Biochemical and Biophysical Research Communications 420 (2012) 217–222

Contents lists available at SciVerse ScienceDirect

Biochemical and Biophysical Research Communications

journal homepage: www.elsevier.com/locate/ybbrc

Calcium–calmodulin signaling induced by epithelial cell differentiation upregulates BRAK/CXCL14 expression via the binding of SP1 to the BRAK promoter region

Takeharu Ikoma [a], Shigeyuki Ozawa [a], Kenji Suzuki [a], Tadanori Kondo [a], Yojiro Maehata [b], Masaichi Chang-il Lee [b], Ryu-Ichiro Hata [c], Eiro Kubota [a,*]

[a] Department of Oral and Maxillofacial Surgery, Kanagawa Dental College, Yokosuka 238-8580, Japan
[b] Department of Clinical Care Medicine Division of Pharmacology, Kanagawa Dental College, Yokosuka 238-8580, Japan
[c] Oral Health Science Research Center, Yokosuka 238-8580, Japan

ARTICLE INFO

Article history:
Received 3 January 2012
Available online 20 February 2012

Keywords:
Chemokine BRAK/CXCL14
Differentiation
Epithelial cell

ABSTRACT

The chemokine BRAK/CXCL14 (BRAK) is expressed in normal squamous epithelium, but is not expressed or is expressed at negligible levels in head and neck squamous cell carcinoma. Malignant cells are known to be dedifferentiated compared with normal epithelial cells, suggesting a role for differentiation cues in the expression of BRAK. Thus, we examined the relationship between BRAK expression and stages of differentiation level in epithelial cells. Immunohistochemical analysis showed that BRAK protein was expressed in cells above the spinous cell layer in normal epithelia. In HSC-3 cells in culture, expression of BRAK mRNA was significantly upregulated by cell contact in a cell density-dependent manner, and mRNA expression of cell differentiation markers such as involucrin, cystatin-A, TGM1, TGM3, and TGM5 was concomitantly augmented. Furthermore, the upregulation of BRAK induced by cell contact was suppressed by chlorpromazine, a specific inhibitor of calmodulin. We previously reported that GC boxes and a TATA-like sequence in the BRAK promoter region are associated with the expression of BRAK. Using a promoter assay and ChIP, we demonstrated that binding of the stimulating protein-1 (SP1) transcription factor to a GC box upstream of the BRAK transcription start site was necessary for cell density-dependent upregulation of BRAK. These results indicated that upregulation of BRAK was accompanied by differentiation of epithelial cells induced by calcium/calmodulin signaling, and that SP1 binding to the BRAK promoter region played an important role in this signaling.

1. Introduction

Stratification of squamous epithelia is maintained by self-renewing cells in the basal layer [1,2]. These cells give rise to epithelial cells, which undergo differentiation as they migrate towards the surface of the epithelium [3]. In epithelial cells, cell–cell contact causes release of calcium ion from the endoplasmic reticulum and promotes cell differentiation through calcium/calmodulin (Ca/CaM) signaling. Differentiation is accompanied by upregulation of epithelial cell differentiation markers, including involucrin and transglutaminase [4]. Differentiation of skin epithelial cells is thus induced by cell–cell contact, enabling formation of the cornified envelope [5,6].

The chemokine BRAK/CXCL14 suppresses oral carcinoma tumor progression [7]. BRAK was first reported to have chemoattractant activity in B cells, monocytes, and dendritic cells [8–10], and it inhibits angiogenesis during tumor growth [11]. Histochemical analysis revealed that head and neck squamous cell carcinoma (HNSCC), derived from oral epithelial cells, expresses BRAK at a very low level, or not at all compared to normal epithelium [12]. Understanding this discrepancy between normal and malignant cells in terms of BRAK mRNA expression is likely to shed light on the role of BRAK in normal epithelial cells.

Recently, we reported that a TATA-like sequence located −65 to −60 bp upstream of the transcription start site in the BRAK gene plays a crucial role in the transcriptional activity of BRAK. In addition, the BRAK promoter region contains 4 GC boxes, 2 of which (located −14 to −9 bp and −10 to −5 bp upstream of the transcription start site) are important for BRAK mRNA expression [13]. Furthermore, we found that BRAK mRNA expression was undetectable in 10 of 18 HNSCC cell lines (56%) [14]. The BRAK promoter was inactivated by methylation in 59% of lung cancer cell lines [15], and targets of methylation in promoters are thought to include GC boxes but not TATA-like sequences. Taken together, these sequences seem to play an important role in the regulation of BRAK mRNA expression.

SP1 is a ubiquitously expressed transcription factor that interacts with GC/GT boxes in the promoter or enhancer regions of many constitutively expressed housekeeping genes and in many

* Corresponding author. Fax: +81 46 822 8888.
E-mail address: kubotaei@kdcnet.ac.jp (E. Kubota).

0006-291X/$ - see front matter © 2012 Elsevier Inc. All rights reserved.
doi:10.1016/j.bbrc.2012.01.157

inducible genes. It may prevent methylation of CpG islands in the genome to keep genes activated, and may participate in remodeling of the chromatin structures. This transcription factor is believed to be especially important in modulation of early developmental genes in undifferentiated cells and in regulation of cell cycle-associated genes [16]. Recently, SP1 protein level and binding activity was also reported to be increased with cell density [17]. This evidence suggests that SP1 is important for BRAK mRNA expression via Ca/CaM signaling induced by cell–cell contact.

In the present study, we examined how BRAK gene expression is influenced by cell–cell contact stimulation in epithelial cells, and elucidated the role of the SP1 transcription factor in BRAK expression.

2. Materials and methods

2.1. Immunohistochemical staining

We used preprocessed head and neck cancer tissues (CB-A219 (II), Cosmobio, Tokyo, Japan), which included normal tissues, for immunohistochemical staining. After deparaffinization and dehydration, the slides were treated with proteinase K (TAKARA BIO, Shiga, Japan) for antigen retrieval, incubated with 0.3% H_2O_2 in absolute methanol for 30 min to block endogenous peroxidase activity, then incubated with Protein Block (DAKO, Glostrup, Denmark) for 10 min at room temperature. The Avidin/Biotin Blocking Kit (Vector Laboratories, Burlingame, CA, USA) was used according to the manufacturer's protocol. Staining was performed using rabbit anti -Cxcl14/BRAK antibody (Abcam, Cambridge, UK) at 1:500 dilution. Rabbit immunoglobulin fraction (DAKO) was used as a negative control. Biotin-conjugated swine anti-rabbit IgG (DAKO) was used as a secondary antibody. The sections were reacted with diaminobenzidine after incubation with avidin-peroxidase.

2.2. Cell culture

Squamous cell line HSC-3, derived from the tongue of a male patient, was provided by the Japanese Collection of Research Bioresources (JCRB) Cell Bank (#JCRB0623). These cells were cultured in Dulbecco's modified Eagle's medium (DMEM, Sigma–Aldrich, St. Louis, MO, USA) containing gentamicin sulfate (50 mg/l) (WAKO Pure Chemical Industries, Osaka, Japan) and Fungizone (250 μg/l) (Invitrogen, Carlsbad, CA, USA) but no serum. This medium is referred to as DMEM-0. Medium supplemented with 10% fetal bovine serum (Thermo Electron, Melbourne, Australia) is called DMEM-10. Cultures were grown at 37 °C in an atmosphere of 95% air and 5% CO_2. Cell numbers were counted with a Coulter Counter (Beckman Coulter, Fullerton, CA, USA) and seeded according cell numbers (0.38, 0.75, 1.5, 3.0, and 6.0×10^5 cells/cm^2) with or without chlorpromazine (WAKO).

2.3. Reverse transcription and real-time quantitative PCR (qPCR) analyses

Total RNA extracted by using TRIzol® Reagent (Invitrogen), was reverse-transcribed with SuperScript First-strand Synthesis System (Invitrogen) and amplified with ExTaq DNA polymerase (TAKARA BIO). For qPCR analysis, we used Brilliant SYBR Green qPCR Master Mix (Stratagene, Cedar Creek, TX, USA). The following primer sets were used: for RT-PCR of BRAK, 5′-AATGAAGCCAAAGTACCCGC-3′ (forward) and 5′-AGTCCTTTGCACAAGTCTCC-3′ (reverse), which yielded a 232-bp product; for β-actin, 5′-AAAGACCTGTACGCCAACAC-3′ (forward) and 5′-CTCGTCATACTCCTGCTTGG-3′ (reverse), which yielded a 224-bp product; for involucrin, 5′-CACTGGCTCCACTTATTTCG-3′ (forward) and 5′-CTCACTCACCTGAGGTTGGGATTG-3′ (reverse), which yielded a 158-bp product; for TGM1, 5′-GATCGCATCACCCTTGAGTTAC-3′ (forward) and 5′-CGCAGGTTCAGATTCTGCC-3′ (reverse), which yielded a 143-bp product; for TGM3, 5′-TGGCAATACTCTGACTATCAGCA-3′ (forward) and 5′-CACATTCAGCCAGGGGTTAAA-3′ (reverse), which yielded a 148-bp product; for TGM5, 5′-ATGGCCCAAGGGCTAGAAGT-3′ (forward) and 5′-AGCTCCGGTTCCTGAAGTACA-3′ (reverse), which yielded a 148-bp product; for cystatin-A, 5′-AACCCGCCACTCCAGAAATC-3′ (forward) and 5′-CACCTGCTCGTACCTTAATGTAG-3′ (reverse), which yielded a 153-bp product. qPCR thermal cycle conditions were as follows: denaturation at 94 °C for 30 s, annealing at 58 °C for 30 s, and extension at 72 °C for 30 s.

2.4. Construction of luciferase reporter gene vectors and BRAK promoter assays

We typically added a trinucleotide for stabilization and a *Kpn*I or an *Xho*I site for cloning to the 5′ end of each primer as follows: 5′-GCGGGTACCCAAAGCAAAAAGAGGAT-3′ (forward) and 5′-GCGCTCGAGCAGGGAAATGGGGAGG-3′ (reverse), which amplified 2000 bp upstream from the transcription start point. For a reverse primer, the anti-codon sequence of the translational start site was mutated to AAT from CAT. The amplified products were then cloned into the pGL4.10 firefly luciferase reporter vector (luc2, Promega, Madison, WI, USA). DNA sequences of the constructs were confirmed by sequencing with a CEQ2000 DNA analysis system and Genome Lab™ DTCS-Quick Start Kit (Beckman Coulter). The empty pGL4.10 firefly luciferase reporter vector was used as a blank, and the sea pansy luciferase vector pGL4.73 (hRluc/SV40, Promega) was used for normalization of transfection efficiency in all experiments. Vectors with a mutated sequence were produced using the Quick Change® II Site-Directed Mutagenesis Kit (Stratagene); sequences were mutated from G to A, A to G, T to C, or C to T. Mutations were verified by DNA sequencing. Cells were transfected using FuGENE® 6 (Roche Diagnostics K.K., Tokyo, Japan) and plated according to cell number (0.38 or 6.0×10^5 cells/cm^2) with or without chlorpromazine after 24 h. Luciferase activities were determined using the Dual-Glo Luciferase Assay System (Promega) according to the manufacturer's protocol.

2.5. Chromatin immunoprecipitation assay

Cells were plated (0.38 or 6.0×10^5 cells/cm^2) with or without chlorpromazine. After 24 h of incubation, we performed chromatin immunoprecipitation (ChIP) assays using the MAGnify™ Chromatin Immunoprecipitation System according to the manufacturer's protocol. Primers used were as follows: for PCR amplification of BRAK promoter region, 5′-TCCCCTCACCACATTGAG-3′ (forward) and 5′-CGCTCTCTCCACAGCATCC-3′ (reverse), yielding a 125-bp product. PCR products were analyzed by agarose gel electrophoresis and 0.01% ethidium bromide staining for 20 min. Anti-SP1 antibody (Abcam) was used in this assay.

2.6. Statistical analysis

Student's *t*-test was used for comparisons between 2 groups, with $P < 0.001$ being considered statistically significant. Relationships between mRNA expression and cell density were analyzed through correlation, and $R > 0.9$ was considered a significant correlation.

3. Results

3.1. Localization of BRAK in squamous epithelial tissue

Epithelial cells are immature in the basal layer and differentiate during migration toward the upper layer. Involucrin, cystatin-A,

TGM1, TGM3, and TGM5, known as differentiation markers for epithelial cells, are expressed in the spinous and granular layers but not in the basal layer. We examined localization of BRAK protein in squamous epithelia using immunohistochemistry to determine the relationship between the expression of BRAK and the differentiation state of epithelial cells. Whereas control specimens were unstained by anti-Cxcl14/BRAK antibody as shown in Fig. 1A, BRAK protein was detected in the spinous and granular layers but not in the basal layer (Fig. 1B).

3.2. Regulation of BRAK mRNA expression by cell density

Cell–cell contact is known to induce differentiation of epithelial cells. We determined whether cell–cell contact induced the expression of BRAK mRNA in HSC-3 cells, a model for immature epithelial cells. HSC-3 cells were plated at specific densities (0.38, 0.75, 1.5, 3.0, and 6.0×10^5 cells/cm^2) for 24 h (Fig. 2A). Cell–cell contact was confirmed in cultures at densities over 1.5×10^5 cells/cm^2 at 24 h. After 24 h, expression of BRAK mRNA was dramatically upregulated in a cell density-dependent manner (Fig. 2B), and expression of the differentiation markers involucrin, cystatin-A, TGM1, TGM3, and TGM5 increased in parallel with BRAK (Fig. 2C–G).

3.3. Regulation of BRAK mRNA expression through Ca/CaM signaling in a cell density-dependent manner

Because cell–cell contact induces calcium release from endoplasmic reticulum, we investigated whether chlorpromazine inhibits cell density-dependent upregulation of BRAK mRNA expression. As previously described, expression of BRAK mRNA was upregulated with an increase in cell density. This upregulation was suppressed by chlorpromazine treatment (Fig. 3A); a similar effect of chlorpromazine was observed for the various differentiation markers (Fig. 3B–F).

3.4. Analysis of BRAK promoter activity induced by cell contact

Previously, we reported that GC boxes play a crucial role in the BRAK promoter [13]. Therefore, we asked whether these promoter elements are associated with the upregulation of BRAK mRNA expression by increased cell density. BRAK promoter activity was upregulated 9-fold by cell density stimulation. In contrast, upregulation of BRAK promoter activity by cell density stimulation was suppressed in a mutated vector lacking the tandem GC boxes −14 to −5 bp upstream of the transcription start site (Fig. 4A). Furthermore, chlorpromazine suppressed the upregulation of BRAK promoter activity induced by cell density stimulation (Fig. 4B). Because SP1 was reported to be activated in a cell density-dependent manner [17], we examined the binding activity of SP1 to BRAK promoter region using a ChIP assay. The binding activity of SP1 to the BRAK promoter region was upregulated 9-fold by cell density stimulation. Furthermore, the upregulation of this binding activity was suppressed by chlorpromazine (Fig. 4C and D).

4. Discussion

BRAK is a chemokine that is expressed in many normal cells and tissues but is absent from or is expressed at very low levels in transformed cells and cancerous tissues, including HNSCC [12]. A better understanding of the regulation of BRAK gene expression might thus be very important to understand the function of this chemokine in tumor progression as well as in other physiological and pathological processes [8,12,18,19].

We hypothesized that BRAK expression is altered in association with differentiation of epithelial cells. In immunohistochemical analysis of normal epithelium, we found that BRAK protein was detected in the spinous and granular layers, but not in the basal layer of the epithelium, which is the least differentiated layer. These data suggested that BRAK is expressed concomitantly with differentiation of epithelial cells. Using an in vitro model system, we first confirmed that augmentation of BRAK mRNA expression synchronized with the expression of various differentiation markers of normal epithelial cells. BRAK expression was further upregulated as cell density increased. This suggests that the frequency of cell–cell contact affects the transcriptional level of the BRAK gene. We also found that cell adhesion stimuli induced the Ca/CaM signaling pathway, initiating binding of the transcription factor SP1 to the BRAK promoter region.

The widely used in vitro keratinocyte differentiation model employs keratinocytes in a low-Ca^{2+} solution. These cells morphologically resemble basal cells of squamous epithelia, and keratinocytes incubated in high-Ca^{2+} solution differentiate morphologically and express various differentiation markers [4]. It was reported that cell–cell contact may induce differentiation of epithelial cells via release of calcium from the endoplasmic reticulum, and adequate concentration of extracellular calcium is necessary for the differentiation of epithelial cells. Ca^{2+} concentrations above 1.2 mM were reported to be sufficient to induce differentiation of epithelial cells [20]. Concentration of Ca^{2+} in our experiments was set to 1.8 mM, which was sufficient for epithelial cell differentiation. In our current experiments, BRAK was significantly upregulated at a cell density ranging from 1.5 to 6.0×10^5 cells/cm^2, where cell–cell contact could be easily established.

It was reported that cell–cell contact initiates formation of a molecular complex consisting of E-cadherin, p120-catenin, and β-catenin at the plasma membrane [21]. Subsequent events include induction of phospholipase C2 and phosphoinositide metabolism, followed by increase in inositol 1,4,5-triphosphate level, after formation of the complex triggers release of calcium from the endoplasmic reticulum [21]. This leads to activation of calcium-sensitive

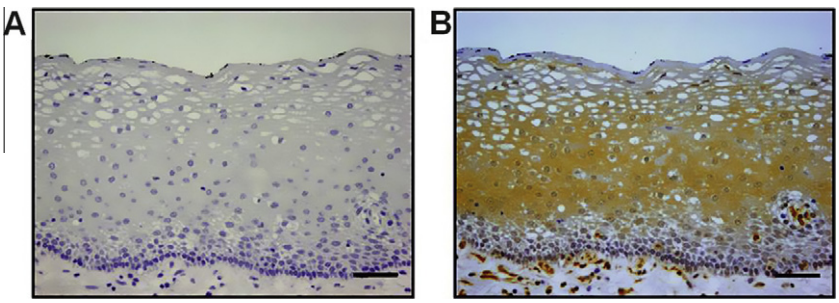

Fig. 1. Immunohistochemical localization of BRAK in normal gingival tissues. Staining is shown with rabbit immunoglobulin fraction as the negative control (A), and with rabbit anti-Cxcl14/BRAK antibody at 1:500 (B). Scale bar = 200 μm.

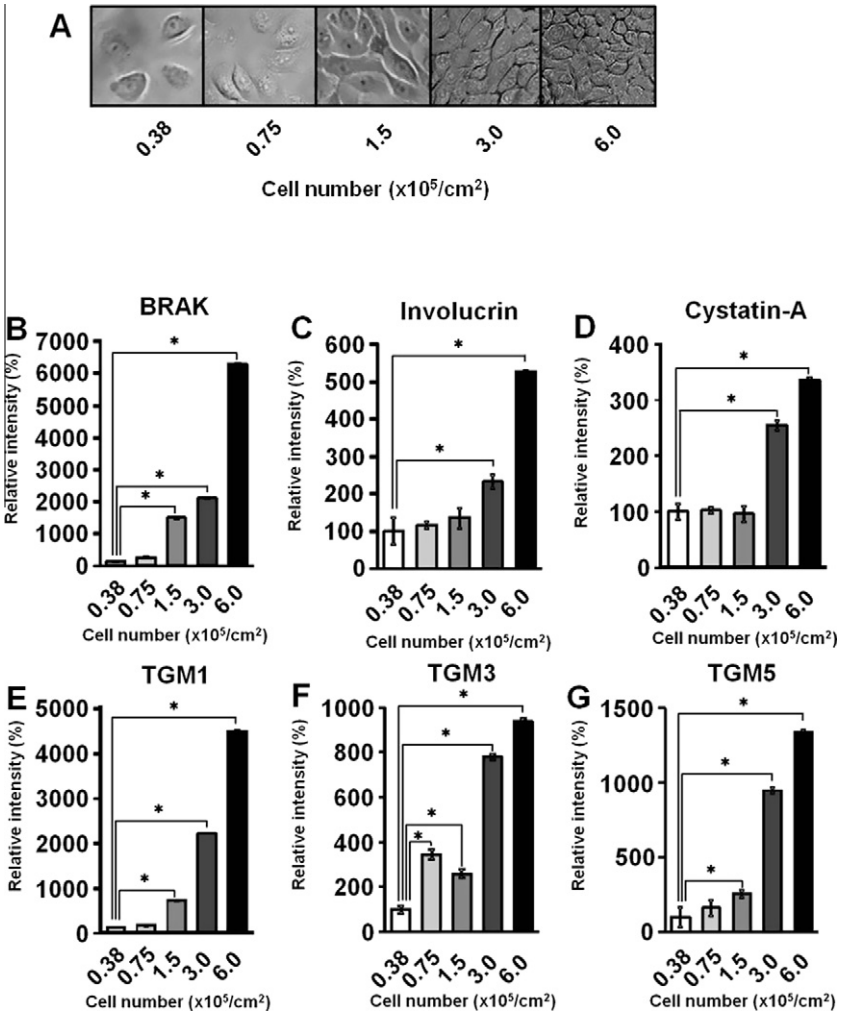

Fig. 2. Cell density-dependent BRAK mRNA expression. (A) HSC-3 cells cultured in DMEM-10 at different densities (0.38, 0.75, 1.5, 3.0, and 6.0 × 10^5 cells/cm^2) for 24 h. Total RNA was extracted and mRNA level for (B) BRAK, (C) involucrin, (D) cystatin-A, (E) TGM1, (F) TGM3, and (G) TGM5 were determined by real-time quantitative PCR. Relative intensity normalized to β-actin. $^*P < 0.001$ (Student's *t*-test); values are presented as mean ± SD ($n = 3$). Relationship between BRAK mRNA expression and cell density was indicated by correlation coefficients, and $R > 0.9$ was considered a significant correlation. Expression levels and cell density were significantly correlated for all genes analyzed, with *R* values of 0.987 (BRAK), 0.985 (involucrin), 0.976 (cystatin-A), 0.997 (TGM1), 0.924 (TGM3), and 0.969 (TGM5).

kinases such as protein kinase C, which in turn phosphorylate proteins that activate a series of signaling events triggering cellular responses. The released calcium binds to calmodulin, and this cell activation step upregulates mRNA expression of keratinocyte differentiation markers including involucrin, cystatin-A, and TGM in epithelial cells. We also found that this Ca/CaM signaling pathway is associated with the upregulation of BRAK mRNA in a cell density-dependent manner. Chlorpromazine, a calmodulin antagonist, suppressed this cell density-dependent augmentation of BRAK mRNA expression. Thus, cell–cell adhesion signaling might trigger Ca^{2+} influx into the cytoplasm or release of Ca^{2+} from the endoplasmic reticulum to further induce transcription of the BRAK gene in epithelial cells.

Chemokine expression is regulated through inducible transcription factors such as NF-kB and activator protein (AP-1) [22–24]. The promoters that control chemokine expression may differ depending on cell type or on the various stimuli that influence target cells. It was reported that BRAK is overexpressed in breast [25] and prostate [26] cancers but not in lung [15] and oral cancers [8,12,18]. In most cancer cells, the BRAK promoter region is amenable to methylation, and this epigenetic change reduces BRAK expression and influences tumor cell growth in vivo. Although several cytokine promoters have a common NF-kB-binding site, each individual promoter also binds to other transactivators as well as repressors that interact with NF-kB to direct transcription. The binding sites for the transcription factors AP-1 and nuclear factor activated by interleukin 6, for example, are present in the promoters for CXCL8, IL-6, and CCL5 genes, where positive cooperation between these transcription factors and NF-kB enhances transcription [22–24].

The transcription factor AP-1 binds to DNA sequences located −87 to −81 bp upstream of the BRAK transcriptional start site [13]. AP-1 augmented BRAK mRNA expression in breast cancer [27]. We previously reported that BRAK mRNA expression was not detected in 10 of 18 HNSCC cell lines (56%) [14]. In this context, it is noteworthy that the BRAK promoter was inactivated by methylation in lung cancer [15]. This kind of aberrant DNA methylation has been established as one of the major mechanisms by which tumor suppressor genes are silenced in cancer. In the present experiments, we showed that GC boxes, known as targets of methyltransferase, play a crucial role in cell density-induced upregulation of BRAK mRNA expression. The BRAK promoter region contains 4 GC boxes, 2 of which regulate BRAK mRNA expression [13].

Another transcription factor known for the effects on cytokine gene expression is SP1 [17]. Here we show that SP1, a transcription

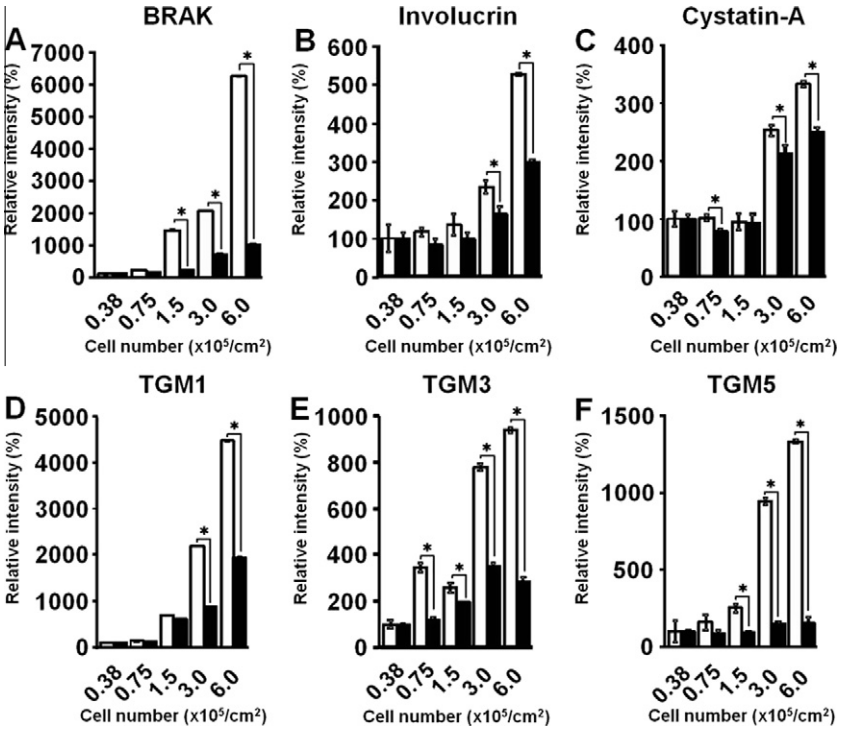

Fig. 3. mRNA levels in HSC-3 cells at various densities (0.38, 0.75, 1.5, 3.0, and 6.0×10^5 cells/cm^2) in the presence (closed column) or absence (open column) of chlorpromazine (10 nM). Total RNA was extracted 24 h after addition of chlorpromazine, and mRNA levels for (B) BRAK, (C) involucrin, (D) cystatin-A, (E) TGM1, (F) TGM3, and (G) TGM5 were determined by qPCR. Relative intensity normalized to β-actin. $^*P < 0.001$ (Student's *t*-test); values are presented as the mean ± SD ($n = 3$). Expression levels and cell density were significantly correlated for all genes analyzed, with *R* values of 0.987 (BRAK), 0.985 (involucrin), 0.976 (cystatin-A), 0.997 (TGM1), 0.924 (TGM3), and 0.969 (TGM5).

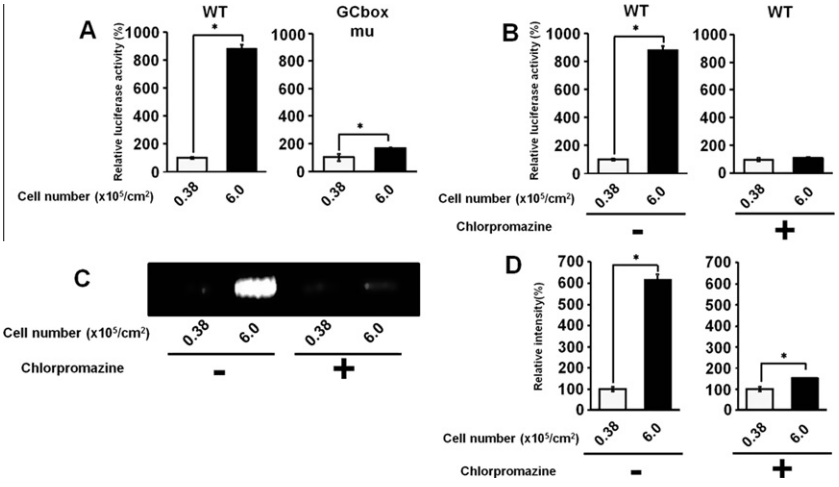

Fig. 4. Upregulation of BRAK promoter activity by binding SP1 to the promoter region. (A and B) Relative promoter activity of reporter gene constructs containing the 5′ region of the human BRAK/CXCL14. Cells at 2 densities (0.38 and 6.0×10^5 cells/cm^2) were transfected with the BRAK promoter vector and incubated with or without chlorpromazine after 24 h. Cells transfected with the wild-type (WT) promoter vector showed 9 times higher promoter activity with increasing cell density. The GC box-mutated BRAK promoter did not show augmented promoter activity (A), and chlorpromazine (10 nM) treatment of cells expressing the WT BRAK promoter inhibits promoter activity (B). (C and D) SP1 binding to the BRAK promoter, analyzed by ChIP. Cells were plated as above and incubated with or without chlorpromazine for 24 h. PCR products were visualized by ethidium bromide staining after agarose gel electrophoresis (C). Relative SP1 binding level was quantified by Image Quant 5.0 (D).

factor that interacts with GC/GT boxes in the promoter or enhancer regions of many housekeeping and inducible genes, binds to the BRAK promoter region when Ca/CaM signaling was induced by cell–cell contact in epithelial cells. The HSC-3 neoplastic cell line used in this experiment constitutively expressed BRAK mRNA, establishing the line as an appropriate model for normal epithelial cells in terms of transcriptional regulation of BRAK gene. Such transcriptional regulation may differ between cell types. Recently, the mitogen-activated protein kinase p38, which exists in 4 isoforms, p38α, p38β, p38γ, and p38δ, was reported to influence the differentiation of keratinocytes [28]. We found that BRAK expression induced by ultraviolet (UV) stress was specifically upregulated by p38δ in HSC-3 cells [29]. This may indicate that BRAK expression in epithelial cells is differentially controlled even by the type of stimuli. Induced BRAK expression in epithelial cells after UV irradiation may contribute to recovery from UV damage.

We have shown that BRAK gene transcription occurred concomitantly with the differentiation of squamous epithelial cells via the

Ca/CaM signaling pathway. Furthermore, we confirmed that SP1 binding to the BRAK promoter region upregulated BRAK expression. Thus, the differential activation of inducible transcription factors and their accessibility to the BRAK promoter may explain the cell type-specific and stimulus-specific expression of BRAK, and these results may further clarify BRAK function in normal epithelial cells.

Acknowledgments

This research was supported by the Grants-in-Aid for Scientific Research from the Ministry of Education, Culture, Sports, Science, and Technology of Japan [21792037 to Shigeyuki Ozawa and 21390543 to Eiro Kubota].

References

[1] S. Papini, D. Cecchetti, D. Campani, Fitzgerald W, Grivel JC, Chen S, Margolis L, Revoltella RP, Isolation and clonal analysis of human epidermal keratinocyte stem cells in long-term culture, Stem Cells 21 (2003) pp. 481–494.
[2] S. Ro, B. Rannala, Evidence from the stop-EGFP mouse supports a niche-sharing model of epidermal proliferative units, Exp. Dermatol. 14 (2005) 838–843.
[3] L. Alonso, E. Fuchs, Stem cells of the skin epithelium, Proc. Natl. Acad. Sci. USA 30 (Suppl. 1) (2003) pp. 11830–11835.
[4] S. Pillai, D.D. Bikle, M.L. Mancianti, P. Cline, M. Hincenbergs, Calcium regulation of growth and differentiation of normal human keratinocytes: modulation of differentiation competence by stages of growth and extracellular calcium, J. Cell. Physiol. 143 (1990) 294–302.
[5] J.L. Charest, J.M. Jennings, W.P. King, A.P. Kowalczyk, A.J. García, Cadherin-mediated cell–cell contact regulates keratinocyte differentiation, J. Invest. Dermatol. 129 (2009) 564–572.
[6] A.C. Steven, P.M. Steinert, Protein composition of cornified cell envelopes of epidermal keratinocytes, J. Cell Sci. 107 (1994) 693–700.
[7] S. Ozawa, Y. Kato, R. Komori, Y. Maehata, E. Kubota, R. Hata, BRAK/CXCL14 expression suppresses tumor growth in vivo in human oral carcinoma cells, Biochem. Biophys. Res. Commun. 348 (2006) 406–412.
[8] T.D. Shellenberger, M. Wang, M. Gujrati, A. Jayakumar, R.M. Strieter, M.D. Burdick, C.G. Ioannides, C.L. Efferson, A.K. El-Naggar, D. Roberts, G.L. Clayman, M.J. Frederick, BRAK/CXCL14 is a potent inhibitor of angiogenesis and a chemotactic factor for immature dendritic cells, Cancer Res. 64 (2004) 8262–8270.
[9] M.A. Sleeman, J.K. Fraser, J.G. Murison, S.L. Kelly, R.L. Prestidge, D.J. Palmer, J.D. Watson, K.D. Kumble, B cell- and monocyte-activating chemokine (BMAC), a novel non-ELR alpha-chemokine, Int. Immunol. 12 (2000) 677–689.
[10] G.V. Shurin, R.L. Ferris, I.L. Tourkova, L. Perez, A. Lokshin, L. Balkir, B. Collins, G.S. Chatta, M.R. Shurin, Loss of new chemokine CXCL14 in tumor tissue is associated with low infiltration by dendritic cells (DC), while restoration of human CXCL14 expression in tumor cells causes attraction of DC both in vitro and in vivo, J. Immunol. 174 (2005) 5490–5498.
[11] K. Izukuri, K. Suzuki, N. Yajima, S. Ozawa, S. Ito, E. Kubota, R. Hata, Chemokine CXCL14/BRAK transgenic mice suppress growth of carcinoma cell transplants, Transgenic Res. 19 (2010) 1109–1117.
[12] M.J. Frederick, Y. Henderson, X. Xu, M.T. Deavers, A.A. Sahin, H. Wu, D.E. Lewis, A.K. El-Naggar, G.L. Clayman, In vivo expression of the novel CXC chemokine BRAK in normal and cancerous human tissue, Am. J. Pathol. 156 (2000) 1937–1950.
[13] R. Komori, S. Ozawa, Y. Kato, H. Shinji, S. Kimoto, R. Hata, Functional characterization of proximal promoter of gene for human BRAK/CXCL14, a tumor-suppressing chemokine, Biomed. Res. 31 (2010) 123–131.
[14] S. Ozawa, Y. Kato, S. Ito, R. Komori, N. Shiiki, K. Tsukinoki, S. Ozono, Y. Maehata, T. Taguchi, Y. Imagawa-Ishiguro, M. Tsukuda, E. Kubota, R. Hata, Restoration of BRAK/CXCL14 gene expression by gefitinib is associated with antitumor efficacy of the drug in head and neck squamous cell carcinoma, Cancer Sci. 100 (2009) 2202–2209.
[15] M. Tessema, D.M. Klinge, C.M. Yingling, K. Do, L. Van Neste, S.A. Belinsky, Re-expression of CXCL14, a common target for epigenetic silencing in lung cancer, induces tumor necrosis, Oncogenesis 29 (2010) 5159–5170.
[16] B.Y. Park, C.S. Hong, F.A. Sohail, J.P. Saint-Jeannet, Developmental expression and regulation of the chemokine CXCL14 in *Xenopus*, Int. J. Dev. Biol. 53 (2009) 535–540.
[17] E.L. Cheng, Y. Li, J. Sugar, B.Y. Yue, Cell density regulated expression of transcription factor Sp1 in corneal stromal cultures, Exp. Eye Res. 73 (2001) 17–24.
[18] C.M. McKinnon, K.A. Lygoe, L. Skelton, R. Mitter, H. Mellor, The atypical Rho GTPase RhoBTB2 is required for expression of the chemokine CXCL14 in normal and cancerous epithelial cells, Oncogenesis 27 (2008) 6856–6865.
[19] R. Hromas, H.E. Broxmeyer, C. Kim, H. Nakshatri, K. Christopherson 2nd, A. Azam, Y.H. Hou, Cloning of BRAK, a novel divergent CXC chemokine preferentially expressed in normal versus malignant cells, Biochem. Biophys. Res. Commun. 255 (1999) 703–706.
[20] C.L. Tu, W. Chang, D.D. Bikle, The role of the calcium sensing receptor in regulating intracellular calcium handling in human epidermal keratinocytes, J. Invest. Dermatol. 127 (2007) 1074–1083.
[21] Z. Xie, D.D. Bikle, The recruitment of phosphatidylinositol 3-kinase to the E-cadherin–catenin complex at the plasma membrane is required for calcium-induced phospholipase C-gamma1 activation and human keratinocyte differentiation, J. Biol. Chem. 282 (2007) 8695–8703.
[22] J.S. Wolf, Z. Chen, G. Dong, J.B. Sunwoo, C.C. Bancroft, D.E. Capo, N.T. Yeh, N. Mukaida, C. Van Waes, IL (interleukin)-1alpha promotes nuclear factor-kappaB and AP-1-induced IL-8 expression, cell survival, and proliferation in head and neck squamous cell carcinomas, Clin. Cancer Res. 7 (2001) pp. 1812–1820.
[23] P. Roux, C. Alfieri, M. Hrimech, E.A. Cohen, J.E. Tanner, Activation of transcription factors NF-kappaB and NF-IL-6 by human immunodeficiency virus type 1 protein R (Vpr) induces interleukin-8 expression, J. Virol. 74 (2000) 4658–4665.
[24] J.G. Mastronarde, B. He, M.M. Monick, N. Mukaida, K. Matsushima, G.W. Hunninghake, Induction of interleukin (IL)-8 gene expression by respiratory syncytial virus involves activation of nuclear factor (NF)-kappa B and NF-IL-6, J. Infect. Dis. 174 (1996) 262–267.
[25] M. Allinen, R. Beroukhim, L. Cai, C. Brennan, J. Lahti-Domenici, H. Huang, D. Porter, M. Hu, L. Chin, A. Richardson, S. Schnitt, W.R. Sellers, K. Polyak, Molecular characterization of the tumor microenvironment in breast cancer, Cancer Cell 6 (2004) 17–32.
[26] S.R. Schwarze, J. Luo, W.B. Isaacs, D.F. Jarrard, Modulation of CXCL14 (BRAK) expression in prostate cancer, Prostate 64 (2005) 67–74.
[27] H. Pelicano, W. Lu, Y. Zhou, W. Zhang, Z. Chen, Y. Hu, P. Huang, Mitochondrial dysfunction and reactive oxygen species imbalance promote breast cancer cell motility through a CXCL14-mediated mechanism, Cancer Res. 69 (2009) 2375–2383.
[28] R.L. Eckert, J.F. Crish, T. Efimova, S.R. Dashti, A. Deucher, F. Bone, G. Adhikary, G. Huang, R. Gopalakrishnan, S. Balasubramanian, Regulation of involucrin gene expression, J. Invest. Dermatol. 123 (2004) 13–22.
[29] S. Ozawa, S. Ito, Y. Kato, E. Kubota, R. Hata, Human p38 delta MAP kinase mediates UV irradiation induced up-regulation of the gene expression of chemokine BRAK/CXCL14, Biochem. Biophys. Res. Commun. 396 (2010) 1060–1064.

Biochemical and Biophysical Research Communications 420 (2012) 223–229

Contents lists available at SciVerse ScienceDirect

Biochemical and Biophysical Research Communications

journal homepage: www.elsevier.com/locate/ybbrc

Requirement of protein L-isoaspartyl *O*-methyltransferase for transcriptional activation of trefoil factor 1 (TFF1) gene by estrogen receptor alpha

Jong Woo Park [a,1], Jae Cheol Lee [a,1], Shin Won Ha [a], So Young Bang [a], Eun Kyung Park [a], Sang Ah Yi [a], Min Gyu Lee [a], Dae Sung Kim [a], Ki Hong Nam [a], Ji Hee Yoo [a], So Hee Kwon [b,*], Jeung-Whan Han [a,*]

[a] *Research Center for Epigenome Regulation, School of Pharmacy, Sungkyunkwan University, Republic of Korea*
[b] *College of Pharmacy, Yonsei Institute of Pharmaceutical Sciences, Yonsei University, Republic of Korea*

ARTICLE INFO

Article history:
Received 9 February 2012
Available online 20 February 2012

Keywords:
PIMT
Protein methylation
Co-activator
Transcriptional regulation

ABSTRACT

Lysine- and arginine-specific methyltransferases have been shown to act as either direct or secondary transcriptional co-activator of the estrogen receptor (ERα). However, little is known about the role of protein L-isoaspartyl *O*-methyltransferase (PIMT) on transcriptional regulation. Here, we show that PIMT acts as a co-activator for ERα-mediated transcription. Activation of the estrogen response element (ERE) promoter by β-estradiol (E_2) was suppressed by knockdown of PIMT, and enhanced by overexpression of wild-type PIMT. However, the ERE promoter activity was resistant to E_2 stimulation in cells overexpressing a catalytically inactive PIMT mutant, G88A. Consistent with these results, the expression of the endogenous ERα response gene trefoil factor 1 (TFF1) by E_2 was completely abrogated by PIMT depletion and decreased to approximately 50% when PIMT mutant G88A was expressed. In addition, over-expression of PIMT significantly increased the levels of TFF1 mRNA in the presence or absence of E_2. Interestingly, PIMT interacted with ERα and was distributed to the cytosol and the nucleus. The chromatin immunoprecipitation analysis revealed that PIMT was recruited to the promoter of TFF1 gene together with ERα in an E_2-dependent manner, which was accompanied by uploading of RNA polymerase II on the promoter. Taken together, the results suggest that PIMT may act as a co-activator in ERα-mediated transcription through its recruitment to the promoter via interacting with ERα.

1. Introduction

Nuclear receptors (NRs) play an important role in endocrine processes, differentiation, and responses to extracellular stimuli through regulating the expression of specific target genes, and constitute a large superfamily of DNA binding transcriptional regulators [1–3]. The majority of NRs share common functional domains. The DNA binding domain maps near the central portion of the polypeptide chain and has a repeat of the C4 zinc-finger motif. The hormone binding domain, located at the *C*-terminal end, contains a hormone-dependent activation domain. In addition, all the NRs have a unique *N*-terminal region of variable length that contains a constitutively active trans-activation region (AF-1) and several autonomous trans-activation domains [4].

Hormone-dependent activation of transcription, which is mediated by NRs, is a complex, multistep process [5]. Once NRs bind to specific enhancer elements in the promoter region, NRs activate the gene by recruiting the transcriptional initiation complex to the promoter and by inducing local remodeling of chromatin. The NRs bound to specific enhancer elements recruit co-activators of the p160 family (SRC-1, GRIP1, ACTR) [5]. These co-activators recruit secondary co-activators including histone acetylases (p300, CBP) and arginine-specific protein methyltransferases (CARM1, PRMT1) which modulates chromatin remodeling through histone modification [6,7]. In the presence of a p160 co-activator, for example, CARM1 and p300 function together to yield a higher level of activation than can be achieved by factor alone. The same is true for CARM1 and PRMT1 [8]. The acetylation of multiple lysine residues within the core histones by p300 may act cooperatively with the methylation of specific arginine residues in H3 by CARM1 [6]. Such cooperation appears to be the case for PRMT1. Recent study shows that menin, an integral component of MLL1/MLL2 histone methyltransferase complexes specific for Lys-4 of histone H3 (H3K4), is a transcriptional co-activator of the NR for estrogen and vitamin D [9]. In addition, G9a acts as repressor for specific transcription factors through inducing methylation of Lys-9 of histone H3. Also, G9a functions as a co-activator for NRs, cooperating synergistically with NR co-activators GRIP1, CARM1, and p300 [10], suggesting an important role of arginine- and lysine-specific methyltransferases in transcriptional regulation by NRs.

* Corresponding authors. Fax: +82 32 749 4105 (S.H. Kwon), +82 31 290 7796 (J.-W. Han).
E-mail addresses: soheekwon@yonsei.ac.kr (S.H. Kwon), jhhan551@skku.edu (J.-W. Han).
[1] These authors contributed equally to this work.

0006-291X/$ - see front matter © 2012 Elsevier Inc. All rights reserved.
doi:10.1016/j.bbrc.2012.02.072

Besides arginine- and lysine-specific methyltransferases, protein-carboxyl-*O*-methyltransferasemethylates the free carboxyl groups of glutamyl or aspartyl residues. Protein L-isoaspartyl *O*-methyltransferase (PIMT), a subclass of protein-carboxyl-*O*-methyltransferase, catalyzes the methylation of L-isoaspartyl, and to a lesser extent D-aspartyl residues that arise from the spontaneous deamidation and isomerization of protein asparaginyl and aspartyl residues [11]. Methylation of isoaspartate containing peptides and various proteins *in vitro* initiates conversion of the atypical β-linkage to a normal α-linkage, suggesting that PIMT may serve as a repair function *in vivo* [12,13]. Interestingly, recent studies have shown that histone H2B is a major endogenous substrate for PIMT in the nucleus of cultured rat PC12 cells and PIMT knockout mouse cells [13,14]. In chicken nucleosomes, isoaspartate accumulates mainly in histone H2A and can be methylated by PIMT [15]. Thus, the observation that methylation of isoaspartate occurs in histone H2A and H2B raises the possibility that PIMT plays an important role in transcriptional regulation.

In this study, we report the first evidence that PIMT can act as a co-activator for ERα-mediated transcription. We also find that PIMT is recruited into the promoter region of the estrogen-regulated trefoil factor 1 (TFF1) gene in an E_2 (β-estradiol)-dependent manner and its activity is essential for transcriptional activation of the TFF1 gene. These results provide a molecular mechanism for E_2-dependent transcriptional regulation by PIMT.

2. Materials and methods

2.1. Plasmids and mutagenesis

For the expression of recombinant human PIMT in *Escherichia coli* and mammalian cell lines, PIMT cDNA was PCR-amplified from the pool of MCF7 cDNA using a 5′ primer (5′-ccgGAATTCcgcctg-gaaatccggcggc) and a 3′ primer (5′- ccgCTCGAGcttccacctggac-cactgct), which included EcoRI and XhoI sites at the 5′ and 3′ ends, respectively. The amplified gene, after digestion with EcoRI and XhoI, was inserted into the same sites of pGEX-4T-3 (GE Healthcare Life Sciences) and PCMV-Flag (BD biosciences) plasmids. All mutations were confirmed by DNA sequencing. The ER mammalian expression vector for ER was the pHE0 plasmid encoding human ERα. The luciferase-expressing reporter gene construct was MMTV-ERE-Luc [16]. Mutagenesis was performed by PCR with pGEX-4T-3-PIMT and PCMV-Flag-PIMT as a template. The site chosen was within motif I (PDVGSGSGILY), one of the three conserved motifs of protein methyltransferases and *S*-adenosyl-L-methionine binding sites reported [17].

2.2. Luciferase reporter gene assay

293T cells were plated at 1×10^5 cells/well in 12-well plates and transiently transfected with plasmids using Lipofectamine 2000 (Invitrogen). After 24 h of transfection, cells were incubated for an additional 24 h in phenol red-free 5% FBS-DMEM treated with dextran-coated charcoal (Gemini Bioproducts), 20 mM Na-HEPES (pH 7.2), penicillin and streptomycin, with or without 50 nM E_2. The luciferase activity of cell lysates was measured using the Firefly Luciferase® Reporter Assay System according to the manufacturer's instructions (Promega). The results from five independent experiments are presented as the relative luciferase unit per milligram protein (mean ± standard deviation).

2.3. RNA extraction and RT-PCR

Total RNA was extracted using the easy-BLUE™ total RNA extraction kit (iNtRON Biotechnology). RNA integrity was checked by agarose gel electrophoresis and ethidium bromide staining. The primers used in RT-PCR reactions were as follows: TFF1, 5′-AAAG AATTAGCTTAGGCCTAGACG-3′ (forward) and 5′-GGATTTGCTGATA GACAG- AGACGA-3′ (reverse); GAPDH, 5′-TGATGACATCAAG AAGGTGGTGAAG-3′ (forward) and 5′-TCCTTGGAGGCCATGTAG GC-CAT-3′ (reverse). PCR products were analyzed by 1.5% agarose gel electrophoresis.

2.4. Chromatin immunoprecipitation (ChIP) assay

MCF7 cells were grown in phenol red-free 5% FBS-DMEM treated with dextran-coated charcoal in 150 mm dishes for 3 days, and then treated with or without 50 nM E_2 for 30 min. The cross-linked, sheared chromatin was used for immunoprecipitation with anti-PIMT, anti-ERα, anti-Pol II, or rabbit/mouse normal IgG, and protein A agarose with rotation at overnight at 4 °C. Immunoprecipitated DNA was purified by phenol-chloroform extraction, precipitated by ethanol, and resuspended in 20 μl of TE buffer. PCR amplifications were performed with 0.01–5 μl DNA using 30–35 cycles. The following primers were used: TFF1 (−353/−31), 5′-GGCCATCTCTCACTATGAATCACTTCTGC-3′ (forward) and 5′-GGCAGGCTCTGTTTGCTTAAAGAGCG-3′ (reverse), PCR products were run on 1.8% agarose gels and analyzed by ethidium bromide staining.

2.5. RNA interference

Stealth™RNAi (Invitrogen) oligonucleotides for PIMT were designed to target PIMT mRNA, and annealed as follows: siPIMT, 5′-AACAUGCAGUAAG- GAUUCCACUUCC-3′ (sense) and 5′-GGAAGUGGAAUCCUUACUGCAUGUU-3′ (antisense); scrambled siRNA (negative control siRNA duplexes, 12935-300, Invitrogen). For transfection of siRNA, MCF7 cells were plated into 6-well plates, grown until reaching 70–80% confluence, and transfected with 40 or 80 pmole of siRNA duplex using Lipofectamine 2000 (Invitrogen) following the manufacturer's instructions.

2.6. Immunoprecipitationand western blot

Cell lysates were cleared with protein A beads (Santa Cruz Biotechnology) for 1 h at 4 °C. 1 μg anti-PIMT (BD biosciences), anti-ERα (Santa Cruz Biotechnology) or normal rabbit/mouse IgG (Santa Cruz Biotechnology) was added to the cell lysates and incubated at overnight at 4 °C on a rotator. 30 μl protein A beads were added and incubated for another 3 h. Beads were washed three times with PBS and subjected to SDS-PAGE. Blots were probed with anti-PIMT (BD biosciences) or anti-ERα (Santa Cruz Biotechnology) at 1 μg/20 ml blocking buffer (5% non-fat milk in TBS-T: 150 mM NaCl, 10 mM Tris–HCl, pH 8.0%, and 0.1% Tween-20). HRP-conjugated secondary antibodies (Santa Cruz Biotechnology) were used at 1 μg/10 ml blocking buffer and ECL reagents (Amersham Biosciences) were used for detection.

2.7. Cytosolic and nuclear extract preparation

The cells were washed with cold 1x phosphate-buffered saline (PBS, pH 7.2) and suspended in 500 μl of Buffer A (10 mM HEPES (pH 7.9) containing 1.5 mM $MgCl_2$, 10 mM KCl, 1 mM EDTA, 1 mMdithiothreitol, 0.5 μg/ml leupeptin, 1 mM phenylmethylsulfonylfluoride (PMSF), 1 μM pepstatin A, and 0.05% Nonidet P-40) and left on ice for 10 min. The nuclei were separated from the cytosolic fraction by centrifuge at 4 °C at 3000 rpm for 10 min. The nuclear pellet was resuspended and sonicated in 400 μl of Buffer B (20 mM HEPES (pH 7.9) containing 1.5 mM $MgCl_2$, 420 mMKCl, 25% glycerol, 0.2 mM EDTA, 1 mMdithiothreitol, 0.5 μg/ml leupeptin, 1 mM PMSF, and 1 μM pepstatin A), and left on ice for 30 min. Nuclear extracts were separated by centrifugation at 4 °C at 15,000 rpm for 20 min.

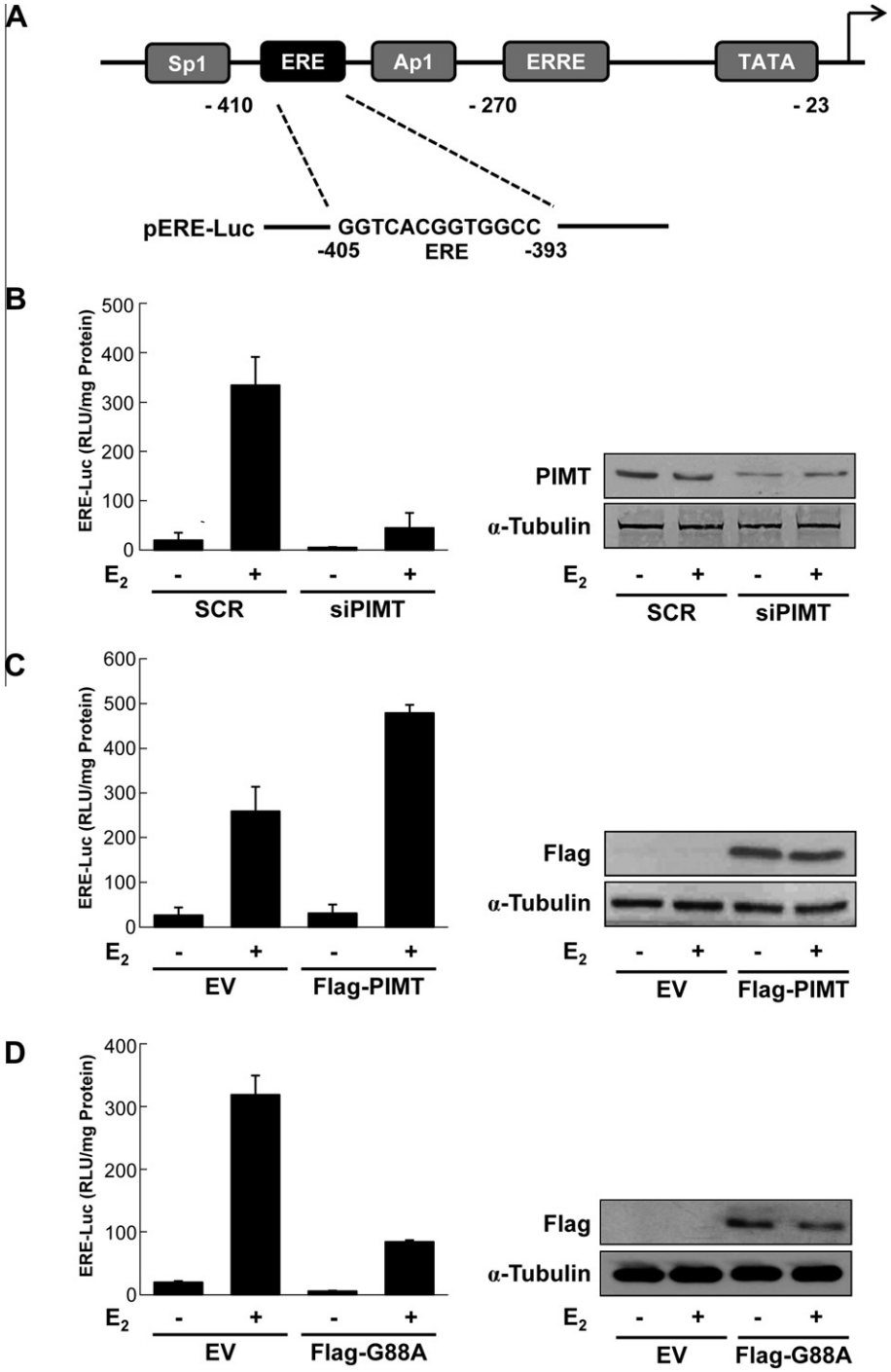

Fig. 1. Co-activator function of PIMT in ERα-dependent transcription, (A) Description of the TFF1 5′-flanking proximal promoter region and the luciferase reporter plasmids containing ERE-promoter. (B) 293T cells in 12-well plates were transiently transfected with MMTV-ERE reporter gene together with ERα expression vector, and PIMT siRNA or scrambled siRNA (as a control) prior to treatment with 50 nM E_2 or ethanol (vehicle). (C and D) 293T cells in 12-well plates were transiently transfected with MMTV-ERE reporter gene together with EREexpression vector, and with Flag-tagged PIMT (Flag-PIMT), its catalytic dead mutant (Flag-G88A) or empty vector (EV), and followed by treatment with 50 nM E_2 or ethanol (vehicle). PIMT expression levels were determined by Western blot analysis. The data from five independent experiments are shown as the relative luciferase unit per milligram protein (mean ± SD).

3. Results

3.1. PIMT functions as a co-activator in ERα-mediated transcription

To explore the functional role of PIMT in transcriptional regulation by the ERα, we first tested whether PIMT can enhance or inhibit transcriptional activation of reporter plasmids by ERα. 293T cells were transfected with expression vectors for ERα and a luciferase reporter gene containing the estrogen response element (ERE) (Fig. 1A). In addition, siRNA against PIMT or expression vectors for PIMT and a catalytically inactive PIMT mutant, G88A, were transfected and their effect on the expression of an ERα-regulated reporter plasmid was measured. E_2 stimulation dramatically increased the ERE promoter activity. However, the depletion of PIMT

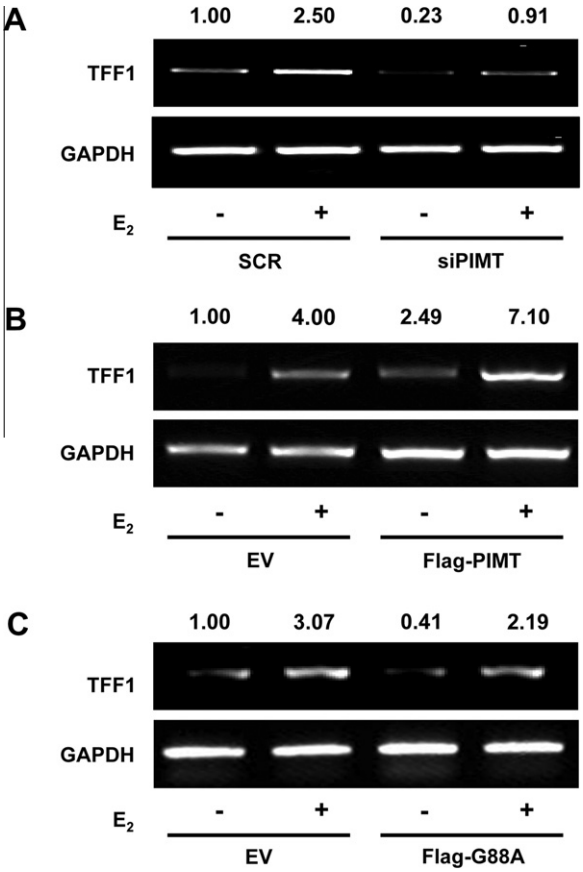

Fig. 2. Involvement of PIMT in activation of the ERα target gene TFF1, MCF7 cells were transfected with (A) PIMT siRNA or scrambled siRNA; (B) Flag-PIMT or EV; (C) Flag-G88A or EV. After 72 h, cells were stimulated with or without 50 nM E_2 for 30 min. Changes in TFF1 mRNA levels were determined as described in Experimental Procedures. Values are normalized to GAPDH levels and the representative from three independent experiments. Density values were analyzed by NIH Image J software.

resulted in an 87% reduction in E_2-mediated stimulation of the promoter activity, when compared with scrambled siRNA-transfected control cells (Fig. 1B). Furthermore, over-expression of PIMT induced approximately two-fold stimulation of the promoter activity in response to E_2, while overexpression of a catalytically inactive PIMT mutant, G88A, was resistant to E_2 stimulation (Fig. 1C and D). Collectively, these findings demonstrate that the methylation activity of PIMT is specifically required for ERα-mediated transcriptional activation.

3.2. PIMT mediates E_2-induced transcription of TFF1

Since PIMT was essential for the activation of the ERE promoter by E_2 (Fig. 1), we next tried to confirm the role of PIMT in the transcription of TFF1, an endogenous estrogen-response gene, containing an imperfect ERE within its promoter [18–20]. After E_2 stimulation for 30 min, the levels of TFF1 expression in PIMT siRNA-transfected cells were completely reduced (Fig. 2A). In the absence of E_2, depletion of PIMT also resulted in a decrease (<70%) in TFF1 mRNA levels. In contrast, PIMT over-expression markedly increased the levels of TFF1 mRNA in the absence or presence of E_2 (Fig. 2B). To examine whether the methytransferase activity of PIMT is essential for TFF1 mRNA induction, we next analyzed changes of TFF1 mRNA level in cells expressing G88A mutant (Fig. 2C). The expression of mutant PIMT reduced TFF1 mRNA level in E_2-stimulated cells (<40%), compared with those in vector control cells. These findings indicate that PIMT is a critical co-activator of E_2-mediated TFF1 transcription.

3.3. PIMT interacts with ERα and is distributed to the cytosol and the nucleus

To examine the interaction of PIMT with ERαin MCF7 cells, we performed immunoprecipitation using antibodies against PIMT and ERα. PIMT was co-immunoprecipitated with anti-ERα, but not with IgG (Fig. 3A). Similarly, ERαwas also detected in immunoprecipitates with anti-PIMT. However, the interaction of PIMT with ERα was not affected by E_2 treatment (data not shown).

PIMT is known to methylate various nuclear protein *in vitro* and *in vivo* including histone H2A, H2B, and non-chromosomal nuclear proteins, indicating that PIMT may be localized to the nucleus [21]. To test this, MCF7 cells were subjected to sub-cellular fractionation. Although the PIMT was mainly detected in the cytosol fraction, the nuclear fractions also contained small, but significant amount of PIMT (Fig. 3B). Taken together, these results indicate that PIMT is capable of interacting with ER and localized both in the cytosol and the nucleus.

3.4. PIMT is recruited to the TFF1 promoter by E_2 treatment

To further characterize the mechanisms by which PIMT regulates the expression of TFF1, we first examined whether PIMT is recruited into the promoter. To analyze the occupancy of PIMT at the TFF1 promoter, we designed primer sets which covered ERα binding site (Fig. 4A). E_2 treatment induced the recruitment of PIMT to the promoter, while PIMT was marginally recruited to the promoter in the absence of E_2 (Fig. 4B). Moreover, in the PIMT-depleted cells, PIMT recruitment by E_2 was completely suppressed (Fig. 4C). ERα recruitment by E_2 was marginally affected by PIMT as shown by a slight decrease in ERα recruitment in PIMT-depleted cells (Fig. 4C). To further investigate the relationship between PIMT recruitment and transcriptional initiation, we examined the recruitment of Pol II to the regulatory elements of the TFF1 gene. E2 treatment caused a two-fold increase in the recruitment of Pol II to the promoter. However depletion of PIMT reduced the recruitment of Pol II by E2 treatment. In the absence of E_2,

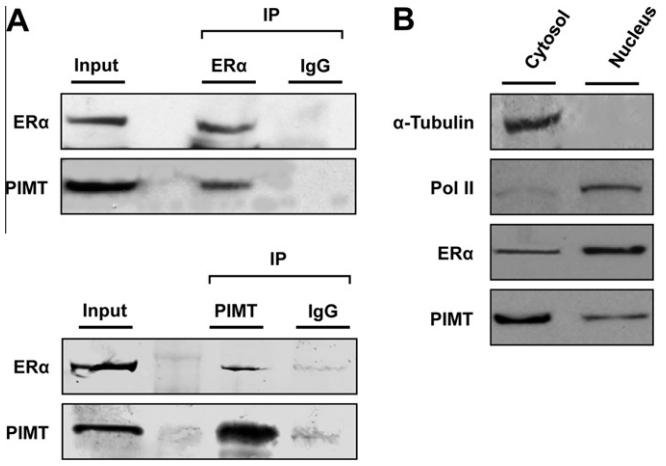

Fig. 3. Interaction of PIMT with ERα and localization of PIMT in the nucleus, (A) MCF7 cell extracts were immunoprecipitated with anti-PIMT, anti-ERα or normal rabbit/mouse IgG. The immunoprecipitates were Western-blotted with indicated antibodies. (B) MCF7 cells were rinsed twice with ice-cold PBS, and cytoplasmic and nuclear extracts were prepared as described in Experimental Procedures. The cellular localization of PIMT and ERα was detected with anti-PIMT, anti-ERα, anti-Pol II (nuclear fraction standard), or anti-α-tubulin antibodies (cytosolic fraction standard).

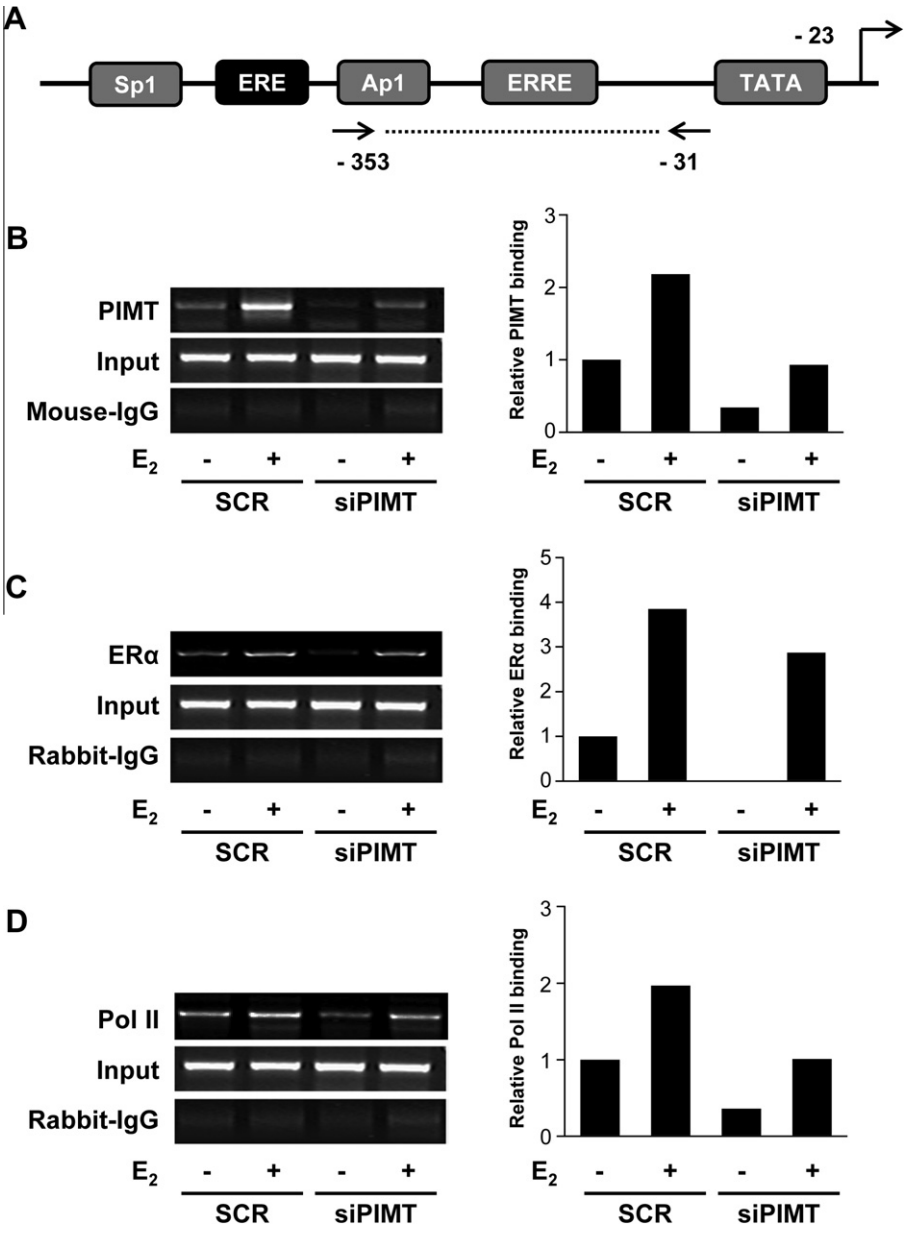

Fig. 4. Recruitment of PIMT, ERα and Pol II to the TFF1 promoter byE_2 stimulation. (A) Description of the TFF1 gene. Arrows, location of primers in the TFF1 promoter. (B–D) MCF7 cells were transfected with PIMT siRNA or scrambled siRNA. After 72 h, cells were treated with or without 50 nM E_2 for 30 min. Changes in recruitment of PIMT (B), ERα (C) and Pol II (D) into TFF1 promoter following treatment with E_2 were determined by ChIP analysis.

depletion of PIMT also further decreased the recruitment of Pol II below those observed in scrambled siRNA-transfected untreated control cells (Fig. 4D). These results suggest that PIMT might be involved in the transcriptional initiation of TFF1 gene via regulating ERα recruitment into the promoter.

4. Discussion

PIMT has been shown to function as a protein repair enzyme, which can restore loss of activity associated with isoaspartate formation through catalyzing the conversion of β–linked isopeptide bonds back to the conventional α–liked form [22]. However, in the case of asparagine deamidation, PIMT cannot restore the normal asparagine side chain. Therefore, it has been hypothesized that methylation of isoaspartate may regulate protein activity beyond damage and repair. In this study, we report the first evidence that PIMT can act as a direct co-activator for ERα-mediated transcription. PIMT interacted with ERα and was localized both in the cytosol and the nucleus. PIMT was recruited to the promoter region of the estrogen-regulated TFF1 gene along with ERα in an E_2-dependent manner. Depletion of PIMT by RNA silencing decreased the recruitment of ERα to the promoter (about 30%), leading to suppression of Pol II uploading to the promoter as well as the expression of TFF1 mRNA. In addition, over-expression of the catalytically inactive PIMT mutant, G88A, caused the ERE promoter activity and endogenous TFF1 gene transcription to be resistant to E_2 stimulation, indicating that the methylation activity of PIMT is specifically required for E_2-mediated transcriptional activation.

The transcriptional activation by ERα requires the recruitment of various co-regulators onto its target gene promoters in response to E_2 [23,24]. Currently, the function of these co-regulators has been explained by two mechanistic models. First, the co-regulators transmit the signal of a ligand-induced ERα conformational change

to the basal transcription machinery [25]. Second, the co-regulators recruited to the promoter via their complex formation with ERα induce chromatin remodeling, leading to changes in accessibility of Pol II to the promoter [26]. Here, we demonstrate that PIMT may play a role as a co-activator in ERα-mediated transcription. PIMT bound ERα and was recruited to the promoter (Fig. 4B). The LXXLL motifs have been shown to mediate binding of transcriptional co-activators to ligand-bound NRs [27]. PIMT contains one LXXLL-like motif in the region between amino acid 71 and 76. Thus, the interaction of PIMT with ERα may be mediated via the LXXLL-like motif in PIMT. In part, the binding of PIMT to ERα seems to increase the DNA binding affinity of ERα, because depletion of PIMT led to a 30% reduction of ERα recruitment to the promoter (Fig. 4B). Interestingly, ERα contains an aspartyl (Asp) residue at position 351, which is important for trans-activation and obtaining an active conformation as a nuclear receptor [28]. Asp351 is located within the ligand binding domain of ERα and replacement of Asp351 with lysine completely abolished E_2-dependent trans-activation by impairing the ability of ERα to bind p160 co-activators. Based on the observation, it is assumed that the L-isoaspartyl residue arising from the spontaneous isomerization of aspartyl residue 351 may be methylated by PIMT; therefore, affecting either its DNA binding affinity or its sub-cellular distribution. Thus, it will be very interesting to identify whether aspartyl residue 351 can serve as a substrate for PIMT.

Targeted reduction of PIMT expression by RNA silencing led to the complete suppression of TFF1 gene transcription, while reducing the partial DNA binding affinity of ERα (Fig. 2A and 4C). This finding indicates that additional other mechanisms may be involved in PIMT-dependent transcription by ERα. Two major types of chromatin remodeling have been widely investigated for ERα-mediated transcription. First,ATP-dependent chromatin remodeling factorsalter the structure and the position of nucleosomes at the promoters of ERα target genes [29,30]. The second class of remodeling factors includes a diverse group of single/multi-subunit factors that affect post-translational modifications of histone tails [31,32]. The well-known histone-modifying factors acting in ERα-mediated transcription are histone acetyltransferases, and histone methyltransferases, as well as the arginine methyltransferases [10,33–35]. These remodeling factors are recruited to the promoter proximal region of ERα target genes [31,32] and facilitate either remodeling or removal of the underlying nucleosome, thereby increasing the accessibility of promoter regions to the transcription machinery. Interestingly, histone H2B is found to be a major nuclear substrate for PIMT in the rat and mouse cells [13,14]. In chicken nucleosomes, isoaspartate accumulates primarily in histone H2A and can be methylated by PIMT [15]. Thus, it will be very interesting to identify the carboxyl methylation sites in histone H2A and H2B *in vivo* and investigate their effects on chromatin remodeling.

Collectively, the present study on the identification of PIMT as a regulator of ERα contributes to an expanding list of molecules that act as co-activators of ERα-mediated transcription and have a pivotal role in growth control and oncogenesis.

Acknowledgments

This research was supported by Basic Science Research Program through the National Research Foundation of Korea (NRF) funded by the Ministry of Education, Science and Technology (2011-0028282, 2011-0028283, 2011-0028284).

References

[1] R.M. Evans, The steroid and thyroid hormone receptor superfamily, Science 240 (1988) pp. 889–895.
[2] M. Beato, P. Herrlich, G. Schutz, Steroid hormone receptors: many actors in search of a plot, Cell 83 (1995) 851–857.
[3] M.J. Tsai, B.W. O'Malley, Molecular mechanisms of action of steroid/thyroid receptor superfamily members, Ann. Rev. Biochem. 63 (1994) 451–486.
[4] M. Robinson-Rechavi, H. Escriva Garcia, V. Laudet, The nuclear receptor superfamily, J. Cell Sci. 116 (2003) 585–586.
[5] P. Webb, P. Nguyen, J. Shinsako, C. Anderson, W. Feng, M.P. Nguyen, D. Chen, S.M. Huang, S. Subramanian, E. McKinerney, B.S. Katzenellenbogen, M.R. Stallcup, P.J. Kushner, Estrogen receptor activation function 1 works by binding p160 coactivator proteins, Mol. Endocrinol. 12 (1998) 1605–1618.
[6] D. Chen, S.M. Huang, M.R. Stallcup, Synergistic, p160 coactivator-dependent enhancement of estrogen receptor function by CARM1 and p300, J. Biol. Chem. 275 (2000) 40810–40816.
[7] C. Teyssier, H. Ma, R. Emter, A. Kralli, M.R. Stallcup, Activation of nuclear receptor coactivator PGC-1alpha by arginine methylation, Genes Dev. 19 (2005) 1466–1473.
[8] H. Wang, Z.Q. Huang, L. Xia, Q. Feng, H. Erdjument-Bromage, B.D. Strahl, S.D. Briggs, C.D. Allis, J. Wong, P. Tempst, Y. Zhang, Methylation of histone H4 at arginine 3 facilitating transcriptional activation by nuclear hormone receptor, Science 293 (2001) 853–857.
[9] K.M. Dreijerink, K.W. Mulder, G.S. Winkler, J.W. Hoppener, C.J. Lips, H.T. Timmers, Menin links estrogen receptor activation to histone H3K4 trimethylation, Cancer Res. 66 (2006) 4929–4935.
[10] D.Y. Lee, J.P. Northrop, M.H. Kuo, M.R. Stallcup, Histone H3 lysine 9 methyltransferase G9a is a transcriptional coactivator for nuclear receptors, J. Biol. Chem. 281 (2006) 8476–8485.
[11] E.D. Murray.Jr., S. Clarke, Synthetic peptide substrates for the erythrocyte protein carboxyl methyltransferase. Detection of a new site of methylation at isomerized L-aspartyl residues, J. Biol. Chem. 259 (1984) pp. 10722–10732.
[12] S. Clarke, Aging as war between chemical and biochemical processes: protein methylation and the recognition of age-damaged proteins for repair, Ageing Res. Rev. 2 (2003) 263–285.
[13] G.W. Young, S.A. Hoofring, M.J. Mamula, H.A. Doyle, G.J. Bunick, Y. Hu, D.W. Aswad, Protein L-isoaspartylmethyltransferase catalyzes in vivo racemization of Aspartate-25 in mammalian histone H2B, J. Biol. Chem. 280 (2005) 26094–26098.
[14] A.L. Young, W.G. Carter, H.A. Doyle, M.J. Mamula, D.W. Aswad, Structural integrity of histone H2B in vivo requires the activity of protein L-isoaspartate O-methyltransferase, a putative protein repair enzyme, J. Biol. Chem. 276 (2001) 37161–37165.
[15] W.G. Carter, D.W. Aswad, Formation, localization, and repair of L-isoaspartyl sites in histones H2A and H2B in nucleosomes from rat liver and chicken erythrocytes, Biochemistry 47 (2008) 10757–10764.
[16] D. Chen, H. Ma, H. Hong, S.S. Koh, S.M. Huang, B.T. Schurter, D.W. Aswad, M.R. Stallcup, Regulation of transcription by a protein methyltransferase, Science 284 (1999) 2174–2177.
[17] A. Hamahata, Y. Takata, T. Gomi, M. Fujioka, Probing the S-adenosylmethionine-binding site of rat guanidinoacetatemethyltransferase. Effect of site-directed mutagenesis of residues that are conserved across mammalian non-nucleic acid methyltransferases, Biochem. J. 317 (Pt 1) (1996) 141–145.
[18] A.M. Nunez, M. Berry, J.L. Imler, P. Chambon, The 5'flanking region of the pS2 gene contains a complex enhancer region responsive to oestrogens, epidermal growth factor, a tumour promoter (TPA), the c-Ha-rasoncoprotein and the c-jun protein, EMBO J. 8 (1989) 823–829.
[19] J. Kim, L.N. Petz, Y.S. Ziegler, J.R. Wood, S.J. Potthoff, A.M. Nardulli, Regulation of the estrogen-responsive pS2 gene in MCF-7 human breast cancer cells, J. Steroid Biochem. Mol. Biol. 74 (2000) 157–168.
[20] D. Lu, Y. Kiriyama, K.Y. Lee, V. Giguere, Transcriptional regulation of the estrogen-inducible pS2 breast cancer marker gene by the ERR family of orphan nuclear receptors, Cancer Res. 61 (2001) 6755–6761.
[21] D.P. Quick, P.J. Orchard, J.A. Duerre, Carboxyl methylation of nonhistone chromosomal proteins, Biochemistry 20 (1981) 4724–4729.
[22] K.J. Reissner, D.W. Aswad, Deamidation and isoaspartate formation in proteins: unwanted alterations or surreptitious signals?, Cell Mol. Life Sci. 60 (2003) 1281–1295.
[23] R. Metivier, G. Penot, M.R. Hubner, G. Reid, H. Brand, M. Kos, F. Gannon, Estrogen receptor-alpha directs ordered, cyclical, and combinatorial recruitment of cofactors on a natural target promoter, Cell 115 (2003) 751–763.
[24] Y. Shang, X. Hu, J. DiRenzo, M.A. Lazar, M. Brown, Cofactor dynamics and sufficiency in estrogen receptor-regulated transcription, Cell 103 (2000) 843–852.
[25] B. Belandia, M.G. Parker, Nuclear receptors: a rendezvous for chromatin remodeling factors, Cell 114 (2003) 277–280.
[26] C. Rachez, B.D. Lemon, Z. Suldan, V. Bromleigh, M. Gamble, A.M. Naar, H. Erdjument-Bromage, P. Tempst, L.P. Freedman, Ligand-dependent transcription activation by nuclear receptors requires the DRIP complex, Nature 398 (1999) 824–828.
[27] A. Aranda, A. Pascual, Nuclear hormone receptors and gene expression, Physiol. Rev. 81 (2001) 1269–1304.
[28] J.H. Kim, M.H. Lee, B.J. Kim, S.J. Han, H.Y. Kim, M.R. Stallcup, Role of aspartate 351 in transactivation and active conformation of estrogen receptor alpha, J. Mol. Endocrinol. 35 (2005) 449–464.

[29] S.K. Yoshinaga, C.L. Peterson, I. Herskowitz, K.R. Yamamoto, Roles of SWI1, SWI2, and SWI3 proteins for transcriptional enhancement by steroid receptors, Science 258 (1992) pp. 1598–1604.
[30] Z.Q. Huang, J. Li, L.M. Sachs, P.A. Cole, J.A. Wong, Role for cofactor-cofactor and cofactor-histone interactions in targeting p300, SWI/SNF and mediator for transcription, EMBO J. 22 (2003) 2146–2155.
[31] D. Dubik, T.C. Dembinski, R.P. Shiu, Stimulation of c-myc oncogene expression associated with estrogen-induced proliferation of human breast cancer cells, Cancer Res. 47 (1987) 6517–6521.
[32] J.S. Foster, J. Wimalasena, Estrogen regulates activity of cyclin-dependent kinases and retinoblastoma protein phosphorylation in breast cancer cell, Mol. Endocrinol. 10 (1996) 488–498.
[33] K.C. Lee, J. Li, P.A. Cole, J. Wong, W.L. Kraus, Transcriptional activation by thyroid hormone receptor-beta involves chromatin remodeling, histone acetylation, and synergistic stimulation by p300 and steroid receptor coactivators, Mol. Endocrinol. 17 (2003) 908–922.
[34] T. Carling, K.C. Kim, X.H. Yang, J. Gu, X.K. Zhang, S. Huang, A histone methyltransferase is required for maximal response to female sex hormones, Mol. Cell. Biol. 24 (2004) 7032–7042.
[35] H. Kim, K. Heo, J.H. Kim, K. Kim, J. Choi, W. An, Requirement of histone methyltransferase SMYD3 for estrogen receptor-mediated transcription, J. Biol. Chem. 284 (2009) 19867–19877.

Biochemical and Biophysical Research Communications 420 (2012) 230–235

Contents lists available at SciVerse ScienceDirect

Biochemical and Biophysical Research Communications

journal homepage: www.elsevier.com/locate/ybbrc

Short-time glucose exposure of embryonic carcinoma cells impairs their function as terminally differentiated cardiomyocytes

Julia M. Knelangen [a,*], Randy Kurz [b], Undraga Schagdarsurengin [c], Bernd Fischer [a], Anne Navarrete Santos [a]

[a] Department of Anatomy and Cell Biology, Martin-Luther-University Halle-Wittenberg, Germany
[b] Division of Molecular Biological–Biochemical Processing Technology, Center for Biotechnology and Biomedicine, University of Leipzig, Germany
[c] Department of Urology, Pediatric Urology and Andrology, Justus-Liebig-University Giessen, Germany

ARTICLE INFO

Article history:
Received 16 February 2012
Available online 3 March 2012

Keywords:
P19 embryonic carcinoma cells
Cardiac differentiation
Glucose
CpG methylation

ABSTRACT

The fetal and postnatal phenotype is influenced by developmental conditions experienced prenatally. Among prenatal development metabolic factors are of particular importance as they are supposed to predispose for pathophysiological alterations later in life and to pioneer functional impairment in senescence (metabolic programming). Till now the mechanisms of metabolic programming are not well understood.

We have investigated various concentrations of glucose during differentiation of pluripotent P19 embryonic carcinoma cells (ECC) into cardiomyocytes. Undifferentiated P19 cells were exposed to 5 mM (low), 25 mM (control), 40 mM or 100 mM (high) glucose for 48 h during embryoid body (EB) formation, followed by plating and differentiation into cardiomyocytes in vitro with standard glucose supplementation (25 mM) for 10–15 days. The amount of cardiac clusters, the frequency of spontaneous beatings as well as the expression of metabolic and cardiac marker genes and their promoter methylation were measured.

We observed a metabolic programming effect of glucose during cardiac differentiation. Whereas the number of beating clusters and the expression of the cardiac marker alpha myosin heavy chain (α-MHC) were comparable in all groups, the frequencies of beating clusters were significantly higher in the high glucose group compared to low glucose. However, neither the insulin receptor (IR) or insulin like growth factor 1 receptor (IGF1R) nor the metabolic gene glucose transporter 4 (GLUT4) were influenced in RNA expression or in promoter methylation.

Our data indicate that a short time glucose stress during embryonic cell determination leads to lasting effects in terminally differentiated cell function.

1. Introduction

Embryonic cells have an astonishing capacity to adapt quickly to metabolic changes. A molecular "cell memory" can store this "stress" information, leading to a modified metabolic programming with consequences for further development and differentiation. Environmental and metabolic factors act in early life to program the risks for cardiovascular and metabolic disease in adult life and even premature death [1]. Barker and colleagues were the first to propose the "Developmental Origins of Health and Disease" (DOHaD hypothesis) [2]. Although extensive human epidemiological and animal model data support this hypothesis, the underlying mechanisms are still poorly understood [3].

There is growing evidence that metabolic programming occurs as early as during the first days in ontogeny during embryo preimplantation development [4]. The most fascinating information from such studies is that metabolic factors do not influence only immediate events of blastocyst morphogenesis but also the fetal and postnatal phenotype. For example, maternal protein restriction in the rat during the few days of the preimplantation development leads to altered growth and elevated systolic blood pressure in offspring [5,6].

One of the key player in metabolic and growth regulation is the insulin/IGF/-receptor system. It regulates glucose transport, glycolysis and gluconeogenesis on one side and cell proliferation, apoptosis and organ size on the other. Dysregulation leads to metabolic diseases such as diabetes mellitus and the metabolic syndrome. Therefore this system is one of the most likely candidates for

Abbreviations: ECC, embryonic carcinoma cells; IGF1R, insulin like growth factor 1 receptor; GLUT 4, glucose transporter 4; IR, insulin receptor; α-MHC, alpha myosin heavy chain.

* Corresponding author. Address: Martin Luther University, Faculty of Medicine, Department of Anatomy and Cell Biology, Grosse Steinstrasse 52, D-06097 Halle (Saale), Germany. Fax: +49 3455571700.
E-mail address: julia.knelangen@medizin.uni-halle.de (J.M. Knelangen).

0006-291X/$ - see front matter © 2012 Elsevier Inc. All rights reserved.
doi:10.1016/j.bbrc.2012.02.105

metabolic programming. From the blastocyst stage glucose is the most frequently utilized carbohydrate and plays a fundamental role in embryogenesis. Glucose reaches the early embryo through uterine secretions or the placenta in a direct correlation to the maternal blood glucose level. In diabetic rabbits the uterine glucose concentration is 3-fold increased compared to the physiological level of healthy animals [7].

The glucose transporter 4 (GLUT4) is responsible for insulin-mediated glucose uptake in adipose tissue, skeletal muscle and heart. Upon insulin stimulation, GLUT4 translocates from intracellular storages to the plasma membrane and mediates glucose intake into the cell from the circulation [8].

To analyze potential mechanisms involved in metabolic programming we have cultured pluripotent P19 embryonic carcinoma cells (ECC) in hypo- and hyperglycemic media. P19 cells have been shown to reliably differentiate into cardiac, skeletal and smooth muscle cells. The in vitro cardiac cell differentiation recapitulates the in vivo differentiation of the embryonic myocardium.

As functional endpoints of cardiac cell differentiation the number of beating clusters and the frequency of spontaneously beating cardiomyocytes were counted by (i) video detection and (ii) multi-electrode array (MEA) [9]. Thereby, the MEA technology functioned as a second independent and highly reliable method to determine cardiac cell function. The transcription profile of insulin receptor (IR), insulin like growth factor 1 receptor (IGF1R), glucose transporter 4 (GLUT4) and of the cardiac marker alpha myosin heavy chain (α-MHC) were measured. As a potential mechanism for metabolic programming the specific DNA methylation of IR, IGF1R and GLUT4 was analyzed. We used bisulfite sequencing to determine the pattern of methylation in the various experimental P19 ECC groups.

2. Material and methods

2.1. Differentiation of P19 cells into cardiomyocytes in vitro

The embryonic carcinoma cell line P19 was cultured as described before [10].

The cardiac differentiation of ECC proceeds in hanging drops (Fig. 1) [11]. Cells were cultured in differentiation medium supplemented with 1% dimethyl sulfoxide (DMSO) (Sigma–Aldrich, Germany) as inducer of cardiac differentiation. Drops of differentiation medium (20 μl) with 400 cells each were placed onto the lids of Petri dishes filled with PBS and cultured for 2 d. The ECC aggregated and formed so-called embryoid bodies (EBs). During the 48 h of EB formation the cells were cultured with low glucose (5 mM), standard glucose (25 mM) and high glucose concentrations (40 mM or 100 mM). Subsequent culture from day 2 to day 5 + 10 was performed under standard conditions (25 mM glucose). The cell aggregates formed were transferred into non-adhesive bacteriological grade Petri dishes and maintained for 3 days in suspension in differentiation medium. The 5-d-old EBs were placed onto 0.1% gelatine-coated dishes and cultured for another 5–10 d (5 + 5 d, 5 + 10 d). The first spontaneously beating clusters appeared 1 d after plating.

2.2. Determination of cardiomyocyte contractility

Cardiac cell function was examined by counting beating clusters and by two different measurements of beating frequencies in the EB outgrowths:

1. Frequency was detected at day 5 + 7 by using a video camera installed to a microscope. The registration is based on light–dark changes and every EB was recorded once for 60 s. The experiment was repeated three times with 24 EBs in each group.
2. For the extracellular recording of field potentials, EBs were cultured on a planar 0.2% gelatine-coated multielectrode array (MEA) with 60 substrate-integrated titanium nitride electrodes. An internal electrode was used as reference electrode. To measure the electrogenic properties of cardiomyocytes, the biochip was connected to a heatable MEA1060 amplifier system (Multi Channel Systems). Recording of electric activity of cardiomyocytes was carried out simultaneously on all electrodes at a sampling rate of 4 kHz. Data were analyzed and processed off-line using a toolbox programmed with MATLAB (The Mathworks,

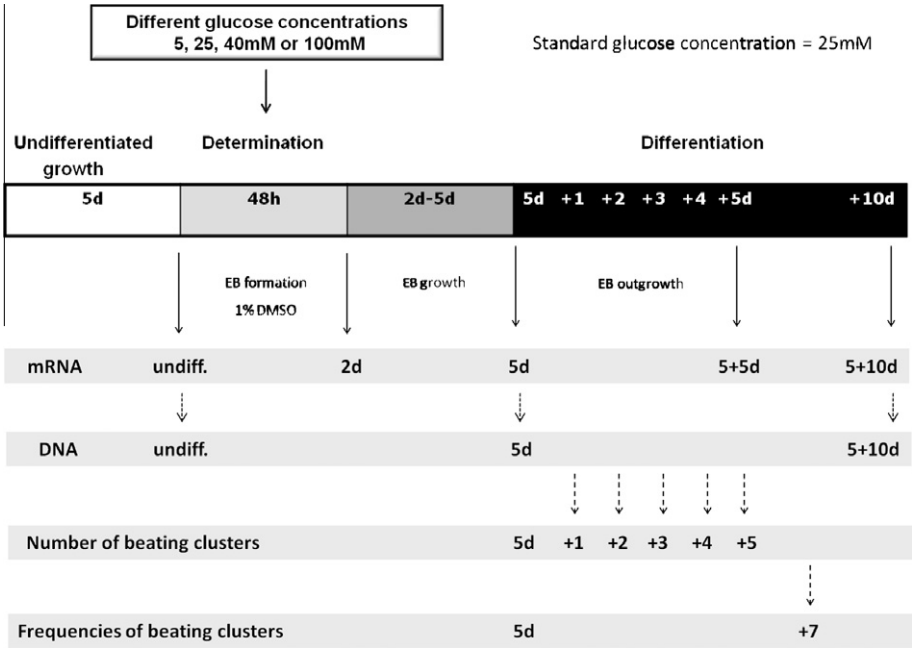

Fig. 1. Schematic time schedule for the differentiation and analysis of P19 cells into cardiomyocytes in vitro. During determination period (48 h) cells were cultured with different glucose concentrations (5 mM, 25 mM, 40 mM, 100 mM) and subsequently differentiated into cardiomyocytes under standard glucose concentration (25 mM). EB = embryoid body, d = days.

Natick, MA, USA) to identify voltage signals [12,13]. To analyze alterations in beating frequency the peak-to-peak distance of the negative amplitude of the field potential was calculated. Each experiment was repeated three times by recording each EB 15 min every second at day 5 + 7.

2.3. RNA extraction and reverse transcription

Messenger RNA levels of the target genes were measured at 2 d, 5 d, 5 + 5 d and 5 + 10 d. Total RNA from P19 cells was extracted as published by Chomczynski and Sacchi [14]. For isolation of total EB-RNA 15 EBs were pooled and the *RNAspin Mini RNA Isolation Kit* (GE Healthcare, Germany) was used. Total RNA (2 μg) was reverse transcribed in a final volume of 100 μl. The Superscript II RT-kit, dNTPs, and *Taq* polymerase were purchased from Invitrogen (Germany), and random primer, Rnase inhibitor, and Dnase I from Roche Diagnostics (Germany).

2.4. Real-time PCR

The transcription levels of 18S, GLUT4, IR, IGF1R and α-MHC were analyzed by qRT-PCR using an ABI-PRISM 5700 Sequence Detection System (Applied Biosystems, USA). Reactions were performed in duplicate measurement using SYBR green Master Mix (Applied Biosystems, USA) with the appropriate primer set (Table 1a) to determine a mean C_T-value for each sample. C_T values of the different samples were compared with the $\Delta\Delta C_T$ method described by Livak and Schmittgen [15]. Expression of 18S rRNA was homogenous in all samples and served as internal reference. All experiments were repeated three times. Levels of significance between groups were calculated using Student's *t* test after proven normal distribution (SigmaPlot). Data are expressed as mean ± SEM. Transcription levels with a $p < 0.05$ were considered as differentially expressed.

2.5. DNA isolation and methylation analysis

The CpG methylation of promoter regions from the target genes GLUT4, IGF1R and IR was investigated by combined bisulfite restriction analysis (COBRA) and by bisulfite sequencing. First, DNA samples of undifferentiated P19 cells, adult mouse heart and EBs at 5 d and 5 + 10 d treated with low (5 mM), standard (25 mM) and high glucose concentration (40 mM) were collected. Therefore, P19 cells and pooled EBs were transferred into 400 μl proteinase K-buffer supplemented with 15 μl proteinase K (20 μg/ml) and incubated for 3 h at 56 °C. The DNA was isolated applying the standard phenol/chloroform procedure. Subsequently, the remaining RNA was enzymatically degraded. The following bisulfite treatment of the DNA was performed as described by Shapiro and co-authors [16]. Purification of the bisulfite-treated DNA was performed with the *Wizard clean-up system* (Promega, Germany) and amplified with the *Taq* polymerase from Invitek (Germany), using primer combinations listed in Table 1b.

For bisulfite sequencing, the PCR products were purified from agarose gel using a gel extraction kit (QIAGEN, Germany) following the manufacturer's protocol. Cloning and sequencing of the PCR fragments was performed as previously described [17]. For bisulfite-modified DNA sequence of the promoter region of the target genes see additional file 1 (Supplemental material).

Table 1
(a) Primer sequences for qPCR; (b) Primer sequences for COBRA.

Name	Primer combination
(a)	
18S	Fw: 5′-AGAAACGGCTACCACATCCAA-3′
	Rv: 5′-CTGTATTGTTAI I I I CGTCACTACCT-3′
α-MHC	Fw: 5-ATCATTCCCAACGAGCGAAA-3
	Rv: 5′-GCCGGAAGTCCCCATAGAGA-3′
GLUT4	Fw: 5′-TGACGCACTAGCTGAGCTGAA-3′
	Rv: 5′-AGGAGCTGGAGCAAGGACATT-3′
IGF1-R	Fw: 5′-CCAGAGCAAAGGGGACATAA-3′
	Rv: 5′-TGATTCGGTTCTTCCAGGTC-3
IR	Fw: 5′-GCAACTGTTCGGAACCTGATGACC-3′
	Rv: 5′-GCGCCAGTCCTGGAAGTGATAGTA-3′
(b)	
GLUT4	Fw: 5′-AGTTATTGGTTTTTTGGATTATTTTTT-3′
	Rv: 5′-AAATAACTCCAACAAAATAACATAAAACCC-3′
IGF1-R	Fw: 5′-TTGTTTGGGTTTTTTTTTTAGGGTTGG-3′
	Rv: 5′-CACACCTAAAAAAAAAAAAAACCCCTAAAAA-3′
IR	Fw: 5′-AAAAAGAGAGAGATATATTTTAGAGGGAAGA-3′
	Rv: 5′-AACAATAACTTAACACTATAAATCATCTCCC-3′

3. Results

3.1. Analysis of cardiac differentiation und function

The various P19 experimental groups were grown in 100, 40 mM (high), 5 mM (low) or 25 mM (standard) glucose during embryoid body formation. The following culture from day 2 to day 5 + 10 was performed under standard conditions (25 mM glucose) in all groups (Fig. 1). This 2 day exposure to low or high glucose during the determination period did not influence the number of beating clusters (Fig. 2a). However, even though the number and the time of developing beating clusters was comparable in all groups, clear differences in beating frequencies were measured between the EBs cultured under low and high glucose conditions (Fig. 2b). The MEA analysis demonstrated also an effect of glucose stress during the determination period of ECC on beating frequencies (Fig. 2c). The contractions/min in finally differentiated cardiomyocytes was significantly reduced in the group cultured with 5 mM glucose (65 contractions/min) compared to the 100 mM group (95 contractions/min). The mean frequency was about 72 contractions/min.

The cardiac marker α-MHC showed a typical differentiation-dependent transcription profile without differences in experimental groups (5 mM, 40 mM glucose) (Fig. 3a).

3.2. Transcriptional regulation of target genes

The expression of the glucose transporter 4 (GLUT4) increased from day 2 to day 5 + 5 in all groups (Fig. 3b). At day 5 + 5 d the GLUT4 amount from 5 mM EBs was two times higher compared to 25 mM and 40 mM EBs. Transcript amounts of the insulin receptor (IR) and insulin like growth factor 1 receptor (IGF1R) were not influenced by hypo- or hyperglycemic media during the determination phase (data not shown).

3.3. DNA methylation of the analyzed promoter regions

One potential mechanism for transcriptional regulation is the CpG-methylation within the gene promoters. Analyzing the target promoters by bisulfite sequencing we found that a glucose stress during determination of ECC differentiation did not affect the methylation status of the promotor regions of GLUT4, IR and of IGF1R (Table 2). Methylation was not detected in any of analyzed CpG positions regarding GLUT4 and IGF1R. In contrast, all analyzed CpG positions within the IR gene were found to be methylated in P19 cells.

4. Discussion

The murine P19 embryonic carcinoma cell (ECC) model was used to recapitulate developmental processes of cardiomyogenesis

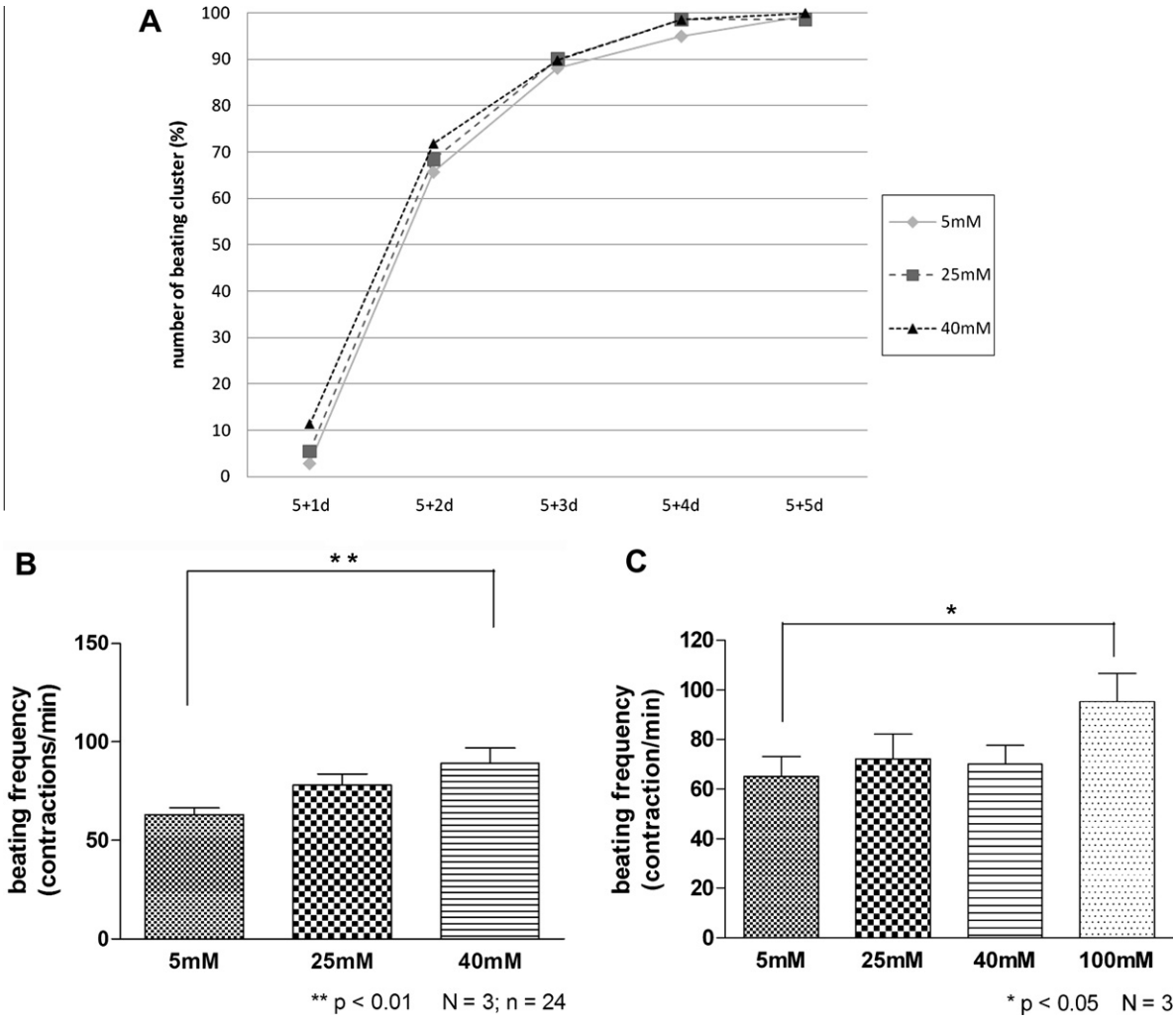

Fig. 2. Analysis of cardiac differentiation and function by counting the appearance of beating clusters (A) and determination of cluster beating frequencies (B and C) after culture with different glucose concentrations during determination period. (A) The amount of beating clusters in plated embryoid bodies was counted at different time points. After 5 days of differentiation, each EB was set into a well of a 24-well plate and analyzed from day 6 (5 d + 1) to day 10 (5 d + 5) for spontaneously beating clusters. The relative amount of beating clusters in percent (%) at different time points of differentiation is shown at day 6 (5 + 1 d), 7 (5 + 2 d), 8 (5 + 3 d), 9 (5 + 4 d) and 10 (5 + 5 d). (b + c) Frequencies of spontaneously beating cardiomyocytes were measured by video detection (B) and multielectrode array (MEA, C) in plated embryoid bodies at day 5 + 7.

in vitro [18]. ECCs have a high capacity to form cardiomyocytes in vitro and exhibit during differentiation the biochemical and physiological properties of their embryonic equivalents in vivo during cardiomyogenesis [19,20]. For the first time we can show that a metabolic programming of ECC results in changes of cardio-physiological features and can be induced by an exposure to hyper- and hypoglycemia during embryonic cell determination. Metabolic stress during embryonic and fetal developmental can occur in terms of malnutrition [21,22], immunological challenges to the mother [23] and/or metabolic diseases like diabetes mellitus type 1 and 2 [24,25]. It is well known that particularly a lack of maternal insulin and the hyperglycemia caused by maternal diabetes mellitus lead to a dysregulation of embryonic and fetal development [26] and especially affects the fetal cardiovascular system [27].

Recent studies indicate that preimplantation exposure to high glucose levels have an impact on the offspring and that poor maternal glycemic control increases the risk of miscarriage [28]. Exposure of P19 ECC to high glucose from day 0 to day 2 led to significant changes in terminally differentiated cardiac cell function, indicating a critical window for cardiac cell physiology during early cell determination. The chosen time period was found to be glucose sensitive for programming of embryonic cells. Wyman and colleagues determined a glucose sensitive window in early embryogenesis in a mouse in vivo model by demonstrating that maternal diabetes during oogenesis, fertilization, and early cleavage was correlated with significantly more morphological changes [29]. The employed glucose concentrations simulated a metabolic stress for embryonic cells. Preimplantation mouse embryos exposed to hyperglycemia, whether in vivo or in vitro, experienced a delay in development from the 2-cell to blastocyst stage [30]. A hyperglycemic exposure for >24 h is toxic for early embryos [31]. The other extreme, an absence of glucose, reduced blastocyst and trophectodermal cell numbers [32]. Kwong et al. investigated the effect of maternal periconceptional low protein diet in pregnant rats. Such offspring had altered birth weights and altered postnatal growth, hypertension and different organ proportions. The low protein diet caused a moderate hyperglycemia, which shows that altered glucose concentrations with their metabolic programming effects can be induced in different ways [6].

Epigenetic modifications like DNA methylation are currently discussed as the most likely mechanisms of metabolic programming in embryonic cells [33,34]. During adipogenic differentiation of 3T3L1 preadipocytes the methylation of specific CpG regions and methylation sensitive transcription factors can regulate transcription of GLUT4 [35]. The alteration of GLUT4 transcription in differ-

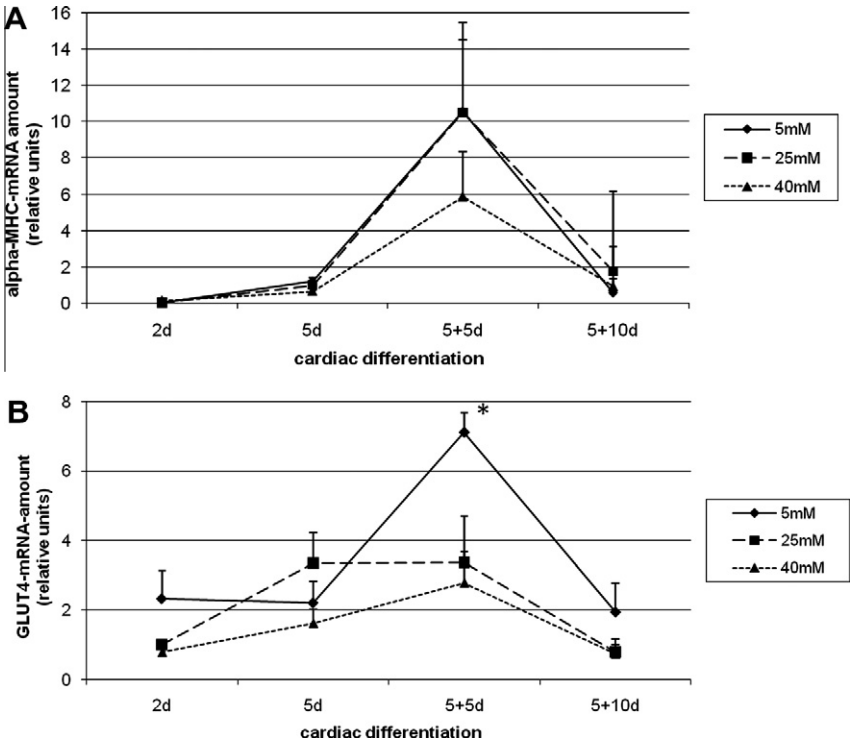

Fig. 3. Relative mRNA amounts of α-MHC (A) and GLUT4 (B) from cardiac differentiating P19 cells cultured during determination period with different glucose concentrations. Using qRT-PCR the expression profiles of undifferentiated P19 cells, EBs from 2 days (2 d) 5 days (5 d), and plated EB at day 10 (5 + 5 d) and day 15 (5 + 10 d) were characterized. The qPCR was analyzed by $\Delta\Delta C_T$ method with 18S rRNA as standard. Incubation with 5, 25 and 40 mM glucose was performed during determination period (0–2 d). *Asterisk* indicates statistical significance to the 25 mM glucose standard media (∗).

Table 2
Summary of methylation analysis of the promotor regions of GLUT4, IGF1R and IR.

Samples		Genes		
		GLUT4 #12-CpG-	IGF1-R #18-CpG-	IR #2-CpG
Undifferentiated P19 cells		non	non	met
EB 5 d	5 mM	non	non	met
	25 mM	non	non	met
	40 mM	non	non	met
EB 5 + 10 d	5 mM	non	non	met
	25 mM	non	non	met
	40 mM	non	non	met
Female adult heart		non	non	met
Male adult heart		non	non	met

non = methylation was not detected in any CpG position of the analyzed region.
met = methylation was detected in all CpG positions of the analyzed region.

entiated ECC was not regulated by DNA methylation as shown by COBRA and bisulfite sequencing. All CpG positions in the analyzed promotor region were unmethylated. Rüegg et al. demonstrated the involvement of DNA methylation in GLUT4 regulation by the estrogen receptor β [8] and provided another indication for epigenetic regulation of GLUT4 expression.

We did not find a different transcriptional regulation or changes in the promoter methylation of the IGF1R or the IR due to the altered glucose concentrations. By comparing diabetic mice with a non-diabetic control group, Nikoshkov et al. have not seen differences in the IR promoter methylation in the heart and skeletal muscles, but showed an increase in IGF1 promotor methylation [36].

Due to the fact that we had no changes in the DNA methylation status, we propose that other epigenetic mechanisms are responsible for our described metabolic programming of embryonic cells. Further epigenetic modifications potentially involved in metabolic programming are histone modifications and non-coding RNA molecules such as microRNAs [37]. By characterizing the microRNA expression during adipogenic differentiation in the murine embryonic stem cell line CGR8 we did not found an alteration in the micro-RNA profile caused by a 2 day exposure to different glucose concentrations (5 mM vs. 25 mM glucose) [38].

A maternal diabetes with a poor glycemic control is a major risk factor for the offspring to develop cardiovascular malformations [39]. Noteworthy, the peri-implantation nutritional environment of the embryo is already able to program cardiovascular dysfunction in the young adult independently of reductions in birth weight or accelerated postnatal catch-up growth as shown in a sheep model [40]. The cardiac differentiation of P19 cells is a suitable model to study metabolic imprinting. Even a moderate metabolic stress during cell determination alters the function of terminally differentiated cardiomyocytes what can lead to lifetime consequences. Current data and results from our studies clearly implicate that periconceptional and early pregnancy care is crucial and indispensable in the prevention of metabolic and cardiovascular diseases.

Grants

This work was supported by the German National Academic Foundation and the German Research Council Grant DFG NA418.

Disclosures

The authors have nothing to disclose.

Acknowledgments

We thank Dr. Sarah Tonack for her help with P19 cell culture and Prof. Reinhard Dammann for his advice in methylation specific

primer design. Thanks to Prof. Dr. Ursula Müller-Werdan for allocating the video detection system and also to Prof. Dr. Andrea Robitzki for providing the MEA technology. Thank you to Dr. Insa Schroeder for reading the manuscript.

Appendix A. Supplementary data

Supplementary data associated with this article can be found, in the online version, at doi:10.1016/j.bbrc.2012.02.105.

References

[1] I.C. Mcmillen, J.S. Robinson, Developmental origins of the metabolic syndrome: prediction, plasticity, and programming, Physiol. Rev. 85 (2005) 571–633.
[2] D.J. Barker, C.N. Hales, C.H. Fall, C. Osmond, K. Phipps, P.M. Clark, Type 2 (non-insulin-dependent) diabetes mellitus, hypertension and hyperlipidaemia (syndrome X): relation to reduced fetal growth, Diabetologia 36 (1993) 62–67.
[3] R.A. Waterland, K.B. Michels, Epigenetic epidemiology of the developmental origins hypothesis, Annu. Rev. Nutr. 27 (2007) 363–388.
[4] T.P. Fleming, W.Y. Kwong, R. Porter, E. Ursell, I. Fesenko, A. Wilkins, D.J. Miller, A.J. Watkins, J.J. Eckert, The embryo and its future, Biol. Reprod. 71 (2004) 1046–1054.
[5] W. Kwong, A. Wild, P. Roberts, A. Willis, T. Fleming, Maternal undernutrition during the preimplantation period of rat development causes blastocyst abnormalities and programming of postnatal hypertension, Development 127 (2000) 4195–4202.
[6] W.Y. Kwong, D.J. Miller, A.P. Wilkins, M.S. Dear, J.N. Wright, C. Osmond, J. Zhang, T.P. Fleming, Maternal low protein diet restricted to the preimplantation period induces a gender-specific change on hepatic gene expression in rat fetuses, Mol. Reprod. Dev. 74 (2007) 52–60.
[7] N. Ramin, R. Thieme, S. Fischer, M. Schindler, T. Schmidt, B. Fischer, A.N. Santos, Maternal diabetes impairs gastrulation and insulin and IGF-I receptor expression in rabbit blastocysts, Endocrinology 151 (2010) 4158–4167.
[8] J. Rüegg, W. Cai, M. Karimi, N.B. Kiss, E. Swedenborg, C. Larsson, T.J. Ekström, I. Pongratz, Epigenetic regulation of glucose transporter 4 by estrogen receptor β, Mol. Endocrinol. 25 (2011) 2017–2028.
[9] A. Rothermel, R. Kurz, M. Rüffer, W. Weigel, H.G. Jahnke, A.K. Sedello, H. Stepan, R. Faber, K. Schulze-Forster, A.A. Robitzki, Cells on a chip – The use of electric properties for highly sensitive monitoring of blood-derived factors involved in angiotensin II type 1 receptor signalling, Cell. Physiol. Biochem. 16 (2005) 51–58.
[10] S. Tonack, K. Kind, J.G. Thompson, A.M. Wobus, B. Fischer, A. Navarrete Santos, Dioxin affects glucose transport via the arylhydrocarbon receptor signal cascade in pluripotent embryonic carcinoma cells, Endocrinology 148 (2007) 5902–5912.
[11] V.A. Maltsev, A.M. Wobus, J. Rohwedel, M. Bader, J. Hescheler, Cardiomyocytes differentiated in vitro from embryonic stem cells developmentally express cardiac-specific genes and ionic currents, Circ. Res. 75 (1994) 233–244.
[12] K. Banach, M.D. Halbach, P. Hu, J. Hescheler, U. Egert, Development of electrical activity in cardiac myocyte aggregates derived from mouse embryonic stem cells, Am. J. Physiol. Heart Circ. Physiol. 287 (2003) H2114–2123.
[13] U. Egert, T. Knott, C. Schwarz, M. Nawrot, A. Brandt, S. Rotter, M. Diesmann, MEA tools: an open source tool box for the analysis of multi-electrode data with MATLAB, J. Neurosci. Methods 117 (2002) 33–42.
[14] P. Chomczynski, N. Sacchi, Single-step method of RNA isolation by acid guanidinium thiocyanate-phenol-chloroform extraction, Anal. Biochem. 162 (1987) 156–159.
[15] K.J. Livak, T.D. Schmittgen, Analysis of relative gene expression data using real-time quantitative PCR and the 2-[delta][delta]CT method, Methods 25 (2001) 402–408.
[16] R. Shapiro, B. Braverman, J.B. Louis, R.E. Servis, Nucleic acid reactivity and conformation. II. Reaction of cytosine and uracil with sodium bisulfite., J. Biol. Chem. 248 (1973) 4060–4064.
[17] A. Navarrete Santos, S. Tonack, M. Kirstein, S. Kietz, B. Fischer, Two insulin-responsive glucose transporter isoforms and the insulin receptor are developmentally expressed in rabbit preimplantation embryos, Reproduction 128 (2004) 503–516.
[18] J. Rohwedel, K. Guan, C. Hegert, A.M. Wobus, Embryonic stem cells as an in vitro model for mutagenicity, cytotoxicity and embryotoxicity studies: present state and future prospects, Toxicol. In Vitro 15 (2001) 741–753.
[19] I.S. Skerjanc, Cardiac and skeletal muscle development in P19 embryonal carcinoma cells, Trends Cardiovasc. Med. 9 (1999) 139–143.
[20] A.C. Fijnvandraat, A.C.G. van Ginneken, P.A.J. de Boer, J.M. Ruijter, V.M. Christoffels, A.F.M. Moorman, R.H. Lekanne Deprez, Cardiomyocytes derived from embryonic stem cells resemble cardiomyocytes of the embryonic heart tube, Cardiovasc. Res. 58 (2003) 399–409.
[21] A.J. Watkins, E. Ursell, R. Panton, T. Papenbrock, L. Hollis, C. Cunningham, A. Wilkins, V.H. Perry, B. Sheth, W.Y. Kwong, J.J. Eckert, A.E. Wild, M.A. Hanson, C. Osmond, T.P. Fleming, Adaptive responses by mouse early embryos to maternal diet protect fetal growth but predispose to adult onset disease, Biol. Reprod. 78 (2008) 299–306.
[22] A.J. Watkins, E.S. Lucas, C. Torrens, J.K. Cleal, L. Green, C. Osmond, J.J. Eckert, W.P. Gray, M.A. Hanson, T.P. Fleming, Maternal low-protein diet during mouse pre-implantation development induces vascular dysfunction and altered renin-angiotensin-system homeostasis in the offspring, Br. J. Nutr. 103 (2010) 1762–1770.
[23] C.L. Williams, J.L. Teeling, V.H. Perry, T.P. Fleming, Mouse maternal systemic inflammation at the zygote stage causes blunted cytokine responsiveness in lipopolysaccharide-challenged adult offspring, BMC Biol. 9 (2011) 49.
[24] T.D. Clausen, E.R. Mathiesen, T. Hansen, O. Pedersen, D.M. Jensen, J. Lauenborg, L. Schmidt, P. Damm, Overweight and the metabolic syndrome in adult offspring of women with diet-treated gestational diabetes mellitus or type 1 diabetes, JCEM 94 (2009) 2464–2470.
[25] T.D. Clausen, E.R. Mathiesen, T. Hansen, O. Pedersen, D.M. Jensen, J. Lauenborg, P. Damm, High prevalence of type 2 diabetes and pre-diabetes in adult offspring of women with gestational diabetes mellitus or type 1 diabetes: the role of intrauterine hyperglycemia, Diabetes Care 31 (2008) 340–346.
[26] L. Aerts, F.A.V. Assche, Animal evidence for the transgenerational development of diabetes mellitus, Int. J. Biochem. Cell Biol. 38 (2006) 894–903.
[27] B.E. Reinking, E.W. Wedemeyer, R.M. Weiss, J.L. Segar, T.D. Scholz, Cardiomyopathy in offspring of diabetic rats is associated with activation of the MAPK and apoptotic pathways, Cardiovasc. Diabetol. 8 (2009) 43.
[28] L. Jovanovic, R.H. Knopp, H. Kim, W.T. Cefalu, X. Zhu, Y.J. Lee, J.L. Simpson, A.J.L. Mills, Elevated pregnancy losses at high and low extremes of maternal glucose in early normal and diabetic pregnancy: evidence for a protective adaptation in diabetes, Diabetes Care 28 (2005) 1113–1117.
[29] A. Wyman, A.B. Pinto, R. Sheridan, K.H. Moley, One-cell zygote transfer from diabetic to nondiabetic mouse results in congenital malformations and growth retardation in offspring, Endocrinology 149 (2008) 466–469.
[30] K. Moley, M. Chi, J. Manchester, D. McDougal, O. Lowry, Alterations of intraembryonic metabolites in preimplantation mouse embryos exposed to elevated concentrations of glucose: a metabolic explanation for the developmental retardation seen in preimplantation embryos from diabetic animals, Biol. Reprod. 54 (1996) 1209–1216.
[31] R.B. Fraser, S.L. Waite, K.A. Wood, K.L. Martin, Impact of hyperglycemia on early embryo development and embryopathy: in vitro experiments using a mouse model, Hum. Reprod. 22 (2007) 3059–3068.
[32] G. Leppens-Luisier, F. Urner, D. Sakkas, Facilitated glucose transporters play a crucial role throughout mouse preimplantation embryo development, Hum. Reprod. 16 (2001) 1229–1236.
[33] R.A. Waterland, Epigenetic mechanisms and gastrointestinal development, J. Pediatr. Nutr. Gastrointest. Tract Dev. Funct. 149 (2006) S137–S142.
[34] M.E. Blewitt, N.K. Vickaryous, A. Paldi, H. Koseki, E. Whitelaw, Dynamic reprogramming of DNA methylation at an epigenetically sensitive allele in mice, PLoS Genet. 2 (2006) e49.
[35] N. Yokomori, M. Tawata, T. Onaya, DNA demethylation during the differentiation of 3T3-L1 cells affects the expression of the mouse GLUT4 gene, Diabetes 48 (1999) 685–690.
[36] A. Nikoshkov, V.G. Sunkari, O. Savu, E. Forsberg, S.-B. Catrina, K. Brismar, Epigenetic DNA methylation in the promoters of the Igf1 receptor and insulin receptor genes in db/db mice, Epigenetics 6 (2011) 405–409.
[37] S. Moshe, The early life environment and the epigenome, Biochim. Biophys. Acta (BBA) – General Subjects 1790 (2009) 878–885.
[38] J.M. Knelangen, M.B. van der Hoek, W.-C. Kong, J.A. Owens, B. Fischer, A.N. Santos, MicroRNA expression profile during adipogenic differentiation in mouse embryonic stem cells, Physiol. Genomics 43 (2011) 611–620.
[39] C.A. Loffredo, P.D. Wilson, C. Ferencz, Maternal diabetes: an independent risk factor for major cardiovascular malformations with increased mortality of affected infants, Teratology 64 (2001) 98–106.
[40] D.S. Gardner, S. Pearce, J. Dandrea, R. Walker, M.M. Ramsay, T. Stephenson, M.E. Symonds, Peri-implantation undernutrition programs blunted angiotensin II evoked baroreflex responses in young adult sheep, Hypertension 43 (2004) 1290–1296.

Biochemical and Biophysical Research Communications 420 (2012) 236–240

Contents lists available at SciVerse ScienceDirect

Biochemical and Biophysical Research Communications

journal homepage: www.elsevier.com/locate/ybbrc

Phospholamban mutants compete with wild type for SERCA binding in living cells

Simon J. Gruber, Suzanne Haydon, David D. Thomas *

Department of Biochemistry, Molecular Biology and Biophysics, University of Minnesota Medical School, Minneapolis, MN 55455, USA

ARTICLE INFO

Article history:
Received 17 February 2012
Available online 1 March 2012

Keywords:
SERCA
PLB
HEK
FRET
Competition

ABSTRACT

We have used fluorescent fusion proteins stably expressed in HEK cells to detect directly the interaction between the sarcoplasmic reticulum Ca-ATPase (SERCA) and phospholamban (PLB) in living cells, in order to design PLB mutants for gene therapy. Ca^{2+} cycling in muscle cells depends strongly on SERCA. Heart failure (HF), which contributes to 12% of US deaths, typically exhibits decreased SERCA activity, and several potential therapies for HF aim to increase SERCA activity. We are investigating the use of LOF-PLB mutants (PLB_M) as gene therapy vectors to increase SERCA activity. Active SERCA1a and WT-PLB, tagged at their N termini with fluorescent proteins (CFP and YFP), were coexpressed in stable HEK cell lines, and fluorescence resonance energy transfer (FRET) was used to detect their interaction directly. Phosphorylation of PLB, induced by forskolin, caused an increase in FRET from CFP-SERCA to YFP-PLB, indicating that SERCA inhibition can be relieved without dissociation of the complex. This suggests that a LOF mutant might bind to SERCA with sufficient affinity to complete effectively with WT-PLB, thus relieving SERCA inhibition. Therefore, we transiently expressed a series of PLB_M in the CFP-SERCA/YFP-PLB cell line, and found decreased FRET, implying competition between PLB_M and WT-PLB for binding to SERCA. These results establish this FRET assay as a rapid and quantitative means of screening PLB_M for optimization of gene therapy to activate SERCA, as needed for gene therapy in HF.

1. Introduction

The sarcoplasmic reticulum (SR) Ca-ATPase (SERCA) is an integral membrane protein that pumps Ca^{2+} from the cytosol into the SR lumen in muscle cells, thus maintaining low cytosolic [Ca^{2+}] in resting myocytes and potentiating contraction. In cardiac muscle, SERCA is inhibited at submicromolar [Ca^{2+}] by the single-pass transmembrane protein phospholamban (PLB), which can be phosphorylated to relieve SERCA inhibition [1]. Because SERCA activity or expression is reduced in many instances of heart failure (HF) [2,3], SERCA activation is a widely pursued goal for development of new therapies [3]. A gene therapy approach using rAAV to overexpress SERCA2a in heart tissue recently concluded phase II clinical trials with promising results [4], and small-molecule SERCA activators are also being sought [5]. PLB-based approaches involve overexpression of a pseudophosphorylated PLB (S16E) [6] or a protein phosphatase I inhibitor to increase the phosphorylation of PLB [7]. Here we explore expression of loss-of-function PLB mutants (PLB_M) to displace WT-PLB and activate SERCA.

Clear understanding of the mechanism by which PLB inhibits SERCA (Fig. 1A) is critical to designing an effective therapy. In the conventional model, supported by crosslinking and immunoprecipitation [8,9], SERCA inhibition can only be relieved by dissociation of PLB (“Dissociation Model”, Fig. 1A left), but recent spectroscopic studies suggest that PLB remains bound to SERCA even after activation by PLB phosphorylation or Ca^{2+} (“Subunit Model”, Fig. 1A right) [10–13]. If this model is valid, an alternative therapeutic approach is suggested – a loss-of-function PLB mutant (PLB_M), introduced by gene therapy, could relieve SERCA inhibition if it binds tightly to SERCA, thus competing with endogenous PLB (Fig. 1B). Evidence favoring this hypothesis in a reconstituted membrane system was recently published [14]. In the present study we have used fluorescent fusion proteins to detect directly the SERCA-PLB interaction in living cells. We used fluorescence microscopy to determine whether phosphorylation of YFP-PLB dissociates it from CFP-SERCA (Fig. 1A), and to measure the ability of several PLB_M to compete with YFP-PLB for CFP-SERCA binding (Fig. 1B).

2. Materials and methods

2.1. Generation of stable cell lines expressing fluorescent fusion proteins

ECFP and EYFP mammalian vectors (Clonetech), containing the monomeric A206K mutation, were fused to the N-terminus of

Abbreviations: CFP, cyan fluorescent protein; FRET, fluorescence resonance energy transfer; K_d, dissociation constant; LOF, loss of function; PKA, protein kinase A; PLB, phospholamban; PLB_M, PLB mutant; SDS, sodium dodecyl-sulfate; SERCA, sarco-endoplasmic reticulum Ca^{2+}-ATPase; SR, sarcoplasmic reticulum; WT, wild-type; YFP, yellow fluorescent protein.

* Corresponding author. Address: 312 Church St. SE, 5-290 NHH, Minneapolis, MN 55455, USA. Fax: +1 612 624 5121.
E-mail address: ddt@umn.edu (D.D. Thomas).

0006-291X/$ - see front matter © 2012 Elsevier Inc. All rights reserved.
doi:10.1016/j.bbrc.2012.02.125

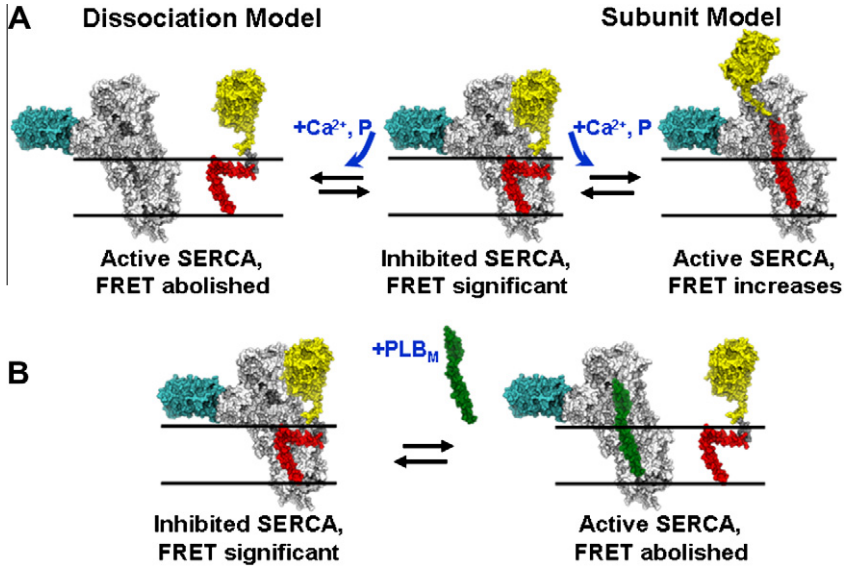

Fig. 1. SERCA inhibition relief scheme. (A) Alternative mechanisms for relief of SERCA inhibition can be distinguished by FRET from CFP-SERCA to YFP-PLB. (B) Proposed gene therapy approach, based on subunit model, is testable by FRET.

rabbit SERCA1a and canine PLB respectively. HEK293 cells (ATCC) were cultured in Dulbecco's Modified Eagle Medium (DMEM) without phenol red (Gibco/Invitrogen), supplemented with 10% fetal bovine serum (Atlanta Biologicals), at 37 °C and 10% CO_2. Cells were transiently transfected using Lipofectamine (Invitrogen), and stable cell lines were generated by G418 (Sigma) selection. Surviving clones expressing CFP-SERCA and YFP-PLB were further selected by fluorescence expression seen via fluorescence microscopy. The goal was to obtain measurable CFP fluorescence with a substantial excess of YFP over CFP.

2.2. Transient expression of non-fluorescent PLB_M for competition measurements

Mutations in WT-PLB cDNA (resulting in PLB_M in plasmid pRH132) were made using the QuickChange XLII mutagenesis kit (Agilent). PLB_M were expressed in stable CFP-SERCA/YFP-PLB cell lines using 293fectin (Invitrogen). The amount of PLB_M DNA used, volume of 293fectin, and time after transfection to maximize competition were all optimized so that PLB_M expression was within 20% of that observed for the stable expression of YFP-PLB. Final conditions in a six-well plate required 1.25 pmol DNA with 9 μL 293fectin, and photobleaching measurements were acquired 48 h after transfection.

2.3. Western blots to quantify PLB and SERCA content

Cells were pelleted and homogenized 48 h after transient transfection with PLB_M DNA or after 5 min. incubation in 40 μM forskolin [15]. Cell homogenates were run on 4–20% Tris–HCl gels (Criterion, Biorad) at 5 μg total homogenate protein along with standard curves of PLB (synthetic, WT or phosphorylated) and rabbit light SR ([16]), transferred to Immobilon-FL membranes (Millipore), and blocked for 1 h in 1x TBS/casein (Bio-rad). Primary antibodies for unphosphorylated PLB (Ab2D12, Abcam), PLB phosphorylated at S16 (Ab285, Merck), SERCA1 (IIH11, Abcam), or GFP variants (1GFP63, Abcam) were visualized using IR secondary antibodies (goat-anti-mouse or goat-anti-rabbit) from LI-COR Biosciences. Blots were scanned on the Odyssey (LI-COR Biosciences). Concentrations of PLB (phosphorylated and unphosphorylated forms) and PLB_M were determined with high accuracy using synthetic standards run on the same blots as the cell homogenates [17,18]. The slopes of standard curves were calculated from summed monomer and pentamer band intensities of three load concentrations for each standard (0.2, 0.4, and 0.8 pmol), using LI-COR Odyssey software and median, one-pixel background subtraction. Band intensities for both monomer and pentamer of YFP-PLB in cell homogenates were summed, and concentrations of both YFP-uPLB (C_U) and YFP-pPLB (C_P) were calculated by solving simultaneous equations, using the standard slopes [17,18]. X_P (the fraction of phosphorylated YFP-PLB) was then calculated by $X_P = C_P/(C_U + C_P)$ [17,18]. A GFP antibody was used to label duplicate blots of the cell homogenates and indicated that total [YFP-PLB] was unaffected by incubation with forskolin. Blots with the SERCA antibody showed that all samples used in phosphorylation experiments had essentially the same CFP-SERCA expression levels (36 ± 5 nmol SERCA/g total protein). The molar ratio of YFP-PLB to SERCA was found to be 7.8 ± 0.9, and the transient expression of PLB_M was consistently observed to be similar (7.1 ± 1.2).

2.4. Fluorescence resonance energy transfer (FRET) measurements in live HEK cells

Acceptor-selective photobleaching of cells co-expressing CFP-SERCA and YFP-PLB was done essentially as described previously [19] on an Eclipse TE200 microscope (Nikon Instruments), using CFP (excitation 430 nm/24, emission 470 nm/24) and YFP (excitation 500 nm/20, emission 535 nm/30) filters in automated filter wheels (Ludl) driven by MetaMorph software (Molecular Devices). Images were acquired using a 40x dry objective (0.55 numerical aperture), an X-Cite metal-halide lamp (EXFO), and a Cascade II CCD camera (Photometrics). A 10-ms exposure time was used in both channels with no neutral density filters, or a 100-ms exposure time was used with two neutral density filters, to reduce CFP photobleaching over the course of the experiment. Images at both emission wavelengths were then acquired at 20-s intervals before and after the start of 20-s exposures to high intensity light at YFP-specific excitation wavelengths. Photobleaching intervals were continued until YFP intensity was reduced to less than 5% of its starting value. The fractional decrease of fluorescence emission intensity of the donor (CFP-SERCA) caused by the presence of an acceptor (YFP-WT-PLB) is defined as the FRET efficiency

$E = 1 - (F_{DA}/F_D)$, where F_{DA} and F_D are the fluorescence intensities in the presence and absence of acceptor, respectively. F_{DA} was measured as the CFP intensity prior to the start of the YFP photobleach. F_D was determined by the *y*-axis intercept of the linear fit to a data plot of YFP intensity (on *x*-axis) to CFP intensity (*y*-axis) over the course of the photobleach for each cell, to account for any CFP photobleaching and incomplete YFP photobleaching [19]. FRET values were calculated for all cells in each experimental condition and averaged together to determine $FRET_{ave}$. To eliminate any changes in $FRET_{ave}$ due to differences in YFP-PLB expression levels, only cells with YFP intensities common to all experimental conditions were included in the $FRET_{ave}$ calculation.

3. Results

3.1. PLB phosphorylation

We expressed CFP-SERCA and YFP-PLB stably in HEK cells (at a molar ratio of 7.8 PLB/SERCA, to ensure saturation), then measured FRET using acceptor-selective photobleaching (Fig. 2). The control FRET value of the parent cell line was 15.4 ± 1.2%, measured repeatedly and on different days over several weeks. This stable cell line was critical to evaluating perturbations due to PLB phosphorylation or competition with PLB_M. FRET was calculated for every cell and averaged together based on initial YFP intensity.

FRET between CFP-SERCA and YFP-PLB increased significantly when PLB phosphorylation was induced by incubating the cells in forskolin (fsk), which activates the PKA pathway at adenylyl cyclase (Fig. 3A). Immunoblots from the same cells, using antibodies specific for phosphorylated and unphosphorylated PLB, verify that phosphorylation of YFP-PLB increased substantially (from 51% to 87%) after forskolin treatment (Fig. 3B). Increased FRET indicates increased SERCA-PLB association or a shorter donor–acceptor distance within the SERCA-PLB complex. If the Dissociation Model of SERCA regulation were valid, we would expect a decrease in FRET (Fig. 1A, left). Thus this data clearly supports the Subunit Model (Fig. 1A, right), in which phosphorylation changes the structure of the SERCA-PLB complex but does not dissociate it.

FRET measurements were used to calculate the distance between CFP and YFP before and after induction of PLB phosphorylation. Since FRET is a linear combination of the values for unphosphorylated (U) and phosphorylated (P) PLB, $FRET = X_U \times FRET_U + X_P \times FRET_P$, where X_P (= $1 - X_U$) is the fraction of PLB that is phosphorylated. Solving two simultaneous equations (before and after fsk), we find that the FRET values for the bound SERCA-PLB complex in the absence and presence of phosphorylation are $FRET_U = 0.07 \pm 0.02$ and $FRET_P = 0.23 \pm 0.04$. Since YFP-PLB is in large excess over CFP-SERCA, and since phosphorylation actually increases FRET, we assume that all CFP donors are participating in FRET. Assuming a single interprobe distance *R* in each case, $R = (1/FRET - 1)^{-1/6} \times 4.92$ nm, giving $R = 7.7 \pm 0.4$ nm (unphosphorylated) and 6.0 ± 0.2 nm (phosphorylated) [20]. Thus phosphorylation of PLB causes a change in the structure of the SERCA-PLB complex that decreases the CFP-YFP distance by $\Delta R = 1.7 \pm 0.6$ nm ($p < 0.01$, $n = 8$), consistent with the Subunit Model in Fig. 1A (right).

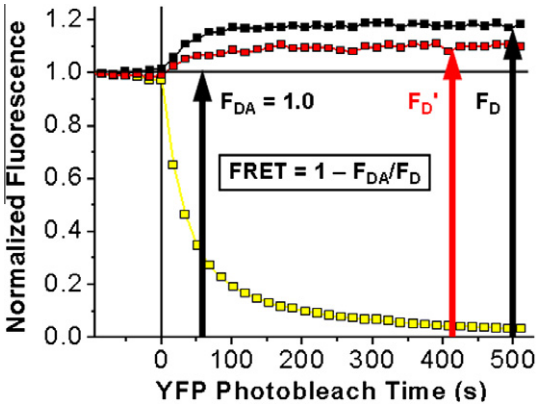

Fig. 2. FRET from CFP-SERCA to YFP-PLB in live HEK cells. Normalized fluorescense was measured for YFP (yellow) or CFP (black or red). YFP acceptors were selectively photobleached, and FRET was calculated as shown. Black: control. Red: FRET is reduced after transient expression of PLB_M. (For interpretation of the references to color in this figure legend, the reader is referred to the web version of this article.)

3.2. PLB_M competition

In contrast to the increased FRET induced by PLB phosphorylation, FRET between CFP-SERCA and YFP-PLB decreased significantly when unlabeled PLB_M was added (Fig. 2, Fig. 4). FRET measurements, following transient transfection of unlabeled PLB_M into the stable CFP-SERCA/YFP-PLB HEK cell line, showed that all PLB_M studied here compete effectively with YFP-PLB for SERCA binding, and several reduced FRET by approximately half (Fig. 4). Expression levels of YFP-PLB and PLB_M were similar, so a 50% decrease in FRET indicates that PLB_M has a SERCA affinity similar to that of YFP-PLB. Further addition of YFP-PLB or a cytosolic protein (activation-induced deaminase, AID, used as a control) did not affect FRET (Fig. 4), indicating that CFP-SERCA is saturated with YFP-PLB at the start of each competition experiment. The data in Fig. 4 were obtained from PLB variants based on the human sequence. Essentially the same results were obtained when these same mutations (WT, P21G, and S16E) were studied on the background of the monomeric AFA-PLB mutant (not shown).

Several PLB_M compete effectively with YFP-PLB, with a potency (affinity) equal to or greater than that of unlabeled WT-PLB (Fig. 4). The pseudo-phosphorylated mutant S16E, which rescues HF phenotypes in animal models when introduced via rAAV [6], is a potent competitor, reducing CFP-YFP FRET by 45%. Two other LOF PLB_M, P21G and L31A, also showed competition; this is important, since these mutants, unlike S16E, can still be phosphorylated by PKA at S16 and are thus preferable as gene therapy candidates. I40A, a superinhibitory (GOF) mutant of PLB [21], showed similar competitive potency as WT and several LOF mutants (Fig. 4).

In the competition experiments, we assume that the effect of unlabeled PLB_M is to decrease the fraction of CFP-SERCA that is bound to YFP-PLB:

$$FRET' = X_B \times FRET,$$

where FRET and FRET′ are values observed before and after transient expression of unlabeled PLB_M, and X_B is the mole fraction of CFP-SERCA that remains bound to YFP-PLB after PLB_M expression. Since the levels of YFP-PLB and PLB_M are very similar, this means that, to a good approximation,

$$K_A(PLB_M)/K_A(PLB) = FRET/FRET' - 1,$$

where K_A is the affinity ($1/K_D$) of the PLB variant for CFP-SERCA. Since most of the PLB_M tested, as well as WT-PLB, decreased FRET by about half (FRET/FRET′ = 2) (Fig. 4), each has about the same SERCA affinity as YFP-PLB. The exception is L31A, which gave FRET/FRET′ = 0.7, so its SERCA affinity is about half that of the others.

4. Discussion

We showed previously that the SERCA-PLB interaction can be measured by FRET in living cells transiently expressing fluorescent fusion proteins CFP-SERCA and YFP-PLB [22]. The present study establishes a stable cell line to make precise FRET measurements

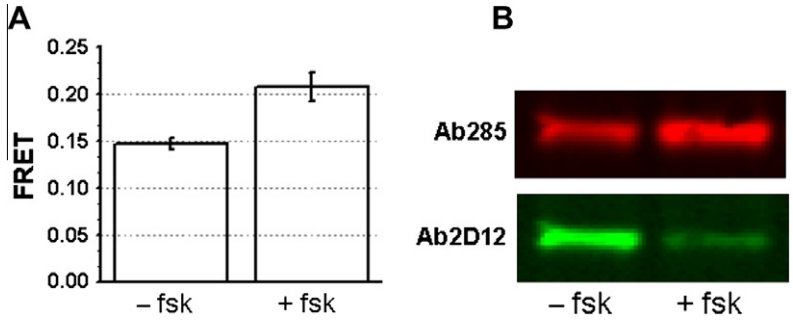

Fig. 3. Effect of PLB phosphorylation on SERCA-PLB FRET in live cells. (A) FRET in live cells, before and after 5 min incubation in 40 μM forskolin (fsk), increases from 0.15 ± 0.01 to 0.21 ± 0.02 (SEM, $n = 8$, $p < 0.01$). (B) Immunoblot of cell homogenates from (A) shows increased YFP-PLB phosphorylation, by increased Ab285 (red, specific for pPLB) and decreased Ab2D12 (green, specific for uPLB). Quantitative densitometry, using purified uPLB and pPLB standards [17], shows that phosphorylation increased from 51 ± 4% to 87 ± 5% in PLB monomer (shown) and pentamer bands. (For interpretation of the references to color in this figure legend, the reader is referred to the web version of this article.)

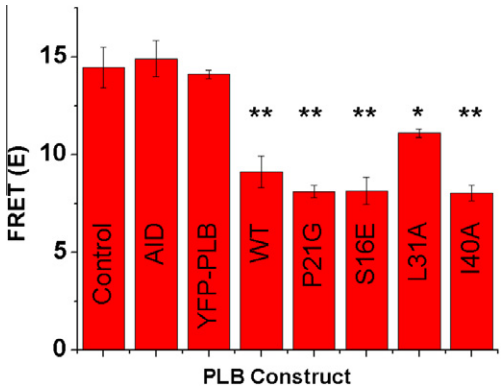

Fig. 4. FRET competition in live cells. Decreased FRET indicates that unlabeled PLB_M constructs compete effectively with YFP-PLB for binding to CFP-SERCA. $n \geqslant 3$ for each PLB_M, significant difference from control is indicated by $^{**}(p < 0.001)$ and $^{*}(p < 0.01)$.

over time (Fig. 2), making it possible to compare the effects of numerous perturbations, such as PLB phosphorylation (Fig. 3) or the introduction of unlabeled PLB_M to compete for SERCA binding (Fig. 2, Fig. 4). We used this assay to resolve several controversies regarding SERCA/PLB regulation. We found that FRET between SERCA and PLB actually increases upon phosphorylation (Fig. 3), clearly contradicting the Dissociation Model in favor of the Subunit Model (Fig. 1A). Since PLB inhibition can be relieved by phosphorylation without decreasing SERCA affinity, a loss-of-function mutation might do the same (Fig. 1B). This hypothesis was confirmed by the competition experiments, in which all mutants tested showed competition with WT-PLB for SERCA binding (Fig. 2, Fig. 4).

This system offers the potential for probing the fundamental regulatory mechanism of the SERCA-PLB system in living cells [22,23], but our main motivation is therapeutic development. This direct and rapid competition assay in HEK cells provides a platform for evaluating further PLB_M for gene therapy treatment of HF to activate SERCA (Fig. 1). The effectiveness of S16E, the pseudophosphorylated PLB_M, to compete significantly for SERCA binding in HEK cells (Fig. 4) helps explain its success as a gene therapy tool in animal models of HF [6]. Introduction of S16E-PLB into the human heart could cause chronic inotropic stimulation and is otherwise unregulated, so it is not optimal for gene therapy [24]. Better PLB_M must be developed, with intact phosphorylation sites.

L31A-PLB is a well-known LOF mutant [14], but it still competes with WT-PLB, albeit less effectively than S16E-PLB (Fig. 4), in agreement with recent FRET experiments on purified proteins [14]. The P21G mutant, designed from magnetic resonance-based structural analysis [25], provides encouraging evidence that a LOF PLB_M with an intact phosphorylation site can be just as effective as S16E (Fig. 4). Most of the PLB_M tested show similar SERCA affinity as WT-PLB, but none shows significantly tighter binding (Fig. 4). We are currently developing double mutants, combining LOF mutations with other mutations that increase SERCA affinity [25]. We envision an assortment of mutants to fine-tune SERCA activity to treat distinct HF syndromes. Our FRET competition assay in live cells provides a rapid and inexpensive method for screening potential therapeutic PLB_M mutants before they are tested in animals or humans. This FRET assay also has the potential for high-throughput screening of small molecules as potential HF drugs to activate SERCA [14,26].

Acknowledgments

We thank Razvan Cornea, Seth Robia, J. Michael Autry, John Rubin, and Gianluigi Veglia for helpful discussions, and Octavian Cornea for helping to prepare the manuscript for publication. Spectroscopy experiments were performed at the Biophysical Spectroscopy Center, University of Minnesota.

This work was supported by NIH Grants to DDT (GM27906, AR057220). SH and SJG were supported by the Minnesota Muscle Training Grant (NIH AR007612), and SJG is currently supported by a predoctoral fellowship from the American Heart Association (Midwest Affiliate 11PRE5710019).

References

[1] H.K. Simmerman, J.H. Collins, J.L. Theibert, A.D. Wegener, L.R. Jones, Sequence analysis of phospholamban. Identification of phosphorylation sites and two major structural domains, J. Biol. Chem. 261 (1986) 13333–13341.
[2] D.H. MacLennan, E.G. Kranias, Phospholamban: a crucial regulator of cardiac contractility, Nat. Rev. Mol. Cell. Biol. 4 (2003) 566–577.
[3] K.F. Frank, B. Bolck, K. Brixius, E.G. Kranias, R.H. Schwinger, Modulation of SERCA: implications for the failing human heart, Basic Res. Cardiol. 97 (Suppl 1) (2002) 172–178.
[4] M. Jessup, B. Greenberg, D. Mancini, T. Cappola, D.F. Pauly, B. Jaski, A. Yaroshinsky, K.M. Zsebo, H. Dittrich, R.J. Hajjar, Calcium upregulation by percutaneous administration of gene therapy in cardiac disease (CUPID): a phase 2 trial of intracoronary gene therapy of sarcoplasmic reticulum Ca^{2+}-ATPase in patients with advanced heart failure, Circulation 124 (2011) 304–313.
[5] G. Hasenfuss, J.R. Teerlink, Cardiac inotropes: current agents and future directions, Eur. Heart J. 32 (2011) 1838–1845.
[6] M. Hoshijima, Y. Ikeda, Y. Iwanaga, S. Minamisawa, M.O. Date, Y. Gu, M. Iwatate, M. Li, L. Wang, J.M. Wilson, Y. Wang, J. Ross Jr., K.R. Chien, Chronic suppression of heart-failure progression by a pseudophosphorylated mutant of phospholamban via in vivo cardiac rAAV gene delivery, Nat. Med. 8 (2002) 864–871.
[7] P. Nicolaou, R.J. Hajjar, E.G. Kranias, Role of protein phosphatase-1 inhibitor-1 in cardiac physiology and pathophysiology, J. Mol. Cell. Cardiol. 47 (2009) 365–371.

[8] M. Asahi, E. McKenna, K. Kurzydlowski, M. Tada, D.H. MacLennan, Physical interactions between phospholamban and sarco(endo)plasmic reticulum Ca^{2+}-ATPases are dissociated by elevated Ca^{2+}, but not by phospholamban phosphorylation, vanadate, or thapsigargin, and are enhanced by ATP, J. Biol. Chem. 275 (2000) 15034–15038.

[9] Z. Chen, B.L. Akin, L.R. Jones, Ca^{2+} binding to site I of the cardiac Ca^{2+} pump is sufficient to dissociate phospholamban, J. Biol. Chem. 285 (2010) 3253–3260.

[10] S. Negash, Q. Yao, H. Sun, J. Li, D.J. Bigelow, T.C. Squier, Phospholamban remains associated with the Ca^{2+}- and Mg^{2+}-dependent ATPase following phosphorylation by cAMP-dependent protein kinase, Biochem. J. 351 (2000) 195–205.

[11] B. Mueller, C.B. Karim, I.V. Negrashov, H. Kutchai, D.D. Thomas, Direct detection of phospholamban and sarcoplasmic reticulum Ca-ATPase interaction in membranes using fluorescence resonance energy transfer, Biochemistry 43 (2004) 8754–8765.

[12] C.B. Karim, Z. Zhang, E.C. Howard, K.D. Torgersen, D.D. Thomas, Phosphorylation-dependent conformational switch in spin-labeled phospholamban bound to SERCA, J. Mol. Biol. 358 (2006) 1032–1040.

[13] P. Bidwell, D.J. Blackwell, Z. Hou, A.V. Zima, S.L. Robia, Phospholamban binds with differential affinity to calcium pump conformers, J. Biol. Chem. 286 (2011) 35044–35050.

[14] E.L. Lockamy, R.L. Cornea, C.B. Karim, D.D. Thomas, Functional and physical competition between phospholamban and its mutants provides insight into the molecular mechanism of gene therapy for heart failure, Biochem. Biophys. Res. Commun. 408 (2011) 388–392.

[15] K. Maruyama, D.H. MacLennan, Mutation of aspartic acid-351, lysine-352, and lysine-515 alters the Ca^{2+} transport activity of the Ca^{2+}-ATPase expressed in COS-1 cells, Proc. Natl. Acad. Sci. USA 85 (1988) 3314–3318.

[16] W. Birmachu, F.L. Nisswandt, D.D. Thomas, Conformational transitions in the calcium adenosinetriphosphatase studied by time-resolved fluorescence resonance energy transfer, Biochemistry 28 (1989) 3940–3947.

[17] N.A. Ablorh, F. Nitu, K. Engebretsen, D.D. Thomas, J.S. Holger, Insulin-dependent rescue from cardiogenic shock is not mediated by phospholamban phosphorylation, Clin. Toxicol. (Phila) 47 (2009) 296–302.

[18] N.-A. Ablorh, T. Miller, F.R. Nitu, S.J. Gruber, C.B. Karim, D.D. Thomas, Accurate quantitation of phospholamban phosphorylation by immunoblot, Anal. Biochem. (2012) (accepted).

[19] J.M. Autry, J.E. Rubin, S.D. Pietrini, D.L. Winters, S.L. Robia, D.D. Thomas, Oligomeric interactions of sarcolipin and the Ca-ATPase, J. Biol. Chem. 286 (2011) 31697–31706.

[20] E.M. Kelly, Z. Hou, J. Bossuyt, D.M. Bers, S.L. Robia, Phospholamban oligomerization, quaternary structure, and sarco(endo)plasmic reticulum calcium ATPase binding measured by fluorescence resonance energy transfer in living cells, J. Biol. Chem. 283 (2008) 12202–12211.

[21] Y. Kimura, M. Asahi, K. Kurzydlowski, M. Tada, D.H. MacLennan, Phospholamban domain Ib mutations influence functional interactions with the Ca^{2+}-ATPase isoform of cardiac sarcoplasmic reticulum, J. Biol. Chem. 273 (1998) 14238–14241.

[22] S.L. Robia, K.S. Campbell, E.M. Kelly, Z. Hou, D.L. Winters, D.D. Thomas, Forster transfer recovery reveals that phospholamban exchanges slowly from pentamers but rapidly from the SERCA regulatory complex, Circ. Res. 101 (2007) 1123–1129.

[23] D.L. Winters, J.M. Autry, B. Svensson, D.D. Thomas, Interdomain fluorescence resonance energy transfer in SERCA probed by cyan-fluorescent protein fused to the actuator domain, Biochemistry 47 (2008) 4246–4256.

[24] R.G. Crystal, Cardiac gene therapy: pumping the heart, Gene Therapy 10 (2003) 2–3.

[25] K.N. Ha, N.J. Traaseth, R. Verardi, J. Zamoon, A. Cembran, C.B. Karim, D.D. Thomas, G. Veglia, Controlling the inhibition of the sarcoplasmic Ca^{2+}-ATPase by tuning phospholamban structural dynamics, J. Biol. Chem. 282 (2007) 37205–37214.

[26] J.M. Muretta, A. Kyrychenko, A.S. Ladokhin, D.J. Kast, G.D. Gillispie, D.D. Thomas, High-performance time-resolved fluorescence by direct waveform recording, Rev. Sci. Instrum. 81 (2010) 103101.

Biochemical and Biophysical Research Communications 420 (2012) 241–246

Contents lists available at SciVerse ScienceDirect

Biochemical and Biophysical Research Communications

journal homepage: www.elsevier.com/locate/ybbrc

Adhesive force behavior of single ATDC5 cells in chondrogenic culture

Yusuke Kambe, Nobumasa Hayashi, Naohide Tomita *

Department of Mechanical Engineering, Graduate School of Engineering, Kyoto University, Yoshida-honmachi, Sakyo-ku, Kyoto 606-8501, Japan

ARTICLE INFO

Article history:
Received 5 February 2012
Available online 7 March 2012

Keywords:
Cell mechanics
Cell adhesion
ATDC5 cells
Differentiation
Cell detachment test
Cytoskeleton

ABSTRACT

Cellular mechanical properties are implicated in numerous cell behaviors, but their involvement in cell differentiation process has remained unclear. Since mechanical interactions between chondrogenic cells and their surrounding environment heavily affect the maintenance of their differentiation phenotype, here, using a chondrogenic cell strain ATDC5, we evaluated cell mechanical properties (e.g., adhesive force and spring constant) and gene expression levels in differentiation culture. The adhesive force appeared to be affected by both cellular cytoskeletal and adhesive constructions. Treatment with Y27632, which accordingly inhibits actin polymerization, decreased the adhesive force while increased chondrogenic gene expressions, suggesting the both of them are interrelated via the mediation of actin cytoskeleton. However, the mechanical property did not represent chondrogenic differentiative stages as obviously as the biochemical characteristics. Meanwhile, interestingly, changes in cell distribution maps of the force in the differentiation process indicated that the cells have different levels of mechanical properties in the undifferentiated state, whereas they tend to converge when the differentiative stage is in a lull. These results reaffirm the cellular diversity during differentiation from a mechanical perspective and provide important information to the fields of generation and scaffold-based tissue regeneration, where cell–substrate adhesion plays a role.

1. Introduction

Mechanical properties of single cells are important for various cell activities, such as survival, migration, and signal transduction. Their relations to cell differentiation have also been investigated [1–4]. Darling et al. [2], with an atomic force microscopy (AFM), measured elastic and viscoelastic properties of differentiated human mesenchymal stem cells (MSCs) such as chondrocytes, osteoblasts, and adipocytes, and showed that, in spread morphology, the three types of cells exhibited significantly different mechanical characteristics. Using a micropipette aspiration technique for single cells in suspension, Yu et al. [4] demonstrated that human MSCs undergoing osteogenesis had higher Young's moduli than control MSCs. These results confirmed that cellular mechanical characteristics are involved in cell differentiation. Past studies also measured mechanical properties of cells during their differentiation [1,4] or dedifferentiation [3] process, however changes of the property in the process were neither statistically analyzed nor adequately discussed; instead the characteristic at a time point in the process was compared with that of a control group. It is thus still unclear whether mechanical properties of cells are meaningful enough to characterize cellular differentiative stages.

Articular chondrocytes, a mesenchymal lineage, function in frequently-loaded circumstances *in vivo*, and their mechanical environment strongly affect the activity of the cells even *in vitro*. For example, the maintenance of chondrogenic phenotype of chondrocytes was influenced by the elasticity of a scaffold [5]. Moreover, adherent morphologies of chondrocytes are well known to be related to their differentiation phenotype. Chondrocytes which adhere and spread well on a substrate tend to exhibit fibroblast-like shape and express more cartilage-nonspecific extracellular matrices (ECMs) like collagen type I relative to cartilage-specific ECMs like collagen type II and aggrecan, whereas chondrocytes with spherical morphology are considered to maintain the chondrogenic phenotype [6–8]. Hence mechanical interactions between chondrogenic cells and scaffolds can be involved in their differentiation. Cell–material adhesion has been mechanically evaluated by measuring force to detach cells from a substrate. However, most of these studies showed the dependency of the cell adhesive force on substrate types and/or incubation time [9–16], and few studies have focused on the relationship between mechanical cell adhesiveness and cell differentiation.

The motivation of this study is to clarify changes in mechanical properties of individual cells during chondrogenic differentiation process, focusing on cell adhesion. We used the murine chondrogenic cell line ATDC5, which is illustrative of chondrogenesis in the early stage of endochondral ossification, and the cells differentiate into chondrocytes from undifferentiated mesenchymal cells

* Corresponding author. Fax: +81 75 753 9200.
E-mail address: ntomita@chachan.mbox.media.kyoto-u.ac.jp (N. Tomita).

0006-291X/$ - see front matter © 2012 Elsevier Inc. All rights reserved.
http://dx.doi.org/10.1016/j.bbrc.2012.02.130

during *in vitro* culture [17,18]. Biochemical phenotypic changes during differentiation culture with insulin were evaluated by Alcian blue and Alizarin red S stainings and relative messenger RNA (mRNA) expression levels. Mechanical properties of single cells were measured by using a cell detachment test established previously [13,16]. In this test vertical force was applied to individual cells to pull them away from a substrate, and we obtained the adhesive force and spring constant of single ATDC5 cells. Additionally, cell morphology was observed by immunofluorescence staining of F-actin.

2. Materials and methods

2.1. ATDC5 cells and culture conditions

The murine chondrogenic cell line, ATDC5 (RCB0565), was provided by RIKEN BRC through the National Bio-Resource Project of MEXT, Japan. The cells were seeded onto either a 24-well plate (Asahi Glass Co. Ltd., Japan) or a 6-well plate (Asahi Glass Co. Ltd.) at 1.1×10^4 cells/cm^2 and cultured with DMEM/F12 (a mixture of Dulbecco's modified Eagle's medium and Ham's F12 medium) (Sigma–Aldrich Co., USA) containing 5% heat-inactivated fetal bovine serum (FBS) (Nacalai Tesque Inc., Japan) and 1% antibiotic mixture (10,000 units/ml penicillin, 10 mg/ml streptomycin, and 25 μg/ml amphotericin B) (Nacalai Tesque Inc.) at 37 °C in a humidified atmosphere of 95% air and 5% CO_2. This medium, which shall be referred to as the maintenance medium, was changed every 2 days. Once the cells became confluent (on day 4 after seeding), the maintenance medium was replaced with fresh maintenance medium supplemented with 1% ITS mixture (1 mg/ml insulin, 550 μg/ml transferrin, and 670 ng/ml sodium selenite) (Invitrogen Corp., USA) to induce differentiation in chondrocyte-like cells [18]. This medium, which shall be referred to as the differentiation medium, was changed every 2 days.

2.2. Real-time PCR analysis

ATDC5 cells cultured on a 6-well plate were washed twice with ice-cold phosphate-buffered saline (PBS) (Nacalai Tesque Inc.) after 3, 7, 10, 14, or 17 days in culture. Total RNA was then extracted from the cells using a TriPure Isolation Reagent (Roche Diagnostics, Germany) and a High Pure RNA Tissue Kit (Roche Diagnostics). Complementary DNA (cDNA) was synthesized by reverse-transcription polymerase chain reaction (PCR) using a Transcriptor First Strand cDNA Synthesis Kit (Roche Diagnostics) and a thermal cycler (PC-320, Astec Co. Ltd., Japan). Three different samples were used ($n = 3$).

Quantitative real-time PCR was performed using a LightCycler® FastStart DNA Master^{PLUS} SYBR Green I (Roche Diagnostics), and SYBR Green PCR amplification and real-time fluorescence detection were performed using the LightCycler® ST300 (Roche Diagnostics). Primers (Sigma–Aldrich Co., USA) were designed for β-actin, sex determining region Y-box containing gene 9 (Sox9), aggrecan, collagen type II αI chain, and collagen type X αI chain, where β-actin was used as a house-keeping gene. The primer sequences are shown in Table S1.

2.3. Evaluation of mechanical properties of single ATDC5 cells

After culturing for 3, 7, 10, 14, or 17 days on a 24-well plate, ATDC5 cells were removed from the plate by mixing with 0.25% trypsin/1 mM EDTA (Nacalai Tesque Inc.) and washed twice with PBS. The cells were seeded onto a fibronectin-coated ultra-thin glass plate (45 × 1.5 mm; thickness, 30 μm; Young's modulus, 71.4 GPa) (Matsunami Glass Ind. Ltd., Japan) at 3.1×10^3 cells/cm^2 and incubated with the maintenance medium at 37 °C in a humidified atmosphere of 95% air and 5% CO_2 for 6 h. After incubation, the cell detachment test was done as described previously [13,16]. Briefly, the ultra-thin glass plate seeded with ATDC5 cells was fixed to a holder and completely submerged into a chamber filled with a mixture of phenol red-free L-15 medium (Invitrogen Corp.), 5% FBS, and 1% antibiotic mixtures, pre-warmed to 37 °C. The plate acted as a cantilever, and a micropipette aspirator was used to capture a single cell adhering to the substrate. The cell was then detached by pulling the micropipette at a constant rate of 5 μm/s using a motorized single-axis stage (KS101-20HD, Suruga Seiki Co. Ltd., Japan). The detachment process was observed through a video microscope (DG-2, Scalar Co., Japan) connected to a time-lapse video capture board able to acquire 29.97 frames per second (GV-MVP/RX3, I-O Data Device Inc., Japan). This measurement was performed at room temperature (RT). The fibronectin substrate was prepared as described in Section S1.3. The number of measurements at 3, 7, 10, 14, and 17 days of culture was $n = 26$, 29, 24, 28, and 22, respectively.

Each digital frame of the detachment animation was analyzed by lab specific image analysis software. Using this software, the 32-bit image was transformed into 8-bit grayscale according to the National Television System Committee coefficients, and digitized with a threshold based on the Otsu method [19]. Then, the position of the ultra-thin glass plate at the cell was determined. By analyzing the digital frames of the detachment process, we obtained a time–deflection curve like the one shown in Fig. S1A.

The reaction force of a leaf spring at the cell ($F(t)$) was given by $F(t) = 3IEL^{-3}\omega(t)$, where t is the measurement time from when pulling began, I is the moment of inertia of the sectional area of the glass plate, E is the Young's modulus of the glass plate, L is the length from the fixed edge of the leaf spring to the cell, and $\omega(t)$ is the deflection at L at t. Cell adhesive force (F_{ad}) was defined and calculated using the maximum deflection.

The displacement of the micropipette in the tensile direction at the time t ($\Delta x_{pipette}(t)$) was calculated by $\Delta x_{pipette}(t) = vt$, where v was the pulling velocity (5 μm/s). The elongation of the cell in the detachment process at the time t ($\Delta h(t)$) was given by $\Delta h(t) = \Delta x_{pipette}(t) - \omega(t)$, and a cell elongation–force curve, similar to the one shown in Fig. S1B, was obtained. The apparent spring constant of the cell (k_{cell}) was defined by fitting a straight line from the origin to the maximum-force point on the curve.

2.4. Y27632 treatment to ATDC5 cells

The ATDC5 cells were seeded onto either a 24-well plate or a 6-well plate and cultured with the maintenance medium as described in Section 2.1. On day 4 in culture, the maintenance medium was replaced with the differentiation medium supplemented with 10 μM Y27632 (Wako Pure Chemical Industries Ltd., Japan), which is a Rho-associated protein kinase (ROCK) inhibiter. The medium and the inhibitor were changed every 2 days.

On day 7 after seeding, the real-time PCR analysis, immunofluorescence staining of F-acitn, and cell detachment test were conducted as described in Sections S1.3, 2.2, and 2.3, respectively. The number of measurements was $n = 3$ (gene expression levels) and 13 (mechanical properties).

2.5. Statistical analysis

Data on the mechanical properties of single cells were not always normally distributed according to the Shapiro–Wilks test and were log-transformed before statistical analysis. Quantitative data on the gene expression level, cell adhesive force, and cell spring constant were analyzed using one-way ANOVA followed by Tukey or Tukey–Kramer post hoc comparisons as appropriate.

Effects of the Y27632 treatment on the gene expression levels and mechanical properties were analyzed by two-sided Student's *t*-test. A value of $p < 0.05$ was considered significant.

3. Results

3.1. mRNA expression levels

Fig. 1 shows the changes in mRNA expression levels for Sox9, aggrecan, and collagens type II and type X over the culture period, with all measurements normalized to the expression level at the baseline (3 days). Expression levels of chondrogenic marker genes (Sox9, aggrecan, and collagen type II) exhibited similar time evolutions. They tended to increase with culture time and peaked at 14 days, when the levels were significantly higher than the previous period. Sox9 and aggrecan gene expressions on day 17 were statistically greater than those on days 3, 7, and 10. The gene expression level of collagen type X, which is hypertrophic and calcified chondrocyte-specific [20,21], increased with time in culture. This temporal change was different from those of the other genes in this study. In particular, the collagen type X gene expression on day 17 was significantly higher than the previous time points.

3.2. Mechanical properties of single ATDC5 cells

The time-dependent changes in the adhesive force and spring constant of single ATDC5 cells are shown in Fig. 2. Both characteristics did not fluctuate during 3 and 10 days in culture, but experienced a negative peak on day 14, when the mechanical properties were statistically lower than those on days 3 and 7. In Fig. 2C, the values for the spring constant of each cell were plotted against the adhesive force of the cell to examine their relationships. The correlation coefficient for them was 0.42.

Distributions of the adhesive force at each time point were shown in Fig. 3. Vertical axis represents the probability of observations, which is calculated by dividing the number of population in a certain range of the mechanical property by the total number of observations. The ATDC5 cells showed an almost even distribution of the adhesive force ranged from 0 to 250 nN at 3 days. As culture time advanced, the distribution range tended to be narrower, showing a peak around 100 nN. Especially, on day 14, about 80% of cells exhibited adhesion force lower than 100 nN. However, the cells at 17 days represented broad distributions of the force like day 3. Similar tendencies were observed in cell distribution maps of the cell spring constant (Fig. S4).

3.3. Effects of the Y27632 treatment

The representative images of F-actin, gene expressions, and mechanical properties of ATDC5 cells with (Y27632) or without (Control) the Y27632 treatment are shown in Fig. 4. On day 7, more defibrinated actin filaments were observed in the cells of the Y27632 group, compared to the Control group. The treatment with Y27632 increased the gene expression levels, showing significant differences in the levels of the chondrogenic marker genes, while both the adhesive force and spring constant of individual ATDC5 cells were remarkably decreased by the treatment.

4. Discussion

Mechanical properties of cells have been quantified through a variety of techniques. In this study, the adhesive force and spring constant of single ATDC5 cells were measured by detaching the cells vertically from a substrate. Both characteristics showed a similar time evolution, suggesting that they were temporally affected by same factors. One of them can be cellular internal construction

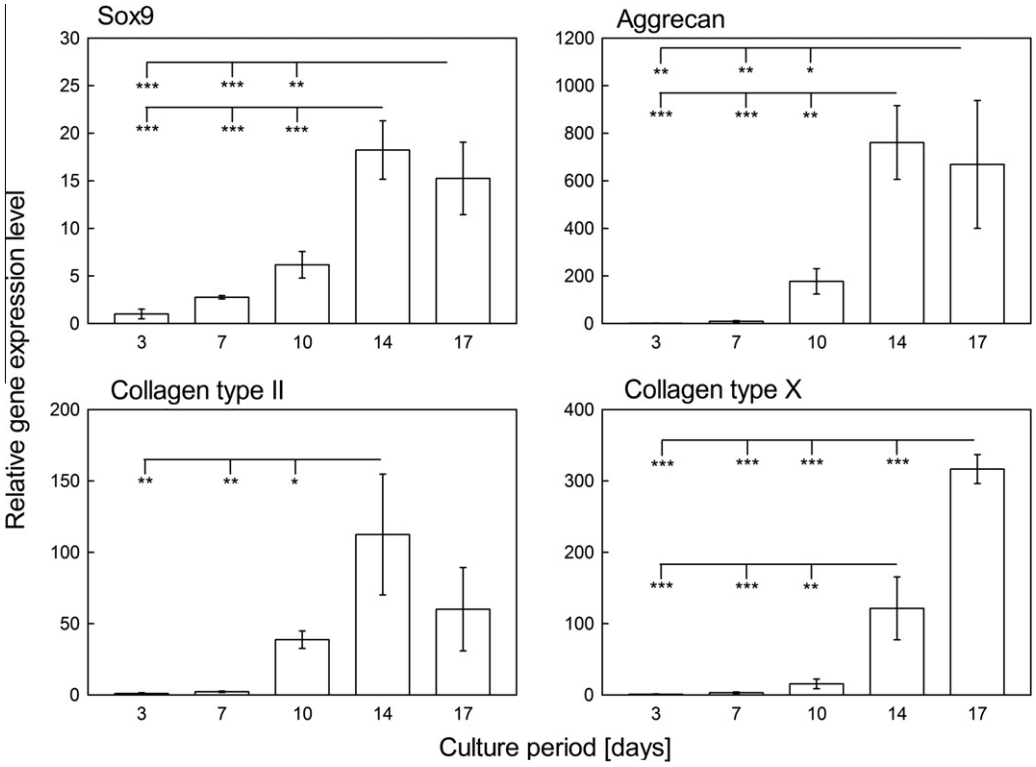

Fig. 1. Temporal changes in relative mRNA expression levels of Sox9, aggrecan, and collagens type II and type X in ATDC5 cells cultured on a 6-well plate normalized to the expression level at baseline (3 days). Data is shown in the form: mean ± SD. Asterisks indicate significant differences ($^{*}p < 0.05$, $^{**}p < 0.01$, $^{***}p < 0.001$; post hoc comparisons, following to one-way ANOVA).

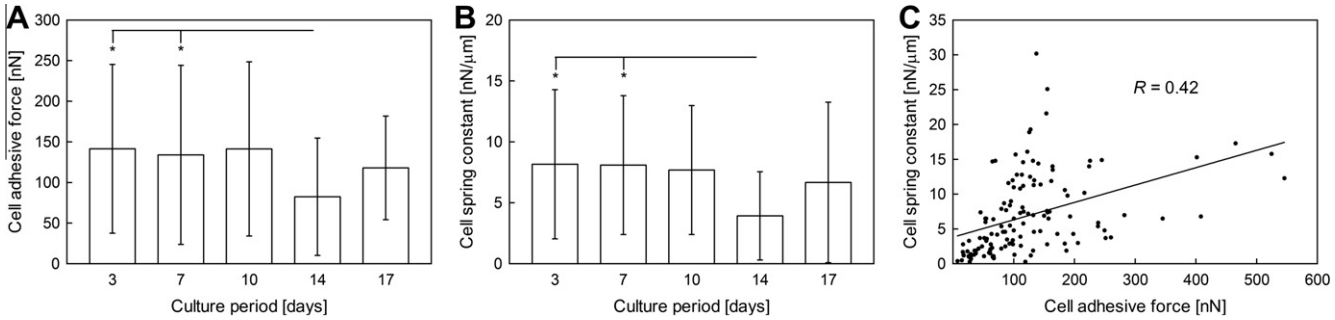

Fig. 2. Time-dependent transitions in the adhesive force (A) and spring constant (B) of single ATDC5 cells trypsinized and incubated on fibronectin for 6 h after culturing for 3, 7, 10, 14, and 17 days. Data is shown in the form: mean ± SD. Asterisks indicate significant differences ($^*p < 0.05$; post hoc comparisons, following to one-way ANOVA). Spring constant of each ATDC5 cell was represented as a function of cell adhesive force (C). Line fitting was done using liner approximation method. *R*: correlation coefficient. Dot number = 129.

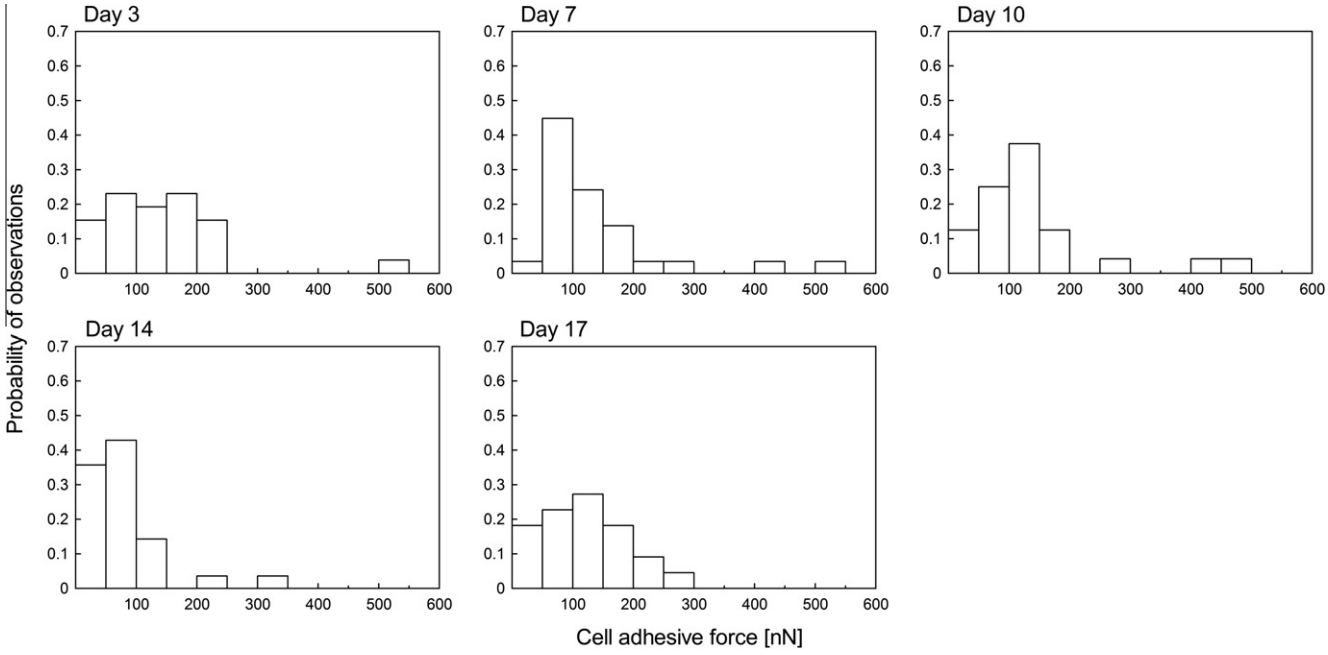

Fig. 3. Cell distribution map of the adhesion force on days 3, 7, 10, 14, and 17.

since cytoskeletal structures are well known to affect cell stiffness [22,23] and cell adhesive force to a substrate [10,11,13–15]. Our results also showed that the ATDC5 cells typically exhibited a spherical shape with immature actin fibers on day 14 (Fig. S3), when the mechanical properties were the lowest. More directly, the treatment with a ROCK inhibitor Y27632, which eventually inhibits actin polymerization [24,25], statistically decreased both the adhesive force and the spring constant. However, the two properties of each cell did not have a strong correlation. With respect to the adhesive force, the formation of focal adhesions, derived from bindings between transmembrane cell-adhesive molecules (e.g., integrins) and extracellular ligands (e.g., Arg-Gly-Asp sequences), is reported to have a strong impact [9,12–16]. For example, the blocking of an integrin subunit by its antibody significantly weakened the adhesive force of fibroblasts [14], and the expression of focal adhesion kinase (FAK), which is a member to construct a focal adhesion, strengthened the force [12]. As integrins bind to actin cytoskeleton, mediated by anchor molecules like FAK, cell-adhesive constructions can mutually affect the adhesive force with the cytoskeletal architecture. This might lead the weak correlation of the adhesive force with the spring constant, which appears to mainly include the information about cytoskeletal structures.

Cells in long-term cultures are affected not only by putative differentiation process but also by processes as e.g., contact inhibition. These processes do not necessarily have to influence the differentiation of the ATDC5 cells but can heavily change the actin cytoskeleton and cell adhesion. However, in terms of the chondrogenic differentiation, it has been shown that Sox9 expression and activity are regulated by actin organization [26,27]. Woods et al. [26] reported that the RhoA-induced development of actin stress fibers suppressed Sox9 gene expression, while the inhibition of RhoA/ROCK signaling by Y27632 led a cortical actin architecture and enhanced Sox9 gene expression. Our results also demonstrated that the vigorous inhibition of actin polymerization by Y27632 not only weakened the adhesive force but also promoted the chondrogenic gene expressions of the ATDC5 cells on day 7, even when the effects of contact inhibition-induced changes in cellular structures are considered to be comparatively small. Therefore, changes in the constructions of cytoskeleton and cell adhesion can affect both the mechanical properties and differentiation of the ATDC5 cells. This result also suggests the involvement of mechanical cell adhesiveness in chondrogenic differentiation, mediated by the cellular structure.

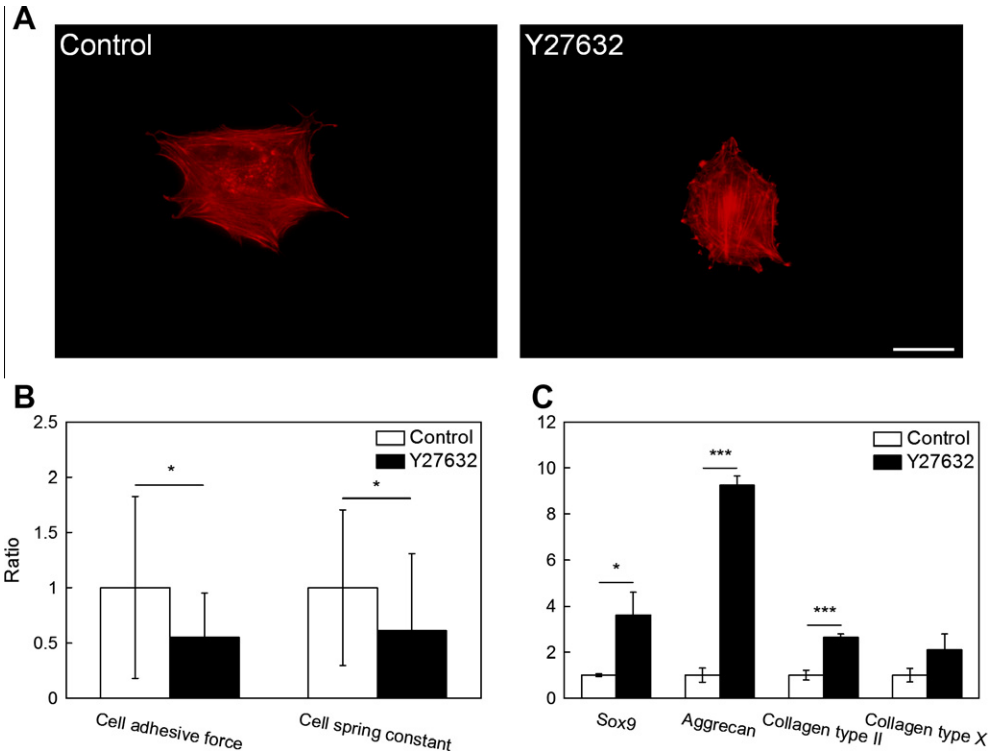

Fig. 4. Effects of the treatment with Y27632 on properties of ATDC5 cells. Immunofluorescence staining of F-actin in a cell incubated on a fibronectin substrate for 6 h after culturing for 7 days (A). Scale bar = 20 μm. Relative adhesive force and spring constant of single ATDC5 cells trypsinized and incubated on fibronectin for 6 h after culturing for 7 days normalized to the value at baseline (Control) (B). Relative gene expression levels of Sox9, aggrecan, and collagens type II and type X in the cells cultured on a 6-well plate for 7 days normalized to the expression level at baseline (Control) (C). Data is shown in the form: mean ± SD. Asterisks indicate significant differences ($^{*}p < 0.05$, $^{***}p < 0.001$; two-sided Student's *t*-test).

From these observations, we inferred that the differentiation-dependent changes in the adhesive force of individual ATDC5 cells were evaluated in this study. The photographs of Alcian blue staining exhibited that the ATDC5 cells gradually produced sulfate glycosaminoglycan as the chondrogenic culture advanced (Fig. S2). Additionally, quantitative real-time PCR analysis showed that chondrogenic gene expression levels (Sox9, aggrecan, and collagen type II) maintained an upward trend during 3 and 14 days, showing a strong increase from days 10 to 14. However, they tended to decrease between 14 and 17 days in culture. In contrast, hypertrophic and calcific marker gene expression (collagen type X) kept increasing throughout the culture period. These results are consistent with those reported elsewhere [28,29]. Taking these facts into account, it is suggested that the ATDC5 cells mainly differentiated into chondrocytes from anaplastic cells until day 14 and then to hypertrophic and calcified chondrocytes between 14 and 17 days in this study. This suggestion is also supported by the result of Alizarin red S staining because calcium deposition were observed at day 14 and the mineralization progressed to day 17 (Fig. S2).

Under these differentiation processes, changes in the adhesive force of single ATDC5 cells were examined. Chondrocyte-like cells (day 14) had a significantly lower adhesive force than the cells on the way to the differentiation into chondrcoytes (days 3 and 7). However, the force did not fluctuate between 3 and 10 days in spite of the increasing tendency of the chondrogenic marker genes in that period. Additionally, no statistical differences in the mechanical characteristic were detected between days 10 and 14, when the gene expressions increased dramatically. On the other hand, focusing on the time evolution of the cell distribution map of the adhesive force, the distribution tended to become narrower and its peak appeared to shift toward lower value as the cells differentiated into chondrocytes from anaplastic mesenchymal cells between days 3 and 14. The force then got to range widely again with the progression of hypertrophy and calcification from 14 to 17 days. These temporal tendencies were also observed in the distribution of the cell spring constant (Fig. S4). Thus the cells could have various levels of mechanical properties in undifferentiated and transitional states, whereas they tended to show comparatively-unified degree of the properties when the differentiation process is in a lull. The results shown by Darling et al. [2] may also support this suggestion. Using an AFM, they demonstrated that human MSCs, chondrocytes, and osteoblasts had elasticity distributions similar to the adhesive force distributions of the ATDC5 cells on days 3, 14, and 17, respectively.

The results of this study suggest that, when evaluated as a bulk, the mechanical adhesiveness of single ATDC5 cells do not reflect chondrogenic differentiation process as clearly as cellular biochemical properties such as gene expressions. However, the mechanical characteristics of the cells had large population variations and were not necessarily normally distributed, suggesting that subpopulations of cells with different properties existed as Darling et al. [2] mentioned previously. In fact, individual ATDC5 cells are unequal in chondrogenic culture because their chondrogenic differentiation is performed with the formation of cartilage nodules [17,18]. Therefore, with the recognition that cells have diversity, the mechanical characteristic can be useful to pursue differentiation stages; the phase of chondrogenic differentiation appears to be featured by the range and peak of cell distribution of the adhesive force. Furthermore, these findings can provide the significance of mechanical interactions between individual cells and their surrounding environment in the fields of generation and scaffold-based tissue regeneration, where cell–substrate adhesion plays a role.

Acknowledgments

The authors would like to thank the Kyoto University-Venture Business Laboratory for the use of their experimental laboratory. This study was supported by Agri-Health Translational Research Project (Ministry of Agriculture, Forestry and Fisheries of Japan).

Appendix A. Supplementary data

Supplementary data associated with this article can be found, in the online version, at doi:10.1016/j.bbrc.2012.02.130.

References

[1] A.M. Collinsworth, S. Zhang, W.E. Kraus, G.A. Truskey, Apparent elastic modulus and hysteresis of skeletal muscle cells throughout differentiation, Am. J. Physiol. Cell Physiol. 283 (2002) C1219–C1227.
[2] E.M. Darling, M. Topel, S. Zauscher, P.V. Thomas, F. Guilak, Viscoelastic properties of human mesenchymally-derived stem cells and primary osteoblasts, chondrocytes, and adipocytes, J. Biomech. 41 (2008) 454–464.
[3] E.M. Darling, P.E. Pritchett, B.A. Evans, R. Superfine, S. Zauscher, F. Guilak, Mechanical properties and gene expression of chondrocytes on micropatterned substrates following dedifferentiation in monolayer, Cell. Mol. Bioeng. 2 (2009) 395–404.
[4] H. Yu, C.Y. Tay, W.S. Leong, S.C.W. Tan, K. Lio, L.P. Tan LP, Mechanical behavior of human mesenchymal stem cells during adipogenic and osteogenic differentiation, Biochem. Biophys. Res. Commun. 393 (2010) 150–155.
[5] E. Schuh, J. Kramer, J. Rohwedel, H. Notbohm, R. Müller, T. Gutsmann, N. Rotter, Effect of matrix elasticity on the maintenance of the chondrogenic phenotype, Tissue Eng. Part A 16 (2010) 1281–1290.
[6] K. von der Mark, V. Gauss, H. von der Mark, P. Müller, Relationship between cell shape and type of collagen synthesised as chondrocytes lose their cartilage phenotype in culture, Nature 267 (1977) 531–532.
[7] P.D. Benya, J.D. Shaffer, Dedifferentiated chondrocytes reexpress the differentiated collagen phenotype when cultured in agarose gels, Cell 30 (1982) 215–224.
[8] K.R. Brodkin, A.J. García, M.E. Levenston, Chondrocyte phenotypes on different extracellular matrix monolayers, Biomaterials 25 (2004) 5929–5938.
[9] A. Yamamoto, S. Mishima, N. Maruyama, M. Sumita, Quantitative evaluation of cell attachment to glass, polystyrene, and fibronectin- or collagen-coated polystyrene by measurement of cell adhesive shear force and cell detachment energy, J. Biomed. Mater. Res. 50 (2000) 114–124.
[10] G. Hoben, W. Huang, B.S. Thoma, R.G. LeBaron, K.A. Athanasiou, Quantification of varying adhesion levels in chondrocytes using the cytodetacher, Ann. Biomed. Eng. 30 (2002) 703–712.
[11] W. Huang, B. Anvari, J.H. Torres, R.G. LeBaron, K.A. Athanasiou, Temporal effects of cell adhesion on mechanical characteristics of the single chondrocyte, J. Orthop. Res. 21 (2003) 88–95.
[12] C.C. Wu, H.W. Su, C.C. Lee, M.J. Tang, F.C. Su, Quantitative measurement of changes in adhesion force involving focal adhesion kinase during cell attachment, spread, and migration, Biochem. Biophys. Res. Commun. 329 (2005) 256–265.
[13] K. Yamamoto, N. Tomita, Y. Fukuda, S. Suzuki, N. Igarashi, T. Suguro, Y. Tamada, Time-dependent changes in adhesive force between chondrocytes and silk fibroin substrate, Biomaterials 28 (2007) 1838–1846.
[14] N. Cai, C.C. Wong, S.C.W. Tan, V. Chan, K. Liao, Temporal effect of functional blocking of β_1 integrin on cell adhesion strength under serum depletion, Langmuir 25 (2009) 10939–10947.
[15] Y. Kambe, K. Yamamoto, K. Kojima, Y. Tamada, N. Tomita, Effects of RGDS sequence genetically interfused in the silk fibroin light chain protein on chondrocyte adhesion and cartilage synthesis, Biomaterials 31 (2010) 7503–7511.
[16] Y. Kambe, Y. Takeda, K. Yamamoto, K. Kojima, Y. Tamada, N. Tomita N, Effect of RGDS-expressing fibroin dose on initial adhesive force of a single chondrocyte, Biomed. Mater. Eng. 20 (2010) 309–316.
[17] T. Atsumi, Y. Ikawa, Y. Miwa, K. Kimata, A chondrogenic cell line derived from a differentiating culture of AT805 teratocarcinoma cells, Cell Differ. Dev. 30 (1990) 109–116.
[18] C. Shukunami, C. Shigeno, T. Atsumi, K. Ishizeki, F. Suzuki, Y. Hiraki, Chondrogenic differentiation of clonal mouse embryonic cell line ATDC5 in vitro: differentiation-dependent gene expression of parathyroid hormone (PTH)/PTH-related peptide receptor, J. Cell Biol. 133 (1996) 457–468.
[19] N. Otsu, A threshold selection method from gray-level histograms, IEEE Trans. Syst. Man Cybern. B: Cybern. 9 (1979) 62–66.
[20] P. Castagnola, B. Dozin, G. Moro, R. Cancedda, Changes in the expression of collagen genes show two stages in chondrocyte differentiation in vitro, J. Cell Biol. 106 (1988) 461–467.
[21] L.C. Gerstenfeld, W.J. Landis, Gene expression and extracellular matrix ultrastructure of a mineralizing chondrocyte cell culture system, J. Cell Biol. 104 (1991) 1435–1441.
[22] K. Nagayama, Y. Nagano, M. Sato, T. Matsumoto, Effect of actin filament distribution on tensile properties of smooth muscle cells obtained from rat thoracic aortas, J. Biomech. 39 (2006) 293–301.
[23] S.C.W. Tan, W.X. Pan, G. Ma, N. Cai, K.W. Leong, K. Liao, Viscoelastic behaviour of human mesenchymal stem cells, BMC Cell Biol. 9 (2008) 40.
[24] M. Hirose, T. Ishizaki, N. Watanabe, M. Uehata, O. Kranenburg, W.H. Moolenaar, F. Matsumura, M. Maekawa, H. Bito, S. Narumiya, Molecular dissection of the Rho-associated protein kinase (p160ROCK)-regulated neurite remodeling in neuroblastoma N1E-115 cells, J. Cell Biol. 141 (1998) 1625–1636.
[25] M. Maekawa, T. Ishizaki, S. Boku, N. Watanabe, A. Fujita, A. Iwamatsu, T. Obinata, K. Ohashi, K. Mizuno, S. Narumiya, Signaling from Rho to the actin cytoskeleton through protein kinases ROCK and LIM-kinase, Science 285 (1999) 895–898.
[26] A. Woods, G. Wang, F. Beier, RhoA/ROCK signaling regulates Sox9 expression and actin organization during chondrogenesis, J. Biol. Chem. 280 (2005) 11626–11634.
[27] D. Kumar, A.B. Lassar, The transcriptional activity of Sox9 in chondrocytes is regulated by RhoA signaling and actin polymerization, Mol. Cell. Biol. 29 (2009) 4262–4273.
[28] B. Newman, L.I. Gigout, L. Sudre, M.E. Grant, G.A. Wallis, Coordinated expression of matrix Gla protein is required during endochondral ossification for chondrocyte survival, J. Cell Biol. 154 (2001) 659–666.
[29] T.D. Challa, Y. Rais, E.M. Ornan, Effect of adiponectin on ATDC5 proliferation, differentiation and signal pathways, Mol. Cell. Endocrinol. 323 (2010) 282–291.

Biochemical and Biophysical Research Communications 420 (2012) 247–252

Contents lists available at SciVerse ScienceDirect

Biochemical and Biophysical Research Communications

journal homepage: www.elsevier.com/locate/ybbrc

LIMK2d, a truncated isoform of Lim kinase 2 regulates neurite growth in absence of the LIM kinase domain

Julie Tastet [a,b], Patrick Vourc'h [a,d,*], Frédéric Laumonnier [a], Béatrice Vallée [b], Caroline Michelle [a], Anne Duittoz [c], Hélène Bénédetti [b], Christian R. Andres [a,d]

[a] UMR INSERM U930, CNRS ERL 3106, Université François Rabelais, Tours, France
[b] CNRS UPR 4301, CBM, Orléans, France
[c] UMR 6175 INRA, CNRS, Haras Nationaux, Nouzilly, France
[d] Laboratoire de Biochimie et Biologie moléculaire, CHRU de Tours, 2, Bd Tonnellé, 37044 Tours, France

ARTICLE INFO

Article history:
Received 20 February 2012
Available online 3 March 2012

Keywords:
LIMK2
Alternative splicing
Neurite outgrowth

ABSTRACT

Lim kinase 2 isoforms, LIMK2a and LIMK2b, phosphorylate cofilin leading to remodeling of actin cytoskeleton during neuronal differentiation. The expression and function of the LIMK2d isoform, missing the kinase domain, remain unknown. We analyzed the expression of LIMK2 splice variants in adult rat brain and in cultures of rat neural stem cells by RT-QPCR. All three splice variants were expressed in adult cortex, hippocampus and cerebellum. *Limk2a* and *Limk2d* expression, but not *Limk2b*, increased during neuronal differentiation. We studied the localization and function of LIMK2d isoform by transfecting Hela, NSC-34, and hippocampal rat neuron cultures. Similarly to LIMK2b, LIMK2d was expressed in the cytoplasm, neurites and dendritic spines, but not in the nucleus. Similarly to LIMK2a, LIMK2d over-expression in NSC-34 cells increased neurite length, but independently of cofilin phosphorylation or of direct interaction with actin. Overall, these results indicate that LIMK2d is a third LIMK2 isoform which regulates neurite extension and highlights the possible existence of a kinase independent function of LIMK2.

1. Introduction

Remodeling of actin cytoskeleton is a key mechanism for neuritogenesis and synaptogenesis [1,2]. The Rho-GTPases pathway controls this mechanism. It involves the small GTP-binding proteins Rac, Cdc42 and Rho, and their downstream effectors PAK1–4 and ROCK1–2 (For review [3]). These effectors phosphorylate Lim kinase 1 (LIMK1) and Lim kinase 2 (LIMK2) which inactivate by phosphorylation the cofilin/actin depolymerisation factor (ADF) leading to reduced actin depolymerisation [4,5]. Abnormalities in regulation of actin dynamics resulting from mutation in genes encoding regulators and effectors of Rho-GTPase family members have been implicated in cognitive deficits and mental retardation [6].

LIMK1 and LIMK2, the unique members of the LIM kinase family, display 50% of identity [7]. Most of the studies performed to date on the neuronal function of LIM kinases have been performed on LIMK1 [8–10]. In the central nervous system (CNS), the *LIMK2* gene (22q12.2) encodes two isoforms of high molecular weights known as LIMK2a (72 kDa) and LIMK2b (70 kDa) [11–14]. LIMK2a and LIMK2b contain two LIM domains, one PDZ domain and one serine/threonine kinase domain. They are both phosphorylated by the ROCK effectors and phosphorylate cofilin [4,15,16].

Immunohistochemistry analysis showed LIMK2 expression in several regions in the developing central nervous system (CNS), and particularly in the spinal cord and the olfactory bulb. In the adult CNS, high expression of LIMK2 was observed in neurons of the hippocampus and cerebral cortex, and in the Purkinje cells of the cerebellum [14]. Abnormalities in LIMK2 expression, such as single knockdown of *Limk2* in cultured dorsal root ganglia (DRG) neurons, is associated with decreased rate of growth cone extension [17]. Moreover double *Limk1*/*Limk2* knockout mice showed more severe impairment of synaptic function than *Limk1* KO mice [18]. These observations support a role for LIMK2 isoforms in CNS development and in cognitive processes. A third splice variant of LIMK2,

Abbreviations: bFGF, basic fibroblast growth factor; DRG, dorsal root ganglia; EGF, epidermal growth factor; GAPDH, glyceraldehyde-3-phosphate dehydrogenase; IP, immunoprecipitated proteins; LIM, Lin-11, Isl-1, Mec-3; LIMK, LIM kinase; LTP, long term potentiation; NGF, nerve growth factor; NSC, neural stem cells; PAK, p-21 activated kinase; PDLIM5, PDZ and LIM domain protein 5; PDZ, PSD-95, Dlg, ZO-1; PKC, protein kinase C; PVDF, polyvinylidene fluoride; ROCK, Rho associated protein kinase; RT-QPCR, reverse transcription-quantitative real-time PCR; SDS, sodium dodecyl sulfate; SN, supernatant.

* Corresponding author at: UMR INSERM U930, CNRS ERL 3106, Université François Rabelais, Tours, France. Fax: +33 2 47 36 61 85.
E-mail address: vourch@med.univ-tours.fr (P. Vourc'h).

0006-291X/$ - see front matter © 2012 Elsevier Inc. All rights reserved.
http://dx.doi.org/10.1016/j.bbrc.2012.02.134

named LIMK2d, was isolated from a rat brain cDNA library [19] but never studied. The sequence of this isoform predicts a truncated LIM domain, a truncated PDZ domain and lacks the serine/threonine kinase domain present in LIMK2a and LIMK2b. We analyzed the expression and function of this LIMK2d isoform in neurons.

2. Materials and methods

2.1. Cell cultures

Primary cultures of rat neural stem cells (NSC) from E14 rat embryos were obtained as previously described [20]. After 7 days of culture, the neurospheres were transferred in poly-D-lysine (25 μg/mL) (Sigma–Aldrich®, St. Louis, MO) coated plates containing Neurobasal-A with N2 supplement, 2 mM L-glutamine, 20 ng/mL bFGF, 100 U/mL penicillin and 100 μg/mL streptomycin. Two days after, removal of bFGF and addition of 10 ng/mL of nerve growth factor (NGF 2.5 S) promoted neuronal differentiation. Primary cultures of hippocampal neurons from E17 rat embryos were adapted from Laumonnier et al. (2010) [21]. Cells were cultured during 17 days at a density of 30,000 cells/cm^2. At 17 days of culture, neurons were stimulated during 5 min with a solution containing 20 mM NaCl, 5.4 mM KCl, 1.8 mM $CaCl_2$, 25 mM Tris–HCl (pH = 7.4), 15 mM glucose, 50 μM *N*-methyl-D-Aspartate and 10 μM glycine.

NIH/3T3 cells (European Collection of Cell cultures, Salisbury, UK) and HeLa cells (TeBu-Bio, Le Perray en Yvelines, France) were cultured in Dulbecco's Modified Eagle Medium (DMEM) with Glutamax® (Invitrogen™), 4.5 g/L glucose, 10% fetal bovine serum. NSC-34 cells were cultured in DMEM containing 4.5 g/L glucose, 0.58 g/L L-glutamine and 10% fetal bovine serum, 100 U/mL penicillin and 100 μg/mL streptomycin (Sigma–Aldrich®). Neurite outgrowth was induced by serum starvation for 36 h.

2.2. Expression vectors and transfection

Limk2d splice variant sequence was obtained from rat frontal cortex mRNA by RT-PCR using AccuPrime Taq DNA Polymerase (Invitrogen™). Sequences of primers are indicated in Table 1. *Limk2d* cDNA was inserted into pcDNA6.2/N-EmGFP-GW/TOPO (Invitrogen™) and amplified in TOP10 *E. coli* bacteria according to the manufacturer's instructions. Plasmids were extracted using the PureYield Plasmid Midiprep System (Promega, Charbonnières, France) and sequenced. Transfections were conducted with Lipofectamine 2000 according to the manufacturer's instructions (Invitrogen™), 24 h after plating for NIH/3T3 cells (70% confluence), HeLa cells (70% confluence) and hippocampal neurons (14 days of culture) and one hour after plating for NSC-34 cells (30% confluence). Medium were replaced with DMEM without serum 4 h after transfection of NSC-34 cells and neurite outgrowth was assessed 36 h later.

2.3. Immunocytochemical analysis and morphological analysis

Cells were fixed with 4% paraformaldehyde (Sigma–Aldrich®) in Phosphate Buffer Saline (PBS) for 30 min at room temperature (RT). After 1 h at RT in 1% bovine serum albumin, 5% horse serum, 0.2% triton X-100 in PBS, NIH/3T3 cells were incubated over night at 4 °C with mouse monoclonal primary antibody against actin (sc-8432, 1/50, Santa Cruz Biotechnology Inc., Heidelberg, Germany) and hippocampal neurons with rabbit polyclonal antibody against βIII-tubulin (MMS- 435P, 1/2000, Covance®, Paris, France). This was followed by incubation for 1 h at RT with Cy3 conjugated donkey antibody against mouse IgG or against rabbit IgG. Preparations were mounted with Prolong Gold Antifade (Invitrogen™) and observed under Nikon DMX 1200 microscope or Olympus Fluoview 500 confocal laser scanning microscope. We determined the length of the longest neurite and neurite complexity (Sholl's method) of GFP-LIMK2d or GFP expressing NSC-34 cells [22,23].

2.4. Semi quantitative RT-PCR

RNA were extracted from tissues from adult female rats (Wistar, Janvier Cerj, Le Genest saint-isle, France), from cultures of rat NSC during proliferation (D7) and differentiation (D9 and D13) and from cultures of rat hippocampal neurons after 4 days (D4) and 17 days of culture (D17), 1 h (D17 1 h) and 12 h (D17 12 h) after NMDA stimulation. Total RNA were extracted using Trizol (Invitrogen™) and treated with DNase I (Invitrogen™).

Reverse transcription was performed on 250 ng of treated RNA using superscript II reverse transcriptase kit (Invitrogen™). The expression of *Limk2b* splice variant was evaluated by semi-quantitative RT-PCR relatively to *Gapdh* expression. Length of specific amplicons of *Limk2b* splice variant was too long (970 pb) to measure its expression by real-time quantitative RT-PCR. *Gapdh* and *Limk2b* cDNA were amplified in a 60 μL reaction mixture containing buffer I 1X, 0.2 μM of each primer, 2.4 U AccuPrime enzyme and 10 μL cDNA (*Tm* = 62 °C). 10 μL of these products underwent electrophoresis on 1.2% agarose gel before capture with ChemiDoc XRS camera and quantification by QuantityOne software (BioRad). The fluorescence was quantified after 30 cycles.

We measured by quantitative real time RT-PCR the expression of *Limk2a* and *Limk2d* splice variants relatively to *Gapdh* expression using Platinum® SYBR® Green qPCR SuperMix-UDG kit (Invitrogen™). The reaction was performed in a LightCycler 480 (Roche Diagnostic, Meylan, France, *Tm* = 60 °C). The efficiency of amplification was calculated on cDNA at concentrations ranging from 1 to 1/10,000. The expression of *Limk2* splice variants were determined by $E^{cp_{isoform}}/E'^{cp_{Gapdh}}$ (E and E′: efficiencies of PCR). Primers are listed in Table 1.

2.5. Western blot analysis

GFP-LIMK2d or GFP transfected NIH/3T3 cells were lysed in a buffer containing 50 mM Tris, 100 mM NaCl, 5 mM EDTA, 0.1% Triton X-100, 50 mM sodium fluoride, 10 μg/mL aprotinin, 10 mM pyrophosphate, 1 mM sodium orthovanadate, 20 mM p-nitrophenylphosphate, 1 μg/mL leupeptin, 50 ng/mL okadaic acid, 1 mM phenylmethanesulfonyl fluoride and 20 mM β-glycerophosphate. 20 μg of proteins were separated by SDS–PAGE in a

Table 1
Sequences of primers used for RT-PCR and cloning.

Gene	Forward primer (5′-3′)	Reverse primer (5′-3′)	Amplified fragment length
Gapdh	CTGCACCACCAACTGCTTAG	GTCTTCTGGGTGGCAGTGAT	108 pb
Rat *Limk2a*	GGGCTGTGGCAACTATGTTC	ACATCGGAACACCGGAAG	89 pb
Rat *Limk2b*	GTCTGTCCCGGCTTACTTC	GAGTCACCTTGATGGCCTG	970 pb
Rat *Limk2d*	CCAGCAGCTACTCACCGCAG	TGGCTTTGTGAGTCACCTGAC	124 pb
*Limk2*d for cloning	ATGGGGAGTTACTTGTCTGTC	CAGCGAATTAACTCCTTCATGA-CCATCACTTTGCCTGTGGCTTTG-TGAGTCACCTGAC	1050 pb

4–15% acrylamide gel and transferred to a polyvinylidene fluoride (PVDF) membrane. Membrane was treated with 5% milk in Tris buffer saline containing 0.1% tween-20. To assess the expression of GFP and GFP-LIMK2d proteins, the membrane was incubated with polyclonal goat anti-GFP antibody (sc-5385, 1/500, Santa Cruz Biotechnology® Inc., Heidelberg, Germany) or polyclonal goat anti-LIMK2 antibody (sc-8390, 1/200, Santa Cruz Biotechnology® Inc.) which recognized all LIMK2 isoforms (epitope located between LIM and PDZ domain) overnight at 4 °C. To measure the amount of cofilin and phosphocofilin, membrane was incubated with polyclonal rabbit anti-cofilin antibody (ab42824, 1/1000, Abcam, Paris, France) or polyclonal rabbit anti-phospho-cofilin antibody (ab12866, 1/1500, Abcam). Horseradish peroxydase-conjugated rabbit anti-goat antibody (81–1620, 1/2500, Zymed®-Invitrogen™, Carlsbad, CA) or donkey anti-rabbit antibody (W401B, 1/2500, Promega, Charbonnières, France) were used as secondary antibodies before chemiluminescence analysis using ECL (Pierce-Thermo Fischer Scientific Inc., Rockford, IL) and quantification by QuantityOne software (Bio-Rad). Cofilin and phosphocofilin were detected on two separate gels. GAPDH expression was used for normalization using polyconal goat anti-GAPDH antibody (sc-48166, 1/250, Santa Cruz Biotechnology® Inc.) and secondary donkey anti-goat antibody (V8051, 1/2500, Promega). Cofilin and phosphocofilin signal intensities were normalized with GAPDH before calculating phosphocofilin/cofilin ratio.

2.6. Immunoprecipitation analysis

Forty microliter of anti-GFP agarose conjugate antibody (sc-5385 AC, 500 μg/mL, Santa Cruz Biotechnology® Inc.) were incubated 2 h at RT with 30 mM Tris, 120 mM NaCl, 5 mM EDTA, 1% Triton X-100. GFP-LIMK2d and GFP HeLa cells were lysed 24 h after transfection using the buffer previously described. Cell lysate was incubated with anti-GFP agarose conjugate antibodies overnight. Proteins not bound to the antibodies formed the supernatant fraction (SN). Proteins bound to antibodies and then eluted with 30 μL of denaturating solution (200 mM Tris pH 6.8, 4% SDS, 40% glycerol, 1 M β-mercaptoethanol, 0.02% bromophenol blue) formed the immunoprecipitated fraction (IP). Proteins were separated by SDS–PAGE in a 4–15% acrylamide gel and transferred to a PVDF membrane before treatment with 5% milk in Tris buffer saline containing 0.1% tween-20. Membrane was incubated with polyclonal mouse anti-GFP antibody (33–2600, 1/500, Invitrogen™) or monoclonal mouse anti-actin antibody (sc-8432, 1/500, Santa Cruz Biotechnology® Inc.) and horseradish peroxydase-conjugated sheep anti-mouse secondary antibody (W4021, 1/2500, Promega) before revelation by chemiluminescence.

2.7. Statistical analysis

Statistical analyses were performed using CA Prism software (GraphPad Software Inc., La Jolla). *Limk2* RNA expression and cofi-

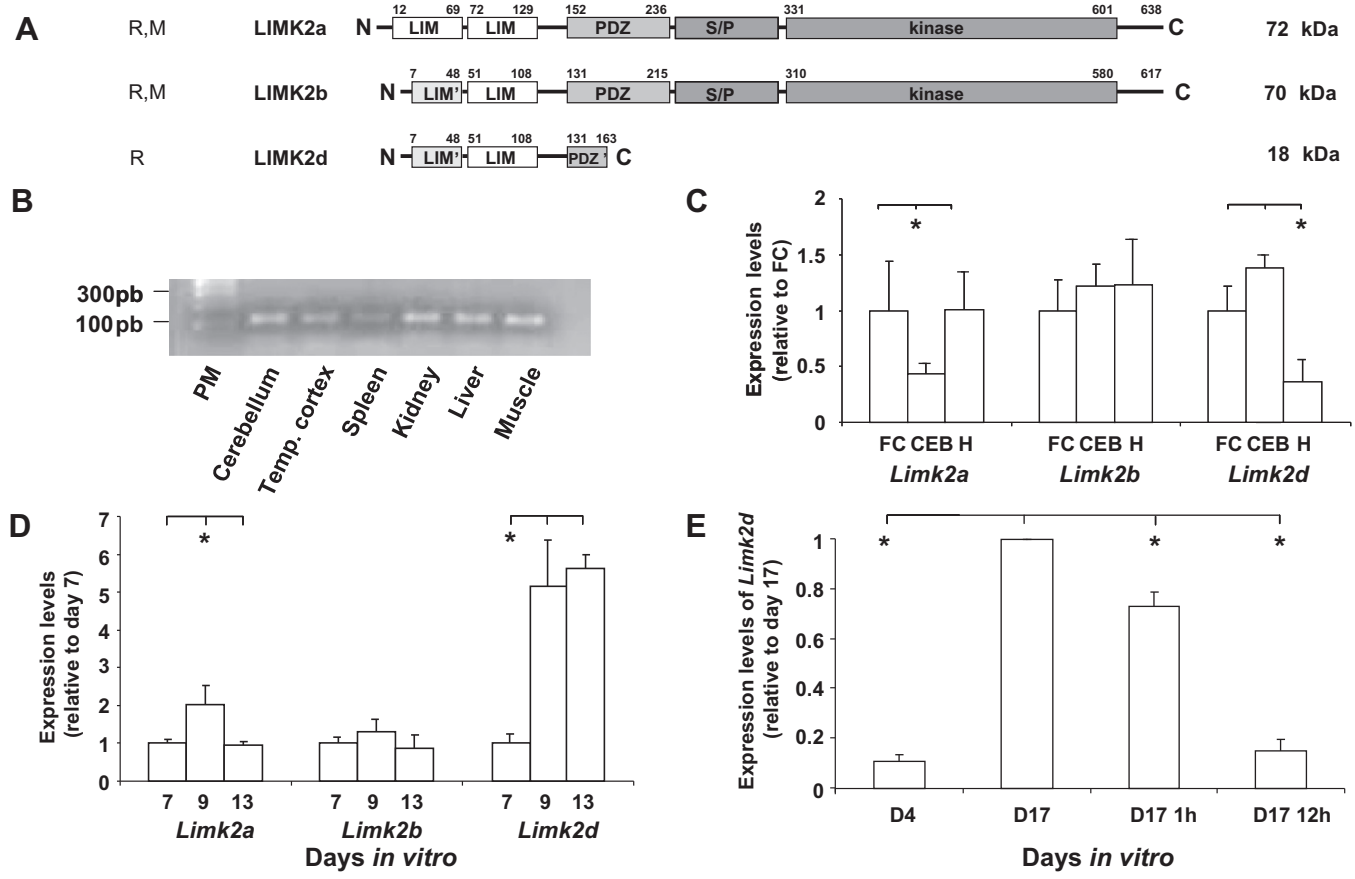

Fig. 1. LIMK2 isoforms in rat. (A) LIMK2 isoforms expressed in rodents. Protein sequences were obtained in NCBI, Ensembl and Uniprot databases and aligned with ClustalW. (B) Expression levels of *Limk2d* mRNA in cerebellum, temporal cortex, spleen, kidney, liver and muscle of adult rat. (C) Expression of *Limk2* splice variants in brain tissues from adult rats: frontal cortex (FC), cerebellum (CEB) and hippocampus (H). Results were normalized to the expression in frontal cortex. (D) Expression levels of *Limk2* splice variants in culture of neural stem cells from rat embryos during proliferation (D7) and differentiation steps (D9 and D13). Results were normalized to the expression at D7. (E) Expression levels of *Limk2d* splice variant in culture of hippocampal neurons after 4 (D4) and 17 days of culture (D17), and 1 h (D17 1 h) or 12 h (D17 12 h) after NMDA stimulation. Results were normalized to D17 (maximum of expression). Data are mean ± SEM of three independent experiments (*$p \leqslant 0.05$).

lin phosphorylation were compared by using a Mann-Withney non-parametric test. For analysis of neurite length, homogeneity of 3 experiments and comparison of the neurite length of GFP or GFP-LIMK2d cells were assessed by Chi square test.

3. Results

3.1. Expression of LIMK2 splice variants in rodents

Two LIMK2 isoforms (a and b) are expressed both in rat and mouse [19]. LIMK2a, the longest one, contains two LIM domains, one PDZ domain, one serine/proline rich domain and one serine/threonine kinase domain. LIMK2b differs from LIMK2a by a truncated *N*-terminal LIM domain (Fig. 1A). Nunoue et al. (1995) [19] reported another isoform expressed in rat, LIMK2d. This isoform has truncated LIM and PDZ domains and lacks the serine/threonine kinase domain (Fig. 1A, Supplementary Fig. 1).

Several studies reported the importance of the Rho-GTPases pathway activating LIMK during brain development and function. Most of knowledge on LIMK2 concerns LIMK2a and LIMK2b isoforms. We focused our studies on LIMK2d splice variant because it was identified in a rat brain cDNA library and was not further studied [19]. We first showed that *Limk2d* expression was not restricted to nervous system, but was detected in a large set of tissues (Fig. 1B). In the adult brain, *Limk2a*, *2b* and also *2d* mRNA were expressed in all regions studied, but at various levels (Fig. 1C). *Limk2d* mRNA was particularly well expressed in frontal cortex and cerebellum. In frontal cortex, the expression ratio between *Limk2d* and *Limk2a* was 0.3. We also detected this isoform by immunoprecipitation in rat cerebellum extract (Supplementary Fig. 2).

To assess a possible role for *Limk2d* during brain development, we analyzed its expression during differentiation of rat neural stem cells in culture (Fig. 1D). Neural stem cells, proliferating as neurospheres for 7 days, expressed all three splice variants *Limk2a*, *2b* and *2d*. The expression of *Limk2a* and particularly *Limk2d* significantly increased after two days of neural differentiation ($p \leqslant 0.05$). This important increase in expression was maintained for *Limk2d* after one week of differentiation. In hippocampal neurons, *Limk2d* expression increased after synaptogenesis and decreased 1 h and 12 h after neuron stimulation with NMDA and glycine (Fig. 1E, $p = 0.038$). These results supported a role for *Limk2d* during neuronal differentiation and maturation.

3.2. LIMK2d promotes neurite outgrowth

We transfected hippocampal neurons with a plasmid overexpressing a GFP-LIMK2d fused protein, and monitored its cellular localization. The correct expression of this protein was confirmed by western blot (Fig. 2A). GFP-LIMK2d was expressed in the soma, in neurites as well as in dendritic spines (Fig. 2B). To determine a possible function of LIMK2d during neuronal differentiation, we

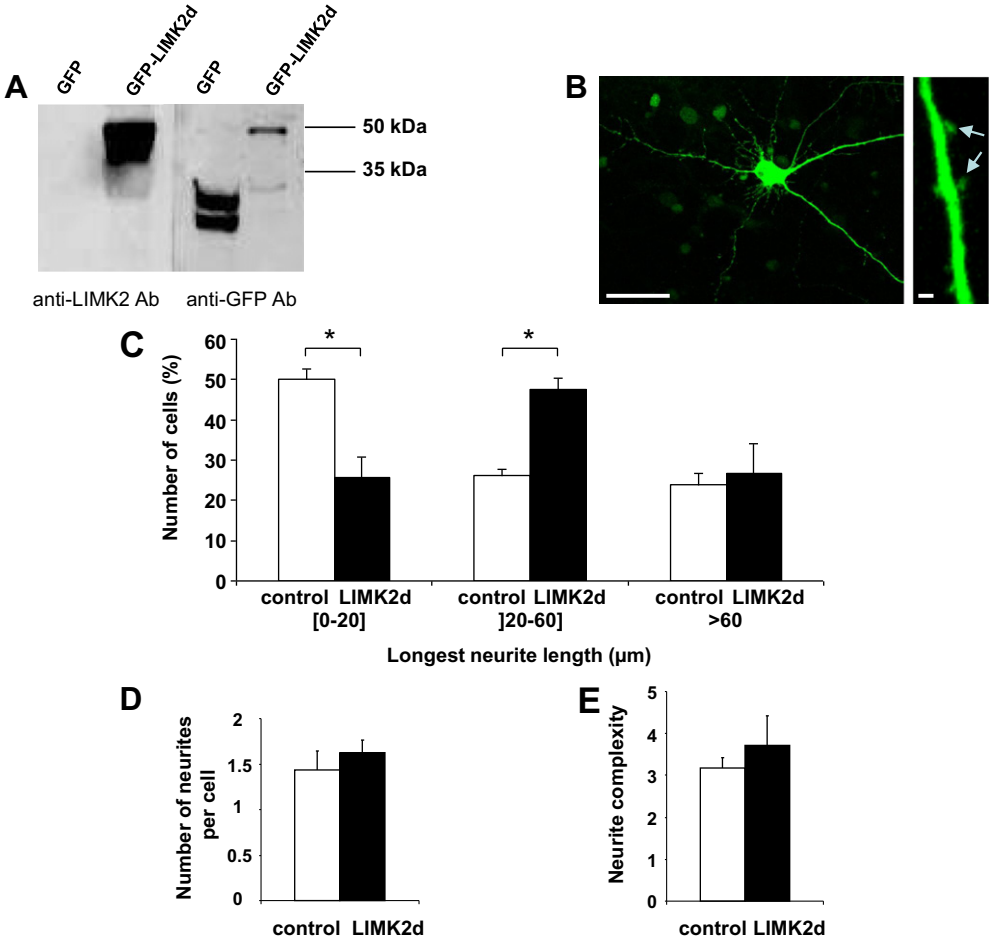

Fig. 2. LIMK2d localization and function in neuronal cells. (A) Expression of GFP or GFP-LIMK2d proteins into HeLa cells by western blot using an anti-LIMK2 (left panel) or anti-GFP (right panel) antibody. (B) Localization of GFP-LIMK2d protein in transfected hippocampal neurons at 14 days of culture. Localization was monitored 24 h after transfection. Scale bars: 30 µm (left panel), 1 µm (right panel). Effect of GFP-LIMK2d over-expression on length (C), number (D) and complexity of neurites (E) of NSC-34 cells. Data are means ± SEM of three independent experiments ($^{*}p \leqslant 0.05$). White bars: cells expressing GFP; black bars: cells expressing GFP-LIMK2d.

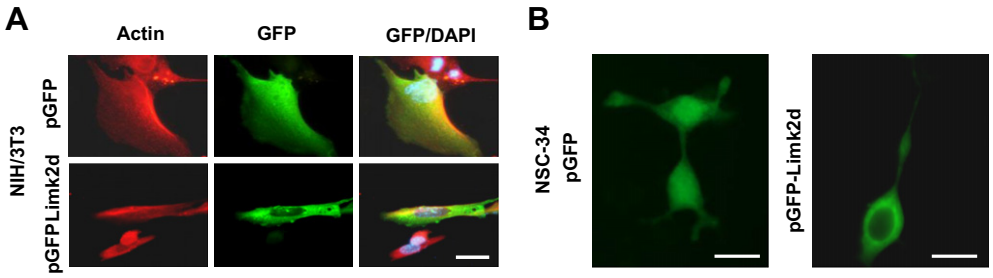

Fig. 3. Cytoplasmic expression of LIMK2d. (A) Localization of GFP and GFP-LIMK2d protein in NIH/3T3 cells observed 24 h after transfection by immunocytochemistry with an antibody anti-actin (in red) and counterstained with DAPI. (B) NSC-34 cells expressing GFP and GFP-LIMK2d. Scale bars: 30 μm (For interpretation of the references to color in this figure legend, the reader is referred to the web version of this article.).

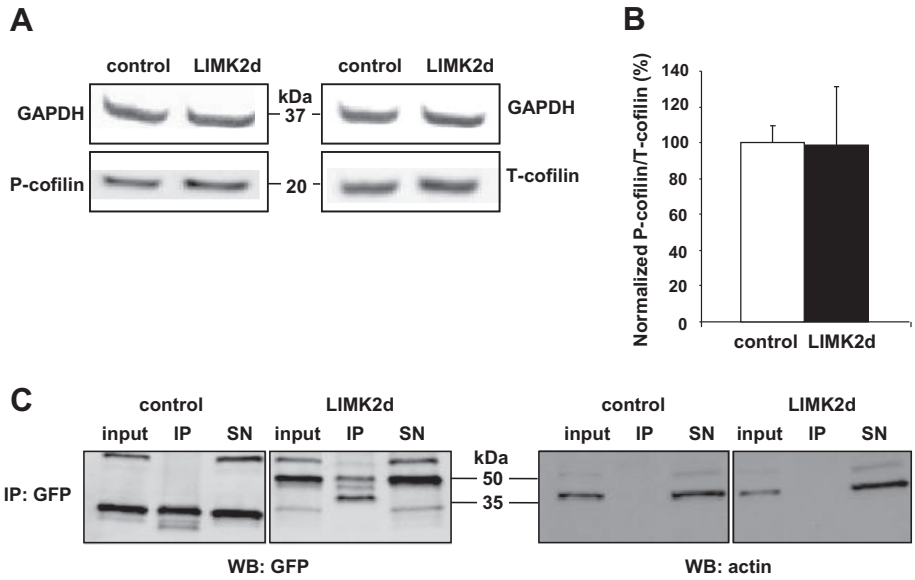

Fig. 4. Study of cofilin phosphorylation and actin binding. (A, B) Measure of cofilin phosphorylation in HeLa cells expressing GFP (control) or GFP-LIMK2d (LIMK2d) protein by western blot. Results represent the ratio between the level of phosphorylated cofilin and total cofilin normalized to values obtained in GFP-expressing cells. Data are means ± SEM of three independent experiments ($^{*}p \leqslant 0.05$). (C) Immunoprecipitation of GFP and GFP-LIMK2d proteins and western blot analysis using an anti-GFP antibody (left panel) or an anti-actin antibody (right panel). Input, proteins from cell lysate before immunoprecipitation; IP, proteins immunoprecipitated; SN, supernatant.

next transfected a neuronal cell line (NSC-34) by GFP-LIMK2d or GFP expressing constructs. GFP-LIMK2d cells displayed longer longest neurites compared to control cells (GFP alone) ($p = 0.023$; Fig. 2C). The number and complexity of neurites were not affected (Fig. 2D and E). Therefore, the small isoform, LIMK2d, promotes neurite outgrowth.

We next investigated the molecular mechanism of LIMK2d-induced neurite outgrowth. We first observed that GFP-LIMK2d was localized only in the cytoplasm of transfected NIH/3T3 and NSC-34 cells and not in the nucleus (Fig. 3A and B). LIMK2d does not possess a kinase domain, in contrast to LIMK2a and LIMK2b, and thus normally could not phosphorylate cofilin. We hypothesized that LIMK2d could bind cofilin and consequently prevent its phosphorylation by LIMK2a and b thereby affecting actin polymerization. We measured the ratio phosphorylated cofilin/total cofilin by western blotting of lysates from GFP-LIMK2d or GFP expressing cells. The ratio was equal in both cultures, indicating that LIMK2d did not affect cofilin phosphorylation (Fig. 4A and B). We next asked whether LIMK2d could regulate neurite outgrowth by direct interaction with actin, similarly to other proteins containing only LIM and PDZ domains [24,25]. Immunoprecipitation experiments showed that GFP-LIMK2d did not interact with actin (Fig. 4C). These results showed that LIMK2d is a new cytoplasmic factor promoting neurite outgrowth by a different mechanism than other LIMK proteins.

4. Discussion

Previous works revealed the expression of several isoforms for LIMK2 in the central nervous system of rodents. The longest ones, LIMK2a and LIMK2b, are expressed in rat and mouse. Another isoform, LIMK2d, expressed in the rat CNS, has truncated LIM and PDZ domains and lacks the kinase domain. We reported that *Limk2d* was widely expressed in cerebral and non cerebral tissues. In cerebral tissues, this splice variant had a distinct pattern of expression compared to *Limk2a* and *Limk2b*. *Limk2d* expression was highest in frontal cortex and cerebellum whereas *Limk2a* showed higher expression in frontal cortex and hippocampus. *Limk2b* expression was similar in the three brain regions analyzed. This suggested that LIMK2d may have distinct functions from LIMK2a and b in the central nervous system.

In a first approach, to get insights into these functions, we showed that *Limk2d* expression increased during the differentiation of neural stem cells. We then performed transfection experiments *in vitro* in order to overproduce GFP-LIMK2d into hippocampal neurons. We observed that LIMK2d was localized in the soma, dendrites and dendritic spines in mature hippocampal neurons and that *Limk2d* expression decreased after stimulation of these cells. This observation supports a role for LIMK2d in neuronal activity during brain development, maturation and function. As the regulation of ADF/cofilin activity is important for the synap-

tic receptors trafficking after induction of LTP [26], our results suggested that LIMK2d may have a function in LTP alongside to LIMK2a and b.

To test a possible role for LIMK2d in neurite outgrowth, we overproduced GFP-LIMK2d protein in NSC-34 cells. We observed a significant increase in neurite length but not number or complexity. Similarly to LIMK2b, GFP-LIMK2d protein was expressed only in the cytoplasm of NIH/3T3 cells, NSC-34 and hippocampal neurons. This is in accordance with its sequence as LIMK2d does not possess any NLS signal. Endo and his colleagues (2007) [17] suggested that neurite outgrowth is induced by the regulation of cofilin phosphorylation by the LIM kinases and by the slingshot phosphatases. LIMK2d does not possess the kinase domain of LIMK2a or b. We hypothesized that it might compete with LIMK2a and b thereby preventing the phosphorylation of ADF/cofilin. This hypothesis was not confirmed in HeLa cells. Another hypothesis for LIMK2d action on neurite outgrowth comes from a previous study reporting that PDLIM5, an actin-binding protein containing LIM domains, regulates actin polymerization in neurons [24]. However, we could not observe, as in the case of PDLIM5, an interaction between LIMK2d and actin *in vitro*. Another possibility may be that the role of LIMK2d on neurite outgrowth could be the consequence of an interaction between its LIM domains and one of the numerous proteins interacting with such domains [27]. For instance, an interaction with PKC, (as described for LIMK1; [28]) might play a role on neurite outgrowth [29].

Therefore, as LIMK2a and LIMK2b, LIMK2d controls neurite extension, which is a crucial process in the formation and plasticity of the neuronal network. Since LIMK2 isoforms present important structural differences, further investigations will be needed to understand the specific functions of each isoform.

Acknowledgments

This work was supported by the Région Centre, la Ligue contre le Cancer, the Centre National de la Recherche, Scientifique, the Institut National de la Santé et de la Recherche Médicale, the Université François Rabelais de Tours and the Ministère de l'Enseignement supérieur et de la Recherche.

Appendix A. Supplementary data

Supplementary data associated with this article can be found, in the online version, at doi:10.1016/j.bbrc.2012.02.134.

References

[1] P. Hotulainen, C.C. Hoogenraad, Actin in dendritic spines: connecting dynamics to function, J. Cell Biol. 189 (2010) 619–629.
[2] M. Stiess, F. Bradke, Neuronal polarization: the cytoskeleton leads the way, Dev. Neurobiol. 71 (2010) 430–444.
[3] O. Bernard, LIM kinases, regulators of actin dynamics, Int. J. Biochem. Cell Biol. 39 (2007) 1071–1076.
[4] S. Arber, F.A. Barbayannis, H. Hanser, C. Schneider, C.A. Stanyon, O. Bernard, P. Caroni, Regulation of actin dynamics through phosphorylation of cofilin by LIM-kinase, Nature 393 (1998) 805–809.
[5] T. Sumi, K. Matsumoto, Y. Takai, T. Nakamura, Cofilin phosphorylation and actin cytoskeletal dynamics regulated by rho- and Cdc42-activated LIM kinase 2, J. Cell Biol. 147 (1999) 1519–1532.
[6] E.E. Benarroch, Rho GTPases: role in dendrite and axonal growth, mental retardation, and axonal regeneration, Neurology 68 (2007) 1315–1318.
[7] I. Okano, J. Hiraoka, H. Otera, K. Nunoue, K. Ohashi, S. Iwashita, M. Hirai, K. Mizuno, Identification and characterization of a novel family of serine/threonine kinases containing two *N*-terminal LIM motifs, J. Biol. Chem. 270 (1995) 31321–31330.
[8] M. Takemura, T. Mishima, Y. Wang, J. Kasahara, K. Fukunaga, K. Ohashi, K. Mizuno, Ca2+/calmodulin-dependent protein kinase IV-mediated LIM kinase activation is critical for calcium signal-induced neurite outgrowth, J. Biol. Chem. 284 (2009) 28554–28562.
[9] Z. Wen, L. Han, J.R. Bamburg, S. Shim, G.L. Ming, J.Q. Zheng, BMP gradients steer nerve growth cones by a balancing act of LIM kinase and Slingshot phosphatase on ADF/cofilin, J. Cell Biol. 178 (2007) pp. 107–119.
[10] M. Endo, K. Ohashi, Y. Sasaki, Y. Goshima, R. Niwa, T. Uemura, K. Mizuno, Control of growth cone motility and morphology by LIM kinase and Slingshot via phosphorylation and dephosphorylation of cofilin, J. Neurosci. 23 (2003) 2527–2537.
[11] C. Ikebe, K. Ohashi, T. Fujimori, O. Bernard, T. Noda, E.J. Robertson, K. Mizuno, Mouse LIM-kinase 2 gene: cDNA cloning, genomic organization, and tissue-specific expression of two alternatively initiated transcripts, Genomics 46 (1997) 504–508.
[12] T. Mori, I. Okano, K. Mizuno, M. Tohyama, A. Wanaka, Comparison of tissue distribution of two novel serine/threonine kinase genes containing the LIM motif (LIMK-1 and LIMK-2) in the developing rat, Mol. Brain Res. 45 (1997) pp. 247–254.
[13] M. Yildirim, W.G. Janssen, N.E. Tabori, M.M. Adams, G.S. Yuen, K.T. Akama, B.S. McEwen, T.A. Milner, J.H. Morrison, Estrogen and aging affect synaptic distribution of phosphorylated LIM kinase (pLIMK) in CA1 region of female rat hippocampus, Neuroscience 152 (2008) 360–370.
[14] K. Acevedo, N. Moussi, R. Li, P. Soo, O. Bernard, LIM kinase 2 is widely expressed in all tissues, J. Histochem. Cytochem. 54 (2006) 487–501.
[15] M. Maekawa, T. Ishizaki, S. Boku, N. Watanabe, A. Fujita, A. Iwamatsu, T. Obinata, K. Ohashi, K. Mizuno, S. Narumiya, Signaling from Rho to the actin cytoskeleton through protein kinases ROCK and LIM-kinase, Science 285 (1999) 895–898.
[16] N. Yang, O. Higuchi, K. Ohashi, K. Nagata, A. Wada, K. Kangawa, E. Nishida, K. Mizuno, Cofilin phosphorylation by LIM-kinase 1 and its role in Rac mediated actin reorganization, Nature 393 (1998) 809–812.
[17] M. Endo, K. Ohashi, K. Mizuno, LIM kinase and slingshot are critical for neurite extension, J. Biol. Chem. 282 (2007) 13692–13702.
[18] Y. Meng, H. Takahashi, J. Meng, Y. Zhang, G. Lu, S. Asrar, T. Nakamura, Z. Jia, Regulation of ADF/cofilin phosphorylation and synaptic function by LIM kinase, Neuropharmacology 47 (2004) 746–754.
[19] K. Nunoue, K. Ohashi, I. Okano, K. Mizuno, LIMK-1 and LIMK-2, two members of a LIM motif-containing protein kinase family, Oncogene 11 (1995) 701–710.
[20] I. Martin, C.R. Andres, S. Vedrine, R. Tabagh, C. Michelle, M.L. Jourdan, N. Heuze- Vourc'h, P. Corcia, A. Duittoz, P. Vourc'h, Effect of the oligodendrocyte myelin glycoprotein (OMgp) on the expansion and neuronal differentiation of rat neural stem cells, Brain Res. 1284 (2009) 22–30.
[21] F. Laumonnier, C. Shoubridge, C. Antar, L.S. Nguyen, H. Van Esch, T. Kleefstra, S. Briault, J.P. Fryns, B. Hamel, J. Chelly, H.H. Ropers, N. Ronce, S. Blesson, C. Moraine, J. Gecz, M. Raynaud, Mutations of the UPF3B gene, which encodes a protein widely expressed in neurons, are associated with nonspecific mental retardation with or without autism, Mol. Psychiatry 15 (2010) 767–776.
[22] D.A. Sholl, The measurable parameters of the cerebral cortex and their significance in its organization, Prog. Neurobiol. 2 (1956) 324–333.
[23] B. Bindu, P.A. Alladi, B.M. Mansooralikhan, B.N. Srikumar, T.R. Raju, B.M. Kutty, Short-term exposure to an enriched environment enhances dendritic branching but not brain-derived neurotrophic factor expression in the hippocampus of rats with ventral subicular lesions, Neuroscience 144 (2007) 412–423.
[24] S. Herrick, D.M. Evers, J.Y. Lee, N. Udagawa, D.T. Pak, Postsynaptic PDLIM5/Enigma Homolog binds SPAR and causes dendritic spine shrinkage, Mol. Cell. Neurosci. 43 (2010) pp. 188–200.
[25] G.R. Phillips, T.R. Anderson, L. Florens, C. Gudas, G. Magda, J.R. Yates, D.R. Colman, Actin-binding proteins in a postsynaptic preparation: Lasp-1 is a component of central nervous system synapses and dendritic spines, J. Neurosci. Res. 78 (2004) 38–48.
[26] J. Gu, C.W. Lee, Y. Fan, D. Komlos, X. Tang, C. Sun, K. Yu, H.C. Hartzell, G. Chen, J.R. Bamburg, J.Q. Zheng, ADF/cofilin-mediated actin dynamics regulate AMPA receptor trafficking during synaptic plasticity, Nat. Neurosci. 13 (2010) pp. 1208–1215.
[27] I. Bach, The LIM domain: regulation by association, Mech. Dev. 91 (2000) pp. 5–17.
[28] S. Kuroda, C. Tokunaga, Y. Kiyohara, O. Higuchi, H. Konishi, K. Mizuno, G.N. Gill, U. Kikkawa, Protein-protein interaction of zinc finger LIM domains with protein kinase C, J. Biol. Chem. 271 (1996) 31029–31032.
[29] P. Yang, Z.Q. Li, L. Song, Y.Q. Yin, Protein kinase C regulates neurite outgrowth in spinal cord neurons, Neurosci. Bull. 26 (2010) pp. 117–125.

Biochemical and Biophysical Research Communications 420 (2012) 253–256

Contents lists available at SciVerse ScienceDirect

Biochemical and Biophysical Research Communications

journal homepage: www.elsevier.com/locate/ybbrc

Site-specific conjugation of a lanthanide chelator and its effects on the chemical synthesis and receptor binding affinity of human relaxin-2 hormone

Fazel Shabanpoor [a,b], Ross A.D. Bathgate [a,c], Alessia Belgi [a,c], Linda J. Chan [a,b], Vinojini B. Nair [a,b], John D. Wade [a,b], Mohammed Akhter Hossain [a,b,*]

[a] Florey Neuroscience Institutes, The University of Melbourne, Parkville, VIC 3010, Australia
[b] School of Chemistry, The University of Melbourne, Parkville, VIC 3010, Australia
[c] Department of Biochemistry and Molecular Biology, The University of Melbourne, Parkville, VIC 3010, Australia

ARTICLE INFO

Article history:
Received 22 February 2012
Available online 7 March 2012

Keywords:
Protein
Peptide
Lanthanide
Circular dichroism
Relaxin
Solid phase synthesis

ABSTRACT

Diethylenetriamine pentaacetic acid (DTPA) is a popular chelator agent for enabling the labeling of peptides for their use in structure–activity relationship study and biodistribution analysis. Solid phase peptide synthesis was employed to couple this commercially available chelator at the N-terminus of either the A-chain or B-chain of H2 relaxin. The coupling of the DTPA chelator at the N-terminus of the B-chain and subsequent loading of a lanthanide (europium) ion into the chelator led to a labeled peptide (Eu-DTPA-(B)-H2) in low yield and having very poor water solubility. On the other hand, coupling of the DTPA and loading of Eu at the N-terminus of the A-chain led to a water-soluble peptide (Eu-DTPA-(A)-H2) with a significantly improved final yield. The conjugation of the DTPA chelator at the N-terminus of the A-chain did not have any impact on the secondary structure of the peptide determined by circular dichroism spectroscopy (CD). On the other hand, it was not possible to determine the secondary structure of Eu-DTPA-(B)-H2 because of its insolubility in phosphate buffer. The B-chain labeled peptide Eu-DTPA-(B)-H2 required solubilization in DMSO prior to carrying out binding assays, and showed lower affinity for binding to H2 relaxin receptor, RXFP1, compared to the water-soluble A-chain labeled peptide Eu-DTPA-(A)-H2. The mono-Eu-DTPA labeled A-chain peptide, Eu-DTPA-(A)-H2, thus can be used as a valuable probe to study ligand–receptor interactions of therapeutically important H2 relaxin analogs. Our results show that it is critical to choose an approriate site for incorporating chelators such as DTPA. Otherwise, the bulky size of the chelator, depending on the site of incorporation, can affect yield, solubility, structure and pharmacological profile of the peptide.

1. Introduction

Human gene 2 relaxin (H2 relaxin) is the human ortholog of the relaxin peptide that was discovered in 1926 [1]. It has been grouped in the insulin and insulin-like growth factors family of peptide hormones due to their structural resemblances [2]. H2 relaxin is a heterodimer of two peptide chains (A-chain and B-chain with 24 and 29 residues, respectively) held together by three disulfide bonds [3], which is a common feature of all 10 members in insulin-relaxin superfamily [2].

The relaxin receptor has been identified to be a G protein-coupled receptor (GPCR) known as RXFP1 (relaxin family peptide receptor 1) [4]. Relaxin binds and activates its receptor using a binding cassette (RXXXRXXI) located on the helical region of the B-chain together with some residues at the C-terminus of the A-chain [5–7]. The interaction of relaxin with its receptor leads to various biologic effects many of which are mediated as a result of activation of the G_S-cAMP dependent pathway [8]. Initially, relaxin was regarded as a hormone of pregnancy due to its effect in softening of cervical tissue during pregnancy and hence facilitating the delivery of young [9]. Relaxin also possesses potent anti-fibrotic effects by inhibiting collagen synthesis and enhancing its breakdown by increasing matrix metalloproteinases [10]. It can also stimulate angiogenesis and promotes wound healing possibly by increasing the expression of the vascular endothelial growth factors (VEGF) [11,12]. In addition, relaxin can also induce vasodilation in heart, liver and kidney by increasing nitric oxide (NO) production, via stimulation of NO synthase and endothelin B (ETB) receptor [13]. Currently, relaxin is in Phase III clinical trial for the treatment of acute heart failure (AHF) [13,14]. Apart from these beneficial agonist effects, a recent study has shown that relaxin is involved in prostate cancer growth and metastasis [15]. Hence an antagonist of relaxin can be of immense value in developing a potential treatment for prostate cancer.

* Corresponding author at: Florey Neuroscience Institutes, The University of Melbourne, Parkville, VIC 3010, Australia. Fax: +61 3 9348 1707.
E-mail address: akhter.hossain@florey.edu.au (M.A. Hossain).

0006-291X/$ - see front matter © 2012 Elsevier Inc. All rights reserved.
http://dx.doi.org/10.1016/j.bbrc.2012.02.141

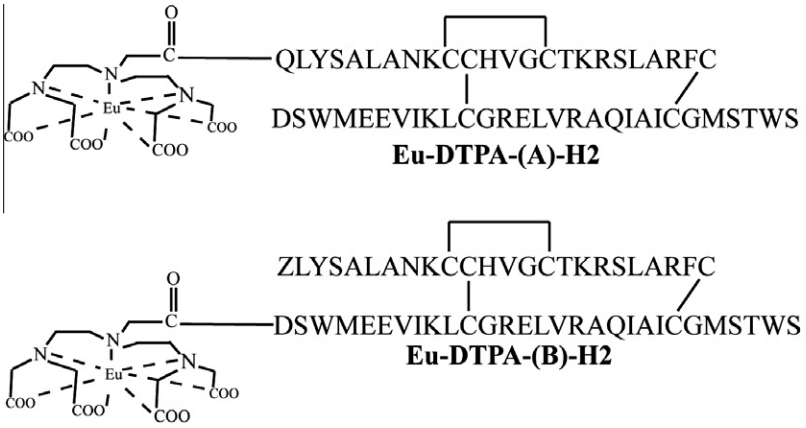

Fig. 1. Primary structures of H2 relaxin with DTPA chelator coupled to the N-terminus of the A- or B-chain.

The development of a new generation of relaxin agonists and antagonists with improved therapeutic indices necessitates the synthesis of various novel analogs. The receptor binding characterization of these analogs requires the use of a labeled probe. In the past, we have used isotopically (33P) labeled H2 relaxin [16], which was both laborious and expensive to obtain. We also had to characterize the labeled peptide each time due to variation in activity from batch to batch. In the current study, we have used chemical synthesis to mono-label relaxin on both A- and B-chains with a commercially available lanthanide chelate (Fig. 1). The activity of the two labeled peptides was studied using a whole cell binding assay. These lanthanide (europium) labeled H2 relaxin peptides would be cheaper, more user-friendly and non-hazardous compared to isotopically labeled H2 relaxin analogs.

2. Materials and methods

2.1. Peptide synthesis

All linear peptides were assembled on solid support using Fmoc chemistry as previously described [17]. The protocol used was similar for most parts except combination reaction. Due to the poor solubility of the B-chain, the combination reaction was carried out in 6 M GnHCl/0.1 M Gly-NaOH buffer (pH 8.5). Please see the Supplementary section for details of all the reaction steps.

2.2. Circular dichrosim spectroscopy

The secondary α-helical content of the peptides were measured as described previously [17,18]. For this study, the peptides were made up to a concentration of 0.2 μM in phosphate buffer saline pH 7.4. The recorded spectra in millidegrees of ellipticity (θ) were converted to mean residue ellipticity (MRE) in deg cm^2 $dmol^{-1}$.

2.3. Cell culture and ligand binding assays

Human embryonic kidney cells, (HEK 293T) stably expressing RXFP1 were plated in 96 well viewplate (PerkinElmer, Australia). Saturation and competition binding experiments were carried out as previously described [17]. Briefly, H2 relaxin with DTPA chelator conjugated to the N-terminus of A-chain was dissolved in H_2O whereas H2 relaxin with DTPA chelator on the B-chain was dissolved in 20% DMSO. The saturation binding experiment was carried using increasing concentrations of labeled peptides (0.1–1 nM) and the non-specific binding was determined in presence of H2 relaxin (0.5 nM). The competition binding experiments was carried out using a single concentration of the europium-labeled H2 peptides (0.5 nM) in presence of increasing concentrations of H2 relaxin. Each concentration point was in triplicate from 3 to 5 independent experiments. The binding data were analyzed using GraphPad PRISM 5 and expressed as mean ± SEM. The saturation data were fitted into one site hyperbolic model and the competition binding data were fitted using a one site binding model.

3. Results

Each of the A- and B-chains of H2 relaxin was synthesized separately. The B-chain with and without conjugated DTPA chelator was purified after cleavage from solid support (Scheme 1, Supplementary Material). The B-chain without DTPA chelator had a yield of about 35% compared to 20% for B-chain conjugated with the chelator. The A-chain was further modified by first forming the intra-A-chain disulfide bond and the tBu group was converted to 2-pyridylsulfenyl group that is very reactive to thiol moiety. Each of these steps had about 50–60% yield for both A-chain with and without DTPA coupled. The A-chains were successfully combined with the B-chain to form the first inter-chain disulfide bonds via thiolysis of the S-pyridinyl by the free thiol of Cys 10 of the B-chain. The final step of the synthesis was the formation of the second inter-chain disulfide bond, which was carried out via iodine oxidation of the Acm groups on CysA24 and CysB22. H2 relaxin with DTPA chelator coupled to the N-terminus of the A-chain was obtained in a yield of about 12% whereas H2 relaxin with DTPA conjugated at the N-terminus of the B-chain had very low yield (3%) starting from the B-chain. Finally, DTPA was loaded with europium using $EuCl_3$ and purified by RP-HPLC buffer using TEA acetate buffer (pH 6.5) to prevent the liberation of europium from the DTPA chelator. The Eu-DTPA-labeled H2 relaxins, Eu-DTPA-(A)-H2 and Eu-DTPA-(B)-H2 (Fig. 1), were purified by analytical RP-HPLC in greater than 98% purity and the peptide content (A-chain labeled: 85%, B-chain labeled: 81%) was determined by amino acid analysis. The reaction progress and products in each reaction step were analyzed with RP-HPLC and MALDI-TOF/TOF.

The effect of DTPA conjugation on the secondary structure of the H2 relaxin was determined by CD spectroscopy. The α-helical content of Eu-DTPA-(A)-H2 (37%) was similar to the native H2 relaxin (36%) (Fig. 2) indicating that DTPA labeled at the N-terminus does not affect the secondary structure of H2 relaxin.

The receptor binding affinity was calculated by measuring the dissociation constant (Kd) from saturation binding curves (Fig. 3A). The receptor binding affinity of Eu-DTPA-(A)-H2 (0.50 ± 0.04 nM, $n = 3$) was slightly higher compared to Eu-DTPA-(B)-H2 (0.85 ± 0.08 nM, $n = 3$) and the difference is statistically significant ($p < 0.01$, t-test). A single concentration (0.5 nM) of each labeled

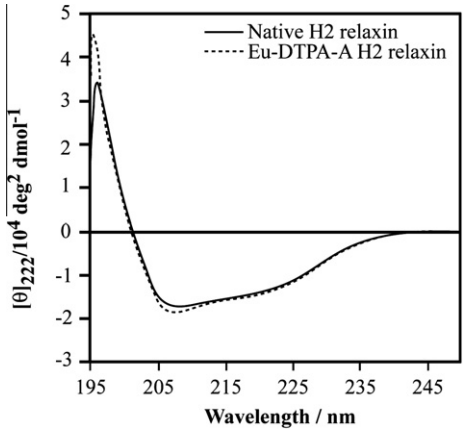

Fig. 2. CD spectroscopy profiles of native H2 relaxin, Eu-DTPA-(A) H2 relaxin. Both peptides exhibit similar α-helicity profiles.

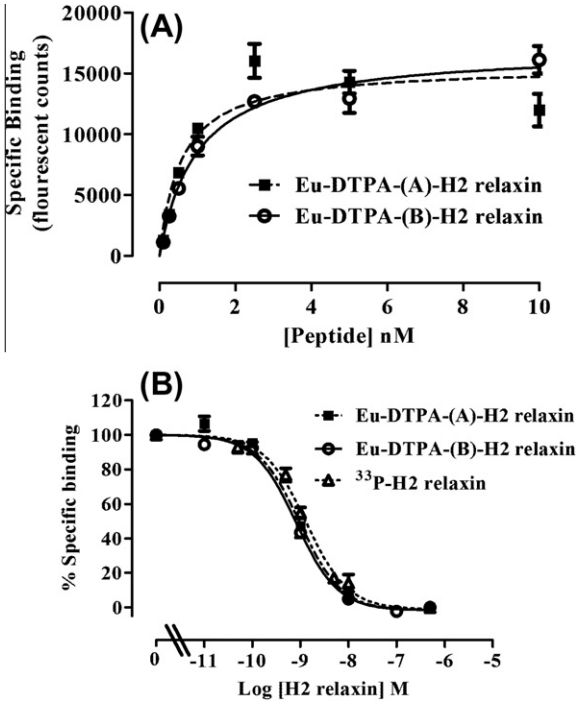

Fig. 3. Receptor binding curves of Eu-DTPA copupled H2 relaxins in HEK-293T stably expressing RXFP1. (A) The dissociation constant (Kd) was determined by saturation binding usingdifferent concentrations of labeled peptides. Non-specific binding was determined in the presence of 500 nM H2 relaxin. (B) The competition binding experiment was carried out using a single concentration of the europium-labeled H2 peptides (0.5 nM) or ^{33}P-labeled H2 relaxin in presence of increasing concentrations of H2 relaxin. The binding data were analyzed using Graphpad PRISM 5. The data were expressed as mean ± SEM from 3 to 5 independent experiments. The saturation data were fitted into one site hyperbolic model and the competition binding data were fitted using a one site binding model.

peptide was used in competition binding assay to determine the receptor binding affinity of the native H2 relaxin. The receptor binding affinity (pKi) of H2 relaxin was found to be 9.30 ± 0.02 (n = 3), 9.31 ± 0.05 (n = 5), and 9.24 ± 0.16 (n = 3) in presence of Eu-DTPA-(A)-H2, Eu-DTPA-(B)-H2, ^{33}P-H2 relaxin, respectively (Fig. 3B).

4. Discussion

H2 relaxin is a pleiotropic peptide hormone, which is currently in Phase III clinical trials for the treatment of acute heart failure. The large size of this hormone is a major limitation, which has been addressed by the design of smaller analogs [19]. The proteolytic stability is also a major issue, which is yet to be addressed to improve its half-life in circulation. Furthermore, in patients with prostate cancer, it has been demonstrated that H2 relaxin can cause growth and metastasis of the cancer [15] and in a rodent xenograft model of prostate cancer a H2 relaxin antagonist was shown to block cancer growth [20]. Therefore, a H2 receptor antagonist may be a potential treatment for prostate cancer. However, the development of any H2 relaxin agonist and antagonist requires the screening of various analogs for their receptor binding affinity, which in turn needs a labeled probe. Previously, radioactively or isotopically labeled H2 relaxin has been used but there are many limitations to the use of such probes as their short-half lives, high cost, batch variation, and safety.

It is possible to undertake post-synthesis labeling of synthetic H2 relaxin with commercially available activated Eu-DTTA chelate, *N1-(p-isothiocyanato* benzyl)-diethylenetriamine-*N,N2,N,N3-tetra-acetic* acid [17]. However, this would create a multiple site-labeled peptide as there are 4 free primary amine sites in H2 relaxin. Using modem solid phase peptide synthesis, we have produced mono-labeled H2 relaxin analogs. We have used a commercially available lanthanide chelator at either N-terminus of A-chain or B-chain on solid support. The diethylenetriamine pentaacetic acid (DTPA) is an effective chelating agent for a variety of lanthanide as well as radionuclides. It can be readily coupled to specific sites within the peptides on solid support. In the first instance, the DTPA chelator was coupled to the N-terminus of the B-chain that resulted labeled peptide Eu-DTPA-(B)-H2. This was based on our previous studies on INSL3 [17] and INSL5/relaxin-3 [21] where we showed that coupling DTPA at the N-terminus of the B-chain did not have any impact on the secondary structure and receptor binding affinity of the peptides. However, in the case of H2 relaxin, this resulted in a significant decrease in solubility of the B-chain, which yielded a very low amount of final product. Due to its poor solubility in H_2O, it was solubilized in 20% DMSO for use in the binding assays. The use of organic solvents in solubilizing the peptide for bioassays is generally not preferred due to their toxic effects on the live cells. Therefore, in order to address the insolubility problem, we conjugated the DTPA chelator to the N-terminus of the A-chain that resulted in a labeled peptide Eu-DTPA-(A)-H2. The solubility of Eu-DTPA-(A)-H2 was better and the final yield obtained was much higher compared to Eu-DTPA-(B)-H2. More importantly, the final product was water-soluble and it was used directly in the binding assays without using any organic solvent.

In order to obtain an insight into the solution structure of Eu-DTPA-(A)-H2 and Eu-DTPA-(B)-H2, we attempted to record some CD spectra. The conjugation of DTPA at the N-terminus of the A-chain had no effect on the secondary structure of the peptide. However, CD spectrum of the Eu-DTPA-(B)-H2 could not be obtained due to its poor solubility in phosphate buffer saline.

The receptor binding affinity of Eu-DTPA-(A)-H2 was higher compared to Eu-DTPA-(B)-H2 which may be due to the poor solubility. Despite the lower receptor binding affinity of Eu-DTPA-(B)-H2, H2 relaxin exhibited similar receptor binding affinity in the presence of both labeled peptides. The affinity of the two Eu-DPTA-H2 relaxin variants is similar to that obtained using both ^{33}P- and ^{125}I-labeled H2 relaxin [22].

In summary, we have successfully synthesized two mono-Eu-DTPA conjugated peptide ligands using modern solid phase synthesis technology. In vitro receptor assays showed that the choice of a site for incorporation of a chelator like DTPA is critical as its large size can adversely alter the biophysical property and consequently affect the pharmacological activity of the peptides. Our mono-Eu-DTPA labeled peptide, Eu-DTPA-(A)-H2 retains full activity and as it does not undergo isotope decay and is stable for long

periods at -20 °C it is a useful probe to study ligand–receptor interactions of therapeutically important H2 relaxin analogs.

Acknowledgments

This research was funded by NHMRC (Australia) project grants 350284 and 508995 to JDW and RADB. We are grateful to Tania Ferraro & Sharon Layfield for assistance with biochemical assays and to Feng Lin for amino acid analysis. During these studies, MAH was the recipient of a Reid Trust Fellowship, and is currently a Florey Trust Foundation Fellow. RADB is an NHMRC Senior Research Fellow. JDW is an NHMRC Principal Research Fellow. Studies at the FNI were supported by the Victorian Government's Operational Infrastructure Support Program.

Appendix A. Supplementary data

Supplementary data associated with this article can be found, in the online version, at doi:10.1016/j.bbrc.2012.02.141.

References

[1] F. Hisaw, Experimental relaxation of the pubic ligament of the guinea pig, Proc. Soc. Exp. Biol. Med. 23 (1926) 661–663.
[2] F. Shabanpoor, F. Separovic, J.D. Wade, The human insulin superfamily of polypeptide hormones, Vitam. Horm. 80 (2009) 1–31.
[3] C. Eigenbrot, M. Randal, C. Quan, J. Burnier, L. O'Connell, E. Rinderknecht, A.A. Kossiakoff, X-ray structure of human relaxin at 1.5 A. Comparison to insulin and implications for receptor binding determinants, J. Mol. Biol. 221 (1991) 15–21.
[4] R.A. Bathgate, R. Ivell, B.M. Sanborn, O.D. Sherwood, R.J. Summers, International Union of Pharmacology LVII: recommendations for the nomenclature of receptors for relaxin family peptides, Pharmacol. Rev. 58 (2006) 7–31.
[5] E.E. Bullesbach, C. Schwabe, The relaxin receptor-binding site geometry suggests a novel gripping mode of interaction, J. Biol. Chem. 275 (2000) 35276–35280.
[6] E.E. Bullesbach, S. Yang, C. Schwabe, The receptor-binding site of human relaxin II. A dual prong-binding mechanism, J. Biol. Chem. 267 (1992) 22957–22960.
[7] J.I. Park, J. Semyonov, W. Yi, C.L. Chang, S.Y. Hsu, Regulation of receptor signaling by relaxin A chain motifs: derivation of pan-specific and LGR7-specific human relaxin analogs, J. Biol. Chem. 283 (2008) 32099–32109.
[8] S.Y. Hsu, K. Nakabayashi, S. Nishi, J. Kumagai, M. Kudo, O.D. Sherwood, A.J. Hsueh, Activation of orphan receptors by the hormone relaxin, Science 295 (2002) 671–674.
[9] O.D. Sherwood, Relaxin's physiological roles and other diverse actions, Endocr. Rev. 25 (2004) 205–234.
[10] I. Mookerjee, N.R. Solly, S.G. Royce, G.W. Tregear, C.S. Samuel, M.L. Tang, Endogenous relaxin regulates collagen deposition in an animal model of allergic airway disease, Endocrinology 147 (2006) 754–761.
[11] R.D. Koos, A.A. Kazi, M.S. Roberson, J.M. Jones, New insight into the transcriptional regulation of vascular endothelial growth factor expression in the endometrium by estrogen and relaxin, Ann. NY Acad. Sci. 1041 (2005) 233–247.
[12] S. Palejwala, L. Tseng, A. Wojtczuk, G. Weiss, L.T. Goldsmith, Relaxin gene and protein expression and its regulation of procollagenase and vascular endothelial growth factor in human endometrial cells, Biol. Reprod. 66 (2002) 1743–1748.
[13] J.R. Teerlink, M. Metra, G.M. Felker, P. Ponikowski, A.A. Voors, B.D. Weatherley, A. Marmor, A. Katz, J. Grzybowski, E. Unemori, S.L. Teichman, G. Cotter, Relaxin for the treatment of patients with acute heart failure (Pre-RELAX-AHF): a multicentre, randomised, placebo-controlled, parallel-group, dose-finding phase IIb study, Lancet 373 (2009) 1429–1439.
[14] S.L. Teichman, E. Unemori, J.R. Teerlink, G. Cotter, M. Metra, Relaxin: review of biology and potential role in treating heart failure, Curr. Heart Fail. Rep. 7 (2010) 75–82.
[15] S. Feng, I.U. Agoulnik, A. Truong, Z. Li, C.J. Creighton, E.M. Kaftanovskaya, R. Pereira, H.D. Han, G. Lopez-Berestein, T. Klonisch, M.M. Ittmann, A.K. Sood, A.I. Agoulnik, Suppression of relaxin receptor RXFP1 decreases prostate cancer growth and metastasis, Endocr. Relat. Cancer 17 (2010) 1021–1033.
[16] S. Sudo, J. Kumagai, S. Nishi, S. Layfield, T. Ferraro, R.A. Bathgate, A.J. Hsueh, H3 relaxin is a specific ligand for LGR7 and activates the receptor by interacting with both the ectodomain and the exoloop 2, J. Biol. Chem. 278 (2003) 7855–7862.
[17] F. Shabanpoor, R.A. Hughes, R.A. Bathgate, S. Zhang, D.B. Scanlon, F. Lin, M.A. Hossain, F. Separovic, J.D. Wade, Solid-phase synthesis of europium-labeled human INSL3 as a novel probe for the study of ligand-receptor interactions, Bioconjug. Chem. 19 (2008) 1456–1463.
[18] F. Shabanpoor, R.A. Hughes, S. Zhang, R.A. Bathgate, S. Layfield, M.A. Hossain, G.W. Tregear, F. Separovic, J.D. Wade, Effect of helix-promoting strategies on the biologic activity of novel analogs of the B-chain of INSL3, Amino Acids 38 (2010) 121–131.
[19] M.A. Hossain, K.J. Rosengren, C.S. Samuel, F. Shabanpoor, L.J. Chan, R.A. Bathgate, J.D. Wade, The minimal active structure of human relaxin-2, J. Biol. Chem. 286 (2011) 37555–37565.
[20] J.D. Silvertown, J.C. Symes, A. Neschadim, T. Nonaka, J.C. Kao, A.J. Summerlee, J.A. Medin, Analog of H2 relaxin exhibits antagonistic properties and impairs prostate tumor growth, Faseb J. 21 (2007) 754–765.
[21] F. Shabanpoor, F. Separovic, J.D. Wade, General method for selective labeling of double-chain cysteine-rich peptides with a lanthanide chelate via solid-phase synthesis, J. Pept. Sci. 17 (2011) 169–173.
[22] M.A. Hossain, K.J. Rosengren, L.M. Haugaard-Jonsson, S. Zhang, S. Layfield, T. Ferraro, N.L. Daly, G.W. Tregear, J.D. Wade, R.A. Bathgate, The A-chain of human relaxin family peptides has distinct roles in the binding and activation of the different relaxin family peptide receptors, J. Biol. Chem. 283 (2008) 17287–17297.

Biochemical and Biophysical Research Communications 420 (2012) 257–262

Contents lists available at SciVerse ScienceDirect

Biochemical and Biophysical Research Communications

journal homepage: www.elsevier.com/locate/ybbrc

L-type voltage-operated calcium channels, *N*-methyl-D-aspartate receptors and neuronal nitric-oxide synthase form a calcium/redox nano-transducer within lipid rafts

D. Marques-da-Silva, C. Gutierrez-Merino *

Dept. Biochemistry and Molecular Biology, Faculty of Sciences, University of Extremadura, Badajoz 06006, Spain

ARTICLE INFO

Article history:
Received 24 February 2012
Available online 3 March 2012

Keywords:
Cerebellar granule neurons
Lipid rafts
Calcium/redox signaling
NMDA receptors
L-type calcium channels
nNOS

ABSTRACT

Cytosolic calcium plays a leading role in the control of neuronal excitability, plasticity and survival. This work aims to experimentally assess the possibility that lipid rafts of the plasma membrane can provide a structural platform for a faster and tighter functional coupling between calcium and nitric-oxide signaling in neurons. Using primary cerebellar granule neurons (CGN) in culture this hypothesis has been experimentally assessed with fluorescence resonance energy transfer imaging, preparations of lipid rafts-enriched membrane fragments and western blotting. The results obtained in this work demonstrated that major calcium entry systems of the plasma membrane of CGN (L-type calcium channels and *N*-methyl-D-aspartate receptors) and nitric-oxide synthase are separated by less than 80 nm from each other within lipid rafts-associated sub-microdomains, suggesting a new role of lipid rafts as neuronal calcium/redox nano-transducers.

1. Introduction

A highly efficient and rapid functional coupling is particularly relevant for neuronal activity, and studies on calcium signaling in neurons have played a pioneer role to demonstrate the outstanding role of sub-cellular compartmentation in the control of neuronal activity [1–3].

Calcium entry through L-VOCC and NMDAr play a major role in the maintenance of cytosolic calcium needed for mature cerebellar granule neurons (CGN) survival and excitability [4–6], and alterations of their functional response by ROS or redox modulation can lead to CGN death in culture either by apoptosis or by excitotoxicity [6–9]. Moreover, a sustained alteration of intracellular calcium homeostasis in neurons is a common feature in oxidative stress-mediated neurodegeneration, and plasma membrane calcium transport systems have been shown to be molecular targets for ROS generated in neurodegenerative insults and diseases [10,11]. In primary cultures of mature CGN the entry of calcium through L-VOCC plays a major role to keep cytosolic calcium within the optimal 70–200 nM concentration range needed for survival of these neurons *in vitro* [5,6,9].

Calcium entry through opening of L-VOCC can generate transients of micromolar calcium concentration up to distances close to 100 nm from the L-VOCC pore depending on the calcium buffering capacity of its microenvironment [3]. L-VOCC have been shown to be associated with lipid rafts in cardiomyocytes [12,13], the L-VOCC subunit α22 has been shown to partition within lipid rafts in cerebellum bound to caveolin [14], and we have shown that in mature CGN in culture L-VOCC is associated with lipid rafts [15]. Lipid rafts define cellular sub-microdomains of the plasma membrane anchoring caveolins, flotillin and also actin microfilaments [12]. The presence of caveolins associated with neuronal plasma membrane in microdomains without the morphological appearance of "caveola invaginations" has been documented during last decade, revised in [16]. Furthermore, it has been suggested that these caveolin-rich nanodomains can serve to focalize cell signaling transduction in neurons [16–18]. Indeed, it has been shown that caveolin-1 interacts with nNOS [19] and that the actin cytoskeleton modulates the activity of NMDAr [20].

Lipid rafts of the plasma membrane are dynamic nanodomains of a size between 10 and 200 nm [21]. FRET is a spectroscopic ruler that allows to measure distances in the nanometer scale range [22,23]. Quantitative FRET-imaging is a powerful tool for the analysis of cellular sub-microdomains, because intensity readings of

Abbreviations: CGN, cerebellar granule neurons; CTB, cholera toxin subunit B; FRET, fluorescence or Förster resonance energy transfer; IgG, immunoglobulin G; L-VOCC, L-type voltage-operated calcium channels; NMDAr, *N*-methyl D-aspartate receptor; nNOS, neuronal nitric-oxide synthase; PBS, phosphate-buffered saline; ROS, reactive oxygen species.

* Corresponding author. Fax: +34 924 289419.
E-mail addresses: dorinda1@unex.es (D. Marques-da-Silva), carlosgm@unex.es (C. Gutierrez-Merino).

0006-291X/$ - see front matter © 2012 Elsevier Inc. All rights reserved.
doi:10.1016/j.bbrc.2012.02.145

volume elements of sub-micrometers section size can yield information on their structure in the nanometer scale range. FRET between membrane-bound proteins labeled with fluorescent antibodies is a case of FRET from one donor to multiple acceptors which can be used to identify proteins separated less than 100 nm within lipid rafts sub-microdomains [15,24,25].

In this work, we have extended our studies using FRET-imaging approaches, preparations of lipid rafts-enriched membrane fragments and western blotting to show that L-VOCC, NMDAr and nNOS co-localize within lipid rafts-associated sub-microdomains of a size lower than 200 nm.

2. Materials and methods

2.1. Preparation of rat cerebellar granule neurons (CGN)

CGN were obtained from dissociated cerebella of 7 days-old Wistar rats as described previously [6,15,24,26,27].

2.2. Isolation of lipid rafts

Lipid rafts were isolated running sucrose gradients as in previous works [15,25], following a method adapted from the protocols described in [28,29]. Samples were analyzed by SDS–PAGE followed by Western blotting.

2.3. Western blotting

SDS–PAGE were run at a concentration of 7.5%, 10.4% or 12.5% acrylamide depending upon the molecular weights of the target proteins, using 2 μg protein of CGN lysates in each lane. Gels were transferred to nitrocellulose membranes of 0.2 μm average pore size (Trans-BloT Transfer Medium, BioRad), as in [15,25].

2.4. Fluorescence microscopy imaging and FRET analysis

Fluorescence microscopy images of CGN were acquired with a Hamamatsu Orca-R2 CCD camera (binning mode 2×2) attached to a Nikon Diaphot 300 epifluorescence microscope (objective NCF Plan ELWD 20×), and quantitative analysis of the average fluorescence intensity of selected neuronal soma was done with the HCImage software, as described previously [15,24,25]. Images were acquired with an excitation filter of 470 nm, and 510 nm dichroic mirror/520 nm emission filter (donor-green fluorescence) and 580 nm dichroic mirror/590 nm emission filter (acceptor-red fluorescence). Acquired images were exported as TIFF pseudo-color images for further processing using the Image J software. Direct-fluorescence intensity images are presented in gray scale (black: very low or no-signal, and white: saturated signal).

FRET measurements were performed with mature CGN fixed and stained with primary and fluorescence-labeled secondary antibodies as in [15,24,25]. The basic criteria used to confirm the occurrence of FRET and calculation of FRET-efficiency was the simultaneous occurrence of quenching of the green fluorescence (GF) and an increase of the ratio between red (acceptor fluorescence) and green fluorescence intensities (ratio red/green) in CGN stained with Alexa488- and Cy3-secondary antibodies, as discussed in more detail in [15]. To quantitate the effects of the treatment for labeling with the second primary antibody/IgG-Cy3 complex in the green and red fluorescence intensities of CGN stained with the first primary antibody plus IgG-Alexa488 we have carried out control experiments performing these treatments without the second primary antibody. These control experiments showed that on average this treatment resulted in 12 ± 3% quenching of the green fluorescence of the IgG-Alexa488 antibody, and no statistically significant change of the red fluorescence intensity. This has been taken into account in all the calculations of the quenching of green fluorescence afforded by CGN double labeling with antibodies shown in this work.

2.5. Chemicals and reagents

Primary antibodies: goat anti-NMDAr (sc-1468), rabbit anti-L-VOCC (sc-25686), mouse anti-nNOS (sc-5302), goat anti-H-Ras (sc-32026), rabbit anti-caveolin-1 (sc-894), rabbit anti-caveolin-2 (sc-7942), goat anti-caveolin-2 (sc-1858), goat anti-flotillin-1 (sc-16640) and rabbit anti-flotillin-1 (sc-25506) were supplied by Santa Cruz Biotechnology (Santa Cruz, CA, USA). Fluorescence-labeled secondary antibodies used to label the primary antibodies listed above: anti-rabbit IgG-Alexa488 (cat. no. A11008), anti-goat IgG-Alexa488 (cat. no. A11055) and anti-mouse IgG-Alexa488 (cat. no. A11001) from Invitrogen (Molecular Probes, Eugene, OR, USA), and anti-rabbit IgG-Cy3 (cat. no. C2306) and anti-goat IgG-Cy3 (cat. no. C2821) from Sigma (St. Louis, MO, USA). Anti-goat, anti-rabbit and anti-mouse IgG horseradish peroxidase and Super-Signal West Dura Extended Duration Substrate used in Western blotting were supplied by Pierce (Rockford, IL, USA).

DM-bodipy dihydropyridine (cat. no. D7443), ST-bodipy dihydropyridine (cat. no. S7445) and cholera toxin subunit B conjugated with Alexa555 (cat. no. C34776) were supplied by Invitrogen (Molecular Probes, Eugene, OR, USA). All other reagents and chemicals were of analytical grade from Sigma–Aldrich or Roche-Merck (Darmstadt, Germany).

2.6. Statistical analysis

Results are expressed as mean ± standard error (s.e.). Statistical analysis was carried out by Mann–Whitney non-parametric test. Significant difference was accepted at the $p < 0.05$ level. All the results were confirmed with duplicate measurements of at least three different CGN preparations.

3. Results

3.1. Lipid rafts membrane fractions are enriched in transport systems relevant for cytosolic calcium homeostasis and also in ROS-producing redox systems

Membrane fragments prepared from CGN lysates were fractionated in sucrose density gradients as indicated in the Methods. Western Blot analysis of the fractions showed that typical lipid rafts markers, H-Ras, flotillin, caveolin-1 and caveolin-2 were largely enriched in fractions 1–5 (Fi. 1). NMDAr, L-VOCC and nNOS were found to be highly enriched in the fractions 1–5 (Fig. 1), as it was also shown earlier for L-VOCC [15]. On these grounds, we have experimentally ascertained this conclusion by FRET-imaging in fixed mature CGN.

3.2. L-VOCC and NMDAr co-localize within cholera toxin B-binding sites and caveolin-rich sub-microdomains in the neuronal plasma membrane of mature C

Fluorescence microscopy images of CGN double stained with anti-L-VOCC/IgG-Alexa488 and anti-NMDAr/IgG-Cy3 were obtained with an excitation filter of 470 nm, i.e. with a negligible direct excitation of the Cy3-dye. The images showed an extensive co-localization of both antibodies as shown by merge images displayed in Fig. 2. The results obtained for a total number of 1400 neuronal somas of, at least, three different CGN preparations ($n \geqslant 6$) were accumulated and subjected to detailed pixel-analysis

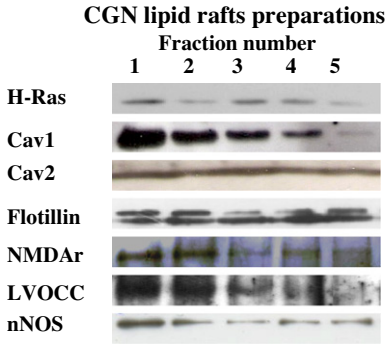

Fig. 1. NMDAr, L-VOCC and nNOS are associated with lipid rafts isolated from mature CGN in culture. NMDAr, L-VOCC and nNOS distribution in membrane fractions were determined by Western blotting using anti-NMDAr (sc-1468), anti-L-VOCC (sc-25686), anti-nNOS (sc-5302). Fraction's distribution of protein raft markers: H-Ras (anti-H-Ras sc-32026), caveolin-1 (anti-caveolin-1 sc-894), caveolin-2 (anti-caveolin-2 sc-1858) and flotillin (anti-flotillin-1 sc-16640). Fractions 1–5 enriched in protein lipid rafts markers are also enriched in cholesterol as shown in a recent work of our laboratory [25]. Western blotting shown are representative of the results obtained in experiments done with at least three different preparations of lipid rafts. The same amounts of protein were used in each fraction for these experiments.

with the Image J software (Fig. 2). With the magnification and binning used to acquire the images, one pixel has a square section size of ~0.7 μm × 0.7 μm. Double staining of CGN led to a marked shift of the green fluorescence histograms towards lower intensity and mean values, whereas the red fluorescence histograms are shifted towards higher intensity and mean values. A very large FRET-efficiency for this pair is revealed by (i) an average 64 ± 6% quenching of the intensity of donor fluorescence (green Alexa488 fluorescence emission) and (ii) 9.6-fold increase of the ratio between red and green fluorescence intensities, from 0.50 ± 0.08 for CGN stained only with the donor anti-L-VOCC/IgG-Alexa488 up to 4.8 ± 0.5 for CGN double stained with the same donor and anti-NMDAr/IgG-Cy3. Therefore, these results led to the conclusion that donor (Alexa488) and acceptor (Cy3) dyes are separated by an average distance lower than the R_0 value for this FRET pair, i.e. <5 nm. Taking into account the average size of the IgG antibodies used for labeling of both proteins are T-shape of dimensions of approx. 25 × 18 nm [30] and that for the case of multiple acceptors around each donor the FRET-efficiency is lower than 2% for a donor/acceptor pair separated by a distance $\geqslant 2R_0$ [23], this indicated that L-VOCC and NMDAr are separated by less than 80 nm. We confirmed this point using an alternate FRET approach with shorter distance range. To this end we used the fluorescent L-VOCC ligand ST-bodipy dihydropyridine, a much smaller size molecule, as acceptor of NMDAr labeled with anti-NMDAr/IgG-Alexa488. Fluorescence microscopy images of CGN double stained with anti-NMDAr/IgG-Alexa488 and 80 nM ST-bodipy dihydropyridine revealed the occurrence of FRET also for this donor/acceptor pair (Fig. 2). Moreover, the average efficiency of FRET was high, e.g. 49 ± 5% quenching of the green fluorescence of the donor, pointing out that the binding site of ST-bodipy dihydropyridine is at approximately 6 ± 1 nm distance from donor Alexa488 dyes of the antibodies bound to NMDAr. Taking into consideration the average diameter sizes of L-VOCC and NMDAr (~10–15 nm), the location of the dihydropyridine binding site in the center of the large globular extracellular domain of L-VOCC [31,32] and the size of primary + secondary IgG antibodies complex (~35 nm), this result leads to the conclusion that L-VOCC and NMDAr are vicinal proteins in the plasma membrane.

The quantitative pixel-analysis of FRET-imaging also confirmed that NMDAr extensively co-localized within FRET-distance with L-VOCC, as no indications of segregation of two separated populations was observed in the pixel-intensity distributions in FRET-imaging, see Fig. 2. Because we have shown an extensive association of L-VOCC in mature CGN in culture with lipid rafts [15], we have performed FRET-imaging using fluorescent cholera toxin B (CTB) and antibodies against lipid rafts-associated proteins like caveolins 1 and 2 and flotillin.

Fig. 2 also shows the results obtained in FRET-imaging experiments using anti-NMDAr/IgG-Alexa488 as donor and as acceptors CTB-Alexa555 (Fig. 2), anti-caveolin-2/IgG-Cy3 (Supplementary Figs. S1 and S2), anti-caveolin-1/IgG-Cy3 (Supplementary Fig. S2), and anti-flotillin/IgG-Cy3 (Supplementary Fig. S2). The percentage of quenching of donor fluorescence (see Figs. 2 and S2), pointed out a remarkably high efficiency of FRET for all these pairs. It is to be noted that the value obtained for the efficiency of FRET between anti-NMDAr/IgG-Alexa488 and CTB-Alexa555 is identical to the 66 ± 9% value obtained in separate experiments for CGN stained with the donor/acceptor pair: 8 nM DM-bodipy dihydropyridine (a green fluorescent L-VOCC blocker [33,34])/0.5 μg/ml cholera toxin subunit B conjugated with Alexa555 (CTB-A555).

3.3. nNOS is within FRET-distance from NMDAr and L-VOCC

nNOS association with PDZ-domains of proteins bound to the neuronal cytoskeleton is a well established experimental observation [35]. As NMDAr also binds to proteins containing PDZ-domains [36], nNOS should be expected to be anchored near NMDAr.

Selected fluorescence microscopy images of CGN double stained with anti-nNOS/IgG-Alexa488 and anti-NMDAr/IgG-Cy3 are presented in Fig. 3. Both, direct inspection of merge images and pixels-intensity analysis within neuronal soma demonstrated the occurrence of significant FRET between Alexa488- and Cy3-tagged antibodies. Moreover, green fluorescence quenching and the increase of red fluorescence were derived from a shift of a large part of the Gaussian distribution of pixels towards lower and higher fluorescence intensity values, respectively (Supplementary Fig. S3), demonstrating an extensive co-localization of nNOS and NMDAr within a distance supporting an average 46 ± 5% FRET-efficiency.

The nNOS co-localization within FRET-distance of protein markers associated with lipid rafts was also assessed by microscopy imaging. Fig. 3 shows the results obtained in FRET-imaging experiments using anti-nNOS/IgG-Alexa488 as donor and as acceptors CTB-Alexa555, anti-caveolin-1/IgG-Cy3 and anti-caveolin-2/IgG-Cy3. The percentage of quenching of donor fluorescence showed large variations for these different pairs (Fig. 3), pointing out that FRET-efficiency varied from 16 to 60%. The lower FRET-efficiency from anti-nNOS/IgG-Alexa488 as donor to anti-caveolin-1/IgG-Cy3 with respect to anti-caveolin-2/IgG-Cy3 indicated a smaller distance of close approach for the pair nNOS/caveolin-2 than for the pair nNOS/caveolin-1. In contrast, the lower FRET-efficiency from anti-nNOS/IgG-Alexa488 as donor to CTB-Alexa555 with respect to anti-caveolin-2/IgG-Cy3 can be rationalized, at least in part, in terms of the extracellular location of CTB-binding sites in the plasma membrane, while nNOS is intracellular.

4. Discussion

Our results highlight the occurrence of a large clustering of NMDAr and L-VOCC in caveolin-rich and lipid rafts-associated sub-microdomains of an average size $\leqslant$ 100 nm. Taking into account the molecular sizes of NMDAr and L-VOCC, their location within domains of a size lower than 100 nm in a rigid lipid environment (lipid rafts) strongly suggest that these nanodomains operate as a "calcium-microchip like structure" of the plasma membrane for a tight control of neuronal excitability by calcium

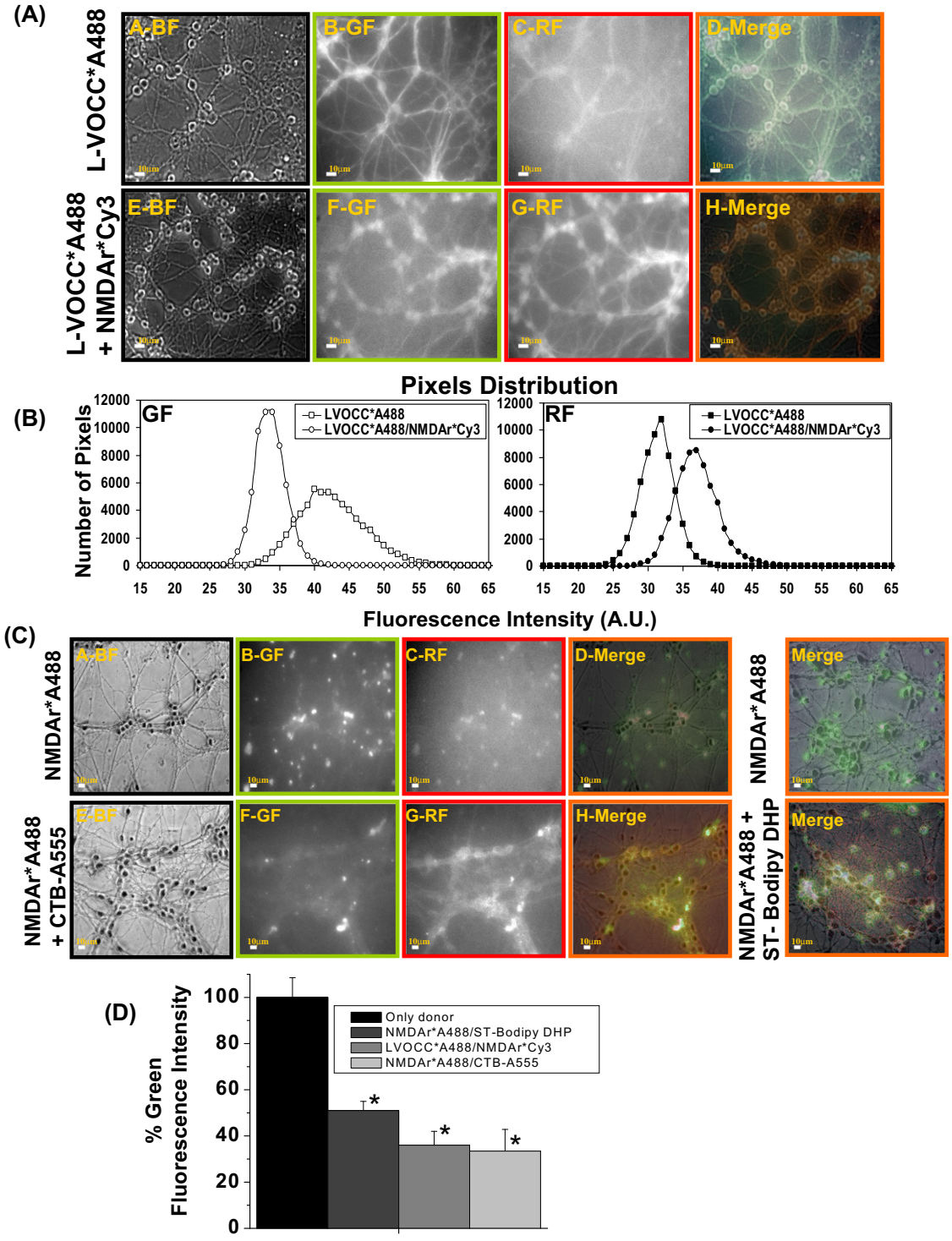

Fig. 2. Extensive FRET between NMDAr and L-VOCC tagged with antibodies forming an appropriate donor/acceptor pair, between NMDAr labeled with antibodies and the fluorescent L-VOCC antagonist ST-bodipy-dihydropyridine (ST-bodipy-DHP) and also with the lipid rafts marker cholera toxin subunit B conjugated with Alexa555 (CTB-A555). Panel A: Representative quantitative fluorescence microscopy images of CGN stained with anti-L-VOCC (sc-25686)/IgG-Alexa488 (L-VOCC∗A488, A–D) or with anti-L-VOCC/IgG-Alexa488 and anti-NMDAr (sc-1468)/IgG-Cy3 (L-VOCC∗A488/NMDAr∗Cy3, E–H). Merged images of green (GF) and red fluorescence (RF) are pasted over a bright field (BF) mask. Green and red areas display the donor and acceptor fluorescence, respectively, and the orange-yellow areas point out the higher intensity FRET regions (D and H). The exposure time for green fluorescence images was 168.3 ms and for red fluorescence images was 224 ms. Panel B: Distribution of the fluorescence intensity of pixels of 1400 neuronal somas selected from fluorescence microscopy images like those shown in the Panel A obtained with three different CGN preparations. Distribution of pixels versus fluorescence intensity in green fluorescence images and red fluorescence images. Panel C: *Left side*: Representative quantitative fluorescence microscopy images of CGN stained with anti-NMDAr (sc-1468)/IgG-Alexa488 (NMDAr∗A488, A–D) or with anti-NMDAr/IgG-Alexa488 and 0.5 μg/ml cholera toxin subunit B conjugated with Alexa555 (NMDAr∗A488/CTB-A555) (E–H). *Right side*: Representative quantitative merge fluorescence microscopy images of CGN stained with anti-NMDAr (sc-1468)/IgG-Alexa488 (NMDAr∗A488) or with anti-NMDAr/IgG-Alexa488 and 80 nM ST-bodipy-dihydropyridine (NMDAr∗A488/ST-Bodipy-DHP). The exposure time for green fluorescence images was 205.7 ms and for red fluorescence images was 243.1 ms. Other experimental details as in Panel A. Panel D: Quenching of the donor fluorescence (green fluorescence) obtained from the analysis of fluorescence intensity data. The results shown in panel D are the mean ± s.e. evaluated from the fluorescence intensity readings of more than 1000 neuronal somas of at least three different CGN preparations. (∗) $p < 0.05$, i.e. statistically significant, with respect to the control (CGN labeled with the donor only).

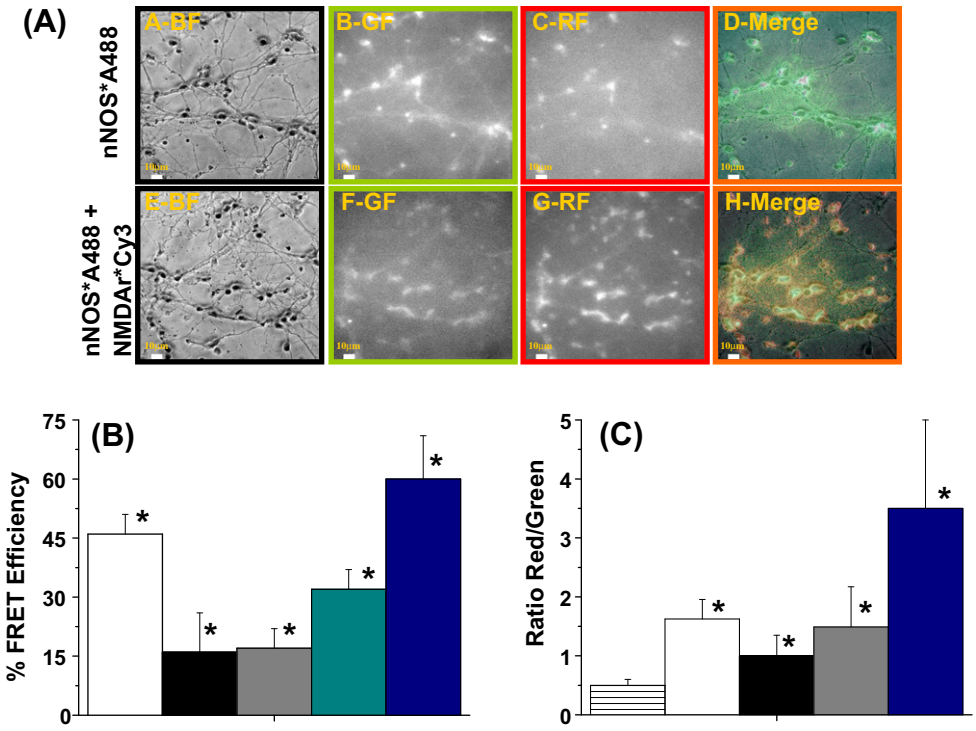

Fig. 3. FRET from nNOS tagged with IgG-Alexa488 (as fluorescence donor) to CTB-A555 and to NMDAr, L-VOCC and caveolins tagged with IgG-Cy3 antibodies. Panel A: Representative quantitative fluorescence microscopy images of CGN stained with anti-nNOS (sc-5302)/IgG-Alexa488 (nNOS∗A488, A–D) or with anti-nNOS/IgG-Alexa488 and anti-NMDAr (sc-1468)/IgG-Cy3 (nNOS∗A488/NMDAr∗Cy3, E–H). Merged images of green (GF) and red fluorescence (RF) are pasted over a bright field (BF) mask. Green and red areas display the donor and acceptor fluorescence, respectively, and the orange-yellow areas point out the higher intensity FRET regions (D and H). The exposure time for green fluorescence images was 243.1 ms and for red fluorescence images was 261.8 ms. Panel B: FRET-efficiency obtained from the quenching of green fluorescence intensity for CGN double stained with anti-nNOS/IgG-Alexa488//anti-NMDAr/IgG-Cy3 (nNOS∗A488/NMDAr∗Cy3, white), anti-nNOS/IgG-Alexa488//anti-L-VOCC/IgG-Cy3 (nNOS∗A488/L-VOCC∗Cy3, black), anti-nNOS/IgG-Alexa488//anti-caveolin-1/IgG-Cy3 (nNOS∗A488/Cav1∗Cy3, gray), anti-nNOS/IgG-Alexa488//CTB-A555 (nNOS∗A488/CTB-A555, cyan) and anti-nNOS/IgG-Alexa488//anti-Cav2/IgG-Cy3 (nNOS∗A488/Cav2∗Cy3, blue). Panel C: Ratio of Red/Green fluorescence obtained from the analysis of fluorescence intensity data for CGN stained as indicated in the Panel B. The bar with horizontal lines in panel C is the ratio value for CGN stained only with the donor (nNOS∗A488). The results shown in panels B and C are the mean ± s.e. evaluated from the green fluorescence intensity readings of more than 1000 neuronal soma of at least three different CGN preparations in each case. (∗) $p < 0.05$, i.e. statistically significant, with respect to the control (CGN labeled only with the donor).

signaling. Our calculated distance for NMDAr and L-VOCC separation within these nanodomains is ⩽40 nm. As shown in Parekh [3], at this short distance L-VOCC activation can transiently rise the local Ca^{2+} concentration nearby NMDAr up to the 10–100 μM range. As this calcium concentration is high enough to strongly stimulate the secretion of L-Glu in the vicinity of the NMDAr, our data suggest that L-VOCC activation can eventually potentiate the activation of neighbor NMDAr.

Considering the volume and geometry of IgG [30], the value of the distance for 50% FRET-efficiency of the donor/acceptor pairs used herein (R_0 values), between 5 and 6 nm [37], and the fact that FRET-efficiency is lower than 10% for a separation distance of $2R_0$ in the case of a highly packed geometry of multiple acceptors around each donor [23], the results led to the conclusion that L-VOCC, NMDAr and nNOS are largely clustered in lipid rafts sub-microdomains and separated by less than 80 nm. Activation of L-VOCC can generate a calcium microdomain with calcium concentrations higher than 1 μM up to a distance close to 100 nm with low calcium buffering capacity, as the mean path length is 70–80 nm in the presence of 0.1 mM of calcium chelators with a calcium dissociation constant lower than 250 nM [3]. Our results also pointed out the presence of nNOS within this distance in lipid rafts sub-microdomains. The presence of nNOS within these sub-microdomains is consistent with previous reports pointing out that both nNOS and NMDAr bind to PDZ-domains of proteins of the neuronal cytoskeleton [35,36] and that nNOS interacts with caveolin-1 [19]. Owing to the dependence on free Ca^{2+} concentration of NO production by nNOS, $EC_{50} \approx 0.2–0.4$ μM [38], a vicinal sub-cellular location is the simplest way to elicit the activation of this enzyme after NMDAr and/or L-VOCC activation and also to optimize the inhibition by NO of the excessive influx of Ca^{2+} via NMDAr.

Acknowledgments

This work has been funded by Grant BFU2007-67740 of the Spanish Ministerio de Ciencia y Tecnología, with FEDER co-financing. DMS is a Predoctoral Fellow of the Spanish Ministerio de Ciencia y Tecnología. Our laboratory technician Maria I. Piedehierro helped in CGN preparations and performance of western blotting.

Appendix A. Supplementary data

Supplementary data associated with this article can be found, in the online version, at doi:10.1016/j.bbrc.2012.02.145.

References

[1] M.J. Berridge, Neuronal calcium signalling, Neuron 21 (1998) 13–26.
[2] M. Brini, E. Carafoli, Calcium signalling: a historical account, recent developments and future perspectives, Cell Mol. Life Sci. 57 (2000) 354–370.
[3] A.B. Parekh, Ca^{2+} microdomains near plasma membrane Ca^{2+} channels: impact on cell function, J. Physiol. 586 (2008) 3043–3054.
[4] R. Balazs, O.S. Jorgensen, N. Hack, *N*-methyl-D-aspartate promotes the survival of cerebellar granule cells in culture, Neuroscience 27 (1988) 437–451.
[5] J.L. Franklin, E.M. Johnson Jr., Suppression of programmed neuronal death by sustained elevation of cytoplasmic calcium, Trends Neurosci. 15 (1992) 501–508.

[6] Y. Gutierrez-Martin, F.J. Martin-Romero, F. Henao, C. Gutierrez-Merino, Alteration of cytosolic free calcium homeostasis by SIN-1: high sensitivity of L-type Ca^{2+} channels to extracellular oxidative/nitrosative stress in cerebellar granule cells, J. Neurochem. 92 (2005) 973–989.
[7] H. Ischiropoulos, D. Duran, J. Horwitz, Peroxynitrite-mediated inhibition of DOPA synthesis in PC12 cells, J. Neurochem. 65 (1995) 2366–2372.
[8] J.L. Trackey, T.F. Uliasz, S.J. Hewett, SIN-1-induced cytotoxicity in mixed cortical cell culture: peroxynitrite-dependent and -independent induction of excitotoxic cell death, J. Neurochem. 79 (2001) 445–455.
[9] M.A. Garcia-Bereguiain, A. Samhan-Arias, F.J. Martin-Romero, C. Gutierrez-Merino, Hydrogen sulfide raises cytosolic calcium in neurons through activation of L-type Ca^{2+} channels, Antioxid. Redox Signal. 10 (2008) 31–42.
[10] C. Hidalgo, P. Donoso, Crosstalk between calcium and redox signalling: from molecular mechanisms to health implications, Antioxid. Redox Signal. 10 (2008) 1275–1312.
[11] C. Gutierrez-Merino, Redox modulation of neuronal calcium homeostasis and its deregulation by reactive oxygen species, in: C. Gutierrez-Merino, C. Leeuwenburgh (Eds.), Free Radicals in Biology and Medicine, Research Signpost, Kerala, India, 2008, pp. 67–101.
[12] K.M.M. ÓConnell, J.R. Martens, M.M. Tamkun, Localization of ion channels to lipid raft domains within the cardiovascular system, Trends Cardiovasc. Med. 14 (2004) 37–42.
[13] R.C. Balijepalli, J.D. Foell, D.D. Hall, J.W. Hell, T.J. Kamp, Localization of cardiac L-type Ca^{2+} channels to a caveolar macromolecular signaling complex is required for β_2-adrenergic regulation, Proc. Natl. Acad. Sci. USA 103 (2006) 7500–7505.
[14] A. Davies, L. Douglas, J. Hendrich, J. Wratten, A. Tran van Minh, I. Foucault, D. Koch, W.S. Pratt, H.R. Saibil, A.C. Dolphin, The calcium channel 22 subunit partitions with CaV2.1 into lipid rafts in cerebellum: implications for localization and function, J. Neurosci. 26 (2006) 8748–8757.
[15] D. Marques-da-Silva, A.K. Samhan-Arias, T. Tiago, C. Gutierrez-Merino, L-type calcium channels and cytochrome b_5 reductase are components of protein complexes tightly associated with lipid rafts microdomains of the neuronal plasma membrane, J. Proteomics 73 (2010) 1502–1510.
[16] B.P. Head, P.A. Insel, Do caveolins regulate cells by actions outside of caveolae?, Trends Cell Biol 17 (2007) 51–57.
[17] B.P. Head, H.H. Patel, Y.M. Tsutsumi, Y. Hu, T. Mejia, R.C. Mora, P.A. Insel, D.M. Roth, J.C. Drummond, P.M. Patel, Caveolin-1 expression is essential for N-methyl-D-aspartate receptor-mediated Src and extracellular signal-regulated kinase 1/2 activation and protection of primary neurons from ischemic cell death, Faseb J. 22 (2008) 828–840.
[18] M. Toselli, G. Biella, V. Taglietti, E. Cazzaniga, M. Parenti, Caveolin-1 expression and membrane cholesterol content modulate N-type calcium channel activity in NG108-15 cells, Biophys. J. 89 (2005) 2443–2457.
[19] Y. Sato, I. Sagami, T. Shimizu, Identification of Caveolin-1-interacting sites in neuronal nitric-oxide synthase. Molecular mechanism for inhibition of NO formation, J. Biol. Chem. 279 (2004) 8827–8836.
[20] E. Bonfoco, M. Leist, B. Zhivotovsky, S. Orrenius, S.A. Lipton, P. Nicotera, Cytoskeletal breakdown and apoptosis elicited by NO donors in cerebellar granule cells require NMDA receptor activation, J. Neurochem. 67 (1996) 2484–2493.
[21] L.J. Pike, Rafts defined: a report on the keystone symposium on lipid rafts and cell function, J. Lipid Res. 47 (2006) 1597–1598.
[22] L. Stryer, Fluorescence energy transfer as a spectroscopic ruler, Annu. Rev. Biochem. 47 (1978) 819–846.
[23] C. Gutierrez-Merino, F. Centeno, E. Garcia-Martin, J.M. Merino, Fluorescence energy transfer as a tool to locate functional sites in membrane proteins, Biochem. Soc. Trans. 22 (1994) 784–788.
[24] A.K. Samhan-Arias, M.A. Garcia-Bereguiain, F.J. Martin-Romero, F.J.C. Gutierrez-Merino, Clustering of plasma membrane-bound cytochrome b5 reductase within 'lipid rafts' microdomains of the neuronal plasma membrane, Mol. Cell. Neurosci. 40 (2009) 14–26.
[25] A.K. Samhan-Arias, D. Marques-da-Silva, N. Yanamala, C. Gutierrez-Merino, Stimulation and clustering of cytochrome b_5 reductase in caveolin-rich lipid microdomains is an early event in oxidative stress-mediated apoptosis of cerebellar granule neurons, J. Proteomics, in press. doi:10.1016/j.jprot.2011.12.007.
[26] F.J. Martin-Romero, E. Garcia-Martin, C. Gutierrez-Merino, Inhibition of the oxidative stress produced by plasma membrane NADH oxidase delays low-potassium induced apoptosis of cerebellar granule cells, J. Neurochem. 82 (2002) 705–715.
[27] A. Samhan-Arias, F.J. Martin-Romero, C. Gutierrez-Merino, Kaempferol blocks oxidative stress in cerebellar granule cells and reveals a key role for the plasma membrane NADH oxidase activity in the commitment of apoptosis, Free Radic. Biol. Med. 37 (2004) 48–61.
[28] J. Herreros, T. Ng, G. Schiavo, Lipid rafts act as specialized domains for tetanus toxin binding and internalization into neurons, Mol. Biol. Cell. 12 (2001) 2947–2960.
[29] J.L. MacDonald, L.J. Pike, A simplified method for the preparation of detergent-free lipid rafts, J. Lipid Res. 46 (2005) 1061–1067.
[30] E.O. Saphire, P.W.H.I. Parren, C.F. Barbas 3rd, D.R. Burtona, I.A. Wilson, Crystallization and preliminary structure determination of an intact human immunoglobulin, b12: an antibody that broadly neutralizes primary isolates of HIV-1, Acta Crystallogr. D57 (2001) 168–171.
[31] G.H. Hockerman, B.D. Johnson, T. Scheuer, W.A. Catterall, Molecular determinants of high affinity phenylalkylamine block of L-type calcium channels, J. Biol. Chem. 270 (1995) 22119–22122.
[32] T. Brauns, H. Prinz, S.D. Kimball, R.P. Haughland, J. Striessnig, H. Glossmann, L-type calcium channels: binding domains for dihydropyridines and benzothiazepines are located in close proximity to each other, Biochemistry 36 (1997) 3625–3631.
[33] H.G. Knaus, T. Moshammer, K. Friedrich, H.C. Kang, R.P. Haugland, H. Glossmann, In vivo labeling of L-type Ca^{2+} channels by fluorescent dihydropyridines: evidence for a functional, extracellular heparin-binding site, Proc. Natl. Acad. Sci. USA 89 (1992) 3586–3590.
[34] W. Berger, H. Prinz, J. Striessnig, H.C. Kang, R. Haugland, H. Glossmann, Complex molecular mechanism for dihydropyridine binding to L-type Ca^{2+}-channels as revealed by fluorescence energy transfer, Biochemistry 33 (1994) 11875–11883.
[35] J.E. Brenman, D.S. Bredt, Synaptic signalling by nitric-oxide, Curr. Opin. Neurobiol. 7 (1997) 374–378.
[36] K. Prybylowski, K. Chang, N. Sans, L. Kan, S. Vicini, R.J. Wenthold, The synaptic localization of NR2B-containing NMDA receptors is controlled by interactions with PDZ proteins and AP-2, Neuron 47 (2005) 845–857.
[37] R.P. Haugland, The Handbook: a Guide to Fluorescent Probes and Labeling Techniques, tenth ed., Invitrogen Corp, Carlsbad, CA, USA, 2005.
[38] D.S. Bredt, S.H. Snyder, Nitric-oxide: a physiologic messenger molecule, Annu. Rev. Biochem. 63 (1994) 175–195.

Biochemical and Biophysical Research Communications 420 (2012) 263–268

Contents lists available at SciVerse ScienceDirect

Biochemical and Biophysical Research Communications

journal homepage: www.elsevier.com/locate/ybbrc

Insights into substrate recognition by the *Escherichia coli* Orf135 protein through its solution structure

Kumiko Kawasaki [a], Teppei Kanaba [a], Momoko Yoneyama [b], Naoko Murata-Kamiya [c], Chojiro Kojima [b], Yutaka Ito [a], Hiroyuki Kamiya [d], Masaki Mishima [a,*]

[a] Graduate School of Science and Engineering, Tokyo Metropolitan University, 1-1 Minamiosawa, Hachioji 192-0397, Japan
[b] Graduate School of Biological Sciences, Nara Institute of Science and Technology, 8916-5 Takayama-cho, Ikoma, Nara 630-0192, Japan
[c] Graduate School of Medicine, University of Tokyo, 7-3-1 Hongo, Bunkyo-ku, Tokyo 113-0033, Japan
[d] Graduate School of Science and Engineering, Ehime University, 2-5 Bunkyo-cho, Matsuyama 790-8577, Japan

ARTICLE INFO

Article history:
Received 19 February 2012
Available online 5 March 2012

Keywords:
Orf135
Solution structure
Oxidatively damaged nucleotides
Nudix hydrolase

ABSTRACT

Escherichia coli Orf135 hydrolyzes oxidatively damaged nucleotides such as 2-hydroxy-dATP, 8-oxo-dGTP and 5-hydroxy-CTP, in addition to 5-methyl-dCTP, dCTP and CTP. Nucleotide pool sanitization by Orf135 is important since nucleotides are continually subjected to potential damage by reactive oxygen species produced during respiration. Orf135 is a member of the Nudix family of proteins which hydrolyze nucleoside diphosphate derivatives. Nudix hydrolases are characterized by the presence of a conserved motif, even though they recognize various substrates and possess a variety of substrate binding pockets. We investigated the tertiary structure of Orf135 and its interaction with a 2-hydroxy-dATP analog using NMR. We report on the solution structure of Orf135, which should contribute towards a structural understanding of Orf135 and its interaction with substrates.

1. Introduction

Reactive oxygen species generated during respiration can damage a variety of cellular molecules such as nucleotides. These oxidized DNA precursors form aberrant base pairs which can generate mutations. Among these, 8-oxoguanine (8-oxo-G) and its derivatives are well known, and the system in place to avoid mutation by 8-oxo-G has been well studied. 8-Oxo-G mispairs with adenine, and can subsequently cause mutation during replication. In *Escherichia coli,* MutT hydrolyzes 8-oxo-deoxyguanosine triphosphate (8-oxo-dGTP) to its monophosphate to prevent incorporation into the genome [1]. Further, 8-oxo-G within the genome can be excised by MutM, an 8-oxo-G DNA glycosylase, and mispaired adenine can be excised by MutY, an adenine DNA glycosylase [2–5]. Recently, human NUDT5 is also thought to play a role in nucleotide pool sanitization by hydrolyzing 8-oxo-deoxyguanosine diphosphate (8-oxo-dGDP) to 8-oxo-deoxyguanosine monophosphate (8-oxo-dGMP) [6].

In addition to 8-oxo-G, it has been shown that 2-hydroxy-deoxyadenosine triphosphate (2-hydroxy-dATP) is a highly mutagenic precursor since it induces GC-TA transversion during replication [7]. Mammalian MutT homolog 1 (MTH1) sanitizes oxidized DNA precursors including 2-hydroxy-dATP and prevents mutations in organisms. Human MTH1 hydrolyzes 8-oxo-dGTP, 2-hydroxy-dATP, 2-hydroxy-ATP and 8-oxo-dATP to their respective monophosphate forms. *E. coli* Orf135 hydrolyzes 2-hydroxy-dATP, 8-oxo-dGTP and 5-hydroxy-CTP [8–10]. A possible role of Orf135 is to hydrolyze oxidatively damaged nucleotides including 2-hydroxy-dATP, and thereby sanitize the nucleotide pool in cells. In fact, it is known that the frequency of spontaneous and H_2O_2-induced mutations is two- to threefold higher in the *orf135*$^-$ strain compared with the wild-type [11]. Additionally, it is known that Orf135 also hydrolyzes 5-methyl-dCTP, dCTP and CTP [12], although the biological significance of this remains unknown.

Orf135, MutT, MTH1 and NuDT5 are members of the Nudix family of proteins which hydrolyze dNTPs, NADH, GDP-mannose, ADP-ribose, diadenosine polyphosphates and diphosphoinositol polyphosphates [13]. Since these substrates consist of a nucleoside diphosphate group linked to some other moiety, the substrates are referred to by the acronym Nudix (Nucleoside DIphosphate linked to X) [13]. Nudix enzymes generally possess a characteristic signature among the family of hydrolases, and are characterized by the presence of a conserved array of 23 amino acids comprising $GX_5EX_7REUXEEXGU$, where U represents a bulky hydrophobic amino acid. From a structural point of view, the motif contains a conserved helix, in which conserved glutamic acid residues

Abbreviations: NOE, nuclear Overhauser effect; NOESY, NOE spectroscopy; TOCSY, total correlation spectroscopy; HSQC, heteronuclear single quantum correlation spectroscopy; r.m.s., root mean square.

* Corresponding author. Fax: +81 42 673 2525.
E-mail address: mishima-masaki@tmu.ac.jp (M. Mishima).

0006-291X/$ - see front matter © 2012 Elsevier Inc. All rights reserved.
http://dx.doi.org/10.1016/j.bbrc.2012.02.146

Table 1[a]

	SA	$SA_{water\ refined}$
Total number of distance constraints	3504	
Intra residue	603	
Short range ($\|i-j\|=1$)	965	
Middle range ($\|i-j\|=2,3,4$)	574	
Long range ($\|i-j\|>4$)	1292	
Hydrogen bond constraints	35×2	
Dihedral constraints		
ϕ, φ	93, 93	
Residual dipole couplings		
$^1D_{NH}$	90	
R.m.s. deviations from experimental constraints[b]		
Distance (Å)	$0.013\pm4\times10^{-4}$	$0.0200\pm5\times10^{-4}$
Angle (°)	0.23 ± 0.06	0.50 ± 0.08
R.m.s. deviations from idealized covalent geometry		
Bonds (Å)	$0.0011\pm5\times10^{-6}$	$0.0040\pm5\times10^{-5}$
Angles (°)	0.284 ± 0.001	0.54 ± 0.01
Impropers (°)	0.163 ± 0.006	1.33 ± 0.08
RDC Q-factor	11.8 ± 0.5%	6 ± 0.8%
PROCHECK Ramachandran plot (1–24,31–131)		
Residues in most favored regions (%)	89.6	93.4
Residues in additional allowed regions (%)	9.9	6.0
Residues in generously allowed regions (%)	0.3	0.6
Residues in disallowed regions (%)	0.2	0.0
Average atomic r.m.s. deviations from the average structure		
Back bone (1–24, 31–131) (Å)	0.26	0.41
All heavy (1–24, 31–131) (Å)	0.72	0.88

[a] These statistics comprise the ensemble of the 20 structures obtained from 100 starting structures. Structure calculations were performed using CNS version 1.2.
[b] None of these structures exhibited distance violations >0.5 Å, dihedral angle violations >5°.

protrude and chelate metal ions, which plays a crucial role in hydrolysis [13]. Although the hydrolysis center of Nudix enzymes is well conserved, the substrate recognition pockets display structural variation, thus reflecting the variety of substrates which bind the enzymes. Detailed structural information of Orf135 is required in an effort to delineate the nature of the enzyme–substrate interactions involved.

In this study, we have determined the solution structure of Orf135 by NMR techniques. Based on inspection of the determined structure and monitoring the NMR signals when adding substrate, we have identified a substrate binding pocket. We also discuss the molecular recognition mechanism of Orf135 and detail a structure comparison with other Nudix enzymes. Molecular recognition of the 2-hydroxy-A base is a particularly important issue. To date, structural investigations of MTH1 have provided the sole information pertaining to the molecular recognition of 2-hydroxy-A [14].

2. Materials and methods

2.1. Sample preparation and NMR experiments

Orf135 was expressed and purified as previously described [15]. Briefly, the protein was expressed as a GST-fusion protein in *E. coli* BL21 Star (DE3) (Invitrogen), and subsequently purified by GSH column chromatography. Following the removal of GST by HRV3C proteinase, Orf135 was finally purified by gel-filtration chromatography. Purified Orf135 was prepared in KH_2PHO_4-K_2HPO_4 (pH 6.8) 93% H_2O/7% ^2H_2O buffer containing 50 mM KCl for the NMR experiments. NMR experiments were performed on a Bruker DMX500, a Bruker AVANCE 500 with cryogenic probe, a Bruker AVANCE 600 with cryogenic probe, or a Bruker DRX800 with triple axis gradient probe at 303 K. All spectra were processed using NMRPipe [16], and analyzed by Sparky [17]. The ^1H, ^{13}C and ^{15}N assignments were obtained from standard multidimensional NMR methods [15].

2.2. Structure determination

Inter-proton distances were derived from 2D NOESY, 3D ^{15}N edited NOESY–HSQC, and 3D ^{13}C edited NOESY–HSQC. Additionally, dihedral ϕ and ψ angles derived from TALOS were also used [18]. Residual $^1D_{NH}$ couplings were obtained by comparison with ^{15}N–^1H couplings obtained from isotropic and anisotropic samples. The anisotropic sample was prepared by adding 15 mg/ml Pf1 phage. The couplings were measured using 3D HNCO-TROSY experiments performed in an interleaved manner [19]. Structural restraint collection was performed using CYANA version 3.00 with the CANDID protocol [20]. An ensemble of 100 Orf135 structures were calculated using CNS version 1.2 based on the obtained structural restraints including residual $^1D_{NH}$ couplings using a standard simulated annealing protocol [21]. Finally, structures were refined with a water refinement protocol using CNS version 1.2 [22].

The final 20 lowest energy ensemble structures were checked by PROCHECK-NMR [23], and graphics were created using MOLMOL [24] and PyMOL (DeLano Scientific, San Carlos, CA). The lowest energy structure among the ensemble was used as a representative structure in order to perform structural comparisons, and to generate ribbon and molecular surface models.

2.3. Substrate binding analyses

Signal perturbations of ^1H and ^{15}N amide resonances of ^{15}N uniformly labeled Orf135 were monitored upon addition of an equimolar amount of non-hydrolyzed ribonucleotide analog of 2-hydroxy-dATP, α, β-methylene 2-hydroxy-adenosine triphosphate (2-hydroxy-AMPCPP) to 0.2 mM Orf135 sample in 20 mM HEPES buffer (pH 7.5) containing 20 mM KCl, 1 mM DTT, 1 mM $MgCl_2$ and 5% ^2H_2O. The ^1H–^{15}N HSQC experiments were performed at 303 K. Reduced signal intensities were analyzed using Sparky [17]. Changes in signal intensity were evaluated by calculating the ratio of the intensity difference caused by perturbation and reference spectra, (Iref − Iper)/Iref, where Iref and Iper represent signal intensities in the reference and perturbed spectrum, respectively.

3. Results and discussion

3.1. Structure determination and description of overall structure

The elution volume of Orf135 in the gel filtration chromatography corresponded to the molecular weight of the monomer, while the line shapes of the NMR spectrum were relatively narrow. These data indicated that Orf135 exists as a monomer in solution. Almost all of the ^1H, ^{13}C and ^{15}N NMR signals were assigned using standard multi-dimensional NMR techniques [15]. More than three thousand distance restraints derived from NOEs were collected, and 90 N–H residual dipole couplings were also used (Table 1). Fig. 1A depicts the backbone of the final 20 structures derived from NMR data showing that the atomic coordinates throughout the protein molecule have been well defined, with the exception of the C-terminal residues and the long loop located between strand β2 and helix α1 (Fig. 1A and B). It should be noted that steady state {^1H}–^{15}N heteronuclear NOE indicated that the former part of this loop is flexible in solution (residues 25–30). As shown in Fig. 1C, the values are relatively low, which indicate flexibility, in contrast to the secondary structure parts associated with higher values, which indicate rigidity. The average r.m.s. deviation calculated

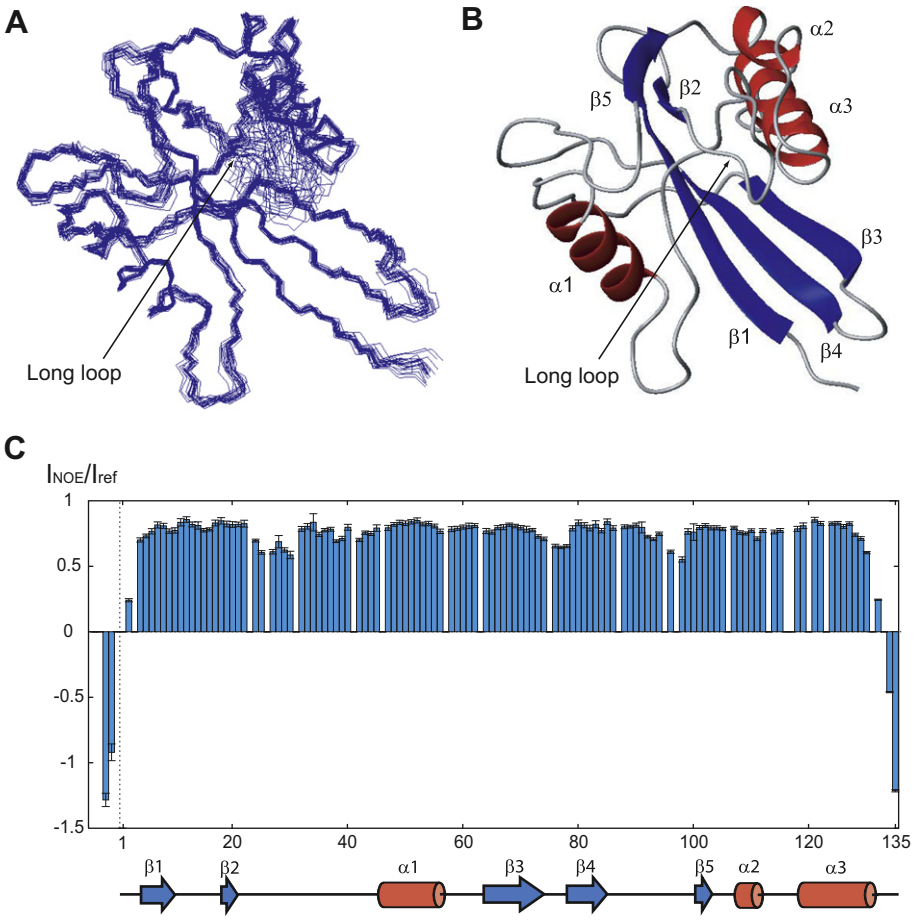

Fig. 1. Solution structure of Orf135. (A) Backbone superposition of the final 20 simulated annealing structures of Orf135. (B) Ribbon drawing of the representative structure of Orf135. The molecular orientation is the same as in (A) and the four stranded β-sheet and α-helices are depicted in blue and red, respectively. α-Helices, β-strands and the long loop are labeled. (C) $\{^1H\}$–^{15}N NOE versus amino acid residue for Orf135. The data are represented by the intensity ratio I_{NOE}/I_{ref}, where I_{ref} and I_{NOE} were measured in the absence or presence of ^1H saturation, respectively. The error bars were calculated based on the signal-to-noise ratios. The secondary structure elements of Orf135 are described below. Amino acids derived from expression vector are shown as minus residue numbers.

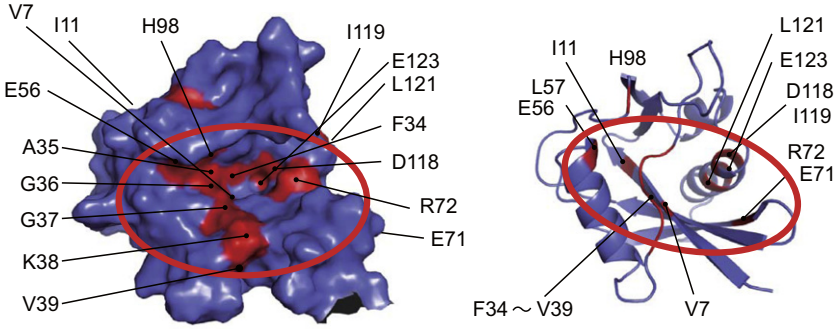

Fig. 2. Substrate binding site. Molecular surface model (left) and ribbon drawing (right) of Orf135 structure. The residues perturbed by 2-hydroxy-AMPCPP binding are highlighted in red and labeled. The 2-hydroxy-AMPCPP binding site is shown in the red circle.

from the averaged structure was 0.41 and 0.88 Å for the backbone and all heavy atoms of the well-defined region (residues 1–24, 31–131), respectively. Statistical data for the structures are given in Table 1.

Orf135 adopts an α + β fold consisting of five β-strands and three α-helices: β1(3–13), β2(16–21), β3(65–74), β4(77–86), β5(102–107), α1(45–56), α2(106–109) and α3(118–130). Additionally, there is a partially flexible long loop as described, connected with strand β2 and helix α1 (Fig. 1B). The main frame of the fold comprises a curled β-sheet made up of five strands. The Nudix motif (residues 37–59) is composed of an amphipathic helix of about 3 turns, α1, and a preceding loop. Notably, the long loop and large β-sheet form a cleft adjacent to the Nudix helix (α1) on the molecular surface (Figs. 1B and 2).

3.2. The substrates binding site

The substrate binding site was investigated by monitoring amide signals of the HSQC spectra of Orf135. Upon addition of 2-hydroxy-AMPCPP, some signals of Orf135 were significantly per-

turbed, in fast to intermediate exchange manners, resulting in decreases in signal intensities with slight changes in chemical shift. We mapped the distribution of significantly perturbed residues on the molecular surface of Orf135 and found that it was confined to the cleft region, suggesting that the cleft represents the 2-hydroxy-AMPCPP binding site (Fig. 2). The location of this substrate binding site is consistent with other Nudix enzymes such as MutT and MTH1. Notably, the flexible region of the long loop is located on the rim of the cleft, and can be described as the "roof" of the substrate binding site. This flexible loop may fold upon substrate binding. In the apo MutT crystal structure, coordinates of the corresponding region were not observed, possibly due to its flexibility, and the structure was folded upon complex formation with 8-oxo-dGMP, in which R23 and H28 interact with sugar and α-phosphate of 8-oxo-dGMP [25]. The key residues required for substrate recognition as identified by mutation analysis were located inside the cleft and exposed on the molecular surface. 5-Methyl-dCTP was also found to bind the same cleft as determined from NMR analysis (data not shown).

3.3. Structure comparison and implications for molecular recognition

Here, we discuss the molecular mechanism pertaining to the recognition of oxidatively damaged base by Orf135 as determined by structure comparison with MutT and MTH1 in conjunction with the results of the mutational studies. Fig. 3 shows the structure comparison of Orf135 with MutT and MTH1.

Firstly, we discuss the molecular recognition of the 2-hydroxy-A base. Mutational studies showed that the D118A mutant of Orf135 displayed no activity for 2-hydroxy-dATP, while activity for 8-oxo-dGTP was retained [10]. Orf135 and MTH1 commonly have aspartic acid at this position (D118 and D119 for Orf135 and human MTH1, respectively). However, the substrate recognition mechanism of these two enzymes should differ from one another since the shape of the binding pocket differs (Fig. 3B, C, E). In MTH1, the side chain of W117 is located in the vicinity of D119 and its aromatic ring may contribute towards ligand binding through stacking interactions [26], although there is no corresponding residue in Orf135. Additionally, R72 of Orf135, also found to be important for 2-hydroxy-A-specific recognition as determined from mutational studies, is located within the putative binding site (Fig. 3B and E). In MutT, the corresponding residue is Y73, and the side chain is oriented outwards.

Based on these data, we have proposed a Orf135:2-hydroxy-dATP complex model (Fig. S1). The N6 and N1 atoms of the 2-hydroxy-A ring may form hydrogen bonds with the carboxyl group of D118, and the O2 atom may form hydrogen bonds with the guanidino group of R72. The N6 atom may also form a hydrogen bond with the backbone amide of F34. We manually made this docking model based on the determined structure, and the potential donor and corresponding acceptor atoms that participate in possible intermolecular hydrogen bonds could be located within 3.5 Å. We therefore concluded that discrimination of 2-hydroxy-A from adenine by Orf135 may be executed by hydrogen bonding mediated by the N1 and O2 atoms. Consequently, Orf135 can directly recognize oxidation of the adenine ring.

The other interesting issue relates to 8-oxo-G recognition by Orf135. In the crystal structure of the MutT:8-oxo-dGMP complex, 8-oxo-dGMP forms hydrogen bonds with the backbone amide and carbonyl group of F34, and interestingly adopts a syn-conformation around the glycoside bond between the base and sugar. The side chain of N119 also plays a key role in recognizing the 8-oxo-dGMP. The amino group of N119 forms hydrogen bonds with the 8-oxo-G base (Fig. 3A, D). As expected from the sequence similarity, the tertiary structure of Orf135 is similar to that of MutT (Fig. 3A, B, D). The DALI server, which quantitatively evaluates tertiary structure similarities, showed a high z-score of 15.6, and the r.m.s.d. of back bone Cα, N, C, and O atoms was 2.1 Å with the apo

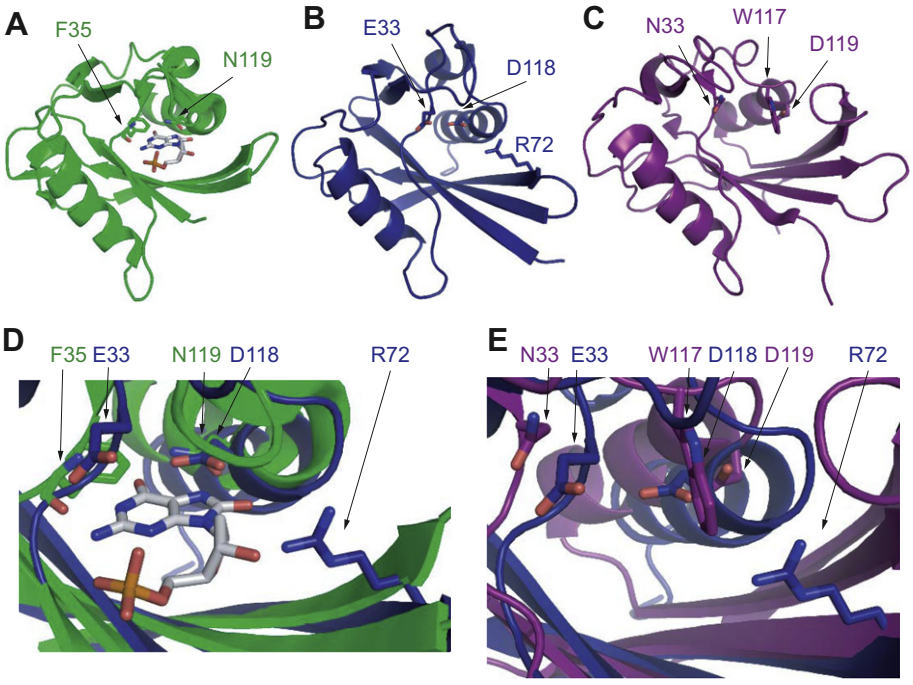

Fig. 3. Structure comparison of Orf135 with MutT and MTH1. A, Crystal structure of the MutT/8-oxo-dGMP complex. 8-oxo-dGMP is shown in stick representation. MutT residues (F34 and N119) important for the recognition of 8-oxo-dGMP are shown in stick representation and labeled. Nitrogen, oxygen and phosphorus atoms are colored blue, red and orange, respectively. B, Solution structure of Orf135. The molecular orientations are the same as in A. Key residues (E33, R72 and D118) involved in the recognition of 8-oxo-dGMP and 2-hydroxy-dATP are shown in stick representation and labeled. C, Solution structure of MTH1. The molecular orientations are the same as in A. Key residues (N33, W117 and D119) involved in the recognition of 2-hydroxy-dATP are shown in stick representation and labeled. D, Closer view of oxidatively damaged nucleotide binding site of the MutT/8-oxo-dGMP complex (green) and Orf135 (navy). E, Closer view of the nucleotide binding site of Orf135 (navy) and MTH1 (magenta).

MutT crystal structure (PDB:3A6S) [25], indicating that the structures are highly similar to one another. Consistent with the similarity in global structure, the shape of the binding pocket was also found to be similar in both enzymes. The common shape of the binding pocket seems to be generated by the side chain of conserved F34. Briefly, the aromatic ring of F34 is surrounded by the hydrophobic side chains of I15, I17, L19, L114 and L122, which form a hydrophobic core in Orf135. In MutT, the side chain of F35 is surrounded by the side chains of I10, I18, I20, I123 and F115. These interactions represent common characteristic features of MutT and Orf135, and the presence of this hydrophobic core may be useful in distinguishing the MutT-type enzyme from other Nudix enzymes. It should be noted that the shape of the binding pocket in MTH1 and NUDT5 differs in comparison with MutT-type enzymes. The key phenylalanine residue is not conserved in MTH1 or NUDT5.

Although Orf135 and MutT share a similar substrate binding pocket shape, substrate specificity differs. The critical difference between MutT and Orf135 is substitution of asparagine to aspartic acid at position 118 (position 119 in MutT). It is interesting to note that Orf135 can recognize 8-oxo-G, albeit with low affinity, even though the key asparagine residue is absent. This can be accounted for by considering that 8-oxo-dG favors a syn-conformation in solution, and that a syn-conformation was also found in the MutT complex. Accordingly, assuming that 8-oxo-dGTP also adopts a syn-conformation in the complex with Orf135, we generated a docking model (Fig. S2). In this model, E33 is an attractive candidate for interaction with 8-oxo-G. The carboxyl group of the side chain of E33 may form hydrogen bonds with the N1 and N2 atoms of 8-oxo-G. In fact, E33 plays a critical role in the recognition of 8-oxo-dGTP. The E33A mutant displayed no activity for 8-oxo-dGTP, while activity for 2-hydroxy-dATP was retained [10]. It should be noted that the structure of the purine ring around the N1 and N2 atoms of 8-oxo-G is identical to that of guanine. Since this part of 8-oxo-G is not unique, the same hydrogen bonds could form with guanine. In order to effect this interaction, the base must adopt a syn-conformation. Given its preference to adopt a syn-conformation, 8-oxo-dGTP may be a better substrate for Orf135 compared with dGTP. Consequently, Orf135 does not directly recognize the oxidized structure of 8-oxo-G, but recognizes the syn-conformer.

Finally, this study should contribute towards a further understanding of the substrate specificity of Nudix enzymes. For example, the DALI server showed the highest similarity score of 18.9 to the recently published Nudix enzyme (PDB:3HHJ) [27]. This enzyme was reported as a putative MutT homolog in the literature [27], is very similar in structure to *E. coli* MutT and Orf135, and possesses a "MutT-type" substrate binding pocket made by a conserved phenylalanine residue. However, the enzyme lacks a side-chain NH_2 group at amino acid position 125 (corresponding to D118 in Orf135) since this position is substituted by an aspartic acid residue. Thus, we speculate that the enzyme substrate specificity may resemble Orf135 more than that of MutT.

Recently, investigations of Nudix enzymes and proteins containing the Nudix motif have infiltrated a variety of fields [28,29]. In addition to widely used homology sequence searches based on the Nudix motif, other features including the conservation of key amino acid residues whose importance was found through structural studies may contribute towards future biochemical studies of novel Nudix enzymes and proteins containing the Nudix motif.

Acknowledgments

This work was supported in part by the Grant-in-Aid for Scientific Research on Innovative Areas, "Structural Cell Biology" and "Transient Macromolecular Complex" from the Japanese Ministry of Education, Culture, Sports, and Technology (to M.M.). T.K. is a recipient of a Sasagawa Scientific Research Grant.

Appendix A. Supplementary data

Supplementary data associated with this article can be found, in the online version, at doi:10.1016/j.bbrc.2012.02.146.

References

[1] H. Maki, M. Sekiguchi, MutT protein specifically hydrolyses a potent mutagenic substrate for DNA synthesis, Nature 355 (1992) 273–275.
[2] K.G. Au, M. Cabrera, J.H. Miller, P. Modrich, *Escherichia coli* mutY gene product is required for specific A-G––C.G mismatch correction, Proc. Natl. Acad. Sci. USA 85 (1988) 9163–9166.
[3] M. Cabrera, Y. Nghiem, J.H. Miller, MutM, a second mutator locus in *Escherichia coli* that generates G.C––T.A transversions, J. Bacteriol. 170 (1988) 5405–5407.
[4] M.L. Michaels, C. Cruz, A.P. Grollman, J.H. Miller, Evidence that MutY and MutM combine to prevent mutations by an oxidatively damaged form of guanine in DNA, Proc. Natl. Acad. Sci. USA 89 (1992) 7022–7025.
[5] J. Tchou, H. Kasai, S. Shibutani, M.H. Chung, J. Laval, A.P. Grollman, S. Nishimura, 8-Oxoguanine (8-hydroxyguanine) DNA glycosylase and its substrate specificity, Proc. Natl. Acad. Sci. USA 88 (1991) 4690–4694.
[6] T. Arimori, H. Tamaoki, T. Nakamura, H. Kamiya, S. Ikemizu, Y. Takagi, T. Ishibashi, H. Harashima, M. Sekiguchi, Y. Yamagata, Diverse substrate recognition and hydrolysis mechanisms of human NUDT5, Nucleic Acids Res. 39 (2011) 8972–8983.
[7] M. Inoue, H. Kamiya, K. Fujikawa, Y. Ootsuyama, N. Murata-Kamiya, T. Osaki, K. Yasumoto, H. Kasai, Induction of chromosomal gene mutations in *Escherichia coli* by direct incorporation of oxidatively damaged nucleotides. New evaluation method for mutagenesis by damaged DNA precursors in vivo, J. Biol. Chem. 273 (1998) 11069–11074.
[8] H. Kamiya, N. Murata-Kamiya, E. Iida, H. Harashima, Hydrolysis of oxidized nucleotides by the *Escherichia coli* Orf135 protein, Biochem. Biophys. Res. Commun. 288 (2001) 499–502.
[9] K. Fujikawa, H. Kasai, The oxidized pyrimidine ribonucleotide, 5-hydroxy-CTP, is hydrolyzed efficiently by the *Escherichia coli* recombinant Orf135 protein, DNA Repair (Amst) 1 (2002) 571–576.
[10] E. Iida, K. Satou, M. Mishima, C. Kojima, H. Harashima, H. Kamiya, Amino acid residues involved in substrate recognition of the Escherichia coli Orf135 protein, Biochemistry 44 (2005) 5683–5689.
[11] H. Kamiya, E. Iida, N. Murata-Kamiya, Y. Yamamoto, T. Miki, H. Harashima, Suppression of spontaneous and hydrogen peroxide-induced mutations by a MutT-type nucleotide pool sanitization enzyme, the *Escherichia coli* Orf135 protein, Genes Cells 8 (2003) 941–950.
[12] S.F. O'Handley, C.A. Dunn, M.J. Bessman, Orf135 from *Escherichia coli* is a Nudix hydrolase specific for CTP, dCTP, and 5-methyl-dCTP, J. Biol. Chem. 276 (2001) 5421–5426.
[13] A.S. Mildvan, Z. Xia, H.F. Azurmendi, V. Saraswat, P.M. Legler, M.A. Massiah, S.B. Gabelli, M.A. Bianchet, L.W. Kang, L.M. Amzel, Structures and mechanisms of Nudix hydrolases, Arch. Biochem. Biophys. 433 (2005) 129–143.
[14] M. Mishima, Y. Sakai, N. Itoh, H. Kamiya, M. Furuichi, M. Takahashi, Y. Yamagata, S. Iwai, Y. Nakabeppu, M. Shirakawa, Structure of human MTH1, a Nudix family hydrolase that selectively degrades oxidized purine nucleoside triphosphates, J. Biol. Chem. 279 (2004) 33806–33815.
[15] K. Kawasaki, M. Yoneyama, N. Murata-Kamiya, H. Harashima, C. Kojima, Y. Ito, H. Kamiya, M. Mishima, (1)H, (13)C and (15)N NMR assignments of the *Escherichia coli* Orf135 protein, Biomol. NMR Assign., 2011.
[16] F. Delaglio, S. Grzesiek, G.W. Vuister, G. Zhu, J. Pfeifer, A. Bax, NMRPipe: a multidimensional spectral processing system based on UNIX pipes, J. Biomol. NMR 6 (1995) 277–293.
[17] T.D. Goddard, D.G. Kneller, SPARKY3, University of California, San Francisco, 1999.
[18] G. Cornilescu, F. Delaglio, A. Bax, Protein backbone angle restraints from searching a database for chemical shift and sequence homology, J. Biomol. NMR 13 (1999) 289–302.
[19] Y. Daiwen, V. Ronald, A.M. Geoffrey, C.W.Y., E.K. Lewis, TROSY-based HNCO pulse sequences for the measurement of 1HN–15N, 15N–13CO, 1HN–13CO, 13CO–13C′ and 1HN–13C′ dipolar couplings in 15N, 13C, 2H-labeled proteins, J. Biomol. NMR 14 (1999) 333–343.
[20] T. Herrmann, P. Guntert, K. Wuthrich, Protein NMR structure determination with automated NOE assignment using the new software CANDID and the torsion angle dynamics algorithm DYANA, J. Mol. Biol. 319 (2002) 209–227.
[21] A.T. Brunger, P.D. Adams, G.M. Clore, W.L. DeLano, P. Gros, R.W. Grosse-Kunstleve, J.S. Jiang, J. Kuszewski, M. Nilges, N.S. Pannu, R.J. Read, L.M. Rice, T. Simonson, G.L. Warren, Crystallography & NMR system: a new software suite for macromolecular structure determination, Acta Crystallogr. D 54 (1998) 905–921.
[22] J.P. Linge, M.A. Williams, C.A. Spronk, A.M. Bonvin, M. Nilges, Refinement of protein structures in explicit solvent, Proteins 50 (2003) 496–506.

[23] R.A. Laskowski, J.A. Rullmannn, M.W. MacArthur, R. Kaptein, J.M. Thornton, AQUA and PROCHECK-NMR: programs for checking the quality of protein structures solved by NMR, J. Biomol. NMR 8 (1996) 477–486.
[24] R. Koradi, M. Billete, K. Wuthrich, MOLMOL: a program for display and analysis of macromolecular structures, J. Mol. Graph. 14 (1996) 51–55.
[25] T. Nakamura, S. Meshitsuka, S. Kitagawa, N. Abe, J. Yamada, T. Ishino, H. Nakano, T. Tsuzuki, T. Doi, Y. Kobayashi, S. Fujii, M. Sekiguchi, Y. Yamagata, Structural and dynamic features of the MutT protein in the recognition of nucleotides with the mutagenic 8-oxoguanine base, J. Biol. Chem. 285 (2010) 444–452.
[26] M. Takahashi, F. Maraboeuf, Y. Sakai, H. Yakushiji, M. Mishima, M. Shirakawa, S. Iwai, H. Hayakawa, M. Sekiguchi, Y. Nakabeppu, Role of tryptophan residues in the recognition of mutagenic oxidized nucleotides by human antimutator MTH1 protein, J. Mol. Biol. 319 (2002) 129–139.
[27] G.W. Buchko, T.E. Edwards, J. Abendroth, T.L. Arakaki, L. Law, A.J. Napuli, S.N. Hewitt, W.C. Van Voorhis, L.J. Stewart, B.L. Staker, P.J. Myler, Structure of a Nudix hydrolase (MutT) in the Mg(2+)-bound state from *Bartonella henselae*, the bacterium responsible for cat scratch fever, Acta Crystallogr. Sect. F. Struct. Biol. Cryst. Commun. 67 (2011) 1078–1083.
[28] A.G. McLennan, The Nudix hydrolase superfamily, Cell Mol. Life Sci. 63 (2006) 123–143.
[29] E. Kraszewska, The plant Nudix hydrolase family, Acta Biochim. Pol. 55 (2008) 663–671.

Biochemical and Biophysical Research Communications 420 (2012) 269–274

Contents lists available at SciVerse ScienceDirect

Biochemical and Biophysical Research Communications

journal homepage: www.elsevier.com/locate/ybbrc

Crystal structure and substrate-binding mode of a novel pectate lyase from alkaliphilic *Bacillus* sp. N16-5

Yingying Zheng [a], Chun-Hsiang Huang [a], Wenting Liu [a,b], Tzu-Ping Ko [c], Yanfen Xue [d], Cheng Zhou [d], Rey-Ting Guo [a], Yanhe Ma [a,d,*]

[a] Industrial Enzymes National Engineering Laboratory, Tianjin Institute of Industrial Biotechnology, Chinese Academy of Sciences, Tianjin 300308, China
[b] Tianjin University of Science and Technology, Tianjin 300457, China
[c] Institute of Biological Chemistry, Academia Sinica, Taipei 115, Taiwan
[d] State Key Laboratory of Microbial Resources, Institute of Microbiology, Chinese Academy of Sciences, Beijing 100101, China

ARTICLE INFO

Article history:
Received 15 February 2012
Available online 3 March 2012

Keywords:
Pectin
Pectate lyase
Trigalacturonate
Ca^{2+} binding
Crystal structure

ABSTRACT

The pectate lyase (Bsp165PelA) from *Bacillus* sp. N16-5 has great potential in industrial applications because it shows high specific activity under extremely alkaline conditions. Besides, activity measurement of Bsp165PelA does not require addition of calcium, in a way different from the other pectate lyases. Here we report crystal structures of Bsp165PelA in apo-form and in complex with trigalacturonate. The parallel β-helix, active site residues and substrate binding cleft are similar to those in the other pectate lyases from Polysaccharide Lyase family 1. However, some of the highly conserved Ca^{2+} binding residues and secondary structures are altered in Bsp165PelA, making it difficult to coordinate with Ca^{2+} as in the other pectate lyases. We found Bsp165PelA forms some direct enzyme–substrate interactions instead of using Ca^{2+} ions bridging in the extremely alkaline environment.

1. Introduction

Pectate is the de-esterified product of pectin, which is the major component of plant cell walls. The pectate backbone mainly consists of polygalacturonate, a homopolymer of D-galacturonic acid (Gal*p*A). The degradation of pectate requires either hydrolases or lyases. Pectate lyases (Pels) (EC 4.2.2.2) cleave α-1,4-linked galacturonate units of pectate by β-elimination, giving rise to an unsaturated C4–C5 bond at the non-reducing end of the newly formed oligogalacturonate [1]. Pels are normally secreted by plant pathogenic microbes and are believed to be the major virulence factor of pathogenesis in a broad range of plants [2,3].

Pels constitute a family of isozymes that share 29–91% amino acid sequence similarity [4]. Accordingly, Pels are classified into Polysaccharide Lyase (PL) families 1, 2, 3, 9 and 10 (http://www.cazy.org/Polysaccharide-Lyases.html). Among these PL members, Pels from the PL family 1 have been extensively studied. Most isozymes exert catalytic activity under alkaline conditions with a pH optimum around 9.0 [5]. In addition, Ca^{2+} is believed to be required for the pectolytic activity of all Pels [6].

Several apo-form and complex structures of Pels that contained Ca^{2+} and/or oligogalacturonate substrate have been determined [1,6–10]. All of these related structures show a parallel β-helix topology, in which the β strands are folded into a large right-handed coil. The major differences among various Pels exist in the size and conformation of the loops that protrude from and cover the parallel β-helix core. According to the sequence alignment and site-directed mutagenesis studies, these protruding loops constitute the pectolytic active site [11].

In previous reports, Ca^{2+} was found to be essential for Pels activity. The need for Ca^{2+} is also suggested by structural studies. There are two classes of Ca^{2+} in the Pels structures. One is denoted the primary Ca^{2+}, which binds to the enzyme molecule in the absence of substrate [9]. The other two or three Ca^{2+} ions are called additional Ca^{2+}, which bridge the enzyme and oligogalacturonate in the complex [8,12]. The primary Ca^{2+} has been observed in four other Pels structures: the pectate lyase from *Bacillus* sp. strain KSM-P15 (belonging to PL family 3, not discussed in this paper) [13], BsPel from *B. subtilis* [1], PelC from *Erwinia chrysanthemi* [9] and Bsp47Pel from *Bacillus* sp. TS 47 (PDB ID: 1VBL). The complex structure of an inactive PelC mutant and pentagalacturonate revealed three additional Ca^{2+} ions linking the substrate and the enzyme [8]. Similarly, two additional Ca^{2+} ions were found in BsPel from *B. subtilis* in the presence of pentagalacturonate [12].

Previously, we over-expressed and characterized an alkaliphilic pectate lyase Bsp165PelA from *Bacillus* sp. N16-5 [14]. The enzyme

* Corresponding author at: Industrial Enzymes National Engineering Laboratory, Tianjin Institute of Industrial Biotechnology, Chinese Academy of Sciences, 32 XiQiDao, Tianjin Airport Economic Park, Tianjin 300308, China. Fax: +86 10 64807616.
E-mail address: mayanhe@im.ac.cn (Y. Ma).

0006-291X/$ - see front matter © 2012 Elsevier Inc. All rights reserved.
http://dx.doi.org/10.1016/j.bbrc.2012.02.148

characteristics of Bsp165PelA are significantly different from the other Pels. It showed a specific activity of above 1000 U/mg, which is the highest among all Pels identified so far. Bsp165PelA has a high pH optimum of 11.5 and can maintain full pectolytic activity with only a trace amount of Ca^{2+}. These characteristics make it a great candidate for industrial use. To better understand the 3D structure and catalytic mechanism, we solved the structures of Bsp165PelA in apo-form and in complex with trigalacturonate (TGA). These structures can help elucidate the substrate and Ca^{2+} binding mode and provide more information for engineering to improve enzyme characteristics for industrial applications.

2. Materials and methods

2.1. Protein expression, purification and crystallization

Expression and purification of Bsp165PelA were carried out as described previously [14]. The final sample was concentrated to 12.5 mg/ml.

Bsp165PelA were crystallized using the sitting drop method from Hampton Research (Laguna Niguel, CA) by mixing 2 μl of the protein solution (12.5 mg/ml in 25 mM Tris–HCl, 150 mM NaCl, pH 8.0) with 2 μl of the mother liquor, equilibrating with 500 μl of the mother liquor at room temperature. The optimized crystallization conditions for all crystals mentioned here are 0.18 M Li_2SO_4, 0.085 M Tris–HCl, pH 8.5, 24% polyethylene glycol 4000, and 15% v/v glycerol anhydrous. Within 3 days, the crystals grew to dimensions of about 0.2 mm × 0.6 mm × 0.1 mm. Crystals of Bsp165PelA in complex with TGA were obtained by soaking the crystal in the reservoir solution containing 10 mM TGA for 30 min.

2.2. Data collection, structural determination and refinement

The X-ray diffraction data sets from the apo-form Bsp165PelA and the complex were collected to 1.54 and 1.90 Å resolution, respectively, at beam line BL13B1 of the National Synchrotron Radiation Research Center (NSRRC, Hsinchu, Taiwan). The data were processed using the program HKL2000 [15]. The crystals belong to the space group $P2_12_12$ with 1 monomer/asymmetric unit. Prior to use in structural refinements, 5% randomly selected reflections were set aside for calculating R_{free} as a monitor [16]. The crystal structure of Bsp165PelA was determined by the molecular-replacement method with CNS [17], using as a template the structure of pectate lyase from *Xanthomonas campestris* (PDB ID: 2QXZ), which has 33% sequence identity with Bsp165PelA. The initial phase angles were largely improved by solvent flipping using the CNS program [17]. Manual model building, water picking and SO_4^{2-} addition were performed with Coot [18]. Subsequent computational refinement used PHENIX [19]. The Bsp165PelA–TGA complex structure was determined by using the molecular-replacement method with PHASER [20]. The $2Fo - Fc$ difference Fourier map showed clear electron densities for all amino acid residues except the disordered residues 1 and 2. Incorporation of substrates and water molecules was according to 1.0σ map level by using Coot [18] and PHENIX [19]. The data collection and refinement statistics of these crystals are summarized in Table 1. All figures were prepared by using PyMol (http://pymol.sourceforge.net/).

2.3. Activity assay

Pectolytic activity was assayed at 50 °C and pH 11.5 in 50 mM glycine-NaOH buffer. One unit of enzymatic activity was defined as the amount of protein that produced 1 μmol of unsaturated oligogalacturonides per minute.

Table 1
Summary of X-ray data collections and refinement statistics.

	Native	TGA-soak
Data collection		
Space group	$P2_12_12$	$P2_12_12$
Unit-cell parameters		
a (Å)	134.9	137.9
b (Å)	48.5	48.2
c (Å)	52.9	52.5
Resolution (Å)	25.0–1.54 (1.60–1.54)	25.0–1.90 (1.97–1.90)
Unique reflections	51969 (5155)	28061 (2631)
Redundancy	7.8 (7.5)	10.0 (10.2)
Completeness (%)	99.3 (99.8)	98.6 (94.5)
Average I/σ (I)	33.4 (7.5)	36.4 (12.8)
R_{merge} (%)[a]	5.9 (30.1)	5.0 (22.3)
Refinement		
No. of reflections	51866 (2648)	27967 (1408)
R_{work}	0.166 (0.170)	0.154 (0.178)
R_{free}	0.191 (0.212)	0.204 (0.269)
R.m.s.d. bonds (Å)	0.014	0.014
R.m.s.d. angles (°)	1.539	1.442
Dihedral angles (%)		
Most favored	84.1	84.8
Allowed	14.9	14.2
Disallowed	1.1	1.1
No. of non-H atoms/average B (Å²)		
Protein	2528/15.4	2528/27.1
Water	349/31.2	184/37.3
Ligand (TGA)	–	36/33.0
Ion (SO_4)	10/30.1	25/65.3
PDB ID code	3VMV	2VMW

Values in parentheses are for the highest resolution shell.
[a] $R_{merge} = \Sigma_{hkl}\Sigma_i|I_i(hkl) - \langle I(hkl)\rangle|\Sigma_{hkl}\Sigma_i I_i(hkl)$

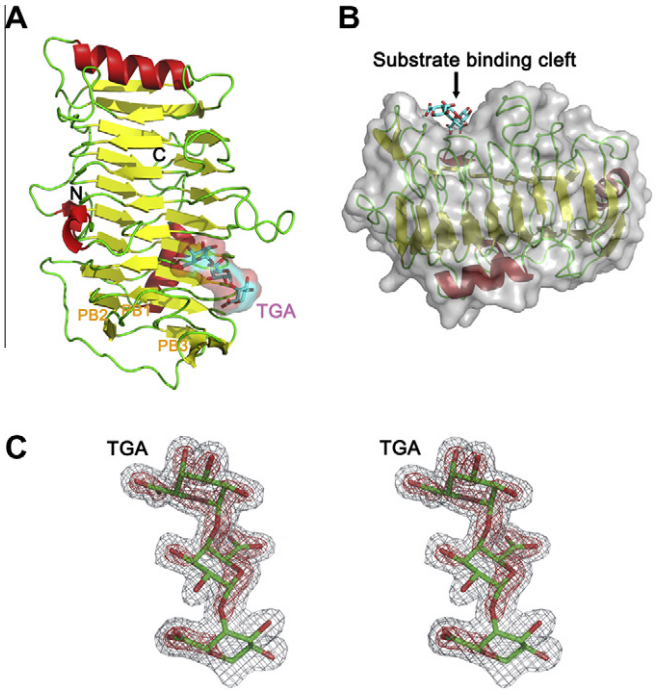

Fig. 1. Overall fold of Bsp165PelA. (A) Overall structure of Bsp165PelA bound with TGA. The three β sheets are denoted PB1, PB2 and PB3. A surface representation of the bound TGA is also shown. (B) A surface model of Bsp165PelA is shown in gray. The arrow indicates the substrate-binding cleft. (C) A stereo view of the electron density map of TGA. The $2Fo - Fc$ maps are contoured at 1.0σ level (green) and 2.5σ level (red).

2.4. RCSB protein data bank accession numbers

The atomic coordinates and structure factors of the *Bacillus* sp. N16-5 Bsp165PelA in apo-form (PDB ID: 3VMV) and in complex with trigalacturonate (PDB ID: 3VMW) have been deposited in the RCSB Protein Data Bank.

3. Results and discussion

3.1. Overall structure

The predominant structural motif of Bsp165PelA is a right-handed parallel β-helix formed by three parallel β-sheets (Fig. 1A). These three parallel β-sheets are referred to as PB1, PB2 and PB3. The loops or turns between the parallel β-sheets, which lack significant secondary structures, are named T1 (connecting PB1 and PB2), T2 (connecting PB2 and PB3), and T3 (connecting PB3 and PB1). There is little similarity in the detailed structures of the T3 and T1 loops in PL family 1 [21]. The most obvious difference lies in the long loop extending from the core structure in the T3 region [3,21]. At this position, Bsp165PelA adopts a simple loop while PelC from *E. chrysanthemi* adopts a compound loop according to the established taxonomy of loops [22] (Fig. 1). The tertiary structure of Bsp165PelA is similar to those of the other Pels [1,6,8,10,23–25], with seven complete turns in the parallel β-helix. In total, PB1 has ten strands while PB2 and PB3 have nine and seven strands, respectively.

3.2. The substrate-binding site

According to sequence alignment (Fig. 2), Bsp165PelA is highly homologous to the Pels from PL family 1. Thin-layer chromatography experiments proved that the major pectolytic product is TGA [14]. TGA should be stable as a product and no longer to be degraded when soaked into the crystal. In addition, TGA provides us with valuable information about substrate binding. In the Bsp165PelA–TGA complex structure, a long groove is formed between turn T3 and β sheet PB1, in which TGA is located (Fig. 1A and B). Judging by the structural superposition with PelC from *E. chrysanthemi*, which shows 30% sequence identity with Bsp165PelA, the location and structure of substrate binding cleft are similar in these two enzymes (Fig. 3A). The oligogalacturonates superimpose well to each other. TGA binds to the subsites from +2 to +4 and the electron density for TGA is very clear (Fig. 1C).

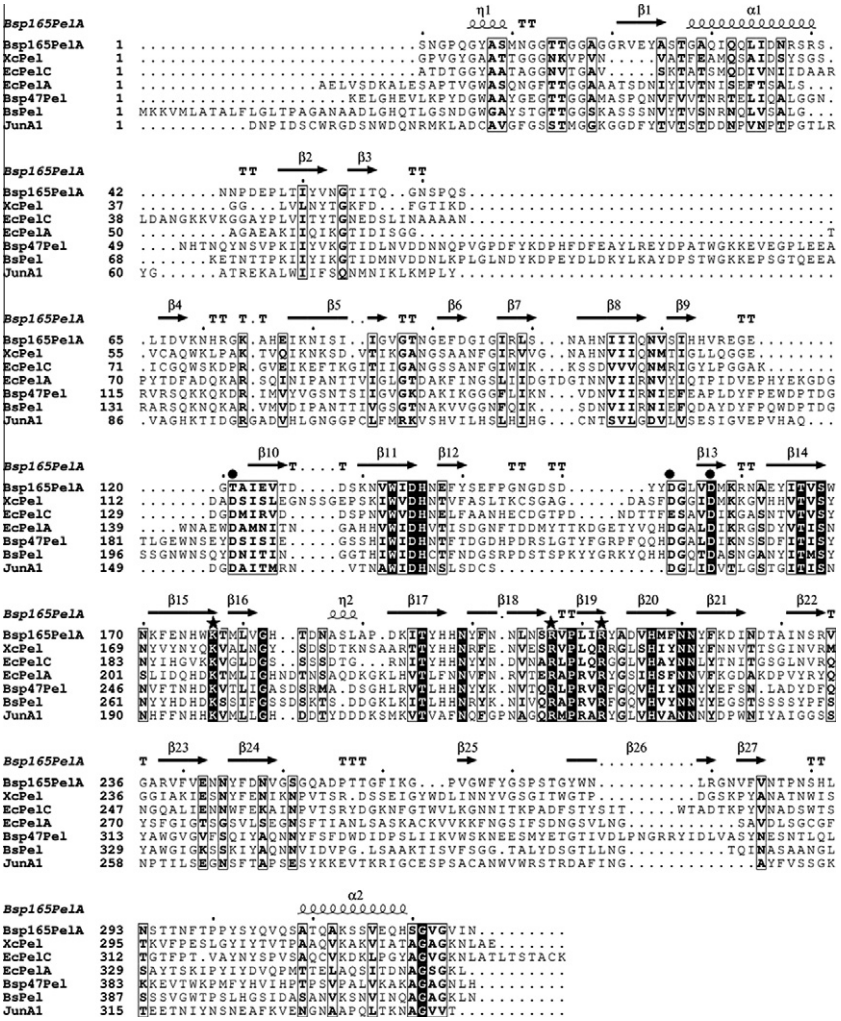

Fig. 2. Sequence alignment of Bsp165PelA and other Pels belonging to the PL family 1. Sequence alignment was performed with ClustalX [27]. Bsp165PelA (*Bacillus* sp. N16-5, pectate lyase), XcPel (*Xanthomonas cappestris* 33913, pectate lyase II), EcPelC (*Erwinia chrysanthemi*, PelC), EcPelA (*Erwinia chrysanthemi*, PelA), Bsp47Pel (*Bacillus* sp. TS 47, PelA), BsPel (*B. substilus* subsp. *subtilis* str. 168, pectate lyase), JunA1 (*Juniperus Ashei*). Strictly conserved residues are highlighted by black background and conservatively substituted residues are boxed. The secondary structural elements (helices-α, strands-β, turns-T, and 3_{10} helices-η) of Bsp165PelA are shown above the aligned sequences. The conserved catalytic sites are indicated by asterisks and the conserved calcium binding sites by circles. The figure was produced using ESPript [28].

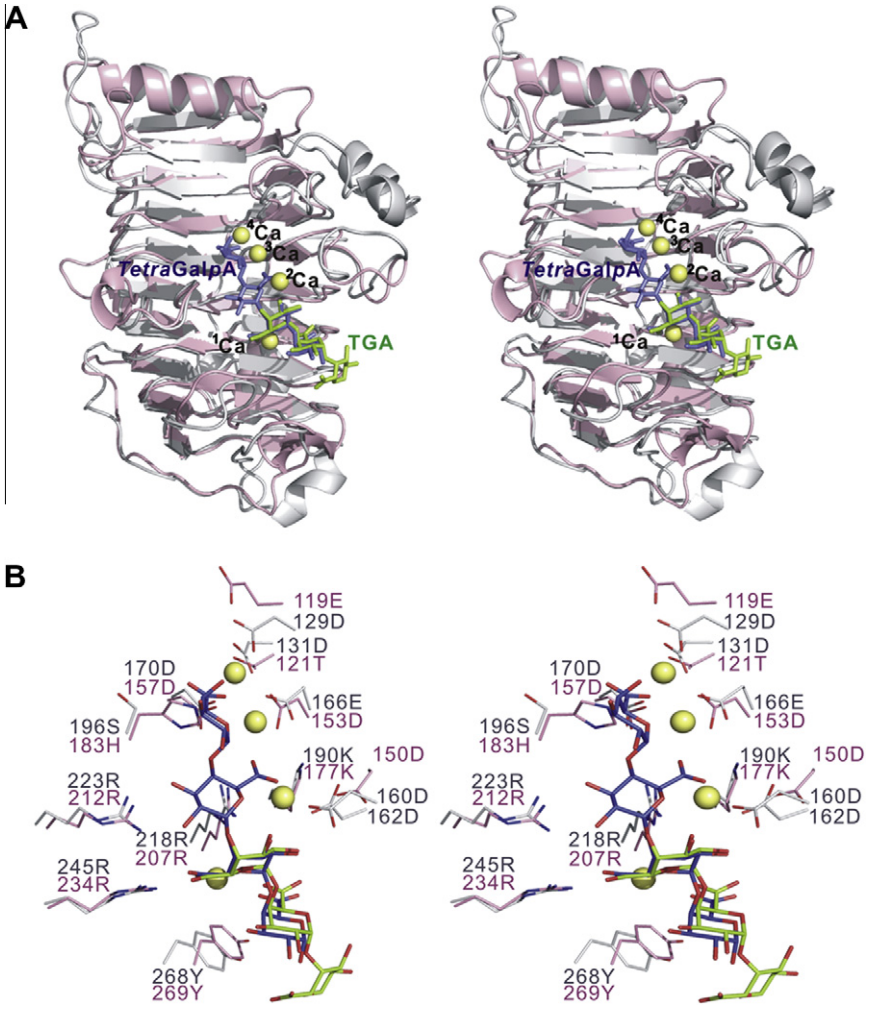

Fig. 3. Structure comparison of Bsp165PelA-TGA with PelC-tetragalacturonate-Ca^{2+}. (A) The Bsp165PelA-TGA (pink) is superimposed with *Erwinia chrysanthemi* PelC-tetragalacturonate-Ca^{2+} (gray; PDB ID: 2EWE). Tetragalacturonate (TetraGal*p*A) and TGA are shown in purple and green, respectively. Four Ca^{2+} ions are showed as yellow spheres. (B) Detailed interactions in the substrate binding clefts of Bsp165PelA–TGA and PelC-tetragalacturonate-Ca^{2+} are compared.

Table 2
Amino acids coordinated with Ca^{2+} ions in complex structures of Pels.

Ca^{2+}	PelC	BsPel	Bsp47Pel	Bsp165PelA
PDB code	2EWE	2O17	1VBL	3VMW
$^{1}Ca^{2+}$	Lys218	–		–
$^{2}Ca^{2+}$	Asp160	Asp172		–
	Asp162	Asn179		–
$^{3}Ca^{2+}$	Glu166-Oδ1	Asp222-Oδ1		Asp153-Oδ1
	Glu166-Oδ2	Asp222-Oδ2		Asp153-Oδ2
$^{4}Ca^{2+}$ (primary Ca^{2+})	Asp129	–		–
	Asp131-Oδ1	Asp183-Oδ1	Asp190-Oδ1	–
	Asp131-Oδ2	Asp183-Oδ2	Asp190-Oδ2	–
	Glu166	Asp222	Asp229	Asp153
	Asp170	Asp226	Asp233	Asp157

–: no ligand was found.

3.3. Ca^{2+} binding sites

Ca^{2+} is believed to be required for pectolytic activity by all Pels [26]. In former reports, the purified PelC from *E. chrysanthemi* and BsPel from *B. subtilis* did not show any activity without adding Ca^{2+} [6,12]. Surprisingly, Bsp165PelA in our study showed full activity after the same purification steps of ion-exchange and gel filtration as for the other Pels. Addition of Ca^{2+} did not further increase the enzyme activity. However, the activity was completely lost after EDTA treatment, and could not be restored by dialysis that removed EDTA. Bsp165PelA retrieves its full activity only if Ca^{2+} with a final concentration of 0.2 mM is added (data not shown). These

results suggest that Bsp165PelA is also Ca^{2+}-dependent but has a lower requirement for Ca^{2+} comparing with the other Pels. Even a trace amount of Ca^{2+} left by purification is sufficient. This characteristic is highly valuable for industrial use, as enzyme production without further addition of Ca^{2+} can effectively reduce the manufacture cost.

According to our former result, Bsp165PelA cleaves polygalacturonate to yield major product of trimer [14]. To get the complex of Bsp165PelA, Ca^{2+} ions and TGA crystallized turned out not working. Instead, we obtained a Bsp165PelA–TGA complex crystal in the absence of Ca^{2+}.

Some previous reports have identified conserved residues that bind to Ca^{2+} ions or the oligogalacturonate in the Pels structures. The amino acids associated with Ca^{2+} binding are listed in Table 2. Electrostatic interactions dominate in the complex of enzyme-Ca^{2+}-oligogalacturonate, where the negatively charged uronic acid moieties in the oligogalacturonate interact primarily with the positively charged groups in the protein or the Ca^{2+} ions.

Although the location and coordination numbers of primary Ca^{2+} in all three reported structures are the same, there are small differences among these Ca^{2+} binding sites. In the wild-type PelC [8], the primary Ca^{2+} coordinates to seven ligands including both carboxyl oxygens of Asp131, one carboxyl oxygen from each of Asp129, Glu166, and Asp170, and two water molecules. The primary Ca^{2+} in BsPel [1] also has seven ligands: two carboxyl oxygens each from Asp223 and Asp227, both carboxyl oxygens of Asp184 and three water molecules. The binding ligands in Bsp47Pel are similar. Notably, the Asp which in the other Pels donates two carboxyl oxygens for the primary Ca^{2+} is substituted by Thr121 in Bsp165PelA (Fig. 3B). However, Thr121 cannot form any electrostatic interaction with the primary Ca^{2+}. Because the Asp at this position is highly conserved in the Pels superfamily, the replacement by a Thr in Bsp165PelA might be the reason for the reduced affinity for primary Ca^{2+}. In addition, Asp129 in PelC is replaced by Glu119 in Bsp165PelA. The loop in which Glu119 is located deviates from the substrate binding cleft that the distance between Ca^{2+} and carboxyl oxygen is increased from 2.3 Å (Asp129 in PelC) to 4.7 Å (Glu119 in Bsp165PelA), which is too far for direct electrostatic interaction. In total, for the primary Ca^{2+}, at least three ligands present in the other Pels are missing in Bsp165PelA. Thus it is very likely that Bsp165PelA does not bind the primary Ca^{2+}. In addition, the optimal pH of Bsp165PelA is 11.5, at which there are lots of hydroxyl ions in the environment that will compete effectively with amino acids for direct coordination to Ca^{2+}. For instance, the Ca^{2+} affinity of PelC decreases 10-fold at pH 11.2 comparing to that at pH 9.5. In our study, the electron density map does not show any evidence of Ca^{2+} being present at this position, even if the crystals of Bsp165PelA were soaked in mother liquid containing high concentrations of Ca^{2+}.

One of the proposed functions of primary Ca^{2+} is to induce a substrate conformation that could be recognized by Pels. We found that His183 in Bsp165PelA can interacts with Gal*p*A_-1 intensively (Fig. 4). But in all three structures containing primary Ca^{2+} mentioned above, a Ser or an Ala replaces the His at this position (Figs. 2 and 3B), which does not provide any interaction with Gal*p*A_-1. So we hypothesize that the function of primary Ca^{2+} might be taken over by amino acids in Bsp165PelA through direct interaction/recognition between the enzyme and substrate.

The additional Ca^{2+} binding in Bsp165PelA was investigated by superimposing our enzyme structure with PelC from *E. chrysanthemi* (Fig. 3). PelC can bind three additional Ca^{2+} ions in the presence of substrate. $^{3}Ca^{2+}$ bridges substrate to both carboxyl oxygens of Glu166 in PelC. In Bsp165PelA, Glu166 was replaced by Asp153 in the corresponding position. We believe that Bsp165PelA can also bind a Ca^{2+} ion at this position in the presence of substrate. In PelC, Asp160 and Asp162 in a loop participate in the

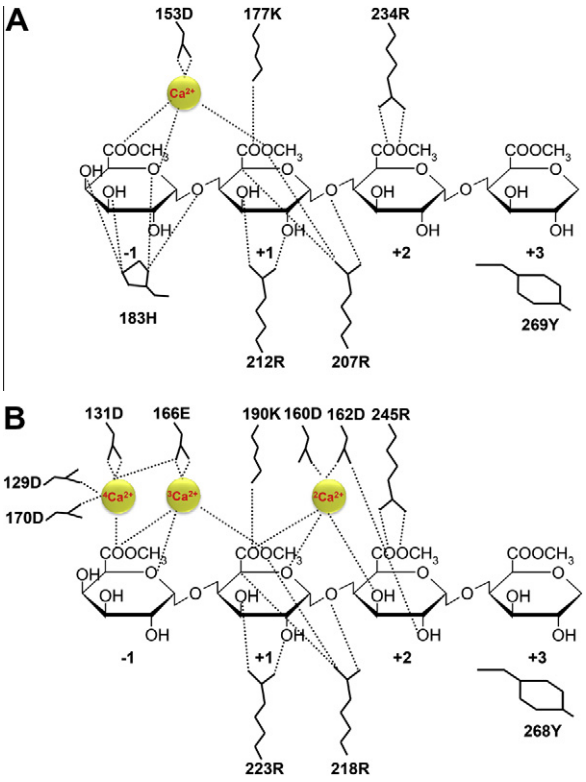

Fig. 4. Schematic representation of interactions in the Bsp165PelA and PelC substrate binding cleft. (A) The predicted Ca^{2+} position and −1, +1 subsites are obtained by structural superimposing of Bsp165PelA–TGA with *Erwinia chrysanthemi* PelC-tetragalacturonate-Ca^{2+} (PDB ID: 2EWE). The +2 and +3 subsites are from the Bsp165PelA–TGA structure. Hydrogen bonds are indicated by dashed lines. 269Y interacts with TGA by stacking effect. (B). Interactions in the PelC substrate-binding cleft. $^{1}Ca^{2+}$ is not shown in this schematic drawing since it only interacts with PelC when the mutant R218 K was used.

interaction with $^{2}Ca^{2+}$. However, in Bsp165PelA, the loop in which these two amino acids are located deviates prominently from the substrate binding cleft. No structurally similar residues lie within the distance for electrostatic interactions with $^{2}Ca^{2+}$. So we suspect that Bsp165PelA does not bind to Ca^{2+} at this position even in the presence of substrate. Coordination between the $^{1}Ca^{2+}$ and protein can only be seen in the mutant of R219L PelC structure, in which $^{1}Ca^{2+}$ is bound to Lys219. But in the wild type, $^{1}Ca^{2+}$ cannot coordinate with any amino acid but the substrate. Similarly, BsPel from *B. subtilis* has only two additional Ca^{2+} ions and does not bind to a third Ca^{2+} ion at this position. So $^{1}Ca^{2+}$ might be unimportant for catalysis.

Taken together, considering the number of ligands, it is likely that Bsp165PelA may bind to only one Ca^{2+} ion (Fig. 4). The complex structure of an inactive Bsp165PelA mutant in complex with oligogalacturonate and Ca^{2+} that we are working on may support our conclusion in the future.

In summary, the structures of pectate lyase Bsp165PelA from *Bacillus* sp. N16-5 in apo-form and in complex with TGA were solved in this study. Data from sequence alignment and structural superposition showed that the β-sheet topology and catalytic amino acids are conserved in Bsp165PelA. Yet some of the highly conserved Ca^{2+} binding sites are altered in Bsp165PelA, making it difficult to coordinate with some Ca^{2+} ions. Based on these structures, we proposed that Bsp165PelA might need only one Ca^{2+} ion for catalytic activity instead of three or four Ca^{2+} ions in the other Pels. This proposal explains the lower Ca^{2+} requirement for the Bsp165PelA activity and may help guide Pels engineering for industrial use.

Acknowledgments

The synchrotron data collection was conducted at beam line BL13B1 of NSRRC (National Synchrotron Radiation Research Center, Taiwan, ROC) supported by the National Synchrotron Radiation Research Center (Hsinchu, Taiwan, ROC). The research project was supported by the Ministry of Sciences and Technology of China (973 program 2011CBA00805) and the Knowledge Innovative Program of CAS (KSCX2-EW-G-8).

References

[1] R. Pickersgill, J. Jenkins, G. Harris, W. Nasser, J. Robert-Baudouy, The structure of *Bacillus subtilis* pectate lyase in complex with calcium, Nat. Struct. Biol. 1 (1994) 717–723.
[2] M.C. Marin-Rodriguez, J. Orchard, G.B. Seymour, Pectate lyases, cell wall degradation and fruit softening, J. Exp. Bot. 53 (2002) 2115–2119.
[3] S.R. Herron, J.A. Benen, R.D. Scavetta, J. Visser, F. Jurnak, Structure and function of pectic enzymes: virulence factors of plant pathogens, Proc. Natl. Acad. Sci. USA 97 (2000) 8762–8769.
[4] S. Heffron, B. Henrissat, M.D. Yoder, S. Lietzke, F. Jurnak, Structure-based multiple alignment of extracellular pectate lyase sequences, Mol. Plant Microbe. Interact. 8 (1995) 331–334.
[5] F. Tardy, W. Nasser, J. Robert-Baudouy, N. Hugouvieux-Cotte-Pattat, Comparative analysis of the five major *Erwinia chrysanthemi* pectate lyases: enzyme characteristics and potential inhibitors, J. Bacteriol. 179 (1997) 2503–2511.
[6] M.D. Yoder, F. Jurnak, The refined three-dimensional structure of pectate lyase C from *Erwinia chrysanthemi* at 2.2 Angstrom resolution (implications for an enzymatic mechanism), Plant Physiol. 107 (1995) 349–364.
[7] L.M. Thomas, C.N. Doan, R.L. Oliver, M.D. Yoder, Structure of pectate lyase A: comparison to other isoforms, Acta Crystallogr. D Biol. Crystallogr. 58 (2002) 1008–1015.
[8] R.D. Scavetta, S.R. Herron, A.T. Hotchkiss, N. Kita, N.T. Keen, J.A. Benen, H.C. Kester, J. Visser, F. Jurnak, Structure of a plant cell wall fragment complexed to pectate lyase C, Plant cell 11 (1999) 1081–1092.
[9] S.R. Herron, R.D. Scavetta, M. Garrett, M. Legner, F. Jurnak, Characterization and implications of Ca^{2+} binding to pectate lyase C, J. Biol. Chem. 278 (2003) 12271–12277.
[10] Z. Xiao, H. Bergeron, S. Grosse, M. Beauchemin, M.L. Garron, D. Shaya, T. Sulea, M. Cygler, P.C. Lau, Improvement of the thermostability and activity of a pectate lyase by single amino acid substitutions, using a strategy based on melting-temperature-guided sequence alignment, Appl. Environ. Microbiol. 74 (2008) 1183–1189.
[11] N. Kita, C.M. Boyd, M.R. Garrett, F. Jurnak, N.T. Keen, Differential effect of site-directed mutations in pelC on pectate lyase activity, plant tissue maceration, and elicitor activity, J. Biol. Chem. 271 (1996) 26529–26535.
[12] A. Seyedarabi, T.T. To, S. Ali, S. Hussain, M. Fries, R. Madsen, M.H. Clausen, S. Teixteira, K. Brocklehurst, R.W. Pickersgill, Structural insights into substrate specificity and the anti beta-elimination mechanism of pectate lyase, Biochemistry 49 (2010) 539–546.
[13] M. Akita, A. Suzuki, T. Kobayashi, S. Ito, T. Yamane, The first structure of pectate lyase belonging to polysaccharide lyase family 3, Acta Crystallogr. D Biol. Crystallogr. 57 (2001) 1786–1792.
[14] G. Li, L. Rao, Y. Xue, C. Zhou, Y. Zhang, Y. Ma, Cloning, expression, and characterization of a highly active alkaline pectate lyase from alkaliphilic *Bacillus* sp. N16-5, J. Microbiol. Biotechnol. 20 (2010) 670–677.
[15] Z. Otwinowski, W. Minor, Processing of X-ray diffraction data collected in oscillation mode, Methods Enzymol. 276 (1997) 307–326.
[16] A.T. Brunger, Assessment of phase accuracy by cross validation: the free R value. Methods and applications, Acta Crystallogr. D Biol. Crystallogr. 49 (1993) 24–36.
[17] A.T. Brunger, P.D. Adams, G.M. Clore, W.L. DeLano, P. Gros, R.W. Grosse-Kunstleve, J.S. Jiang, J. Kuszewski, M. Nilges, N.S. Pannu, R.J. Read, L.M. Rice, T. Simonson, G.L. Warren, Crystallography & NMR system: a new software suite for macromolecular structure determination, Acta Crystallogr. D Biol. Crystallogr. 54 (1998) 905–921.
[18] P. Emsley, K. Cowtan, Coot: model-building tools for molecular graphics, Acta Crystallogr. D Biol. Crystallogr. 60 (2004) 2126–2132.
[19] P.D. Adams, R.W. Grosse-Kunstleve, L.W. Hung, T.R. Ioerger, A.J. McCoy, N.W. Moriarty, R.J. Read, J.C. Sacchettini, N.K. Sauter, T.C. Terwilliger, PHENIX: building new software for automated crystallographic structure determination, Acta Crystallogr. D Biol. Crystallogr. 58 (2002) 1948–1954.
[20] A.J. McCoy, R.W. Grosse-Kunstleve, P.D. Adams, M.D. Winn, L.C. Storoni, R.J. Read, Phaser crystallographic software, J. Appl. Crystallogr. 40 (2007) 658–674.
[21] J. Jenkins, R. Pickersgill, The architecture of parallel beta-helices and related folds, Prog. Biophys. Mol. Biol. 77 (2001) 111–175.
[22] C.S. Ring, D.G. Kneller, R. Langridge, F.E. Cohen, Taxonomy and conformational analysis of loops in proteins, J. Mol. Biol. 224 (1992) 685–699.
[23] M.D. Yoder, F. Jurnak, Protein motifs. 3. The parallel beta helix and other coiled folds, FASEB J. 9 (1995) 335–342.
[24] S.E. Lietzke, R.D. Scavetta, M.D. Yoder, F. Jurnak, The refined three-dimensional structure of pectate lyase E from *Erwinia chrysanthemi* at 2.2 Å resolution, Plant Physiol. 111 (1996) 73–92.
[25] E.W. Czerwinski, T. Midoro-Horiuti, M.A. White, E.G. Brooks, R.M. Goldblum, Crystal structure of Jun a 1, the major cedar pollen allergen from *Juniperus ashei*, reveals a parallel beta-helical core, J. Biol. Chem. 280 (2005) 3740–3746.
[26] B. Henrissat, S.E. Heffron, M.D. Yoder, S.E. Lietzke, F. Jurnak, Functional implications of structure-based sequence alignment of proteins in the extracellular pectate lyase superfamily, Plant Physiol. 107 (1995) 963–976.
[27] J.D. Thompson, T.J. Gibson, F. Plewniak, F. Jeanmougin, D.G. Higgins, The CLUSTAL_X windows interface. flexible strategies for multiple sequence alignment aided by quality analysis tools, Nucleic Acids Res. 25 (1997) 4876–4882.
[28] P. Gouet, X. Robert, E. Courcelle, ESPript/ENDscript: extracting and rendering sequence and 3D information from atomic structures of proteins, Nucleic Acids Res. 31 (2003) 3320–3323.

Biochemical and Biophysical Research Communications 420 (2012) 275–280

Contents lists available at SciVerse ScienceDirect

Biochemical and Biophysical Research Communications

journal homepage: www.elsevier.com/locate/ybbrc

Expression of prohibitins on the surface of activated T cells

Hajime Yurugi [a], Shuhei Tanida [a], Akiko Ishida [a], Kaoru Akita [a], Munetoyo Toda [a], Mizue Inoue [b], Hiroshi Nakada [a,*]

[a] Department of Molecular Biosciences, Faculty of Life Sciences, Kyoto Sangyo University, Kamigamo-Motoyama, Kitaku, Kyoto 603-8555, Japan
[b] Avian Influenza Research Center, Kyoto Sangyo University, Kamigamo-Motoyama, Kitaku, Kyoto 603-8555, Japan

ARTICLE INFO

Article history:
Received 27 February 2012
Available online 6 March 2012

Keywords:
Prohibitin
T cell regulation
Signal transduction

ABSTRACT

Prohibitins (prohibitin-1 and -2) comprise a family of highly conserved proteins that are mainly localized to mitochondria. Recent studies showed that prohibitins are up-regulated upon T cell activation and play an essential role in maintaining mitochondrial homeostasis. In the present study, we found that a considerable proportion of prohibitin-1 and -2 induced in response to T cell activation was expressed on the surface of activated T cells. When mouse and human T cells were stimulated with PMA and ionomycin, prohibitins expressed on the cell surface were increased significantly, peaking at 48 h after stimulation. Stimulation of mouse T cells with anti-CD3 and anti-CD28 antibodies also remarkably induced the cell surface expression of prohibitins. Their expression on the cell surface was also detected in T cell leukemia cells such as Jurkat cells. In Jurkat cells, prohibitin-1 and -2 were co-localized with CD3 on the cell surface, and anti-CD3 antibody-induced signaling, the MAP kinase cascade, was inhibited on treatment with protein A magnetic beads co-conjugated with anti-CD3 antibody and anti-prohibitin-1 or anti-prohibitin-2 antibody. These results suggest that prohibitins expressed on the surface of activated T cells are involved in the T cell receptor-mediated signaling cascade.

1. Introduction

Although prohibitins (prohibitin-1 and -2) are primarily localized to mitochondria, recent studies showed that they are present in multiple cellular compartments and possess diverse functions [1–3]. Prohibitin-1 and -2 have molecular masses of approximately 30 kDa and 37 kDa, respectively, and form a high molecular mass complex. In mitochondria, they are located in the inner membrane, where they stabilize mitochondrial respiratory enzymes [4,5]. Nuclear prohibitins play a role as transcriptional regulators in combination with some transcriptional factors such as p53 and E2F1, which control proliferation and apoptosis, respectively [6,7]. The nuclear localization of prohibitins has often been described in breast and prostate cancer cell lines [8,9]. It has also been reported that prohibitin-2 interacts and inhibits the transcriptional activity of estrogen receptor [10]. Prohibitins were originally identified as B cell receptor-associated proteins, and revealed to be relevant to modulate signaling in B cells [11]. Prohibitins have also been shown to regulate the activation of c-Raf in epithelial cancer cells [12]. Recently, Ross et al. reported that prohibitins are markedly induced upon T cell activation and are responsible for maintaining mitochondrial integrity [13]. Furthermore, genetic deletion of prohibitin-1 or -2 in mice is lethal before embryonic day 9.0, indicating that prohibitins play a pivotal role at an early embryonic stage [14,15]. In the present study, we found that expression of prohibitins on the cell surface was induced remarkably upon T cell activation. Their cell surface expression was also observed in T cell leukemia cells. Co-localization of prohibitins with CD3, and the inhibitory effects of anti-prohibitin-1 and anti-prohibitin-2 antibodies on anti-CD3 antibody-induced signaling suggest that prohibitin-1 and prohibitin-2 on the cell surface play an important role in the regulation of T cell signaling.

2. Materials and methods

2.1. Animals and cells

Balb/c mice (5–7w, female) were purchased from SHIMIZU Laboratory Supplies Co. Ltd. and kept under SPF conditions. T cell leukemia cell lines, Molt-3, Molt-4, and Jurkat cells, were obtained from ATCC. Primary T cells and T cell leukemia cells were cultured in RPMI-1640 supplemented with 10% heat inactivated fetal calf serum (Cell Culture Bioscience), 2 mM L-glutamine, 50 IU/ml penicillin, and 50 μg/ml streptomycin.

2.2. Preparation and activation of T cells

Mouse T cells were obtained from mouse spleens using a Pan T Cell Isolation Kit II (Miltenyi Biotec). Mouse $CD4^+$ and $CD8^+$ T cells

* Corresponding author. Fax: +81 75 705 1888.
E-mail address: hnakada@cc.kyoto-su.ac.jp (H. Nakada).

0006-291X/$ - see front matter © 2012 Elsevier Inc. All rights reserved.
http://dx.doi.org/10.1016/j.bbrc.2012.02.149

were separated using anti-CD4 antibody- and anti-CD8 antibody-conjugated microbeads (Miltenyi Biotec), respectively. Human T cells were prepared from peripheral blood mononuclear cells (PBMCs) of healthy donors using anti-CD3 antibody-conjugated microbeads (Miltenyi Biotec). Mouse and human T cells (1.5×10^6 cells) were stimulated with 100 nM phorbol 12-myristate 13-acetate (PMA) and 500 ng/ml ionomycin. Mouse T cells were also stimulated with anti-mouse CD3 antibody (BioLegend, clone 145-2C11), which was coated on a culture plate (6 well, BD), in the presence of 5 μg/ml anti-mouse CD28 antibody (BioLegend, clone 37.51) and 100 U/ml mouse IL-2 (CST).

2.3. Analysis of induced prohibitins

Some activated and non-activated T cells were solubilized with lysis buffer (50 mM Tris–HCl, pH 7.5, 150 mM NaCl, 1% Triton-X100, 2 mM EDTA, and 1% protease inhibitor cocktail (nacalai tesque)) at the indicated times after stimulation. Each lysate was subjected to SDS–PAGE, followed by Western blotting. Other activated and non-activated T cells were treated with EZ-Link sulfo-NHS biotin (Thermo Scientific) according to the manufacturer's instructions. After washing with PBS containing 0.1 M glycine, the cells were solubilized as described above. Streptavidin-Sepharose (GE Healthcare) was added to each cell lysate containing the same amount of proteins, followed by stirring at 4 °C for 1 h. After washing with lysis buffer, proteins precipitated with the resin were dissolved in SDS–PAGE sample buffer, and then subjected to SDS–PAGE, followed by Western blotting. After blocking with PBS containing 5% BSA, the membranes were treated with mouse anti-prohibitin-1 (Neo Markers, clone II-14-10), rabbit anti-prohibitin-1 (ABGENT), rabbit anti-prohibitin-2 (BETHYL), and mouse anti-ß-actin (SIGMA) antibodies, followed by incubation with HRP-conjugated anti-rabbit IgG antibody or HRP-conjugated anti-mouse IgG antibody (Invitrogen). The bands were visualized using an ECL system (GE Healthcare), and their intensities were determined with Image J software.

2.4. Immunocytochemical staining of Jurkat cells

Jurkat cells (5×10^5 cells) were treated with 5 μg/ml mouse anti-human CD3 antibody (Millipore, clone UCHT1) plus 2.5 μg/ml rabbit anti-prohibitin-1 antibody (ABGENT) or rabbit anti-prohibitin-2 antibody (BETHYL) at 4 °C for 1 h. After washing with PBS, the cells were stained with Alexa Fluor 488-conjugated anti-mouse IgG antibody (Molecular Probes), and Alexa Fluor 594-conjugated anti-rabbit IgG antibody (Molecular Probes). After fixing with 4% paraformaldehyde, nuclei were stained with DAPI, and then the cells were mounted using Prolong Gold Antifade Reagent (Invitrogen).

2.5. Stimulation of Jurkat cells with anti-CD3 antibody-bound protein A magnetic beads and analysis of ERK phosphorylation

Jurkat cells were treated by the following three methods. (1) Prohibitins and CD3 were co-cross-linked using protein A magnetic beads conjugated with mouse anti-human CD3 antibody and rabbit anti-prohibitin-1 or rabbit anti-prohibitin-2 antibody. (2) Prohibitins and CD3 were separately cross-linked using protein A magnetic beads conjugated with anti-CD3 antibody and anti-prohibitin-1 or anti-prohibitin-2 antibody independently. (3) Jurkat cells were stimulated with protein A magnetic beads conjugated with anti-CD3 antibody in the presence of soluble anti-prohibitin-1 or anti-prohibitin-2 antibody. A control experiment was performed using isotype rabbit IgG instead of anti-prohibitin-1 or -2 antibody. IgG-bound protein A magnetic beads, the amount of which was arranged to bind 9 μg of IgG, were added to a suspension of Jurkat cells (5×10^4 cells). After incubation at 37 °C for 10 min, the cells were collected, dissolved in SDS–PAGE sample buffer, and then subjected to SDS–PAGE, followed by Western blotting. After blocking with PBS containing 5% BSA, the membranes were treated with mouse anti-phosphorylated ERK1/2 antibody and rabbit anti-ERK1/2 antibody (CST), followed by treatment with HRP-conjugated anti-mouse IgG antibody or HRP-conjugated anti-rabbit IgG antibody (Invitrogen). The bands were visualized and their intensities were determined as described above.

2.6. Statistical analysis

Student's *t* test was used to determine the significance of differences between sample means.

3. Results and discussion

3.1. Elevated expression of prohibitin-1 and -2 on the surface of activated T cells

Mouse T cells were prepared from mouse spleens, and stimulated with PMA and ionomycin as described under Section 2. Activated mouse T cells obtained at 48 h after stimulation with PMA and ionomycin were stained with trypan blue, dead cells being estimated to comprise less than 5% of the total cells (data not shown). At 0, 24, 48, and 72 h after stimulation, some activated and non-activated cells were lysed and the lysates was directly subjected to SDS–PAGE, followed by Western blotting. Prohibitins were detected and their levels were compared. Total prohibitin-1 and -2 of mouse T cells were increased about 2- and 2.5-fold, respectively, at 48 h after stimulation with PMA and ionomycin (Fig. 1A). Other activated and non-activated cells were treated with biotin to label the cell surface proteins. After lysis, biotin-labeled proteins were precipitated with Streptavidin-Sepharose. The precipitate was subjected to SDS–PAGE, followed by Western blotting and detection with anti-prohibitin-1 and -2 antibodies. It should be noted that although cell surface prohibitin-1 and -2 were hardly detected in naive T cells, they were remarkably elevated and peaked at 48 h after stimulation. Prohibitin-1 and -2 on the cell surface were increased about 66- and 28-fold, respectively (Fig. 1A). To confirm that biotin-labeled prohibitins were not derived from intracellular membranes and cytosol, contamination by other subcellular proteins in the biotin-labeled protein fraction was examined. As shown in Supplementary Fig. S1, negligible levels of intracellular proteins such as ß-actin, lamin B, and voltage-dependent anion channel (VDAC), which are present in the cytosol, nuclei, and mitochondria, respectively, were detected. These data corresponded to the level of dead cells estimated by trypan blue-staining, suggesting that these intracellular proteins were artificially labeled with biotin due to damaged plasma membrane of dead cells. About 20% and 29% of prohibitin-1 and -2, respectively, were detected in the biotin-labeled protein fraction, indicating that a considerable proportion of induced prohibitins were expressed on the cell surface.

To see if this induction of prohibitin-1 and -2 in activated T cells is restricted to distinct subpopulations of T cells, we separated $CD4^+$ and $CD8^+$ T cells, and then similar experiments were performed. As shown in Fig. 1B, marked induction of prohibitins on the cell surface was observed irrespective of whether the cells were $CD4^+$ or $CD8^+$ ones, indicating that prohibitins were commonly induced in T cells. Since non-physiological stimulation with PMA and ionomycin may mimic antigen receptor stimulation, we also tried to stimulate T cells with anti-CD3 and anti-CD28 antibodies. As shown in Fig. 1C, prohibitins were also induced and cell surface expression of prohibitins was elevated similarly.

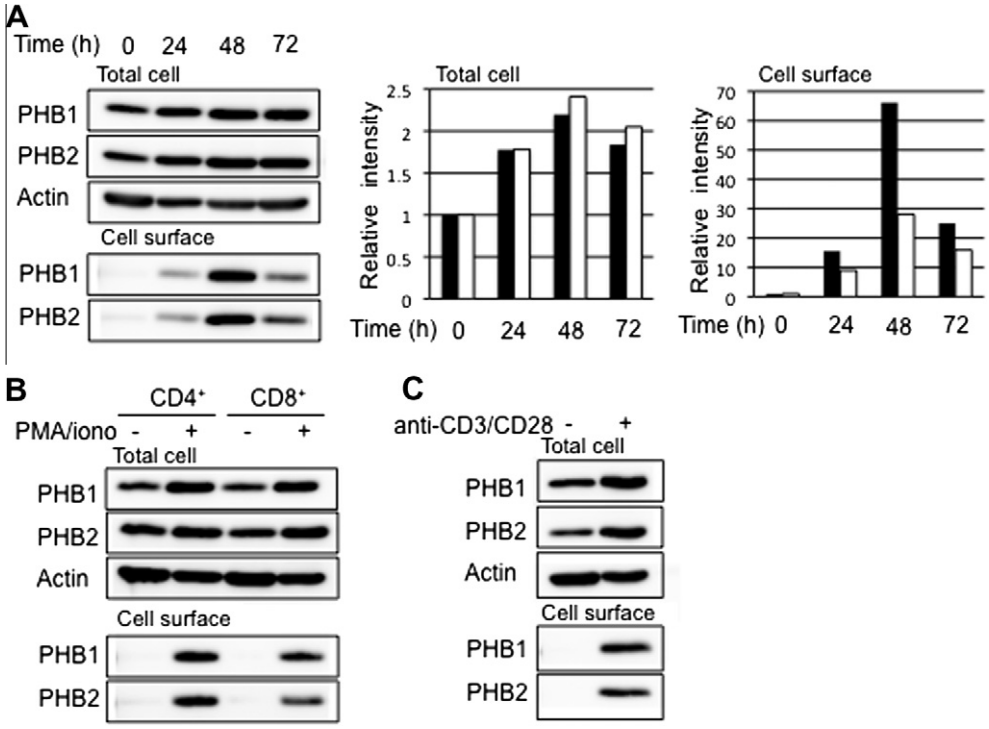

Fig. 1. Expression of prohibitin-1 and -2 on the surface of mouse activated T cells. (A) Mouse T cells were prepared from spleens as described under Materials and methods. T cells were stimulated with PMA and ionomycin, and cells were recovered at 0, 24, 48, and 72 h after stimulation. Some cells were treated with biotin, and cell surface proteins were prepared using streptavidin-Sepharose as described under Section 2. Whole cell lysates and cell surface proteins were subjected to SDS–PAGE, followed by Western blotting and detection of prohibitin-1 (PHB1), prohibitin-2 (PHB2), and ß-actin. Histograms show the relative intensities of the prohibitin-1 (closed bars) and -2 (opened bars) bands (averages of duplicate experiments), in which each density was normalized as to ß-actin and the value for T cells at 0 time was taken as 1. (B) Mouse $CD4^+$ and $CD8^+$ T cells were separated as described under Section 2. These cells were stimulated with PMA and ionomycin, recovered at 48 h after stimulation, and then prohibitins were detected as in A. (C) Mouse T cells were stimulated with anti-CD3 and anti-CD28 antibodies, and a similar experiment to that in B was performed.

Human T cells were obtained from PBMCs and stimulated similarly. Human prohibitin-1 and -2 were also increased about 5.4- and 2.7-fold, respectively, at 48 h after stimulation. Prohibitin-1 and -2 on the surface of human activated T cells were also elevated 16- and 23-fold, respectively (Fig. 2). However, unlike in the case of mouse T cells, prohibitin-2 was induced more prominently than prohibitin-1 on the cell surface. This different level of induction cannot be explained at present. Elucidation of the induction mechanism may be necessary to clarify this. Such a study is currently under investigation. Ross et al. reported that prohibitin-1 and -2 are up-regulated upon activation of primary human T cells, and that induced prohibitins are located in the mitochondrial inner membrane. Prohibitin-1 and -2 expressed on the surface of mouse T cells at 48 h after stimulation were roughly estimated to comprise 20% and 29% of total prohibitin-1 and -2, respectively, as described above. This estimation means that residual intracellular prohibitins were also elevated by stimulation, and that they may be mainly localized to mitochondria, this being consistent with the results reported by Ross et al. Expression of prohibitin-1 and -2 on the cell surface has been demonstrated in B lymphocytes [11], intestinal epithelial cells [16], and adipose endothelial cells [17]. It appears likely that the subcellular localization of prohibitins is cell type-dependent. Notably, we have found that the subcellular distribution of prohibitins in T cells was changed with the cellular physiological conditions, suggesting their significant biological role. At present, it is uncertain whether prohibitins induced on the cell surface are directly incorporated into the plasma membrane after their synthesis or translocated from an intracellular compartment such as mitochondria. It has been suggested that prohibitin-1 may be able to be translocated between the mitochondria and the plasma membrane [3,17]. In addition, we also compared cell surface prohibitins with intracellular ones with respect to their apparent molecular size. Biotin-labeled cell surface prohibitins and biotin-unlabeled intracellular ones were applied to gel filtration on Sephadex G-75. Both prohibitin-1 and -2, irrespective of whether they were cell surface and intracellular ones, showed similar elution patterns and were mostly eluted in the excluded fractions as shown in Supplementary Fig. S2, suggesting that cell surface prohibitins also form multi- and hetero-complexes.

3.2. Cell surface prohibitins on T cell leukemia cells

Cell surface proteins on T cell leukemia cell lines, Jurkat, Molt-3, and Molt-4 cells, were labeled with biotin. Biotin-labeled proteins were prepared and prohibitins were detected as described above. All the cells examined expressed prohibitin-1 and -2 on the cell surface as shown in Fig. 3A. Jurkat cells were immunochemically stained with anti-prohibitin-1 and -2 antibodies, and anti-CD3 antibody. Prohibitin-1 and -2 were immunochemically detected on the cell surface, as shown in Fig. 3B. It should be noted that their distribution was not uniform, but patchy on the cell surface, and that prohibitin-1 and -2 were completely co-localized with CD3, suggesting that prohibitins are located in the rafts including CD3-T cell receptor complexes. Lipid rafts are known to be the sites in the plasma membrane where many cellular signaling events are initiated. Thus, cell surface prohibitins in activated T cells and T cell leukemia cells may function as signaling components.

3.3. Inhibition of ERK signaling by anti-prohibitin-1 and -2 antibodies in Jurkat cells

Jurkat cells were stimulated for 10 min with anti-CD3 antibody in three different combinations with anti-prohibitin-1 or -2

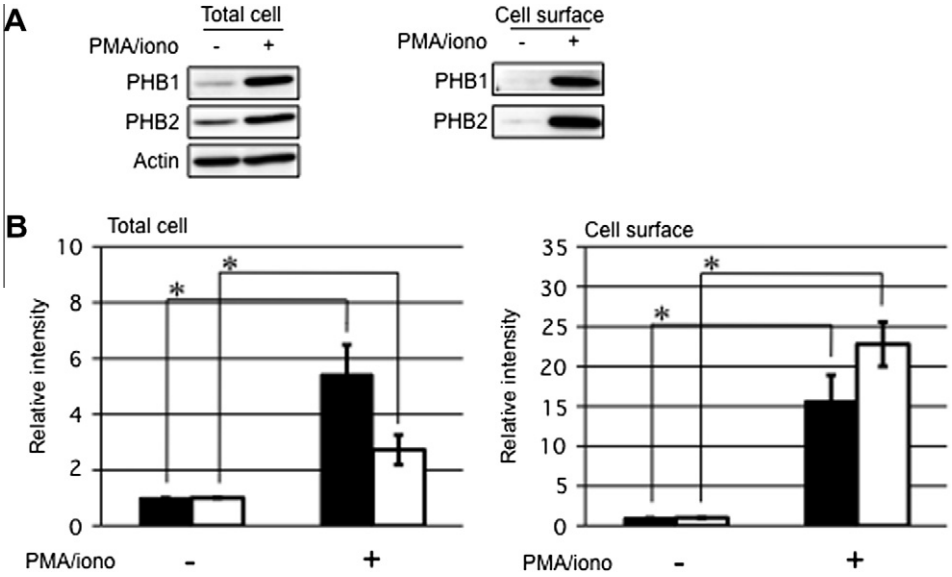

Fig. 2. Expression of prohibitin-1 and -2 on the surface of human activated T cells. Human T cells were prepared from PBMCs and stimulated as described in Fig. 1A. (A) Total and cell surface prohibitins were detected as described under Section 2. Representative data for four experiments are shown. (B) The levels of prohibitin-1 (closed bars) and -2 (opened bars) were compared as the relative intensities of bands as described in Fig. 1A. Data are expressed as means ± SD ($n = 4$, $^{*}p < 0.05$).

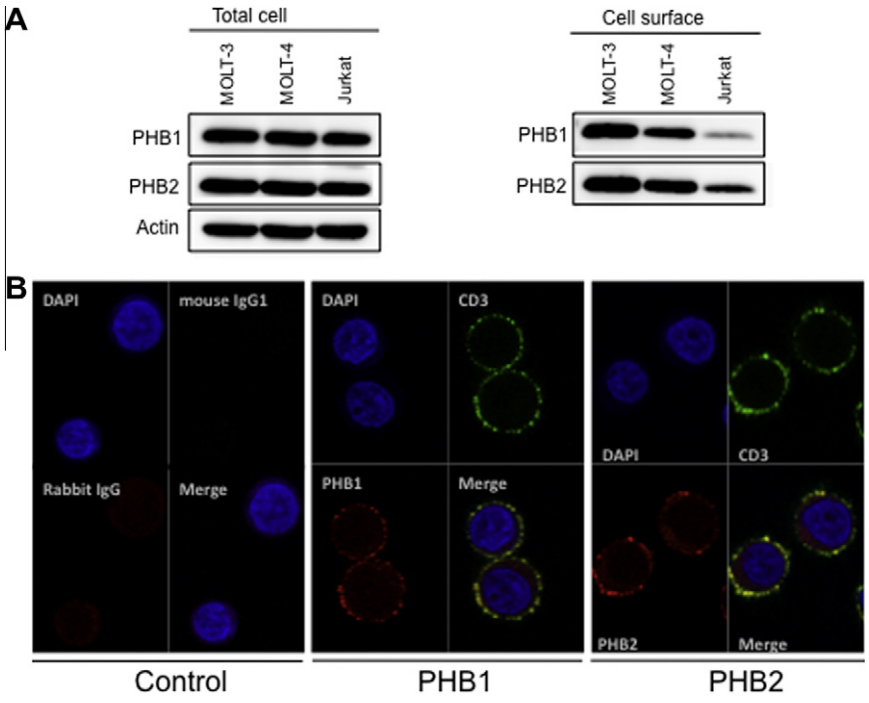

Fig. 3. Expression of prohibitin-1 and -2 on the surface of T cell leukemia cells. (A) Cell surface prohibitins on Molt-3, Molt-4, and Jurkat cells were analyzed as described in Fig. 1A. (B) Jurkat cells were treated with 5 μg/ml anti-CD3 antibody plus 2.5 μg/ml anti-prohibitin-1 or -2 antibody, and then with each secondary antibody, followed by fixation and staining of nuclei with 4% paraformaldehyde and DAPI, respectively. A control experiment was performed using isotype mouse IgG and rabbit IgG. After mounting, the samples were observed by confocal microscopy.

antibody, and the cell lysates were subjected to SDS–PAGE, followed by Western blotting. Phosphorylated ERK1/2 and total ERK1/2 were detected on PVDF membrane. When prohibitins and CD3 on the cell surface of Jurkat cells were co-cross-linked using protein A magnetic beads conjugated with anti-CD3 antibody and anti-prohibitin-1 or anti-prohibitin-2 antibody, anti-prohibitin-1 antibody inhibited about 40% of the phosphorylation of ERK1/2, and anti-prohibitin-2 about 20% and 30% of the phosphorylation of ERK1 and ERK2, respectively, suggesting that prohibitin-1 and -2 may be involved in the ERK cascade that is brought about by T cell activation (Fig. 4). This effect of anti-prohibitin-1 and -2 antibodies on the ERK phosphorylation decreased until 30 min after stimulation (data not shown). When Jurkat cells were treated with protein A magnetic beads conjugated with anti-CD3 antibody and anti-prohibitin-1 or -2 antibody separately, anti-prohibitin-1 and -2 antibodies slightly decreased the phosphorylation of ERK1/2 (data not shown). Furthermore, Jurkat cells were treated with protein A magnetic beads conjugated with anti-CD3 antibody in the

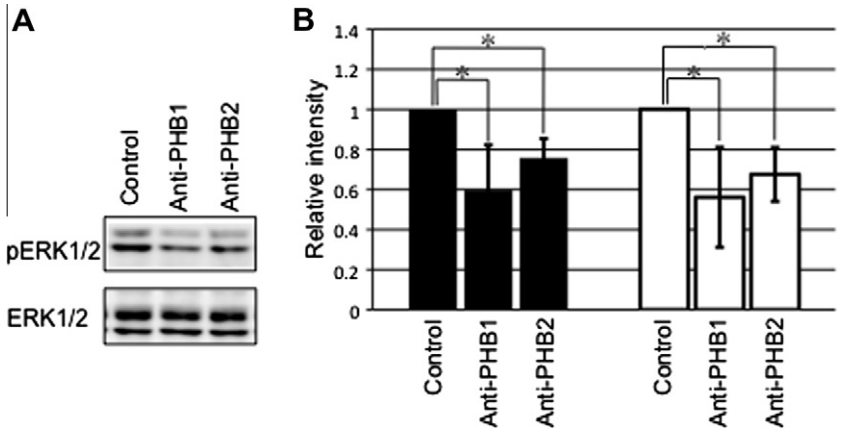

Fig. 4. Effects of anti-prohibitin-1 and -2 antibodies on T cell receptor-mediated signaling. (A) Jurkat cells (5×10^4 cells) were treated with anti-CD3 antibody plus anti-prohibitin-1 or -2 antibody-bound protein A magnetic beads at 37 °C for 10 min. The cells were dissolved in SDS–PAGE sample buffer, and subjected to SDS–PAGE, followed by Western blotting and detection with anti-phosphorylated ERK1/2 and anti-ERK1/2 antibodies as described under Section 2. A control experiment was performed using isotype rabbit IgG instead of anti-prohibitin-1 and -2 antibodies. Representative data for four experiments are shown. (B) The histogram shows the relative intensities of the phosphorylated ERK1 (closed bars) and phosphorylated ERK2 (opened bars) bands, in which each density was normalized as to ß-actin and the value for control experiment was taken as 1. Data are expressed as means ± SD ($n = 4$, $^*p < 0.05$).

presence of soluble anti-prohibitin-1 or -2 antibody. In this case, an effect of anti-prohibitin-1 or -2 antibody was hardly detected (data not shown). These results indicate that prohibitins inhibit T cell receptor signaling only when they are co-cross-linked with CD3 like programed death-1 (PD-1) [18]. These results are consistent with the report that the Vi polysaccharide of *Salmonella typhi* can interact with prohibitins on the surface of intestinal epithelial cells and down-modulate the MAP kinase cascade, leading to inhibition of inflammatory responses [16]. Rajalingam et al. reported that prohibitin-1 is required for Ras-mediated Raf activation, which occurs in association with the plasma membrane, and proposed that prohibitin might play a role in the plasma membrane scaffold that ensures the Ras-Raf interaction [12]. Thus, these facts suggest a crucial role of prohibitin-1 on the cell surface. In addition, cell surface prohibitins may be a direct target for modulating these cellular functions. Cytotoxic T lymphocyte antigen-4 (CTLA-4) and PD-1 are known to be induced on the surface of activated T cells like prohibitins [19–22]. They are T cell-co stimulation receptors and critical negative regulators of T cell activation. Antibodies against CTLA-4 and PD-1 have been examined as to therapies for inflammatory diseases and cancer [23,24]. Although the precise roles of cell surface prohibitins in T cell receptor-mediated signaling remain to be elucidated, prohibitins may also be therapeutic targets for the regulation of T cell activation.

Acknowledgment

This study was supported by a Private University Strategic Research Foundation Support Program.

Appendix A. Supplementary data

Supplementary data associated with this article can be found, in the online version, at doi:10.1016/j.bbrc.2012.02.149.

References

[1] S. Mishra, L.C. Murphy, L.J. Murphy, The prohibitins: emerging roles in diverse functions, J. Cell. Mol. Med. 10 (2006) 353–363.
[2] S. Mishra, S.R. Ande, B.L.G. Nyomba, The role of prohibitin in cell signaling, FEBS J. 277 (2010) 3937–3946.
[3] S. Mishra, L.C. Murphy, B. Nyomba, L.J. Murphy, Prohibitin: a potential target for new therapeutics, Trends Mol. Med. 11 (2005) 192–197.
[4] M.A. Sanz, W.Y. Tsang, E.M. Willems, L.A. Grivell, B.D. Lemire, H. van der Spek, et al., The mitochondrial prohibitin complex is essential for embryonic viability and germline function in *Caenorhabditis elegans*, J. Biol. Chem. 278 (2003) 32091.
[5] L.G. Nijtmans, L. de Jong, M. Artal Sanz, P.J. Coates, J.A. Berden, J.W. Back, et al., Prohibitins act as a membrane-bound chaperone for the stabilization of mitochondrial proteins, EMBO J. 19 (2000) 2444–2451.
[6] H. Chander, M. Halpern, L. Resnick-Silverman, J.J. Manfredi, D. Germain, Skp2B attenuates p53 function by inhibiting prohibitin, EMBO Rep. 11 (2010) 220–225.
[7] B. Joshi, D. Ko, D. Ordonez-Ercan, S.P. Chellappan, A putative coiled-coil domain of prohibitin is sufficient to repress E2F1-mediated transcription and induce apoptosis, Biochem. Biophys. Res. Commun. 312 (2003) 459–466.
[8] G. Fusaro, P. Dasgupta, S. Rastogi, B. Joshi, S. Chellappan, Prohibitin induces the transcriptional activity of p53 and is exported from the nucleus upon apoptotic signaling, J. Biol. Chem. 278 (2003) 47853–47861.
[9] S.C. Gamble, M. Odontiadis, J. Waxman, J.A. Westbrook, M.J. Dunn, R. Wait, et al., Androgens target prohibitin to regulate proliferation of prostate cancer cells, Oncogene 23 (2004) 2996–3004.
[10] J.-W. Kim, M. Akiyama, J.-H. Park, M.-L. Lin, A. Shimo, T. Ueki, et al., Activation of an estrogen/estrogen receptor signaling by BIG3 through its inhibitory effect on nuclear transport of PHB2/REA in breast cancer, Cancer Sci. 100 (2009) 1468–1478.
[11] M. Terashima, K.M. Kim, T. Adachi, P.J. Nielsen, M. Reth, G. Köhler, et al., The IgM antigen receptor of B lymphocytes is associated with prohibitin and a prohibitin-related protein, EMBO J. 13 (1994) 3782–3792.
[12] K. Rajalingam, C. Wunder, V. Brinkmann, Y. Churin, M. Hekman, C. Sievers, et al., Prohibitin is required for Ras-induced Raf-MEK-ERK activation and epithelial cell migration, Nat. Cell Biol. 7 (2005) 837–843.
[13] J.A. Ross, Z.S. Nagy, R.A. Kirken, The PHB1/2 phosphocomplex is required for mitochondrial homeostasis and survival of human T cells, J. Biol. Chem. 283 (2008) 4699–4713.
[14] B. He, Q. Feng, A. Mukherjee, D.M. Lonard, F.J. DeMayo, B.S. Katzenellenbogen, et al., A repressive role for prohibitin in estrogen signaling, Mol. Endocrinol. 22 (2008) 344–360.
[15] S.-Eun Park, J. Xu, A. Frolova, L. Liao, B.W. O'Malley, B.S. Katzenellenbogen, Genetic deletion of the repressor of estrogen receptor activity (REA) enhances the response to estrogen in target tissues in vivo, Mol. Cell. Biol. 25 (2005) 1989–1999.
[16] A. Sharma, A. Qadri, Vi polysaccharide of Salmonella typhi targets the prohibitin family of molecules in intestinal epithelial cells and suppresses early inflammatory responses, Proc. Natl. Acad. Sci. USA 101 (2004) 17492–17497.
[17] M.G. Kolonin, P.K. Saha, L. Chan, R. Pasqualini, W. Arap, Reversal of obesity by targeted ablation of adipose tissue, Nat. Med. 10 (2004) 625–632.
[18] Y. Latchman, C.R. Wood, T. Chernova, D. Chaudhary, M. Borde, I. Chernova, et al., PD-L2 is a second ligand for PD-1 and inhibits T cell activation, Nat. Immunol. 2 (2001) 261–268.
[19] P. Waterhouse, J.M. Penninger, E. Timms, A. Wakeham, A. Shahinian, K.P. Lee, et al., Lymphoproliferative disorders with early lethality in mice deficient in Ctla-4, Science 270 (1995) 985–988.
[20] C. Nakaseko, S. Miyatake, T. Iida, S. Hara, R. Abe, H. Ohno, et al., Cytotoxic T lymphocyte antigen 4 (CTLA-4) engagement delivers an inhibitory signal through the membrane-proximal region in the absence of the tyrosine motif in the cytoplasmic tail, J. Exp. Med. 190 (1999) 765–774.

[21] Y. Agata, A. Kawasaki, H. Nishimura, Y. Ishida, T. Tsubata, H. Yagita, et al., Expression of the PD-1 antigen on the surface of stimulated mouse T and B lymphocytes, Int. Immunol. 8 (1996) 765–772.
[22] Y. Ishida, Y. Agata, K. Shibahara, T. Honjo, Induced expression of PD-1, a novel member of the immunoglobulin gene superfamily, upon programed cell death, EMBO J. 11 (1992) 3887–3895.
[23] D.R. Leach, M.F. Krummel, J.P. Allison, Enhancement of antitumor immunity by CTLA-4 blockade, Science 271 (1996) 1734–1736.
[24] J.M. Kremer, R. Westhovens, M. Leon, E. Di Giorgio, R. Alten, S. Steinfeld, et al., Treatment of rheumatoid arthritis by selective inhibition of T-cell activation with fusion protein CTLA4Ig, N. Engl. J. Med. 349 (2003) 1907–1915.

Biochemical and Biophysical Research Communications 420 (2012) 281–287

Contents lists available at SciVerse ScienceDirect

Biochemical and Biophysical Research Communications

journal homepage: www.elsevier.com/locate/ybbrc

BMP signaling is responsible for serum-induced Id2 expression

Hisanori Kurooka [a,c,*], Takeshi Nakahiro [a,b], Kentaro Mori [a], Kazuo Sano [b], Yoshifumi Yokota [a,c,*]

[a] Division of Molecular Genetics, Department of Biochemistry and Bioinformative Sciences, School of Medicine, Faculty of Medical Sciences, University of Fukui, Fukui, Japan
[b] Division of Dentistry and Oral Surgery, Department of Sensory and Locomotor Medicine, School of Medicine, Faculty of Medical Sciences, University of Fukui, Fukui, Japan
[c] Research and Education Program for Life Science, University of Fukui, Fukui, Japan

ARTICLE INFO

Article history:
Received 27 February 2012
Available online 6 March 2012

Keywords:
Serum
Id2
Dorsomorphin
BMP signaling
Smad

ABSTRACT

Ids function as negative regulators of basic helix–loop–helix transcription factors and their expression is rapidly induced by serum stimulation in various cell types. In this study, we investigated the molecular basis of serum-induced expression of the mouse *Id2* gene in NIH3T3 cells. A small-molecule inhibitor of bone morphogenetic protein (BMP) type I receptor kinases blocked the serum induction of *Id2* mRNA. The chemical compound and several inhibitory proteins specific for BMP signaling suppressed the serum-induced activation of the luciferase construct with the mouse *Id2* 4.6-kb promoter region. Importantly, serum stimulation evoked rapid phosphorylation of Smad1/5/8 and significant activation of the reporter plasmid containing the recently identified BMP-responsive element (BRE) of the mouse *Id2*. Mutation analysis demonstrated that the binding sites for Smad proteins in the *Id2* BRE were critical for serum response of the 4.6-kb whole construct. Gel shift and chromatin immunoprecipitation (ChIP) assays confirmed the serum-inducible binding of Smad1/5/8 and Smad4 to the *Id2* BRE *in vitro* and *in vivo*. Finally, a knockdown experiment revealed the functional importance of Smad1 in the serum induction of *Id2* expression. Thus, we concluded that BMP signaling is primarily responsible for the serum-induced *Id2* expression. Our results also suggest that some of the cellular effects caused by serum are mediated through BMP signaling.

1. Introduction

Id proteins are negative regulators of basic helix–loop–helix transcription factors that control cell fate determination. Four members of the Id family, Id1 to Id4, have been identified in mammals. Extensive analyses of knock-out mice have demonstrated that Ids play essential roles in various processes including neurogenesis, angiogenesis, and immune cell development [1].

The expression of the *Id* genes is up-regulated in response to diverse stimuli [1]. Above all, it is rapidly induced by stimulation with serum [2–5]. While serum stimulates cell proliferation, it maintains stem or progenitor cells in undifferentiated states. Deprivation of serum from culture medium induces differentiation of embryonic stem cells into neural precursors [5] and of myoblasts into myotubes [2]. These effects are tightly associated with down-regulation of the *Id* genes, suggesting that Ids function as key molecules to prevent differentiation in these cells. Although serum exerts the cellular effects through multiple signaling pathways, it remains unclear which pathway is responsible for the serum-induced *Id* gene expression.

Another representative stimulus that can induce *Id* gene expression is bone morphogenetic protein (BMP), which displays pleiotropic activities in cell differentiation, pluripotency, and tissue morphogenesis [6]. BMP signaling is initiated by binding of the ligands to their transmembrane type I and type II receptors [6]. Both types of receptors encode serine/threonine kinases and the activated type I receptor phosphorylates the receptor-regulated (R) Smads, Smad1, Smad5, and Smad8, in the cytoplasm. The phosphorylated R-Smads form complexes with the common-partner (Co) Smad, Smad4, and then move into the nucleus, where the complexes bind to the regulatory regions of the downstream target genes [6]. Recently, we have identified the BMP-responsive element (BRE) in the promoter region of the mouse *Id2* gene [7]. Similar BREs are present in those of *Id1* [8] and *Id3* [9].

Here we provide evidence that BMP signaling is a primary pathway responsible for serum-induced expression of the *Id2* gene. We show that inhibition of BMP signaling leads to a significant decrease in the serum induction of *Id2* expression and demonstrate

Abbreviations: BMP, bone morphogenetic protein; BRE, BMP-responsive element; ChIP, chromatin immunoprecipitation; R-Smad, receptor-regulated Smad; Co-Smad, common-partner Smad; FBS, fetal bovine serum; TGF-β, transforming growth factor-β; dn, dominant negative.

* Corresponding authors. Address: Division of Molecular Genetics, Department of Biochemistry and Bioinformative Sciences, School of Medicine, Faculty of Medical Sciences, University of Fukui, 23-3 Matsuoka-Shimoaizuki, Eiheiji, 910-1193 Fukui, Japan. Fax: +81 776 61 8164.

E-mail addresses: hkurooka@u-fukui.ac.jp (H. Kurooka), yokota@u-fukui.ac.jp (Y. Yokota).

0006-291X/$ - see front matter © 2012 Elsevier Inc. All rights reserved.
doi:10.1016/j.bbrc.2012.02.150

that Smad proteins play a pivotal role. Our results suggest that some of the cellular effects caused by serum are mediated through BMP signaling.

2. Materials and methods

2.1. Cell culture, drugs, and antibodies

Mouse fibroblast NIH3T3 cells were cultured in Dulbecco's modified Eagle's medium (DMEM; Wako, Tokyo, Japan) containing 10% fetal bovine serum (FBS; Thermo Scientific HyClone, Logan, UT). For serum stimulation, cells were starved by culture in DMEM containing 0.2% FBS for 24 h and the medium was then replaced with DMEM containing 10% FBS. PD98059 and SB203580 were purchased from Calbiochem (San Diego, CA). SP600125, LY294002, dorsomorphin, SB431542, puromycin, and normal rabbit IgG were from Sigma–Aldrich (St. Louis, MO). Antibodies against phosphorylated Smad1/5/8 (#9511; Cell Signaling, Beverly, MA), Smad1/5/8 (N-18), Smad4 (B-8), NF-YA (H-209) (Santa Cruz Biotechnology, Santa Cruz, CA), NF-YB (Diagnode, Liège, Belgium), and Smad1 (Zymed, South San Francisco, CA) were used.

2.2. Western blot analysis

Western blot analysis was basically carried out as described previously [10]. Forty micrograms of total protein was resolved by 10% SDS–PAGE, transferred onto a nitrocellulose filter, and immunoblotted with various antibodies.

2.3. RNA isolation, Northern blot analysis, and RT-PCR

Total RNA was extracted using an RNeasy kit (Qiagen, Valencia, CA). For Northern blot analysis, 5 μg of RNA was separated by electrophoresis on a 1.2% agarose-formaldehyde gel and transferred onto a nylon membrane using standard protocols. The membrane was hybridized with [α-^{32}P]dCTP-labeled DNA probes for mouse *Id2* and *Gapdh* [7]. For semiquantitative RT-PCR analysis, reverse transcription and PCR were executed as described previously [11], with slight modification. Cycle conditions were as follows: 30 or 35 cycles at 94 °C for 30 s, 58 °C for 30 s, 72 °C for 1 min. The primers used for PCR are listed in Supplementary Table 1.

2.4. Plasmids

All the firefly luciferase plasmids were constructed using pGL4.12 (Promega, Madison, WI). pGL4.12-Id2/4.6-kb was as previously reported [12] and pGL4.12-Id2/BRE was derived from pGL3-Id2/BRE [7]. Mutations of the BRE were introduced into pGL4.12-Id2/4.6-kb by site-directed mutagenesis. As an internal control, phRL-TK (Promega) was used. The coding regions of mouse ALK1, ALK2, ALK3, and ALK5 were amplified by RT-PCR. Their dominant-negative forms, ALK1(K228R), ALK2(K235R), ALK3(K261R), and ALK5(K232R), were generated by substituting arginine for the critical lysine in the kinase domains and then subcloned into pFLAG-CMV-14 (Sigma). pcDNA3-FLAG-mouse Smad6 was kindly provided by Dr. K. Tsuchida (Fujita Health University). To silence the mouse Smad1 expression, the target sequence was chosen as follows: 5′-GGATGGACAAGTCAGACAG-3′ [13]. The annealed oligonucleotides were inserted into pSUPER-puro (Oligoengine, Madison, WI) to create pSUPER-mSmad1.

2.5. Luciferase assay

NIH3T3 cells were transfected with plasmids using FuGENE 6 reagent (Roche Diagnostics, Tokyo, Japan) according to the manufacturer's instructions. After 24 h, the cells were serum-starved by culture in DMEM containing 0.2% FBS for a further 24 h. The medium was then replaced with fresh DMEM containing 10% FBS and the cells were incubated for an additional 8 h. Luciferase assays were performed using the Dual-Glo Luciferase Assay System (Promega), as previously described [10]. The firefly luciferase activity was measured and normalized to the renilla luciferase activity conferred by phRL-TK.

2.6. Electrophoretic mobility shift assay (EMSA)

EMSA was carried out as described previously [7]. Ten micrograms of nuclear extract incubated with [γ-^{32}P]dATP-labeled oligonucleotides was electrophoresed on a 5% polyacrylamide gel. For the supershift experiment, 2 μg of anti-Smad1/5/8 or 0.5 μg of anti-Smad4 antibody was added to the reaction.

2.7. Chromatin immunoprecipitation (ChIP) assay

ChIP assay was conducted as described previously [7,12]. In brief, cells were cross-linked with 1% formaldehyde in medium for 10 min at room temperature, followed by quenching with 125 mM glycine for 5 min. Two and half micrograms of each antibody was used for immunoprecipitation. The samples were resuspended in 100 μl of TE for input DNA and 20 μl of TE for ChIP DNA, and analyzed by PCR using the following primer pairs: BRE, 5′-CTTGCAGGCATTGATCAGCTG-3′ (−2903) and 5′-TTTTGTTCTCAC AGCTGTGTCCATT-3′ (−2630); proximal promoter, 5′-ACACTGTACT CAATTTGCCACCC-3′ (−226) and 5′-GCTGCTCGTAGGAGGAGAG ACC-3′ (+76).

2.8. RNA interference

NIH3T3 cells were transfected with pSUPER-mSmad1 or the control vector using FuGENE HD reagent (Roche). Two days after transfection, the cells were subjected to puromycin (2 μg/ml) selection for 10 days. Drug-resistant clones were then isolated and the positive clones were selected by immunoblotting with anti-Smad1 antibody.

3. Results

3.1. Dorsomorphin suppresses serum-induced expression of the mouse Id2 gene

It has been reported that expression of the human and mouse *Id2* genes is rapidly induced by serum stimulation in various cell types [2,4,12]. However, it remains to be determined which intracellular signaling pathway is responsible for serum-induced *Id2* gene expression. To address this issue, we treated serum-stimulated NIH3T3 cells with several kinase inhibitors: PD98059 for MEK, SB203580 for p38 MAPK, SP600125 for JNK, LY294002 for PI3K, dorsomorphin for the BMP type I receptors, and SB431542 for the transforming growth factor-β (TGF-β) type I receptors. Northern blot analysis showed that dorsomorphin completely blocked the induction of *Id2* mRNA, whereas the other inhibitors did not reduce it (Fig. 1A). We also examined the effect of dorsomorphin on the serum-induced *Id2* expression using the luciferase construct with the mouse *Id2* 4.6-kb promoter region (see Fig. 3A). The reporter plasmid exhibited a marked response to serum (about 16-fold increase) and the response was suppressed by dorsomorphin in a dose-dependent manner (Fig. 1B). These observations suggest that BMP signaling is involved in the serum induction of *Id2* expression.

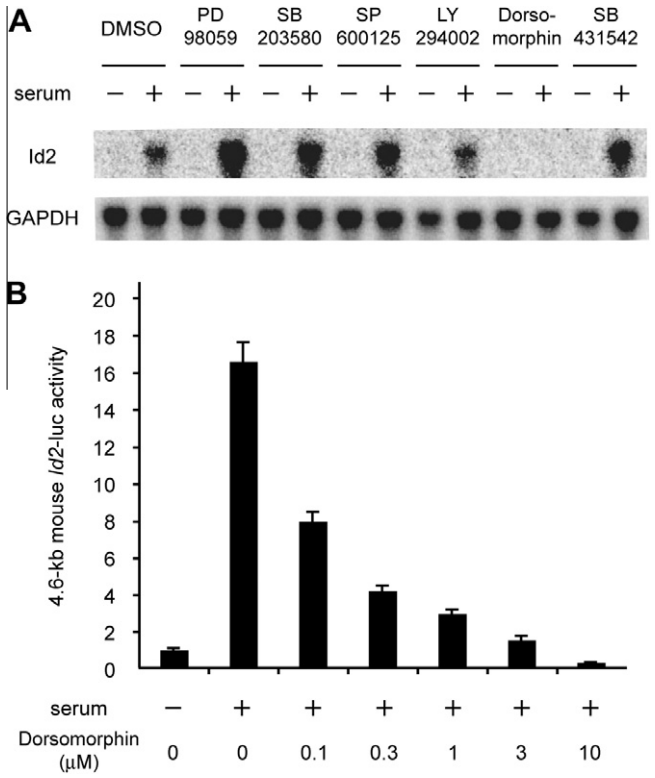

Fig. 1. Dorsomorphin suppresses serum-induced expression of the mouse *Id2* gene. (A) Serum-starved NIH3T3 cells were pre-treated for 30 min with 50 μM PD98059, 10 μM SB203580, 20 μM SP600125, 10 μM LY294002, 10 μM dorsomorphin, 5 μM SB431542, or 0.1% DMSO. The cells were stimulated with serum for 2 h in the presence of each inhibitor. *Id2* expression was examined by Northern blot analysis. (B) NIH3T3 cells were transfected with pGL4.12-mouse *Id2*/4.6-kb, serum-starved for 24 h, and stimulated with serum for 8 h in the presence (0.1–10 μM) or absence of dorsomorphin. The error bars indicate the standard error of the mean.

3.2. Serum-induced Id2 expression is suppressed by inhibition of BMP signaling

From the above observations, it is assumed that BMP signaling is activated by stimulation with serum. We then assessed phosphorylation of the BMP R-Smads, Smad1/5/8, in NIH3T3 cells. Substantial phosphorylation of Smad1/5/8 proteins was detected at 30 min–1 h after serum stimulation (Fig. 2A). The level of phosphorylation declined at 2 h and was sustained until 4 h after the stimulation.

Although dorsomorphin is utilized as a potent inhibitor of the BMP type I receptors, it can inhibit some other kinases with comparable potency [14]. To avoid cross-inhibition, we tried to interfere with BMP signaling in other ways. We first examined the expression of four BMP-activated type I receptors (ALK1, ALK2, ALK3, and ALK6) and one TGF-β-activated type I receptor (ALK5). RT-PCR analysis showed that ALK2 and ALK5 were highly, and ALK3 was modestly expressed in the mouse fibroblasts (Fig. 2B). It was also found that expression levels of ALK1 were low and those of ALK6 were negligible. These findings prompted us to test the ability of dominant-negative (dn) forms of the expressed receptors to suppress the serum response of the *Id2* reporter. The response was considerably suppressed by dn-ALK1 and dn-ALK2, and only slightly by dn-ALK3, all of which are dominant-negative forms of the BMP type I receptors (Fig. 2C). In contrast, it was not affected by dn-ALK5, a dominant-negative form of the TGF-β type I receptor. Moreover, we examined the effect of Smad6, the inhibitory Smad protein specific for BMP signaling [6]. Forced expression of Smad6 resulted in repression of the serum-induced promoter activity (Fig. 2D). Taken together, these results suggest that BMP signaling pathway, possibly *via* ALK1 and/or ALK2, is responsible for the serum-induced *Id2* expression.

3.3. Smads binding sites are required for serum-induced activation of the Id2 BRE

Besides its serum response, *Id2* is immediately induced by BMP stimulation [6,7,15]. Since the BMP-responsive element (BRE) was recently identified in mouse *Id2* [7], we investigated whether it could be potentiated by serum stimulation. Importantly, the reporter containing the *Id2* BRE exhibited a significant response to serum, although its activity was half as much as the 4.6-kb construct (Fig. 3A). Serum-induced activation of the *Id2* BRE was also observed in myoblast (C2C12) and epithelial (A549, HeLa, and HepG2) cells (data not shown).

As shown in Fig. 3B, the *Id2* BRE is homologous to the *Id1* BRE [8] and contains the two conserved bipartite sequences (GGCGCC-N_5-GNCN) consisting of the binding sites for Smad1/5/8 (GGCGCC-1 or GGCGCC-2) and for Smad4 (CGCC in the reverse orientation of GGCG, or GTCT) [6]. We demonstrated previously that both of the sequences are necessary for BMP response of the *Id2* BRE in C2C12 cells [7]. Since our data clearly showed that serum stimulation activated the BMP signaling and the *Id2* BRE, Smad proteins are likely to be important for the serum induction of *Id2* expression. On the other hand, the transcription factor RFX1 was reported to be involved in serum-induced expression of the mouse *Id2* gene [12]. Interestingly, RFX1 binds to the sequence adjacent to the CGCC site within the upstream bipartite sequence (Fig. 3B). To compare the contribution of the transcription factors to the serum response, their binding sites were mutated in the context of the 4.6-kb construct. When the RFX1 site was mutated, the serum induction was decreased by approximately 25% compared with that of the wild-type construct (Fig. 3C). The induction was diminished by nearly 60% when the CGCC and GGCGCC-1 sites were mutated. Mutation of the other palindrome, GGCGCC-2, resulted in about 80% reduction and the induction almost disappeared as a result of simultaneous mutation of the two palindromes. These results suggest that Smads play a central role in serum-induced *Id2* expression.

3.4. Serum-inducible binding of Smads to the Id2 BRE and a critical role of Smad1 in serum-induced Id2 expression

Subsequently, we analyzed the serum-inducible binding of Smads to the *Id2* BRE. To this end, EMSA was performed using two oligonucleotide probes (probes A and B) that contain the distinct bipartite sequences (Fig. 3B). As shown in Fig. 4A, formation of DNA–protein complexes was enhanced by serum stimulation with both probes. The serum-induced DNA–protein complexes were supershifted by specific antibody against Smad1/5/8 or Smad4 for each probe, indicating that the Smad proteins bind to the two fragments in a serum-dependent manner. We next examined their *in vivo* DNA binding by ChIP assay. Phosphorylated Smad1/5/8 appeared around the *Id2* BRE only when cells had been stimulated with serum (Fig. 4B). The binding of Smad4 was increased by serum, although it was detected even in the absence of serum. Around the proximal promoter region, no binding of Smads was observed in the presence or absence of serum. The two subunits of the NF-Y trimer complex, NF-YA and NF-YB [16], bound to the proximal promoter, ensuring that this locus is accessible. Their binding was not altered by serum, in agreement with a previous report describing the constant binding of NF-YA to the same region before and after treatment with retinoic acid [17].

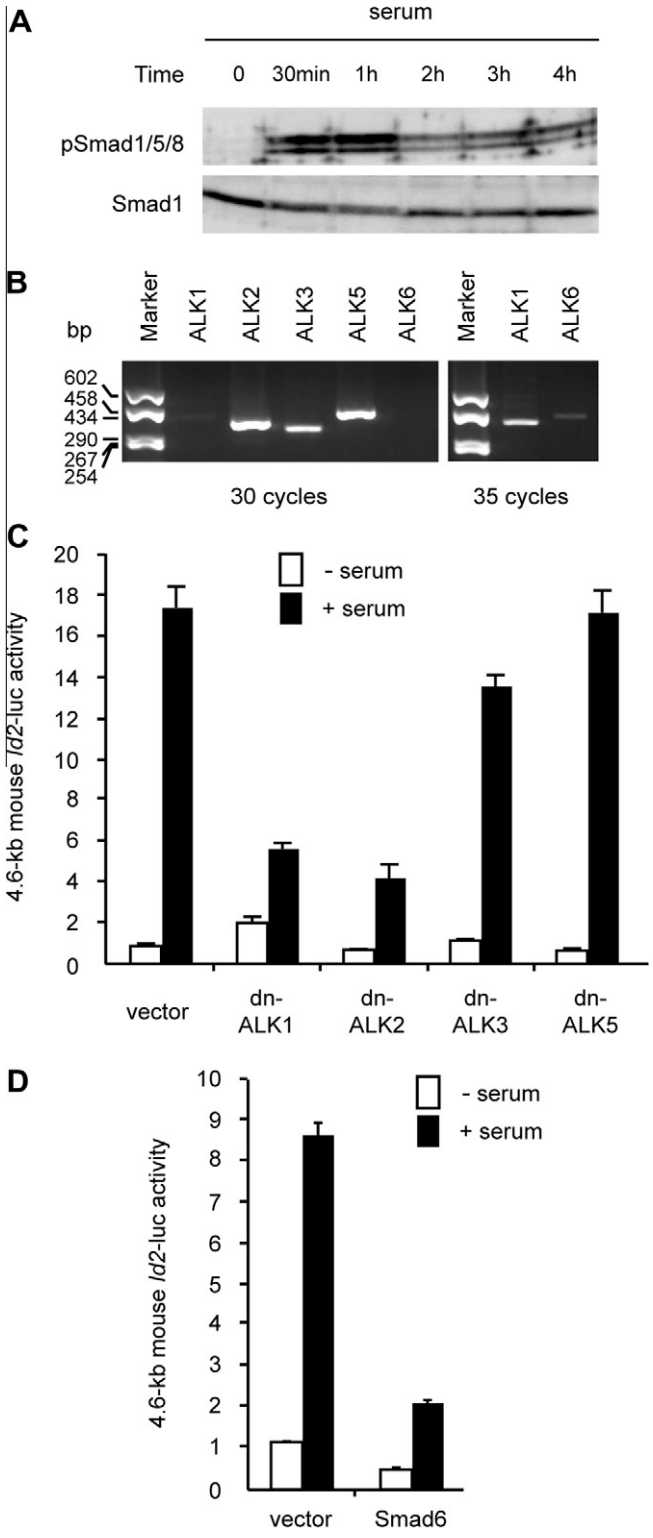

Fig. 2. Inhibition of BMP signaling suppresses serum-induced *Id2* expression. (A) NIH3T3 cells were harvested at 0 min (control), 30 min, 1 h, 2 h, 3 h, and 4 h after serum stimulation. The cell lysates were subjected to immunoblotting with anti-phospho-Smad1/5/8 or anti-Smad4 antibody. (B) Expression of the BMP and TGF-β type I receptors was examined by RT-PCR. Sizes of the molecular weight markers are depicted in the left margin. Cycle numbers for PCR are also indicated. (C) NIH3T3 cells were co-transfected with pGL4.12-*Id2*/4.6-kb and the dominant-negative ALK expression plasmids or the empty vector. The cells were serum-starved for 24 h and then treated with or without serum for 8 h. (D) NIH3T3 cells were co-transfected with pGL4.12-*Id2*/4.6-kb and the wild-type Smad6 expression plasmid or the empty vector. The cells were serum-starved for 24 h and then treated with or without serum for 8 h. The error bars indicate the standard error of the mean.

These data demonstrate that Smad1/5/8 and Smad4 selectively bind to the *Id2* BRE in a serum-dependent manner.

To confirm the involvement of Smads in the serum induction of *Id2* expression, we established cell lines in which *Smad1* was

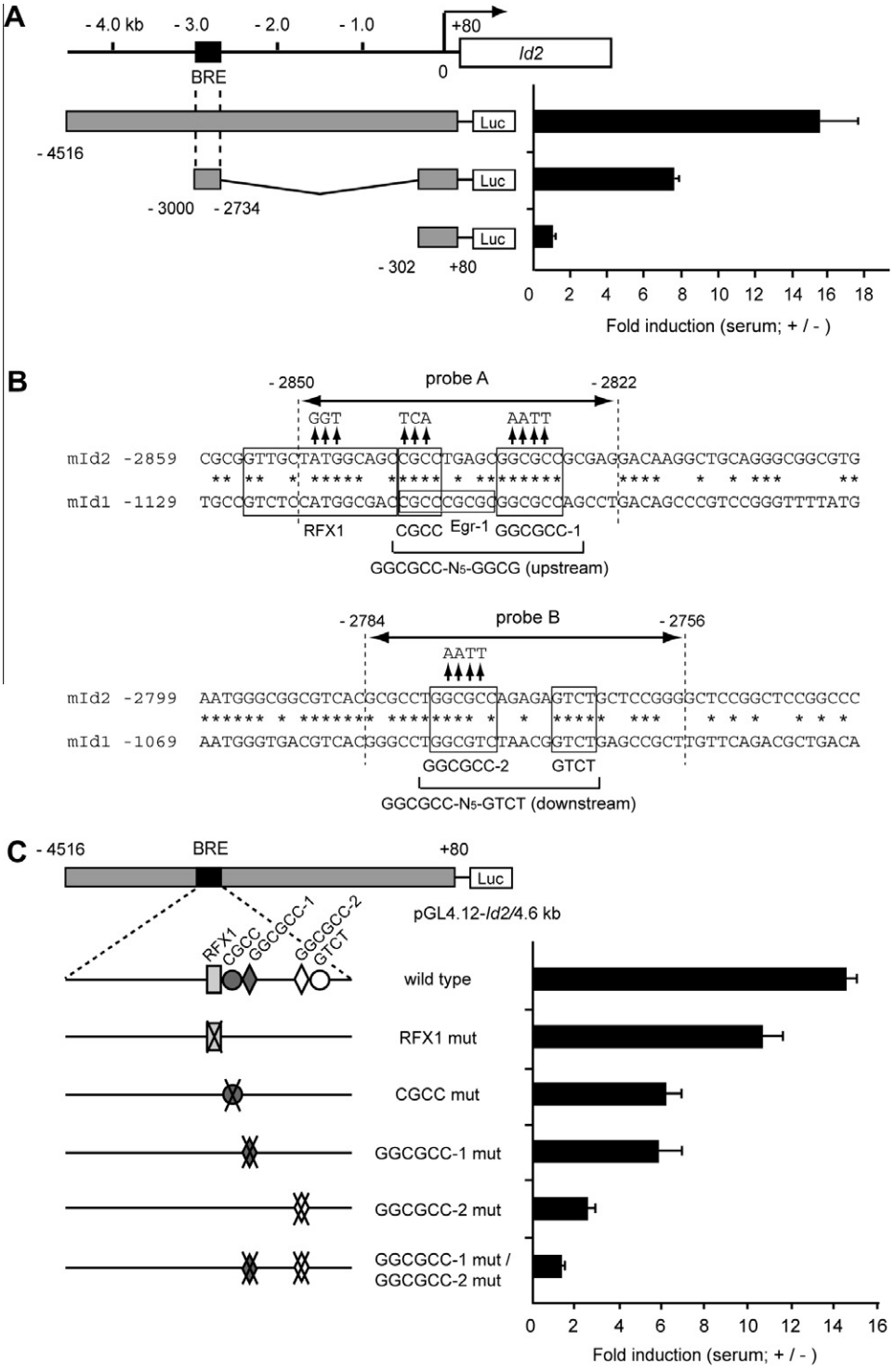

Fig. 3. Analysis of the *Id2* BMP-responsive element (BRE) in serum response. (A) The structures of the 4.6-kb upstream region of the mouse *Id2* promoter and the 267-bp BRE are illustrated at the top. Luciferase reporter constructs are drawn on the left. The positions are numbered from the transcription start site. The right graph represents fold-induction values of the luciferase activity in the presence of serum compared with those in its absence. The error bars indicate the standard error of the mean. (B) Sequence alignment of the mouse *Id2* BRE with the mouse *Id1* BRE. Asterisks indicate identical nucleotides between *Id1* and *Id2*. The binding sites for Smad1/5/8 (GGCGCC-1 and GGCGCC-2), Smad4 (CGCC and GTCT), RFX1, and Egr-1 are boxed. Substituted amino acids in mutation analysis are shown by vertical arrows. The left-and-right arrows indicate the positions corresponding to probes A and B used in EMSA (Fig. 4A). It should be noted that the two probes harbor the bipartite sequences (upstream, GGCGCC-N_5-GGCG; downstream, GGCGCC-N_5-GTCT) important for binding of the BMP R-Smad/Co-Smad complexes. (C) Luciferase assays were performed with reporter plasmids bearing mutations of the binding sites for RFX1 and Smads in the *Id2* BRE. The constructs are schematically presented on the left and the crosses indicate the mutated sites. The serum-induced luciferase activity is shown as fold induction.

constitutively suppressed by shRNA. Western blot analysis showed that expression levels of Smad1 in the two knockdown clones were both reduced about 4-fold compared with those in the control clones (Fig. 4C). The serum responses of the *Id2* BRE reporter in

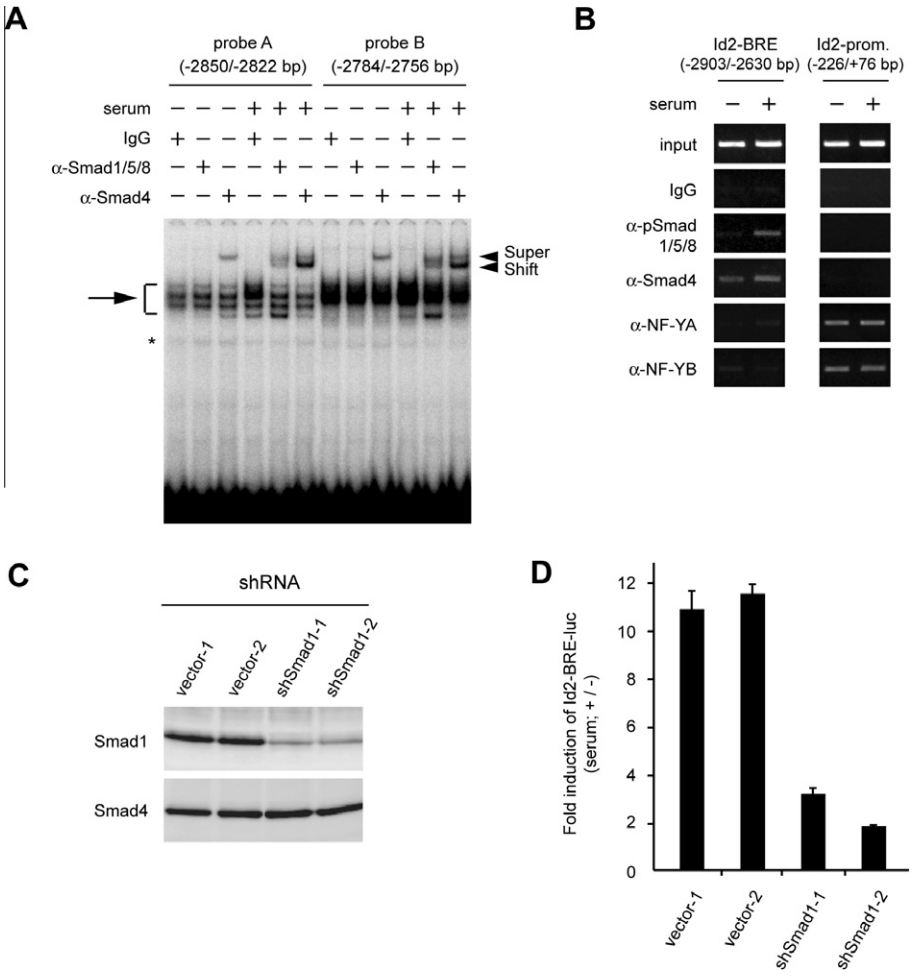

Fig. 4. Roles of Smads in serum-induced *Id2* expression. (A) EMSA was carried out using nuclear extracts prepared from NIH3T3 cells treated with or without serum for 1 h. Probes A and B correspond to the regions shown in Fig. 3B. The arrow and asterisk indicate the DNA–protein complexes and non-specific binding, respectively. Anti-Smad1/5/8 or anti-Smad4 antibody was employed in supershift experiment. IgG served as a negative control. Arrowheads indicate the supershifted complexes. (B). ChIP assays were conducted using the chromatins prepared from NIH3T3 cells treated with or without serum for 1 h. The antibodies used in immunoprecipitation are indicated on the left. IgG served as a negative control. The regions spanning from −2903 to −2630 and from −226 to +76 were amplified by PCR with the primer sets described in Section 2. (C) NIH3T3 cells were transfected with pSUPER-mSmad1 or the control vector and subsequently the puromycin-resistant clones were isolated. Two control clones (vector-1 and vector-2) and two knockdown clones (shSmad1–1 and shSmad1–2) were analyzed by immunoblotting with anti-Smad1 or anti-Smad4 antibody. (D) The control and Smad1 knockdown clones were transfected with pGL4.12-Id2/BRE, serum-starved for 24 h, and then treated with or without serum for 8 h. The serum-induced luciferase activity is shown as fold induction. The error bars indicate the standard error of the mean.

the knockdown cell lines were consistently smaller than those in the control ones (Fig. 4D). This indicates that Smad1 is critical for serum-induced expression of the *Id2* gene.

4. Discussion

In this study, we investigated the signaling pathways implicated in serum-induced *Id2* expression. Although MEK/ERK pathway is responsible for serum induction of the immediate early genes such as c-Fos and Egr-1 [18], it does not seem to regulate the *Id2* induction positively. The MEK inhibitor PD98059 did not inhibit, but rather augmented the serum induction of *Id2* mRNA (Fig. 1A), consistent with the observation that inhibition of MEK/ERK led to activation of BMP signaling [19]. We also explored the involvement of TGF-β signaling since it generally suppresses, but sometimes induces, the *Id* gene expression [1,11,20]. However, the serum induction of *Id2* was not impaired by either the chemical inhibitor or the dominant-negative form of the type I receptor for TGF-β signaling. In contrast, it was effectively suppressed by dorsomorphin (Fig. 1) and by the several inhibitory proteins specific for BMP signaling (Fig. 2). These results strongly suggest that BMP signaling is activated by serum and is responsible for serum-induced *Id2* expression.

Our data indicated that Smad1/5/8 was rapidly phosphorylated by serum stimulation in the mouse fibroblasts, NIH3T3 cells (Fig. 2A). Likewise, serum-induced phosphorylation of the BMP R-Smads has been reported in endothelial, mesenchymal, and epithelial cells [21,22]. In addition, accumulating evidence has revealed that serum contains a small but significant amount of BMPs, particularly BMP4, BMP6, and BMP9 [22–24]. Therefore, it is conceivable that some of the cellular effects caused by serum are mediated through BMP signaling. This notion is supported by recent studies showing that inhibition of BMP signaling with dorsomorphin or the BMP antagonist noggin promoted myogenic differentiation of muscle satellite cells [25,26].

As well as the phosphorylation of the BMP R-Smads, the serum-induced activation of the *Id2* BRE is not cell type-specific. This implies that the serum-induced *Id2* expression is under the control of the canonical BMP signaling pathway. In fact, we showed that the Smads binding sites were indispensable for serum response of the *Id2* 4.6-kb reporter construct (Fig. 3C). Furthermore, we demonstrated that Smad1/5/8 and Smad4 bound to the *Id2* BRE in a

serum-dependent manner and that Smad1 was critical for the serum induction of *Id2* (Fig. 4). Nevertheless, we cannot exclude the possibility that other transcription factors play some roles. In this regard, we reevaluated the contribution of RFX1 and found that it was less important than we had expected. As opposed to Smads, the binding of RFX1 is serum-independent [12] and its role in the serum induction may be auxiliary. On the other hand, serum-induced expression of the mouse *Id1* gene was regulated by Egr-1 [3], whose binding site overlaps with the upstream bipartite sequence of the *Id1* BRE (Fig. 3B). However, its involvement in *Id2* induction seems unlikely because the *Id2* BRE has no consensus sequence for *Egr-1* (CGCCC(C/G/T)CGC).

In conclusion, we have demonstrated that serum-induced expression of the *Id2* gene is primarily mediated though BMP signaling. Since some of the immediate early genes including the other *Ids* and *JunB* also respond to both serum and BMP [4,5,15,23], it is interesting to see if their serum-induced expression is similarly mediated through BMP signaling.

Acknowledgments

We are grateful to Y. Matsui for technical assistance. We also thank K. Tsuchida for the Smad6 expression plasmid. This work was supported by Grants-in-Aid for Scientific Research from the Japan Society for the Promotion of Science (H.K.: #20570128, Y.Y.: #21390092).

Appendix A. Supplementary data

Supplementary data associated with this article can be found, in the online version, at doi:10.1016/j.bbrc.2012.02.150.

References

[1] J. Perk, A. Iavarone, R. Benezra, Id family of helix–loop–helix proteins in cancer, Nat. Rev. Cancer 5 (2005) 603–614.
[2] M. Kurabayashi, S. Dutta, L. Kedes, Serum-inducible factors binding to an activating transcription factor motif regulate transcription of the Id2A promoter during myogenic differentiation, J. Biol. Chem. 269 (1994) 31162–31170.
[3] O. Tournay, R. Benezra, Transcription of the dominant-negative helix-loop-helix protein Id1 is regulated by a protein complex containing the immediate-early respomse gene Egr-1, Mol. Cell. Biol. 16 (1996) 2418–2430.
[4] V.R. Iyer, M.B. Eisen, D.T. Ross, G. Schuler, T. Moore, J.C.F. Lee, J.M. Trent, L.M. Staudt, J. Hudson Jr., M.S. Boguski, D. Lashkari, D. Shalon, D. Botstein, P.O. Brown, The transcriptional program in the response of human fibroblasts to serum, Science 283 (1999) 83–87.
[5] Q.L. Ying, J. Nichols, I. Chambers, A. Smith, BMP induction of Id proteins suppresses differentiation and sustains embryonic stem cell self-renewal in collaboration with STAT3, Cell 115 (2003) 281–292.
[6] K. Miyazono, Y. Kamiya, M. Morikawa, Bone morphogenetic protein receptors and signal transduction, J. Biochem. 147 (2010) 35–51.
[7] T. Nakahiro, H. Kurooka, K. Mori, K. Sano, Y. Yokota, Identification of BMP-responsive elements in the mouse Id2 gene, Biochem. Biophys. Res. Commun. 399 (2010) 416–421.
[8] O. Korchynskyi, P. ten Dijke, Identification and functional characterization of distinct critically important bone morphogenetic protein-specific response elements in the Id1 promoter, J. Biol. Chem. 277 (2002) 4883–4891.
[9] T.G. Shepherd, B.L. Thériault, M.W. Nachtigal, Autocrine BMP4 signaling regulates ID3 proto-oncogene expression in human ovarian cancer cells, Gene 414 (2008) 95–105.
[10] H. Kurooka, Y. Yokota, Nucleo-cytoplasmic shuttling of Id2, a negative regulator of basic helix–loop–helix transcription factors, J. Biol. Chem. 280 (2005) 4313–4320.
[11] O. Scherner, S.K. Meurer, L. Tihaa, A.M. Gressner, R. Weiskirchen, Endoglin differentially modulates antagonistic transforming growth factor-β1 and BMP-7 signaling, J. Biol. Chem. 282 (2007) 13934–13943.
[12] K.R. Wang, T. Nemoto, Y. Yokota, RFX1 mediates the serum-induced immediate early response of Id2 gene expression, J. Biol. Chem. 282 (2007) 26167–26177.
[13] J.A. Freudenberg, W.T. Chen, Induction of Smad1 by MT1-MMP contributes to tumor growth, Int. J. Cancer 121 (2007) 966–977.
[14] J. Vogt, R. Traynor, G.P. Sapkota, The specificities of small molecule inhibitors of the TGFβ and BMP pathways, Cell Signal. 23 (2011) 1831–1842.
[15] A. Hollnagel, V. Oehlmann, J. Heymer, U. Rüther, A. Nordheim, Id genes are direct targets of bone morphogenetic protein induction in embryonic stem cells, J. Biol. Chem. 274 (1999) 19838–19845.
[16] R. Mantovani, The molecular biology of the CCAAT-binding factor NF-Y, Gene 239 (1999) 15–27.
[17] S. van Wageningen, M.C. Breems-de Ridder, J. Nigten, G. Nikoloski, C.A.J. Erpelinck-Verschueren, B. Löwenberg, T. de Witte, D.G. Tenen, B.A. van der Reijden, J.H. Jansen, Gene transactivation without direct DNA binding defines a novel gain-of-function for PML-RARα, Blood 111 (2008) 1634–1643.
[18] L.O. Murphy, J. Blenis, MAPK signal specificity: the right place at the right time, Trends Biochem. Sci. 31 (2006) 268–275.
[19] J. Yang, R.J. Davies, M. Southwood, L. Long, X. Yang, A. Sobolewski, P.D. Upton, R.C. Trembath, N.W. Morrel, Mutations in bone morphogenetic protein type II receptor cause dysregulation of Id gene expression in pulmonary artery smooth muscle cells, Circ. Res. 102 (2008) 1212–1221.
[20] M. Sugai, H. Gonda, T. Kusunoki, T. Katakai, Y. Yokota, A. Shimizu, Essential role of Id2 in negative regulation of IgE class switching, Nat. Immunol. 4 (2003) 25–30.
[21] I.R. Gupta, M. Macias-Sivia, S. Kim, X. Zhou, T.D. Piscione, C. Whiteside, J.L. Wrana, N.D. Rosenblum, BMP-2/ALK3 and HGF signal in parallel to regulate renal collecting duct morphogenesis, J. Cell Sci. 113 (2000) 269–278.
[22] L. David, C. Mallet, M. Keramidas, N. Lamandé, J.M. Gasc, S. Dupuis-Girod, H. Plauchu, J.J. Feige, S. Bailly, Bone morphogenetic protein-9 is a circulating vascular quiescence factor, Circ. Res. 102 (2008) 914–922.
[23] K. Kodaira, M. Imada, M. Goto, A. Tomoyasu, T. Fukuda, R. Kamijo, T. Suda, K. Higashio, T. Katagiri, Purification and identification of a BMP-like factor from bovine serum, Biochem. Biophys. Res. Commun. 345 (2006) 1224–1231.
[24] B. Herrera, G.J. Inman, A rapid and sensitive bioassay for the simultaneous measurement of multiple bone morphogenetic proteins. Identification and quantification of BMP4, BMP6 and BMP9 in bovine and human serum, BMC Cell Biol. 10 (2009) 20.
[25] Y. Ono, F. Calhabeu, J.E. Morgan, T. Katagiri, H. Amthor, P.S. Zammit, BMP signaling permits population expansion by preventing premature myogenic differentiation in muscle satellite cells, Cell Death Differ. 18 (2011) 222–234.
[26] M. Yanagisawa, A. Mukai, K. Shiomi, S.Y. Song, N. Hashimoto, Community effect triggers terminal differentiation of myogenic cells derived from muscle satellite cells by quenching Smad signaling, Exp. Cell Res. 317 (2011) 221–233.

Biochemical and Biophysical Research Communications 420 (2012) 288–292

Contents lists available at SciVerse ScienceDirect

Biochemical and Biophysical Research Communications

journal homepage: www.elsevier.com/locate/ybbrc

Smad7 sensitizes A549 lung cancer cells to cisplatin-induced apoptosis through heme oxygenase-1 inhibition

Woo-Kwang Jeon [a], Hey-Young Hong [a], Won-Chan Seo [a], Kyu-Hyoung Lim [b], Hui-Young Lee [b], Woo-Jin Kim [b], Seo-Young Song [b], Byung-Chul Kim [a,*]

[a] Department of Biochemistry, College of Natural Sciences, Kangwon National University, Chuncheon 200-701, Republic of Korea
[b] Department of Internal Medicine, Kangwon National University Hospital, School of Medicine, Kangwon National University, Chuncheon 200-701, Republic of Korea

ARTICLE INFO

Article history:
Received 26 February 2012
Available online 6 March 2012

Keywords:
Smad7
HO-1
Apoptosis
Akt
A549 cells

ABSTRACT

Smad7, an inhibitory Smad, acts as a key regulator forming autoinhibitory feedback loop in transforming growth factor-beta (TGF-β) signaling. However, a growing body of evidences suggests that Smad7 is capable of apoptotic function. In the present study, we have demonstrated a proapoptotic function of Smad7 as a negative regulator of survival protein heme oxygenase-1 (HO-1). The HO-1 protein level was elevated in cisplatin-resistant A549 human lung cancer cells and blockade of HO-1 activation sensitized the cells to apoptosis. Interestingly, overexpression of Smad7 decreased HO-1 gene expression and its enzymatic activity. Notably, Smad7 reduced Akt activity and infection with adenovirus expressing a constitutively active form of the Akt reversed the inhibitory effects of Smad7 to HO-1, indicating a negative action mechanism of Smad7 to Akt-HO-1-linked survival pathway. Consistently, Smad7 sensitized A549 cells to cisplatin-induced apoptosis and these effects were dependent on HO-1 and Akt inhibition. Based on these findings, we suggest that targeting Smad7 may be an efficient strategy for overcoming drug-resistance in cancer therapy.

1. Introduction

Heme oxygenase-1 (HO-1) is a microsomal enzyme, catalyzing the breakdown of heme into equimolar amounts of carbon monoxide (CO), biliverdin, and free iron using molecular oxygen and reducing equivalents from NADPH:cytochrome P450 reductase [1,2]. HO-1 contributes to the cellular homeostasis and defense reaction against oxidative injury through the antioxidant activities of biliverdin and its metabolite, bilirubin, as well as the cytoprotective action of CO. Therefore, the expression of HO-1 must be tightly controlled in normal cells. A growing body of evidences indicates, however, that HO-1 is elevated in a variety of human cancers, including breast, liver, lung, pancreas, and prostate cancers [3–6]. Indeed, HO-1 activation may play a role in carcinogenesis and can potently influence the growth and metastasis of tumors.

Smad7 is an inhibitory Smad, which forms autoinhibitory feedback loop in transforming growth factor-beta (TGF-β) signaling [7]. However, growing body of evidences indicate that Smad7 may be involved in another signaling pathway [8,9] and have another cellular functions [10–12]. For example, Smad7 increases sensitization of cells to apoptosis through nuclear factor-kappa B inhibition and c-Jun N-terminal kinase activation. In view of these observations, we sought to gain further insight into the role of Smad7 in cell death. In the present study, we found that Smad7 represent a pro-apoptotic function that promotes sensitivity to cisplatin in cancer cells by suppressing the expression of survival protein HO-1.

2. Materials and methods

2.1. Materials

Cisplain was purchased from Sigma Chemical Co. (St. Louis, MI). The *N*-acetyl-Asp-Glu-Val-Asp-ρ-nitroanlide (Ac-DEVD-pNA) was purchased from Enzyme Systems Products (Dublin, CA). Zinc protoporphyrin IX was purchased from Sigma Chemical Co. (St. Louis, MI).

2.2. Cell culture and generation of stable cell lines

A549 human lung carcinoma cells were obtained from American Type Culture Collection (Manassas, VA). The cells were cultured in RPMI1640 medium supplemented with 2 mM L-glutamine, 10% heat-inactivated fetal bovine serum, 100 U/mL penicillin, and 100 μg/mL streptomycin. Generation of the A549-HO-1 stable cell

* Corresponding author. Address: Department of Biochemistry, College of Natural Sciences, Kangwon National University, 191-1 Hyoja-2-dong, Chuncheon 200-701, Republic of Korea. Fax: +82 33 242 0459.
E-mail address: bckim@kangwon.ac.kr (B.-C. Kim).

0006-291X/$ - see front matter © 2012 Elsevier Inc. All rights reserved.
http://dx.doi.org/10.1016/j.bbrc.2012.02.151

lines were performed as described in [13]. Cells stably expressing the HO-1 gene were screened for resistance to neomycin, and verified through immunoblot analysis.

2.3. Plasmids and adenoviral infections

To construct the HO-1 expression vector, PCR amplification was performed by using two oligonucleotides (5′-AAGCTTATGGAGCGTCCGCAACCCGA-3′ and 5′-CTCGAGAGTTCATGCCCTGGGAGCC-3′). The amplified fragment of HO-1 was subcloned into HindIII-XhoI sites of pcDNA-hemagglutinin (HA) (Clontech). The plasmid pHO-1-Luc, which contains a 4.9-kb human promoter upstream of the luciferase gene, was provided by Dr. Norbert Leitinger (Department of Vascular Biology and Thrombosis Research, University of Vienna, Vienna, Austria). Adenoviral vector encoding Akt1 (CA), constitutively active form of Akt1, was kindly provided by Dr. Seok Hee Park (Sungkyunkwan University, Suwon, Korea). Recombinant adenoviruses expressing LacZ, FLAG-tagged Smad7, and active Akt1 was used at a multiplicity of infection (m.o.i.) ranging from 0 to 250 from single viruses as described by Fujii et al. [14].

2.4. RNA isolation and reverse transcriptase-polymerase chain reaction (RT-PCR)

Total RNA was extracted using the phenol-guanidinium isothiocyanate method [15]. RT-PCR was performed by the Access RT-PCR system (Promega, Madison, WI) according to the manufacturer's instructions using the following human HO-1-specific primers: forward, 5′-TTACCTTCCCGAACATCGAC-3′, and reverse, 5′-GCATAAATTCCCACTGCCAC-3′, human glyceraldehyde-3-phosphate dehydrogenase (GAPDH) was amplified as a control, using the following primers: forward, 5′-TGAAGGTCGGTGTGAACGCATTTGGC-3′, reverse, 5′-TTCTGGGTGGCAGTGATGGC-3′. PCR products were visualized on 1.2% agarose gels stained with ethidium bromide using the BioDoc-ItTM system (Ultraviolet Products, Upland, CA).

2.5. DNA transfection and reporter assay

The A549 cells were transfected using Fugene 6 (Roche, Mannheim, Germany). To control variations in cell numbers and transfection efficiency, all clones were cotransfected with 0.2 μg of CMV-β-GAL, a eukaryotic expression vector in which Escherichia coli β-galactosidase (Lac Z) structural gene is under the transcriptional control of the CMV promoter. Luciferase reporter activity was assessed on a luminometer with a luciferase assay system (Promega, Madison, WI) according to the manufacturer's protocol. Transfection experiments were performed in duplicate with two independently isolated sets, and these results were averaged.

2.6. Immunoblot analysis

Cytosolic extracts were obtained in 1% Triton X-100 lysis buffer (50 mM Tris–Cl, pH 8.0, 150 mM sodium chloride, 1 mM EDTA, 1 mM EGTA, 2.5 mM sodium pyrophosphate, 1 mM sodium orthovanadate, 1 mM β-glycerophosphate, 1 μg/mL leupeptin, and 1 mM phenylmethylsulfonyl fluoride). Western blotting was performed using anti-HO-1 (Santa Cruz Biotechnology, Santa Cruz, CA), anti-phospho-Akt (Cell Signaling Technology, Beverly, MA), Anti-poly(ADP-ribose) polymerase (Upstate), anti-FLAG (Sigma, St. Louis, MO), and anti-β-actin (Sigma, St. Louis, MO) antibodies. Protein samples were heated at 95 °C for 5 min and analyzed by SDS–PAGE. Immunoblot signals were developed by Super Signal Ultra chemiluminescence detection reagents (Pierce Biotechnology, Rockford, IL). For immunoprecipitation, the cell lysates were incubated with the appropriate antibody (Ab) for 1 h, followed by incubation with Gamma-bind beads (Amersham Pharmacia Biosciences) at 4 °C for 1 h. Beads were washed four times with the buffer used for cell solubilization. Immune complexes then were eluted by boiling for 3 min in 2× Laemmli buffer (pH 6.8), and then extracts were analyzed by immunoblotting as described above.

2.7. HO-1 enzyme activity

HO-1 activity was measured as described previously [16]. HO-1 activity was calculated as picomole of bilirubin formed/mg of microsomal protein/h and normalized to the hemin-treated control to eliminate intra-assay variation.

2.8. Annexin V/PI double staining

Apoptosis was detected using AnnexinV plus propodium iodide (PI) for apoptosis detection according to the manufacturer's instructions (Biosource, Camarillo, CA, USA). In brief, cells were harvested by trypsinization and rinsed with cold PBS twice. After centrifugation (4 °C, 1000×*g*) for 10 min, cells were suspended by 200 mL binding buffer and then treated with 10 mL Annexin VFITC and 5 mL PI for 15 min at room temperature. Flow cytometric analysis of cells was performed with a FACSCalibur using CellQuest software as per manufacturer instructions (Becton Dickinson). Cytometric analysis was repeated three times.

2.9. Caspase-3 assay

Caspase-3 activity in cytosolic extracts was determined with a spectrophotometric assay, as described previously [17]. Briefly, the peptide substrate *N*-acetyl-Asp-Glu-Val-Asp-ρ-nitroanlide (Ac-DEVD-pNA) was added to the cell lysates in assay buffer (50 mM HEPES, pH 7.4, 100 mM NaCl, 0.1% CHAPS, 10 mM dithiothreitol, 1 mM EDTA, 10% glycerol) and incubated at 37 °C. The cleavage of the substrate was monitored at 405 nm.

2.10. Statistical analysis

All data presented are expressed as mean ± SD, and a representative of three or more independent experiments. Statistical analyses were assessed by Student's *t*-test for paired data. Results were considered significant at $p < 0.05$.

3. Results and discussion

3.1. HO-1 decreases sensitivity to cisplatin-induced apoptosis

Heme oxygenase-1 (HO-1) is considered as an enzyme facilitating cell survival and tumor progression [3–6]. First, we analyzed the expression level of HO-1 in BEAS2B, A549, and NCI-H322 cells. Highly elevated HO-1 protein expression was detected in A549 lung cancer cells compared with BEAS2B lung epithelial cells and NCI-H322 lung cancer cells (Fig. 1A). To determine relationship between HO-1 level and cell death, we treated the anticancer agent cisplatin and assayed the caspase activity in those cells. Cisplatin treatment led to a significant increase of caspase-3 activity in BEAS2B and NCI-H322 cells (Fig. 1B). In contrast, A549 cells were less susceptible to cisplatin-induced caspase-3 activation (Fig. 1B). Pretreatment of the HO-1 inhibitor zinc protoporphyin IX (ZnPP) in A549 cells significantly reversed the decreased caspase-3 activity in a dose-dependent manner (Fig. 1C). These results suggest that HO-1 can contribute to the resistance of cancer cells to cisplatin-induced apoptosis.

3.2. Overexpression of Smad7 decreases HO-1 expression and activity

It has been reported that Smad7 sensitizes cancer cells to apoptotic cell death [12]. To investigate whether Smad7 influences

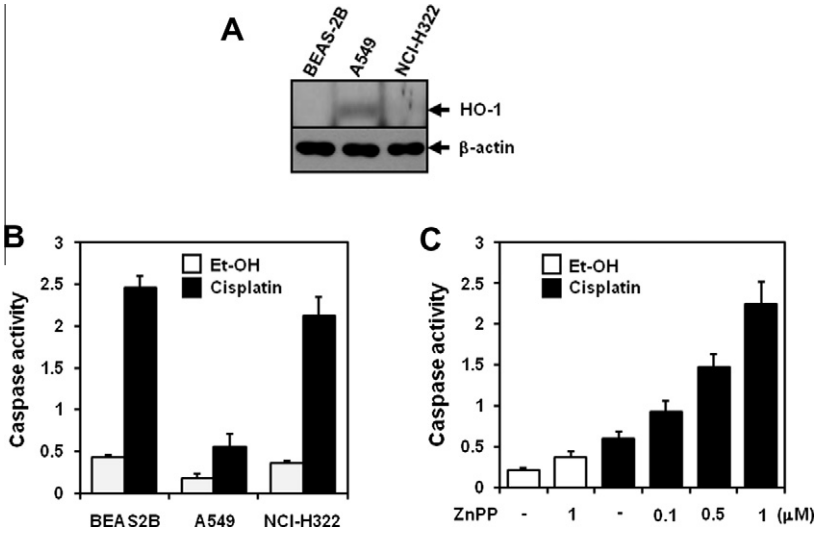

Fig. 1. The effect of HO-1 in cisplatin resistance of A549 cells. (A) The HO-1 protein level was analyzed in BEAS2B, A549, and NCI-H322 cells using immunoblot analysis. (B) Cells were treated with cisplatin (50 μM) for 24 h. (C) Cells were pre-treated with the indicated concentrations of ZnPP for 30 min and then treated with cisplatin (50 μM) for 24 h. Capsae-3 activities were determined as described under Section 2. The enzyme activity is represented as ΔA_{405}/min/mg protein.

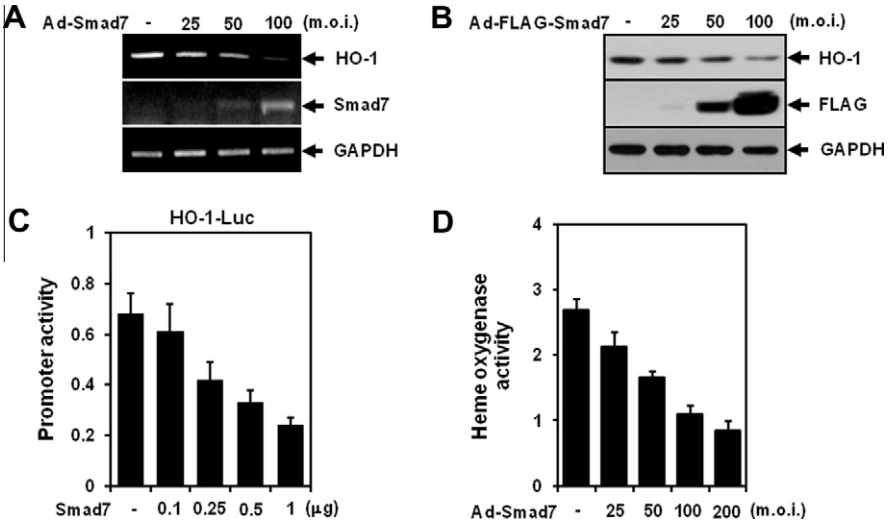

Fig. 2. Inhibition of HO-1 expression and activity by Smad7. A549 cells were infected with adenovirus carrying the Smad7 gene (Ad-Smad7) at the indicated amounts of m.o.i. (A) HO-1, Smad7, and GAPDH mRNA levels were analyzed by RT-PCR. (B) Immunoblots of whole cell lysates were probed with antibodies specific to HO-1, FLAG, and GAPDH. (C) Cells were co-transfected with HO-1-Luc and pCMV-Smad7 at indicated concentrations for 24 h. Luciferase activities were normalized on the basis of β-galactosidase expression to adjust for variation in transfection efficiency. (D) A549 cells were infected with adenovirus carrying the Smad7 gene (Ad-Smad7) at the indicated amounts of m.o.i. HO-1 activity was measured as described under Section 2.

HO-1 expression, A549 cells were infected with adenovirus carrying the LacZ (Ad-LacZ) or Smad7 (Ad-Smad7) gene. Successful infection and exogenous expression with adenoviral vector carrying the Smad7 gene was confirmed by RT-PCR (Fig. 2A) and immunoblot analysis (Fig. 2B). Interestingly, overexpression of Smad7 dose-dependently decreased the HO-1 expression at both mRNA (Fig. 2A) and protein (Fig. 2B) levels. Consistent with these results, transient transfection of A549 cells with Smad7 reduced the HO-1-Luc reporter activity (Fig. 2C). Furthermore, HO-1 enzyme activity was also dose-dependently suppressed by overexpression of Smad7 (Fig. 2D). These findings suggest that Smad7 is a negative regulator of HO-1.

3.3. Smad7 negatively regulates HO-1 through Akt inhibition

Because it has been well known that Akt plays a key role in the up-regulation of HO-1 expression [18], we assessed the ability of Smad7 to inhibit Akt phosphorylation at Ser-426, which triggers activation of Akt. As shown in Fig. 3A, the exogenously expressed Smad7 dose-dependently reduced the endogenous phosphorylation of Akt at Ser-426. To explore the potential role of Akt in the regulation of HO-1 activation, we tested the effect of Akt on inhibition of HO-1 by Smad7. Co-transfection of Akt with Smad7 resulted in a remarkable rescue of the decreased HO-1-Luc reporter activity by Smad7 (Fig. 3B). Similar effect on HO-1 activity was observed in A549 cells co-infected with adenoviruses carrying the Smad7 (AdSmad7) and the constitutively active form of Akt (Ad-Akt(CA)) gene (Fig. 3C).

3.4. Smad7 decreases resistance to cisplatin through inhibition of Akt and HO-1

Finally, we examined whether Smad7 relieves the Akt-HO-1-mediated resistance to cisplatin-induced apoptotic response.

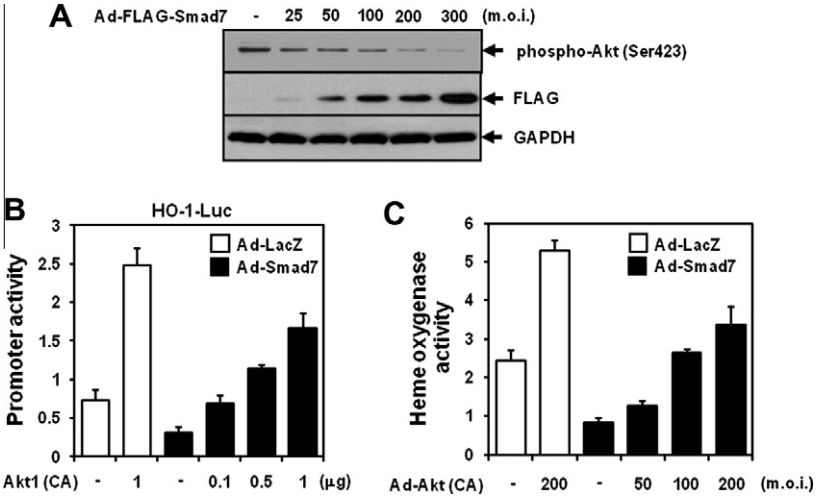

Fig. 3. Smad7 suppress HO-1 through Akt inhibition. (A) A549 cells were infected with adenovirus carrying the Smad7 gene (Ad-Smad7) at the indicated amounts of m.o.i. The extent of phosphorylated Akt, FLAG, and GAPDH was analyzed by immunobloting. (B) A549 cells were co-transfected with HO-1-Luc and pcDNA-Akt for 24 h. After transfection, cells were infected with Ad-LacZ or Ad-Smad7 for additional 24 h. Luciferase activities were normalized on the basis of β-galactosidase expression to adjust for variation in transfection efficiency. (C) Cells were co-infected with Ad-Akt (CA) and Ad-LacZ or Ad-Smad7 for 24 h. HO-1 activity was measured as described under Section 2.

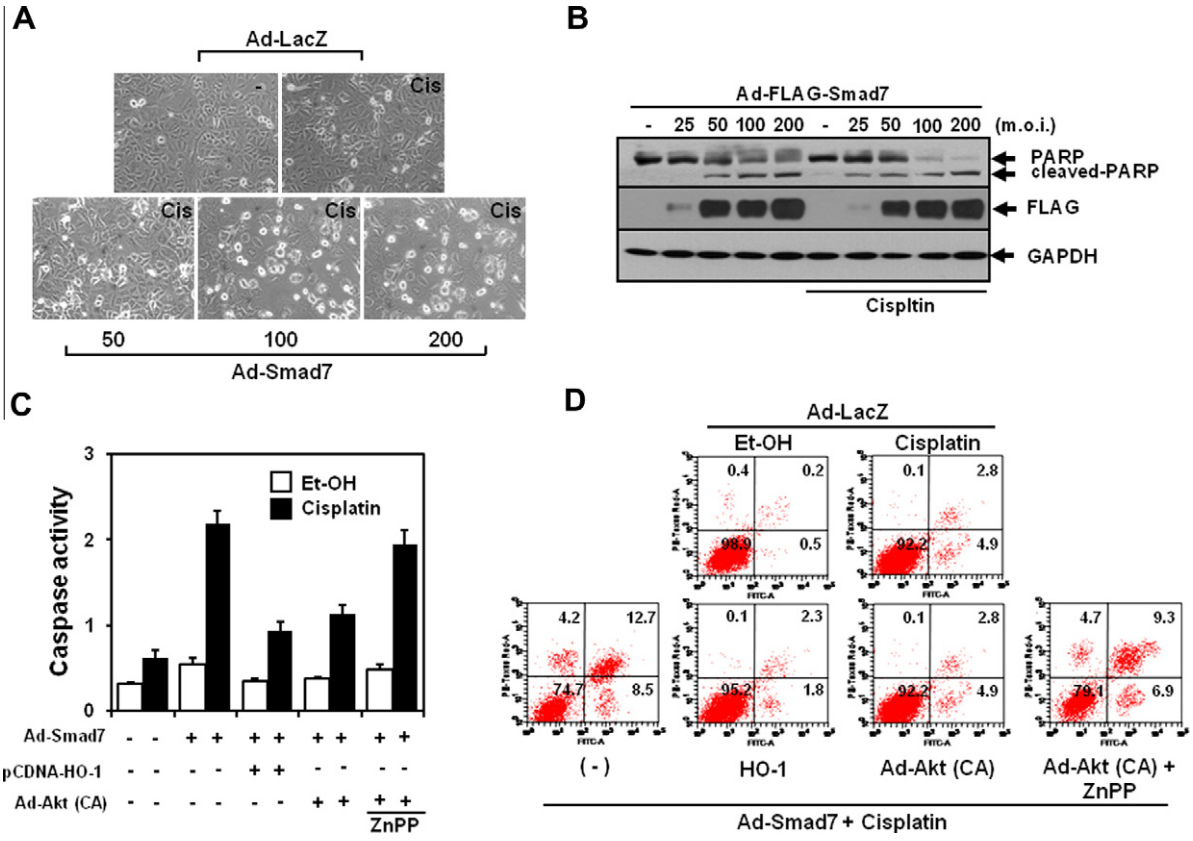

Fig. 4. Smad7 increases A549 cells sensitivity to cisplatin through inhibition of Akt and HO-1. (A) Cells were infected with Ad-LacZ or Ad-Smad7 for 24 h and then incubated without or with cisplatin for 24 h. Changes in cellular morphologies were observed by phase-contrast microscopy (magnification, 200×). (B) Cells were infected with Ad-Smad7 at the indicated amounts of m.o.i. At 24 h after infection, cells were incubated without or with cisplatin for 24 h. The cell lysates were immunoblotted with the anti-PARP, anti-FLAG, and anti-GAPDH antibody. A549-pcDNA or A549-HO-1 cells were infected with Ad-Smad7 or Ad-Akt (CA) for 24 h. At 24 h after infection, cells were pre-treated without or with ZnPP for 30 min and then incubated with cisplatin (50 μM) for 24 h. (C) Caspase activity were determined as described under Section 2. The enzyme activity is represented as ΔA_{405}/min/mg protein. (D) Flow cytometric analysis of apoptosis induction by cisplatin was shown by Annexin V/PI double staining.

Overexpression of Smad7 induced apoptotic cell death in cisplatin-treated A549 human lung cells, detected morphological cellular changes (Fig. 4A), degradation of poly (ADP-ribose) polymerase (Fig. 4B), activation of caspase-3 (Fig. 4C), and increased subG1 population (Fig. 4D). However, exogenously expressed HO-1 in Smad7-infected cells rendered them resistant to cisplatin-induced caspase-3 activation (Fig. 4B) and apoptosis (Fig. 4C). Similar results were observed in A549 cells that were infected with

adenovirus carrying Akt (CA) gene (Fig. 4C and D) and addition of the HO-1 inhibitor ZnPP to the cells increased sensitivity to cisplatin-induced apoptosis (Fig. 4C and D).

Resistance to death signal of tumor cell is the most important obstacles in chemotherapy of cancer. A growing body of evidences indicates that tumor cells defend themselves from oxidative damage by stimulating antioxidant capacity [19]. Because HO-1 passes a potent anti-oxidant activity and is often upregulated in tumor tissues, inhibition of HO-1 may contributes to sensitization of cancer cells to drug-induced apoptosis. In the present study, we showed that Smad7 inhibits Akt-dependent HO-1 activation and suppression of HO-1 expression significantly increased cisplatin sensitivity of A549 lung cancer cells. Thus we believe that pharmacologic augmentation of Smad7 expression can be an important strategy for overcoming drug-resistance in cancer therapy.

Acknowledgments

This study was supported by a grant from the National R&D Program for Cancer Control, Ministry for Health and Welfare, Republic of Korea (1020420).

References

[1] H.Y. Lin, S.C. Shen, C.W. Lin, L.Y. Yang, Y.C. Chen, Baicalein inhibition of hydrogen peroxide-induced apoptosis via ROS-dependent heme oxygenase 1 gene expression, Biochim. Biophys. Acta 1773 (2007) 1073–1086.
[2] S. Sharma, O. Dewald, J. Adrogue, R.L. Salazar, P. Razeghi, J.D. Crapo, R.P. Bowler, M.L. Entman, H. Taegtmeyer, Induction of antioxidant gene expression in a mouse model of ischemic cardiomyopathy is dependent on reactive oxygen species, Free. Rad. Biol. Med. 40 (2006) 2223–2231.
[3] C. Zou, H. Zhang, Q. Li, H. Xiao, L. Yu, S. Ke, L. Zhou, W. Liu, W. Wang, H. Huang, N. Ma, Q. Liu, X. Wang, W. Zhao, H. Zhou, X. Gao, Heme oxygenase-1: a molecular brake on hepatocellular carcinoma cell migration, Carcinogenesis 32 (2011) 1840–1848.
[4] M. Sunamura, D.G. Duda, M.H. Ghattas, L. Lozonschi, F. Motoi, J. Yamauchi, S. Matsuno, S. Shibahara, N.G. Abraham, Heme oxygenase-1 accelerates tumor angiogenesis of human pancreatic cancer, Angiogenesis 6 (2003) 15–24.
[5] C.M. Raval, P.J. Lee, Heme oxygenase-1 in lung disease, Curr. Drug Targets 11 (2010) 1532–1540.
[6] J. Alicja, W. Halina, D. Jozef, Heme oxygenase-1 in tumors; Is it a false friend?, Antioxidant Redox Signal 9 (2007) 2099–2118.
[7] J. Massague, TGF-β signal transduction, Annu. Rev. Biochem. 67 (1998) 753–791.
[8] L. Ulloa, J. Doody, J. Massagué, Inhibition of transforming growth factor-beta/SMAD signalling by the interferon-gamma/STAT pathway, Nature 397 (1999) 710–713.
[9] M. Bitzer, G. von Gersdorff, D. Liang, A. Dominguez-Rosales, A.A. Beg, M. Rojkind, E.P. Böttinger, A mechanism of suppression of TGF-beta/SMAD signaling by NF-kappa B/RelA, Genes Dev. 14 (2000) 187–197.
[10] S. Edlund, S. Bu, N. Schuster, P. Aspenström, R. Heuchel, N.E. Heldin, P. ten Dijke, C.H. Heldin, M. Landström, Transforming growth factor-β1 (TGF-β)-induced apoptosis of prostate cancer cells involves Smad7-dependent activation of p38 by TGF-β-activated kinase 1 and mitogen-activated protein kinase kinase 3, Mol. Biol. Cell 14 (2003) 529–544.
[11] B.C. Kim, H.J. Lee, S.H. Park, S.R. Lee, T.S. Karpova, J.G. McNally, A. Felici, D.K. Lee, S.J. Kim, Jab1/CSN5, a component of the COP9 signalosome, regulates transforming growth factor beta signaling by binding to Smad7 and promoting its degradation, Mol. Cell. Biol. 24 (2004) 2251–2262.
[12] S. Hong, S. Lim, A.G. Li, C. Lee, Y.S. Lee, E.K. Lee, S.H. Park, X.J. Wang, S.J. Kim, Smad7 binds to the adaptors TAB2 and TAB3 to block recruitment of the kinase TAK1 to the adaptor TRAF2, Nat. Immunol. 8 (2007) 504–513.
[13] H.Y. Hong, W.K. Jeon, B.C. Kim, Up-regulation of heme oxygenase-1 expression through the Rac1/NADPH oxidase/ROS/p38 signaling cascade mediates the anti-inflammatory effect of 15-deoxy-$\Delta^{12,14}$-prostaglandin J_2 in murine macrophages, FEBS Lett. 582 (2008) 861–868.
[14] A. Brederlau, R. Faigle, M. Elmi, A. Zarebski, S. Sjöberg, M. Fujii, K. Miyazono, K. Funa, The bone morphogenetic protein type Ib receptor is a major mediator of glial differentiation and cell survival in adult hippocampal progenitor cell culture, Mol. Biol. Cell 15 (2004) 3863–3875.
[15] M.P. Sherman, E.E. Aeberhard, V.Z. Wong, J.M. Grisavage, L.J. Ignarro, Pyrrolidine dithiocarbamate inhibits induction of nitric oxide synthase activity in rat alveolar macrophages, Biochem. Biophys. Res. Commun. 191 (1993) 1301–1308.
[16] W.K. Jeon, H.Y. Hong, B.C. Kim, Genipin up-regulates heme oxygenase-1 via PI3-kinase-JNK1/2-Nrf2 signaling pathway to enhance the anti-inflammatory capacity in RAW264.7 macrophages, Arch. Biochem. Biophys. 512 (2011) 119–125.
[17] K. Kim, Z. Lu, E.D. Hay, Direct evidence for a role of beta-catenin/LEF-1 signaling pathway in induction of EMT, Cell Biol. Int. 26 (2002) 463–476.
[18] S.S. Hamdulay, B. Wang, G.M. Birdsey, F. Ali, O. Dumont, P.C. Evans, D.O. Haskard, C.P. Wheeler-Jones, J.C. Mason, Celecoxib activates PI-3K/Akt and mitochondrial redox signaling to enhance heme oxygenase-1-mediated anti-inflammatory activity in vascular endothelium, Free. Radic. Biol. Med. 48 (2010) 1013–1023.
[19] A.I. Rojo, M. Salina, M. Salazar, S. Takahashi, G. Suske, V. Calvo, M.R. de Sagarra, A. Cuadrado, Regulation of heme oxygenase-1 gene expression through the phosphatidylinositol 3-kinase/PKC-zeta pathway and Sp1, Free Radic. Biol. Med. 41 (2006) 247–261.

Biochemical and Biophysical Research Communications 420 (2012) 293–296

Contents lists available at SciVerse ScienceDirect

Biochemical and Biophysical Research Communications

journal homepage: www.elsevier.com/locate/ybbrc

Cdc25A promotes cell survival by stimulating NF-κB activity through IκB-α phosphorylation and destabilization

Hey-Young Hong [a], Jiyeon Choi [a], Young-Wook Cho [b], Byung-Chul Kim [a,*]

[a] Department of Biochemistry, College of Natural Sciences, Kangwon National University, 192-1 Hyoja-2-dong, Chuncheon 200-701, Republic of Korea
[b] Korea Basic Science Institute, Chuncheon Center, Gangwondaehak-gil 1, Chuncheon 200-701, Republic of Korea

ARTICLE INFO

Article history:
Received 26 February 2012
Available online 6 March 2012

Keywords:
Cdc25A
NF-κB
Iκ-Bα
Ubiquitination
Apoptosis

ABSTRACT

Cell division cycle 25A (Cdc25A), a dual specificity protein phosphatase, exhibits anti-apoptotic activity, but the underlying molecular mechanisms are poorly characterized. Here we report that Cdc25A inhibits cisplatin-induced apoptotic cell death by stimulating nuclear factor-kappa B (NF-κB) activity. In HEK-293 cells, Cdc25A decreased protein level of inhibitor subunit kappa B alpha (Iκ-Bα) in association with increased serine 32-phosphorylation, followed by stimulation of transcriptional activity of NF-κB. Inhibition of NF-κB activity by chemical inhibitor or overexpression of Iκ-Bα in Cdc25A-elevated cancer cells resistant to cisplatin improved their sensitivity to cisplatin-induced apoptosis. Our data show for the first time that Cdc25A has an important physiological role in NF-κB activity regulation and it may be an important survival mechanism of cancer cells.

1. Introduction

Cdc25A is a member of cell division cycle 25 (Cdc25) family of protein with highly conserved dual-specific phosphatase activity [1,2]. It plays a key role in G1/S phase transition during normal cell division through the activation of cyclin E/cyclin-dependent kinase2 (CDK2) complex [3] and in the G2/M checkpoint mechanisms activated in response to DNA damage [4,5]. Therefore, dysregulation of Cdc25A levels results in checkpoint bypass and genomic instability. Indeed, Cdc25A overexpression has been reported in many high-grade tumors [6–8] and often correlates with poor progression in human cancers. Cdc25A overexpression also critically contributes to the resistance of tumor cells to chemotherapy-mediated cell death [9]. However, the underlying molecular mechanisms remain to be elucidated.

The nuclear factor κB (NF-κB) is a family of transcription factors that regulates the expression of various genes involved in cell survival signaling [10,11]. The prototypical and ubiquitously expressed NF-κB complex is the p50/p65 heterodimer, of which RelA or p65 subunit directly regulate expression of Bcl-2 and IAP family survival proteins [12,13]. In the classical pathway, NF-κB remains in cytosol in an inactive state, complexed with inhibitor subunit kappa B (IκB). Under activation stimulus, IκB is phosphorylated by IκB kinases, IKKα and IKKβ, which is subsequently ubiquitinated and degraded by the 26S proteasome, thus leading to the nuclear translocation and transcriptional activation of NF-κB [14]. In the present study, we demonstrate that Cdc25A stimulates NF-κB activity by destabilizing IκB protein through inducing its phosphorylation and ubiquitination. Our study supports a novel function of Cdc25A as a positive regulator of NF-κB.

2. Materials and methods

2.1. Materials

Cisplatin was purchased from Sigma Chemical Co. (St. Louis, MI). Small interfering ribonucleic acids (siRNAs) for control and human p65/RelA were purchased from Santa Cruz Biotechnology (Santa Cruz, CA). The *N*-acetyl-Asp-Glu-Val-Asp-ρ-nitroanlide (Ac-DEVD-pNA) was purchased from Enzyme Systems Products (Dublin, CA).

2.2. Cell culture

HEK-293, a human kidney embryonic cell line, and the estrogen-independent and invasive human breast cancer cells, MDA-MB231 and MDA-MB435, were obtained from American Type Culture Collection (Manassas, VA). The cells were cultured in Dulbecco's modified Eagle's medium supplemented with 2 mM L-glutamine, 10% heat-inactivated fetal bovine serum, 100 U/ml penicillin, and 100 μg/ml streptomycin.

2.3. DNA transfection and reporter assay

The HEK-293 cells were transfected using Fugene 6 (Roche, Mannheim, Germany). To control variations in cell numbers and

* Corresponding author. Fax: +82 33 242 0459.
E-mail address: bckim@kangwon.ac.kr (B.-C. Kim).

0006-291X/$ - see front matter © 2012 Elsevier Inc. All rights reserved.
http://dx.doi.org/10.1016/j.bbrc.2012.02.152

transfection efficiency, all clones were co-transfected with 0.2 μg of CMV-β-GAL, a eukaryotic expression vector in which *Escherichia coli* β-galactosidase (Lac Z) structural gene is under the transcriptional control of the CMV promoter. Luciferase reporter activity was assessed on a luminometer with a luciferase assay system (Promega, Madison, WI) according to the manufacturer's protocol. Transfection experiments were performed in duplicate with two independently isolated sets, and these results were averaged.

2.4. Indirect immunofluorescence

HEK-293 cells were plated at 1×10^5 cells onto 18 mm glass cover slips 24 h prior to transfection. The cells were co-transfected with GFP-p65/RelA and pCMA-FLAG or pCMV-FLAG-Cdc25A for 24 h. The coverslips were fixed in cold 3.5% paraformaldehyde for 5 min, permeabilized in cold methanol for 2 min and incubated for 5 min in 50 mM glycine. The GFP-p65/RelA and FLAG-Cdc25A were then detected by incubation with anti-GFP rabbit polyclonal antibody (FL; Santa Cruz Biotechnology, Santa Cruz, CA) and anti-FLAG mouse monoclonal antibody (M5; Sigma, St. Louis, MO) for 2 h at room temperature. After washing in phosphate-buffered saline (PBS), the coverslips were incubated for 1 h at room temperature with fluorescein isothiocyanate (FITC) conjugated goat anti-mouse IgG and rhodamine (TRITC) conjugated goat anti-rabbit IgG secondary antibodies (Molecular Probes). Stained cells were washed, mounted in medium containing 4,6-diamino-2-phenylindole (DAPI) (h-1200; Vector Laboratories, Burlingame, CA) and examined using a Olympus Fluoview-FV300 confocal microscope.

2.5. Immunoblot analysis

Cytosolic extracts were obtained in 1% Triton X-100 lysis buffer (50 mM Tris–Cl, pH 8.0, 150 mM sodium chloride, 1 mM EDTA, 1 mM EGTA, 2.5 mM sodium pyrophosphate, 1 mM sodium orthovanadate, 1 mM b-glycerophosphate, 1 lg/ml leupeptin, and 1 mM phenylmethylsulfonyl fluoride). Western blotting was performed using anti-IκBα (FL; Santa Cruz Biotechnology, Santa Cruz, CA), anti-p65 (C-20; Santa Cruz Biotechnology, Santa Cruz, CA), antiphospho-IκBα (14D4; Cell Signaling Technology, Beverly, MA), and anti-β-actin (AC-15; Sigma, St. Louis, MO) antibodies. Protein samples were heated at 95 °C for 5 min and analyzed by SDS–PAGE. Immunoblot signals were developed by Super Signal Ultra chemiluminescence detection reagents (Pierce Biotechnology, Rockford, IL). For immunoprecipitation, the cell lysates were incubated with the appropriate antibody (Ab) for 1 h, followed by incubation with Gamma-bind beads (Amersham Pharmacia Biosciences) at 4 °C for 1 h. Beads were washed four times with the buffer used for cell solubilization. Immune complexes then were eluted by boiling for 3 min in 2× Laemmli buffer (pH 6.8), and then extracts were analyzed by immunoblotting as described above.

2.6. Caspase-3 assay

Caspase-3 activity in cytosolic extracts was determined with a spectrophotometric assay, as described previously [15]. Briefly, the peptide substrate *N*-acetyl-Asp-Glu-Val-Asp-ρ-nitroanlide (Ac-DEVD-pNA) was added to the cell lysates in assay buffer

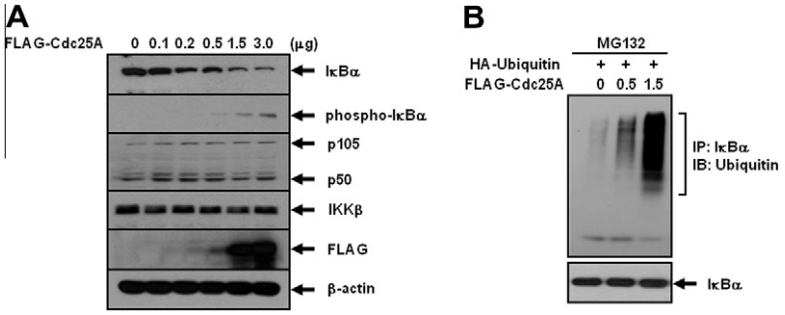

Fig. 1. Phosphorylation, ubiquitination, and proteasomal degradation of IκBα by Cdc25A. (A) HEK-293 cells were transfected with pCMV-FLAG-Cdc25A at indicated concentrations for 24 h. Whole cell lysates were analyzed for IκBα, phosphor-IκBα (Ser-32), p65, p105, p50, IKKβ, FLAG, and b-actin by immunoblotting. (B) HEK-293 cells co-transfected with HA-ubiquitin and FLAG-Cdc25A were treated with MG-132 (0.5 μM) for 12 h. Cell lysates were immunoprecipitated with anti-IκBα followed by immunoblot analysis with anti-ubiquitin and anti-IκBα.

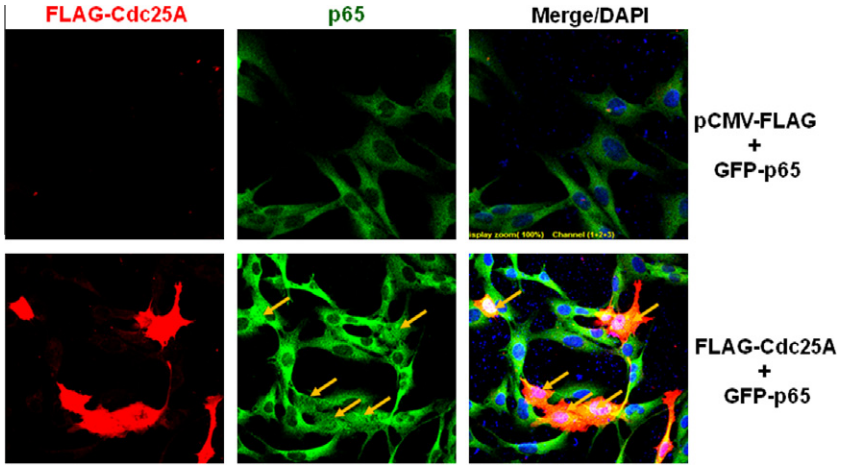

Fig. 2. Nuclear translocation of p65/RelA induced by Cdc25A. HEK-293 cells were transfected with vector control or FLAG-Cdc25A for 24 h. Expression and subcellular localization of FLAG-Cdc25A and p65/RelA were observed by immunofluorescence. Nuclei are stained with DAPI, 4′-6-diamidino-2-phenylindole. Arrows indicate cells expressed exogenous Cdc25A.

(50 mM HEPES, pH 7.4, 100 mM NaCl, 0.1% CHAPS, 10 mM dithiothreitol, 1 mM EDTA, 10% glycerol) and incubated at 37 °C. The cleavage of the substrate was monitored at 405 nm.

2.7. Statistical analysis

All data presented are expressed as mean ± SD, and a representative of three or more independent experiments. Statistical analyses were assessed by Student's *t*-test for paired data. Results were considered significant at $P < 0.05$.

3. Results and discussion

3.1. The phosphorylation and ubiquitin-mediated degradation of IκB-α induced by Cdc25A

Because Cdc25A plays an important role in determining the survival of cancer cells to chemotherapeutic agents [9], we examined the effect of Cdc25A to proteins of NF-κB survival pathway. In HEK-293 cells, overexpression of Cdc25A resulted in the phosphorylation on the Ser32 and subsequent degradation of IκB-α in a concentration-dependent manner (Fig. 1A). In contrast, p65/RelA protein level was increased (Fig. 1A). Protein levels of p50, p105, and IKKβ were not changed under same conditions (Fig. 1A). Because phosphorylation of IκB-α on Ser32 is crucial for its ubiquitination and posterior proteasome degradation, we next tested whether Cdc25A induces ubiquitination of IκB-α. The polyubiquitinated IκB-α was confirmed using immunoprecipitation with a specific anti-ubiquitin antibody in cells co-transfected with plasmids encoding ubiquitin with or without vectors expressing Cdc25A (Fig. 1B).

3.2. Nuclear localization of p65/RelA induced by Cdc25A

The phosphorylation and degradation of IκB-α leads to the nuclear accumulation of NF-κB [14]. We next examined whether

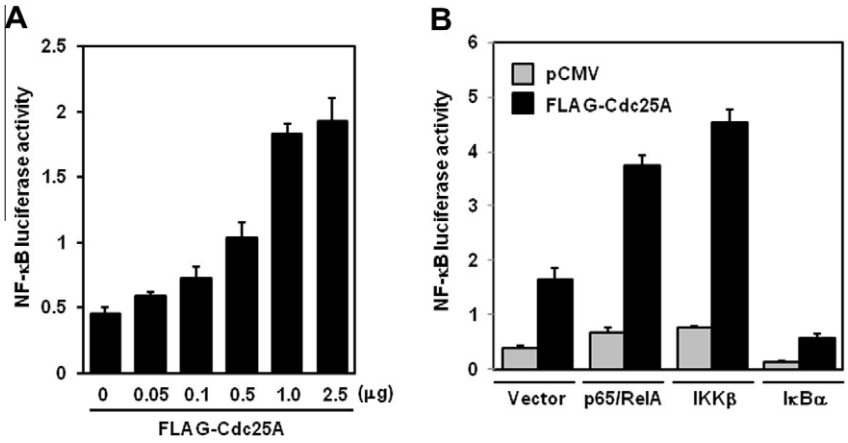

Fig. 3. Stimulation of NF-κB-dependent transcriptional activity induced by Cdc25A. (A) HEK-293 cells were co-transfected with NF-κB-Luc and pCMV-FLAG-Cdc25A at indicated concentrations for 24 h. (B) HEK-293 ells were co-transfected with NF-κB-Luc, pCMV-FLAG-Cdc25A and pcDNA-p65 or pcDNA-IKKβ or pcDNA-IκBα for 24 h. Luciferase activities were normalized on the basis of b-galactosidase expression to adjust for variation in transfection efficiency.

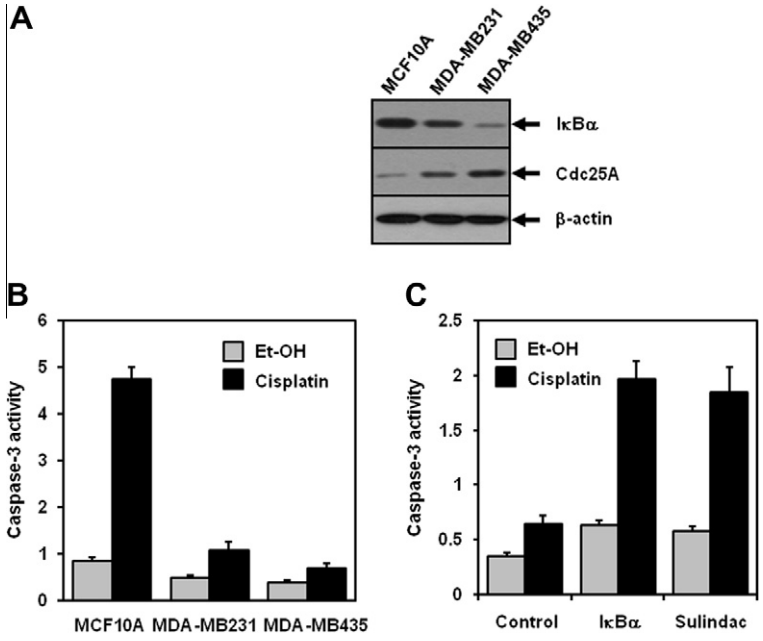

Fig. 4. Inhibition of cisplatin-induced apoptosis by Cdc25A-NF-κB axis. (A) Cdc25A and IκBα expression level were tested in MCF10A, MDA-MB231, and MDA-MB435 cells using immunoblot analysis. (B) Capsae-3 activities were determined in MCF10A, MDA-MB231, and MDA-MB435 cells as described under Section 2. (C) MDA-MB435 cells were transfected with vector control or IkBa. At 24 h after transfection, cells were incubated in the absence or presence of sulindac for 30 min before exposed to cisplatin (50 μM) for 24 h. The enzyme activity is represented as ΔA_{405}/min/mg protein.

Cdc25A can induces translocation of p65/RelA into the nucleus by indirect immunofluorescence and confocal microscopy. As would be expected, p65/RelA resides mainly in the cytoplasm in cells transfected with empty vector, whereas p65/RelA was detected primarily in the nucleus in cells transfected with Cdc25A (Fig. 2).

3.3. Stimulation of NF-κB transcriptional activity induced by Cdc25A

We examined whether overexpression of Cdc25A enhances the transcriptional activity of NF-κB. In HEK-293 cells, Cdc25A increased the NF-κB-Luc reporter gene activity in a dose-dependent manner (Fig. 3A). This effect was further enhanced by co-transfection of Cdc25A with IKKβ or p65, whereas overexpression of Iκ-Bα completely abolished it (Fig. 3B).

3.4. Cdc25A mediates the resistance of cancer cells to cisplatin through NF-κB activation

The transcription factor NF-κB is a key mediator of cell survival signaling. We thus determined whether NF-κB activation by Cdc25A confer antiapoptotic property to cancer cells. We firstly analyzed the correlation between expression of Cdc25A and Iκ-Bα and resistance to cisplatin-induced cell death. As shown in Fig. 4A, B, highly invasive human breast cancer cell lines that are resistance to cisplatin-induced apoptosis, such as MAD-MB231 and MDA-MB435, showed elevated Cdc25A expression and lower Iκ-Bα protein level compared with MCF10A cells that are sensitive to cisplatin-induced apoptosis. Furthermore, our data showed that NF-κB inhibition by pharmacological inhibitor, sulindac, or overexpression of Iκ-Bα sensitized MDA-MB435 cells to cisplatin-induced activation of caspase-3, as a key regulator of apoptosis (Fig. 4B).

Cdc25A has been reported to be elevated in many types of cancer and contributes to the resistance of tumor cells to chemotherapy-mediated cell death, but the underlying mechanisms are less understood. In this study, we examined whether the anti-apoptotic effect of Cdc25A is mediated through NF-κB survival pathway. Our results provide the first evidence that Cdc25A is a potent stimulator of the ubiquitious transcription factor NF-κB. The phosphorylation of Iκ-Bα at Ser 32 and subsequent its proteasomal degradation induced by Cdc25A positively modulated the nuclear translocation of p65/rRelA and its transcriptional activity, which explain the anti-apoptotic effect of Cdc25A in cancer cells.

Acknowledgment

This research was supported by Basic Science Research Program through the National Research Foundation of Korea(NRF) funded by the Ministry of Education, Science and Technology (2009-0072203).

References

[1] J. Rudolph, Cdc25 phosphatases: structure, specificity, and mechanism, Biochemistry 46 (2007) 3595–3604.
[2] P. De Wulf, F. Montani, R. Visintin, Protein phosphatases take the mitotic stage, Curr. Opin. Cell Biol. 6 (2009) 806–815.
[3] I. Blomberg, I. Hoffmann, Etopic expression of Cdc25A accelerates the G(1)/S transition and leads to premature activation of cyclin E-and cyclin A-dependent kinases, Mol. Cell Biol. 19 (1999) 6183–6194.
[4] J. Bartek, J. Lukas, Pathways governing G1/S transition and their response to DNA damage, FEBS Lett. 490 (2001) 117–122.
[5] D. Ray, H. Kiyokawa, CDC25A phosphatase: a rate-limiting oncogene that determines genomic stability, Cancer Res. 68 (2008) 1251–1253.
[6] R. Boutros, V. Lobjois, B. Ducommun, CDC25 phosphatases in cancer cells: key players? Good targets?, Nat Rev. 7 (2007) 495–507.
[7] K. Kristjansdottir, J. Rudolph, Cdc25 phosphatases and cancer, Chem. Biol. 11 (2004) 1043–1051.
[8] M.G. Cangi, B. Cukor, P. Soung, S. Signoretti, G. Moreira Jr., M. Ranashinge, B. Cady, M. Pagano, M. Loda, Role of the Cdc25A phosphatase in human breast cancer, J. Clin. Invest. 106 (2000) 753–761.
[9] L. Brault, D. Bagrel, Activity of novel Cdc25 inhibitors and preliminary evaluation of their potentiation of chemotherapeutic drugs in human breast cancer cells, Life Sci. 82 (2008) 315–323.
[10] A. Kumar, Y. Takada, A.M. Boriek, B.B. Aggarwal, Nuclear factor-kappaB: its role in health and disease, J. Mol. Med. 82 (2004) 434–448.
[11] A.S. Baldwin Jr., Series introduction: the transcription factor NF-kappaB and human disease, J. Clin. Invest. 107 (2001) 3–6.
[12] C.Y. Wang, D.C. Guttridge, M.W. Mayo, A.S. Baldwin Jr., NF-kappaB induces expression of the Bcl-2 homologue A1/Bfl-1 to preferentially suppress chemotherapy-induced apoptosis, Mol. Cell. Biol. 19 (1999) 5923–5929.
[13] T.D. Gilmore, Introduction to NF-κB: players, pathways, perspectives, Oncogene 25 (2006) 6680–6684.
[14] M. Karin, Y. Ben-Neriah, Phosphorylation meets ubiquitination: the control of NF-κB activity, Annu. Rev. Immunol. 18 (2000) 621–663.
[15] K. Kim, Z. Lu, E.D. Hay, Direct evidence for a role of beta-catenin/LEF-1 signaling pathway in induction of EMT, Cell Biol. Int. 26 (2002) 463–476.

Biochemical and Biophysical Research Communications 420 (2012) 297–301

Contents lists available at SciVerse ScienceDirect

Biochemical and Biophysical Research Communications

journal homepage: www.elsevier.com/locate/ybbrc

Distribution and histologic effects of intravenously administered amorphous nanosilica particles in the testes of mice

Yuki Morishita [a], Yasuo Yoshioka [a,*], Hiroyoshi Satoh [a], Nao Nojiri [a], Kazuya Nagano [b], Yasuhiro Abe [c], Haruhiko Kamada [b,d], Shin-ichi Tsunoda [b,d], Hiromi Nabeshi [e], Tomoaki Yoshikawa [a], Yasuo Tsutsumi [a,b,d,*]

[a] Laboratory of Toxicology and Safety Science, Graduate School of Pharmaceutical Sciences, Osaka University, 1-6 Yamadaoka, Suita, Osaka 565-0871, Japan
[b] Laboratory of Biopharmaceutical Research, National Institute of Biomedical Innovation, 7-6-8 Saitoasagi, Ibaraki, Osaka 567-0085, Japan
[c] Cancer Biology Research Center, Sanford Research/USD, 2301 E. 60th Street N, Sioux Falls, SD 57104, USA
[d] The Center for Advanced Medical Engineering and Informatics, Osaka University, 1-6 Yamadaoka, Suita, Osaka 565-0871, Japan
[e] Division of Foods, National Institute of Health Sciences, 1-18-1, Kamiyoga, Setagaya-ku, Tokyo 158-8501, Japan

ARTICLE INFO

Article history:
Received 25 February 2012
Available online 6 March 2012

Keywords:
Biodistribution
Nanomaterials
Safety
Reproductive toxicity

ABSTRACT

Amorphous nanosilica particles (nSP) are being utilized in an increasing number of applications such as medicine, cosmetics, and foods. The reduction of the particle size to the nanoscale not only provides benefits to diverse scientific fields but also poses potential risks. Several reports have described the *in vivo* and *in vitro* toxicity of nSP, but few studies have examined their effects on the male reproductive system. The aim of this study was to evaluate the testicular distribution and histologic effects of systemically administered nSP. Mice were injected intravenously with nSP with diameters of 70 nm (nSP70) or conventional microsilica particles with diameters of 300 nm (nSP300) on two consecutive days. The intratesticular distribution of these particles 24 h after the second injection was analyzed by transmission electron microscopy. nSP70 were detected within sertoli cells and spermatocytes, including in the nuclei of spermatocytes. No nSP300 were observed in the testis. Next, mice were injected intravenously with 0.4 or 0.8 mg nSP70 every other day for a total of four administrations. Testes were harvested 48 h and 1 week after the last injection and stained with hematoxylin–eosin for histologic analysis. Histologic findings in the testes of nSP70-treated mice did not differ from those of control mice. Taken together, our results suggest that nSP70 can penetrate the blood-testis barrier and the nuclear membranes of spermatocytes without producing apparent testicular injury.

1. Introduction

With recent developments in nanotechnology, various kinds of nanomaterials have been designed and produced throughout the world. The small particle size and large surface area relative to volume enables nanomaterials to display a number of useful properties that are different from those of bulk materials, including high levels of electrical conductivity, tensile strength, electronic reactivity, and tissue permeability [1]. Because of these properties, nanomaterials have been widely used in consumer and industrial applications. In particular, amorphous nanosilica particles (nSP) possess a variety of unique properties, such as ease of synthesis, relatively low cost, and availability of sites for surface modifications [2,3], and nSP are increasingly being used for applications including cosmetics, foods, and drugs. However, several reports have shown that nSP might induce adverse effects such as pulmonary inflammation [4] and hemolysis [5]. Because nanomaterials have the potential to improve the quality of human life, it is essential to insure their safety and obtain the information necessary for designing safe nanomaterials. For the development of safe nanomaterials, we have been investigating the biologic distribution and biologic effects of nSP. We have already found that nSP can pass through biologic barriers, such as skin, the blood-brain barrier [6], and the blood-placental barrier [7] in mice. In addition, we found that nSP induces oxidative stress and DNA damage [8], allergic immune responses [9], and pregnancy complications [7] in mice, although the administration dose of nSP was higher than the dose of the human occupational exposure situation. Furthermore, we showed that surface modification of nSP with amine or carboxyl groups altered the intracellular distribution of the nSP and had an effect on cell proliferation [10], and suppressed toxic biologic effects of nSP such as pregnancy complications [7], indicating that surface modification prevented adverse effects of nSP and would be an approach to create safer nanomaterials.

* Corresponding authors. Address: Laboratory of Toxicology and Safety Science, Graduate School of Pharmaceutical Sciences, Osaka University, 1-6 Yamadaoka, Suita, Osaka 565-0871, Japan. Fax: +81 6 6879 8234.
E-mail addresses: yasuo@phs.osaka-u.ac.jp (Y. Yoshioka), ytsutsumi@phs.osaka-u.ac.jp (Y. Tsutsumi).

0006-291X/$ - see front matter © 2012 Elsevier Inc. All rights reserved.
doi:10.1016/j.bbrc.2012.02.153

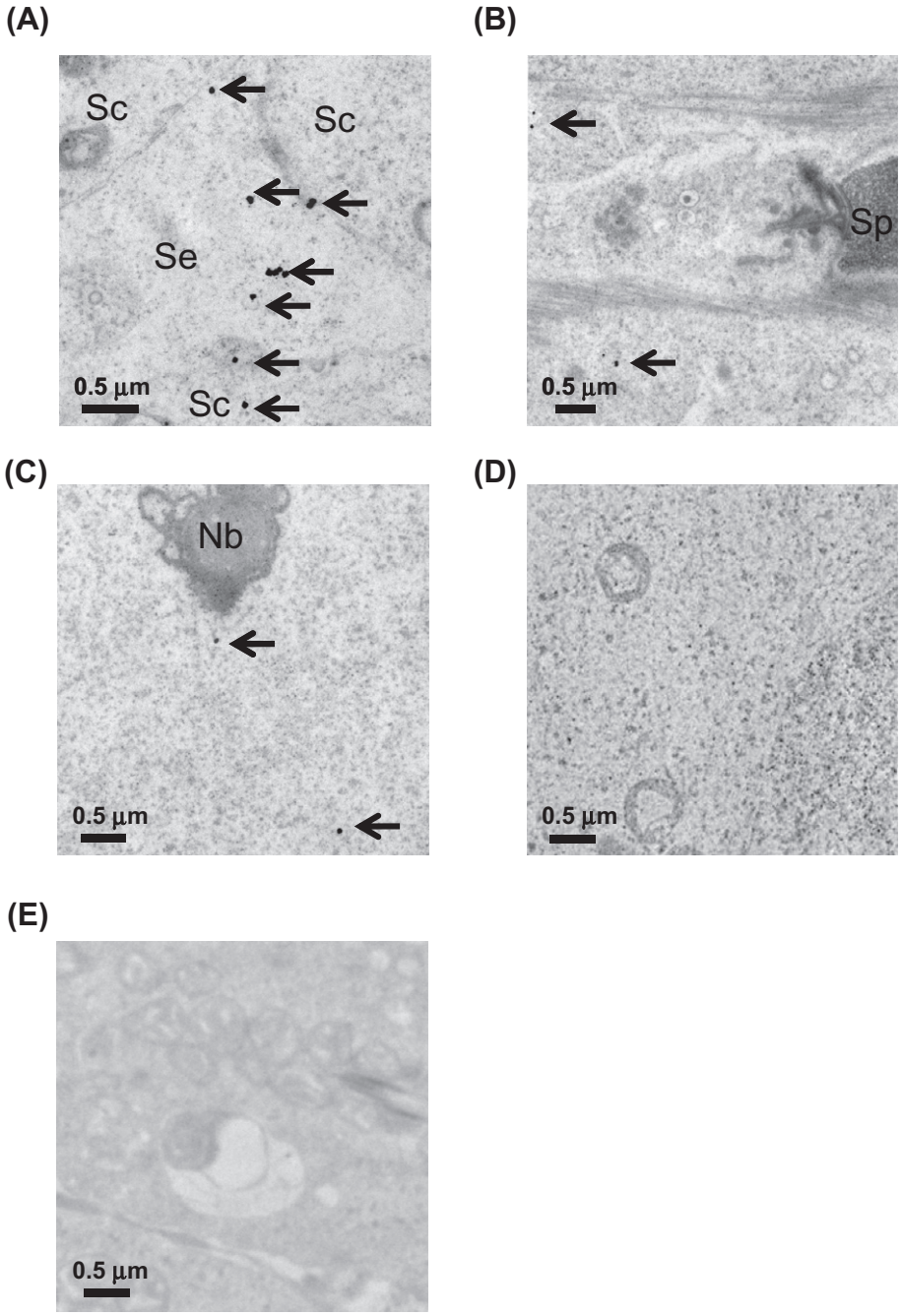

Fig. 1. Transmission electron micrographs of silica particles biodistribution in the testis. BALB/c mice were intravenously administered 0.8 mg of nSP70, nSP300, or saline on two consecutive days. Arrows indicate nSP70 present in Sertoli cells and spermatocytes (A), near sperm (B), and in the nucleus of a spermatocyte (C). No particles were observed in testes of nSP300 (D) or control mice (E). Sc: spermatocyte, Se: Sertoli cell, Sp: sperm, Nb: nuclear body.

Rates of male infertility continue to increase, and male infertility has been a difficult problem to solve [11]. Male infertility is for the most part caused by dysfunction of the testes. The testes are sensitive to many chemicals, such as endocrine disruptors [12], pesticides [13,14], and anticancer agents [15]. Therefore, to insure the reproductive safety of nSP, it is important to investigate their biologic effects on the testis. The toxicity of nanomaterials [16,17] and nanoparticle-rich diesel exhaust [18,19] to male reproductive functions has been investigated. For example, Bai et al. showed that multiwalled carbon nanotubes are distributed to the testis, where they induce reversible damage [17]. However, few studies have investigated the effect of nSP on the male reproductive system or the distribution of nanomaterials in testis and male germ cells, although information about the intra-testicular distribution would greatly help to elucidate the effect of nanomaterials on male reproductive systems.

Here, we qualitatively evaluated the intra-testicular distribution of nSP after intravenous administration in mice, including penetration of the blood-testis barrier and the distribution of nSP to germ cells. We also investigated the histologic effects of nSP on the testis.

2. Materials and methods

2.1. Silica particles

Amorphous silica particles (nSP70, 70-nm diameter; nSP300, 300-nm diameter) were purchased from Micromod Partikeltech-

nologie (Rostock-Warnemuende, Germany). The silica particles were used after 5 min of sonication (280 W output; Ultrasonic Cleaner, AS One, Osaka, Japan) and 1 min of vortexing.

2.2. Physicochemical examination of silica particles

Silica particles were diluted with PBS to 0.25 mg/mL (nSP70) or 0.5 mg/mL (nSP300), and the average particle size and zeta potential were measured using the Zetasizer Nano-ZS (Malvern Instruments Ltd., Worcestershire, UK). The mean size and the size distribution of silica particles were measured with the dynamic light scattering method. The zeta potential was measured by using laser Doppler electrophoresis.

2.3. Animals

BALB/c mice (male, 9 weeks old) were purchased from Japan SLC (Shizuoka, Japan). Mice were allowed to habituate to the animal room for 1 week prior to their use. The experimental protocols conformed to the ethical guidelines of Osaka University and the National Institute of Biomedical Innovation, Japan.

2.4. Transmission electron microscopy

BALB/c mice were injected intravenously through the tail vein with 100 μL (0.8 mg) of nSP70 or nSP300 on two consecutive days. The mice were anaesthetized and killed 24 h after the second injection, and the testes were fixed in 2.5% glutaraldehyde for 2 h. Small pieces of tissue collected from these samples were washed with phosphate buffer, postfixed in sodium cacodylate-buffered 1.5% osmium tetroxide for 60 min at 48 °C, dehydrated using a series of ethanol concentrations, and embedded in Epon resin. The samples were examined under a Hitachi electron microscope (H-7650; Hitachi, Tokyo, Japan).

2.5. Histology

Mice were given four doses of 100 μL (0.4 or 0.8 mg) nSP70 or saline (control), given intravenously through the tail vein every other day. Testes were collected 48 h or 1 week after the last administration. The testes were weighed and fixed in 10% neutral buffered formalin solution, dehydrated in a graded series of ethanol and xylene solutions, and embedded in paraffin. Sections were cut with a microtome, deparaffinized, rehydrated in a graded series of ethanols, and stained with hematoxylin and eosin.

2.6. Plasma biochemical analysis

Liver function was evaluated by measuring the plasma levels of alanine aminotransferase (ALT) and aspartate aminotransferase (AST). Nephrotoxicity was evaluated by measuring the plasma level of blood urea nitrogen (BUN). These markers were assayed by using a biochemical autoanalyzer, FUJI DRI-CHEM 7000 (Fujifilm, Tokyo, Japan).

2.7. Statistical analysis

All results are presented as means ± standard deviation (SD). Differences were compared by using Bonferroni's method after analysis of variance (ANOVA).

3. Results

Here we used nanosilica particles with diameters of 70 nm (nSP70) and conventional microsilica particles with diameters of 300 nm (nSP300). All of the silica particles were confirmed to be smooth-surfaced spheres, as we had previously described [6]. The hydrodynamic diameters of nSP70 and nSP300 were 77.0 and 269.3 nm, respectively, with zeta potentials of −21.6 and −31.3, respectively. The size distribution spectrum of each silica particle showed a single peak, and the hydrodynamic diameter corresponded almost precisely to the primary particle size for each sample, indicating that the silica used in this study were well-dispersed in solution (data not shown).

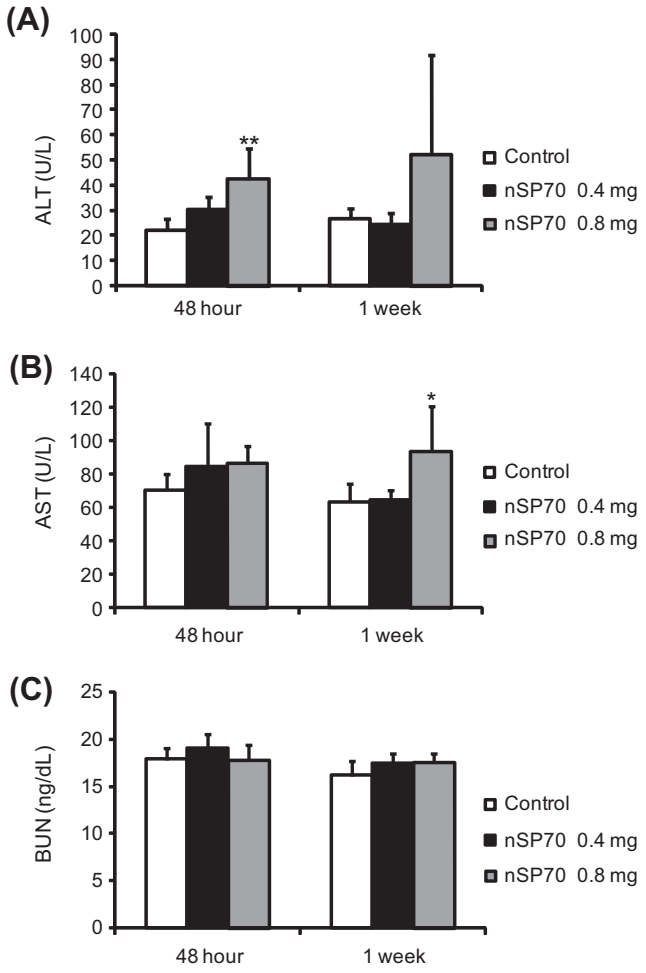

Fig. 2. Changes in liver and kidney damage markers in mouse plasma. Mice were given 0.4 or 0.8 mg nSP70 or saline intravenously every other day for a total of 4 doses. ALT (A), AST (B), and BUN (C) levels in plasma were evaluated 48 h and 1 week after the last injection. All data were presented as means ± SD ($n = 5$; $^{*}P < 0.05$, $^{**}P < 0.01$ versus value for control).

We had already found that nSP70 can enter the blood circulation after dermal administration [6]. To assess the biodistribution from the blood circulation, we used TEM to analyze the intratesticular distribution of each silica particle after intravenous injection. Dots with sharp outlines and appropriate sizes (70 nm for nSP70, 300 nm for nSP300) were identified as silica particles. The nSP70 were found in Sertoli cells, spermatocytes, and near sperm (Fig. 1A, B) and in both the cytoplasm and nuclei of spermatocytes (Fig. 1C). No particles were observed in testes of mice injected with nSP300 or of control mice (Fig. 1D, E). Although TEM provides only qualitative information, these results suggest that nSP70 were able to penetrate the blood-testis barrier and into the nuclei of spermatocytes, whereas nSP300 were not. The findings for nSP70, but not nSP300, are consistent with our previous results showing that nSP70 is distributed to placenta through blood-placental barrier [7].

Next, to evaluate whether nSP70 produce histologic effects on the testis, we administered four doses of 0.4 or 0.8 mg nSP70 intravenously every other day. The blood levels of ALT (Fig. 2A), ALT (Fig. 2B), and BUN (Fig. 2C) remained within the physiologic range, indicating that nSP70 did not induce liver and kidney damage at the administered doses, although some significant changes were observed in ALT and AST. Furthermore, the testes were weighed and analyzed histologically 48 h and 1 week after the last injection. Testis weights (Fig. 3A) and histologic findings (Fig. 3B) were not different in the testes of nSP70-treated mice and control mice. These results indicate that nSP70 can penetrate the blood-testis barrier without producing apparent testicular injury.

4. Discussion

In this study, we showed that nSP70, but not nSP300, were able to cross the blood-testis barrier. The limited histologic effects on the testes indicated that nSP70 may be actively transported across it without producing apparent testicular injury, although further investigation of the function of the blood-testis barrier in nSP70-treated mice is needed. By imaging fluorescently labeled nanoparticles, Kim et al. showed that 50-nm magnetic nanoparticles can also penetrate the mouse blood-testis barrier [20]. Therefore, the penetration of the blood-testis barrier is not specific to nSP. On the other hand, it is known that high-molecular-weight species (>500 Da) do not penetrate the blood-testis barrier by passive diffusion [21]. In fact, De Jong et al. showed with inductively coupled plasma mass spectrometry that gold nanoparticles larger than 50 nm were not distributed in the testis after intravenous administration [22]. Although differences in the dose or duration of administration and in the detection method might account for the different results, these findings suggest that the testicular distribution of nanomaterials might depend on the type of material. In this study, we evaluated the testicular distribution of nSP qualitatively, but testicular distribution of nanomaterials has also been evaluated quantitatively [17,23]. For example, Bai et al. measured the radioactivity of ^{64}Cu-labeled multiwalled carbon nanotubes in the testes of mice [17]. In future, the testicular distribution of nSP should also be quantitatively analyzed to further assess the reproductive safety of nSP.

We showed that nSP70 cause little overt testicular injury, although production of reproductive hormones and sperm function should also be examined. In contrast to our results with nSP70, intravenous administration of multiwalled carbon nanotubes do induce testis damage [17]. The total dose of nanomaterials that we administered in the current report was about five times higher than the total dose in the previous nanotube study. Therefore, we presume that nSP70 are safer to the testis than are multiwalled carbon nanotubes, although the duration of administration should also be taken into consideration.

Although nSP70 produced little testicular injury, the presence of nSP70 in the nuclei of spermatocytes suggests that DNA in the male germ line might be affected by nSP70. Abnormal DNA in the male germ line has been associated with an increased incidence of morbidity in the offspring [24], and paternal exposure to environmental factors has been suggested to influence biologic functions in offspring [25–27]. Therefore, the transgenerational effects of nSP as well as the direct effects on sperm should be evaluated in future studies.

In conclusion, this study showed that nSP70 can penetrate the blood-testis barrier without producing apparent testicular injury.

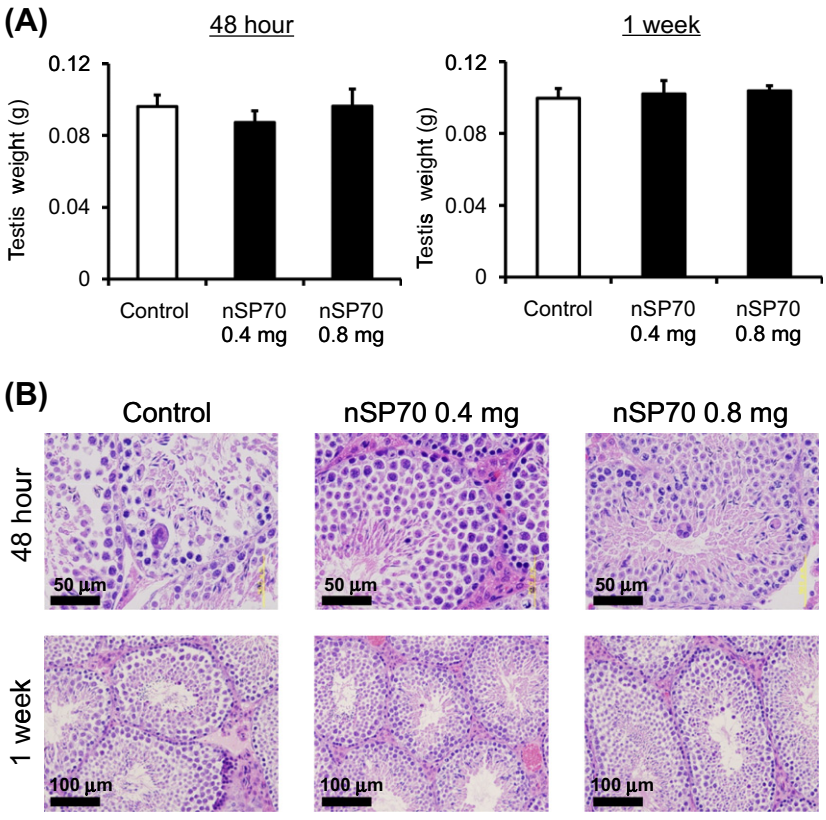

Fig. 3. Weight and pathological examination of the testis after four doses of nSP70. BALB/c mice were intravenously administered 0.4 or 0.8 mg of nSP70 or saline every other day for a total of four doses. Testes were weighed (A) and stained with hematoxylin–eosin (B) 48 h and 1 week after the last injection. Testis weight and histologic findings did not differ between nSP70-treated mice and control mice. All data were presented as means ± SD ($n = 5$).

Acknowledgments

This study was supported in part by Grants-in-Aid for Scientific Research from the Ministry of Education, Culture, Sports, Science and Technology of Japan (MEXT), and from the Japan Society for the Promotion of Science (JSPS); and by a the Knowledge Cluster Initiative (MEXT); by Health Labour Sciences Research Grants from the Ministry of Health, Labor and Welfare of Japan (MHLW); by a Global Environment Research Fund from Minister of the Environment; by Food Safety Commission (Cabinet Office); by The Cosmetology Research Foundation; by The Smoking Research Foundation; by The Takeda Science Foundation.

References

[1] O. Salata, Applications of nanoparticles in biology and medicine, J. Nanobiotechnol. 2 (2004) 3.
[2] T.K. Barik, B. Sahu, V. Swain, Nanosilica-from medicine to pest control, Parasitol Res. 103 (2008) 253–258.
[3] B. Fadeel, A.E. Garcia-Bennett, Better safe than sorry: understanding the toxicological properties of inorganic nanoparticles manufactured for biomedical applications, Adv. Drug Deliv. Rev. 62 (2010) 362–374.
[4] A.S. Yazdi, G. Guarda, N. Riteau, S.K. Drexler, A. Tardivel, I. Couillin, J. Tschopp, Nanoparticles activate the NLR pyrin domain containing 3 (Nlrp3) inflammasome and cause pulmonary inflammation through release of IL-1alpha and IL-1beta, Proc. Natl. Acad. Sci. USA 107 (2010) 19449–19454.
[5] T. Yu, A. Malugin, H. Ghandehari, Impact of silica nanoparticle design on cellular toxicity and hemolytic activity, ACS Nano 5 (2011) 5717–5728.
[6] H. Nabeshi, T. Yoshikawa, K. Matsuyama, Y. Nakazato, K. Matsuo, A. Arimori, M. Isobe, S. Tochigi, S. Kondoh, T. Hirai, T. Akase, T. Yamashita, K. Yamashita, T. Yoshida, K. Nagano, Y. Abe, Y. Yoshioka, H. Kamada, T. Imazawa, N. Itoh, S. Nakagawa, T. Mayumi, S. Tsunoda, Y. Tsutsumi, Systemic distribution, nuclear entry and cytotoxicity of amorphous nanosilica following topical application, Biomaterials 32 (2011) 2713–2724.
[7] K. Yamashita, Y. Yoshioka, K. Higashisaka, K. Mimura, Y. Morishita, M. Nozaki, T. Yoshida, T. Ogura, H. Nabeshi, K. Nagano, Y. Abe, H. Kamada, Y. Monobe, T. Imazawa, H. Aoshima, K. Shishido, Y. Kawai, T. Mayumi, S. Tsunoda, N. Itoh, T. Yoshikawa, I. Yanagihara, S. Saito, Y. Tsutsumi, Silica and titanium dioxide nanoparticles cause pregnancy complications in mice, Nat. Nanotechnol. 6 (2011) 321–328.
[8] H. Nabeshi, T. Yoshikawa, K. Matsuyama, Y. Nakazato, S. Tochigi, S. Kondoh, T. Hirai, T. Akase, K. Nagano, Y. Abe, Y. Yoshioka, H. Kamada, N. Itoh, S. Tsunoda, Y. Tsutsumi, Amorphous nanosilica induce endocytosis-dependent ROS generation and DNA damage in human keratinocytes, Part Fibre Toxicol. 8 (2011) 1.
[9] T. Yoshida, Y. Yoshioka, M. Fujimura, K. Yamashita, K. Higashisaka, Y. Morishita, H. Kayamuro, H. Nabeshi, K. Nagano, Y. Abe, H. Kamada, S. Tsunoda, N. Itoh, T. Yoshikawa, Y. Tsutsumi, Promotion of allergic immune responses by intranasally-administrated nanosilica particles in mice, Nanoscale Res. Lett. 6 (2011) 195.
[10] H. Nabeshi, T. Yoshikawa, A. Arimori, T. Yoshida, S. Tochigi, T. Hirai, T. Akase, K. Nagano, Y. Abe, H. Kamada, S. Tsunoda, N. Itoh, Y. Yoshioka, Y. Tsutsumi, Effect of surface properties of silica nanoparticles on their cytotoxicity and cellular distribution in murine macrophages, Nanoscale Res. Lett. 6 (2011) 93.
[11] S.S. Howards, Treatment of male infertility, N. Engl. J. Med. 332 (1995) 312–317.
[12] C.B. Herath, W. Jin, G. Watanabe, K. Arai, A.K. Suzuki, K. Taya, Adverse effects of environmental toxicants, octylphenol and bisphenol A, on male reproductive functions in pubertal rats, Endocrine 25 (2004) 163–172.
[13] S.Y. Zhang, Y. Ito, O. Yamanoshita, Y. Yanagiba, M. Kobayashi, K. Taya, C. Li, A. Okamura, M. Miyata, J. Ueyama, C.H. Lee, M. Kamijima, T. Nakajima, Permethrin may disrupt testosterone biosynthesis via mitochondrial membrane damage of Leydig cells in adult male mouse, Endocrinology 148 (2007) 3941–3949.
[14] A.T. Farag, A.H. Radwan, F. Sorour, A. El Okazy, S. El-Agamy el, K. El-Sebae Ael, Chlorpyrifos induced reproductive toxicity in male mice, Reprod. Toxicol. 29 (2010) 80–85.
[15] N. Elangovan, T.J. Chiou, W.F. Tzeng, S.T. Chu, Cyclophosphamide treatment causes impairment of sperm and its fertilizing ability in mice, Toxicology 222 (2006) 60–70.
[16] S. Yoshida, K. Hiyoshi, T. Ichinose, H. Takano, S. Oshio, I. Sugawara, K. Takeda, T. Shibamoto, Effect of nanoparticles on the male reproductive system of mice, Int. J. Androl. 32 (2009) 337–342.
[17] Y. Bai, Y. Zhang, J. Zhang, Q. Mu, W. Zhang, E.R. Butch, S.E. Snyder, B. Yan, Repeated administrations of carbon nanotubes in male mice cause reversible testis damage without affecting fertility, Nat. Nanotechnol. 5 (2010) 683–689.
[18] C. Li, S. Taneda, K. Taya, G. Watanabe, X. Li, Y. Fujitani, Y. Ito, T. Nakajima, A.K. Suzuki, Effects of inhaled nanoparticle-rich diesel exhaust on regulation of testicular function in adult male rats, Inhal. Toxicol. 21 (2009) 803–811.
[19] D.H. Ramdhan, Y. Ito, Y. Yanagiba, N. Yamagishi, Y. Hayashi, C. Li, S. Taneda, A.K. Suzuki, G. Watanabe, K. Taya, M. Kamijima, T. Nakajima, Nanoparticle-rich diesel exhaust may disrupt testosterone biosynthesis and metabolism via growth hormone, Toxicol. Lett. 191 (2009) 103–108.
[20] J.S. Kim, T.J. Yoon, K.N. Yu, B.G. Kim, S.J. Park, H.W. Kim, K.H. Lee, S.B. Park, J.K. Lee, M.H. Cho, Toxicity and tissue distribution of magnetic nanoparticles in mice, Toxicol. Sci. 89 (2006) 338–347.
[21] Y. Jin, I. Uchida, K. Eto, T. Kitano, S. Abe, Size-selective junctional barrier and Ca(2+)-independent cell adhesion in the testis of Cynops pyrrhogaster: expression and function of occludin, Mol. Reprod. Dev. 75 (2008) 202–216.
[22] W.H. De Jong, W.I. Hagens, P. Krystek, M.C. Burger, A.J. Sips, R.E. Geertsma, Particle size-dependent organ distribution of gold nanoparticles after intravenous administration, Biomaterials 29 (2008) 1912–1919.
[23] S.K. Balasubramanian, J. Jittiwat, J. Manikandan, C.N. Ong, L.E. Yu, W.Y. Ong, Biodistribution of gold nanoparticles and gene expression changes in the liver and spleen after intravenous administration in rats, Biomaterials 31 (2010) 2034–2042.
[24] R.J. Aitken, G.N. De Iuliis, R.I. McLachlan, Biologic and clinical significance of DNA damage in the male germ line, Int. J. Androl. 32 (2009) 46–56.
[25] M.D. Anway, A.S. Cupp, M. Uzumcu, M.K. Skinner, Epigenetic transgenerational actions of endocrine disruptors and male fertility, Science 308 (2005) 1466–1469.
[26] S.F. Ng, R.C. Lin, D.R. Laybutt, R. Barres, J.A. Owens, M.J. Morris, Chronic high-fat diet in fathers programs beta-cell dysfunction in female rat offspring, Nature 467 (2010) 963–966.
[27] B.R. Carone, L. Fauquier, N. Habib, J.M. Shea, C.E. Hart, R. Li, C. Bock, C. Li, H. Gu, P.D. Zamore, A. Meissner, Z. Weng, H.A. Hofmann, N. Friedman, O.J. Rando, Paternally induced transgenerational environmental reprogramming of metabolic gene expression in mammals, Cell 143 (2010) 1084–1096.

Biochemical and Biophysical Research Communications 420 (2012) 302–307

Contents lists available at SciVerse ScienceDirect

Biochemical and Biophysical Research Communications

journal homepage: www.elsevier.com/locate/ybbrc

Molecular characterization of the *Trypanosoma cruzi* specific RNA binding protein TcRBP40 and its associated mRNAs

Eloise P. Guerra-Slompo, Christian M. Probst, Daniela P. Pavoni, Samuel Goldenberg, Marco A. Krieger, Bruno Dallagiovanna *

Instituto Carlos Chagas, Fiocruz-Paraná, Rua Professor Algacyr Munhoz Mader 3775, 81350-010 CIC Curitiba, Brazil

ARTICLE INFO

Article history:
Received 14 February 2012
Available online 7 March 2012

Keywords:
Trypanosoma cruzi
RNA Recognition Motif
TcRBP40
Reservosomes

ABSTRACT

Trypanosoma cruzi is the causative agent of Chagas disease, a neglected disorder that affects millions of people in the Americas. *T. cruzi* relies mostly upon post-transcriptional regulation to control stage specific gene expression. RNA binding proteins (RBPs) associate with functionally related mRNAs forming ribonucleoprotein complexes that define post-transcriptional operons. The RNA Recognition Motif (RRM) is the most common and ancient family of RBPs. This family of RBPs has been identified in trypanosomatid parasites and only a few of them have been functionally characterized. We describe here the functional characterization of TcRBP40, a *T. cruzi* specific RBP, and its associated mRNAs. We used a modified version of the recombinant RIP-Chip assay to identify the mRNAs with which it associates and *in vivo* TAP-tag assays to confirm these results. TcRBP40 binds to an AG-rich sequence in the 3′UTR of the associated mRNAs, which were found to encode mainly putative transmembrane proteins. TcRBP40 is differentially expressed in metacyclogenesis. Surprisingly, in epimastigotes, it is dispersed in the cytoplasm but is concentrated in the reservosomes, a *T. cruzi* specific organelle, which suggests a putative new function for this parasite organelle.

1. Introduction

Chagas' disease is a parasitic illness that compromises the quality of life of millions of people in the Americas. The causative agent is *Trypanosoma cruzi*, a flagellated protozoon from the kinetoplastid order, which infects mammalian hosts through transmission by a triatomine insect. Its life cycle has at least four well defined forms. [1]. In kinetoplastids there is no evidence of transcriptional regulation of protein-coding genes. Transcription occurs on polycistronic units guided by non-canonical RNA polymerase II promoters [2]. These promoters show no specific regulation of transcriptional initiation for the whole polycistron or for individual genes. These findings strongly suggest that regulation of gene expression occurs mainly at the post-transcriptional level [3].

RNA binding proteins (RBPs) associate with mRNA molecules and other regulatory proteins, forming ribonucleoprotein (mRNP) complexes, which are involved in several levels of RNA regulation [4]. The RNA Recognition Motif (RRM) is the most common RNA interacting domain found in proteins. It has 70–90 aminoacids and two known motifs of 8 and 5 aminoacids, RNP-1 and RNP-2 respectively, which interact directly with the RNA molecule [5]. In *T. cruzi* De Gaudenzi and cols. [6] identified 77 non-redundant RRM proteins within the parasite genome. Genome-wide profiling of the mRNA expression patterns in *T. brucei* suggests the existence of multiple post-transcriptional operons in trypanosome parasites [7].These operons contain transcripts with a variety of functions, though mRNAs of known metabolic pathways were often co-regulated, strongly suggesting the existence of RNA regulons [8–10].

The ribonomic approach has been used to identify the bound mRNAs of different RBPs in several organisms [11]. In trypanosomatids, some RBPs have been characterized using this approach. TcPUF6 and TbPUF9 mRNA targets were identified by affinity purification of tagged proteins and microarray hybridization [12,13]. Alternatively, an immunoprecipitation method was used for purification of TcUBP1 and TcRBP3 targets, [14]. Altogether, these studies show that RBPs are responsible for the regulation of specific sets of RNAs in the cell. Here we report the functional characterization of TcRBP40, a *T. cruzi* specific RRM protein.

2. Materials and methods

2.1. Parasites

The *T. cruzi* clone Dm28c [15] was used throughout this work. Epimastigote forms were maintained at 28 °C in liver infusion

* Corresponding author. Fax: +55 41 33163267.
E-mail address: brunod@tecpar.br (B. Dallagiovanna).

0006-291X/$ - see front matter © 2012 Elsevier Inc. All rights reserved.
http://dx.doi.org/10.1016/j.bbrc.2012.02.154

tryptose (LIT) medium supplemented with 10% heat inactivated fetal bovine serum (FBS). Metacyclic trypomastigotes and amastigotes were prepared as described [16].

2.2. Bioinformatic analysis

A consensus domain was created based on RRMs from other eukaryotes. Proteins from the *T. cruzi* genome database (GeneDB) containing RRM were identified with HMMER2.0 [17,18]. Retrieved matches were analyzed according to the e-value number of domain. Low-score sequences were manually analyzed. The TMHMM program was used for predicting transmembrane motifs on default parameters.

2.3. Cloning and expression of the TcRBP40 recombinant protein

The coding region of TcRBP40 from *T. cruzi* Dm 28c genomic DNA was PCR-amplified and cloned into the pDEST17 vector (Gateway®, Invitrogen), for the production of an *N*-terminal His-tagged recombinant protein. Cell culture was stress-induced with 3% ethanol for 1 h prior to IPTG induction (0.1 mM). The recombinant protein was purified in native conditions, using Ni–NTA Agarose (Qiagen) as recommended.

2.4. Production of polyclonal antiserum and Western blot analysis

A polyclonal antiserum was raised in Swiss mice as described [18]. This study was carried out in strict accordance with the recommendations in the guide for animal use of the FIOCRUZ Committee on Animal Experimentation, protocol number P-0434/07. Protein extracts from the different parasite forms were prepared as described in [18].

2.5. RNA pull-down assay

For the recombinant protein pull-down assays, 50 μg of recombinant His-tag TcRBP40 protein were bound to 100 uL of Ni–NTA resin (Qiagen) overnight at 4 °C. 100 μg of total RNA from epimastigotes were incubated with the bound protein in 500 μl EMSA buffer at 4 °C for 2 h, in the presence of Heparine and Spermidine as competitors. Bound and supernatant samples were separated. The bound sample was washed with the same buffer three times, for 10 min each. After washing, RNAs present in the bound and supernatant fractions were purified.

2.6. RNA purification and amplification

RNA was extracted using the RNeasy mini kit (Qiagen). Linearly amplified RNA (aRNA) was generated with the MessageAmp™II aRNA Amplification kit (Ambion), in accordance with the manufacturer's instructions.

2.7. Microarray analysis

The microarray was constructed with 70-mer oligonucleotides. All coding regions (CDS) identified in the genome (version 3) were clustered by the BLASTClust program, using parameters of 40% coverage and 75% identity. For probe design, the software ArrayOligoSelector (v. 3.8.1) was used, with a parameter of 50% G+C content. This obtained 10,359 probes for the longest *T. cruzi* CDS of each cluster, 393 probes corresponding to the genes of an external group (Cryptosporidium hominis), and 64 spots containing only spotting solution (SSC 3x), giving a total of 10,816 spots. These oligonucleotides were spotted from a 50 μM solution onto poly-L-lysine coated slides and cross-linked with 600 mJ UV. Probes were identified according to the *T. cruzi* Genome Consortium annotation (http://www.genedb.org). We compared bound and unbound to TcRBP40 protein mRNA, extracted from independent pull-down assays, in a dye-swap design. Images were analyzed by Spot software. The Limma package [19] was used for background correction by the normexp method, intra-slide normalization by the printtiploess method and inter-slide normalization by the quantile method. Microarray data have been deposited on ArrayExpress, with accession number E-MEXP-3057.

2.8. Tandem affinity purification assay

The coding sequence of the *TcRBP40* gene was inserted into a p*Tc*TAPN vector. *T. cruzi* epimastigotes (5×10^7 cells) were transfected with 30 μg of vector DNA as described [12]. We added 250 μg/ml geneticin 24 h and 500 μg/ml 72 h after electroporation, for the selection of transfected parasites. TAP-tag assays of bound proteins and RNAs were performed as previously described [12]. The tagged proteins were purified on IgG-Sepharose columns (Amersham).

2.9. cDNA synthesis and PCR

cDNA was synthesized from 1 μg of total or affinity-purified RNAs, with an oligo-dT primer (USB Corporation) and reverse transcriptase (ImProm-II™ Reverse Transcriptase, Promega), as recommended. PCR conditions and primers are described in Table S3. Bands were quantified by Scion Image 4.0.3.2 software (http://www.scioncorp.com) and fold changes were calculated by test/control ratio. Two-step real-time reverse transcription-PCR assays were performed using the ABI PRISM 7000 sequence detection system (Applied Biosystems). For relative quantification, the standard curve method was used, based on cycle threshold values. Gene expression was normalized against the *TcL9* control gene [18].

2.10. Gel shift assays

Binding reactions and EMSA were performed as previously described [20]. Probes were all end-labeled with T4 polynucleotide kinase (Roche) and [γ-^{32}P]ATP (Amersham Biosciences), as recommended, following probe purification. Binding reactions were performed by adding 1 μg of the recombinant TcRBP40 protein to the reaction mixture. Oligoribonucleotides were obtained from Midland Certified Reagent Co. and are shown in Table S3.

2.11. Immunofluorescence assays

Immunofluorescence assays were performed as described [18]. Serum dilutions were: mouse anti-TcRBP40 1:100 and rabbit anti-cruzipain 1:200. AlexaFluor 488 conjugated anti mouse and AlexaFluor 546 conjugated anti rabbit secondary antibodies (1:400) (Molecular Probes, Invitrogen) were used. Sub-cellular localization images were acquired using a Leica SP5 Laser Confocal Microscope (Mannheim, Germany).

3. Results

3.1. The T. cruzi RRM protein family

With the aim to characterize RBP protein families in *T. cruzi*, we performed an *in silico* search for RRM-containing proteins within the parasite's genome. First, we defined a consensus RRM domain based on RRM proteins which were deposited in the Pfam databank. The HMMER algorithm scored for seventy-four conserved aminoacid positions. The resulting matrix was used to search the

T. cruzi GeneDB database. We identified 160 gene entries in *T. cruzi* matching the consensus domain sequence. Accounting for the reported redundancy of the parasite genome, our search identified 80 proteins bearing the RRM motif (Table S1).

We identified six new proteins, named according to the proposed nomenclature for the RBP family in trypanosomatids [6]. We manually searched for the presence of at least one of the conserved RNP1 or RNP2 motifs in the RRM domain. We then performed BLAST searches in GenBank and a new manual Pfam analysis, confirming them as RRM-containing proteins. We also found two proteins (classified as RRM-like proteins) whose domains resemble the conserved motif, but do not fulfill the previous requirements. Unexpectedly, four proteins identified in the previous related study were not found in our study. One of them was confirmed as an RRM protein coding for a member of the U2AF protein complex. The other three proteins did not retrieve any RRM match, and therefore were included in the table as not confirmed. Considering the data presented, we can conclude that *T. cruzi* has 81 RRM proteins.

We selected TcRBP40 for further characterization. TcRBP40 was only identified in the *T. cruzi* genome, with no orthologues in other sequenced trypanosome genomes. The protein has 127 aminoacids, a predicted molecular weight of 14.3 kDa and a unique RRM (Fig. S1A).

We expressed a 17 kDa recombinant protein that was recovered as a soluble fusion polypeptide with an amino-terminal histidine tag (Fig. S1B). The ability of the purified recombinant protein to form complexes with the four synthetic homoribopolymer probes under standard conditions was tested by EMSA (data not shown).

3.2. TcRBP40 association with mRNAs

To identify the mRNAs that associate with TcRBP40, we used a previously described *in vitro* approach, the recombinant RIP-Chip [21]. The recombinant soluble protein was used to perform a pull-down assay to purify RNAs specifically bound to the protein, under EMSA competitive conditions. Mock assays using nikel-agarose columns with no protein rendered undetectable amounts of RNA. Amplified RNAs were labeled for microarray competitive hybridization using the non-bound fraction as the reference population. To select the putative associated transcripts we considered only spots rendering signals with a fold-change at least four times and a 1% FDR value as positive.

We retrieved 148 genes which associated with TcRBP40 (Table S2). As a control, we compared our results with those obtained with a similar assay using the RRM protein TcRBP19 [22] and we found only 15 transcripts that were shared by both proteins. Analyzing the functions of the enriched transcripts of TcRBP40, 115 of them are annotated as coding for hypothetical proteins. Among the few annotated proteins we found some to be involved in nucleic acid metabolism and protein folding processes (Fig. 1A). We also searched for conserved domains that could indicate any putative function. Almost half of these proteins contained putative transmembrane domains. We analyzed the complete proteomic repertoire of *T. cruzi*, excluding redundancy and large protein families, and calculated the frequency of transmembrane motifs. The percentage of proteins bearing putative transmembrane domains (25%, $p < 10^{-6}$), compared with the percentage found in the TcRBP40 (46%) shows the preferential association of TcRBP40 with this type of proteins (Fig. 1A).

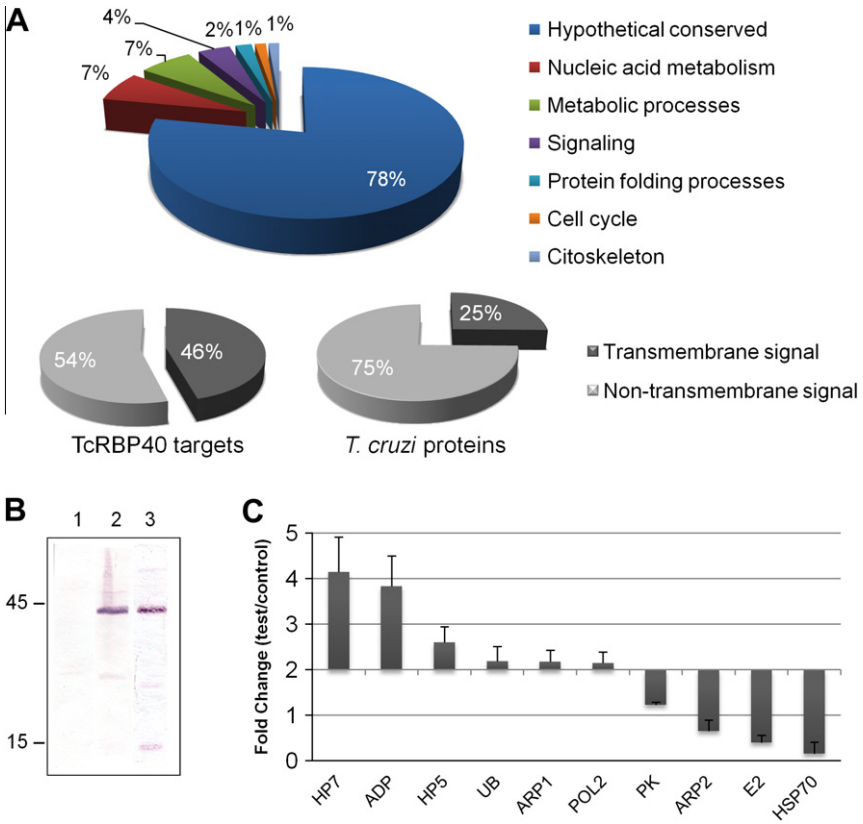

Fig. 1. Functional annotation of TcRBP40 putative targets. A) Gene entries were grouped according to biological function (GO) in upper panel. Bellow, proteins coded by TcRBP40 associated mRNAs and total *T. cruzi* proteins classified according to the presence of a putative transmembrane domain. B) Western blot of cells transfected with TAP-tag vector, incubated with TcRBP40 antibody (lane 3), showing the 45 kDa tagged protein and 15 kDa endogenous protein. Lane 2, the same extract incubated with anti-CBP tag. Control cells were transfected with vector alone, and incubated with anti-CBP (lane 1). C) Quantification of RT-PCR of mRNAs purified in TAP-tag assays. mRNAs showing a 2-fold enrichment were considered as positives. Genes named as in *Table S2*.

A TcRBP40-tagged protein was overexpressed in epimastigote forms to perform purification of *in vivo* formed complexes. We used the episomal p*Tc*TAPN vector to generate two independent transfectant clones. These populations expressed a protein of about 45 kDa resulting from the fusion with the 30 kDa tag (Fig. 1B).

We performed *in vivo* purification of the TcRBP40-RNA complexes using affinity chromatography on IgG-Sepharose columns. As a control, the vector alone was transfected and RNA from cell extracts was also purified. Precipitated RNAs were extracted and analyzed by RT-PCR using primers for 10 randomly selected genes. We obtained an enrichment of at least 2-fold for six of the genes that were tested (Fig. 1B).

Overexpression of the tagged TcRBP40 protein resulted in no evident morphological or structural changes of the cells. Moreover, transfected epimastigotes showed no altered *in vitro* growth curves and, when differentiated into metacyclic forms, no differences in the rate of cell infection were observed (not shown). We investigated whether TcRBP40 overexpression can cause changes in steady-state transcript levels of associated mRNAs. No significant changes in the abundance of TcRBP40 targets were observed (not shown).

3.3. TcRBP40 recognizes an AG-rich element in UTRs

To identify the RNA recognition element in the target transcripts, we carried out EMSAs. We searched Genbank for ESTs that could include the 3′UTRs of the confirmed transcripts. We found sequences of up to 44 nucleotides into the putative 3′ intergenic region of the RNA polymerase II subunit 9 mRNA. We considered these 44 nt as the putative 3′UTR and synthesized an RNA probe for EMSA. The recombinant protein formed a stable complex with the probe (Fig. 2B).

Three overlapping probes spanning the entire putative UTR were synthesized and tested (Fig. 2A). The recombinant protein formed complexes with all of the probes (not shown). Competition assays using the UTR1 labeled probe and the others as cold competitors showed that increasing concentrations of the other two UTR fragments did not abolish the formation of TcRBP40 complexes (Fig. 2C). When the UTR3 probe was tested, formed complexes were displaced by the cold competitors (Fig. 2D). Similar negative results were obtained with the UTR2 probe (not shown). Analysis of this initial portion showed that it has an AG-rich motif. AG-rich tracts were also present in the putative 3′UTRs of the other confirmed targets. Furthermore, the MEME algorithm also identified an AG-rich element in all positive sequences, while this motif was not present in the false positive transcripts identified (Fig. S2). The UTR1 labeled probe was competed with the probes bearing the different homoriboplymers and also with both $(AG)_{15}$ and $(UG)_{15}$ cold probes. None of these probes were able to compete with the UTR1 probe efficiently (Fig. S3).

3.4. TcRBP40 is preferentially localized in reservosomes in epimastigote forms

Antibodies against the recombinant protein were used in Western blot analysis of total protein extracts from different parasite forms. We detected a 14 kDa band, corresponding to the expected molecular mass of TcRBP40, in epimastigote forms but not in the infective metacyclic forms. A detailed analysis of the metacyclogenesis differentiation extracts showed that the protein is present in stressed and differentiating parasites and is not detected in fully differentiated metacyclic forms (Fig. 3).

In cell-derived amastigotes and cellular trypomastigotes TcRBP40 was localized in the cytoplasm in a granular distribution (Fig. 4C). As expected, no signal was observed in the metacyclic trypomastigote forms (Fig. 4B). When epimastigote forms were analyzed, TcRBP40 showed a diffuse pattern of expression throughout the cytoplasm with a strong signal localized in discrete foci in

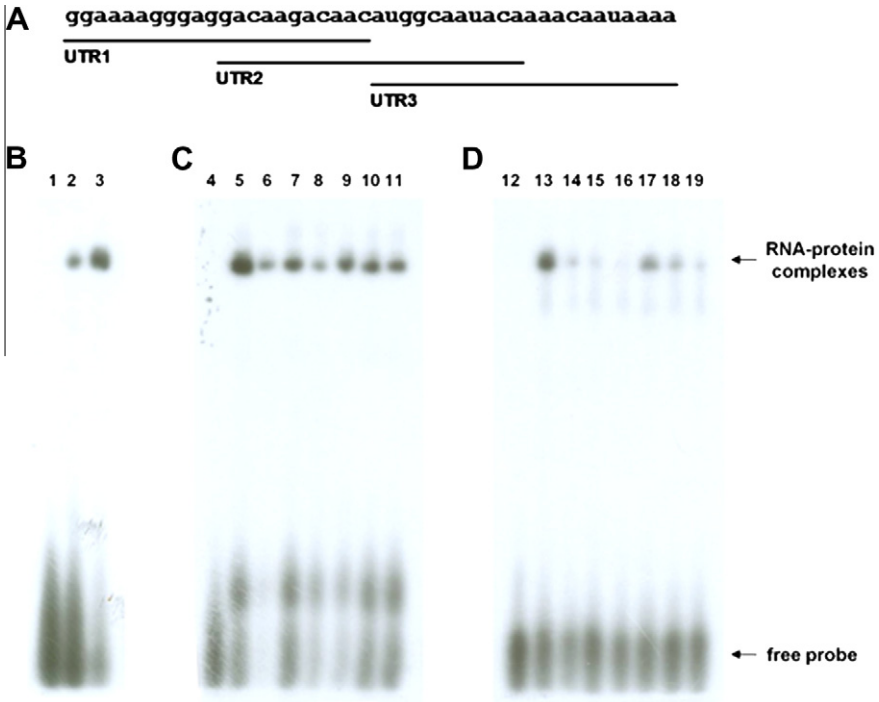

Fig. 2. Identification of TcRBP40 binding element. (A) 3′UTR sequence of RNA polymerase II subunit 9 mRNA. Overlapping lines indicate the 3 probes, named UTR1–3. B) TcRBP40 protein complex formation with the entire 3′UTR. Lanes 2 and 3 assays with increasing protein concentrations. (C and D) Competitive binding of TcRBP40 with UTR1 (C) and UTR3 (D) cold probes. Lanes 5 and 13 contains labeled probes with TcRBP40 recombinant protein. Competition assays with increasing concentrations (2, 5 and 10×) of UTR2 cold probe (6–8) and UTR3 cold probe (9–11) competing with UTR1 labeled probe, and UTR1 cold probe (14–16) and UTR2 cold probe (17–19) competing with UTR3 labeled probe. 1, 4, and 12 are the respective free probes.

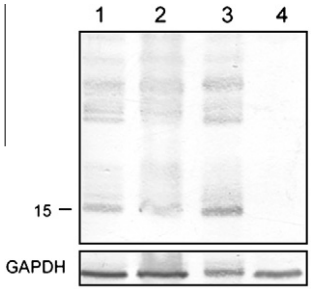

Fig. 3. Expression of TcRBP40 protein on *T. cruzi* metacyclogenesis. Western blot of protein extracts from various stages of the parasite's life cycle: (1) epimastigotes; (2) stressed epimastigotes; (3) adhered stressed epimastigotes for 24 h; (4) metacyclic trypomastigotes. Lower pannel shows loading control using anti-GAPDH serum.

the posterior region of the cell (Fig. 4A). These foci resemble the localization of reservosomes, a *T. cruzi* specific specialized organelle [23]. The posterior localization of TcRBP40 is even more evident in nutritionally-stressed epimastigotes (Fig. 4B), and is also observed in differentiating epimastigotes albeit slightly reduced as also occurs with reservosomes. We performed co-localization studies with cruzipain, a specific reservosome marker [24]. Confocal microscopy assays showed that both proteins co-localize in the interior of reservosomes (Fig. 4D).

4. Discussion

De Gaudenzi and cols. [6] described and annotated the RRM containing protein family in Tritryps. In the present study, we performed a new search for RRM containing RBPs using a slightly different approach. As expected, most of the previously characterized proteins were identified, even though we found some new putative members of this family. These differences are probably due to the different approaches used in both searches, as most of the new putative RRM proteins identified showed low identity scores. However, functional analyses are necessary to define these proteins as real RBPs.

We selected the TcRBP40 protein because it is a *T. cruzi* specific RBP. RBPs are usually regulators of gene expression, and species-specific RBPs could establish and regulate new or different gene regulatory networks [26]. The identification and characterization of these regulatory networks could help in the understanding of the processes that define and control the particular features of each parasite [25].

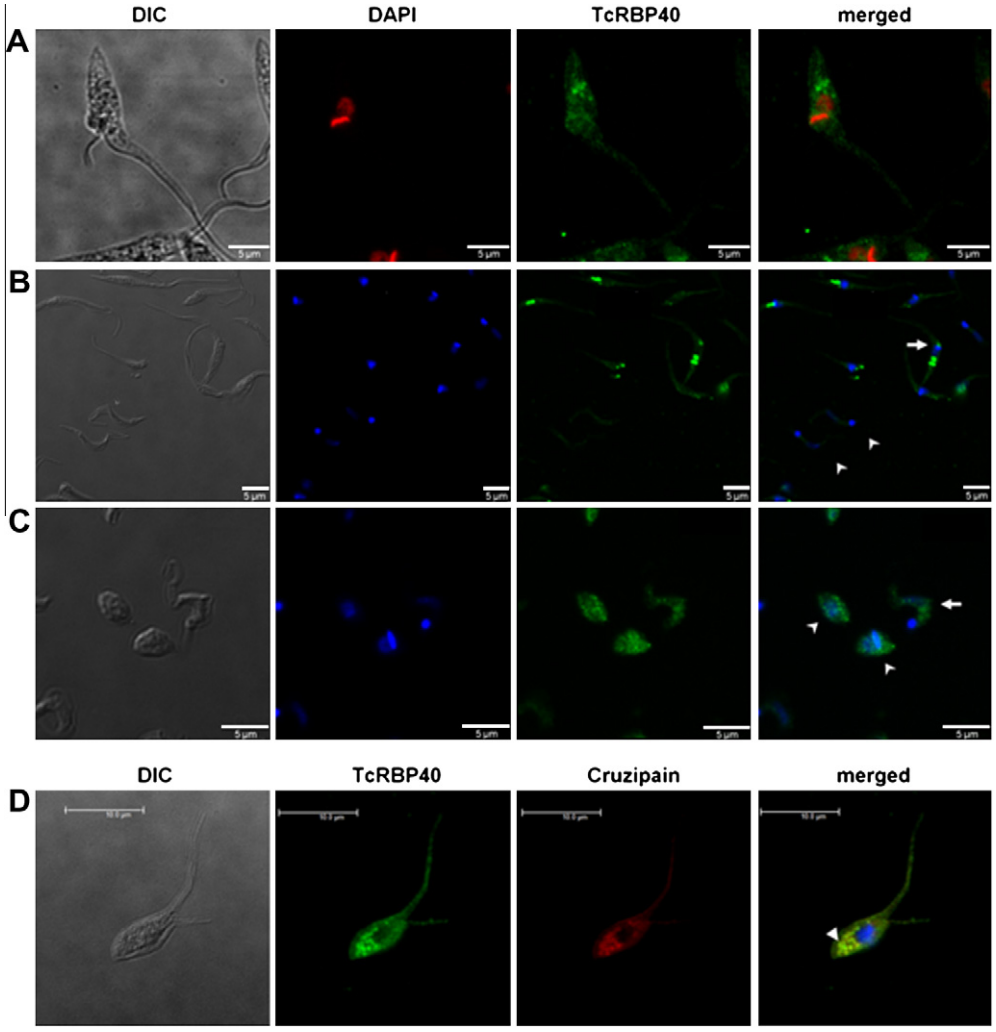

Fig. 4. Cellular localization of TcRBP40 at different life-stages. (A) Epimastigote (B) Metacyclic trypomastigote (arrowheads) and stressed forms (arrow); (C) Amastigote (arrowheads) and cellular trypomastigote forms (arrow); (D) Co-localization of TcRBP40 and cruzipain in epimastigotes. Arrowhead shows reservosomes. DIC: differential interference contrast; DAPI: nucleus and kinetoplast staining. Bars = 5 μm.

In vitro characterization of RNA–protein complexes using recombinant proteins raise concerns about the specificity of this kind of approach. However, stringent conditions competed for binding site and made it possible to select putative targets in the pull-down and microarray assays. A comparison of our results with other studies that used similar assays with different *T. cruzi* RBPs showed that, in our experimental conditions, we were able to select candidate transcripts for the protein and confirmed more than half of the tested transcripts. Specifically bound transcripts were identified, showing that the *in vitro* approach can be considered as an alternative strategy due to its simplicity and straightforwardness.

Binding assays suggest that TcRBP40 recognizes an AG-rich element present in the 3′UTR of the transcripts. EMSA results show that it binds to this element with low specificity, as TcRBP40 can bind different sequences in this assay. The low specificity could also explain the percentage of false positives observed in the pull-down assays.

It has been suggested that RBPs may bind and regulate functionally related mRNAs. In trypanosomes this kind of analysis is hampered by the high percentage of hypothetical proteins in the genomes. Even though, bioinformatic analysis of the hypothetical protein coding genes showed the preferential association of TcRBP40 with mRNAs coding for proteins with predicted transmembrane localization domains.

Surprisingly, when the cellular localization of TcRBP40 was analyzed in epimastigote forms, TcRBP40 appeared throughout the cytoplasm but concentrated particularly in reservosomes. The protein localization changes along the parasite life cycle to a cytoplasmic distribution in amastigotes and cellular trypomastigotes. These changes in the cellular localization of TcRBP40 could be related to its regulatory function. It has been observed that other RBPs change its distribution in response to biological stimuli [12,27]. Reservosomes are *T. cruzi* specific organelles present in the insect epimastigote forms and are related to the accumulation and storage of nutrients. Reservosomes are exhausted during metaciclogenesis as a response to the nutritional stress that triggers the differentiation process [23]. The presence of TcRBP40 in this organelle could suggest a new role of reservosomes in the biology of the parasite. Recently, the proteome of reservosomes was described showing the presence of a significant percentage of proteins involved in nucleic acid metabolism [28]. Further work is needed to assess whether reservosomes are involved in RNA metabolism. We cannot discard the possibility of a different function of TcRBP40 in this organelle as moonlighting proteins have been described in trypanosomes [29]. Characterizing regulatory proteins that are specific to a certain species could be essential to understand differences in the biology of related parasitic protozoa.

Acknowledgements

The authors thank Juan Cazullo for anti-cruzipain antibody; Michel Batista for *T. cruzi* vectors; Nilson Fidencio and Andréia Dallabonna for technical assistance; Maurílio J. Soares for help with microscopy assays; Andréa Ávila and Alejandro Correa for critical reading of the manuscript.

This study was supported by grants from Conselho Nacional de Desenvolvimento Científico e Tecnológico (CNPq) and Fundação Oswaldo Cruz. M.A.K., S.G. and B.D. received fellowships from CNPq and E.P.G.S. from CAPES.

Appendix A. Supplementary data

Supplementary data associated with this article can be found, in the online version, at doi:10.1016/j.bbrc.2012.02.154.

References

[1] A. Rassi Jr., A. Rassi, J.A. Marin-Neto, Chagas disease, Lancet 375 (2010) 1388–1402.
[2] N.G. Kolev, J.B. Franklin, S. Carmi, H. Shi, S. Michaeli, C. Tschudi, The transcriptome of the human pathogen Trypanosoma brucei at single-nucleotide resolution, PLoS Pathog. 6 (2010) e1001090.
[3] S. Haile, B. Papadopoulou, Developmental regulation of gene expression in trypanosomatid parasitic protozoa, Curr. Opin. Microbiol. 10 (2007) 569–577.
[4] B.M. Lunde, C. Moore, G. Varani, RNA-binding proteins: modular design for efficient function, Nat. Rev. Mol. Cell Biol. 8 (2007) 479–490.
[5] C.G. Burd, G. Dreyfuss, Conserved structures and diversity of functions of RNA-binding proteins, Science 265 (1994) 615–621.
[6] J. De Gaudenzi, A.C. Frasch, C. Clayton, RNA-binding domain proteins in Kinetoplastids: a comparative analysis, Eukaryot. Cell 4 (2005) 2106–2114.
[7] M. Ouellette, B. Papadopoulou, Coordinated gene expression by post-transcriptional regulons in African trypanosomes, J. Biol. 8 (2009) 100.
[8] S. Kabani, K. Fenn, A. Ross, A. Ivens, T.K. Smith, P. Ghazal, K. Matthews, Genome-wide expression profiling of in vivo-derived bloodstream parasite stages and dynamic analysis of mRNA alterations during synchronous differentiation in *Trypanosoma brucei*, BMC Genomics 10 (2009) 427.
[9] B.C. Jensen, D. Sivam, C.T. Kifer, P.J. Myler, M. Parsons, Widespread variation in transcript abundance within and across developmental stages of *Trypanosoma brucei*, BMC Genomics 10 (2009) 482.
[10] R. Queiroz, C. Benz, K. Fellenberg, J.D. Hoheisel, C. Clayton, Transcriptome analysis of differentiating trypanosomes reveals the existence of multiple post-transcriptional regulons, BMC Genomics 10 (2009) 495.
[11] J.D. Keene, RNA regulons: coordination of post-transcriptional events, Nat. Rev. Genet. 8 (2007) 533–543.
[12] B. Dallagiovanna, A. Correa, C.M. Probst, F. Holetz, P. Smircich, A.M. de Aguiar, F. Mansur, C.V. da Silva, R.A. Mortara, B. Garat, G.A. Buck, S. Goldenberg, M.A. Krieger, Functional genomic characterization of mRNAs associated with TcPUF6, a pumilio-like protein from *Trypanosoma cruzi*, J. Biol. Chem. 283 (2008) 8266–8273.
[13] S.K. Archer, VS.D. Luu, R.A. de Queiroz, S. Brems, C. Clayton, *Trypanosoma brucei* PUF9 regulates mRNAs for proteins involved in replicative processes over the cell cycle, PLoS Pathog. 5 (2009) e1000565.
[14] G. Noe, J.G. De Gaudenzi, A.C. Frasch, Functionally related transcripts have common RNA motifs for specific RNA-binding proteins in trypanosomes, BMC Mol. Biol. 9 (2008) 107.
[15] V.T. Contreras, T.C. Araujo-Jorge, M.C. Bonaldo, N. Thomaz, H.S. Barbosa, N. Meirelles Mde, S. Goldenberg, Biological aspects of the Dm 28c clone of *Trypanosoma cruzi* after metacyclogenesis in chemically defined media, Mem. Inst. Oswaldo Cruz 83 (1988) 123–133.
[16] V.T. Contreras, J.M. Salles, N. Thomas, C.M. Morel, S. Goldenberg, In vitro differentiation of *Trypanosoma cruzi* under chemically defined conditions, Mol. Biochem. Parasitol. 16 (1985) 315–327.
[17] S.R. Eddy, Profile hidden Markov models, Bioinformatics 14 (1998) 755–763.
[18] S.C. Nardelli, A.R. Avila, A. Freund, M.C. Motta, L. Manhaes, T.C. de Jesus, S. Schenkman, S.P. Fragoso, M.A. Krieger, S. Goldenberg, B. Dallagiovanna, Small-subunit rRNA processome proteins are translationally regulated during differentiation of *Trypanosoma cruzi*, Eukaryot. Cell 6 (2007) 337–345.
[19] J.M. Wettenhall, G.K. Smyth, LimmaGUI: a graphical user interface for linear modeling of microarray data, Bioinformatics 20 (2004) 3705–3706.
[20] M.A. Duhagon, B. Dallagiovanna, B. Garat, Unusual features of poly[dT-dG].[dC-dA] stretches in CDS-flanking regions of *Trypanosoma cruzi* genome, Biochem. Biophys. Res. Commun. 287 (2001) 98–103.
[21] W.H. Townley-Tilson, S.A. Pendergrass, W.F. Marzluff, M.L. Whitfield, Genome-wide analysis of mRNAs bound to the histone stem-loop binding protein, RNA 12 (2006) 1853–1867.
[22] L. Perez-Diaz, M.A. Duhagon, P. Smircich, J. Sotelo-Silveira, C. Robello, M.A. Krieger, S. Goldenberg, N. Williams, B. Dallagiovanna, B. Garat, *Trypanosoma cruzi*: molecular characterization of an RNA binding protein differentially expressed in the parasite life cycle, Exp. Parasitol. 117 (2007) 99–105.
[23] R.C. Figueiredo, D.S. Rosa, M.J. Soares, Differentiation of *Trypanosoma cruzi* epimastigotes: metacyclogenesis and adhesion to substrate are triggered by nutritional stress, J. Parasitol. 86 (2000) 1213–1218.
[24] T. Souto-Padron, O.E. Campetella, J.J. Cazzulo, W. de Souza, Cysteine proteinase in *Trypanosoma cruzi*: immunocytochemical localization and involvement in parasite-host cell interaction, J. Cell Sci. 96 (Pt 3) (1990) 485–490.
[25] S.M. Beverley, Protozomics: trypanosomatid parasite genetics comes of age, Nat. Rev. Genet. 4 (2003) 11–19.
[26] K.D. Mansfield, J.D. Keene, The ribonome: a dominant force in co-ordinating gene expression, Biol. Cell 101 (2009) 169–181.
[27] A. Cassola, J.G. De Gaudenzi, A.C. Frasch, Recruitment of mRNAs to cytoplasmic ribonucleoprotein granules in trypanosomes, Mol. Microbiol. 65 (2007) 655–670.
[28] C. Sant'Anna, E.S. Nakayasu, M.G. Pereira, D. Lourenco, W. de Souza, I.C. Almeida, E.S.N.L. Cunha, Subcellular proteomics of *Trypanosoma cruzi* reservosomes, Proteomics 9 (2009) 1782–1794.
[29] P.W. Collingridge, R.W. Brown, M.L. Ginger, Moonlighting enzymes in parasitic protozoa, Parasitology 137 (2010) 1467–1475.

Biochemical and Biophysical Research Communications 420 (2012) 308–314

Contents lists available at SciVerse ScienceDirect

Biochemical and Biophysical Research Communications

journal homepage: www.elsevier.com/locate/ybbrc

Serum profiling based on fucosylated glycoproteins for differentiating between chronic hepatitis B and hepatocellular carcinoma

Jian Liao [a,b], Ruixiu Zhang [a], Haihua Qian [a], Lu Cao [a], Yu Zhang [a], Wen Xu [a], Jing Li [a], Mengchao Wu [a], Zhengfeng Yin [a,*]

[a] Molecular Oncology Laboratory, Eastern Hepatobiliary Surgery Hospital, Second Military Medical University, Shanghai 200438, China
[b] Institute for Laboratory Medicine, Fuzhou General Hospital of Nanjing Command, Fuzhou 350025, Fujian Province, China

ARTICLE INFO

Article history:
Received 17 February 2012
Available online 7 March 2012

Keywords:
Hepatitis B virus
Hepatocellular carcinoma
Fucosylation
MALDI-TOF MS profiling
Defucosylation

ABSTRACT

Chronic infection with hepatitis B virus (HBV) is associated with the majority of cases of hepatocellular carcinoma (HCC) in China. Despite this, there is no effective method for the early detection of HBV-induced liver cancer. Aberrant fucosylation is known to occur during the development of HCC. We, therefore, developed a method of applying matrix-assisted laser desorption/ionization time-of-flight mass spectrometry (MALDI-TOF MS) to analyze the relationship between aberrant fucosylation, tumor genesis and progression of HBV-associated HCC, and to establish proteomic profiling of serum for early diagnosis of HCC. The MALDI-TOF MS was based on *Lens culinaris* agglutinin (LCA) lectin magnetic beads and their affinity for separation. The method was applied initially to a 'training' cohort of 111 serum samples obtained from subjects in China with no liver disease ($n = 26$), chronic hepatitis B without cirrhosis ($n = 21$), HBV-infected cirrhosis ($n = 32$), or HBV-infected HCC ($n = 32$). In contrast to previous findings, the results of our profiling analysis demonstrated defucosylation on some of the glycoproteins involved in HCC. HCC was then diagnostically classified in a 'blind test' cohort ($n = 96$). In this group we demonstrated that, HCC could be distinguished from all serum samples, HBV-associated chronic liver disease, and HBV-associated cirrhosis with a sensitivity/specificity of 70%/70%, 78%/74%, and 81%/82%, respectively. When combined with serum alpha-fetoprotein detection (AFP > 20 ng/mL), the sensitivity/specificity improved to 78%/88%, 85%/88%, and 89%/91%, respectively. In conclusion, serum glycoprotein fucosylation abnormalities have diverse forms in patients with HCC. MALDI-TOF MS profiling of aberrant serum fucosylated glycoproteins distinguished HCC from controls with high accuracy.

1. Introduction

In China, HCC is the third leading cause of cancer death [1]. The HCC epidemic in China is associated with hepatitis B viral (HBV) infection. China has the highest prevalence of HBV in the world [2], with up to 80% of HCC cases in the Chinese population being attributed to HBV [3]. The natural progression of HBV infection to hepatitis, cirrhosis, and HCC is slow and studies of HBV progression to HCC are expected to provide new insights on the management of this increasing problem.

Currently available systemic therapies demonstrate poor to modest response rates and do not improve survival in patients with HCC. The slow development and late detection of HCC suggest that the identification of biomarkers of disease progression and early detection represent attractive strategies for improving the prognosis of HCC.

Current diagnosis of HCC relies on clinical information, liver imaging and serum alpha-fetoprotein (AFP) measurement. AFP is the serum marker that is most widely used for the diagnosis, and surveillance of HCC [4,5]. However, AFP levels have been found to be normal in up to 40% of patients with HCC, particularly during the early stages indicating the low sensitivity of this marker [4]. Furthermore, elevated AFP levels may also be detected in patients with cirrhosis or exacerbations of chronic hepatitis indicating low specificity [5]. By contrast, AFP with core-fucosylation has been shown to be a very specific marker for HCC [6]. This marker is referred to as AFP-L3 because it is detected at the L3 fraction on *Lens culinaris* agglutinin (LCA) lectin-electorophoresis. At a cut off level of 10% of total AFP, the reported specificities of AFP-L3 as a

* Corresponding author. Address: Molecular Oncology Laboratory, Eastern Hepatobiliary Surgery Hospital, Second Military Medical University, 225 Changhai Road, Shanghai 200438, China. Fax: +86 21 81875354.
E-mail addresses: pamperslj28@yahoo.cn (J. Liao), crossecho@yahoo.com.cn (R. Zhang), qhhlb@yahoo.com.cn (H. Qian), caolu0909@yahoo.com.cn (L. Cao), oct0072004@yahoo.com.cn (Y. Zhang), andrew_xw@hotmail.com (W. Xu), lijinggava5945@tom.com (J. Li), wumengchao@yahoo.com.cn (M. Wu), yinzfk@yahoo.com.cn (Z. Yin).

0006-291X/$ - see front matter © 2012 Elsevier Inc. All rights reserved.
http://dx.doi.org/10.1016/j.bbrc.2012.02.155

method of detecting HCC range from 90% to 92.0% [6]. Based on these observations, AFP-L3 has gained approval from the US Food and Drug Administration (FDA) in 2005 as the diagnostic assay for HCC [7].

However, AFP is not present in all patients with HCC, which limits the use of AFP and AFP-L3 as a primary screen for HCC and highlights the need for more sensitive serum biomarkers for HCC for future work.

The molecular mechanism of aberrant fucosylation in HCC is not clear, but it is known that the abnormalities are not restricted to AFP [7]. Results from several groups have indicated that other liver-derived glycoproteins, such as Golgi protein-73 (GP73) and kininogen, also become fucosylated with the development of HCC. A recent study has proposed that these glycoforms may be valuable biomarkers of HCC [8,9]. However, the majority of previous studies have been performed on individual or very small numbers of patients who have the most abundant serum glycoproteins [10].

It has been proposed that the combination of a biomarker panel of fucosylated glycoproteins might provide a more reliable diagnostic standard [11]. However, a comprehensive comparative analysis of all the fucosylated glycoproteins in HCC patients has yet to be performed. This type of study has been limited by the absence of a suitable technology to allow the examination of large pools of unknown fucosylated glycoproteins.

In the present study, we developed a method for applying of matrix-assisted laser desorption/ionization time-of-flight mass spectrometry (MALDI-TOF MS) which uses LCA magnetic glyco-capturing beads to analyze the relation between glycoprotein fucosylation abnormalities and the onset and development of HBV-associated HCC in the sera of patients with HBV-HCC and controls. We used this method to define a specific proteomic profile that could potentially be used for early diagnosis of HBV-HCC.

2. Materials and methods

2.1. Study subjects

Serum samples ($n = 207$) from patients and healthy controls were collected from the Eastern Hepatobiliary Surgery Hospital (Shanghai, China) from November 2007 to October 2009. This study was approved by the Biomedical Ethics Committee of Eastern Hepatobiliary Surgery Hospital, and written informed consent was obtained from all participants. Demographic and clinical information were obtained and a blood sample was collected from each subject. Each subject's hepatitis B viral (HBV) and C viral (HCV) infection status was assessed by enzyme immunoassay for anti-HBV, anti-HCV surface antigen, and by polymerase chain reaction for HBV DNA.

Four groups of consecutive subjects were enrolled (Table 1). The first group ($n = 52$) included subjects with no history of liver disease and normal liver biochemistry, no risk factors for viral hepatitis, and alcohol consumption less than 40 g/week. The second group ($n = 42$) consisted of patients with chronic hepatitis B (CHB) based on HBsAg (+), HBeAg (+), HBV DNA (+), HCsAg (−), and abnormal liver biochemistry. The third group ($n = 54$) consisted of patients with HBV-infected cirrhosis. Diagnosis of cirrhosis was based on liver histology or clinical, laboratory, and imaging evidence of hepatic decompensation or portal hypertension [12]. Each of the patients with cirrhosis had a normal hepatic ultrasound (US). If serum AFP was elevated, a contrast computed tomography (CT) scan or magnetic resonance imaging (MRI) of the liver within 3 months before enrollment and 6 months after enrollment showed no liver mass. The fourth group ($n = 59$) consisted of patients with HBV-infected HCC. The diagnosis of HCC was made by histopathology [13]. Tumor staging was determined using the United Network of Organ Sharing-modified tumor-node-metastasis staging system for HCC.

Table 1
Serum sample numbers used in training and blinded test cohorts.

	Training cohort	Blind test cohort	Total
Healthy	26	26	52
CHB	21	21	42
HBV-Cirrhosis	32	22	54
HBV-HCC	32	27	59
Total	111	96	207

Abbreviations: HBV, hepatitis B virus; CHB, chronic hepatitis B; HBV-Cirrhosis, HBV-infected cirrhosis; HBV-HCC, HBV-infected hepatocellular carcinoma.

2.2. Blood sample preparation

Blood from patients with HCC was collected preoperatively in glass tubes without additive (BD Vacutainer™ Franklin Lakes, NJ) and was allowed to clot at room temperature for 40 min. Serum was separated by centrifugation at 2000 rpm for 15 min, immediately split into 200 μL aliquots and frozen at −80 °C until analysis. The time from collection to frozen storage was no more than 60 min.

The processing, collection, and storage protocols for all individuals were identical. Each sample used for proteomic profiling had not been thawed more than once. Blood samples from patients with HCC were drawn before initiation of treatment. Samples of each group were randomly divided into a 'training' cohort and a blind 'test' cohort (Table 1).

2.3. Serum protein fractionation and tryptic digestion

Serum samples were thawed and purified using LCA magnetic beads (Bruker Daltonics, Germany). Ten microliters of serum was mixed with 2 μL of beads and the samples were purified by binding, washing and elution in accordance with the manufacturer's protocol. Each incubation step took 1 min. Elution was carried out with 10 μL of elution buffer. A portion of the eluted sample (5 μL) was lyophilized and rehydrated in 25 μL of 100 mM NH_4HCO_3 containing 50 ng of trypsin. The portion was digested overnight at 37 °C.

2.4. MALDI-TOF MS

For MALDI-TOF MS analysis, 1 μL of digested sample was mixed with 0.5 μL of matrix solution (0.4 mg/mL α-cyano-4-hydroxycinnamic acid in ethanol:acetone 2:1) and allowed to dry onto the MALDI sample plate (600 μm AnchorChip™, Bruker Daltonics, Germany). Laser desorption was targeted randomly on the sample plate and samples were measured using an Autoflex II MALDI-TOF mass spectrometer (Bruker Daltonics, Germany) operated in positive ion linear (reflection) mode. Ionization was achieved by irradiation with a 50 Hz nitrogen laser ($\lambda = 337$ nm). Spectra were the mean of 100 ionizations with fixed laser power in linear geometry mode and mass maps were obtained in reflectron mode. The spectra were calibrated externally with a mixture of protein/peptide standards in the range of 1000–10,000 Da (Bruker Daltonics, Germany). Three MALDI preparations (MALDI spots) were measured from each sample. For each MALDI spot, 400 spectra were acquired (50 laser shots at eight different spot positions). The spectra from all samples (training cohort) were imported into CLINPROT™ software (Bruker Daltonics, Germany) for spectra processing, model building, model recognition, and internal model validation. The spectra were processed in the following order: (1) spectra normalization to total ion current; (2) spectra recalibration using

prominent peaks; (3) baseline subtraction, peak smoothing (Savitsky–Golay algorithm) and peak detection; (4) calculation of peak areas for each spectrum. Peak detection was performed using S/N $\geqslant$ 5 and peak areas were calculated using a zero level integration type.

All MALDI-TOF MS spectra were analyzed with flexAnalysis™ (Bruker Daltonics, Germany) to detect the peak intensities of interest and CLINPROT™ software (Bruker Daltonics, Germany) to compile the peaks across the spectra obtained from all samples of the training set. This analysis allowed for discrimination between HCC and control samples. The Supervised Neural Network (SNN) contained in this software suite was used for selecting clusters of signals for the model to discriminate the two populations. A leave-20%-out cross-validation was calculated to avoid over-fitting of pattern recognitions. The spectra from all samples of the blinded test cohort were processed by the same method. The spectra data of two sets were used for internal and external model validation.

2.5. Sample processing and MALDI analysis

Each serum sample from the training cohort was analyzed by LCA magnetic beads enriched fucosylated glycoproteins, and then by trypsin digestion. The MALDI-TOF approach was applied to exhibited spectral peaks in the 1000–10,000 m/z range, as well as the effect of pre-processing and normalization. Each serum sample was tested in duplicate. Using ClinprotTools ver. 2.1 (Bruker Daltonics, Germany) to statistically analyze the differences in peak positions and intensities.

2.6. Blinding

The analysts were blinded to the origin of the samples. Initially the established model was used to distinguish HCC from all serum samples. Then healthy samples were excluded, and the analysts attempted to distinguish HCC from samples with HBV-associated disease. In the final step the analysts attempted to exclude chronic hepatitis B, and distinguish HCC from all cirrhosis samples.

2.7. Statistical analysis

The processed spectra were analyzed using Students t-tests and Wilcoxon tests. Values of $P < 0.05$ were considered to be statistically significant.

3. Results

Demographic information and etiology of liver diseases of all the patients and healthy volunteers are provided in Table 2.

3.1. MALDI analysis

The complete mass spectrum comparison of serum samples from healthy, CHB, HBV-Cirrhosis and HBV-HCC groups are shown in Fig. 1. MALDI-TOF analysis of patients in the four groups resulted in 89 distinguishable peaks in the 1000–10,000 m/z range, with 36 peaks having differential expression and statistical significance ($P < 0.05$; data not shown). Twelve peaks shown to have differential expression and statistical significance ($P < 0.005$) are shown in Table 3.

To assess the classification efficiency, the mean ± SD of the mass of the 12 peaks in the four groups were calculated. Two significantly differently expressed peptides, 2263.41 Da and 5199.24 Da, were used for this analysis. A sample spectrum showing the average peak value for these peptides in the four groups and the corresponding concentrations are shown in Fig. 2. The levels of the 2263.41 Da and 5199.24 Da peptides were highest in the healthy group and decreased with disease severity in the CHB and HBV-Cirrhosis groups. Expression of both peptides increased in the HBV-HCC group, but the degree of expression was lower than in the healthy group. Thus peptides 2263.41 Da and 5199.24 Da appeared to have general discriminatory potential (Fig. 3).

3.2. Classification models analysis and blind test

A Supervised Neural Network (SNN) in CLINPROT, established using the detected peaks from the training cohort was used to generate cross-validated classification models.

Having established the correct classification of the more clinically relevant scenarios for surveillance of HBV disease progression, from chronic hepatitis to cirrhosis, we next examined HCC using specific HCC diagnostic classification models. The peptide peaks of HCC diagnostic classification models are shown in Table 4. The accuracy of the models data from the blinded test cohort was validated with the analysts blinded as to the origin of the samples.

HBV-HCC was distinguished from all serum samples (HBV-HCC versus HBV-Cirrhosis plus CHB plus healthy samples) with a sensitivity of 70% and a specificity of 70% (Table 5). When both chronic hepatitis B and HBV-associated cirrhosis samples were combined and compared with HBV-HCC samples, sensitivity and specificity increased to 78% and 74%, respectively (Table 5). HBV-HCC samples were distinguished from HBV-Cirrhosis samples with a sensitivity of 81% and a specificity of 82% (Table 5).

To test whether the accuracy of classification could be increased by including clinical data, AFP values were included in the analysis of all the diagnostic classification models. These values were considered by the algorithm to be additional 'peaks' to be used in conjunction with those from the MALDI analyses to build new classification models. As seen in Table 5, inclusion of AFP values > 20 ng/mL increased sensitivity/specificity of the correct classification of disease states to 78%/88%, 85%/88%, and 89%/91%, respectively, in both cohorts.

4. Discussion

An association between the fucosylation abnormality of glycoproteins and liver cancer is becoming increasingly evident [7–10]. The successful clinical use of fucosylated AFP (AFP-L3) has made researchers aware that different proteins with fucosylation abnormalities exist in human sera that may be markers that assist in the diagnosis of liver cancer. The usual experimental process is enrichment of fucosylation with special agglutinins, followed by detection with two-dimensional electrophoresis (2-DE) or liquid chromatography–mass spectrometry technology. However, this is a time and labor consuming process which is seldom employed clinically. Furthermore, identifying which proteins with fucosylation abnormalities are suitable for diagnosis of liver cancer requires verification one by one [14,15]. Other researchers suggest that it is necessary to detect the glycoproteome with fucosylation abnormalities before making an early diagnosis of liver cancer [9,10].

The agglutinin magnetic bead-based CLINPROT system adopted in our study combined agglutinin affinity technology with time-of-flight mass spectrometry (TOF MS), making it possible to rapidly detect and analyze proteomics with glycosylation abnormalities [16]. There are no previous reports on applying the LCA affinity based CLINPROT technology to establish a serum fucosylation abnormality peptide group fingerprint model associated with liver cancer.

In our study, healthy, CHB, HBV-Cirrhosis, and HBV-HCC groups were based on a gradual progression of HBV infection, from viral infection to hepatitis to cirrhosis and HCC. This finding suggests

Table 2
Demographic information and etiology of liver diseases.

Training cohort	Healthy	CHB	HBV-Cirrhosis	HBV-HCC
Num.	26	21	32	32
Male/female	16/10	17/4	29/3	28/4
Age (years)	46.8 ± 11.6	40.3 ± 6.9	48.5 ± 11.4	52.0 ± 10.4
ALT (U/L)	20.2 ± 6.7	112.5 ± 78.8	54.7 ± 104.2	70.6 ± 71.0
AST (U/L)	18.0 ± 4.8	98.5 ± 75.4	62.4 ± 67.8	72.8 ± 52.1
AFP (ng/mL)	2.5 ± 1.0	17.0 ± 27.9	25.4 ± 57.8	13810.6 ± 26999.7
< 20	26	17	26	4
20–200	0	4	5	5
> 200	0	0	1	23
TNM stage (I/II/III/IV)	NA	NA	NA	12/14/4/2
Blind test cohort	Healthy	CHB	HBV-Cirrhosis	HBV-HCC
Num.	26	21	22	27
Male/female	14/12	18/3	19/3	24/3
Age (years)	49.1 ± 12.8	40.9 ± 7.1	48.3 ± 10.7	51.2 ± 13.0
ALT (U/L)	17.0 ± 4.7	118.8 ± 74.4	35.9 ± 27.0	69.6 ± 46.2
AST (U/L)	17.5 ± 3.1	94.5 ± 59.5	50.8 ± 48.0	75.2 ± 63.4
AFP (ng/mL)	2.5 ± 1.0	28.2 ± 76.6	28.7 ± 81.7	2590.1 ± 7289.0
< 20	26	17	18	8
20–200	0	3	2	4
> 200	0	1	2	15
TNM stage (I/II/III/IV)	NA	NA	NA	13/10/3/1

Note: data are presented as the mean ± SD where appropriate.
Abbreviations: HBV, hepatitis B virus; CHB, chronic hepatitis B; HBV-Cirrhosis, HBV-infected cirrhosis; HBV-HCC, HBV-infected hepatocellular carcinoma; ALT, alanine aminotransferase; AST, aspartate aminotransferase; AFP, alpha fetoprotein; TNM, primary tumor/lymph node/distant metastasis; NA, not applicable.

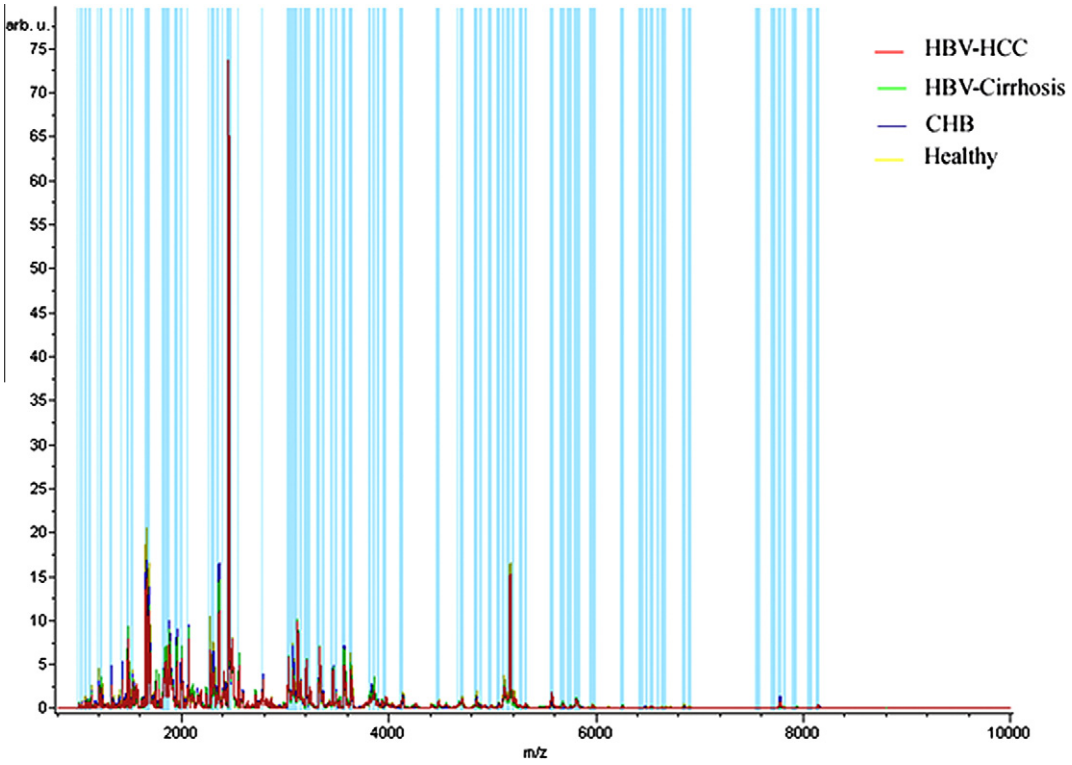

Fig. 1. Complete mass spectrum comparison of serum samples from healthy, CHB, HBV-Cirrhosis, and HBV-HCC subjects in the 1000–10,000 *m*/*z* range. Red line: HBV-HCC group; Green line: HBV-Cirrhosis group; Blue line: CHB group; Yellow line: Healthy group. Vertical blue bar representing the four groups in the peptide peaks detected. *Abbreviations:* HBV, hepatitis B virus; CHB, chronic hepatitis B; HBV-Cirrhosis, HBV-infected cirrhosis; HBV-HCC, HBV-infected hepatocellular carcinoma.

that the method not only diagnoses HCC, but also provides information on the relationship between fucosylation abnormalities of glycoproteins and the onset and development of HCC.

In most previous research it has been reported that high levels of fucosylation occurs in many glycoproteins [9,10,14,15]. In our study we showed that with some glycoproteins, such as the 2263.41 Da peptide and 5199.24 Da peptide, the fucosylation protein levels were highest in the healthy group and decreased in the HBV-HCC group (Fig. 2). Similar results have also been found in our another experiment on the glycoproteins with fucosylation abnormalities in sera of the healthy people, patients of chronic liver disease (CLD) and HCC patients with two-dimensional electrophoresis (data

Table 3
Mass spectral characteristics of peptides with differential expression among four groups ($P < 0.005$).

m/z	D_{Ave}	P value	Ave1	Ave2	Ave3	Ave4	SD1	SD2	SD3	SD4
2263.41	61.3	0.00000101	75.8	47.74	50.8	109.03	32.36	26.33	22.06	34.75
5199.24	21.37	0.0000185	30.99	16.66	27.49	38.03	19.3	6.02	12.38	14.2
2293.81	94.65	0.000043	112.06	96.63	128.8	191.27	62.43	34.09	43.6	68.28
4871.87	8.06	0.000127	16.38	14.07	18.35	22.13	4.4	3.95	7.31	5.05
2542.93	38.37	0.000141	69.11	83.55	71.91	45.18	21.61	27.19	30.9	15.13
1644.33	82.16	0.000433	134.31	95.88	148.63	178.04	53.87	47.7	63.97	51.73
1186.58	17.14	0.000433	21.83	17.19	27.24	34.33	11.75	7.61	12	14.91
6838.5	8.31	0.000591	9.78	8.97	10.68	17.28	4.73	3.6	3.95	7.98
1664.32	66.73	0.000718	101.52	76.84	122.3	143.58	45.83	35.7	53.99	45.65
5139.36	12.66	0.00177	24.46	18.83	24.54	31.49	8.93	8.15	11.73	8.44
1855.83	24.99	0.00285	58.69	59.78	60.11	83.68	21.32	18.88	16.11	26.08
7766.09	10.44	0.00285	20.87	20.42	30.85	30.87	10.93	29.41	28.88	17.16

Note: 1: HBV-HCC; 2: HBV-Cirrhosis; 3: CHB; 4: healthy.
m/z: the mass/charge characteristic of each protein/peptides.
D_{Ave}: difference between the maximal and minimal average peak area.
P value of Wilcoxon test (2 class) or Kruskal–Wallis (> 2 class).
Ave N: peak area (intensity) average of class N.
SD N: standard deviation of the peak area average of class i.
Abbreviations: HBV, hepatitis B virus; CHB, chronic hepatitis B; HBV-Cirrhosis, HBV-infected cirrhosis; HBV-HCC, HBV-infected hepatocellular carcinoma.

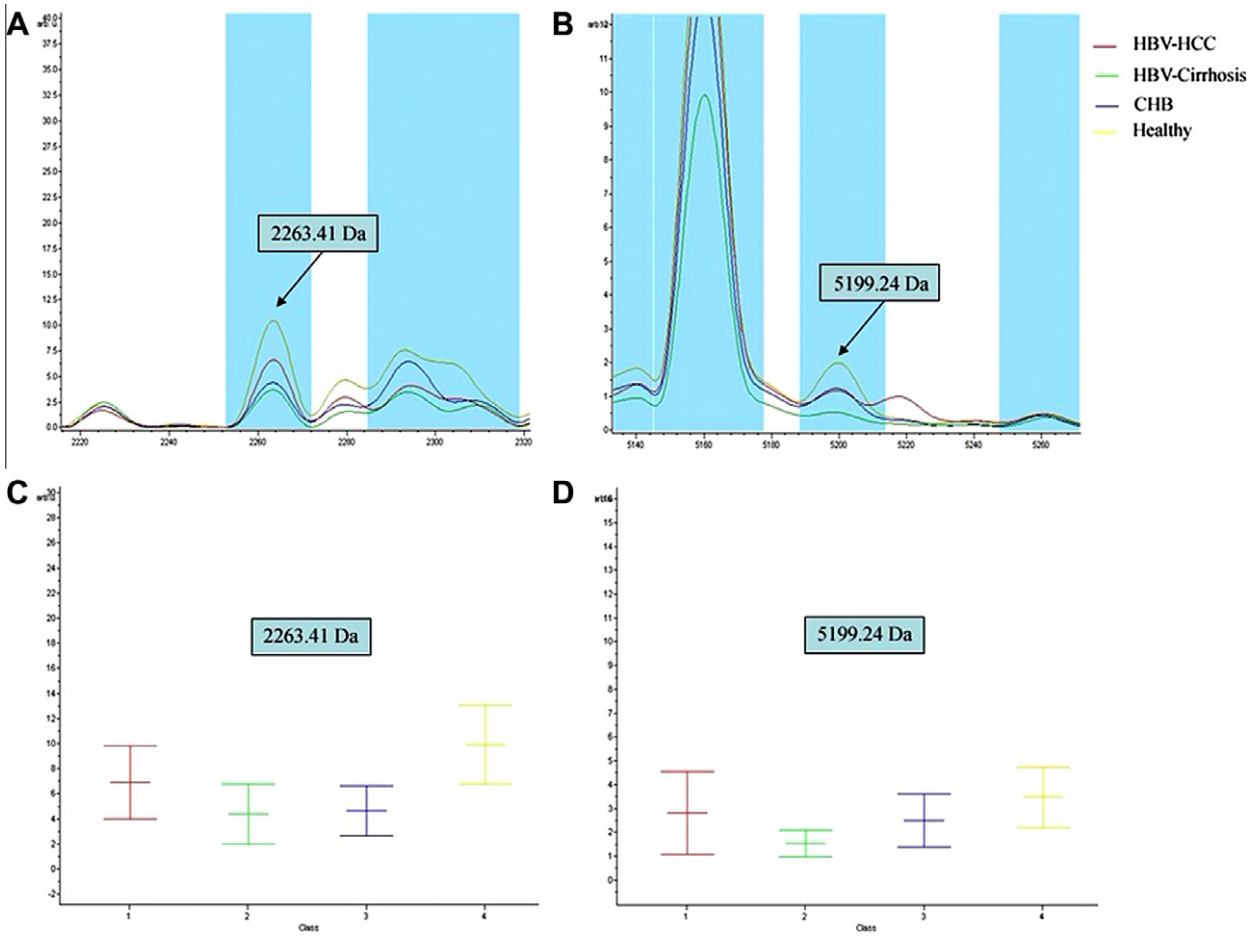

Fig. 2. Sample spectrum showing an average peak value for peptides 2263.41 Da (A) and 5199.24 Da (B) in each group. Corresponding peptide concentrations (mean ± SD) are shown in the lower box-plot for peptides 2263.41 Da (C) and 5199.24 Da (D). Levels of the 2263.41 Da (A, C) and 5199.24 Da (B, D) peptides were highest in the healthy group and decreased with disease severity in CHB group and HBV-Cirrhosis group. Expression of both peptides increased in the HBV-HCC group, but the remained lower than in the healthy group. Red line: HBV-HCC group; Green line: HBV-Cirrhosis group; Blue line: CHB group; Yellow line: Healthy group. 2263.41 Da and 5199.24 Da are the mass of peptide peaks. *Abbreviations:* HBV, hepatitis B virus; CHB, chronic hepatitis B; HBV-Cirrhosis, HBV-infected cirrhosis; HBV-HCC, HBV-infected hepatocellular carcinoma.

not show). Other studies in cancer patients have shown that a large range of glycoproteins are fucosylated as a result of the actions of fucosyltransferase [17]. In our study we demonstrated that defucosylation occurred in certain glycoproteins in HCC. It can therefore be speculated that there might be cellular enzymes that catalyase the opposite effect of fucosyltransferase, and that these enzymes might be activated in liver cancer to facilitate defucosylation on some of the fucosylation glycoproteins.

The mechanism causing defucosylation of glycoproteins in HCC has yet to be defined. However, the existence of different forms of

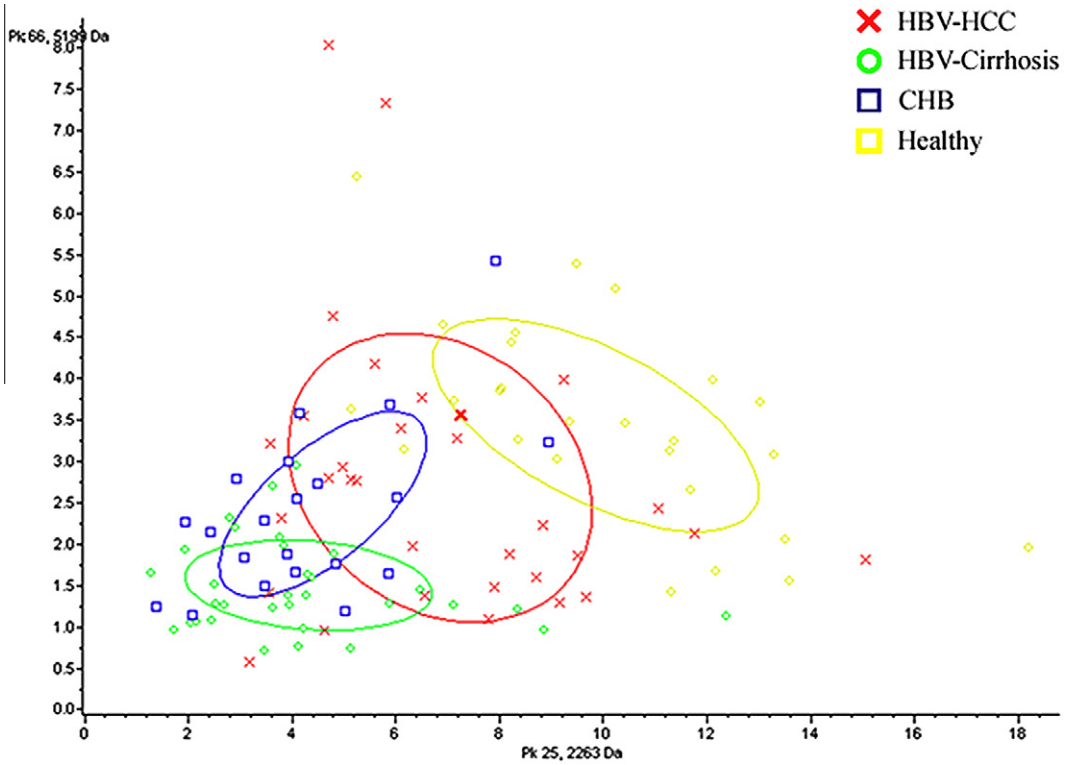

Fig. 3. Bivariate plot of two peptide peaks 2263.41 Da and 5199.24 Da showing general distinction between distributions in four groups. The yellow, blue, green and red symbols show samples from the training cohorts of healthy, CHB, HBV-Cirrhosis and HBV-HCC groups respectively. 2263.41 Da and 5199.24 Da are the mass of peptide peaks. The *x*-axis values represent the relative expression of peptide 2263.41 Da in each group. The y-axis shows the relative expression of peptide 5199.24 Da in each group. *Abbreviations:* HBV, hepatitis B virus; CHB, chronic hepatitis B; HBV-Cirrhosis, HBV-infected cirrhosis; HBV-HCC, HBV-infected hepatocellular carcinoma.

Table 4
Peaks of the HCC diagnostic classification models.

Condition	Peaks of the classification model (m/z)
HBV-HCC vs. HBV-Cirrhosis + CHB + Healthy	4838.07, 1871.54, 3227.09, 5260.74, 3051.4, 2474.13, 3322.01
HBV-HCC vs. HBV-Cirrhosis + CHB	1073.61, 3556.64, 1833.66, 1741, 4837.76
HBV-HCC vs. HBV-Cirrhosis	3847.71, 1517.64, 6891.23, 5955.53, 1871.31

Abbreviations: HBV, hepatitis B virus; CHB, chronic hepatitis B; HBV-Cirrhosis, HBV-infected cirrhosis; HBV-HCC, HBV-infected hepatocellular carcinoma.

Table 5
Blind test results of HCC diagnostic classification models and the results of joint detection AFP.

Condition	Sensitivity	Specificity
HBV-HCC vs. HBV-Cirrhosis + CHB + Healthy	70% (19/27)	70% (48/69)
HBV-HCC vs. HBV-Cirrhosis + CHB + Healthy (+AFP > 20 ng/ml)	78% (21/27)	88% (61/69)
HBV-HCC vs. HBV-Cirrhosis + CHB	78% (21/27)	74% (32/43)
HBV-HCC vs. HBV-Cirrhosis + CHB (+AFP > 20 ng/ml)	85% (23/27)	88% (38/43)
HBV-HCC vs. HBV-Cirrhosis	81% (22/27)	82% (18/22)
HBV-HCC vs. HBV-Cirrhosis (+AFP > 20 ng/ml)	89% (24/27)	91% (20/22)

Abbreviations: HBV, hepatitis B virus; CHB, chronic hepatitis B; HBV-Cirrhosis, HBV-infected cirrhosis; HBV-HCC, HBV-infected hepatocellular carcinoma.

fucosylation abnormality indicates a complex relationship between the fucosylation abnormality and HCC.

Our diagnostic classification model was established through pairwise comparisons between the HCC group and the control groups. The control groups were divided into the healthy people plus CHB plus HBV-Cirrhosis, CHB plus HBV-Cirrhosis, and HBV-Cirrhosis by the severity the disease. Blind testing revealed the sensitivity/specificity for HCC as 70%/70%, 78%/74%, and 81%/82% in all serum samples (healthy people plus CHB plus HBV-Cirrhosis), the HBV-CLD group (CHB plus HBV-Cirrhosis), and the HBV-Cirrhosis group, respectively (Table 5).

Both sensitivity and specificity were shown to increase with the severity of diseases in the control group, indicating that this diagnostic model may be suitable for distinguishing HCC from the HBV-Cirrhosis, which is helpful for the early diagnosis of HCC. Furthermore, the sensitivity (81%) for distinguishing HCC from HBV-Cirrhosis in our model was higher than that of AFP detection (56%) (AFP > 200 ng/mL). When the diagnostic model was combined with AFP detection (AFP > 20 ng/mL), there was significantly improved sensitivity and specificity for HCC diagnosis indicating that this model may have potential for clinical use.

In conclusion, we have shown that fucosylation abnormalities of glycoproteins are a complicated and mutable process, and that the onset and development of HCC does not simply involve high fucosylation. A serum fucosylation abnormality peptide fingerprint diagnosis model has been established using LCA magnetic bead affinity based MALDI-TOF MS technology to analyze the relationship between glycoprotein fucosylation abnormalities and the onset and development of HBV-HCC. Preliminary verification has been undertaken for the clinical diagnosis of HCC. The combination of this diagnostic model and AFP detection provides a favorable basis for future clinical use for diagnosing HCC. Our study lacks com-

parative data with other cancers which will be the subject of future research.

Acknowledgments

Supported by China National Key Projects for Infectious Disease (No. 2008ZX10002-021 and No. 2012ZX10002012), and the National Natural Science Foundation of China (No. 30901732).

References

[1] D.M. Parkin, F. Bray, J. Ferlay, et al., Global cancer statistics, 2000, CA, Cancer J. Clin. 55 (2005) (2002) 74–108.
[2] J. Liu, D. Fan, Hepatitis B in China, Lancet 369 (2007) 1582–1583.
[3] J.A. Marrero, Hepatocellular carcinoma, Curr. Opin. Gastroenterol. 22 (2006) 248–253.
[4] A.M. Di Bisceglie, J.H. Hoofnagle, Elevations in serum alpha-fetoprotein levels in patients with chronic hepatitis B, Cancer 64 (1989) 2117–2120.
[5] M. Sherman, K.M. Peltekian, C. Lee, Screening for hepatocellular carcinoma in chronic carriers of hepatitis B virus: incidence and prevalence of hepatocellular carcinoma in a North American urban population, Hepatology 22 (1995) 432–438.
[6] K. Taketa, S. Okada, N. Win, et al., Evaluation of tumor markers for the detection of hepatocellular carcinoma in Yangon General Hospital, Myanmar, Acta Med. Okayama 56 (2002) 317–320.
[7] A. Mehta, T.M. Block, Fucosylated glycoproteins as markers of liver disease, Dis. Markers 25 (2008) 259–265.
[8] J.A. Marrero, P.R. Romano, O. Nikolaeva, et al., GP73, a resident Golgi glycoprotein, is a novel serum marker for hepatocellular carcinoma, J. Hepatol. 43 (2005) 1007–1012.
[9] X.F. Zhang, E.C. Lai, X.F. Kang, et al., Lens culinaris agglutinin-reactive fraction of alpha-fetoprotein as a marker of prognosis and a monitor of recurrence of hepatocellular carcinoma after curative liver resection, Ann. Surg. Oncol. 18 (2011) 2218–2223.
[10] M.A. Comunale, M. Wang, J. Hafner, et al., Identification and development of fucosylated glycoproteins as biomarkers of primary hepatocellular carcinoma, J. Proteome Res. 8 (2009) 595–602.
[11] R. Saldova, L. Royle, C.M. Radcliffe, et al., Ovarian cancer is associated with changes in glycosylation in both acute-phase proteins and IgG, Glycobiology 17 (2007) 1344–1356.
[12] J.A. Marrero, R.J. Fontana, S. Fu, et al., Alcohol, tobacco and obesity are synergistic risk factors for hepatocellular carcinoma, J. Hepatol. 42 (2005) 218–224.
[13] J. Bruix, M. Sherman, J.M. Llovet, et al., Clinical management of hepatocellular carcinoma. Conclusions of the Barcelona-2000 EASL conference. European Association for the Study of the Liver, J. Hepatol. 35 (2001) 421–430.
[14] T.M. Block, M.A. Comunale, M. Lowman, et al., Use of targeted glycoproteomics to identify serum glycoproteins that correlate with liver cancer in woodchucks and humans, Proc. Natl. Acad. Sci. USA 102 (2005) 779–784.
[15] M.A. Comunale, M. Lowman, R.E. Long, et al., Proteomic analysis of serum associated fucosylated glycoproteins in the development of primary hepatocellular carcinoma, J. Proteome Res. 5 (2006) 308–315.
[16] K. Sparbier, S. Koch, I. Kessler, et al., Selective isolation of glycoproteins and glycopeptides for MALDI-TOF MS detection supported by magnetic particles, J. Biomol. Tech. 16 (2005) 407–413.
[17] E. Miyoshi, K. Moriwaki, T. Nakagawa, Biological function of fucosylation in cancer biology, J. Biochem. 143 (2008) 725–729.

Biochemical and Biophysical Research Communications 420 (2012) 315–320

Contents lists available at SciVerse ScienceDirect

Biochemical and Biophysical Research Communications

journal homepage: www.elsevier.com/locate/ybbrc

Monoubiquitination of pro-amphiregulin regulates its endocytosis and ectodomain shedding

Shinji Fukuda [a,*], Hisayo Nishida-Fukuda [a], Hironao Nakayama [a], Hirofumi Inoue [a,b,c], Shigeki Higashiyama [a,c,*]

[a] Department of Biochemistry and Molecular Genetics, Ehime University Graduate School of Medicine, Shitsukawa, Toon, Ehime 791-0295, Japan
[b] Ehime-Nikon Bio Imaging Core-Laboratory, Shitsukawa, Toon, Ehime 791-0295, Japan
[c] Department of Cell Growth and Tumor Regulation, Proteo-Medicine Research Center (ProMRes), Ehime University, Shitsukawa, Toon, Ehime 791-0295, Japan

ARTICLE INFO

Article history:
Received 22 February 2012
Available online 7 March 2012

Keywords:
Amphiregulin
Epidermal growth factor receptor
Ubiquitination
Ectodomain shedding

ABSTRACT

All members of epidermal growth factor (EGF) family are expressed as transmembrane precursors on cell surfaces and then proteolytically converted to soluble ligands for EGF receptor (EGFR) by a disintegrin and metalloproteases (ADAMs). As enzyme-substrate complex formation is essential for this "ectodomain shedding", alteration of cell surface retention could affect their physical interaction with ADAMs and eventually contribute to shedding efficiency. Here, we showed that monoubiquitination of pro-amphiregulin (pro-AREG, an EGFR ligand) accelerated its half-life on cell surface. Monoubiquitination occurred at lysine 240 of pro-AREG as the primary acceptor site. Using a chimeric protein of pro-AREG and a monomeric ubiquitin mutant (pro-AREGmUb), immunocytochemical analysis and a cell surface biotinylation assay revealed that a significant portion of pro-AREGmUb was expressed on the cell surface, immediately endocytosed, and predominantly localized to early endosomes. Importantly, ectodomain shedding of pro-AREGmUb induced by tetradecanoyl phorbol acetate was significantly reduced in comparison to wild-type pro-AREG. These results suggested that pro-AREG monoubiquitination and the subsequent trafficking to intracellular organelles is a novel shedding regulatory mechanism that contributes to the secretion of EGFR ligands in growth factor signaling.

1. Introduction

Cell surface proteins are dynamically controlled during cell growth and differentiation. The proteolytic release of extracellular domains from transmembrane proteins is an important regulatory event occurring on the plasma membrane for cell signaling. The process, ectodomain shedding, is executed by members of the a disintegrin and metalloproteases (ADAMs) family of transmembrane-metalloproteases, which have a profound impact on the regulation of membrane-anchored growth factors and cytokines, their receptors, and cell adhesion molecules [1,2]. Epidermal growth factor receptor (EGFR) ligands consist of seven members, including EGF, amphiregulin (AREG), heparin binding EGF-like growth factor (HB-EGF), transforming growth factor α (TGFα), betacellulin, epiregulin, and epigen, which are also representative membrane-anchored growth factors and appear to be primary ADAMs substrates [3].

In normal cells, ectodomain shedding and secretion of soluble EGFR ligands should be tightly regulated [3]. In contrast, enhanced ectodomain shedding of EGFR ligands has been reported in tumor cells, causing aberrant EGFR signaling hyperactivation followed by tumor progression [4]. To date, the regulatory mechanism of ectodomain shedding still remains to be elucidated, but it is conceivable that intracellular localization of EGFR ligands could serve as an important determinant in the spatial regulation of ectodomain shedding, because colocalization of EGFR ligands and ADAMs is essential for the proteolytic event. The amino acid sequences of the EGFR ligand cytoplasmic domains affect their intracellular localization. In polarized epithelial cells, pro-AREG and pro-TGFα are selectively delivered to basolateral membranes [5–7], and a recent study identified a basolateral sorting motif within the pro-AREG cytoplasmic domain [8]. Notably, this cytoplasmic domain has been reported to specify pro-TGFα cleavage to form soluble growth factor [9]. These results suggest a possible link between intracellular localization of EGFR ligands and ectodomain shedding, and also imply the importance of cytoplasmic domains when considering physical interactions between EGFR ligands and ADAMs.

Based on these observations, we hypothesized that the modification of cytoplasmic domains of EGFR ligands regulates their intracellular localization, thereby eventually affecting ectodomain

* Corresponding authors. Address: Department of Biochemistry and Molecular Genetics, Ehime University Graduate School of Medicine, Ehime University, Shitsukawa, Toon, Ehime 791-0295, Japan. Fax: +81 89 960 5256.
E-mail addresses: sfukuda@m.ehime-u.ac.jp (S. Fukuda), shigeki@m.ehime-u.ac.jp (S. Higashiyama).

0006-291X/$ - see front matter © 2012 Elsevier Inc. All rights reserved.
http://dx.doi.org/10.1016/j.bbrc.2012.02.156

shedding. Accumulating evidence has established that ubiquitination at lysine residues of various transmembrane proteins influences their intracellular localization, and the best-studied example is ubiquitin modification of EGFR in regards to its internalization and degradation [10,11]. As EGFR ligands are synthesized as transmembrane proteins and their cytoplasmic domains are accessible by cytoplasmic ubiquitin ligases, it could be possible that cytoplasmic domains of EGFR ligands are also modified by ubiquitin. In this study, a ligand for EGFR, AREG, was examined to determine whether it possessed a sequence for ubiquitin conjugation and the results suggested that monoubiquitination of the pro-AREG cytoplasmic domain was involved in endocytosis and subsequent ectodomain shedding.

2. Materials and methods

2.1. Cells and plasmids

MCF7 and HT1080 cells were obtained from American Type Culture Collection (Manassas, VA, USA) and RIKEN Cell Bank (RIKEN Bioresource Center, Ibaraki, Japan), respectively. Expression vectors encoding enhanced green fluorescent protein-GTP-binding protein (EGFP-Rabs) were kindly provided by Dr. Fukuda (Tohoku University, Sendai City, Japan) [12,13]. Expression vectors encoding lysine substitution mutants were generated by site-directed mutagenesis using pro-AREGwt-pME18SIII as a template [14]. FLAG-ubiquitin-pcDNA3.1 was generated by subcloning PCR-amplified ubiquitin cDNA into pcDNA3.1 with the FLAG epitope. According to information regarding EGFR-Ub-mut (EGFR-$Ub^{K48R/\Delta GG}$, [10]), wild-type (wt) ubiquitin was converted to $Ub^{K48R/\Delta GG}$ and fused to pro-AREGwt, generating a pro-AREGmUb chimera. Residue 107 to the C-terminus of wt and uncleavable pro-AREG (pro-AREGuc) was fused to alkaline phosphatase (AP) [15] and subcloned into pcDNA3.1, generating AP-tagged constructs.

2.2. Transfection, immunoprecipitation, and western blot analysis

Ubiquitinated pro-AREG endogenously expressed in MCF7 was detected by lysing 1×10^7 cells with 1 mL of RIPA buffer solution supplemented with Protease inhibitor cocktail (F. Hoffman-La Roche, Ltd., Basel, CH). Debris was removed by centrifugation and the supernatants were incubated with 0.5 μg anti-AREG antibodies (AF262, R&D Systems, Inc., Minneapolis, MN, USA) for 4 h with rotation. Then, protein G sepharose (bed volume, 30 μL) were added and incubated a further 2 h. Beads were washed 3 times with 800 μL of wash buffer (Tris–HCl, pH 8.0, 150 mM NaCl, 0.1% NP40, v/v). The eluted immunoprecipitates were boiled in Laemmli SDS buffer for 3 min, separated by SDS–PAGE, and analyzed by western blotting using antibodies against AREG, ubiquitin (P4D10, Cell Signaling Technology, Inc., Danvers, MA, USA) and β-actin (AC-15, Sigma–Aldrich, St. Louis, MO, USA). To determine the lysine residue responsible for ubiquitination, HT1080 cells were transfected with expression plasmids encoding pro-AREGwt and mutant derivatives together with FLAG-ubiquitin using Lipofectamine2000 (Invitrogen, Life Technologies, Grand Island, NY, USA) according to the recommended protocol. The next day, cell lysates were immunoprecipitated with anti-AREG antibodies as described above. To remove the putative pro-AREG binding protein conjugated with ubiquitin, immunoprecipitates were denatured by boiling for 5 min, immunoprecipitated again using anti-AREG antibodies, and analyzed using anti-FLAG antibody.

2.3. Immunocytochemistry

Conventional immunocytochemistry was performed by fixing cells with 4% paraformaldehyde for 20 min and permeabilizing them in phosphate buffered saline (PBS) containing 1% TritonX-100 (v/v) for 5 min. After subsequent incubation in blocking buffer (PBS containing 10% fetal bovine serum and 1% TritonX-100, v/v), cells were incubated with antibodies (as described in figure legends). The next day, antibodies were removed by rinsing and the cells were stained with secondary antibodies and Hoechst33342 (Molecular Probes, Life Technol.); secondary antibodies were anti-goat IgG-FITC (705-095-147), anti-goat IgG-Cy3 (705-165-147), and anti-mouse IgG-FITC (715-165-151, Jackson ImmunoResearch Laboratories, Inc., West Grove, PA, USA). In the antibody uptake experiment, HT1080 cells were transfected with empty vector or expression plasmids encoding pro-AREGwt or pro-AREGmUb. The following day, living transfected cells were incubated with anti-AREG antibodies (2 μg/mL) at 37 °C for 30 min and then fixed. After permeabilization, cells were stained with anti-early endosome-associated protein (EEA1) antibody (14/EEA1, BD Transduction Laboratories, Lexington, KY, USA). Primary antibodies and nuclei were detected by the secondary antibodies above and Hoechst33342.

2.4. Other cell based assays

The cell surface biotinylation assay and the AP assay were carried out essentially as described previously [15,16]. Biotinylated bands were detected and quantified by ImageQuant LAS 4000 (GE Healthcare, Buckinghamshire, UK). The result of the AP assay was presented as mean ± standard deviation. Student's *t*-test was used to compare mean values. A *p*-value of <0.01 was defined as statistical significance.

3. Results

3.1. Pro-AREG was monoubiquitinated at lysine 240

To examine whether pro-AREG was modified by ubiquitination, endogenous pro-AREG was enriched by immunoprecipitation from whole cell lysates of MCF7, a human breast cancer carcinoma cell line from which AREG was initially identified [17]. HT1080, a human fibrosarcoma cell line, was used as a negative control that does not express any detectable levels of AREG protein (Fig. 1A). Immunoprecipitation and immunoblotting using antibodies against extracellular domains of pro-AREG allowed detection of endogenous pro-AREG as multiple bands in MCF7 (Fig. 1B, left panel). Based on a previous study [18], approximately 40-, 35-, and <20-kDa were judged as glycosylated full-length, non-glycosylated full-length, and N-terminal-processed pro-AREG, respectively. Western blot analysis of the immunoprecipitates revealed that ubiquitinated pro-AREG was detected at ~50-kDa with smeared high molecular weight species from MCF7 but not in control precipitates (Fig. 1B, right panel). These results suggested that, in the steady state, a portion of MCF7 endogenous pro-AREG was ubiquitinated.

As there are three lysine residues in the cytoplasmic domain of pro-AREG, the responsive lysine for ubiquitination was identified by constructing seven pro-AREG mutants (mut 1–7), which possessed lysine (K) to arginine (R) substitutions (Fig. 1C). These mutants were coexpressed with FLAG-tagged ubiquitin in HT1080 cells, immunoprecipitation by anti-AREG antibodies, and analyzed using anti-FLAG antibody. The most prominent signal was detected at ~50-kDa (Fig. 1D, right panel), suggesting that monoubiquitination of full-length pro-AREG occurred in HT1080 as well as MCF7. The other ubiquitinated forms were presumed to be monoubiquitinated pro-AREG produced by HT1080-specific

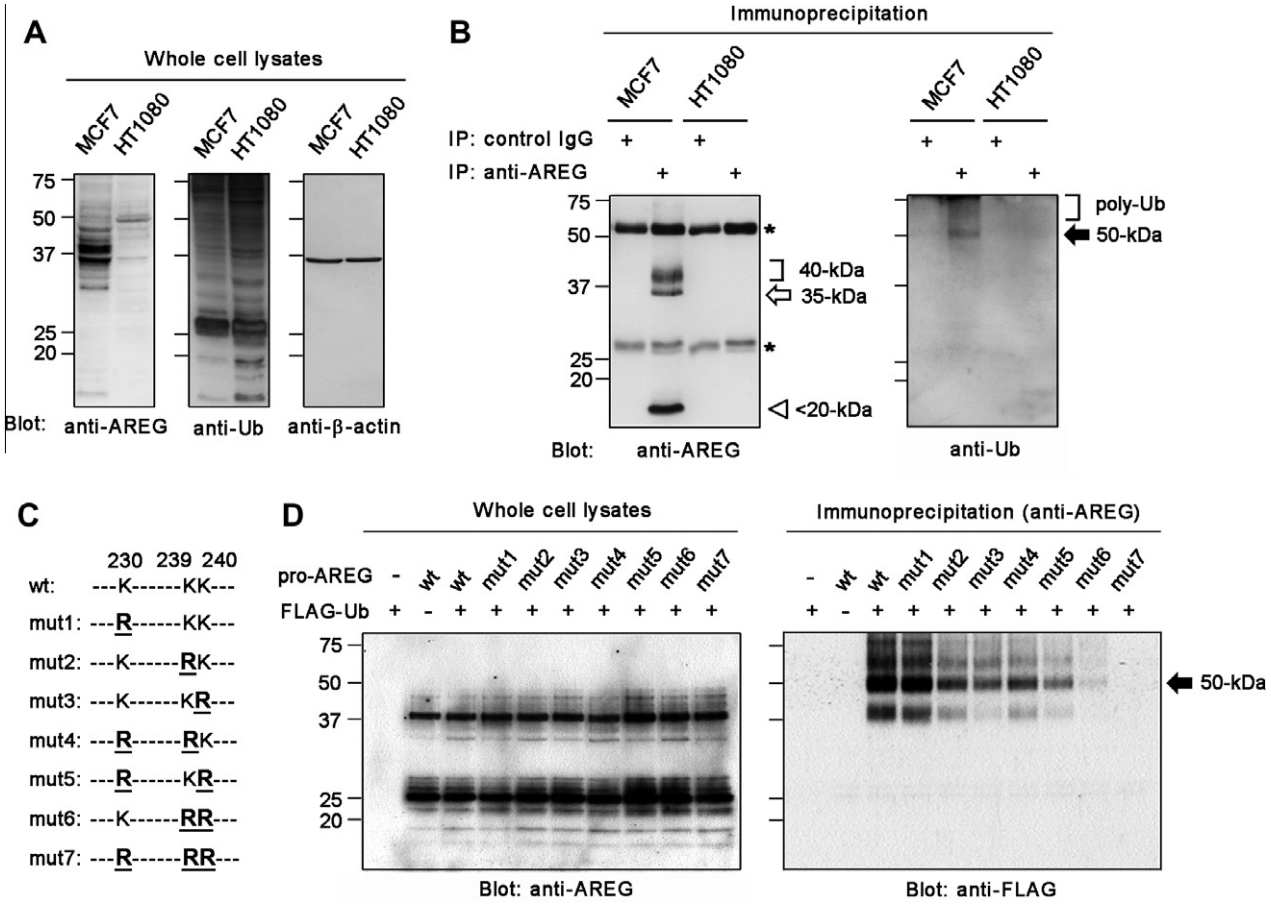

Fig. 1. Modification of pro-AREG by monoubiquitination. (A) Expression of pro-AREG, ubiquitin, and β-actin in whole cell lysates of MCF7 and HT1080 by western blot analysis. (B) Ubiquitinated pro-AREG in MCF7. Lysates in (A) were subjected to immunoprecipitation with anti-AREG antibodies. Precipitates were analyzed by SDS–PAGE and western blotting using anti-AREG (left) and anti-ubiquitin (right) antibodies. Left panel: parentheses (40-kDa), white arrow (35-kDa), white arrowhead (20-kDa), and asterisks indicate glycosylated full-length, non-glycosylated full-length, N-terminus-processed pro-AREG, and IgG chains, respectively. Right panel: black arrow (50-kDa) and parentheses (poly-Ub) indicate monoubiquitinated and polyubiquitinated pro-AREG, respectively. (C) Amino acid sequences of pro-AREG derivatives. Lysine (K) to arginine (R) substitutions are underlined. (D) Ubiquitination of pro-AREG in HT1080. HT1080 were transfected with expression vectors encoding wt, mutant pro-AREG, and FLAG epitope-tagged ubiquitin. After the immunoprecipitation with AREG antibodies, immunoprecipitates were analyzed by the FLAG antibody. Left panel: expression of pro-AREG derivative. Right panel: Ubiquitinated AREG detected by the FLAG antibody. The black arrow (50-kDa) indicates monoubiquitinated pro-AREG.

N-terminal processing/glycosylation and polyubiquitinated pro-AREG.

Ubiquitination was not affected when K230 was substituted to arginine and barely detectable with mut 6 and 7 (Fig. 1D, right panel, wt and mut 1, 6, and 7), which excluded K230 being the responsive residue. Ubiquitination of mut 3 and 5, which carried an arginine substitution at K240 in common, was significantly impaired in comparison to mut 2 and 4 (Fig. 1D, right panel, mut 2–5). Taken together with the MCF7 results, these data suggested that K240 was the primary ubiquitin acceptor site in the cytoplasmic domain of pro-AREG and that K239 also acted as a potential ubiquitination site. In further experiments, the focus was on the possible role of pro-AREG monoubiquitination.

3.2. Pro-AREGmUb mutant predominantly localized at early endosomes, but not recycling endosome

A previous study has shown that a monoubiquitination event is sufficient for EGFR internalization [10]. The role of monoubiquitinated pro-AREG was studied in detail by use of a fusion protein composed of pro-AREGwt and a previously reported ubiquitin mutant (hereafter we referred to as pro-AREGmUb). The mutated ubiquitin possessed a lysine to arginine substitution at the major polyubiquitination residue K48 and also lacked two carboxyl-terminal glycine residues ($Ub^{K48R\Delta GG}$, [10]). Plasmids encoding pro-AREGwt and pro-AREGmUb were transfected into cells and the intracellular localization in the steady state was analyzed by immunocytochemistry. Pro-AREGwt was found to be localized at plasma membranes as well as in the intracellular compartment, while pro-AREGmUb predominantly accumulated at intracellular vesicles (Fig. 2A). The organelle type at which pro-AREGmUb located was identified by cotransfection of cells with pro-AREGmUb and EGFP-Rab cDNAs; Rab5, Rab7, and Rab11 are known to be distributed primarily on early, late, and recycling endosomes, respectively [12,13]. Pro-AREGmUb primarily colocalized with EGFP-Rab5 and, to some extent, with EGFP-Rab7 but scarcely colocalized with EGFP-Rab11 at all (Fig. 2B). These results suggested that monoubiquitination of pro-AREG affected intracellular trafficking, leading to its accumulation at early and late endosomes, but not in recycling endosomes.

3.3. Pro-AREGmUb mutant was delivered to the cell surface and rapidly endocytosed

Next, the question was addressed as to whether the pro-AREG and monoubiquitin chimera was (1) transported to the plasma membrane, followed by endosomal targeting, or (2) directly transported to early endosomes immediately after protein synthesis without targeting to the cell surface. The intracellular trafficking

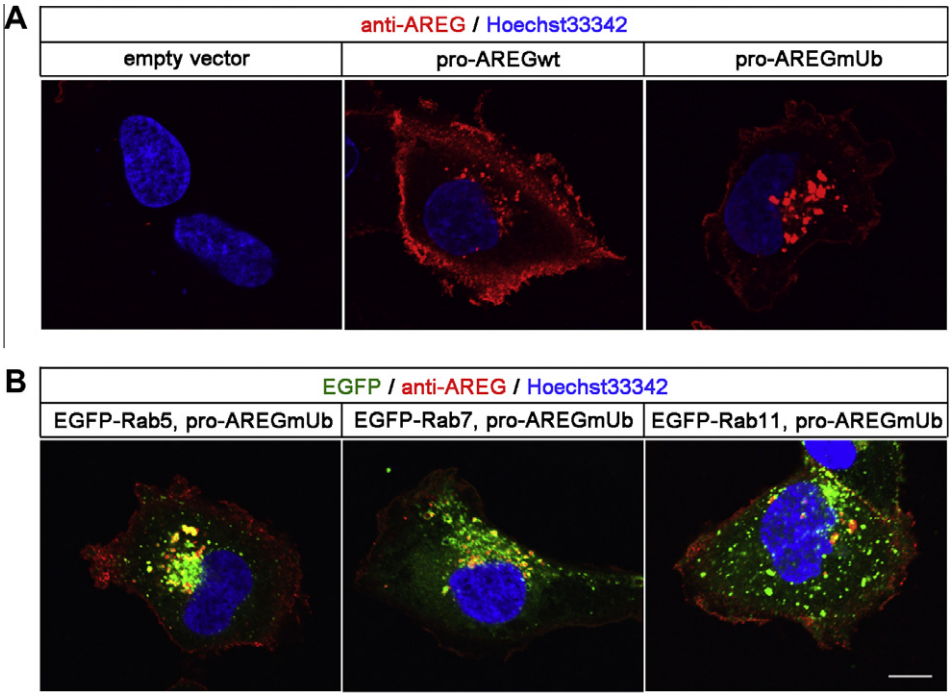

Fig. 2. pro-AREG-monoubiquitin chimera mainly localized in early endosomes. (A) HT1080 transfected with empty vector or vectors encoding pro-AREGwt or pro-AREGmUb. Cells were fixed, permeabilized, and immunostained with anti-AREG antibodies (red); nuclei were stained with Hoechst33342 (blue). Scale bar: 20 μm. (B) HT1080 transfected as in (A), together with plasmids that express EGFP-Rab5, EGFP-Rab7, or EGFP-Rab11. GFP-Rabs proteins, pro-AREGmUb, and nuclei are shown in green, red, and blue, respectively. Scale bar: 20 μm.

of pro-AREGwt and pro-AREGmUb was tracked by adding anti-AREG antibodies to the culture medium, which then bound to pro-AREG on cell surfaces of living HT1080 cells. After a 30 min incubation, the cells were fixed, stained with an early endosomal marker, EEA1, and the primary antibodies were detected using their secondary antibodies. In empty vector-transfected cells, no anti-AREG signal was observed, excluding nonspecific incorporation of antibodies into transfected cells (Fig. 3A, left). We detected anti-AREG antibodies incorporated into pro-AREGwt- and pro-AREGmUb-expressing HT1080 (Fig. 3A, middle and right). Immunostaining revealed that pro-AREGmUb significantly colocalized with EEA1 (Fig. 3A, right) and, in part, also merged with a lysosome marker, lysosome-associated membrane protein (Lamp1, data not shown).

In a parallel experiment, the amounts of pro-AREGwt and pro-AREGmUb expressed on cell surfaces were compared by labeling with a membrane impermeable biotin reagent. After cycloheximide treatment, pro-AREGwt and pro-AREGmUb were immunoprecipitated using anti-AREG antibodies, separated by SDS–PAGE, and analyzed by horseradish peroxidase (HRP)-conjugated streptavidin. The results showed that pro-AREGmUb as well as pro-AREGwt were expressed on cell surfaces, but the full-length and N-terminus-processed forms of pro-AREGmUb present on cell surface rapidly disappeared from the surfaces, compared with pro-AREGwt (Fig. 3B). These results suggested that, after protein synthesis, a significant portion of pro-AREGmUb was transported to the cell surface, but then rapidly endocytosed by the ubiquitin-mediated mechanism and localized at early and late endosomes.

3.4. Ectodomain shedding was abrogated when pro-AREG was fused to monoubiquitin

As pro-AREGmUb rapidly disappeared from plasma membranes where TPA-activated ADAMs cleave pro-AREG [19], the frequency of enzyme/substrate encounters might be altered. Therefore, it was hypothesized that monoubiquitination could affect pro-AREG shedding. The effect of monoubiquitination on the ectodomain shedding was examined using a quantitative alkaline phosphatase (AP) assay that estimated shedding efficiency of pro-AREG [15]. The expression level of AP-pro-AREGmUb was slightly lower than that of wild-type and uncleavable (uc) AP-pro-AREG due to the accelerated turnover (Fig. 4A). In these cells, the expression of AP-pro-AREG derivatives was driven by the simian virus 40 early promoter, suggesting that variability in their expression was post-translationally regulated by the monoubiquitin moiety. Based on the observed AP activity released into the culture medium, TPA stimulation induced >10-fold increase in the amount of shed AP-pro-AREGwt, whereas that of AP-pro-AREGuc was completely abrogated (Fig. 4B). In the case of AP-pro-AREGmUb, although the amount of the released AP was severely reduced in comparison to with pro-AREGwt, a ~3.8-fold increase in the release of shed AP-pro-AREGmUb was observed after TPA stimulation (Fig. 4B). Taken together, these results suggested that monoubiquitination and subsequent pro-AREG endocytosis exerted an inhibitory effect on the ectodomain shedding through regulation of intracellular localization.

4. Discussion

In the present study, we report that pro-AREG is a substrate for ubiquitin modification mainly at the lysine 240. The fusion protein pro-AREGmUb was rapidly endocytosed and predominantly localized to early but not recycling endosomes. Furthermore, unstimulated and TPA-induced pro-AREG ectodomain shedding was abrogated by fusion to the monoubiquitin moiety. Based on these observations, transmembrane protein ubiquitination on the cell surface and subsequent endocytosis is proposed to be one of the

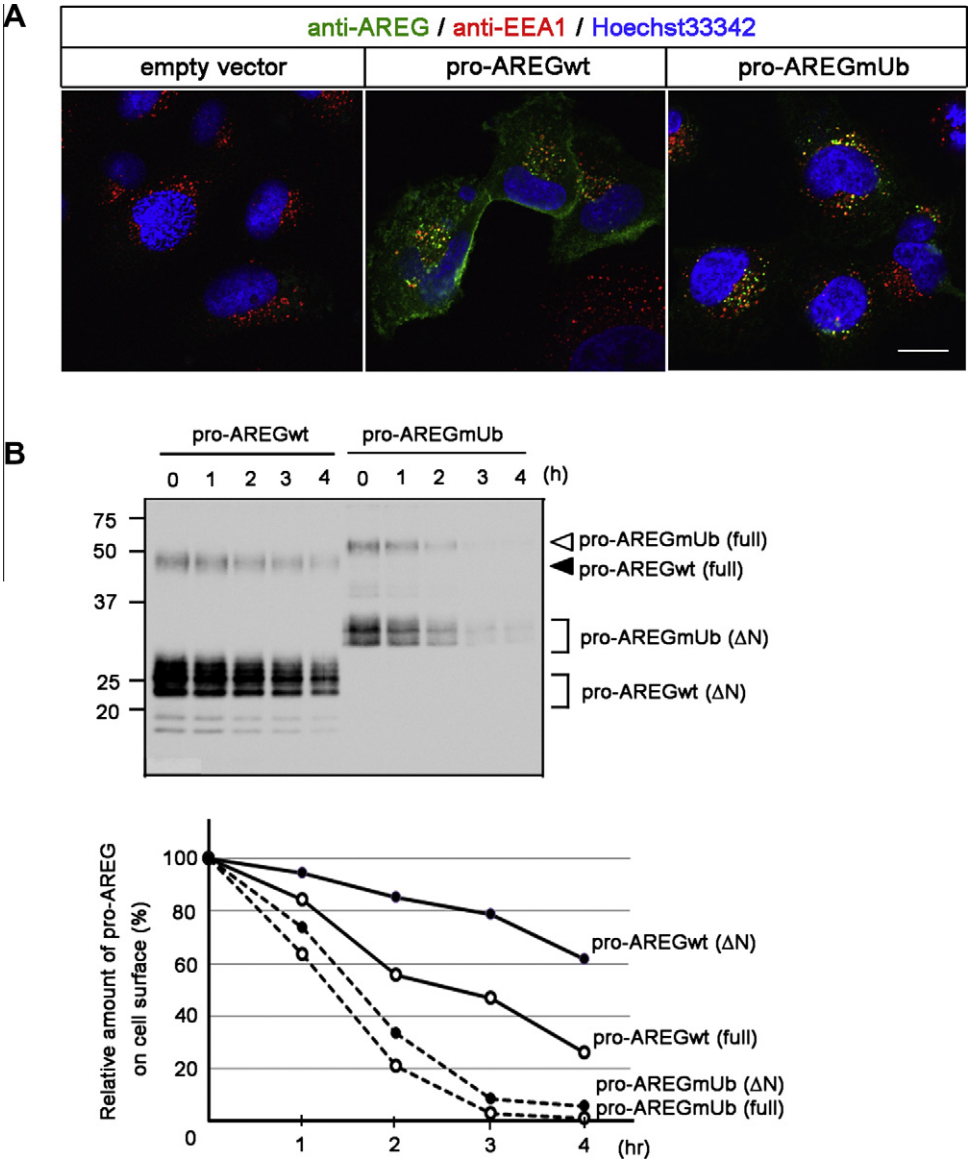

Fig. 3. Pro-AREGmUb chimera was expressed on the cell surface and rapidly internalized. (A) Antibody incorporation assay. HT1080 cells were transfected with plasmids as in Fig. 2A. Living cells were incubated with anti-AREG antibodies and then fixed. Cells were permeabilized and stained with anti-EEA1 antibody. Primary antibodies were detected by their respective secondary antibodies (anti-AREG, green; anti-EEA1, red). Nuclei were stained with Hoechst33342 (blue). Scale bar: 40 μm. (B) The amount of pro-AREGwt and pro-AREGmUb on cell surface. HT1080 cells transfected with plasmids encoding pro-AREGwt or pro-AREGmUb were treated with cycloheximide (10 μg/mL) for 4 h (defined as time point 0). After incubation (0–4 h), cell surface proteins were labeled with biotin and immunoprecipitated with anti-AREG antibodies. Precipitated pro-AREG was detected by avidin-HRP, and the band intensity of relative amounts of cell-surface pro-AREG was quantified. Note that cell surface biotinylation does not label non-glycosylated pro-AREG because it localizes to the intracellular compartment.

shedding regulatory mechanisms that eventually down-regulates conversion from the proform to soluble form.

Previously, we have shown that the full-length and carboxy-terminal fragments (CTFs) of pro-AREG and pro-HB-EGF translocate to the perinucleus and nuclear envelope and to engage in transcription [14,20]. However, the physiological significance of CTFs, particularly their roles in ectodomain shedding, remains elusive. Recent efforts have identified a large number of interaction partners with ADAMs [1], but considering the spatiotemporal regulation of ectodomain shedding, we have to pay much attention to the involvement of the shedding substrate-binding proteins. Naked 2 (NKD2), a negative regulator of the canonical Wnt signaling, has been reported to bind to pro-TGFα's cytoplasmic tail and escort it to the basolateral membrane of MDCK cells [21]. Although NKD2 acts in the anterograde trafficking of pro-TGFα, and pro-AREG does not interact with NKD2, the report strongly suggests that cytoplasmic domain-binding protein-dependent regulation of intracellular trafficking of EGFR ligands would be crucial. Based on the present results, ubiquitin modification is speculated to possibly have changed the interaction partner of pro-AREG, thereby limiting the duration of pro-AREG retention on the plasma membrane.

The binding of EGFR ligands to EGFR acts as a trigger for the conjugation of ubiquitin to EGFR by the multidomain c-Cbl protein [10,21], whereas here pro-AREG ubiquitination was observed under steady-state conditions. Examination of the properties of pro-AREG mut 7, in which all cytoplasmic domain lysine residues were arginine-substituted, found that the intracellular localization and shedding efficiency of mut 7 were indistinguishable from that of

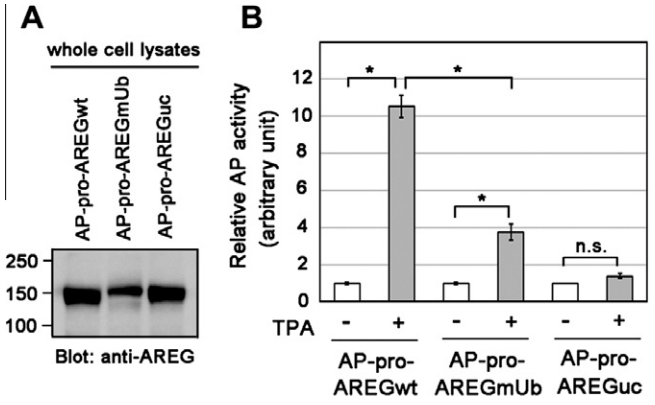

Fig. 4. Ectodomain shedding of pro-AREG is abrogated by ubiquitin conjugation. (A) Expression of AP-tagged proAREG derivatives in HT1080 cells. (B) AP activity released into the culture medium in response to the TPA stimulation. Cells were transfected with expression plasmids encoding AP-tagged pro-AREGwt, pro-AREGmUb, or pro-AREGuc (negative control). Cells were treated with 100 nM TPA for 30 min and AP activity in the conditioned medium was measured. Data are indicated as mean ± standard deviation; * and n.s. indicate $p < 0.01$ and not significant by the Student's *t*-test, respectively.

pro-AREGwt (data not shown). Although ubiquitinated pro-AREG was reproducibly detected under the present experimental condition, these results indicated that pro-AREG ubiquitination occurred at a low frequency in the steady state. In further studies, it would be necessary to identify signals or enzymes that efficiently induce ubiquitination and to uncover their related physiological significance in the regulation of pro-AREG function. Monoubiquitination-mediated endocytosis of transmembrane substrates for ADAMs could be an important posttranslational regulatory mechanism of ectodomain shedding, because this process could directly and immediately compete with an ADAM-mediated overproduction of soluble ligands at the posttranslational level, when cells are exposed to excess environmental shedding stimuli, such as high doses of ultraviolet irradiation or severe wounding.

Overexpression of AREG mRNA and protein has been reported in a wide variety of human epithelial carcinomas from breast, lung, colon, and liver [22]. It has also been reported that pro-AREG is involved in resistance to radiation and chemotherapeutic agents [22,23]. In the present study, as the amount of released ectodomain was reduced by fusing pro-AREG to ubiquitin, it might be possible that ubiquitination-inducing signals or enzymes could suppress aberrant activation of EGFR signaling through the reduction of AREG secretion. Future investigations to elucidate the molecular mechanism for pro-AREG cytoplasmic domain modification would provide valuable clues not only for full understanding of the regulation of EGFR ligand activity but also for the development of a therapeutic target for cancer treatment.

Acknowledgments

We thank the members of our laboratory. We are grateful to Dr. Fukuda (Tohoku University, Japan) for the gift of EGFP-Rab constructs. This work was supported by a Grant-in-Aid for Scientific Research to S. Fukuda (No. 70398238) and S. Higashiyama (No. 20390082) from the Ministry of Education, Culture, Sports, Science and Technology of Japan.

References

[1] D.R. Edwards, M.M. Handsley, C.J. Pennington, The ADAM metalloproteinases, Mol. Aspects Med. 29 (2008) 258–289.
[2] G. Murphy, The ADAMs: signalling scissors in the tumour microenvironment, Nat. Rev. Cancer 8 (2008) 929–941.
[3] S. Higashiyama, D. Nanba, H. Nakayama, H. Inoue, S. Fukuda, Ectodomain shedding and remnant peptide signalling of EGFRs and their ligands, J. Biochem. (Tokyo) 150 (2011) 15–22.
[4] K.J. Wilson, J.L. Gilmore, J. Foley, M.A. Lemmon, D.J. Riese 2nd, Functional selectivity of EGF family peptide growth factors: implications for cancer, Pharmacol. Ther. 122 (2009) 1–8.
[5] P.J. Dempsey, R.J. Coffey, Basolateral targeting and efficient consumption of transforming growth factor-alpha when expressed in Madin-Darby canine kidney cells, J. Biol. Chem. 269 (1994) 16878–16889.
[6] L. Damstrup, S.K. Kuwada, P.J. Dempsey, C.L. Brown, C.J. Hawkey, H.S. Poulsen, H.S. Wiley, R.J. Coffey Jr., Amphiregulin acts as an autocrine growth factor in two human polarizing colon cancer lines that exhibit domain selective EGF receptor mitogenesis, Br. J. Cancer 80 (1999) 1012–1019.
[7] C.L. Brown, R.J. Coffey, P.J. Dempsey, The proamphiregulin cytoplasmic domain is required for basolateral sorting, but is not essential for constitutive or stimulus-induced processing in polarized Madin-Darby canine kidney cells, J. Biol. Chem. 276 (2001) 29538–29549.
[8] J.D. Gephart, B. Singh, J.N. Higginbotham, J.L. Franklin, A. Gonzalez, H. Folsch, R.J. Coffey, Identification of a novel mono-leucine basolateral sorting motif within the cytoplasmic domain of amphiregulin, Traffic 12 (2011) 1793–1804.
[9] M.W. Bosenberg, A. Pandiella, J. Massague, The cytoplasmic carboxy-terminal amino acid specifies cleavage of membrane TGF alpha into soluble growth factor, Cell 71 (1992) 1157–1165.
[10] K. Haglund, S. Sigismund, S. Polo, I. Szymkiewicz, P.P. Di Fiore, I. Dikic, Multiple monoubiquitination of RTKs is sufficient for their endocytosis and degradation, Nat. Cell Biol. 5 (2003) 461–466.
[11] S. Sigismund, T. Woelk, C. Puri, E. Maspero, C. Tacchetti, P. Transidico, P.P. Di Fiore, S. Polo, Clathrin-independent endocytosis of ubiquitinated cargos, Proc. Natl. Acad. Sci. USA 102 (2005) 2760–2765.
[12] T. Matsui, T. Itoh, M. Fukuda, Small GTPase Rab12 regulates constitutive degradation of transferrin receptor, Traffic 12 (2011) 1432–1443.
[13] R. Misaki, T. Nakagawa, M. Fukuda, N. Taniguchi, T. Taguchi, Spatial segregation of degradation- and recycling-trafficking pathways in COS-1 cells, Biochem. Biophys. Res. Commun. 360 (2007) 580–585.
[14] M. Isokane, M. Hieda, S. Hirakawa, M. Shudou, K. Nakashiro, K. Hashimoto, H. Hamakawa, S. Higashiyama, Plasma-membrane-anchored growth factor pro-amphiregulin binds A-type lamin and regulates global transcription, J. Cell Sci. 121 (2008) 3608–3618.
[15] S. Tokumaru, S. Higashiyama, T. Endo, T. Nakagawa, J.I. Miyagawa, K. Yamamori, Y. Hanakawa, H. Ohmoto, K. Yoshino, Y. Shirakata, Y. Matsuzawa, K. Hashimoto, N. Taniguchi, Ectodomain shedding of epidermal growth factor receptor ligands is required for keratinocyte migration in cutaneous wound healing, J. Cell Biol. 151 (2000) 209–219.
[16] K. Goishi, S. Higashiyama, M. Klagsbrun, N. Nakano, T. Umata, M. Ishikawa, E. Mekada, N. Taniguchi, Phorbol ester induces the rapid processing of cell surface heparin-binding EGF-like growth factor: conversion from juxtacrine to paracrine growth factor activity, Mol. Biol. Cell 6 (1995) 967–980.
[17] M. Shoyab, V.L. McDonald, J.G. Bradley, G.J. Todaro, Amphiregulin: a bifunctional growth-modulating glycoprotein produced by the phorbol 12-myristate 13-acetate-treated human breast adenocarcinoma cell line MCF-7, Proc. Natl. Acad. Sci. USA 85 (1988) 6528–6532.
[18] C.L. Brown, K.S. Meise, G.D. Plowman, R.J. Coffey, P.J. Dempsey, Cell surface ectodomain cleavage of human amphiregulin precursor is sensitive to a metalloprotease inhibitor. Release of a predominant N-glycosylated 43-kDa soluble form, J. Biol. Chem. 273 (1998) 17258–17268.
[19] U. Sahin, G. Weskamp, K. Kelly, H.M. Zhou, S. Higashiyama, J. Peschon, D. Hartmann, P. Saftig, C.P. Blobel, Distinct roles for ADAM10 and ADAM17 in ectodomain shedding of six EGFR ligands, J. Cell Biol. 164 (2004) 769–779.
[20] M. Hieda, M. Isokane, M. Koizumi, C. Higashi, T. Tachibana, M. Shudou, T. Taguchi, Y. Hieda, S. Higashiyama, Membrane-anchored growth factor, HB-EGF, on the cell surface targeted to the inner nuclear membrane, J. Cell Biol. 180 (2008) 763–769.
[21] K. Roepstorff, M.V. Grandal, L. Henriksen, S.L. Knudsen, M. Lerdrup, L. Grovdal, B.M. Willumsen, B. van Deurs, Differential effects of EGFR ligands on endocytic sorting of the receptor, Traffic 10 (2009) 1115–1127.
[22] B. Busser, L. Sancey, E. Brambilla, J.L. Coll, A. Hurbin, The multiple roles of amphiregulin in human cancer, Biochim. Biophys. Acta 2011 (1816) 119–131.
[23] M. Yoshida, T. Shimura, S. Fukuda, T. Mizoshita, S. Tanida, H. Kataoka, T. Kamiya, T. Nakazawa, S. Higashiyama, T. Joh, Nuclear translocation of pro-amphiregulin induces chemoresistance in gastric cancer, Cancer Sci. (2012) in press. doi:10.1111/j.1349-7006.2012.02204.x.

Biochemical and Biophysical Research Communications 420 (2012) 321–324

Contents lists available at SciVerse ScienceDirect

Biochemical and Biophysical Research Communications

journal homepage: www.elsevier.com/locate/ybbrc

The N-terminal domain determines the affinity and specificity of H1 binding to chromatin

Christine Öberg, Sergey Belikov *

Karolinska Institute, Department of Cell and Molecular Biology, P.O. Box 285, SE-17177 Stockholm, Sweden

ARTICLE INFO

Article history:
Received 28 February 2012
Available online 7 March 2012

Keywords:
Linker histone
Histone H1
Xenopus oocytes
Histone H1 N-terminal domain
Chromatin

ABSTRACT

Linker histone H1, one of the most abundant nuclear proteins in multicellular eukaryotes, is a key component of the chromatin structure mainly due to its role in the formation and maintenance of the 30 nm chromatin fiber. It has a three-domain structure; a central globular domain flanked by a short N-terminal domain and a long, highly basic C-terminal domain. Previous studies have shown that the binding abilities of H1 are at large determined by the properties of the C-terminal domain; much less attention has been paid to role of the N-terminal domain. We have previously shown that H1 can be reconstituted via cytoplasmic mRNA injection in *Xenopus* oocytes, cells that lack somatic H1. The heterologously expressed H1 proteins are incorporated into *in vivo* assembled chromatin at specific sites and the binding event is monitored as an increase in nucleosomal repeat length (NRL). Using this setup we have here compared the binding properties of wt-H1.4 and hH1.4 devoid of its N-terminal domain (ΔN-hH1.4). The ΔN-hH1.4 displays a drastically lower affinity for chromatin binding as compared to the wild type hH1.4. Our data also indicates that ΔN-hH1.4 is more prone to unspecific chromatin binding than the wild type. We conclude that the N-terminal domain of H1 is an important determinant of affinity and specificity of H1-chromatin interactions.

1. Introduction

The linker histone, often collectively called H1, is located at the surface of the nucleosome, interacting with the DNA at its entry and exit points. Despite being the key molecule in formation and maintenance of the higher order chromatin structure [1] and its vital role in mammalian development [2] histone H1 is not as well studied as the core histones. Histone H1 consists of a globular "winged-helix" domain flanked by lysine rich C- and N-terminal domains [3]. Multicellular organisms have several different linker histone subtypes, present simultaneously in the same cell type. Individual H1 variants demonstrate both apparent inter-species conservation and pronounced intra-species divergence. Within one species the H1 globular domain tends to be highly conserved while the N- and C-terminal domains are more divergent. The C-terminal tail comprises almost half of the protein and thus, much of the heterogeneity between subtypes can be attributed to this part (reviewed in [4]). The C-terminal domain has been implicated to be a major contributor to H1s binding abilities [5] and much effort has been spent elucidating the role of the C-terminal domain in the maintenance of higher order chromatin structure [6]. The N-terminal domain has received much less attention. It is known that the N-terminal affects H1's behavior in terms of chromatin binding since deletion of the N-terminal domain results in reduced affinity for chromatin binding as shown by FRAP-studies [5].

The *Xenopus* oocyte is a giant cell that can be used as an "*in vivo* test tube" for studies of DNA–protein interactions. By microinjection of *in vitro* synthesized mRNA in the cytoplasm these cells can be programmed to express (a) protein(s) of interest. ssDNA is introduced via intranuclear injection and will then undergo second strand DNA synthesis concomitantly with chromatin assembly [7,8]. *Xenopus laevis* oocytes lack somatic H1 [9,10] and, thus, are especially well suited for *in vivo* studies of histone H1-DNA interactions mediated by heterologously expressed linker histones. We have previously used this approach to study linker histone H1 binding to chromatin. The binding event was monitored as a shift in the nucleosome repeat length (NRL) obtained from *in situ* micococcal nuclease (MNase) digestion [11]. This showed that the binding of linker histones, $xH1^0$ and H1A, is saturable as monitored by an increase in the NRL that reached a plateau and stays constant within a wide range of H1 concentrations [11]. We have then exploited this method to analyze the chromatin structural effects by various linker histone H1 subtypes (Öberg and Belikov, to be published elsewhere).

Abbreviations: NRL, nucleosomal repeat length; MNase, micrococcal nuclease; ΔN-hH1.4, human hH1.4 devoid of its N-terminal domain.

* Corresponding author. Fax: +46 832 3672.
E-mail addresses: christine.oberg@ki.se (C. Öberg), sergey.belikov@ki.se (S. Belikov).

0006-291X/$ - see front matter © 2012 Elsevier Inc. All rights reserved.
http://dx.doi.org/10.1016/j.bbrc.2012.02.157

Here we use the same method to address the role of N-terminal domain of the human somatic subtype histone H1.4 in its interaction with chromatin *in vivo*. Our results imply that the N-terminal domain is an important contributor both to the affinity and to the specificity of the hH1.4-chromatin interactions *in vivo*.

2. Methods

2.1. mRNA synthesis

Plasmids for *in vitro* production of the hH1.4/ΔN-hH1.4 mRNA were generated by PCR amplification of hH1.4 cDNA, NCBI reference sequence number NM_005321.2, cDNA clone using specific primers that generated BamHI and NotI sites in the 5′ and 3′ end of the inserts, respectively (available upon request). For the ΔN-hH1.4 construct the primers were chosen so that the 34 first amino acid of H1 was removed. The resulting fragments were inserted into the RN3P-vector [11,12] between the BamHI and NotI sites.

2.2. Xenopus oocyte preparation

The handling of the frogs as well as the experiments have been approved of by the Central commission for animal research (Centrala försöksdjursnämnden, CFN), reference number N61/09. Preparation of *Xenopus* oocytes and oocyte injections were performed as described earlier [13,14]. Briefly, the linker histone variants were expressed in the oocytes by cytosolic injection of 23 nl mRNA solutions (see figure legends for details). After 4–6 h incubation in oocyte media [13] at 19 °C, 7 ng of M13mp18 single stranded DNA (USB, P/N 71706) was co-injected with α-[P^{33}]$^-$dCTP (NEG613H, Perkin Elmer) in a volume of 18.3 nl in the oocyte nucleus.

2.3. MNase digestion

Oocytes were harvested 24 h after DNA injection and digested with micrococcal nuclease (MNase). The oocytes were homogenized with a Dounce homogenizer in the volume of 18 μl × number of oocytes (at least 15 oocytes were used) in 15 mM Tris–HCl pH 8.1, 50 mM KCl, 1 mM dithiothreitol (DTT), 5% glycerol and 1 mM $CaCl_2$. Three aliquotes of homogenate containing 3.3 oocytes each were digested with 8.2 U MNase (USB, P/N 70196Y) for 5 min at 15 °C. The reaction was stopped by the addition of 2× STOP-solution; 10 mM Tris–HCl pH 8.0, 10 mM EDTA, 1% SDS and 0.1 mg/ml proteinase K and sample incubated over night in 37 °C. The DNA was extracted twice with phenol:chloroform mix (2:1), isopropanol precipitated and treated with 5 μg RNase A for at least 1 h at 37 °C and finally extracted once with phenol:chloroform mix and isopropanol precipitated. DNAs were dissolved in a mix of 8 μl 5 mM Tris (8.0) and 1 mM EDTA supplemented with 4 μl 6× Orange DNA loading dye (Fermentas, #R0631). 4 μl were loaded on a 1.3% agarose gel (0.5× TBE solution).

2.4. Analysis of NRL to monitor H1-chromatin binding

The agarose gels were dried and scanned using a Fuji Bio-Imaging FLA-7000 analyzer and analyzed using Image Gauge V4.1 Software. The profiles of the MNase digestion pattern were exported as an Excel-file and reconstituted using PeakFit® v.4.12 (Seasolve Software Inc., USA). The MNase digestion pattern was smoothened using the Loess algorithm and the size marker ladders were smoothened using the FFT filtering, which is more suitable for these sharp peaks. The program estimates the maxima of the MNase and the marker profiles. The marker DNA lengths were plotted as a function of the electrophoretic mobility. The equation for this graph was used for determination of the size of the three nucleosomal band, which was used to calculate NRL.

2.5. Quantification of expressed protein

Eight oocytes per group were incubated in 3 mCi/ml of ^{14}C-lysine (NEC280E, Perkin Elmer). The linker histones were extracted in 5% perchloric acid and resolved in SDS–PAGE. The relative intensity of the bands corresponding to H1 was determined by the Image Gauge V4.1 Software. Relative protein amount was expressed in arbitrary units accounting for the difference in lysine content between the wt H1.4 and ΔN-H1.4.

3. Results

The role of the N-terminal domain of linker histone H1.4 was addressed by expression of increasing amounts of either hH1.4wt or ΔN-hH1.4 in the *Xenopus* oocytes as described previously [11]. The intracellular level of linker histones was monitored by ^{14}C-labeled lysine incorporation and subsequent analysis of the gel (Fig. 1A). Protein expression is presented in arbitrary units, and thus the particular unit counts have no relation to absolute molar amounts, but only to their ratios and relative amounts. Evidently hH1.4wt and ΔN-hH1.4 have a different number of lysines; this has been taken into account when comparing the relative protein expression levels. Introduction of H1 into the system results in incorporation of H1s in the newly assembled chromatin that can be seen by the slower migration of polynucleosomal DNA on the agarose gel, i.e. as an upward shift in the nucleosome ladder after digestion with micrococcal nuclease, MNase. This reflects the increase in nucleosome repeat length, NRL (Fig. 1B). The analysis of the agarose gel was done using Image Gauge software (Fujifilm). Since it is difficult to determine the maxima of the peaks of the MNase cleavage pattern with high precision we used a computer based curve-fitting algorithm by the program PeakFit® (Seasolve Software Inc., USA) to estimate the position of each maximum. The DNA size corresponding to trinucleosomal band was calculated by using the known DNA standard as a reference and used for NRL estimation.

The increase in NRL was plotted as a function of the relative protein amount as shown in Fig. 1C. In order to strengthen our data by statistical evaluation each group of oocytes was divided into three parts and digested with MNase and analyzed individually. Isolated DNAs were run side by side on the agarose gel (see Supplementary File 1). Both hH1.4wt and ΔN-hH1.4 results in a stepwise increase in the NRL with a final increase in NRL of roughly 20 bp, from 161.5 ± 0.4 bp to 181.6 ± 0.8 bp for hH1.4 and to 181.9 ± 3.6 bp for ΔN-hH1.4. Importantly, the NRL concentration curves for hH1.4 and ΔN-hH1.4 reach a plateau indicating that the binding of both H1 variants to chromatin is saturable, and thus, specific. However, at high concentrations of ΔN-hH1.4 (see lanes 6 and 7 in Fig. 1B) the regular nucleosome ladder is gradually replaced by a smear indicating unspecific ΔN-hH1.4 binding to chromatin at indicated concentrations of ΔN-hH1.4 (see also [11]). The deterioration of the pattern at the highest concentration of ΔN-hH1.4 makes it difficult to determine the maxima of the peaks, and results in the big standard deviation. The fact that the effect of both histones on the NRL is saturable, and thus, the H1-chromatin interaction reflects a specific binding event is in agreement with previously obtained *in vitro* and *in vivo* data [11,15]. We observed that three to four times higher levels of ΔN-hH1.4 as compared to wt hH1.4 are required to reach saturating effect on the NRL (Fig. 1C). This indicates that the truncated protein has a lower affinity for chromatin binding.

Chromatin containing hH1.4 shows "canonical" MNase digestion profiles and corresponding scans reveals matching pattern

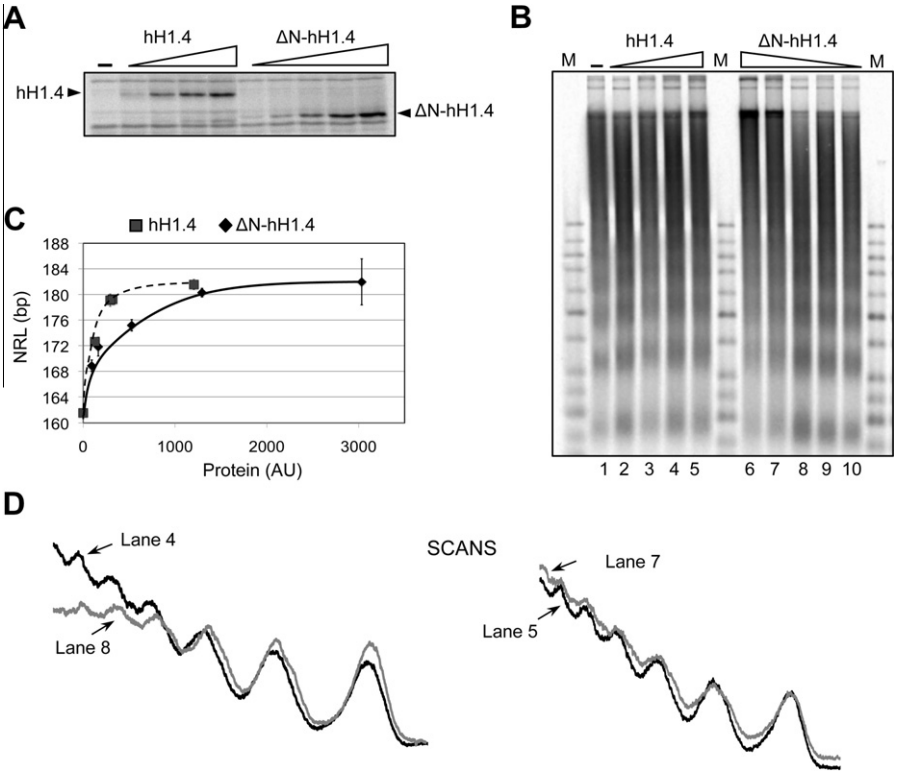

Fig. 1. (A) Expression of hH1.4 and ΔN-hH1.4 as monitored by incorporation of ^{14}C-labeled lysines. The different number of lysines in hH1.4 and ΔN-hH1.4 has been accounted for when determining protein amount. (B) 5.5, 2.8, 1.4 and 0.7 ng of mRNA coding for hH1.4wt and 5.2, 3.5, 1.5, 0.92, 0.66 ng mRNA coding for ΔN-hH1.4 were injected to express increasing amounts of hH1.4 and ΔN-hH1.4, respectively. At the two highest concentrations of ΔN-hH1.4, lane 6 and 7, the nucleosomal ladder is disturbed. (C) Saturation curves for hH1.4 and ΔN-hH1.4. Both result in an increase of roughly 20 bp, from 161.5 in the DNA only control to 181.6 ± 0.8 bp for hH1.4 and 181.9 ± 3.6 bp for ΔN-hH1.4 at saturating amount. Three to four times more ΔN-hH1.4 than hH1.4 is needed to reach saturation. (D) The scans of lane 4 as compared to lane 8 and of lane 7 as compared to lane 5 are shown.

within a wide range of concentrations used (see Fig. 1B, lanes 2–5 and 1D, scans for lanes 4 and 5). ΔN-hH1.4 containing chromatin demonstrates the similar type of pattern at low H1 concentrations (Fig. 1B, lanes 8–10 and Fig. 1D scans for lanes 4 and 8). However, already at the second highest concentration of ΔN-hH1.4 the digestion pattern becomes "smeary" with lower amplitude of MNase-induced nucleosome ladder (compare lanes 7 and 8 in Fig. 1B and corresponding scans in Fig. 1D). Interestingly, at the same concentration the effect of hH1.4 on NRL reaches a plateau, i.e. hH1.4 binding reaches saturation (Fig. 1C). This, however, did not render any significant smearing of the MNase ladder. (compare lanes 5 and 7 in Fig. 1B; see also Fig. 1C and corresponding scans in Fig. 1D, see also [11]). From this we conclude that the smearing of the MNase-pattern observed at the two highest concentrations of ΔN-hH1.4 is not simply due to vast protein overexpression but rather indicate that saturation cannot be reached without significant amount of unspecifically bound ΔN-hH1.4.

4. Discussion

In a previous study using the *Xenopus* oocyte system we demonstrated that ubiquitously expressed H1 subtypes that usually coexist in most cell types of higher eukaryotes do differ in their effects on the NRL (Öberg and Belikov, to be published elsewhere). Here we show that the lack of N-terminal domain does not have any role in the hH1.4 induced increase in the NRL since the final increase in NRL is the same both in the absence and presence of N-terminal domain (Fig. 1). However, the ΔN-hH1.4 displays a considerably lower affinity for chromatin binding as illustrated by the three to four fold higher levels of H1 protein needed to reach saturation. The lack of N-terminus seems to impair the ability of hH1.4 to bind specifically to chromatin, and a larger fraction of the protein takes part in unspecific chromatin interactions, as reflected by the progressive deterioration of the pattern. Thus, ΔN-hH1.4 is more prone to unspecific chromatin binding than its wild type counterpart and it is not surprising that more protein is needed to reach saturation as compared to the wild type hH1.4.

Our results support the notion that the N-terminus may be primarily involved in the proper binding of H1 at the appropriate location within the nucleosome. This is in line with previous data showing that H1 without N-terminus does not position itself properly on the nucleosome *in vitro*, as seen by less protection from MNase digestion [16]. Data by Vyas and Brown indicate that the N-terminal domain is the primary determinant of H1.2 and H1^0 chromatin binding characteristics [17]. Using FRAP analysis the

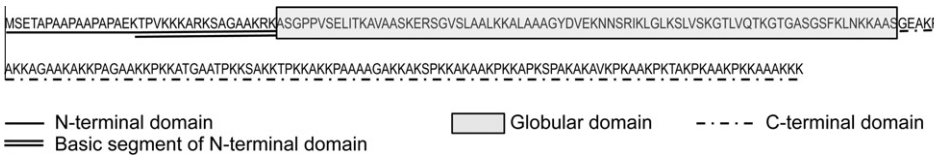

Fig. 2. Amino acid sequence of hH1.4 (NCBI reference sequence number NM_005321.2).

authors elegantly showed that swapping of the N-terminal domains between these two H1 subtypes result in swapping of their chromatin binding characteristics, i.e. their N-terminal domains were important determinants of their different chromatin binding affinities.

The hH1.4 N-terminus can be divided into two distinct parts that are fairly well conserved within paralogs [4,18] (Fig. 2). The part proximal to the globular domain is rich in lysines while the distal segment is rich in alanines and prolines [18]. We speculate that the proximal part may help the H1 to bind properly on the nucleosome surface. To gain further insight into the role of the H1 N-terminal domain it would be interesting to perform N-terminal domain swapping experiments and also to test H1 devoid of only the alanine/proline rich or basic part of N-terminus. It would also be of interest to randomize the order of the amino acids in the N-terminal domain, as it was done previously in studies of the C-terminal domain [19,20].

A recent study has made it clear that the globular domain and the C-terminal domain of H1 bind to chromatin with intramolecular cooperativity [21]. We suggest that the N-terminal domain also may play a role in this cooperativity since our data show that the lack of N-terminal domain affects histone H1 binding affinity and specificity. A previous study has shown that globular domains of H1 subtypes H1(0) and H1C bind to the nucleosome via distinct interaction surfaces [22]. We speculate that the N-terminal domains of the different H1 subtypes also have different modes of interaction with nucleosome and/or linker DNA. If that is the case then these different modes of interaction can help explain the different affinity for effect on chromatin structure that previous studies have demonstrated for the H1 subtypes [23,24].

Acknowledgments

Authors would like to express their appreciation and gratitude to Örjan Wrange for continuous support and help during implementation of this Project. This work was supported by the Swedish Cancer Foundation (project number 110702) and the Swedish Research Council – Medicine (project number K2008-66X-15337-04-3). CÖ was supported by Karolinska Institute funding for PhD students (KID) and by The Royal Swedish Academy of Sciences, KVA.

Note added in proof

The paper we refer to in the text as "(Öberg and Belikov, to be published elsewhere)" is now accepted for publication in Journal of Molecular Biology.

Appendix A. Supplementary data

Supplementary data associated with this article can be found, in the online version, at doi:10.1016/j.bbrc.2012.02.157.

References

[1] A. Routh, S. Sandin, D. Rhodes, Nucleosome repeat length and linker histone stoichiometry determine chromatin fiber structure, Proc. Natl. Acad. Sci. USA 105 (2008) 8872–8877.
[2] Y. Fan, T. Nikitina, E.M. Morin-Kensicki, J. Zhao, T.R. Magnuson, C.L. Woodcock, A.I. Skoultchi, H1 linker histones are essential for mouse development and affect nucleosome spacing in vivo, Mol. Cell. Biol. 23 (2003) 4559–4572.
[3] J. Allan, P.G. Hartman, C. Crane-Robinson, F.X. Aviles, The structure of histone H1 and its location in chromatin, Nature 288 (1980) 675–679.
[4] A. Izzo, K. Kamieniarz, R. Schneider, The histone H1 family: specific members, specific functions?, Biol Chem. 389 (2008) 333–343.
[5] M.J. Hendzel, M.A. Lever, E. Crawford, J.P. Th'ng, The C-terminal domain is the primary determinant of histone H1 binding to chromatin in vivo, J. Biol. Chem. 279 (2004) 20028–20034.
[6] T.L. Caterino, J.J. Hayes, Structure of the H1 C-terminal domain and function in chromatin condensation, Biochem. Cell. Biol. 89 (2011) 35–44.
[7] L.Y. Lee, X. Liang, M. Hook, E.L. Brown, Identification and characterization of the C3 binding domain of the *Staphylococcus aureus* extracellular fibrinogen-binding protein (Efb), J. Biol. Chem. 279 (2004) 50710–50716.
[8] G. Almouzni, A.P. Wolffe, Replication-coupled chromatin assembly is required for the repression of basal transcription in vivo, Genes Dev. 7 (1993) 2033–2047.
[9] R. Hock, A. Moorman, D. Fischer, U. Scheer, Absence of somatic histone H1 in oocytes and preblastula embryos of *Xenopus laevis*, Dev. Biol. 158 (1993) 510–522.
[10] S. Dimitrov, G. Almouzni, M. Dasso, A.P. Wolffe, Chromatin transitions during early *Xenopus* embryogenesis: changes in histone H4 acetylation and in linker histone type, Dev. Biol. 160 (1993) 214–227.
[11] S. Belikov, C. Astrand, O. Wrange, Mechanism of histone H1-stimulated glucocorticoid receptor DNA binding in vivo, Mol. Cell. Biol. 27 (2007) 2398–2410.
[12] M. Zernicka-Goetz, J. Pines, K. Ryan, K.R. Siemering, J. Haseloff, M.J. Evans, J.B. Gurdon, An indelible lineage marker for *Xenopus* using a mutated green fluorescent protein, Development 122 (1996) 3719–3724.
[13] C. Astrand, S. Belikov, O. Wrange, Histone acetylation characterizes chromatin presetting by NF1 and Oct1 and enhances glucocorticoid receptor binding to the MMTV promoter, Exp. Cell Res. 315 (2009) 2604–2615.
[14] S. Belikov, C. Astrand, O. Wrange, FoxA1 binding directs chromatin structure and the functional response of a glucocorticoid receptor-regulated promoter, Mol. Cell. Biol. 29 (2009) 5413–5425.
[15] D.V. Fyodorov, J.T. Kadonaga, Chromatin assembly in vitro with purified recombinant ACF and NAP-1, Methods Enzymol. 371 (2003) 499–515.
[16] J. Allan, T. Mitchell, N. Harborne, L. Bohm, C. Crane-Robinson, Roles of H1 domains in determining higher order chromatin structure and H1 location, J. Mol. Biol. 187 (1986) 591–601.
[17] P. Vyas, D.T. Brown, The N- and C-terminal domains determine the differential nucleosomal binding geometry and affinity of linker histone isotypes H10 and H1C, J. Biol. Chem. (2012), in press.
[18] L. Bohm, T.C. Mitchell, Sequence conservation in the N-terminal domain of histone H1, FEBS Lett. 193 (1985) 1–4.
[19] X. Lu, J.C. Hansen, Identification of specific functional subdomains within the linker histone H10 C-terminal domain, J. Biol. Chem. 279 (2004) 8701–8707.
[20] X. Lu, B. Hamkalo, M.H. Parseghian, J.C. Hansen, Chromatin condensing functions of the linker histone C-terminal domain are mediated by specific amino acid composition and intrinsic protein disorder, Biochemistry 48 (2009) 164–172.
[21] T.J. Stasevich, F. Mueller, D.T. Brown, J.G. McNally, Dissecting the binding mechanism of the linker histone in live cells: an integrated FRAP analysis, EMBO J. 29 (2010) 1225–1234.
[22] E.M. George, T. Izard, S.D. Anderson, D.T. Brown, Nucleosome interaction surface of linker histone H1c is distinct from that of H1(0), J. Biol. Chem. 285 (2010) 20891–20896.
[23] J.P. Th'ng, R. Sung, M. Ye, M.J. Hendzel, H1 family histones in the nucleus, Control of binding and localization by the C-terminal domain, J. Biol. Chem. 280 (2005) 27809–27814.
[24] J. Clausell, N. Happel, T.K. Hale, D. Doenecke, M. Beato, Histone H1 subtypes differentially modulate chromatin condensation without preventing ATP-dependent remodeling by SWI/SNF or NURF, PLoS One 4 (2009) e0007243.

Biochemical and Biophysical Research Communications 420 (2012) 325–330

Contents lists available at SciVerse ScienceDirect

Biochemical and Biophysical Research Communications

journal homepage: www.elsevier.com/locate/ybbrc

Preclinical evaluation of combined antineoplastic effect of DLC1 tumor suppressor protein and suberoylanilide hydroxamic acid on prostate cancer cells

Xiaoling Zhou [1], Xu-Yu Yang [1], Nicholas C. Popescu *

Laboratory of Experimental Carcinogenesis, Center for Cancer Research, National Cancer Institute, National Institutes of Health, Bethesda, MD 20892, USA

ARTICLE INFO

Article history:
Received 28 February 2012
Available online 7 March 2012

Keywords:
DLC1
Tumor suppressor gene
SAHA
Apoptosis
RhoA activity
Inhibition prostate tumor growth in vivo

ABSTRACT

Deleted in liver cancer (DLC1), a tumor suppressor gene in multiple cancers, is recurrently down regulated or inactivated by epigenetic mechanisms in primary prostate carcinomas (PCAs). In this study the methylation and acetylation profile of the DLC1 promoter region was examined in three PCA cell lines with low or undetectable DLC1 expression: LNCaP, its derivative C4-2B-2, and 22Rv1. Two histone deacetylase inhibitors (HDAC), suberoylanilide hydroxamic acid (SAHA) and trichostatin A (TSA) induced histone acetylation of the DLC1 promoter in all three lines. DLC1 promoter methylation and deacetylation were detected in LNCaP and C4-2B-2 cells while in 22Rv1 cells DLC1 is silenced by deacetylation. Treatment with SAHA or TSA efficiently increased DLC1 expression in all lines, particularly in 22Rv1 cells, and activated the DLC1 promoter through the same Sp1 sites. The 22Rv1 cell line was selected to evaluate the efficacy of combined DLC1 transduction and SAHA treatment on tumor growth in athymic mice. Individually, DLC1 transduction and SAHA exposure reduced the tumor size by 75–80% compared to controls and in combination almost completely inhibited tumor growth. The antitumor effect was associated with the induction of apoptosis and inhibition of RhoA activity. SAHA alone significantly reduced RhoA activity, showing that this RhoGTPase is a target for SAHA. These results, obtained with a reliable preclinical in vivo test, predict that combined therapeutic agents targeting the pathways governing DLC1 function and HDAC inhibitors may be beneficial in management of prostate cancer.

1. Introduction

Human cancer is regarded as a genetic disorder originating from a single precursor cell by cumulative acquisition of multiple genetic or epigenetic alterations. Over the past several years the trend in cancer therapy has been increasingly focused on therapeutics based on epigenetic changes in cancer cells. Epigenetic changes commonly down regulate or inactivate tumor suppressor genes (TSGs) by promoter hypermethylation or histone deacetylation [1]. Agents that reverse the inhibitory effect of epigenetic processes such as Vidaza, Decitabine, Zebularine or suberoylanilide hydroxamic acid (SAHA), have been developed and shown promise in clinical trials used alone or in combination.

DLC-1 (deleted in liver cancer) that encodes a Rho GTPase-activating protein is an established TSG and functions as a metastasis suppressor in several common cancers [2–5]. Down regulation of the DLC-1 expression is mediated by genetic and epigenetic changes in many forms of cancer and in certain cancers is more frequently deleted than the well-known TSGs [4,5]. However, the epigenetic mechanisms are the major contributing factors in deregulation of DLC-1 in various cancers [4].

Among solid tumors prostate carcinoma (PCA) provides a good example for the role of epigenetic mechanisms in negative regulation of DLC1 expression. DLC1 has been found to be down regulated or silenced by epigenetic modifications in a high number of primary PCAs [6].

Because DLC1 transduction and histone deacetylase (HDAC) inhibitors exert antineoplastic functions, their combined action could be exploited for a more effective cancer therapy. We opted to test the antioncogenic action of SAHA, the most advanced HDAC inhibitor proven to have therapeutic efficacy in certain types of cancer [7,8]. Based on these considerations, we undertook present study to evaluate the combinatorial effect of SAHA and DLC-1 in vivo, as a conclusive preclinical test. The major finding in this study is the robust inhibitory effect of combined SAHA and DLC1 transduction on tumor growth in nude mice of highly tumorigenic PCA 22Rw1 cells. Importantly, inhibition of tumor growth was associated with reduction of RhoA activity and induction of apoptosis.

Abbreviations: DLC1, deleted in liver cancer; PCAs, prostate carcinomas; HDAC, histone deacetylase inhibitors; SAHA, suberoylanilide hydroxamic acid; TSA, trichostatin A.

* Corresponding author. Address: Laboratory of Experimental Carcinogenesis, National Cancer Institute, 37 Convent Drive, MSC 4262, Bethesda, MD 20892-4262, USA.

E-mail address: popescun@mail.nih.gov (N.C. Popescu).

[1] These authors contributed equally to this work.

0006-291X/$ - see front matter © 2012 Elsevier Inc. All rights reserved.
http://dx.doi.org/10.1016/j.bbrc.2012.02.158

2. Materials and methods

2.1. Cell lines and culture conditions

The human PCA cell lines 22Rv1 and LNCaP were obtained from the American Type Culture Collection (ATCC, Manassas, VA). LNCaP and 22Rv1 cells were cultured in RPMI 1640 and DMEM/F12 medium, respectively (Invitrogen, Carlsbad, CA). C4-2B cell, a metastatic androgen-independent PCA cell line derived from LNCaP, was purchased from ViroMed (Minneapolis, MN) and was cultured in T medium (Invitrogen). All cell culture medium were supplemented with fetal bovine serum (10%), penicillin/streptomycin (100 U/ml) and the cell cultures were maintained in a humidified atmosphere containing 5% CO_2 at 37 °C.

2.2. Chemicals and administration

SAHA (Selleck Chemicals LLC, Houston, TX) and trichostatin A (TSA) (Sigma, St. Louis, MO) were prepared as 10 mM or 1 mM stock solution in dimethylsulphoxide (DMSO), respectively. For in vitro experiments, cells were treated with 5 μM of SAHA or 0.5 μM TSA of for 24 or 48 h after seeding. For in vivo experiments, mice received 50 mg/kg SAHA daily by i.p. injection for 21 days. The injection volume was kept constant at 1 μl/g body weight.

2.3. Methylation-specific PCR (MSP)

MSP for detection of DLC1 promoter methylation was carried out with minor modifications as previously described [6].

2.4. Chromatin immunoprecipitation assay (ChIP)

Histone acetylation detection was carried out using an acetyl-histone H3 immunoprecipitation (ChIP) assay Kit (Millipore, Billerica, MA) according to the manufacturer's instructions. Two sets of primers spanning different DLC1 promoter regions were used, the primer sets are Chip-F1: 5-GCT AGA GGG CGG CCT GAG GC-3, Chip-R1: 5-CAG TCG GAG CGA ACT GTC TC-3; Chip-F2: 5-AGA-GGAGAGGCGGGGCCT-3, Chip-R2: 5-CTTAGCGACGGGCTGTTCTCC-3, which yield products of 124 bp and 215 bp in length, respectively.

2.5. Real-time RT-PCR

PCA cell lines, 22Rv1, C4-2-B2, and LNCaP were treated with 5 μM SAHA or 0.5 μM TSA or DMSO for 24 h and harvested. Total RNAs were isolated using RNeasy kit (Qiagen, Valencia, CA) and first-strand cDNAs were synthesized from 1 μg of total RNA by a SuperScript III system (Invitrogen) according to the manufacture's instructions. Real-time PCR reactions were performed using TaqMan® Universal PCR Master Mix (Applied Biosystems, Carlsbad, CA). The $2^{-\Delta\Delta Ct}$ method was used to calculate the relative fold difference of DLC1 mRNA.

2.6. Construction of fragments from DLC-1 promoter region

DLC1 promoter construct −577/+117-pGL3b was kindly provided by Drs. Yung-Jue Bang and Tai Young Kim. Five truncated fragments from DLC1 promoter region (−374/−203, −374/186, −293/+26, −203/+26, −189/+26, numbered relative to the transcription start site + 1) were generated by PCR using the following primers: F (−374): 5-CTT GTG ACC TTT GCC TTT GC-3; F (−293): 5-GGG AAA CAT TCC AGC CTT C-3; F (−203): 5-CTG GGC GGG GCG GGG CTA G-3; F (−189): 5-GCT AGA GGG CGG CCT GAG GC-3; R (203): 5-CCC CGC CTC TCC TCT GTC CCG -3; R (−186): 5-TAG CCC CGC CCC GCC CAG-3; R (+26): 5-CAG TCG GAG CGA ACT GTC TC-3, respectively. The resulting PCR products were inserted into the Topo TA pCR2.1-vector (Invitrogen) and subcloned into KpnI/XhoI-cut pGL3-basic vector (Promega, Madison, WI). The sequences and orientations of the inserts were verified directly by DNA sequencing.

2.7. Transient transfection and luciferase assay

The effect of SAHA and TSA on DLC-1 promoter activity was determined by transient transfection and luciferase assay. The truncated DLC-1 promoter-luciferase constructs were transfected into 22Rv1 cells using Lipofectamine 2000 (Invitrogen). After 24 h post-transfection, cells were treated with 5 μM SAHA or 0.5 μM of TSA, for additional 24 h. Cell lysates were collected for luciferase assays with britelite™ plus Reporter Gene Assay System (Waltham, MA 02451) according to the manufacturer's instructions. Luciferase activities were measured using a Vector2, 1420 Multulabel counter (Perkin Elmer, San Jose, CA) and normalized for total protein concentration determined using BCA assay (Pierce, Rockford, IL).

2.8. In vivo tumorigenicity assay

All procedures involving animals were reviewed and approved by NCI Animal Care and Use Committee. The stably transfected 22Rv1 cells expressing a DLC1-luciferasion protein were generated by inserting the full-length wtDLC1 into pPK-CMV-F4 vector (PromoKine, Heidelberg, Germany) followed by selection with 750 μg/ml of neomycin. To establish subcutaneous tumors, 6-week-old BALB/c AnNCr-nu/nu male mice (NCI-Frederick, Frederick, MD) were injected with 3×10^6 exponentially growing 22Rv1 cells. When tumors in each treatment group reached a similar size (5×5 mm, around 6–8 days), 50 mg/kg (50 μg/g) SAHA or DMSO were administrated daily by intraperitoneal injections for 21 days. The injection volume was kept constant at 1 μl/g body weight. Tumor size was measured using a digital caliper and average tumor volume was calculated using the standard formula: tumor volume = $(W^2 \times L) \times 0.5$. To quantify the tumor size, luciferase bioluminescent images were measured using Xenogen IVIS system according to the manufacturer's instruction (Caliper Life Sciences, Hopkinton, MA). Data presented are representative of three independent experiments. The significant differences between means was determined by Student's t test. A P value of <0.05 was considered statistically significant.

2.9. Rho activation, apoptosis and cell cycle

An adenoviral vector carrying human DLC1 cDNA was prepared and purified as previously described [9]. The effects of DLC1 and SAHA alone or in combination on cell cycle, apoptosis and RhoA activation were tested as previously described [10]. The DNA histograms have been gated to include only single cells and the data were analyzed with CellQuest software (BD Bioscience, San Jose, CA). Active RhoA level in SAHA and solvent treated cells were determined by an ELISA-based RhoA activation assay (G-LISA, Cytoskeleton, Inc. Denver, CO) according to the manufacturer's instructions.

3. Results

3.1. Methylation and acetylation profile of PCA cells

Three PCA cell lines, LNCaP, its derivative metastatic C4-2B-2 and highly tumorigenic 22Rv1 lines were selected for this study. The cells from all three lines express either a negligible level of

or lacking endogenous DLC1 [6,9]. LNCaP and 22Rv1 but not C4-2B-2 cells that are metastatic to bone have been previously examined for the epigenetic modifications responsible for DLC1 down regulation. Thus, we decided to reexamine all three lines under identical conditions. DLC1 promoter methylation was detected in LNCaP and C4-2B-2 cells and not in 22Rv1 (Fig. 1A). In our previous study using 22Rv1 cells, direct evidence showing that TSA induced DLC-1 mRNA re-expression is mediated through acetylation of the DLC1 promoter region has been presented [6]. To determine whether promoter methylation was exclusively responsible for DLC1 deregulation in LNCaP and C4-2B-2 cells, we compared the effect of SAHA and TSA on histone acetylation using ChIP assay for two sets of primers from DLC1 promoter region. In all three cell lines, DLC1 specific amplification products of fragments 124 bp and 201 bp were detected in cells treated with either SAHA or TSA, indicating that DLC1 promoter is both methylated and acetylated in LNCaP and C4-2B-2 cells (Fig. 1B).

3.2. Restoration of DLC1 expression by HDAC inhibitors

Based on these results, we then tested the effectiveness of SAHA and TSA in inducing DLC1 mRNA expression in these lines. The level of DLC1 transcriptional re-expression after exposure to SAHA or TSA was 22–35-fold higher over the control samples and as expected, DLC1 expression was 13 fold higher in 22Rv1 cells than in LNCaP and C4-2B-2 cells (Fig. 1C).

3.3. Activation of DLC1 promoter by HDAC inhibitors

In gastric cancer cells, others have demonstrated that TSA activates DLC1 promoter activity through Sp1 sites located at −219 and −174 relative to the transcription start site, thus providing possible clues for the mechanism responsible for the induction of DLC1 expression through TSA-mediated chromatin modifications [11]. To see whether SAHA and TSA activate the DLC1 promoter through the same sites we constructed several DLC1 promoter fragments covering a series of Sp1 binding sites and linked them to a luciferase reporter gene (Fig. 2A). The promoter activity driven by these fragments was measured after exposure to SAHA or TSA. The DLC1 promoter fragments most responsive to both HDAC inhibitors were fragment F1 (−293/+26) and F6 (−577/+177) (Fig. 2B). Seemingly, these Sp1 sites are essential for both SAHA and TSA -mediated DLC1 promoter activation. Fragment F2 (−203/+26) containing three Sp1 sites, and fragment F3 (−189/+26) containing the fourth Sp1 site, also elicit a significant capacity to activate the DLC1 promoter (Fig. 2B). Fragment F4 (−374/-203) containing the first Sp1 site and F5 (−374/−186) carrying three sp1 sites had a similar capacity. Overall, these observations suggest that not all Sp sites are equally responsive on HDAC inhibitors - mediated DLC-1 promoter activation.

3.4. SAHA and/or DLC1 inhibition of tumor growth in vivo

Once relevant information on interaction of the two HDAC inhibitors were generated, we proceeded with the central aim of present study, to assess the therapeutic efficacy of combined DLC1 transduction and SAHA treatment on 22Rv1 tumor growth in nude mice. 22Rv1 cells are highly tumorigenic, as only 6–10 days after injection of all animals developed small palpable tumors. At this time SAHA or solvent was administrated i.p. daily for 21 days. The kinetics of tumor growth was monitored regularly using digital caliper and quantitative measurements of bioluminescent images. Either DLC1 transduction or exposure to SAHA had an inhibitory effect on tumor growth as early as 13 days, and after 21 days at the end point of the experiment, the size of the tumors was reduced by 70–88% (Fig. 3A, B). The size of tumors developed in mice inoculated with DLC1 transfected cells and treated with SAHA was reduced as compared to either DLC1 or SAHA treatment alone (Fig. 3A, B). Quantitative data analysis showed that combined DLC1 transduction and exposure to SAHA had a robust inhibitory effect on tumor growth, and bioluminescent signals of the tumors were reduced to less than 2% (Fig. 3B).

To evaluate the toxicity of SAHA, the weight of all animals was checked twice a week and their general condition monitored daily. Among 40 mice from both control and DLC1 vector injected with SAHA for 16 and 19 days, 4 did not survive, most likely due to SAHA toxicity. In contrast, DLC1 transduction did not affect their survival, but contributed to slight weight loss.

3.5. Reduction of RhoA activity, induction of apoptosis and. cell cycle progression

To gain insights into mechanisms involved in the process of SAHA and DLC1 inhibitory effects of tumor growth, we next examined the effects on RhoA activity, induction of apoptosis and cell cycle progression in 22Rv1 cells (Fig. 4). An ELISA-based RhoA activation assay was employed to determine whether re-expression of DLC1 and exposure to SAHA affect RhoA activity in 22Rv1 cells. The level of active GTP-bound RhoA was 57% lower in cells transduced with DLC1, 66% lower in SAHA treated cells and up to 87% in

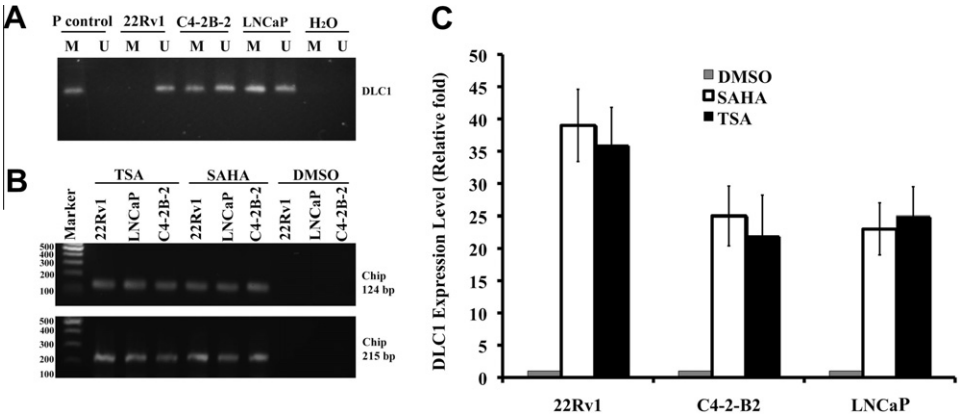

Fig. 1. SAHA and TSA restore DLC1 expression in prostate cancer cells. (A) Methylation of DLC1 promoter in 22Rv1, LNCaP and C4-2-B2 cells. P control, universal methylated human DNA; M, methylated; U, unmethylated. (B) Chromatin immunoprecipitation analysis of histone H3 acetylation on the DLC1 promoter. 22Rv1, LNCaP, and C4-2-B2 were treated with TSA or SAHA. Two sets of primers spanning different DLC1 promoter regions were used, which yield products of 124 bp and 215 bp in length, respectively. M, DNA marker. (C) Restoration of DLC1 expression lines 22Rv1, C4-2-B2 and LNCaP cells by SAHA and TSA. DLC1 expression level was measured by real-time PCR.

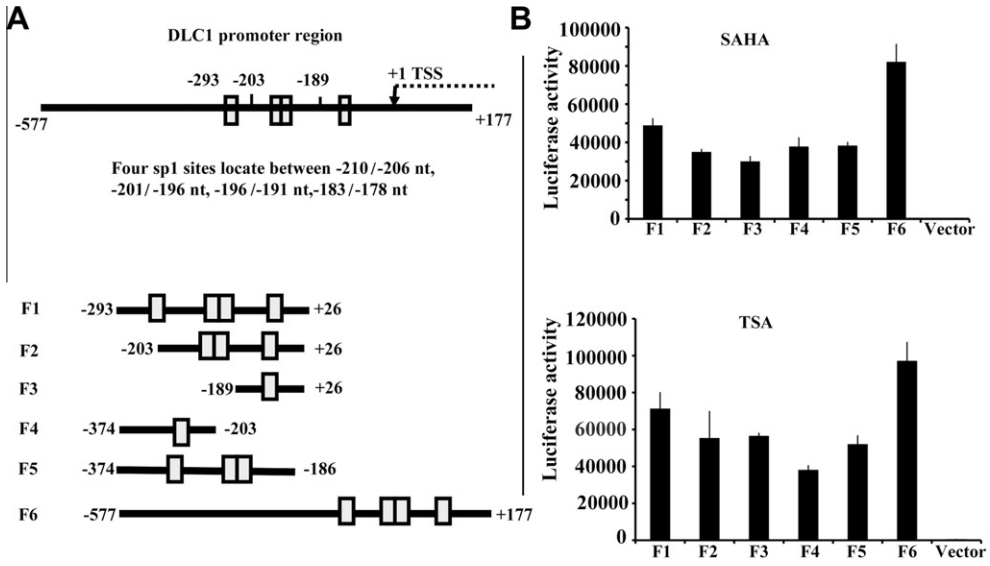

Fig. 2. SAHA and TSA activate DLC1 promoter with the same Sp1 sites. (A) Schematic representation of the DLC1 promoter region, which spans from −577 to +177 and contains four Sp1sites locate between −210/−206, −201/−196, −196/−191, −183/−178. Fragments with different combinations of Sp1 sites are shown in the bottom. The numbers refer to the transcription start site (left panel). (B) Activation of the truncated constructs of DLC-1 promoter in 22Rv1 cells. The constructs were transiently transfected into 22Rv1 cells followed by treatment with TSA or SAHA. Luciferase activity was measured and normalized to protein concentration. Data presented are representative of three independent experiments (right panel).

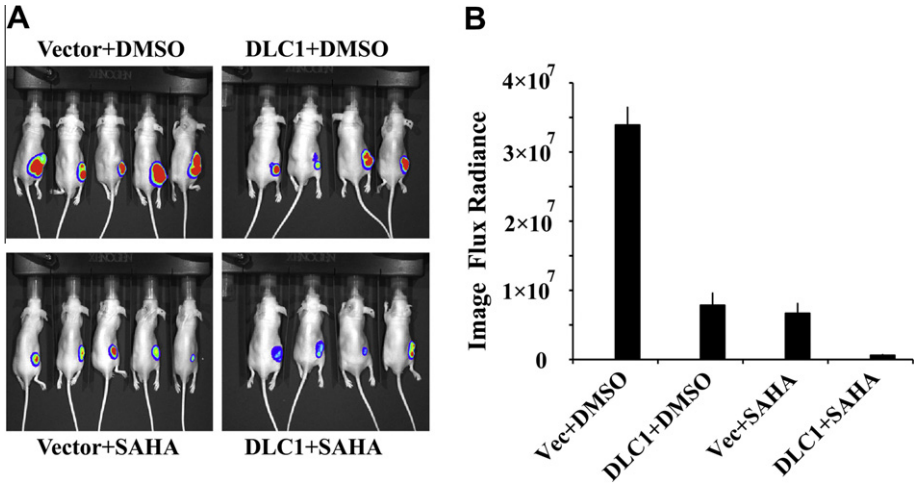

Fig. 3. SAHA and/or DLC1 effect of in vivo tumor growth of 22Rv1 cells. Exponentially growing 22Rv1 cells were injected subcutaneously in BALB/c AnNCr-nu/nu male mice, 50 mg/kg (50 μg/g) SAHA or DMSO were administrated daily by intraperitoneal injections for 21 days beginning after all animals developed palpable tumors. The bioluminescent signal was acquired and illustrated as a pseudocolor image (A) and quantitative data from the region of interest are shown as the photon counts (B).

combination as compared with controls vector and solvent treated cells ($P = 0.035$, Fig. 4A).

For apoptosis and cell cycle analysis, 22Rv1 cells were transfected with the DLC1 expression vector, the vector only or exposed to SAHA for 24 h. We detected a significant accumulation of subG1 cells in cells treated with DLC1, SAHA, and DLC1 plus SAHA (arrows, Fig. 4B–D), indicative of apoptosis, compared to the control (Fig. 4A). The populations in G1 and G2 phase were not significantly affected (Fig. 4).

4. Discussion

Recurrent loss of DNA copy number and loss of heterozygosity on the short arm of chromosome 8, non randomly affecting the region 8p21-22 harboring the DLC1 gene, have been detected in several earlier studies with in PCAs. Subsequently, it has been firmly demonstrated that promoter methylation and histone deacetylation are major mechanisms for the down regulation and silencing of DLC1 expression in primary PCAs [6]. In a recent genome-wide array analysis of copy number alterations of PCAs, the highest frequencies of loss DNA copy number was found to be confined on chromosomes 8p and 6q and affected the DLC1 and WWOX gene loci, respectively. Both genes were found to be involved in the apoptosis pathway and associated with increasing disease grade. Based on these results and our previous data with epigenetic deregulation of DLC1, this study concluded that DLC1 is involved in pathogenesis of prostate cancer [12].

Here we examined three PCA cell lines with low level, or lacking DLC1 expression to identify the mechanism responsible for DLC1 deregulation. Both promoter methylation and histone deacetylation were detected in LNCaP and C4-2B-2 cells but only deacetylation in 22Rv1cells. Treatment of cells from all three lines with SAHA or TSA efficiently restored DLC1 expression and activated the DLC1 promoter through the same Sp1 sites. Also, we showed

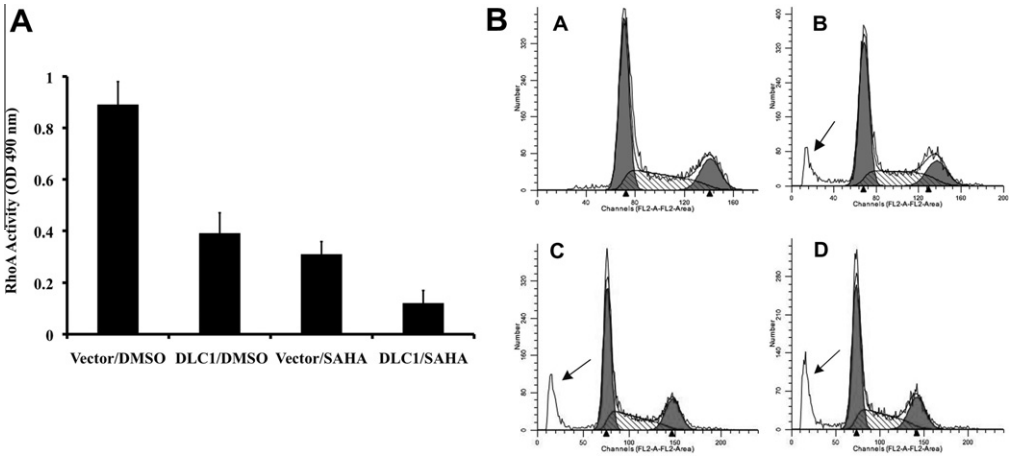

Fig. 4. Effects of SAHA on RhoA activity, apoptosis and cell cycle progression. (A) Effect of SAHA and DLC1 on RhoA activity. DLC1 or vector only transduced 22Rv1 cells were treated with SAHA or DMSO. Twenty-four hours after treatment, cells were lysed and equal amounts of cell lysates were subjected to G-Lisa RhoA assay. (B) Effects of SAHA and DLC1 on apoptosis and cell cycle. DLC1 or vector only transduced 22Rv1 cells were treated with SAHA or DMSO. The percentage of cells in the sub-G1 phase (arrow) was significantly increased upon DLC1 or/and SAHA treatment for 24 h. Vector and DMSO (a), DLC1 and DMSO (b), Vector and SAHA (c), DLC1 plus SAHA (d).

that not all the Sp1 sites confer the same DLC1 promoter responsiveness to both HDAC inhibitors, and this difference might due to the uneven distribution of these Sp1 sites.

22Rv1 cell line was used for in vivo tumorigenicity assay because these cells do not express endogenous DLC1 due to histone deacetylation. Restoration of DLC1 expression combined with SAHA treatment resulted in significant inhibition of tumor development in nude mice. This effect on tumor growth in vivo is consistent with the synergistic inhibitory effect of DLC1 and SAHA on cell migration and anchorage independent growth of 22Rv1 cells in vitro [13]. 22Rv1 cell line was established from PCA xenograft, CWR22 [14]. SAHA treatment of xenotransplanted CWR22 tumors in nude mice caused a 97% reduction of tumor size compared to controls [15]. Current results and those with CWR22 transplanted tumors clearly show that these tumor cells lacking DLC1 expression are highly susceptible to SAHA.

The antitumor effect of DLC1 and SAHA in 22Rv1 cells was associated with the induction of apoptosis and inhibition of RhoA activity, both known contributing factors in the inhibition of tumor cell growth. Accumulating evidence indicates that inactivation of DLC1 may represent the most frequent mechanism for aberrant activation of RhoGTPases in human oncogenesis [16]. The suppressive effect on tumor cell growth and tumorigenicity induced by DLC1 requires RhoGAP activity, which can negatively regulate Rho GTPases, most commonly RhoA [5,17–19]. As expected, DLC1 transduction of 22Rv1 cells reduced RhoA activity and the addition of SAHA enhanced this effect. However, the most important and unanticipated finding with multiple implications, was the significant inhibitory effect of SAHA alone on RhoA activity. This finding certainly requires further confirmation with other types of cancer cells, yet raises the possibility that RhoA and perhaps other RhoGTPases are targets for SAHA or different HDAC inhibitors. It also adds a new antitumor action of SAHA [7,8,20–24].

In clinical trials SAHA has been considerably more effective in hematological malignancies than in solid tumors [7]. As previously discussed in detail, DLC1 is most frequently inactivated by epigenetic mechanisms in over 80% of patients with acute lymphoblastic leukemia and non-Hodgkin's lymphoma and multiple myeloma [10]. Because inactivation or down regulation of DLC1 expression is commonly associated with an increase RhoA activity, SAHA might be more effective in hematological malignancies than in solid tumors.

Despite the antitumor effects of HDAC inhibitors in multiple cancers, it is increasingly documented that combinatorial treatment with DNA demethylating agents may enhance the therapeutic efficacy. Both agents efficiently restore DLC1 expression in cancer cells and their combined use has been highlighted as an attractive therapeutic approach [25]. Both promoter methylation and acetylation are responsible for the reduction of DLC1 expression in androgen-independent C4-2B-2 cells that metastasize to bone. Thus, these cells are ideal for testing the effect of combined of DNA demethylating agents and HDAC inhibitors in DLC1-negative and DLC1 transduced cells. Such experiments are in progress.

Given the high incidence of primary PCA with low or lacking DLC1 expression, we propose that DLC1 deficiency may serve as an independent diagnostic factor in prostate cancer. In a recent article, it has been suggested that DLC1 is a therapeutic target for future cancer treatment in conjunction with other factors [26]. Current results with in vivo inhibition tumor growth show that DLC1-negative PCA cells are susceptible to antitumor action of SAHA. The development of novel therapies of prostate cancer is a clinical priority. Thus, taking into consideration the large number of patients with disabled DLC1 expression, SAHA alone or in combination with other agents may be therapeutically beneficial in prostate cancer.

Acknowledgments

This work was supported by the Intramural Research Program of the National Cancer Institute, NIH.

References

[1] P.A. Jones, S.B. Baylin, The epigenomics of cancer, Cell 128 (2007) 683–692.
[2] B.Z. Yuan, M.J. Miller, C.L. Keck, D.B. Zimonjic, S.S. Thorgeirsson, N.C. Popescu, Cloning, characterization and chromosomal localization of a gene frequently deleted in human liver cancer (DLC-1) homogous to rat RhoGAP, Cancer Res. 58 (1998) 2196–2199.
[3] S. Goodison, J. Yuan, D. Sloan, R. Kim, C. Li, N.C. Popescu, V. Urquidi, The RhoGAP protein DLC-1 functions as a metastasis suppressor in breast cancer cells, Cancer Res. 65 (2005) 6042–6053.
[4] M.E. Durkin, B.Z. Yuan, X. Zhou, D.B. Zimonjic, D.R. Lowy, S.S. Thorgeirsson, N.C. Popescu, DLC-1: a Rho GTPase-activating protein and tumour suppressor, J. Cell. Mol. Med. 11 (2007) 1185–1207.
[5] W. Xue, A. Krasnitz, R. Lucito, R. Sordella, L. Vanaelst, C. Cordon-Cardo, S. Singer, F. Kuehnel, M. Wigler, S. Powers, L. Zender, S.W. Lowe, DLC1 is a chromosome 8p tumor suppressor whose loss promotes hepatocellular carcinoma, Genes Dev. 22 (2008) 1439–1444.
[6] M. Guan, X. Zhou, N. Soulitzis, D.A. Spandidos, N.C. Popescu, Aberrant methylation and deacetylation of deleted in liver cancer-1 gene in prostate cancer: potential clinical applications, Clin. Cancer Res. 12 (2006) 1412–1419.

[7] C. McGuire, J. Lee, Brief review of Vorinostat, Clin. Med. Insights: Therapeutics 2 (2010) 83–87.
[8] H.J. Kim, S.C. Bae, Histone deacetylase inhibitors: molecular mechanisms of action and clinical trials as anti-cancer drugs, Am. J. Transl. Res. 3 (2011) 166–179.
[9] M. Guan, V. Tripathi, X. Zhou, N.C. Popescu, Adenovirus-mediated restoration of expression of the tumor suppressor gene DLC1 inhibits the proliferation and tumorigenicity of aggressive, androgen-independent human prostate cancer cell lines:prospects for gene therapy, Cancer Gene Ther. 15 (2008) 371–381.
[10] V. Ullmannova-Benson, M. Guan, X. Zhou, V. Tripathi, X.Y. Yang, D.B. Zimonjic, N.C. Popescu, DLC1 tumor suppressor gene inhibits migration and invasion of multiple myeloma cells through RhoA GTPase pathway, Leukemia 23 (2009) 383–390.
[11] T.Y. Kim, I.S. Kim, H.S. Jong, J.W. Lee, T.Y. Kim, M. Jung, Y.J. Bang, Transcriptional induction of DLC-1 gene through Sp1 sites by histone deacetylase inhibitors in gastric cancer cells, Exp. Mol. Med. 40 (2008) 639–646.
[12] Cheng, A.M. Levin, Y.C. Tai, S. Plummer, G.K. Chen, C. Neslund-Dudas, G. Casey, B.A. Rybicki, J.S. Witte, Copy number alterations in prostate tumors and disease aggressiveness, Genes Chromosomes Cancer 51 (2012) 66–76.
[13] X. Zhou, X-Y. Yang, N.C. Popescu, Synergistic antineoplastic effect of DLC1 tumor suppressor protein and histone deacetylase inhibitor, suberoylanilide hydroxamicacid (SAHA), on prostate and liver cancer cells: perspectives for therapeutics, Int. J. Oncol. 36 (2010) 999–1005.
[14] R.M. Sramkoski, T.G. Pretlow 2nd, J.M. Giaconia, T.P. Pretlow, S. Schwartz, M.S. Sy, S.R. Marengo, J.S. Rhim, D. Zhang, J.W. Jacobberger, A new human prostate carcinoma cell line, 22Rv1, In Vitro Cell Dev. Biol. Anim. 35 (1999) 403–409.
[15] L.M. Butler, D.B. Agus, H.I. Scher, B. Higgins, A. Rose, C. Cordon-Cardo, H.T. Thaler, R.A. Rifkind, P.A. Marks, V.M. Richon, Suberoylanilide hydroxamic acid, an inhibitor of histone deacetylase, suppresses the growth of prostate cancer cells in vitro and in vivo, Cancer Res. 60 (2000) 5165–5170.
[16] X.-Y. Yang, M. Guan, D. Vigil, C.J. Der, D.R. Lowy, N.C. Popescu, p120Ras-GAP binds the DLC1 Rho-GAP tumor suppressor protein and inhibits its RhoA GTPase and growth suppressing activities. Oncogene 28 (2009) 1401–1409.
[17] E. Sahai, C.J. Marshall, RHO-GTPases and cancer, Nat. Rev. Cancer 2 (2002) 133–142.
[18] A.B. Jaffe, A. Hall, Rho GTPases in transformation and metastasis, Adv. Cancer Res. 84 (2002) 57–80.
[19] D. Vigil, J. Cherfils, K.L. Rossman, C.J. Der, Ras superfamily GEFs andGAPs: validated and tractable targets for cancer therapy?, Nat Rev. Cancer 10 (2010) 842–857.
[20] R.W. Johnstone, Histone-deacetylase inhibitors: novel drugs for the treatment ofcancer, Nat. Rev. Drug Discov. 1 (2002) 287–299.
[21] S. Minucci, P.G. Pelicci, Histone deacetylase inhibitors and the promise of epigenetic (and more) treatments for cancer, Nat. Rev. Cancer 6 (2006) 38–51.
[22] A.A. Lane, B.A. Chabner, Histone deacetylase inhibitors in cancer therapy, J. Clin. Oncol. 27 (2009) 5459–5468.
[23] N. Batty, G.G. Malouf, J.P. Issa, Histone deacetylase inhibitors as anti-neoplastic agents, Cancer Lett. 280 (2009) 192–200.
[24] V.M. Richon, J. Garcia-Vargas, J.S. Hardwick, Development of vorinostat: current applications and future perspectives for cancer therapy, Cancer Lett. 280 (2009) 201–210.
[25] A. Lahoz, Hall, DLC1: a significant GAP in the cancer genome, Genes Dev. 22 (2008) 1724–1730.
[26] X. Cao, C. Voss, B. Zhao, T. Kaneko, S.S-C. Li, Differential regulation of the activity of deleted in liver cancer 1 (DLC1) by tensin control cell migration and transformation, Proc. Natl. Acad. Sci. USA 109 (2012). 1455-146.

Biochemical and Biophysical Research Communications 420 (2012) 331–335

Contents lists available at SciVerse ScienceDirect

Biochemical and Biophysical Research Communications

journal homepage: www.elsevier.com/locate/ybbrc

Evidence that truncated TrkB isoform, TrkB-Shc can regulate phosphorylated TrkB protein levels

Jenny Wong *, Brett Garner

Illawarra Health and Medical Research Institute and the School of Biological Sciences, University of Wollongong, Wollongong, NSW 2522, Australia

ARTICLE INFO

Article history:
Received 28 February 2012
Available online 7 March 2012

Keywords:
Brain-derived neurotrophic factor
Shc
Protein stability

ABSTRACT

Tropomyosin receptor kinase B (TrkB) is best known as the receptor for brain-derived neurotrophic factor (BDNF). In humans, three major isoforms of TrkB, the full-length receptor (TrkB-TK+) and two C-terminal truncated receptors (TrkB-TK− and TrkB-Shc) are expressed in various tissues. In comparison to TrkB-TK+ and TrkB-TK−, TrkB-Shc is less well characterized. In this study, we analyzed the biological function of the TrkB-Shc receptor in response to exogenous BDNF treatment. In experiments transiently overexpressing TrkB-Shc in CHOK1 cells, we found that TrkB-Shc protein levels were rapidly decreased when cells were exposed to exogenous BDNF. When we assessed the functional impact of TrkB-Shc on TrkB-TK+ activity, we found that phosphorylated TrkB-TK+ protein levels were significantly decreased in the presence of TrkB-Shc and moreso following BDNF exposure. Interestingly, while the reduction of phosphorylated TrkB-TK+ protein was more pronounced in the presence of TrkB-Shc following BDNF exposure, the stability of TrkB-Shc protein itself was increased. Our findings suggest that cells may increase TrkB-Shc protein levels in response to exogenous BDNF exposure to regulate TrkB-TK+ activity by increasing degradation of activated receptor complexes as a means to prevent overactivation or inappropriate temporal and spatial activation of BDNF/TrkB-TK+ signaling.

1. Introduction

Tropomyosin receptor kinase B (TrkB) is best known as the receptor for brain-derived neurotrophic factor (BDNF), although it has also been demonstrated to bind neurotrophin-4/5 and neurotrophin-3 [1,2]. TrkB is a member of the Trk receptor family of type III receptor tyrosine kinases that is linked to various cell signaling cascades including Akt, ERK1/2, and PLCγ. The mammalian full-length TrkB receptor (TrkB-TK+) was discovered more than two decades ago and since then at least 36 possible alternative transcript variants and protein isoforms have been identified [3]. In humans, three major isoforms of TrkB, the full-length and two C-terminal truncated receptors are expressed.

The full-length TrkB receptor, TrkB-TK+, consists of an N-terminal signal sequence followed by numerous domains including a cysteine- and leucine-rich sequence followed by a second cysteine-rich domain, 2 immunoglobulin (Ig)-like domains that also include the BDNF-binding region, a transmembrane domain, an Shc-binding motif, a catalytic tyrosine kinase domain near the C-terminus that is necessary for activating second messenger signaling [1,4], and a C-terminal PLCγ-docking site. TrkB-TK+ is the principal mediator of the neurotrophic effects of BDNF. Upon ligand binding, monomeric TrkB-TK+ homodimerizes and undergoes trans-phosphorylation at key tyrosine residues in the C-terminal domain that couple it to downstream signaling pathways.

The two truncated TrkB receptor isoforms include TrkB-TK− and TrkB-Shc. Both truncated isoforms are generated from alternatively spliced transcripts and are truncated at the C-terminus, thus lacking the tyrosine kinase domain [5,6]. However, the TrkB-TK− and TrkB-Shc receptors differ in that each contain unique amino acid sequences at their C-terminus. The TrkB-Shc isoform includes the Shc binding domain that is absent in TrkB-TK− [6].

Both truncated TrkB receptors show differential tissue and cell-type expression. TrkB-TK− is expressed in multiple tissues including brain, heart, lung, skeletal muscle, kidney, and pancreas [6]. In the brain, TrkB-TK− is expressed by both neurons and glia [7–9]. In contrast, TrkB-Shc is expressed in the spinal cord and multiple brain regions including the cerebellum, cortex, pons, hind brain, and diencephalon [6]. Interestingly, TrkB-Shc mRNA is detected in neurons but not in astrocytes [6].

Abbreviations: BDNF, brain-derived neurotrophic factor; CHOK1, Chinese hamster ovary K1; CHX, cycloheximide; TrkB, tropomyosin receptor kinase B; TrkB-TK+, full-length TrkB.

* Corresponding author. Address: Illawarra Health and Medical Research Institute, University of Wollongong, Northfields Avenue, Wollongong, NSW 2522, Australia. Fax: +61 2 4221 8130.
E-mail address: jwong@uow.edu.au (J. Wong).

0006-291X/$ - see front matter Crown Copyright © 2012 Published by Elsevier Inc. All rights reserved.
http://dx.doi.org/10.1016/j.bbrc.2012.02.159

In comparison to TrkB-TK−, the function of TrkB-Shc is not fully elucidated. *In vitro*, TrkB-TK− has been demonstrated to inhibit neurotrophin signaling either by sequestering or trapping neurotrophins (when expressed in glia) and thereby preventing binding and signal transduction via TrkB-TK+ homodimers [10,11] and/or act as a dominant-negative receptor by forming inactive heterodimers with TrkB-TK+ and hence, preventing neurotrophin signaling [12,13]. To date, similar co-transfection studies *in vitro* using TrkB-TK+ and TrkB-Shc have demonstrated that TrkB-Shc cannot be tyrosine phosphorylated [6] also suggesting a dominant negative function. However, Haapasalo et al. [14] demonstrated that co-expression of TrkB-Shc leads to increased cell surface expression levels of the TrkB-TK+ receptor in N2a neuronal cells and primary hippocampal neurons but did not investigate the phosphorylation state of TrkB.

In this study, we further characterize the biological function of the TrkB-Shc receptor in response to brief BDNF exposure. We report that TrkB-Shc protein levels are regulated by exogenous BDNF and that binding results in the regulation of phosphorylated TrkB-TK+ protein levels.

2. Materials and methods

2.1. Materials

Chemicals and reagents used are listed below with the supplier. From Life Technologies: Dulbecco's modified Eagle's medium/Ham's F-12 medium (DF12 1:1 mixture); fetal bovine serum; glutamax, Lipofectamine 2000; myc antibody. From Sigma: bovine-serum albumin fraction V; BDNF (Sigma; recombinant protein Cat # B3795); cycloheximide; protease inhibitor cocktail; β-actin antibody. Other reagents were bicinchoninic acid assay and phosphatase inhibitor cocktail (Pierce); phospho-TrkB antibody (Epitomics); mouse and rabbit peroxidase-conjugated affinity purified secondary antibodies (Dako); Immobilon-P enhanced chemiluminescence reagent (Millipore).

2.2. Cell culture, transfections and treatments

Chinese Hamster Ovary K1 (CHOK1) cells were obtained from the American Type Culture Collection and grown at 37 °C in a 5% CO_2 atmosphere. CHOK1 cells were cultured in Dulbecco's modified Eagle's medium/Ham's F-12 medium (DF12 1:1 mixture) containing 10% (v/v) FBS supplemented with 2 mM glutamax (Life Technologies).

2.3. Western blotting

CHOK1 cells were plated at a density of 5×10^5 in 12 well plates and transfected with overexpression plasmids as indicated in the figures and figure legends [pcDNA3.1 (empty vector), pcDNA3.1-TrkB-Shc-myc and/or pcDNA3.1-TrkB-TK+ (500 ng/well)] for 24 h using Lipofectamine 2000 (2 μl/well). Cells were treated with 15 ng of BDNF (Abcam; recombinant protein Cat # AB9794) post-transfection in 0.1% BSA-DF12 medium for 15 min and then harvested or switched to 0.1% BSA-DF12 containing 100 μg/ml cycloheximde (without BDNF) and incubated for an additional 3 h before harvest. Cells were harvested for total protein using RIPA buffer supplemented with protease inhibitors (2 mM AEBSF, 0.015 mM aprotinin, 0.038 mM leupeptin, 0.030 mM pepstatin A, 0.028 mM E-64, 0.08 mM bestatin) (Sigma) and phosphatase inhibitors (Pierce). Protein concentrations were determined by the bicinchoninic acid method. Fifteen or twenty micrograms of each sample were mixed with 5× SDS loading buffer (containing β-mercaptoethanol), boiled at 95 °C for 5 min, and separated on 10% SDS–PAGE gels. Proteins were transferred onto nitrocellulose membranes and blocked using 5% (w/v) non-fat milk, 0.1% (v/v) Tween-20 in TBS (TBST) at room temperature for 1 h. Membranes were incubated with primary antibodies overnight at 4 °C: phospho-TrkB (1:5000) (Epitomics); myc (1:5000) (Invitrogen) and β-actin (1:10,000) (Sigma). Membranes were washed 3 × 10 min with TBST and incubated with mouse or rabbit peroxidase-conjugated affinity purified secondary antibody for 1 h (Dako). After further washing, bound antibodies were detected with Immobilon-P enhanced chemiluminescence reagent (Millipore) and visualized by autoradiography. Immunoreactive species were quantitated by densitometry using Image J (version 1.37v) (National Institutes of Health USA). The brightness/contrast of images have been adjusted using Adobe Photoshop CS (version 8).

2.4. Data presentation and statistics

All results shown are representative of 2–4 separate experiments as detailed in the figure legends. Data are presented as mean + standard error of the mean (SEM). Where appropriate, statistical differences were determined by student *t*-tests using STATISTICA 7 (StatSoft Inc., 2000, STATISTICA for Windows). A p-value $\leqslant 0.05$ (two-tailed) was considered statistically significant.

3. Results

3.1. TrkB-Shc protein expression is regulated by BDNF

Previously, cell surface expression of TrkB-TK+ was shown to be reduced by concentrations of BDNF that could stimulate TrkB-TK+ phosphorylation [14]. Since TrkB-Shc is also capable of binding BDNF, we determined whether its protein expression could be modulated by BDNF exposure. Using CHOK1 cells transiently transfected with myc-tagged TrkB-Shc, we found that expression of TrkB-Shc protein levels was significantly reduced when cells were briefly incubated with 15 ng of BDNF ($t = -2.95$, df = 4, $p = 0.04$) (Fig. 1A, B). Treatment of cells with BDNF did not affect β-actin protein levels (Fig. 1A).

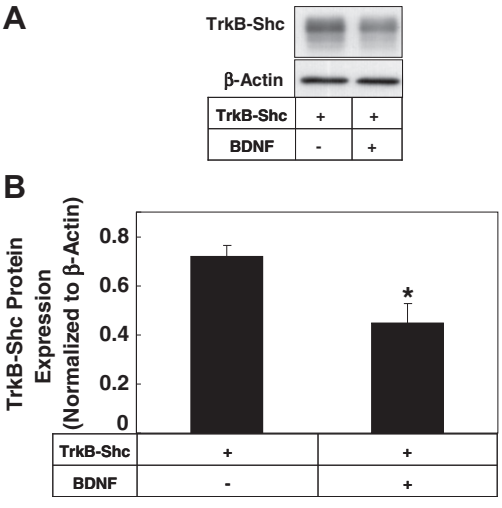

Fig. 1. Effect of BDNF on TrkB-Shc protein levels. CHOK1 cells were transfected with TrkB-Shc-myc for 24 h and treated with 15 ng BDNF for 15 min before harvest. Proteins were separated by SDS–PAGE and immunoprobed. (A) Representative western blot image. (B) Bands were quantitated by densitometry and presented as protein expression normalized to β-actin + SEM. $^*p = 0.04$. Representative of $n = 4$ independent experiments.

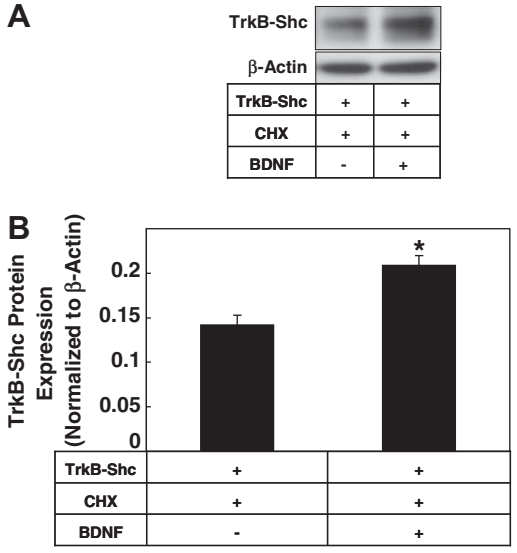

Fig. 2. Effect of BDNF on TrkB-Shc protein stability. CHOK1 cells transfected with TrkB-Shc-myc for 24 h were treated with 15 ng BDNF for 15 min and then incubated with cycloheximide for 3 h before harvest. Proteins were separated by SDS–PAGE and immunoprobed. (A) Representative western blot image. (B) Bands were quantitated by densitometry and presented as protein expression normalized to β-actin + SEM. $^{*}p = 0.04$. Representative of $n = 2$ independent experiments.

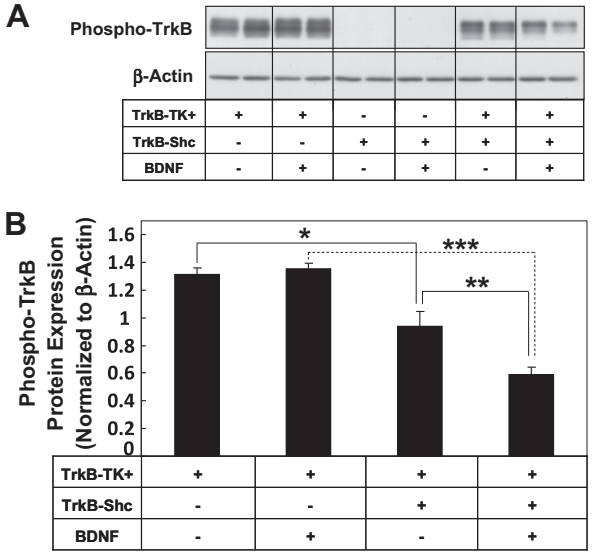

Fig. 3. Effect of TrkB-Shc on phosphorylated TrkB-TK+ protein levels. CHOK1 cells were co-transfected with either empty vector + TrkB-TK+, empty vector + TrkB-Shc-myc, or TrkB-TK+ + TrkB-Shc-myc for 24 h and treated with 15 ng BDNF for 15 min before harvest. Proteins were separated by SDS–PAGE and immunoprobed. (A) Representative western blot image. (B) Bands were quantitated by densitometry and presented as protein expression normalized to β-actin + SEM. $^{*}p = 0.05$, $^{**}p = 0.01$ and $^{***}p = 0.001$. Representative of $n = 3$ independent experiments.

3.2. TrkB-Shc protein stability is increased following exposure to BDNF

The rapid change in TrkB-Shc protein levels suggested that BDNF exposure might have an effect on TrkB-Shc protein stability. To test this, we assessed the stability of TrkB-Shc protein levels before and after BDNF exposure by blocking protein synthesis with cycloheximide. Inhibition of protein synthesis using cycloheximide enables the assessment of protein stability as protein degraded would not be replaced by newly synthesized protein. We found significantly higher levels of TrkB-Shc protein in cells exposed to BDNF for 15 min in comparison to non-exposed cells ($t = 4.31$, df = 2, $p = 0.04$) (Fig. 2A, B). β-Actin protein levels were not affected by any of the treatment conditions (Fig. 2A).

3.3. TrkB-Shc functions as a dominant negative receptor by attenuating TrkB protein phosphorylation and increasing its turnover

We next determined whether TrkB-Shc could regulate BDNF-stimulated TrkB-TK+ activity by examining phosphorylated TrkB-TK+ protein levels in CHOK1 cells co-transfected with both TrkB-Shc and TrkB-TK+. In cells transfected with TrkB-TK+ alone, we were able to detect phosphorylated TrkB-TK+ protein in the absence of BDNF exposure (Fig. 3A). This is consistent with previous reports of auto-phosphorylation of the TrkB-TK+ receptor [6,15]. Interestingly, BDNF exposure for 15 min produced a small but non-significant increase in phosphorylated TrkB-TK+ protein levels compared to the vehicle-treated controls suggesting that TrkB-TK+ phosphorylation may be near saturation (Fig. 3A, B). Phosphorylated TrkB-TK+ protein was not detected in conditions where only the TrkB-Shc receptor was overexpressed, consistent with TrkB-Shc lacking the tyrosine kinase domain that is present in TrkB-TK+ (Fig. 3A). In the absence of BDNF exposure, we observed a significant decrease in phosphorylated TrkB-TK+ protein levels in cells co-expressing both TrkB-TK+ and TrkB-Shc compared to cells overexpressing TrkB-TK+ alone ($t = -3.13$, df = 3, $p = 0.05$) (Fig. 3A, B). However, in the presence of BDNF an even greater reduction in phosphorylated TrkB protein levels was observed in cells co-expressing TrkB-TK+ and TrkB-Shc ($t = -8.42$, df = 4, $p = 0.001$). When both TrkB-TK+ and TrkB-Shc were co-expressed in cells, we observed a significant decrease in phosphorylated TrkB-TK+ protein levels in the presence of BDNF compared to cells co-expressing TrkB-TK+ and TrkB-Shc in the absence of BDNF ($t = -5.25$, df = 3, $p = 0.02$). No significant changes were observed in β-actin protein levels (Fig. 3A).

We next examined the stability of phosphorylated TrkB-TK+ levels in the presence and absence of exogenous BDNF and in combination with TrkB-Shc expression. Interestingly, when we inhibited protein synthesis using cycloheximde, we observed that in cells exposed to BDNF, the stability of phosphorylated TrkB-TK+ protein was significantly reduced compared to non-exposed cells ($t = -11.69$, df = 2, $p = 0.007$) (Fig. 4A, B). In cells co-expressing TrkB-Shc, we found that stability was highly reduced in all conditions compared to cells expressing TrkB-TK+ alone (compare Fig. 4A and Fig. 4C). β-Actin protein levels were not significantly altered by any of the conditions tested (Fig. 4A, C).

4. Discussion

In this current study, we found that TrkB-Shc protein levels can be regulated by exogenous BDNF exposure. When cells were treated with BDNF at a time and quantity known to induce TrkB-TK+ phosphorylation, we observed a rapid decrease in TrkB-Shc protein levels. However, subsequent to BDNF exposure, TrkB-Shc protein levels were found to be more stable with increased levels of expression compared to control conditions. Importantly, when we assessed the functional impact of TrkB-Shc on TrkB-TK+ activity, we found that phosphorylated TrkB-TK+ protein levels were significantly decreased in the presence of TrkB-Shc and even moreso following BDNF exposure.

Previous studies have demonstrated cellular and sub-cellular co-localization of TrkB-Shc with TrkB-TK+ [6,14]. Moreover, co-expression of TrkB-Shc has been shown to inhibit TrkB-TK+ phosphorylation [6]. In this study, we confirmed that TrkB-Shc negatively impacts TrkB-TK+ phosphorylation, but importantly, we extend upon this observation by demonstrating that TrkB-Shc

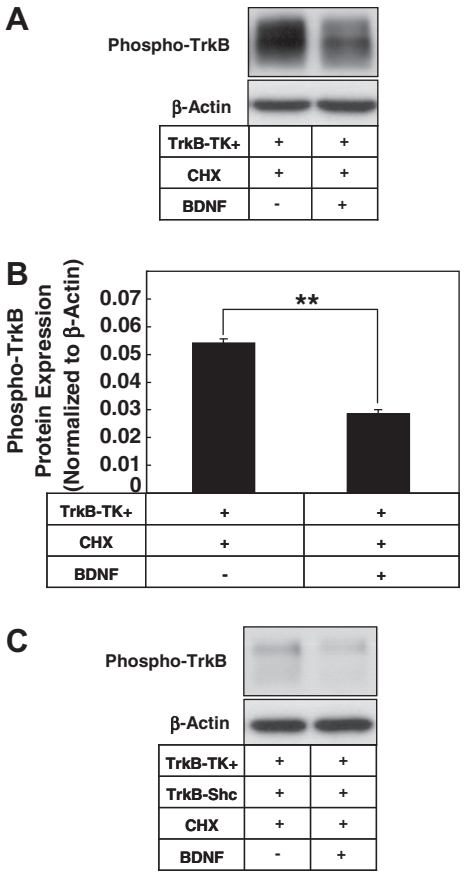

Fig. 4. Effect of TrkB-Shc on the stability of phosphorylated TrkB-TK+. CHOK1 cells co-transfected with either empty vector + TrkB-TK+ or TrkB-TK+ + TrkB-Shc-myc for 24 h were treated with 15 ng BDNF for 15 min and then incubated with cycloheximide for 3 h before harvest. Proteins were separated by SDS–PAGE and immunoprobed. (A and C) Representative western blot images. (A) and (C) are from the same blot and have the same exposure. (B) Bands in (A) were quantitated by densitometry and presented as protein expression normalized to β-actin + SEM. $^{**}p = 0.007$. Representative of $n = 2$ independent experiments.

inhibits TrkB-TK+ phosphorylation by decreasing phosphorylated TrkB protein stability and thus, increasing its turnover. Interestingly, while the reduction of phosphorylated TrkB-TK+ protein was more pronounced in the presence of TrkB-Shc following BDNF exposure, the stability of TrkB-Shc protein itself was increased. This would suggest that in addition to functioning as a dominant negative receptor to hinder or inhibit BDNF/TrkB-TK+ signaling (via reducing TrkB-TK+ phosphorylation), cells might increase TrkB-Shc protein levels in response to BDNF as a mechanism to regulate TrkB-TK+ activity by increasing degradation of activated receptor complexes, a manner akin to feedback regulatory loops observed in metabolic pathways.

4.1. Why limit BDNF activation?

While BDNF signaling via TrkB is important in multiple aspects related to neuronal viability and differentiation, overactivation or inappropriate temporal and spatial activation of BDNF/TrkB-TK+ signaling during brain development or "leakage" of BDNF to adjacent neurons or brain regions can negatively impact brain function. For instance, during embryonic brain development and early neurogenesis, increased expression of truncated TrkB receptors in non-neuronal cells has been described [10]. Expression of truncated TrkB has been demonstrated to bind to BDNF with high avidity and affinity followed by rapid internalization [10]. This suggests that expression of truncated TrkB receptors can act as efficient and selective barriers to prevent diffusion of BDNF to adjacent brain regions to enable independent development and maturation of multiple structures and different neuronal populations at various periods during brain development [10]. At present, the role of TrkB-Shc in brain development and neurogenesis is largely unexplored. Considering that TrkB-Shc is expressed by neurons and shares similar function to TrkB-TK−, we predict that expression of TrkB-Shc in development may also function to limit BDNF diffusion and dispersion to neighboring neurons and/or brain regions. Further studies into the function of TrkB-Shc during brain development using *in vivo* models would be required to address this issue.

Our findings also have implications with regard to the therapeutic application of BDNF to stimulate TrkB-TK+ activation in neurodegenerative diseases (e.g. Alzheimer's Disease). At present, infusion of high doses of BDNF into the brain is required as the neurotrophin has limited diffusion potential [16–18]. Considering that TrkB-Shc and TrkB-TK+ share identical ligand binding domains, the limited diffusion of BDNF from injected to target sites or limited activation of TrkB-TK+ receptors may likely be due to the presence of truncated TrkB isoforms. In regions that are neuron-enriched, we predict that TrkB-Shc may function similarly to TrkB-TK− [10,19] in limiting BDNF diffusion and TrkB-TK+ activation.

In contrast to under activation of TrkB-TK+ activity in neurodegenerative diseases, over activation of BDNF/TrkB-TK+ signaling can also be deleterious to neuronal viability. Studies have demonstrated that BDNF signaling is increased and localized in areas implicated in epileptogenesis [20,21]. Seizure activity increases the expression of BDNF mRNA and protein. However, it has been demonstrated that BDNF signal transduction via TrkB is responsible for the development of the epileptic state *in vivo* [22]. In studies using the kindling model to induce epileptogenesis in conditional TrkB knockout mice, it was demonstrated that a reduction in TrkB activity, rather than the reduction in BDNF expression, was associated with impairment of epileptogenesis [20,21]. Moreover, in transgenic mouse models of mesio-temporal lobe epilepsy overexpressing TrkB-TK+ or truncated TrkB-T1 receptors, it was shown that the development of epileptogenesis in the hippocampus following intra-hippocampal injections of kainic acid was significantly increased in mice with increased TrkB signaling (TrkB-TK+ overexpressing mice) but delayed in mutants with reduced TrkB signaling (TrkB-T1 overexpressing mice) [23]. Thus, while increases in truncated TrkB isoforms may be deleterious to neuronal viability and function in certain brain disorders where neurotrophin signaling is reduced, in other disorders of the brain, such as epileptogensis where increased TrkB signaling is detrimental for neuronal survival, increased expression of truncated TrkB receptors, such as TrkB-Shc, in neurons may be beneficial.

In summary, we report a novel role for TrkB-Shc in the feedback regulation of TrkB-TK+ activation in response to BDNF stimulation. Our findings have important implications in regard to TrkB function in current disease models, in brain development, and in the application of BDNF for the treatment of neurodegenerative diseases and suggest that future research into TrkB-TK+ activation and downstream signaling should consider the role of the truncated TrkB receptors.

Acknowledgments

This work was funded by the Illawarra Health and Medical Research Institute and a National Health and Medical Research Council of Australia (NHMRC) Postdoctoral Training Fellowship (568884) awarded to JW. BG is supported by an Australian Research Council Future Fellowship (FT0991986).

References

[1] R. Klein, V. Nanduri, S.A. Jing, F. Lamballe, P. Tapley, S. Bryant, C. Cordon-Cardo, K.R. Jones, L.F. Reichardt, M. Barbacid, The trkB tyrosine protein kinase is a receptor for brain-derived neurotrophic factor and neurotrophin-3, Cell 66 (1991) 395–403.

[2] M. Barbacid, The Trk family of neurotrophin receptors, J. Neurobiol. 25 (1994) 1386–1403.

[3] K. Luberg, J. Wong, C.S. Weickert, T. Timmusk, Human TrkB gene: novel alternative transcripts, protein isoforms and expression pattern in the prefrontal cerebral cortex during postnatal development, J. Neurochem. 113 (2010) 952–964.

[4] R. Klein, L.F. Parada, F. Coulier, M. Barbacid, TrkB, a novel tyrosine protein kinase receptor expressed during mouse neural development, Embo J. 8 (1989) 3701–3709.

[5] R. Klein, D. Conway, L.F. Parada, M. Barbacid, The trkB tyrosine protein kinase gene codes for a second neurogenic receptor that lacks the catalytic kinase domain, Cell 61 (1990) 647–656.

[6] P. Stoilov, E. Castren, S. Stamm, Analysis of the human TrkB gene genomic organization reveals novel TrkB isoforms, unusual gene length, and splicing mechanism, Biochem. Biophys. Res. Commun. 290 (2002) 1054–1065.

[7] K. Ohira, K. Shimizu, A. Yamashita, M. Hayashi, Differential expression of the truncated TrkB receptor, T1, in the primary motor and prefrontal cortices of the adult macaque monkey, Neurosci. Lett. 385 (2005) 105–109.

[8] K. Ohira, H. Kumanogoh, Y. Sahara, K.J. Homma, H. Hirai, S. Nakamura, M. Hayashi, A truncated tropomyosin-related kinase B receptor, T1, regulates glial cell morphology via Rho GDP dissociation inhibitor 1, J. Neurosci. 25 (2005) 1343–1353.

[9] K. Ohira, M. Hayashi, Expression of TrkB subtypes in the adult monkey cerebellar cortex, J. Chem. Neuroanat. 25 (2003) 175–183.

[10] S. Biffo, N. Offenhauser, B.D. Carter, Y.A. Barde, Selective binding and internalisation by truncated receptors restrict the availability of BDNF during development, Development 121 (1995) 2461–2470.

[11] M. Snapyan, M. Lemasson, M.S. Brill, M. Blais, M. Massouh, J. Ninkovic, C. Gravel, F. Berthod, M. Gotz, P.A. Barker, A. Parent, A. Saghatelyan, Vasculature guides migrating neuronal precursors in the adult mammalian forebrain via brain-derived neurotrophic factor signaling, J. Neurosci. 29 (2009) 4172–4188.

[12] F.F. Eide, E.R. Vining, B.L. Eide, K. Zang, X.Y. Wang, L.F. Reichardt, Naturally occurring truncated trkB receptors have dominant inhibitory effects on brain-derived neurotrophic factor signaling, J. Neurosci. 16 (1996) 3123–3129.

[13] N. Ninkina, J. Adu, A. Fischer, L.G. Pinon, V.L. Buchman, A.M. Davies, Expression and function of TrkB variants in developing sensory neurons, Embo J. 15 (1996) 6385–6393.

[14] A. Haapasalo, I. Sipola, K. Larsson, K.E. Akerman, P. Stoilov, S. Stamm, G. Wong, E. Castren, Regulation of TRKB surface expression by brain-derived neurotrophic factor and truncated TRKB isoforms, J. Biol. Chem. 277 (2002) 43160–43167.

[15] J. Wong, H.G. Woon, C.S. Weickert, Full length TrkB potentiates estrogen receptor alpha mediated transcription suggesting convergence of susceptibility pathways in schizophrenia, Mol. Cell. Neurosci. 46 (2011) 67–78.

[16] H.W. Horch, L.C. Katz, BDNF release from single cells elicits local dendritic growth in nearby neurons, Nat. Neurosci. 5 (2002) 1177–1184.

[17] K.D. Anderson, R.F. Alderson, C.A. Altar, P.S. DiStefano, T.L. Corcoran, R.M. Lindsay, S.J. Wiegand, Differential distribution of exogenous BDNF, NGF, and NT-3 in the brain corresponds to the relative abundance and distribution of high-affinity and low-affinity neurotrophin receptors, J. Comp. Neurol. 357 (1995) 296–317.

[18] S.D. Croll, C.R. Chesnutt, J.S. Rudge, A. Acheson, T.E. Ryan, J.A. Siuciak, P.S. DiStefano, S.J. Wiegand, R.M. Lindsay, Co-infusion with a TrkB-Fc receptor body carrier enhances BDNF distribution in the adult rat brain, Exp. Neurol. 152 (1998) 20–33.

[19] R.H. Fryer, D.R. Kaplan, L.F. Kromer, Truncated trkB receptors on nonneuronal cells inhibit BDNF-induced neurite outgrowth in vitro, Exp. Neurol. 148 (1997) 616–627.

[20] X.P. He, R. Kotloski, S. Nef, B.W. Luikart, L.F. Parada, J.O. McNamara, Conditional deletion of TrkB but not BDNF prevents epileptogenesis in the kindling model, Neuron 43 (2004) 31–42.

[21] R. Kotloski, J.O. McNamara, Reduction of TrkB expression de novo in the adult mouse impairs epileptogenesis in the kindling model, Hippocampus 20 (2010) 713–723.

[22] D.K. Binder, S.D. Croll, C.M. Gall, H.E. Scharfman, BDNF and epilepsy: too much of a good thing?, Trends Neurosci 24 (2001) 47–53.

[23] C. Heinrich, S. Lahteinen, F. Suzuki, L. Anne-Marie, S. Huber, U. Haussler, C. Haas, Y. Larmet, E. Castren, A. Depaulis, Increase in BDNF-mediated TrkB signaling promotes epileptogenesis in a mouse model of mesial temporal lobe epilepsy, Neurobiol. Dis. 42 (2011) 35–47.

Biochemical and Biophysical Research Communications 420 (2012) 336–342

Contents lists available at SciVerse ScienceDirect

Biochemical and Biophysical Research Communications

journal homepage: www.elsevier.com/locate/ybbrc

VCC-1 over-expression inhibits cisplatin-induced apoptosis in HepG2 cells

Zhitao Zhou [a], Xiao Lu [a], Ping Zhu [a], Wei Zhu [b], Xia Mu [c], Rongmei Qu [a], Ming Li [a,*]

[a] School of Biotechnology, Southern Medical University, Guangzhou 510515, China
[b] Department of Toxicology, Guangzhou Center for Disease Control and Prevention, Guangzhou 510440, China
[c] Guizhou Provincial People's Hospital, Guiyang 550004, China

ARTICLE INFO

Article history:
Received 25 February 2012
Available online 7 March 2012

Keywords:
Chemokine
Hepatocellular carcinoma
VCC-1
Apoptosis

ABSTRACT

Vascular endothelial growth factor-correlated chemokine 1 (VCC-1), a recently described chemokine, is hypothesized to be associated with carcinogenesis. However, the molecular mechanisms by which aberrant VCC-1 expression determines poor outcomes of cancers are unknown. In this study, we found that VCC-1 was highly expressed in hepatocellular carcinoma (HCC) tissue. It was also associated with proliferation of HepG2 cells, and inhibition of cisplatin-induced apoptosis of HepG2 cells. Conversely, down-regulation of VCC-1 in HepG2 cells increased cisplatin-induced apoptosis of HepG2 cells. In summary, these results suggest that VCC-1 is involved in cisplatin-induced apoptosis of HepG2 cells, and also provides some evidence for VCC-1 as a potential cellular target for chemotherapy.

1. Introduction

Hepatocellular carcinoma (HCC) is one of the most common malignant neoplasms in the world especially, in sub-Saharan Africa and Southeast Asia including China [1,2]. Surgical resection or liver transplantation still remains the most important therapeutic approach for patients with HCC. However, the recurrence rate of HCC after curative treatment is high in the remnant liver [3,4]. Chemotherapy is of limited value in the treatment of HCC because of chemoresistance.

Chemokines are a family of low molecular weight (8–10 kDa) proteins or peptides that bind to their cognate G protein-coupled receptors (GPCRs). Chemokines and receptors regulate the development and migration of various cell types. Recent studies have found that chemokines and their receptors play important roles in processes of cell proliferation, survival, apoptosis, angiogenesis, and metastasis [5–8]. Many studies have indicated that chemokine receptors in HCC are involved in carcinogenesis [9]. VCC-1 (VEGF-correlated chemokine 1) is a recently described CXC chemokine related to interleukin (IL)-8 and VEGF. It is also known as chemokine (C-X-C motif) ligand 17 (CXCL17; gene ID: 284340). The receptor for VCC-1 is still unknown. VCC-1 was found to be significantly up-regulated in various breast carcinoma and colon tumors, and constitutively expressed in lung, stomach, and colon tissue [10,11]. Expression levels of VCC-1 were shown to be up-regulated in intraductal papillary mucinous adenoma (IPMA), but absent in intraductal papillary mucinous carcinoma (IPMC) [12]. Over-expression of VCC-1 has also been found to result in increased proliferation of SMMC-7721 cells [13].

In the current study, by measuring expression and distribution of VCC-1 in hepatocellular carcinoma (HCC), we proposed to examine the role of VCC-1 in tumor growth, and evaluate the effects on the apoptotic rate of HepG2 cells exposed to cisplatin.

2. Materials and methods

2.1. Cell cultures

The human hepatocellular carcinoma cell line, HepG2, was obtained from the American Type Culture Collection (Manassas, VA, USA). The human HCC cell line SMMC-7721 was obtained from the Cell Bank of Type Culture Collection of Chinese Academy of Sciences (Shanghai, China). All cell lines were maintained routinely in RPMI 1640 medium supplemented with 10% fetal bovine serum (FBS), 100 U/ml penicillin and 100 μg/ml streptomycin at 37 °C in a humidified atmosphere of 5% CO_2.

2.2. Plasmids and transfections

A VCC-1 expression vector pcDNA3.1-VCC-1 was provided by Dr. X. Mu (School of Biotechnology, Southern Medical University, Guangzhou, China) [13]. The pGPU6/GFP/Neo-shRNA expression vectors against human VCC-1, PGPU6/GFP/Neo-VCC-1 (shRNA-VCC-1), and a negative control (PGPU6/GFP/Neo-shNC, shRNA-NC) were produced by Genepharma Co., Inc. (Shanghai, China). HepG2 cells were

Abbreviations: VCC-1, VEGF-correlated chemokine 1; HCC, hepatocellular carcinoma; CXCL17, chemokine (C-X-C motif) ligand 17.

* Corresponding author. Fax: +86 2061648550.
E-mail address: limimg2010@yahoo.cn (M. Li).

0006-291X/$ - see front matter © 2012 Elsevier Inc. All rights reserved.
http://dx.doi.org/10.1016/j.bbrc.2012.02.160

transfected separately with the expression constructs pcDNA3.1-VCC-1 and shRNA-VCC-1 using Lipofectamine™ 2000 (Invitrogen, Carlsbad, USA) according to the manufacturer's protocols. Parental cells transfected with the empty vectors pcDNA3.1 and shRNA-NC were used as controls.

2.3. RT-PCR

Total RNA was isolated from cultured cells using Trizol (Invitrogen), and cDNA was synthesized using RT-PCR kit (TaKaRa, Tokyo, Japan) according to the manufacturer's instructions. The sequences of the primers were as follows: CTCGAGATGAAAGTTCTAATCTCT TCCC (forward), and GGATCCCAAAGGCAGAGCAAAG (reverse) for VCC-1, CAAGGTCATCCATGACAACTTTG (forward), and GTCCACCA CCCTGTTGCTGTAG (reverse) for GAPDH. The amplified products were analyzed by 0.8% agarose gel electrophoresis. The results were expressed as the relative expression of VCC-1 normalized to GAPDH.

2.4. Western blot analysis

Western blot analysis was performed as previously described [13]. Total cell protein was extracted with lysis buffer on ice, and equal amounts of protein were separated by 15% sodium dodecyl sulfate polyacrylamide gel electrophoresis, and transferred to a PVDF membrane using a standard protocol. The membrane was probed with anti-VCC-1 antibody (10 μg/ml, R&D Systems, Minneapolis, USA), and GAPDH (DAKO, Denmark) as an internal control. The membranes were incubated with horseradish peroxidase-conjugated goat anti-rabbit immunoglobulin G for 1 h at room temperature. Positive bands were detected using an ECL system (Pierce, Chicago, USA). The results were expressed as the relative expression of VCC-1 normalized to that of GAPDH. The Western blot analyses were performed in triplicate.

2.5. MTT assay

Cell proliferation was measured by an MTT [3-(4,5-dimethylthiazol-2-yl)-2, 5-diphenyltetrazolium bromide] assay as previously described [13]. Cells were cultured in 96-well plates at a density of 1000 cells/well for 1, 2, 3, 4, 5, and 6 days. At each time point, 20 ml of MTT was added to each well followed by 4 h incubation. Then, the medium was removed, and 150 ml of dimethyl sulfoxide was added. The optical density (OD) of each well was measured using a microplate reader set at 570 nm.

2.6. Flow cytometric assay

Cells were collected and resuspended at a density of 1×10^6 cells in 500 μl of binding buffer containing 1 μl of annexin V-PE and 5 μl 7-amino actinomycin D (7-AAD) [14], and analyzed by a FACSCalibur flow cytometer (BD Biosciences). Data are presented as mean ± SEM of three independent experiments.

2.7. DAPI analysis

The nuclear chromatin of apoptotic cells was stained with 4, 6-diamidino-2-phenylindole (DAPI) as previously described [15]. After treatment with cisplatin, cells were stained with DAPI solution (1 g/ml) at 37 °C for 15 min, and subsequently washed with phosphate-buffered saline. The stained cells were examined under a fluorescence microscope (Nikon Corp.) at 460 nm.

2.8. Electron microscopy

For electron microscopic analysis, the cells were fixed with 2.5% glutaraldehyde. After fixation and dehydration through an acetone series, samples were embedded in Spurr's medium. Ultrathin sections (40–60 nm) were placed on grids, and double-stained with uranyl acetate and lead citrate. Images were obtained from a Hitachi 7500 electron microscope.

2.9. Tissue samples

Hepatocellular carcinoma tissue samples were obtained from 148 patients who had undergone surgical resection at Southern Medical University (Guangzhou, China). In each case, the removed liver tissue was histologically divided into cancerous and paired non-cancerous specimens after the surgical resection. The morphological classification of the carcinomas was conducted according to the Edmondson grading system. All samples were fixed in 10% formalin, embedded in paraffin, and sliced into 3 μm sections. Informed consent was obtained from each patient before entering the study.

2.10. Immunohistochemical staining

The slides were prepared for immunohistochemical staining with an anti-human VCC-1 antibody (10 μg/ml, R&D). Immunoreactivity was detected using an EnVision™ Detection Kit (DAKO). The nuclei were counterstained with hematoxylin. Slides incubated with PBS instead of the primary antibody were used as negative controls in every experiment. In addition, the slides of HCC specimens and corresponding adjacent non-HCC livers were stained by immunohistochemistry, and the percentage of immunopositive cells assessed by visual inspection. The HCC specimens with less than 10% immunopositive cells were considered to be negative.

2.11. Statistical analysis

All experiments were performed in triplicate, and the data were expressed as means ± SD. The significance of differences between experimental conditions was determined by one-way analysis of variance with SPSS 13.0. The relationship between VCC-1 status and clinicopathological variables was tested by χ^2 and Fisher exact tests. Differences were considered significant at $P < 0.05$.

3. Results

3.1. Alteration of VCC-1 gene expression in HepG2 cells by gene transfection and gene disruption

To investigate the role of the VCC-1 gene in the control of tumor development, we altered VCC-1 gene expression in HepG2 cells. As expected, HepG2 cells transfected with the recombinant plasmid pcDNA3.1-VCC-1 resulted in significantly higher levels of VCC-1 mRNA (Fig. 1A) and protein (Fig. 1C). Inhibition of VCC-1 gene expression by transfection of VCC-1 shRNA resulted in significantly down-regulated VCC-1 mRNA levels in HepG2 cells compared with the control cells (Fig. 1E). Western blot assays confirmed that the VCC-1 protein levels were significantly decreased in the shRNA transfected cells compared with the control cells (Fig. 1G).

3.2. Increased VCC-1 gene expression promoted cell proliferation in HepG2 cells

MTT assays were used for measurement of cell proliferation. As shown in Fig. 2A, HepG2 cells transfected with the pcDNA3.1-VCC-1 grew much faster compared with non-transfected cells or mock transfected cells. There was a significant difference in the average growth rate from day 3 to day 6 ($P < 0.05$). Similar results were also

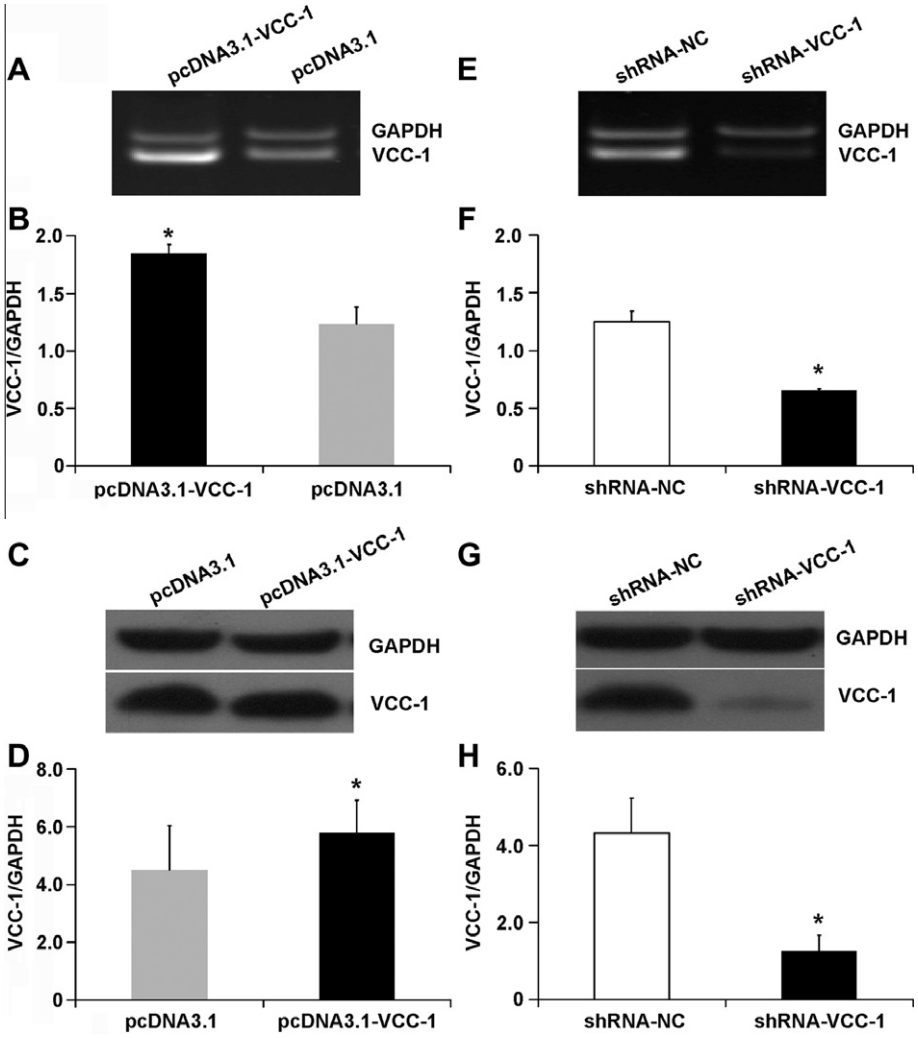

Fig. 1. Expression analysis of VCC-1 under various experimental conditions. HepG2 cells transfected with the VCC-1 expression vector pcDNA3.1-VCC-1 and then VCC-1 mRNA (RT-PCR, A) and protein (Western blot, C) were determined as described in Section 2. Expression of VCC-1 in the cells transfected with the shRNA-VCC-1 was confirmed by RT-PCR (E) and Western blot (G). Parent HepG2 cells transfected with the empty vector were used as controls. (B, D, F, and H) VCC-1/GAPDH density ratio ($n = 3$). $^*P < 0.05$ compared with vector control.

confirmed in SMMC-7721 cells (Fig. 2B), which indicated that VCC-1 gene expression increased cell proliferation in hepatocellular carcinoma.

3.3. Aberrant VCC-1 gene expression in HepG2 cells alters the rate of apoptosis

To further investigate the involvement of VCC-1 in the control of tumor cell apoptosis, we compared the effect of aberrant VCC-1 expression on cell apoptosis induced by a chemotherapeutic drug. The data demonstrated that VCC-1 over-expression resulted in a significant decrease in cisplatin-induced apoptosis in HepG2 cells. HepG2 cells transfected with the empty vector and exposed to various concentrations of cisplatin for 12 h had early apoptosis rates of 15.42%, 29.74%, 48.56% and 62.44% in response to 50, 100, 200 and 300 μM cisplatin, respectively. In contrast, HepG2 cells transfected with the pcDNA3.1-VCC-1 revealed decreased early apoptosis rates of 12.99%, 18.55%, 36.97% and 57.47% in response to 50, 100, 200 and 300 μM cisplatin, respectively (Fig. 2E). We also observed that decreased VCC-1 expression in HepG2 cells after shRNA-VCC-1 transfection significantly increased early apoptosis rates (Fig. 2G). Similar results were also confirmed in SMMC-7721 cells (Fig. 2F and H). These results strongly suggested that VCC-1 contributes to an anti-apoptotic response in hepatocellular carcinoma.

3.4. Aberrant VCC-1 gene expression in HepG2 cells alters cell morphology

To further understand whether over-expression of VCC-1 promotes the growth of HepG2 cells through inhibition apoptosis in HepG2 cells, we next examined the apoptotic morphological changes after cisplatin treatment. Various morphological changes that occur during apoptosis have been identified by light and electron microscopy observation [16]. After 12 h treatment with various concentrations of cisplatin, marked morphological changes were observed. With DAPI staining, we found that cisplatin-treated cells displayed typical apoptotic morphology, which included cell shrinkage, fragmentation, and irregularity by reverse fluorescence microscopy [17]. As shown in Fig. 3A, HepG2 cells transfected with the pcDNA3.1-VCC-1 had normal morphology, and only a small number of cells were dyed. In comparison, the cells transfected with the shRNA-VCC-1 had more obvious damage in cell morphology in contrast to the control.

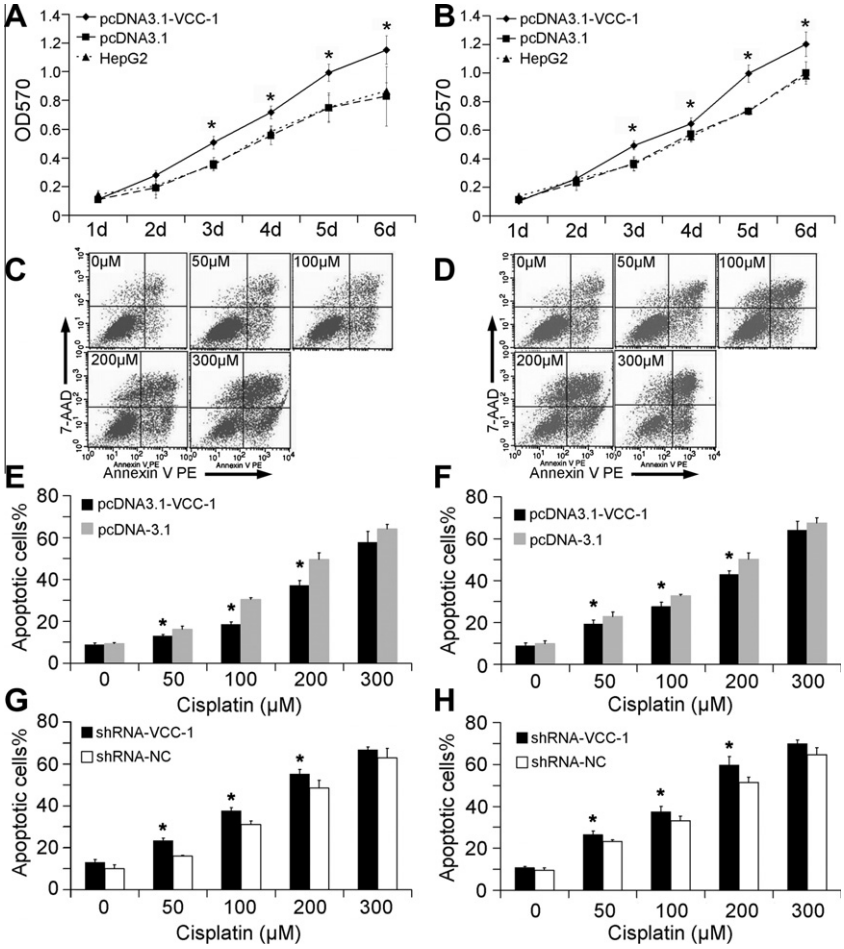

Fig. 2. The effect of VCC-1 expression on the cell growth and apoptosis of HCC cells. The growth curve of HepG2 (A) and SMMC-7721 (B) cells exposed to exogenous VCC-1. Cells transfected with the empty vector pcDNA3.1 served as controls. Flow cytometric analysis of apoptotic cells in HepG2 (C) and SMMC-7721 (D) by PE annexin V and 7-AAD staining. Representative dot plots showing cells transfected with the pcDNA3.1-VCC-1. Percentage of annexin V-positive apoptotic cells in HepG2 (E and G) and SMMC-7721 cells (F and H). The cells were transfected with the pcDNA3.1-VCC-1 (E and F) or shRNA-VCC-1 (G and H). The empty vector served as controls. Data shown are means ± SEM of three independent experiments. $^{*}P < 0.05$ compared with vector groups.

The morphologic characteristics of apoptotic cells were also clearly observed by transmission electron microscopy (Fig. 3C). Treatment with cisplatin at 50 μM produced no obvious morphologic changes in either cell line at 12 h. With 100 μM cisplatin treatment, marked morphologic changes were observed. In the cells transfected with the shRNA-VCC-1, "budding" and chromatin condensation appeared. With 200 μM cisplatin treatment, a significant increase in the number of shRNA-VCC-1 cells with progressive nuclear shrinkage, and cellular fragmentation was clearly evident. There were also many apoptotic bodies.

3.5. Increased VCC-1 expression in human hepatocellular carcinoma

To evaluate the correlation between VCC-1 expression and tumor development, we measured the VCC-1 expression in clinical HCC specimens using immunohistochemical staining. Fig. 4 shows representative results in the resected HCC tissue specimens. We observed the positive staining of VCC-1, which was mainly located in the cytoplasm (Fig. 4A). The average rate for VCC-1 positive staining in the HCC group was around 83%, and 124 out of 148 HCC samples were found to be positive for VCC-1 (Table 1). By contrast, all of the samples from non-cancerous human liver were negative for VCC-1 staining ($N = 30$). Therefore, this result demonstrated increased VCC-1 expression in human hepatocellular carcinoma cells.

4. Discussion

Chemokines are members of a super-family of chemotactic cytokines, initially characterized because of their association with inflammatory responses, and by stimulation of leukocyte chemotaxis during inflammation [18]. Chemokines interact with G protein-coupled receptors. It is now known that they have many roles, including in homeostasis, cell proliferation, hematopoiesis, host–virus interactions and angiogenesis [19]. Many studies have been conducted on chemokines and their receptors in hepatocellular carcinoma. In hepatocellular carcinoma, chemokines play multiple roles in cell invasion, metastasis, survival and growth [20]. VCC-1 is a newly identified chemokine, also known as VEGF co-regulated chemokine 1, which now is designated as CXCL17 [10,12].

In the current study, we examined the expression of VCC-1 in HCC and non-cancerous liver samples by immunohistochemistry staining. VCC-1 has been reported to be highly expressed in human breast cancer, colon carcinomas [10], and constitutively expressed on bronchial and bronchiolar epithelium [11]. In agreement with these findings, our results showed that the expression of VCC-1 in HCC tissue was much higher than that in adjacent non-cancerous tissue. In addition, increased VCC-1 expression was also observed in colon, gastric, pancreatic, breast, lung, bladder, and uterine cervical cancers (data not shown). In

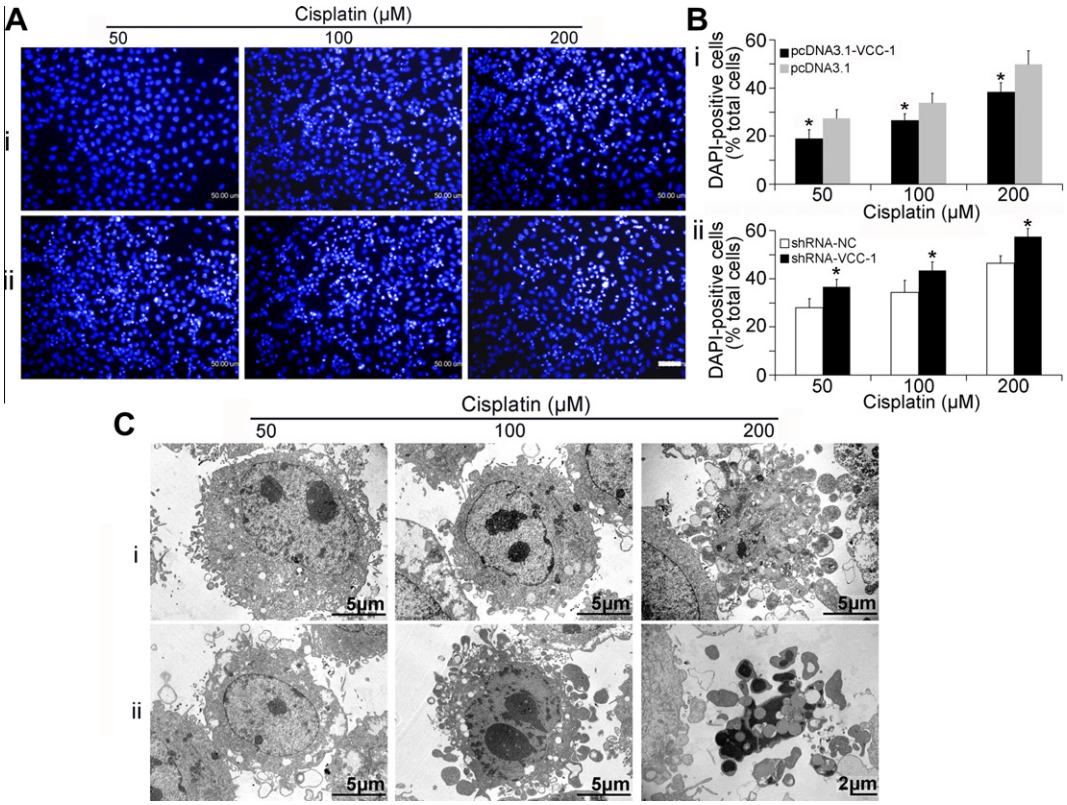

Fig. 3. The morphology of apoptotic cells. (A) Representative micrographs showing cells stained with DAPI. The HepG2 cells were transfected with the pcDNA3.1-VCC-1 (i) or shRNA-VCC-1 (ii), and cultures treated for 12 h with the indicated concentrations of cisplatin. Scale bars, 100 μm. (B) The percentage of DAPI-positive cells is shown as means ± SEM of five fields from three separate experiments as shown in (A), $^{*}P < 0.05$ compared with vector groups. (C) Electron microscopy analysis of apoptotic cells in HepG2. The cells were transfected with the pcDNA3.1-VCC-1 (i) or shRNA-VCC-1 (ii), and cultures treated for 12 h with the indicated concentrations of cisplatin.

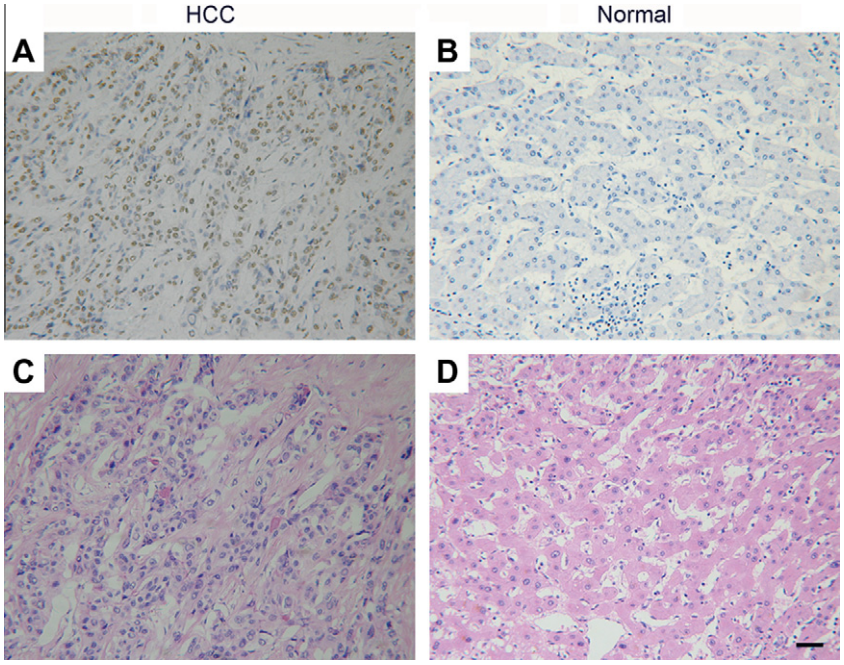

Fig. 4. Representative immunohistochemical staining for VCC-1. (A) VCC-1 expression in HCC, (B) non-cancerous liver did not express VCC-1. Histological analysis of HCC (C) and non-cancerous liver (D) by H&E staining. The scale bars indicate 50 μm.

contrast, Hiraoka et al. reported that the expression of VCC-1 was up-regulated exclusively in IPMA, and down-regulated in IPMC. It was found to be induced in IPMA and associated with dendritic cells (DC) infiltration [12]. Mu et al. indicated that the over-expression VCC-1 in HCC cell lines could enhance cellular proliferation, tumor growth and invasiveness [13]. These studies indicated

Table 1
Correlation of VCC-1 status and clinicopathologic features in hepatocellular carcinoma.

Characteristic	$n = 148$	VCC-1 expression		P value
		Negative n (%)	Positive n (%)	
Age				0.045*
<50 years	71	16(23)	55(77)	
⩾50 years	77	8(10)	69(90)	
Sex				0.632
Female	13	1(8)	12(92)	
Male	135	23(17)	112(83)	
Tumor size				0.785
<5 cm	34	5(15)	29(85)	
⩾5 cm	114	19(17)	95(83)	
Stage				0.287
I	5	0	5(100)	
I–II	5	0	5(100)	
II	86	13(15)	73(85)	
II–III	22	7(32)	15(68)	
III	30	4(13)	26(87)	

* $P < 0.05$.

that VCC-1 played a causative role in promoting the tumor growth progression of HCC, and that loss of VCC-1 in tumors might also contribute to the regulation of immunologic responses to tumors.

HCC is one of the most common cancers in worldwide. Hepatitis C virus (HCV) and hepatitis B virus (HBV) infections are the major risk factors for its development [21–24]. Surgical resection or liver transplantation remains the most important first-line treatment. However, tumor recurrence is still a major reason for failure of surgical therapy. HCC recurs or develops *de novo* in 50–80% of patients within 5 years after resection, the majority occurring within 2 years [25,26], and 50–90% of post-operative deaths are due to recurrent disease [27]. Therefore, there is a need for more effective adjuvant treatments to improve survival after resection and liver transplantation. Radiotherapy and chemotherapy are the conventional second-line treatments.

Cisplatin is an effective chemotherapeutic agent, displaying significant clinical activity against a variety of tumors including hepatocellular carcinoma [28–30]. Cisplatin exerts its cytotoxic effect by forming DNA–Pt adducts, which in turn activate a complex network of pathways that finally culminate in apoptosis [31]. The induction of apoptosis in tumor cells is a major goal of cancer chemotherapy. In this study, we observed that cisplatin inhibited cell growth, and induced apoptotic cell death in human HepG2 cells. With annexin V/7-AAD staining, we were able to distinguish viable cells from the apoptotic cells. The cisplatin-induced apoptosis was further demonstrated morphologically, which showed obvious cell shrinkage and deep condensation of the nuclei with large gaps around the nuclei. The condensed chromatin showed large sharply marginated electron dense masses that abutted the nuclear envelopes. Extensive plasma membrane blebbing occurred followed by karyorrhexis, and separation of cell fragments into apoptotic bodies during a process called "budding". These results showed that the HepG2 cells underwent apoptosis in response to cisplatin treatment.

Evasion of apoptosis is one of the basic features of cancer [32]. VCC-1 has been shown to co-regulate apoptosis along with CXCL-8, GRO-1, and VEGF [10]. Over-expression of CXCL-8 in colorectal cancer cells has been shown to lead to evasion of apoptosis, and significant resistance to the cytotoxic effects of oxaliplatin [33]. In addition, CXCL-8 and its receptors were demonstrated to be involved in the processes of invasion and metastasis in human gastric cancer cell lines [34]. CXCL12 expression was found to correlate well with decreased apoptosis in human myelodysplastic syndrome [35]. CXCL12–CXCR4 was demonstrated to stimulate the proliferation of HCC [36], and the CXCR4/CXCL12 axis was shown to increase cell migration and survival of hepatomas [37]. CCL25–CCR9 interactions in ovarian cancer cells inhibit cisplatin-induced cell death [38]. In agreement with these findings, our results showed that apoptosis was significantly increased in the down-regulated VCC-1 group compared with the control group. HepG2 cells transfected with the recombinant plasmid pcDNA3.1-VCC-1 became more resistant to cisplatin induced apoptosis. Taken together, these observations demonstrated that VCC-1 may play a crucial role in cell growth and tumorigenicity. The over-expression of VCC-1 decreased the cisplatin-induced apoptosis, which suggests that VCC-1 may exert its function by the inhibition of the intracellular apoptosis signaling pathway.

In conclusion, our data suggested that the recently described chemokine, VCC-1, plays a crucial role in control of tumor development, and up-regulation of VCC-1 expression in HepG2 cells increases cellular proliferation rates, and decreases rates of apoptosis. Immunochemical staining of clinical specimens demonstrated that the expression levels of VCC-1 were significantly up-regulated in HCC tissues. In addition, we have shown that cisplatin-induced apoptotic rates in HepG2 cells were related to changes in expression levels of the VCC-1 gene. However, it is unclear whether the over-expression of VCC-1 is associated with the induction of apoptosis or cell survival in cisplatin-treated cells. A detailed mechanistic study is needed to address this issue. Taken together, our data suggested that VCC-1 plays an important role in the development of hepatocellular carcinoma, and may serve as an important target for the HCC therapy in the future.

Acknowledgments

We are grateful to Dr. Wang Hongwei from Nanjing University for critical review and comments on this manuscript.

This work was supported by a Grant from the National High Technology Research and Development Program of China (863 Program, No. 2006AA02A311).

References

[1] B. Rampone, B. Schiavone, A. Martino, C. Viviano, G. Confuorto, Current management strategy of hepatocellular carcinoma, World J. Gastroenterol. 15 (2009) 3210–3216.
[2] K. Okuda, Hepatocellular carcinoma, J. Hepatol. 32 (2000) 225–237.
[3] J.P. Duffy, J.R. Hiatt, R.W. Busuttil, Surgical resection of hepatocellular carcinoma, Cancer J. 14 (2008) 100.
[4] T. Mizuta, I. Ozaki, Y. Eguchi, T. Yasutake, S. Kawazoe, K. Fujimoto, K. Yamamoto, The effect of menatetrenone, a vitamin K2 analog, on disease recurrence and survival in patients with hepatocellular carcinoma after curative treatment, Cancer 106 (2006) 867–872.
[5] A. Viola, A.D. Luster, Chemokines and their receptors: drug targets in immunity and inflammation, Annu. Rev. Pharmacol. Toxicol. 48 (2008) 171–197.
[6] S. Singh, A. Sadanandam, R.K. Singh, Chemokines in tumor angiogenesis and metastasis, Cancer Metastasis Rev. 26 (2007) 453–467.
[7] D. Raman, P.J. Baugher, Y.M. Thu, A. Richmond, Role of chemokines in tumor growth, Cancer Lett. 256 (2007) 137–165.
[8] Z. Albert, Chemokines in neoplastic progression, Semin. Cancer Biol. 14 (2004) 181–185.
[9] L.R. Roberts, Chemokines as attractive targets in liver carcinogenesis, Am. J. Gastroenterol. 100 (2005) 499–501.
[10] E. Weinstein, R. Head, D. Griggs, D. Sun, R. Evans, M. Swearingen, M. Westlin, R. Mazzarella, VCC-1, a novel chemokine, promotes tumor growth, Biochem. Biophys. Res. Commun. 350 (2006) 74–81.
[11] M.T. Pisabarro, B. Leung, M. Kwong, R. Corpuz, G.D. Frantz, N. Chiang, R. Vandlen, L.J. Diehl, N. Skelton, H.S. Kim, Cutting edge: novel human dendritic cell-and monocyte-attracting chemokine-like protein identified by fold recognition methods, J. Immunol. 176 (2006) 2069.
[12] N. Hiraoka, R. Yamazaki-Itoh, Y. Ino, Y. Mizuguchi, T. Yamada, S. Hirohashi, Y. Kanai, CXCL17 and ICAM2 are associated with a potential anti-tumor immune response in early intraepithelial stages of human pancreatic carcinogenesis, Gastroenterology 140 (2011) 310–321 (e314).
[13] X. Mu, Y. Chen, S. Wang, X. Huang, H. Pan, M. Li, Overexpression of VCC-1 gene in human hepatocellular carcinoma cells promotes cell proliferation and invasion, Acta Biochim. Biophys. Sin. 41 (2009) 631–637.

[14] L. Dreolini, F. Takei, Activation of LFA-1 by ionomycin is independent of calpain-mediated talin cleavage, Biochem. Biophys. Res. Commun. 356 (2007) 207–212.
[15] S.-H. Kang, H.-J. Lee, S.-J. Jeong, H.-Y. Kwon, J.-H. Kim, S.-M. Yun, J.-H. Kim, H.-J. Lee, E.-O. Lee, K.S. Ahn, K.S. Ahn, S.-H. Kim, Protective effect of Bojungbangdocktang on cisplatin-induced cytotoxicity and apoptosis in MCF-10A breast endothelial cells, Environ. Toxicol. Pharmacol. 28 (2009) 430–438.
[16] G. Hacker, The morphology of apoptosis, Cell Tissue Res. 301 (2000) 5–17.
[17] D. Du, S. Liu, J. Chen, H. Ju, H. Lian, J. Li, Colloidal gold nanoparticle modified carbon paste interface for studies of tumor cell adhesion and viability, Biomaterials 26 (2005) 6487–6495.
[18] M. Thelen, Dancing to the tune of chemokines, Nat. Immunol. 2 (2001) 129–134.
[19] A. Zlotnik, Chemokines and cancer, Int. J. Cancer 119 (2006) 2026–2029.
[20] F. Huang, X.P. Geng, Chemokines and hepatocellular carcinoma, World J. Gastroenterol. 16 (2010) 1832.
[21] T.H.-H. Chen, C.-J. Chen, M.-F. Yen, S.-N. Lu, C.-A. Sun, G.-T. Huang, P.-M. Yang, H.-S. Lee, S.W. Duffy, Ultrasound screening and risk factors for death from hepatocellular carcinoma in a high risk group in Taiwan, Int. J. Cancer 98 (2002) 257–261.
[22] H. Tsukuma, T. Hiyama, S. Tanaka, M. Nakao, T. Yabuuchi, T. Kitamura, K. Nakanishi, I. Fujimoto, A. Inoue, H. Yamazaki, T. Kawashima, Risk factors for hepatocellular carcinoma among patients with chronic liver disease, N. Engl. J. Med. 328 (1993) 1797–1801.
[23] R.F. Velázquez, M. Rodríguez, C.A. Navascués, A. Linares, R. Pérez, N.G. Sotorríos, I. Martínez, L. Rodrigo, Prospective analysis of risk factors for hepatocellular carcinoma in patients with liver cirrhosis, Hepatology 37 (2003) 520–527.
[24] P. Ferenci, M. Fried, D. Labrecque, J. Bruix, M. Sherman, M. Omata, J. Heathcote, T. Piratsivuth, M. Kew, J.A. Otegbayo, S.S. Zheng, S. Sarin, S.S. Hamid, S.B. Modawi, W. Fleig, S. Fedail, A. Thomson, A. Khan, P. Malfertheiner, G. Lau, F.J. Carillo, J. Krabshuis, A. Le Mair, Hepatocellular carcinoma (HCC): a global perspective, J. Clin. Gastroenterol. 44 (2010) 239–245, 210.1097/MCG.1090b1013e3181d1046ef1092.
[25] E. Lai, W. Lau, The continuing challenge of hepatic cancer in Asia, Surgeon 3 (2005) 210–215.
[26] C.H. Cha, L. Ruo, Y. Fong, W.R. Jarnagin, J. Shia, L.H. Blumgart, R.P. DeMatteo, Resection of hepatocellular carcinoma in patients otherwise eligible for transplantation, Ann. Surg. 238 (2003) 315.
[27] W.Y. Lau, E. Lai, Hepatocellular carcinoma: current management and recent advances, Hepatobiliary Pancreat. Dis. Int. 7 (2008) 237–257.
[28] J.M. Llovet, J. Bruix, Systematic review of randomized trials for unresectable hepatocellular carcinoma: chemoembolization improves survival, Hepatology 37 (2003) 429–442.
[29] J.M. Llovet, M.I. Real, X. Monta a, R. Planas, S. Coll, J. Aponte, C. Ayuso, M. Sala, J. Muchart, R. Sol, Arterial embolisation or chemoembolisation versus symptomatic treatment in patients with unresectable hepatocellular carcinoma: a randomised controlled trial, Lancet 359 (2002) 1734–1739.
[30] C.M. Lo, H. Ngan, W.K. Tso, C.L. Liu, C.M. Lam, R.T.P. Poon, S.T. Fan, J. Wong, Randomized controlled trial of transarterial lipiodol chemoembolization for unresectable hepatocellular carcinoma, Hepatology 35 (2002) 1164–1171.
[31] A. Muller, E. Sonkoly, C. Eulert, P.A. Gerber, R. Kubitza, K. Schirlau, P. Franken Kunkel, C. Poremba, C. Snyderman, L.O. Klotz, Chemokine receptors in head and neck cancer: association with metastatic spread and regulation during chemotherapy, Int. J. Cancer 118 (2006) 2147–2157.
[32] M. Agostini, P. Tucci, G. Melino, Cell death pathology: perspective for human diseases, Biochem. Biophys. Res. Commun. 414 (2011) 451–455.
[33] Y. Ning, P.C. Manegold, Y.K. Hong, W. Zhang, A. Pohl, G. Lurje, T. Winder, D. Yang, M.J. LaBonte, P.M. Wilson, Interleukin-8 is associated with proliferation, migration, angiogenesis and chemosensitivity in vitro and in vivo in colon cancer cell line models, Int. J. Cancer 128 (2011) 2038–2049.
[34] Y. Kitadai, K. Haruma, N. Mukaida, Y. Ohmoto, N. Matsutani, W. Yasui, S. Yamamoto, K. Sumii, G. Kajiyama, I.J. Fidler, Regulation of disease-progression genes in human gastric carcinoma cells by interleukin 8, Clin. Cancer Res. 6 (2000) 2735–2740.
[35] Y. Zhang, H. Zhao, D. Zhao, L. Sun, Y. Zhi, X. Wu, W. Huang, W. Da, SDF-1/CXCR4 axis in myelodysplastic syndromes: correlation with angiogenesis and apoptosis, Leuk. Res. 36 (2012) 281–286.
[36] P. Mavier, N. Martin, D. Couchie, A.M. Préaux, Y. Laperche, E.S. Zafrani, Expression of stromal cell-derived factor-1 and of its receptor CXCR4 in liver regeneration from oval cells in rat, Am. J. Pathol. 165 (2004) 1969.
[37] E. Bertran, L. Caja, E. Navarro, P. Sancho, M.M. Murillo, A. Vinyals, I. Fabregat, Role of CXCR4/SDF-1 [alpha] in the migratory phenotype of hepatoma cells that have undergone epithelial–mesenchymal transition in response to the transforming growth factor-[beta], Cell. Signal. 21 (2009) 1595–1606.
[38] E. Johnson, R. Singh, C. Johnson-Holiday, W. Grizzle, E. Partridge, J. Lillard, S. Singh, CCR9 interactions support ovarian cancer cell survival and resistance to cisplatin-induced apoptosis in a PI3K-dependent and FAK-independent fashion, J. Ovarian Res. 3 (2010) 15.

Biochemical and Biophysical Research Communications 420 (2012) 343–349

Contents lists available at SciVerse ScienceDirect

Biochemical and Biophysical Research Communications

journal homepage: www.elsevier.com/locate/ybbrc

The G protein-coupled receptor GPR30 mediates the proliferative and invasive effects induced by hydroxytamoxifen in endometrial cancer cells

Gui-Qiang Du [a], Long Zhou [a], Xiao-Yue Chen [a], Xiao-Ping Wan [a,*], Yin-Yan He [b]

[a] Department of Obstetrics and Gynecology, The International Peace Maternity and Child Health Hospital of the China Welfare Institute Affiliated to Shanghai Jiao Tong University, 910, Hengshan Road, Shanghai, China
[b] Department of Obstetrics and Gynecology, Shanghai First People's Hospital, Shanghai Jiao Tong University, Shanghai, China

ARTICLE INFO

Article history:
Received 18 February 2012
Available online 7 March 2012

Keywords:
Endometrial cancer
GPR30
Tamoxifen
Hydroxytamoxifen

ABSTRACT

The selective ER modulator tamoxifen (TAM[1]) is the most widely used ER antagonist for treatment of women with hormone-dependent breast tumor. However, long-term treatment is associated with an increased risk of endometrial cancer. The aim of the present study was to demonstrate new insight into the role of G-protein coupled receptor 30 (GPR30) in the activity of TAM, which promoted endometrial cancer. In endometrial cancer cell lines ISHIKAWA and KLE, the potential of 4-hydroxytamoxifen (OHT), the active metabolite of TAM, 17β-estradiol (E2) and G1, a non-steroidal GPR30-specific agonist to promote cell proliferation and invasion was evaluated. All agents above induced high proliferative and invasive effects, while the down-regulation of GPR30 or the interruption of MAPK signal pathway partly or completely prevented the action of the regent. Moreover, the RNA and protein expression of GPR30 was up-regulated by G1, E2 or OHT in both cell lines. The present study provided a new insight into the mechanism involved in the agonistic activity exerted by TAM in the uterus.

1. Introduction

Estrogen is vital hormone, which regulates the growth and differentiation of many tissues, and is the one of the risk factors for endometrial cancer and breast tumors, which accounts for 40% of cancer among the women [1]. The estrogen binding to estrogen receptors (ER) α and β was the main mechanism responsible for the diverse effects [2]. Approximately 50% of all breast cancers demonstrated elevated levels of ER. Consequently, ERα antagonists such as tamoxifen (TAM) and raloxifene have been used clinically and demonstrated advantages in treating ERα-positive breast cancer [3,4]. Although primarily considered an anti-estrogen, TAM also exhibited some mild estrogenic effects in the uterus, bone, and the cardiovascular system [5]. Studies have suggested that incidence and severity of endometrial cancer increased in women treated with TAM [6]. TAM and its active metabolite 4-hydroxytamoxifen (OHT) stimulated the proliferation of uterine cell growth in vivo and cultured human endometrial carcinoma cells [7–9].

The G-protein coupled receptor 30 (GPR30) is a membrane-associated estrogen receptor, that might alter gene expression independently of the nuclear ERs [10]. GPR30 belongs to the seven-transmembrane GPCR family, which signals through heterotrimeric guanine nucleotide-binding proteins to alter the activity of effector proteins. Cellular activation by GPR30 occurs through a mechanism involving transactivation of epidermal growth factor receptors (EGFRs) via a G protein-dependent pathway and activation of mitogen activated protein kinase (MAPK), adenylyl cyclase, and phosphoinositide 3-kinase (PI3K) [10–12]. GPR30 acted in physiological processes such as the attenuation of liver injury and pubertal adrenal development [13,14], and mediated the proliferative effects of estrogen in a number of cancer cell lines [15,16]. Furthermore, it has been shown that 17β-estradiol (E2) and G1, a GPR30-specific ligand, stimulated the production and activity of matrix metalloproteinase (MMP), the proteolysis of which was involved in cancer invasion and metastasis, increased secretion of interleukin-6, the activation of which was associated with tumor growth, and mediated invasion and carcinogenesis in endometrial cancer cell line in a GPR30 dependent manner [17,18]. The classical ERα antagonists TAM also acted as GPR30 agonists [10,19].

To demonstrate the possible role of GPR30 in the mediating the signal of TAM in endometrial cancer cell, experiments and found E2, G1 and OHT promote the proliferation and invasion in a GPR30-dependent manner in ISHIKAWA and KLE human endometrial cancer cells. Moreover, GPR30 was also up-regulated by the

* Corresponding author.
E-mail address: wanxiaoping61@126.com (X.-P. Wan).

[1] *Abbreviations:* GPR30, G protein-coupled receptor 30; E2, 17β-estradiol; MMP, Matrix metal-loproteinase; MAPK, Mitogen-activated protein kinase; TAM, Tamoxifen; OHT, 4-Hydroxytamoxifen; ShGPR30-pGFP-V-RS, Short hairpin RNA (shRNA) constructs against GPR30 in pGFP-V-RS; shiv-pGFP-V-RS vector, HuSH 29-mer noneffective against enhanced GFP vector; EGFR, Epidermal growth factor receptor; ERK, Extracellular-signal-regulated kinase; DMEM, Dulbecco's modified Eagle's medium.

0006-291X/$ - see front matter © 2012 Elsevier Inc. All rights reserved.
http://dx.doi.org/10.1016/j.bbrc.2012.02.161

same agents. The results showed insights into the mechanism through which OHT exerted an action in the endometrial cancer cells.

2. Materials and methods

2.1. Cell culture

The human endometrial cell line ISHIKAWA and KLE was obtained from the Chinese Academy of Sciences Committee Type Culture Collection cell bank. The cells were grown in Dulbecco's modified Eagle's medium (DMEM)/F12 (11030; Gibco, Auckland, New Zealand) supplemented with 10% fetal bovine serum (FBS) (16000-44; Gibco, Carlsbad, CA), 100 units/ml penicillin, and 100 μg/ml streptomycin in a humidified atmosphere of 5% CO_2/95% air at 37 °C.

2.2. Stable transfection

One hundred thousand cells were plated into 24-well dishes with 500 μl regular growth medium per well on the day before transfection. According to the manufacturer's instructions, the cells were transfected with short hairpin RNA (shRNA) constructed against GPR30 in pGFP-V-RS (TG316565; OriGene Technologies, Rockville, MD) (Fig. 1A), and the HuSH 29-mer non-effective against enhanced GFP vector (pRS.TR30003; OriGene Technologies) using Lipofectamine 2000 reagent (Invitrogen, Carlsbad, CA). To obtain a stable cell line, selection pressure was maintained with puromycin at a concentration of 0.5–1.0 μg/ml in the growth medium for two weeks. Clonal populations of cells were selected by transferring well-isolated single clumps of cells (the clonal ancestor and cells divided from it) into a six-well plate, and the growth of these cells were continued in the selection medium for two additional passages.

2.3. Real-time RT-PCR

Total RNA was extracted from the cells using TRI Reagent (TR118; Molecular Research Center, Cincinnati, OH). The cDNA was generated with oligo (dT) 18 primers using a Revert Aid First Strand cDNA Synthesis Kit (K1622; Fermentas Life Science, St. Leon-Rot, Germany). A 50 μl PCR amplification of single-strand cDNA was performed with 40 cycles of denaturation (94 °C) for 60 s, annealing (55 °C) for 30 s, and elongation (72 °C) for 30 s using PerfectShot Ex Taq (Loading Dye Mix) (DRR05TA; Takara, Dalian, China). The primer sequences were as mentioned in Supplementary material Table 1.

2.4. Proliferation assay

Cells were seeded in 96-well plates at 2×10^5 cells/ml and cultured for 24 h. The cells were then transferred to phenol red-free and serum-free medium (DMEM/F12, 11039; Gibco, Carlsbad, CA) and cultured for 24 h, followed by the addition of G1 (371705; Calbiochem, Darmstadt, Germany), E2 (E2758-250MG; Sigma Aldrich, St. Louis, MO) or OHT (H7904-5MG; Sigma Aldrich, St. Louis, MO) in the presence or absence of the MAPK inhibitor U0126 (30 μM) (9903; Cell Signaling Technology, Beverly, MA). The cells were further cultured with phenol red-free DMEM/F12 containing 5% dextran-coated charcoal-treated FBS (S181F; Biowest, Nuaillé, France). Cell proliferation was evaluated using a Cell Counting Kit-8 (CK04-11; Dojindo Molecular Technologies, Gaithersburg,

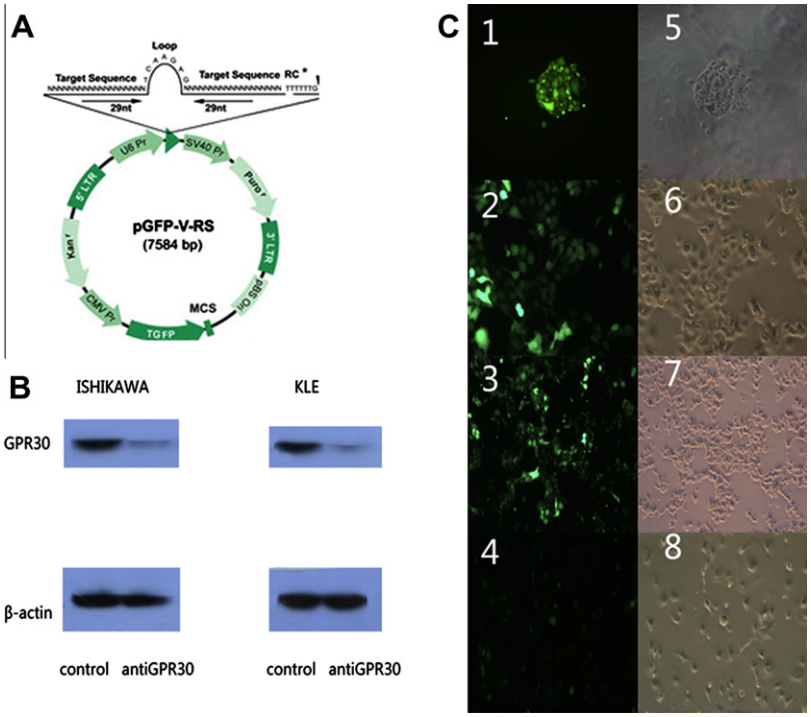

Fig. 1. Expression of GPR30 is stably down-regulated in KLE and ISHIKAWA cell lines. (A) The pGFP-V-RS plasmid vector pattern. The pGFP-V-RS plasmid vector was created with an integrated turboGFP element to readily verify transfection efficiency. It also incorporates both a kanamycin and puromycin resistance elements for greater selection capabilities .The shRNA expression cassette consists of a 29 nt GPR30-specific sequence, a 7 nt loop, and another 29 nt reverse complementary sequence, all under the control of the human U6 promoter. A termination sequence (TTTTTT) is located immediately downstream of the second 29 nt reverse complementary sequence to terminate the transcription by RNA Pol III. (B) The expression level of GPR30 protein in ISHIKWA and KLE cells transfected with ShGPR30-pGFP-V-RS (AntiGPR30) or shiv-pGFP-V-RS (Control) were detected using western-blot. (C) Cells were then visualized by fluorescence microscopy after stable transfection with pGFP-V-RS: ISHIKAWA cells transfected with ShGPR30-pGFP-V-RS under fluorescence (1) or white light (5); ISHIKAWA cells transfected with shiv-pGFP-V-RS under fluorescence (2) or white light (6); KLE cells transfected with ShGPR30-pGFP-V-RS under fluorescence (3) or white light (7); KLE cells transfected with shiv-pGFP-V-RS under fluorescence (4) or white light (8). Magnification (1,5,2,6) ×200; (3,7,4,8) ×100. (For interpretation of the references to color in this figure legend, the reader is referred to the web version of this article.)

MD). The controls were treated with vehicle (0.1% dimethyl sulfoxide or ethanol in phenol red-free DMEM/F12).

2.5. Transwell® assay

The cell culture inserts (8 lm pore size, 6.5 mm diameter; Corning, Corning, NY, USA) coated with 5 lL pure Matrigel (356237, BD Biosciences) were placed in a 24-well plate. Before use, the Matrigel was rehydrated with 100 μl warm DMEM for 2 h. The lower chamber was filled with 800 lL DMEM with 1% FBS. The cells were allowed to invade for 12 h in 5% CO_2 at 37 °C. The cells were plated in the upper chamber, and were treated as in "Proliferation assay". The lower chamber was filled with 800 lL DMEM/F12 containing 5% dextran-coated charcoal-treated FBS. The cells were then incubated at 37 °C for 48 h. After swabbing of non-invaded cells in the upper chambers, cells that migrated to the lower chambers were fixed with 3.7% paraformaldehyde in PBS and stained with hematoxylin. For quantification, the cells that had migrated to the lower surface were counted under a light microscope in five predetermined fields at a magnification of ×100. The assay was repeated three times, and the results are expressed as a percentage to the mean number of three controls. Each experiment was carried out in triplicate and repeated three times.

2.6. Sandwich ELISA assay

Cells were seeded in 24-well plates at 1×10^6 cells/ml, cultured, and starved as described above. The cells were incubated with G1 (10^{-8} M), E2 (10^{-7} M) or OHT (10^{-7} M) in the presence or absence of U0126 (30 μM). The cells were further cultured for 48 h with phenol red-free DMEM/F12 containing 5% dextran-coated charcoal-treated FBS and the supernatants were harvested. Each supernatant was centrifuged at 200g and stored at −80 °C until detection. The concentrations of human MMP-2 and MMP-9 were determined according to the manufacturers' instructions by ELISA kits (MMP-9, BMS2016/2; Bender MedSystems, Campus Vienna Biocenter, Vienna, Austria; MMP-2, SMP200; R&D Systems, Minneapolis, MN, USA). The MMP-9 assay sensitivity was 0.05 ng/ml, and the intra-assay and inter-assay CV of 7.3% and 10.2%, respectively. For MMP-2, the assay sensitivity was 0.16 ng/ml, and the intra-assay and inter-assay CV were 4.8% and 7.6%, respectively.

2.7. Western blotting

Cells were grown in 10-cm dishes and exposed to ligands. After two rinses with ice-cold PBS, the cells were scraped and lysed in ice-cold HNTG buffer (50 mmol/l HEPES [pH 7.5], 150 mmol/l NaCl, 10% glycerol, 1% Triton X-100, 1.5 mmol/l $MgCl_2$, 1 mmol/l EDTA, 10 mmol/l sodium PPI, 100 μmol/l sodium orthovanadate, 100 mmol/l NaF, 10 μg/ml aprotinin, 10 μg/ml leupeptin, and 1 mmol/l phenylmethylsulfonyl fluoride) on ice for 30 min. Total protein was measured using Bio-Rad protein assay reagent according to the manufacturer's protocol. Twenty micrograms of protein was separated on 10% sodium dodecylsulfate polyacrylamide electrophoresis gels and transferred to nitrocellulose membranes. After blocking with 10% bovine serum albumin in 1× Tris-buffered saline, the membrane was incubated at 4 °C overnight with various primary antibodies against GPR30 (1:250 dilutions, ab39742, Abcam, UK) and β-actin (1:1000 dilutions, 4697s, Cell Signaling Technology, USA). The membranes were washed three times with PBS and then incubated with peroxidase-linked secondary antibody (1:10,000) for 1 h at room temperature. The signals were developed using an ECL kit (Pierce), scanned, and analyzed with TotalLab software. The relative expression of target proteins was presented as the ratio to β-actin.

2.8. Statistics

Statistical analysis was performed using the *t*-test or one way analysis of variance. All tests were performed using Statistical Product and Service Solutions software version 17.0 (SPSS Inc., Chicago, IL). The *p*-value <0.05 was considered statistically significant.

3. Results

3.1. Expression of GPR30 was stably down-regulated by transfection with ShGPR30-pGFP-V-RS

The commercial plasmid pGFP-V-RS (Fig. 1A) contained an inserted sh sequence that either suppressed the expression of GPR30 (ShGPR30-pGFP-V-RS) or was invalid (shiv-pGFP-V-RS). The vector also contained the pCMV driven tGFP gene, which encoded the tGFP protein constitutively in mammalian cells. The transfected ISHIKAWA and KLE cells in stable condition were obtained after 30 d. The interferential efficiency of the different vectors was then determined using western-blot assay. The expression of GPR30 protein was down-regulated significantly in the cells transfected with ShGPR30-pGFP-V-RS compared with the control (Fig. 1B). The successfully transfected cells were also examined under a microscope, and green fluorescence from tGFP protein expressed by pGFP-V-RS was observed (Fig. 1C).

3.2. GPR30 signaling induced by hydroxytamoxifen stimulated proliferation of endometrial cancer cell line ISHIKAWA and KLE

Proliferation assays were conducted, to determine GPR30 signaling induced by hydroxytamoxifen induced growth of endometrial cancer cells. It was observed that several doses of E2, OHT and G1 enhanced the proliferation of cell lines including KLE and ISHIKAWA after 48 h culture. The proliferation-promoting activity induction peaked at a concentration of 10^{-6}–10^{-7} M E2, 10^{-7} M OHT and 10^{-8} M G1 in KLE cells, and at a concentration of 10^{-7} M E2, 10^{-7} M OHT and 10^{-8} M G1 in ISHIKAWA cells (Fig. 2A). After treatment of 6 d with E2 (10^{-7} M), OHT (10^{-7} M) and G1 (10^{-8} M), it was observed that a longer duration of treatment had a greater proliferation-promoting effect (Fig. 2B). The stimulation of proliferation by E2, OHT and G1 was disrupted by U0126, an inhibitor of MAPK (Fig. 2C). The cells transfected with ShGPR30-pGFP-V-RS showed decline in proliferation, even in the presence of E2, OHT and G1, as compared to the negative control group (Fig. 2D). These results suggested that GPR30-mediated MAPK pathway had a crucial signaling role in the proliferation of the endometrial cancer cell line induced by E2, OHT and G1.

3.3. GPR30 signaling induced by hydroxytamoxifen increased MMP production of endometrial cancer cell line ISHKAWA and KLE

OHT promoted ISHIKAWA and KLE cell proliferation via GPR30 signaling, and its effect on MMP production via GPR30 signaling was evaluated. The MMP-2 (Fig. 3A) and MMP-9 (Fig. 3B) production increased when ISHIKAWA and KLE cells were treated with E2, OHT or G1 (Fig. 3). Moreover, the increase in secretion of MMP-9 and MMP-2 was blocked by the presence of U0126 or down-regulation of GPR30 protein expression (Fig. 3A and B).

3.4. GPR30 signaling induced by hydroxytamoxifen promoted invasion of endometrial cancer cell line ISHKAWA and KLE

The effect of E2, OHT and G1 on ISHKAWA and KLE invasion was determined by a Transwell® assay. ISHIKAWA and KLE cells without transfection or transfected with ShGPR30-pGFP-V-RS or

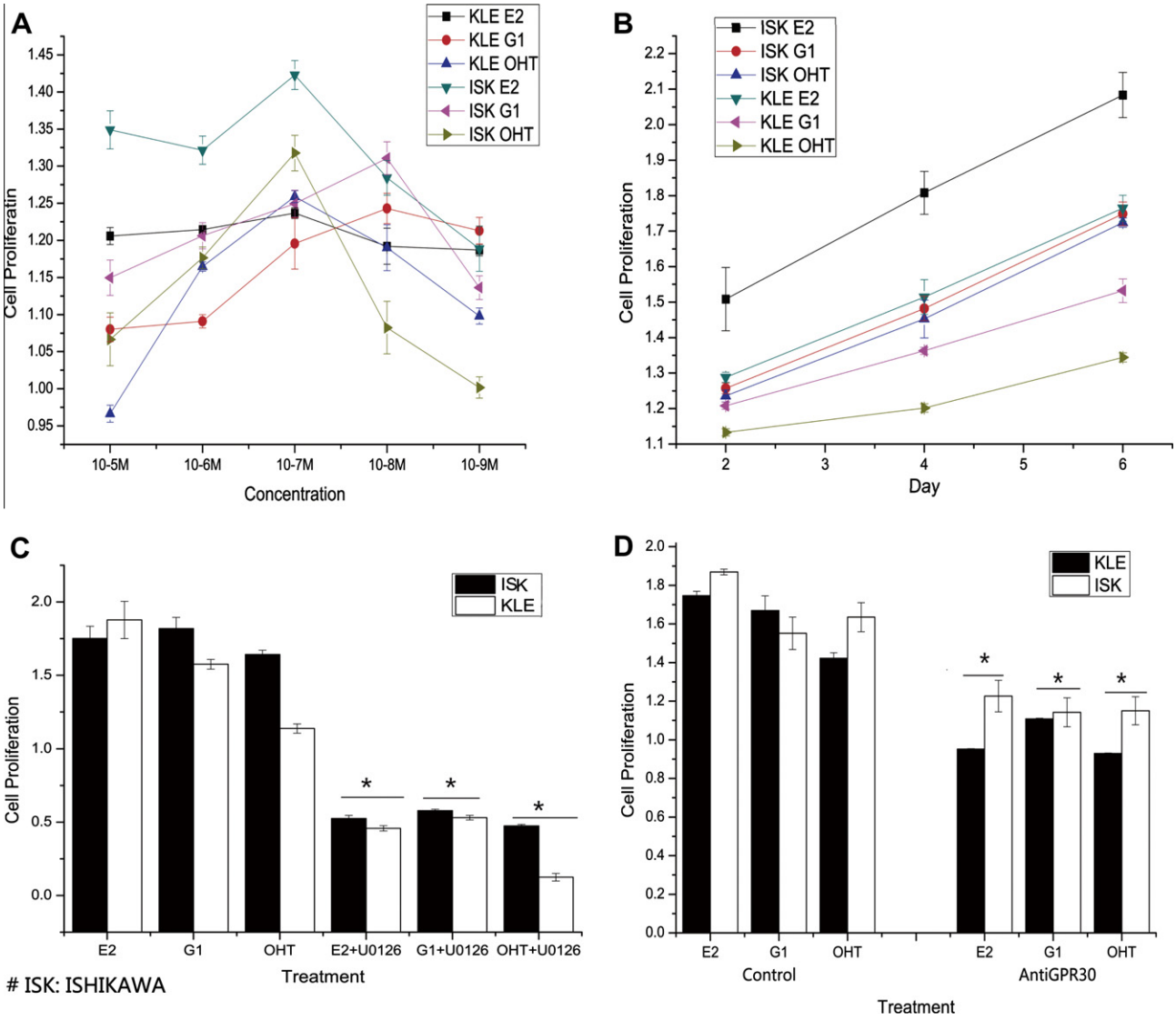

Fig. 2. G protein-coupled receptor 30 via the MAPK pathway stimulates proliferation of the endometrial cancer cell line. (A) Cells were treated with E2 (10^{-5}–10^{-9} M), OHT (10^{-5}–10^{-9} M) or G1 (10^{-5}–10^{-9} M) in medium containing 5% charcoal-stripped FBS, then analyzed after 48 h. (B) Cells were treated with E2 (10^{-7} M), OHT (10^{-7} M) or G1 (10^{-8} M), then analyzed on the indicated day. (C) Cells were treated with E2 (10^{-7} M), OHT (10^{-7} M) or G1 (10^{-8} M) with or without U0126 (30 μM) for 96 h before evaluation of cell proliferation. $^{*}P < 0.05$ versus the group with the same treatment but U0126. (D) Cells transfected with ShGPR30-pGFP-V-RS (AntiGPR30) or shiv-pGFP-V-RS (Control) were treated with E2 (10^{-7} M),OHT (10^{-7} M) or G1 (10^{-8} M) for 96 h before evaluation of cell proliferation. $^{*}P < 0.05$ versus the control cell line with the same treatment. The proliferation of cells treated with vehicle was set as 1, from which all the cell proliferation data in the figures was calculated. Vehicle: 0.1% dimethyl sulfoxide (versus G1) or ethanol (versus E2, OHT) in phenol red-free and serum-free DMEM/F12. Medium was refreshed and treatments were renewed every 2 d. Each data point is the mean ± SD of three independent experiments. (For interpretation of the references to color in this figure legend, the reader is referred to the web version of this article.)

shiv-pGFP-V-RS were treated with E2 (10^{-7} M), OHT (10^{-7} M) or G1 (10^{-8} M). The results revealed that incubation with U0126 markedly decreased cell invasion compared to the control (Fig. 3C). Furthermore, reduction of GPR30 inhibited ISHKAWA and KLE cell invasion, induced by E2, OHT or G1 (Fig. 3D). These data suggested that GPR30 signaling mediated invasive effects induced by OHT in endometrial cancer cell lines via the MAPK pathway.

3.5. GPR30 expression was up-regulated by hydroxytamoxifen in endometrial cancer cell line ISHKAWA and KLE

It was observed that the GPR30 had a role in mediating effects of E2, OHT and G1, and it was further studied that there was impact of these ligands on GPR30 expression. A concentration course study performed by real time quantitative RT-PCR revealed that the mRNA expression of GPR30 were induced by E2, OHT or G1 treatments in ISHIKAWA and KLE cells (Fig. 4A). In both cell types, E2, OHT and G1 up-regulated GPR30 protein levels (Fig. 4B). Cumulatively, the data indicated that the GPR30 responded to E2, OHT and G1 in endometrial cancer cell line ISHKAWA and KLE.

4. Discussion

One major concern with TAM therapy for breast cancer was the carcinogenic effect in the endometrium. The previous studies have demonstrated that the TAM was converted into reactive species forming DNA adducts, which led to endometrial carcinogenesis [20]. Cell- and promoter-specific factors have been reported, and were involved in the mechanism, that caused TAM act as an estrogen agonist in the uterus [21]. Moreover, co-regulator proteins

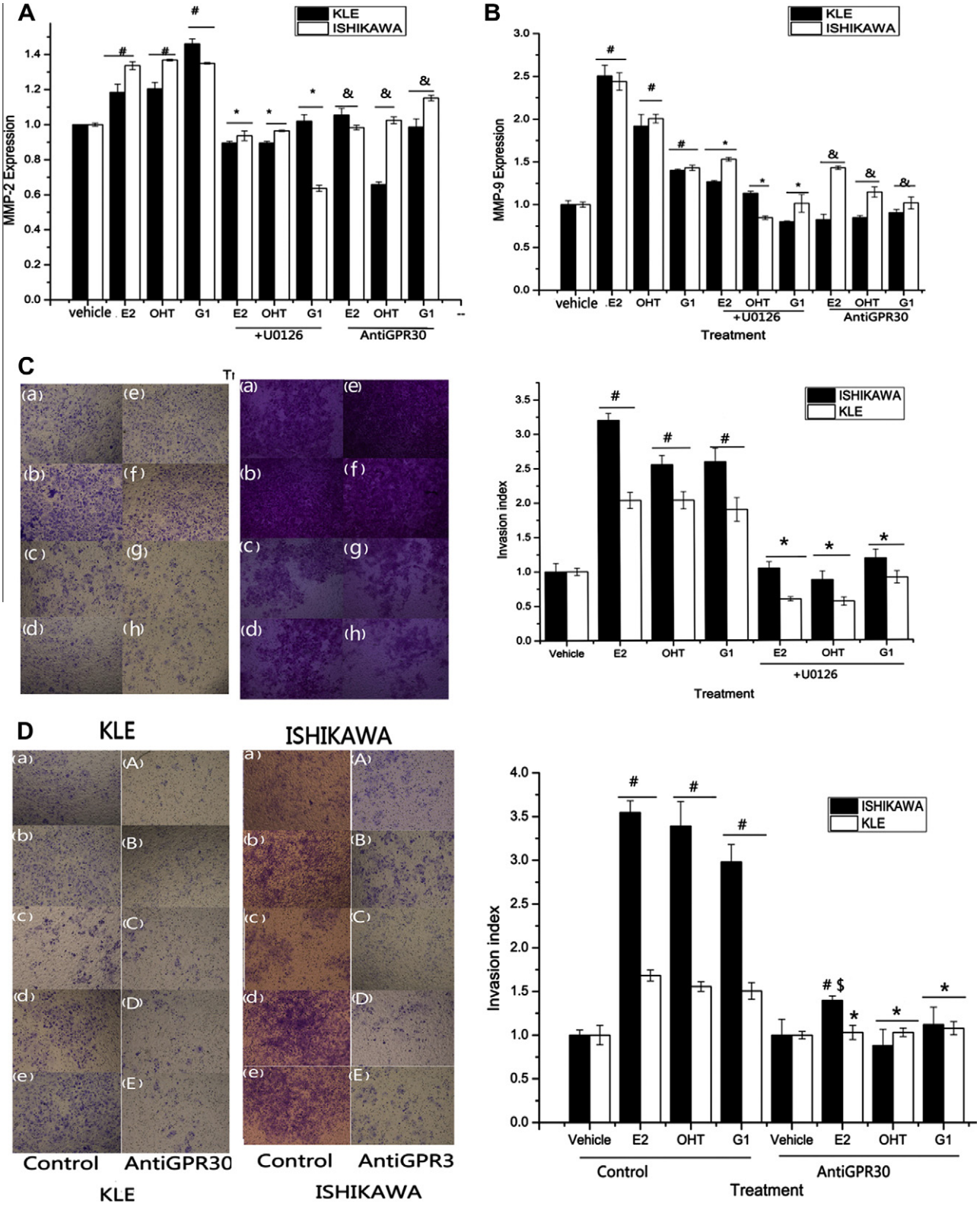

Fig. 3. G protein-coupled receptor 30 stimulates invasion in endometrial cancer cell line via the MAPK pathway. Enzyme-linked immunosorbent assay (ELISA) was made for MMP-2 (Fig. a) and MMP-9 (Fig. b). $^{\#}P < 0.05$ compared with vehicle; $^{*}P < 0.05$ compared with the group with the same treatment but U0126; $^{\&}P < 0.05$ compared with the groups transfected with shiv-pGFP-V-RS vector with the same treatment. In Transwell® assay, KLE and ISHIKAWA cells with no transfection or stable transfection with shiv-pGFP-V-RS (Control) or ShGPR30-pGFP-V-RS (AntiGPR30) were treated as follows, Fig. c (A) vehicle (0.1% dimethyl sulfoxide/phenol-free DMEM/F12); (B) G1 (10^{-8} M); (C) G1 (10^{-8} M) with U0126 (30 μM); (D) vehicle (0.1% ethanol/phenol-free DMEM/F12); (E) E2 (10^{-7} M); (F) OHT (10^{-7} M); (G) E2 (10^{-7} M) with U0126 (30 μM); (H) OHT (10^{-7} M) with U0126 (30 μM); Fig. D: (a, A) vehicle (0.1% dimethyl sulfoxide/phenol-free DMEM/F12); (b, B) G1 (10^{-8} M); (c, C) vehicle (0.1% ethanol/phenol-free DMEM/F12); (d, D) E2 (10^{-7} M); (e, E) OHT (10^{-7} M). Cell invasion was then assessed and photomicrographs taken. $^{\#}P < 0.05$ compared with the vehicle group. $^{*}P > 0.05$ compared with the vehicle group. $^{\$}P < 0.05$ compared with the ISHIKAWA cells treated with E2 in the "Control" group. Magnification ×100. All data are expressed as mean ± SD of three independent experiments.

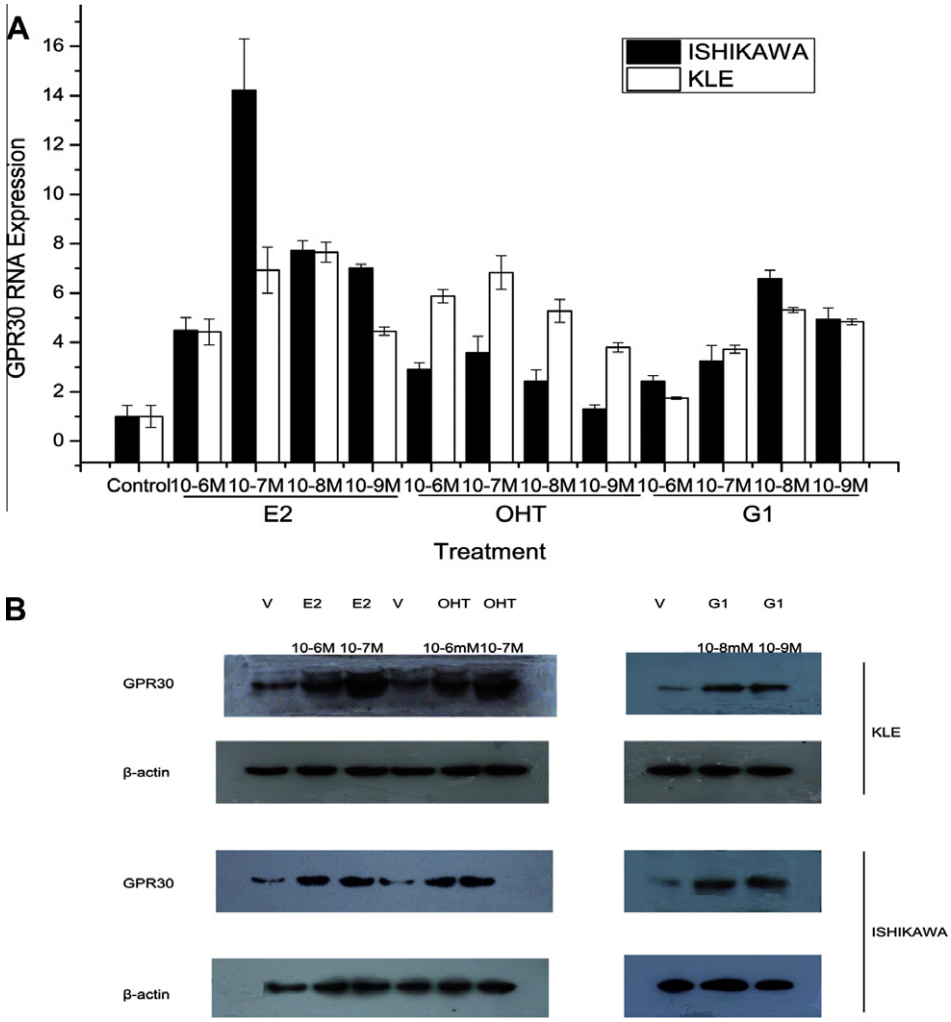

Fig. 4. TAM up-regulate GPR30 expression levels in ISHIKAWA and KLE cells. The RNA expression levels of ISHIKAWA and KLE cells were determined using real-time RT-PCR (A). Immunoblots of GPR30 from cells treated for 48 h with vehicle, E2, OHT or G1 (B) V: Vehicle, 0.1% dimethyl sulfoxide (versus G1) or ethanol (versus E2, OHT) in phenol red-free and serum-free DMEM/F12. Data are expressed as mean ± SD of three independent experiments.

facilitating ERα interaction with the general transcriptional machinery and chromatin led to differential ability of partial agonists/antagonists modify gene expression [22].

It has been reported that the interaction between either TAM or E2 with GPR30 triggered rapid cellular responses to estrogen signals at the plasma membrane level [10,19,23]. In the present study, it was evaluated and demonstrated that in endometrial cancer cells, OHT acquired the ability to induce cell proliferation and invasion in a GPR30-mediated fashion. Treatment able to block GPR30 signaling, such as U0126, the specific inhibitors of the MAPK pathway, or the ShGPR30-pGFP-V-RS transfection, both prevented the enhancement of proliferation and invasion in a similar manner. These results suggested that the GPR30 signal had a pathway involved in the carcinogenic effect of OHT.

In the present study, it was observed that the GPR30 expression was induced by OHT in endometrial cancer cell line. It was assumed that the OHT by up-regulating the GPR30 expression induced the GPR30 signal. The GPR30 expression was induced by epidermal growth factor (EGF) through the EGFR/ERK transduction pathway activated in GPR30 signaling and the recruitment of c-fos to the activator protein-1 site located within GPR30 promoter sequence in endometrial and tamoxifen-resistant breast cancer cells [24]. It was reported that, in a GPR30-mediated fashion, TAM induced expression of c-fos, which belonged to a family of transcription factor [15,23]. The GPR30 signal activated the EGFR/ERK pathway through the release of heparin-binding EGF [11,25], it was assumed that a positive feedback loop occurred within the ligand/EGFR/c-fos/GPR30 signaling network, through which OHT induced the expression of GPR30.

Several studies have examined the expression of GPR30 in vivo. Immunohistochemistry for GPR30 was conducted on tumors from patients with endometrial adenocarcinoma, and GPR30 overexpression was observed more frequently in endometrial carcinomas exhibiting deep myometrial invasion, high grade, biologically aggressive histological subtype, advanced stage, and significantly worse overall survival rate [26]. There was a significant correlation observed between G protein-coupled estrogen receptor expression and endometrial pathology in breast cancer patients receiving TAM [27]. All the in vivo studies demonstrated an association between GPR30 and the occurrence and development of endometrial cancer induced by TAM.

It has been observed that the GPR30 mediated c-fos expression, only after E2 treatment in breast cancer cells [23] and also after OHT treatment in endometrial tumor cells [15], although E2 and the ER antagonists TAM bind to GPR30 directly [10]. This suggested that GPR30 function might be dependent on the cellular context and induced a reverse response of TAM in breast tissues as compared to endometrium.

It has been largely documented that treatment with TAM was associated with an increased incidence of proliferative and neoplastic endometrial changes. The present study showed insights into the molecular mechanisms by which TAM led to these side effects and GPR30 may be the target that could be selectively abrogated.

Acknowledgments

The study was supported by National Natural Science Foundation of China (Nos. 30872760 and 81001154) and the Bureau grant of Shanghai Municipal Health Bureau (2005ZD002).

Appendix A. Supplementary data

Supplementary data associated with this article can be found, in the online version, at doi:10.1016/j.bbrc.2012.02.161.

References

[1] M.C. Pike, C.L. Pearce, A.H. Wu, Prevention of cancers of the breast, endometrium and ovary, Oncogene 23 (2004) 6379–6391.
[2] Y. Shang, Molecular mechanisms of oestrogen and SERMs in endometrial carcinogenesis, Nature Reviews Cancer 6 (2006) 360–368.
[3] J.A. Scott, W.L. McGuire, New molecular markers of prognosis in breast cancer, endocrine-dependent tumors, Raven, New York, 1991. 179–196.
[4] V.C. Jordan, M. Morrow, Tamoxifen, raloxifene, and the prevention of breast cancer, Endocrine reviews 20 (1999) 253–278.
[5] D.P. McDonnell, The molecular pharmacology of SERMs, Trends in Endocrinology and Metabolism 10 (1999) 301–311.
[6] L. Bernstein, D. Deapen, J.R. Cerhan, S.M. Schwartz, J. Liff, E. McGann-Maloney, J.A. Perlman, L. Ford, Tamoxifen therapy for breast cancer and endometrial cancer risk, Journal of the National Cancer Institute 91 (1999) 1654–1662.
[7] A. Jamil, J. Croxtall, J. White, The effect of anti-oestrogens on cell growth and progesterone receptor concentration in human endometrial cancer cells (Ishikawa), Journal of molecular endocrinology 6 (1991) 215–221.
[8] L.B. Schwartz, L. Krey, R. Demopoulos, S.R. Goldstein, L.E. Nachtigall, K. Mittal, Alterations in steroid hormone receptors in the tamoxifen-treated endometrium*, American Journal of Obstetrics and Gynecology 176 (1997) 129–137.
[9] M.M. Gottardis, S.P. Robinson, P.G. Satyaswaroop, V.C. Jordan, Contrasting actions of tamoxifen on endome-trial and breast tumor growth in the athymic mouse, Cancer Research 48 (1988) 812–815.
[10] P. Thomas, Y. Pang, E. Filardo, J. Dong, Identity of an estrogen membrane receptor coupled to a G protein in human breast cancer cells, Endocrinology 146 (2005) 624.
[11] E. Filardo, Estrogen-induced activation of Erk-1 and Erk-2 requires the G protein-coupled receptor homolog, GPR30, and occurs via trans-activation of the epidermal growth factor receptor through release of HB-EGF (2000).
[12] E.J. FILARDO, Estrogen action via the G protein-coupled receptor, GPR30: stimulation of adenylyl cyclase and cAMP-mediated attenuation of the epidermal growth factor receptor-to-MAPK signaling axis, Molecular Endocrinology (2002).
[13] C. Wang, E.R. Prossnitz, S.K. Roy, Expression of G protein-coupled receptor 30 in the hamster ovary: differential regulation by gonadotropins and steroid hormones, Endocrinology 148 (2007) 4853.
[14] M.S. Baquedano, N. Saraco, E. Berensztein, C. Pepe, M. Bianchini, E. Levy, J. Goni, M.A. Rivarola, A. Belgorosky, Identification and developmental changes of aromatase and estrogen receptor expression in prepubertal and pubertal human adrenal tissues, Journal of Clinical Endocrinology & Metabolism 92 (2007) 2215.
[15] A. Vivacqua, The G protein-coupled receptor GPR30 mediates the proliferative effects induced by 17β-estradiol and hydroxytamoxifen in endometrial cancer cells, Molecular Endocrinology 20 (2005) 631–646.
[16] L. Albanito, A. Madeo, R. Lappano, A. Vivacqua, V. Rago, A. Carpino, T.I. Oprea, E.R. Prossnitz, A.M. Musti, S. Ando, G protein-coupled receptor 30 (GPR30) mediates gene expression changes and growth response to 17β-estradiol and selective GPR30 ligand G-1 in ovarian cancer cells, Cancer Research 67 (2007) 1859.
[17] Y.-Y. He, B. Cai, Y.-X. Yang, X.-L. Liu, X.-P. Wan, Estrogenic G protein-coupled receptor 30 signaling is involved in regulation of endometrial carcinoma by promoting proliferation, invasion potential, and interleukin-6 secretion via the MEK/ERK mitogen-activated protein kinase pathway, Cancer Science 100 (2009) 1051–1061.
[18] Y.Y. He, G.Q. Du, B. Cai, Q. Yan, L. Zhou, X.Y. Chen, W. Lu, Y.X. Yang, X.P. Wan, Estrogenic transmembrane receptor of GPR30 mediates invasion and carcinogenesis by endometrial cancer cell line RL95-2, Journal of Cancer Research and Clinical Oncology (2012) 1–9.
[19] C.M. Revankar, D.F. Cimino, L.A. Sklar, J.B. Arterburn, E.R. Prossnitz, A transmembrane intracellular estrogen receptor mediates rapid cell signaling, Science 307 (2005) 1625.
[20] S. Shibutani, A. Ravindernath, N. Suzuki, I. Terashima, S.M. Sugarman, A.P. Grollman, M.L. Pearl, Identification of tamoxifen-DNA adducts in the endometrium of women treated with tamoxifen, Carcinogenesis 21 (2000) 1461.
[21] H. Lee, F. Jiang, Q. Wang, S.V. Nicosia, J. Yang, B. Su, W. Bai, MEKK1 activation of human estrogen receptor α and stimulation of the agonistic activity of 4-hydroxytamoxifen in endometrial and ovarian cancer cells, Molecular Endocrinology 14 (2000) 1882–1896.
[22] C.L. Smith, Z. Nawaz, B.W. O'Malley, Coactivator and corepressor regulation of the agonist/antagonist activity of the mixed antiestrogen, 4-hydroxytamoxifen, Molecular Endocrinology 11 (1997) 657–666.
[23] M. Maggiolini, A. Vivacqua, G. Fasanella, A.G. Recchia, D. Sisci, V. Pezzi, D. Montanaro, A.M. Musti, D. Picard, S. Andò, The G protein-coupled receptor GPR30 mediates c-fos up-regulation by 17β-estradiol and phytoestrogens in breast cancer cells, Journal of Biological Chemistry 279 (2004) 27008.
[24] A. Vivacqua, R. Lappano, P. De Marco, D. Sisci, S. Aquila, F. De Amicis, S.A.W. Fuqua, S. Ando, M. Maggiolini, G protein-coupled receptor 30 expression is up-regulated by EGF and TGF in estrogen receptor-positive cancer cells, Molecular Endocrinology 23 (2009) 1815–1826.
[25] E. Filardo, P. Thomas, GPR30: a seven-transmembrane-spanning estrogen receptor that triggers EGF release, Trends in Endocrinology and Metabolism 16 (2005) 362–367.
[26] H.O. Smith, K.K. Leslie, M. Singh, C.R. Qualls, C.M. Revankar, N.E. Joste, E.R. Prossnitz, GPR30: a novel indicator of poor survival for endometrial carcinoma, American Journal of Obstetrics and Gynecology 196 (2007) 386 e381–386. e311.
[27] T. Ignatov, H. Eggemann, A. Semczuk, B. Smith, J. Bischoff, A. Roessner, S.D. Costa, T. Kalinski, A. Ignatov, Role of GPR30 in endometrial pathology after tamoxifen for breast cancer, American Journal of Obstetrics and Gynecology 203 (2010) 595 e595–599.e516.

Biochemical and Biophysical Research Communications 420 (2012) 350–356

Contents lists available at SciVerse ScienceDirect

Biochemical and Biophysical Research Communications

journal homepage: www.elsevier.com/locate/ybbrc

In vitro binding properties of tumor suppressor p53 with PUMA and NOXA

So Young Park [1], Mi Suk Jeong [1], Se Bok Jang *

Department of Molecular Biology, College of Natural Sciences, Pusan National University, Jangjeon-dong, Geumjeong-gu, Busan 609-735, Republic of Korea

ARTICLE INFO

Article history:
Received 23 February 2012
Available online 13 March 2012

Keywords:
p53
PUMA
NOXA
Interaction
Apoptosis

ABSTRACT

The p53-upregulated modulator of apoptosis (Puma) and Noxa, are direct targets in p53-mediated apoptosis localized to the mitochondria. Tumor suppressor p53 induces apoptosis by transcriptional induction of Puma and Noxa, which encode proapoptotic BH3-only member Bcl-1 family proteins. However, at a molecular level, the mechanism of action of Puma and Noxa proteins remain poorly defined. In addition, there have been no reports on whether or not p53 directly interacts with Puma and Noxa, *in vitro*. Here, we provide evidence indicating that the DNA binding domain (DBD) of p53 directly interacted with the BH3 domains of human PUMA and NOXA. Our studies revealed that PUMA has a weak affinity for p53, but NOXA has significant affinity for p53. In this study, we developed a molecular docking model using homology modeling based on the structures of truncated p53, PUMA and NOXA. In addition, we investigated whether or not six mutants of p53 (K101A, T102A, L111A, D186A, G199A and S227A) were able to bind to PUMA and NOXA. Four structure-based mutations (T102A, L111A, D186A and G199A) disrupted the p53-PUMA/NOXA interaction. Our study suggested that these four mutations lowered the stability of the p53 DBD domain and induced aggregation of structurally destabilized p53, and thus disrupted the p53-PUMA/NOXA interaction.

1. Introduction

A broad spectrum of p53 target genes have been identified including genes that regulate cell cycle arrest, DNA repair, autophagy, and a series that regulate cell death through various pathways [1–10]. Oncogene activation causes aberrant DNA replication, and such DNA replicative stress, i.e., "oncogenic stress" may activate p53 and result in elimination of such hazardous cells. p53 is one of the most important tumor suppressors within the cell, and as a result, is frequently found to be inactivated in human cancers [11]. It functions mainly as a transcription factor by binding to specific DNA response elements and integrates a multitude of cellular signals via protein–protein interactions to initiate an appropriate cellular response [12]. To understand the mechanism of the p53-mediated tumor surveillance system, it is important to analyze the molecular mechanism of p53-induced apoptosis.

Pro-apoptotic BH3 (Bcl-2 homology 3)-only members of the Bcl-2 protein family are essential initiators of developmentally programmed cell death and stress-induced apoptosis [13]. Mammalian noxa and puma/bbc-3 are both induced by the p53 tumor suppressor protein and may be critical initiators of DNA damage-induced apoptosis [11,14,15]. Puma appears to be critical for γ-irradiation-induced NPC (Neural precursor cells) apoptosis in postnatal cerebellar external granule cells [16]. However, it is unclear if other BH3-only molecules, such as Noxa, are involved in this process as well, or if Puma has a similar function in telencephalic NPCs.

The roles of Puma and Noxa in p53-mediated apoptosis have been analyzed using gene knockout mice [16–18]. Mice embryonic fibroblasts (MEFs), deficient in *Noxa*, and MEFs from *Puma*-deficient mice both show resistance to oncogene-dependent apoptosis. Additionally, thymocytes from *Puma*-deficient mice, but not *Noxa*-deficient mice, are resistant to DNA-damage-induced apoptosis. Noxa and Puma show overlapping and, in some cases, different functions in p53-mediated apoptosis. Recently, it was confirmed that Puma and Noxa synergistically induce apoptosis [19]. However, the molecular mechanism underlying this synergism remains unclear.

To elucidate the mutual relationships between human p53 and PUMA/Noxa in their respective signal transduction pathways, we investigated the interactions between the recombinant BH3 domains (BH3s) of human PUMA/NOXA and the DNA binding domain of p53. Using several biochemical and biophysical assays, we demonstrated a direct protein–protein interaction between p53 and PUMA/NOXA, *in vitro*. Mutagenesis studies implicated the amino acids K101, T102, L111, D186, G199 and S227, as participants in the p53-PUMA/NOXA interactions. Of six mutations produced by substitution of Ala, four mutants were unable to associate as a result of p53 to PUMA/NOXA signal transductions. The p53-PUMA/NOXA structures described herein provide a structural basis for the observed changes in the site-specific variants. These

* Corresponding author. Fax: +82 51 581 2544.
E-mail address: sbjang@pusan.ac.kr (S.B. Jang).
[1] These authors contributed equally to this article.

0006-291X/$ - see front matter © 2012 Elsevier Inc. All rights reserved.
http://dx.doi.org/10.1016/j.bbrc.2012.03.001

findings provide additional insights into the mechanism underlying p53-induced apoptosis.

2. Materials and methods

2.1. Protein cloning, expression and extraction

The p53 (92-293) was subcloned into the C-terminal His-tagged fusion protein vector pET-26b for purification. The p53 and PUMA were amplified by polymerase chain reaction (PCR) using oligonucleotides incorporating *Nde*I and *Xho*I sites on the 5′ primer, and a 3′ primer containing a stop codon.p53 (92-293), 5′-GGAATTCCATATGCCCCTGTCATCTTCTGTC-3′and 5′-CCGCTCGAGCCCTTTCTTGCGGAGATTC-3′.

Then, the full-length NOXA was subcloned into a glutathione S-transferase (GST)-fused protein vector pGEX-4T1 for the pull-down experiment. PUMA and NOXA were amplified by PCR with oligonucleotides incorporating *Bam*HI/*Xho*I and *Eco*RI/*Xho*I sites on the 5′ primer, and the 3′ primer containing a stop codon.PUMA (96-152), 5′-CGCGGATCCTCGCTCTCGCTGGCGGAG-3′and 5′-CCGCTCGAGGTACT GTGCGTTGAGGTCGTC-3′;NOXA (1-54), 5′-CCGGAATTCATGCCT GGGA AGAAGGC-3′and 5′-CCGCTCGAGGGTT CCTGAGCAG AAGAG-3′.The sequences of the double-stranded oligonucleotides used for site-directed mutagenesis of the six different p53 residues to alanine, were as follows:K101A, 5′-CTGTCCCTTCCCAGGCAACCTACCAGGGand 5′-CCCT GGTAGGTTGCCTGGGAAGGGACAG;T102A,5′-TCCCTTCCCAGAAAG CC TACCAGGGCAGand 5′-CTG CCCTGGTAGGC TTTCTG GGAA GGGA;-L111A, 5′-CTACGGTTTCCGTG CG GGCTTCTTGCATTCand 5′-GAAT GCAAGAAGCCCGCACGGAAACCGTAG ;D186A, 5'-TGCTCAGATAG CGC TGGTCTGGCCCCTCand 5'-GAGGGGC CAGACCAG CGCTATCTGAGCA;-G199A, 5′-TTATCCG AGTGGA AGC AAATTT GCGT GTGGand 5′-CCA-CACGCA AATTTGCTTCCACTCGGATAA; S227A, 5′-GCCTGA GGTTG GCGCTGACTG TACCACCand 5′-GGT GGTACAGTCAGCG CCAACC TCA GGC.

The plasmids with positive p53, PUMA, and NOXA expression were identified by restriction endonuclease digestion and further verified by DNA sequencing using a Macrogen automatic DNA sequencer. The constructs were transformed into the expression host *Escherichia coli* BL21 (DE3). A single colony was inoculated into 20 mL of Luria-Bertani (LB) medium containing 50 μg/mL of ampicillin (PUMA/NOXA), and 10 μg/mL of kanamycin (p53), and then the bacteria were grown overnight at 37 °C. These cells were then added to six 2-L flasks, each containing 500 mL of LB and 50 μg/mL of ampicillin. The cultures were grown at 37 °C until an OD_{600} of 0.5 was reached. The expression of these proteins was induced using 0.5 mM isopropyl-thio-β-D-galactopyranoside (IPTG). The bacterial cells were induced for 5 h at 25 °C for p53, 5 h at 37 °C for PUMA/NOXA, and then harvested by centrifugation at 3830*g* for 25 min. The cell pellets were either used immediately or stored frozen at −70 °C.

The p53 cell pellets were then resuspended in lysis buffer A [50 mM Tris-HCl with a pH of 7.5, 200 mM NaCl, and 1 mM dithiothreitol (DTT)] and PUMA/NOXA in Phosphate buffer saline (PBS). After sonicating the cell suspensions on ice (Branson Sonifier 450), the resulting cell lysates were centrifuged at 20,017*g* for 45 min to remove insoluble cellular debris. The insoluble fractions were then directly resuspended in 2× sodium dodecyl sulfate (SDS) loading buffer, followed by incubation at 95 °C for 5 min. The soluble and insoluble portions were fractionated on 15% SDS-polyacrylamide gel electrophoresis (SDS-PAGE) gels and visualized by Coomassie blue staining. The supernatants were collected and used for protein purification.

2.2. Purification

The His-tagged p53 fusion protein was applied to a Ni-NTA (Amersham Pharmacia Biotech) column for purification. The supernatants obtained from the protein extraction were loaded onto the Ni-NTA column and pre-equilibrated with buffer A. The column was washed with buffer A containing imidazole, and elution of the bound proteins was achieved by varying the imidazole amount (20–200 mM). Protein elution was monitored at 280 nm and the resulting fractions were analyzed using 15% SDS-PAGE. Then, gel filtration was performed by Fast protein liquid chromatography (FPLC) using a Superdex 200 10/300 GL column. The proteins were loaded onto a column equilibrated with buffer A and separated at a flow rate of 1.5 mL/min.

The clear PUMA and NOXA supernatants were loaded onto a Glutathione-Sepharose 4 Fast Flow (Amersham-Pharmacia Biotech; binding capacity of 10 mg of GST per milliliter of resin) at a flow rate of 2.5 mL/min, and were then washed extensively using 20 mL of PBS. The PUMA and NOXA fusion proteins were eluted with 10 mL of 10 mM reduced glutathione dissolved in 50 mM Tris–HCl. The PUMA and NOXA proteins were then concentrated by centrifugation at 2500 rpm using ultrafiltration devices to a final volume of 10 mL. Then, gel filtration was performed using a Superdex 200 10/300 GL column.

2.3. Western blotting

The purified p53 and PUMA/NOXA proteins from the 15% SDS-PAGE analysis were transferred onto a nitrocellulose membrane and 115 V was applied for 1 h. The membrane was blocked for 1 h using 5% skim milk in Tween-PBS buffer containing 1% Tween 20. The membrane was then incubated with primary antibody [His-probe (G-18) diluted to 1:5000; Santa Cruz Biotechnology, Inc. and GST (B-14) diluted to 1:5000, Santa Cruz Biotechnology, Ins.] for 12 h or 1 h. After washing with Tween-PBS, the membrane was incubated for 1 h with goat anti-rabbit IgG-HRP, for reaction with the His secondary antibody (Santa Cruz Biotechnology, Inc.), and with goat anti-mouse IgG-HRP for the GST secondary antibody which was diluted at a ratio of 1:10,000 in blocking buffer.

2.4. GST pull-down assay

For the pull-down assay, 20 μg of purified His-p53 and their mutants were mixed with 20 μg of purified GST, GST-PUMA or GST-NOXA, in a 1.5 ml microcentrifuge tube. This was followed by incubation for 12 h at 4 °C with gentle rotation. Then, the pre-equilibrated glutathione–Sepharose 4B beads were added with PBS for a 1 h reaction at 4 °C. Beads were then centrifuged at 600*g* for 3 min and washed five times with 1 ml of PBS. Proteins bound to the beads were eluted [50 mM Tris–HCl (pH 7.5), 30 mM reduced glutathione] and then resolved on a 12% SDS polyacrylamide gel. The proteins were subsequently analyzed by Western blot using anti-His (Santa Cruz Biotech) and anti-GST (Santa Cruz Biotech).

2.5. Fluorescence spectroscopy

Fluorescence emission spectra were obtained using an Edinburgh (UK) FLS920 Time correlated single photon counting spectrometer (TCSPC) with 1 cm path length cuvettes containing excitation and emission slits of 20 nm in width. The fluorescence emission spectra of p53 and PUMA/NOXA were obtained in order to identify their characteristic chemical structures, namely their double bonds and aromatic groups. The emission intensity was recorded at 305–465 nm with an excitation wavelength of 295 nm. PUMA/NOXA and p53, each at concentration of 5 μM, were preincubated together for 25 min at 25 °C. All spectra were obtained at a protein concentration of 50 μg/mL at 24 °C. Ten spectra for each protein sample were collected, averaged, and subjected to baseline correction by subtraction of the buffer spectrum.

2.6. Biacore biosensor analysis

Measurements of the apparent dissociation constants (K_D) between p53 and PUMA/NOXA were carried out using a Biacore 2000 biosensor (Biosensor, Sweden). The p53 (20 μg/mL in 10 mM sodium acetate with a pH of 5.0) was covalently bound to the carboxylated dextran matrix at a concentration corresponding to 5000 response units (RU) by an amine-coupling method, as suggested by the manufacturer. A flow path involving two cells was employed to simultaneously measure the kinetic parameters from one flow cell containing the p53-immobilized sensor chip, to the other flow cell containing an underivatized chip. For kinetic measurements at room temperature, PUMA/NOXA samples with concentrations ranging from 250 to 5000 nM were prepared by dilution in HBS buffer (150 mM NaCl, 3 mM EDTA, 0.005% surfactant P20 and 10 mM HEPES) with a pH of 7.4. Each sample was injected, along with 50 μL of p53 solution, into the flow cells (association phase) at a rate of 10 μL/min. The immobilized ligand was regenerated by injecting 10 μL of 50 mM NaOH at a rate 10 μL/min during the cycles.

2.7. UV-Vis Absorption

Absorbance measurements were carried out using a Shimadzu UV-1650 PC UV–Vis Spectrophotometer with 1.0 cm quartz cells. The UV absorbance spectra of the p53 and PUMA/NOXA were obtained using concentrations of 0.5 mg/ml. Thermal unfolding was performed using the same set up and buffer. To examine the effect of temperature conditions, the p53 and PUMA/NOXA samples were incubated at various temperatures (20–60 °C) for 5 min. The pH-dependent unfolding studies were carried out under various pH conditions (pH 5.5–pH 9.5). The UV spectra of the p53, PUMA and NOXA were recorded in the 280–340 nm range.

2.8. 3D structure prediction of p53 and PUMA/NOXA

Models of p53 and PUMA/NOXA were constructed using SWISS-MODEL software, a program for relative protein structure modeling [20]. The results of an ExPASy search with the PDB revealed three reference proteins: p53 (92-290) (PDB ID: 2XWR), PUMA (130-152) (PDB ID: 2ROC) and NOXA (18-45) (PDB ID: 2JM6). Structur-

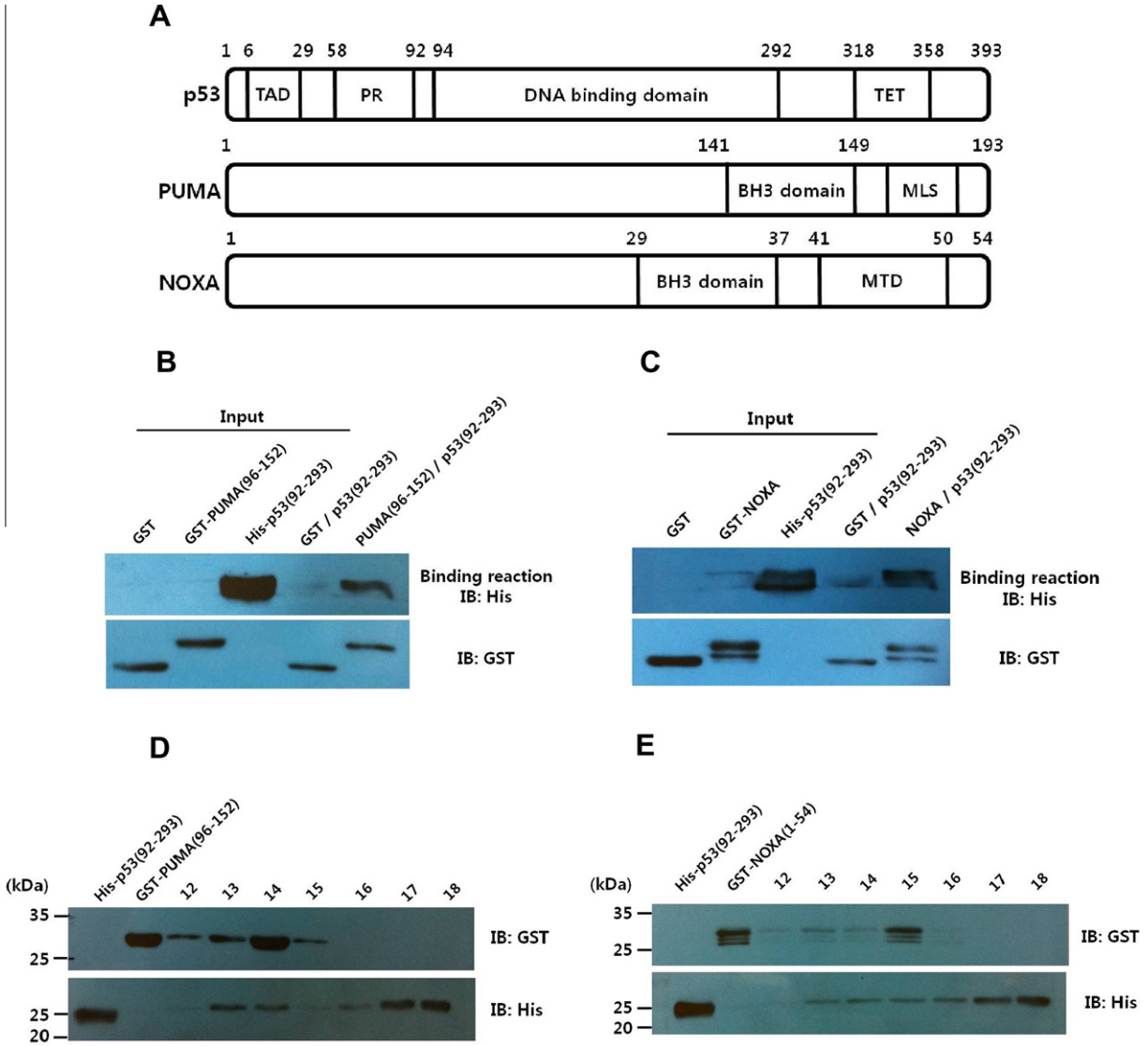

Fig. 1. (A) Schematic representation of the full-length p53, PUMA, and NOXA. (B and C) The map of p53 DNA binding domains that interact with PUMA (96-152) and NOXA (1-54) using an *in vivo* GST pull-down assay. GST-PUMA/NOXA fusion proteins bound to glutathione-sepharose 4B beads. After pull-down, the beads were washed and the samples were separated via SDS-PAGE. The protein interactions were detected by Western blot. (D and E) After size-exclusion chromatography, the binding of p53 to PUMA/NOXA was shown by Western blot analysis.

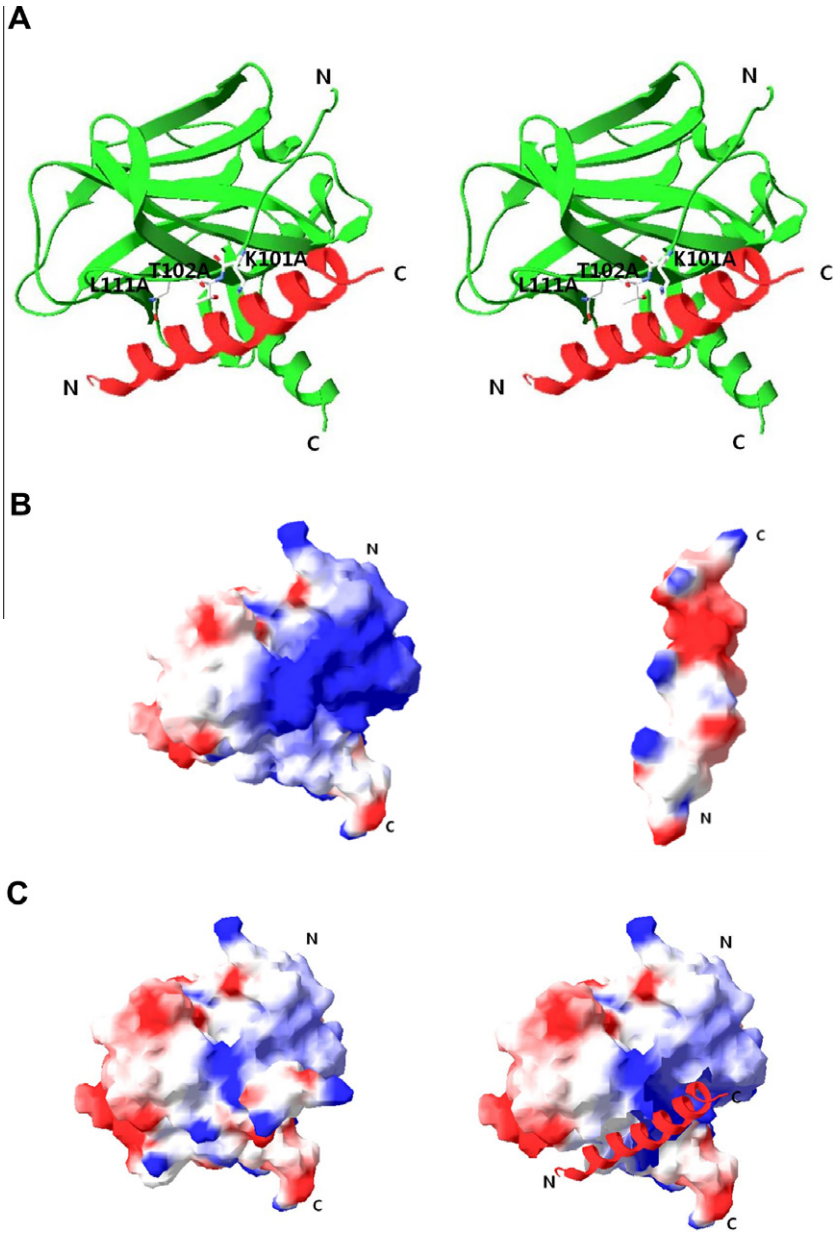

Fig. 2. (A) A stereoview of the modeled p53 and PUMA complex structure. Molecules are shown as ribbon representations in a white window. The p53 is shown in green and PUMA is shown in red. The binding sites between p53 and PUMA/NOXA are also illustrated. (B) Molecules are shown as surface representations in a white window. Blue and red represent positive and negative electrostatic potential, respectively. Structures are shown as surface representations for p53 (left panel) and PUMA (right panel). (C) The p53 moiety bound with PUMA is shown (left panel) along with the electrostatic potential of the p53 surface as viewed from the PUMA binding site (right panel). (For interpretation of the references to colour in this figure legend, the reader is referred to the web version of this article.)

ally conserved regions (SCRs) for the model and the template were compared by multiple sequence alignment using CLUSTAL W.

3. Results and discussion

While a great deal of progress has been made in structural and functional p53 research, the direct interaction between p53 and PUMA/NOXA, *in vitro,* has not yet been determined. Achievement of this goal may help interpret and explain the complicated biological actions of p53 and PUMA/NOXA. The domain structure of p53 is shown in Fig. 1A. The p53 protein had an intrinsic N-terminal region comprising the transactivation domain (TAD, amino acids (aa) 6–29) and proline-rich region (PR, aa 58–92). The structured DNA binding domain (DBD, aa 94–292) and tetramerization domain (TET, aa 318–358) were connected via a flexible linker. Full-length PUMA and NOXA proteins contained BH (Bcl-2 homology) with 3 domains each (Fig. 1A). Also, PUMA and NOXA each contained mitochondria-localization signal (MLS) and mitochondrial targeting domain (MTD). The DNA binding domain (DBD) is the core domain. Approximately 95% of the known cancer-causing mutants of p53 are altered in this domain. To investigate whether or not the p53 DBD interacts with the PUMA/NOXA BH3s, recombinant PUMA/NOXA and p53 were isolated. The soluble PUMA/NOXA and p53 proteins were purified to homogeneity and analyzed.

We evaluated the interaction of p53 with PUMA and NOXA, *in vitro,* using a series of biochemical and biophysical measurements. His-tagged p53 fusion protein was effective in pull-down of both GST-PUMA and NOXA, with BH3s (Fig. 1B and C). These results indicated that PUMA and NOXA interact with p53, *in vitro*. Furthermore, we were able to confirm the interaction between

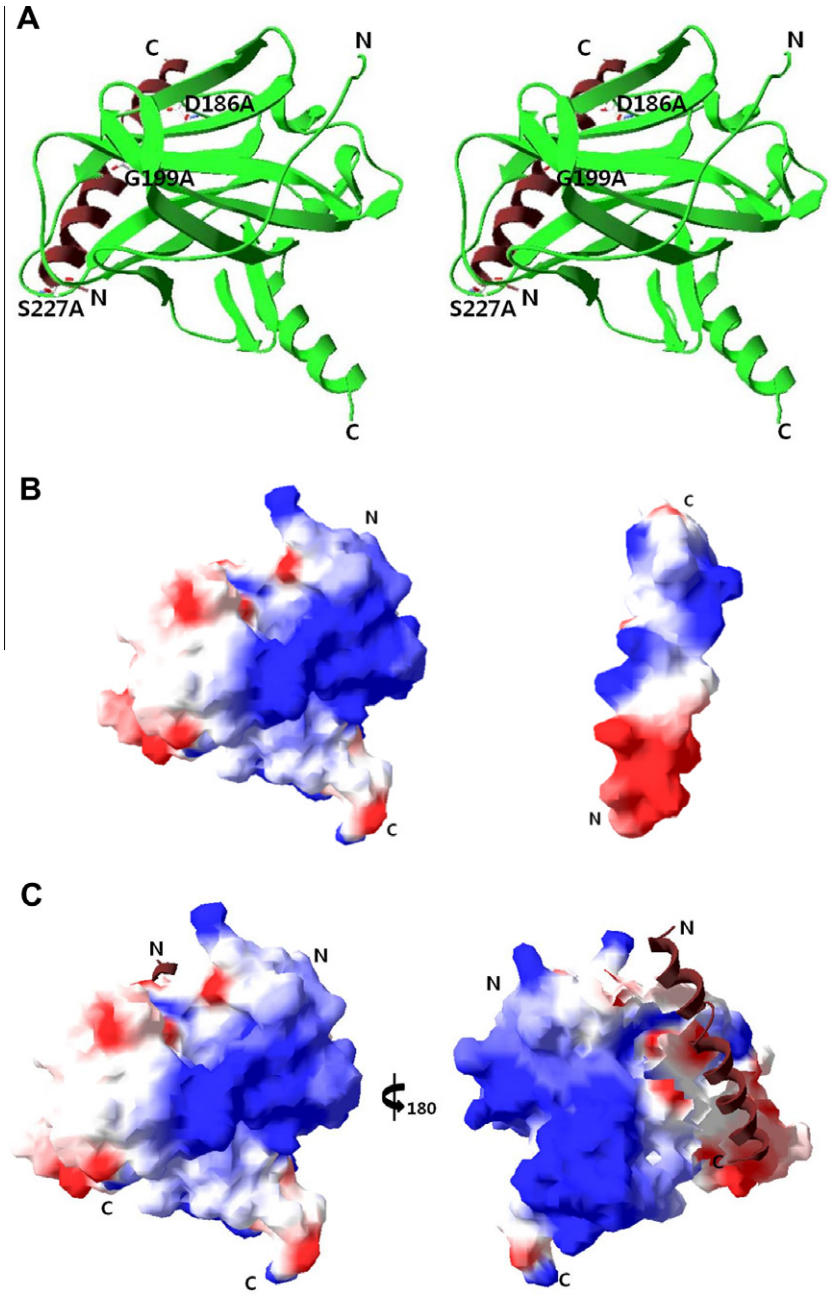

Fig. 3. (A) The interaction between p53 and NOXA was modeled. Molecules are shown as ribbon representations in a white window. The p53 in shown in green and NOXA in brown. (B) Molecules are shown as surface representations in a white window. Blue and red represent positive and negative electrostatic potential, respectively. Structures are shown as surface representation for p53 (left panel) and NOXA (right panel). (C) The electrostatic potential of the p53 surface as viewed from the NOXA binding site (left panel). The p53 moiety bound with NOXA is shown (right panel). (For interpretation of the references to colour in this figure legend, the reader is referred to the web version of this article.)

p53 and PUMA/NOXA using a size-exclusion column. The purified p53 and PUMA/NOXA proteins were mixed in a 1:1 molar ratio. After incubation for 12 h at 4 °C, the mixture was loaded onto a Superdex 200 10/300 GL column (Amersham Pharmacia Biotech). Binding between p53 and PUMA/NOXA was detected by Western blot analysis (Fig. 1D and E).

To investigate the structural aspects of the interaction between p53 and PUMA/NOXA, we assumed a p53 (92-293) structure similar to human p53 structure (PDB ID: 2XWR, 89-293) (Figs. 2A and 3A). Next, we modeled the PUMA (96-152) structure using the known structure of truncated PUMA (PDB ID: 2ROC, 130-155). Most positive charges in the p53 structure were densely packed in the binding pocket (Fig. 2B). The positively charged p53 binding pocket binds to the negatively charged pocket of PUMA. Because BH3 protein surface features dictate their mode of interactions with partners, the electrostatic surface differential is critical for interactions with partner proteins. Also, we modeled NOXA (1-54) using the known structure of truncated NOXA (PDB ID: 2JM6, 18-45) (Fig. 3A and B). Interestingly, these results indicated that PUMA and NOXA interact with p53 at different sites. In PUMA, most residues in the N- and C-regions had negative charges. In NOXA, most residues in the N-regions had negative charges, whereas most residues of the C-region had positive charges in a globular fold. These charges may promote formation of the PUMA/NOXA complexes (Figs. 2C and 3C).

We predicted interaction sites using the modeled complex structures including the mutations. Six residues were chosen for

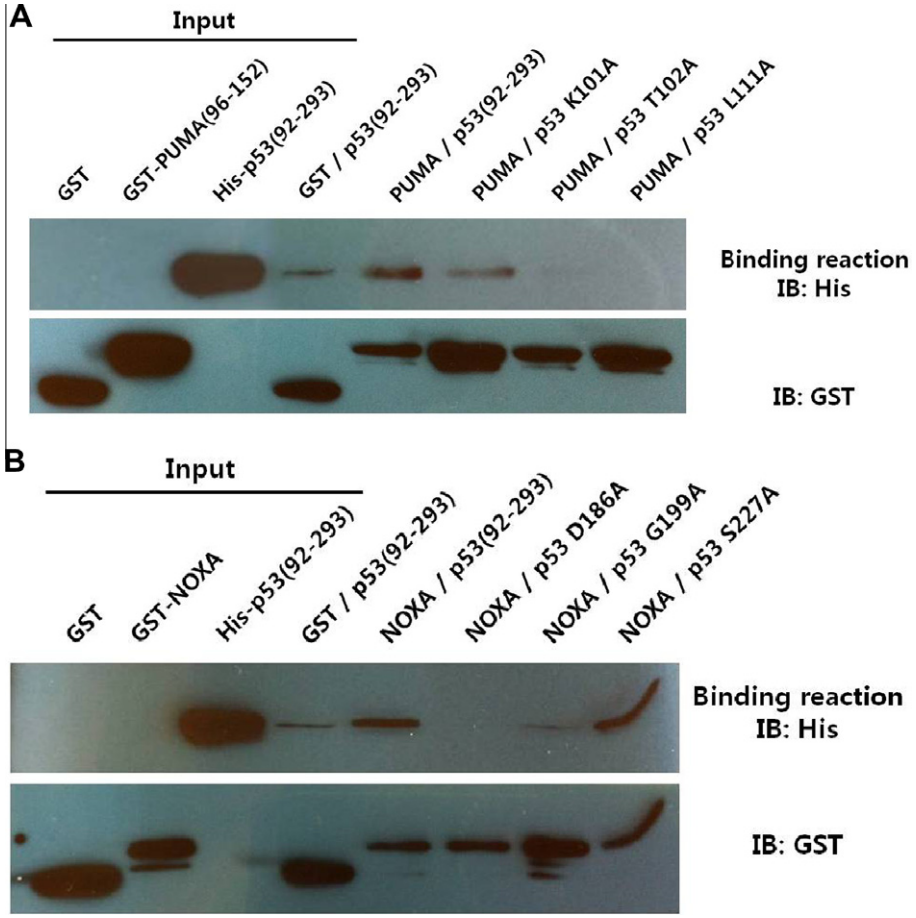

Fig. 4. Structure-based mutagenesis and analysis of binding region mutations. (A) Analysis of structure-based mutations of p53 and PUMA as revealed by *in vitro* GST-tag pull-down assay. A defective interaction was indicated for T102A and L111A. (B) Pull-down of p53 and NOXA as revealed by *in vitro* GST-tag pull-down assay. A defective interaction was indicated for D186A and G199A .

mutations in order to investigate the interaction between the p53 and PUMA/NOXA complexes (Figs. 2A and 3A). The p53 mutations were K101A, T102A and L111A for PUMA, and D186A, G199A and S227A for NOXA. Interestingly, the T102A and L111A mutations for PUMA, and the D186A and G199A mutations for NOXA, disrupted their interaction (Fig. 4A and B). These four mutations structurally destabilized p53 and induced their aggregation. These results indicate that the predicted interaction sites in the modeled complex structures play important roles in the structural stability of the p53 and PUMA/NOXA protein complexes.

To further investigate the interaction between PUMA/NOXA and p53, the fluorescence emission spectra of purified PUMA and NOXA were measured with λ_{max} curve detection at 330 nm (Fig. S1A and B). Spectra of both p53-PUMA/NOXA complexes were of lower intensity than that observed when simply combining PUMA/NOXA and p53. The fluorescence intensities were approximately 15,900N for PUMA, 7500N for NOXA, and 1800N for p53. The interaction was most likely accompanied by significant conformational changes in either one or both proteins, and is likely mediated as the residues of the aromatic groups are buried within the 3D protein structure. Furthermore, the less rigid hydrophobic environment required for the conformational changes associated with PUMA/NOXA and p53 can were observed as a decrease in fluorescence intensity. Assessing our findings as a whole, we concluded that both the PUMA and NOXA BH3 regions interact with p53.

The binding affinities of PUMA/NOXA for p53 were also estimated by surface plasmon resonance spectroscopy (Biacore; Fig. S2A and B). Sensorgrams of PUMA/NOXA binding to p53 were used to calculate the kinetic binding constants. Background sensorgrams were then subtracted from the experimental sensorgrams to yield representative specific binding constants. We found that p53 physically bound both PUMA and NOXA with an apparent K_D of 359 nM for PUMA, and a K_D of 113 nM for NOXA (Table 1). We found that p53 interacted strongly with NOXA and weakly with PUMA as a result of their DBD and BH3 domain conformations.

Table 1
Kinetic parameters of the binding of p53 to PUMA and NOXA[a].

	Conc of analyte (nM)	k_a ($M^{-1}s^{-1}$)	k_d (s^{-1})	K_D (M)
PUMA				
	5000	5.25×10^3	1.60×10^{-3}	3.05×10^{-7}
	2500	1.02×10^4	1.42×10^{-4}	1.39×10^{-7}
	1000	2.37×10^4	1.34×10^{-4}	5.65×10^{-8}
	500	3.68×10^4	1.41×10^{-4}	3.83×10^{-8}
	250	4.52×10^4	1.23×10^{-5}	2.72×10^{-8}
K_D (nM)$_{avg}$				113
NOXA				
	5000	3.26×10^3	2.44×10^{-3}	7.49×10^{-7}
	2500	3.24×10^3	9.69×10^{-4}	2.99×10^{-7}
	500	8.50×10^3	2.49×10^{-3}	2.93×10^{-7}
	250	1.51×10^4	1.47×10^{-3}	9.73×10^{-8}
K_D (nM)$_{avg}$				359

[a] The association rate constant (k_a) was determined from a plot of ln[Abs(dR/dt)] *versus* time, where R is the intensity of the surface plasmon resonance signal at time, t. The dissociation rate constant (k_d) was determined from a plot of ln(R_0/R) *versus* time, where R_0 is the resonance signal intensity at time zero. The apparent K_D was calculated from the kinetic constants: K_D (M) = k_d/k_a.

In order to examine the change of the protein's secondary or tertiary structure under different temperature and pH conditions, UV absorption spectra of the p53 and PUMA/NOXA proteins were measured. The intensity of the p53 proteins increased gradually with pH increasing from 5.5 to 9.5. The peaks in the difference spectra of the proteins were related to the p53 conformational changes. At lower pH conditions, p53 was less soluble, and at high pH conditions, p53 was more soluble. However, at more extreme pH conditions (9.5–10.5), p53 produced a large conformational change, encouraging aggregation. The p53 conformational changes also depended on temperature. The p53 protein UV absorption spectra indicated large conformational changes above 40 °C (Fig. S3A). Thus, we found that p53 protein stability was sensitive to both pH and temperature. On the other hand, the PUMA/NOXA protein stabilities were nearly independent of pH and temperature in the range where p53 undergoes conformational changes. PUMA/NOXA were destabilized and accompanied by large structural changes only at the more extreme condition of pH 9.5 and 60 °C (Fig. S3B and C).

In this study, we carried out the purification and characterization of truncated PUMA/NOXA and p53 proteins in *E. coli*. Furthermore, by performing a series of biochemical and biophysical measurements, we confirmed that PUMA/NOXA both interact with p53, *in vitro*. Intriguingly, the BH3 of NOXA bound with higher affinity to the DNA binding domain of p53, than that of PUMA. Furthermore, we observed that six mutations showed different levels of expressions and characterization as compared to the wild-type. To study the functional role of p53 mutations in tumor suppression, we will further explore the structure of these mutant proteins and their interactions using X-ray and NMR techniques. This study provided important data regarding the PUMA/NOXA structure, the binding activity of PUMA/NOXA BH3s to the p53 DNA binding domain, and protein–protein interactions involving tumor suppressor DNA binding domain as a transcriptional activator factor.

Acknowledgment

This work was supported by The Bio-Scientific Research Grant funded by The Pusan National University (PNU, Bio-Scientific Research Grant) (PNU-2010-101-20100613214).

Appendix A. Supplementary data

Supplementary data associated with this article can be found, in the online version, at http://dx.doi.org/10.1016/j.bbrc.2012.03.001.

References

[1] T. Soussi, G. Lozano, P53 Mutation heterogeneity in cancer, Biochem. Biophys. Res. Commun. 331 (2005) 834–842.
[2] M.H. Kubbutat, S.N. Jones, K.H. Vousden, Regulation of p53 stability by Mdm2, Nature 387 (1997) 299–303.
[3] Y. Haupt, R. Maya, A. Kazaz, M. Oren, Mdm2 promotes the rapid degradation of p53, Nature 387 (1997) 296–299.
[4] D. Menendez, A. Inga, M.A. Resnick, The expanding universe of p53 targets, Nat. Rev. Cancer 9 (2009) 724–737.
[5] K. Nakano, E. Balint, M. Ashcroft, K.H. Vousden, A ribonucleotide reductase gene is a transcriptional target of p53 and p73, Oncogene 19 (2000) 4283–4289.
[6] M.B. Kastan, Q. Zhan, W.S. el-Deiry, F. Carrier, T. Jacks, W.V. Walsh, B.S. Plunkett, B. Vogelstein, A.J.Jr. Fornacer, A mammalian cell cycle checkpoint pathway utilizing p53 and GADD45 is defective in ataxia-telangiectasia, Cell 71 (1992) 587–597.
[7] H. Tanaka, H. Arakawa, T. Yamaguchi, K. Shiraishi, S. Fukuda, K. Matsui, Y. Takei, Y. Nakamura, A ribonucleotide reductase gene involved in a p53-dependent cell cycle checkpoint for DNA damage, Nature 404 (2000) 42–49.
[8] D. Crighton, S. Wilkinson, J. O'Prey, N. Syed, P. Smith, P.R. Harrison, M. Gasco, O. Garrone, T. Crook, K.M. Ryan, DRAM, a p53-induced modulator of autophagy, is critical for apoptosis, Cell 126 (2006) 121–134.
[9] J. O'Prey, J. Skommer, S. Wilkinson, K.M. Ryan, Analysis of DRAM-related proteins reveals evolutionarily conserved and divergent roles in the control of autophagy, Cell Cycle 8 (2009) 2260–2265.
[10] K. Nakano, K.H. Vousden, PUMA, a novel proapoptotic gene, is induced by p53, Mol. Cell 7 (2001) 683–694.
[11] J. Yu, L. Zhang, P.M. Hwang, K.W. Kinzler, B. Vogelstein, PUMA induces the rapid apoptosis of colorectal cancer cells, Mol. Cell 7 (2001) 673–682.
[12] E. Natan, C. Baloglu, K. Pagel, S.M. Freund, N. Morgner, C.V. Robinson, A.R. Fersht, A.C. Joerger, Interaction of the p53 DNA-binding domain with its n-terminal extension modulates the stability of the p53 tetramer, J. Mol. Biol 409 (2011) 358–368.
[13] D.C.S. Huang, A. Strasser, BH3-only proteins-essential initiators of apoptotic cell death, Cell 103 (2000) 839–842.
[14] E. Oda, R. Ohki, H. Murasawa, J. Nemoto, T. Shibue, T. Yamashita, T. Tokino, T. Taniguchi, N. Tanaka, Noxa, a BH3-only member of the Bcl-2 family and candidate mediator of p53-induced apoptosis, Science 288 (2000) 1053–1058.
[15] J. Han, C. Flemington, A.B. Houghton, Z. Gu, G.P. Zambetti, R.J. Lutz, L. Zhu, T. Chittenden, Expression of bbc3, a pro-apoptotic BH3-only gene, is regulated by diverse cell death and survival signals, Proc. Natl. Acad. Sci. USA 98 (2001) 11318–11323.
[16] J.R. Jeffers, E. Parganas, Y. Lee, C. Yang, J. Wang, J. Brennan, K.H. MacLean, J. Han, T. Chittenden, J.N. Ihle, P.J. McKinnon, J.L. Cleveland, G.P. Zambetti, Puma is an essential mediator of p53-dependent and -independent apoptotic pathways, Cancer Cell 4 (2003) 321–328.
[17] T. Shibue, K. Takeda, E. Oda, H. Tanaka, H. Murasawa, A. Takaoka, Y. Morishita, S. Akira, T. Taniguchi, N. Tanaka, Integral role of NOXA in p53-mediated apoptotic response, Genes Dev. 17 (2003) 2233–2238.
[18] A. Villunger, E.M. Michalak, L. Coultas, F. Mullauer, G. Bock, M.J. Ausserlechner, J.M. Adams, A. Strasser, P53- and drug-induced apoptotic responses mediated by BH3-only proteins puma and NOXA, Science 302 (2003) 1036–1038.
[19] W. Nakajima, N. Tanaka, Synergistic induction of apoptosis by p53-inducible Bcl-2 family proteins NOXA and Puma, J. Nippon Med. Sch. 74 (2007) 148–157.
[20] N. Guex, M.C. Peitsch, SWISS-MODEL and the Swiss-Pdb Viewer: an environment for comparative protein modeling, Electrophoresis 18 (1997) 2714–2723.

Biochemical and Biophysical Research Communications 420 (2012) 357–363

Contents lists available at SciVerse ScienceDirect

Biochemical and Biophysical Research Communications

journal homepage: www.elsevier.com/locate/ybbrc

Transcellular distribution heterogeneity of Annexin A5 represents a protective response to lupus-related thrombophilia: A pilot Proteomics-based study

Di Zhou [a], Na Luo [a], Qiao Wu [b], Yi You [a], Zhifang Zhai [a], Zhirong Mou [b], Yuzhang Wu [b], Fei Hao [a,*]

[a] Department of Dermatology, Southwest Hospital, PLA, Third Military Medical University, 30 Gaotanyan Street, Chongqing 400038, PR China
[b] Institute of Immunology of PLA, Third Military Medical University, 30 Gaotanyan Street, Chongqing 400038, PR China

ARTICLE INFO

Article history:
Received 14 February 2012
Available online 8 March 2012

Keywords:
Annexin A5
Proteomics
Systemic lupus erythematosus
Thrombophilia

ABSTRACT

Lupus-related vascular events are becoming a formidable obstacle to the improvement of long-term prognosis of systemic lupus erythematosus (SLE) and the existent findings lack for systematization. Proteomics is a strategic approach but its applications in this regard are rare and primarily involve proteome acquisition or biomarker screening, rather than functional identification. To provide further insight, we investigated the proteomic diversity of peripheral blood mononuclear cells (PBMCs) in SLE and the possible role of the identified Annexin A5 (AnxA5) in pathogenesis. The study involved 214 SLE and 183 healthy women. The two-dimensional electrophoresis gel images showed 649 ± 25 and 676 ± 19 protein spots from the PBMCs of the patients and controls, respectively. From these protein spots, 30 differentially expressed proteins were chosen, and 16 of these proteins were identified by mass spectrometer. Western blotting confirmed the over-expressed candidate, AnxA5, from the PBMCs of the patients (SLE:control = 1.607:1, $P = 0.0004$), but ELISAs indicated decreased levels of sera AnxA5 in the patients compared to healthy donors (SLE vs. control = 26.8 ± 3.0 vs. 49.0 ± 3.3 ng/mL, $P < 0.0001$). A positive correlation was demonstrated between the manifestation of thrombosis and AnxA5 (Mann–Whitney $Z = -2.084$, $P = 0.037$), not anti-AnxA5, while searching for correlations between clinical parameters and the two molecular levels of patient sera. The coagulation assays using plasma from SLE patients revealed that elevated AnxA5 could shorten prothrombin time, activated partial thromboplastin time and prolonged thrombin time ($P < 0.001$). Our data demonstrated the proteomic differences in the PBMCs between SLE patients and healthy persons. Moreover, the heterogeneous transcellular distribution, increased intracellular concentrations and decreased serum levels of AnxA5 represent a protective response to lupus-related thrombophilia; AnxA5 mostly participate in the common coagulation pathway in the thrombogenesis of SLE.

1. Introduction

Systemic lupus erythematosus (SLE) is an important model of autoimmunity characterized by multiple organ involvement and capricious clinical manifestation. Before the 1960s, SLE was a catastrophic disease worldwide, with an approximately 50% five-year survival rate [1]. In subsequent decades, the pathogenesis studies and the use of corticosteroids, cytotoxic drugs and antibiotics led to a dramatic reduction in its severity and mortality, especially nephritis and infection [2,3]. Unfortunately, although these regimens prolonged the patient's life spans, some unpredictable complications also followed. Lupus nephritis and infection are no longer the most frequent primary causes of death [4]. Instead, patients now suffer from increasing thrombosis-related symptoms, which can be very serious, sometimes even lethal [5].

To clarify the etiopathogenesis, which remains unclear, current studies focused on how the autoimmunity begins, with respect to genetic susceptibility, invasive autoantibody alteration, obstacles to the elimination of apoptosis, cytokine and immune regulation pathway dysfunction [6–8]. Vascular events have hindered the improvement of long-term prognosis and there are meaningful detections on potential biomarkers such as antiphospholipid antibodies, Annexin A5 (AnxA5) and β2 glycoprotein I [9,10]. However, these findings are not abundant enough to verify the cascade of lupus-related vascular events.

Abbreviations: AnxA5, annexin A5; APS, antiphospholipid syndrome; aPTT, activated partial thromboplastin time; CTX, cyclophosphamide; ELISA, enzyme-linked immunosorbent assay; Fib, fibrinogen; IEF, isoelectric focusing; Ig, immunoglobulin; INR, international normalized ratio; IPG, immobilized pH gradient; mAb, monoclonal antibody; MS, mass spectrometer; MW, molecular weight; PBMCs, peripheral blood mononuclear cells; pH, power of hydrogen; pI, pH of isoelectric point; PPP, platelet-poor plasma; PSTs, peptide sequence tags; PT, prothrombin time; SDS–PAGE, sodium dodecyl sulphate polyacrylamide gel; SLE, systemic lupus erythematosus; TT, thrombin time; 2-DE, two-dimensional electrophoresis.

* Corresponding author. Fax: +86 23 68752522.
E-mail addresses: zhoudi83@hotmail.com (D. Zhou), ronaderma@msn.com (N. Luo), wuqiao001268@163.com (Q. Wu), youyitmmu@yahoo.cn (Y. You), zhaizf1004@163.com (Z. Zhai), mouzr@yahoo.com (Z. Mou), wuyuzhang@yahoo.com (Y. Wu), haofei62@medmail.com.cn (F. Hao).

0006-291X/$ - see front matter © 2012 Elsevier Inc. All rights reserved.
http://dx.doi.org/10.1016/j.bbrc.2012.02.162

Among the extant approaches, Proteomics has the capacity for high-throughput screening and possesses unique advantages. The combination of proteome isolation, identification and functional analyses has enabled the study of protein function in the post-genomic era. To our knowledge, the applications of Proteomics in this field are rare, and the few studies undertaken were suspended mostly at the stage of proteome acquisition or biomarker screening, rather than function probing [11].

In the present study, we used Proteomics to identify differentially regulated proteins between SLE patients and healthy controls. Then, using clinical parameters and bioinformatics analyses, we hypothesized that AnxA5, a candidate of intracellular overexpression in SLE, might possess the capacity for protection; this protection may avoid SLE patients plagued by antiphospholipid syndrome (APS), a typical thrombotic disease. We performed pilot studies to confirm the heterogeneity in the transcellular distribution of AnxA5. This heterogeneity may be also correlated with thrombus-related manifestations.

2. Materials and methods

2.1. Reagents and antibodies

Most of the reagents and equipments were purchased from Pharmacia (GE Healthcare, UK) and Bio-Rad (USA) unless otherwise stated. Several consumables were from Roche (Switzerland), Millipore, Sigma–Aldrich and Thermo Scientific (USA). The mouse anti-human AnxA5 mAb was from Abnova, Taiwan. Antibodies against AnxA5 were obtained from R&D Systems (USA) and precoated by Biovalue as a quantitative enzyme-linked immunosorbent assay (ELISA) system. Human anti-AnxA5 Platinum ELISA kits were from Bender MedSystems (eBioscience, Austria). Mouse anti-βactin IgG and peroxidase-conjugated goat anti-mouse IgG were home products of Zhongshan Biology. Basic inorganic chemicals were native made from Kelong and Boyi Chemistry.

2.2. Study subjects and sample applications

The study participants consisted of 214 Mongoloid female SLE patients from the Department of Dermatology and 183 age-gender-matched volunteers from the Health Examination Center and Blood Transfusion Center, Southwest Hospital, Chongqing, China. The participants were recruited from July 2007 to November 2011. Some participants with proven infections and other systemic or autoimmune diseases were excluded during screening. Each patient fulfilled at least 4 of the 11 diagnostic criteria defined by the American College of Rheumatology [12], and the severity of the SLE was evaluated using the SLE Disease Activity Index 2000 score [13]. The clinical characteristics are summarized in Table 1. Peripheral blood mononuclear cells (PBMCs) from 14 patients and 9 controls were isolated from approximately 20 mL heparinized venous blood by Ficoll-Hypaque centrifugation. These samples were used for isoelectric focusing (IEF) and two-dimensional electrophoresis (2-DE). The PBMCs of other 47 patients and 31 volunteers were separately isolated from approximately 5 mL blood for use in Western blotting. The sera of 123 patients and 113 volunteers were collected in succession before use. So did the platelet-poor plasma (PPP) from 30 patients and 30 volunteers. This study was approved by the ethics committee of the hospital and a written formal consent of the participant was signed before every acquisition.

2.3. IEF and 2-DE

Following the protocols used previously with few modifications [14,15], the soluble proteins of the PBMCs were extracted by detergent lysis. Once quantitated by the 2-D Quant Kit, the individual lysate from every participant was rehydrated with 18 cm IPG non-linear strips overnight. IEF was performed according to the following parameters: 3 h at 30 V, 1 h at 200 V, 1 h at 500 V, 1 h at 1000 V, upgrading to 8000 V within 30 min and held constant until the total voltage × time reached approximately 60 kV h. After equilibrated twice, the strips were loaded on a 12.5% sodium dodecyl sulfate polyacrylamide gel (SDS–PAGE) and electrophoresed at 40 mA per gel. All electrophoresed gels were stained using the Silver Stain method improved by Gharahdaghi et al. [16] and scanned with a GS-800 Calibrated Densitometer.

Table 1
Characteristics of the SLE patients involved in the study.

Parameter	No.
Sum	214
Gender	Female
Age: Mean (SD) [range] years	34.0 (11.0) [11–60]
Duration: Mean (SD) [range] months	45.4 (50.7) [1–348]
Rash	119 (55.6%)
Photosensitivity	50 (23.4%)
Raynaud phenomenon	30 (14.0%)
Mucosal ulcers	8 (3.7%)
Arthritis	57 (26.6%)
Serositis	5 (2.3%)
Hematuria	35 (16.4%)
Proteinuria (positive or >150 mg/d)	58 (27.1%)
Pyuria	43 (20.1%)
Neurologic disorder	3 (1.4%)
Vasculitis	8 (3.7%)
Thrombosis	9 (4.2%)
Fever (>38 °C)	10 (4.7%)
Anti-nuclear antibodies	208 (97.2%)
Thrombocytopenia ($<100 \times 10^9$/L)	105/18 (17.1%)[a]
Leukopenia ($<4 \times 10^9$/L)	106/33 (31.1%)[a]
Anti-dsDNA antibodies	212/50 (23.6%)[a]
Anti-Sm antibodies	212/88 (41.5%)[a]
Anti-Cardiolipin IgG	138/52 (37.7%)[a]
Low complement 3 (<0.6 g/L)	102/41 (40.2%)[a]
Prednisone: Mean (SD) [range] mg	14.0 (17.6) [0–60]
Immunosuppressant	82 (38.3%)

[a] Because some participants from outpatient had not received these laboratory examinations, the three values sequentially represent the patients who received these examinations, the positive patients and the percentage.

2.4. Image analysis and MS identification

The scanned images were analyzed using PDQuest software version 7.1. The image pairs of higher quality were chosen as primary match gels, which were used to check the match rates of the spots. Based on the analytical match rates of the software, the highest quality pair among the primary gels was chosen as the actual match gels. Spots with a gradation ratio greater than 2 or less than 0.5 were marked on the match gels. The spots from the other images in both groups were compared to the marked spots on the match gels. After statistically confirming the reproducibility of the gradation diversity, spot excision and tryptic digestion were appropriately executed [15]. The supernatant of the prepared digested peptides was loaded on an ion-trap high-performance liquid chromatography chip tandem mass spectrometer (MS), according to manufacturer's manual (Agilent Technologies, USA). Peptide sequence tags (PSTs) from each spot were obtained. Acquired PSTs were searched in the UniProtKB/Swiss-Prot database. After excluding duplicate and unreasonable results based on the molecular weight (MW) gradient, pH of isoelectric point (pI) level and distribution *in vivo*, the proteins with the greatest number of matched PSTs were considered of actually differential expression.

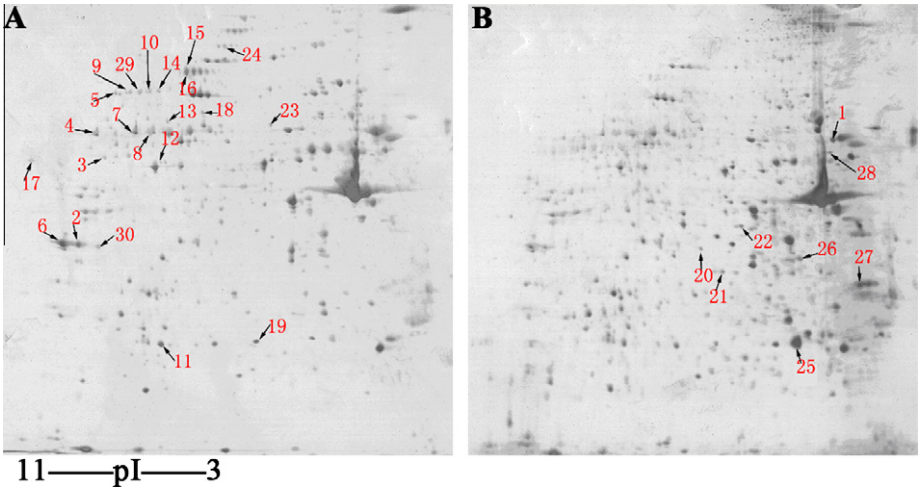

Fig. 1. The proteome diversity of PBMCs from patients with SLE and healthy controls. A (Control) and B (SLE) show the 2 matched gel images of the PBMC cytoplasmic protein 2-DE. The numbers represent the candidate protein spots chosen for MS identification. The results of identified spots are listed in Table 2.

Table 2
Profiles of identified proteins by MS.

Spot no.	Protein name	UniProt ID	Theory pI/Mw (Da)	No. of peptides matched	Sequence coverage (%)	Alteration[a]
2	Glyceraldehyde-3-phosphate dehydrogenase	P04406	8.57/36053.4	9	34	↓
3	Integrin-linked protein kinase	Q13418	8.30/51419.5	14	28	↓↓
4	Adenylylcyclase-associated protein 1	Q01518	8.27/51855.7	22	69	↓
5	Transketolase	P29401	7.58/67878.0	10	19	↓
6	Proline-serine-threonine phosphatase-interacting protein 2	Q9H939	8.73/38832.4	5	14	↓
11	Triosephosphate isomerase	P60174	6.45/26669.6	17	59	↓
12	Tyrosine-protein kinase CSK	P41240	6.62/50704.6	15	34	↓↓
15	Dynamin-1-like protein	O00429	6.37/81877.6	2	3	↓
17	Elongation factor 1-alpha 1	P68104	9.10/50141.1	3	4	↓↓
18	T-complex protein 1 subunit zeta	P40227	6.24/58024.5	13	22	↓↓
19	Heat shock protein beta-1	P04792	5.98/22782.6	10	40	↓
20	Phosphoglycerate kinase 1	P00558	8.30/44615.0	12	37	↑↑
22	Alpha-enolase	P06733	7.01/47169.2	8	22	↑
25	Osteoclast-stimulating factor 1	Q92882	5.45/23786.9	2	17	↑
27	Annexin A5	P08758	4.94/35936.9	6	19	↑↑
28	Heat shock cognate 71 kDa protein	P11142	5.38/70898.4	11	15	↑

Relative specific expression or deficiency was determined when the gradation of one matched spot could not reach the minimal sensitivity of GS-800 Calibrated Densitometer and the ratio was almost infinity or nearly zero.
Up-regulated or down-regulated expression suggests that the average gradation ratio of the two matched spots is more than 2 or less than 0.5.
[a] ↑, up-regulated expression in PBMCs from SLE patients; ↑↑, relative specific expression in PBMCs from SLE patients; ↓, down-regulated expression in PBMCs from SLE patients; ↓↓, relative specific deficiency in PBMCs from SLE patients.

2.5. Western blotting

Following quantitation by Bradford method, the PBMC lysates from the 47 patients and 31 controls were electrophoresed separately using 12.5% SDS–PAGE. The gels were electro-transferred onto a polyvinylidene difluoride membrane and blocked overnight at 4 °C. The blocked membrane was first incubated with 1:500 diluted AnxA5 mAb for 1 h and then with 1:5000 diluted conjugated antibody for 30 min. Unbound antibodies were washed to remove and enhanced chemiluminescence was fixed onto Kodak film. βactin was used as an internal reference. The gradation on film was measured by Quantity One version 4.6.2.

2.6. Quantitative ELISA

After sera from 123 patients and 113 volunteers were obtained, the level of AnxA5 was determined by a quantitative ELISA. Sera level of anti-AnxA5 was also determined quantitatively shortly after the assays of the antigen. ELISAs were performed according to the manufacturers' instructions. Optical densities were measured by the Paradigm Detection Platform (Beckman Colter, USA).

2.7. Coagulation assays

Citrated blood was collected from 30 patients and 30 volunteers, and centrifuged to be PPP. The approximate concentrations of recombined AnxA5 (Biovalue, China) were determined using previous ELISA data and double immunodiffusion. Subsequently, 7 clinical coagulation assays—prothrombin time (PT), PT%, PT INR, activated partial thromboplastin time (aPTT), aPTT ratio, fibrinogen (Fib) and thrombin time (TT)—were performed with an automated blood coagulation analyzer CA-7000 (Sysmex, Japan) from three paired bunches of the PPP. Either three groups from SLE or healthy women were PPP only; PPP with AnxA5 (600 ng/mL, volume ratio of 1:10 and incubated at 37 °C for 5 min) and PPP

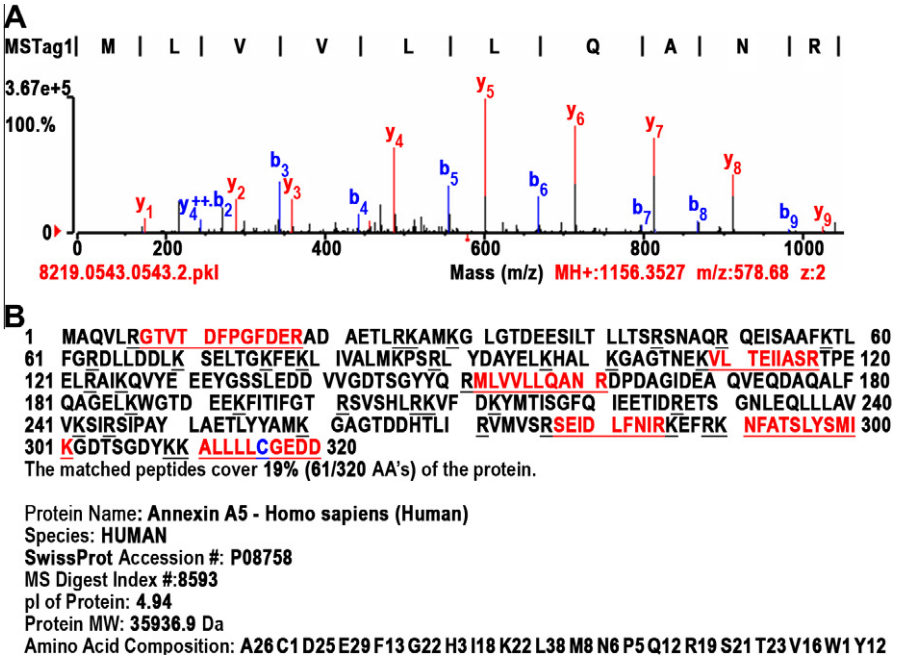

Fig. 2. MS identification and database searching results of spot 27 from Fig. 1B. A typical mass spectrogram of spot 27. This PST matched the third peptide sequence (amino acid counts from 152 to 161) shown in Fig. 2B. Mass (*m*/*z*), mass electron ratio; MH+, the relative molecular mass of the ionized peptide; *z*, the electric charge of the ionized peptide. (B) The result of a UniProtKB/Swiss-Prot database search for spot 27, which was identified as AnxA5. The red sequences with homochromatic underlining are the matched peptides detected by MS. AAs, amino acids.

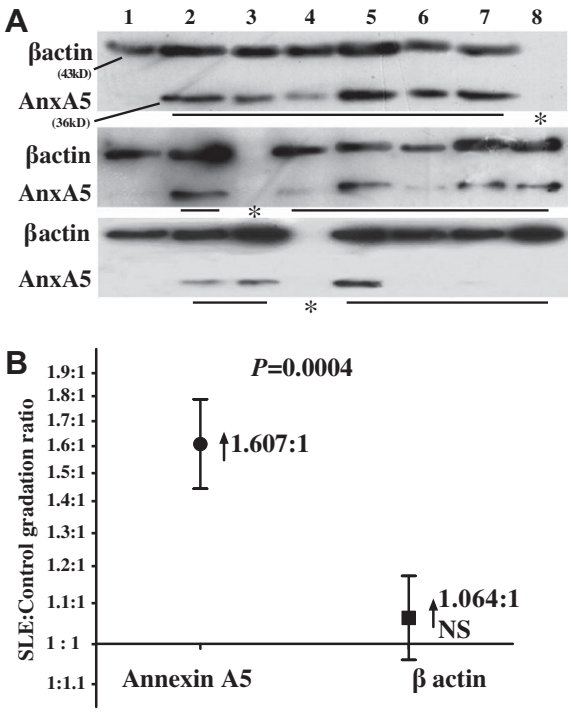

Fig. 3. Verification of PBMCs upregulation of AnxA5. (A) A portion of Western blot results. Although not uniform, the upregulation of AnxA5 in the PBMCs of SLE patients were statistically significant. The left bands represent healthy controls. The bands of SLE are underlined. The three empty lanes labeled with asterisks represent MW markers. (B) SLE:control gradation ratio was defined as the relative ratio of AnxA5 or βactin between SLE patients and healthy controls. This ratio confirmed the intracellular overexpression of AnxA5 among patients. The *Y*-axis was set in a nonlinear scale to display the ratios more robustly, and the origin was 1:1, which indicated that the band gradation of AnxA5 or βactin in the patient group equaled the gradation of the control group at the origin.

pre-mixed with a 1:10 volume ratio of bovine serum albumin (BSA) as an unrelated control.

2.8. Statistical analysis

All the results were acquired from unrelated equal experiments repeated at least twice, except the 2-DEs and their initial IEFs from 8 of the patients due to insufficient samples. The data were analyzed with SPSS software version 11.5. Several statistical methods were chosen when appropriate. *P* values of 0.05 or below were considered statistically significant (two-tailed test).

3. Results

3.1. 2-DE images and variability analysis

The 2 matched gels exhibited 1084 spots in total. Of these spots, 241 spots on both gels were considered matched spots (mean CV = 49.13, correlation coefficient = 0.508). 649 ± 25 spots were detected in the patient group with a match rate of 59 ± 5% among intragroup individuals, whereas these data in the control group were 676 ± 19 and 61 ± 4%, respectively. Based on the visible gradation diversity, 153 spots were selected. There were acceptable concordances among the repeated 2-DEs, and the weakest match rate of identical spots from single individual was 76%. Once diversity reproducibility was confirmed, 30 spots in total—22 from the control and 8 from the patient group—were chosen from the selected 153 for further study (Fig. 1).

3.2. MS identification

Among the 30 spots analyzed by MS, 28 exhibited qualified mass spectrograms. After filtering the results, 16 reasonable results, each representing a protein, were obtained. Among these, 5 were overexpressed at the proteome level in the patient group,

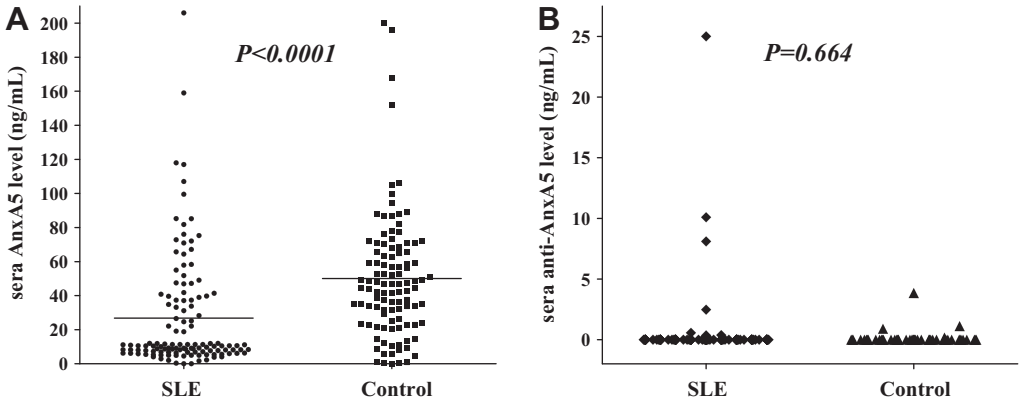

Fig. 4. Sera AnxA5 and anti-AnxA5 concentrations of SLE patients and healthy controls. (A) Sera AnxA5 concentrations of SLE patients and healthy controls. The decrease was overturned from the intracellular result shown in Fig. 3A, B. (B) Sera anti-AnxA5 concentrations of the SLE patients and the healthy controls. With the exception of several subjects, most of the participants were negative.

Table 3
Summary of correlations between sera molecular levels and clinical parameters.

Statistical value/*P*	AnxA5 (ng/mL)	Anti-AnxA5 (ng/mL)
AnxA5	–	–
Anti-AnxA5	−0.054/0.555	–
Age	−0.016/0.857	0.085/0.351
Duration	0.114/0.209	0.082/0.368
ANA titer	0.010/0.910	0.030/0.744
Anti-Cardiolipin IgG	−0.040/0.658	−0.106/0.244
nRNP/Sm	0.008/0.929	0.017/0.853
Sm	−0.120/0.189	0.080/0.382
SS-A	−0.111/0.224	0.162/0.074
RO-52	−0.092/0.313	0.242/0.007**
SS-B	0.079/0.387	0.064/0.483
Scl-70	−0.137/0.134	−0.039/0.669
PM-Scl	−0.027/0.767	−0.022/0.806
JO-1	−0.027/0.767	−0.022/0.806
Centromere protein B	−0.022/0.810	0.352/0.000**
PCNA	−0.026/0.773	−0.032/0.728
dsDNA	−0.005/0.957	−0.026/0.779
Nucleosome	−0.031/0.735	−0.079/0.388
Histone	−0.161/0.076	0.165/0.069
Ribosomal P-protein	0.013/0.884	−0.115/0.206
AMA M2	0.015/0.870	−0.065/0.475
Raynaud phenomenon	−0.402/0.688	−2.522/0.012*
Arthritis	−0.192/0.848	−0.675/0.500
Proteinuria	−1.083./0.279	−0.726/0.468
Rash	−1.205/0.228	−0.943/0.346
Vasculitis	−1.953/0.051	−1.499/0.134
Thrombosis	−2.084/0.037*	−1.272/0.203
Photosensitivity	−1.172/0.241	−1.372/0.170
Alopecia	−0.441/0.659	−2.427/0.015*
Mucosal ulcers	−1.141/0.254	−0.497/0.619
Serositis	−0.960/0.337	−0.349/0.727
Fever	−1.015/0.310	−0.762/0.446
Thrombocytopenia	−0.905/0.365	−0.497/0.619
Leukopenia	−0.621/0.535	−0.715/0.474

Statistical values were Spearman's (ρ_s) for the quantitative/semi-quantitative data from AnxA5 to AMA M2 and Mann–Whitney *Z* for the qualitative data from Raynaud phenomenon to the end. Statistically significant results are in bold and labeled with asterisks. *$P < 0.05$; **$P < 0.01$ (two-tailed). All the 15 autoantibodies, from nRNP/Sm to AMA M2, were determined using EUROLINE ANA-Profile 3 (Euroimmun, Germany); nRNP, nuclear ribonuclear protein; PCNA, proliferating cell nuclear antigen; AMA M2, anti-mitochondrial antibody M2.

and the other 11 exhibited oppositely (Table 2). Fig. 2A shows a typical PST of spot 27, which was identified as AnxA5 (UniProt ID: P08758) from the UniProtKB/Swiss-Prot database. The precise matched peptides are shown in Fig. 2B. AnxA5 was widely thought to be an anticoagulant *in vivo* [17,18]. In our study, AnxA5 upregulation was observed in 5 of the 6 patients who exhibited duplicate 2-DE results. Interestingly, a review of the clinics revealed that 3 of the 6 patients had serum-positive reactions to cardiolipin, but only one suffered thrombophlebitis confirmed by biopsy and met the diagnostic criteria of APS [19].

3.3. Upregulation of AnxA5 in SLE PBMCs

Using Western blotting, we confirmed the difference in the AnxA5 diversity of PBMCs between patients and volunteers, and this difference was significant according to the relative gradation values (SLE:control = 1.607:1, $P = 0.0004$, Fig. 3). No significant difference was observed in the results from the screening of the cytomembrane protein lysate. Reviewing the correlations indicated the cluster without cyclophosphamide (CTX) treatment exhibited much higher AnxA5 than the CTX-treated cluster (untreated:-treated = 1.974:1.170, $P = 0.014$, without dose-dependence). We could not verify any other direct or significant correlation between AnxA5 and the other clinical parameters.

3.4. Quantitative ELISA

Unlike in PBMCs, quantitative ELISAs demonstrated the AnxA5 concentrations of the patient sera (26.8 ± 3.0 ng/mL) were significantly lower than the healthy donors (49.0 ± 3.3 ng/mL, Fig. 4A). The sera anti-AnxA5 levels did not greatly differ from each other (SLE vs. control = 0.38 ± 2.53 vs. 0.11 ± 0.56 ng/mL, $P = 0.664$; SLE anti-AnxA5 positive rate = 5.69%, extremum value = 25.01 ng/mL, Fig. 4B). The correlations between 2 molecules in the patient group and the clinical parameters are listed in Table 3. Although AnxA5 levels decreased in the patient's sera compared to the control group, several patients showed the opposite trend. The elevated AnxA5 levels in the latter group of patients also led to a significantly positive correlation between the AnxA5 concentration and thrombosis among these patients (6 patients among 123, Mann–Whitney $Z = -2.084$, $P = 0.037$).

The correlation between anti-AnxA5 concentrations and thrombosis was not significant (Mann–Whitney $Z = -1.272$, $P = 0.203$). However, this statistic may be controversial because it would become highly significant if we assumed a linear correlation between them (Pearson's (r) = 0.377, $P < 0.001$). In addition, since there was no significant correlation between AnxA5 and anti-AnxA5 levels (Spearman's (ρ_s) = −0.054, $P = 0.555$) or between anti-AnxA5 qualitation and thrombosis (Chi-square = 1.416, $P = 0.234$), we might inferred that serum AnxA5 levels could probably be an independent correlation factor of thrombosis.

Table 4
Overview of the PPP coagulation assays performed from the SLE patients in parallel and healthy controls intervened by AnxA5.

Coagulation assay value (Mean ± SD)	SLE (Null)	SLE (BSA)	SLE (AnxA5)	Healthy control (AnxA5)
PT (s)	11.8 ± 2.0	11.4 ± 1.4	10.8 ± 1.2***	10.9 ± 1.3*
PT%	92.9 ± 20.5	97.1 ± 20.0	108.0 ± 19.8***	106.3 ± 20.2*
PT INR	1.02 ± 0.18	0.99 ± 0.13	0.94 ± 0.10***	0.95 ± 0.11**
APTT (s)	35.6 ± 11.6	34.8 ± 11.9	28.1 ± 7.3***	28.3 ± 6.8**
APTT ratio	1.28 ± 0.42	1.25 ± 0.42	1.02 ± 0.26***	1.05 ± 0.28*
Fib (g/L)	2.77 ± 1.00	2.80 ± 0.95	2.87 ± 0.93	2.83 ± 0.96
TT (s)	16.0 ± 1.6	16.1 ± 1.2	17.4 ± 1.5***	16.7 ± 1.3

Intervenors of PPP are listed in brackets of the head line. All significant results are compared to the SLE (Null) group values and labeled with asterisks in bold. *$P < 0.05$; **$P < 0.01$; ***$P < 0.001$ (two-tailed). Reference ranges: PT (s): 10.0–14.0 s; PT%: 65–130%; PT INR: 0.80–1.21; APTT (s): 22.7–32.7 s; APTT ratio: 0.82–1.20; Fib (g/L): 1.80–3.70 g/L; TT (s): 14.0–21.0 s.

3.5. Coagulation assays

Table 4 shows the results of the coagulation assays of PPP samples from 30 identical SLE patients and one group of samples from 30 healthy controls (data of healthy controls intervened by BSA or Null not shown). No significant differences were observed between the Null groups and the BSA-treated groups in any assay ($P > 0.05$). PT is the screening test of the extrinsic coagulation pathway and clinically similar to PT% and PT INR. APTT Ratio and aPTT, the screening test of the intrinsic coagulation pathway, are also clinically alike. Comparing to the control groups of SLE, intervention of AnxA5 significantly shorten PT (AnxA5 vs. Null = 10.8 ± 1.2 vs. 11.8 ± 2.0 s) and aPTT (AnxA5 vs. Null = 28.1 ± 7.3 vs. 35.6 ± 11.6 s). The elongation of TT caused by AnxA5 in SLE group was also observed (AnxA5 vs. Null = 17.4 ± 1.5 vs. 16.0 ± 1.6 s). Interestingly, the intervention of AnxA5 in healthy control group displayed a similar trend to the SLE groups on PT, aPTT and TT, but the alterations were not as numerically significant or statistically dramatic as these in SLE.

4. Discussion

It is well known AnxA5 is a distinctive annexin with anticoagulant activity that is rarely observed in the annexin family. AnxA5 is also widely expressed in multiple tissues. Its functions are involved in several physiological processes, which have not been completely elucidated [17]. Our observations indicate a heterogeneity in the transcellular distribution of AnxA5 in SLE patients, which is upregulated in PBMCs and downregulated in sera. Once this heterogeneity was disturbed, the morbidity of lupus-related thrombophilia appeared to become more significant. Although we used a similar proteomic approach on 2-DE and MS closing to Dai et al. [11], our work involved a greater isoelectric range (pH 3–11), which allowed the candidates to be considered more representative. In addition, after searching previous studies for the 16 proteins, we conducted pilot functional studies to the target AnxA5 *in vitro*. With the exception of the flaw of several unrepeatable IEFs, the strategy applied in our study can be considered more integrated, and this analysis may be more detailed.

As we know the hypothesis proposed by Rand et al. [18], the competition of antiphospholipid antibodies against AnxA5 has been verified in some lupus-related cases. Inferring from this, the levels of sera AnxA5 in such cases should be elevated, rather than decreased as found in our study. Even despite the hypothesis, this aspect of our results also conflicts with the observations made by Van Heerde et al. [9]. In addition to the different ethnicities of the participants in these studies, different anticoagulation methods, sera against EDTA-anticoagulated plasma, or some other factor may also have contributed to these conflicting results. We attempt to make two conditional inferences. First, if the conflict between our findings and those of previous studies is due to anticoagulation differences and extracellular AnxA5 is truly elevated in both ethnicities, then there should be an AnxA5 consumption mechanism in some SLE patients during sera formation *in vitro*. The patients without this consumption mechanism or not so efficiently would be at a higher risk of thrombo-embolic complications. Second, if the profiles of AnxA5 distribution cannot be reversed by anticoagulation, there should at least be an AnxA5 intracellular enrichment mechanism, which was associated with a protective response to thrombophilia among Mongoloid SLE women. For example, in the model of the pinocytic pathway mediated by surface-expressed phosphatidylserine and AnxA5 [20], this mechanism might be a special cell entry corridor of nearby function-correlated membrane proteins such as tissue factor, the primary initial stimulator of coagulation cascade [21]. The model was verified on tumor cell lines *in vitro* and other possibilities were not excluded, however, considering the abundant abnormal apoptosis and phosphatidylserine externalization in SLE [7,22], we still could suspect that the heterogeneity might be caused by the same model, which would lead to the consequences we observed.

With respect to autoantibodies, our data indicate that the anti-AnxA5 elevation in Mongoloid SLE is not as distinct as in other ethnicities, and the anti-AnxA5 positive rate was much lower [23–25]. However, its certainty and meaning might not be thoroughly effable yet. If according to Pearson's (r), anti-AnxA5 intensively suggested thrombosis. Meanwhile, anti-AnxA5 had no significant association with AnxA5, of which finding would be similar to the evidence described by Hrycek and Cieslik [25]. Namely, this disassociation might suggest AnxA5 and anti-AnxA5 could participate in the pathogenesis of lupus-related thrombosis, but partly they might involve relatively independent pathways. A detailed analysis demonstrated that this assumed linear correlation between anti-AnxA5 and thrombosis was mostly caused by the extremum value. In fact, this patient suffering from tender splinter hemorrhages and thrombus of the fingertips confirmed by cutaneous biopsy, had a much higher level of serum anti-AnxA5 than the others. If this participant was excluded, the significance would have been eliminated, causing a similar result to that determined by the nonparametric Mann–Whitney Z. Additionally, several patients without diagnosable thrombosis and a few controls displayed low or moderate levels of anti-AnxA5. Therefore, although our samples were not enough to precisely clarify this phenomenon, we could roughly infer that a distinctly high titer of serum anti-AnxA5 might be a risk factor of lupus-related thromboembolism, as lower titers might not.

The alterations in coagulation assays caused by AnxA5 were also partly unpredicted. The coordinated shortening of PT and aPTT indicated that extracellular AnxA5 could promote the hypercoagulation state of lupus that is involved in the common blood coagulation pathway, which was consistent with previous results. However, TT, also the screening assays of the common coagulation pathway, was prolonged at the identical assays. This finding seemed to suggest that AnxA5 was not simply an anticoagulant in all cases all the time. As we know that TT measurement focuses

on the timing and is completed when insoluble fibrin strands first become observable. Thus, this discrepancy may be due to some artificial flaws. For instance, AnxA5 could act as a calcium occupant *in vitro*, causing AnxA5-intervened TT to be prolonged due to the decline of available calcium ions [17,26], but this might not suggest the shift of actual termination of coagulation process. Additionally, we were unable to ignore the fact that most varieties were still within the normal ranges, and many functional coagulation assays are still screening tests with unsatisfactory sensitivity. From our observations, we could only conclude with some confidence that AnxA5 might mostly participate in the common coagulation pathway in the thrombogenesis of SLE.

Besides AnxA5, 15 other potential protein candidates were identified. Each protein might contribute to the understanding of pathogenesis or the development of more effective drugs. For example, elongation factor 1 may interact with ribosomes and induce conditional onset [27]; gene locus polymorphisms of heat shock protein family may also be genetic risk factors for SLE [28]. Despite the limitations of fineness and repeatability, such as the restricted choice of PBMCs for the labor intensity and sample volume demands of 2-DE, deficiency of participants and clinical parameters, especially those outpatients, this study provides a better understanding of SLE and lupus-related thrombophilia. It might serve as a pilot study for further etiologic studies and drug exploration.

Acknowledgments

This study was supported by National Basic Research Program of China (Nos. 2007CB512401 and 2007CB512805), National Natural Science Foundation of China (Nos. 30671886, 30800995, 81000696 and 81071293) and Innovation Grants of Southwest Hospital (2008BB5033).

References

[1] M. Merrell, L.E. Shulman, Determination of prognosis in chronic disease, illustrated by systemic lupus erythematosus, J. Chronic Dis. 1 (1955) 12–32.
[2] J.L. Decker, J.H. Klippel, P.H. Plotz, et al., Cyclophosphamide or azathioprine in lupus glomerulonephritis. A controlled trial: results at 28 months, Ann. Intern. Med. 83 (1975) 606–615.
[3] N. Kasitanon, L.S. Magder, M. Petri, Predictors of survival in systemic lupus erythematosus, Medicine (Baltimore) 85 (2006) 147–156.
[4] S. Rosner, E.M. Ginzler, H.S. Diamond, et al., Arthritis. Rheum. 25 (1982) 612–617.
[5] R. Cervera, M.A. Khamashta, J. Font, et al., Morbidity and mortality in systemic lupus erythematosus during a 10-year period: a comparison of early and late manifestations in a cohort of 1000 patients, Medicine (Baltimore) 82 (2003) 299–308.
[6] Y. Deng, B.P. Tsao, Genetic susceptibility to systemic lupus erythematosus in the genomic era, Nat. Rev. Rheumatol. 6 (2010) 683–692.
[7] W.H. Shao, P.L. Cohen, Disturbances of apoptotic cell clearance in systemic lupus erythematosus, Arthritis. Res. Ther. 13 (2011) 202.
[8] M. Nakou, G. Bertsias, I. Stagakis, et al., Gene network analysis of bone marrow mononuclear cells reveals activation of multiple kinase pathways in human systemic lupus erythematosus, PLoS One 5 (2010) e13351.
[9] W.L. Van Heerde, C.P. Reutelingsperger, C. Maassen, et al., The presence of antiphospholipid antibodies is not related to increased levels of annexin A5 in plasma, J. Thromb. Haemost. 1 (2003) 532–536.
[10] H. Zheng, Y. Chen, W. Ao, et al., Antiphospholipid antibody profiles in lupus nephritis with glomerular microthrombosis: a prospective study of 124 cases, Arthritis Res. Ther. 11 (2009) R93.
[11] Y. Dai, C. Hu, Y. Huang, et al., A proteomic study of peripheral blood mononuclear cells in systemic lupus erythematosus, Lupus 17 (2008) 799–804.
[12] M.C. Hochberg, Updating the American College of Rheumatology revised criteria for the classification of systemic lupus erythematosus, Arthritis Rheum. 40 (1997) 1725.
[13] D.D. Gladman, D. Ibanez, M.B. Urowitz, Systemic lupus erythematosus disease activity index 2000, J. Rheumatol. 29 (2002) 288–291.
[14] Y.J. He, Y.Z. Wu, Z.R. Mou, et al., Proteomics-based identification of HSP60 as a tumor-associated antigen in colorectal cancer, Proteomics Clin. Appl. 1 (2007) 336–342.
[15] R.S. Xia, F. Hao, Z.R. Mou, et al., Identification of proteins involved in aggregation of human dermal papilla cells by proteomics, J. Dermatol. Sci. 48 (2007) 189–197.
[16] F. Gharahdaghi, C.R. Weinberg, D.A. Meagher, et al., Mass spectrometric identification of proteins from silver-stained polyacrylamide gel: a method for the removal of silver ions to enhance sensitivity, Electrophoresis 20 (1999) 601–605.
[17] V. Gerke, S.E. Moss, Annexins: from structure to function, Physiol. Rev. 82 (2002) 331–371.
[18] J.H. Rand, X.X. Wu, H.A. Andree, et al., Pregnancy loss in the antiphospholipid-antibody syndrome–a possible thrombogenic mechanism, N. Engl. J. Med. 337 (1997) 154–160.
[19] S. Miyakis, M.D. Lockshin, T. Atsumi, et al., International consensus statement on an update of the classification criteria for definite antiphospholipid syndrome APS, J. Thromb. Haemost. 4 (2006) 295–306.
[20] H. Kenis, H. van Genderen, A. Bennaghmouch, et al., Cell surface-expressed phosphatidylserine and annexin A5 open a novel portal of cell entry, J. Biol. Chem. 279 (2004) 52623–52629.
[21] S. Ravassa, A. Bennaghmouch, H. Kenis, et al., Annexin A5 down-regulates surface expression of tissue factor: a novel mechanism of regulating the membrane receptor repertoir, J. Biol. Chem. 280 (2005) 6028–6035.
[22] E. Tinazzi, M. Dolcino, A. Puccetti, et al., Gene expression profiling in circulating endothelial cells from systemic sclerosis patients shows an altered control of apoptosis and angiogenesis that is modified by iloprost infusion, Arthritis Res. Ther. 12 (2010) R131.
[23] J. Matsuda, N. Saitoh, K. Gohchi, et al., Anti-annexin V antibody in systemic lupus erythematosus patients with lupus anticoagulant and/or anticardiolipin antibody, Am. J. Hematol. 47 (1994) 56–58.
[24] G. Lakos, E. Kiss, N. Regeczy, et al., Antiprothrombin and antiannexin V antibodies imply risk of thrombosis in patients with systemic autoimmune diseases, J. Rheumatol. 27 (2000) 924–929.
[25] A. Hrycek, P. Cieslik, Annexin A5 and anti-annexin antibodies in patients with systemic lupus erythematosus, Rheumatol. Int. (2011).
[26] W. Wang, J. Xu, T. Kirsch, Annexin-mediated Ca2+ influx regulates growth plate chondrocyte maturation and apoptosis, J. Biol. Chem. 278 (2003) 3762–3769.
[27] T. Uchiumi, R.R. Traut, K. Elkon, et al., A human autoantibody specific for a unique conserved region of 28 S ribosomal RNA inhibits the interaction of elongation factors 1 alpha and 2 with ribosomes, J. Biol. Chem. 266 (1991) 2054–2062.
[28] B.G. Furnrohr, S. Wach, J.A. Kelly, et al., Polymorphisms in the Hsp70 gene locus are genetically associated with systemic lupus erythematosus, Ann. Rheum. Dis. 69 (2010) 1983–1989.

Biochemical and Biophysical Research Communications 420 (2012) 364–367

Contents lists available at SciVerse ScienceDirect

Biochemical and Biophysical Research Communications

journal homepage: www.elsevier.com/locate/ybbrc

Identification of an intra-molecular disulfide bond in the sodium channel β1-subunit

Raffaella Barbieri, Debora Baroni, Oscar Moran *

Istituto di Biofisica, Consiglio Nazionale delle Ricerche, Via De Marini, 6, 16149 Genova, Italy

ARTICLE INFO

Article history:
Received 14 February 2012
Available online 8 March 2012

Keywords:
Sodium channel
Beta subunit: transfected cells
Epilepsy
Diagonal electrophoresis
GEFS+

ABSTRACT

The sodium channel β1 subunit is non-covalently associated with the pore-forming α-subunits, and has been proposed to act as a modulator of channel activity, regulator of channel cell surface expression and cell adhesion molecule. Its importance is evident since mutations of the β1 subunit cause neurologic and cardiovascular disorders. The first described β1 subunit mutation is the C121W, that is related to generalized epilepsy with febrile seizures plus (GEFS+), a childhood genetic epilepsy syndrome. This mutation changed a conserved cysteine residue in position 121 into a tryptophan, putatively disrupting a disulfide bridge that should normally maintain the β1 extracellular immunoglobulin-like fold. Using the 2-D-diagonal-SDS–PAGE technique, we demonstrated the existence of this putative disulfide bridge in the Ig-like extracellular domain of the β1 subunit and its disruption in the epileptogenic C121W mutant.

1. Introduction

Voltage-gated Na^+ channels (NaCh) are heteromeric membrane proteins responsible for the generation of action potential in most excitable tissues. It is formed by a single pore-forming α subunit in association with one or more β subunits [1,2]. Auxiliary β subunits are not required for the heterologous expression of NaCh function, but they modulate the expression levels and the functional properties of the α subunit [3,4]. β subunits belong to the Ig super-family of cell adhesion molecules (CAM) [4,5] and may interact with different cytoskeleton and extracellular matrix proteins [6,7]. NaCh auxiliary β subunits are encoded by 4 different genes SCN1B, SCN2B, SCN3B, SCN4B. Two splice variants of the gene SCN1B, β1 and β1B, are known in humans.

With the exception of β1B, all NaCh auxiliary subunits are type 1 trans-membrane proteins containing an extracellular N-terminal with an Ig-like domain similar to the myelin P0 glycoprotein, one transmembrane domain and an intracellular C-terminal domain. β2 and β4 are covalently bound to the α subunits, whereas β1 and β3 associate non-covalently [3,5,8,9]. Conversely, β1B is a soluble protein that may function as a ligand for cell adhesion [10]. The auxiliary β subunits, in association with pore-forming α-subunits, are highly expressed in excitable cells, including central and peripheral neurons, skeletal and cardiac muscle cells.

Mutations of the sodium channel β1 subunit are involved in human cardiac and neurological disorders. The best known disease correlated to a β1 subunit mutation is the generalized epilepsy with febrile seizures plus, type 1 (GEFS+, GEFSP1 OMIM 604233), a childhood epilepsy syndrome [11,12]. This syndrome is caused by a miss-sense mutation, C121W, substituting a conserved cysteine (C) residue with a tryptophan (W). Based on the homology of β1 subunit with other proteins of the same family, it was proposed that this mutation disrupts a putative conserved disulfide bond, that is thought to be critical for the interaction between the two β-sheets that compose the Ig fold [11]. This fact would prevent the proper folding of the β1 protein, and consequently, its interaction with the α subunit or other macromolecules, or its cell surface expression. However, to now, there is no experimental evidence that the extracellular domain of β1 subunit actually contains a disulfide bridge, or that mutation C121W effectively disrupts this bond.

By using bi-dimensional diagonal gel electrophoresis (2-D-diagonal-SDS–PAGE), we have demonstrated the existence of the disulfide bond in rat NaCh β1 subunit and furthermore we have confirmed that in the C121W subunit, where a conserved cysteine residue is substituted with a tryptophan.

2. Materials and methods

2.1. Cells

Permanent transfected cell lines were prepared as described elsewhere [13–15]. In brief, the full-length rat β1-subunit was inserted into the bicistronic expression vector pIRES (Clontech, Mountain View, Ca, USA) in the XbaI–SalI site, and successively the rat Nav1.4 α-subunit in the EcoRI site. The resulting construct contained the sequence α1.4-subunit–IRES–β1-subunit. Site-directed mutagenesis was accomplished using the Pfu DNA polymerase using the QuikChange kit (Stratagene) [15]. The correct direction of the inserts, and the presence of the mutation was checked in each

* Corresponding author.
E-mail address: oscar.moran@cnr.it (O. Moran).

0006-291X/$ - see front matter © 2012 Elsevier Inc. All rights reserved.
http://dx.doi.org/10.1016/j.bbrc.2012.02.163

case by a multiple enzyme restriction map and DNA sequencing. Chinese hamster ovary (CHO) was grown in standard conditions, in Ham's F10 medium supplemented with 10% fetal calf serum, 2 mM glutamine and 0.05 mg/100 ml gentamicin (Sigma–Aldrich, Saint Louis, MO, USA). Cells were transfected by electroporation with the constructs containing the rat Nav 1.4 α-subunit and the rat WT or the C121W β1-subunits. Monoclonal cell lines were selected according to a resistance to the 800 μg/ml Geneticin (G-418; Sigma) [13,14].

2.2. RT-PCR

First-strand cDNA was synthesized from 2.5 μg of each RNA using RevertAid First Strand cDNA Synthesis Kit and random hexamers according to the manufacturer's instructions (Fermentas, Burlington, Canada). The oligonucleotide primer pairs described in Table 1 (Bio-Fab Research, Roma, Italy), were used to amplify by RT-PCR the section of the cDNA samples coding for the Nav1.4 and the WT or C121W β1 subunits. Table 1 shows also the sequence of the oligonucleotide primers used to amplify glyceraldehyde-3-phosphate-dehydrogenase (GDH), which was assayed as housekeeping gene.

RT-PCR products were resolved by electrophoresis in 1% agarose gels, stained with ethidium bromide and visualized under an UV transiluminator. Amplicon sizes were determined by comparison with a DNA molecular weight marker (SM0333, Fermentas) that was routinely run on the gels. Controls without reverse transcriptase were used to check for the absence of contaminating DNA. Each experiment, including the RNA extraction, RT-PCR and gel electrophoresis was done in triplicate, from different cell pulls.

2.3. Protein electrophoresis

SDS–PAGE was performed according to standard protocols. Cells were lysed in 62.5 mM Tris, 2% SDS and a cocktail of protease inhibitors (1 mM 4-(2-Aminoethyl)benzenesulfonyl fluoride hydrochloride, 0.8 mM Aprotinin, 0.2 mM Leupeptin, 40 mM, Bestatin, 15 mM Pepstatin A, 14 mM E-64; Sigma–Aldrich) and boiled for 5 min. Samples were supplemented with SDS/sample buffer without reducing agents (4% w/v SDS, 125 mM Tris–HCl, 0.001% w/v bromphenol blue, 20% glycerol, pH 6.8) and then loaded onto 12% polyacrylamide gel. The run was performed by using Protean II System (Bio-Rad Laboratories, Milan, Italy).

The gels were blotted on a PVDF membrane (Millipore, Billerica, MA, USA) using standard methods [16]. The blots were blocked in 5% dry fat milk in 0.5 M Tris, 2 M NaCl, 0.1% Tween-20 and then incubated with primary antibodies specific either for SCN1B diluted1:1000 (Abnova Corporation, Heidelberg, Germany) or for sodium channel α subunits, diluted 1:1000 (Acris Antibody Gmbh, Herford, Germany) using the SNAP i.d. system (Millipore catalogue N° WBAVDBASE, Worcester, MA, USA) according to the manufacturer's instructions. Anti-rabbit peroxidase-conjugated secondary antibody diluted 1:3000 (Santa Cruz biotechnology, Inc., Santa Cruz, CA, USA) was used for visualization with ECL system (GE Healthcare Europe, Milan, Italy). To perform second-dimension SDS–PAGE separation [17], single lanes excised from first dimension gels were cut out and incubated with a reducing buffer (0.5% dithiothreitol (DTT), 0.1% SDS, 0.125 M Tris–HCl pH 6.8) for 1 h at room temperature with gentle rocking on a orbital rotator. To avoid disulfide bond reforming, the reduced samples were alkylated with a solution of iodoacetamide (2.5% w/v). An excised lane was then placed horizontally on a top of a larger SDS–PAGE reducing gel (12% polyacrylamide), sealed with hot agarose and run in Protean II xi large-format vertical system (Bio-Rad). Molecular weight standard from Fermentas (SM184) was used to verify protein molecular weight correspondence. Two identical gel preparations were compared with Silver staining or with antibody detection.

Table 1
Primers used to detect the NaCh α and the β1 subunits, and the housekeeper GDH, from retro-transcripts of mRNA extracted from CHO cells.

Product		Primer
NaCh α1.4	Forward	5′-CTTCATCGGTGTCATCATCG-3′
	Reverse	5′-GGAGACAGATGACCAGAGCC-3′
NaCh β1	Forward	5′-TGAGACCGAGGCAGTGTATG-3′
	Reverse	5′-GTCGCCAGAGTGGTTGTAGG-3′
GDH	Forward	5′-CAAGGTCATCCATGACAACTTTG-3′
	Reverse	5′-GTCCACCACCCTGTTGCTGTAG-3′

3. Results

First, we verified the expression of NaCh α and β1 subunits in control and transfected cells. Fig. 1 shows transcription products corresponding to α1.4 and β1 subunit cDNAs revealed by RT-PCR. In control CHO cells there is not a detectable expression of neither the pore-forming nor the auxiliary subunits (lanes 2 and 3, respectively). Conversely, in the CHO cells transfected with the constructs containing either α1.4 and WT-β1subunits (lanes 4 and 5) or α1.4 and C121W-β1subunits (lanes 6 and 7), about the same concentration of NaCh subunit cDNAs was detected. These data were confirmed by the Western blot analysis of cell extracts prepared from each CHO cell group. Fig. 2 shows the bands corresponding to α1.4 and β1 NaCh proteins (227 kDa and 25 kDa, respectively) revealed in control untransfected or in α1.4 and WT-β1 or α1.4 and C121W-β1 CHO transfected cells. It is noteworthy to observe that in control untransfected CHO cells there is not any resolvable NaCh expression signal (lane 1). Differently, a well identifiable band, for both NaCh subunits, is detectable in the CHO cells transfected with the bicistronic constructs containing either the α1.4 subunit and WT- (lane 2) or α1.4 and C121W-β1 subunit (lane 3). A further control of the expression of the NaCh was done by patch-clamp recording of sodium currents (data not shown). These experiments confirmed that sodium current density and electrophysiologic properties were fully reproducible along time in select cell lines used in this study.

Successively, to investigate the presence of the hypothesized disulfide bridge in the NaCh β1 subunit we applied the diagonal electrophoresis. The results of these bi-dimensional electrophoresis experiments are shown in Fig. 3. The electrophoresis of the samples in the first dimension was done in the absence of any reducing agent in the polyacrylamide gel, while the second-dimension was done in a gel in strong reducing conditions. It is known that proteins that do not have disulfide bonds run at the same molecular weight under both conditions, placing on a hypothetical diagonal line connecting the opposite corners of the gel. However, those proteins containing intra-molecular disulfide bonds, will run faster on the gel under reducing conditions, as the gyration radius of the polypeptide is strongly modified by their disruption and will be detected as spots outside the diagonal, on the upper-right side of the gel. To confirm the identity of the NaCh β1 subunit, we compared the position on the gel of the spot with the band of 25 kDa of a Western blot of the same sample, revealed with an antibody against the β1 subunit. The comparison of the gels and western blot images containing cell extracts of CHO cell transfected either with α1.4 and WT-β1 or α1.4 and C121W shows that the spot corresponding to WT-β1 subunit lied above the diagonal, whereas when the same experiment was conducted using CHO cells transfected with α1.4 and C121W β1 subunit, the spot lied out of the diagonal in coincidence with the 25 kDa β1 subunit band on the Western blot (see Fig. 3). Similar experiment done with no transfected CHO cells yielded a clear diagonal without the 25 kDa spot out of the diagonal,

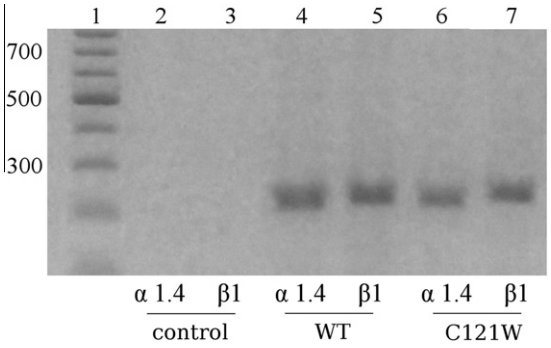

Fig. 1. Detection of transcription products of the sodium channel in stably transfected CHO cells. The bands represent the PCR products of retro-transcribed mRNA coding for the NaCh α and β1 subunits, as indicated in each lane. Lane 1 is the molecular size marker. Lane 2 and 3 are the products of control, no transfected, CHO cells. Observe the virtually absence of a signal for the NaCh transcripts. Lanes 4 and 5 are the amplicons of the NaCh transcripts of CHO cells expressing the α1.4 and WT β1 subunits; lanes 6 and 7 correspond to the transcripts present in CHO cells expressing the NaCh α and the mutant C121W β1 subunits. Observe that the intensity of the bands corresponding to the α and β1 subunits are similar in both cell lines.

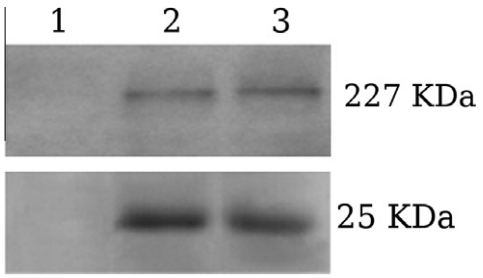

Fig. 2. Western blotting of sodium channel α- (~227 kDa) and β1-subunits (~25 kDa) stably expressed in CHO cells. Lanes 1 correspond to control CHO cells, that do not express neither the α nor β1 subunits. Sodium channel protein is detected in cells expressing the NaCh in a bicistronic construct with the α subunit and the WT (lane 2) and the mutant (lane 3) β1subunits.

as expected (data not shown). We repeated the experiments on three different cell pools for each isoform, with exactly the same results. Therefore, we concluded that the NaCh β1 subunit does present a disulfide bridge, and the pathologic mutation C121W produces a disruption of this covalent interaction.

4. Discussion

The main goal of this work was to prove experimentally that the NaCh β1 subunit has a disulfide bridge, and that it is disrupted by the C121W mutation. This covalent intra-chain interaction should maintain two beta foils of the Ig-motive of the extracellular domain of the β1-subunit linked [3,7,11,12]. The disruption of this cysteine bridge should cause a molecule destabilization, and consequently a modification of the whole NaCh [11,14], perhaps leading to the GEFS + syndrome manifestation [11,12].

The experiments were done in CHO cells expressing the complete NaCh, composed of the α and β1 subunits. We chose to analyze the β1 subunit in a system that expressed also the pore-forming α subunit to avoid any possible disturbance caused by the absence of the β1 natural partner. Therefore, we used CHO cells transfected with plasmids coding for both subunits, separated by an IRES sequence, that allows the expression of two proteins from a single RNA. Preliminary control experiments demonstrated that the bicistronic plasmids, containing either the WT or the mutant β1- subunit, produced indeed about the same amount of both mRNA, as revealed by a semi-quantitative RT-PCR (see Fig. 1), and they also enable the expression of the corresponding proteins, as observed by Western blotting (see Fig. 2).

We attempted to solve this query by using a biochemical approach based on a bi-dimensional electrophoresis. Two-dimensional SDS–polyacrylamide diagonal gels have been used since the 1970s for analysis of proteins in erythrocyte membrane or ribosomes [18,19], T cell receptor [20,21], immunoglobulin [22], and CD8 molecules [23]. This method was also used for protein purification prior to amino acid sequencing and can be used to investigate both soluble and membrane proteins, and also to determine whether disulfide bonds are intra-molecular or inter-molecular [17]. As mentioned before, the removal of a disulfide bridge causes a main change on the mobility of a protein. Polypeptides that lost a disulfide bridge displace away from the diagonal formed by all others proteins, when the electrophoresis is run in reducing conditions. If the disulfide bond is intra-molecular, the polypeptides acquire a relatively faster mobility in non-reducing conditions, as the molecules keep more compact, and therefore migrate to a position at the right side of the diagonal. Differently, if the disulfide bridges are inter-molecular, the reduction produces two (or more) lower molecular mass polypeptides, that migrate faster in reducing conditions, and accommodate on the left side

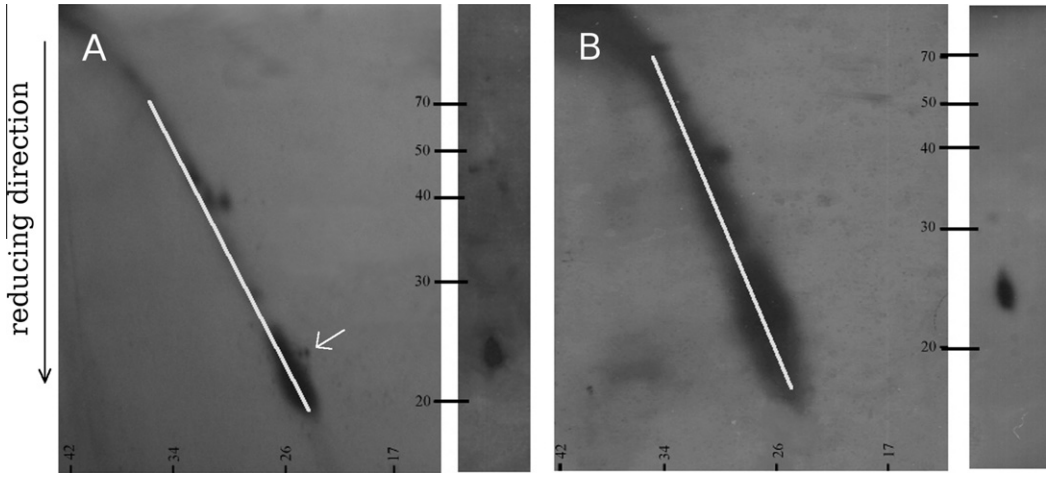

Fig. 3. Bidimensional diagonal-SDS–PAGE analysis of WT (A) and C121W mutant β1 subunits (B). Electrophoresis in non-denaturing conditions was run in the first dimension, and that with denaturing reagents (0.5% DTT) was run in the second dimension, as indicated. The molecular mass markers are shown on each axis. The diagonal electrophoresis was silver stained. The white line was drawn over the diagonal formed by proteins running with the same mobility in both dimensions. The arrow indicates the position of the characteristic spot of 25 kDa out of the diagonal that could be observed only in the preparations containing the WT β1 subunit. At the right of each bi-dimensional electrophoresis panel, it is shown the corresponding Western blot, revealed with an anti-β1 antibody, to identify the position of the β1 subunit.

of the diagonal. Concerning the NaCh β1-subunit, we can confirm the presence of an intra-molecular disulfide bridge, as predicted from the homology with other members of the protein family.

The second question, regarding the involvement of residue 121 on the disulfide bridge, was also afforded by the same method. In this case, we could not observe any extra spot of 25 kDa, corresponding to the β1 subunit, on the right side of the diagonal of the bi-dimensional electrophoresis (see Fig. 3B). This confirms that, most probably, cysteine in position 121 is part of the disulfide bridge of the extracellular domain of the NaCh β1 subunit. Thus, the pathologic mutation C121W likely produces a protein with a less stable extracellular domain, that would impair the α-β1 subunits interactions (or the interactions of β1 subunit with other molecules), leading to a malfunctioning pathological channel.

In conclusion, we have proved the existence of a disulfide bridge in the extracellular domain of the NaCh β1 channel, involving the cysteine in position 121. Furthermore, the epileptogenic C121W mutation produces the disruption of this extracellular disulfide bridge.

Acknowledgment

This work was partially supported by Fondazione Carige and Fondazione Compagnia di San Paolo. We thank Dr. F. Gambale for comments and corrections.

References

[1] W.A. Catterall, Cellular and molecular biology of voltage-gated sodium channels, Physiol. Rev. 72 (1992) S15–48.
[2] W.A. Catterall, From ionic currents to molecular mechanisms: the structure and function of voltage-gated sodium channels, Neuron 26 (2000) 13–25.
[3] L.L. Isom, K.S. De Jongh, D.E. Patton, B.F. Reber, J. Offord, H. Charbonneau, et al., Primary structure and functional expression of the beta 1 subunit of the rat brain sodium channel, Science 256 (1992) 839–842.
[4] T. Tseng, A.M. McMahon, V.T. Johnson, E.Z. Mangubat, R.J. Zahm, M.E. Pacold, et al., Sodium channel auxiliary subunits, J. Mol. Microbiol. Biotechnol. 12 (2007) 249–262.
[5] L. Isom, D. Ragsdale, K. De Jongh, R. Westenbroek, B. Reber, T. Scheuer, et al., Structure and function of the beta 2 subunit of brain sodium channels, a transmembrane glycoprotein with CA motif, Cell 83 (1995) 433–442.
[6] J.D. Malhotra, K. Kazen-Gillespie, M. Hortsch, L.L. Isom, Sodium channel beta subunits mediate homophilic cell adhesion and recruit ankyrin to points of cell–cell contact, J. Biol. Chem. 275 (2000) 11383–11388.
[7] L.L.I. Isom, Cellular and molecular biology of sodium channel beta-subunits: therapeutic implications for pain? I. Cellular and molecular biology of sodium channel beta-subunits: therapeutic implications for pain?, Am J. Physiol. Gastrointest. Liver Physiol. 278 (2000) G349–53.
[8] K. Morgan, E. Stevens, B. Shah, P. Cox, A. Dixon, K. Lee, et al., B3: an additional auxiliary subunit of the voltage-sensitive sodium channel that modulates channel gating with distinct kinetics, Proc. Natl. Acad. Sci. USA 97 (2000) 2308–2313.
[9] F.H. Yu, R.E. Westenbroek, I. Silos-Santiago, K.A. McCormick, D. Lawson, P. Ge, et al., Sodium channel beta4, a new disulfide-linked auxiliary subunit with similarity to beta2, J. Neurosci. 23 (2003) 7577–7585.
[10] G.A. Patiño, L.R.F. Claes, L.F. Lopez-Santiago, E.A. Slat, R.S.R. Dondeti, C. Chen, et al., A functional null mutation of SCN1B in a patient with Dravet syndrome, J. Neurosci. 29 (2009) 10764–10778.
[11] R. Wallace, D. Wang, R. Singh, I. Scheffer, A. George, H. Phillips, et al., Febrile seizures and generalized epilepsy associated with mutation of the Na+-channels b1-subunit gene SCN1B, Nat. Genet. 19 (1998) 366–370.
[12] R.H. Wallace, I.E. Scheffer, G. Parasivam, S. Barnett, G.B. Wallace, G.R. Sutherland, et al., Generalized epilepsy with febrile seizures plus: mutation of the sodium channel subunit SCN1B, Neurology 58 (2002) 1426–1429.
[13] L. Ferrera, O. Moran, Beta1-subunit modulates the Nav1.4 sodium channel by changing the surface charge, Exp Brain Res 172 (2006) 139–150.
[14] O. Moran, F. Conti, P. Tammaro, Sodium channel heterologous expression in mammalian cells and the role of the endogenous beta1-subunits, Neurosci. Lett. 336 (2003) 175–179.
[15] P. Tammaro, F. Conti, O. Moran, Modulation of sodium current in mammalian cells by an epilepsy-correlated β1-subunit mutation, Biochem. Biophys. Res. Commun. 291 (2002) 1095–1101.
[16] U.K. Laemmli, Cleavage of structural proteins during the assembly of the head of bacteriophage T4, Nature 227 (1970) 680–685.
[17] A. Aitken, M. Learmonth, in: J.M. Walker (Ed.), Diagonal Electrophoresis for Detecting Disulfide Bridges in the Protein Protocols Handbook, Humana Press, Totowa, NJ, USA, 2002, pp. 589–593.
[18] A. Sommer, R.R. Traut, Diagonal polyacrylamide-dodecyl sulfate gel electrophoresis for the identification of ribosomal proteins crosslinked with methyl-4-mercaptobutyrimidate, Proc. Natl. Acad. Sci. USA 71 (1974) 3946–3950.
[19] K. Wang, F.M. Richards, An approach to nearest neighbor analysis of membrane proteins. Application to the human erythrocyte membrane of a method employing cleavable cross-linkages, J. Biol. Chem. 249 (1974) 8005–8018.
[20] J.P. Allison, B.W. McIntyre, D. Bloch, Tumor-specific antigen of murine T-lymphoma defined with monoclonal antibody, J. Immunol. 129 (1982) 2293–2300.
[21] C. Hannum, J.H. Freed, G. Tarr, J. Kappler, P. Marrack, Biochemistry and distribution of the T cell receptor, Immunol. Rev. 81 (1984) 161–176.
[22] B.H. Dulis, T.M. Kloppel, H.M. Grey, R.T. Kubo, Regulation of catabolism of IgM heavy chains in a B lymphoma cell line, J. Biol. Chem. 257 (1982) 4369–4374.
[23] J.W. Goding, A.W. Harris, Subunit structure of cell surface proteins: disulfide bonding in antigen receptors, Ly-2/3 antigens, and transferrin receptors of murine T and B lymphocytes, Proc. Natl. Acad. Sci. USA 78 (1981) 4530–4534.

Biochemical and Biophysical Research Communications 420 (2012) 368–373

Contents lists available at SciVerse ScienceDirect

Biochemical and Biophysical Research Communications

journal homepage: www.elsevier.com/locate/ybbrc

Expression of human carbonyl reductase 3 (CBR3; SDR21C2) is inducible by pro-inflammatory stimuli

Petra Malátková [a], Bettina Ebert [b], Vladimír Wsól [a], Edmund Maser [b,*]

[a] Department of Biochemical Sciences, Faculty of Pharmacy, Charles University, Heyrovského 1203, CZ-50005 Hradec Králové, Czech Republic
[b] Institute of Toxicology and Pharmacology for Natural Scientists, University Medical School Schleswig-Holstein, Brunswiker Str. 10, 24105 Kiel, Germany

ARTICLE INFO

Article history:
Received 24 February 2012
Available online 8 March 2012

Keywords:
Carbonyl reductase 3
Inflammation
NFκB
Transcriptional regulation

ABSTRACT

Until today, the physiologic role of human carbonyl reductase 3 (CBR3; SDR21C2), a member of the short-chain dehydrogenase/reductase superfamily remains obscure. Since the transcriptional regulation is closely related to the function of a protein, elucidation of the regulation of CBR3 should help to understand its physiologic role. We recently identified CBR3 as a novel target gene of Nrf2, a cellular sensor of oxidative stress. In this study, we provide for the first time evidence that pro-inflammatory stimuli induce the expression of the *CBR3* gene. Treatment of human cancer cells HT-29 (colon) and HepG2 (liver) with TNF-α, IL-1β, and LPS induced CBR3 expression differentially. While TNF-α (50 ng/ml) or IL-1β (1 and 10 ng/ml), induced CBR3 mRNA expression in HT-29 cells (up to 10-fold) and HepG2 cells (up to 20-fold), LPS activated the *CBR3* gene only in HepG2 cells. Furthermore, overexpression of the NFκB subunits p65 and p50 alone or in combination elevated CBR3 mRNA levels (3.9-fold) in HT-29 cells. According to our results, CBR3 is a novel target gene of inflammatory stimuli, and elucidation of its detailed role in inflammation deserves further investigation.

1. Introduction

As carbonyl groups often govern the biologic activity of endo- and xenobiotics, enzymes mediating carbonyl reduction drive numerous physiologic processes (e.g., steroid biotransformation) as well as the detoxification of potentially harmful exogenous (e.g., drugs, environmental pollutants) and endogenous (e.g., lipid peroxidation products) compounds [1].

So far, three carbonyl reductases (CBRs) have been identified in humans (CBR1 [SDR21C1], CBR3 [SDR21C2] and CBR4 [SDR45C1]) all of which belong to the short-chain dehydrogenase/reductase (SDR) superfamily [2].

Since the identification of CBR3 in 1998 [3] some progress has been made with regard to its tissue-specific distribution, but still the understanding of its molecular function is incomplete [4]. Although being considered an enzyme in the reductive metabolism of anthracyclines such as doxorubicin and daunorubicin [5,6], the poor catalytic efficiencies for other tested carbonyl compounds imply that the expected function of CBR3 in xenobiotic carbonyl metabolism is very unlikely [7,8]. Therefore, the physiologic role of CBR3 in the human body remains obscure. Elucidation of its transcriptional regulation may shed light on the physiologic role of CBR3, since molecular mechanisms that regulate an enzyme's expression are often closely related to its function.

In a recent study, we could identify CBR3 as a novel Nrf2 (nuclear factor-erythroid 2 related factor 2)-target gene [9], which was later confirmed by others [10]. Since Nrf2 mediates the transcriptional activation of genes in response to oxidative stress [13], CBR3 might fulfill antioxidant functions. However, as the promoter of CBR3 contains putative binding sites for various other transcription factors, some additional environmental conditions may be involved in the regulation of CBR3 as well.

Recently, two potential NFκB (nuclear-factor kappa-B) consensus motifs were identified in the 5′-UTR of the *CBR3* gene which are located −1160 and −593 basepairs upstream of the transcriptional start site [11]. Moreover, our preliminary promoter analysis revealed the existence of even a third putative NFκB binding site (nt −364: 5′-GGGGTTTTCCC-3′). Meanwhile, it is widely accepted that oxidative stress and inflammation are two cellular events which are closely connected. For instance, NFκB attenuates the production of reactive oxygen species (ROS) via increased expression of antioxidant proteins. By contrast, transcriptional targets of NFκB itself promote the production of ROS, especially enzymes important for the inflammatory response, such as cyclooxygenase-2 (COX-2) and inducible nitric oxide synthase (iNOS) [12].

Abbreviations: CBR3, carbonyl reductase 3; IL-1, interleukin-1; LPS, lipopolysaccharides; NFκB, nuclear-factor kappa-B; qPCR, quantitative real-time RT-PCR; sqPCR, semi-quantitative RT-PCR; TNF-α, tumor necrosis factor-α.

* Corresponding author. Fax: +49 431 597 3558.
E-mail address: maser@toxi.uni-kiel.de (E. Maser).

0006-291X/$ - see front matter © 2012 Elsevier Inc. All rights reserved.
http://dx.doi.org/10.1016/j.bbrc.2012.03.002

NFκB comprises a family of transcription factors [e.g., p65 (RelA) and p50 (NFκB1) among others] that control a wide range of critical physiologic processes in the organism including inflammation, immune response and cell survival [13]. These various subunits form homodimers and heterodimers with each other [14,15]. In their inactive form, NFκB dimers are associated with inhibitory proteins such as IκBα that retains them in the cytoplasm. IκBα itself is regulated by NFκB, thereby providing an autoregulatory feedback loop allowing for the control of the inflammatory response [13]. A great variety of biologic factors (e.g., pathogens, cytokines) and environmental conditions (e.g., UV irradiation, oxidative stress) trigger the formation of NFκB dimers that translocate to the nucleus where they bind to NFκB response elements of target genes [16].

There are two main signaling pathways activating NFκB, referred to as "classical" (canonical) and "alternative" (non-canonical) pathway [17]. The former is activated by endogenous inflammatory stimuli (e.g., pro-inflammatory cytokines such as tumor necrosis factor-α [TNF-α] and interleukin-1 [IL-1]), and in response to invading microorganisms or their products (e.g., lipopolysaccharides [LPS]).

The aim of this study was to infer whether CBR3 expression is regulated via pro-inflammatory stimuli in the model cell lines HT-29 and HepG2. According to our findings, this is the first report providing clear evidence that the expression of the *CBR3* gene is induced under inflammatory conditions.

2. Materials and methods

2.1. Cell culture materials and cell lines

Cell culture media and supplements were purchased from PAA Laboratories GmbH (Cölbe, Germany). The human colon cancer cell line HT-29 was obtained from the Deutsche Sammlung für Mikroorganismen und Zellkulturen (DSMZ, Braunschweig, Germany) and the human hepatoma cell line HepG2 was from Cell lines service (CLS, Eppelheim, Germany).

2.2. Plasmids

Expression plasmids for NFκB subunits p65 and p50 were constructed by Warner Greene [18] and obtained from Addgene (Addgene Inc., Cambridge, MA, USA) (pCMV4 p65: Addgene plasmid 21966 and pCMV4 p50: Addgene plasmid 21965). Plasmids were purified from bacterial cultures with the QIAGEN plasmid Midi kit (Qiagen, Hilden, Germany).

2.3. Cell culture

HT-29 cells were maintained in Dulbecco's modified Eagle's medium (DMEM, high glucose) supplemented with 2 mM L-glutamine, 1% of non-essential amino acids and 10% heat-inactivated fetal calf serum (FCS). HepG2 cells were cultured in DMEM/Ham's F12 (1:1) supplemented with 2 mM L-glutamine and 10% FCS. All cells were routinely cultured without antibiotics in a humidified atmosphere of 5% CO_2 in air at 37 °C.

2.4. Gene expression experiments

Cells were seeded in 60 mm Petri dishes or six-well plates (9.3 cm^2) and grown until they reached 60–90% of confluence. Recombinant TNF-α and IL-1β were purchased from Cell Systems (Troisdorf, Germany) and LPS was from Sigma–Aldrich (Deisenhofen, Germany). Stock solutions were prepared in sterile H_2O (IL-1β and LPS) or sterile H_2O containing 0.1% BSA (TNF-α) and stored as aliquots at −20 °C until used. After serum-starvation for 18–24 h, the cells were incubated with test compounds freshly dissolved in serum-free medium for times as indicated in the figures. The medium was replaced with fresh serum-free medium and test compounds every 24 h. All experiments were performed 2–5 times.

2.5. Transient transfections

Cells were seeded in six-well plates and allowed to recover for 24 h. Expression plasmids pCMV4 p65 and pCMV4 p50 were diluted in 250 µl of OptiMEM I (Invitrogen, Karlsruhe, Germany), combined with 250 µl of OptiMEM I containing 10 µl of Lipofectamine 2000™ (Invitrogen, Karlsruhe, Germany), and, after incubation for 20 min at room temperature, the mixture was added to the cells. The medium was replaced after 7 h with fresh culture medium. Transfected cells were harvested for RNA isolation after 24 h incubation.

2.6. RNA-isolation and cDNA synthesis

RNA was isolated using the MasterPure™ RNA Purification Kit (Epicentre Biotechnologies, Madison, Wisconsin, USA). The cell-monolayer was washed with phosphate buffered saline (PBS) and RNA isolation was performed following the manufacturer's protocol including removal of contaminating DNA and with an additional ethanol wash step. cDNA synthesis was carried out as described before [9].

2.7. Semi-quantitative RT-PCR (sqPCR)

Semi-quantitative RT-PCR (sqPCR) was performed using Phire Hot-start DNA polymerase (Biozym Scientific, Hessisch Oldendorf, Germany) as described in detail elsewhere [9]. β-Actin served as the house-keeping gene. The following primers were used: β-Actin (fwd: 5'-ACTCTTCCAGCCTTCCTTCCT, rev: 5′-AGGTTTTGTCAAGAA AGGGTGT), CBR3 (fwd: 5′-GCTCAACGTACTGGTCAACAAC, rev: 5′-ATCCTCGATAAGACCGTGACC), IκBα (fwd: 5′-CTACACCTTGCCTGT-GAGCA, rev: 5′-GCTCGTCCTCTGTGAACTCC), COX-2 (fwd: 5′-GA ATGGGGTGATGAGCAGTT, rev: 5′-GGTCAATGGAAGCCTGTCAT), p50 (fwd: 5′-TGCCAACAGCAGATGGCCCAT, rev: 5′-AAACATGAG CCGCACCACGCT), p65 (fwd: 5′-AAGTTCCTATAGAAGAGCAGCG, rev: 5′-TGCTCTTGAAGGTCTCATATG).

Densitometric analyses were carried out with GIMP2.0 software.

2.8. Quantitative real-time RT-PCR (qPCR)

Real-time PCR (qPCR) experiments were run on an AB 7500 Fast Real-time PCR system (Life Technologies, Darmstadt, Germany). Two micrograms of RNA were reverse transcribed into cDNA in a total volume of 35 µl. Each cDNA sample was diluted 2-fold and 2 µl of this dilution were used for qPCR analyses. One 20 µl reaction contained 1 µl of TaqMan Gene expression Assay Hs01025918_m1 (CBR3) or Hs99999903_m1 (ATCB, β-Actin), 10 µl of TaqMan Fast Universal PCR Mastermix, 2 µl cDNA and 7 µl sterile H_2O. The thermal cycling conditions included an initial activation-step at 95 °C for 20 s, followed by 40 cycles of denaturation (95 °C, 3 s) and annealing/extension (60 °C, 30 s). Samples and no-template controls were run in triplicate. The fold-changes in the mRNA expression levels were calculated by the comparative quantitation ($2^{-\Delta\Delta Ct}$) method by using the instrument's software.

2.9. Statistical analysis

Statistical analyses were performed with the GraphPad Prism5 software. Differences between mean values were determined by a two-tailed paired Student's *t*-test or a one-way ANOVA followed by a Tukey's post-test. Statistically significant differences were set at $P \leqslant 0.05$, $P \leqslant 0.001$, and $P \leqslant 0.0001$ indicated highly significant data.

3. Results and discussion

The existence of putative NFκB binding sites in the promoter region of the *CBR3* gene [11] was the basis for our working hypothesis that CBR3 may be up-regulated during inflammation. This idea was supported by data from high-throughput experiments available from the public database GEO ("Gene Expression Omnibus", http://www.ncbi.nlm.nih.gov/geo/). For example, elevated levels of CBR3 mRNA were detected in colon biopsy samples from patients suffering from ulcerative colitis, a type of inflammatory bowel disease (GEO profiles: **GDS3119**) and in bronchial epithelial cells treated with interferon gamma (IFN-γ), a prototypical inflammatory cytokine (GEO profiles: **GDS1256**). Although these microarray data provide valuable information about the regulation of a certain gene, a PCR-based validation of these data is always essential.

In our study, the cell lines HT-29 and HepG2 were chosen as suitable models because of their low constitutive level of CBR3 expression.

3.1. Pro-inflammatory stimuli increased CBR3 expression in HT-29 cells

To investigate the role of inflammation in the up-regulation of CBR3, HT-29 cells were incubated with TNF-α (25 and 50 ng/ml), IL-1β (10 and 20 ng/ml) and LPS (100 and 1000 ng/ml) for 4, 8 and 24 h. While IL-1β treatment (20 ng/ml) led to a slight increase in the expression of CBR3 mRNA after 24 h (2.2-fold; Fig. 1A), TNF-α caused the strongest increase in the expression of CBR3 mRNA from 4 h through 24 h (see Fig. 2A, B). The effect of LPS after 8 h was marginal (1.5-fold, 1000 ng/ml; not shown).

Since the NFκB activators used in this experiment mediate their effects through binding to specific receptors (e.g., TNF receptors [TNF-α], IL-1 receptors [IL-1β], and Toll-like receptors [LPS]), our findings might result from a cell-specific expression of these cognate receptors. Most interestingly, mature colon cells per se show a relatively low inflammatory response upon exposure to LPS, a fact which results from a micro RNA (miRNA-146)-mediated repression of the NFκB-signaling pathway [19], thereby preventing an unwanted chronic inflammation in response to the normal gut flora. In our study, the low effect of LPS on CBR3 expression in HT-29 colon cells, which is in contrast to the strong response of HepG2 liver cells to LPS (see below) might be explained by this miRNA-based mechanism.

3.2. Time- and concentration-dependent up-regulation of CBR3 by TNF-α in HT-29 cells

Because TNF-α had the strongest effect in HT-29 cells, we examined the effect of this cytokine on CBR3 expression in more detail. HT-29 cells were incubated with 50 ng/ml of TNF-α under serum-free conditions. After 2, 4, 8, 12, 24 and 48 h of treatment, the amounts of CBR3, COX-2 and IκBα mRNA were determined. As presented in Fig. 2A, TNF-α increased the expression of CBR3 throughout the whole time course of the incubation. Densitometric analysis (Fig. 2B) of four independent cell culture experiments that

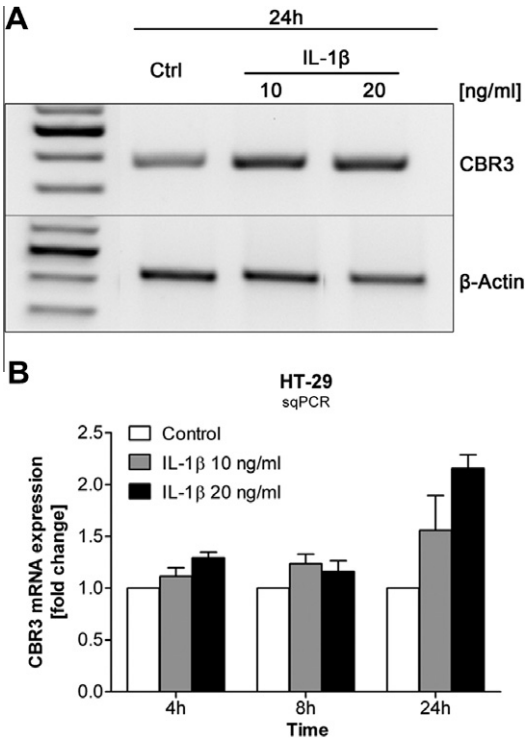

Fig. 1. CBR3 expression in HT-29 cells after exposure to IL-1β. HT-29 cells were treated with IL-1β (10 and 20 ng/ml) or serum-free medium only for 4, 8 and 24 h and changes in the mRNA expression were assayed by means of sqPCR. One representative gel of the treatment with IL-1β for 24 h (A) is shown. Panel (B) shows the densitometric analysis of two representative experiments of the IL-1β treatment. Bars represent means of $n = 2$ experiments ± the standard deviation. The CBR3 mRNA expression was normalized to that of β-actin, and the untreated control ("Ctrl") was set to 1.

were subjected to semi-quantitative RT-PCR (sqPCR) revealed that CBR3 mRNA levels continuously increased from the 2 h-treatment on (2-fold increase vs. control, $P < 0.05$) until it reached a peak after 48 h (9.2-fold vs. control, $P < 0.05$). Also, the mRNA levels of two established NFκB-target genes, COX-2 and IκBα that served as controls for the activation of the NFκB signaling pathway, were induced, indicating that TNF-α successfully activated NFκB in HT-29 cells.

Next, to investigate a possible concentration-dependency in response to TNF-α, HT-29 cells were exposed to 10, 25, 50 and 100 ng/ml of TNF-α for 24 h. Indeed, TNF-α was shown to increase CBR3 mRNA expression in a concentration-dependent manner (Fig. 2C, D). sqPCR analysis (Fig. 2D) revealed that CBR3 mRNA was inducible even by the lowest concentration of 10 ng/ml of TNF-α (2.3-fold, $P < 0.05$), and this effect was continuously growing with increasing concentrations of TNF-α up to 6.6-fold compared to the control ($P < 0.001$) when 100 ng/ml of TNF-α was applied. Again, the exposure to TNF-α led to an elevated level of the NFκB-driven control genes COX-2 and IκBα in HT-29 cells (Fig. 2C).

3.3. Overexpression of the NFκB subunits p65 and/or p50 increased the level of CBR3 mRNA in HT-29 cells

To directly activate the NFκB pathway, HT-29 cells were transfected with the expression vectors pCMV4 p65 and pCMV4 p50 encoding the NFκB subunits p65 and p50, respectively. In this experiment, either two different concentrations (2 μg and 6 μg) of each pCMV4 p65 or pCMV4 p50, respectively, were transfected into the cells alone or in combination (2 μg each). The increased amounts of p65 mRNA (lanes 2, 3, and 6 in Fig. 3A) or p50 mRNA

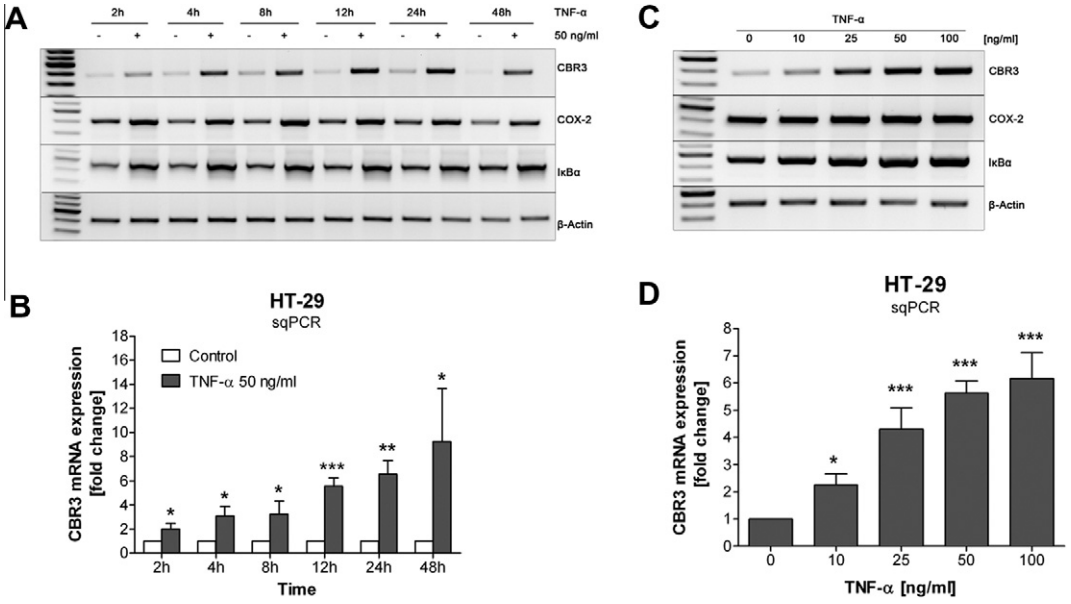

Fig. 2. Time- and concentration-dependent effect of TNF-α on CBR3 mRNA expression in HT-29 cells. HT-29 cells were incubated for 2, 4, 8, 12, 24 and 48 h with (+) or without (−) TNF-α (50 ng/ml) and sqPCR was performed with β-actin as the house-keeping gene. (A) CBR3 mRNA as well as the NFκB-regulated control genes COX-2 and IκBα were induced by TNF-α during the whole time-course. (B) Densitometric analyses of four independent experiments show changes in the CBR3 mRNA expression relative to untreated cells. Bars represent means of $n = 4$ experiments ± the standard deviation (three asterisks denote $P < 0.001$; two asterisks denote $P < 0.01$; one asterisk denotes $P < 0.05$; two-tailed paired Student's t-test). (C, D) Different concentrations of TNF-α (0, 10, 25, 50, and 100 ng/ml) were applied for 24 h and sqPCR was performed. (C) A representative gel shows the effect on CBR3 and NFκB-regulated control genes COX-2 and IκBα. (D) Densitometric analysis of five independent experiments. Bars represent means of $n = 5$ experiments ± the standard deviation (three asterisks denote $P < 0.001$; one asterisk denotes $P < 0.05$; ANOVA).

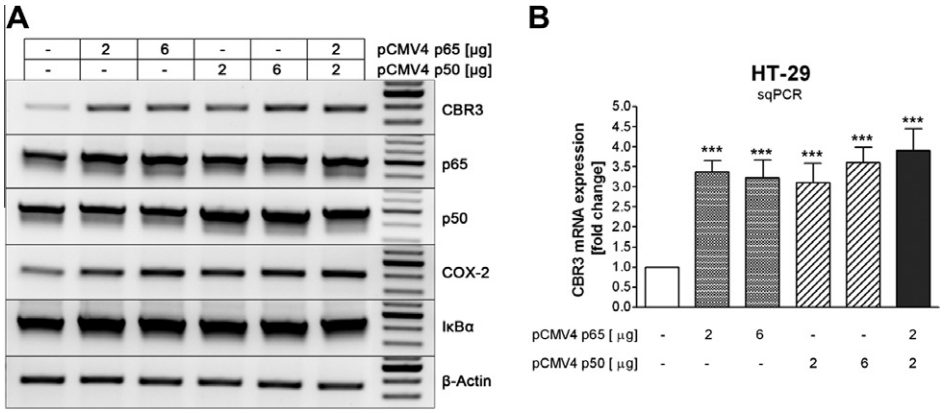

Fig. 3. Transfection of HT-29 cells with NFκB subunits p65 and/or p50 induced CBR3 expression. HT-29 cells were transfected with different amounts of expression plasmids *pCMV4 p50* ("p50") and/or *pCMV4 p65* ("p65") and the changes in the expression of CBR3, p65, p50, as well as of the control genes COX-2 and IκBα were determined by sqPCR. Amounts (in µg) of transfected plasmid DNA are indicated in the table above or below the figures, respectively. (A) One representative gel is shown. (B) The graph shows the densitometric analyses of $n = 3$ independent experiments ± the standard deviation (three asterisks denote $P < 0.001$; ANOVA). The non-transfected control was set to 1.

(lanes 4–6) 24 h post-transfection indicated that the plasmids had been successfully delivered into the cells. Moreover, the activation of the NFκB signaling pathway after transfection of p65 and/or p50 was monitored by the induction of the NFκB target genes COX-2 and IκBα.

As shown in Fig. 3B, sqPCR analysis of four individual experiments revealed that all transfections elevated the levels of CBR3 mRNA in a range from 3.1-fold to 3.9-fold compared to non-transfected cells. Interestingly, the transfection of 2 µg of only one of both expression vectors was sufficient to cause a 3.4-fold (pCMV4 p65) or 3.1-fold (pCMV4 p50) induction of the *CBR3* gene ($P < 0.0001$). A similar effect on CBR3 mRNA expression was observed after co-transfection of both the NFκB subunits p65 and p50 (3.9-fold vs. control, $P < 0.0001$).

Activation of the classical NFκB pathway provokes the translocation of p65 and p50, which act in most of the cases as a p65:p50 heterodimer [14]. However, p65:p65 or p50:p50 homodimers are able to activate gene transcription as well [15]. In HT-29 cells, overexpression of either p65 or p50 already had an equivalent inducing effect on CBR3 mRNA expression, whereas co-transfection with both expression plasmids further enhanced the CBR3 gene transcription only slightly. If both homodimers (p65:p65 and p50:50) and heterodimers (p65:p50) were involved in the transcription of CBR3 mRNA, one would expect a much larger amount of CBR3 mRNA in p50 and p65 co-transfected cells. Thus, the same effectiveness of overexpressed subunits alone and in combination indicates the involvement of p65:p50 heterodimers rather than homodimers. In our case it seems that the plasmid-expressed

p50 or p65 subunits form dimers with the p65 and p50 subunits that were already endogenously present in HT-29 cells.

3.4. CBR3 mRNA expression is inducible by pro-inflammatory stimuli in HepG2 cells and IL-1β regulates CBR3 in a time- and concentration-dependent manner

In order to test, whether the results obtained with HT-29 cells are reproducible in a cell line originating from another tissue, HepG2 cells were incubated with TNF-α, IL-1β, and LPS. All tested NFκB-activators strongly induced CBR3 mRNA expression in HepG2 cells. As shown in Fig. 4A, IL-1β (10 and 20 ng/ml) was the most effective inducer, followed by TNF-α (50 ng/ml) and LPS (1000 ng/ml). Therefore, IL-1β was chosen to study its effect on CBR3 mRNA expression in HepG2 cells in more detail.

From our preliminary experiments it was obvious that HepG2 cells responded more promptly than HT-29 cells with regard to CBR3 up-regulation by pro-inflammatory stimuli. Accordingly, for HepG2 cells, a shorter period of time (2–8 h) was chosen. HepG2 cells were exposed to two different concentrations of IL-1β (1 ng/ml and 10 ng/ml) under serum-free conditions and the changes in CBR3 mRNA expression levels were determined after 2, 4, and 8 h by means of sqPCR (Fig. 4B, C). Again, to monitor the activation of the NFκB-signaling pathway, IκBα served as a control gene that exhibited an expression pattern similar to that of CBR3 when HepG2 cells were subjected to IL-1β-treatment (Fig. 4B). Noteworthy, the second NFκB-regulated control gene, COX-2 was undetectable in this cell line.

As presented in Fig. 4C, even after the shortest incubation time of 2 h, IL-1β-treatment (1 ng/ml and 10 ng/ml) could provoke a strong elevation of CBR3 mRNA expression (4.2-fold and 10.5-fold, respectively; $P < 0.05$ and $P < 0.001$). Interestingly, treatment with 10 ng/ml of IL-1β beyond 2 h did not further increase the amount of CBR3 mRNA, but rather decreased the CBR3 mRNA (to 7.8-fold; $P < 0.001$).

Two out of four individual experiments were additionally verified by quantitative real-time PCR (qPCR) (Fig. 4D). Clearly, due to the two different methods, values of fold-inductions differed between sqPCR and qPCR, especially when the mRNA levels reach the point of saturation in the sqPCR. However, the results turned out to be comparable: IL-1β-treatment for 2 h (1 ng/ml and 10 ng/ml) clearly induced *CBR3* gene expression to 3.7- and 20.7-fold, respectively. A slight further increase was observed after 4 h only at a concentration of 1 ng/ml of IL-1β (5.5-fold vs. control). As seen upon sqPCR after 8 h of incubation with IL-1β (1 ng/ml and 10 ng/ml) the CBR3 mRNA expression declined to 1.5- and 4.1-fold vs. control.

Taken together, our results clearly demonstrate that in HepG2 cells *CBR3* gene expression is up-regulated by IL-1β in a time- and concentration-dependent manner.

Comparing the results obtained with both cell lines, the most striking difference between HT-29 and HepG2 towards pro-inflammatory cytokines was the very prompt response of HepG2 cells followed by a rapid decline in the mRNA levels of both CBR3 and the control gene IκBα (cf. Fig. 4B). The corresponding effect in HT-29 cells (cf. Fig. 2A) was comparatively slow but more persistent. In addition, CBR3 mRNA inducibility was more pronounced in HepG2 cells than in HT-29 cells. Different IκBα activities in colonic cells and hepatocytes may explain the high and rapid increase in CBR3 mRNA in HepG2 cells in contrast to the low but prolonged effects in HT-29 cells. For HT-29 cells as well as for some other human colonic epithelial cells it is known that IκBα-degradation is incomplete after NFκB stimulation, however, without preventing the NFκB binding activity [20]. In contrast, NFκB activation in HepG2 cells caused a strong and rapid proteolysis of IκBα followed by a prompt re-synthesis of IκBα, resulting in an inhibition of NFκB-mediated gene transcription [21]. In addition, different mRNA-stabilities may also contribute to the observed effects. In summary, our findings imply a cell-specific regulation of CBR3 by pro-inflammatory stimuli.

In conclusion, we provide for the first time evidence that the *CBR3* gene is activated under inflammatory conditions. Treatment of cancer cell lines with either TNF-α (HT-29) or IL-1β (HepG2) regulated the expression of CBR3 mRNA in a time- and

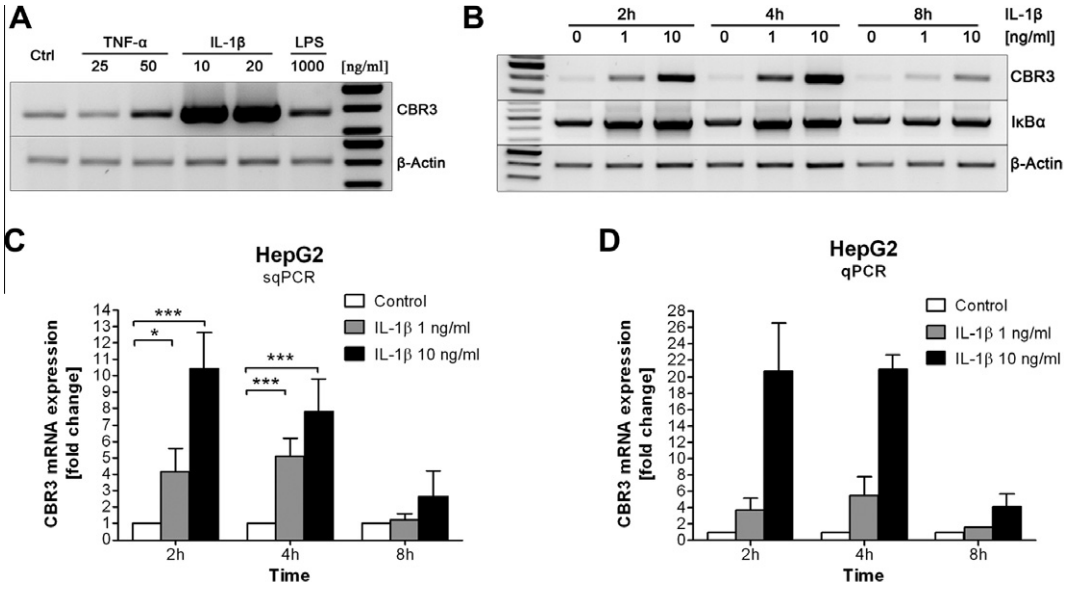

Fig. 4. Time- and concentration-dependent effect of IL-1β on CBR3 mRNA expression in HepG2 cells. (A) HepG2 cells were treated with TNF-α (25 and 50 ng/ml), IL-1β (10 and 20 ng/ml), LPS (1000 ng/ml) or serum-free medium only (control; "Ctrl") for 4 h. Expression levels of CBR3 mRNA were examined by sqPCR. One representative gel is shown. (B) HepG2 cells were incubated for 2, 4 and 8 h with 1 ng/ml and 10 ng/ml of IL-1β or serum-free medium only (0 ng/ml) and the expression of CBR3 mRNA and that of the NFκB-regulated control gene IκBα was determined by sqPCR. (C) The densitometric analysis of four independent experiments is shown. Bars represent means of $n = 4$ experiments ± the standard deviation (three asterisks denote $P < 0.001$; one asterisk denotes $P < 0.05$; ANOVA). (D) Two representative experiments were analyzed by real-time RT-PCR (qPCR). Bars represent means of $n = 2$ experiments ± the standard deviation.

concentration-dependent manner. However, there were striking differences between both cell lines, pointing to a possible cell-specific regulation of CBR3. The identification of the functional NFκB binding sites is currently on-going in our lab by means of reporter gene assays and chromatin immuno-precipitation (ChIP) analyses. Nevertheless, still the greatest challenge is the identification of physiologic substrates that will help to decipher the exact role of CBR3 in the human body.

Acknowledgment

This work was supported by the Deutsche Forschungsgemeinschaft (MA 1704/5-2) and the grant SVV-2012-265-004 from the Grant Agency of Charles University.

References

[1] U. Oppermann, Carbonyl reductases: the complex relationships of mammalian carbonyl- and quinone-reducing enzymes and their role in physiology, Annu. Rev. Pharmacol. Toxicol. 47 (2007) 293–322.
[2] T. Matsunaga, S. Shintani, A. Hara, Multiplicity of mammalian reductases for xenobiotic carbonyl compounds, Drug Metab. Pharmacokinet. 21 (2006) 1–18.
[3] K. Watanabe, C. Sugawara, A. Ono, Y. Fukuzumi, S. Itakura, M. Yamazaki, H. Tashiro, K. Osoegawa, E. Soeda, T. Nomura, Mapping of a novel human carbonyl reductase, CBR3, and ribosomal pseudogenes to human chromosome 21q22.2, Genomics 52 (1998) 95–100.
[4] P. Malatkova, E. Maser, V. Wsol, Human carbonyl reductases, Curr. Drug Metab. 11 (2010) 639–658.
[5] O.S. Bains, M.J. Karkling, J.M. Lubieniecka, T.A. Grigliatti, R.E. Reid, K.W. Riggs, Naturally occurring variants of human CBR3 alter anthracycline in vitro metabolism, J. Pharmacol. Exp. Ther. 332 (2010) 755–763.
[6] S. Lal, E. Sandanaraj, Z.W. Wong, P.C. Ang, N.S. Wong, E.J. Lee, B. Chowbay, CBR1 and CBR3 pharmacogenetics and their influence on doxorubicin disposition in Asian breast cancer patients, Cancer Sci. 99 (2008) 2045–2054.
[7] E.S. Pilka, F.H. Niesen, W.H. Lee, Y. El-Hawari, J.E. Dunford, G. Kochan, V. Wsol, H.J. Martin, E. Maser, U. Oppermann, Structural basis for substrate specificity in human monomeric carbonyl reductases, PLoS One 4 (2009) e7113.
[8] T. Miura, T. Nishinaka, T. Terada, Different functions between human monomeric carbonyl reductase 3 and carbonyl reductase 1, Mol. Cell Biochem. 315 (2008) 113–121.
[9] B. Ebert, M. Kisiela, P. Malatkova, Y. El-Hawari, E. Maser, Regulation of human carbonyl reductase 3 (CBR3; SDR21C2) expression by Nrf2 in cultured cancer cells, Biochemistry 49 (2010) 8499–8511.
[10] Q. Cheng, J.L. Kalabus, J. Zhang, J.G. Blanco, A conserved antioxidant response element (ARE) in the promoter of human carbonyl reductase 3 (CBR3) mediates induction by the master redox switch Nrf2, Biochem. Pharmacol. 83 (2012) 139–148.
[11] J. Zhang, J.G. Blanco, Identification of the promoter of human carbonyl reductase 3 (CBR3) and impact of common promoter polymorphisms on hepatic CBR3 mRNA expression, Pharm. Res. 26 (2009) 2209–2215.
[12] M.J. Morgan, Z.G. Liu, Crosstalk of reactive oxygen species and NF-kappaB signaling, Cell Res. 21 (2011) 103–115.
[13] H.L. Pahl, Activators and target genes of Rel/NF-kappaB transcription factors, Oncogene 18 (1999) 6853–6866.
[14] S. Ghosh, M. Karin, Missing pieces in the NF-kappaB puzzle, Cell 109 (Suppl) (2002) S81–S96.
[15] A. Rahman, K.N. Anwar, A.L. True, A.B. Malik, Thrombin-induced p65 homodimer binding to downstream NF-kappa B site of the promoter mediates endothelial ICAM-1 expression and neutrophil adhesion, J. Immunol. 162 (1999) 5466–5476.
[16] F.E. Chen, G. Ghosh, Regulation of DNA binding by Rel/NF-kappaB transcription factors: structural views, Oncogene 18 (1999) 6845–6852.
[17] T.D. Gilmore, Introduction to NF-kappaB: players, pathways, perspectives, Oncogene 25 (2006) 6680–6684.
[18] D.W. Ballard, E.P. Dixon, N.J. Peffer, H. Bogerd, S. Doerre, B. Stein, W.C. Greene, The 65-kDa subunit of human NF-kappa B functions as a potent transcriptional activator and a target for v-Rel-mediated repression, Proc. Natl. Acad. Sci. USA 89 (1992) 1875–1879.
[19] E. Sonkoly, A. Pivarcsi, MicroRNAs in inflammation, Int. Rev. Immunol. 28 (2009) 535–561.
[20] C. Jobin, S. Haskill, L. Mayer, A. Panja, R.B. Sartor, Evidence for altered regulation of I kappa B alpha degradation in human colonic epithelial cells, J. Immunol. 158 (1997) 226–234.
[21] Y. Han, T. Meng, N.R. Murray, A.P. Fields, A.R. Brasier, Interleukin-1-induced nuclear factor-kappaB-IkappaBalpha autoregulatory feedback loop in hepatocytes. A role for protein kinase calpha in post-transcriptional regulation of ikappabalpha resynthesis, J. Biol. Chem. 274 (1999) 939–947.

Biochemical and Biophysical Research Communications 420 (2012) 374–379

Contents lists available at SciVerse ScienceDirect

Biochemical and Biophysical Research Communications

journal homepage: www.elsevier.com/locate/ybbrc

Rev-erbα regulates circadian rhythms and *StAR* expression in rat granulosa cells as identified by the agonist GSK4112

Huatao Chen [a], Guiyan Chu [a,1], Lijia Zhao [a], Nobuhiko Yamauchi [a], Yasufumi Shigeyoshi [b], Seiichi Hashimoto [c], Masa-aki Hattori [a,*]

[a] Department of Animal and Marine Bioresource Sciences, Graduate School of Agriculture, Kyushu University, Fukuoka, Japan
[b] Department of Anatomy and Neurobiology, Kinki University School of Medicine, Osaka, Japan
[c] Graduate School of Medicine, The University of Tokyo, Tokyo, Japan

ARTICLE INFO

Article history:
Received 24 February 2012
Available online 8 March 2012

Keywords:
Rev-erbα
Circadian rhythm
StAR
GSK4112
Granulosa cell

ABSTRACT

The *Rev-erbα* gene is regarded as a circadian clock gene and clock-regulated gene which regulates the circadian transcriptional/translational loop in a subtle way. Here, we first detected the circadian oscillation in mature granulosa cells from antral follicles using a real-time monitoring system of *Per2* promoter activity with the addition of FSH. Then we used GSK4112, an agonist ligand of Rev-erbα, to investigate the function of Rev-erbα. GSK4112 treatment significantly reduced the *Per2-dLuc* amplitude and induced the *Per2* oscillation phase advance shift. GSK4112 significantly inhibited *Bmal1* mRNA expression, whereas it did clearly stimulate expression of *StAR* mRNA in a dose-dependent manner. Our data are the first to show the Rev-erbα function in the steroid biosynthesis of rat granulosa cells, and to suggest that Rev-erbα may coordinate circadian rhythm and metabolism in rat ovaries.

1. Introduction

The nuclear hormone receptor (NHR) Rev-erbα plays critical roles in many physiologic networks, such as circadian rhythm, adipogenesis, lipid metabolism, and inflammation [1–4]. Rev-erbα, originally defined as a unique orphan receptor, is encoded by the opposite DNA strand of the thyroid hormone receptor-α [5,6]. Because Rev-erbα lacks the activation function 2 (AF-2) domain present at the C-terminal of the ligand-binding domain (LBD) of NHRs, it usually acts as a transcriptional repressor through recruitment of a complex of nuclear receptor corepressor (N-CoR) and histone deacetylsae 3 [7–9]. Recently, it was reported that recruitment of this complex to Rev-erbα is potentiated by Rev-erbα binding to heme, whose intracellular concentrations fluctuate in a circadian manner [10,11]. Two additional studies proved that heme, identified as a novel natural ligand of Rev-erbα, plays a vital role in the regulation of Rev-erbα activity in some physiologic signal pathways [12,13]. Subsequently, GSK4112 (GSK) was identified as a small synthetic agonist for Rev-erbα, which was competitive with heme, and shared a similar function with heme in the regulation of adipogenesis [13,14]. Another study also illustrated that GSK has the potential to reset the peripheral circadian clock in a phasic manner through the recruitment of N-CoR to Rev-erbα [15].

Circadian rhythms are associated with reproductive processes. In mammals, the central pacemaker controlling circadian rhythms resides in the suprachiasmatic nuclei (SCN) of the hypothalamus [16]. Circadian clocks also exist in a wide range of peripheral tissues [17–19]. The master clock in the SCN can synchronize and regulate downstream oscillators in peripheral tissues [17,20,21]. Recent findings have revealed that peripheral circadian oscillators also have similar molecular mechanisms similar to that of SCN. The peripheral clocks are also cell-autonomous and self-sustained, and can be uncoupled from the SCN by restricted feeding [22,23]. As an important reproductive organ, rat ovaries show circadian gene expression [19,24,25]. Our previous studies showed that FSH induced the circadian oscillation of *Per2* in rat granulosa cells (GCs) [26]. Consistent with our studies, a recent report illustrated that FSH causes large phase shifts when applied to cultured rat GCs [25]. The above two reports firmly support the idea that FSH can provide important endocrine cues and synchronized circadian clockwork in rat GCs. Substantial reports proved that circadian clocks exist in ovaries and can be regulated by hormonal signals. However, the issues of how circadian clocks in the ovary influence the downstream genes and what genes integrate the circadian clock and metabolism in the ovary remain largely unknown.

Rev-erbα is a critical component of circadian clockwork [2,3,27]. It acts as a domain clock-controlled gene under the regulation of Bmal1-Clock heterodimer; in turn it has been shown to

* Corresponding author. Address: Department of Animal and Marine Bioresource Sciences, Graduate School of Agriculture, Kyushu University, Hakozaki, Higashi-ku, Fukuoka 812-8581, Japan. Fax: +81 92 642 2938.
E-mail address: mhattori@agr.kyushu-u.ac.jp (M.-a. Hattori).
[1] Present address: The institute of Medical Plant Development, Beijing, China.

0006-291X/$ - see front matter © 2012 Elsevier Inc. All rights reserved.
http://dx.doi.org/10.1016/j.bbrc.2012.02.164

suppress *Bmal1* transcription through binding to RORα response elements (RORE) presenting in *Bmal1* promoters [3,28]. In a recent report, *Rev-erbα* mRNA expression was detected and varied significantly in the ovaries of wild-type mice across 24 h at diestrus [29]. In addition, Rev-erbα expression was found in ovarian GC tumors identified in a recent report [30]. Given the vital role of Rev-erbα in many physiologic pathways and the expression of Rev-erbα in ovarian cells, we hypothesized that Rev-erbα might act as a relay from circadian rhythm to hormone metabolism and might be involved in the regulation of GC function. In the present study, we first examined the Per2 oscillations and several canonical clocks genes expression profiles in rat GCs after synchronization by FSH. Subsequently, we investigated the role of Rev-erbα in the mature GCs via using a synthetic ligand, GSK.

2. Materials and methods

2.1. Animals

The mouse *Per2* promoter region that is sufficient for circadian oscillations was fused to a destabilized luciferase (*dLuc*) reporter gene [31]. *Per2-dLuc* transgenic rats were generated in accordance with the method described in the patent publication number WO/2002/081682 (Y.S. New Technology Institute, Utsunomiya, Japan). Transgenic rats were maintained under 12-h light and 12-h dark (zeitgeber time, ZT0: 0800 h light on; ZT12: 2000 h light off) with water and food *ad libitum*. All experiments were performed under the control of the Guidelines for Animal Experiments in the Faculty of Medicine, Kyushu University, and Law No. 105 and Notification No. 6 of the Government of Japan.

2.2. Preparation and culture of cells

Mature GCs were prepared according to a previous report [32]. Approximately 1×10^6 GCs were plated on a 35-mm collagen-coated dish (Iwaki, Tokyo, Japan) with 2 ml DMEM/F12 supplemented with 1× antibiotic–antimycotic (AA; Nacalai Tesque, Kyoto, Japan) and 5% charcoal-treated FBS (Invitrogen, Carlsbad, CA). Cultures were carried out in a humidified atmosphere of 95% air and 5% CO_2 at 37 °C. Cells were cultured for 48 h prior to other treatments.

2.3. Real-time monitoring of Per2-dLuc oscillations

Attached mature GCs were exposed to serum-free medium supplemented with 15 mM HEPES, 0.1 mM luciferin (Wako, Tokyo, Japan), 0.1% BSA (Nacalai Tesque), and 1× AA in the presence of 100 ng/ml ovine FSH (NIH-oFSH-S16), then subjected to luminescence determination. Luciferase activity was chronologically monitored at 37 °C with Kronos AB-2500 (ATTO, Tokyo, Japan) interfaced to a computer for continuous data acquisition, as previously described [33]. In some experiments, the monitoring was in the presence of GSK or DMSO (vehicle control).

2.4. RNA extraction, RT-PCR and qPCR

Cultured cells were harvested at the indicated times, and total RNA was isolated using RNeasy Mini kit (Qiagen), according to the manufacturer's protocol. RNA samples were treated with RNase-free DNase I (Qiagen). The cDNAs were generated by reverse transcription with random primers using a High Capacity Reverse Transcription kit (Applied Biosystems). Primer sets used for RT-PCR and qPCR are listed in Supplemental Table 1. RT-PCR reactions were carried out in total volume of 20 μl containing 1 μl cDNA (10 ng/μl), dNTP at a final concentration of 0.2 mM, 200 nM of each primer and 0.4 unit KOD-plus-enzyme (Toyobo, Osaka, Japan). Amplification was performed in a programmable thermocycler (Biometra, Germany). The samples were first denatured at 94 °C for 2 min, followed by 28 cycles (*Gapdh*, internal control) or 30 cycles (*StAR*) (94 °C/15 s, 60 °C/30 s, and 68 °C/15 s), and followed by 68 °C for 5 min. The PCR products were analyzed by electrophoresis on 2% agarose gels. The bands were stained by ethidium bromide, and visualized by UV fluorescence. qPCR was performed in a 15-μl volume containing a 30-ng cDNA sample in a Master SYBR Green I mixture (Roche Diagnostics) and 500 nM specific primers, with a Mx3000P Real-time qPCR System (Stratagene) using the parameters recommended by the manufacturer as previously described [32]. All reactions were performed in triplicate and displayed amplification efficiency between 80% and 120%. Relative quantitate of each mRNA was performed using the comparative quantity (copies) method creating standard curves. The quantity for each sample was normalized to *Gapdh*.

2.5. Statistical analyses

All data are presented as means ± SEM of at least three separate experiments, each performed with triplicate samples. The amplitude of *Per2-dLuc* was documented by Cosinor analysis using Timing Series Single 6.3 (Expert Soft Tech., Richelieu, France). The statistical differences of examined values of target genes in cultured GCs were determined by either Student's *t*-test, one-way ANOVA or two-way ANOVA using SigmaPlot software (Ver. 11.2; Systat Software, San Jose, CA, USA). Differences were considered significant at $p < 0.05$ or less.

3. Results

3.1. Analysis of Per2-dLuc oscillation and clock gene expression in mature GCs after synchronization by FSH

The circadian rhythm of *in vitro Per2* promoter activity was first investigated using mature GCs prepared from antral follicles of *Per2-dLuc* transgenic rats. The *Per2* circadian oscillation was generated in the presence of 100 ng/ml FSH. After synchronization by FSH, oscillations were clearly observed in mature GCs, albeit with a rapid and steady decrease of amplitude (Fig. 1A). To further analyze the clock system in mature GCs in the presence of FSH, clock gene transcripts known to comprise the core oscillator (*Bmal1, Clock, Per2, Rev-erbα*) as well as the clock-controlled gene *StAR* and the maturation marker gene *Lhr* were measured at indicated time points according to the first phase. The results are presented in Fig. 1B. Circadian rhythms of *Per2* and *Bmal1* transcripts were obviously anti-phase in mature GCs. In addition, the *Per2* transcript profile was consistent with *Per2* circadian oscillation. The *Per2* transcript level was 24-h rhythmic in GCs (one-way ANOVA, $p < 0.01$). In addition, the circadian variation of the *Bmal1* transcript was small but nonetheless statistically significant ($p = 0.0458$). The expression of the *StAR* gene showed robustly significant changes over the 24-h sampling period ($p = 0.002$). Expression of *Rev-erbα* mRNA changed two-fold across 24 h ($p < 0.01$), with the maximum expression coinciding with troughs in oscillating *Bmal1* mRNA levels. There were no changes in the expression of *Clock* mRNA and *Lhr* mRNA across 24 h (one-way ANOVA, $p > 0.05$).

3.2. GSK treatment altered the Per2 oscillations in mature GCs

To determine whether GSK has an effect on the modulation of circadian rhythm in GCs through increasing the activity of Rev-erbα, the circadian rhythm of *in vitro Per2* promoter activity was investigated using mature GCs. The *Per2* circadian oscillation was

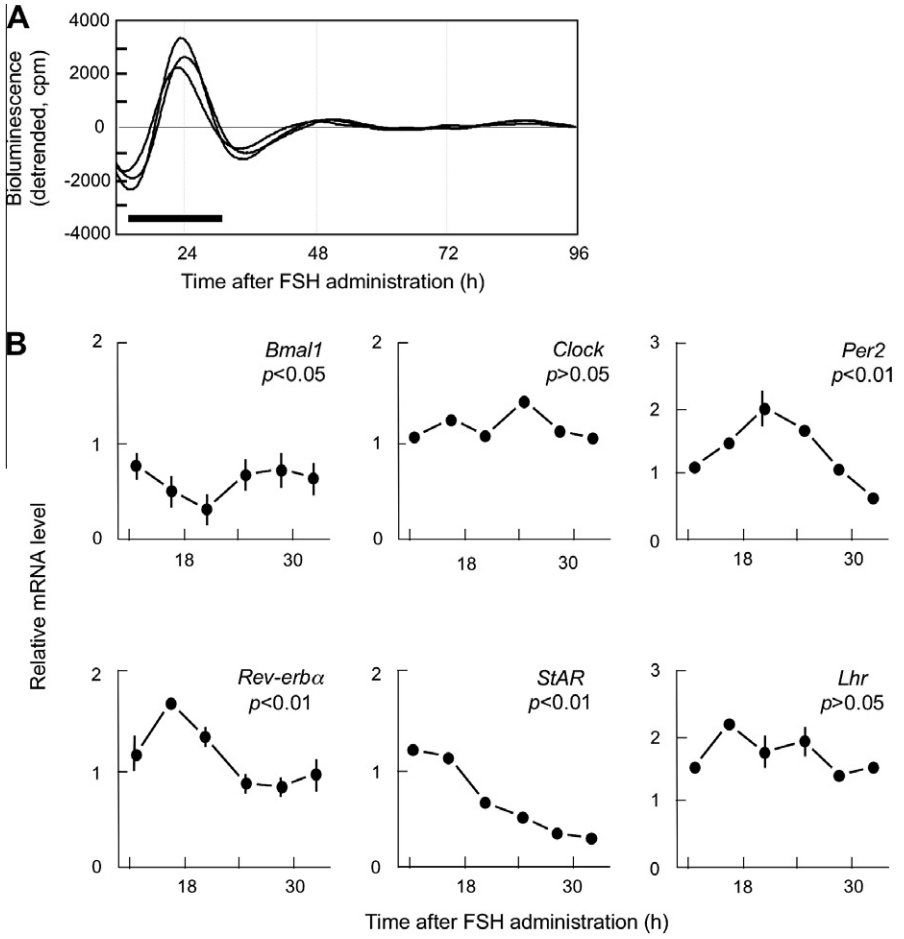

Fig. 1. Circadian rhythms of *Per2-dLuc* expression and clock gene transcript prifiles in the mature GCs in the presence of FSH. (A) Records of bioluminescence showing circadian profiles of *Per2-dLuc* expression rhythms in mature GCs (the onset of bioluminescent measurement with 100 ng/ml FSH was set as 0 day). (B) According to the first *Per2-dLuc* phase, total RNA was collected at the indicated times (*solid line* in *panel* A). qPCR analysis of transcript levels were performed using their specific primers. *Gapdh* was used as an internal control. Each value represents the mean ± SEM of three separate experiments. One-way ANOVA was used to determine significant differences among each value ($p < 0.05$ or less).

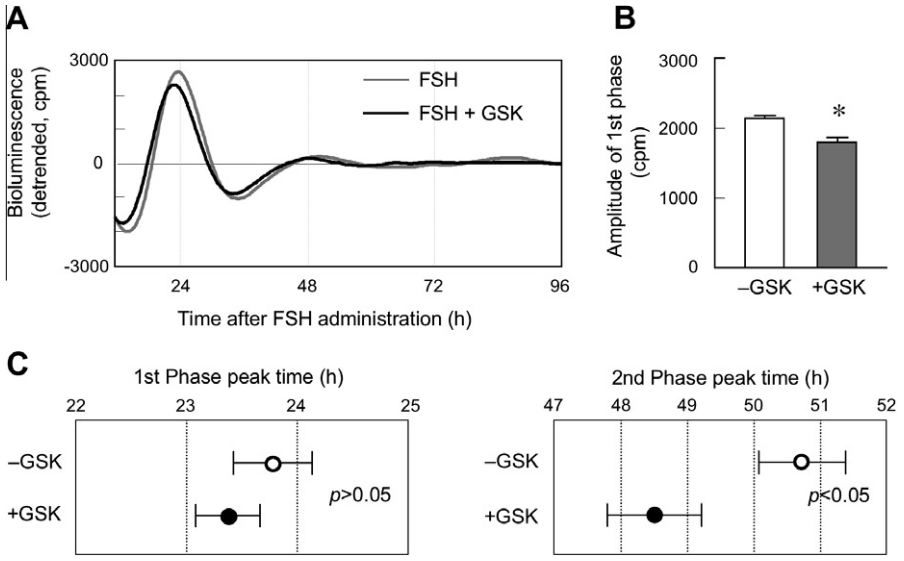

Fig. 2. Effects of exogenous treatment with or without GSK (0.01 mM) in the presence of FSH on circadian rhythms of *Per2-dLuc* expression in mature GCs. (A) Representative records of bioluminescence showing the effect of GSK on rhythmic expression of *Per2-dLuc* in cultured mature GCs. (B) Amplitude of *Per2-dLuc* expression rhythms after treatment with vehicle or vehicle + GSK documented by Cosinor analysis. $^{*}p < 0.05$. (C) Peak times in the first and second phases of *Per2-dLuc* expression rhythms treated with or without GSK. Each point represents the mean ± SEM of six separate experiments.

synchronized by FSH, with or without 0.01 mM GSK. Oscillations were clearly observed in different treatments (Fig. 2A). It is interesting to note that GSK significantly decreased the amplitude of *Per2-dLuc* compared to FSH treatment alone (Fig. 2B). Also, GSK induced *Per2-dLuc* oscillation phase advance shifts in the peak time of the second phase though the first phase did not show a significant difference between GSK and vehicle-only treatment (Fig. 2C).

3.3. The mRNA expression of circadian clock genes, StAR gene and Lhr gene under the modulation of GSK

In order to examine the function of Rev-erbα in mature GCs, we further investigated the mRNA expression of genes. GCs were treated with FSH in the presence or absence of 0.01 mM GSK as above indicated. Twenty-four hours later, cells were then harvested for RNA extraction and qPCR analysis. The mRNA expression of *Clock, Lhr,* and *Rev-erbα* were not significantly different for GSK and vehicle-only treatment (Fig. 3A). However, it seemed significant that *StAR* gene expression was greatly increased with the addition of GSK (4.2-fold). We further investigated whether its effects on *StAR* gene expression were time dependent. By sampling synchronized mature GCs at four time points over a 24-h period, a rhythmicity was observed in the basal expression of the circadian clock genes *Bmal1* and *Rev-erbα*, when analyzed by one-way ANOVA (Fig. 3B). *Clock* transcript levels showed no significant change in the presence or absence of GSK (two-way ANOVA, $p > 0.05$). Reasonably, the expression level of the *Bmal1* gene was significantly repressed in the presence of GSK (two-way ANOVA, $p < 0.05$). Consistent with Fig. 3A, the *StAR* transcript level showed a significant increase across the 24-h period in the presence of GSK. In addition, RT-PCR analysis revealed GSK stimulatory effect on *StAR* expression (Fig. 3C). Because heme is a natural ligand of Rev-erbα, the influence of heme was removed according to a previously described method [14]. qPCR data showed that GSK also significantly increased *StAR* mRNA expression in a dose-dependent manner with the depletion of endogenous heme (Fig. 3D).

4. Discussion

Rev-erbα is an important NHR in the regulation of cell physiology. Substantial evidence has shown that *Rev-erbα* is a circadian clock component in the maintenance of circadian rhythms [3,27]. GSK, as an agonist of Rev-erbα, can significantly suppress *Bmal1* gene expression through recruitment of NCo-R complex [13,14]. Here our result proved that *Bmal1* mRNA expression was indeed suppressed with the addition of GSK compared to FSH treatment only. Also, the amplitude of *Per2-dLuc oscillation* was significantly reduced in the presence of GSK. This result is quite reasonable: since *Per2* is directly under the regulation of Bmal1, the inhibition of *Bmal1* expression may downregulate *Per2* mRNA expression. Consistent with our hypothesis, a study illustrated that the expression level of *mPer2* was near baseline levels in *Bmal1*$^{-/-}$ mice [34]. In addition, our result indicated that GSK exert a *Per2* oscillation phase-shift effect on mature GCs synchronized by FSH. Indeed, a previous report showed that GSK can reset the circadian clock in rat-1 fibroblasts and mice primary lung fibroblasts in a phasic

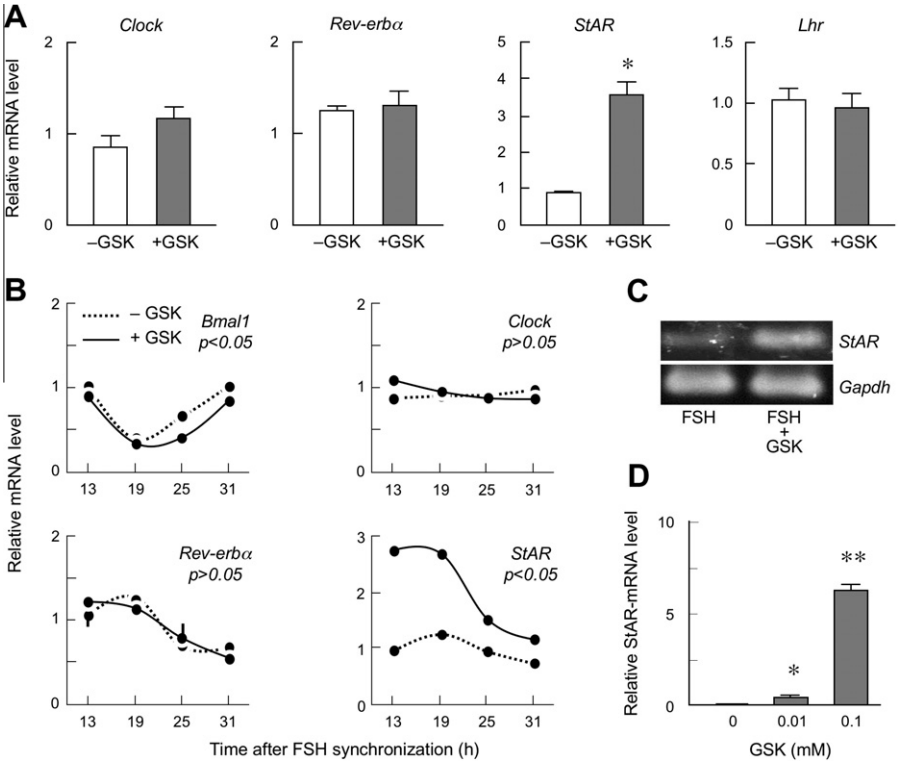

Fig. 3. Gene expression profiles fluctuation regulated by GSK. (A) Expression mRNA level of *Clock*, *Rev-erbα*, *StAR* and *Lhr* with or without GSK in the presense of FSH. Mature GCs were cultured two days *in vitro* and then treated with vehicle or vehicle + GSK (time: 0 h) in the presence of FSH. The RNA samples were collected at 24 h after the addition of GSK. Data are means ± SEM of three independent determinations. $^{*}p < 0.05$. (B) Circadan gene expression profiles under the influence of GSK. Mature GCs were synchronized by FSH with or without GSK. The RNA samples were collected at four time points according to the first *Per2-dLuc* phase. Data were analyzed by one-way ANOVA to determine variations of selected genes within one group of four timepoints. Two-way ANOVA was used to determine significant differences between FSH treatment and FSH + GSK treatment groups. (C) Stimulatory effects of GSK on *StAR* mRNA expression as revealed by RT-PCR. The RNA samples were collected at 24 h after the addition of GSK. (D) Dose-dependent induction of *StAR* mRNA level by GSK with the depletion of exogenous heme. Mature GCs were cultured two days in DMEM/F12 with the supplementation of 5% FBS. Cells were then switched to serum-free DMEM/F12 for overnight incubation to deplete heme. Then, either DMSO (vehicle control) or GSK (0.01 mM and 0.1 mM) was added and incubated with GCs for another 16 h before harvest. $^{*}p < 0.05$, $^{**}p < 0.01$.

manner [15]. The present findings proved that GSK suppressed *Bmal1* expression and altered circadian rhythms in mature GCs, as in previous studies [8,13–15]. This indicated that GSK is indeed functional in mature GCs.

In this study, we also examined the role of Rev-erbα in the regulation of *StAR*, an important gene that regulates the rate-limiting step of steroidogenesis in gonadal cells. *StAR* expression is involved with many transcription factors, such as SF-1, CCAAT/enhancer binding proteins, Sp1, DAX-1, and other transcription factors [35]. However, the role of Rev-erbα in the regulation of *StAR* expression is largely unknown. Here we showed that the Rev-erbα agonist GSK can significantly upregulate *StAR* expression in mature GCs. The result might indicate that Rev-erbα has an effect in the regulation of *StAR* expression. It is interesting to note that Rev-erbα regulates *StAR* gene expression in largemouth bass as illustrated by a recent study [36]. That study proved that a putative RORE was presented at the promoter of the *StAR* gene within largemouth bass, rats, mice and other species. It also showed that mutation of the response element significantly impeded dbcAMP-induced activation of *StAR*. Therefore it is concluded that the *StAR* gene can be directly under the regulation of Rev-erbα, which can modulate *StAR* gene expression as a repressor. In contrast, our observation appeared paradoxical, since recent studies have consistently shown that Rev-erbα is a transcriptional silencer [3,7,28]. We identified that Rev-erbα can significantly induce *StAR* expression as an activator in mature GCs. Interestingly, our result is not without precedent. For example, a recent study proved that Rev-erbβ, as a homolog of Rev-erbα, is a transcriptional activator of *Srebp-1c* in both the presence and absence of heme [37]. Moreover, the literature has suggested that some nuclear receptors can perform dual functions as transcriptional activators and repressors [38]. Apart from the AF-2 present at the C-terminal LBD, NHRs can also regulate gene expression using their N-terminus activation function-1 (AF-1) domain [39,40]. Interestingly, previous studies have shown that Rev-erbα contains a functional AF-1 domain [41]. Based on the fact that the rat *StAR* gene promoter contains putative RORE, we posit that Rev-erbα can directly modulate *StAR* gene expression as an activator. Our observations raise the interesting question of whether Rev-erbα functions in a species- and gene-specific manner, and strongly indicate that Rev-erbα can directly induce and silence gene expression. In addition, some studies have reported that *StAR* is a clock-controlled gene under the regulation of the Clock-Bmal1 heterodimer in reproductive tissues and cells [29,42,43]. Also, our study proved that *StAR* mRNA displays a 24-h pattern of changing expression. Therefore, we propose that *StAR* is a gene under the dual regulation of Bmal1 and Rev-erbα.

Acknowledgments

This work was supported by a Grant-in-Aid for Scientific Research (B) from the Japan Society for the Promotion of Sciences (JSPS; 22380152) (to M-A. H). Huatao Chen was supported by the China Scholarship Council (Grant # 2010630069).

Appendix A. Supplementary data

Supplementary data associated with this article can be found, in the online version, at http://dx.doi.org/10.1016/j.bbrc.2012.02.164.

References

[1] H. Duez, B. Staels, Rev-erbα gives a time cue to metabolism, FEBS Lett. 582 (2008) 19–25.
[2] L. Yin, J. Wang, P.S. Klein, et al., Nuclear receptor Rev-erbα is a critical lithium-sensitive component of the circadian clock, Science 311 (2006) 1002–1005.
[3] N. Preitner, F. Damiola, L.L. Molina, et al., The orphan nuclear receptor REV-ERBα controls circadian transcription within the positive limb of the mammalian circadian oscillator, Cell 110 (2002) 251–260.
[4] S.N. Ramakrishnan, G.E. Muscat, The orphan Rev-erbα nuclear receptors: a link between metabolism, circadian rhythm and inflammation?, Nucl Recept. Signal. 4 (2006) e009.
[5] M.A. Lazar, R.A. Hodin, D.S. Darling, et al., A novel member of the thyroid/steroid hormone receptor family is encoded by the opposite strand of the rat c-ErbAα transcriptional unit, Mol. Cell. Biol. 9 (1989) 1128–1136.
[6] N. Miyajima, R. Horiuchi, Y. Shibuya, et al., Two *erbA* homologs encoding proteins with different T_3 binding capacities are transcribed from opposite DNA strands of the same genetic locus, Cell 57 (1989) 31–39.
[7] L. Yin, M.A. Lazar, The orphan nuclear receptor Rev-erbα recruits the N-CoR/histone deacetylase 3 corepressor to regulate the circadian Bmal1 gene, Mol. Endocrinol. 19 (2005) 1452–1459.
[8] C. Crumbley, T.P. Burris, Direct regulation of *Clock* expression by REV-ERB, PLoS One 6 (2011) e17298.
[9] C.A. Phelan, R.T. Gampe, M.H. Lambert, et al., Structure of Rev-erbα bound to N-CoR reveals a unique mechanism of nuclear receptor-co-repressor interaction, Nat. Struct. Mol. Biol. 17 (2010) 808–815.
[10] P.M. Rogers, L. Ying, T.P. Burris, Relationship between circadian oscillations of Rev-erbα expression and intracellular levels of its ligand, heme, Biochem. Biophys. Res. Commun. 368 (2008) 955–958.
[11] L. Yin, N. Wu, J.C. Curtin, et al., Rev-erbα, a heme sensor that coordinates metabolic and circadian pathways, Science 318 (2007) 1786–1789.
[12] S. Raghuram, K.R. Stayrook, P.X. Huang, et al., Identification of heme as the ligand for the orphan nuclear receptors REV-ERBα and REV-ERBβ, Nat. Struct. Mol. Biol. 14 (2007) 1207–1213.
[13] N. Kumar, L.A. Solt, Y. Wang, et al., Regulation of adipogenesis by natural and synthetic REV-ERB ligands, Endocrinology 151 (2010) 3015–3025.
[14] D. Grant, L. Yin, J.L. Collins, et al., GSK4112, a small molecule chemical probe for the cell biology of the nuclear heme receptor Rev-erbα, ACS Chem. Biol. 5 (2010) 925–932.
[15] Q.J. Meng, A. McMaster, S. Beesley, et al., Ligand modulation of REV-ERBα function resets the peripheral circadian clock in a phasic manner, J. Cell Sci. 121 (2008) 3629–3635.
[16] T. Ueyama, K.E. Krout, X. Van Nguyen, et al., Suprachiasmatic nucleus: a central autonomic clock, Nat. Neurosci. 2 (1999) 1051–1053.
[17] T. Yamamoto, Y. Nakahata, H. Soma, et al., Transcriptional oscillation of canonical clock genes in mouse peripheral tissues, BMC Mol. Biol. 5 (2004).
[18] A. Balsalobre, Clock genes in mammalian peripheral tissues, Cell. Tissue Res. 309 (2002) 193–199.
[19] B.N. Karman, S.A. Tischkau, Circadian clock gene expression in the ovary: effects of luteinizing hormone, Biol. Reprod. 75 (2006) 624–632.
[20] S.M. Reppert, D.R. Weaver, Molecular analysis of mammalian circadian rhythms, Annu. Rev. Physiol. 63 (2001) 647–676.
[21] U. Schibler, P. Sassone-Corsi, A web of circadian pacemakers, Cell 111 (2002) 919–922.
[22] F. Damiola, N. Le Minh, N. Preitner, et al., Restricted feeding uncouples circadian oscillators in peripheral tissues from the central pacemaker in the suprachiasmatic nucleus, Gene Dev. 14 (2000) 2950–2961.
[23] R. Hara, K.K. Wan, H. Wakamatsu, et al., Restricted feeding entrains liver clock without participation of the suprachiasmatic nucleus, Genes Cells 6 (2001) 269–278.
[24] J. Fahrenkrug, B. Georg, J. Hannibal, et al., Diurnal rhythmicity of the clock genes *Per1* and *Per2* in the rat ovary, Endocrinology 147 (2006) 3769–3776.
[25] T. Yoshikawa, M. Sellix, P. Pezuk, et al., Timing of the ovarian circadian clock is regulated by gonadotropins, Endocrinology 150 (2009) 4338–4347.
[26] P.J. He, M. Hirata, N. Yamauchi, et al., Gonadotropic regulation of circadian clockwork in rat granulosa cells, Mol. Cell. Biochem. 302 (2007) 111–118.
[27] G. Triqueneaux, S. Thenot, T. Kakizawa, et al., The orphan receptor Rev-erbα gene is a target of the circadian clock pacemaker, J. Mol. Endocrinol. 33 (2004) 585–608.
[28] F. Guillaumond, H. Dardente, V. Giguere, et al., Differential control of Bmal1 circadian transcription by REV-ERB and ROR nuclear receptors, J. Biol. Rhythms 20 (2005) 391–403.
[29] M.J. Boden, T.J. Varcoe, A. Voultsios, et al., Reproductive biology of female *Bmal1* null mice, Reproduction 139 (2010) 1077–1090.
[30] M. Alexiadis, N. Eriksson, S. Jamieson, et al., Nuclear receptor profiling of ovarian granulosa cell tumors, Horm. Cancer 2 (2011) 157–169.
[31] H.R. Ueda, W.B. Chen, A. Adachi, et al., A transcription factor response element for gene expression during circadian night, Nature 418 (2002) 534–539.
[32] G.Y. Chu, K. Yoshida, S. Narahara, et al., Alterations of circadian clockworks during differentiation and apoptosis of rat ovarian cells, Chronobiol. Int. 28 (2011) 477–487.
[33] M. Hirata, P.J. He, N. Shibuya, et al., Progesterone, but not estradiol, synchronizes circadian oscillator in the uterus endometrial stromal cells, Mol. Cell. Biochem. 324 (2009) 31–38.
[34] M.K. Bunger, L.D. Wilsbacher, S.M. Moran, C.A. Bradfield, et al., *Mop3* is an essential component of the master circadian pacemaker in mammals, Cell 103 (2000) 1009–1017.
[35] A.J. Reinhart, S.C. Williams, D.M. Stocco, Transcriptional regulation of the *StAR* gene, Mol. Cell. Endocrinol. 151 (1999) 161–169.
[36] J. Kocerha, M.S. Prucha, K.J. Kroll, et al., Regulation of steroidogenic acute regulatory protein transcription in largemouth bass by orphan nuclear receptor signaling pathways, Endocrinology 151 (2010) 341–349.

[37] S.N. Ramakrishnan, P. Lau, L.M. Crowther, et al., *Rev-erbβ* regulates the *Srebp-1c* promoter and mRNA expression in skeletal muscle cells, Biochem. Biophys. Res. Commun. 388 (2009) 654–659.

[38] F.A. Pereira, M.J. Tsai, S.Y. Tsai, COUP-TF orphan nuclear receptors in development and differentiation, Cell. Mol. Life Sci. 57 (2000) 1388–1398.

[39] K.D.S.A. Wansa, J.M. Harris, G.E.O. Muscat, The activation function-1 domain of Nur77/NR4A1 mediates trans-activation, cell specificity, and coactivator recruitment, J. Biol. Chem. 277 (2002) 33001–33011.

[40] K.D.S.A. Wansa, J.M. Harris, G. Yan, P. Ordentlich, G.E.O. Muscat, The AF-1 domain of the orphan nuclear receptor NOR-1 mediates trans-activation, coactivator recruitment, and activation by the purine anti-metabolite 6-mercaptopurine, J. Biol. Chem. 278 (2003) 24776–24790.

[41] L.J. Burke, M. Downes, V. Laudet, et al., Identification and characterization of a novel corepressor interaction region in RVR and Rev-erbAα, Mol. Endocrinol. 12 (1998) 248–262.

[42] J.D. Alvarez, A. Hansen, T. Ord, P. Bebas, et al., The circadian clock protein BMAL1 is necessary for fertility and proper testosterone production in mice, J. Biol. Rhythms 23 (2008) 26–36.

[43] N. Nakao, S. Yasuo, A. Nishimura, et al., Circadian clock gene regulation of steroidogenic acute regulatory protein gene expression in preovulatory ovarian follicles, Endocrinology 148 (2007) 3031–3038.

Biochemical and Biophysical Research Communications 420 (2012) 380–384

Contents lists available at SciVerse ScienceDirect

Biochemical and Biophysical Research Communications

journal homepage: www.elsevier.com/locate/ybbrc

Mechanisms involved in inhibition of chondrogenesis by activin-A

Sho Mitsugi [a,b], Wataru Ariyoshi [b], Toshinori Okinaga [b], Takeshi Kaneuji [b], Yoshihiro Kataoka [a,b], Tetsu Takahashi [a], Tatsuji Nishihara [b,*]

[a] Division of Oral and Maxillofacial Reconstructive Surgery, Department of Oral and Maxillofacial Surgery, Kyushu Dental College, Kitakyushu 803-8580, Japan
[b] Division of Infections and Molecular Biology, Department of Health Promotion, Kyushu Dental College, Kitakyushu 803-8580, Japan

ARTICLE INFO

Article history:
Received 24 February 2012
Available online 8 March 2012

Keywords:
Activin-A
Chondrocyte
Smad
JNK
Akt

ABSTRACT

Objectives: Activin-A, a member of the TGF-β family, is known to be present in bone and cartilage. Although, involvement of the TGF-β family in chondrogenesis has been reported, the mechanism by which activin-A regulates chondrogenesis has not been fully elucidated. The aim of this study was to investigate the effects of activin-A on chondrocyte differentiation *in vitro*.
Materials and methods: Monolayer cultures of mouse chondrocyte ATDC cells were pretreated with a variety of inhibitors of major signaling pathways prior to addition of activin-A. The expressions of *sox9*, *runx2*, and *osterix* mRNA were detected using real-time PCR. To determine chondrocyte differentiation, sulfated glycosaminoglycans were stained with Alcian blue. To further elucidate the role of activin-A on chondrogenesis regulation, phosphorylation of Smad2/3, ERK, JNK, and Akt proteins was determined by western blotting.
Results: Activin-A suppressed the transcription of *sox9*, *runx2*, and *osterix* mRNA, as well as sulfated glycosaminoglycans accumulation. Activin-A also inhibited constitutive phosphorylation of JNK and Akt proteins. Furthermore, inhibition of the JNK and PI3K-Akt pathways by chemical inhibitors suppressed chondrogenesis in ATDC5 cells.
Conclusions: These results indicate that activin-A may suppress chondrocyte differentiation in ATDC5 cells via down-regulation of JNK and Akt phosphorylation.

1. Introduction

Osteoarthritis (OA), one of the most common joint disorders worldwide, is characterized by cartilage degeneration and osteophyte formation in joints. Articular cartilage has received much attention in OA studies, because gross articular cartilage damage is the most obvious pathologic feature leading to joint dysfunction. Recent studies have reported that endochondral ossification is an essential process in pathologic disorders such as osteophyte formation during OA progression [1,2].

In chondrogenesis, the transcription factor *sox9* is considered to be the master chondrogenic factor. *Sox9* is a member of a high-mobility-group DNA-binding domain that exhibits a high degree of homology with that of the mammalian testis-determining factor, *SRY* (*sex* determining region of Y chromosome) and is required for expression of such cartilage specific matrix proteins as collagen type II, IX, XI, and aggrecan [3,4]. Heterozygous mutations in the human *sox9* gene cause the skeletal malformation syndrome camptomelic dysplasia [5,6]. Studies in mice have shown that *sox9* is required for multiple steps along the chondrocyte differentiation pathway. In addition, *sox9*-deficient cells are known to not participate in mesenchymal condensation and do not express extra-cellular matrix (ECM) genes, which are known to be activated by *sox9* in chondrocytes [7]. *Sox9*-deficient cells are excluded from cartilage primordia throughout embryonic development [8]. In addition, cartilage is highly hypoplastic in *Col2a1-Cre-sox9*$^{flox/flox}$ conditional knockout mice, in which *sox9* expression is lost in condensed mesenchymal cells before differentiation into chondrocytes [9]. These findings suggest that expression of *sox9* in differentiated chondrocyte lineage cells is essential for cell survival.

Members of the transforming growth factor β (TGF-β) family are pleiotropic cytokines that are involved in inducing various kinds of cell differentiation [10]. Activins are closely related to their natural antagonists, inhibins, which are comprised of a common α subunit coupled to 1 of 2 β subunits leading to inhibin-A (αβA) or inhibin-B (αβB). Homo- and heterodimerization of the αβA and αβB subunits

Abbreviations: OA, osteoarthritis; SRY, sex determining region of Y chromosome; ECM, extracellular matrix; DMEM, Dulbecco's modified Eagle's medium; FBS, fetal bovine serum; TGF-β, transforming growth factor β; ERK, extracellular signal-regulated kinase; JNK, c-Jun N-terminal kinase; FBS, fetal bovine serum; PI3K, phosphatidylinositol-3-kinase; PBS, phosphate-buffered saline; RT-PCR, reverse-transcription polymerase chain reaction; SDS–PAGE, SDS–polyacrylamide gel electrophoresis; R-SMADs, regulatory transcription factors of the SMAD family; TAK1, TGF-β activated kinase-1.

* Corresponding author. Address: 2-6-1 Manazuru, Kokurakita-ku, Kitakyushu 803-8580, Japan. Fax: +81 93 581 4984.
E-mail address: tatsujin@kyu-dent.ac.jp (T. Nishihara).

0006-291X/$ - see front matter © 2012 Elsevier Inc. All rights reserved.
http://dx.doi.org/10.1016/j.bbrc.2012.03.003

result in formation of activin-A (βAβA), activin-AB (βAβB), or activin-B (βBβB) [11]. Although activin-A is known to be present in bone and cartilage, neither activin-B nor activin-AB have been detected in bone [12]. Although several studies have reported the role of activin-A in bone metabolism, conflicting evidence exists concerning the role of activin-A in bone formation and destruction, while it has also been reported to inhibit and stimulate osteoblastogenesis *in vitro*, and promote osteoclast formation *in vitro* [13–16]. *In vivo* studies have revealed that direct administration of activin-A increases bone mineral density [17], whereas overexpression of inhibin-A, which blocks activin-A and other TGF-β family members, increases bone mass [18,19].

Several researchers have reported involvement of the TGF-β family in chondrogenesis, though less attention has been paid to the impact of activin-A signaling on chondrocyte differentiation. In the present study, we examined the mechanisms by which activin-A inhibits chondrocyte differentiation in chondrogenesis.

2. Materials and methods

2.1. Reagents and antibodies

Dulbecco's modified Eagle's medium (DMEM) and Ham's F-12 medium were obtained from Gibco BRL (Grand Island, NY, USA). Recombinant human activin-A was kindly provided by Institute for Innovation, Ajinomoto Co. (Kanagawa, Japan). Anti-phospho-Smad2 monoclonal, anti-Smad2/3 polyclonal, anti-phospho-extracellular signal-regulated kinase (ERK) monoclonal, anti-ERK polyclonal, anti-phospho-c-Jun N-terminal kinase (JNK) monoclonal, anti-phospho-Akt monoclonal, and anti-Akt polyclonal antibodies were purchased from Cell Signaling Technology Inc. (Beverly, MA, USA). Anti-JNK monoclonal antibody was obtained from R&D Systems Inc. (Minneapolis, MN, USA) and anti-β-actin monoclonal antibody was purchased from Sigma (St. Louis, MO, USA).

2.2. Cell culture

Mouse chondrocyte ATDC5 cells were purchased from Riken Cell Bank (Ibaraki, Japan) and maintained in a 1:1 mixture of DMEM/Ham's F-12 medium containing 5% fetal bovine serum (FBS), 100 U/ml penicillin G and 100 μg/ml streptomycin, 10 μg/ml human transferring, and 3×10^{-8} M sodium selenite at 37 °C in an atmosphere of 5% CO_2.

ATDC5 cells were incubated in a serum-free 1% FBS for 24 h, then treated with FBS-free medium for the experiment, and incubated with activin-A for the indicated times. For signaling inhibition assays, ATDC5 cells were pre-treated with inhibitors of type I TGF-β receptor kinase (A-83-01, Santa Cruz Biotechnology, Santa Cruz, CA, USA), ERK (U0126, Calbiochem, San Diego, CA, USA); JNK (SP600125, Calbiochem), or phosphatidylinositol-3-kinase (PI3K)/Akt (LY294002, Calbiochem) for 1 h, then treated with activin-A for the indicated times in the presence or absence of each inhibitor.

2.3. Alcian blue staining

Chondrogenic differentiation of ATDC5 cells was determined by staining sulfated glycosaminoglycans with Alcian blue. ATDC5 cells (2.5×10^5 cells/ml) were seeded into 6-well plates, and cultured with activin-A (50 ng/ml) and human recombinant insulin (10 μg/ml) for 40 days. The medium was changed every 2 days. Cultured cells were washed and fixed with 4% paraformaldehyde at room temperature for 10 min. After washing in phosphate-buffered saline (PBS; pH7.2), the cells were incubated overnight at room temperature with Alcian Blue Solution (pH2.5; Nacalai tesque, Kyoto Japan). After being rinsed with distilled water, the results were recorded with a digital camera.

2.4. Quantitative real-time reverse-transcription polymerase chain reaction (RT-PCR)

Total RNA was extracted using an RNeasy Mini Kit (QIAGEN Inc., Valencia, CA, USA), according to the manufacturer's instructions. Obtained RNA was transcribed with SuperScript Reverse Transcriptase II (Invitrogen, Carlsbad, CA, USA) and amplified using a Mastercycler gradient (Ependorf AG, Hamburug, Germany). PCR products were detected using FAST SYBR® Green Master Mix (Applied Biosystems, Foster Cith, CA, USA) using the following primer sequences: *gapdh* forward: 5′-GACGGCCGCATCTTCTTGA-3′ and reverse: 5′-CACACCGACCTTCACCATTTT-3′, *runx2* forward: 5′-GCCGAGCTCCGAA ATGC-3′ and reverse: 5′-AGATCGTTGAACCTGGCTACTTG-3′, *osterix* forward: 5′-TCTGTTCCAAGCGCTTTACCA-3′ and reverse: 5′-CGTGGGTGCGCTGA TGT-3′, and *sox9* forward: 5′-ACCCACCACTCCCAAAACC-3′ and reverse: 5′-CGCCCCTCTCGCTTCAG-3′. Thermal cycling and fluorescence detection were performed using a StepOne™ Real-Time System (Applied Biosystems). The fold increase in copy numbers of mRNA was calculated as the relative ratio of the target gene to *gapdh*.

2.5. Western blotting analysis

The total protein was extracted using Cell Lysis Buffer (Cell Signaling Technology). Protein contents were measured using a DC protein assay kit (Bio-Rad, Hercules, CA, USA). Equivalent amounts of total protein per sample were electrophoresed using SDS–polyacrylamide gel electrophoresis (SDS–PAGE) and then transferred to polyvinylidene difluoride membranes (Millipore Corp., Bedford, MA, USA). Non-specific binding sites were blocked by immersing the membrane in 10% skim milk in PBS for 60 min at room temper-

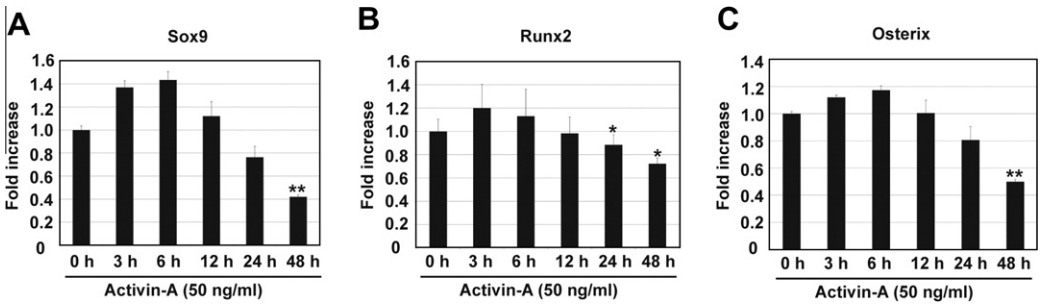

Fig. 1. Activin-A suppresses *sox9*, *runx2*, and *osterix* expression. ATDC5 cells were incubated with activin-A (50 ng/ml) for the indicated times, then total RNA was isolated and reverse-transcribed into cDNA using PCR amplification with SYBR green. PCR amplification was performed using primers specific for (A) *sox9*, (B) *runx2*, and (C) *osterix* and *gapdh*. Fold changes in *sox9*, *runx2*, and *osterix* mRNA copy number values shown represent the average ± SD of data derived from triplicate cultures. $^{*}P < 0.05$; $^{**}P < 0.01$, by Student's *t*-test.

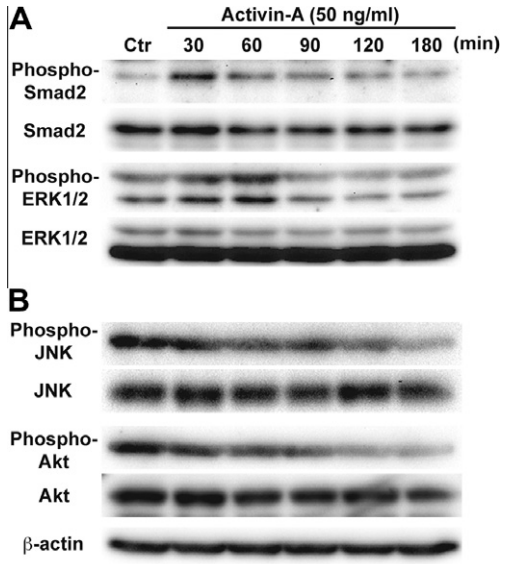

Fig. 2. Activin-A enhances smad2 and ERK phosphorylation, and suppresses JNK and Akt phosphorylation. ATDC5 cells were incubated with activin-A (50 ng/ml) for the indicated times, then whole cell lysates were analyzed by SDS–PAGE and western blotting analyses. (A) Expressions of phosphorylated Smad2 and ERK1/2. (B) Expressions of phosphorylated JNK and Akt. Following visualization, the western blots were stripped and re-probed for Smad2, ERK, JNK, Akt, and β-actin.

ature. After that, the membrane was washed 4 times with PBS, followed by incubation with the diluted primary antibody at 4 °C. Anti-phopsho-Smad2, anti-Smad2/3, anti-phospho-ERK1/2, anti-ERK1/2, anti-phospho-JNK, anti-JNK, anti-phospho-Akt, anti-Akt, and anti-β-actin were used as the primary antibodies, while horseradish peroxidase-conjugated anti-mouse and anti-rabbit IgG were used as secondary antibodies (GE Healthcare, Little Chalfont, UK). After washing the membranes, chemiluminescence was produced using ECL reagent (Amersham Pharmacia Biotech, Upspsala, Sweden).

2.6. Statistical analysis

Statistical differences were determined using an unpaired Student's *t*-test with Bonferroni's correction for multiple comparisons. *P* values less than 0.05 were considered significant. All data are expressed as the mean ± standard deviation (SD).

3. Results

3.1. Effect of activin-A on chondrocyte differentiation

To determine the effect of activin-A on chondrocyte differentiation, we assessed the mRNA expressions of *sox9*, *runx2*, and *osterix* as typical markers of chondrocyte differentiation. As early as after 24 h of incubation with activin-A, there was a decrease in *sox9* mRNA copies as compared to the untreated control chondrocytes (Fig. 1A). This effect of activin-A was time-dependent, with the

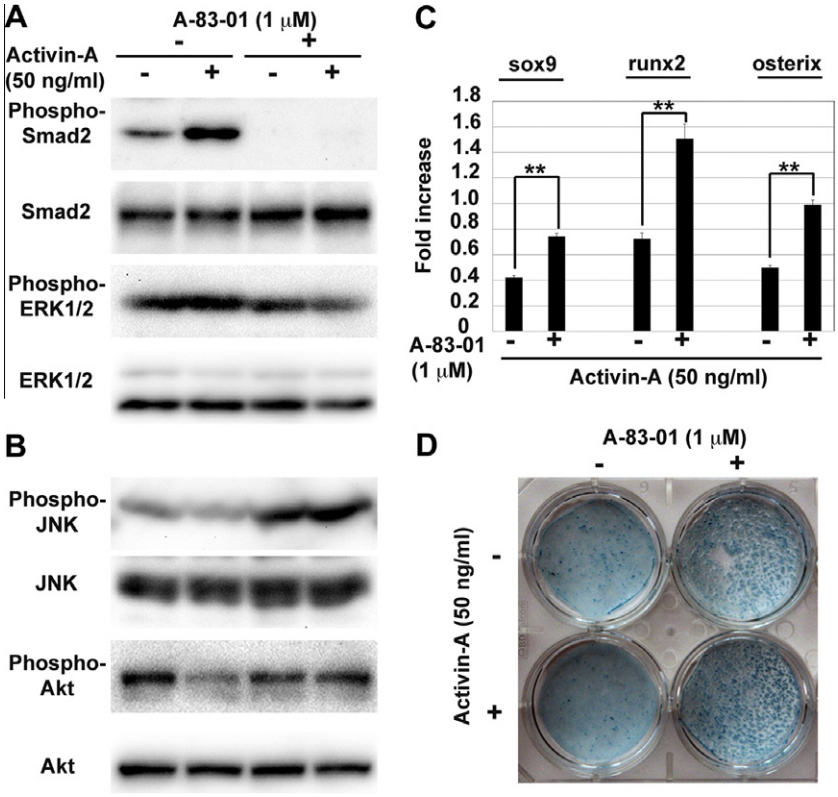

Fig. 3. Type I TGF-β receptor kinase inhibition recovered activin-A-dependent suppression of chondrogenesis. ATDC5 cells were pre-incubated with A-83-01 (1 μM) for 60 min as well as during the addition of activin-A (50 ng/ml) for the indicated times. Whole cell lysates were analyzed by SDS–PAGE and western blotting analyses. (A) Expressions of phosphorylated Smad2 and ERK1/2. (B) Expressions of phosphorylated JNK and Akt. Following visualization, the western blots were stripped and re-probed for Smad2, ERK, JNK, Akt, and β-actin. (C) Total RNA was isolated and reverse-transcribed into cDNA using PCR amplification with SYBR green. PCR amplification was performed using *sox9*, *runx2*, *osterix*, and *gapdh*. Fold changes in *sox9*, *runx2*, and *osterix* mRNA copy number values shown represent the average ± SD of data derived from triplicate cultures. $^{**}P < 0.01$, by Student's *t*-test. (D) ATDC5 cells were cultured with activin-A (50 ng/ml) in the presence or absence of A-83-01 (1 μM) for 40 days. Cultured cells were fixed with 4% paraformaldehyde and stained with Alcian blue.

maximum reduction observed after 48 h. As shown in Fig. 1B, C, treatment with activin-A also produced a statistically significant reduction in *runx2* and *osterix* mRNA expression by 24 h, and reached maximal reduction at 48 h.

3.2. Effect of activin-A on signal transduction

Next, we examined the phosphorylation levels of signaling molecules in the process of chondrogenic differentiation in ATDC5 by western blotting. Treatment with activin-A enhanced the amount of phosphorylated Smad2 (Phospho-Smad2) and ERK1/2 (phospho-ERK1/2) protein after 30 min (Fig. 2A). Furthermore, the levels of phosphorylated JNK (phospho-JNK) and Akt (phospho-Akt) were down-regulated following addition of activin-A in a time dependent manner up to 180 min (Fig. 2B). However, activin-A caused no change in p38 MAPK phosphorylation (data not shown).

3.3. Effect of type I TGF-β receptor kinase inhibitor on activin-A dependent suppression of chondrogenesis

To evaluate the role of Smad2, a key transducer of activin-A signaling in the regulation of chondrogenesis, ATDC5 cells were treated with type I TGF-β receptor kinase inhibitor (A-83-01) prior to stimulation with activin-A. The activin-A-induced phosphorylation of Smad2 and ERK was blocked by A-83-01 (Fig. 3A). In contrast, type I TGF-β receptor kinase inhibition prevented the inhibition of JNK and Akt phosphorylation by activin-A (Fig. 3B). Real-time RT-PCR revealed that A-83-01 blocked down-regulation of the mRNA expressions of *sox9*, *runx2*, and *osterix* by activin-A (Fig. 3C). To assess the effect of targeting activin-A on chondrocyte differentiation, we determined the effect of activin-A on cartilaginous matrix accumulation *in vitro*. Activin-A blocked the matrix accumulation of ATDC5, whereas A-83-01 prevented its inhibitory activity (Fig. 3D).

3.4. Effects of chemical inhibitors of signaling pathways on activin-A dependent suppression of chondrogenesis

To further elucidate the participation of the signaling molecules in response to activin-A, ATDC5 cells were treated with chemical inhibitors of the signaling pathway. Following treatment with SP600125 and LY294002, a substantial inhibition of JNK and Akt phosphorylation was observed (Fig. 4A). Both inhibitors down-regulated the expression of *sox9* mRNA (Fig. 4B, C). However, inhibitors of ERK (U0126) did not change *sox9* mRNA expression (data not shown).

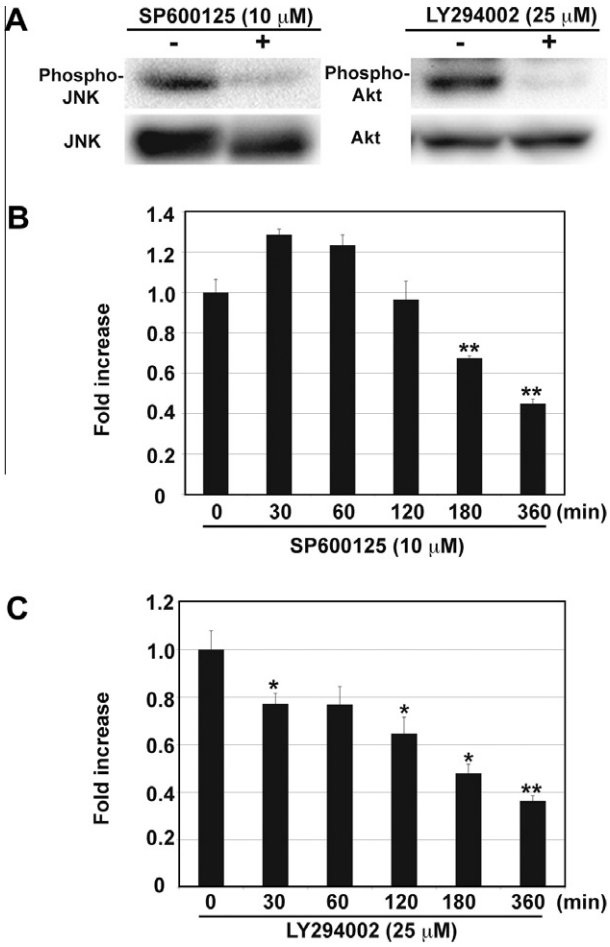

Fig. 4. Inhibitors of JNK and PI3K-Akt pathways suppress *sox9* mRNA expression. ATDC5 cells were incubated with SP600125 (10 μM) or LY294002 (10 μM) for the indicated times. (A) Whole cell lysates were probed using antibodies specific for phosphorylated JNK and Akt. Following visualization, the western blots were stripped and re-probed for JNK and Akt. (B, C) Total RNA was isolated and reverse-transcribed into cDNA using PCR amplification with SYBR green. PCR amplification was performed using *sox9*, and *gapdh*. Fold changes in *sox9* mRNA copy number values shown represent the average ± SD of data derived from triplicate cultures. $^{*}P < 0.05$; $^{**}P < 0.01$, by Student's *t*-test.

4. Discussion

In the present study, we used a clonal population of murine chondrogenic ATDC5 cells to elucidate the direct effect of activin-A on chondrocyte differentiation. ATDC5 cells were originally isolated from a differentiating culture of AT805 murine feeder-independent teratocarcinoma stem cells that expressed a fibroblastic cell phenotype in the growth phase on the basis of chondrogenic potential [20]. This cell line is known to be a useful *in vitro* model for examining chondrogenic differentiation [21,22] and endochondral ossification [21,23,24]. The main advantage of this system is that it does not contain any osteoblast/bone marrow stromal cells, which may also be targets of activin-A activity. We focused on chondro-progenitor cells to examine the effects of activin-A on differentiation and proteoglycan synthesis.

We found that activin-A suppressed chondrogenesis-related gene expression, including expressions of *sox9*, *runx2*, and *osterix in vitro*, while blocking activin-A signaling stimulated chondrocyte differentiation (Fig. 1). These findings are consistent with reports showing that activin-A acts as an inhibitor of chondrogenic differentiation in limb bud mesodermal cells [25], while they are in contrast with other studies showing that activin-A slightly stimulates proteoglycan synthesis in bovine articular cartilage [26]. We have no explanation for the reason of the discrepancy, though it may be due to differences in the cell lines used in these studies. Interestingly, we found that A-83-01 alone increased proteoglycan synthesis of ATDC5 (Fig. 3D). One explanation for this observation is that this agent binds activin-A, which endogenously enhanced proteoglycan synthesis.

TGF-β has been widely proven to regulate cell differentiation by triggering a large variety of signaling cascades, including the Smad family, and is tightly controlled by feedback mechanisms at different levels. Among them, activation of Ras, ERK1/2, and JNK by TGF-β signaling have been reported in primary intestinal epithelial cells and some breast cancer cell lines [27,28]. In addition, TGF-β activated kinase-1 (TAK1), a member of the MEKK family and activator of JNK and p38 MAPK pathways [29,30], is rapidly activated by TGF-β in certain cell systems, notably in murine C2C12 monocytes [31]. In the present study, we demonstrated that Smad2/3 and, ERK1/2 pathways were rapidly and transiently activated following

treatment with activin-A in ATDC5. Conversely, activin-A treatment caused a transient suppression of JNK and Akt phosphorylation (Fig. 2). Inhibition of Smad2/3 phosphorylation by type I TGF-β receptor kinase inhibitor revealed that these alternations of ERK1/2, JNK, and PI3K-Akt pathways are required for Smad2/3 phosphorylation (Fig. 3).

OA is generally thought to result from matrix destruction due to production of proteinases caused by a cryptic stimulus. However, the molecular mechanisms of cartilage destruction in OA remain largely unknown. Previous studies have revealed that the endochondral ossification process plays a crucial role in OA development as well as in physiological skeletal growth [2,32,33]. This process starts with hypertrophic differentiation of chondrocytes characterized by type X collagen expression, followed by conversion of non-vascularized and hypotoxic cartilage tissue into highly vascular invasion [34]. Aberrant expression of key markers involved in skeletogenesis, including *sox9*, was observed in mouse OA models [35]. Furthermore, significantly elevated expressions of *runx2* and *osterix* were observed in bone samples obtained from OA patients [36]. Our results in the present study showed that activin-A reduced the gene expression of *sox9*, *runx2* and *osterix*, suggesting that the activin-A administration may be useful as pharmacotherapy for treatment of OA.

In conclusion, we found that activin-A inhibited chondrogenesis in ATDC5 cells via down-regulation of JNK and Akt phosphorylation, suggesting the possible involvement of activin-A in regulation of chondrogenesis in pathophysiological conditions *in vivo*.

References

[1] H.M. Knonenberg, Developmental regulation of the growth plate, Nature 423 (2003) 332–336.
[2] H. Kawaguchi, Endochondral ossification signals in cartilage degradation during osteoarthritis progression in experimental mouse models, Mol. Cells 25 (2008) 1–6.
[3] V. Lefebvre, W. Huang, V.R. Harley, et al., SOX9 is a potent activator of the chondrocyte-specific enhancer of the pro alpha (II) collagen gene, Mol. Cell Biol. 17 (1997) 2336–2346.
[4] V. Lefebvre, P. Li, B.A. de Crombrugghe, B, A new bone form of Sox5 (L-Sox5), Sox6 and Sox9 are coexpressed in chondrogenesis and cooperatively activate the type II collagen gene, Embo J. 17 (1998) 5718–5733.
[5] J.W. Foster, M.A. Dominguez-Steglich, S. Guioli, et al., Campomelic dysplasia and autosomal sex reversal caused by mutations in an SRY-related gene, Nature 372 (1994) 525–530.
[6] T. Wagner, J. Wirth, J. Meyer, et al., Autosomal sex reversal and campomelic dysplasia are caused by mutations in and around the SRYrelated gene SOX9, Cell 79 (1994) 1111–1120.
[7] W. Bi, J.M. Deng, Z. Zhang, R.R. Behringer, et al., Sox9 is required for cartilage formation, Nat. Genet. 22 (1999) 85–89.
[8] W. Bi, J.M. Deng, Z. Zhang, et al., Sox9 is required for cartilage formation, Nat. Genet. 22 (1999) 85–89.
[9] H. Akiyama, M.C. Chaboissier, J.F. Martin, et al., The transcription factor Sox9 has essential roles in successive steps of the chondrocyte differentiation pathway and is required forexpression of Sox5 and Sox6, Genes Dev. 16 (2002) 2813–2828.
[10] Y. Shi, J. Massague, Mechanisms of TGF-β signaling from cell membrane to nucleus, Cell 113 (2003) 685–700.
[11] Y.G. Chen, Q. Wnag, S.L. Lin, et al., Activin signaling and its role in regulation of cell proliferation, apoptosis, and carcinogenesis, Exp. Biol. Med. 231 (2006) 534–544.
[12] Y. Ogawa, D.K. Schmidt, R.M. Nathan, et al., Bovine bone activin enhances bone morphogenetic protein-induced ectopic bone formation, J. Biol. Chem. 267 (1992) 14233–14237.
[13] T. Ikenoue, S. Jingushi, K. Urabe, et al., Inhibitory effects of activin-A on osteoblast differentiation during cultures of fetal rat calvarial cells, J. Cell Biochem. 75 (1999) 206–214.
[14] D. Gaddy-Kurten, J.K. Coker, E. Abe, et al., Inhibin suppresses and activin stimulates osteoblastogenesis and osteoclastogenesis in murine bone marrow cultures, Endocrinology 143 (2002) 74–83.
[15] M. Eijken, S. Swagemakers, M. Koedam, et al., The activin A-follistatin system: potent regulator of human extracellular matrix mineralization, FASEB J. 11 (2007) 2949–2960.
[16] K. Fuller, K.E. Bayley, T.J. Chambers, Activin-A is and essential cofactor for osteoclast induction, Biochem. Biophys. Res. Commun. 268 (2000) 2–7.
[17] Y. Oue, H. Kanatani, M. Kiyoki, et al., Effect of local injection of activin A on bone formation in newborn rats, Bone 15 (1994) 361–366.
[18] D.S. Perrien, N.S. Akel, P.K. Edwards, et al., Inhibin A is an endocrine stimulator of bone mass and strength, Endocrinology 148 (2007) 1654–1665.
[19] L.F. Bonewald, G.R. Mundy, Role of transforming growth factor-beta in bone remodeling, Clin. Orthp. Relat. Res. 250 (1990) 261–276.
[20] T. Atsumi, Y. Miwa, K. Kimata, et al., A chondrogenic cell line derived from a differentiating culture of AT805 teratocarcinoma cells, Cell. Diff. Dev. 30 (1990) 109–116.
[21] C. Shukunami, K. Ishizeki, T. Atusmi, et al., Cellular hypertrophy and calcification of embryonal carcinoma-derived chondrogenic cell line ATDC5 in vitro, J. Bone Miner. Res. 12 (1997) 1174–1188.
[22] S. Yamashita, M. Andoh, H. Ueno-Kudoh, et al., Sox-9 directly promotes Bapx1 gene expression to repress Runx2 in chondrocytes, Exp. Cell Res. 315 (2009) 2231–2240.
[23] H. Akiyama, Y. Hiraki, C. Shigeno, et al., 1α, 25-dihydroxyvitamin D3 inhibits cell growth and chondrogenesis of a clonal mouse EC cell line, ATDC5, J. Bone Miner. Res. 11 (1996) 22–28.
[24] C. Shukunami, C. Shigeno, T. Atumi, et al., Chondrogenic differentiation of clonal mouse embryonic cell line ATDC5 in vitro: Differentiation-dependent gene expression of parathyroid hormone (PTH)/PTH-related peptide receptor, J. Cell Biol. 133 (1996) 457–468.
[25] P. Chen, Y.M. Yu, A.H. Reddim, Chondrogenesis in chick limb bud mesodermal cells: reciprocal modulation by activin and inhibin, Exp. Cell. Res. 206 (1993) 119–127.
[26] F.P. Luytenm, P. Chen, V. Paralkar, et al., Reconbinant bone morphogenetic protein-4, transforming growth factor-β_1, and activin-A enhance the cartilage phenotype of articular chondrocytes *in vitro*, Exp. Cell Res. 210 (1994) 224–229.
[27] M.T. Hartsough, R.S. Frey, P.A. Zipfel, et al., Altered transforming growth factor signaling in epithelial cells when ras activation is blocked, J. Biol. Chem. 37 (1996) 22368–22375.
[28] R.S. Frey, K.M. Mulder, Involvement of extraxwllular signal-related kinase 2 and stress-activated protein kinase/Jin N-terminal kinase activation by transforming growth factor beta in the negative growth control of breast cancer cells, Cancer Res. 57 (1997) 628–633.
[29] M.K. Zabin, J. Bundy, H. Ernst, et al., Distinct spatial and temporal distributions of aggrecan and versican in the embryonic chick heart, Anat. Rec. 256 (1999) 366–380.
[30] K. Yamaguchi, K. Shirakabe, H. Shibuya, et al., Identification of a member of the MAPKKK family as a potential mediator of TGF-beta signal transduction, Science 270 (1995) 2008–2011.
[31] H. Hanafusa, J. Ninomiya-Tsuji, N. Masuyama, et al., Involvement of the p38 mitogen-activated protein kinase pathway in transforming growth factor-beta0induced gene expression, J. Biol. Chem. 274 (1999) 27161–27167.
[32] N. Boos, A.G. Nerlich, I. Wiest, et al., Immunohistochemical analysis of type-X-collagen expression in osteoarthritis of the hip joint, J. Orthop. Res. 17 (1999) 495–502.
[33] S. Kamemura, Y. Kawasaki, K. Hoshi, et al., Contribution of runt-related transcription factor 2 to the pathogenesis of osteoarthritis in mice after induction of knee joint instability, Arthritis Rheum. 54 (2006) 2462–2470.
[34] H.M. Kronenberg, Developmental regulation of the growth plate, Nature 423 (2003) 332–336.
[35] R. Monemdjou, F. Vasheghani, H. Fahmi, et al., Cartilage-specific deletion of PPARγ results in abnormal endochondral ossification, and cartilage growth and development, Arthritis Rheum., in press.
[36] J. Dragovic, D.B. Logar, R. Komadina, et al., Osteoblastogenesis and adipogenesis are higher in osteoarthritic than in osteoporotic bone tissue, Arc. Med. Res. 42 (2011) 392–397.

Biochemical and Biophysical Research Communications 420 (2012) 385–390

Contents lists available at SciVerse ScienceDirect

Biochemical and Biophysical Research Communications

journal homepage: www.elsevier.com/locate/ybbrc

Heregulin-β1-induced GPR30 upregulation promotes the migration and invasion potential of SkBr3 breast cancer cells via ErbB2/ErbB3–MAPK/ERK pathway

Shu-Qin Ruan [a], Zhan-Huai Wang [a], Shan-Wei Wang [b], Zhi-Xuan Fu [a], Kan-Lun Xu [b], Dong-Bo Li [c], Su-Zhan Zhang [a,*]

[a] Cancer Institute (Key Laboratory of Cancer Prevention and Intervention, China National Ministry of Education, Key Laboratory of Molecular Biology in Medical Sciences, Zhejiang Province, China), The Second Affiliated Hospital, School of Medicine, Zhejiang University, Hangzhou 310009, PR China
[b] Department of Pathology, The Second Affiliated Hospital, School of Medicine, Zhejiang University, Hangzhou 310009, PR China
[c] Division of Cardiovascular Medicine, Zhengzhou University People's Hospital, Zhengzhou University, Zhengzhou 450000, PR China

ARTICLE INFO

Article history:
Received 27 February 2012
Available online 8 March 2012

Keywords:
GPR30
Heregulin
Tamoxifen
Migration
Invasion
Breast cancer

ABSTRACT

Estrogen receptor (ER)-negative breast cancer cells are probably more aggressive with larger metastatic potential than ER-positive cells. Loss of ER in recurrent breast cancer is associated with poor response to endocrine therapy. G protein-coupled receptor 30 (GPR30) is expressed in half of ER-negative breast cancers. Tumor cell-derived heregulin-β1 (HRG-β1) is also found mainly in ER-negative cancer. In SkBr3 breast cancer cells that lack ER but express GPR30, HRG-β1 upregulates mRNA and protein levels of GPR30 by promoting ErbB2–ErbB3 heterodimerization and activating the downstream MAPK–ERK signaling pathway. Moreover, GPR30 boosts HRG-β1-induced migration and invasion of SkBr3 cells after combinative treatment with E2, 4-hydroxy-tamoxifen or the specific GPR30 agonist G-1, which are blocked by the specific GPR30 antagonist G-15 or the transfection with the small interfering RNA for GPR30. The ErbB2 inhibitor AG825 and the MEK1/2 inhibitor U0126 also partly inhibit the enhanced migration and invasion. Therefore, HRG-β1-induced migration and invasion partly depend on the upregulation of GPR30 expression through activation of the ErbB2–ERK pathway in SkBr3 cells. The results of this study indicate that the crosstalk between GPR30 and HRGs signaling is important for endocrine therapy resistance and may provide a new therapeutic way to treat breast cancer.

1. Introduction

Breast cancer is a highly heterogeneous disease in clinical and histologic forms. Five subtypes of breast cancer are proposed according to molecular analyses: luminal A and luminal B, both of which are estrogen receptor (ER)-positive; basal (ER-negative); ErbB2-overexpressing; and normal-like [1]. The decision to use endocrine therapy for breast cancer remains primarily based on the presence of ERs in tumor today [2]. Trastuzumab treatment is offered as an option for metastatic and adjuvant breast cancer over-expressing ErbB2. However, tumors in the same subtype are not likely to respond to the same treatment. Thus, the recent classification may not be enough for personalized therapy selection, and other molecular markers need to be discovered.

G protein-coupled receptor 30 (GPR30) belongs to the G protein-coupled receptors (GPCRs) family and is classified as a new ER because of its high affinity with 17β-estradiol (E2) [3]. Previous studies have demonstrated that an estrogen-dependent signaling response is observed not only in MCF-7 cells expressing ER-α, ER-β, and GPR30, but also in SkBr3 cells expressing only GPR30 [4]. Tamoxifen (TAM) and fulvestrant (ICI 182,780) are used as endocrine therapy drugs in clinical practice because they inhibit the classical estrogen receptors α and β signals in breast cancer. However, recent results indicate that TAM and fulvestrant activate multiple cellular-signaling pathways via GPR30 [5]. Moreover, a study of 321 primary breast tumors showed that 60% maintain GPR30 expression, including half of all ER-negative tumors [6]. GPR30 expression was found to correlate very strongly with tumor size, ErbB2 expression, and distant metastasis. GPR30 may become a risk factor in patients that are treated with TAM because TAM is a potent GPR30 agonist. Thus, activation of GPR30 might actually promote tissue invasion perhaps independently of ER status for those GPR30-positive breast cancers [7].

Abbreviations: GPR30, G protein-coupled receptor 30; TAM, tamoxifen; GPCR, G protein-coupled receptor; E2, 17-β-estradiol; 4-OHT, 4-hydroxy-tamoxifen; HRG, heregulin; ER, estrogen receptor; EGFR, epidermal growth factor receptor; EGF, epidermal growth factor; TGF, transforming growth factor; SDS–PAGE, sodium dodecyl sulfate–polyacrylamide gels; PVDF, polyvinylidene fluoride; siRNA, small interfering RNA.

* Corresponding author. Address: Cancer Institute, The Second Affiliated Hospital, School of Medicine, Zhejiang University, Jiefang Road#88, Hangzhou 310009, Zhejiang, PR China. Fax: +86 571 87214404.
E-mail address: suzhanzhang@gmail.com (S.-Z. Zhang).

0006-291X/$ - see front matter © 2012 Elsevier Inc. All rights reserved.
http://dx.doi.org/10.1016/j.bbrc.2012.03.004

Discordance of ER status between the primary and metastatic sites in breast cancer was frequently reported. In most studies, ER was lost during the metastatic progress [8]. Comparing the ER status of circulating tumor cells (CTCs) with the primary tumor in metastatic breast cancer patients, ER can change during the course of the disease [9]. Most of the CTCs were ER-negative despite the presence of an ER-positive primary tumor. In clinical studies, more than 10% of cancer cells that express ER in primary breast cancer is judged as ER-positive and recommended for hormone therapy. The remaining ER-negative cancer cells may become the source of recurrence and metastasis in the future because they do not respond to the endocrine treatment. ER-negative cell clusters are likely to represent a population of a more aggressive cell clone that is under clonal evolution. The size of ER-negative cell clusters appeared to increase with tumor progression [10].

Heregulins are a family of ligands for ErbB3 and ErbB4 that consists of four members: HRG1, HRG2, HRG3, and HRG4. HRGs promote ErbB3 and ErbB4 heterodimerization with other ErbB family members and activate downstream signaling transduction pathways, leading to multiple cellular responses [11]. HRGs have been proposed as an oncogene because of their important functions in various tumors [12], and are also involved in the acquisition of a hormone-independent phenotype [13] and endocrine treatment resistance [14].

The crosstalk between GPCRs and ErbBs is a good example of the interaction in multiple signaling pathways. GPR30, as a member of GPCRs, can transactivate the epidermal growth factor receptor (EGFR) signaling pathway [4]. In turn, EGFR ligands epidermal growth factor (EGF) and transforming growth factor (TGF)-α upregulate GPR30 expression in endometrial and breast cancer cells [15,16]. This positive loop has been implied to contribute to endocrine therapy resistance in breast cancer.

Few reports on the crosstalk between GPCRs and HRGs are available [17,18]. To date, little is known about the HRG2, HRG3, and HRG4 proteins. HRG1 expression in human cancers has been observed in thyroid cancers, ovarian cancers, breast cancers, and prostate tumors, further implicating its role in tumor pathogenesis [12]. HRG1 can be subdivided into α, β, and γ isoforms, with both α and β isoforms binding to the ErbB3 and ErbB4 receptors. HRG1-β is more potent than HRG1-α, and shows higher receptor affinity [19]. HRGs primarily function as paracrine signaling proteins [11]; thus, the recombinant human HRG-β1 was selected as the exogenous HRG1 to examine its ability to mediate GPR30 expression in the present study. Previous reports have revealed that EGF or HRG-β1 stimulation of ErbB2-overexpressing cells enhances vascular endothelial growth factor (VEGF) up-regulation, although HRG-β1 can up-regulate VEGF in the absence of ErbB2 over-expression [20]. SkBr3 cells were chosen as the experimental model for the present study because they express GPR30 and over-express ErbB2, but lack both ERα and ERβ [4]. In the present research, the relationship between GPR30 and HRGs in ER-negative breast cancer cells was assessed for the first time. The results improved our understanding on the mechanism of endocrine therapy resistance and may offer new perspectives for designing therapies for breast cancer.

2. Materials and methods

2.1. Cell culture and reagents

SkBr3 cells were maintained in DMEM medium (Gibco) with 10% fetal bovine serum (FBS, Gibco). The following reagents were prepared as stock according to the recommendations of the manufacturer: Recombinant human HRG-β1 (PeproTech), E2, 4-hydroxytamoxifen (4-OHT), and AG825 (Sigma–Aldrich); AG1478, LY294002, U0126, and PD98059 (Cell Signaling Technology); G-1 (Merck) and G-15 (Tocris Bioscience). All stock solutions were diluted with phenol red-free growth medium for treatments.

2.2. Western blot analysis and immunoprecipitation

Equal amounts of protein lysates were separated using 8–10% SDS–PAGE and subsequently transferred onto PVDF membranes. The membranes were incubated overnight at 4 °C with primary antibodies. After being washed with TBST, the membranes were then incubated with appropriate secondary antibody for 1 h at room temperature. Blots were visualized using EZ-ECL chemiluminescence detection kit for HRP (Bioind).

Equal amounts of proteins for immunoprecipitation were incubated with a primary antibody for 2 h at 4 °C, followed by overnight incubation with 20 μl of protein A agarose beads (Beyotime). The samples were washed three times with RIPA buffer, resuspended in 20 μl 2× SDS loading buffer, and boiled for 5 min. The proteins were then detected using western blot analysis as described above. Agarose-conjugated normal rabbit IgG (MBL) served as the negative control IgG.

The following monoclonal (m) and polyclonal (p) antibodies (Ab) were used: anti GPR30 pAb (1:250), anti-ERK2 pAb (1:2000), and anti-EGFR phospho (pY845) pAb (1:1000) (Abcam); anti-ErbB2 phospho (pY1248) pAb (1:1000) and anti-ErbB3 pAb (1:1000) (Bioworlde); anti-EGFR pAb (1:1000) and anti-Akt pAb (1:1000) (Biovision); anti-α-tublin mAb (1:2000) (Beyotime); anti-EGFR phospho (pY1068) mAb (1:5000), anti-EGFR phospho (pY1173) mAb (1:5000), anti-ErbB2 mAb (1:5000), anti-ErbB2 phospho (pY1221/pY1222) mAb (1:5000), anti-ErbB3 phospho (pY1289) mAb (1:5000), anti-ErbB4 (C-TERM) mAb (1:5000), anti-ErbB4 phospho (pY1188) mAb (1:1000), anti-Erk1 (pT202/pY204)/Erk2 (pT185/pY187) phospho mAb (1:10,000), and anti-Akt1 phospho (pS473) mAb (1:5000) (Epitomics).

2.3. Real-time quantitative polymerase chain reaction (qPCR)

Total RNA was extracted using TRIzol reagent (Invitrogen). cDNA was synthesized using PrimeScript RT reagent kit (TaKaRa) and was amplified using SYBR Premix Ex Taq (TaKaRa) following the protocols of the manufacturer. A StepOnePLUS Real-Time PCR system (Applied Biosystems) was used for qPCR. The amount of GPR30 mRNA was normalized to the internal control GAPDH. The relative target gene expression was calculated using the $2^{-\triangle\triangle Ct}$ method. The primers used were: 5′-GGTGCCAGGACAATGAAATACTC-3′ (GPR30 forward) and 5′-GATCCGCACATGACAGGTTTATTG-3′ (GPR30 reverse); 5′-GAAGGTGAAGGTCGGAGTCAAC-3′ (GAPDH forward) and 5′-CCTGGAAGATGGTGATGGGATT-3′ (GAPDH reverse).

2.4. Small interfering RNA (siRNA) transfection

Cells were grown to 80% confluence prior to transfection. siRNA against GPR30 (SiGPR30) or nonspecific presynthesized control siRNA (scrambled siRNA) were transiently transfected using Lipofectamine 2000 reagent (Invitrogen) following the instructions of the manufacturer. The sequences of SiGPR30 were 5′-GCUGUACAUUGAGCAGAAATT-3′ for sense and 5′-UUUCUGCUCAAUGUACAGCTT-3′ for antisense (GenePharma).

2.5. Migration and invasion assays

Migration experiments were performed using Boyden chambers (Costar). Cells were serum-starved for 24 h, and then incubated with the indicated treatment conditions for 24 h in phenol red and serum-free medium. Subsequently, these cells were seeded in the upper chambers at a concentration of 1×10^5 cells/well with

the indicated reagents. Approximately, 400 μl of phenol red-free medium containing 10% FBS has been previously added to the bottom wells. Cells on the bottom side of the membrane were fixed and counted after incubation at 37 °C for 48 h.

The operations in invasion assays were similar with the aforementioned migration experiments, except that the chambers were coated with 40 μl Matrigel (BD) diluted in a serum-free medium (matrigel:medium = 1:3 ratio).

2.6. Statistical analysis

Data were expressed as means ± standard deviation. The statistical analysis was performed using ANOVA followed by Newman–Keuls' test. A value of $P < 0.05$ was considered statistically significant.

3. Results and discussion

3.1. HRG-β1 up-regulates GPR30 expression in SkBr3 cells

After receiving 20 ng/ml HRG-β1 treatment for 12 h, GPR30 mRNA expression increased significantly and reached a higher level at 24 h (Fig. 1A). The elevation of GPR30 protein expression was also in a time- and concentration-dependent manner (Fig. 1B). GPR30 expression levels no longer rose continually and remained constant when the concentration of HRG-β1 exceeded 20 ng/ml and the time was over 24 h. HRG-β1 has been certified to enhance VEGF up-regulation in ErbB2-overexpressing cells [20]. Our results indicated that HRG-β1 increased GPR30 expression on mRNA and protein levels in SkBr3 cells that over-express ErbB2.

3.2. Activation of ErbB2/ErbB3–MAPK/ERK signaling pathway is involved in the mediation of GPR30 by HRG-β1

The regulatory mechanism of GPR30 was still at its preliminary stage in the past years. EGF, TGF-α, and hypoxia-inducible factor-1α (HIF-1α) have been proven to up-regulate GPR30 in several cell types [15,16,21], in which EGFR–ERK signaling pathway has a central role. HRG-β1, as a ligand for ErbB3 and ErbB4, can promote ErbB3 or ErbB4 heterodimerization with other ErbB family members, especially with ErbB2 [11]. ErbB2–ErbB3 complex and their downstream signaling are becoming increasingly important in cancer development, despite the traditional focus on EGFR or EGFR–ErbB2 pathway in cancer research [22]. Based on these findings, the possible signaling transduction pathway involved in the regulation of GPR30 by HRG-β1 in SkBr3 cells was subsequently examined. The phosphorylation of the tyrosine kinase domain residue of the ErbB family members was first evaluated after HRG-β1 addition. In EGFR, no phosphorylation was observed at Tyr1086, Tyr845, and Tyr1173, and no change was observed at Tyr1068 (data not shown). In ErbB2, the phosphorylation levels of Tyr1221/1222 and Tyr1248 sites were the same as the untreated cells (Fig. 2A). The immediate increase in the phosphorylation of ErbB3 at its Tyr1289 site persisted for at least 1 h, which was paralleled by the activation of the downstream signaling elements ERK1/2 and Akt (Fig. 2A). The total and phosphorylated ErbB4 were almost not observed (data not shown), which was consistent with previous studies [23].

Through immunoprecipitation, more ErbB2–ErbB3 heterodimer formations were observed in the SkBr3 cells after HRG-β1 treatment (Fig. 2B). EGFR–ErbB2 or ErbB2–ErbB4 heterodimer formation was not observed (data not shown). Increased phosphorylation of ErbB3 combined with ErbB2 was also detected after a 15 min treatment with HRG-β1 (Fig. 2B). These results suggested that ErbB2–ErbB3 was the primary heterodimer after HRG-β1 treatment. In SkBr3 cells, ErbB3 was only trans-phosphorylated by ErbB2 because of the impaired kinase activity of ErbB3 and the absence of ErbB4 [24]. Therefore, ErbB2–ErbB3 signaling was presumed to be very important in GPR30 up-regulation by HRG-β1. ErbB2–ErbB3 complex has been reviewed to have more potential than EGFR–ErbB2 in promoting the occurrence and development of breast cancer that over-express ErbB2 [25].

Considering that HRG-β1-induced stimulation of ErbB2–ErbB3 may activate the downstream signaling MAPK/ERK and PI3K/Akt, specific pharmacal inhibitors were used to certify the signaling pathway connected with the regulation of GPR30 expression. The ErbB2 inhibitor AG 825, the MAPK kinase inhibitor PD 98059, and the MEK1/2 inhibitor U0126 blocked ERK1/2 activation and inhibited the HRG-β1-induced GPR30 expression, whereas the EGFR inhibitor AG 1478 and the PI3K inhibitor LY294002 did not exhibit any inhibitory effect (Fig. 2C). U0126 is a highly selective inhibitor of MEK1 and MEK2, but PD 98059 is a selective inhibitor

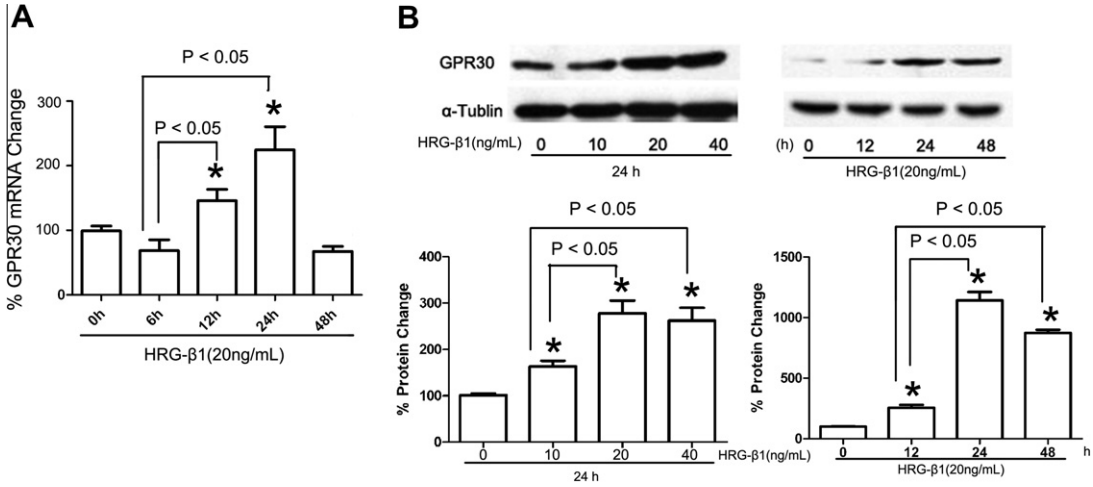

Fig. 1. Regulation of GPR30 expression by HRG-β1 in SkBr3 cells. (A) GPR30 mRNA expression was evaluated by real-time PCR. At different time points, mRNA was acquired after cells were treated with 20 ng/ml HRG-β1. GPR30 expression was normalized to GAPDH. Data shown are the mean ± SD of three independent experiments. $^{*}P < 0.05$ for cells that received treatment at different times vs. 0 h. (B) GPR30 protein expression was evaluated by Western blot. Cells were treated with different concentrations of HRG-β1 for 24 h, or with 20 ng/ml HRG-β1 for different periods. α-Tublin served as the loading control. Data represent three independent experiments. $^{*}P < 0.05$ for cells that received various treatments vs. control group.

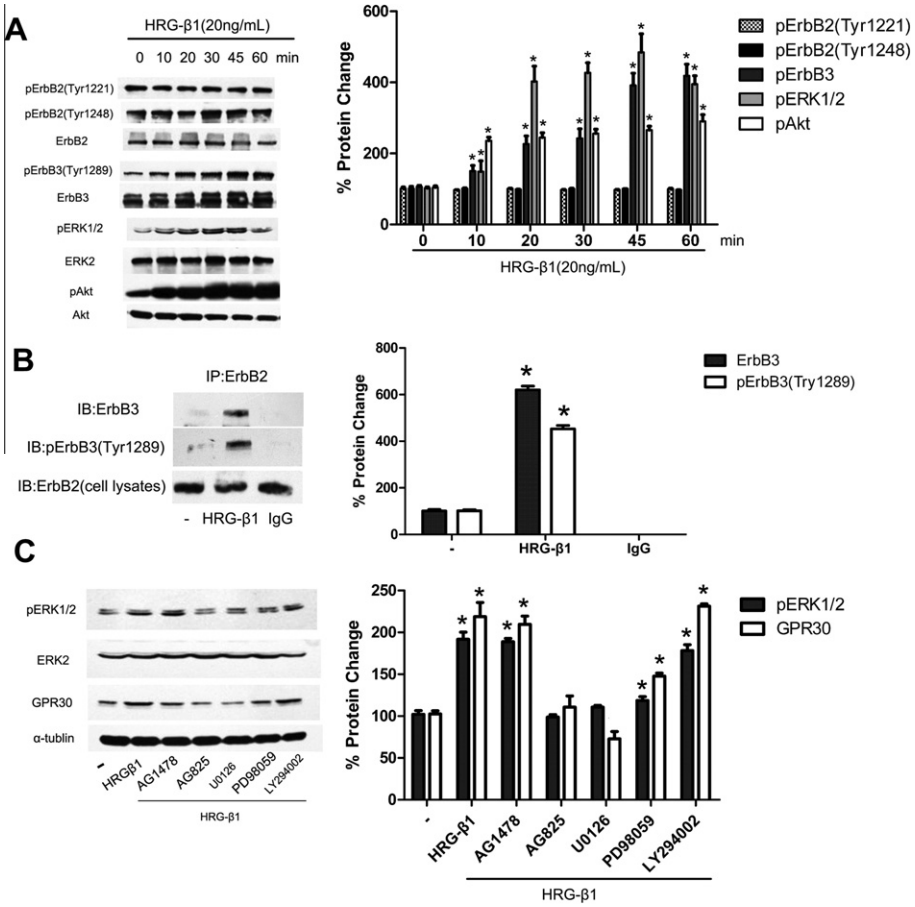

Fig. 2. Mediation of HRG-β1-induced GPR30 expression through the ErbB2–ERK signaling transduction pathway in SkBr3 cells. (A) After treatment with 20 ng/ml HRG-β1 for different periods, the total and phosphorylated protein of ErbB2, ErbB3, ERK1/2, and Akt were examined via Western blot analysis. Data represent three independent experiments. $^{*}P < 0.05$ for cells that received treatment at different times vs. 0 min. (B) After treatment with 20 ng/ml HRG-β1 for 15 min, the conformation of ErbB2/ErbB3 and pErbB3 (Tyr1289)/ErbB2 complexes was detected via coimmunoprecipitation assays. In the control samples, nonspecific IgG was used instead of the primary antibody. The cell lysate ErbB2 served as the loading control. Data represent three independent experiments. $^{*}P < 0.05$ for cells that received treatment vs. vehicle (–). (C) Cells were treated with 20 ng/ml HRG-β1 alone or in combination with the EGFR inhibitor tyrphostin AG1478 (10 μM), the ErbB2 inhibitor tyrphostin AG 825 (10 μM), the MAPK kinase inhibitor PD98059 (10 μM), the MEK1/2 inhibitor U0126 (10 μM), and the PI3K inhibitor LY294002 (10 μM). All inhibitors were pretreated for 1 h. After 24 h treatment, GPR30 and ERK1/2 phosphorylation were examined via Western blot analysis. α-Tublin was determined as the loading control. Data represent three independent experiments. $^{*}P < 0.05$ for cells that received treatment vs. vehicle (–).

of MEK1, which may be the reason for the stronger inhibitory effect of U0126 than PD 98059 on ERK1/2 activation and GPR30 expression. Our results further indicated that HRG-β1 mediated GPR30 expression through ErbB2–ERK signaling transduction pathway because ErbB3 requires the assistance of ErbB2 to function properly in SkBr3 cells as mentioned above. Previous reports indicated that ErbB2–ERK signaling pathway has been suggested to play a role in regulating GPCR expressions [26].

3.3. GPR30 up-regulation is involved in the enhanced migration and invasion by HRG-β1 in SkBr3 cells

ER-negative breast cancer is more aggressive than ER-positive disease [27], which has the inherent insensitivity to hormonal agents (tamoxifen, aromatase inhibitors). In addition, half of all ER-negative tumors express GPR30 [6]. Moreover, the ER antagonists in breast tissues, TAM and ICI 182780, act as GPR30 agonists [28]. GPR30 has been found to play a potential role in cancer progression [29] and in the development of TAM resistance [30]. Meanwhile, both HRGs and ErbB2 are linked to endocrine therapy resistance. The binding of HRGs to their receptors and the activation of the ErbB2 are relative to the decreased response to E2 in breast carcinomas. HRGs can down-regulate ER protein expression and lead to a more endocrine-independent phenotype [13]. Tumor cells-derived HRG-β1 was found mainly in ER-negative breast cancer [31]; therefore, the up-regulation of GPR30 by HRG-β1 might play a role in the biologic behavior of ER-negative breast cancer cells.

In the current study, the combination of E2, 4-OHT, or the specific GPR30 agonist G-1 with HRG-β1 treatments evidently enhanced the migration (Fig. 3A, C) and invasion (Fig. 3B, D) of SkBr3 cells stimulated by each reagent used alone. The effects of migration and invasion were partly blocked by the specific GPR30 antagonist G-15. This finding was further confirmed by GPR30 knockdown using siRNA for GPR30. These findings implied that breast cancer cells expressing GPR30 with endocrine treatment may have more potential metastasis after HRG-β1 stimulation.

As aforementioned, ErbB2–ERK signaling pathway was involved in GPR30 up-regulation by HRG-β1, which probably plays a role in the mediation of cellular biologic functions as well. The potential signaling pathway involved in the migration and invasion by HRG-β1 was subsequently investigated. The enhanced migration (Fig. 3C) and invasion (Fig. 3D) of SkBr3 cells stimulated by the combination of G-1 with HRG-β1 or each reagent used alone were partly blocked by the ErbB2 inhibitor AG825 and the MEK1/2 inhibitor U0126. Therefore, the migration and invasion induced

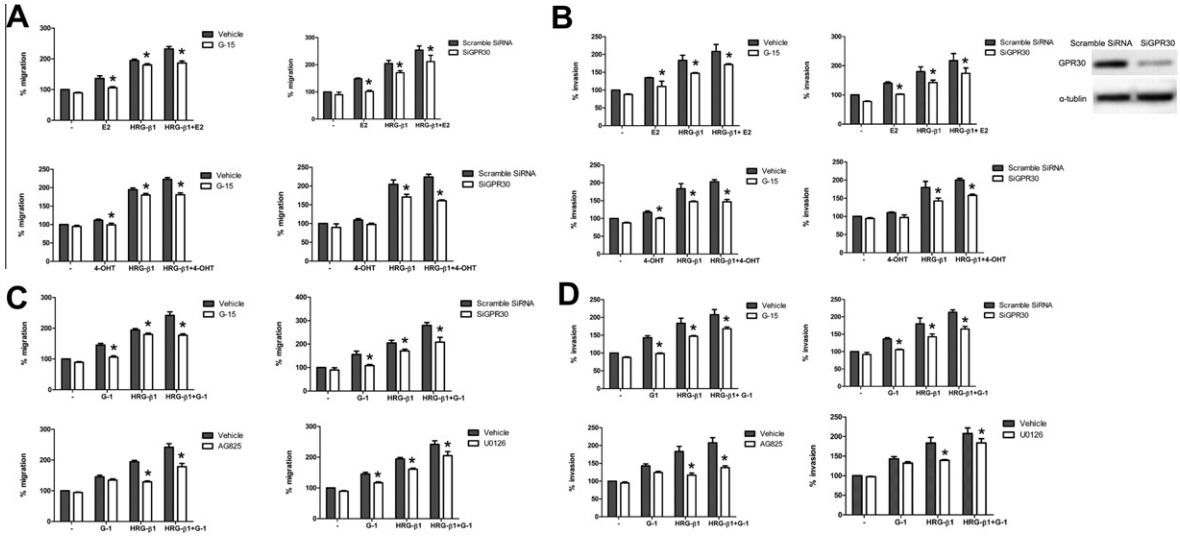

Fig. 3. Involvement of GPR30 in the migration and invasion promoted by HRG-β1 in SkBr3 cells. After incubated with the indicated reagents for 48 h, cells were counted under eight high-power fields per filter. Each data point is the mean ± SD of three independent experiments. (A, B) The migration and invasion of SkBr3 cells induced by 10 nM E2, 100 nM 4-OHT alone, or in combination with 20 ng/ml HRG-β1 were abolished by 1 μM G-15 or GPR30 silencing. $^{*}P < 0.05$, for cells that received vehicle vs. G-15, or for cells transfected with scrambled siRNA vs. siGPR30. (C), (D) The migration and invasion of SkBr3 cells induced by 1 μM G-1 alone or in combination with 20 ng/ml HRG-β1 were abolished by 1 μM G-15, GPR30 silencing, 10 μM AG825 or 10 μM U0126. $^{*}P < 0.05$, for cells that received vehicle vs. different inhibitors, or for cells transfected with scrambled siRNA vs. siGPR30.

by HRG-β1 partly depends on the up-regulation of GPR30 expression through the activation of ErbB2–ERK pathway in SkBr3 cells.

In follow-on research, the relationship between HRGs and GPR30 needs to be assessed in tissue samples of breast cancer patients, especially in samples that over-express ErbB2. Considering that changes of receptor status may take place between the primary tumor and the metastatic sites, examination of the receptor expression in the associated metastatic tumor is also necessary before and after endocrine therapy as far as possible.

In conclusion, the data presented in this study revealed that HRG-β1 up-regulates GPR30 expression in SkBr3 breast cancer cells through ErbB2/ErbB3–MAPK/ERK signaling pathway. Moreover, GPR30 boosts HRG-β1-induced migration and invasion of SkBr3 cells after combinative treatment with E2, 4-OHT, or G-1, which is blocked by inhibiting ErbB2–ERK pathway. All of these results imply that the communication between GPR30 and HRG-β1 may play an important role in endocrine therapy resistance and metastasis of breast cancer. Moreover, the current findings may facilitate the development of new strategies in controlling human breast cancer. The combination of GPR30 antagonist with the inhibitor of ErbBs signaling pathway may become a promising therapy method for ER-negative breast cancers that express GPR30.

Acknowledgments

This work was supported by National Natural Science Foundation of China (No. 30801341) and The Research Fund for the Doctoral Program of Higher Education (China, No. 200803351107).

References

[1] C.M. Perou, T. Sorlie, M.B. Eisen, M. van de Rijn, S.S. Jeffrey, C.A. Rees, J.R. Pollack, D.T. Ross, H. Johnsen, L.A. Akslen, O. Fluge, A. Pergamenschikov, C. Williams, S.X. Zhu, P.E. Lonning, A.L. Borresen-Dale, P.O. Brown, D. Botstein, Molecular portraits of human breast tumours, Nature 406 (2000) 747–752.

[2] A.U. Buzdar, G. Hortobagyi, Update on endocrine therapy for breast cancer, Clin. Cancer Res. 4 (1998) 527–534.

[3] E.J. Filardo, P. Thomas, GPR30: a seven-transmembrane-spanning estrogen receptor that triggers EGF release, Trends Endocrinol. Metab. 16 (2005) 362–367.

[4] E.J. Filardo, J.A. Quinn, K.I. Bland, A.J. Frackelton, Estrogen-induced activation of Erk-1 and Erk-2 requires the G protein-coupled receptor homolog, GPR30, and occurs via trans-activation of the epidermal growth factor receptor through release of HB-EGF, Mol. Endocrinol. 14 (2000) 1649–1660.

[5] E.R. Prossnitz, L.A. Sklar, T.I. Oprea, J.B. Arterburn, GPR30: a novel therapeutic target in estrogen-related disease, Trends Pharmacol. Sci. 29 (2008) 116–123.

[6] E.J. Filardo, C.T. Graeber, J.A. Quinn, M.B. Resnick, D. Giri, R.A. DeLellis, M.M. Steinhoff, E. Sabo, Distribution of GPR30, a seven membrane-spanning estrogen receptor, in primary breast cancer and its association with clinicopathologic determinants of tumor progression, Clin. Cancer Res. 12 (2006) 6359–6366.

[7] D.P. Pandey, R. Lappano, L. Albanito, A. Madeo, M. Maggiolini, D. Picard, Estrogenic GPR30 signalling induces proliferation and migration of breast cancer cells through CTGF, EMBO J. 28 (2009) 523–532.

[8] L. Pusztai, G. Viale, C.M. Kelly, C.A. Hudis, Estrogen and HER-2 receptor discordance between primary breast cancer and metastasis, Oncologist 15 (2010) 1164–1168.

[9] B. Aktas, V. Muller, M. Tewes, J. Zeitz, S. Kasimir-Bauer, C.R. Loehberg, B. Rack, A. Schneeweiss, T. Fehm, Comparison of estrogen and progesterone receptor status of circulating tumor cells and the primary tumor in metastatic breast cancer patients, Gynecol. Oncol. 122 (2011) 356–360.

[10] Y.H. Hsiao, M.C. Chou, C. Fowler, J.T. Mason, Y.G. Man, Breast cancer heterogeneity: mechanisms, proofs, and implications, J. Cancer 1 (2010) 6–13.

[11] D.L. Falls, Neuregulins: functions, forms, and signaling strategies, Exp. Cell Res. 284 (2003) 14–30.

[12] L.M. Gilmour, K.G. Macleod, A. McCaig, J.M. Sewell, W.J. Gullick, J.F. Smyth, S.P. Langdon, Neuregulin expression, function, and signaling in human ovarian cancer cells, Clin. Cancer Res. 8 (2002) 3933–3942.

[13] T.W. Grunt, M. Saceda, M.B. Martin, R. Lupu, E. Dittrich, G. Krupitza, H. Harant, H. Huber, C. Dittrich, Bidirectional interactions between the estrogen receptor and the cerbB-2 signaling pathways: heregulin inhibits estrogenic effects in breast cancer cells, Int. J. Cancer 63 (1995) 560–567.

[14] R.J. Pietras, J. Arboleda, D.M. Reese, N. Wongvipat, M.D. Pegram, L. Ramos, C.M. Gorman, M.G. Parker, M.X. Sliwkowski, D.J. Slamon, HER-2 tyrosine kinase pathway targets estrogen receptor and promotes hormone-independent growth in human breast cancer cells, Oncogene 10 (1995) 2435–2446.

[15] L. Albanito, D. Sisci, S. Aquila, E. Brunelli, A. Vivacqua, A. Madeo, R. Lappano, D.P. Pandey, D. Picard, L. Mauro, S. Ando, M. Maggiolini, Epidermal growth factor induces G protein-coupled receptor 30 expression in estrogen receptor-negative breast cancer cells, Endocrinology 149 (2008) 3799–3808.

[16] A. Vivacqua, R. Lappano, P. De Marco, D. Sisci, S. Aquila, F. De Amicis, S.A. Fuqua, S. Ando, M. Maggiolini, G protein-coupled receptor 30 expression is up-regulated by EGF and TGF alpha in estrogen receptor alpha-positive cancer cells, Mol. Endocrinol. 23 (2009) 1815–1826.

[17] A.K. Fu, W.M. Cheung, F.C. Ip, N.Y. Ip, Identification of genes induced by neuregulin in cultured myotubes, Mol. Cell. Neurosci. 14 (1999) 241–253.

[18] A.M. Ratchford, O.J. Baker, J.M. Camden, S. Rikka, M.J. Petris, C.I. Seye, L. Erb, G.A. Weisman, P2Y2 nucleotide receptors mediate metalloprotease-dependent phosphorylation of epidermal growth factor receptor and ErbB3 in human salivary gland cells, J. Biol. Chem. 285 (2010) 7545–7555.

[19] H.S. Lu, D. Chang, J.S. Philo, K. Zhang, L.O. Narhi, N. Liu, M. Zhang, J. Sun, J. Wen, D. Yanagihara, A. Et, Studies on the structure and function of glycosylated and nonglycosylated neu differentiation factors. Similarities and differences of the alpha and beta isoforms, J. Biol. Chem. 270 (1995) 4784–4791.

[20] S. Xiong, R. Grijalva, L. Zhang, N.T. Nguyen, P.W. Pisters, R.E. Pollock, D. Yu, Up-regulation of vascular endothelial growth factor in breast cancer cells by the heregulin-beta1-activated p38 signaling pathway enhances endothelial cell migration, Cancer Res. 61 (2001) 1727–1732.

[21] A.G. Recchia, E.M. De Francesco, A. Vivacqua, D. Sisci, M.L. Panno, S. Ando, M. Maggiolini, The G protein-coupled receptor 30 is up-regulated by hypoxia-inducible factor-1{alpha} (HIF-1{alpha}) in breast cancer cells and cardiomyocytes, J. Biol. Chem. 286 (2011) 10773–10782.

[22] R. Pinkas-Kramarski, A.E. Lenferink, S.S. Bacus, L. Lyass, M.L. van de Poll, L.N. Klapper, E. Tzahar, M. Sela, E.J. van Zoelen, Y. Yarden, The oncogenic ErbB-2/ErbB-3 heterodimer is a surrogate receptor of the epidermal growth factor and betacellulin, Oncogene 16 (1998) 1249–1258.

[23] A. DeFazio, Y.E. Chiew, R.L. Sini, P.W. Janes, R.L. Sutherland, Expression of c-erbB receptors, heregulin and oestrogen receptor in human breast cell lines, Int. J. Cancer 87 (2000) 487–498.

[24] M. Breuleux, Role of heregulin in human cancer, Cell. Mol. Life Sci. 64 (2007) 2358–2377.

[25] J. Baselga, S.M. Swain, Novel anticancer targets: revisiting ERBB2 and discovering ERBB3, Nat. Rev. Cancer 9 (2009) 463–475.

[26] M. Shi, D. Liu, H. Duan, L. Qian, L. Wang, L. Niu, H. Zhang, Z. Yong, Z. Gong, L. Song, M. Yu, M. Hu, Q. Xia, B. Shen, N. Guo, The beta2-adrenergic receptor and Her2 comprise a positive feedback loop in human breast cancer cells, Breast Cancer Res. Treat. 125 (2011) 351–362.

[27] R.B. Brunn, C. Kamby, Immunohistochemical detection of estrogen receptors in paraffin sections from primary and metastatic breast cancer, Pathol. Res. Pract. 185 (1989) 856–859.

[28] P. Thomas, Y. Pang, E.J. Filardo, J. Dong, Identity of an estrogen membrane receptor coupled to a G protein in human breast cancer cells, Endocrinology 146 (2005) 624–632.

[29] H.O. Smith, K.K. Leslie, M. Singh, C.R. Qualls, C.M. Revankar, N.E. Joste, E.R. Prossnitz, GPR30: a novel indicator of poor survival for endometrial carcinoma, Am. J. Obstet. Gynecol. 196 (386) (2007) e1–9 (discussion 386.e9-11).

[30] A. Ignatov, T. Ignatov, C. Weissenborn, H. Eggemann, J. Bischoff, A. Semczuk, A. Roessner, S.D. Costa, T. Kalinski, G-protein-coupled estrogen receptor GPR30 and tamoxifen resistance in breast cancer, Breast Cancer Res. Treat. 128 (2011) 457–466.

[31] G. Perez-Tenorio, O. Stal, Activation of AKT/PKB in breast cancer predicts a worse outcome among endocrine treated patients, Br. J. Cancer 86 (2002) 540–545.

Biochemical and Biophysical Research Communications 420 (2012) 391–396

Contents lists available at SciVerse ScienceDirect

Biochemical and Biophysical Research Communications

journal homepage: www.elsevier.com/locate/ybbrc

Identification of methylation-dependent regulatory elements for intergenic miRNAs in human H4 cells

Kwang Hee Lee [a,c], Hyunyoung Kim [b], Byeong Jae Lee [c,d,*], Kiejung Park [a,*]

[a] Division of Bioinformatics and Bio-Medical Informatics, Center for Genome Science, National Institute of Health, Republic of Korea
[b] Division of Brain Disease, Center for Bio-Medical Science, National Institute of Health, Republic of Korea
[c] Laboratory of Molecular Genetics and Genomics, Interdisciplinary Program in Bioinformatics, Institute of Molecular Biology and Genetics, Seoul National University, Seoul 151-742, Republic of Korea
[d] School of Biological Sciences, Institute of Molecular Biology and Genetics, Seoul National University, Seoul 151-742, Republic of Korea

ARTICLE INFO

Article history:
Received 27 February 2012
Available online 8 March 2012

Keywords:
Intergenic microRNA
DNA methylation
Regulatory element

ABSTRACT

MicroRNAs (miRNAs) are important post-transcriptional regulators of various biological processes. Although our knowledge of miRNA expression and regulation has been increased considerably in recent years, the regulatory elements for miRNA gene expression (especially for intergenic miRNAs) are not fully understood. In this study, we identified differentially methylated regions (DMRs) within 1000 bp upstream from the start site of intergenic miRNAs in human neuroglioma cells using microarrays. Then we identified a unique sequence pattern, $C[N]_6CT$, within the DMRs using motif analysis. Interestingly, treatment of cells with a methyl transferase inhibitor (5-aza-2-deoxycytidine, DAC) significantly increased expression of miRNA genes with a high frequency of the $C[N]_6CT$ motif in DMRs. Statistical analysis showed that the frequency of the $C[N]_6CT$ motif in DMRs is highly correlated with intergenic miRNA gene expression, suggesting that $C[N]_6CT$ motifs associated with DNA methylation regions play a role as regulatory elements for intergenic miRNA gene expression.

1. Introduction

MicroRNAs (miRNAs) are small, non-coding RNA molecules that act as post-transcriptional regulators of gene expression by inhibiting translation or degrading mRNA genes through partial or complete base pairing with complementary sequences of target genes [1]. In addition, some miRNAs participate in the remodeling of chromatin structures [2]. miRNAs are initially transcribed as large precursor RNAs, or primary miRNAs (pri-miRNA), and sequentially processed by Drosha and Dicer to produce ~22-nucleotide-long active mature miRNAs [3–5]. miRNAs are highly conserved in multiple organisms and play crucial roles in development, cell differentiation, determination of cell fate, and cancer [6,7].

miRNA genes can be classified into two categories according to their genomic contexts: intronic and intergenic miRNAs. Intronic miRNAs are embedded within other genes. Therefore, they are thought to be transcribed by sharing promoters with host genes [8]. On the other hand, intergenic miRNAs are believed to have independent transcription units because they are positioned within flanking regions or in antisense orientation to annotated genes [9]. Intronic miRNAs are generally believed to be transcribed by RNA polymerase II (pol II); however, it remains unclear what type of RNA polymerase is responsible for intergenic miRNA transcription, although pol II and RNA polymerase III (pol III) are obvious candidates. For example, pri-miR-23a~27a~24-2 and pri-miR-21 are transcribed by pol II and have a 5′-7-methylguanosine cap structure and a 3′-polyadenylated [poly(A)] tail similar to the structure of mRNAs [10,11], while miR-517a and miR-517c, which are interspersed among Alu repeats in the human chromosome 19, are transcribed by pol III [12].

The transcriptional start site of intergenic miRNA genes usually occurs within 2 kb upstream from the start site of miRNAs [13]. Using computational methods, several conserved sequence patterns for intergenic miRNA genes, including putative promoters, have been proposed from various species [14,15]. Among these, CT repeats are most well known. They are highly conserved among four species, such as *Caenorhabditis elegans*, *Homo sapiens*, *Arabidopsis thaliana* and *Oryza sativa*, and are abundant within 1000 bp upstream sequences from miRNA hairpins [14]. Another sequence pattern, GANNNNGA, was identified within 1000 bp upstream of

Abbreviations: DMPs, differentially methylated probes; DMRs, differentially methylated regions; DAC, 5-aza-2-deoxycitidine; pol II, RNA polymerase II; pol III, RNA polymerase III; pri-miRNA, primary miRNA.

* Corresponding authors. Address: Division of Bioinformatics and Bio-Medical Informatics, Center for Genome Science, National Institute of Health, Building 2, Room 521, Osong 363-951, Republic of Korea. Fax: +82 43 719 8869 (K. Park).
E-mail address: kjpark63@gmail.com (K. Park).

0006-291X/$ - see front matter © 2012 Elsevier Inc. All rights reserved.
http://dx.doi.org/10.1016/j.bbrc.2012.03.005

worm miRNAs [15]. However, there is no direct evidence that these conserved patterns play a role as promoter or regulatory elements. Currently, the transcriptional mechanisms of most intergenic miRNAs are largely unknown.

Epigenetic signatures such as DNA methylation and histone modification, and the regulation of expression of miRNA genes are tightly linked similarly to other genes [16–19]. Recently it was reported that hypermethylation of the human miR-124 loci, which is the most abundant miRNA in the adult brain and plays a key role in neurogenesis, inhibits miR124a expression and results in brain tumors [20–22]. Interestingly, some miRNAs control the expression of epigenetic regulators, including DNA methyltransferases and histone deacethylases [23,24]. The fact that miRNA gene expression can be regulated by DNA methylation indicates the feasibility of using methylated sequences to predict miRNA gene promoters or regulatory elements.

In this study, we found a novel sequence motif, $C[N]_6CT$, for intergenic miRNA gene expression by predicting sequence patterns in the differentially methylated regions (DMRs), and by examining the relationship between the occurrence of this motif and methylation dependence of gene expression.

2. Materials and methods

2.1. Cell lines and culture

H4 cells, a human neuroglioma cell line, were purchased from the American Type Culture Collection and cultured in Dulbecco's modified Eagle's medium (DMEM; Invitrogen, Carlsbad, CA, USA) supplemented with 10% fetal bovine serum (FBS; Invitrogen, Carlsbad, CA, USA) and 1% antibiotics-antimycotics (Invitrogen, Carlsbad, CA, USA) at 37 °C in a humidified incubator containing 5% CO_2.

2.2. Identification of miRNAs from sequence and annotation data

The genomic coordinates of 1049 human miRNAs were obtained from the miRBase (ver. 16.0) [25], and all sequences and the annotated data were from the UCSC genome browser (http://genome.ucsc.edu). A total of 1049 miRNAs were classified into 621 intronic and 428 intergenic miRNAs according their genome contexts.

2.3. Probe design

Sequences up to 1000 bp upstream from the start site of 428 intergenic miRNAs were retrieved and cleaved into 60-bp-long sequences overlapped by 40 bp of adjacent sequence (Fig. 1A). Chopped sequences were filtered based on sequence redundancy, low GC ratios (GC ratio < 0.6), and low melting temperatures (Tm < 85 °C). A total of 7646 sequences were selected as probes for printing on an Agilent 15K array platform to build a customized array chip (Chip No. 253347810001).

2.4. Microarray experiment

Genomic DNA was isolated from H4 cells cultured in the presence or absence of 5 μM DAC, an inhibitor of DNA methyltransferase. Briefly, after sonicating the genomic DNA (0.5 μg), the fragments were incubated with 2 μg recombinant methylation-specific binding protein (MBD2bt) at 4 °C for 4 h on a rocking platform. The enriched methylated DNA was amplified using a Whole Genome Amplification Kit (GenomePlex®, Sigma–Aldrich, St. Louis, MO, USA) as recommended by the manufacturer's instructions. The amplified DNA from DAC-treated and untreated cells were labeled with cyanine 5 (Cy5) and cyanine 3 (Cy3), respectively. The labeled DNA samples were purified using a PCR Purification Kit (QIAquick, Qiagen, Valencia, CA, USA) and co-hybridized to the customized microarrays according to the manufacturer's protocol. The microarrays contained a total of 7646 oligonucleotide probes, including control probes and those covering the sequences upstream of the miRNA genes.

2.5. Microarray data analysis

The hybridized images were analyzed using an Agilent DNA Microarray Scanner and data quantification was performed using Feature Extraction software version 10.7.3.1 (Agilent Technologies, Palo Alto, CA, USA). Preprocessing of raw data and normalization steps were performed using R software (http://www.r-project.org). Background-corrected intensity data were normalized using the intensity-dependent LOWESS method to remove the dye bias within each array. The *p*-values for each probe were calculated using linear fit models implemented in the Limma package (http://bioconductor.org/), and the probes within the threshold (p-value < 0.05) were selected as differentially methylated probes.

2.6. Reverse transcription PCR reaction

Total RNA was isolated using the RecoverAll, Total Nucleic Acid Isolation Kit (Ambion, Austin, TX, USA), according to the manufacturer's protocol. RNA quantity and purity was determined using the NanoDrop 1000 spectrophotometer (Thermo Scientific, Rockford, IL, USA). Reverse transcription was performed using the TaqMan MicroRNA Reverse Transcription Kit (Applied Biosystems, Foster City, CA, USA). All reactions were performed as per the manufacturer's protocol. *Rnu6b* was used as a negative control.

2.7. Quantitative real-time PCR

Quantitative real-time PCR was performed to amplify miRNAs with specific primer sets against target miRNAs (Applied Biosystems, Foster City, CA, USA) using the ABI-7500 Real Time PCR system according to the manufacturer's protocol. Template (10 ng) was amplified in 20 μl reaction volumes. PCR conditions were as follows: 50 °C for 2 min, 95 °C for 10 min, 50 cycles of 95 °C for 15 s, and 60 °C for 1 min. Experiments were performed in triplicate.

2.8. Motif analysis

MEME software [26] was used to search for top-ranking degenerate motifs within the probe sequences in each cluster, and its optional parameters were set as follows: optimum motif width was set to 8–12 bp, occurrence of motif in the input sequences was set to any number of repetitions in the input sequence, and other parameters were left as default. Alignment of DMR sequences was performed using ClustalX (ver. 2.0.12) software [27] with the default parameters.

3. Results

3.1. Identification of DMRs

To identify DMRs in the upstream of miRNA genes, microarray analysis was performed using our custom chips. A total of 7646 probes against the 5′-flanking region of 428 intergenic miRNA genes were designed (Fig. 1A) and implemented on the Agilent 15K array chip platform. Genomic DNA was isolated from H4 cells cultured in the absence or presence of 5-aza-2-deoxycytidine (DAC). Methylated sequences were enriched using MBD2bt

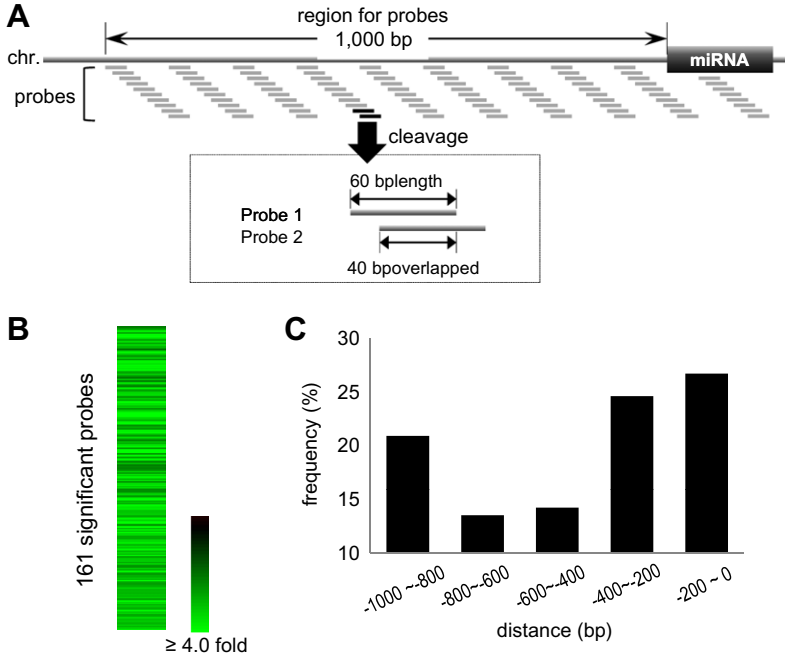

Fig. 1. Clustering and distribution of differentially methylated probes. (A) A schematic diagram of our custom designed probes. Probe sequences were retrieved from candidate regions and cleaved into 60-bp lengths with a 40-bp overlap with the adjacent probe. (B) Profiles of 161 differentially methylated probes (DMPs) identified from the 5′-flanking regions of 98 intergenic miRNAs. Green color designates hypomethylated probes, while black color represents non-methylated. (C) Distribution of DMPs in 200-bp intervals. The frequency is represented as a percentile of DMPs in each interval. (For interpretation of the references to color in this figure legend, the reader is referred to the web version of this article.)

proteins. The methyl group-enriched DNAs were labeled with fluorescent dyes and then hybridized with the probes on chips (see Section 2).

The signal intensities of the 7646 probe spots on each chip were obtained after LOESS normalization. The Pearson's correlation of signal intensities between chips was 0.99 (Supplementary Fig. S1). By performing a linear fitting and Bayes function analysis, a total of 161 probes (adjusted p-value < 0.05) were found to have different methylation levels between DAC-treated and untreated samples (Fig. 1B) and these were defined as differentially methylated probes (DMPs). These DMPs were derived from 98 intergenic miRNAs. The sequences of the DMPs are shown in Supplementary Table S1.

To determine the distribution of the DMPs on the 5′-flanking region of each gene, we calculated the relative distance of DMPs from the 5′-end of each intergenic miRNA and constructed a frequency graph for DMPs in 200-bp intervals. As shown in Fig. 1C, the majority of DMPs were located within 400 bp upstream from the start site of each miRNA, suggesting that the major DMR, which is defined as the contig of DMPs, overlaps with the region containing the transcriptional regulatory elements such as promoter and proximal sequence elements. Interestingly, there is an additional DMR (20.9% of total DMPs) spanning from -800 to -1000 where enhancers are usually found.

3.2. Prediction of sequence motifs from DMPs

Because altering genome DNA methylation usually affects the efficiency of gene expression, it can be assumed that a specific sequence motif that regulates the transcription of its target miRNA gene is located within DMRs. Therefore, we analyzed the DMP sequences to predict a sequence motif using MEME software [26], which is used to predict statistically overrepresented sequence motifs.

After performing MEME with DMP sequences, we obtained six significant sequence patterns (p-value < 1.00e−05; Fig. 2A) which were 8–11 bp long. The most significantly overrepresented pattern was CNNNNNNCT (C[N]$_6$CT, p-value = 3.22e−18). N designates a non-conserved nucleotide. CTANCCTC, CTCTNCNC, TCTNNNTNT, GAGGTNTGATC, and CNNAGNGAC were also selected as significant patterns, the p-values of which were 2.15e−07, 5.26e−07, 2.34e−05, 2.80e−05, and 8.22e−05, respectively. It should be noted that there was a significant difference between the p-values for the C[N]$_6$CT pattern and CTANCCTC (11 logarithmic order), suggesting that C[N]$_6$CT is a major sequence motif in DMRs. Interestingly, CTANCCTC and CTCTNCNC patterns, as well as C[N]$_6$CT, contain two cytosine residues at positions 1 and 8, suggesting the cytosine residues at these positions are important for these patterns.

When performing multiple sequence alignment with 161 DMPs using the ClustalX program [27], only a single consensus sequence, CNNNNNNC (C[N]$_6$C), was found in all DMPs, which was also composed of conserved cytosine residues at position 1 and 8 (see Supplementary Fig. S2). It should be noted that this C[N]$_6$C motif is highly similar to the C[N]$_6$CT pattern predicted by MEME. These results suggest that the two conserved cytosine residues at positions 1 and 8 are likely embedded in the regulatory elements, and that the C[N]$_6$CT pattern may be a potential regulatory motif for intergenic miRNA gene expression. Thus, we selected the C[N]$_6$CT pattern as a candidate motif of regulatory element for intergenic miRNA expression.

We next examined the C[N]$_6$CT pattern within 1000 bp upstream of 98 intergenic miRNAs that contain DMPs, and identified a total of 1766 C[N]$_6$CT motifs. Among the 1766 C[N]$_6$CT motifs, 189 (10.7%) were located in DMPs (Supplementary Table S2). Overall, the number of C[N]$_6$CT motifs found in DMPs is small compared to that found in non-DMPs. However, further analysis of this motif showed that each gene contains a different frequency of C[N]$_6$CT motifs in its DMPs. For example, miR-200c has three DMRs, and 16 out of 22 C[N]$_6$CT motifs (72.7%) are concentrated in the DMRs (top line in Fig. 2B). In miR-124-1, there are four largely methylated regions that contain 11 out of 28 C[N]$_6$CT motifs (39.3%)

A

Consensus	motif logo	p-value [a]
CNNNNNNCT		3.22e-18
CTANCCTC		2.15e-07
CTCTNCNC		5.26e-07
TCTNNNTNT		2.34e-05
GAGGTNTGATC		2.80e-05
CNNAGNGAC		8.22e-05

B

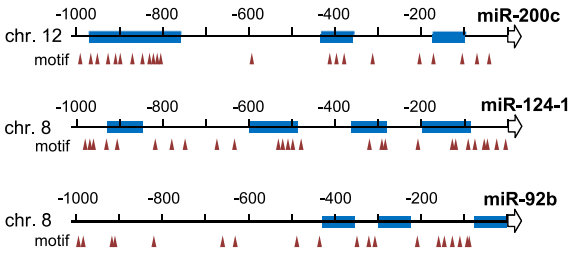

Fig. 2. Identification of significant sequence patterns and the distribution of C[N]$_6$CT motifs on the 5′-flank of intergenic miRNA genes. (A) Six highly significant motifs were identified in the DMRs using MEME software (see Section 2). Consensus designates the conserved sequence at each position. N represents non-conserved nucleotides. Motif logos are the graphically represented sequences showing homology at each position. The *p*-value designates significance of the sequences calculated against the random sequences. (B) Schematic representation of the genomic region encompassing miR-200c, miR-124-1, and miR-92b showing the distribution of C[N]$_6$CT motifs. The blue box represents DMR, which is the contig of DMPs. C[N]$_6$CT motifs are marked with triangles. All features were drawn based on the distance from the 5′-end of each miRNA.

(middle line in Fig. 2B). On the other hand, miR-92b contains three methylated regions, but there is no C[N]$_6$CT motif in these regions (bottom line in Fig. 2B).

3.3. Effect of demethylation on intergenic miRNA expression

It is important to determine whether the expression level of intergenic miRNA changes depending on the frequency of C[N]$_6$CT motifs in DMRs. Therefore, we first treated H4 cells with DAC to demethylate DNA. Then we isolated total RNA and measured the expression levels using quantitative PCR analysis against eight selected intergenic miRNA genes: one miRNA which had the highest frequency of C[N]$_6$CT motifs in DMRs (miR-200c), two with a 30–40% frequency (miR-124-1, miR-375), two with a 20–30% frequency (miR-34c, miR-210), one with a 10–20% frequency (miR-212), and two with less than 10% frequency (miR-3188 and miR-92b), all of which had more than three DMRs in their upstream regions but had no or only one C[N]$_6$CT motif in the DMRs (see Supplementary Table S2). *Rnu6b* was used as a negative control. As shown in Fig. 3, the expression levels of six of eight intergenic miRNAs (miR-200c, miR-124-1, miR-375, miR-34c, miR-210, and miR-212) increased significantly in DAC-treated cells compared to untreated normal cells. The expression level of miR-200c, which shows the highest frequency of C[N]$_6$CT motifs in DMRs (72.7%), was increased by 22.3-fold after DAC treatment. The expression levels of miR-124-1, miR-375, miR-34c, miR-210, and miR-212 were also increased by 11.3, 9.4, 8.4, 3.5, and 13.2-fold after DAC treatment, respectively. On the other hand, DAC treatment did not significantly change the expression levels of miR-92b or miR-3188. It should be noted that the frequencies of the C[N]$_6$CT motif in the DMR of miR-92b and miR-3188 are less than 10%, although they have more than three DMRs. These results strongly suggest that the frequency of C[N]$_6$CT motifs in DMRs is related to intergenic miRNA expression.

3.4. Correlations between the C[N]$_6$CT motif in DMRs and intergenic miRNA expression

Because the expression of intergenic miRNA genes were changed after DAC treatment in a motif-frequency dependent manner,

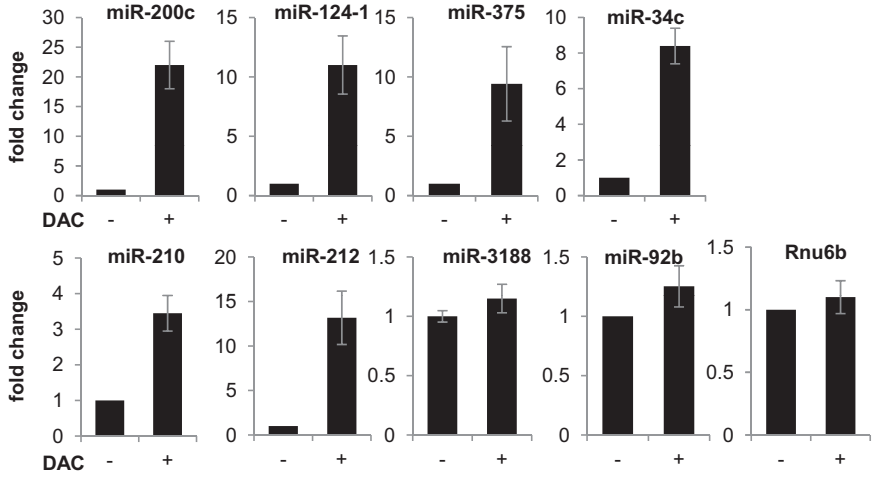

Fig. 3. Measurement of intergenic miRNA gene expression by qPCR. The intergenic miRNA levels were measured by qPCR. *Rnu6b* was used as a negative control. The *x*-axis shows the experimental condition treated with (+) and without (−) DAC, respectively. The *y*-axis represents the relative fold change of expression level of each intergenic miRNA after treating the cells with DAC. The fold change of non-treated cells was set to 1. The gene symbol is marked above each panel.

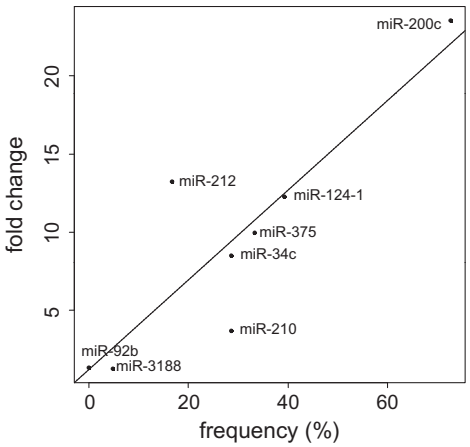

Fig. 4. Pearson's correlations between the expression levels and the frequency of the C[N]$_6$CT motif in DMRs of intergenic miRNAs. The *y*-axis represents fold change measured by RT-qPCR and the *x*-axis represents the frequency of the motifs within DMRs. The calculated Pearson's correlation (*R*) was 0.86.

we analyzed the relationship between the frequency of the C[N]$_6$CT motif in DMRs and the expression of intergenic miRNAs induced by demethylation. Correlation analysis between the fold changes of gene expression and the frequency of C[N]$_6$CT motifs in DMRs was performed with the eight miRNA genes described in the previous section. After performing Pearson's correlation test using those miRNAs, we obtained a high correlation value of 0.87 (p-value = 4.3e−03) between the frequency of C[N]$_6$CT motifs in DMRs and the fold changes in miRNA expression after demethylation (Fig. 4).

These results indicate that the frequency of C[N]$_6$CT motifs in DMRs plays a role in the expression efficiency of intergenic miRNAs in conjunction with the methylation status, and strongly suggests that the C[N]$_6$CT sequence pattern in DMRs is a methylation-dependent regulatory motif for intergenic miRNA expression.

4. Discussion

After identifying 161 DMPs within 1000 bp upstream of human intergenic miRNAs using microarray analysis, we searched for motifs within the DMRs and found a sequence motif, C[N]$_6$CT, which is conserved in the DMRs. Previous studies have reported that CT-repeat microsatellites are abundant within 1000 bp upstream of most intergenic miRNA ([14] and references therein). Some motifs containing CT-repeats, including (CCT)n, (CCTT)n, (CGCT)n, and (CCTCT)n, have previously been identified in plants [28,29]. Among these, the (CCT)n and (CCTCT)n motifs are very similar to the C[N]$_6$CT motif, which have two cytosine residues at positions 1 and 8. In other words, when n equals 3 in (CCT)n, the sequence of the motif will be CCTCCTCCT, which can be represented as C[N]$_6$CT. Similarly, (CCTCT)n can also be represented as CC[N]$_6$CT when n equals 2. Therefore, the C[N]$_6$CT motif is highly similar to (CCT)n and (CCTCT)n.

The C[N]$_6$CT motif must be located in DMRs to play a role as a regulatory element because the expression was increased in the genes with high frequency of the C[N]$_6$CT motif in DMRs after DAC treatment. It is possible that the cytosine residues at positions 1 and 8 of the C[N]$_6$CT motif in DMRs are methylated because they are found in methylated regions. The fact that this motif is associated with the expression of intergenic miRNA genes in a motif-frequency dependent manner suggests that the C[N]$_6$CT motif regulates gene expression by methylation/demethylation of cytosine.

Our findings indicate that the regulation of gene expression by C[N]$_6$CT motif is closely associated with DNA methylation status and the frequency of C[N]$_6$CT motif occurrence in DMRs of intergenic miRNA gene. This motif may be a regulatory factor binding site for transcription factors or demethylase. Combining the DNA methylation signature with the C[N]$_6$CT motif may be useful for computationally predicting novel intergenic miRNAs.

Acknowledgments

This work was supported by intramural grants from the Korea National Institute of Health (2011-N72001-00) and in part by the Priority Research Centers Program and Basic Science Research Program through the National Research Foundation of Korea (NRF) funded by the Ministry of Education, Science and Technology (Grant Nos. 2009-0094020 and 2011-0012947 to BJL). KHL was supported by Brain Korea 21 Research Fellowship from the Korea Ministry of Education and Human Resources Development.

Appendix A. Supplementary data

Supplementary data associated with this article can be found, in the online version, at doi:10.1016/j.bbrc.2012.03.005.

References

[1] D.P. Bartel, MicroRNAs: genomics, biogenesis, mechanism, and function, Cell 116 (2004) 281–297.
[2] A.S. Yoo, B.T. Staahl, L. Chen, G.R. Crabtree, MicroRNA-mediated switching of chromatin-remodelling complexes in neural development, Nature 460 (2009) 642–646.
[3] Y. Lee, C. Ahn, J. Han, H. Choi, J. Kim, J. Yim, J. Lee, P. Provost, O. Radmark, S. Kim, V.N. Kim, The nuclear RNase III Drosha initiates microRNA processing, Nature 425 (2003) 415–419.
[4] G. Hutvagner, J. McLachlan, A.E. Pasquinelli, E. Balint, T. Tuschl, P.D. Zamore, A cellular function for the RNA-interference enzyme Dicer in the maturation of the let-7 small temporal RNA, Science 293 (2001) 834–838.
[5] R.F. Ketting, S.E. Fischer, E. Bernstein, T. Sijen, G.J. Hannon, R.H. Plasterk, Dicer functions in RNA interference and in synthesis of small RNA involved in developmental timing in *C. elegans*, Genes Dev. 15 (2001) 2654–2659.
[6] I. Alvarez-Garcia, E.A. Miska, MicroRNA functions in animal development and human disease, Development 132 (2005) 4653–4662.
[7] C.M. Croce, G.A. Calin, MiRNAs, cancer, and stem cell division, Cell 122 (2005) 6–7.
[8] A. Rodriguez, S. Griffiths-Jones, J.L. Ashurst, A. Bradley, Identification of mammalian microRNA host genes and transcription units, Genome Res. 14 (2004) 1902–1910.
[9] M. Lagos-Quintana, R. Rauhut, W. Lendeckel, T. Tuschl, Identification of novel genes coding for small expressed RNAs, Science 294 (2001) 853–858.
[10] Y. Lee, M. Kim, J. Han, K.H. Yeom, S. Lee, S.H. Baek, V.N. Kim, MicroRNA genes are transcribed by RNA polymerase II, EMBO J. 23 (2004) 4051–4060.
[11] X. Cai, C.H. Hagedorn, B.R. Cullen, Human microRNAs are processed from capped, polyadenylated transcripts that can also function as mRNAs, RNA 10 (2004) 1957–1966.
[12] G.M. Borchert, W. Lanier, B.L. Davidson, RNA polymerase III transcribes human microRNAs, Nat. Struct. Mol. Biol. 13 (2006) 1097–1101.
[13] H.K. Saini, S. Griffiths-Jones, A.J. Enright, Genomic analysis of human microRNA transcripts, Proc. Natl. Acad. Sci. USA 104 (2007) 17719–17724.
[14] X. Zhou, J. Ruan, G. Wang, W. Zhang, Characterization and identification of microRNA core promoters in four model species, PLoS Comput. Biol. 3 (2007) e37.
[15] L. Heikkinen, S. Asikainen, G. Wong, Identification of phylogenetically conserved sequence motifs in microRNA 5′ flanking sites from *C. elegans* and *C. briggsae*, BMC Mol. Biol. 9 (2008) 105.
[16] N.D. Heintzman, R.K. Stuart, G. Hon, Y. Fu, C.W. Ching, R.D. Hawkins, L.O. Barrera, S. Van Calcar, C. Qu, K.A. Ching, W. Wang, Z. Weng, R.D. Green, G.E. Crawford, B. Ren, Distinct and predictive chromatin signatures of transcriptional promoters and enhancers in the human genome, Nat. Genet. 39 (2007) 311–318.
[17] F. Ozsolak, L.L. Poling, Z. Wang, H. Liu, X.S. Liu, R.G. Roeder, X. Zhang, J.S. Song, D.E. Fisher, Chromatin structure analyses identify miRNA promoters, Genes Dev. 22 (2008) 3172–3183.
[18] H. Suzuki, S. Takatsuka, H. Akashi, E. Yamamoto, M. Nojima, R. Maruyama, M. Kai, H.O. Yamano, Y. Sasaki, T. Tokino, Y. Shinomura, K. Imai, M. Toyota, Genome-wide profiling of chromatin signatures reveals epigenetic regulation of MicroRNA genes in colorectal cancer, Cancer Res. 71 (2011) 5646–5658.
[19] M. Toyota, H. Suzuki, Y. Sasaki, R. Maruyama, K. Imai, Y. Shinomura, T. Tokino, Epigenetic silencing of microRNA-34b/c and B-cell translocation gene 4 is associated with CpG island methylation in colorectal cancer, Cancer Res. 68 (2008) 4123–4132.
[20] X. Agirre, A. Vilas-Zornoza, A. Jimenez-Velasco, J.I. Martin-Subero, L. Cordeu, L. Garate, E. San Jose-Eneriz, G. Abizanda, P. Rodriguez-Otero, P. Fortes, J. Rifon, E.

Bandres, M.J. Calasanz, V. Martin, A. Heiniger, A. Torres, R. Siebert, J. Roman-Gomez, F. Prosper, Epigenetic silencing of the tumor suppressor microRNA Hsa-miR-124a regulates CDK6 expression and confers a poor prognosis in acute lymphoblastic leukemia, Cancer Res. 69 (2009) 4443–4453.

[21] X. Cao, S.L. Pfaff, F.H. Gage, A functional study of miR-124 in the developing neural tube, Genes Dev. 21 (2007) 531–536.

[22] J. Silber, D.A. Lim, C. Petritsch, A.I. Persson, A.K. Maunakea, M. Yu, S.R. Vandenberg, D.G. Ginzinger, C.D. James, J.F. Costello, G. Bergers, W.A. Weiss, A. Alvarez-Buylla, J.G. Hodgson, MiR-124 and miR-137 inhibit proliferation of glioblastoma multiforme cells and induce differentiation of brain tumor stem cells, BMC Med. 6 (2008) 14.

[23] M. Fabbri, R. Garzon, A. Cimmino, Z. Liu, N. Zanesi, E. Callegari, S. Liu, H. Alder, S. Costinean, C. Fernandez-Cymering, S. Volinia, G. Guler, C.D. Morrison, K.K. Chan, G. Marcucci, G.A. Calin, K. Huebner, C.M. Croce, MicroRNA-29 family reverts aberrant methylation in lung cancer by targeting DNA methyltransferases 3A and 3B, Proc. Natl. Acad. Sci. USA 104 (2007) 15805–15810.

[24] E.J. Noonan, R.F. Place, D. Pookot, S. Basak, J.M. Whitson, H. Hirata, C. Giardina, R. Dahiya, MiR-449a targets HDAC-1 and induces growth arrest in prostate cancer, Oncogene 28 (2009) 1714–1724.

[25] S. Griffiths-Jones, R.J. Grocock, S. van Dongen, A. Bateman, A.J. Enright, MiRBase: microRNA sequences, targets and gene nomenclature, Nucleic Acids Res. 34 (2006) D140–D144.

[26] T.L. Bailey, N. Williams, C. Misleh, W.W. Li, MEME: discovering and analyzing DNA and protein sequence motifs, Nucleic Acids Res. 34 (2006) W369–W373.

[27] M.A. Larkin, G. Blackshields, N.P. Brown, R. Chenna, P.A. McGettigan, H. McWilliam, F. Valentin, I.M. Wallace, A. Wilm, R. Lopez, J.D. Thompson, T.J. Gibson, D.G. Higgins, Clustal W and Clustal X version 2.0, Bioinformatics 23 (2007) 2947–2948.

[28] S. Fujimori, T. Washio, K. Higo, Y. Ohtomo, K. Murakami, K. Matsubara, J. Kawai, P. Carninci, Y. Hayashizaki, S. Kikuchi, M. Tomita, A novel feature of microsatellites in plants: a distribution gradient along the direction of transcription, FEBS Lett. 554 (2003) 17–22.

[29] C. Molina, E. Grotewold, Genome wide analysis of Arabidopsis core promoters, BMC Genom. 6 (2005) 25.

Biochemical and Biophysical Research Communications 420 (2012) 397–403

Contents lists available at SciVerse ScienceDirect

Biochemical and Biophysical Research Communications

journal homepage: www.elsevier.com/locate/ybbrc

Activation of the Wnt/β-catenin signaling pathway is associated with glial proliferation in the adult spinal cord of ALS transgenic mice

Yanchun Chen [a,b], Yingjun Guan [a,b,*], Huancai Liu [c], Xin Wu [a], Li Yu [a], Shanshan Wang [a], Chunyan Zhao [a], Hongmei Du [a], Xin Wang [d,*]

[a] Department of Histology and Embryology, Weifang Medical University, Weifang, Shandong, PR China
[b] Department of Histology and Embryology, Shandong University School of Medicine, Jinan, Shandong, PR China
[c] Department of Orthopedic, Affiliated Hospital, Weifang Medical University, Weifang, Shandong, PR China
[d] Department of Neurosurgery, Brigham and Women's Hospital, Harvard Medical School, Boston, MA, USA

ARTICLE INFO

Article history:
Received 18 February 2012
Available online 9 March 2012

Keywords:
Amyotrophic lateral sclerosis
Wnt signaling pathway
Spinal cord
Proliferation
Transgenic mice

ABSTRACT

Amyotrophic lateral sclerosis (ALS) is a neurodegenerative disease characterized by the progressive and fatal loss of motor neurons. In ALS, there is a significant cell proliferation in response to neurodegeneration; however, the exact molecular mechanisms of cell proliferation and differentiation are unclear. The Wnt signaling pathway has been shown to be involved in neurodegenerative processes. Wnt3a, β-catenin, and Cyclin D1 are three key signaling molecules of the Wnt/β-catenin signaling pathway. We determined the expression of Wnt3a, β-catenin, and Cyclin D1 in the adult spinal cord of $SOD1^{G93A}$ ALS transgenic mice at different stages by RT-PCR, Western blot, and immunofluorescence labeling techniques. We found that the mRNA and protein of Wnt3a and Cyclin D1 in the spinal cord of the ALS mice were upregulated compared to those in wild-type mice. In addition, β-catenin translocated from the cell membrane to the nucleus and subsequently activated transcription of the target gene, Cyclin D1. BrdU and Cyclin D1 double-positive cells were increased in the spinal cord of these mice. Moreover, Wnt3a, β-catenin, and Cyclin D1 were also expressed in both neurons and astrocytes. The expression of Wnt3a, β-catenin or Cyclin D1 in mature $GFAP^{+}$ astrocytes increased. Moreover, BrdU/Cyclin D1/GFAP triple-positive cells were detected in the ALS mice. Our findings suggest that neurodegeneration activates the Wnt/β-catenin signaling pathway, which is associated with glial proliferation in the adult spinal cord of ALS transgenic mice. This mechanism may be significant in clinical gene therapy.

1. Introduction

Amyotrophic lateral sclerosis (ALS) also known as Lou Gehrigis diseases, is an adult-onset neurodegenerative disease, characterized by the progressive and fatal loss of motor neurons in the brainstem and spinal cord [1]. Although most cases of ALS are sporadic in origin, 10–15% are familial (familial ALS) [2]. Among this particular, approximately 20% possess a mutation in the gene that encodes for the enzyme copper/zinc superoxide dismutase (SOD1) [3]. Although more than 125 different mutations in SOD1 have been identified in patients with familial ALS [4], most of the disease symptoms caused by these mutations are similar, suggesting that the progressive degeneration of motor neurons in ALS is caused by one or several factors. The putative mechanisms of the progressive degeneration of motor neurons include growth factor deficiency, mitochondrial abnormalities, axonal disorganization, oxidative stress, inflammation, and excitotoxicity, among others [5,6]. The exact mechanisms responsible for motor neuron degeneration in ALS, however, are not completely understood and few therapeutic options have emerged for slowing down disease progression. Our previous study [7] showed that there was a significant cell proliferation in response to neurodegeneration in ALS, however, the exact molecular mechanisms of cell proliferation and differentiation are unclear.

Canonical Wnt/β-catenin signaling plays an important role in a variety of cellular events, including cell proliferation, differentiation, migration and morphogenesis. In the presence of Wnt, binding of Wnts to a Frizzled receptor and low-density lipoprotein receptor-related protein 5/6 (LRP5/6) co-receptor triggers the recruitment of the cytoplasmic component, Disheveled, which

Abbreviations: ALS, amyotrophic lateral sclerosis; SOD1, copper/zinc superoxide dismutase 1; GSK-3β, glycogen synthase kinase 3 beta; LRP, low-density lipoprotein receptor-related protein; TCF/LEF, the lymphoid enhancer factor/T-cell factor.

* Corresponding authors. Address: Department of Histology and Embryology, Weifang Medical University, Shandong, PR China (Y. Guan).

E-mail addresses: guanyj@wfmc.edu.cn (Y. Guan), xwang@rics.bwh.harvard.edu (X. Wang).

0006-291X/$ - see front matter © 2012 Elsevier Inc. All rights reserved.
http://dx.doi.org/10.1016/j.bbrc.2012.03.006

inhibits the phosphorylation of β-catenin by glycogen synthase kinase 3 beta (GSK-3β). This results in an increase in the stability of β-catenin and its translocation to the nucleus, where it can interact with members of the lymphoid enhancer factor/T-cell factor (TCF/LEF) transcription factors and subsequently regulate the expression of downstream target genes, such as c-myc and Cyclin D1 [8,9]. The Wnt signaling pathway has also previously been demonstrated to be involved in neurodegenerative processes. The down-regulated Wnt signaling pathway was found to be associated with rat brain degeneration in Alzheimer's disease (AD) [10], and abnormalities of the Wnt signaling pathway were found to be related to Huntington's disease (HD) [11]. The roles of the Wnt signaling pathway in the pathogenesis of ALS have not yet been reported.

In this study, the expression of Wnt3a, β-catenin, and Cyclin D1 in the adult spinal cord of $SOD1^{G93A}$ transgenic mice was analyzed. To find new targets for the treatment of ALS, our study examined the role of Wnt/β-catenin signaling in the cell proliferation and differentiation in the spinal cord of ALS transgenic mice, which may have important significance in clinical gene therapy.

2. Materials and methods

2.1. Experimental animals and tissue preparation

Mice carrying the mutated human $SOD1^{G93A}$ gene and wild-type human SOD1 gene were obtained from Jackson Laboratories (Bar Harbor, ME, USA). Mice were crossbred and genotyping was performed using genomic DNA from mouse-tail tissue, as suggested by the Jackson Laboratory genotyping protocol. The Animal Ethics Committee of the University approved all working protocols. Mice were sacrificed at an early, middle, and end stage (95 d, 108 d and 122 d, respectively) and spinal cords were quickly removed. The samples were either saved in liquid nitrogen for molecular biology analysis or immersed and fixed in 4% paraformaldehyde for immunohistological analysis. The methods of tissue processing and bromodeoxyuridine injection strategy were described previously [7].

2.2. RNA extraction & reverse transcriptase PCR

Total RNA was obtained from spinal cord tissue using Trizol Reagent (Invitrogen) following the instructions of the manufacturer. The total RNA (2 μg) was reverse-transcribed with SuperScript II Reverse Transcriptase (Invitrogen). RNA samples were treated with RNase-free DNase I (Fermentas). A PCR was performed with the following primers: (β-catenin) sense, 5′TTTCCCAGTCCTTCACGCAAG3′; antisense, 5′TAGAGCAGACAGACAGCACCTTC3′; (Cyclin D1) sense, 5′TGTGAGGAGCAGAAGTGCGAAGA3′; antisense, 5′TGTTCACCAGAAGCAGTTCCATTTG3′; (β-actin) sense, 5′GTCGTACCACAGGCATTGTGATGG3′; antisense, 5′GCAATGCCTGGGTACATGGTGG3′. The band intensity was evaluated using UVI Soft Image Acquisition and Analysis software (UVItec, Cambridge, UK). Endogenous β-actin expression was used as a control.

2.3. Real-time PCR

Real-time PCR was performed with the Rotor-Gene 3000 Real-time PCR System (Corbett Research). The following primers were used: (Wnt3a) sense, 5′CTTTCGCAGTGACACGCTC3′; antisense, 5′CCTGGCATCGGCAAACT3′; (β-actin) sense, 5′CCTGTACGCCAACACAGTGC3′; antisense, 5′ATACTCCTGCTTGCTGATCC3′. Amplification was performed with the following program cycle: initial melting temperature, 95 °C for 5 min followed by 40 cycles of 95 °C for 10 s, 59 °C for 15 s, 72 °C for 20 s, and 83 °C for 5 s. The cycle number at which a statistically significant increase in the Wnt3a gene was first detected (threshold cycle, Ct) was normalized to the Ct for β-actin, which was used as an endogenous reference gene. The difference in the relative expression between ALS and wild-type mice was calculated using the $2^{-\Delta\Delta Ct}$ method.

2.4. Western blot analysis

The isolated spinal cords were mechanically homogenized in lysis buffer (50 mM Tris–HCl (pH 7.4), 50 mM NaCl, 1% Triton X-100, 1 mM EDTA, 20 mM NaF, 2 mM Na_3VO_4, 1 mM PMSF, 1 μg/ml aprotinin, 1 μg/ml leupeptin, and 1 μg/ml pepstatin). Homogenates were clarified by centrifugation at 14,000*g* for 15 min at 4 °C, and total extracts were obtained from the supernatant. Proteins were separated by SDS–PAGE electrophoresis (100 μg of total protein per well) and then transferred onto nitrocellulose membranes. The membranes were then blocked in 5% fat free milk with 0.05% Tween®-20 for 1 h at room temperature with constant agitation, followed by overnight incubation in rabbit anti-Wnt3a antibody (Abcam), rabbit anti-β-catenin (6B3) antibody (Cell Signaling), rabbit anti-Cyclin D1 antibody (Epitomics), mouse anti-β-actin antibody (Sigma) at 4 °C. Immunoreactive bands were visualized by peroxidase-conjugated secondary antibodies (Jackson ImmunoResearch) and subsequent ECL-development.

2.5. Preparation of nuclear protein extraction

Nuclear protein from the spinal cords was extracted according to the NE-PER Nuclear and Cytoplasmic Extraction Reagents manufacturer's instructions (Thermo). Rabbit anti-LMNB1 antibody (Proteintech Group, Inc.) and rabbit anti-β-catenin (6B3) antibody (Cell Signaling) were used. Nuclear β-catenin protein levels were normalized to those of LMNB1, which was used as an internal control.

2.6. Immunofluorescence labeling

Sections were blocked in 10% goat serum for 30 min at 37 °C, and incubated with primary antibody overnight at 4 °C. The following primary antibodies were applied: rabbit anti-Wnt3a IgG (Abcam), rabbit anti-β-catenin IgG (Cell Signaling) and rabbit anti-Cyclin D1 IgG (Epitomics). The samples were soaked for 2 h in 0.01 M PBS, pH 7.4 with 0.1% Triton X-100 containing goat anti-rabbit IgG conjugated to Cy3 (Jackson ImmunoResearch). Finally, the nuclei were stained with Hoechst33258. For BrdU staining, cryosections were pretreated with 2 N HCl at 37 °C for 30 min and incubated with 0.4% (w/v) prewarmed pepsin in 0.01 N HCl at 37 °C for 10 min. For double labeling, two compatible primary antibodies were simultaneously applied overnight at 4 °C. The following primary antibodies were applied: mouse anti-BrdU IgG (Sigma), rabbit anti-Wnt3a IgG (Abcam), rabbit anti-β-catenin IgG (Cell Signaling), chicken anti-GFAP IgY (Abcam), chicken anti-β-tubulinIII IgY (Abcam), and rabbit anti-Cyclin D1 IgG (Epitomics). The samples were then incubated for 2 h in 0.01 M PBS, pH 7.4 with 0.1% Triton X-100 containing two of the following secondary antibodies: goat anti-mouse IgG conjugated to FITC (Jackson ImmunoResearch), or goat anti-rabbit IgG conjugated to Cy3 (Jackson ImmunoResearch) or goat anti-Chicken IgY-H&L (DyLight®488) (Abcam). For triple labeling, three compatible primary antibodies were simultaneously applied overnight at 4 °C. The following secondary antibodies were used: goat anti-mouse IgG conjugated to FITC (Jackson ImmunoResearch), goat anti-rabbit IgG conjugated to Cy3 (Jackson ImmunoResearch) and donkey anti-chicken IgY conjugated to Cy5 (Millipore). As negative controls, we performed staining in the absence of the primary antibodies by only adding

PBS to the sections. Sections were documented with a fluorescence or laser scanning confocal microscope.

2.7. Statistical analysis

The data are represented as mean ± standard deviation (SDs) and analyzed using one-way ANOVA procedures. The significance level is defined as $p < 0.05$.

3. Results and discussion

3.1. Neurodegeneration upregulates the expression of Wnt3a in the spinal cord of ALS mice with disease progression

Wnt3a, one type of secreted protein in the Wnt/β-catenin signaling pathway, initiates Wnt signaling. We performed real-time PCR analysis to examine possible changes in Wnt3a mRNA expression over time. Our results showed that Wnt3a mRNA levels were upregulated at the age of 95 d, 108 d, and 122 d in the spinal cord of ALS mice compared with wild-type mice (Fig. 1A). Wnt3a protein levels were also upregulated (Fig. 1B and C), where we observed a consistent change in the expression of Wnt3a protein that corresponded with those of Wnt3a mRNA. To investigate the distribution and localization of Wnt3a, we analyzed the expression of Wnt3a by immunofluorescence labeling. Wnt3a-positive cells were detected in the gray and white matter of the spinal cord, with a few Wnt3a-positive cells found in the central canal. Within the gray matter, the majority of the Wnt3a-positive cells were located in the ventral horn. Nerve fibers were also positive within the white matter. In ALS mice, the distribution of Wnt3a was similar to that in wild-type mice, and the majority of Wnt3a-positive cells were in the ventral horn of the gray matter

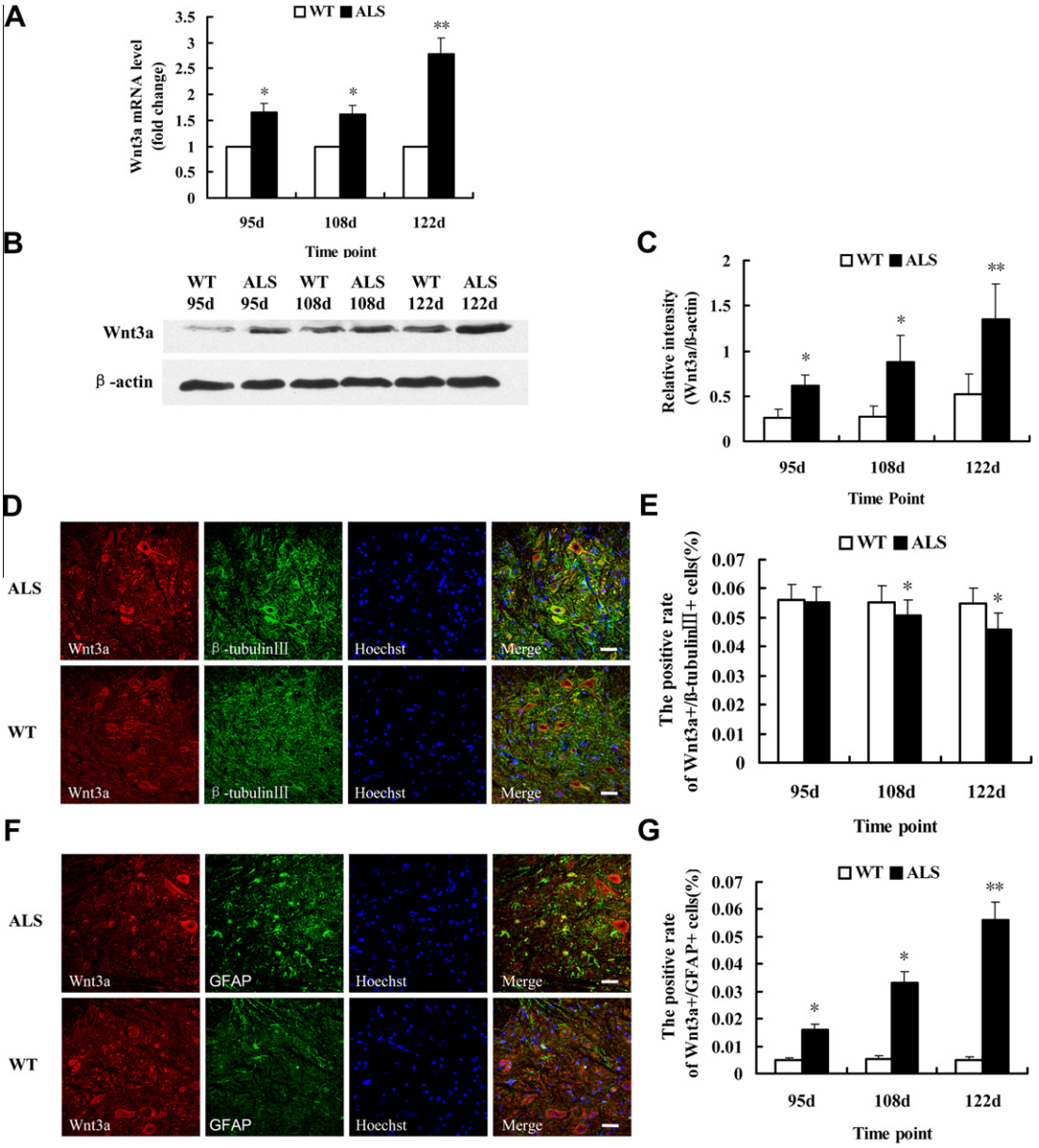

Fig. 1. The expression of Wnt3a in the adult spinal cord of ALS and wild-type (WT) mice. (A) The relative mRNA levels of Wnt3a analyzed by real-time PCR ($n = 4$). (B) Representative Western blot of Wnt3a. β-actin was used as an internal control. (C) The relative intensity of Wnt3a protein analyzed by Western blot ($n = 5$). (D) Wnt3a/β-tubulinIII colocalization in gray matter of 122-day-old mice. (E) The percentage of positive $Wnt3a^+/\beta\text{-tubulinIII}^+$ cells in the ventral horn of gray matter ($n = 4$). (F) Wnt3a/GFAP colocalization in the gray matter of 122-day-old mice. (G) The percentage of positive $Wnt3a^+/GFAP^+$ cells in the gray matter ($n = 4$). Scale bar = 50 μm. $^*p < 0.05$, $^{**}p < 0.01$ vs. wild-type littermates.

(Fig. 1D), the locus of neurodegeneration. Moreover, within the white matter, the number of myelinated axons decreased due to neuronal loss [12].

BrdU and Wnt3a double immunofluorescence staining were used to demonstrate the localization of Wnt3a in proliferating cells; however, no BrdU/Wnt3a double-positive cells were detected (data not shown). This may suggest that there was a lack of Wnt3a expression in proliferating cells. Wnt3a/β-tubulinIII and Wnt3a/GFAP double immunofluorescence staining were performed to demonstrate the localization of Wnt3a in differentiated cells, such as in β-tubulinIII$^+$ neurons and GFAP$^+$ mature astrocytes. Our results revealed that in wild-type mice, most of the Wnt3a-positive cells were immunopositive for β-tubulinIII (Fig. 1D) and a few of the Wnt3a-positive cells were immunopositive for GFAP (Fig. 1F), suggesting that Wnt3a was expressed predominantly in β-tubulinIII$^+$ neurons and in a few GFAP$^+$ mature astrocytes. In ALS mice, especially at 122 d (considered to be the end stage of the ALS disease model), the number of Wnt3a/GFAP double-positive cells were markedly increased (Fig. 1G), but Wnt3a/β-tubulinIII double-positive cells in the ventral horn, the locus of neurodegeneration, were decreased (Fig. 1E). This may suggest that the expression of Wnt3a in neurons decreased due to neuronal loss [12] and that the expression of Wnt3a in mature astrocytes had increased with neurodegeneration. This is consistent with our previous studies demonstrating mature GFAP$^+$ astrocytes were found to be markedly increased at the end stage of ALS [7]. The increasing astrocytes in response to neurodegeneration were proven to protect neurons from damage in ALS [13].

The direct activation of the Wnt signaling pathway by Wnt3a ligand had previously been demonstrated to prevent the toxic ef-

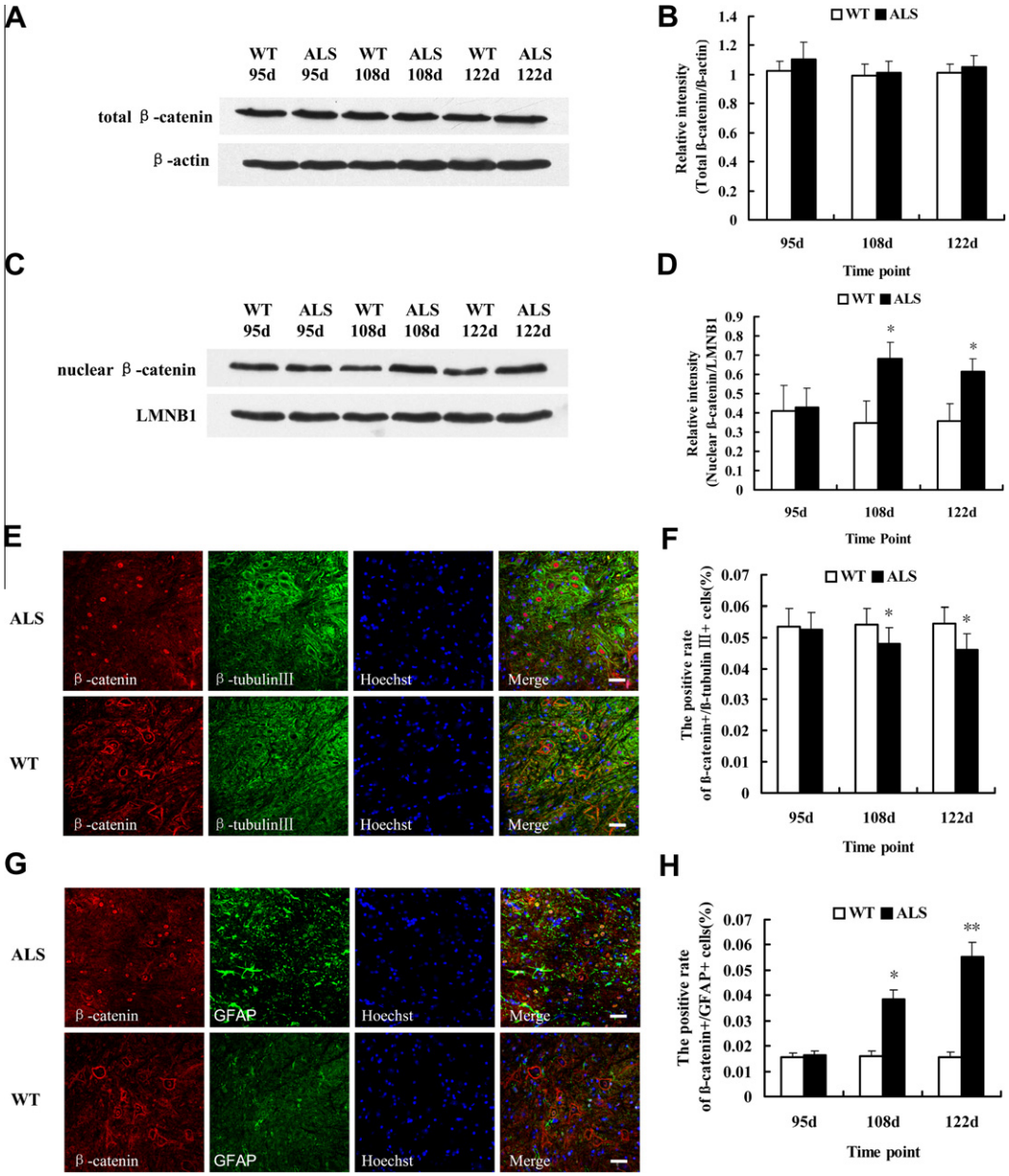

Fig. 2. The expression of β-catenin in the adult spinal cord of ALS and wild-type (WT) mice. (A) Representative Western blot of total β-catenin protein. β-actin was used as an internal control. (B) The relative intensity of total β-catenin protein as analyzed by Western blot (n = 5). (C) Representative Western blot of nuclear β-catenin protein. LMNB1 was used as an internal control. (D) The relative intensity of the nuclear β-catenin protein was analyzed by Western blot (n = 5). (E) β-catenin/β-tubulinIII colocalization in the gray matter of 108-day-old mice. (F) The percentage of positive β-catenin$^+$/β-tubulinIII$^+$ cells in the ventral horn of gray matter (n = 4). (G) β-catenin/GFAP colocalization in the gray matter of 108-day-old mice. (H) The percentage of positive β-catenin$^+$/GFAP$^+$ cells in the gray matter (n = 4). Scale bar = 50 μm. $^*p < 0.05$, $^{**}p < 0.01$ vs. wild-type littermates.

fects induced by amyloid-β-peptide (Aβ) in rat hippocampal neurons. Wnt3a inhibited GSK-3β activity and tau phosphorylation, and protected hippocampal neurons from apoptosis induced by Aβ. Frzb-1, a secreted Wnt antagonist protein, was able to reverse the Wnt3a neuroprotective effects on cell survival against Aβ toxicity, suggesting that Wnt3a loss-of-function may play a role in triggering neurodegeneration in AD [9,14]. Activation of the nuclear factor erythroid-2-related transcription factor 2 (Nrf2) in astrocytes coordinates the upregulation of antioxidant defenses and conferred protection to neighboring neurons. Overexpression of Nrf2 in astrocytes protected motor neurons from mutant hSOD1 toxicity and significantly delayed onset and extended survival in ALS mice [15].

3.2. β-catenin translocates from the cell membrane to the nucleus in the spinal cord of ALS mice

β-catenin is an important key regulatory factor, which can transmit the Wnt signal from the cytoplasm to the nucleus. Loss of membrane β-catenin and the accumulation of cytoplasmic or nuclear β-catenin may prompt abnormal changes in β-catenin protein expression. In this study, our results showed that there were no clear changes in β-catenin mRNA and total protein levels (Fig. 2A and B) in the spinal cord between wild-type and ALS mice. At the middle (108 d) and end stage (122 d) of the ALS disease model, we found that nuclear β-catenin protein levels in the ALS spinal cord were increased (Fig. 2C and D), suggesting that β-cate-

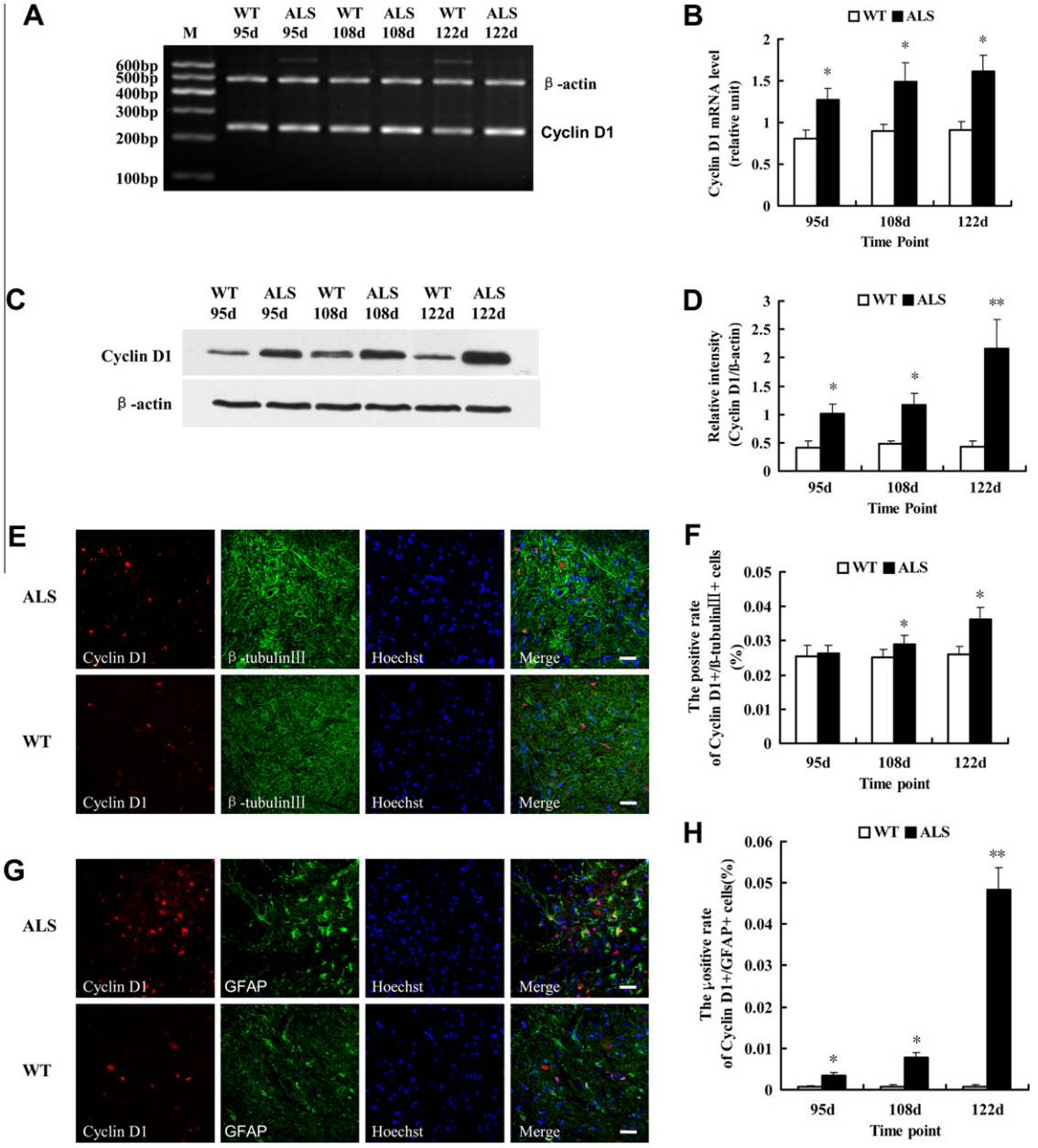

Fig. 3. The expression of Cyclin D1 in the adult spinal cord of ALS and wild-type (WT) mice. (A) Representative RT-PCR of Cyclin D1. β-actin was used as an internal control. (B) The relative mRNA levels of Cyclin D1 as analyzed by RT-PCR ($n = 5$). (C) Representative Western blot of Cyclin D1 protein. β-actin was used as an internal control. (D) The relative intensity of Cyclin D1 protein as analyzed by Western blot ($n = 5$). (E) Cyclin D1/β-tubulinIII colocalization in the gray matter of 122-day-old mice. (F) The percentage of positive Cyclin $D1^+$/β-$tubulinIII^+$ cells in the ventral horn of gray matter ($n = 4$). (G) Cyclin D1/GFAP colocalization in the gray matter of 122-day-old mice. (H) The percentage of positive Cyclin $D1^+$/$GFAP^+$ cells in the gray matter ($n = 4$). Scale bar = 50 μm.*$p < 0.05$, **$p < 0.01$ vs. wild-type littermates.

nin translocated to the cell nucleus during the progression of ALS, leading to the upregulation of nuclear β-catenin protein levels. The results obtained from our immunofluorescence labeling showed that β-catenin-positive cells were localized mainly to the nuclei at the middle (108 d) and end stage (122 d) of ALS, compared with wild-type mice, implying that during the progression of ALS, there was a loss of membrane β-catenin and an accumulation of nuclear β-catenin. Nuclear translocation of β-catenin from the cell membrane or the cytoplasm is a sign of activation of the canonical Wnt signaling pathway. The activitiation of Wnt/β-catenin signaling pathway are likely to be associated with the upregulation of Wnt3a.

BrdU/β-catenin double-positive cells were detected in neither wild-type nor ALS mice (data not shown). β-catenin/β-tubulinIII and β-catenin/GFAP double-positive cells were detected in both ALS and wild-type mice, but most of the β-catenin-positive cells were also immunopositive for β-tubulinIII (Fig. 2E), although a few were GFAP-positive (Fig. 2G). This shows that β-catenin is mainly expressed in β-tubulinIII$^+$ neurons, with small amount in mature GFAP$^+$ astrocytes. In ALS mice, especially at day 122, the number of β-catenin/GFAP double-positive cells were increased (Fig. 2H) and the number of β-catenin/β-tubulinIII double-positive cells in the ventral horn were decreased (Fig. 2F), suggesting that the expression of β-catenin in mature GFAP$^+$ astrocytes increased and the expression of β-catenin in β-tubulinIII$^+$ neurons decreased as a result of the loss of neurons at the end stage of neurodegenerative disease [12]. Reactive astrocytes have a protective effect on neurons. Recent evidence supports the role of β-catenin as a survival factor in AD. Tau hyperphosphorylation accompanied by increases in the nuclear translocation of β-catenin prevented cells from undergoing apoptosis. Further, reduced levels of β-catenin antagonized the anti-apoptotic effect of tau [16].

3.3. Upregulation of Cyclin D1 in the spinal cord of ALS mice is associated with glial proliferation

As one type of downstream target gene of the Wnt/β-catenin signaling pathway, Cyclin D1 is an important nuclear transcription factor, which can regulate the cell cycle. High levels of Cyclin D1 mRNA and protein promoted cell proliferation [17].

RT-PCR tests revealed that Cyclin D1 mRNA was upregulated in the ALS spinal cord compared with the wild-type spinal cord at the age of 95 d, 108 d, and 122 d; the changes of Cyclin D1 mRNA at 122 d were observed to be the most robust (Fig. 3A and B). Increased Cyclin D1 mRNA levels resulted in increased protein levels (Fig. 3C and D). The results of our immunofluorescence labeling

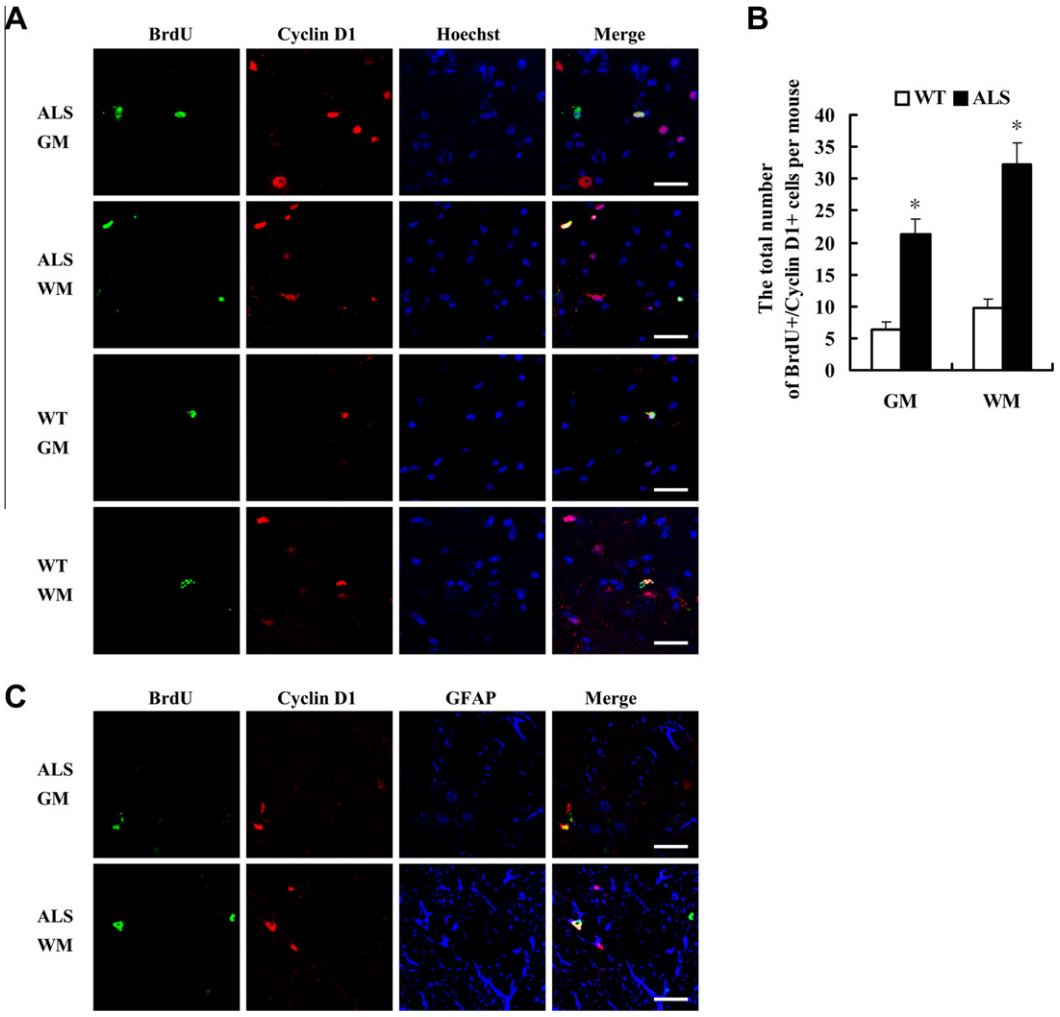

Fig. 4. BrdU/Cyclin D1 and BrdU/Cyclin D1/GFAP colocalization in the adult spinal cord of ALS and wild-type (WT) mice. (A) BrdU/Cyclin D1 colocalization in the gray matter (GM) and white matter (WM) of 95-day-old mice. (B) The analysis of BrdU/Cyclin D1 double positive cells in the gray matter (GM) and white matter (WM) of 95-day-old ALS and wild-type (WT) mice. The total number of labeled cells were counted ($n = 5$). For each mouse, 10 representative slides were selected. (C) Triple immunofluorescence staining of BrdU, Cyclin D1 and GFAP in the adult spinal cord of 95-day-old ALS mice. Immunohistochemistry images were taken of the gray matter (GM) and white matter (WM). Scale bar = 50 μm. $^*p < 0.05$ vs. wild-type littermates.

showed that Cyclin D1-positive cells were detected in the gray matter, white matter, and the central canal in both ALS and wild-type mice. The number of Cyclin D1-positive cells were distinctly increased in the gray and white matter as well as in the central canal of spinal cord in ALS mice at the age of 95 d, 108 d, and 122 d.

Double immunofluorescence staining suggested that Cyclin D1 was expressed in both proliferating and differentiated cells. BrdU and Cyclin D1 double-positive cells were detected in the gray and white matter of spinal cord in both ALS and wild-type mice (Fig. 4A). The number of BrdU and Cyclin D1 double-positive cells in the spinal cord of ALS mice (95-day-old) were increased (Fig. 4B), suggesting an increase in the expression of Cyclin D1 in proliferating cells. Cyclin D1/β-tubulinIII and Cyclin D1/GFAP double-positive cells were detected in both sets of mice (Fig. 3E and G), implying that Cyclin D1 expressed in β-tubulinIII$^+$ neurons and mature GFAP$^+$ astrocytes. In ALS mice, the number of Cyclin D1/GFAP and Cyclin D1/β-tubulinIII double-positive cells both increased during ALS progression (Fig. 3F and H). In particular, we found a robust increase in Cyclin D1/GFAP double-positive cells, suggesting that the expression of Cyclin D1 in GFAP$^+$ mature astrocytes had increased markedly. Because of the progressive degeneration of motor neurons and the increasing number of astrocytes in ALS, the upward trends of Cyclin D1/β-tubulinIII were lower than that of Cyclin D1/GFAP.

To identify the differentiation of proliferating cells, triple labeling of BrdU/Cyclin D1/β-tubulinIII and BrdU/Cyclin D1/GFAP was performed. Our results showed that BrdU/Cyclin D1/GFAP triple-positive cells were detected in ALS mice (Fig. 4C); however, BrdU/Cyclin D1/β-tubulinIII triple-positive cells were not detected (data not shown), implying that proliferating cells expressing Cyclin D1 may be differentiated largely into glial cells and not neurons.

Taken together with our study, these findings demonstrate that as target genes of the Wnt/β-catenin signaling pathway, the upregulation of Cyclin D1 mRNA and protein are likely to be associated with the activation of the Wnt/β-catenin signaling pathway. Upregulation of Wnt3a induces the translocation of β-catenin from the cell membrane to the nucleus, activating the Wnt/β-catenin signaling pathway. Nuclear translocation of β-catenin activates transcription of Cyclin D1 by acting on TCF/LEF binding sites. Upregulation of Cyclin D1 leads to cells entering into the S-phase, and causes an increase in cell proliferation and the proliferating cells differentiated largely into glial cells. Activation of the Wnt/β-catenin signaling pathway increased the expression of β-catenin and Cyclin D1 mRNA and protein, which played an important role in the genesis and development of Alzheimer's disease [18].

Recent studies have shown that the Wnt/β-catenin signaling pathway is capable of regulating cell proliferation and differentiation [19–21]. Wnt3a signaling induced β-catenin nuclear translocation and activated the Wnt pathway in rat bone marrow mesenchymal stem cells (rMSC), thereby promoting the proliferation, myogenic differentiation, and migration of rMSC [19]. β-catenin also plays an important role in regulating the cell proliferation or differentiation [20]. Cyclin D1, a known direct target gene of Wnt/β-catenin signaling, was activated by an increased expression of Wnt1 in the developing mid/hindbrain, thus potentially enhancing the proliferation of local precursors [21].

In conclusion, activation of the Wnt/β-catenin signaling pathway is associated with glial proliferation in the adult spinal cord of ALS transgenic mice, which may protect neurons from further damage during the progression of ALS. Further research is needed to gather more evidence to demonstrate the protective roles of the Wnt/β-catenin signaling pathway. Drugs targeting the key signaling molecules that activate the Wnt/β-catenin signaling pathway may be a new avenue to pursue for ALS treatment.

4. Sources of funding

This work was funded by grants obtained from the National Natural Science Foundation of China (30871314) and the Shandong Provincial Education Department of China (J11 LF16).

Acknowledgments

We are thankful to He Li's lab in Tongji Medical College of Huazhong University of Science and Technology.

References

[1] V.B. Tripathi, A. Al-Chalabi, Molecular insights and therapeutic targets in amyotrophic lateral sclerosis, CNS Neurol. Disord.: Drug Targets 7 (2008) 11–19.
[2] G.M. Alexander, K.L. Erwin, N. Byers, J.S. Deitch, B.J. Augelli, E.P. Blankenhorn, T.D. Heiman-Patterson, Effect of transgene copy number on survival in the G93A SOD1 transgenic mouse model of ALS, Brain Res. Mol. Brain Res. 130 (2004) 7–15.
[3] C. Crosio, C. Valle, A. Casciati, C. Iaccarino, M.T. Carri, Astroglial inhibition of NF-kappaB does not ameliorate disease onset and progression in a mouse model for amyotrophic lateral sclerosis (ALS), PLoS One 6 (2011) e17187.
[4] P. Pasinelli, R.H. Brown, Molecular biology of amyotrophic lateral sclerosis: insights from genetics, Nat. Rev. Neurosci. 7 (2006) 710–723.
[5] H. Ilieva, M. Polymenidou, D.W. Cleveland, Non-cell autonomous toxicity in neurodegenerative disorders: ALS and beyond, J. Cell Biol. 187 (2009) 761–772.
[6] A. Neymotin, N.Y. Calingasan, E. Wille, N. Naseri, S. Petri, M. Damiano, K.T. Liby, R. Risingsong, M. Sporn, M.F. Beal, M. Kiaei, Neuroprotective effect of Nrf2/ARE activators, CDDO ethylamide and CDDO trifluoroethylamide, in a mouse model of amyotrophic lateral sclerosis, Free Radical. Biol. Med. 51 (2011) 88–96.
[7] Y.J. Guan, X. Wang, H.Y. Wang, K. Kawagishi, H. Ryu, C.F. Huo, E.M. Shimony, B.S. Kristal, H.G. Kuhn, R.M. Friedlander, Increased stem cell proliferation in the spinal cord of adult amyotrophic lateral sclerosis transgenic mice, J. Neurochem. 102 (2007) 1125–1138.
[8] N.C. Inestrosa, E. Arenas, Emerging roles of Wnts in the adult nervous system, Nat. Rev. Neurosci. 11 (2010) 77–86.
[9] E.M. Toledo, M. Colombres, N.C. Inestrosa, Wnt signaling in neuroprotection and stem cell differentiation, Prog. Neurobiol. 86 (2008) 281–296.
[10] N.C. Inestrosa, L. Varela-Nallar, C.P. Grabowski, M. Colombres, Synaptotoxicity in Alzheimer's disease: the Wnt signaling pathway as a molecular target, IUBMB Life 59 (2007) 316–321.
[11] J.D. Godin, G. Poizat, M.A. Hickey, F. Maschat, S. Humbert, Mutant huntingtin-impaired degradation of beta-catenin causes neurotoxicity in Huntington's disease, EMBO J. 29 (2010) 2433–2445.
[12] A.Y. Chiu, P. Zhai, M.C. Dal Canto, T.M. Peters, Y.W. Kwon, S.M. Prattis, M.E. Gurney, Age-dependent penetrance of disease in a transgenic mouse model of familial amyotrophic lateral sclerosis, Mol. Cell Neurosci. 6 (1995) 349–362.
[13] W.W. Yang, R.L. Sidman, T.V. Taksir, C.M. Treleaven, J.A. Fidler, S.H. Cheng, J.C. Dodge, L.S. Shihabuddin, Relationship between neuropathology and disease progression in the SOD1(G93A) ALS mouse, Exp. Neurol. 227 (2011) 287–295.
[14] A.R. Alvarez, J.A. Godoy, K. Mullendorff, G.H. Olivares, M. Bronfman, N.C. Inestrosa, Wnt-3a overcomes beta-amyloid toxicity in rat hippocampal neurons, Exp. Cell Res. 297 (2004) 186–196.
[15] M.R. Vargas, D.A. Johnson, D.W. Sirkis, A. Messing, J.A. Johnson, Nrf2 activation in astrocytes protects against neurodegeneration in mouse models of familial amyotrophic lateral sclerosis, J. Neurosci. 28 (2008) 13574–13581.
[16] H.L. Li, H.H. Wang, S.J. Liu, Y.Q. Deng, Y.J. Zhang, Q. Tian, X.C. Wang, X.Q. Chen, Y. Yang, J.Y. Zhang, Q. Wang, H. Xu, F.F. Liao, J.Z. Wang, Phosphorylation of tau antagonizes apoptosis by stabilizing beta-catenin, a mechanism involved in Alzheimer's neurodegeneration, Proc. Natl. Acad. Sci. USA 104 (2007) 3591–3596.
[17] O. Tetsu, F. McCormick, Beta-catenin regulates expression of Cyclin D1 in colon carcinoma cells, Nature 398 (1999) 422–426.
[18] X. Zhang, W.K. Yin, X.D. Shi, Y. Li, Curcumin activates Wnt/beta-catenin signaling pathway through inhibiting the activity of GSK-3beta in APPswe transfected SY5Y cells, Eur. J. Pharm. Sci. 42 (2011) 540–546.
[19] Y.C. Shang, S.H. Wang, F. Xiong, C.P. Zhao, F.N. Peng, S.W. Feng, M.S. Li, Y. Li, C. Zhang, Wnt3a signaling promotes proliferation, myogenic differentiation, and migration of rat bone marrow mesenchymal stem cells, Acta Pharmacol. Sin. 28 (2007) 1761–1774.
[20] L. Zhang, X. Yang, S. Yang, J. Zhang, The Wnt /beta-catenin signaling pathway in the adult neurogenesis, Eur. J. Neurosci. 33 (2011) 1–8.
[21] M. Panhuysen, D.M. Vogt Weisenhorn, V. Blanquet, C. Brodski, U. Heinzmann, W. Beisker, W. Wurst, Effects of Wnt1 signaling on proliferation in the developing mid-/hindbrain region, Mol. Cell Neurosci. 26 (2004) 101–111.

Biochemical and Biophysical Research Communications 420 (2012) 404–410

Contents lists available at SciVerse ScienceDirect

Biochemical and Biophysical Research Communications

journal homepage: www.elsevier.com/locate/ybbrc

The transcription factor STAT2 enhances proteasomal degradation of RCAN1 through the ubiquitin E3 ligase FBW7

Jee Won Lee [a,1], Hye Seon Kang [a,1], Jae Youn Lee [a], Eun Jung Lee [a], Hyewhon Rhim [d], Joo Heon Yoon [b,c], Su Ryeon Seo [e], Kwang Chul Chung [a,c,*]

[a] Department of Systems Biology, College of Life Science and Biotechnology, Yonsei University, Seoul 120-749, Republic of Korea
[b] Department of Otorhinolaryngology, Yonsei University College of Medicine, Seoul 120-752, Republic of Korea
[c] Research Center for Human Natural Defense System, Yonsei University College of Medicine, Seoul 120-752, Republic of Korea
[d] Life Sciences Division, Korea Institute of Science and Technology, Seoul 136-791, Republic of Korea
[e] Department of Molecular Bioscience, College of Biomedical Science, Kangwon National University, Chuncheon 200-701, Republic of Korea

ARTICLE INFO

Article history:
Received 21 February 2012
Available online 9 March 2012

Keywords:
RCAN1
DSCR1
STAT2
Proteasome
FBW7
Inflammation
Interferon-α

ABSTRACT

Down syndrome is the most common genetic disorder and is characterized by three copies of chromosome 21. *Regulator of calcineurin 1* (*RCAN1*) is located close to the Down syndrome critical region (distal part of chromosome 21), and its product functions as an endogenous inhibitor of calcineurin signaling. RCAN1 protein stability is regulated by several inflammatory signaling factors, though the underlying mechanisms remain incompletely understood. Here, we report that RCAN1 interacts with the inflammation-linked transcription factor, signal transducer and activator of transcription 2 (STAT2) in mammalian cells. STAT2 overexpression decreased levels of RCAN1 protein. Decreases in RCAN1 were blocked by a proteasome inhibitor, indicating that STAT2 regulates RCAN1 degradation via the ubiquitin–proteasome system. Co-immunoprecipitation/immunoblot analyses showed that STAT2 enhanced RCAN1 ubiquitination through the ubiquitin E3 ligase FBW7. This pathway appeared to be physiologically relevant, as treatment of cells with interferon-α reduced RCAN1 levels through the activation of STAT2 and FBW7. Together, these results suggest that STAT2 influences diverse cellular processes linked to RCAN1 by negatively affecting RCAN1 protein stability.

1. Introduction

The regulator of calcineurin 1 (RCAN1) was identified as a protein product of the Down syndrome critical region 1 (*DSCR1*; also known as *Adapt78*, *MCIP1*, or *calcipressin 1*) gene on human chromosome 21 [1]. RCAN1 has been shown to be involved in cardiac valve development, cardiac hypertrophy, inflammation, angiogenesis, and cancer [2]. Preferentially expressed in the heart, skeletal muscle, and brain, RCAN1 binds to and regulates calcineurin, a Ca^{2+}/calmodulin-dependent protein phosphatase 2B that mediates many cellular responses, including lymphocyte activation and neuronal and muscle development [3,4]. Although RCAN1 inhibits calcineurin-dependent responses when overexpressed, it regulates calcineurin through two paradoxical actions [3–5]. That is, RCAN1 inhibits calcineurin signaling through an auto-regulatory feedback mechanism, while it stimulates calcineurin after being phosphorylated by the GSK3 family of protein kinases.

RCAN1 gene consists of seven exons plus the first alternative one (exon 1 through 4) [1]. There are four possible transcripts, and the major transcriptional products are isoforms that include exon 1 (RCAN1-1) or 4 (RCAN1-4). RCAN1-1 encodes a protein of 197 amino acids and is primarily abundant in the fetal and adult brains [1]. Recent study revealed an additional start site upstream of exon 1, which leads to the production of RCAN1-1 with 252 amino acids [6]. In order to avoid confusion between these two products, the former short form is referred as RCAN1-1S (short from) and the latter as RCAN1-1L (long-form).

Signal transducer and activator of transcription 2 (STAT2), one of seven mammalian STAT proteins, is known to be a key interferon (IFN)-signaling molecule in the Janus kinase (JAK)/STAT pathway [7]. In response to type I IFN (IFN-α, -β, and -ω) stimulation, IFN-α and -β receptor-associated JAK1 and Tyk2 are phosphorylated and activated [8]. Activated JAKs then phosphorylate tyrosine residues on STAT1 and STAT2, resulting in the dimerization and nuclear translocation of STAT1–STAT2 heterodimers. In the nucleus, STATs interact with IRF-9/p48 protein to form ISGF3 complexes, which then bind to a specific DNA sequence in target

* Corresponding author at: Department of Systems Biology, College of Life Science and Biotechnology, Yonsei University, Seoul 120-749, Republic of Korea. Fax: +82 2 312 5657.
E-mail address: kchung@yonsei.ac.kr (K.C. Chung).
[1] These authors contributed equally to this work.

0006-291X/$ - see front matter © 2012 Elsevier Inc. All rights reserved.
http://dx.doi.org/10.1016/j.bbrc.2012.03.007

genes [9]. Recent studies have shown that STAT2 plays a pivotal role in blood development, immune responses, and myogenic differentiation [10,11].

In this study, we set out to explore additional roles and/or regulatory modes of RCAN1 (RCAN1-1S). Using yeast two-hybrid assay, we identified several previously unreported RCAN1-binding partners, including STAT2. We further explored the interaction between RCAN1 and STAT2 as well as its functional consequences, focusing on the regulatory mechanism of RCAN1 stability. We found that RCAN1 physically interacts with STAT2 in mammalian cells, resulting in decreased RCAN1 protein levels. In addition, STAT2 reduced RCAN1 levels through the ubiquitin E3 ligase FBW7. Furthermore, IFN-α-activated STAT2 enhanced the RCAN1 degradation, providing evidence of a cytokine-induced RCAN1 degradation pathway involving STAT2 and FBW7.

2. Materials and methods

2.1. Materials

Anti-RCAN1 antibody was purchased from Abgent and ECM Biosciences. Anti-STAT2, anti-histone H1, anti-α-tubulin, anti-ubiquitin, and anti-Hsp90 antibodies were purchased from Santa Cruz Biotechnology. Mammalian expression vectors for HA- or Myc-tagged human wild-type RCAN1 (RCAN1-1S) were kindly provided by S. de la Luna and Z. Zhang, respectively. Plasmids encoding Flag- or Myc-tagged STAT2 were provided by R. Fagerlund and J.H. Ahn, respectively. Plasmids encoding Flag-tagged wild-type FBW7 (FBW7-WT) and its dominant-negative mutant lacking the C-terminal 8xWD40 domain (FBW7-Δ8xWD40) were kindly provided by B.E. Clurman, and Myc-tagged FBW7 by H.S. Park. Mammalian construct encoding HA-tagged human wild type ubiquitin was obtained from T. Dawson. HA-tagged mammalian expression vectors encoding RCAN1 mutants with deletions spanning amino acids 1–95 ($RCAN1^{1-95}$), 1–125 ($RCAN1^{1-125}$), 30–197 ($RCAN1^{30-197}$), and 90–197 ($RCAN1^{90-197}$) were constructed by PCR and subcloning into pCMV-HA-4T1 (Clontech). All constructs were confirmed by DNA sequencing.

2.2. Cell culture and DNA transfection

Human sarcoma 2fTGH cells (STAT2 +/+) and STAT2-null human sarcoma U6A cells (STAT2 −/−) were kindly provided by G.R. Stark. These two cell lines and human embryonic kidney 293 (HEK293) cells were maintained in DMEM containing 10% FBS and 100 unit/ml penicillin–streptomycin. The cells were transfected with LipofectAMINE PLUS reagent, according to the manufacturer's protocols.

2.3. Immunoprecipitation and immunoblotting

Cells were rinsed twice with ice-cold phosphate-buffered saline (PBS), scraped with 1% Nonidet P40 lysis buffer (50 mM Tris, pH 7.5; 1.0% Nonidet P-40; 150 mM NaCl; 10% glycerol; 1 mM Na_3VO_4; 1 μg/ml leupeptin; 1 μg/ml aprotinin; 1 mM EGTA; 1 mM EDTA; 10 mM NaF; 0.2 mM phenylmethylsulfonyl fluoride), and briefly sonicated. Lysates were collected by centrifugation at 13,000×*g* for 20 min at 4 °C. Immunoprecipitation followed by immunoblotting was performed as described previoulsy [12].

2.4. Immunocytochemistry

After DNA transfection for 24 h, immunocytochemical analaysis was performed as described previoulsy [12]. Where specified, samples were stained with 4, 6-diamidino-2-phenylindole (DAPI) using the SlowFade Antifade kit (Invitrogen). Fixed cells were visualized using a LSM-510 META confocal microscope (Carl Zeiss, Gottingen, Germany).

2.5. Preparation of cytosolic and nuclear fractions

Cells were washed with ice-cold PBS and suspended in hypotonic buffer (10 mM HEPES, pH 7.9; 1.5 mM $MgCl_2$; 10 mM KCl) supplemented with protease inhibitors, including dithiothreitol, aprotinin, and leupeptin. The cells were then incubated for 30 min on ice, lysed with a disposable syringe, and centrifuged at 1000×*g* for 15 min at 4 °C. The supernatants were saved and used as the cytosolic fraction. The nuclear pellet fractions were washed with hypotonic buffer and lysed with 1.0% NP-40 lysis buffer. Supernatants were collected after centrifugation at 15,000×*g* for 15 min at 4 °C.

2.6. Statistical analysis

Statistical differences were determined using a one-way ANOVA with Tukey post test. All values were expressed as mean ± SD.

3. Results

3.1. RCAN1 specifically binds to STAT2

To investigate the additional cellular roles and/or regulatory modes of RCAN1, we performed yeast two-hybrid screening of a human fetal brain cDNA library using full-length RCAN1 as bait [13,14]. We identified several previously unreported RCAN1-binding partners, including NF-κB-inducing kinase (NIK) [13], Tollip [14], and STAT2 (data not shown). To further assess the interaction between RCAN1 and STAT2 as well as the functional role of this interaction, we investigated whether RCAN1 is specifically associated with STAT2 in mammalian cells. HEK293 cells were transiently transfected with plasmids encoding HA-tagged RCAN1 alone or together with Myc-tagged STAT2, and immunoprecipitation of cell lysates was performed using anti-HA antibody. Immunoblot analysis of anti-HA-immunocomplexes with anti-Myc antibody revealed that ectopically expressed RCAN1 bound to STAT2 in HEK293 cells (Fig. 1A). Interestingly, RCAN1 levels were lower in cells co-transfected with STAT2 and RCAN1 than in cells transfected with RCAN1 alone (Fig. 1A). These results suggest that RCAN1-bound STAT2 negatively affects RCAN1 protein levels in HEK293 cells. Immunocytochemical analysis of HEK293 cells transfected with HA-RCAN1 and Myc-STAT2 confirmed the co-localization of these two proteins, which were mainly present in the cytoplasmic regions (Fig. 1B). To exclude the possibility that this binding occurred due to an artifact of DNA transfection, we tested whether endogenous RCAN1 interacts with endogenous STAT2 in the 2fTGH human sarcoma cell line. Immunoblot analysis of anti-RCAN1 IgG co-immunoprecipitates using anti-STAT2 antiserum demonstrated the specific interaction between these two endogenous proteins in 2fTGH cells (Fig. 1C). Overall, these data suggest that specific interactions occur between RCAN1 and STAT2 in mammalian cells.

To determine which domain(s) within RCAN1 protein is responsible for the interaction with STAT2, several constructs encoding deleted RCAN1 fragments fused to HA (Fig. 1D) were generated, and co-immunoprecipitation/immunoblot assays were performed. As shown in Fig. 1E, immunoblot analysis of anti-STAT2 immunocomplexes with anti-HA IgG revealed that STAT2 bound well to full length RCAN1 as well as several RCAN1 peptides, such as $RCAN1^{1-95}$, $RCAN1^{1-125}$, and $RCAN1^{30-197}$. However, it did not bind to $RCAN1^{96-197}$ (Fig. 1E). This result suggests that

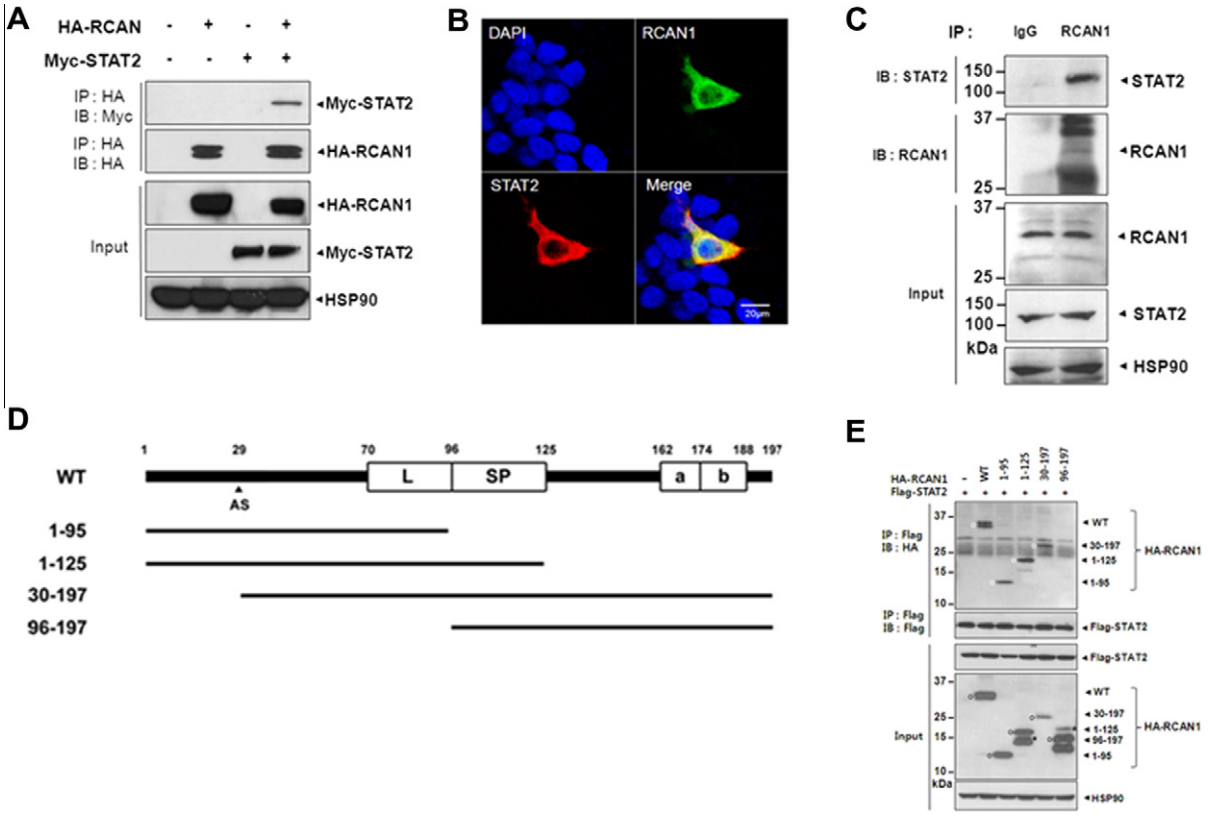

Fig. 1. The interaction between RCAN1 and STAT2. (A) HEK293 cells were mock-transfected or transfected for 24 h with plasmids encoding either HA-RCAN1 and/or Myc-STAT2. The cell lysates were immunoprecipitated with anti-HA antibody, and immunoprecipitates were analyzed by immunoblot with anti-Myc or anti-HA antibodies. The proper expression of transfected proteins in cell lysates was checked with the specified antiserum. Equal loading of the samples was confirmed by immunoblotting with anti-HSP90 antibody. (B) HEK293 cells were co-transfected with HA-RCAN1 and Myc-STAT2 for 24 h, fixed, permeabilized, and labeled with anti-HA or anti-Myc antibody for 24 h. The cells were then stained with TRITC-conjugated anti-rabbit, FITC-conjugated anti-mouse secondary antibodies. Nuclei were counterstained with DAPI. (C) Immunocomplexes prepared with preimmune IgG or anti-RCAN1 antibodies were probed with anti-STAT2 antibodies. The expression of RCAN1 and STAT2 in cell extracts was determined by immunoblotting. (D) Diagram of HA-tagged wild-type RCAN1 and its deletion mutants. (E) HEK293 cells were transfected with Flag-STAT2 alone or together with various HA-tagged deletion RCAN1 mutants, as indicated. Total lysates and anti-Flag immunoprecipitates were analyzed by immunoblot with anti-HA or anti-Flag antibodies. Asterisk indicates the nonspecific bands.

the N-terminal 30–95 amino acid region of RCAN1 is critical for the interaction with STAT2.

3.2. STAT2 overexpression decreases RCAN1 protein levels

As shown in Fig. 1, co-expression of STAT2 appeared to appreciably reduce RCAN1 protein levels compared to expression of RCAN1 alone. Thus, we investigated how the transcription factor STAT2 may lead to a decrease in RCAN1 levels. First, we confirmed that STAT2 reduces RCAN1 levels by transfecting HEK293 cells with HA-tagged RCAN1 either alone or with increasing amounts of Myc-tagged STAT2. We found that increasing the amount of STAT2 decreased RCAN1 levels in a dose-dependent manner (Fig. 2A). Next, we analyzed the effect of STAT2 on the sub-cellular localization of RCAN1 and vice versa. Immunoblot analysis of cytoplasmic and nuclear fractions from HEK293 cell lysates revealed that the sub-cellular localization of STAT2 was not considerably affected by RCAN1 (Fig. 2B). However, RCAN1 was absent from the nucleus in the presence of STAT2 (Fig. 2B). To understand whether endogenous STAT2 similarly affects the level of endogenous RCAN1, we compared RCAN1 levels in the 2fTGH human sarcoma cell line, which contains wild-type STAT2, and the U6A cell line, a mutant human sarcoma cell line lacking STAT2 [14]. Immunoblot analysis of the two cell lysates with anti-RCAN1 antibodies demonstrated that endogenous RCAN1 levels were about 2-fold lower in 2fTGH cells than in U6A cells (Fig. 2C and D). Moreover, the ectopic expression of STAT2 in STAT2-deficient U6A cells decreased RCAN1 levels (Fig. 2E). These results show that STAT2 actually mediates a reduction in RCAN1 protein levels.

3.3. STAT2 enhances RCAN1 degradation via the UPS

RCAN1 has been reported to be processed by the intracellular ubiquitin–proteasome system (UPS) [12]. This finding led us to investigate whether STAT2-induced decreases in RCAN1 occur through the UPS. Pretreatment of HEK293 cells with the proteasome inhibitor MG132 restored RCAN1 levels in STAT2 and RCAN1 co-transfected cells to those seen in control cells transfected with RCAN1 alone (Fig. 3A). To confirm this finding and to assess whether STAT2-induced decrease in RCAN1 may occur through other intracellular protein degradation systems, we analyzed the effect of various protease inhibitors on RCAN1 protein levels under STAT2 overexpression. The protease inhibitors examined were the proteasomal inhibitor lactacystin, the calpain inhibitor calpeptin, the pan caspase inhibitor Z-VAD-FMK, and the lysosomal inhibitor NH_4Cl. Similar to MG132, lactacystin blocked the decrease in RCAN1 levels caused by STAT2 overexpression (Fig. 3B). However, none of the other inhibitors affected STAT2-induced decreases in RCAN1 (Fig. 3B). These results indicate that STAT2 decreases RCAN1 protein level mainly through the UPS.

Next, we tested whether STAT2 affects the ubiquitination of RCAN1. HEK293 cells were transfected with HA-tagged ubiquitin

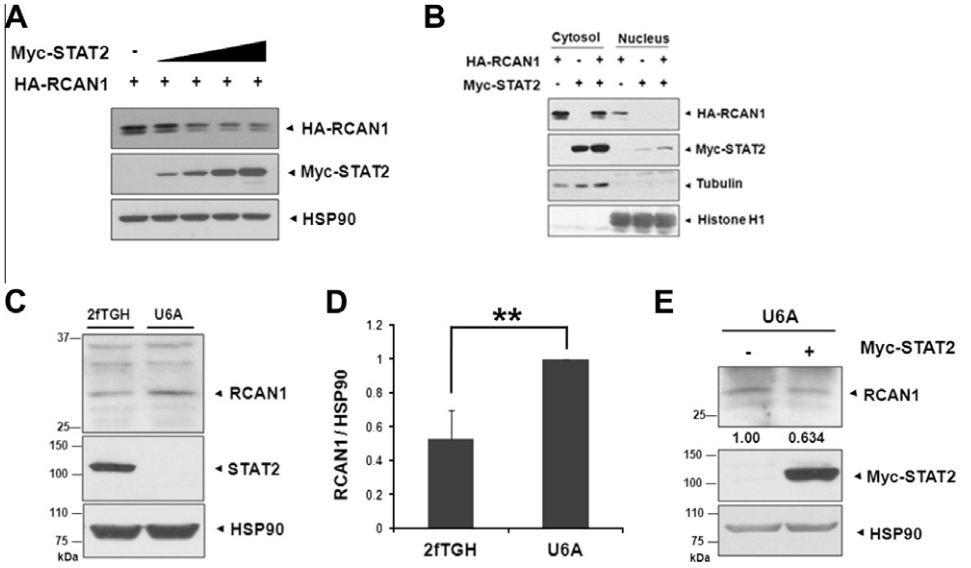

Fig. 2. STAT2 overexpression reduces RCAN1 levels. (A) HEK293 cells were transfected with HA-tagged RCAN1 alone or together with the increasing amounts of Myc-STAT2. RCAN1 and STAT2 levels were determined by immunoblotting with anti-HA and anti-Myc antibody. (B) HEK293 cells were transfected with HA-RCAN1 and/or Myc-STAT2 for 24 h and fractionated into cytosolic and nuclear fractions, which were then analyzed by immunoblot with anti-HA or anti-Myc antibodies. The purity of each fraction was confirmed by immunoblotting of α-tubulin (cytosolic marker) or histone H1 (nuclear marker). (C) Endogenous RCAN1 levels in 2fTGH and U6A cells were analyzed by immunoblotting with anti-RCAN1 antibodies. (D) Quantification of RCAN1 levels in each sample. Error bars indicate ± SD. in triplicate experiments. $^{**}p < 0.05$ compared to 2fTGH. (E) STAT2-deficient U6A cells were transfected for 24 h with Myc-tagged STAT2 plasmid, and endogenous RCAN1 levels were analyzed by immunoblotting and quantified. The values at the bottom of the top panel indicate the relative intensities of RCAN1 bands measured using the ImageJ program (NIH).

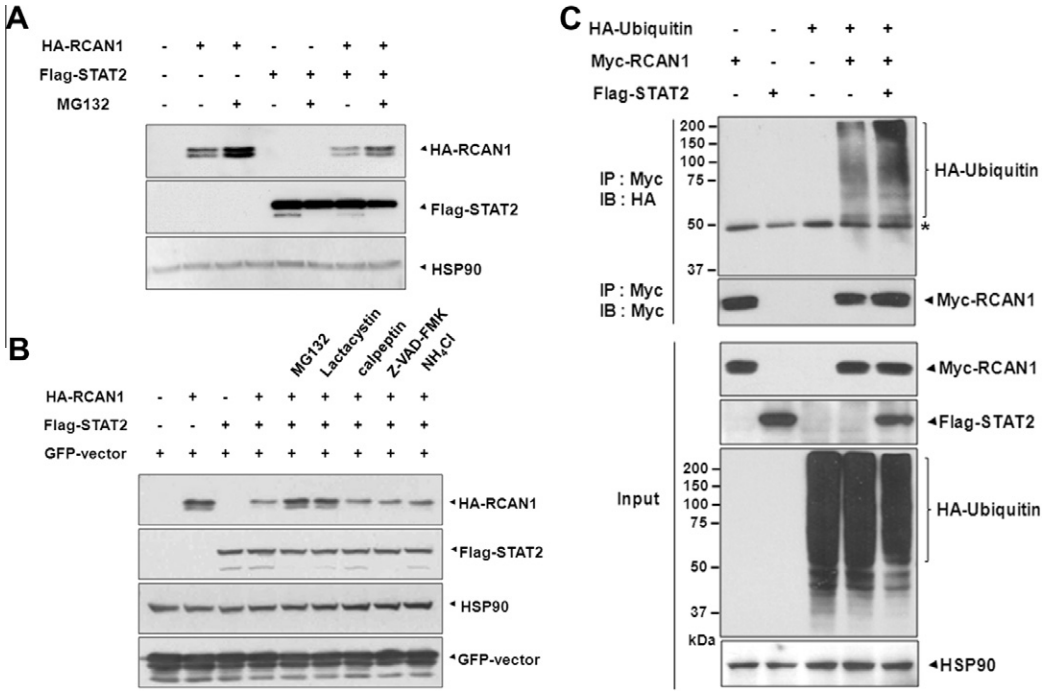

Fig. 3. STAT2-induced decreases in RCAN1 occur via the UPS. HEK293 cells were transfected with HA-RCAN1 alone or together with Flag-STAT2 for 24 h (A). Cells were then left untreated or treated with 10 μM MG132 for 6 h (A & B). Alternatively, they were treated with 10 μM lactacystin, 50 μM calpeptin, 10 μM Z-VAD-FMK, or 15 mM NH_4Cl (B) for 6 h. The expression of HA-RCAN1-S and Flag-STAT2 in cell lysates was assessed by immunoblotting with anti-HA or anti-Flag antibody. Equal loading among samples was confirmed by analyzing HSP90 (A), and equal transfection yield was confirmed using GFP-vector (B). In panel (C), HEK293 cells were transfected for 24 h with HA-tagged ubiquitin alone or along with Myc-tagged RCAN1 ± Flag-tagged STAT2. Cells were then treated with 10 μM MG132 for 6 h. Lysates were immunoprecipitated with anti-Myc antibodies, and immunoprecipitates were analyzed by immunoblotting with anti-HA antibody. Asterisk indicates the nonspecific bands.

alone or along with Myc-tagged RCAN1 ± Flag-tagged STAT2. Cells were then treated with MG132, and the ubiquitination pattern of RCAN1 was examined. Immunoblot analysis of anti-Myc immunocomplexes with anti-HA antiserum revealed that STAT2 overexpression increased the extent of RCAN1 ubiquitination (Fig. 3C). These results indicate that RCAN1 becomes more poly-ubiquitinat-

ed in the presence of STAT2, an outcome that would lead to increased RCAN1 degradation via the proteasome.

3.4. RCAN1 and STAT2 interacts with FBW7 in mammalian cells

The SCF^{FBW7} ubiquitin E3 ligase complex has recently been shown to trigger the degradation of Rcn1, a yeast homologue of RCAN1 [15]. To understand whether RCAN1 is also a substrate for the ubiquitin E3 ligase FBW7 in mammalian systems, we transfected HEK293 cells with plasmids encoding HA-tagged RCAN1 and/or Myc-tagged FBW7 for 24 h, treated the cells with MG132 for another 6 h, and performed immunoprecipitations using anti-HA or anti-Myc antibodies. Immunoblot analysis of immunocomplexes obtained with anti-HA or anti-Flag antibody revealed that RCAN1 also interacted with FBW7 in HEK293 cells (Fig. 4A). This suggests that RCAN1 could be a target for the ubiquitin E3 ligase FBW7 in mammalian cells.

Next, we assessed whether STAT2 also interacts with FBW7. HEK293 cells were transfected with plasmid encoding Myc-STAT2 alone or together with either Flag-tagged wild-type FBW7 or the FBW7-Δ8xWD40 mutant, which lacks the C-terminal 8-times WD40-repeat domain (Fig. 4B). Immunoblot analysis of anti-Flag immunoprecipitates with anti-Myc IgG showed that STAT2 also bound to wild-type FBW7 (Fig. 4C), but not to the FBW7-Δ8xWD40 mutant (Fig. 4D). As the WD40-repeat domains are mainly involved in the substrate recognition of FBW7, this result suggests that a functional link between STAT2 and FBW7 exists.

3.5. FBW7 mediates STAT2-induced degradation of RCAN1

Next, we tested whether STAT2-induced degradation of RCAN1 occurs through FBW7. To check whether RCAN1 is cleaved by FBW7, we co-transfected HEK293 cells with STAT2 and either wild-type FBW7 or the dominant-negative FBW7-Δ8xWD40 mutant. Immunoblot analysis showed that, like STAT2, FBW7-WT significantly decreased RCAN1 levels, while FBW7-Δ8xWD40 had ~2.5-fold less effect (Fig. 4E). In addition, when cells were transfected with RCAN1, STAT2, and FBW7-Δ8xWD40, RCAN1 levels were increased by more than 2-fold, compared to those seen in cells transfected with RCAN1 and STAT2 (Fig. 4E). These data indicate that RCAN1 is a target of the SCF^{FBW7} complex and that STAT2-induced decreases in RCAN1 occur through the action of FBW7.

3.6. Inflammatory signaling reduces RCAN1 levels through STAT2

STAT2 acts as a key IFN-signaling molecule in the JAK/STAT pathway. Accordingly, type I-IFNs (IFN-α, -β, and -ω) activate JAK1 and Tyk2, and the phosphorylation of these kinases subsequently activates STAT2 and the transcription of downstream target genes. To understand the physiological relevance of STAT2-induced alterations in RCAN1, we tested whether the

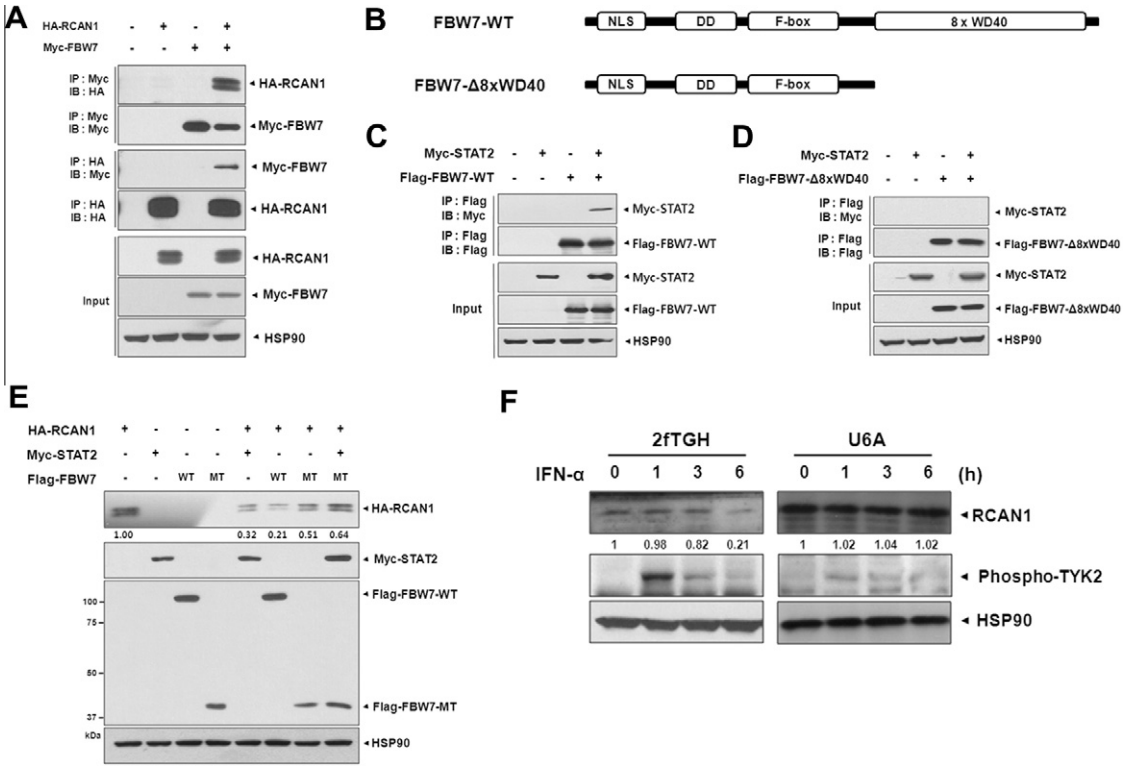

Fig. 4. FBW7 mediates STAT2-induced degradation of RCAN1. (A) HEK293 cells were mock-transfected or transfected with either HA-RCAN1 or Myc-FBW7 alone or together for 24 h. They were then treated with 10 μM MG132 for 6 h. Cell lysates were immunoprecipitated with anti-Myc or anti-HA antibody, and immunoblots were performed with the indicated antiserum. (B) Diagram of wild-type (FBW7-WT) and a FBW7 deletion mutant lacking the eight WD40 repeat domain (FBW7-Δ8xWD40). (C) Cells were mock-transfected or transfected with Myc-STAT2 or Flag-FBW7 alone or together for 24 h. The cell lysates were immunoprecipitated with anti-Flag antibody, and immunoblot analysis was performed using anti-HA antibody. (D) HEK293 cells were either mock-transfected or transfected with Myc-STAT2 and Flag-FBW7-Δ8xWD40, alone or in combination. Immunoprecipitation/immunoblot assays were then performed, as indicated. (E) HEK293 cells were transfected with HA-RCAN1, Flag-STAT2, Flag-FBW7-WT (WT), or Flag-FBW7-Δ8xWD40 (MT) alone or together for 24 h. The cell lysates were subjected to immunoblot analyses with anti-HA or anti-Flag antibodies. The values at the bottom of the top panel indicate the relative quantities of HA-RCAN1 bands. (F) After 2fTGH and U6A cells were treated with IFN-α for the indicated time, endogenous RCAN1 levels in cell extracts were determined by immunoblotting with anti-RCAN1 antibody. Proper inflammatory signaling was confirmed by analyzing phosphorylated TYK2. The values at the bottom of the top panel indicate the relative quantities of endogenous RCAN1 bands.

stimulation of cells with IFN-α can affect RCAN1 protein levels. We compared the effect of an IFN-α stimulus on the levels of endogenous RCAN1 in 2fTGH and STAT2-deficient U6A cells. Immunoblot analysis with anti-RCAN1 antibodies revealed that, in 2fTGH cells, levels of endogenous RCAN1 were decreased after 3 h of treatment with IFN-α (Fig. 4F). In contrast, endogenous RCAN1 levels were not considerably altered in U6A cells, but their levels were highly increased by more than 3.5-fold than 2fTGH cells (Fig. 4F). These data suggest that IFN-α-mediated inflammatory signaling reduces RCAN1 levels through STAT2 activation.

4. Discussion

RCAN1 protein levels are known to be regulated by several degradation pathways, such as the UPS and lysosomal pathway [16–18]. More specifically, the SCF^{CDC4} E3 ubiquitin ligase complex (yeast homologue of FBW7) has been reported to covalently modify Rcn1 (yeast homologue of RCAN1) through poly-ubiquitination and to trigger Rcn1 degradation [15]. This finding is supported by our data showing that RCAN1 becomes ubiquitinated and that inhibition of intracellular proteasomal machinery increases RCAN1 levels. Our data also demonstrate that STAT2 facilitates the ubiquitin-dependent degradation of RCAN1 and its action is mediated through FBW7 E3 ligase. Furthermore, it demonstrates that FBW7-mediated RCAN1 degradation is enhanced by IFN-α treatment.

FBW7 is not the only ubiquitin E3 enzyme that covalently transfers an ubiquitin moiety to RCAN1. For example, β-TrCP, one of the F-box protein components of the SCF ubiquitin ligase, mediates RCAN1 ubiquitination following stimulation with H_2O_2 [19]. Nedd4-2 also acts as a novel E3 enzyme to target RCAN1 for degradation through ubiquitination [20]. Based on these reports, it would be interesting to check if STAT2 recruits these two enzymes. We also recently demonstrated that, similar to STAT2, CREB can activate the degradation of RCAN1, depending on its transcriptional activation [17]. Like the UPS, chaperone-mediated autophagy pathway can also degrade RCAN1 [18].

Here, we have provided evidence that STAT2 negatively regulates the level of RCAN1. Although the action of STAT2 that degrades RCAN1 occurs through FBW7, the detailed mechanism of how STAT2 modulates the SCF E3 enzyme is largely unknown. We speculate that, under resting conditions, FBW7 has difficulty binding to RCAN1 and processing RCAN1 ubiquitination. However, cytokine-activated STAT2 or STAT2 that has accumulated due to increased protein stability might directly and more freely bind to RCAN1 and FBW7, providing a more optimal environment for ubiquitination of RCAN1 by FBW7. The validity of this hypothesis needs to be tested with additional experiments. To date, a few STAT2 binding proteins have been reported, and they are all linked to gene transcription. Examples include STAT1 and p300/CBP [21,22]. The current work provides the first evidence that STAT2 directly binds to the ubiquitin E3 ligase FBW7 and helps the degradation of RCAN1. Similar to STAT2, Smad7 binds to the novel E3 ubiquitin ligase Tiul1 and targets Smad2 for degradation [23]. Studies have shown that CREB triggers RCAN1 degradation via the UPS [18] and that both CREB and STAT2 bind to CREB-binding protein [22]. Given these findings, CREB-mediated RCAN1 degradation likely proceeds through STAT2 action and involves FBW7 recruitment.

RCAN1 protein levels and activity are known to be affected by several factors. For example, RCAN1 interacts physically and functionally with calcineurin A, in some instances inhibiting its Ca^{2+}-induced phosphatase activity [3,5]. Similar to this study, recent studies have also shown that RCAN1 protein stability is regulated by inflammatory signaling. For example, NIK specifically interacts with RCAN1 and phosphorylates its C-terminal region [12]. This phosphorylation increases RCAN1 protein stability and blocks its proteasomal degradation [12]. We also investigated whether inflammatory signaling can affect the RCAN1 levels via STAT2 activation. We found that RCAN1 protein levels are decreased by the cytokine IFN-α. Together, these reports show that STAT2 interplay with RCAN1 can transduce and regulate diverse immune responses through the NFAT and NF-κB signaling pathways.

Acknowledgments

This study was supported by grants from the Korea Healthcare technology R&D Project (A092004 and A111653 to K.C.C.) funded by Ministry for Health, Welfare & Family Affairs, Republic of Korea. This work was also partially supported by grants from the Brain Research Center of the 21st Century Frontier Research Program Technology (2009K-001251 to K.C.C.), the National Research Foundation of Korea (NRF) (2010-0018916 to K.C.C.), and the Basic Science Research Program through NRF (2012-0000810 to K.C.C.) all funded by the Ministry of Education, Science and Technology (MEST), Republic of Korea.

References

[1] J.J. Fuentes, M.A. Pritchard, X. Estivill, Genomic organization, alternative splicing, and expression patterns of the DSCR1 (Down syndrome candidate region 1) gene, Genomics 44 (1997) 358–361.
[2] C.D. Harris, G. Ermak, K.J. Davies, Multiple roles of the DSCR1 (Adapt78 or RCAN1) gene and its protein product calcipressin1 (or RCAN1) in disease, Cell. Mol. Life Sci. 62 (2005) 2477–2486.
[3] J.J. Fuentes, L. Genescà, T.J. Kingsbury, K.W. Cunningham, M. Pérez-Riba, X. Estivill, S. de la Luna, DSCR1, overexpressed in Down syndrome, is an inhibitor of calcineurin-mediated signaling pathways, Hum. Mol. Genet. 9 (2000) 1681–1690.
[4] Z. Hilioti, D.A. Gallagher, S.T. Low-Nam, P. Ramaswamy, P. Gajer, T.J. Kingsbury, C.J. Birchwood, A. Levchenko, K.W. Cunningham, GSK-3 kinases enhance calcineurin signaling by phosphorylation of RCNs, Genes Dev. 18 (2003) 35–47.
[5] B. Rothermel, R.B. Vega, J. Yang, H. Wu, R. Bassel-Duby, R.S. Williams, A protein encoded within the Down syndrome critical region is enriched in striated muscles and inhibits calcineurin signaling, J. Biol. Chem. 275 (2000) 8719–8725.
[6] L. Genesca, A. Aubareda, J.J. Fuentes, X. Estivill, S. De La Luna, M. Perez-Riba, Phosphorylation of calcipressin 1 increases its ability to inhibit calcineurin and decreases calcipressin half-life, Biochem. J. 374 (2003) 567–575.
[7] G.R. Stark, I.M. Kerr, B.R. William, R.H. Silverman, R.D. Schreiber, How cells respond to interferons, Annu. Rev. Biochem. 67 (1998) 227–264.
[8] M.J. Gutch, C. Daly, N.C. Reich, Tyrosine phosphorylation is required for activation of an alpha interferon-stimulated transcription factor, Proc. Natl. Acad. Sci. USA 89 (1992) 11411–11415.
[9] S.A. Veals, C. Schindler, D. Leonard, X.Y. Fu, R. Aebersold, J.E. Darnell, D.E. Levy, Subunit of an alpha-interferon-responsive transcription factor is related to interferon regulatory factor and Myb families of DNA-binding proteins, Mol. Cell. Biol. 12 (1992) 3315–3324.
[10] J.J. O'Shea, M. Gadina, R.D. Schreiber, Cytokine signaling in 2002: new surprises in the Jak/Stat pathway, Cell 109 (2002) 121–131.
[11] K. Wang, C. Wang, F. Xiao, H. Wang, Z. Wu, JAK2/STAT2/STAT3 are required for myogenic differentiation, J. Biol. Chem. 283 (2008) 34029–34036.
[12] E.J. Lee, S.R. Seo, J.W. Um, J. Park, Y. Oh, K.C. Chung, NF-kappaB-inducing kinase phosphorylates and blocks the degradation of Down syndrome candidate region 1, J. Biol. Chem. 283 (2008) 3392–3400.
[13] J.Y. Lee, H.J. Lee, E.J. Lee, S.H. Jang, H. Kim, J.H. Yoon, K.C. Chung, Down syndrome candidate region-1 protein interacts with Tollip and positively modulates interleukin-1 receptor-mediated signaling, Biochim. Biophys. Acta 1790 (2009) 1673–1680.
[14] S. Leung, S.A. Qureshi, I.M. Kerr, J.E. Darnell, G.R. Stark, Role of STAT2 in the alpha interferon signaling pathway, Mol. Cell. Biol. 15 (1995) 1312–1317.
[15] T. Kishi, A. Ikeda, R. Nagao, N. Koyama, The SCF^{CDC4} ubiquitin ligase regulates calcineurin signaling through degradation of phosphorylated Rcn1, an inhibitor of calcineurin, Proc. Natl. Acad. Sci. USA 104 (2007) 17418–17423.
[16] J. Park, Y. Oh, K.C. Chung, Two key genes closely implicated with the neuropathological characteristics in Down syndrome: DYRK1A and RCAN1, BMB Rep. 42 (2009) 6–15.
[17] S.R. Seo, K.C. Chung, CREB activates proteasomal degradation of DSCR1/RCAN1, FEBS Lett. 582 (2008) 1889–1893.
[18] H. Liu, P. Wang, W. Song, X. Sun, Degradation of regulator of calcineurin 1 (RCAN1) is mediated by both chaperone-mediated autophagy and ubiquitin proteasome pathways, FASEB J. 23 (2009) 3383–3392.
[19] S. Asada, A. Ikeda, R. Nagao, H. Hama, T. Sudo, A. Fukamizu, Y. Kasuya, T. Kishi, Oxidative stress-induced ubiquitination of RCAN1 mediated by SCFbeta-TrCP ubiquitin ligase, Int. J. Mol. Med. 22 (2008) 95–104.

[20] S.S. Kim, S.R. Seo, Nedd4-2 ubiquitin ligase interacts with RCAN1 (DSCR1) for the proteasomal degradation, Genes Genom. 32 (2010) 578–582.

[21] X. Li, S. Leung, S. Qureshi, J.E. Darnell, G.R. Stark, Formation of STAT1-STAT2 heterodimers and their role in the activation of IRF-1 gene transcription by interferon-α, J. Biol. Chem. 271 (1996) 5790–5794.

[22] S. Bhattacharya, R. Eckner, S. Grossman, E. Oldread, Z. Arany, A. D'Andrea, D.M. Livingston, Cooperation of Stat2 and p300/CBP in signaling induced by interferon- α, Nature 383 (1996) 344–347.

[23] S.R. Seo, F. Lallemand, N. Ferrand, M. Pessah, S. L'Hoste, J. Camonis, A. Atfi, The novel E3 ubiquitin ligase Tiul1 associates with TGIF to target Smad2 for degradation, EMBO J. 23 (2004) 3780–3792.

Biochemical and Biophysical Research Communications 420 (2012) 411–416

Contents lists available at SciVerse ScienceDirect

Biochemical and Biophysical Research Communications

journal homepage: www.elsevier.com/locate/ybbrc

Isolation of miRNAs that target EGFR mRNA in human lung cancer

Gaku Yamaguchi [a,1], Masakatsu Takanashi [b,1], Masami Tanaka [b,1], Koji Fujita [b], Tatsuo Ohira [a], Masahiko Kuroda [b,*], Norihiko Ikeda [a]

[a] Department of Surgery, Tokyo Medical University, Nishishinjuku, Shinjuku-ku, Tokyo 160-0023, Japan
[b] Department of Molecular Pathology, Tokyo Medical University, Shinjuku, Shinjuku-ku, Tokyo 160-8402, Japan

ARTICLE INFO

Article history:
Received 1 March 2012
Available online 9 March 2012

Keywords:
EGFR
Lung cancer
miR-542-5p

ABSTRACT

Lung cancer, predominantly non-small cell lung cancer (NSCLC), remains the leading cause of cancer-related deaths worldwide. Although epidermal growth factor receptor (EGFR) signaling is important and well studied with respect to NSCLC progression, little is known about how miRNAs mediate EGFR signaling to modulate tumorigenesis. To identify miRNAs that target EGFR, we performed a bioinformatics analysis and found that miR-542-5p down-regulates *EGFR* mRNA and protein expression in human lung cancer cells (H3255, A549, Hcc827). We observed increases in EGFR association with Ago2 in miR-542-5p-transfected cells. Interestingly, we observed an inverse correlation of miR-542-5p expression and EGFR protein levels in human lung cancer tissue samples, suggesting that miR-542-5p directly targets EGFR mRNA. Furthermore, we found that miR-542-5p inhibited the growth of human lung cancer cells. Our findings suggest that miR-542-5p may act as an important modulator of EGFR-mediated oncogenesis, with potential applications as a novel therapeutic target in lung cancer.

1. Introduction

Lung cancer is the most common cancer and the leading cause of cancer-related death worldwide [1]. The epidermal growth factor receptor (EGFR) signaling network plays a central role in the growth and maintenance of epithelial tissues, and EGFR is overexpressed or mutated in most non-small cell lung cancer (NSCLC) cases [2]. Consequently, the EGFR and its downstream signaling effectors are major targets for new therapeutics such as monoclonal antibodies and tyrosine kinase inhibitors [3]. However, the clinical responses of tumors to existing anti-EGFR agents are often limited, and thus a major research focus is the development of novel approaches to block EGFR expression and signaling [4].

MicroRNAs (miRNA) belong to a class of endogenously-expressed, non-coding small RNAs of approximately 22 nucleotides. These small RNAs influence gene regulation by pairing to protein-coding mRNAs to repress their expression via decreased translational efficiency and/or mRNA levels [5]. Growing evidence suggests that dysregulation of miRNA expression contributes to a wide variety of human cancers, including lung cancers [6–11]. Recently, miRNAs have been demonstrated to be diagnostic and prognostic markers in leukemia, lung cancer, and colon cancer [12]. miRNAs may also represent therapeutic targets in human cancers [13]. Interestingly, it has been reported that miR-7 has the ability to coordinately regulate EGFR signaling in multiple human cancer cell types [14]. A miRNA that regulates EGFR may have therapeutic potential against lung cancer.

Computational approaches to miRNA target prediction have used criteria such as sequence complementarity between target mRNAs and a "seed" region within the miRNA, and conservation of predicted miRNA-binding sites across 3′-UTRs from multiple species [15]. Recently, additional features that determine target site functionality have been identified [11,16]. However, the imperfect complementarity of miRNA and target sequences means that identification and functional validation of authentic miRNA targets remains a major challenge.

In the present study we investigate miRNAs that might target EGFR mRNA using computational approaches and identified miR-542-5p as a direct regulator of EGFR mRNA in cancer cells. Furthermore, we showed that miR-542-5p suppressed proliferation of lung cancer cells. Identifying miRNA regulators of EGFR may contribute to the development of novel therapeutics.

2. Materials and methods

2.1. Cell culture and transfection

The HeLa human cervical cancer cell line and the A549 human lung cancer cell line were purchased from the American Type Culture Collection. Cells were cultured according to ATCC instructions. MicroRNAs used in this study were as follows: has-miR-7

* Corresponding author. Address: Department of Molecular Pathology, Tokyo Medical University, 6-1-1, Shinjuku, Shinjuku-ku, Tokyo 160-8402, Japan.
E-mail address: kuroda@tokyo-med.ac.jp (M. Kuroda).
[1] These authors contributed equally.

0006-291X/$ - see front matter © 2012 Elsevier Inc. All rights reserved.
http://dx.doi.org/10.1016/j.bbrc.2012.03.008

sense (5′-UGGAAGACUAGUGAUUUUGUUGU-3′) and antisense (5′-AACAAGUCACAGCCGGCCUCA-3′); hsa-miR-541 sense (5′-AAAGG AUUCUGCUGUCGGUCCCACU-3′) and antisense (5′-UGGUGGGCAC AGAAUCUGGACU-3′); has-miR-542-5p sense (5′-UCGGGGAUCAU CAUGUCAUGAGA-3′) and antisense (5′-ugugacagauugauaacugaaa-3′) miR-nontarget control miRNA sense (5′-AUCCGCGCGAUAG CACGUAUU-3′) and antisense (5′-UACGUACUAUCGCGCGGAUUU-3′). Oligonucleotides were individually transfected into cells using HiPerFect reagent (Qiagen) according to the manufacturer's instructions.

2.2. Western blot analysis

Protein samples were suspended in sodium dodecyl sulfate loading buffer. After boiling, equal amounts (20 μg) of the protein samples were run on 7.5% sodium dodecyl sulfate–polyacrylamide gel electrophoresis gels and transferred to Immobilon membranes (Millipore, Bedford, MA) by semi-dry blotting. The membranes were probed with antibody for EGFR (sc-71033; Santa Cruz Biotechnology) using standard techniques. The signals were visualized by ECL Plus Western blotting detection system (GE Health Care) and detected with LAS-3000 mini (Fujifilm).

2.3. RNA isolation and quantitative RT-PCR

RNAs were isolated from miR-transfected A549 cells using Isogen reagent (Nippon Gene) according to the manufacturer's instructions. miRNA levels were quantified using TaqMan MicroRNA Assays (Applied Biosystems). miRNA levels were normalized based on has-miR-16 levels. Complementary DNA was synthesized using SuperScriptII and Random Hexamers (Invitrogen). Quantitative PCR analysis was run on a Stratagene MX3000P thermocycler and analyzed with MxPro (Stratagene). The EGFR primers used in this study were as follows: forward primer, 5′-GTGACCGTTTGGGAGTTGATGA-3′ and reverse primer, 5′-GGCTGAGGGAGGCGTTCT C-3′.

2.4. Immunohistochemistry and in situ hybridization

Human lung cancer tissues for histologic studies were obtained from Tokyo Medical University Hospital. This study was approved

A

Luciferase GL3-6FAM	Has-mir-663b	Has-miR-1908	Has-miR-452	Has-miR-671-5P	Has-miR-1538	Has-miR-150*	Has-miR-616	Has-miR-1203	Has-miR-575	Lamin A/C
Has-miR-7	Has-miR-1205	Has-miR-1226*	Has-miR-146b-3p	Has-miR-1301	Has-miR-1911	Has-miR-541*	Has-miR-637	Has-miR-1265	Has-miR-1237	Has-miR-517*
Has-miR-24	Has-miR-1207-5p	Has-miR-1914*	Has-miR-432	Has-miR-770-5p	Has-miR-21*	Has-miR-198	Has-miR-663	Has-miR-612	Has-miR-377*	Has-miR-1228*
Has-miR-188-3p	Has-miR-1244	Has-miR-214	Has-miR-520a-5p	Has-miR-760	Has-miR-92a-2*	Has-miR-139-3p	Has-miR-30b*	Has-miR-550	Has-miR-941	Has-miR-1911*
Has-miR-296-3p	Has-miR-1254	Has-miR-193a-5p	Has-miR-526b	Has-miR-934	Has-miR-23b*	Has-miR-330-5p	Has-miR-541	Has-miR-30a*	Has-miR-542-5p	Has-miR-453
Has-miR-423-5p	Has-miR-1269	Has-miR-370	Has-miR-500	Has-miR-1200	Has-miR-130a*	Has-miR-485-5p	Has-miR-665	Has-miR-93*	Has-miR-624*	Has-miR-557
Has-miR-503	Has-miR-1292	Has-miR-378	Has-miR-509-3p	Has-miR-1250	Has-miR-143*	Has-miR-520a-5p	Has-miR-1915	Has-miR-185*	Has-miR-886-5p	Luciferase GL3
eGFP	Has-miR-1471	Has-miR-422a	Has-miR-532-5p	Has-miR-1268	Has-miR-149*	Has-miR-525-5p	Has-miR-1184	Has-miR-194*	Has-miR-412	Negative contorol

B

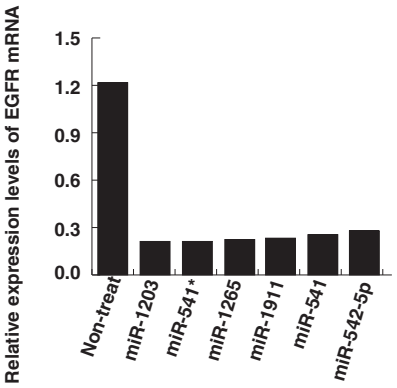

C

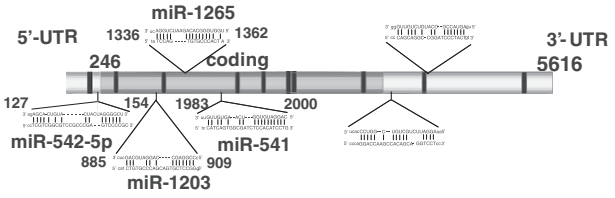

Fig. 1. Identification of miRNAs that target EGFR using 96-well plate transfections. (A) Candidate miRNAs targeting the EGFR sequence on a 96-well plate. (B) Down-regulation of EGFR mRNA by synthetic miRNA. Real-time PCR showed that synthetic miR-1203, miR-541*, miR-1265, miR-1911, miR-541, and miR-542-5p suppress EGFR mRNA in HeLa cells. (C) The predicted binding sites for miR-1203, miR-541*, miR-1265, miR-1911, miR-541, and miR-542-5p in the EGFR mRNA are indicated schematically.

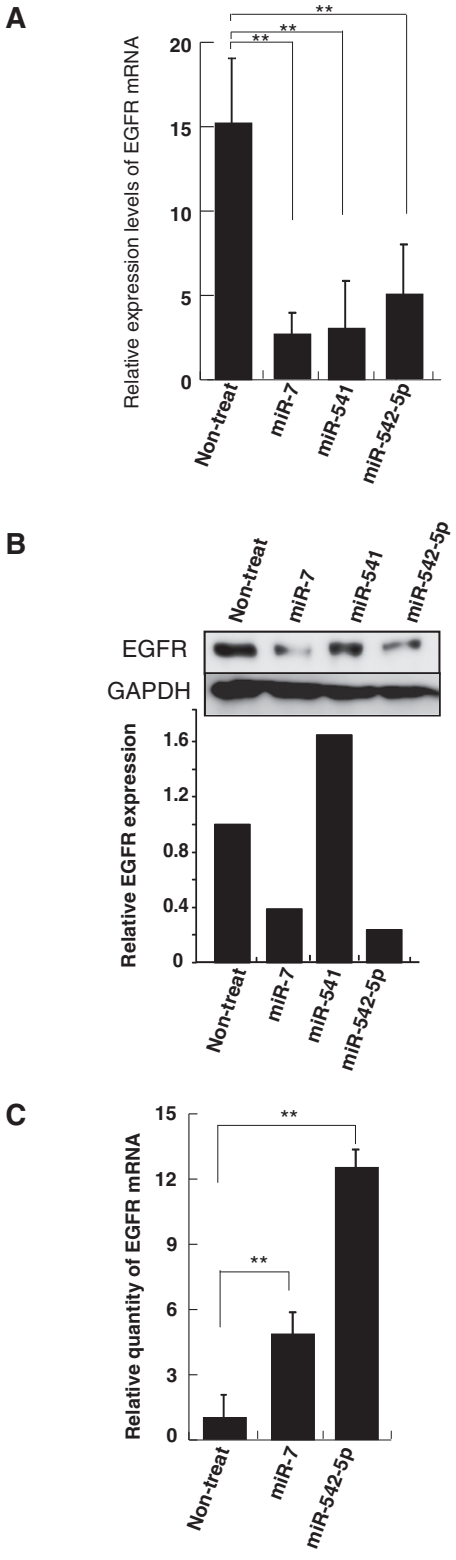

Fig. 2. EGFR is a direct target of miR-542-5p in lung cancer cells. (A) Quantitative analysis of EGFR mRNA by real-time PCR. EGFR mRNA significantly decreased upon transfection of synthetic miR-7, miR-541, and miR-542-5p in A549 cells. *Bars*, mean ± SD. $^{**}P < 0.02$ (B) Regulation of EGFR protein expression by synthetic miR-7, miR-541, and miR-542-5p. A representative western blot analysis of total cell extracts from A549 cells transfected with synthetic miR-7, miR-541, and miR-542-5p is shown in (B). GAPDH was used as a loading control. Densitometry ratios of EGFR to GAPDH were calculated and recorded. (C) Using an anti-Ago2 antibody, we performed RNA co-immunoprecipitation from A549 cells transfected with synthetic miR-7 and miR-542-5p. Reverse-transcribed RNA was PCR-amplified using primers specific for the EGFR mRNA. The averages of three independent experiments are shown. *Bars*, mean ± SD. $^{**}P < 0.02$.

by the institutional review board of Tokyo Medical University, and all patients provided written informed consent.

Immunohistochemical assays were performed on formalin-fixed, paraffin-embedded sections with the Ventana HX System Benchmark (Ventana Medical Systems). An anti-EGFR monoclonal antibody (DAK-H1-WT, DAKO) was applied at a dilution of 1:500. miR-542-5p expression in human lung cancer specimens was detected by *in situ* hybridization with miRCURY LNA probe for miR-542-5p (Exigon) as described previously [17].

2.5. In vitro proliferation assays

We evaluated the effects of miR-7 and miR-542-5p on A549 cell growth using the MTT metabolic growth assay kit (Cell Count Reagent SF, Nacalai Tesque). After transfection with miR-7 or miR-542-5p, cell numbers were assessed by MTT assay 72 h after transfection according to the manufacturer's instructions. Briefly, reagents were added to each well and incubated at 37 °C for 4 h. The reduction of MTT by living cells into a formazan product was visualized using a multiwell scanning spectrophotometer at 450 nm.

2.6. Co-immunoprecipitation

miRNA-542-5p and Ago2 co-immunoprecipitation experiments were performed using Ago2 antibody (Wako Pure Chemical Industries, Tokyo, Japan) as described previously [17]. Total RNA was isolated from the precipitates using TRIzol reagent. Reverse transcription-PCR was performed as described. Parallel immunoprecipitation using rabbit IgG served as a control.

2.7. Statistical analysis

Differences were statistically evaluated using one-way ANOVA followed by Fisher's protected least significant difference test. *P* values < 0.05 were considered statistically significant.

3. Results

3.1. Identification of EGFR target miRNA

First, we used the miRanda system to select candidate miRNAs that might regulate EGFR (NM_201281.1, NM201282.1, NM201283.1, NM201284.1 and NM005228.3). In this analysis, we evaluated the full-length EGFR gene, including the 5′-UTR. We selected a total of 413 candidate miRNAs that could potentially target EGFR (Supplement 1). We narrowed the list of miRNAs based on pairing scores and energies of sequence and synthesized 83 miRNAs (Fig. 1A). We next transfected HeLa cells in 96-well plates with the miRNAs and determined the expression of EGFR mRNA by qRT-PCR analysis. miR-1237, -1203, -541*, -1265, -1911, -541, and -542-5p down-regulated EGFR mRNA in HeLa cells (Fig. 1B, C).

3.2. miR-542-5p directly targets EGFR in lung cancer cell lines

Next, we determined whether the above miRNAs down-regulate EGFR in the A549 lung cancer cell line. We transfected miR-1237, -1203, -541*, -1265, -1911, -541, and -542-5p as well as miR-7, which has been reported to down-regulate EGFR mRNA and protein expression in lung cancer cell lines [14]. In A549 cells, RT-PCR analysis showed that miR-541, miR-542-5p, and miR-7 down-regulate EGFR mRNA (Fig. 2A); however, we could not confirm down-regulation of EGFR mRNA by miR-1237, -1203, -541*, -1265, or -1911.

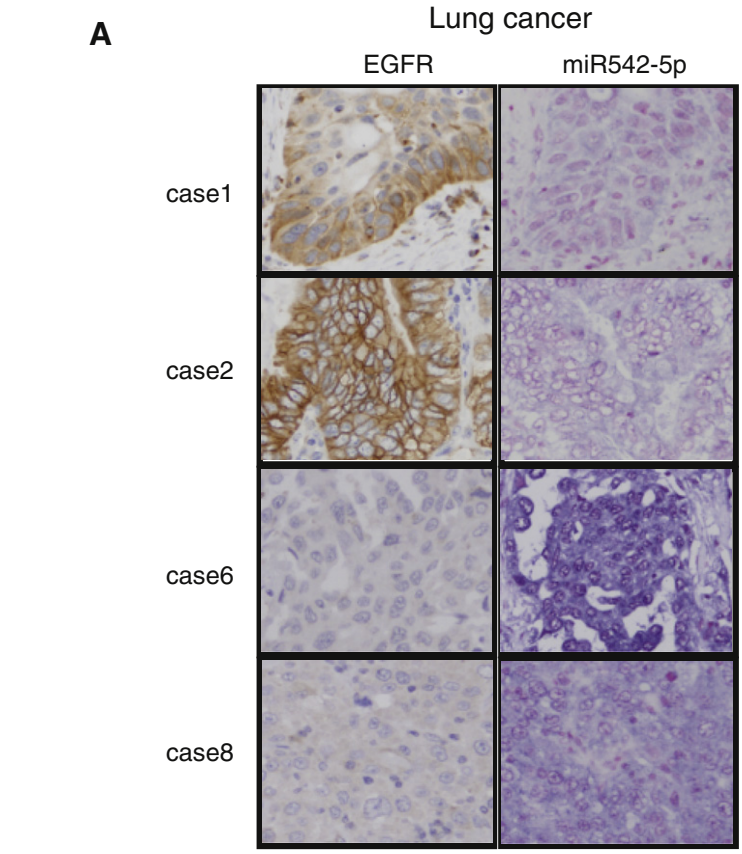

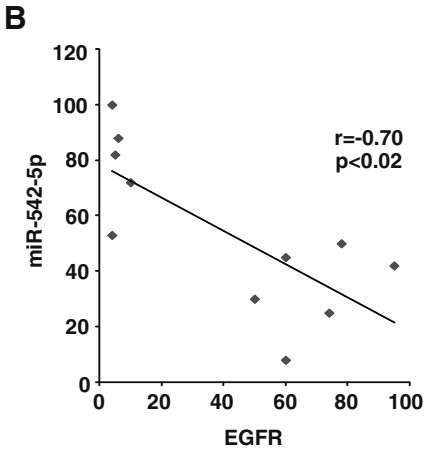

C

	EGFR	miR-542-5p
case1	82	5
case2	72	10
case3	25	74
case4	50	78
case5	8	60
case6	42	95
case7	53	4
case8	45	60
case9	100	4
case10	88	6
case11	30	50

Fig. 3. EGFR expression in human lung cancer cells is inversely related to miR-542-5p expression. (A) We performed *in situ* hybridization for miR-542-5p in concert with immunohistochemical analysis for EGFR. Blue staining represents miRNA positivity, while brown staining represents EGFR positivity. (B) The inverse correlation between miR-542-5p expression and EGFR expression in lung adenocarcinomas is graphically depicted. The mean miR-542-5p and EGFR staining scores were calculated as described [26]. *Bars*, mean ± SD. $^{*}P < 0.02$, ANOVA followed by Tukey–Kramer test. (C) Summary of EGFR and miR-542-5p staining data.

We next investigated whether miR-541 and miR-542-5p suppressed EGFR protein expression. Interestingly, we observed that miR-7 and miR-542-5p down-regulated EGFR protein, whereas miR-541 did not affect EGFR protein levels. These data indicate that miR-542-5p directly suppresses translation of EGFR mRNA. Next, we performed immunoprecipitation assays using an anti-Ago2 antibody. Ago2 is an essential mediator of miRNA-binding to RNA-induced silencing complexes. We therefore analyzed EGFR mRNA levels in Ago2 immunoprecipitates from lysates of HeLa cells transfected with either miR-7 or miR-542-5p. After normalizing EGFR mRNA levels to β-actin mRNA levels in IP samples, we observed increases in EGFR mRNA association with Ago2 in miR-7 and miR-542-5p-transfected cells (Fig. 2C). Together, these data indicate that EGFR mRNA is a direct target of miR-542-5p.

3.3. EGFR is up-regulated in human lung cancer in association with miR-542-5p expression

To investigate the connection between EGFR expression and *miR*-542-5p in lung cancer, we performed immunohistochemical

analysis using anti-EGFR antibodies and *in situ* hybridization using LNA-modified probes specific for *miR*-542-5p in a series of clinical lung cancer samples. Positive staining for *miR*-542-5p was observed in the cytoplasm within these specimens (Fig. 3A). We also detected positive cytoplasmic and membrane staining for EGFR (Fig. 3A). The majority of cases with low *miR*-542-5p staining exhibited strong expression of EGFR protein (Fig. 3B), while most tissues demonstrating high staining for *miR*-542-5p showed low EGFR protein expression. These data demonstrate an inverse correlation of *miR*-542-5p expression with EGFR protein levels *in vivo* ($r = -0.7$, $P < 0.02$, by Spearman's correlation coefficient by rank test), and suggest that dysregulation of *miR*-542-5p is involved in lung carcinogenesis and tumor progression by targeting EGFR.

3.4. Effects of miR-542-5p on a human lung cancer cell line

The EGFR oncoprotein plays a pivotal role in the proliferation of lung cancer cells [18]. Therefore, we investigated whether miR-542-5p would affect the proliferation of the A549 human lung cancer cell line. We transiently transfected either anti-miR-542-5p or miR-7 antagomir into these cells and assessed cell number by MTT assay three days after transfection. Cells transfected with anti-542-5p or miR-7 antagomir exhibited lower proliferative rates than cells transfected with control LNA (Fig. 4: $P < 0.05$). We confirmed the levels of miR-542-5p and miR-7 in cells by quantitative real-time PCR (data not shown). These results suggest that *miR*-542-5p may serve as a molecular target for novel anticancer drugs.

4. Discussion

In the present study, we have demonstrated that miR-542-5p can regulate the expression of EGFR. Furthermore, miR-542-5p has functional effects in cancer cell lines that include reducing cell growth and viability.

Recently, it has been reported that miR-7 down-regulates EGFR mRNA and protein expression in cancer cell lines (lung, breast, and glioblastoma), inducing cell cycle arrest and cell death [14]. We confirmed that miR-7 suppresses EGFR mRNA and protein levels and found that miR-542-5p does as well. Interestingly, miR-542-5p more strongly suppressed cell proliferation than miR-7 (Fig. 4). One possibility for this difference is that miR-7 binds to the 3′-UTR of the EGFR mRNA whereas miR-542-5p binds to the 5′-UTR. Recently, it has become apparent that miRNAs can target sites in 5′-UTRs, and that interactions of miRNAs with gene promoters can regulate gene activity at the transcriptional level [19]. miR-7 has the ability to coordinately down-regulate the expression of multiple members of the EGFR signaling cascade [14]. It is possible that these miRNAs have different potential to down-regulate the expression of multiple members of the EGFR signaling cascade.

Selective inhibitors of EGFR tyrosine kinase activity (EGFR-TKI; i.e., gefitinib and erlotinib) prevent binding of ATP to the ATP-binding pocket of EGFR in a competitive manner, resulting in the loss of catalytic activity [20,21]. Interestingly, it has been reported that the effects of EGFR-TKI are correlated with activating somatic mutations in the epidermal growth factor receptor [22–24]. In contrast, miRNA-542-5p inhibits EGFR by a different mechanism – down-regulating its levels by binding to the 5′-UTR of the EGFR mRNA. Therefore, the suppression of EGFR by miRNA-542-5p should not be affected by mutations in the coding sequence. Agents such as miR-542-5p that down-regulate expression of EGFR as well as some of its signaling effectors may have significant therapeutic potential in a range of human cancer types.

It has recently been reported that miR-543-5p plays a tumor suppressor role in neuroblastoma cells [25], but the proposed target gene was nuclear. In this study, we showed that miR-542-5p overexpression in lung cancer cells decreased cell numbers compared with non-treated cells (Fig. 4). These data indicate that miR-542-5p is a potential novel therapeutic target in lung cancer.

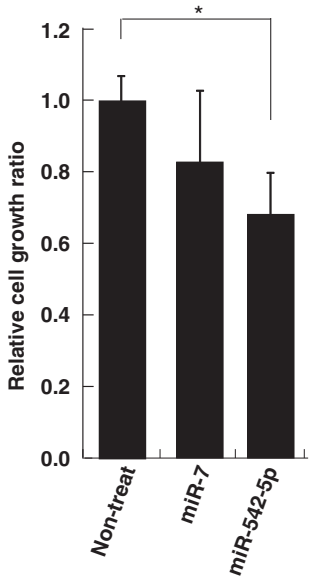

Fig. 4. miR-542-5p modulates the proliferation of human lung cancer cell lines. We determined the number of A549 cells 72 h after transfection with the amiR-7 or miR-542-5p by MTT assay. *Bars*, mean ± SD. (*$P < 0.05$).

Appendix A. Supplementary data

Supplementary data associated with this article can be found, in the online version, at http://dx.doi.org/10.1016/j.bbrc.2012.03.008.

References

[1] A. Jemal, R. Siegel, E. Ward, T. Murray, J. Xu, C. Smigal, M.J. Thun, Cancer statistics, 2006, CA: A Cancer Journal for Clinicians 56 (2006) 106–130.
[2] G.V. Scagliotti, G. Selvaggi, S. Novello, F.R. Hirsch, The biology of epidermal growth factor receptor in lung cancer, Clinical Cancer Research: An Official Journal of the American Association for Cancer Research 10 (2004) 4227s–4232s.
[3] C.L. Arteaga, EGF receptor as a therapeutic target: patient selection and mechanisms of resistance to receptor-targeted drugs, Journal of Clinical Oncology: Official Journal of the American Society of Clinical Oncology 21 (2003) 289s–291s.
[4] R. Bianco, T. Troiani, G. Tortora, F. Ciardiello, Intrinsic and acquired resistance to EGFR inhibitors in human cancer therapy, Endocrine-Related Cancer 12 (Suppl 1) (2005) S159–S171.
[5] D.P. Bartel, MicroRNAs: genomics, biogenesis, mechanism, and function, Cell 116 (2004) 281–297.
[6] K. Inamura, Y. Togashi, K. Nomura, H. Ninomiya, M. Hiramatsu, Y. Satoh, S. Okumura, K. Nakagawa, Y. Ishikawa, Let-7 microRNA expression is reduced in bronchioloalveolar carcinoma, a non-invasive carcinoma, and is not correlated with prognosis, Lung Cancer 58 (2007) 392–396.
[7] J. Takamizawa, H. Konishi, K. Yanagisawa, S. Tomida, H. Osada, H. Endoh, T. Harano, Y. Yatabe, M. Nagino, Y. Nimura, T. Mitsudomi, T. Takahashi, Reduced expression of the let-7 microRNAs in human lung cancers in association with shortened postoperative survival, Cancer Research 64 (2004) 3753–3756.
[8] J. Lu, G. Getz, E.A. Miska, E. Alvarez-Saavedra, J. Lamb, D. Peck, A. Sweet-Cordero, B.L. Ebert, R.H. Mak, A.A. Ferrando, J.R. Downing, T. Jacks, H.R. Horvitz, T.R. Golub, MicroRNA expression profiles classify human cancers, Nature 435 (2005) 834–838.
[9] S.M. Johnson, H. Grosshans, J. Shingara, M. Byrom, R. Jarvis, A. Cheng, E. Labourier, K.L. Reinert, D. Brown, F.J. Slack, RAS is regulated by the let-7 microRNA family, Cell 120 (2005) 635–647.
[10] S. Volinia, G.A. Calin, C.G. Liu, S. Ambs, A. Cimmino, F. Petrocca, R. Visone, M. Iorio, C. Roldo, M. Ferracin, R.L. Prueitt, N. Yanaihara, G. Lanza, A. Scarpa, A. Vecchione, M. Negrini, C.C. Harris, C.M. Croce, A microRNA expression signature of human solid tumors defines cancer gene targets, Proceedings of the National Academy of Sciences of the United States of America 103 (2006) 2257–2261.

[11] A. Grimson, K.K. Farh, W.K. Johnston, P. Garrett-Engele, L.P. Lim, D.P. Bartel, MicroRNA targeting specificity in mammals: determinants beyond seed pairing, Molecular Cell 27 (2007) 91–105.
[12] G.A. Calin, M. Ferracin, A. Cimmino, G. Di Leva, M. Shimizu, S.E. Wojcik, M.V. Iorio, R. Visone, N.I. Sever, M. Fabbri, R. Iuliano, T. Palumbo, F. Pichiorri, C. Roldo, R. Garzon, C. Sevignani, L. Rassenti, H. Alder, S. Volinia, C.G. Liu, T.J. Kipps, M. Negrini, C.M. Croce, A MicroRNA signature associated with prognosis and progression in chronic lymphocytic leukemia, The New England Journal of Medicine 353 (2005) 1793–1801.
[13] J.B. Weidhaas, I. Babar, S.M. Nallur, P. Trang, S. Roush, M. Boehm, E. Gillespie, F.J. Slack, MicroRNAs as potential agents to alter resistance to cytotoxic anticancer therapy, Cancer Research 67 (2007) 11111–11116.
[14] R.J. Webster, K.M. Giles, K.J. Price, P.M. Zhang, J.S. Mattick, P.J. Leedman, Regulation of epidermal growth factor receptor signaling in human cancer cells by microRNA-7, The Journal of Biological Chemistry 284 (2009) 5731–5741.
[15] P. Maziere, A.J. Enright, Prediction of microRNA targets, Drug Discovery Today 12 (2007) 452–458.
[16] S. Griffiths-Jones, H.K. Saini, S. van Dongen, A.J. Enright, MiRBase: tools for microRNA genomics, Nucleic Acids Research 36 (2008) D154–D158.
[17] A. Tsuchida, S. Ohno, W. Wu, N. Borjigin, K. Fujita, T. Aoki, S. Ueda, M. Takanashi, M. Kuroda, MiR-92 is a key oncogenic component of the miR-17-92 cluster in colon cancer, Cancer Science 102 (2011) 2264–2271.
[18] A.F. Gazdar, H. Shigematsu, J. Herz, J.D. Minna, Mutations and addiction to EGFR: the Achilles 'heal' of lung cancers?, Trends in Molecular Medicine 10 (2004) 481–486
[19] U.A. Orom, F.C. Nielsen, A.H. Lund, MicroRNA-10a binds the 5'UTR of ribosomal protein mRNAs and enhances their translation, Molecular Cell 30 (2008) 460–471.
[20] R.S. Herbst, M. Fukuoka, J. Baselga, Gefitinib–a novel targeted approach to treating cancer. Nature reviews, Cancer 4 (2004) 956–965.
[21] S.V. Sharma, D.W. Bell, J. Settleman, D.A. Haber, Epidermal growth factor receptor mutations in lung cancer. Nature reviews, Cancer 7 (2007) 169–181.
[22] T.J. Lynch, D.W. Bell, R. Sordella, S. Gurubhagavatula, R.A. Okimoto, B.W. Brannigan, P.L. Harris, S.M. Haserlat, J.G. Supko, F.G. Haluska, D.N. Louis, D.C. Christiani, J. Settleman, D.A. Haber, Activating mutations in the epidermal growth factor receptor underlying responsiveness of non-small-cell lung cancer to gefitinib, The New England Journal of Medicine 350 (2004) 2129–2139.
[23] J.G. Paez, P.A. Janne, J.C. Lee, S. Tracy, H. Greulich, S. Gabriel, P. Herman, F.J. Kaye, N. Lindeman, T.J. Boggon, K. Naoki, H. Sasaki, Y. Fujii, M.J. Eck, W.R. Sellers, B.E. Johnson, M. Meyerson, EGFR mutations in lung cancer: correlation with clinical response to gefitinib therapy, Science 304 (2004) 1497–1500.
[24] R. Rosell, T. Moran, C. Queralt, R. Porta, F. Cardenal, C. Camps, M. Majem, G. Lopez-Vivanco, D. Isla, M. Provencio, A. Insa, B. Massuti, J.L. Gonzalez-Larriba, L. Paz-Ares, I. Bover, R. Garcia-Campelo, M.A. Moreno, S. Catot, C. Rolfo, N. Reguart, R. Palmero, J.M. Sanchez, R. Bastus, C. Mayo, J. Bertran-Alamillo, M.A. Molina, J.J. Sanchez, M. Taron, Screening for epidermal growth factor receptor mutations in lung cancer, The New England Journal of Medicine 361 (2009) 958–967.
[25] I. Bray, A. Tivnan, K. Bryan, N.H. Foley, K.M. Watters, L. Tracey, A.M. Davidoff, R.L. Stallings, MicroRNA-542-5p as a novel tumor suppressor in neuroblastoma, Cancer Letters 303 (2011) 56–64.
[26] G. Acs, P.J. Zhang, C.M. McGrath, P. Acs, J. McBroom, A. Mohyeldin, S. Liu, H. Lu, A. Verma, Hypoxia-inducible erythropoietin signaling in squamous dysplasia and squamous cell carcinoma of the uterine cervix and its potential role in cervical carcinogenesis and tumor progression, American Journal of Pathology 162 (2003) 1789–1806.

Biochemical and Biophysical Research Communications 420 (2012) 417–421

Contents lists available at SciVerse ScienceDirect

Biochemical and Biophysical Research Communications

journal homepage: www.elsevier.com/locate/ybbrc

The small GTPase Cdc42 modulates the number of exocytosis-competent dense-core vesicles in PC12 cells

Mai Sato [a,1], Tetsuya Kitaguchi [b,1], Rika Numano [c], Kazuya Ikematsu [d], Masaki Kakeyama [e], Masayuki Murata [a], Ken Sato [a], Takashi Tsuboi [a,*]

[a] Department of Life Sciences, Graduate School of Arts and Sciences, The University of Tokyo, 3-8-1 Komaba, Meguro, Tokyo 153-8902, Japan
[b] Cell Signaling Group, Waseda Bioscience Research Institute in Singapore (WABOIS), Waseda University, 11 Biopolis Way, #05-01/02 Helios, Singapore 138667, Singapore
[c] The Electronics-Inspired Interdisciplinary Research Institute (EIIRIS), Toyohashi University of Technology, 1-1 Hibarigaoka, Tennpaku-cho, Toyohashi, Aichi 441-8580, Japan
[d] Forensic Pathology and Science, Graduate School of Biomedical Sciences, Nagasaki University, Nagasaki 852-8523, Japan
[e] Laboratory of Environmental Health Sciences, Center for Disease Biology and Integrative Medicine, Graduate School of Medicine, The University of Tokyo, 7-3-1 Hongo, Bunkyo, Tokyo 113-0033, Japan

ARTICLE INFO

Article history:
Received 1 March 2012
Available online 9 March 2012

Keywords:
Cdc42
Dense-core vesicle
GTPase
Exocytosis
Live cell imaging
Neuroendocrine cells

ABSTRACT

Although the small GTPase Rho family Cdc42 has been shown to facilitate exocytosis through increasing the amount of hormones released, the precise mechanisms regulating the quantity of hormones released on exocytosis are not well understood. Here we show by live cell imaging analysis under TIRF microscope and immunocytochemical analysis under confocal microscope that Cdc42 modulated the number of fusion events and the number of dense-core vesicles produced in the cells. Overexpression of a wild-type or constitutively-active form of Cdc42 strongly facilitated high-KCl-induced exocytosis from the newly recruited plasma membrane vesicles in PC12 cells. By contrast, a dominant-negative form of Cdc42 inhibited exocytosis from both the newly recruited and previously docked plasma membrane vesicles. The number of intracellular dense-core vesicles was increased by the overexpression of both a wild-type and constitutively-active form of Cdc42. Consistently, activation of Cdc42 by overexpression of Tuba, a Golgi-associated guanine nucleotide exchange factor for Cdc42 increased the number of intracellular dense-core vesicles, whereas inhibition of Cdc42 by overexpression of the Cdc42/Rac interactive binding domain of neuronal Wiskott–Aldrich syndrome protein decreased the number of them. These findings suggest that Cdc42 facilitates exocytosis by modulating both the number of exocytosis-competent dense-core vesicles and the production of dense-core vesicles in PC12 cells.

1. Introduction

Peptide hormones are packed into dense-core vesicles at the Golgi complex and are released to the extracellular space in response to Ca^{2+} influx. After the budding from the Golgi complex, the dense-core vesicles translocate to the plasma membrane (transport step). The transported dense-core vesicles morphologically attach to the plasma membrane (docking/tethering step). The vesicles prepare to fuse with the plasma membrane with tight complexes containing soluble *N*-ethylmaleimide-sensitive factor attachment protein receptor (SNARE) protein (priming step), and the readily releasable dense-core vesicles fuse with the plasma membrane following Ca^{2+} influx (fusion step) [1]. To maintain a continuous exocytosis, the refilling of the readily releasable pool by biogenesis and mobilizing the dense-core vesicle pools occurred constantly.

Refilling of the readily releasable pool has been shown to be regulated by trafficking of the dense-core vesicles to the plasma membrane, and this has been implicated in coordinated re-organization of actin filaments [2–4]. Although small GTPase Rho family proteins are involved in actin remodeling, the intracellular distribution and their function in exocytosis are significantly distinct. For example, Cdc42 and Rac1 preferentially exist in the subplasmalemmal region and facilitate exocytosis, whereas RhoA is present on the dense-core vesicles and inhibits exocytosis [5]. In addition to the actin reorganization by Rho family proteins, in particular, Cdc42 has been shown to bind to SNARE proteins directly or indirectly in insulin-secreting cells [6,7]. Therefore, we focused on the role of Cdc42 on the dense-core vesicle exocytosis in neuroendocrine PC12 cells.

In the present study, to clarify the role of Cdc42 on the dense-core vesicle exocytosis, we used total internal reflection fluorescence (TIRF) microscopy to analyze single exocytotic events at a high spatiotemporal resolution. We found that overexpression of a

* Corresponding author. Fax: +81 3 5465 8208.
E-mail address: takatsuboi@bio.c.u-tokyo.ac.jp (T. Tsuboi).
[1] These authors contributed equally to this work.

0006-291X/$ - see front matter © 2012 Elsevier Inc. All rights reserved.
http://dx.doi.org/10.1016/j.bbrc.2012.03.010

wild-type or constitutively-active form of Cdc42 strongly facilitated high-KCl-induced exocytosis from the newly recruited plasma membrane vesicles in the PC12 cells. Furthermore, we found that active Cdc42 increased the total number of intracellular dense-core vesicles in the cells revealed by confocal microscopy. Based on these findings, we propose that Cdc42 induces the biogenesis of dense-core vesicles and regulates the number of exocytosis-competent dense-core vesicles in the neuroendocrine PC12 cells.

2. Materials and methods

2.1. Materials

Anti-chromogranin A (CgA) rabbit polyclonal antibody was from Prof. Kinji Inoue (Saitama University, Japan). Goat anti-rabbit Alexa Fluor 488 IgG was from Invitrogen (Eugene, OR, USA).

2.2. Plasmid constructions

A stop codon deleted monomeric red fluorescent protein (mCherry) fragment [8] was amplified by PCR and inserted into the BamHI-EcoRI site of pcDNA3.1(+) (Invitrogen) as a pcDNA 3.1(+)-mCherry. The full length of Cdc42 was amplified from Marathon-Ready mouse brain cDNA (Clontech) by PCR with the following pairs of oligonucleotides containing a restriction enzyme site (underlined): 5′-GAATTCATGCAGACAATTAAGTGTGTT-3′ and 5′-CTCGAGTCATAGCAGCACACACCTGCG-3′. The fragment was finally inserted into the pcDNA3.1(+)-mCherry vector, and named mCherry-Cdc42(WT). A constitutively-active form (G61L) and dominant-negative form (T17N) of Cdc42 were created by using conventional PCR techniques, and named mCherry-Cdc42(CA) and mCherry-Cdc42(DN), respectively. A stop codon deleted mCherry fragment was amplified by PCR again, and the amplified PCR fragment was inserted into the AgeI-BspEI site of the pEGFP-C1 vector (Clontech) replaced by EGFP with same frame as a pmCherry-C1 vector. The Cdc42/Rac-interactive binding (CRIB) domain of neuronal Wiskott–Aldrich syndrome protein (N-WASP) [4] was amplified from a PC12 cell cDNA library by PCR with the following pair of oligonucleotides containing restriction enzyme site (underlined) and a stop codon (boldface): 5′-GAATTCTGCTCCAAATGGTCCCAA-3′ and 5′-GCGGCGCC**TTA**TGCTTGCCTTCGGAG-3′. The fragment was finally inserted into the pmCherry-C1 vector, and named mCherry-CRIB. Neuropeptide Y-tagged Venus (NPY-Venus) was prepared as described previously [9]. GFP-Tuba and mCherry-Tuba were generous gift from Prof. Frank B. Gertler (Massachusetts Institute of Technology, USA) [10].

2.3. Cell culture

PC12 cells were cultured in Dulbecco's modified Eagle's medium (DMEM, Invitrogen) supplemented with 10% fetal bovine serum, 10% horse serum, 100 U/ml penicillin G, and 100 μg/ml streptomycin, at 37 °C under 5% CO_2. For live-cell imaging, PC12 cells were plated onto poly-L-lysine-coated coverslips, and the cells were co-transfected with 3 μg NPY-Venus and 3 μg of mCherry-Cdc42(WT), mCherry-Cdc42(CA), or mCherry-Cdc42(DN) vectors using LipofectAMINE 2000 (Invitrogen) according to the manufacturer's instructions.

2.4. Total internal reflection fluorescence microscopy

Total internal reflection fluorescence (TIRF) imaging was performed in modified Ringer buffer at 37 °C (RB: 130 mM NaCl, 3 mM KCl, 5 mM $CaCl_2$, 1.5 mM $MgCl_2$, 10 mM glucose, and 10 mM HEPES, pH 7.4). High-KCl stimulation was achieved by perfusion with RB-containing 70 mM KCl (the NaCl concentration was reduced to maintain the osmolality). We mounted a high numerical aperture objective lens (Plan Apochromatic, 100×, NA = 1.45, infinity corrected, OLYMPUS) on an inverted microscope (IX71, OLYMPUS) and introduced an incident light for total internal reflection illumination through the high numerical aperture objective lens via a single mode optical fiber and illumination lens (IX2-RFAEVA-2, OLYMPUS). To observe the NPY-Venus fluorescence image, we used a diode-pumped solid-state 488 nm laser (HPU50100, 20 mW, Furukawa Electronic) for total internal fluorescence illumination and a band pass filter (HQ535/30m, Chroma) as an emission filter. Images were acquired every 300 ms or otherwise as indicated.

2.5. Immunofluorescence

PC12 cells were plated onto poly-L-lysine-coated coverslips and transfected with mCherry-Cdc42(WT), mCherry-Cdc42(CA), mCherry-Cdc42(DN), pmCherry-Tuba, or CRIB-mCherry as described above.

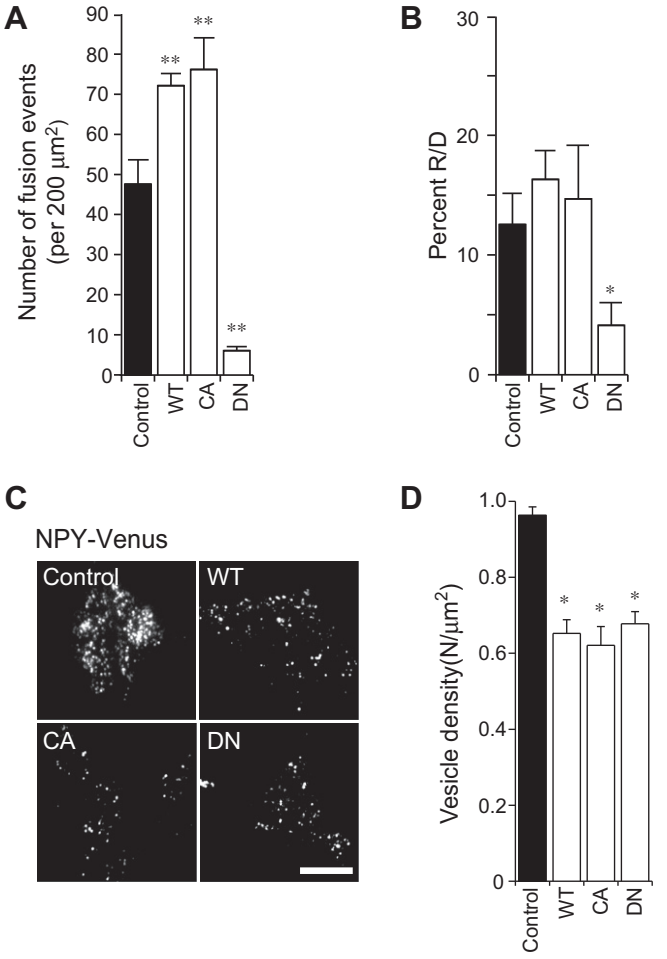

Fig. 1. Cdc42 increased the number of fusion events. (A) The number of fusion events for NPY-Venus during 5 min stimulation in control (Control), wild-type Cdc42 (WT), constitutively-active Cdc42 (CA), or dominant-negative Cdc42 (DN) overexpressing PC12 cells ($n = 15$ cells in each). (B) Percentage of NPY-Venus release events in PC12 cells overexpressing Cdc42 or its mutants during the 5 min stimulation determined from the number of plasma membrane-docked vesicle before stimulation under TIRF microscopy ($n = 15$ cells in each). (C) Typical TIRF images of plasma membrane-docked NPY-Venus vesicles observed in each cells. Scale bar = 10 μm. (D) The density of the plasma membrane-docked NPY-Venus vesicles was measured by counting the vesicles in each image ($n = 7$ cells in each). Data shown as mean values ± SEM; $^{*}P < 0.05$, $^{**}P < 0.01$ in comparison with the control, respectively.

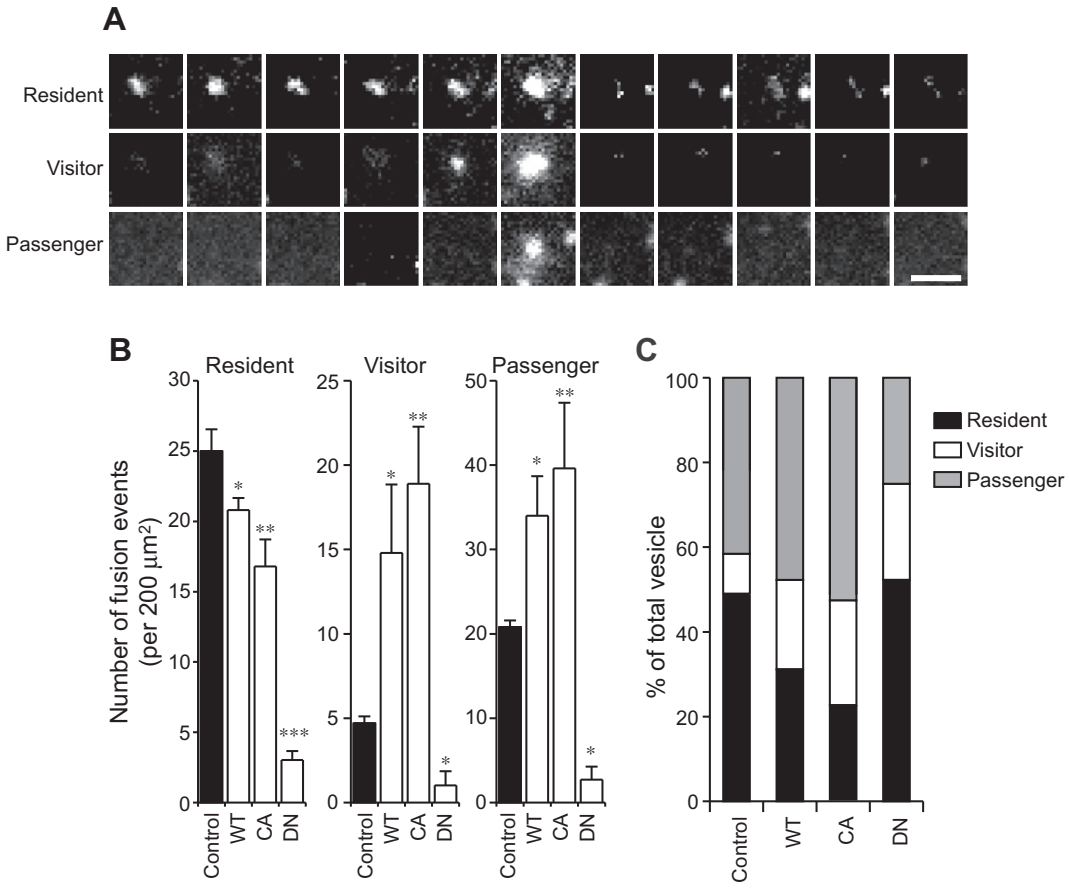

Fig. 2. Cdc42 increased the number of 'passenger' and 'visitor' exocytotic events. (A) Dense-core vesicle exocytotic events were categorized into three types: 'resident' (morphologically previously docked vesicles), 'visitor' (newly docked vesicles in response to stimulation), and 'passenger' (vesicles that abruptly fused without stable docking). Sequential TIRF images were acquired every 100 ms. Scale bar = 1 μm. (B) All fusion events were counted manually in control (Control), wild-type Cdc42 (WT), constitutively-active Cdc42 (CA), or dominant-negative Cdc42 (DN) overexpressing PC12 cells and categorized into three types ($n = 7$ cells in each). The number of fusion events during the stimulation is summed for each category of vesicles. (C) Stacked bar chart represents the percentage of the number of 'resident', 'visitor', and 'passenger' vesicles in (B). Data shown as mean values ± SEM; $^{*}P < 0.05$, $^{**}P < 0.01$, $^{***}P < 0.001$ in comparison with the control, respectively.

48 h after transfection, cells were fixed in 2% paraformaldehyde for 20 min and permeabilized with 0.1% Triton X/phosphate buffered saline (PBS) for 2 min. The cells were blocked for 1 h with 0.1% Triton X/PBS-containing 1% bovine serum albumin (BSA) prior to incubating with primary antibody against CgA. Primary antibody and secondary antibody was diluted 100-fold and 1000-fold, respectively. The medium was replaced with PBS three times after each process. To observe Alexa488-stained CgA, the images were acquired on a Nipkow-disk type confocal microscope (CSU-10, Yokogawa). A 488 nm argon laser provided the excitation light for Alexa488 and the fluorescence was acquired through a 500–530 nm bandpass filter.

2.6. Image analysis

To analyze the TIRF imaging data, single exocytotic events were selected manually and the average fluorescence intensity of an individual vesicle was calculated as previously described [11]. To distinguish between fusion events and vesicle movement (i.e., vesicles that pause at the plasma membrane and then move back inside the cell without fusing), we focused on the fluorescence changes just before the decrease in fluorescent signals. It is known that a rapid transient increase in the fluorescence intensity occurs during a fusion event, whereas, during vesicle movement, the fluorescence intensity gradually decreases to the background level. The number of fusion events during a 5 min period was counted manually based on the above criteria [11].

2.7. Data analysis

Data are presented as means ± standard error of the mean (SEM). The statistical significance of differences between means was assessed by analysis of variance (ANOVA), followed by Newman–Keuls test for multiple comparisons. All analyses were conducted using GraphPad Prism software (GraphPad Software).

3. Results

3.1. Active Cdc42 increased NPY-Venus release

To examine whether active Cdc42 regulates hormone release, we first counted the number of exocytosis visualized by fluorescent protein-tagged hormone (i.e., NPY-Venus) using TIRF microscopy during the 5 min stimulation. While overexpression of Cdc42(WT) or Cdc42(CA) increased the number of fusion events, overexpression of Cdc42(DN) decreased it (Fig. 1A). To confirm whether the modulatory effects by Cdc42 on the number of exocytosis were due to either promotion or suppression of a priming step for the plasma membrane-docked vesicles, we analyzed the ratio of the number of NPY-Venus release events during the 5 min stimulation (R) to the plasma membrane-docked vesicles before stimulation (D) using TIRF microscopy. While the ratio of R to D was significantly decreased with overexpression of Cdc42(DN), no significant differences in the ratio were observed among control, Cdc42(WT), and

Cdc42(CA) overexpressing cells (Fig. 1B). These results suggest that the modulatory effect on the number of fusion events by Cdc42 were caused not only by alteration of priming steps in exocytosis. To further investigate the effect of overexpression of Cdc42 on the docking status of dense-core vesicles on the plasma membrane, we counted the number of plasma membrane-docked vesicles using TIRF microscopy. Interestingly, we found that overexpression of not only Cdc42(WT) and Cdc42(CA) but also Cdc42(DN) significantly decreased the density of plasma membrane-docked vesicles (Fig. 1C, D), indicating that Cdc42 play multiple roles in docking status during exocytosis.

3.2. Cdc42 facilitates the exocytosis from newly recruited plasma membrane vesicles

Despite the number of docked vesicles on the plasma membrane were decreased with overexpression of Cdc42(WT) or Cdc42(CA), the number of fused events were increased in those cells. To resolve this discrepancy, we classified the exocytosed vesicles into three types (i.e., resident, visitor, and passenger) according to the appearance and disappearance of the vesicles at the plasma membrane before and during exocytosis (Fig. 2A). Firstly, NPY-Venus vesicles visible before stimulation were named 'resident'. Secondly, vesicles that had become visible just before and during exocytosis were named 'visitor', which correspond to the vesicles docked at the plasma membrane for some time before exocytosis. Finally, vesicles that fused without stable docking were named 'passenger' [11]. The latter two categories were discriminated based on whether the vesicles were visualized in more than one consecutive frame (>300 ms). We found that overexpression of Cdc42(WT) and Cdc42(CA) increase the number of 'visitor' and 'passenger' events, whereas they cause a decrease in the number of 'resident' events (Fig. 2B). Consistently, overexpression of Cdc42(WT) and Cdc42(CA) in the cells significantly increased the ratio of 'visitor' and 'passenger' events. On the other hand, overexpression of Cdc42(DN) decreased the number of all types of exocytosis, particularly 'passenger' events (Fig. 2C). These results suggest that Cdc42 facilitates exocytosis from the newly recruited plasma membrane vesicles through modification of docking and/or priming steps to increase the amount of hormone.

3.3. Cdc42 increases the number of intracellular dense-core vesicles

Although Cdc42 facilitated the exocytosis from newly recruited plasma membrane vesicles (Fig. 2B, C), the priming step on docked vesicles was not accelerated by active Cdc42 (Fig. 1B). We thus attempted to investigate the effect of Cdc42 on the number of intracellular dense-core vesicles. When we analyzed the number of dense-core vesicles in Cdc42(WT)-, Cdc42(CA)-, and Cdc42(DN)-overexpressed cells by using chromogranin A (CgA) antibody as a dense-core vesicle marker, Cdc42(WT) and Cdc42(CA) increased the total number of dense-core vesicles, whereas Cdc42(DN) had no effect on the number of dense-core vesicles (Fig. 3A, B). We next observed the effect of activation of Cdc42 by overexpression of Tuba, a Golgi-associated guanine nucleotide exchange factor (GEF) for Cdc42 [12], on the total number of dense-core vesicles. As we expected, overexpression of Tuba significantly increased the number of dense-core vesicles, whereas inhibition of Cdc42 activity by overexpression of the Cdc42/Rac interactive binding (CRIB) domain of neuronal Wiskott-Aldrich syndrome protein (N-WASP) significantly decreased the total number of dense-core vesicles (Fig. 3C, D). Taken together, these results suggest that Cdc42 controls the dense-core vesicle biogenesis, and regulates the number of exocytosis-competent dense-core vesicles.

4. Discussion

In the present study, we have demonstrated that the increase in peptide hormone release induced by Cdc42 was attributed to an increase in the number of exocytosis (Fig. 1A). In contrast, Cdc42 decreased the number of plasma membrane-docked vesicles (Fig. 1C, D). This discrepancy could be explained by the notion that Cdc42 promoted the transition of the exocytotic process from the docking step to the priming step. Namely, Cdc42 increased the number of primed vesicles and these vesicles might be fused incidentally to the plasma membrane without secretagogues. Consequently, activation of Cdc42 decreased the number of plasma membrane-docked vesicles. In support this notion, previous studies have shown that Cdc42 bound to SNARE proteins, such as vesicle-associated membrane SNARE protein (VAMP2) and syntaxin-1A, and regulated insulin secretion [6,7]. Thus, activation of Cdc42 presumably accelerates the formation of the SNARE complex to promote the exocytotic process from the docking step to priming step in the PC12 cells.

Based on the above notion, inhibition of Cdc42 activity should increase the number of plasma membrane-docked vesicles by inhibition of the transition of the exocytotic process from the docking

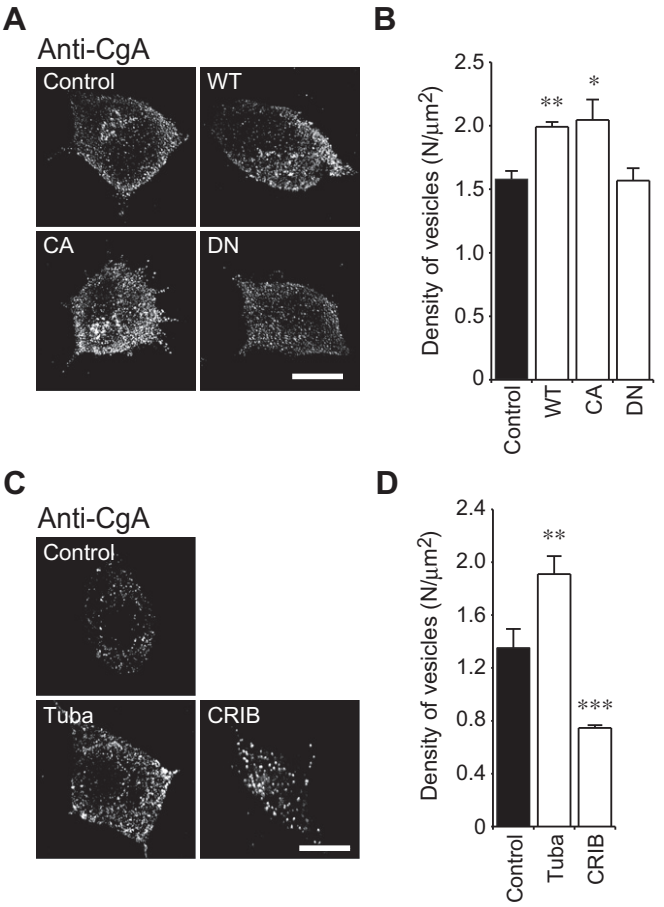

Fig. 3. Cdc42 increased the number of intracellular dense-core vesicles. (A) Confocal images of dense-core vesicles (CgA) observed in control (Control), wild-type Cdc42 (WT), constitutively-active Cdc42 (CA), or dominant-negative Cdc42 (DN) overexpressing PC12 cells. Scale bar = 10 μm. (B) The density of dense-core vesicles was determined by counting the vesicles in each image (n = 7 cells in each). (C) Confocal images of dense-core vesicles (CgA) observed in control (Control), Cdc42 GEF (Tuba), or CRIB domain of N-WASP (CRIB) expressing cells. Scale bar = 10 μm. (D) The density of dense-core vesicles was determined by counting the vesicles in each image (n = 7 cells in each). Data shown as mean values ± SEM; $^{*}p < 0.05$, $^{**}p < 0.01$, $^{***}p < 0.001$ in comparison with the control.

step to the priming step. However, the number of plasma membrane-docked vesicles was decreased (Fig. 1C, D). Thus, Cdc42 could also modulate the exocytotic step before the SNARE complex forms (i.e., biogenesis, transport, and docking/tethering step). In fact, other groups have shown that Cdc42 enhanced the F-actin remodeling on the cell surface [4,13], and that the F-actin localized preferentially to the cortical region forming a peripheral barrier limiting vesicle access to the plasma membrane [14]. Furthermore, the F-actin network is a key element in vesicle transport during exocytosis [15,16]. Thus, the decrease in plasma membrane-docked vesicles caused by inhibition of Cdc42 activity might be ascribed to either the suppression of vesicle docking by actin barrier formation or the attenuation of vesicle transport or biogenesis due to inhibition of actin remodeling.

We have also demonstrated that Tuba increased the total number of dense-core vesicles and CRIB domain of N-WASP decreased them (Fig. 3C, D). Since Tuba is associated with Golgi apparatus [12] and both Cdc42 and N-WASP are involved in the Golgi-to-ER transport, activation of Cdc42 presumably accelerated the biogenesis of dense-core vesicles by modulating the Golgi to ER transport [17,18]. However, the inhibition of Cdc42 activity by CRIB domain of N-WASP decreased the number of intracellular dense-core vesicles, while dominant-negative form of Cdc42 did not (Fig. 3). Since N-WASP is a downstream target of Cdc42, N-WASP probably provides an immediate effect on the biogenesis of dense-core vesicles.

In summary, we have investigated the exocytotic behavior of dense-core vesicles and biogenesis of vesicles by activation or inhibition of Cdc42 function using live cell TIRF microscopy and confocal microscopy, respectively. We propose that Cdc42 regulates not only the number of exocytosis-competent dense-core vesicles but also biogenesis of the dense-core vesicles in the neuroendocrine PC12 cells.

Acknowledgments

The authors thank for Y. Yanagihara, M. Oya, and M. Kishimoto for technical assistance. This research was supported in part by grants from the Ministry of Education, Culture, Sports, Science and Technology of Japan (22790197 to T.K., 21671002 to M.K., and "Program to Foster Young Researchers in Cutting-Edge Interdisciplinary Research" to R.N.) and by the Takeda Science Foundation (R.N. and T.T.).

References

[1] R. Jahn, T. Lang, T.C. Sudhof, Membrane fusion, Cell 112 (2003) 519–533.
[2] T. Lang, I. Wacker, I. Wunderlich, A. Rohrbach, G. Giese, T. Soldati, W. Almers, Role of actin cortex in the subplasmalemmal transport of secretory granules in PC-12 cells, Biophys. J. 78 (2000) 2863–2877.
[3] A. Pendleton, A. Koffer, Effects of latrunculin reveal requirements for the actin cytoskeleton during secretion from mast cells, Cell Motil. Cytoskeleton 48 (2001) 37–51.
[4] S. Gasman, S. Chasserot-Golaz, M. Malacombe, M. Way, M.F. Bader, Regulated exocytosis in neuroendocrine cells: a role for subplasmalemmal Cdc42/N-WASP-induced actin filaments, Mol. Biol. Cell 15 (2004) 520–531.
[5] S. Gasman, S. Chasserot-Golaz, M.R. Popoff, D. Aunis, M.F. Bader, Involvement of Rho GTPases in calcium-regulated exocytosis from adrenal chromaffin cells, J. Cell Sci. 112 (1999) 4763–4771.
[6] S. Daniel, M. Noda, R.A. Cerione, G.W. Sharp, A link between Cdc42 and syntaxin is involved in mastoparan-stimulated insulin release, Biochemistry 41 (2002) 9663–9671.
[7] A.K. Nevins, D.C. Thurmond, A direct interaction between Cdc42 and vesicle-associated membrane protein 2 regulates SNARE-dependent insulin exocytosis, J. Biol. Chem. 280 (2005) 1944–1952.
[8] N.C. Shaner, R.E. Campbell, P.A. Steinbach, B.N. Giepmans, A.E. Palmer, R.Y. Tsien, Improved monomeric red, orange and yellow fluorescent proteins derived from Discosoma sp. red fluorescent protein, Nat. Biotechnol. 22 (2004) 1567–1572.
[9] T. Nagai, K. Ibata, E.S. Park, M. Kubota, K. Mikoshiba, A. Miyawaki, A variant of yellow fluorescent protein with fast and efficient maturation for cell-biological applications, Nat. Biotechnol. 20 (2002) 87–90.
[10] E.M. Kovacs, R.S. Makar, F.B. Gertler, Tuba stimulates intracellular N-WASP-dependent actin assembly, J. Cell Sci. 119 (2006) 2715–2726.
[11] M. Sato, Y. Mori, T. Matsui, R. Aoki, M. Oya, Y. Yanagihara, M. Fukuda, T. Tsuboi, Role of the polybasic sequence in the Doc2alpha C2B domain in dense-core vesicle exocytosis in PC12 cells, J. Neurochem. 114 (2010) 171–181.
[12] A. Kodani, I. Kristensen, L. Huang, C. Sutterlin, GM130-dependent control of Cdc42 activity at the Golgi regulates centrosome organization, Mol. Biol. Cell 20 (2009) 1192–1200.
[13] M. Malacombe, M. Ceridono, V. Calco, S. Chasserot-Golaz, P.S. McPherson, M.F. Bader, S. Gasman, Intersectin-1L nucleotide exchange factor regulates secretory granule exocytosis by activating Cdc42, EMBO J. 25 (2006) 3494–3503.
[14] T. Nakata, N. Hirokawa, Organization of cortical cytoskeleton of cultured chromaffin cells and involvement in secretion as revealed by quick-freeze, deep-etching, and double-label immunoelectron microscopy, J. Neurosci. 12 (1992) 2186–2197.
[15] P. Neco, D. Giner, S. Viniegra, R. Borges, A. Villarroel, L.M. Gutierrez, New roles of myosin II during vesicle transport and fusion in chromaffin cells, J. Biol. Chem. 279 (2004) 27450–27457.
[16] D. Giner, I. Lopez, J. Villanueva, V. Torres, S. Viniegra, L.M. Gutierrez, Vesicle movements are governed by the size and dynamics of F-actin cytoskeletal structures in bovine chromaffin cells, Neuroscience 146 (2007) 659–669.
[17] A. Luna, O.B. Matas, J.A. Martinez-Menarguez, E. Mato, J.M. Duran, J. Ballesta, M. Way, G. Egea, Regulation of protein transport from the Golgi complex to the endoplasmic reticulum by CDC42 and N-WASP, Mol. Biol. Cell 13 (2002) 866–879.
[18] O.B. Matas, J.A. Martinez-Menarguez, G. Egea, Association of Cdc42/N-WASP/Arp2/3 signaling pathway with Golgi membranes, Traffic 5 (2004) 838–846.

Biochemical and Biophysical Research Communications 420 (2012) 422–427

Contents lists available at SciVerse ScienceDirect

Biochemical and Biophysical Research Communications

journal homepage: www.elsevier.com/locate/ybbrc

Flt1 and Flk1 mediate regulation of intraocular pressure and their double heterozygosity causes the buphthalmia in mice

Keigo Sano [a], Osamu Katsuta [b], Satoshi Shirae [b], Yoshiaki Kubota [c], Masatsugu Ema [d], Toshio Suda [e], Masatsugu Nakamura [b], Masanori Hirashima [a,*]

[a] Division of Vascular Biology, Department of Physiology and Cell Biology, Kobe University Graduate School of Medicine, 7-5-1 Kusunoki-cho, Chuo-ku, Kobe, Hyogo 650-0017, Japan
[b] Ophthalmic Research & Development Center, Santen Pharmaceutical Co. Ltd., 8916-16 Takayama-cho, Ikoma-shi, Nara 630-0101, Japan
[c] Center for Integrated Medical Research, School of Medicine, Keio University, 35 Shinanomachi, Shinjuku-ku, Tokyo 160-8582, Japan
[d] Department of Anatomy and Embryology, Institute of Basic Medical Sciences, Graduate School of Comprehensive Human Sciences, University of Tsukuba, 1-1-1 Tennodai, Tsukuba, Ibaraki 305-8575, Japan
[e] The Sakaguchi Laboratory of Developmental Biology, School of Medicine, Keio University, 35 Shinanomachi, Shinjuku-ku, Tokyo 160-8582, Japan

ARTICLE INFO

Article history:
Received 21 February 2012
Available online 9 March 2012

Keywords:
Buphthalmia
Development
Endothelial cell
Intraocular pressure
Mouse
VEGF

ABSTRACT

Flt1 and Flk1 are receptor tyrosine kinases for vascular endothelial growth factor-A which play a crucial role in physiological and pathological angiogenesis. To study genetic interaction between the *Flt1* and *Flk1* genes, we crossed between Flt1 and Flk1 heterozygous ($Flt1^{+/-}$ and $Flk1^{+/-}$) mice. We found that Flt1; Flk1 double heterozygous ($Flt1^{+/-}$; $Flk1^{+/-}$) mice showed enlarged eyes similar to the buphthalmia detected in human congenital glaucoma with elevation of intraocular pressure (IOP). Actually, IOP was elevated in $Flt1^{+/-}$; $Flk1^{+/-}$ mice and also in Flt1 or Flk1 single heterozygous mice. However, none of these mutants showed hallmarks of glaucoma such as ganglion cell death and excavation of optic disc. To clarify the pathological causes for enlarged eyes and elevated IOP, we investigate the mice from matings between $Flt1^{+/-}$ and $Flk1^{+/-}$ mice. $Flt1^{+/-}$ mice showed enlarged Schlemm's canal and disordered collagen fibers in the sclera, whereas $Flk1^{+/-}$ mice showed atrophied choriocapillaris in the choroid. These tissues are a part of the main outflow and alternative uveoscleral outflow pathway of the aqueous humor, suggesting that these pathological changes found in $Flt1^{+/-}$ and $Flk1^{+/-}$ mice are associated with the buphthalmia in $Flt1^{+/-}$; $Flk1^{+/-}$ mice.

1. Introduction

Flt1 and Flk1 are receptor tyrosine kinases for vascular endothelial growth factor-A (VEGF-A) which is a key regulator of physiological and pathological angiogenesis, and of vascular permeability [1]. Gene-targeting studies established a critical but distinct role for these two receptors in vascular development. Flk1 signals are essential for the development of endothelial cells (ECs) and hematopoietic cells during embryogenesis in a cell autonomous manner [2,3], whereas Flt1 is essential for suppressing the overpopulation of ECs as a decoy receptor for the VEGF-A agonist rather than a signaling receptor in ECs [4,5]. High levels of VEGF-A expression was especially shown in epithelial tissues adjacent to fenestrated capillary vessels. In the adult eye, soluble isoform of VEGF-A protein secreted by retinal pigment epithelium (RPE) plays an essential role in the maintenance of choriocapillaris (CC) whose ECs are fenestrated [6–8]. On the other hand, VEGF-A is involved in the onset and progression of diabetic retinopathy and exudative age-related macular degeneration (eAMD) by inducing an abnormal neovascularization in the eye [9]. Indeed, VEGF-blocking antibody, ranibizumab has been developed as an effective drug for eAMD [10].

Intraocular pressure (IOP) is an important clinical index since its elevation causes glaucoma or myopia in humans. IOP is regulated by a balance between the production and excretion of the aqueous humor in the eye. The main outflow pathway of the aqueous humor is composed of chamber angle, trabecular meshwork, and Schlemm's canal, whereas the alternative uveoscleral outflow pathway has also been reported [11]. IOP is thus elevated by an increase in accumulation of extracellular materials in the trabecular and uveoscleral outflow [12]. In the mouse, DBA2/J mouse strain [13,14], Vav2/Vav3-deficient mice [15], and transgenic mice with ocular overexpression of calcitonin receptor-like receptor [16] have been reported to date as genetic mouse models of the elevation of IOP caused by closure of the angle between the cornea and iris in the anterior chamber. On the other hand, mice with a targeted type I collagen mutation [17] and Myocilin transgenic mice [18] have been reported as those with open angle in which detailed mechanisms of impaired outflow pathway of aqueous humor remain to be elucidated.

* Corresponding author. Fax: +81 78 382 5834.
E-mail address: mhirashi@med.kobe-u.ac.jp (M. Hirashima).

0006-291X/$ - see front matter © 2012 Elsevier Inc. All rights reserved.
http://dx.doi.org/10.1016/j.bbrc.2012.03.011

In this study, we aimed to analyze genetic interaction between the *Flt1* and *Flk1* genes and investigated ocular phenotypes in Flt1; Flk1 double heterozygous ($Flt1^{+/-}$; $Flk1^{+/-}$) mice, Flt1 or Flk1 single heterozygous ($Flt1^{+/-}$ or $Flk1^{+/-}$) mice, compared with wild-type (WT) mice.

2. Material and Methods

2.1. Mice

A colony of outbred mice heterozygous for a null allele of Flt1 [4] or Flk1 [2,19] was maintained for these studies. Heterozygous males were crossed to ICR (Japan SLC, Hamamatsu, Japan) random outbred females to generate stock. Mice were genotyped by polymerase chain reaction analysis of ear DNA. Eyes from adult mice were dissected at 3 months of age or older. Animal experiments were approved by the Institutional Animal Care and Use Committee of Kobe University Graduate School of Medicine and Keio University School of Medicine, and carried out in accordance with the animal experimentation guidelines of the Kobe University Graduate School of Medicine and Keio University School of Medicine.

2.2. Measurement of IOP

Every month from 2 to 12 months of age, IOP was measured five times per eye between 1 pm to 3 pm with TonoLab Tonometer (icare Finland) while mice were under sedation within 3–12 min after intraperitoneal injection of ketamine (100 mg/kg) and xylazine (9 mg/kg). Maximal and minimal values were excluded, and intermediate three values were used for the data analysis.

2.3. X-gal staining of the eye

Eyes were fixed in 0.1 M sodium phosphate (pH7.3) containing 2% paraformaldehyde (PFA), 0.05% glutaraldehyde, and 2 mM magnesium chloride at room temperature (RT) for 30 min. The eyes were perforated and further fixed in the same fixative at RT for 1 h. Whole-mount eyes were stained with X-gal as described previously [20], sectioned in paraffin, and counterstained with nuclear fast red (Vector).

2.4. Immunohistochemistry

We used rat anti-PECAM-1 (clone Mec13.3, BD Pharmingen), rat anti-endoglin (clone MJ7/18, eBioscience), and rabbit anti-LYVE-1 (RELIATech) primary antibodies, and Alexa Fluor 488-, Cy3-, or Cy5-conjugated secondary antibodies (Invitrogen and Jackson ImmunoResearch).

Eyes were fixed in PBS containing 1% PFA at 4 °C for 30 min. The eyes were perforated and further fixed in the same fixative at 4 °C for 2 h. The eye was dissected into three regions; the anterior part consisting of the cornea, iris, and ciliary body, the posterior part consisting of sclera and choroid, and the retina, and further fixed in the same fixative at 4 °C for 2 h. The rest of procedure for immunostaining was described previously [21].

2.5. Electron microscopic analysis

Eyes were fixed in 0.1 M phosphate buffer containing 2.5% glutaraldehyde at RT for overnight. The eyes were further fixed in 0.1 M phosphate buffer containing 1% osmium tetroxide at RT for 2 h, dehydrated in ethanol, and embedded in epoxy resin after substituting for *n*-butyl glycidyl ether. Ultrathin sections were treated with uranyl acetate and lead citrate, and visualized on transmission electron microscopy with Hitachi H-7600 (Hitachi High-Technologies).

3. Results

3.1. Enlarged eyes and elevated IOP in $Flt1^{+/-}$; $Flk1^{+/-}$ mice

To study genetic interaction between the Flt1 and Flk1 genes, we crossed between $Flt1^{+/-}$ and $Flk1^{+/-}$ mice to analyze $Flt1^{+/-}$; $Flk1^{+/-}$ mice. Although none of wild-type (WT), Flt1 or Flk1 single heterozygous ($Flt1^{+/-}$ or $Flk1^{+/-}$) mice showed overt phenotypes ($n = 33$, $n = 32$, and $n = 39$ at 4 months old, respectively), about 24% of $Flt1^{+/-}$; $Flk1^{+/-}$ mice ($n = 41$, at 4 months old) showed the enlargement of eyes (Fig. 1A). Since this phenotype is similar to the buphthalmia which is detected in human congenital glaucoma with elevation of IOP, we measured IOP from 2 to 12 months of age for comparison among WT, $Flt1^{+/-}$, $Flk1^{+/-}$ and $Flt1^{+/-}$; $Flk1^{+/-}$ mice. Compared with WT mice, $Flt1^{+/-}$; $Flk1^{+/-}$ mice showed an elevated average IOP by 2.2 mmHg. $Flt1^{+/-}$; $Flk1^{+/-}$ mice with the buphthalmia ($n = 3$) showed a higher average IOP than those without the enlarged eyes ($n = 15$) by 3.5 mmHg at 4 months of age. In addition, $Flt1^{+/-}$ and $Flk1^{+/-}$ mice showed elevated average IOPs by 1.8 mmHg and 1.3 mmHg, respectively (Fig. 1B), although these single heterozygous mutant mice did not exhibit the buphthalmia. Elevation of IOP causes hallmarks of glaucoma such as ganglion cell death and excavation of optic disc. To investigate whether these pathological changes were detected in these mutant mice, we performed TdT-mediated dUTP Nick-End Labeling (TUNEL) staining in paraffin sections of the retina. We did not detect TUNEL-positive apoptotic cells or excavation of the optic disc in any of analyzed mutant mice (Supplementary Fig. S1). These results indicate that $Flt1^{+/-}$; $Flk1^{+/-}$ mice showed the buphthalmia and elevation of IOP without hallmarks of glaucoma.

3.2. Expression patterns of Flt1 and Flk1 in the adult eye

To perform histopathological analysis in $Flt1^{+/-}$; $Flk1^{+/-}$ mice, we first investigated the expression pattern of Flt1 and Flk1 in the adult eye by detecting a lacZ reporter knocked into the *Flt1* or *Flk1* locus [2,4]. X-gal staining of heterozygous mice showed that Flt1 and Flk1 both were detected in endothelial cells of the Schlemm's canal, corneal limbus, ciliary body, iris, and choroid (Fig. 2A–D). However, only Flt1 expression was detected in the retinal vasculature (Fig. 2C, D). In addition to endothelial expression, Flk1 was also detected in the stromal cells and endothelial cells in the cornea, and neural cells in the retina (Fig. 2E, F).

3.3. Enlarged Schlemm's canal and disordered collagen fibers of the sclera in Flt1 heterozygous mice

IOP is regulated by a balance between the production and excretion of the aqueous humor in the eye. The main outflow pathway of the aqueous humor is composed of the chamber angle, trabecular meshwork, and Schlemm's canal. In some genetic glaucoma mice, the elevation of IOP results from the maldevelopment of the outflow tissue, including the closure of the chamber angle, thickened trabecular meshwork, and absence of Schlemm's canal [13–16]. We first performed histological analysis of this main outflow pathway. In sections stained with hematoxylin and eosin or transmission electron micrograms, we did not find an occlusion of chamber angle or an abnormal deposition of extracellular matrix in the trabecular meshwork of enlarged $Flt1^{+/-}$; $Flk1^{+/-}$ eyes (Supplementary Fig. S2). We next investigate the vascular network of the outflow pathway including the Schlemm's canal and corneal limbal blood vessels by whole-mount confocal microscopy of the

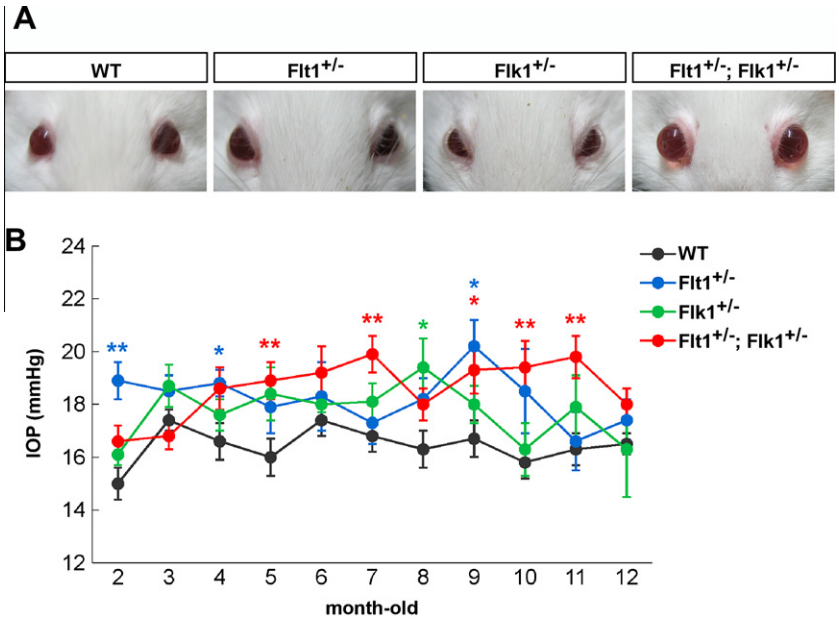

Fig. 1. Appearance of eyes and measurement of IOP. (A) Appearance of eyes is shown from 9-month-old mice whose genotypes are indicated on the top. Enlarged eyes similar to the buphthalmia were detected only in $Flt1^{+/-}$; $Flk1^{+/-}$ mice. (B) IOP was measured from 2 to 12 months of age. $Flt1^{+/-}$, $Flk1^{+/-}$ and $Flt1^{+/-}$; $Flk1^{+/-}$ mice constantly showed elevated average IOPs, compared with WT mice. Data represent the mean ± SEM of 5–20 eyes. Significant difference, $^{*}P < 0.05$, $^{**}P < 0.01$ versus WT by Student's *t*-test.

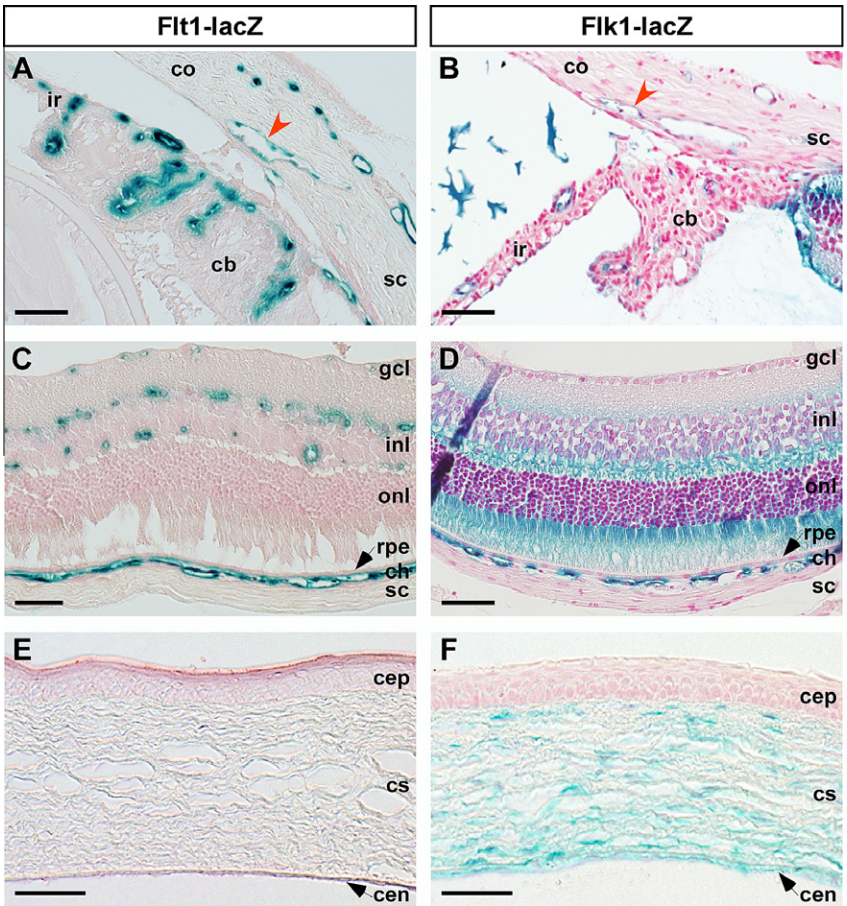

Fig. 2. Expression patterns of Flt1 and Flk1 in the adult eye. Expression analysis was performed by detecting a lacZ reporter knocked into the *Flt1* or *Flk1* locus. (A–D) Flt1 and Flk1 both were expressed in endothelial cells of the Schlemm's canal (arrowhead), corneal limbus, ciliary body (cb), iris (ir), and choroid (ch). (C, D) Flt1 but not Flk1 was expressed in the retinal vasculature. Flk1 is expressed by retinal neural cells in inner nuclear layer (inl) and outer nuclear layer (onl). (E, F) Flk1 but not Flt1 was expressed in the corneal stroma (cs) and corneal endothelium (cen). cep, corneal epithelium; co, cornea; gcl, ganglion cell layer; rpe, retinal pigment epithelium; sc, sclera. Scale bars, 250 μm.

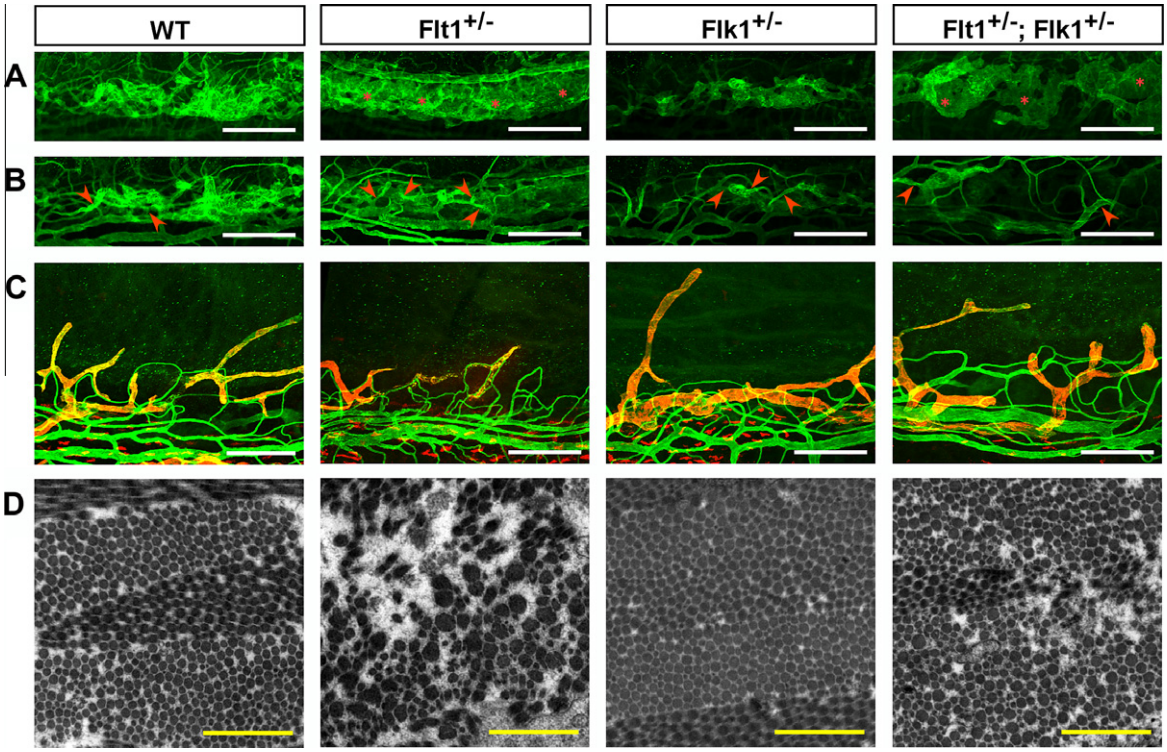

Fig. 3. Enlarged Schlemm's canal and disordered collagen fibers of the sclera in Flt1 heterozygous mice. (A–C) Whole-mount confocal microscopy of the cornea, iris, and ciliary body was performed with antibodies to a pan-endothelial marker PECAM-1 (green) and a lymphatic marker LYVE-1 (red). (A) Enlarged Schlemm's canal (asterisks) was detected in $Flt1^{+/-}$ and $Flt1^{+/-}$; $Flk1^{+/-}$ mice. (B) In different optical sections, collector channels (arrowheads) connecting with the corneal limbal blood vessels were comparable among WT, $Flt1^{+/-}$, $Flk1^{+/-}$, and $Flt1^{+/-}$; $Flk1^{+/-}$ mice. (C) Vascular pattern of blood vessels and LYVE-1^{+} lymphatic vessels in the corneal limbus were also comparable. Scale bars, 250 μm. (D) Transmission electron microscopy of the sclera shows that collagen fibers in the sclera of WT mice and $Flk1^{+/-}$ mice were uniform in size, whereas various sizes and higher density of collagen fibers were detected in the sclera of $Flt1^{+/-}$ and $Flt1^{+/-}$; $Flk1^{+/-}$mice. Scale bars, 2 μm.

cornea, iris, and ciliary body with antibodies to a pan-endothelial marker PECAM-1 and a lymphatic marker LYVE-1. Compared with WT and $Flk1^{+/-}$ mice, we found that the Schlemm's canal was enlarged in $Flt1^{+/-}$ and $Flt1^{+/-}$; $Flk1^{+/-}$mice (Fig. 3A). In different optical sections, we found that collector channels connecting with the corneal limbal blood vessels were comparable among WT, $Flt1^{+/-}$, $Flk1^{+/-}$, and $Flt1^{+/-}$; $Flk1^{+/-}$ mice (Fig. 3B, arrowheads). Vascular pattern of blood vessels and lymphatic vessels in the corneal limbus were also comparable (Fig. 3C). Although our previous study showed that soluble Flk1 plays an important role in inhibiting lymphatic vessel growth into the cornea [22], we did not detect abnormal distribution of lymphatic vessels in the cornea of $Flk1^{+/-}$ mice, indicating that half amount of Flk1 protein is enough for this inhibition of lymphatic growth. These results indicated that Flt1 heterozygosity is associated with enlarged Schlemm's canal.

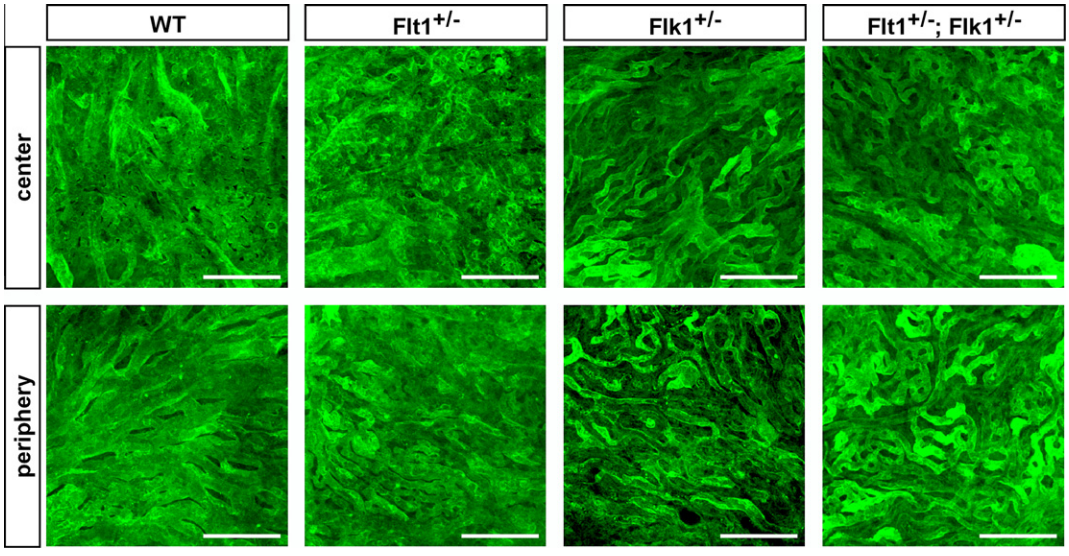

Fig. 4. Atrophied CC in Flk1 heterozygous mice. Whole-mount confocal microscopy of the choroid was performed with antibody to endoglin. A typical dense honeycomb vascular network of the CC was detected in WT and $Flt1^{+/-}$ mice, whereas the CC was atrophied with more avascular areas in both the central and the peripheral choroidal vasculature of $Flk1^{+/-}$ and $Flt1^{+/-}$; $Flk1^{+/-}$ mice. Scale bars, 100 μm.

The sclera contains a plenty amount of collagen fibers and elastic fibers which mechanically support the construction of eyes [23]. To investigate these mechanical fibers in enlarged eyes of $Flt1^{+/-}$; $Flk1^{+/-}$ mice, we performed histological analysis of the sclera. Transmission electron microscopy showed that collagen fibers in the sclera of WT mice and $Flk1^{+/-}$ mice were uniform in size, whereas various sizes and higher density of collagen fibers were detected in the sclera of Flt1 heterozygous mice (Fig. 3D). These results indicated that Flt1 heterozygosity is associated with disordered collagen fibers in the sclera.

3.4. Atrophied CC in Flk1 heterozygous mice

VEGF-A derived from the RPE plays a crucial role in the maintenance of the CC [7] and its receptors, Flt1 and Flk1 both are strongly expressed in CC (Fig. 2C, D). To investigate the vascular structure of CC, we performed whole-mount confocal microscopy of the choroid with antibody to endoglin which labels the CC. In WT and $Flt1^{+/-}$ mice, a typical dense honeycomb vascular network of the CC was detected, whereas the CC was atrophied with more avascular areas in $Flk1^{+/-}$ and $Flt1^{+/-}$; $Flk1^{+/-}$ mice (Fig. 4). The reduced vascular density was observed in both the central and the peripheral choroidal vasculature. To investigate whether the atrophy of CC affect the RPE, we used Phalloidin to label the cortical actin of RPE. Despite abnormal CC patterns in $Flk1^{+/-}$ and $Flt1^{+/-}$; $Flk1^{+/-}$ mice, the organization of the RPE was intact (Supplementary Fig. S3). The vasculature in the retina and iris appeared unaffected in these mutant mice (Supplementary Fig. S4). These results indicated that Flk1 heterozygosity is associated with atrophied CC.

4. Discussion

In this study, we showed enlarged eyes in $Flt1^{+/-}$; $Flk1^{+/-}$ mice. Compared with WT mice, IOP was elevated in $Flt1^{+/-}$, $Flk1^{+/-}$, and $Flt1^{+/-}$; $Flk1^{+/-}$ mice. However, none of them showed hallmarks of glaucoma such as ganglion cell death and excavation of optic disc. Flt1 heterozygosity is associated with enlarged Schlemm's canal and disordered collagen fibers in the sclera, whereas Flk1 heterozygosity is associated with atrophied CC.

Enlarged eyes in $Flt1^{+/-}$; $Flk1^{+/-}$ mice were similar to the buphthalmia which is detected in human congenital glaucoma with elevation of IOP. Indeed, $Flt1^{+/-}$; $Flk1^{+/-}$ mice showed the elevation of IOP, but they did not show hallmarks of glaucoma in the retina. Of note is that average IOPs in $Flt1^{+/-}$; $Flk1^{+/-}$ mice went up and down throughout adulthood although they were constantly higher than those in WT mice by about 1.5 mmHg (Fig. 1B). Previous studies regarding mice with eye projection and hallmarks of glaucoma showed that IOP was more severely elevated [15,16]. It is thus likely that gentle increase in IOP did not induce pathological changes in retinal neural cells. We also detected the elevation of IOP in $Flt1^{+/-}$, and $Flk1^{+/-}$ mice, although they did not exhibit the buphthalmia. Taken together, ocular phenotypes in $Flt1^{+/-}$; $Flk1^{+/-}$ mice were caused by combined effects of Flt1 and Flk1 heterozygosity.

In Flt1 heterozygous mice, we found the enlargement of the Schlemm's canal, suggesting obstruction of the main out flow pathway of the aqueous humor. However, corneal limbal blood vessels and their collector channels with the Schlemm's canal appeared unaffected. Endothelial cells in the Schlemm's canal express many blood endothelial markers [24] and our expression analysis also detected the expression of Flt1 and Flk1. Since Flt1 works as a negative regulator for endothelial cell growth, Schlemm's canal may be enlarged directly by excess VEGF-A protein in Flt1 heterozygous mice. We also found the disorder of collagen fibers in Flt1 heterozygous sclera. Although it remains to be elucidated how Flt1 heterozygosity affects the organization of collagen fibers in the sclera, this is probably a direct result from reduced function of Flt1 rather than from mechanical stress induced by elevated IOP since $Flk1^{+/-}$ mice with elevated IOP show a normal arrangement of collagen fibers in the sclera. In mice with a targeted type I collagen mutation leading to age-dependent collagen accumulation, the age-related elevation of IOP with open anterior chamber angle was reported [17]. Since the sclera is a part of alternative uveoscleral outflow pathway of the aqueous humor, the quality and quantity of collagen fibers in the sclera may affect IOP. Taken together, disordered collagen fibers in Flt1 heterozygous sclera may result in the elevation of IOP.

In Flk1 heterozygous mice, we found the atrophy of the CC, suggesting a change of the blood flow in the choroid and optical blood vessels. This is probably a direct result from reduced function of Flk1 since VEGF-A/Flk1 signals play an important role in maintenance of the CC [7]. A previous study using a fluorescent tracer suggested that the CC is a part of uveoscleral outflow pathway of the aqueous humor [11], suggesting that atrophied CC in Flk1 heterozygous choroid results in the elevation of IOP.

Our histopathological analysis still left some open questions regarding the relationship between vascular phenotypes, eye ball morphology, and regulation of IOP. It is tempting to speculate that, in $Flt1^{+/-}$; $Flk1^{+/-}$ mice, the eye projection by getting collagen fibers loosen in the sclera compensates for increased IOP by vascular defects to keep intact neural tissues in the retina. This study is the first report that $Flt1^{+/-}$; $Flk1^{+/-}$ mice showed the buphthalmia in mice.

Acknowledgments

We thank Dr. Janet Rossant for mutant mice for the *Flt1* and *Flk1* gene; Drs. Akiyoshi Uemura, Yoko Fukushima, Kazuichi Maruyama, and Yoichi Kurebayashi for helpful discussion; and Drs. Noriko Odani, Katsumi Oomachi, Tohru Shibata, and Takashi Yamanouchi for technical supports. This study was supported in part by Grant-in-Aid for JSPS Fellows (K.S.), Grant-in-Aid for Scientific Research (C) (M.H.), the Uehara Memorial Foundation (M.H.), and the Global COE Program "Global Center for Education and Research in Integrative Membrane Biology" from the Ministry of Education, Culture, Sports, Science, and Technology of Japan.

Appendix A. Supplementary data

Supplementary data associated with this article can be found, in the online version, at http://dx.doi.org/10.1016/j.bbrc.2012.03.011.

References

[1] N. Ferrara, H.P. Gerber, J. LeCouter, The biology of VEGF and its receptors, Nat. Med. 9 (2003) 669–676.
[2] F. Shalaby, J. Ho, W.L. Stanford, K.D. Fischer, A.C. Schuh, L. Schwartz, A. Bernstein, J. Rossant, A requirement for Flk1 in primitive and definitive hematopoiesis and vasculogenesis, Cell 89 (1997) 981–990.
[3] Y. Sakurai, K. Ohgimoto, Y. Kataoka, N. Yoshida, M. Shibuya, Essential role of Flk-1 (VEGF receptor 2) tyrosine residue 1173 in vasculogenesis in mice, Proc. Natl. Acad. Sci. U.S.A. 102 (2005) 1076–1081.
[4] G.H. Fong, J. Rossant, M. Gertsenstein, M.L. Breitman, Role of the Flt-1 receptor tyrosine kinase in regulating the assembly of vascular endothelium, Nature 376 (1995) 66–70.
[5] S. Hiratsuka, O. Minowa, J. Kuno, T. Noda, M. Shibuya, Flt-1 lacking the tyrosine kinase domain is sufficient for normal development and angiogenesis in mice, Proc. Natl. Acad. Sci. U.S.A. 95 (1998) 9349–9354.
[6] A.S. Maharaj, M. Saint-Geniez, A.E. Maldonado, P.A. D'Amore, Vascular endothelial growth factor localization in the adult, Am. J. Pathol. 168 (2006) 639–648.
[7] M. Saint-Geniez, T. Kurihara, E. Sekiyama, A.E. Maldonado, P.A. D'Amore, An essential role for RPE-derived soluble VEGF in the maintenance of the choriocapillaris, Proc. Natl. Acad. Sci. U.S.A. 106 (2009) 18751–18756.

[8] M. Saint-Geniez, A.E. Maldonado, P.A. D'Amore, VEGF expression and receptor activation in the choroid during development and in the adult, Invest. Ophthalmol. Vis. Sci. 47 (2006) 3135–3142.
[9] A.N. Witmer, G.F. Vrensen, C.J. Van Noorden, R.O. Schlingemann, Vascular endothelial growth factors and angiogenesis in eye disease, Prog. Retin. Eye Res. 22 (2003) 1–29.
[10] G.D. Yancopoulos, Clinical application of therapies targeting VEGF, Cell 143 (2010) 13–16.
[11] J.D. Lindsey, R.N. Weinreb, Identification of the mouse uveoscleral outflow pathway using fluorescent dextran, Invest. Ophthalmol. Vis. Sci. 43 (2002) 2201–2205.
[12] B.T. Gabelt, P.L. Kaufman, Changes in aqueous humor dynamics with age and glaucoma, Prog. Retin. Eye Res. 24 (2005) 612–637.
[13] S.W. John, R.S. Smith, O.V. Savinova, N.L. Hawes, B. Chang, D. Turnbull, M. Davisson, T.H. Roderick, J.R. Heckenlively, Essential iris atrophy, pigment dispersion, and glaucoma in DBA/2J mice, Invest. Ophthalmol. Vis. Sci. 39 (1998) 951–962.
[14] M. Scholz, T. Buder, S. Seeber, E. Adamek, C.M. Becker, E. Lutjen-Drecoll, Dependency of intraocular pressure elevation and glaucomatous changes in DBA/2J and DBA/2J-Rj mice, Invest. Ophthalmol. Vis. Sci. 49 (2008) 613–621.
[15] K. Fujikawa, T. Iwata, K. Inoue, M. Akahori, H. Kadotani, M. Fukaya, M. Watanabe, Q. Chang, E.M. Barnett, W. Swat, VAV2 and VAV3 as candidate disease genes for spontaneous glaucoma in mice and humans, PLoS ONE 5 (2010) e9050.
[16] L.M. Ittner, K. Schwerdtfeger, T.H. Kunz, R. Muff, K. Husmann, C. Grimm, F. Hafezi, K.S. Lang, M.O. Kurrer, J. Gotz, W. Born, J.A. Fischer, Transgenic mice with ocular overexpression of an adrenomedullin receptor reflect human acute angle-closure glaucoma, Clin. Sci. 114 (2008) 49–58.
[17] F. Mabuchi, J.D. Lindsey, M. Aihara, M.R. Mackey, R.N. Weinreb, Optic nerve damage in mice with a targeted type I collagen mutation, Invest. Ophthalmol. Vis. Sci. 45 (2004) 1841–1845.
[18] V. Senatorov, I. Malyukova, R. Fariss, E.F. Wawrousek, S. Swaminathan, S.K. Sharan, S. Tomarev, Expression of mutated mouse myocilin induces open-angle glaucoma in transgenic mice, J. Neurosci. 26 (2006) 11903–11914.
[19] M. Ema, S. Takahashi, J. Rossant, Deletion of the selection cassette, but not cis-acting elements, in targeted Flk1-lacZ allele reveals Flk1 expression in multipotent mesodermal progenitors, Blood 107 (2006) 111–117.
[20] M. Hirashima, Y. Lu, L. Byers, J. Rossant, Trophoblast expression of fms-like tyrosine kinase 1 is not required for the establishment of the maternal-fetal interface in the mouse placenta, Proc. Natl. Acad. Sci. U.S.A. 100 (2003) 15637–15642.
[21] M. Hirashima, K. Sano, T. Morisada, K. Murakami, J. Rossant, T. Suda, Lymphatic vessel assembly is impaired in Aspp1-deficient mouse embryos, Dev. Biol. 316 (2008) 149–159.
[22] R.J. Albuquerque, T. Hayashi, W.G. Cho, M.E. Kleinman, S. Dridi, A. Takeda, J.Z. Baffi, K. Yamada, H. Kaneko, M.G. Green, J. Chappell, J. Wilting, H.A. Weich, S. Yamagami, S. Amano, N. Mizuki, J.S. Alexander, M.L. Peterson, R.A. Brekken, M. Hirashima, S. Capoor, T. Usui, B.K. Ambati, J. Ambati, Alternatively spliced vascular endothelial growth factor receptor-2 is an essential endogenous inhibitor of lymphatic vessel growth, Nat. Med. 15 (2009) 1023–1030.
[23] P.G. Watson, R.D. Young, Scleral structure, organisation and disease. A review, Exp. Eye Res. 78 (2004) 609–623.
[24] K.M. Perkumas, W.D. Stamer, Protein markers and differentiation in culture for Schlemm's canal endothelial cells, Exp. Eye Res. 96 (2012) 82–87.

Biochemical and Biophysical Research Communications 420 (2012) 428–433

Contents lists available at SciVerse ScienceDirect

Biochemical and Biophysical Research Communications

journal homepage: www.elsevier.com/locate/ybbrc

Androgen receptor is up-regulated by a BLT2-linked pathway to contribute to prostate cancer progression

Jin-Wook Lee, Geun-Young Kim [1], Jae-Hong Kim *

College of Life Sciences and Biotechnology, Korea University, Seoul 136-701, Republic of Korea

ARTICLE INFO

Article history:
Received 18 February 2012
Available online 9 March 2012

Keywords:
AR
Prostate cancer
BLT2
ROS
Survival

ABSTRACT

The androgen receptor (AR) plays a central role in the development and progression of prostate cancer. AR expression is maintained throughout the progression of prostate cancer and is also associated with an aggressive, castration-resistant (CR) phenotype. Despite the critical roles of AR expression in prostate cancer progression, the exact signaling mechanism regulating AR expression remains unclear. In this study, we demonstrated that AR expression was increased by a low-affinity leukotriene B_4 receptor (BLT2)-linked pathway. We found that BLT2 was overexpressed in AR-positive prostate cancer cells, such as LNCaP cells, and BLT2 inhibition, using an inhibitor or siRNA knockdown, clearly attenuated AR expression and triggered apoptosis in these cells. These results suggest a role for BLT2 in AR expression and the survival of AR-positive prostate cancer cells. Moreover, we found that the NADPH oxidase family protein, Nox4, lay downstream of BLT2 and mediated the production of reactive oxygen species (ROS) and subsequent NF-κB stimulation, thereby inducing AR expression. Taken together, our results demonstrate that BLT2 plays a critical role in AR expression via a Nox4-ROS-NF-κB-linked pathway, thereby mediating the survival of AR-positive prostate cancer cells. Our findings point to BLT2 as a key regulator of AR expression and will contribute to the development of novel therapies for AR-positive prostate cancers, including androgen-responsive and CR prostate cancers.

1. Introduction

Prostate cancer is the most frequently diagnosed cancer and is one of the leading causes of cancer-related death in men [1]. Although androgen deprivation, through surgical castration or the administration of anti-androgens, has been widely accepted as a major medical treatment for prostate cancer, most patients with advanced prostate cancer eventually develop resistance to the therapy and progress to a more aggressive, castration-resistant (CR) phenotype [2]. Currently, there are no effective treatments for this stage of prostate cancer. During the progression of prostate cancers from an androgen-responsive to an androgen-refractory CR phenotype, prostate cancer cells still require the expression and activity of the androgen receptor (AR), which suggests that AR is necessary for both androgen-responsive and androgen-refractory CR phenotypes [2]. AR belongs to the steroid receptor superfamily and is a nuclear transcription factor that is responsible for mediating prostate cancer progression, particularly by regulating proliferation and survival [3]. Previous studies have shown that the inhibition of AR expression is in itself sufficient to induce cell death in both androgen-dependent and CR prostate cancer cells [3–6]. Based on these observations, various therapeutic strategies for reducing AR expression are being explored. Despite the critical role of AR expression in prostate cancer progression, the exact signaling mechanism regulating AR expression remains to be determined.

The metabolism of arachidonic acid by the lipoxygenase (LOX) or cyclooxygenase (COX) pathway generates eicosanoids, which have been implicated in the pathogenesis of a variety of human cancers, including prostate cancer, and are now thought to play critical roles in tumor promotion and progression [7]. For example, levels of leukotriene B_4 (LTB_4), a 5-LOX-catalyzed product, and 12(*S*)-hydroxyeicosatetraenoic acid (HETE), a 12-LOX-catalyzed product, are increased in prostate cancer, and these eicosanoids have been suggested to be critically involved in prostate carcinogenesis [7–12]. Additionally, previous studies have shown that BLT2, a putative receptor for LTB_4 and 12(*S*)-HETE, plays a critical role in tumor progression [13–18]. BLT2 is overexpressed in various human cancers, although the contribution of BLT2 to prostate cancer progression has not yet been determined.

Abbreviations: LTB_4, leukotriene B_4; HETE, hydroxyeicosatetraenoic; ROS, reactive oxygen species; NOX, NADPH oxidase; LOX, lipoxygenase.

* Corresponding author. Address: College of Life Sciences and Biotechnology, Korea University, 5-1 Anam-dong, Sungbuk-gu, Seoul 136-701, Republic of Korea. Fax: +82 2 927 9028.

E-mail addresses: ilisamsao@korea.ac.kr (J.-W. Lee), Kmgnyg@hanmail.net (G.-Y. Kim), jhongkim@korea.ac.kr (J.-H. Kim).

[1] Present address: Aab Cardiovascular Research Institute, University of Rochester, 601 Elmwood Avenue, Box CVRI, Rochester, NY 14642, USA.

0006-291X/$ - see front matter © 2012 Elsevier Inc. All rights reserved.
http://dx.doi.org/10.1016/j.bbrc.2012.03.012

In this study, we investigated the role of BLT2 in prostate cancer and found that BLT2 plays a critical role in driving AR expression, thereby affecting the survival of prostate cancer cells. In addition, we examined the downstream cascade responsible for AR expression and found that BLT2 stimulation upregulates NADPH oxidase (Nox)-4 and the subsequent generation of reactive oxygen species (ROS), which leads to the activation of the redox-sensitive transcription factor NF-κB, one of the major transcription factors regulating AR expression [19]. Together, our results suggest that this BLT2-Nox4-ROS-NF-κB cascade mediates AR expression, thus contributing to the progression of prostate cancer.

2. Materials and methods

All of the experiments were performed using the immortalized human prostate epithelial cells (PWR-1E) and prostate cancer cells (LNCaP and CWR22rv-1). The detailed descriptions of the methods that were used in this study are provided in the supplemental materials.

3. Results

3.1. BLT2 plays a role in the survival of AR-positive prostate cancer cells

To investigate the role of BLT2 in AR-positive prostate cancer cells, we initially examined the expression of BLT2 in prostate cancer cells. We found that the level of BLT2 transcripts was significantly increased in AR-positive prostate cancer cells compared with normal prostate epithelial cells. Semi-quantitative RT-PCR and real-time PCR analysis showed that AR-positive LNCaP and CWR22rv-1 prostate cancer cells contained highly increased levels of BLT2 transcripts compared with normal prostate epithelial PWR-1E cells (Fig. 1A). Similarly, we observed by Flow cytometric analysis that the protein levels of BLT2 were elevated in AR-positive prostate cancer cells, especially LNCaP cells, compared with normal epithelial cells (Fig. 1B). Next, to study whether or not BLT2 plays any role in these cells, the effect of the BLT2 antagonist LY255283 was tested. As shown in Fig. 1C, treatment with LY255283 significantly reduced the viability of AR-positive LNCaP and CWR22rv-1 prostate cancer cells, but not normal epithelial PWR-1E cells. Interestingly, we observed that the viability of AR-negative PC-3 and PC-3M prostate cancer cells was not affected by LY255283 treatment (data not shown), which suggests that the effect of BLT2 on survival was specific to AR-positive prostate cancer cells. Next, we tested whether or not the cell death induced by BLT2 inhibition with LY255283 in AR-positive prostate cancer cells resulted from apoptosis. A remarkable level of nuclear DNA fragmentation was clearly detected in LNCaP and CWR22rv-1 cells treated with LY255283 (Fig. 1D). Similarly, nuclear condensation and cleavage of poly ADP-ribose polymerase (PARP) and caspase-9 were demonstrated in the LY255283-treated LNCaP cells (Fig. 1E, F). BLT2 knockdown by siRNA induced apoptotic cell death in LNCaP cells (Fig. 1G). However, BLT2 inhibition did not cause any apoptotic death in PWR-1E control cells (Supplemental Fig. S1A and B). Together, our results suggest that BLT2 plays a role in mediating the AR-dependent survival of prostate cancer cells.

3.2. BLT2 regulates AR expression in AR-positive prostate cancer cells

Next, we examined whether or not BLT2 contributes to AR expression in AR-positive prostate cancer cells. BLT2 inhibition by treatment with LY255283 dramatically reduced the levels of AR at both the protein and transcript levels in AR-positive prostate cancer cells (Fig. 2A). Similarly, BLT2 knockdown by siRNA significantly diminished AR expression in LNCaP cells (Fig. 2B). Moreover, BLT2 stimulation by treatment with a BLT2 agonist, CAY10583 [20], which is also known as Compound A, appeared to further induce AR expression in these cells (Fig. 2C). Together, these results suggest that BLT2 plays a critical role in regulating AR expression, thereby affecting the survival of prostate cancer cells.

3.3. A Nox4-ROS cascade downstream of BLT2 mediates AR expression and survival

Recently, ROS have been suggested to regulate AR [21] and we have previously shown that the BLT2-Nox pathway mediates ROS generation [22–25]. Thus, we hypothesized that BLT2 may mediate AR expression through a Nox-ROS-dependent pathway. We therefore tested the effect of DPI, which is an inhibitor of flavoproteins such as Nox, on the regulation of AR expression and cell survival [26]. As shown in Fig. 3A, B, DPI significantly reduced AR levels and cell survival, which suggests that DPI-sensitive Nox may be involved in AR expression and may thus affect the viability of AR-positive prostate cancer cells. Indeed, Nox1 and Nox4 transcripts were detectable in AR-positive LNCaP prostate cancer cells, and BLT2 overexpression further increased the levels of Nox4 transcripts and AR expression in these cells (Fig. 3C). These results suggest that BLT2-Nox4-derived ROS is likely to be involved in the signaling pathway that leads to AR expression. In accordance with the proposed role of Nox4 downstream of BLT2, we observed that the levels of Nox4 transcripts and ROS generation were significantly diminished by knockdown of BLT2 with siRNA in LNCaP cells (Fig. 3D, E). Moreover, Nox4 knockdown clearly attenuated the level of AR expression in LNCaP cells (Fig. 3F). Together, these results suggest that a BLT2-Nox4-ROS-linked cascade mediates AR expression in AR-positive prostate cancer cells.

3.4. NF-κB acts downstream of BLT2-Nox4-ROS to mediate AR expression and survival

Recently, NF-κB, which is a redox-sensitive transcription factor, has been shown to regulate AR expression [19]. Thus, to test whether or not NF-κB lies downstream of the BLT2-Nox4-ROS cascade leading to AR expression, the effect of the NF-κB inhibitor Bay11-7082 was examined in AR-positive prostate cancer cells. As shown in Fig. 4, NF-κB inhibition by treatment with Bay11-7082 reduced AR transcript and protein levels (Fig. 4A) as well as the viability (Fig. 4B) of LNCaP and CWR22rv-1 cells, which suggests a role for NF-κB in AR expression. In addition, Fig. 4C shows that whereas p65 nuclear translocation was apparent in LNCaP cells transfected with control siRNA, there was no detectable p65 nuclear translocation in the cells transfected with BLT2 siRNA. Thus, NF-κB activity was clearly diminished by BLT2 inhibition. Together, these data suggest that NF-κB is likely to lie downstream of the BLT2-Nox4-ROS cascade in the signaling pathway leading to AR expression in AR-positive prostate cancer cells.

4. Discussion

In this study, we demonstrated that BLT2 played a role in upregulating AR, thereby potentially mediating the survival of AR-positive prostate cancer cells. Additionally, we extensively analyzed the key components mediating AR expression in the BLT2-linked pathway and found that the Nox4-ROS-NF-κB cascade lay downstream of BLT2 in AR-positive LNCaP and CWR22rv-1 prostate cancer cells. Furthermore, we observed that BLT2 blockade reduced tumor formation in a xenograft prostate cancer model (Supplemental Fig. S2). We believe that this finding provides valuable insight into prostate cancer progression, particularly with regard to

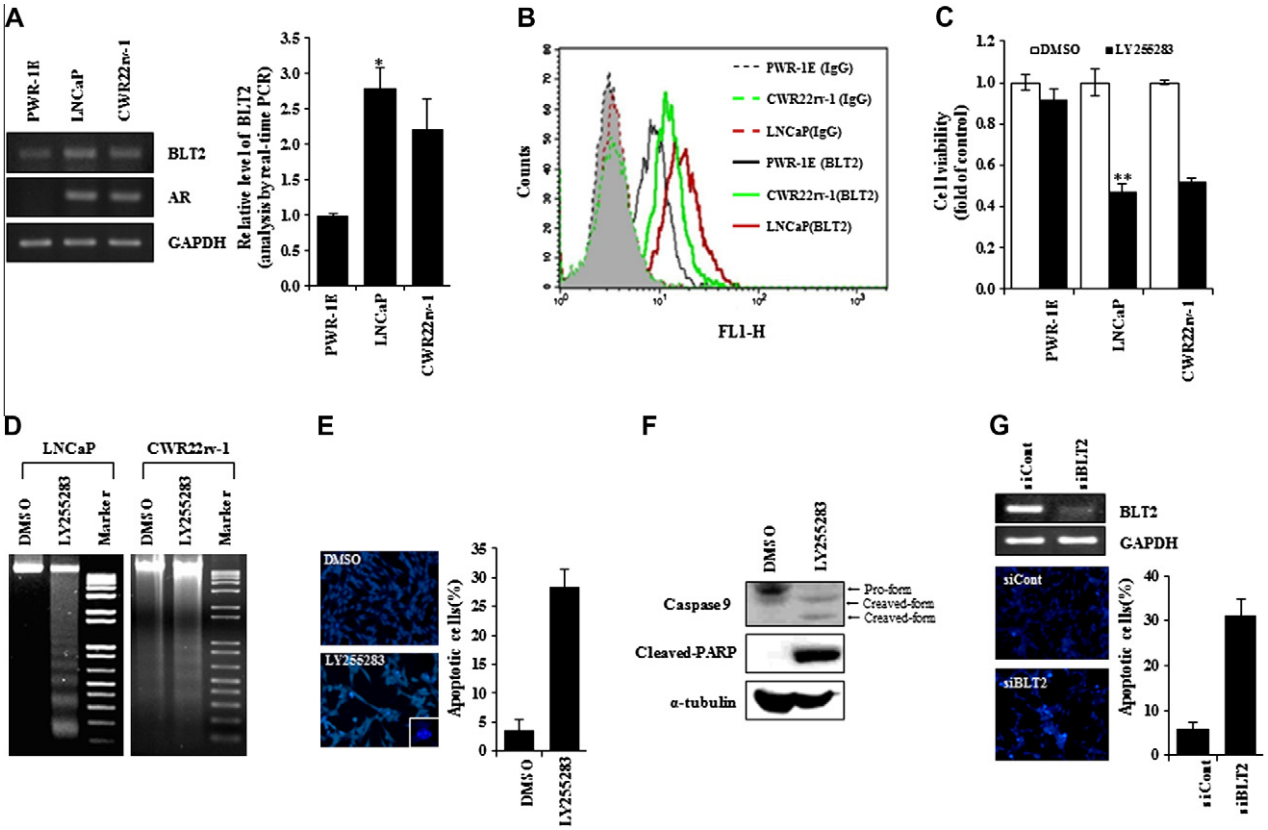

Fig. 1. BLT2 plays a role in the survival of AR-positive prostate cancer cells. (A) Total cellular RNA was isolated, and the levels of each transcript were assessed by semi-quantitative RT-PCR (left panel) and real-time PCR (right panel). Data indicate the means ± SD of three independent experiments (*$P < 0.01$). (B) PWR-1E, LNCaP and CWR22rv-1 cells were stained with primary antibodies against human BLT2 and analyzed by FACS analysis as described in Section 2. (C) PWR-1E, LNCaP and CWR22rv-1 cells were starved and treated with vehicle (DMSO) or 5 μM of LY255283 for 48 h. The MTT assay was then performed as described in the materials and methods. Data indicate the means ± SD of three independent experiments (**$P < 0.001$). (D) LNCaP and CWR22rv-1 cells were starved and treated with vehicle (DMSO) or LY255283 (5 μM) for 48 h. Then, the genomic DNA was isolated, electrophoresed on a 1.8% agarose gel and visualized using ethidium bromide staining. (E) LNCaP cells were incubated with vehicle (DMSO) or LY255283 (5 μM) for 36 h. The cells were stained with Hoechst 33258 (50 μg/ml) as described in Section 2, and the nuclear morphology was observed by fluorescence microscopy. (F) LNCaP cells were treated with vehicle (DMSO) or LY255283 (5 μM) for 48 h, and total cell lysates were used for western blotting to analyze the cleavage of caspase-9 and PARP. α-Tubulin was used as loading control. (G) LNCaP cells were transfected with control or BLT2 siRNA, and the level of BLT2 transcripts was analyzed by semi-quantitative RT-PCR (upper panel). After 72 h of transfection, the cells were stained with Hoechst 33258 as described in Section 2, and the nuclear morphology was observed by fluorescence microscopy (lower panel). Data indicate the means ± SD of three independent experiments.

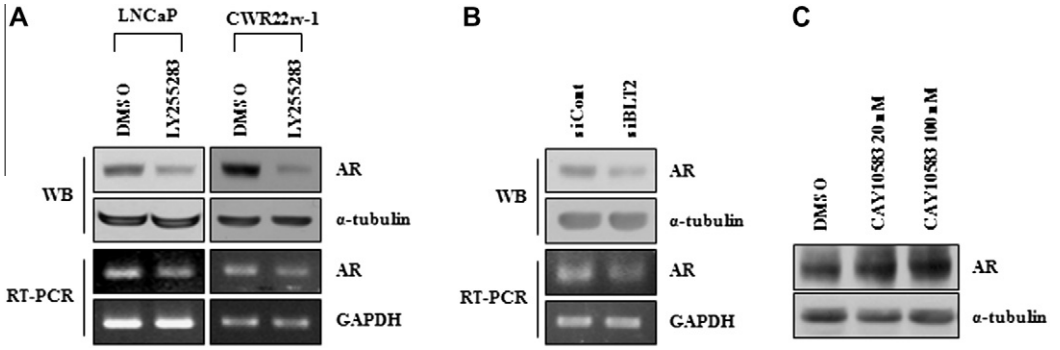

Fig. 2. BLT2 regulates AR expression in AR-positive prostate cancer cells. (A) LNCaP and CWR22rv-1 cells were starved and treated with vehicle (DMSO) or LY255283 (5 μM) for 12 or 24 h. Then, to analyze the level of AR, semi-quantitative RT-PCR was performed using the cells incubated for 12 h (lower panel), and western blotting was performed using the cells incubated for 24 h (upper panel). (B) LNCaP cells were transfected with control or BLT2 siRNA using Oligofectamine. After 24 h, the cells were starved and maintained for an additional 24 or 48 h. Then, the cells incubated for an additional 24 h were used for semi-quantitative RT-PCR (lower panel), and the cells incubated for the additional 48 h were used for western blotting (upper panel). (C) After being starved for 24 h, LNCaP cells were treated with various concentrations of CAY10583 for 24 h. Western blotting was performed to analyze the level of AR, and α-tubulin was used as a loading control.

the mechanism of progression toward androgen-responsive and CR prostate cancer.

Androgen plays a critical role in the development and progression of prostate cancer [2,3]. Prostate cancer cells are typically androgen-dependent, and therefore, androgen deprivation is the standard therapy for this disease. However, virtually most prostate cancer patients treated with androgen deprivation by surgical castration or anti-androgen administration develop resistance to the therapy and progress into a CR phenotype [2,3]. Currently, no effective therapy exists at this stage. In the development of resistance,

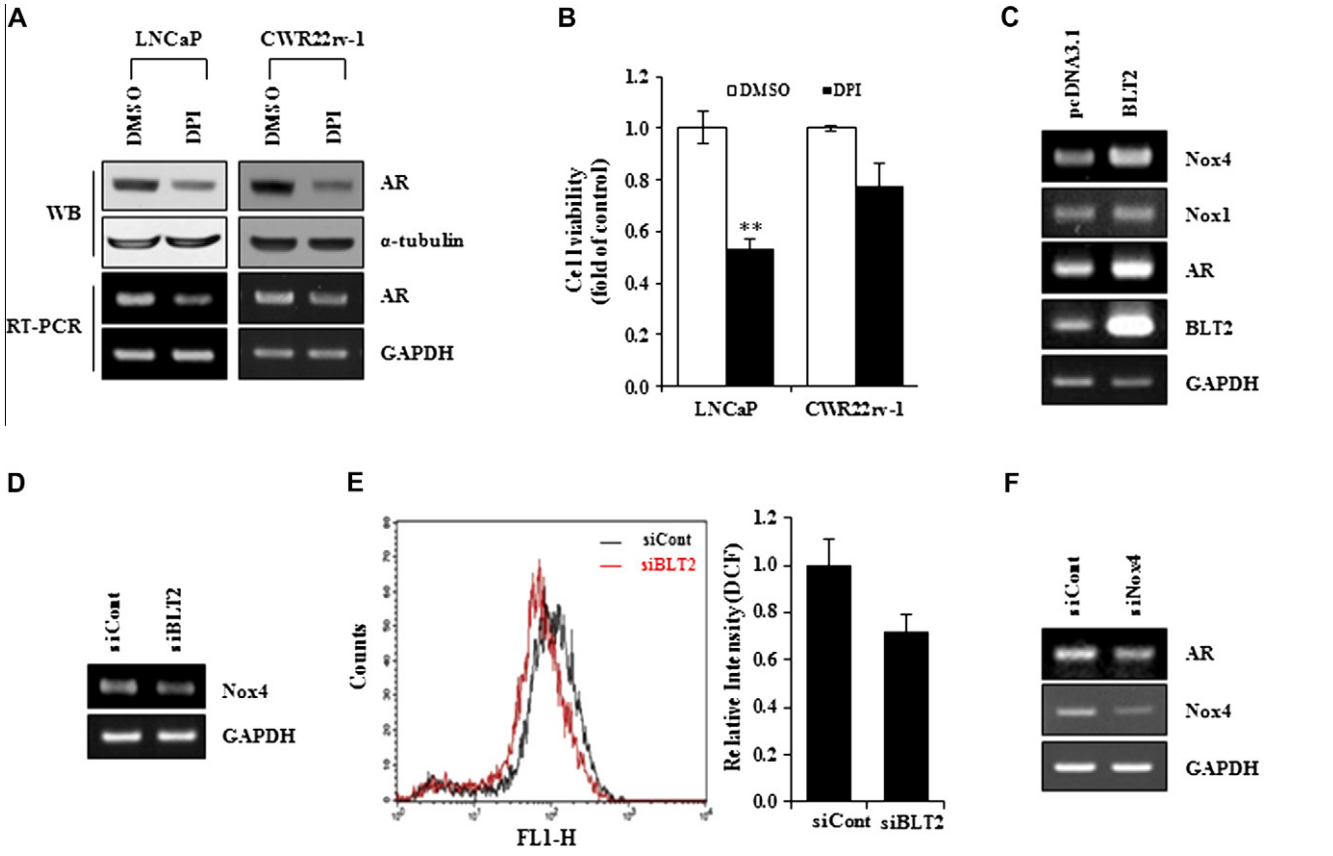

Fig. 3. A Nox4-ROS cascade downstream of BLT2 mediates AR expression and survival. (A) LNCaP and CWR22rv-1 cells were incubated with vehicle (DMSO) or DPI (100 nM) for 12 or 24 h. Then, to analyze the level of AR, semi-quantitative RT-PCR was performed using the cells incubated for 12 h (lower panel), and Western blotting was performed using the cells incubated for 24 h (upper panel). (B) LNCaP and CWR22rv-1 cells were incubated with 100 nM DPI for 48 h, and The MTT assay was then performed. Data indicate the means ± SD of three independent experiments ($^{**}P < 0.001$). (C) LNCaP cells were transfected with pcDNA3.1 or pcDNA3.1-BLT2 using Lipofectamine and then selected with 300 μg/ml of G418 for 15 days. The levels of Nox4, Nox1, AR and BLT2 mRNA were analyzed by semi-quantitative RT-PCR. (D) LNCaP cells were transfected with control or BLT2 siRNA, and the level of Nox4 mRNA was analyzed by semi-quantitative RT-PCR. (E) The intracellular level of ROS was measured in LNCaP cells transfected with control or BLT2 siRNA as described in Section 2. (F) LNCaP cells were transfected with pSuper or pSuper-siNox4 by electroporation as described in Section 2. After 48 h, RNA was isolated, and the levels of AR and Nox4 were analyzed by semi-quantitative RT-PCR.

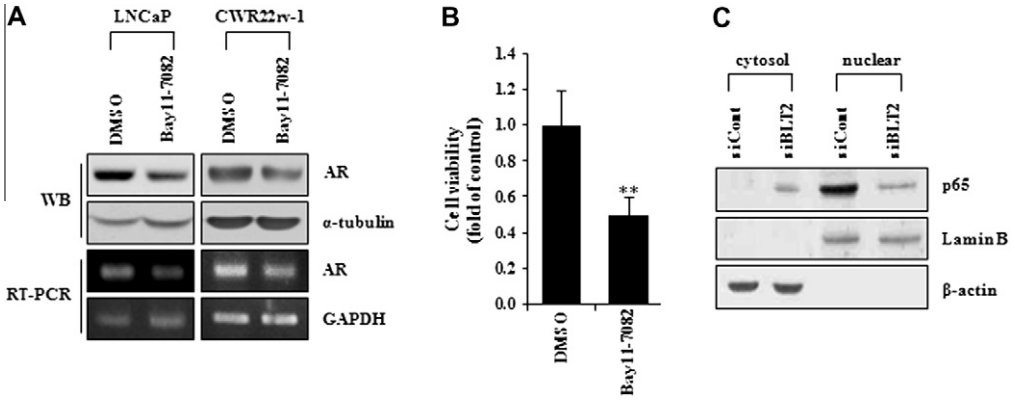

Fig. 4. NF-κB acts downstream of BLT2-Nox4-ROS to mediate AR expression and survival. (A) LNCaP and CWR22rv-1 cells were treated with vehicle (DMSO) or Bay11-7082 (10 μM) for 12 or 24 h. Then, to analyze the level of AR, semi-quantitative RT-PCR was performed using the cells incubated for 12 h (lower panel), and western blotting was performed using the cells incubated for 24 h (upper panel). (B) LNCaP cells were incubated with vehicle (DMSO) or Bay11-7082 (10 μM) for 48 h, and the MTT assay was performed. Data indicate the means ± S.D. of three independent experiments ($^{**}P < 0.001$). (C) LNCaP cells were transfected with control or BLT2 siRNA, and after 24 h, nuclear/cytoplasmic fractionation was performed as described in Section 2. The translocation of the p65 subunit was then analyzed by western blotting. Lamin B and β-actin were used as loading controls.

AR activation by overexpression has been implicated as one of the potential mechanisms [27]. Thus, a marked increase in AR expression is a critical event in the development of resistance for both androgen-responsive and androgen-refractory CR prostate cancer. Although angiotensin II (Ang-II) and interleukin-8 (IL-8) were recently reported to have the potential to induce AR expression, the detail signaling mechanism regulating AR expression remains to be further determined [28,29].

BLT2 is a G-protein-coupled receptor (GPCR) for LTB_4 and 12(*S*)-HETE and has previously been shown to be overexpressed in various human cancers [14–18]. We and others have demonstrated that BLT2 is involved in multiple pleiotropic capacities (e.g., cell proliferation, survival, invasiveness, metastasis, and angiogenesis), depending on the cancer cell type [16–18,22–25]. However, the role of BLT2 in prostate cancer progression has not yet been determined. In this study, our results revealed a previously unsuspected function of BLT2, i.e., a potential capacity to induce AR expression in prostate cancer cells. The inhibition of BLT2 using an inhibitor or siRNA knockdown diminished AR expression (Fig. 2A, B), and stimulation of BLT2 by overexpression upregulated AR (Fig. 3C). In support of the role of BLT2 as an upstream mediator of AR expression, the addition of CAY10583, which is a well-known BLT2 agonist, further increased AR expression in LNCaP cells (Fig. 2C). Additionally, it has previously been shown that LTB_4 and 12(*S*)-HETE are associated with prostate cancer carcinogenesis, and the levels of these ligands have been reported to be increased in prostate cancer patients [7–12], which also supports our observation. To further examine whether or not these ligands act via BLT2 in prostate cancer cells to drive AR expression, we tested the effects of inhibitors of 5-LOX or 12-LOX on AR expression. As expected, treatment with Baicalein, which is an inhibitor of 12-LOX, clearly diminished AR expression and the survival of AR-positive LNCaP prostate cancer cells (Supplemental Fig. S3A and B), and the addition of 12(*S*)-HETE to LNCaP cells further increased AR expression (Supplemental Fig. S3C). However, treatment with MK-886, which is an inhibitor of 5-LOX activating protein (FLAP), did not show any effect on AR expression in LNCaP cells (data not shown). This lack of effect was probably caused by the absence of FLAP protein and the resulting low rate of LTB_4 synthesis in these cells (Lee et al., unpublished observation). Thus, we suspect that 12(*S*)-HETE is a principal ligand for BLT2 and that a 12(*S*)-HETE-BLT2-linked cascade drives AR expression in AR-positive prostate cancer cells to contribute to cell survival. We investigated a potential role for GPR31 in AR-positive prostate cancer cells because GPR31 was recently identified as another receptor for 12(*S*)-HETE [30]. However, we could not detect any inhibitory effect of GPR31 siRNA on the survival of LNCaP cells (data not shown). Based on our observations, we suspect that BLT2 is a major receptor for 12(*S*)-HETE in AR-positive prostate cancer cells.

In this study, we showed that Nox4-derived ROS lie downstream of BLT2 and mediates AR expression, thus affecting survival in AR-positive prostate cancer cells. Consistent with our results, ROS and Nox have previously been suggested to be critical for survival or metastatic potential in prostate cancer cells [31,32], although the signaling mechanism by which ROS contribute to prostate cancer progression has not been investigated yet. Our results suggest that ROS upregulates AR expression by stimulating NF-κB activity. Zhang et al. also demonstrated that NF-κB can directly regulate AR expression in prostate cancer cells, and that levels of NF-κB and AR were strongly correlated in human prostate cancer [19]. Furthermore, it was demonstrated that inhibitors of NF-κB exerted anti-tumor activity in androgen-deprivation-resistant prostate cancer xenografts, which suggests that NF-κB is an important determinant of prostate cancer clinical biology [19]. We propose a hypothetical model that describes how BLT2 regulates AR expression to affect prostate cancer survival. Our results reveal that the upregulation of BLT2 resulted in the generation of ROS via Nox4 and also that NF-κB is a potential downstream component of the BLT2-Nox4-ROS cascade. Thus, we propose that a BLT2-linked pathway leads to the induction of AR expression and subsequently promotes cell survival in AR-positive prostate cancer cells. Further studies will be needed to analyze whether or not BLT2 mediates other parameters (e.g., invasion, metastasis or angiogenesis) in addition to the survival of AR-positive prostate cancer cells.

Considering the critical role of AR in androgen-responsive and androgen-refractory CR prostate cancer, our findings pointing to BLT2 as a key determinant of AR expression will provide valuable insight into the mechanism underlying the progression toward these prostate cancer types. In addition, we believe that these findings will contribute to the development of effective therapies for prostate cancers, including CR prostate cancer.

Acknowledgments

This work was supported by a General Researcher Support Project (2011-0004241) and a Diseases Network Research Program grant from the Ministry of Education, Science & Technology, Republic of Korea (2011-0027753). In addition, this work was supported by a grant from the Korea Healthcare Technology R&D Project, Ministry of Health & Welfare, Republic of Korea (A101032).

Appendix A. Supplementary data

Supplementary data associated with this article can be found, in the online version, at http://dx.doi.org/10.1016/j.bbrc.2012.03.012.

References

[1] A. Jemal, R. Siegel, J. Xu, E. Ward, Cancer statistics, 2010, CA Cancer J. Clin. 60 (2010) 277–300.
[2] B.J. Feldman, D. Feldman, The development of androgen-independent prostate cancer, Nat. Rev. Cancer 1 (2001) 34–45.
[3] M.B. Cohen, O.W. Rokhlin, Mechanisms of prostate cancer cell survival after inhibition of AR expression, J. Cell Biochem. 106 (2009) 363–371.
[4] M.M. Bhuiyan, Y. Li, S. Banerjee, F. Ahmed, Z. Wang, S. Ali, F.H. Sarkar, Down-regulation of androgen receptor by 3,3′-diindolylmethane contributes to inhibition of cell proliferation and induction of apoptosis in both hormone-sensitive LNCaP and insensitive C4–2B prostate cancer cells, Cancer Res. 66 (2006) 10064–10072.
[5] H. Cheng, R. Snoek, F. Ghaidi, M.E. Cox, P.S. Rennie, Short hairpin RNA knockdown of the androgen receptor attenuates ligand-independent activation and delays tumor progression, Cancer Res. 66 (2006) 10613–10620.
[6] X. Liao, S. Tang, J.B. Thrasher, T.L. Griebling, B. Li, Small-interfering RNA-induced androgen receptor silencing leads to apoptotic cell death in prostate cancer, Mol. Cancer Ther. 4 (2005) 505–515.
[7] D. Nie, M. Che, D. Grignon, K. Tang, K.V. Honn, Role of eicosanoids in prostate cancer progression, Cancer Metastasis Rev. 20 (2001) 195–206.
[8] S. Larre, N. Tran, C. Fan, H. Hamadeh, J. Champigneulles, R. Azzouzi, O. Cussenot, P. Mangin, J.L. Olivier, PGE2 and LTB4 tissue levels in benign and cancerous prostates, Prostaglandins Other Lipid Mediat. 87 (2008) 14–19.
[9] N.P. McCabe, S.H. Selman, J. Jankun, Vascular endothelial growth factor production in human prostate cancer cells is stimulated by overexpression of platelet 12-lipoxygenase, Prostate 66 (2006) 779–787.
[10] D. Nie, J. Nemeth, Y. Qiao, A. Zacharek, L. Li, K. Hanna, K. Tang, G.G. Hillman, M.L. Cher, D.J. Grignon, K.V. Honn, Increased metastatic potential in human prostate carcinoma cells by overexpression of arachidonate 12-lipoxygenase, Clin. Exp. Metastasis 20 (2003) 657–663.
[11] J. Ghosh, Inhibition of arachidonate 5-lipoxygenase triggers prostate cancer cell death through rapid activation of c-Jun N-terminal kinase, Biochem. Biophys. Res. Commun. 307 (2003) 342–349.
[12] G.P. Pidgeon, M. Kandouz, A. Meram, K.V. Honn, Mechanisms controlling cell cycle arrest and induction of apoptosis after 12-lipoxygenase inhibition in prostate cancer cells, Cancer Res. 62 (2002) 2721–2727.
[13] A.M. Tager, A.D. Luster, BLT1 and BLT2: the leukotriene B(4) receptors, Prostaglandins Leukot Essent Fatty Acids 69 (2003) 123–134.
[14] R.P. Rocconi, T.O. Kirby, R.S. Seitz, R. Beck, J.M. Straughn Jr., R.D. Alvarez, W.K. Huh, Lipoxygenase pathway receptor expression in ovarian cancer, Reprod. Sci. 15 (2008) 321–326.
[15] M.H. Yoo, H. Song, C.H. Woo, H. Kim, J.H. Kim, Role of the BLT2, a leukotriene B4 receptor, in Ras transformation, Oncogene 23 (2004) 9259–9268.
[16] R. Hennig, T. Osman, I. Esposito, N. Giese, S.M. Rao, X.Z. Ding, W.G. Tong, M.W. Buchler, T. Yokomizo, H. Friess, T.E. Adrian, BLT2 is expressed in PanINs IPMNs, pancreatic cancer and stimulates tumour cell proliferation, Br. J. Cancer 99 (2008) 1064–1073.
[17] J.A. Choi, J.W. Lee, H. Kim, E.Y. Kim, J.M. Seo, J. Ko, J.H. Kim, Pro-survival of estrogen receptor-negative breast cancer cells is regulated by a BLT2-reactive oxygen species-linked signaling pathway, Carcinogenesis 31 (2010) 543–551.
[18] J.M. Seo, K.J. Cho, E.Y. Kim, M.H. Choi, B.C. Chung, J.H. Kim, Up-regulation of BLT2 is critical for the survival of bladder cancer cells, Exp. Mol. Med. 43 (2011) 129–137.
[19] L. Zhang, S. Altuwaijri, F. Deng, L. Chen, P. Lal, U.K. Bhanot, R. Korets, S. Wenske, H.G. Lilja, C. Chang, H.I. Scher, W.L. Gerald, NF-kappaB regulates androgen

receptor expression and prostate cancer growth, Am. J. Pathol. 175 (2009) 489–499.
[20] Y. Iizuka, T. Yokomizo, K. Terawaki, M. Komine, K. Tamaki, T. Shimizu, Characterization of a mouse second leukotriene B4 receptor, mBLT2: BLT2-dependent ERK activation and cell migration of primary mouse keratinocytes, J. Biol. Chem. 280 (2005) 24816–24823.
[21] N. Sharifi, E.M. Hurt, S.B. Thomas, W.L. Farrar, Effects of manganese superoxide dismutase silencing on androgen receptor function and gene regulation: implications for castration-resistant prostate cancer, Clin. Cancer Res. 14 (2008) 6073–6080.
[22] J.A. Choi, E.Y. Kim, H. Song, C. Kim, J.H. Kim, Reactive oxygen species are generated through a BLT2-linked cascade in Ras-transformed cells, Free Radic. Biol. Med. 44 (2008) 624–634.
[23] G.Y. Kim, J.W. Lee, H.C. Ryu, J.D. Wei, C.M. Seong, J.H. Kim, Proinflammatory cytokine IL-1beta stimulates IL-8 synthesis in mast cells via a leukotriene B4 receptor 2-linked pathway, contributing to angiogenesis, J. Immunol. 184 (2010) 3946–3954.
[24] E.Y. Kim, J.M. Seo, K.J. Cho, J.H. Kim, Ras-induced invasion and metastasis are regulated by a leukotriene B4 receptor BLT2-linked pathway, Oncogene 29 (2010) 1167–1178.
[25] E.Y. Kim, J.M. Seo, C. Kim, J.E. Lee, K.M. Lee, J.H. Kim, BLT2 promotes the invasion and metastasis of aggressive bladder cancer cells through a reactive oxygen species-linked pathway, Free Radic. Biol. Med. 49 (2010) 1072–1081.
[26] J.D. Lambeth, NOX enzymes and the biology of reactive oxygen, Nat. Rev. Immunol. 4 (2004) 181–189.
[27] J. Edwards, N.S. Krishna, K.M. Grigor, J.M. Bartlett, Androgen receptor gene amplification and protein expression in hormone refractory prostate cancer, Br. J. Cancer 89 (2003) 552–556.
[28] A. Seaton, P. Scullin, P.J. Maxwell, C. Wilson, J. Pettigrew, R. Gallagher, J.M. O'Sullivan, P.G. Johnston, D.J. Waugh, Interleukin-8 signaling promotes androgen-independent proliferation of prostate cancer cells via induction of androgen receptor expression and activation, Carcinogenesis 29 (2008) 1148–1156.
[29] K. Hoshino, H. Ishiguro, J. Teranishi, S. Yoshida, S. Umemura, Y. Kubota, H. Uemura, Regulation of androgen receptor expression through angiotensin II type 1 receptor in prostate cancer cells, Prostate 71 (2011) 964–975.
[30] Y. Guo, W. Zhang, C. Giroux, Y. Cai, P. Ekambaram, A.K. Dilly, A. Hsu, S. Zhou, K.R. Maddipati, J. Liu, S. Joshi, S.C. Tucker, M.J. Lee, K.V. Honn, Identification of the orphan G protein-coupled receptor GPR31 as a receptor for 12-(S)-hydroxyeicosatetraenoic acid, J. Biol. Chem. 286 (2011) 33832–33840.
[31] B. Kumar, S. Koul, L. Khandrika, R.B. Meacham, H.K. Koul, Oxidative stress is inherent in prostate cancer cells and is required for aggressive phenotype, Cancer Res. 68 (2008) 1777–1785.
[32] S.D. Lim, C. Sun, J.D. Lambeth, F. Marshall, M. Amin, L. Chung, J.A. Petros, R.S. Arnold, Increased Nox1 and hydrogen peroxide in prostate cancer, Prostate 62 (2005) 200–207.

Biochemical and Biophysical Research Communications 420 (2012) 434–439

Contents lists available at SciVerse ScienceDirect

Biochemical and Biophysical Research Communications

journal homepage: www.elsevier.com/locate/ybbrc

Epigallocatechin-3-gallate inhibits apoptosis and protects testicular seminiferous tubules from ischemia/reperfusion-induced inflammation

May Al-Maghrebi [a,*], Waleed M. Renno [b], Nada Al-Ajmi [c]

[a] Department of Biochemistry, Faculty of Medicine, Kuwait University, P.O. Box: 24923, Safat 13110, Kuwait
[b] Department of Anatomy, Faculty of Medicine, Kuwait University, Kuwait
[c] Cell Biology, The Public Authority for Applied Education & Training, Kuwait

ARTICLE INFO

Article history:
Received 1 March 2012
Available online 9 March 2012

Keywords:
EGCG
Testicular torsion
Inflammation
Apoptosis

ABSTRACT

Testicular torsion (TT) is a urologic emergency that may result in future infertility problems. The pathologic process of TT is similar to an ischemia reperfusion injury (IRI). The purpose of this study was to evaluate the effect of epigallocatechin-3-gallate (EGCG) on reversing the damaging consequences of TT-induced IRI by examining its inhibitory effects on the expression of inflammatory and apoptosis mediators in a unilateral TT rat model. Eighteen male Sprague–Dawley rats were divided into 3 groups. Group 1 underwent a sham operation of the left testis under general anesthesia. Group 2 underwent ischemia for 1 h followed by 4 h reperfusion in the presence of saline. The third group was similar to group 2, however, EGCG (50 mg/kg) was injected i.p. 30 min after ischemia induction. The *in vivo* protective effect of EGCG was tested by measuring testicular levels of TNF-α, IL-6 and IL-1β by ELISA and mRNA expression of iNOS, MCP-1, p53, Bax, Bcl-2 and survivin by real-time PCR. Also, testicular morphological changes and damage to spermatogenesis were evaluated using H&E staining and Johnsen's scoring system, respectively. EGCG treatment improved testicular structures in the ipsilateral testis, markedly inhibited germ cell apoptosis (GCA) and significantly decreased testicular cytokine levels. In addition, EGCG was able to down regulate the mRNA expression of iNOS, MCP-1 and pro-apoptosis genes in favor of cell survival. For the first time we show that *in vivo* EGCG treatment rescued the torsed testes from IRI-induced inflammation, GCA and damage to spermatogenesis thus suggesting a new preventive approach to inhibiting the inflammatory and apoptotic consequences of TT-induced IRI.

1. Introduction

Testicular torsion (TT) is caused by twisting of the spermatic cord and leads to ischemia of the testicular tissue due to the obstruction of blood flow to the testis. Extended period of tissue ischemia will result in permanent testicular damage, loss of spermatogenesis and necrosis. Therefore, TT is considered a medical emergency that usually requires immediate surgical intervention to reperfuse the affected testis. Despite return of blood flow after testis detorsion, loss of spermatogenesis is still observed [1]. The ischemia reperfusion injury (IRI) to the testis induced by TT is accompanied by germ cell apoptosis (GCA), increase in intratesticular neutrophils, generation of reactive oxygen species (ROS) and DNA damage [2]. Furthermore, some studies suggest that ROS produced by the recruited neutrophils disturb Bcl-2 family members in the germ cells and thus initiate apoptosis via the mitochondrial pathway [3]. A fine balance between pro-apoptosis molecules and anti-apoptosis molecules can trigger the onset or inhibition of apoptosis.

Coinciding with IRI-induced GCA is the generation of pro-inflammatory cytokines, in particular TNFα, IL-6 and IL-1β. Both TNFα and IL-1β are known to cause inflammation and induce the expression of pro-inflammatory peptides such as iNOS, cyclooxygenase 2 and IL-6 in Sertoli cells [4] as well as in seminiferous peritubular cells [5]. In fact, IL-1α, IL-1β, and TNFα stimulate their own expression as well as each other's production in an amplification loop [6,7]. Inducible nitric oxide synthase (iNOS) is the enzyme responsible for nitric oxide (NO) production and it is known to be expressed in the testes and is involved in spermatogenesis, infertility, sperm maturation and apoptosis of Sertoli and germ cells [8,9]. iNOS is induced in tissues after exposure to inflammatory cytokines or ischemia [10] and produces relatively larger amounts of NO than its other two isoforms, nNOS and eNOS [11], thus it may cause cell death [12]. Therefore, testicular iNOS concentration may define prognosis after IRI. NO was also found to regulate the expression of monocyte chemoattractant protein-1 (MCP-1), a member of the C–C or beta subfamily of chemokines and the principal monocyte-selective chemotactic cytokine [13].

* Corresponding author. Fax: +965 25338908.
E-mail address: malmaghrebi@hsc.edu.kw (M. Al-Maghrebi).

0006-291X/$ - see front matter © 2012 Elsevier Inc. All rights reserved.
http://dx.doi.org/10.1016/j.bbrc.2012.03.013

Interestingly, this chemokine has been shown to be produced by several testicular interstitial cell types *in vitro* [14,15].

Epigallocatechin-3-gallate (EGCG) is the major component of polyphenols in green tea and is widely investigated due to its ability to suppress the inflammatory processes that lead to transformation, inhibit cell proliferation and exert a strong antiradical activity [16,17]. It has been shown that EGCG protects cardiomyocytes against ischemia/reperfusion-induced apoptosis both *in vitro* and *in vivo* [18]. EGCG is also used now as a nutritional supplement due to its many health benefits and positive effects that surpasses any other natural product.

Based on its protective properties, we aimed to investigate whether EGCG treatment can rescue the testes from TT-induced IRI harmful consequences by assessing the morphological changes in testicular tissue, the expression of apoptosis and inflammation genes and measuring testicular cytokine concentrations.

2. Materials and methods

2.1. Animals and surgical procedure

The study included 18 adult male Sprague Dawley rats (8 weeks of age and weighing between 250 and 300 g). Rats were housed in a temperature, humidity, and 12 h light/12 h dark cycle controlled room with food and water *ad libitum*. The rats were randomly assigned into three groups: Sham ($n = 6$); IRI + vehicle ($n = 6$) and IRI + EGCG ($n = 6$). Animals were handled according to the guidelines of experimental animals recommended by Kuwait University for animal welfare and care. All animal experiments were performed following a protocol approved by the ethics committee on animal research at Kuwait University. All surgical procedures were performed under xylazine/ketamine anesthesia (62.5/3.2 mg/kg, i.p.) using sterile conditions with the aid of a surgical microscope. TT and detorsion were performed in the form of 1 h ischemia followed by 4 h of reperfusion, respectively. For the three animal groups, the scrotum was entered through a midline incision. The tunica vaginalis was opened, and the left testis was exposed. The left testicular artery was compressed with a Dumont #7 curved jewelers forceps (Fine Science Tools Inc., North Vancouver, BC, Canada) to completely cut off the blood supply to the testes (ischemia) for 1 h. In the IRI + vehicle group, 250 μl of saline was injected i.p. 30 min after ischemia onset. At the end of 1 h ischemia, the forceps was removed and the left testis was replaced in the scrotum for 4 h of reperfusion followed by animal sacrifice. In the IRI + EGCG group, 50 mg/kg EGCG was dissolved in saline and one dose was injected i.p. 30 min prior to reperfusion. The left testis was then returned to the scrotum for 4 h of reperfusion. In the sham-operated group, the left testis was brought through the incision, exposed for 1 h and then returned to the scrotal sac. Animals in each group were sacrificed together and the testes were harvested, cut into 2 halves and preserved for further histopathologic and biochemical investigations. The right contralateral testes served as a positive internal control.

2.2. Histologic examination

Testicular tissue was immediately immersed and fixed in Bouin's fixative for 24 h before they were washed in PBS buffer and further processed for light microscopy and embedded in paraffin blocks. 4 μm sections were stained with hematoxylin and eosin (H&E). Three sections from each testis (ipsilateral and contralateral) were analyzed under light microscopy. The examiner was blinded to the treatment of each group. As described earlier [19], the Johnsen's score was used to evaluate the morphological impairment to testicular tissue as a result of IRI. Briefly, the Johnsen's method [20] applies a score of 1–10 for each tubule cross-section, whereby a score of 10 indicates complete spermatogenesis and perfect tubules, while a score of 1 means no germ cells and no Sertoli cells present. The Johnsen's score per tubule was expressed as mean ± SEM for each group.

2.3. TUNEL assay

The level of DNA damage was detected via the terminal transferase-mediated dUTP-biotin nick end-labeling (TUNEL) assay, which was performed using an *in situ* cell death detection POD kit (Roche Diagnostics, Mannheim, Germany) following the manufacturer's instructions. Briefly, 4 μm sections were deparaffinized and rehydrated with serial changes of xylene and ethanol followed by Proteinase K treatment (20 mg/L) for 15 min (Sigma–Aldrich, Saint Louis, MI, USA). The sections were then treated with the reaction mixture containing TdT and biotinylated 16-dUTP for 1 h at 37 °C. Labeled DNA was visualized with peroxidase-conjugated antidigoxigenin antibody using 3,3′-diaminobenzidine as the chromogen. One-hundred seminiferous tubules from each testis were evaluated for DNA damage in circular cross sections using randomly selected microscopic fields from three testes in each group. The number of TUNEL-positive nuclei per tubule were counted and expressed as the mean ± SEM.

2.4. ELISA assay

Protein extracts were prepared from fresh testicular tissues homogenized in RIPA lysis solution (50 mM Tris–HCl, pH 8.0, with 150 mM sodium chloride, 1.0% Igepal CA-630, 0.5% sodium deoxycholate, and 0.1% sodium dodecyl sulfate) (Sigma–Aldrich, Saint Louis, MI, USA). A cocktail of protease inhibitors including aprotinin, leupeptine, pepstatine, PMSF (2 μg/ml each) was added to the RIPA lysis solution just before tissue homogenization. Protein concentrations were measured and equal protein amounts were used for each ELISA assay. Protein extracts were analyzed in triplicates for cytokine levels according to the ELISA kit procedures for TNF-α, IL-1β, IL-6 (eBioscience, San Diego, CA, USA).

2.5. RNA isolation and reverse transcription

Total RNA was isolated from testicular tissue using the Trizol reagent (Life Technologies Inc., Gaithersburg, MD, USA). Single-strand complementary DNA (cDNA) was synthesized by random priming of 1–5 μg total RNA using the High Capacity cDNA Reverse Transcription Kit (Applied Biosystems, CA, USA) for 2 h at 85 °C.

2.6. Real-time PCR

Standardized Taqman probe/primers assays for Bax, p53, Bcl-2, survivin, MCP-1 and iNOS were purchased from Applied Biosystems (Carlsbad, CA, USA). Amplification of the above genes was performed in a 96-well reaction plate. The 25 μl reaction mixture in each well contained 3 μL of cDNA, 200 nmol/l of Taqman probe/primers assay and 12.5 μL of qPCR Super Mix (Applied Biosystems, Carlsbad, CA, USA). A non-template PCR negative control reaction and a positive PCR control with a known template size were included. All reactions were run in duplicates. Real-time PCR was performed using the sequence documentation system (SDS) 7000 (Applied Biosystems, Carlsbad, CA, USA). The comparative CT method was used to quantitate mRNA expression [21]. Briefly, the target gene specific signal was normalized to the constitutively expressed β-Actin gene signal using the formula $2^{-\Delta\Delta CT} = 2^{-(CT,\beta\text{-Actin-CT,target gene})}$, resulting in the evaluation of the samples as *n*-fold difference relative to that of β-Actin mRNA expression.

2.7. Statistical analysis

A one-way analysis of variance (ANOVA) was applied to assess significant differences between the mean Johnsen's scores observed in sham, IRI + vehicle, and IRI + EGCG group. The LSD and Bonferroni Post Hoc tests were performed to determine individual probability values for multiple comparisons using SPSS software (v 17.1). t-test (independent) was performed for each group using SPSS software. Statistical analysis for the gene expression and ELISA data was performed using GraphPad Prism (v 5.0). Group differences were compared by ANOVA followed by the Kruskal–Wallis test. All data were expressed as mean ± SEM. P values $\leqslant 0.05$ were considered to indicate statistical significance.

3. Results

3.1. Histologic analysis

The contralateral testes from all three experimental groups including the ipsilateral testes from the sham animals displayed normal morphology of seminiferous tubules. The sham testes showed normal seminiferous tubular diameter, number of germ cell layers and spermatogenesis from spermatogoniun in the basement to spermatozoon in the center of the tubules (Fig. 1A). IRI + vehicle rat testes displayed remarkable morphological changes and tissue damage (Fig. 1C) with significant seminiferous tubular atrophy, reduction in the number of germ cell layers and spermatogenous arrest. In contrast, IRI + EGCG (50 mg/kg i.p.) treated animals displayed normal histologic morphology in the majority of seminiferous tubules of ipsilateral testes (Fig. 1E). High magnifications of the histologic alterations from the sham, IRI + vehicle and IRI + EGCG-experimental groups are also shown (Fig. 1B, D and F).

The mean morphologic testicular damage was assessed by the Johnsen's scoring system in the three experimental groups (Table 1). The testes from the IRI + vehicle group showed significant low scores ($p \leqslant 0.001$) compared to sham-operated and contralateral testes. The average Johnsen's score for the sham and IRI + vehicle group was 9.375 ± 0.125 and 6.875 ± 0.375, respectively. In contrast, the IRI + EGCG testes exhibited significantly ($p \leqslant 0.001$) higher scores (8.313 ± 0.120) compared to the IRI + vehicle group and significantly lower ($p \leqslant 0.03$) than the sham group.

3.2. Evaluation of germ cell apoptosis

Tissue sections from the testes of sham-operated animals stained by TUNEL revealed very few stained nuclei (1.9 ± 0.35) indicating baseline DNA damage (Fig. 2A). However, sections taken

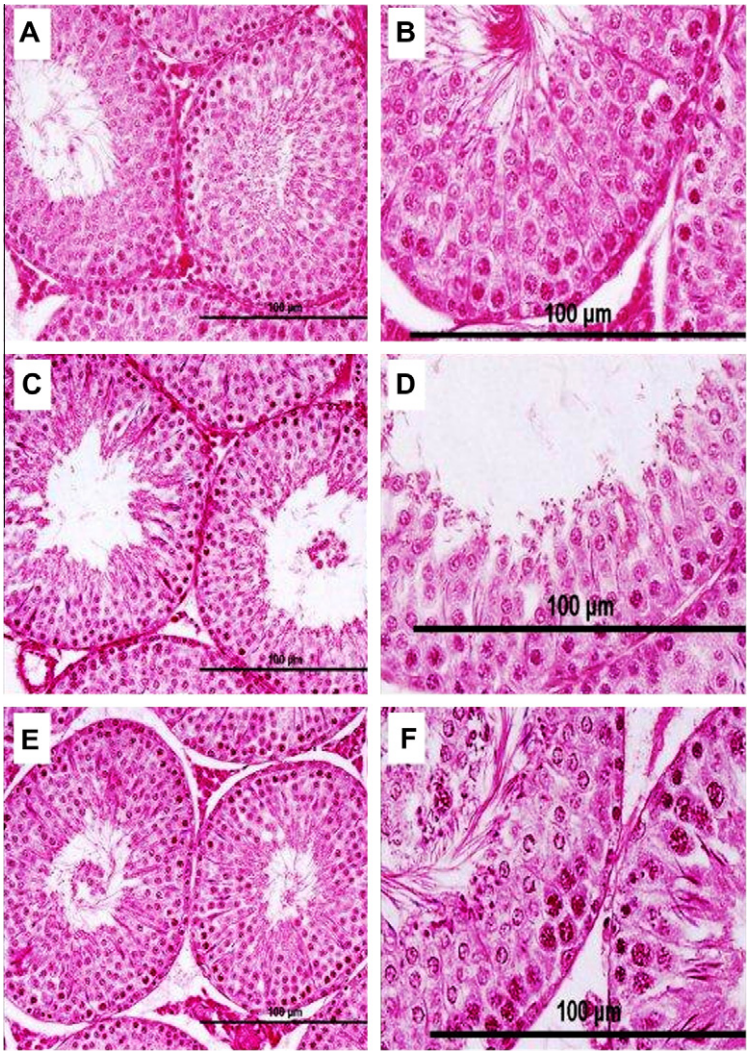

Fig. 1. Histologic analysis of testicular tissue. H & E sections of rat testes showing low (A, C and E) and high (B, D and F) magnifications of the histologic alterations from the sham, IRI + vehicle and IRI + EGCG- experimental groups. A and B are examples of ipsilateral testis from the sham group; C and D represent histologic sections of ipsilateral testis from the IRI + vehicle animal group and E and F are examples of morphological findings of the ipsilateral testis from IRI + EGCG (50 mg/kg, i.p.) group.

Table 1
Mean morphological damage assessed by Johnsen's scoring system.

Animal groups	Ipsilateral testes	Contralateral testes
Sham	9.375 ± 0.125	9.438 ± 0.063
IRI + vehicle	6.875 ± 0.375*	9.313 ± 0.120
IRI + EGCG	8.313 ± 0.120**	9.375 ± 0.125

* $p < 0.001$ injured + saline group compared to sham and injured + EGCG groups and all the contralateral testes; as analyzed by ANOVA followed by Bonferroni and LSD post hoc tests.
** $p < 0.03$ EGCG-treated group III compared to group I and all the contralateral testes; as analyzed by ANOVA followed by Bonferroni and LSD post hoc tests.

4 h after the repair of torsion in the IRI + vehicle group showed significantly increased number of GCA due to DNA damage (28 ± 2.5, $p \leqslant 0.05$) and the seminiferous epithelium were most sensitive to induction of apoptosis (Fig. 2B). Upon EGCG treatment, a significant decrease in GCA was observed (2.8 ± 0.46, $p \leqslant 0.05$) (Fig. 2C) in comparison to IRI + vehicle group and similar to sham levels (Fig. 2D).

3.3. Levels of inflammation markers

Testicular concentration of TNF-α, IL-1β and IL-6 were evaluated in the three experimental groups using ELISA (Table 2). In the IRI + vehicle animals, the levels of TNF-α, IL-1β and IL-6 were significantly increased ($p = 0.0084$, 0.0032 and 0.0179, respectively). Rats injected with EGCG pre-reperfusion showed reduced levels of the three cytokines that were similar to sham levels.

3.4. Expression of apoptosis and inflammation genes

In the ipsilateral testes, a significant increase in the mRNA expression of the pro-apoptosis genes p53 and Bax was obtained after IRI (6.2 ± 0.75, $p \leqslant 0.001$ and 5.37 ± 1.03, $p \leqslant 0.001$, respectively), which was normalized upon EGCG treatment (Fig. 3). On the other hand, the expression of the anti-apoptosis genes Bcl-2 and survivin was not significantly changed by the IRI + vehicle (1.39 ± 0.38, $p > 0.05$ and 0.85 ± 0.15, $p > 0.05$, respectively) or by the IRI + EGCG treatment. Calculation of Bax to Bcl-2 ratio resulted in a 3.86 value, which is considered as positive indicator for the induction of apoptosis. There was a trend toward an increased mRNA expression of the inflammatory markers iNOS and MCP-1 (4.5 ± 0.95, $p \leqslant 0.001$ and 9.28 ± 1.05, $p \leqslant 0.001$, respectively) as a result of IRI. EGCG treatment prior to reperfusion was able to reverse the inflammatory response and decreased the mRNA expression of iNOS and MCP-1 to sham levels.

Table 2
Effect of *in vivo* treatment with EGCG on testicular cytokine levels in rats subjected to unilateral testicular ischemia and reperfusion injury (IRI).

Animal groups	Sham	IRI + vehicle	IRI + EGCG
TNF-α – C	3921 ± 515	4045 ± 341	3800 ± 718
TNF-α – I	3399 ± 329	5675 ± 394[a]	3503 ± 444
IL-6 – C	1988 ± 121	1239 ± 148	1262 ± 145
IL-6 – I	1258 ± 497	3788 ± 386[b]	1438 ± 661
IL-1β – C	4509 ± 349	4883 ± 271	4766 ± 513
IL-1β – I	4533 ± 254	6324 ± 489[c]	4936 ± 266

Cytokine levels are measured as pg/mg tissue. Data are given as mean ± SEM. C = Contralateral and I = Ipsilateral. [a,b,c] Represent p values of 0.0084, 0.0032, 0.0179 in comparison to the sham group. Significant correlation was calculated by ANOVA followed by the Kruskal–Wallis test.

4. Discussion

Testicular torsion can either occur due to a trauma to the testicles, like an accident, or as in most cases happen for no apparent

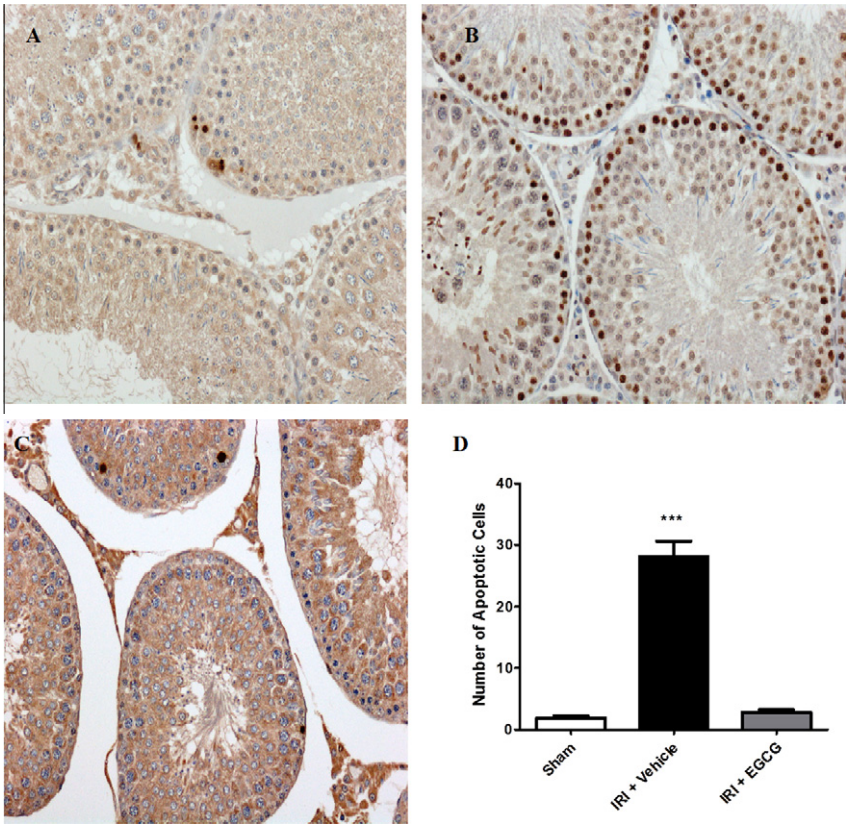

Fig. 2. TUNEL assay analysis for the detection of germ cell apoptosis. IRI + vehicle group (B) displayed a significant increase in germ cell apoptosis in comparison to sham (A) and IRI + EGCG animal group (C) after 4 h of reperfusion of the ipsilateral testes. Bars (D) represent the mean of the results from 6 animals per group ± SEM; *** denotes statistical significance ($p \leqslant 0.0001$).

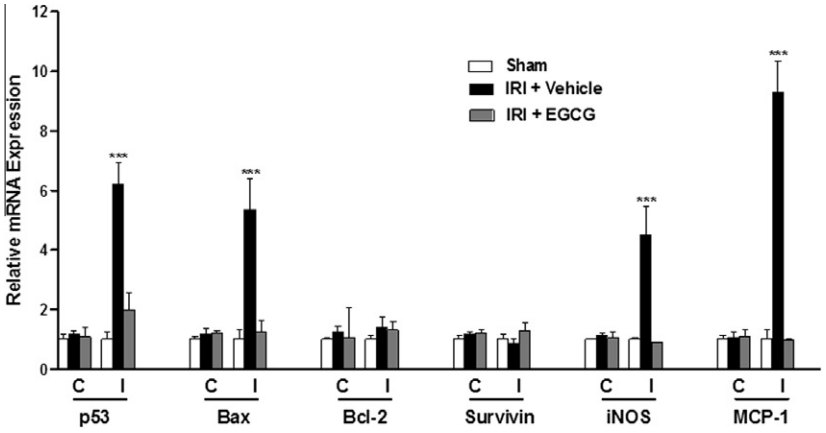

Fig. 3. Gene expression measurement using real-time PCR analysis. Real-time PCR was performed on RNA purified from testicular tissue using Taqman assays for the following genes: Bax, p53, survivin, Bcl-2, MCP-1 and iNOS. Relative mRNA expression was calculated using the $2^{-\Delta\Delta CT}$ method. The expression ratios of the target mRNA against the level of β-actin mRNA are given as bar graphs. The results are representative of reactions run in duplicates on 6 animals per group. *** indicates statistical significance ($p \leqslant 0.001$).

reason. The underlying mechanism of TT is an IRI to the testes, which leads to production of reactive oxygen species, stimulation and secretion of pro-inflammatory cytokines, generation of ROS, apoptosis, testicular atrophy and consequent decrease in spermatogenesis [22,23]. Although the underlying mechanism of GCA in TT is not fully understood, activation of caspases 2 and 3 was demonstrated in both rat and mice models of TT [24,25]. Also, the up-regulation and re-localization of the pro-apoptosis molecule Bax was associated with TT-induced IRI in several studies [26,27]. In our study, the IRI + vehicle showed increased Bax to Bcl-2 ratio suggested a favorable shift toward apoptosis onset and subsequent damage to spermatogenesis. Also, enhanced p53 expression and a positive TUNEL assay indicated the presence of cellular DNA damage. Acute treatment of EGCG prior to testes resulted in a protective effect on the negative outcome of the TT-induced IRI.

Another factor that is also known to induce apoptosis during TT is the stimulation of an inflammatory response. It has been reported that during testes reperfusion, neutrophils and macrophages release free radicals and pro-inflammatory cytokines that can induce apoptosis and thus act as mediators of testicular injury [24,28]. Enhanced expression of TNF-α and IL-1β has been shown after IRI in testicular cells, activated interstitial macrophages [29,30] as well as in other cell types [31]. Furthermore, both cytokines are important regulators of other cytokines, chemokines, adhesion molecules, growth factors and inducible enzymes. IL-6, an acute phase reactant, enhances monocytes and macrophages functions after stimulation. But it also has a modulatory effect on the TNF-α and IL-1β production [32]. There is also evidence that TNF-α and IL-1β can stimulate the expression of the adhesion molecule E-selectin through an NFκB nuclear localization pathway or phosphorylation of JNK [33]. However, the details and order of events of this mechanism is not yet fully elucidated. Another adhesion molecule, MCP-1, was also found to be highly expressed in inflamed rat testes prior to a large invasion of monocytes into the testicular interstitial tissue suggesting a regulatory role of MCP-1 during testes inflammation [15]. Recent studies indicate that the up-regulation of MCP-1 is, in part, regulated by the cytokines TNF-α and IL-1β [34]. Our results are in agreement with the current published reports whereby TNF-α, IL-1β, IL-6 and MCP-1 expression is elevated after IRI of the testis. This enhanced expression was abolished upon EGCG treatment.

NO is a powerful biologic molecule that functions at low concentrations as a signal in many physiologic processes, however at high concentrations could cause DNA damage and cell death [10,35]. During development, NO plays an important function in the conversion of stem cells to spermatozoa and plays a regulatory role within Sertoli cells, pachytene spermatocytes and elongating spermatids [14]. NO is produced by the enzyme iNOS, which has been implicated in the pathogenesis of IRI, and the inhibition of its activity and consequent NO production could offset IRI [4,36,37]. The over expression of iNOS is controlled at the transcriptional level that is induced by various cytokines. Toxic levels of NO due to the overexpression of iNOS were reported in apoptotic germ cells of mice testis [9]. Similarly, we found significant elevations in iNOS mRNA expression after testicular IRI, which correlates with previous studies. Interestingly, iNOS transcriptional up-regulation was suppressed by EGCG treatment. Based on these findings we report for the first time the protective effects of EGCG from the dire consequences of TT-induced-IRI due to its anti-inflammatory and anti-apoptotic properties.

In conclusion, the protective effects of EGCG reported in this study are of clinical importance to patients with testicular torsion. An adjunct interventional use of EGCG prior to testicular detorsion surgery could prevent the destructive effects of TT-induced IRI and possible future infertility problems or removal of damaged testis.

Acknowledgments

This work was supported by Kuwait University Research Grant MB 01/05. The authors would like to acknowledge the following: Ms. Shabeeba Pattillath, Mrs. Preethi George and Mr. Saju Jacob for their excellent technical support.

References

[1] R.T. Ellati, P.K. Kavoussi, T.T. Turner, J.J. Lysiak, Twist and Shout: a clinical and experimental review of testicular torsion, Korean J. Urol. 50 (2009) 1159–1167.
[2] F. Lopez-Neblina, A.H. Toledo, L.H. Toledo-Pereyra, Molecular biology of apoptosis in ischemia and reperfusion, J. Invest. Surg. 18 (2005) 335–350.
[3] P.F. Li, R. Dietz, R. von Harsdorf, P53 regulates mitochondrial membrane potential through reactive oxygen species and induces cytochrome c-independent apoptosis blocked by Bcl-2, EMBO J. 18 (1999) 6027–6036.
[4] F. Taneli, S. Vatansever, C. Ulman, et al., The effect of spermatic vessel ligation on testicular nitric oxide levels and germ cell-specific apoptosis in rat testis, Acta Histochem. 106 (2005) 459–466.
[5] F. Bauche, J.P. Stephan, A.M. Touzalin, B. Jegou, In vitro regulation of an inducible-type NO synthase in the rat seminiferous tubule cells, Biol. Reprod. 58 (1998) 431–438.
[6] C.A. Dinarello, Biological basis for interleukin-1 in disease, Blood 87 (1996) 2095–2147.
[7] E. Stylianou, J. Saklatvala, Interleukin-1, Int. J. Biochem. Cell. Biol. 30 (2000) 1075–1079.

[8] R. Middendorff, D. Muller, S. Wichers, A.F. Holstein, M.S. Davidoff, Evidence for production and functional activity of nitric oxide in seminiferous tubules and blood vessels of the human testis, J. Clin. Endocrinol. Metab. 82 (1997) 4154–4161.
[9] M.K. O'Bryan, S. Schlatt, O. Gerdprasert, et al., Inducible nitric oxide synthase in the rat testis: evidence for potential roles in both normal function and inflammation-mediated infertility, Biol. Reprod. 63 (2000) 1285–1293.
[10] P. Pagliaro, Differential biological effects of products of nitric oxide (NO) synthase: it is not enough to say NO, Life Sci. 73 (2003) 2137–2149.
[11] D.J. Stuehr, Structure-function aspects in the nitric oxide synthases, Ann. Rev. Pharmacol. Toxicol. 37 (1997) 339–359.
[12] Y. Lue, A.P. Sinha Hikim, C. Wang, et al., Functional role of inducible nitric oxide synthase in the induction of male germ cell apoptosis, regulation of sperm number, and determination of testes size: evidence from null mutant mice, Endocrinology 144 (2003) 3092–3100.
[13] D.M. de Kretser, K.L. Loveland, A. Meinhardt, et al., Spermatogenesis, Hum. Reprod. 13 (1998) 1–8.
[14] A. Desai, M.J. Miller, X. Huang, J.S. Warren, Nitric oxide modulates MCP-1 expression in endothelial cells: implications for the pathogenesis of pulmonary granulomatous vasculitis, Inflammation 27 (2003) 213–223.
[15] O. Gerdprasert, M.K. O'Bryan, D.J. Nikolic-Paterson, et al., Expression of monocyte chemoattractant protein-1 and macrophage colony-stimulating factor in normal and inflamed rat testis, Mol. Hum. Reprod. 8 (2002) 518–524.
[16] J.V. Higdon, B. Frei, Tea catechins and polyphenols: health effects, metabolism, and antioxidant functions, Crit. Rev. Food Sci. Nutr. 43 (2003) 89–143.
[17] B.N. Singh, S. Shankar, R.K. Srivastava, Green tea catechin, epigallocatechin-3-gallate (EGCG): mechanisms, perspectives and clinical applications, Biochem. Pharmacol. 82 (2011) 1807–1821.
[18] P.A. Townsend, T.M. Scarabelli, E. Pasini, et al., Epigallocatechin-3-gallate inhibits STAT-1 activation and protects cardiac myocytes from ischemia/reperfusion-induced apoptosis, FASEB J. 18 (2004) 1621–1623.
[19] M. Al-Maghrebi, E.O. Kehinde, J.T. Anim, Long term testicular ischemia–reperfusion injury-induced apoptosis: involvement of survivin down-regulation, Biochem. Biophys. Res. Commun. 395 (2010) 342–347.
[20] S.G. Johnsen, Testicular biopsy score count – a method for registration of spermatogenesis in human testes: normal values and results of 335 hypogonadal males, Hormones 1 (1970) 2–25.
[21] K.J. Livak, T.D. Schmittgen, Analysis of relative gene expression data using real-time quantitative PCR and the 2(−Delta Delta C(T)) Method, Methods 25 (2001) 402–408.
[22] D.W. Filho, M.A. Torres, A.L. Bordin, et al., Spermatic cord torsion, reactive oxygen and nitrogen species and ischemia-reperfusion injury, Mol. Aspects Med. 25 (2004) 199–210.
[23] J.J. Lysiak, The role of tumor necrosis factor-alpha and interleukin-1 in the mammalian testis and their involvement in testicular torsion and autoimmune orchitis, Reprod. Biol. Endocrinol. 10 (2004) 9–19.
[24] S. Zheng, T.T. Turner, J.J. Lysiak, Caspase 2 activity contributes to the initial wave of germ cell apoptosis during the first round of spermatogenesis, Biol. Reprod. 74 (2006) 1026–1033.
[25] N. Yazihan, H. Ataoglu, N. Koku, et al., Protective role of erythropoietin during testicular torsion of the rats, World J. Urol. 25 (2007) 531–536.
[26] J.J. Lysiak, S.D. Turner, T.T. Turner, Molecular pathway of germ cell apoptosis following ischemia/reperfusion of the rat testis, Biol. Reprod. 63 (2000) 1465–1472.
[27] J.J. Lysiak, S. Zheng, R. Woodson, T.T. Turner, Caspase-9-dependent pathway to murine germ cell apoptosis: mediation by oxidative stress, BAX, and caspase 2, Cell Tissue Res. 328 (2007) 411–419.
[28] M.S. Theas, C. Rival, S. Jarazo-Dietrich, et al., Tumour necrosis factor-alpha released by testicular macrophages induces apoptosis of germ cells in autoimmune orchitis, Hum. Reprod. 23 (2008) 1865–1872.
[29] R. Grataroli, D. Vindrieux, A. Gougeon, M. Benahmed, Expression of tumor necrosis factor-alpha-related apoptosis inducing ligand and its receptors in rat testis during development, Biol. Reprod. 66 (2002) 1707–1715.
[30] C. Rival, M.S. Theas, V.A. Guazzone, L. Lustig, Interleukin-6 and IL-6 receptor cell expression in testis of rats with autoimmune orchitis, J. Reprod. Immunol. 70 (2006) 43–58.
[31] M. Guha, W. Bai, J.L. Nadler, R. Natarajan, Molecular mechanisms of tumor necrosis factor alpha gene expression in monocytic cells via hyperglycemia-induced oxidant stress dependent and -independent pathways, J. Biol. Chem. 275 (2000) 17728–17739.
[32] C. Zoja, J.M. Wang, S. Bettoni, et al., Interleukin-1 beta and tumor necrosis factor-alpha induce gene expression and production of leukocyte chemotactic factors, colony-stimulating factors, and interleukin-6 in human mesangial cells, Am. J. Pathol. 138 (1991) 991–1003.
[33] M.A. Read, M.Z. Whitley, S. Gupta, et al., Tumor necrosis factor alpha-induced E-selectin expression is activated by the nuclear factor-kappaB and c-JUN N-terminal kinase/p38 mitogen-activated protein kinase pathways, J. Biol. Chem. 272 (1997) 2753–2761.
[34] C.M. Flory, M.L. Jones, B.F. Miller, J.S. Warren, Regulatory roles of tumor necrosis factor-1alpha and interleukin-1beta in monocyte chemoattractant protein-1-mediated pulmonary granuloma formation in the rat, Am. J. Pathol. 146 (1995) 450–462.
[35] A. Zini, J. Abitbol, S.K. Girardi, et al., Germ cell apoptosis and endothelial nitric oxide synthase (eNOS) expression following ischemia-reperfusion injury to testis, Arch. Androl. 41 (1998) 57–65.
[36] H. Ozturk, H. Buyukbayram, E. Ozdemir, et al., The effects of nitric oxide on the expression of cell adhesion molecules (ICAM-1, UEA-1, and tenascin) in rats with unilateral testicular torsion, J. Pediatr. Surg. 38 (2003) 1621–1627.
[37] Y. Suzuki, E.D. Deitch, S. Mishima, et al., Inducible nitric oxide synthase gene knockout mice have increased resistance to gut injury and bacterial translocation after an intestinal ischemia-reperfusion injury, Crit. Care Med. 28 (2000) 3692–3696.

Biochemical and Biophysical Research Communications 420 (2012) 440–443

Contents lists available at SciVerse ScienceDirect

Biochemical and Biophysical Research Communications

journal homepage: www.elsevier.com/locate/ybbrc

Inhibitory RNA aptamer against SP6 RNA polymerase

Yusuke Mori, Yoshikazu Nakamura, Shoji Ohuchi *

Department of Basic Medical Sciences, Institute of Medical Science, University of Tokyo, 4-6-1 Shirokanedai, Minato-ku, Tokyo 108-8639, Japan

ARTICLE INFO

Article history:
Received 28 February 2012
Available online 9 March 2012

Keywords:
RNA aptamer
SP6 RNA polymerase
SELEX

ABSTRACT

Aptamers are attractive tools for modulating function of a desired target. In this study, we isolated an RNA aptamer that specifically inhibits transcription of SP6 RNA polymerase. The dissociation constant and 50% inhibitory concentration of the aptamer were estimated 9.5 nM and 24.8 nM, respectively. Doped-SELEX and mutational analysis revealed that the aptamer adopts the structure including two stems, two loops, and 5′ single-stranded region. Based on the results, the aptamer could be engineered to circular permutant and binary construct forms without decreasing the activity. The aptamer would be applicable for the construction of expression regulation systems.

1. Introduction

Since the proposal of the central dogma of molecular biology, the importance of RNAs' functions has been recognized, and at present, a wide variety of dynamic roles of RNAs for intracellular events are known [1]. Moreover, functional RNAs has been engineered to manipulate cellular behaviors [2–4]. Compared with proteins, functional RNAs have several attractive features. For example, guide RNAs, similar to short interference RNA, can be designed simply based on base-pairing formations. Concerning structural RNAs, the modular property and the predictability of their two dimensional (2D) architecture enable rational engineering of them. Furthermore, it is also possible to generate novel, artificial RNAs with desired binding or catalytic properties employing an *in vitro* methodology [5,6].

RNA aptamers are such artificial RNAs selected *in vitro* from a large random sequence library based on their high affinity to a target molecule by a process known as SELEX (systematic evolution of ligands by exponential enrichment) [7–11]. Since the establishment of the procedure, a wide variety of aptamers have been generated, and their applications have been extensively studied [9–11].

In this study, we isolated an inhibitory RNA aptamer against SP6 RNA polymerase (RNAP). SP6 RNAP is one of the most commonly used enzymes for *in vitro* transcription [12–14]. In addition, applicability of the RNAP for *in vivo* expression is also demonstrated [15–18]. Thus, the specific inhibitor against SP6 RNAP would be applicable for the construction of a novel regulation system of gene expression.

Abbreviations: RNAP, RNA polymerase; SELEX, systematic evolution of ligands by exponential enrichment.

* Corresponding author. Fax: +81 3 5449 5415.
E-mail address: sohuchi@ims.u-tokyo.ac.jp (S. Ohuchi).

0006-291X/$ - see front matter © 2012 Elsevier Inc. All rights reserved.
http://dx.doi.org/10.1016/j.bbrc.2012.03.014

2. Materials and methods

2.1. RNAP preparations

SP6 RNAP coding sequence was amplified from a plasmid pACSP6R (kind gift from Prof. Changwon Kang of Korea Advanced Institute of Science and Technology) [17,18] by PCR using KOD-Plus-DNA polymerase (Toyobo, Japan) with following primers; 5′-AGCGGATCCA TGCAAGATTT ACACGC-3′ (*Bam*HI restriction site is underlined) and 5′-AGCCTGCAGT TAGGCAAATA CGTATTC-3′ (*Pst*I restriction site is underlined). Otherwise mentioned, all synthetic DNAs were purchased from Operon Biotechnologies (Japan). The amplified fragment was digested by *Bam*HI and *Pst*I, cloned into *Bam*HI/*Pst*I site of an expression vector, pQE-80 (Qiagen). Employing the resulting plasmid, pQE-SP6R, recombinant hexa-histidine-tagged SP6 RNAP was expressed in *Escherichia coli* BL21 (DE3) (Novagen). The protein was purified from the crude cell lysate using HisLink Protein Purification Resin (Promega), followed by ion exchange chromatography using HiTrap CM FF (GE Healthcare) and HiTrap DEAE (GE Healthcare). The recovered fractions containing the protein were dialyzed against buffer D (50 mM Tris–HCl, pH 7.6, 1 M NaCl, 10 mM 2-mercaptoethanol, 10% glycerol) at 4 °C overnight and stored at −20 °C until use.

Recombinant hexa-histidine-tagged T7 RNAP was expressed employing an expression plasmid, pQE-T7R (kind gift from Prof. Tsutomu Suzuki of University of Tokyo, Japan), and purified as described above.

2.2. SELEX

SELEX against SP6 RNAP was performed essentially as described [19] employing the following synthetic DNA as an initial DNA pool;

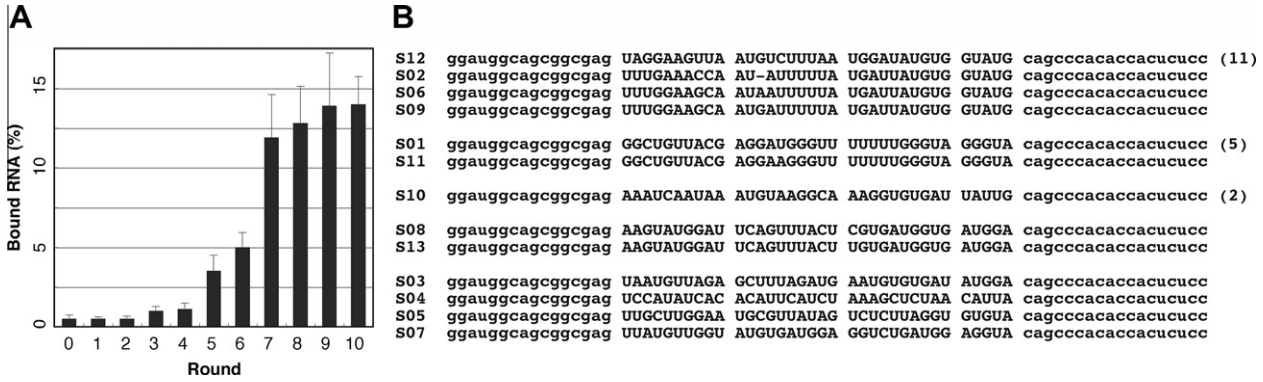

Fig. 1. Progress of SELEX against SP6 RNAP. (A) Affinity enrichment during SELEX. Binding activity of the pool RNA after each round was evaluated by filter-binding assay. Two independent duplicate experiments were performed employing SP6 RNAP (at a final concentration of 10 nM). Error bars indicate standard deviation. (B) Sequences of clones isolated after 10 rounds of SELEX. The numbers in parentheses indicate the frequency with which the sequence was selected. The primer regions are indicated in lowercase letters.

5′-TAATACGACT CACTATAGGA TGGCAGCGGA GAG-N35-CAGCCCA CAC CACTCTCC-3′ (T7 promoter sequence is underlined, and N35 represents 35-nucleotides [nts] of random sequence). The detailed conditions of SELEX are described in Supplemental Table 1.

For the doped-SELEX, the following synthetic DNA (purchased from Gene Design Inc., Japan) was employed as an initial DNA pool; 5′-TAATACGACT CACTATAGCC CCAGGGATGG GGAAAAggat ggcag cggag agttgcttgg aatgcgttat agtctcttag gtgtgtacag cccacaccac tct ccAAAAC TCGGCATCCG TGCCGAG-3′ (uppercase and underlined letters indicate primer binding sites and T7 promoter sequence, respectively. Positions indicated by lowercase letters were 8.1%-doped, that is, mixture of 91.9% of a base identical to that of the parental S05 sequence and 3 × 2.7% of other bases).

2.3. Transcription inhibition assay

For the construction of template DNA for *in vitro* transcription by SP6 RNAP, the DNA fragment between nucleotides 289–486 of plasmid pEGFP (Clontech) was amplified by PCR employing KOD-Plus-DNA polymerase with following primers; 5′-AATTTAGGTG ACACTATAGA GATGGTGAGC AAGGGCGAGG AGC-3′ (SP6 promoter sequence is underlined) and 5′-GGTCAGGGT GGTCACGAGG GTGGG-3′. The amplified fragment was cloned into *Sma*I site of pUC19, re-amplified by PCR, purified by phenol/chloroform extraction and ultrafiltration with Microcon YM-30 (Millipore).

Before the transcription reaction, 2 nM SP6 RNAP was incubated with 50 nM of above template DNA and indicated concentration of the RNA at 37 °C in buffer R [40 mM Tris–HCl, pH 7.6, 6 mM $MgCl_2$, 2 mM spermidine, 10 mM DTT, 0.01% BSA, 0.1 U/μL RNase inhibitor (Takara Bio, Japan)] for 10 min. The reaction was started by adding 0.25 mM of each rNTPs and 0.5–2 μCi/μL [alpha-^{32}P]-GTP (Perkin-Elmer), carried out at 37 °C for 30 min, and stopped by adding equal volume of the stop solution (95% formamide, 20 mM EDTA). The transcript was separated by 6% PAGE containing 8 M urea and quantified by FLA-5100 (Fujifilm Life Science). The 50% inhibitory concentration (IC_{50}) was estimated by curve fitting using Gnuplot 4.5.0 (http://www.gnuplot.info/).

2.4. Filter-binding assay

The filter-binding assay was performed essentially as described [19]. Indicated amounts of SP6 RNAP and [^{32}P]-labeled RNAs were mixed in buffer R, incubated for 20 min at 37 °C, and chilled on ice. The mixture was filtered through a pre-soaked MF-Millipore Membrane Filter (Millipore; HAWP02500) placed in a vacuum manifold, and the filter was washed once with 1 ml of RNase inhibitor-free buffer R. Radioactivity retained on the filter was measured by Cerenkov counting using a scintillation counter. The dissociation constant (K_D) was estimated by curve fitting using Gnuplot 4.5.0.

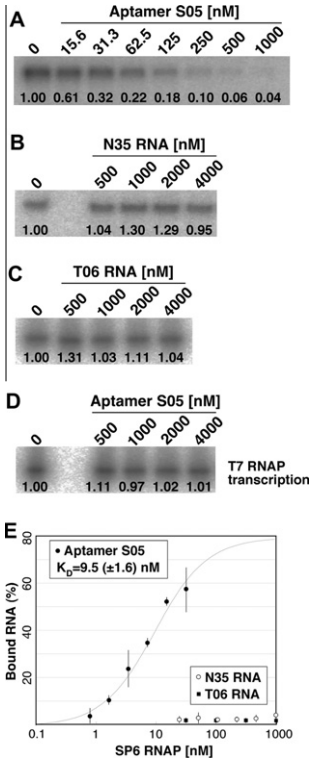

Fig. 2. Inhibitory activity of aptamer S05. *In vitro* transcription was carried out in the presence of indicated concentrations of the RNA. (A) Transcription by SP6 RNAP in the presence of aptamer S05. (B) Transcription by SP6 RNAP in the presence of N35 RNA. (C) Transcription by SP6 RNAP in the presence of T06 RNA. (D) Transcription by T7 RNAP in the presence of aptamer S05. Value under each lane of the gel images indicates the relative amount of transcript compared with that of the reaction in the absence of RNA. Two independent duplicate experiments were performed and the mean values are shown. (E) Estimation of dissociation constant (K_D) by filter-binding assay. The estimated K_D for aptamer S05 and SP6 RNAP was 9.5 nM. Two independent duplicate experiments were performed. Error bars indicate standard deviation.

3. Results and discussion

To generate a specific inhibitor to SP6 RNAP, we intended to isolate inhibitory RNA aptamers against the RNAP. SELEX was carried

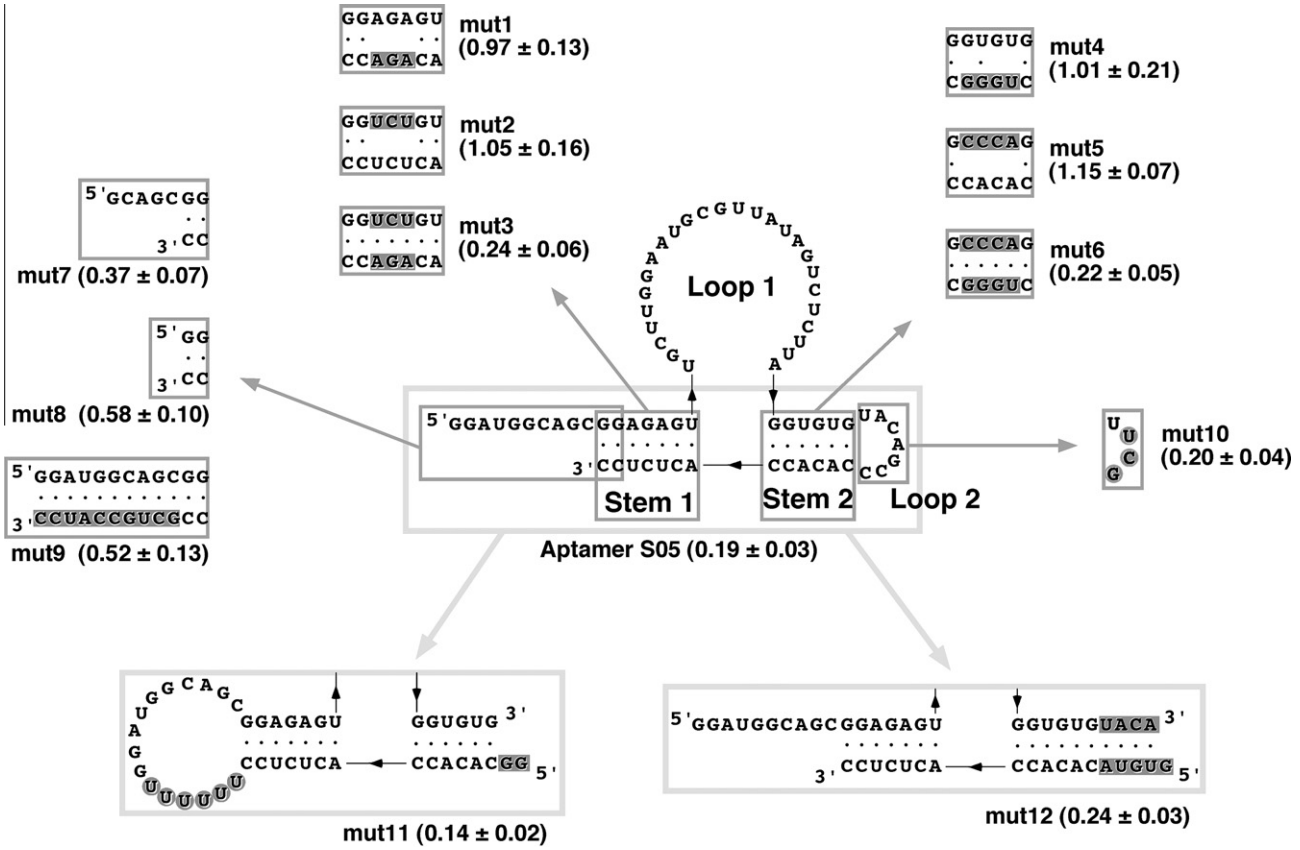

Fig. 3. Mutational analysis of aptamer S05. The two dimensional structure of aptamer S05 is shown at the center. Dots and black arrows indicate base-pairings and 5′-to-3′ orientations, respectively. The mutated regions and mutants are shown in gray squares at arrow roots and tips, respectively. The altered bases are emphasized by gray shadows. Values in the parentheses indicate the relative transcript amounts in the presence of 100 nM RNA.

out against hexa-histidine-tagged SP6 RNAP using an initial pool containing 3×10^{14} variants of 69-nt RNA with 35-nt random sequences.

After 3 rounds of SELEX, slight increase of the pool RNA affinity against SP6 RNAP was observed (Fig. 1A). The pool affinity was progressively enriched, and after 10 rounds, the enrichment reached a plateau. Thus, the variants of the pool were cloned and sequenced. Of 28 clones randomly picked out, 13 independent sequences were isolated. Three sequences appeared multiple times [S12 (eleven), S01 (five), and S10 (twice)], and three (S02, S06, and S09) and one (S11) single-clones showed sequence similarities to S12 and S01, respectively (Fig. 1B). In addition, two single-clones (S08 and S13) had sequences almost identical each other (Fig. 1B).

The isolated 13 independent clones were analyzed for the inhibitory activity against SP6 RNAP, and only one variant, S05, showed strong inhibitory activity. Its IC_{50} (50% inhibitory concentration) value was estimated as 24.8 (±6.7) nM under the typical *in vitro* transcription condition (Fig. 2A). Under this condition, negative control RNAs [the initial pool RNA (N35 RNA) and a 71-nt RNA aptamer (T06 RNA) against T7 RNAP (manuscript in preparation)] showed no apparent inhibition, even when the RNA was added up to 4 μM (Fig. 2B). The dissociation constant (K_D) of aptamer S05 was estimated as 9.5 (±1.6) nM by filer-binding assay, whereas the negative controls showed no apparent binding against SP6 RNAP up to 1 μM (Fig. 2E). As expected from the fact that no reduction was observed on transcription efficiencies by T7 RNAP for the pool RNA preparations during SELEX, aptamer S05 did not inhibit T7 RNAP (31% identical to SP6 RNAP) even at a concentration up to 4 μM, demonstrating the specificity of the aptamer (Fig. 2D).

To elucidate the essential elements of aptamer S05, we first examined several deletions at 5′- or 3′-regions, and found that short deletions reduced the activity (data not shown). Thus, to estimate structure/sequence requirements of aptamer S05 based on artificial phylogeny of the aptamer derivatives, SELEX from an RNA pool of 8.1% mutagenized variants of aptamer S05, or doped-SELEX, was carried out [20]. After 3 rounds of the doped-SELEX, the pool RNA showed the inhibitory activity comparable with that of the parental aptamer (data not shown), and the variants were cloned. Among 45 clones analyzed, 27 clones showed the inhibitory activity comparable with aptamer S05 (Supplemental Fig. 1). According to the prediction by the sequence alignment programs based on consensus 2D structure (MASTR and CMfinder) [21,22], the aptamers adopt the structure including two stems (Stem 1 and Stem 2), two loops (Loop 1 and Loop 2), and 5′ single-stranded (5′ss) region (Fig. 3 and Supplemental Fig. 1). The primary sequence of Loop 1 is highly conserved, whereas that of Loop 2 and 5′ss region are not. The stems are moderately tolerant for mutations, even when the mutations disrupt the base-pairings for some extent (Supplemental Fig. 1).

To confirm the predicted 2D structure, mutational analysis of aptamer S05 was carried out (Fig. 3). When mutations were introduced to disrupt base-pairings of Stem 1 (mut1 and mut2), the activity was significantly reduced. However, the activity was completely retained when the sequence was changed without affecting the base-pairing (mut3). Similar results were obtained for mutations at Stem 2 (mut4, mut5, and mut6). Thus, the secondary structure and not the primary sequence of the stems are important.

With regard to the 5′ss region, four nucleotide truncation of the 9-nt single-stranded fragment (mut7) moderately reduced the activity, and complete deletion (mut8) showed more deleterious effect. Furthermore, addition of an extra 3′ fragment complementary to 5′ss, or change the single-stranded fragment to the extended stem structure (mut9), also showed deleterious effect on the activity. Because the artificial phylogeny indicates that the mutations of 5′ss region are highly bearable (Supplemental Fig. 1), the results suggest that the existence of enough length of single-stranded fragment at 5′ position is required for the full activity in the sequence independent manner.

Finally, Loop 2, the mutation tolerant 7-nt loop, was analyzed. When the loop was replaced with UUCG tetraloop (mut10), no effect on the inhibitory activity was observed. Thus, Loop 2 is likely to have no structural/functional role for the activity.

Based on these results, we designed a Loop 2-lacking derivative by circular permutation (mut11) and found that the variant showed the activity comparable with that of aptamer S05 as intended. Both terminals of the derivative are capped with an extended stem structure to protect the RNA from exonuclease degradation [23], and the aptamer may be efficiently expressed *in vivo*. T7 lysozyme is a specific inhibitor against T7 RNAP, and expression regulation systems employing them are widely used for the production of toxic proteins [24]. The circular permutant aptamer against SP6 RNAP might be used for the similar applications.

We also designed another derivative by dividing aptamer S05 to two fragments (mut12), and the resulting binary aptamer also retained the complete activity. The transcription by SP6 RNAP was suppressed only when both RNA fragments simultaneously existed, and the inhibitory activity could be modulated with an antisense fragment complementary to the aptamer (data not shown). Thus, we expect that the binary aptamer is applicable to the sophisticated design of translation-free, expression regulation systems [25–28].

Acknowledgments

We thank Prof. Changwon Kang of Korea Advanced Institute of Science and Technology and Prof. Tsutomu Suzuki of University of Tokyo (Japan) for providing plasmids, pACSP6R and pQE-T7R, respectively. This work was funded by Grant-in-Aid for Young Scientists (B) from The Ministry of Education, Sports, Culture, Science and Technology of Japan (MEXT) (to S.O.); Core Research for Evolution Science and Technology (CREST) grant from the Japan Science and Technology Agency (to Y.N.), research grants from MEXT (to Y.N.) and The Ministry of Health, Labour and Welfare (to Y.N.).

Appendix A. Supplementary data

Supplementary data associated with this article can be found, in the online version, at http://dx.doi.org/10.1016/j.bbrc.2012.03.014.

References

[1] J.F. Atkins, R.F. Gesteland, T.R. Cech, The RNA Worlds: From Life's Origins to Diversity in Gene Regulation, Cold Spring Harbor Laboratory Press, New York, 2010.
[2] J.C. Liang, R.J. Bloom, C.D. Smolke, Engineering biological systems with synthetic RNA molecules, Mol. Cell. 43 (2011) 915–926.
[3] F.J. Isaacs, D.J. Dwyer, J.J. Collins, RNA synthetic biology, Nature Biotechnol. 24 (2006) 545–554.
[4] H. Saito, T. Inoue, Synthetic biology with RNA motifs, Int. J. Biochem. Cell Biol. 41 (2009) 398–404.
[5] A.D. Ellington, X. Chen, M. Robertson, A. Syrett, Evolutionary origins and directed evolution of RNA, Int. J. Biochem. Cell Biol. 41 (2009) 254–265.
[6] G.F. Joyce, Forty years of in vitro evolution, Angew. Chem. Int. Ed. Engl. 46 (2007) 6420–6436.
[7] A. Ellington, J.W. Szostak, In vitro selection of RNA molecules that bind specific ligands, Nature 346 (1990) 818–822.
[8] C. Tuerk, L. Gold, Systematic evolution of ligands by exponential enrichment: RNA ligands to bacteriophage T4 DNA polymerase, Science 249 (1990) 505–510.
[9] S. Klussmann, The Aptamer Handbook: Functional Oligonucleotides and Their Applications, Wiley-VCH, Weinheim, 2006.
[10] R. Stoltenburg, C. Reinemann, B. Strehlitz, SELEX–a (r)evolutionary method to generate high-affinity nucleic acid ligands, Biomol. Eng. 24 (2007) 381–403.
[11] J.L. Vinkenborg, N. Karnowski, M. Famulok, Aptamers for allosteric regulation, Nature Chem. Biol. 7 (2011) 519–527.
[12] P.A. Krieg, D.A. Melton, In vitro RNA synthesis with SP6 RNA polymerase, Methods Enzymol. 155 (1987) 397–415.
[13] B.M. Paschal, L.A. McReynolds, C.J. Noren, N.M. Nichols, RNA polymerases, Curr. Protoc. Mol. Biol. 84 (2008) 3.8.1–3.8.8.
[14] V.V. Gurevich, Use of bacteriophage RNA polymerase in RNA synthesis, Methods Enzymol. 275 (1996) 382–397.
[15] T.B. Usdin, M.J. Brownstein, B. Moss, S.N. Isaacs, SP6 RNA polymerase containing vaccinia virus for rapid expression of cloned genes in tissue culture, Biotechniques 14 (1993) 222–224.
[16] H. Sagawa, A. Ohshima, I. Kato, A tightly regulated expression system in *Escherichia coli* with SP6 RNA polymerase, Gene 168 (1996) 37–41.
[17] W. Jeong, C. Kang, The histidine-805 in motif-C of the phage SP6 RNA polymerase is essential for its activity as revealed by random mutagenesis, Biochem. Mol. Biol. Int. 42 (1997) 711–716.
[18] I. Shin, C. Kang, Mutational analysis and structure of the phage SP6 promoter, Methods Enzymol. 370 (2003) 658–668.
[19] A. Oguro, T. Ohtsu, Y.V. Svitkin, N. Sonenberg, Y. Nakamura, RNA aptamers to initiation factor 4A helicase hinder cap-dependent translation by blocking ATP hydrolysis, RNA 9 (2003) 394–407.
[20] E.H. Ekland, D.P. Bartel, The secondary structure and sequence optimization of an RNA ligase ribozyme, Nucleic Acids Res. 23 (1995) 3231–3238.
[21] S. Lindgreen, P. Gardner, A. Krogh, MASTR: Multiple alignment and structure prediction of non-coding RNAs using simulated annealing, Bioinformatics 23 (2007) 3304–3311.
[22] Z. Yao, Z. Weinberg, W.L. Ruzzo, CMfinder—a covariance model based RNA motif finding algorithm, Bioinformatics 22 (2006) 445–452.
[23] N. Nakashima, T. Tamura, L. Good, Paired termini stabilize antisense RNAs and enhance conditional gene silencing in *Escherichia coli*, Nucleic Acids Res. 34 (2006) e138.
[24] F.W. Studier, Use of bacteriophage T7 lysozyme to improve an inducible T7 expression system, J. Mol. Biol. 219 (1991) 37–44.
[25] S. Ayukawa, M. Takinoue, D. Kiga, RTRACS: a modularized RNA-dependent RNA transcription system with high programmability, Acc. Chem. Res. 44 (2011) 1369–1379.
[26] J. Kim, K.S. White, E. Winfree, Construction of an in vitro bistable circuit from synthetic transcriptional switches, Mol. Syst. Biol. 2 (2006) 68.
[27] J. Kim, E. Winfree, Synthetic in vitro transcriptional oscillators, Mol. Syst. Biol. 7 (2011) 465.
[28] E. Franco, E. Friedrichs, J. Kim, R. Jungmann, R. Murray, E. Winfree, F.C. Simmel, Timing molecular motion and production with a synthetic transcriptional clock, Proc. Natl. Acad. Sci. USA 108 (2011) E784–E793.

Biochemical and Biophysical Research Communications 420 (2012) 444–449

Contents lists available at SciVerse ScienceDirect

Biochemical and Biophysical Research Communications

journal homepage: www.elsevier.com/locate/ybbrc

Effects of β-(1,3–1,6)-D-glucan on irritable bowel syndrome-related colonic hypersensitivity

Teita Asano [a], Ken-ichiro Tanaka [b], Shintaro Suemasu [a], Tomoaki Ishihara [a], Kayoko Tahara [a], Toshio Suzuki [c], Hidekazu Suzuki [d], Shin Fukudo [e], Tohru Mizushima [a,b,*]

[a] Department of Analytical Chemistry, Faculty of Pharmacy, Keio University, Tokyo 105-8512, Japan
[b] Graduate School of Medical and Pharmaceutical Sciences, Kumamoto University, Kumamoto 862-0973, Japan
[c] Research and Development, Daiso Co., Ltd., Amagasaki 660-0842, Japan
[d] Division of Gastroenterology and Hepatology, Department of Internal Medicine, Keio University School of Medicine, Tokyo 160-8582, Japan
[e] Department of Behavioral Medicine, Tohoku University Graduate School of Medicine, Sendai 980-8575, Japan

ARTICLE INFO

Article history:
Received 29 February 2012
Available online 10 March 2012

Keywords:
Irritable bowel syndrome
Fecal pellet output
Visceral pain response
β-Glucan

ABSTRACT

Irritable bowel syndrome (IBS) is a gastrointestinal disorder characterized by chronic abdominal pain associated with altered bowel habits. Since the prevalence of IBS is very high and thus, involves elevated health-care costs, treatment of this condition by methods other than prescribed medicines could be beneficial. β-(1,3)-D-glucan with β-(1,6) branches (β-glucan) has been used as a nutritional supplement for many years. In this study, we examined the effect of β-glucan on fecal pellet output and visceral pain response in animal models of IBS. Oral administration of β-glucan suppressed the restraint stress- or drug-induced fecal pellet output. β-Glucan also suppressed the visceral pain response to colorectal distension. These results suggest that β-glucan could be beneficial for the treatment and prevention of IBS.

1. Introduction

IBS is a functional gastrointestinal disorder characterized by chronic and recurrent abdominal pain and discomfort (colonic hypersensitivity) that are associated with altered bowel habits but not with any detectable structural or biochemical abnormality [1,2]. IBS is categorized into subtypes according to the predominant bowel habit: diarrhea-predominant IBS, constipation -predominant IBS, and mixed pattern IBS [1]. In spite of the significant impact that IBS has on patient quality-of-life, currently available clinical treatments for IBS have proved unsatisfactory, mainly due to the difficulty in suppressing the visceral pain associated with IBS.

IBS is one of the most common gastrointestinal disorders, estimated to affect 7–15% of the general population in the USA and 6–12% in Asian countries [2,3]. Considering the health-care costs associated with treating the condition, the identification of effective therapies (such as the taking of supplements) that do not involve prescription drugs is beneficial [4,5].

Although the pathogenesis of IBS is not completely understood, studies have suggested that genetic factors, previous inflammation, mental stressors and microbiota play important roles [6]. A number of animal models for IBS has been established and used to evaluate clinical protocols designed to treat the condition. Mental stressor- or drug-induced alterations in defecation have been used as a model for defecation disorders related to IBS in animals [7–9]. Since hypersensitivity to colorectal distension (CRD) was observed in IBS patients [10], monitoring the electrical activity of the abdominal muscles (visceromotor response) in response to CRD is a standard procedure to detect IBS-related abdominal pain (visceral pain) in animals [11,12]. Furthermore, based on the increased colonic level of butyrate in IBS patients [13,14], butyrate enema-induced hypersensitivity to CRD is also considered as a useful animal model for IBS [15,16].

β-Glucans are naturally-occurring polysaccharides found in the cell walls of yeast, fungi, cereal plants and certain bacteria [17,18]. As suggested by the fact that various foods contain β-glucans, they are known to have few toxic and adverse effects [18]. β-Glucans from mushrooms have been used in Japan as anti-tumor drugs due to their immunostimulating activities [17]. In addition, β-(1,3)-D-glucans with β-(1,6) branches have been reported to have various clinically beneficial effects, such as enhancing the

Abbreviations: AUC, area under the curve; β-glucan, β-(1,3)-D-glucan with β-(1,6) branches; CRD, colorectal distention; 5-HT, 5-hydroxytryptamine hydrochloride; IBS, irritable bowel syndrome; LMW, low-molecular-weight; PBS, phosphate-buffered saline; S.E.M, standard error of the mean.

* Corresponding author at: Department of Analytical Chemistry, Faculty of Pharmacy, Keio University, 1-5-30 Shibakoen, Minato-ku, Tokyo 105-8512, Japan. Fax: +81 3 5400 2628.
E-mail address: mizushima-th@pha.keio.ac.jp (T. Mizushima).

0006-291X/$ - see front matter © 2012 Published by Elsevier Inc.
http://dx.doi.org/10.1016/j.bbrc.2012.03.015

bio-defense activity against bacterial, viral, fungal and parasitic challenge, increasing hematopoiesis and radioprotection, stimulating the wound healing response, and decreasing serum lipid levels [17–20]. Interestingly, it was recently reported that β-glucans suppress inflammatory responses in some animal models [21–26], suggesting that β-glucan could be an interesting immunomodulator, causing opposing effects on different aspects of the immune system.

We succeeded in the purification and industrial-scale production of low-molecular-weight β-(1,3–1,6)-D-glucan from *Aureobasidium pullulans* (*A. pullulans*) GM-NH-1A1 strain (LMW β-glucan) [27,28]. The characteristic features of LMW β-glucan are its low molecular weight (about 100 kDa), low viscosity, high water-solubility and high level of β-(1–6) branching (50–80%) [27,28]. We previously reported that LMW β-glucan has various clinically beneficial effects, such as suppression of the allergic response, suppression of restraint stress-induced immunosuppression and anti-tumor and anti-metastatic actions [27–29]. Moreover, we recently reported that LMW β-glucan protects the gastric mucosa against the formation of irritant-induced lesions by increasing levels of defensive factors such as heat shock protein 70 and gastric mucin [30]. In the present study, we use different animal models for IBS to test the hypothesis that LMW β-glucan could be effective in the treatment of this condition. Our results suggest that the oral administration of LMW β-glucan suppresses not only fecal pellet output but also the visceromotor response to CRD (visceral pain response). These findings suggest that LMW β-glucan could be therapeutically effective for the treatment of IBS.

2. Materials and methods

2.1. Chemicals and animals

LMW β-glucan was prepared from the conditioned culture medium of *A. pullulans* GM-NH-1A1, as described previously [27,28]. Analysis of ^{1}H and ^{13}C NMR spectra and gel-filtration chromatography revealed that the LMW β-glucan contains approximately 70% β-(1–6) branches and an average molecular weight of 100 kDa, as described previously [27,28]. Clonidine hydrochloride and castor oil were from WAKO Pure Chemicals (Osaka, Japan). Sodium butyrate, brewer's yeast and carbamyl- β-methylcholine chloride (bethanecol) were obtained from Sigma (St. Louis, MO). Loperamide hydrochloride and 5-hydroxytryptamine hydrochloride (5-HT) were purchased from Nacalai Tesque (Kyoto, Japan). Wild-type mice (C57/BL6, 6–8 weeks of age) and Wistar rats (4–6 weeks of age) were obtained from Charles River (Yokohama, Japan). Wistar-Imamichi rats (4 weeks of age) were purchased from the Institute for Animal Reproduction (Kasumigaura, Japan). The experiments and procedures described here were carried out in accordance with the Guide for the Care and Use of Laboratory Animals as adopted and promulgated by the National Institutes of Health, and were approved by the Animal Care Committees of Keio University and Kumamoto University.

2.2. Analysis of fecal pellet output in mice

Female mice were subjected to restraint stress by being placed individually into a 50 ml Falcon tube (Becton Dickinson, Franklin Lakes, NJ) for 1 h, as described previously [31]. These tubes are small enough to restrain a mouse so that it is able to breathe but unable to move freely. Control mice were left to move freely in the cage. The number of fecal pellets excreted during the 1-h restraint stress period was measured. β-Glucan was dissolved in phosphate-buffered saline (PBS) and administered orally 2 h before animals were subjected to the restraint stress. Control animals were administered PBS.

In a separate experiment, mice were administered one of different drugs that stimulate intestinal motility (bethanecol and 5-HT), cause diarrhea (castor oil) or cause constipation (loperamide and clonidine). Animals were then placed in a cage and the number or wet weight of fecal pellets excreted in the subsequent 1-, 2- or 24-h period determined. Drugs administered subcutaneously were bethanechol (3 mg/kg) and 5-HT (3 mg/kg), while those administered orally were loperamide (10 mg/kg), clonidine (3.5 mg/kg) and castor oil (300 μl/mouse).

β-Glucan was dissolved in PBS and administered orally 2 h before animals were subjected to the restraint stress or drug-treatment. Control animals were administered PBS.

2.3. Electromyography and CRD

Rats were deeply anaesthetized with pentobarbital sodium (40 mg/kg) and then electromyography electrodes (Star Medical, Tokyo, Japan) sutured into the external oblique muscle of the abdomen for electromyogram recording. Electrode leads were tunneled subcutaneously and exteriorized at the nape of the neck for future access. After surgery, rats were housed individually and allowed to recuperate for 6 days before being used for visceromotor response testing.

Repeated CRD was performed as described previously [32]. Rats were restrained in a plastic conical-shape tube (diameter, 6 cm; height, 15 cm), 15 min before electromyography. To reduce confounding effects due to restraint stress, rats were habituated to the tube 30 min per day for 3 days prior to the experiment. A polyethylene bag (length 2 cm) was inserted in the distal colon, positioned 1 cm proximal to rectum, and connected to a balloon catheter which was anchored with tape to the base of the tail. The pressure and volume of the balloon were controlled and monitored by a pressure controller-timing device (Distender Series II; G & J Electronics, Toronto, Canada), connected to the balloon. Rats were subjected to repeated CRD (80 mm Hg, 30 s, 5-min interstimulus interval, 12 times) on day 7. β-Glucan was given orally once daily for 7 days (from day 0 to day 6).

In separate experiments, CRD associated with the use of butyrate enemas was examined as described previously [15]. Rats were instilled with 1 ml sodium butyrate (110 mg/ml, pH 6.9) or saline into the colon twice daily for 3 days (day 1, 2 and 3). Rats were subjected to CRD (10, 20, 40 60 and 80 mm Hg, 20 s, 150-s interstimulus interval) on day 7. β-Glucan was given orally once daily for 7 days (from day 0 to day 6).

Visceromotor responses were monitored by electromyography, as described previously [11,33], 12 h after the last administration of β-glucan. Electromyograph data were collected and analyzed using 8 STAR software (version 6.0–19.2 for Windows; Star Medical, Tokyo, Japan). Responses evoked by contraction of the external oblique musculature were quantified by calculating the area under the curve (AUC) of the voltage alteration graph. The baseline was determined by data collected 20 s (butyrate enema) or 30 s (repeated CRD) before each distention.

2.4. Inflamed paw pressure nociception test

The pain threshold in Wistar-Imamichi rats was measured using a Randall–Sellito test with an analgometer (Ugo basile, Comerio, Italy), as described previously [34]. Brewer's yeast (20%, 1 ml) was injected into one of the hind paws. Seven hours later, an increasing pressure was applied to the underside of the hind limb and the pain threshold was defined as the pressure in grams eliciting a cry from the animal.

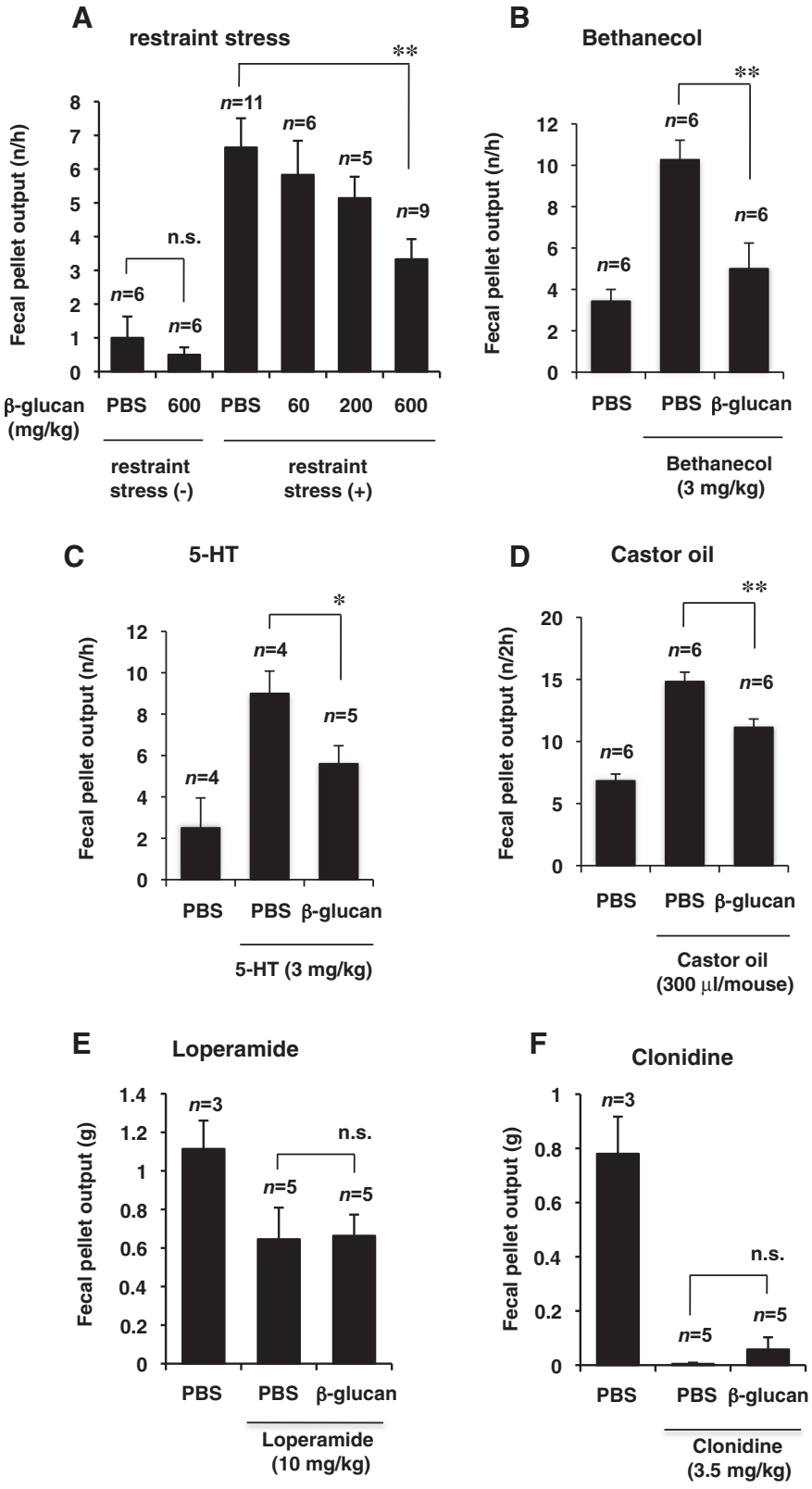

Fig. 1. Effects of LMW β-glucan on restraint stress- or drug-induced alteration of fecal pellet output in mice. Mice were orally administered indicated doses (A) or 600 mg/kg (B–F) of LMW β-glucan or vehicle (PBS). Two hours later, mice were exposed to restraint stress (A) or administered bethanecol (3 mg/kg, *s.c.*) (B), 5-HT (3 mg/kg, *s.c.*) (C), castor oil (300 μl/mouse, *p.o.*) (D), loperamide (10 mg/kg, *p.o.*) or clonidine (3.5 mg/kg, *p.o.*). The number (A–D) or wet weight (E and F) of fecal pellets excreted in the subsequent 0–1 h (A–C), 0–2 h (D) or 0–24 h (E and F) period was determined. Values are mean ± S.E.M $^{*}P < 0.05$; $^{**}P < 0.01$; n.s., not significant.

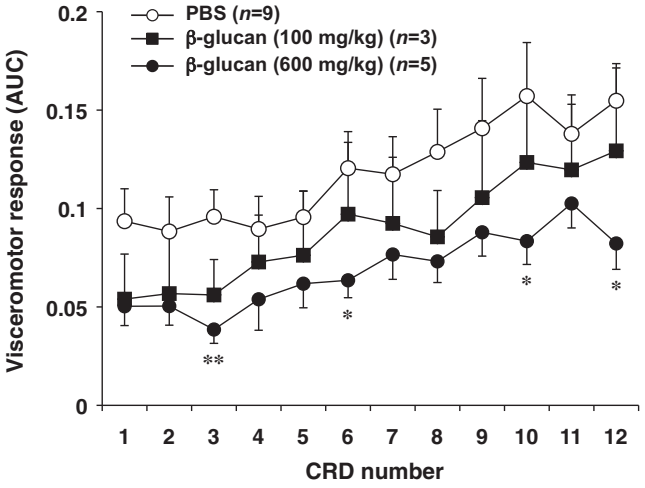

Fig. 2. Effect of LMW β-glucan on the viscermotor response to CRD in rats. The indicated doses (mg/kg) of β-glucan or PBS were orally administered to female Wistar rats once daily for 7 days. Twelve hours after the last administration of LMW β-glucan, rats were subjected to repetitive CRD and the visceromotor response was recorded and analysed as described in Section 2. Values are mean ± S.E.M $^{*}P < 0.05$; $^{**}P < 0.01$.

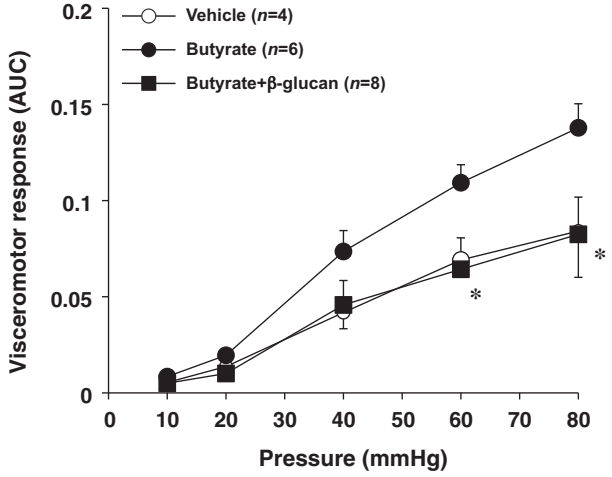

Fig. 3. Effect of LMW β-glucan on butyrate enema-induced colonic hypersensitivity to CRD in rats. Butyrate enemas were administered twice daily on days 1, 2 and 3. Administration of LMW β-glucan (600 mg/kg) (once daily from day 0 to day 6) and monitoring and analysis of the visceromotor response to CRD (on day 7) were performed as described in the legend of Fig. 2. Values are mean ± S.E.M $^{*}P < 0.05$.

2.5. Statistical analysis

All values are expressed as the mean ± S.E.M. Two-way ANOVA followed by the Tukey test or a Student's *t* test for unpaired results was used to evaluate differences between more than two groups or between two groups, respectively. Differences were considered to be significant for values of $P < 0.05$.

3. Results and discussion

3.1. Effect of LMW β-glucan on fecal pellet output in mice

We first examined the effect of a once-only oral administration of LMW β-glucan on restraint stress-induced fecal pellet output in mice. In untreated mice (administered PBS vehicle only), restraint stress (restricted movement by placement of mouse in a 50 ml plastic tube) caused a more than 5-fold increase in fecal pellet output per hour compared to unrestrained mice (Fig. 1A), as described previously [35]. The once-only oral pre-administration of LMW β-glucan suppressed this increase in a dose-dependent manner without affecting the basal level (without restraint stress) of fecal pellet output (Fig. 1A). Similar results were observed in response to a once-daily oral administration of LMW β-glucan for 7 days (data not shown). The LMW β-glucan-dependent suppression of restraint stress-induced fecal pellet output was also confirmed in rats (data not shown).

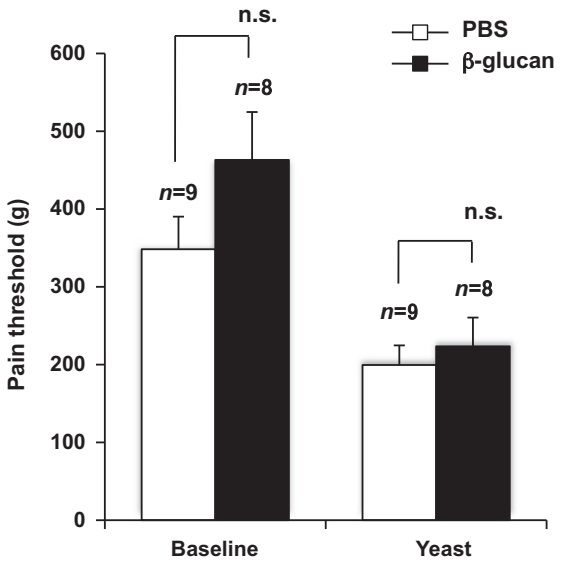

Fig. 4. Effect of LMW β-glucan on the pain response of rats in the inflamed paw pressure test. LMW β-glucan (600 mg/kg) was administered orally as described in the legend of Fig. 2. Twelve hours after the last administration of β-glucan, the inflamed paw pressure test was performed as described in Section 2. The pain threshold before (baseline) and after (yeast) the yeast injection was determined. Values are mean ± S.E.M n.s., not significant.

We also examined the effect of LMW β-glucan on the fecal pellet output induced by drugs that increase intestinal motility (bethanecol and 5-HT) or cause diarrhea (castor oil) [8,36]. As shown in Fig. 1B–D, the oral administration of LMW β-glucan (600 mg/kg) to mice suppressed the fecal pellet output induced by each of these drugs.

We then examined the effect of LMW β-glucan on drug-induced constipation. As shown in Fig. 1E and F, administration of loperamide or clonidine to mice decreased fecal pellet output, as described previously [36]. The oral pre-administration of LMW β-glucan did not alter the fecal pellet output. The results in Fig. 1 thus suggest that orally administered LMW β-glucan suppresses the restraint stress- or drug-induced stimulation of intestinal motility but does not affect the motility in the absence of these stimuli or in presence of constipation-inducing drugs. The mechanism underlying the LMW β-glucan-dependent suppression of intestinal motility is not clear at present.

3.2. Effect of LMW β-glucan on the visceromotor response to CRD in rats

In addition to alterations of fecal pellet output, hypersensitivity to visceral pain is one of the principle pathogenetic pathways for IBS. To study this phenomenon, we examined the effect of LMW β-glucan on visceromotor response to CRD, which has been used as an index of visceral pain response [33]. Rats were used for this analysis since the techniques for measuring the visceromotor response and CRD were established with these animals. As a single oral administration of LMW β-glucan did not significantly affect the visceromotor response to CRD (data not shown), we decided

to determine the effect of LMW β-glucan administered orally once-daily for 7 days. In control rats (PBS-treated), CRD evoked a visceromotor response which increased in amplitude in response to repeated CRDs (Fig. 2), as described previously [32]. Oral pre-administration of LMW β-glucan (600 mg/kg) to animals significantly decreased the visceromotor response to CRD not only after repetitive CRDs but also upon the first CRD (Fig. 2). Pre-administration of LMW β-glucan (100 mg/kg) also showed a tendency to decrease the visceromotor response to CRD, however the effect was not statistically significant (Fig. 2). These results indicate that oral pre-administration of high dose of LMW β-glucan suppresses the visceral pain response to CRD.

Since the visceromotor response to the first CRD was reduced by the pre-administration of LMW β-glucan, the results in Fig. 2 can be interpreted to indicate that LMW β-glucan suppresses the visceral pain response to CRD itself, but does not affect the repeated CRD-induced hypersensitivity to visceral pain. However, although we tried to habituate rats to the tube used for CRD experiment (see Section 2), it is possible that the animals entered into a state of restraint-like stress. Thus, it is also possible that LMW β-glucan suppresses the restraint stress-induced hypersensitivity to visceral pain.

We then examined the effect of LMW β-glucan on the visceral pain response in another animal model, butyrate-induced hypersensitivity to CRD. The butyrate enema is known to reduce the threshold of the visceromotor response to CRD [15,16]. We confirmed that twice-daily butyrate enemas (on days 1, 2 and 3) stimulated the visceromotor response to CRD on day 7 and found that when LMW β-glucan was orally pre-administered once daily from day 0 to day 6, the visceromotor response to CRD was similar to that measured in control rats (not given butyrate enemas) (Fig. 3). This result suggests that LMW β-glucan suppresses butyrate-induced hypersensitivity to CRD.

Finally, we tested whether the inhibitory effect of LMW β-glucan on the pain response is specific for visceral pain. For this purpose, we used the inflamed paw pressure test in which a yeast solution was administered to one of hind paws of rats to induce inflammation and the pressure-induced pain response was subsequently determined. As shown in Fig. 4, oral administration of LMW β-glucan once daily for 7 days did not affect the paw pressure required to elicit a nociception response (pain threshold) in both presence and absence of yeast injection. This finding suggests that LMW β-glucan does not affect the pain response in general but specifically affects the visceral pain response.

In conclusion, we have shown here that the oral administration of LMW β-glucan suppresses not only restraint stress- or drug-induced fecal pellet output, but also suppresses the visceral pain response. The difficulty associated with therapeutic management of IBS can be attributed to the fact that both abdominal pain and bowel habit disorders must be addressed. The results presented in this study thus suggest that LMW β-glucan could prove therapeutically beneficial for the prevention and treatment of IBS, especially in relation to the diarrhea-predominant IBS.

Acknowledgments

This work was supported by Grants-in-Aid of Scientific Research from the Ministry of Health, Labour, and Welfare of Japan, Grants-in-Aid for Scientific Research from the Ministry of Education, Culture, Sports, Science and Technology of Japan, and Grants-in-Aid of the Japan Science and Technology Agency.

References

[1] G.F. Longstreth, W.G. Thompson, W.D. Chey, L.A. Houghton, F. Mearin, R.C. Spiller, Functional bowel disorders, Gastroenterology 130 (2006) 1480–1491.
[2] D.A. Drossman, M. Camilleri, E.A. Mayer, W.E. Whitehead, AGA technical review on irritable bowel syndrome, Gastroenterology 123 (2002) 2108–2131.
[3] M. Shinozaki, S. Fukudo, M. Hongo, T. Shimosegawa, D. Sasaki, K. Matsueda, S. Harasawa, S. Miura, T. Mine, H. Kaneko, T. Arakawa, K. Haruma, A. Torii, T. Azuma, H. Miwa, M. Fukunaga, M. Handa, S. Kitamori, T. Miwa, High prevalence of irritable bowel syndrome in medical outpatients in Japan, J. Clin. Gastroenterol. 42 (2008) 1010–1016.
[4] C.W. Hammerle, C.M. Surawicz, Updates on treatment of irritable bowel syndrome, World J. Gastroenterol. 14 (2008) 2639–2649.
[5] D. Hulisz, The burden of illness of irritable bowel syndrome: current challenges and hope for the future, J Manag. Care Pharm. 10 (2004) 299–309.
[6] E.A. Mayer, S.M. Collins, Evolving pathophysiologic models of functional gastrointestinal disorders, Gastroenterology 122 (2002) 2032–2048.
[7] S. Okano, H. Nagaya, Y. Ikeura, H. Natsugari, N. Inatomi, Effects of TAK-637, a novel neurokinin-1 receptor antagonist, on colonic function in vivo, J. Pharmacol. Exp. Ther. 298 (2001) 559–564.
[8] S. Kobayashi, K. Ikeda, M. Suzuki, T. Yamada, K. Miyata, Effects of YM905, a novel muscarinic M3-receptor antagonist, on experimental models of bowel dysfunction in vivo, Jpn. J. Pharmacol. 86 (2001) 281–288.
[9] R. Moriya, T. Shirakura, H. Hirose, T. Kanno, J. Suzuki, A. Kanatani, NPY Y2 receptor agonist PYY(3–36) inhibits diarrhea by reducing intestinal fluid secretion and slowing colonic transit in mice, Peptides 31 (2010) 671–675.
[10] J. Munakata, B. Naliboff, F. Harraf, A. Kodner, T. Lembo, L. Chang, D.H. Silverman, E.A. Mayer, Repetitive sigmoid stimulation induces rectal hyperalgesia in patients with irritable bowel syndrome, Gastroenterology 112 (1997) 55–63.
[11] J.A. Christianson, G.F. Gebhart, Assessment of colon sensitivity by luminal distension in mice, Nat. Protoc. 2 (2007) 2624–2631.
[12] M. Larsson, S. Arvidsson, C. Ekman, A. Bayati, A model for chronic quantitative studies of colorectal sensitivity using balloon distension in conscious mice – effects of opioid receptor agonists, Neurogastroenterol. Motil. 15 (2003) 371–381.
[13] W.R. Treem, N. Ahsan, G. Kastoff, J.S. Hyams, Fecal short-chain fatty acids in patients with diarrhea-predominant irritable bowel syndrome: in vitro studies of carbohydrate fermentation, J. Pediatr. Gastroenterol. Nutr. 23 (1996) 280–286.
[14] C. Tana, Y. Umesaki, A. Imaoka, T. Handa, M. Kanazawa, S. Fukudo, Altered profiles of intestinal microbiota and organic acids may be the origin of symptoms in irritable bowel syndrome, Neurogastroenterol. Motil. 22 (2010) 512–519, e114–515.
[15] S. Bourdu, M. Dapoigny, E. Chapuy, F. Artigue, M.P. Vasson, P. Dechelotte, G. Bommelaer, A. Eschalier, D. Ardid, Rectal instillation of butyrate provides a novel clinically relevant model of noninflammatory colonic hypersensitivity in rats, Gastroenterology 128 (2005) 1996–2008.
[16] C. Rousseaux, X. Thuru, A. Gelot, N. Barnich, C. Neut, L. Dubuquoy, C. Dubuquoy, E. Merour, K. Geboes, M. Chamaillard, A. Ouwehand, G. Leyer, D. Carcano, J.F. Colombel, D. Ardid, P. Desreumaux, *Lactobacillus acidophilus* modulates intestinal pain and induces opioid and cannabinoid receptors, Nat. Med. 13 (2007) 35–37.
[17] J. Chen, R. Seviour, Medicinal importance of fungal beta-(1→3), (1→6)-glucans, Mycol. Res. 111 (2007) 635–652.
[18] S.V. Tsoni, G.D. Brown, Beta-Glucans and dectin-1, Ann. NY Acad. Sci. 1143 (2008) 45–60.
[19] M. Berdal, H.I. Appelbom, J.H. Eikrem, A. Lund, S. Zykova, L.T. Busund, R. Seljelid, T. Jenssen, Aminated beta-1,3-D-glucan improves wound healing in diabetic db/db mice, Wound Repair Regen. 15 (2007) 825–832.
[20] S. Bell, V.M. Goldman, B.R. Bistrian, A.H. Arnold, G. Ostroff, R.A. Forse, Effect of beta-glucan from oats and yeast on serum lipids, Crit. Rev. Food Sci. Nutr. 39 (1999) 189–202.
[21] G. Sener, E. Eksioglu-Demiralp, M. Cetiner, F. Ercan, B.C. Yegen, Beta-glucan ameliorates methotrexate-induced oxidative organ injury via its antioxidant and immunomodulatory effects, Eur. J. Pharmacol. 542 (2006) 170–178.
[22] A. Bedirli, M. Kerem, H. Pasaoglu, N. Akyurek, T. Tezcaner, S. Elbeg, L. Memis, O. Sakrak, Beta-glucan attenuates inflammatory cytokine release and prevents acute lung injury in an experimental model of sepsis, Shock 27 (2007) 397–401.
[23] O.I. Lyuksutova, E.D. Murphey, T.E. Toliver-Kinsky, C.Y. Lin, W. Cui, D.L. Williams, E.R. Sherwood, Glucan phosphate treatment attenuates burn-induced inflammation and improves resistance to *Pseudomonas aeruginosa* burn wound infection, Shock 23 (2005) 224–232.
[24] J. Soltys, M.T. Quinn, Modulation of endotoxin- and enterotoxin-induced cytokine release by in vivo treatment with beta-(1,6)-branched beta-(1,3)-glucan, Infect. Immun. 67 (1999) 244–252.
[25] H.Z. Toklu, A.O. Sehirli, A. Velioglu-Ogunc, S. Cetinel, G. Sener, Acetaminophen-induced toxicity is prevented by beta-D-glucan treatment in mice, Eur. J. Pharmacol. 543 (2006) 133–140.
[26] V.B. Shah, D.L. Williams, L. Keshvara, Beta-glucan attenuates TLR2- and TLR4-mediated cytokine production by microglia, Neurosci. Lett. 458 (2009) 111–115.
[27] Y. Kimura, M. Sumiyoshi, T. Suzuki, M. Sakanaka, Effects of water-soluble low-molecular-weight beta-1, 3-D-glucan (branch beta-1, 6) isolated from *Aureobasidium pullulans* 1A1 strain black yeast on restraint stress in mice, J. Pharm. Pharmacol. 59 (2007) 1137–1144.
[28] Y. Kimura, M. Sumiyoshi, T. Suzuki, M. Sakanaka, Antitumor and antimetastatic activity of a novel water-soluble low molecular weight beta-1, 3-D-glucan (branch beta-1,6) isolated from *Aureobasidium pullulans* 1A1 strain black yeast, Anticancer Res. 26 (2006) 4131–4141.

[29] Y. Kimura, M. Sumiyoshi, T. Suzuki, M. Sakanaka, Inhibitory effects of water-soluble low-molecular-weight beta-(1,3–1,6) D-glucan purified from *Aureobasidium pullulans* GM-NH-1A1 strain on food allergic reactions in mice, Int Immunopharmacol 7 (2007) 963–972.
[30] K. Tanaka, Y. Tanaka, T. Suzuki, T. Mizushima, Protective effect of beta-(1,3 → 1,6)-D-glucan against irritant-induced gastric lesions, Br. J. Nutr. 106 (2011) 475–485.
[31] T.L. Bale, R. Picetti, A. Contarino, G.F. Koob, W.W. Vale, K.F. Lee, Mice deficient for both corticotropin-releasing factor receptor 1 (CRFR1) and CRFR2 have an impaired stress response and display sexually dichotomous anxiety-like behavior, J. Neurosci. 22 (2002) 193–199.
[32] A. Ravnefjord, M. Brusberg, H. Larsson, E. Lindstrom, V. Martinez, Effects of pregabalin on visceral pain responses and colonic compliance in rats, Br. J. Pharmacol. 155 (2008) 407–416.
[33] K. Saito-Nakaya, R. Hasegawa, Y. Nagura, H. Ito, S. Fukudo, Corticotropin-releasing hormone receptor 1 antagonist blocks colonic hypersensitivity induced by a combination of inflammation and repetitive colorectal distension, Neurogastroenterol. Motil. 20 (2008) 1147–1156.
[34] L.O. Randall, J.J. Selitto, A method for measurement of analgesic activity on inflamed tissue, Arch. Int. Pharmacodyn. Ther. 111 (1957) 409–419.
[35] E. Mazzon, S. Cuzzocrea, Role of TNF-alpha in ileum tight junction alteration in mouse model of restraint stress, Am. J. Physiol. Gastrointest. Liver Physiol. 294 (2008) G1268–G1280.
[36] T. Saito, F. Mizutani, Y. Iwanaga, K. Morikawa, H. Kato, Laxative and anti-diarrheal activity of polycarbophil in mice and rats, Jpn. J. Pharmacol. 89 (2002) 133–141.

Biochemical and Biophysical Research Communications 420 (2012) 450–455

Contents lists available at SciVerse ScienceDirect

Biochemical and Biophysical Research Communications

journal homepage: www.elsevier.com/locate/ybbrc

A regulatory role of Kruppel-like factor 4 in endothelial argininosuccinate synthetase 1 expression in response to laminar shear stress

Gyeong In Mun, Yong Chool Boo *

Department of Molecular Medicine, Cell and Matrix Research Institute, BK21 Medical Education Program for Human Resources, Kyungpook National University School of Medicine, Daegu 700-422, Republic of Korea

ARTICLE INFO

Article history:
Received 1 March 2012
Available online 10 March 2012

Keywords:
Endothelial cells
Shear stress
Argininosuccinate synthetase 1
Nitric oxide synthase 3
Kruppel-like factor 4

ABSTRACT

Endothelial argininosuccinate synthetase 1 (ASS1) regulates the provision of L-arginine to nitric oxide synthase 3 (NOS3). Previous studies demonstrated that endothelial ASS1 expression was induced by laminar shear stress (LSS) and that this enzyme plays a role in maintaining anti-inflammatory microenvironments through enhancing NO production. However, differently from the case of NOS3, the regulatory mechanism for the endothelial ASS1 expression in response to LSS is not well understood. This study addressed a specific issue whether endothelial ASS1 expression is regulated by Kruppel-like factors (KLFs) that are presumed to coordinate endothelial gene expressions in response to LSS. The cDNA microarray data indicated that LSS stimulated the expression of numerous KLFs in human umbilical vein endothelial cells. KLF4 showed the highest fold increase and LSS-dependent increases of KLF4 and most other KLFs were similar in young *versus* senescent endothelial cells. LSS-induced KLF4 expression was verified by RT-PCR and Western blotting. LSS-induced ASS1 expression and NO production were suppressed by a small interfering RNA for KLF4. The ectopic expression of KLF4 led to the increase of ASS1 expression and NO production. The present study demonstrated a key regulatory role of KLF4 in the endothelial ASS1 expression and NO production in response to LSS.

1. Introduction

The endothelium, a monolayer of endothelial cells, plays a key role in the regulation of vascular physiology, not only as a physical interface between circulating blood and the rest of the vessel wall, but also as a chemical factory that produces a variety of substances involved in vasodilatation, blood coagulation, inflammation and immune response [1–2]. Thus, the structural and functional integrities of the endothelium are important for the maintenance of vascular health.

Nitric oxide (NO) produced by nitric oxide synthase 3 (NOS3) in the endothelium is one of the key mediators of vascular responses to various stimuli. NO actively participates in the regulation of vascular tone by promoting smooth muscle relaxation and thus has been named 'endothelium-derived relaxing factor' [3]. NO also inhibits the key events of vascular inflammation such as endothelial cell death or activation, adhesion of monocytes to the inflamed endothelium, transmigration of monocytes beneath the endothelium and proliferation of smooth muscle cells [4]. In these regards, the decreased availability of endothelial NO has been considered a biochemical marker of endothelial dysfunction associated with cardiovascular diseases.

Laminar shear stress (LSS) due to pulsatile blood flow is known to enhance endothelial NO production by increasing both the amount and the catalytic activity of NOS3 [5]. The calcium-dependent calmodulin binding and phosphorylation of NOS3 on multiple sites including Ser^{1177} were identified as the primary mechanisms for NOS3 activation by LSS [5]. The increase of NOS3 protein level was also observed in cultured endothelial cells exposed to chronic LSS [6,7] and in mice trained to exercise [8]. NO production is also governed by the availability of L-arginine, the substrate of NOS3. Argininosuccinate synthetase 1 (ASS1) is the key enzyme that regulates the provision of L-arginine [9]. ASS1 catalyzes the ATP-dependent condensation reaction between L-citrulline and aspartic acid generating L-argininosuccinate, which is used in the subsequent reaction catalyzed by argininosuccinate lyase to form L-arginine. The L-arginine produced in this way can be directed to NO synthesis by NOS3.

Kruppel-like factors (KLFs) have been identified as a group of major transcription factors directing endothelial gene expression

Abbreviations: ASS1, argininosuccinate synthetase 1; GAPDH, glyceraldehyde 3-phosphate dehydrogenase; HUVECs, human umbilical vein endothelial cells; KLF, Kruppel-like factor; LSS, laminar shear stress; NO, nitric oxide; NOS3, nitric oxide synthase 3; RT-PCR, reverse transcriptase-polymerase chain reaction; siRNA, small interfering RNA.

* Corresponding author. Address: Department of Molecular Medicine, Kyungpook National University School of Medicine, 101 Dongin-dong 2-ga, Jung-gu, Daegu 700-422, Republic of Korea. Fax: +82 53 426 4944.
E-mail address: ycboo@knu.ac.kr (Y.C. Boo).

0006-291X/$ - see front matter © 2012 Elsevier Inc. All rights reserved.
http://dx.doi.org/10.1016/j.bbrc.2012.03.016

program in response to LSS [10]. KLF2 has been most intensively studied previously. It plays a key role in the induction of ASS1, NOS3 and thrombomodulin in response to LSS, thus contributing to the establishment of vasodilatory, anti-inflammatory and antithrombotic endothelial microenvironments [11]. The phytogenetic analysis revealed the closest relationship between KLF2 and KLF4 [12], and a recent study identified ASS1 as one of the common transcriptional targets of KLF2 and KLF4 based on the transcriptomic profiling of endothelial cells over-expressing KLF2 and KLF4 [13]. However, no direct evidence is available for the regulatory role of KLF4 in endothelial ASS1 expression in response to LSS.

We previously demonstrated that LSS stimulated both ASS1 and NOS3 expressions, and that the expression of ASS1, but not of NOS3, was suppressed in senescent endothelial cells [7]. ASS1 has also been demonstrated to prevent inflammatory monocyte adhesion under both static and LSS conditions, by increasing NO production and suppressing the expression of cell adhesion molecules [14]. In an attempt to understand the mechanism associated with the endothelial ASS1 expression, the present study addressed a specific issue whether of KLFs, especially KLF4, regulates the endothelial ASS1 expression in response to LSS.

2. Materials and methods

2.1. Cell culture and induction of replicative senescence

Human umbilical vein endothelial cells (HUVECs) obtained from Clonetics Cambrex (Rockland, ME, USA) were cultured in EBM-2 medium containing endothelial growth supplements (Clonetics Cambrex), 10% fetal bovine serum (Gibco BRL, Grand Island, NY, USA) and antibiotics (100 U ml^{-1} penicillin, 100 μg ml^{-1} streptomycin, 0.25 μg ml^{-1} amphotericin B) on 0.2% gelatin-coated 100 mm-culture dishes (BD Biosciences, San Jose, CA, USA) at 37 °C and 5% CO_2. [15] Cells were serially sub-cultured at ratios of 1 to 3∼5 in the same media. The population doubling level (PDL) was calculated using the formula PDL = log[the final cell count/the starting cell count]/log2. Young cells with cumulative PDL 8–12 and senescent cells with cumulative PDL 35–45 were used in the present study. The senescent cells were significantly larger than young cells and expressed a high level of senescence-associated β-galactosidase as verified by *in situ* activity staining [7,16].

2.2. LSS treatments

After changing the growth medium with a fresh one, young and senescent HUVECs on an 100 mm-culture dish (BD Biosciences) were exposed to steady LSS at 12 dyn cm^{-2} or kept under static conditions for 24 h. LSS was provided by rotating a Teflon cone (0.5° cone angle) mounted onto a culture dish, as described previously [17,18]. Cell morphology was examined under an Eclipse TS100 inverted phase microscope from Nikon (Melville, NY, USA).

2.3. Gene expression profiling

Total cellular RNA was extracted from cells using the RNeasy kit (Qiagen, Valencia, CA, USA) and gene expression profiles were analyzed on the GeneChip® HG-U133 Plus 2.0 (Affymetrix, Santa Clara, CA, USA), as reported previously [7]. The complete datasets were deposited in the Gene Expression Omnibus database [Accession Number, GSE13712].

2.4. Reverse transcriptase-polymerase chain reaction (RT-PCR)

Total cellular RNA was extracted from cells using the RNeasy kit (Qiagen). RT-PCR was conducted using the GeneAmp® PCR system 9700 (Applied Biosystems, Foster city, CA, USA) in a reaction mixture (20 μl) containing the Prime RT-PCR Premix (GENETBIO, Nonsan, Korea), 1–125 ng RNA and 10 p mole of gene-specific primer sets (Bioneer, Daejeon, Korea). The sequences of PCR primers were: ASS1 (GeneBank accession number, NM_000050.4) 5′-TCC TGG AGA ACC CCA AGA AC-3′ (sense) and 5′-CTC AGC AAA TTT CAA GCC CA-3′ (antisense); NOS3 (NM_000603.3) 5′-TGC TGG CAT ACA GGA CTC AG-3′ (sense) and 5′-TAG GTC TTG GGG TTG TCA GG-3′ (antisense); KLF4 (NM_004235.4) 5′- GCT CCA TTA CCA AGA GCT CAT G-3′ (sense) and 5′- GTA GTG CCT GGT CAG TTC AT-3′ (antisense); GAPDH (NM_002046.3) 5′-GCC AAA AGG GTC ATC ATC TC-3′ (sense) and 5′-GTA GAG GCA GGG ATG ATG TTC-3′ (antisense). Reaction condition for RT-PCR were the following: A cDNA synthesis at 42 °C for 30 min and heat inactivation of reverse transcriptase at 95 °C for 10 min was followed by 32 cycles of 95 °C for 30 s (denaturation), 55 °C for 30 s (annealing) and 72 °C for 30 s (extension) and a final extension at 72 °C for 5 min. The PCR products were electrophoresed in 1.0% agarose gel with a DNA ladder marker (ELPIS-BIOTECH, Daejeon, Korea). The gel was ethidium bromide-stained and the band intensities were determined using the Gel Doc system (BioRad, Hercules, CA, USA).

2.5. Western blotting

Preparation of cell lysates and Western blotting were done as described previously [14]. Mouse monoclonal antibodies for ASS1 and NOS3 were purchased from BD Transduction Laboratories (San Diego, CA, USA). Rabbit polyclonal antibodies for KLF4 were from Santa Cruz Biotech (Santa Cruz, CA, USA). Mouse monoclonal β-actin antibody was purchased from Sigma-Aldrich (St. Louis, MO USA). Goat anti-mouse and anti-rabbit antibodies conjugated to horse radish peroxidase were purchased from Cell signaling and Santa Cruz Biotech, respectively.

2.6. Transfection with a small interfering RNA (siRNA)

KLF4 siRNA (#1299001, HSS19018) with nucleotide sequences corresponding to the coding region of a human KLF4 gene transcript (NM_004235.4) and a negative control siRNA (#12935200) with scrambled sequences were purchased from Invitrogen (Grand Island, CA, USA). The nucleotide sequences of KLF4 siRNA were: 5′-UCG UCA GCG UCA GCC UCC UCU UCG U-3′ (sense) and 5′-ACG AAG AGG AGG CUG ACG CUG ACG A-3′ (antisense). Transfection of HUVECs with siRNAs was performed using the lipofectamine RNAiMAX (Invitrogen). In brief, cells at ∼50% confluency on an 100 mm-culture dish were treated with a mixture of 100 nM siRNA and 1.25 μl ml^{-1} Lipofectamine RNAiMAX in 5 ml Opti-MEM (Invitrogen) for 4 h.

2.7. Transfection with a plasmid encoding KLF4

Total RNA from HUVECs was used for the synthesis of first-strand cDNA using the Reverse Transcription Master Premix (ELPIS-BIOTECH). Full coding sequence of KLF4 was PCR-amplified from the first-strand cDNA using primers 5′-CCG AAG CTT ACA TTA ATG AGG CAG CCA CCT GGC-3′ and 5′-GCG TCT AGA TTA AAA ATG CCT CTT CAT GTG TAA GGC A-3′ (*HindIII* and *XbaI* sites were incorporated into sense and antisense primers, respectively, as underlined). The PCR products were gel-purified using the QIA Quick gel extraction kit (Qiagen), digested with *HindIII* and *XbaI* (New England Biolabs, Ipswich, MA, USA) and ligated with the pcDNA3.1(+) vector (Invitrogen) using the Ligation Mix Kit (TaKaRa

Bio Inc., Shiga, Japan). The plasmid was cloned and propagated in the *Escherichia coli* strain DH5α (TaKaRa Bio Inc.) and purified using the Maxi-Prep DNA purification kit (Qiagen). The KLF4 coding sequence was verified to be identical to the reference sequence (NM004235.4). Transfection of HUVECs with the KLF4 expression plasmid (or the empty vector) was performed using the TrueFect™ (United BioSystems Inc., Rockville, MD, USA). Briefly, cultured cells at ~90% confluency were treated with 1 μg ml^{-1} plasmid DNA and 3 μl ml^{-1} TrueFect™ in Opti-MEM for 4 h, followed by incubation in a growth medium.

2.8. Assay of NO production

Cells were transfected with siRNAs or plasmids and cultured for 24 h and then exposed to LSS at 12 dyn cm^{-2} or kept under static conditions for 24 h in Dulbecco's modified Eagle's medium (DMEM) without phenol red (Sigma-Aldrich, St. Louis, MO, USA). NO release from cultured endothelial cells was determined by measuring NO metabolites, nitrite plus nitrate, accumulated in culture media as described previously [26].

2.9. Statistical analysis

Data are presented as the means ± SEM. The statistical analyses were conducted using the Sigma Stat 3.1 software program. Significant differences among the groups were determined *via* one-way ANOVA. Duncan's multiple-range test was conducted if differences were identified between the groups at a significance level of $p < 0.05$.

3. Results

Young and senescent HUVECs were exposed to an arterial level of LSS (12 dyn cm^{-2}) or maintained under static conditions for 24 h, and their typical morphologies are shown in Fig. 1A. The cDNA microarray analysis of total mRNA from these cells indicated that the expressions of many KLFs at the mRNA levels were upregulated by LSS treatments irrespectively of cellular senescence (Fig. 1B). KLF4 mRNA level was the most greatly changed by LSS among the KLF family members, and LSS-dependent increases of KLF4 and most other KLFs were similar in young *versus* senescent cells. These changes were apparently similar to that of NOS3, but different from that of ASS1 whose expression level was lowered in senescent cells compared to young cells.

The changes in the mRNA levels of ASS1, NOS3 and KLF4 due to endothelial cell senescence and LSS were also examined by RT-PCR analysis using gene-specific primer sets (Fig. 2A). GAPDH expression was examined as a house-keeping control gene. The results of RT-PCR analysis verified the effect of LSS inducing KLF4 expression in both young and senescent endothelial cells. LSS stimulated both ASS1 and NOS3 expressions, and the expression of ASS1, but not of NOS3, was partially suppressed in senescent endothelial cells, as previously observed [7]. Total proteins were extracted from young and senescent HUVECs cultured under static and LSS conditions were subjected to Western blotting analysis for ASS1, NOS3, KLF4 and β-actin using specific antibodies (Fig. 2B–E). The expression levels of ASS1, NOS3 and KLF4 proteins were increased by LSS while control β-actin expression remained unchanged. ASS1 protein expression was lowered in senescent cells, as noted previously [7].

Because KLF4 expression levels appeared to be highly up-regulated by LSS, next experiments were undertaken to examine whether KLF4 plays a regulatory role in the induction of ASS1 and NOS3 expression in endothelial cells exposed to LSS. To this end, cells were pretreated with a siRNA targeted to the coding region of KLF4 gene transcript or the control scrambled siRNA. Twenty four hours later, cells were exposed to LSS for additional 24 h. Compared to the control siRNA, KLF4 siRNA markedly inhibited the expression of KLF4 and this led to the attenuation of ASS1 and NOS3 expressions due to LSS at the mRNA and

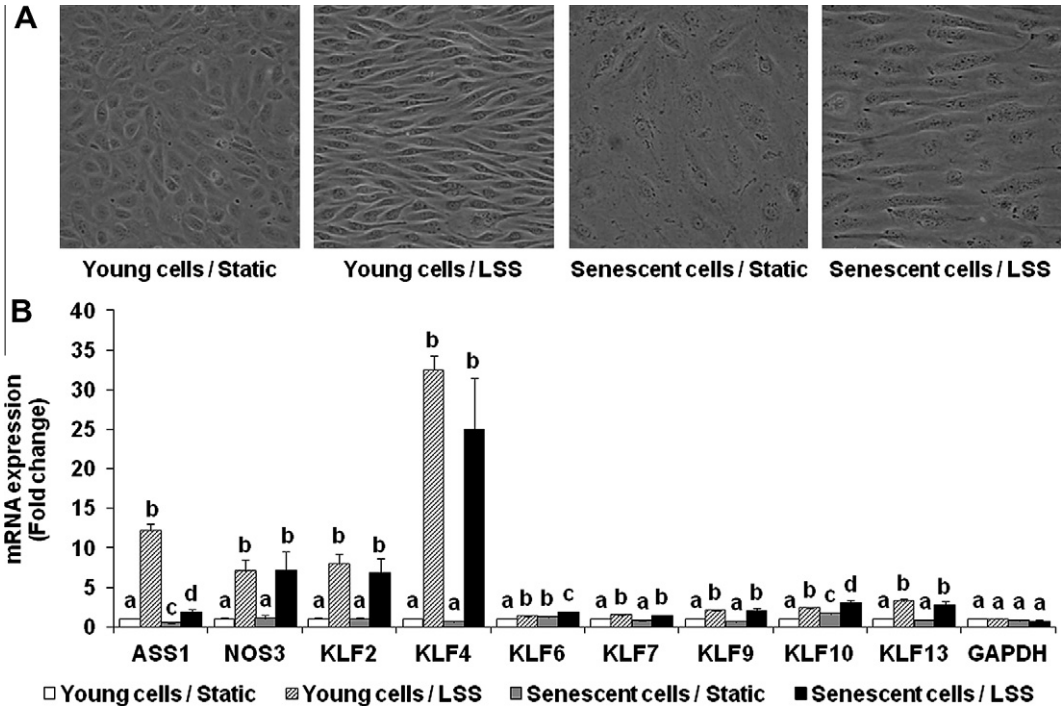

Fig. 1. Differential gene expressions of ASS1, NOS3 and KLFs in young and senescent HUVECs under static and LSS conditions. Cell images were captured under a microscope (original magnification, 200×) (A). Total cellular mRNA was extracted and gene expression profile was analyzed using a cDNA microarray method (B). Fold changes in the mRNA levels of ASS1, NOS3, KLFs and GAPDH are shown (means ± SEM, $n = 3$). Columns not sharing the same letter differ significantly from each other ($p < 0.05$).

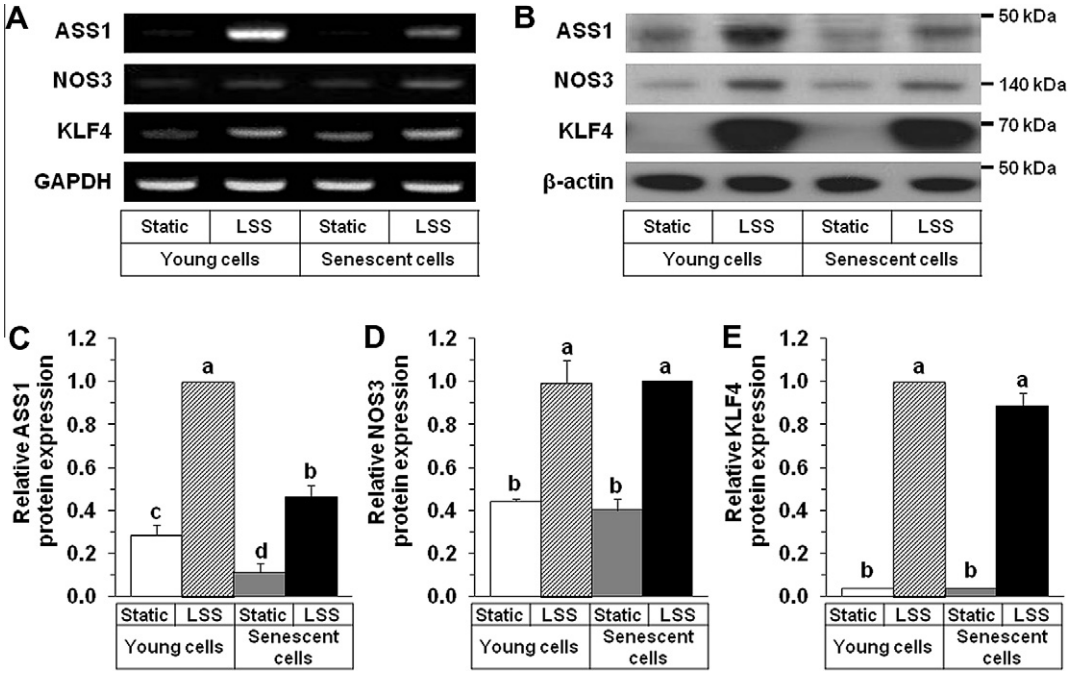

Fig. 2. Effects of endothelial cell senescence and LSS on the expressions of ASS1, NOS3 and KLF4 at the mRNA and protein levels. Young and senescent HUVECs were exposed to LSS at 12 dyn cm^{-2} or maintained under static conditions for 24 h. Expression of ASS1, NOS3, KLF4 and GAPDH or β-actin at the mRNA and protein levels were monitored by RT-PCR (A) and Western blotting (B–E), respectively. Relative protein levels are presented as means ± SEM ($n = 3$). Columns not sharing the same letter differ significantly from each other ($p < 0.05$).

protein levels (Fig. 3A–E). KLF4 siRNA had no effects on GAPDH mRNA expression and β-actin protein expression, supporting the selective gene silencing effect of KLF4 siRNA. It was also confirmed that LSS-stimulated KLF2 mRNA expression was not affected by KLF4 siRNA. KLF4 siRNA lowered the LSS-stimulated NO production (Fig. 3F), supporting the critical role of KLF4 in endothelial physiology.

The regulatory role of KLF4 in the expression of ASS1 and NOS3 was further verified by ectopic expression of KLF4 in endothelial cells. Transfection of HUVECs with the KLF4 expression plasmid (pcDNA-KLF4) increased KLF4 expression to a significantly higher level than the control cells transfected with the empty pcDNA vector (Fig. 4). KLF4 over-expression led to increases in the mRNA and protein levels of ASS1 and NOS3, and NO production (Fig. 4).

4. Discussion

Endothelial NO plays a critical role in maintaining vascular homeostasis. NOS3 catalyzes the conversion of L-arginine to L-citrulline producing NO in endothelial cells. Thus NO production is governed not only by NOS3 activity but by substrate availability. Normal cytosolic levels of L-arginine in endothelial cells (>800 μM) [19] is much higher than NOS3's Michaelis constant (K_M) for L-arginine (~2.9 μM) [20], but NOS3 activity still appears to be dependent on the extracellular availability of L-arginine *in vivo* [21]. To explain this phenomenon called 'arginine paradox', it has been suggested that L-arginine may not be freely diffusible throughout the cell and its subcellular local concentration in the vicinity of NOS3 may be lower than the mean value of the entire cell [22]. In accordance with this model, L-arginine regeneration enzymes and NOS3 are co-localized at caveolae in endothelial cells, constituting 'citrulline-NO cycle' [22–24]. As a rate limiting enzyme of this citrulline-NO cycle, ASS1 can regulate NO production in endothelial cells [25–26]. Indeed, NO production in endothelial cells was quite dependent on the expression level of ASS1 [7,14].

The present study clearly demonstrated an essential regulatory role of KLF4 in ASS1 and NOS3 expressions and NO production in response to LSS through a genetic approach involving siRNA-mediated knockdown and over-expression of KLF4 (Figs. 3 and 4). Potentially ASS1 could supply L-arginine to other NOS enzymes including NOS2. In addition, KLF4 has been shown to stimulate NOS2 expression in macrophages [29]. However, NOS2 protein was not detected by Western blotting in human aortic endothelial cells [16]. Its expression level in HUVECs was also very low and not increased by KLF4 over-expression (data not shown). Thus it was suggested that NOS3 rather than NOS2 may be functionally associated with ASS1 in endothelial cells.

The fold changes of KLF4 expression due to LSS exposure were almost same in young *versus* senescent endothelial cells (Fig. 2). The cDNA microarray data also indicated that the fold increases of most KLFs expression levels due to LSS exposure were almost same in young *versus* senescent endothelial cells (Fig. 1B). Of interest, fold-increases of ASS1 expression due to LSS were almost same in young *versus* senescent endothelial cells, although the basal and LSS-stimulated ASS1 expression levels were significantly lower in senescent cells compared to young cells (Fig. 2). Based these observations, it is tempting to speculate that fold-increases of ASS1 expression due to LSS may be at least partly dependent on transactivation of their gene expressions by KLF4 and other KLF members.

Then, what kind of mechanism is involved in the suppression of the basal and LSS-stimulated ASS1 expression in senescent endothelial cells? Notably, many other transcription factors could contribute to this because transcription of a certain gene is regulated by complicated interaction between *cis*-elements in the gene promoter and many general and gene-specific transcription factors. For example, tumor necrosis factor-α has been shown to down-regulate ASS1 expression in bovine aortic endothelial cells by stimulating NF-κB signaling pathway and reducing Sp1 binding to ASS1 promoter [27]. Alternatively, epigenetic changes due to cellular senescence [28], if any, might contribute to down-regulation of ASS1 expression in senescent endothelial cells. Of interest, a recent study reported the hypermethylation of the ASS1 promoter in several kinds of cancer cell lines that were resistant to platinum

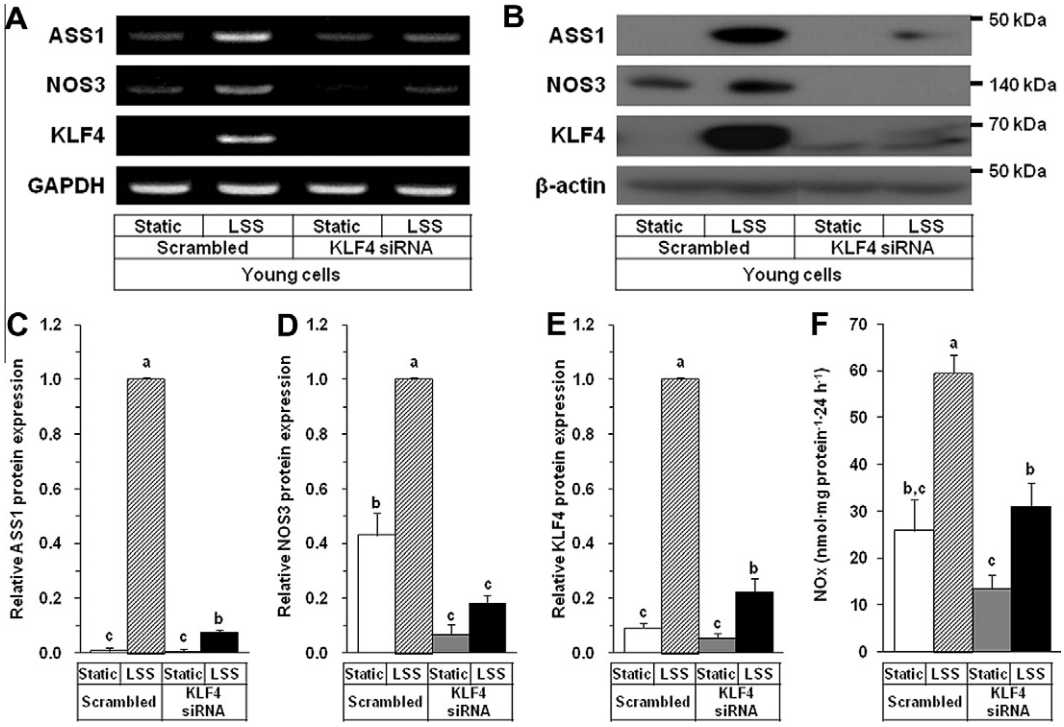

Fig. 3. KLF4 regulates the expressions of ASS1 and NOS3, and the NO production stimulated by LSS in young HUVECs. Young HUVECs were transfected the KLF4 siRNA or the control scrambled siRNA for 4 h and then cultured for 24 h before exposure to LSS at 12 dyn cm^{-2} for 24 h. Expressions of ASS1, NOS3, KLF4 and GAPDH or β-actin at the mRNA and protein levels were monitored by RT-PCR (A) and Western blotting (B–E), respectively. NO production was determined by measuring nitrite plus nitrate accumulated in the conditioned medium (F). Data are presented as means ± SEM ($n = 3$). Columns not sharing the same letter differ significantly from each other ($p < 0.05$).

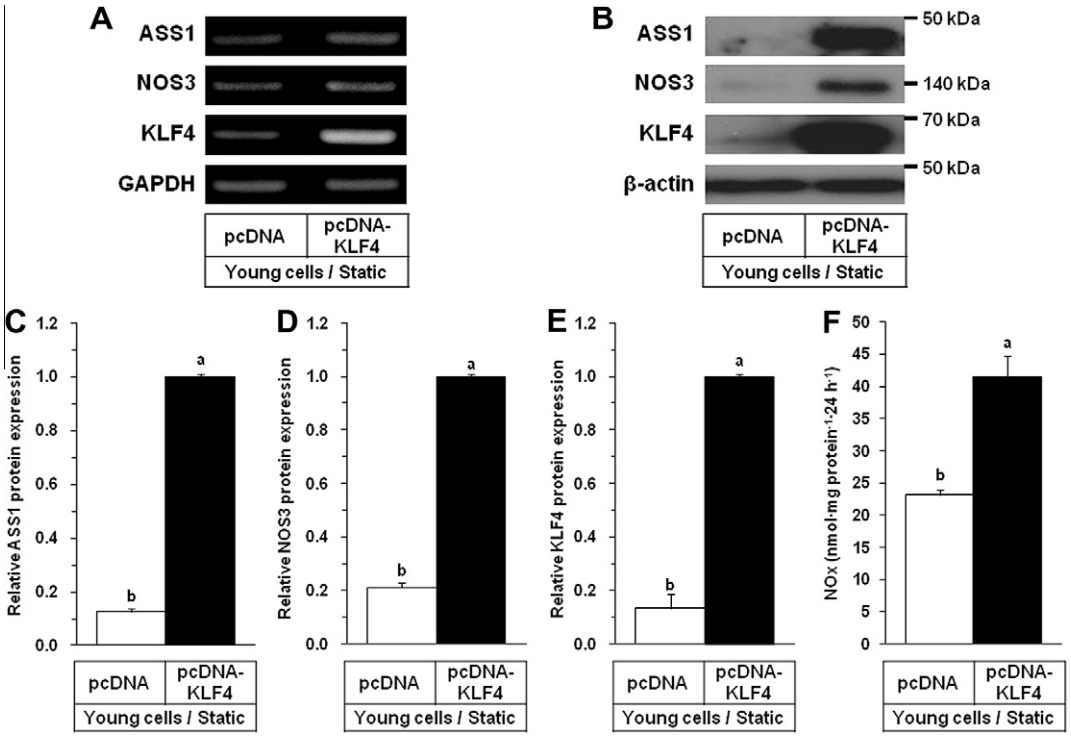

Fig. 4. Over-expression of KLF4 increases the expressions of ASS1 and NOS3 in young HUVECs. Young HUVECs were transfected with pcDNA-KLF4 or pcDNA and cultured for 48 h under static conditions. Expressions of ASS1, NOS3, KLF4 and GAPDH or β-actin at the mRNA and protein levels were monitored by RT-PCR (A) and Western blotting (B–E), respectively. NO production was determined by using the conditioned medium (F). Relative protein levels are presented as means ± SEM ($n = 3$). Columns not sharing the same letter differ significantly from each other ($p < 0.05$).

chemotherapy, implicating that transcriptional silencing of ASS1 may be associated with treatment failure and clinical relapse in ovarian cancer [29]. Preliminary experiments using 5′-aza-2′-deoxycytidine, a mechanism-dependent suicide inhibitor of DNA methylation [30], indicated that endothelial ASS1 expression may also be regulated by the promoter DNA methylation (Supplementary Fig. S1).

In conclusion, the present study established KLF4 as a key regulator of endothelial ASS1 expression in response to LSS. Because NOS3 has been previously noted as a regulatory target of KLF4 [31], it is now suggested that KLF4 effects on the endothelial NO production may be mediated by both ASS1 and NOS3. Various compounds including statins and resveratrol are known to increase KLF4 expression [13], and thus endothelial ASS1 expression is expected to be enhanced by such pharmacological means in addition to physical exercise that increases arterial shear stress levels [32].

5. Disclosures

None.

Acknowledgments

This work was supported by Basic Science Research Program (Grant No. 2009-0071171) and Mid-career Researcher Program (2011-0014527) through NRF grant funded by the MEST, Republic of Korea.

Appendix A. Supplementary data

Supplementary data associated with this article can be found, in the online version, at http://dx.doi.org/10.1016/j.bbrc.2012.03.016.

References

[1] G. Giannotti, U. Landmesser, Endothelial dysfunction as an early sign of atherosclerosis, Herz 32 (2007) 568–572.
[2] P. Libby, Inflammation in atherosclerosis, Nature 420 (2002) 868–874.
[3] R.F. Furchgott, J.V. Zawadzki, The obligatory role of endothelial cells in the relaxation of arterial smooth muscle by acetylcholine, Nature 288 (1980) 373–376.
[4] D.S. Bredt, Endogenous nitric oxide synthesis: biological functions and pathophysiology, Free Radic. Res. 31 (1999) 577–596.
[5] Y.C. Boo, H. Jo, Flow-dependent regulation of endothelial nitric oxide synthase: role of protein kinases, Am. J. Physiol. Cell Physiol. 285 (2003) C499–C508.
[6] M.E. Davis, H. Cai, G.R. Drummond, D.G. Harrison, Shear stress regulates endothelial nitric oxide synthase expression through c-Src by divergent signaling pathways, Circ. Res. 89 (2001) 1073–1080.
[7] G.I. Mun, S.J. Lee, S.M. An, I.K. Kim, Y.C. Boo, Differential gene expression in young and senescent endothelial cells under static and laminar shear stress conditions, Free Radic. Biol. Med. 47 (2009) 291–299.
[8] M.E. Davis, H. Cai, L. McCann, T. Fukai, D.G. Harrison, Role of c-Src in regulation of endothelial nitric oxide synthase expression during exercise training, Am. J. Physiol. Heart Circ. Physiol. 284 (2003) H1449–H1453.
[9] R.J. Haines, L.C. Pendleton, D.C. Eichler, Argininosuccinate synthase: at the center of arginine metabolism, Int. J. Biochem. Mol. Biol. 2 (2011) 8–23.
[10] R.J. Dekker, S. van Soest, R.D. Fontijn, S. Salamanca, P.G. de Groot, E. VanBavel, H. Pannekoek, A.J. Horrevoets, Prolonged fluid shear stress induces a distinct set of endothelial cell genes, most specifically lung Kruppel-like factor (KLF2), Blood 100 (2002) 1689–1698.
[11] K.M. Parmar, H.B. Larman, G. Dai, Y. Zhang, E.T. Wang, S.N. Moorthy, J.R. Kratz, Z. Lin, M.K. Jain, M.A. Gimbrone Jr., G. Garcia-Cardena, Integration of flow-dependent endothelial phenotypes by Kruppel-like factor 2, J. Clin. Invest. 116 (2006) 49–58.
[12] J.J. Bieker, Kruppel-like factors: three fingers in many pies, J. Biol. Chem. 276 (2001) 34355–34358.
[13] G. Villarreal Jr., Y. Zhang, H.B. Larman, J. Gracia-Sancho, A. Koo, G. Garcia-Cardena, Defining the regulation of KLF4 expression and its downstream transcriptional targets in vascular endothelial cells, Biochem. Biophys. Res. Commun. 391 (2010) 984–989.
[14] G.I. Mun, I.S. Kim, B.H. Lee, Y.C. Boo, Endothelial argininosuccinate synthetase 1. Regulates nitric oxide production and monocyte adhesion under static and laminar shear stress conditions, J. Biol. Chem. 286 (2011) 2536–2542.
[15] G.I. Mun, S.M. An, H. Park, H. Jo, Y.C. Boo, Laminar shear stress inhibits lipid peroxidation induced by high glucose plus arachidonic acid in endothelial cells, Am. J. Physiol. Heart Circ. Physiol. 295 (2008) H1966–H1973.
[16] B. van der Loo, M.J. Fenton, J.D. Erusalimsky, Cytochemical detection of a senescence-associated beta-galactosidase in endothelial and smooth muscle cells from human and rabbit blood vessels, Exp. Cell. Res. 241 (1998) 309–315.
[17] Y.C. Boo, G. Sorescu, N. Boyd, I. Shiojima, K. Walsh, J. Du, H. Jo, Shear stress stimulates phosphorylation of endothelial nitric-oxide synthase at Ser1179 by Akt-independent mechanisms: role of protein kinase A, J. Biol. Chem. 277 (2002) 3388–3396.
[18] M.J. Rieder, R. Carmona, J.E. Krieger, K.A. Pritchard Jr., A.S. Greene, Suppression of angiotensin-converting enzyme expression and activity by shear stress, Circ. Res. 80 (1997) 312–319.
[19] A.R. Baydoun, P.W. Emery, J.D. Pearson, G.E. Mann, Substrate-dependent regulation of intracellular amino acid concentrations in cultured bovine aortic endothelial cells, Biochem. Biophys. Res. Commun. 173 (1990) 940–948.
[20] J.S. Pollock, U. Forstermann, J.A. Mitchell, T.D. Warner, H.H. Schmidt, M. Nakane, F. Murad, Purification and characterization of particulate endothelium-derived relaxing factor synthase from cultured and native bovine aortic endothelial cells, Proc. Natl. Acad. Sci. USA 88 (1991) 10480–10484.
[21] J.P. Cooke, P.S. Tsao, Arginine: a new therapy for atherosclerosis?, Circulation 95 (1997) 311–312
[22] K.K. McDonald, S. Zharikov, E.R. Block, M.S. Kilberg, A caveolar complex between the cationic amino acid transporter 1 and endothelial nitric-oxide synthase may explain the ‘‘arginine paradox”, J. Biol. Chem. 272 (1997) 31213–31216.
[23] P.W. Shaul, E.J. Smart, L.J. Robinson, Z. German, I.S. Yuhanna, Y.S. Ying, R.G.W. Anderson, T. Michel, Acylation targets endothelial nitric-oxide synthase to plasmalemmal caveolae, J. Biol. Chem. 271 (1996) 6518–6522.
[24] B.R. Flam, P.J. Hartmann, M. Harrell-Booth, L.P. Solomonson, D.C. Eichler, Caveolar localization of arginine regeneration enzymes, argininosuccinate synthase, and lyase, with endothelial nitric oxide synthase, Nitric oxide 5 (2001) 187–197.
[25] B.R. Flam, D.C. Eichler, L.P. Solomonson, Endothelial nitric oxide production is tightly coupled to the citrulline-NO cycle, Nitric oxide 17 (2007) 115–121.
[26] B.L. Goodwin, L.P. Solomonson, D.C. Eichler, Argininosuccinate synthase expression is required to maintain nitric oxide production and cell viability in aortic endothelial cells, J. Biol. Chem. 279 (2004) 18353–18360.
[27] B.L. Goodwin, L.C. Pendleton, M.M. Levy, L.P. Solomonson, D.C. Eichler, Tumor necrosis factor-alpha reduces argininosuccinate synthase expression and nitric oxide production in aortic endothelial cells, Am. J. Physiol. Heart Circ. Physiol. 293 (2007) H1115–H1121.
[28] C.C. Matouk, P.A. Marsden, Epigenetic regulation of vascular endothelial gene expression, Circ. Res. 102 (2008) 873–887.
[29] L.J. Nicholson, P.R. Smith, L. Hiller, P.W. Szlosarek, C. Kimberley, J. Sehouli, D. Koensgen, A. Mustea, P. Schmid, T. Crook, Epigenetic silencing of argininosuccinate synthetase confers resistance to platinum-induced cell death but collateral sensitivity to arginine auxotrophy in ovarian cancer, Int. J. Cancer 125 (2009) 1454–1463.
[30] D.V. Santi, A. Norment, C.E. Garrett, Covalent bond formation between a DNA-cytosine methyltransferase and DNA containing 5-azacytosine, Proc. Natl. Acad. Sci. USA 81 (1984) 6993–6997.
[31] B. Shen, R.S. Smith Jr., Y.T. Hsu, L. Chao, J. Chao, Kruppel-like factor 4 is a novel mediator of Kallistatin in inhibiting endothelial inflammation via increased endothelial nitric-oxide synthase expression, J. Biol. Chem. 284 (2009) 35471–35478.
[32] J. Padilla, R.A. Harris, L.D. Rink, J.P. Wallace, Characterization of the brachial artery shear stress following walking exercise, Vasc. Med. 13 (2008) 105–111.

Biochemical and Biophysical Research Communications 420 (2012) 456–461

Contents lists available at SciVerse ScienceDirect

Biochemical and Biophysical Research Communications

journal homepage: www.elsevier.com/locate/ybbrc

The role of the Cx43 C-terminus in GJ plaque formation and internalization

Praween Wayakanon [a,b], Rajib Bhattacharjee [a,b], Ken-ichi Nakahama [a,*], Ikuo Morita [a,b]

[a] Department of Cellular Physiological Chemistry, Graduate School, Tokyo Medical and Dental University, 1-5-45 Yushima, Bunkyo-ku, Tokyo 113-8549, Japan
[b] Global Center of Excellence Program, International Research Center for Molecular Science in Tooth and Bone Diseases, Tokyo Medical and Dental University, 1-5-45 Yushima, Bunkyo-ku, Tokyo 113-8549, Japan

ARTICLE INFO

Article history:
Received 2 March 2012
Available online 10 March 2012

Keywords:
Gap junction (GJ)
Connexin 43 (Cx43)
Annular gap junction (AGJ)
C-terminus

ABSTRACT

Connexin 43 (Cx43) is a major gap junction (GJ) protein found in many mammalian cell types. The C-terminal (CT) domain of Cx43 has unique characteristics in terms of amino acid (aa) sequence and its length differs from other connexins. This CT domain can be associated with protein partners to regulate GJ assembly and degradation, which results in the direct control of gap junction intercellular communication (GJIC). However, the essential roles of the CT regions involved in these mechanisms have not been fully elucidated. In this study, we aimed to investigate the specific regions of Cx43CT involved in GJ formation and internalization. Wild type $Cx43_{(382aa)}$ and 10 CT truncated mutants were stably expressed in HeLa cells as GFP or DsRed tagged proteins. First, we found that the deletion of 235–382aa from Cx43 resulted in failure to make GJ and establish GJIC. Second, the Cx43 with 242–382aa CT deletion could form functional GJs and be internalized as annular gap junctions (AGJs). However, the plaques consisting of Cx43 with CT deletions (Δ242–382aa to Δ271–382aa) were longer than the plaques consisting of Cx43 with CT deletions (Δ302–382aa). Third, co-culture experiments of cells expressing wild type $Cx43_{(382)}$ with cells expressing Cx43CT mutants revealed that the directions of GJ internalization were dependent on the length of the respective CT. Moreover, a specific region, 325–342aa residues of Cx43, played an important role in the direction of GJ internalization. These results showed the important roles of the Cx43 C-terminus in GJ expression and its turnover.

1. Introduction

Gap junction (GJ) channels connect the cytoplasms of two apposing cells by docking via a half channel termed a connexon to provide cell–cell communication. Gap junction intercellular communication (GJIC) allows small molecules of less than 1 kDa, including secondary messengers, to pass from one cell to another [1]. Connexons are composed of hexamers of four-transmembrane protein termed connexins (Cxs) [2]. Once transported to the plasma membrane, connexons (hemichannels) routinely assemble in clusters as a double-membrane spanning GJ plaques that are composed of a few to thousands of channels. The size of GJ plaques may vary from a few square nanometers to many square micrometers [3]. The communication via GJ is regulated by the dynamic processes of GJ formation and removal [4]. The removal of GJ from the cell surface involves a unique process. The entire GJ, or a part of it, is endoexocytosed into only one of the two contacting cells [5]. This internalization process generates double-membrane vesicles, termed annular gap junctions (AGJs) or connexosomes. The formation of AGJ vesicles from entire GJs resulted in a rapid reduction in the intercellular communication between two cells [6].

Connexin 43 (Cx43) is a 43 kDa GJ protein widely expressed in many mammalian cell types [7]. It has a short half-life of approximately 1–5 h. Since the turnover of Cx43 is rapid, it has been proposed that Cx43 degradation is important for the regulation of GJIC under pathophysiological conditions [8]. The 17-kDa carboxyl terminal (CT) domain of Cx43 has special features in terms of amino acid sequence and length, which differ from other Cxs [9–11]. It is reported that the Cx43CT domain is extensively phosphorylated by different protein kinases at different motifs containing serine or tyrosine residues [12]. Moreover, this CT domain has been reported to be associated with other proteins to stabilize Cx43 anchoring in plasma membranes [13–15]. Associations of Cx43CT with protein partners have also been proposed to regulate Cx43 assembly and degradation, but the overall functions remain unclear. The aim of this study was to investigate the role of the CT domain of Cx43 in the formation of GJ plaques and in internalization of GJ plaques as an AGJ vesicle. We found that three different amino acid regions in the CT domain of Cx43 played different roles as follows: (1) the region between 235 and 242aa is important for GJ plaque assembly at the plasma membrane; (2) the region between 271 and 302aa is important for sizing of the GJ plaque and AGJ; and (3) the region

* Corresponding author. Fax: +81 3 5803 0212.
E-mail address: nakacell@tmd.ac.jp (K.-i. Nakahama).

0006-291X/$ - see front matter © 2012 Elsevier Inc. All rights reserved.
http://dx.doi.org/10.1016/j.bbrc.2012.03.018

between 325 and 342aa is important for the directionality of GJ internalization. These findings suggest that the formation and internalization of GJ are dependent on the regions of the Cx43 CT domain.

2. Materials and methods

2.1. Cx43-GFP and Cx43-DsRed constructs

DNA fragments coding full-length rat Cx43 (382aa, GenBank ID: NM_012567) and CT truncated mutants [235aa(Δ236–382aa), 242aa(Δ243–382aa), 251aa(Δ252–382aa), 260aa(Δ261–382aa), 271aa(Δ272–382aa), 302aa(Δ303–382aa), 325aa(Δ326–382aa), 342aa(Δ343–382aa), 370aa(Δ371–382aa), and 378aa(Δ379–382aa)] were amplified by a polymerase chain reaction (PCR)-based technique using proofreading DNA polymerase (Pyrobest, Takara, Japan). These DNA fragments were cloned into pEGFP-N3 or a pDsRed monomer (Clonetech, USA). Then, the coding regions of fusion protein were subcloned into a retrovirus expression vector, pQCXIP (Clonetech, USA) (Fig. 1A). To make the deletion mutant Cx43(Δ325–342aa) expressing vector, the Cx43(1–324aa) and Cx43(343–382aa) coding regions were amplified, then these two fragments were ligated via a *Pst*I restriction site (Fig. 3A). All constructs were verified by analysis of restriction enzyme digests and DNA sequencing.

2.2. Cell line and cell culture conditions

Human epitheloid cervix carcinoma cells (HeLa, RIKEN BioResourse Center, Japan) and 293FT cells (Invitrogen, USA) were maintained in Dulbecco's modified Eagle medium (DMEM, Invitrogen, USA) supplemented with 10% fetal bovine serum (FBS) at 37 °C, 100% humidity and 5% CO_2/95% air. Cells were routinely subcultured by trypsinization with 0.05% Trypsin-0.02% EDTA in PBS, and the medium was changed twice a week.

2.3. Establishment of clones expressing the Cx-GFP/DsRed fusion protein

The retrovirus vector and pCL-10A1 (amphotropic vector, Imgenex Corp., USA) were co-transfected to the packaging cell line 293FT using Lipofectamine 2000® (Invitrogen, USA) as described previously [16]. Three days after the transfection, a virus containing conditioned medium was harvested. Then, HeLa cells were infected with the virus containing medium with polybrane (8 μg/ml, Millipore, USA). Three days after infection, Cx43-GFP- or Cx43-DsRed-expressing cells were cultured with 2 μg/ml of puromycin (InvivoGen, USA) containing 10% FBS DMEM for 2 weeks to establish stable clones.

2.4. Immunoblot analysis

Parental HeLa and Cx43 infected cells were harvested on ice in lysis buffer (0.02 M Tris–HCl, 0.137 M NaCl, 0.002 M EDTA, 1% Nonidet P-40 and 10% glycerol, pH 7.6) containing a protease and phosphatase inhibitor cocktail (Sigma, USA). The lysates were then ultrasonicated on ice for 20 s. Total protein concentrations were determined by a Protein Assay kit (Bio-Rad, USA). The protein samples were separated on 8% SDS–polyacrylamide gels, then transferred onto PVDF membranes, and blocked with 5% skim milk (BD transduction, USA) in TBS-T (0.05 M Tris–HCl, 0.150 M NaCl and 0.2% Tween-20, pH7.6). The membranes were incubated with anti-GFP antibody (BD Biosciences, USA) at 1:500 dilution in 5% skim milk in TBS-T at 4 °C overnight. After washing, the membranes were incubated with HRP-conjugated anti-rabbit IgG (GE Healthcare, UK) at 1:1500 dilution at 4 °C for 2 h. The blots were developed using a chemiluminescence method (ECL-plus; GE Healthcare) and were detected by LAS-1000 luminescent image analyzer (Fujifilm, Japan). The blots were reprobed with HRP-conjugated anti-β-actin rabbit polyclonal IgG (MBL, Japan) at 1:500 dilution.

2.5. Cell imagings of Cx43-GFP and -DsRed in living cells

Fluorescence images of GFP- and DsRed-tagged Cx43 were acquired by a LSM 510 META (Carl Zeiss, Germany) confocal microscope. For live cell imaging, cells were placed on a temperature-, CO_2– and humidity-controlled stage. Focus, contrast and brightness settings remained constant during the course of imaging acquisition.

2.6. Quantitative and statistical image analyses

GJ plaque length and AGJ diameter were measured using Zeiss software. Statistical analyses of GJ plaque sizes and AGJ were done in a total of 50 cell-pairs. The experiments were repeated in triplicate. GJ plaques and AGJs were categorized into three groups by size. Then, the ratio of each group was calculated and represented by percentages. Statistical analysis of AGJs internalization directions was also done by counting the number of cells containing internalizing vesicles in a total of 50 cell-pairs in triplicate experiments. The ratio of Cx43-GFP and -DsRed expressing cells containing internalizing AGJs was calculated and represented by percentage values. Data are shown as means ± SEM. Comparisons were made using an independent *t-test* and one-way ANOVA. In all analyses, a p value less than 0.05 was considered statistically significant.

3. Results

3.1. Wild type Cx43 and CT truncated mutants form different sizes of GJ plaques and AGJs

To examine the role of CT in the formation of GJ plaques and AGJs, the wild type Cx43 (382aa) and CT truncated mutants were expressed in non-endogenous connexin-expressing HeLa cells as fusion proteins (with GFP or DsRed) (Fig. 1A). The expression of Cx43-GFP fusion proteins was confirmed by immunoblotting using an antibody against GFP (Fig. 1B). These Cx43 expressing cells showed no different characteristics in terms of cell shape and size compared to parental HeLa cells (data not shown). The wild type $Cx43_{(382aa)}$-GFP and -DsRed were assembled into typical GJ plaques as green and red fluorescent lines at the junction of the infected cells, respectively (arrows in Fig. 1C). The observed GJ plaques from wild type $Cx43_{(382aa)}$-GFP showed variation in length from shorter than 1 μm to a maximum length of 15 μm. Besides GJ plaque formation, wild type $Cx43_{(382aa)}$-GFP formed internalizing AGJ vesicles that originated from a small region or the entire GJ plaque. The AGJs were observed as a circular structure in the cytoplasm. The AGJs from wild type $Cx43_{(382aa)}$-GFP showed variation in diameter from smaller than 1 μm to a maximum of 5 μm (arrow heads in Fig. 1C).

$Cx43_{(235aa)}$-GFP, the shortest CT mutant, did not show any formations of GJ plaque or AGJ (Fig. 1D). On the other hand, $Cx43_{(242aa)}$-GFP, the 7 aa longer CT mutant than $Cx43_{(235aa)}$-GFP could form GJ plaques and AGJ vesicles. This finding suggested an important role of the CT domain 235–242aa of Cx43 in GJ formation at the plasma membrane. Interestingly, GJ plaques and AGJs formed by four mutants ($Cx43_{(242aa)}$-GFP to $Cx43_{(271aa)}$-GFP) were larger than that formed by wild type $Cx43_{(382aa)}$-GFP. The

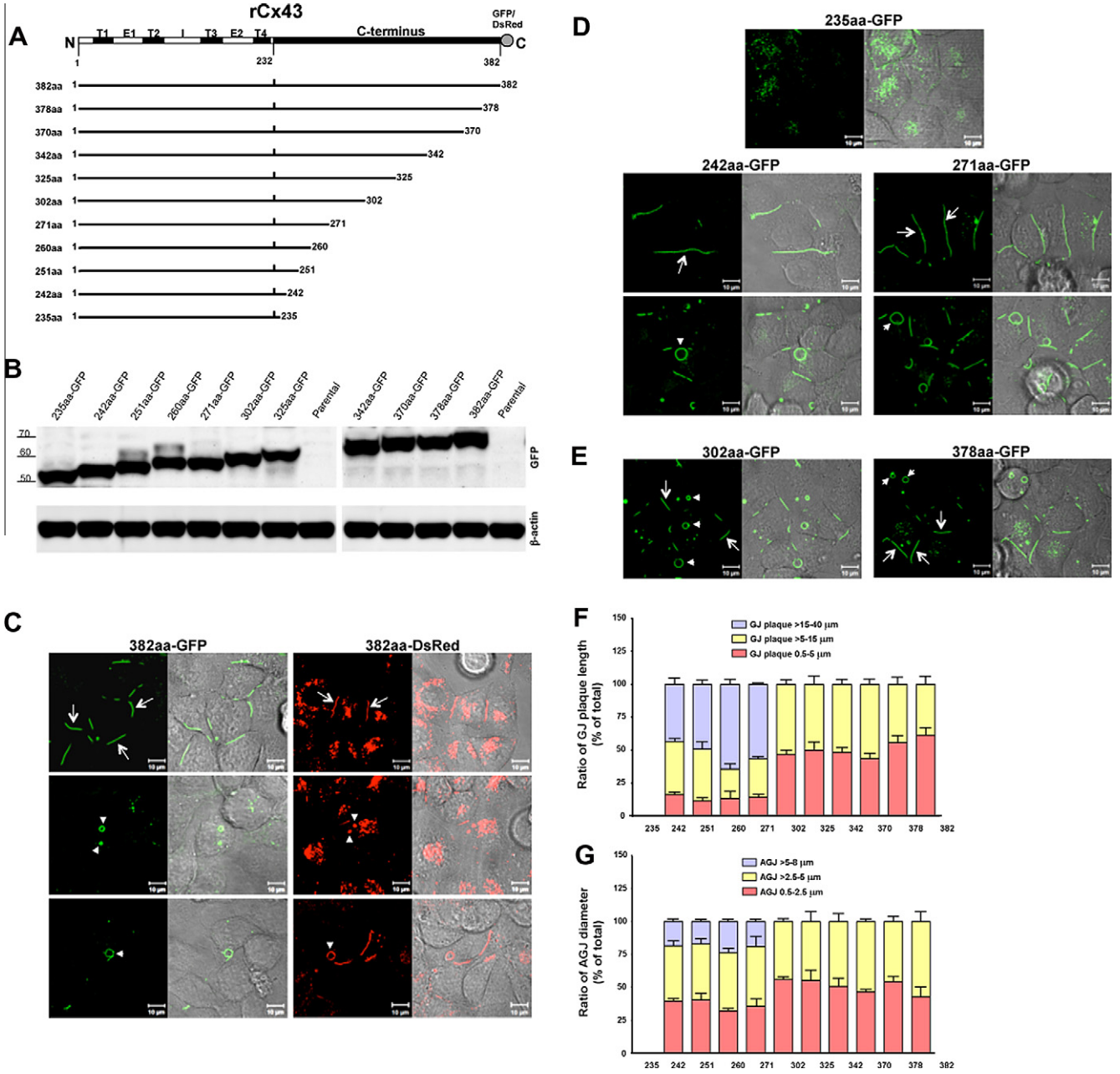

Fig. 1. Formation of GJ plaque and AGJ of wild type Cx43 and CT-truncated mutants. (A) Schematic diagram summarizing a 382aa wild type Cx43 and 10 random truncations of CT. (B) Protein lysates from parental HeLa and cells overexpressing Cx43-GFP were immunoblotted with an anti-GFP antibody. β-actin was used as a protein loading control. (C) Wild type 382aa-GFP (left panel) and 382aa-DsRed (right panel) formed GJ plaques no longer than 15 μm (upper panel, arrows), AGJs 1–3 μm in diameter (middle panel, arrow heads) and large AGJ about 5 μm in diameter (lower panel, arrow head). (D) No GJ plaques could be observed from 235aa-GFP (upper panel). The 242aa- to 271aa-GFP formed large GJ plaques 15–40 μm in length (upper panel, arrows) and AGJs 5–8 μm in diameter (lower panel, arrow heads). (E) 302aa- to 378aa-GFP formed GJ plaques no longer than 15 μm in length (arrows) and AGJs no larger than 5 μm (arrow heads). Schematic diagrams of ratios of (F) GJ plaque length and (G) AGJ diameter in a total of 50 cell-pairs in triplicate experiments. Scale bar = 10 μm.

GJ plaques assembled from these four CT mutants varied in length from shorter than 1 to 40 μm, which is 2.5 times longer than that observed in wild type $Cx43_{(382aa)}$-GFP. These CT mutants also formed large AGJs of about 8 μm in diameter which was 1.6 times larger than that observed in wild type $Cx43_{(382aa)}$-GFP (Fig. 1D, arrow heads). The other five CT mutants ($Cx43_{(302aa)}$-GFP to $Cx43_{(378aa)}$-GFP) formed GJ plaques of up to 15 μm in length and AGJs up to 5 μm in diameter (Fig. 1E, arrows and arrow heads), and these were similar to those observed in wild type $Cx43_{(382aa)}$-GFP. GJ plaques and AGJs were categorized into 3 groups by size (long/large, medium, short/small), and represented as a percentage for each group. About 50% of GJ plaques formed by Cx43CT mutants shorter than 271aa were long, whereas Cx43CT mutants longer than 302aa did not form large GJ plaques (Fig. 1F and 1G). This finding suggests an important role of the amino acid region between 271 and 302aa residues in the C-terminus of Cx43 in the size of GJ plaques and AGJ formations.

Fluorescence recovery after photobleaching (FRAP) experiments showed that all CT mutants, except for $Cx43_{(235aa)}$-GFP, formed functional GJs (Supplementary Fig. 1A).

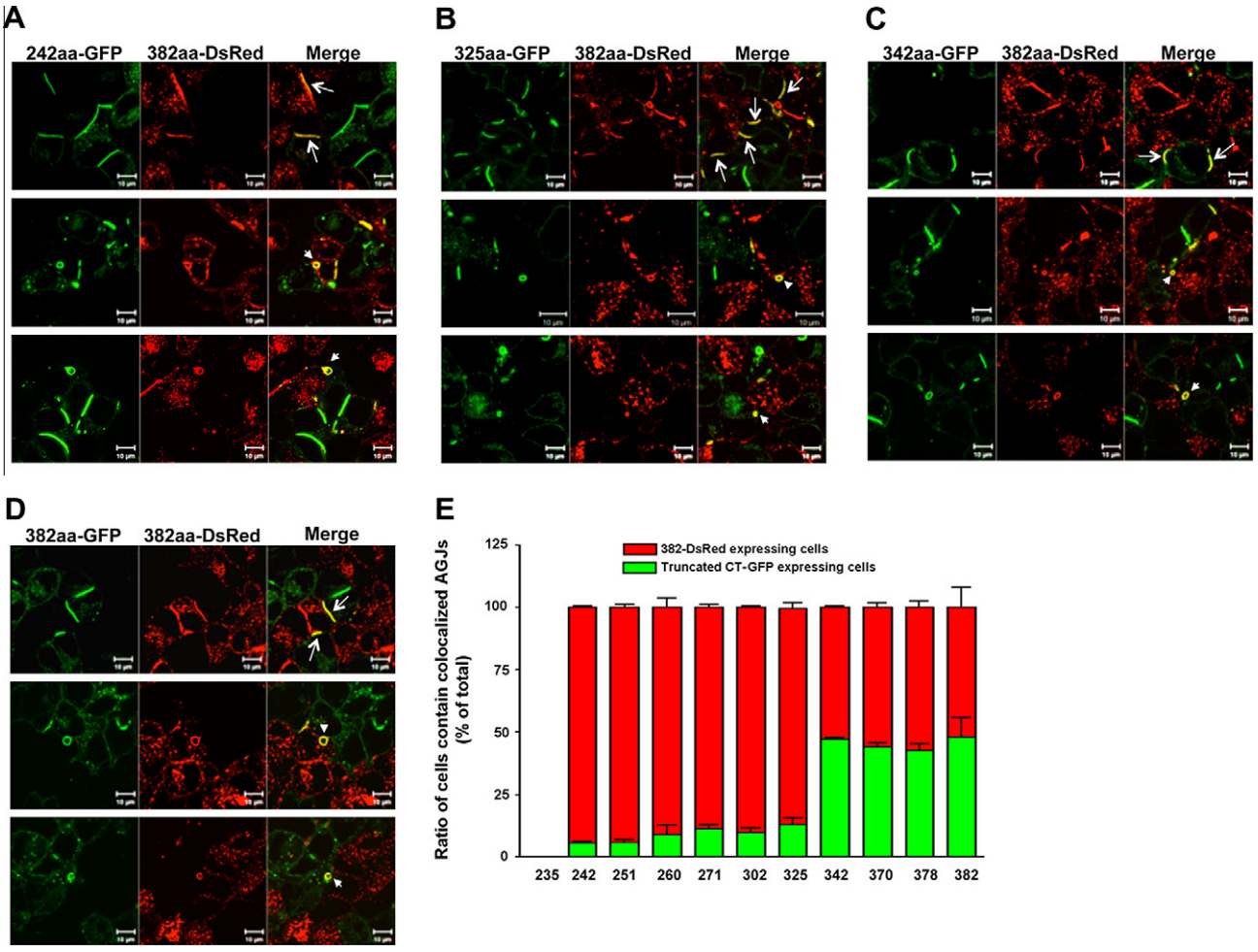

Fig. 2. Directions of AGJ internalization are dependent on the length of the C-terminal domain of Cx43. Colocalized GJ plaques and AGJs between 382aa-DsRed and (A) 242aa-GFP, (B) 325aa-GFP, (C) 342aa-GFP and (D) 382aa-GFP are shown in yellow. Colocalizations of GJ plaque (upper panels, arrows), internalized AGJs into 382aa-DsRed cells (middle panel, arrow heads) and into GFP cells (lower panel, arrow heads). (E) Schematic diagram of the ratio of cells containing colocalized AGJs in a total of 50 cell-pairs in triplicate experiments. Scale bar = 10 μm.

3.2. CT mutants form GJ plaques and AGJs with wild type Cx43 at typical sizes

To investigate the details of Cx43CT's role in GJ plaque size, $Cx43_{(382aa)}$-DsRed-expressing cells were co-cultured with GFP-tagged Cx43CT mutant-expressing cells. All Cx43CT mutants longer than 242aa formed GJ plaques with $Cx43_{(382aa)}$-DsRed as shown in Fig. 2A–C. The length of the GJ plaques and the diameters of AGJs were shorter than 15 μm and smaller than 5 μm respectively, and were similar to those consisting of $Cx43_{(382aa)}$-DsRed and $Cx43_{(382aa)}$-GFP (Fig. 2D). The length of plaque made up of Cx43-$GFP_{(<271aa)}$ was sometimes longer than 15 μm (Fig. 1D and F), and this result suggested that the GJ plaque size and AGJ diameter were restricted not by the connexon of the shorter Cx43-GFP mutant, but by the connexon of $Cx43_{(382aa)}$-DsRed. The function of GJIC among these cells was confirmed by a parachute assay (Supplementary Fig. 1B).

3.3. The Direction of GJ internalization is dependent on the length of Cx43CT

To investigate the role of Cx43CT in the direction of GJ internalization, the cells containing AGJ vesicles between a pair of wild type $Cx43_{(382aa)}$-DsRed and GFP-tagged Cx43CT mutant expressing cells were examined (middle and lower panels in Fig. 2A–D). The ratios of presence of AGJs were randomly examined in a total of 50 cell-pairs and repeated in triplicate experiments (Fig. 2E). A co-culture experiment of $Cx43_{(382aa)}$-DsRed-expressing cells with $Cx43_{(242\ to\ 325aa)}$-GFP expressing cells showed unidirectional internalization of AGJs, that is, AGJs were present in 87–95 percent of wild type $Cx43_{(382aa)}$-DsRed-expressing cells. On the other hand, a co-culture experiment of $Cx43_{(382aa)}$-DsRed-expressing cells with $Cx43_{(342aa\ to\ 382aa)}$-GFP- expressing cells showed bidirectional internalization of AGJs into 52–57 percent of $Cx43_{(382aa)}$-DsRed-expressing cells and 43–48 percent of GFP-expressing cells, respectively. These findings suggest an important role of the region between 325 and 342aa residues of the Cx43 CT domain in the direction of internalization of GJ plaques.

3.4. Deletion of the 325–342aa region confirms the important role of the length of C-terminal domain of Cx43 in the direction of GJ internalization

To investigate whether the region of 18aa between the 325 and 342aa residues of Cx43CT [S^{325}TISNSHAQPFDFPDDNQ^{342}] was important for the direction of GJ plaque internalization, this 18aa region was deleted from the CT of wild type Cx43 and then fused with GFP at the end of CT (Fig. 3A). The expression of $Cx43_{(\Delta 325–342aa)}$-GFP was determined by immublotting using an antibody against GFP (Fig. 3B). The GJ plaque formation and AGJs

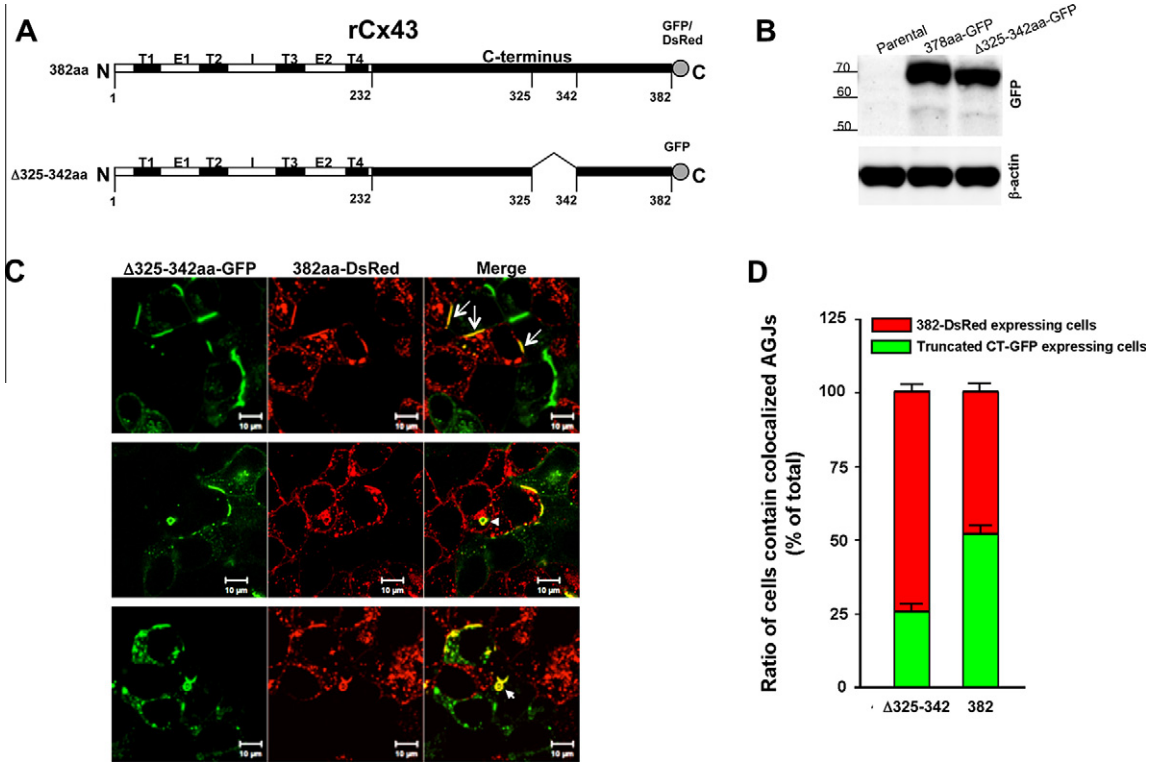

Fig. 3. Deletion of 325–342aa confirms the effect on the direction of AGJ internalization. (A) Schematic diagram summarizing the construction of an 18aa (325–342aa) deletion mutant. (B) Protein lysates from parental HeLa cells, and cells expressing wild type 382aa Cx43-GFP and Δ325–342aa-GFP were immunoblotted with an anti-GFP antibody. β-Actin was used as a protein loading control. (C) Δ325–342aa-GFP cocultured with wild type 382aa-DsRed. Colocalized GJ plaques no longer than 15 μm (upper panel, arrows). Colocalized AGJ no larger than 5 μm internalized into 382aa-DsRed cells (middle panel, arrow head) and into Δ325–342aa-GFP cells (lower panel, arrow head). (D) Schematic diagram of the ratio of cells containing colocalized AGJs in a total of 50 cell-pairs in triplicate experiments. Scale bar = 10 μm.

internalization between $Cx43_{(\Delta 325-342aa)}$-GFP-expressing cells and $Cx43_{(382aa)}$-DsRed-expressing cells were similar to that observed between $Cx43_{(382aa)}$-DsRed-expressing cells and $Cx43_{(242\ to\ 325aa)}$-GFP-expressing cells (Figs. 2E and 3C). That is, the most unidirectional internalization of AGJs into $Cx43_{(382aa)}$-DsRed-expressing cells (middle and lower panels in Fig. 3C). Only 25% of cells expressing $Cx43_{(\Delta 325-342aa)}$-GFP contained AGJs (Fig. 3D). This finding confirmed the important role of the region between 325 and 342aa residues of the Cx43 C-terminal domain in the direction of internalization of GJ.

4. Discussion

In order to determine the role of Cx43CT in GJ formation and internalization, 10 sequentially truncated CT mutants of Cx43 tagged with GFP/DsRed were stably expressed in HeLa cells. This approach aimed to study the formation of GJ plaques and AGJ vesicles originating from different lengths of Cx43CT mutants in living cells by laser scanning confocal microscopy. A previous report showed that the wild type connexins tagged with fluorescence proteins on their CT could be clustered normally into typical GJ plaques [17]. The HeLa cells were used in this study because they do not express endogenous connexins [18]. Moreover, the Cx43-expressing HeLa cells did not show significant differences in cell shape or size compared to typical parental HeLa cells. The wild type $Cx43_{(382aa)}$-GFP or -DeRed formed a GJ plaque as fluorescent lines between 0.5 and 15 μm in length at the membrane junction between two contacting cells. Double-membrane AGJ vesicles between 0.5 and 5 μm in diameter were observed in the cytoplasmic space. The wild type 382aa-GFP and 382aa-DsRed did not show any differences in characteristics in either GJ plaques or AGJs.

Only the shortest mutant of Cx43-GFP, $Cx43_{(235aa)}$-GFP, did not form GJ or GJIC. All other longer mutants from 242aa were assembled into GJ plaques as fluorescent lines at sites of cell–cell apposition. All GJ plaques and AGJs originating from these CT mutants colocalized with caveolin-1 (Cav-1) in an immunostaining experiment (Supplementary Fig. 2). This finding suggested that GJ at the plasma membrane is localized in a lipid raft domain by association with Cav-1. Moreover, it is suggested that the internalization of AGJ is due to caveolae-dependent endocytosis [19]. The FRAP experiment showed that the assembled GJs originating from these CT mutants are functionally efficient (Supplementary Fig. 1). This finding suggested an important role of the amino acid region between 235 and 242aa residues [G^{235}VKDRVKG^{242}] in assembly of GJ plaques at the plasma membrane. This region between 234 and 243aa has been reported previously as a specific tubulin binding domain [20] because Cx43 was reported to be translationally inserted into the endoplasmic reticulum [21] and then transported through the Golgi apparatus [22]. Taken together with our finding, we conclude that region between 235 and 242aa plays an essential role in trafficking of Cx43, along with microtubules, to the cell membrane.

The Cx43CT mutants were classified into two groups according to the size of GJ plaques and AGJs. The first group was composed of four CT mutants from $Cx43_{(242aa)}$-GFP to $Cx43_{(271aa)}$-GFP, that showed GJ plaques between 0.5 and 40 μm in length, and AGJs between 0.5 and 8 μm in diameter. The second group was composed of five truncation mutants from $Cx43_{(302aa)}$-GFP to $Cx43_{(378aa)}$-GFP. They could form GJ plaques no longer than 15 μm and AGJs no larger than 5 μm, sizes similar to GJ and AGJ from wild type $Cx43_{(382aa)}$-GFP. This finding suggested a significant role of the region between 271 and 302aa [C^{271}SSPTAPLSPMSPPGYKLVTGDRNNSSCRNYN^{302}] of Cx43CT in determination of GJ

plaque size and AGJ diameter. These data suggested that this region may be responsible for facilitating the association of Cx43 with protein that plays a role in the endocytic pathway, such as a caveolae-dependent endocytosis [23]. Lacking these 31aa residues may interfere with the internalization of GJ and result in a long GJ plaque remaining at the plasma membrane. The large AGJs may be due to internalization of long GJs. Our finding was supported by recent publications; they reported that the PY motif (xPPxY) of Cx43CT [$P^{283}PGY^{286}$] was associated with Nedd4 [24] and Eps15 [25]. Therefore, Nedd4-mediated ubiquitination of Cx43CT may play a major role in the internalization of GJ plaques in physiological conditions.

One GJ plaque is internalized into only one of the two apposing cells [5]. Therefore, we examined the role of Cx43CT in this unique process of AGJ formation. A significant region of the Cx43 CT domain that is responsible for the direction of internalization was examined by a co-culture experiment with cells expressing GFP-tagged Cx43CT mutants and cells expressing $Cx43_{(382aa)}$-DsRed. When the Cx43CT mutants were smaller than 271aa, the length of GJ plaques formed between the GFP-tagged Cx43CT mutants and the $Cx43_{(382aa)}$-DsRed were shorter than those formed among GFP-tagged Cx43CT mutants. Furthermore, internalization of GJ plaques was observed more in $Cx43_{(382aa)}$-DsRed-expressing cells than in GFP-tagged Cx43CT mutant-expressing cells (unidirectional internalization). Owing to this unidirectional transport of AGJ, the GJ plaque formed between GFP-tagged Cx43CT mutants and the $Cx43_{(382aa)}$-DsRed was of normal size, as observed among $Cx43_{(382aa)}$-DsRed-expressing cells. We also found that the directions of GJ internalization depended on the length of the Cx43CT domain by a co-culture experiment of $Cx43_{(382aa)}$-DsRed-expressing cells with GFP-tagged Cx43CT mutant-expressing cells. The unidirectional internalization of GJ plaques into $Cx43_{(382aa)}$-DsRed-expressing cells was observed when Cx43CT mutants were shorter than 325aa. On the other hand, AGJs originating from Cx43CT mutants longer than 342aa existed almost equally in two apposing cells (bidirectional internalization). This finding suggested the significant role of 18aa residues between 325 and 342aa [S^{325}TISNSHAQPFDFPDDNQ^{342}] of the Cx43CT domain in the direction of GJ internalization. Moreover, we confirmed that this region (325–342aa) was important for directional internalization by a co-culture experiment of $Cx43_{(\Delta 325\text{-}342aa)}$-GFP-expressing cells with $Cx43_{(382aa)}$-DsRed-expressing cells. According to a previous study, phosphorylation sites of casein kinase 1 (CK1) were reported in this region [26]. They suggested that CK1 stimulated Cx43 GJ assembly via serine phosphorylation of Cx43CT. They also observed non-junctional Cx43 accumulation in the plasma membrane by treatment of cells with a CK1 inhibitor; however, the role of CK1 in GJ plaque internalization was not examined. Our data suggest that unidentified protein binding to this region induces active internalization of GJ plaque.

Finally, this study revealed that three important regions in the CT domain of Cx43 may play important roles in GJ formation and internalization. The region between 235 and 242aa residues is important for GJ plaque assembly at the plasma membrane. Moreover, the region between 271 and 302aa residues is important for determining the size of the GJ plaque and AGJ vesicles. Finally, the region between 325 and 342aa residues is important for direction of GJ internalization. These findings will contribute to the molecular understanding of Cx43 turnover.

Acknowledgments

This work was supported by research grant Global COE (Centers of Excellence) Program from the Japan Society for the Promotion of Science, Tokyo, Japan. This work was supported in part by research Grants 21659432 and 20390463 from the Japan Society for Promotion of Science, Tokyo, Japan.

Appendix A. Supplementary data

Supplementary data associated with this article can be found, in the online version, at http://dx.doi.org/10.1016/j.bbrc.2012.03.018.

References

[1] G.S. Goldberg, P.D. Lampe, B.J. Nicholson, Selective transfer of endogenous metabolites through gap junctions composed of different connexins, Nat. Cell Biol. 1 (1999) 457–459.
[2] R. Bruzzone, T.W. White, D.L. Paul, Connections with connexins: the molecular basis of direct intercellular signaling, Eur. J. Biochem. 238 (1996) 1–27.
[3] M.M. Falk, Connexin-specific distribution within gap junctions revealed in living cells, J. Cell Sci. 113 (Pt 22) (2000) 4109–4120.
[4] L.S. Musil, A.C. Le, J.K. VanSlyke, L.M. Roberts, Regulation of connexin degradation as a mechanism to increase gap junction assembly and function, J. Biol. Chem. 275 (2000) 25207–25215.
[5] K. Jordan, R. Chodock, A.R. Hand, D.W. Laird, The origin of annular junctions: a mechanism of gap junction internalization, J. Cell Sci. 114 (2001) 763–773.
[6] B.M. Nickel, B.H. DeFranco, V.L. Gay, S.A. Murray, Clathrin and Cx43 gap junction plaque endoexocytosis, Biochem. Biophys. Res. Commun. 374 (2008) 679–682.
[7] M. Koval, Pathways and control of connexin oligomerization, Trends Cell Biol. 16 (2006) 159–166.
[8] J.E. Saffitz, J.G. Laing, K.A. Yamada, Connexin expression and turnover: implications for cardiac excitability, Circ. Res. 86 (2000) 723–728.
[9] T.W. White, R. Bruzzone, Multiple connexin proteins in single intercellular channels: connexin compatibility and functional consequences, J. Bioenerg. Biomembr. 28 (1996) 339–350.
[10] D.A. Goodenough, J.A. Goliger, D.L. Paul, Connexins, connexons, and intercellular communication, Annu. Rev. Biochem. 65 (1996) 475–502.
[11] A. el Aoumari, C. Fromaget, E. Dupont, H. Reggio, P. Durbec, J.P. Briand, K. Boller, B. Kreitman, D. Gros, Conservation of a cytoplasmic carboxy-terminal domain of connexin 43, a gap junctional protein, in mammal heart and brain, J. Membr. Biol. 115 (1990) 229–240.
[12] P.D. Lampe, A.F. Lau, The effects of connexin phosphorylation on gap junctional communication, Int. J. Biochem. Cell Biol. 36 (2004) 1171–1186.
[13] B.N. Giepmans, W.H. Moolenaar, The gap junction protein connexin43 interacts with the second PDZ domain of the zona occludens-1 protein, Curr. Biol. 8 (1998) 931–934.
[14] A.M. Gumpert, J.S. Varco, S.M. Baker, M. Piehl, M.M. Falk, Double-membrane gap junction internalization requires the clathrin-mediated endocytic machinery, FEBS Lett. 582 (2008) 2887–2892.
[15] W.J. Larsen, H.N. Tung, S.A. Murray, C.A. Swenson, Evidence for the participation of actin microfilaments and bristle coats in the internalization of gap junction membrane, J. Cell Biol. 83 (1979) 576–587.
[16] R. Bhattacharjee, M. Kaneda, K. Nakahama, I. Morita, The steady-state expression of connexin43 is maintained by the PI3K/Akt in osteoblasts, Biochem. Biophys. Res. Commun. 382 (2009) 440–444.
[17] D.W. Laird, K. Jordan, T. Thomas, H. Qin, P. Fistouris, Q. Shao, Comparative analysis and application of fluorescent protein-tagged connexins, Microsc. Res. Tech. 52 (2001) 263–272.
[18] D.F. Hulser, B. Rehkopf, O. Traub, Dispersed and aggregated gap junction channels identified by immunogold labeling of freeze-fractured membranes, Exp. Cell Res. 233 (1997) 240–251.
[19] N. Balasubramanian, D.W. Scott, J.D. Castle, J.E. Casanova, M.A. Schwartz, Arf6 and microtubules in adhesion-dependent trafficking of lipid rafts, Nat. Cell Biol. 9 (2007) 1381–1391.
[20] B.N. Giepmans, I. Verlaan, T. Hengeveld, H. Janssen, J. Calafat, M.M. Falk, W.H. Moolenaar, Gap junction protein connexin-43 interacts directly with microtubules, Curr. Biol. 11 (2001) 1364–1368.
[21] J.T. Zhang, M. Chen, C.I. Foote, B.J. Nicholson, Membrane integration of in vitro-translated gap junctional proteins: co- and post-translational mechanisms, Mol. Biol. Cell 7 (1996) 471–482.
[22] K.L. Puranam, D.W. Laird, J.P. Revel, Trapping an intermediate form of connexin43 in the Golgi, Exp. Cell Res. 206 (1993) 85–92.
[23] A.M. Hommelgaard, K. Roepstorff, F. Vilhardt, M.L. Torgersen, K. Sandvig, B. van Deurs, Caveolae: stable membrane domains with a potential for internalization, Traffic 6 (2005) 720–724.
[24] K. Leykauf, M. Salek, J. Bomke, M. Frech, W.D. Lehmann, M. Durst, A. Alonso, Ubiquitin protein ligase Nedd4 binds to connexin43 by a phosphorylation-modulated process, J. Cell Sci. 119 (2006) 3634–3642.
[25] H. Girao, S. Catarino, P. Pereira, Eps15 interacts with ubiquitinated Cx43 and mediates its internalization, Exp. Cell Res. 315 (2009) 3587–3597.
[26] C.D. Cooper, P.D. Lampe, Casein kinase 1 regulates connexin-43 gap junction assembly, J. Biol. Chem. 277 (2002) 44962–44968.

Biochemical and Biophysical Research Communications 420 (2012) 462–466

Contents lists available at SciVerse ScienceDirect

Biochemical and Biophysical Research Communications

journal homepage: www.elsevier.com/locate/ybbrc

Inhibition of fatty acid translocase cluster determinant 36 (CD36), stimulated by hyperglycemia, prevents glucotoxicity in INS-1 cells

Yong-Woon Kim [a], Jun Sung Moon [b], Ye Jin Seo [a], So-Young Park [a], Jong-Yeon Kim [a], Ji Sung Yoon [b], In-Kyu Lee [c], Hyoung Woo Lee [b], Kyu Chang Won [b,*]

[a] Department of Physiology, School of Medicine, Yeungnam University, Daegu, Republic of Korea
[b] Department of Internal Medicine, School of Medicine, Yeungnam University, Daegu, Republic of Korea
[c] Department of Internal Medicine, School of Medicine, Kyungpook National University, Daegu, Republic of Korea

ARTICLE INFO

Article history:
Received 21 February 2012
Available online 10 March 2012

Keywords:
CD36
Glucotoxicity
Insulin secretion
INS-1 cells

ABSTRACT

The purpose of the present study was to determine whether exposure of pancreatic islets to glucotoxic conditions changes fatty acid translocase cluster determinant 36 (CD36) and examine the role of CD36 on the induction of glucotoxicity. We measured the changes of CD36 and insulin secretion in high glucose (30 mM) exposed INS-1 cells and CD36 suppressed INS-1 cells by transfection of CD36 siRNA. The intracellular peroxide level of INS-1 cells increased in the high glucose media compared to normal glucose (5.6 mM) media. The mRNA levels of insulin and PDX-1, as well as glucose stimulated insulin secretion (GSIS) were decreased in INS-1 cells exposed to high glucose media compared to normal glucose media, while CD36 and palmitate uptake were significantly elevated with exposure to high glucose media for 12 h. The inhibition of CD36 reversed the decreased GSIS and intracellular peroxide level in INS-1 cells. These results suggest that high glucose may exacerbate glucotoxicity via increasing fatty acid influx by elevation of CD36 expression, and that CD36 may be a possible target molecule for preventing glucotoxicity in pancreatic beta-cells.

1. Introduction

Glucotoxicity in the pancreatic beta-cell is defined as nonphysiological and potentially irreversible cellular damage induced by chronic exposure to supraphysiologic glucose concentrations, which leads to defective insulin secretion and worsening glucose regulation [1–3]. Preservation of beta-cells, through tight glycemic regulation, is an essential component of the treatment strategy for type 2 diabetes. It is well known that one of the main mechanisms of glucotoxicity is chronic oxidative stress [1]. However, tight glycemic control alone often fails to complete preservation of beta-cells in type 2 diabetic patients.

Though free fatty acids (FFA) stimulate insulin secretion, chronically elevated FFA impairs pancreatic beta cell function *in vitro* and *in vivo*, which leads to the induction of lipotoxicity [4,5]. FFAs move into cells through a passive concentration-dependent diffusion, and it has been reported that there are active transport systems to enhance FFA uptake [6]. Fatty acid translocase cluster determinant 36 (CD36), which is part of the FFA transporter system, has been identified in several tissues such as muscle, liver, and insulin-producing cells [7]. Several studies [8,9] have reported that induction of CD36 increases uptake of FFA in INS-1 cells and Caco-2/15 cells, suggesting the functional interplay between glucose and FFA in terms of insulin secretion and oxidative metabolism.

Interestingly, the lipotoxic effect of FFA on normal pancreatic beta-cells is induced only by the combined exposure to hyperglycemic conditions [10–12]. It is also reported that hyperglycemic conditions induce the expression of CD36 in intestinal epithelial cells [9]. However, we do not currently know the regulating mechanism and physiological role of CD36 on glucotoxicity in pancreatic beta-cells.

The purpose of this study was to determine whether hyperglycemia enhances the expression of CD36, and whether the accompanying FFA influx can affect pancreatic beta-cell function, and if inhibition of CD36 reverses the deteriorated beta-cell function.

2. Materials and methods

2.1. INS-1 cell culture

INS-1 cells [13] were grown in 5% CO2-95% air at 37 °C in RPMI-1640 medium (GIBCO, Grand Island, NY) containing 11.1 mM pyruvate, 10 mM HEPES, 50 M 2-mercaptoethanol, 100 U penicillin/mL and 100 g streptomycin/mL. The RPMI-1640 medium used in all

* Corresponding author. Address: Department of Internal Medicine, School of Medicine, Yeungnam University, #317-1, Daemyungdong, Namgu, Daegu 705-717, Republic of Korea.
E-mail address: kcwon@med.yu.ac.kr (K.C. Won).

0006-291X/$ - see front matter © 2012 Elsevier Inc. All rights reserved.
http://dx.doi.org/10.1016/j.bbrc.2012.03.020

the experiments contained the supplements described above. The cells were passaged weekly after they had been detached with trypsin–EDTA. All studies were performed using INS-1 cells that were between passages 21 and 29. The glucotoxicity was induced by 3-day treatment of high glucose (30 mM) and confirmed by impaired glucose stimulated insulin secretion (GSIS) in INS-1 cells. CD36 mRNA expression was determined in 12-h exposed INS-1 cells at normal or high glucose condition.

2.2. Evaluation of reactive oxygen species (ROS) with flow cytometry

The intracellular peroxide levels [14] were detected by flow cytometric analysis with using an oxidation-sensitive fluorescein-labeled dye, carboxylated dichlorodi-hydrofluorescein diacetate (carboxy-H2DCFDA, Molecular Probes, Carlsbad, CA, USA). Upon oxidation by intracellular ROS, the non-fluorescent dye is converted into its fluorescent form. The INS-1 cells were labeled with 100 M carboxy-H2DCFDA for 1 h at 37 °C. Following the cell loading of the dye, the cells were washed twice with PBS and then put back into culture conditions for 2 h. The INS-1 cells were then harvested, washed twice with PBS and resuspended in trypsin–EDTA (0.25% trypsin, 2 mM Na4-EDTA, Invitrogen) for 5 min at 37 °C. To disperse the cells into a single cell suspension, INS-1 cells were gently passed 20 times in and out of a 200–1000 μL tip. The cells were then washed twice with ice-cold PBS. The cells were analyzed using a 488 nm argon laser EPICS XL-MCL flow cytometer that was controlled by EXPO 32-ADC software (Beckman Coulter, Fullerton, CA). The ROS values were analyzed based on fluorescence intensity.

2.3. GSIS

Static incubation of the INS-1 rat insulinoma cell line in Krebs–Ringer buffer (KRB) (118 mmol/L NaCl, 4.7 mmol/L KCl, 2.5 mmol/L $CaCl_2$, 1.18 mmol/L KH_2PO_4, 1.18 mmol/L $MgSO_4$, 25 mmol/L $NaHCO_3$, 10 mmol/L HEPES and 0.1% BSA, pH 7.4) that contained either non-stimulatory or stimulatory concentrations of glucose (5.6 mM or 16.7 mM, respectively) was performed for 1 h [11]. The insulin levels in the KRB media collected from the static incubations from the INS-1 cells by using a 95.5 ethanol: hydrochloric acid solution were measured using a enzyme-linked immunosorbent assay (Rat Insulin ELISA kit; Mercodia, Uppsala, Sweden).

2.4. Construction of siRNA for CD36

INS-1 cells were plated at a density of 1×10^6 cells per well in a 6-well plate and subcultured for 2 days in INS-1 medium. The cells were transiently transfected with CD36 siRNA oligos in Lipofectamine™ 2000 Transfection Reagent (Invitrogen, Carlsbad, CA). The cells were incubated for 4 h, washed to remove siRNA, and then cultured in media containing the indicated glucose concentration (11.1 or 30 mM). Cells were harvested 24 h after transfection. The siRNA sequences are as follows: CD36 (siRNA#1, siRNA#2 and siRNA#3-scramble) siRNA#1, CUG AGU AGG UUU UUC UCU U (sence); AAG AGA AAA ACC UAC UCA G (antisence) and siRNA#2, GUU CUU UUC CUC UGA CAU U (sence); AAU GUC AGA GGA AAA GAA C (antisence) and siRNA#3, CAU CAA UUU CUG CAG AAC U (sence); AGU UCU GCA GAA AUU GAU G (antisence).

2.5. Real time PCR

Total RNA was obtained from the INS-1 cells by using Trizol Reagent (Bio Science Technology, Korea). cDNA was synthesized using 1 μg total RNA with oligo-(dT) primers and Prime RT Premix (GENET BIO, Korea). Real-time RT-PCR was performed in the LightCycler (Roche, Germany) as previously described. The following primers were used: for insulin, 5′-ACC CAA GTC CCG TCG TGA AGT-3′ (forward) and 5′-CCA GTT GGT AGA GGG AGC AGA TG-3′ (reverse); for PDX-1,5′-GGC TTA ACC TAA ACG CCA CA-3′ (forward) and 5′-GGG ACC GTC CAA GTT TGT AA-3′ (reverse); for CD36, 5′-GTG GCT AAA TGA GAC TGG GAC C-3′ (forward) and 5′-AGA CCA TCT CAA CCA GGC CC-3′ (reverse); for β-actin, 5′-TAC TGC

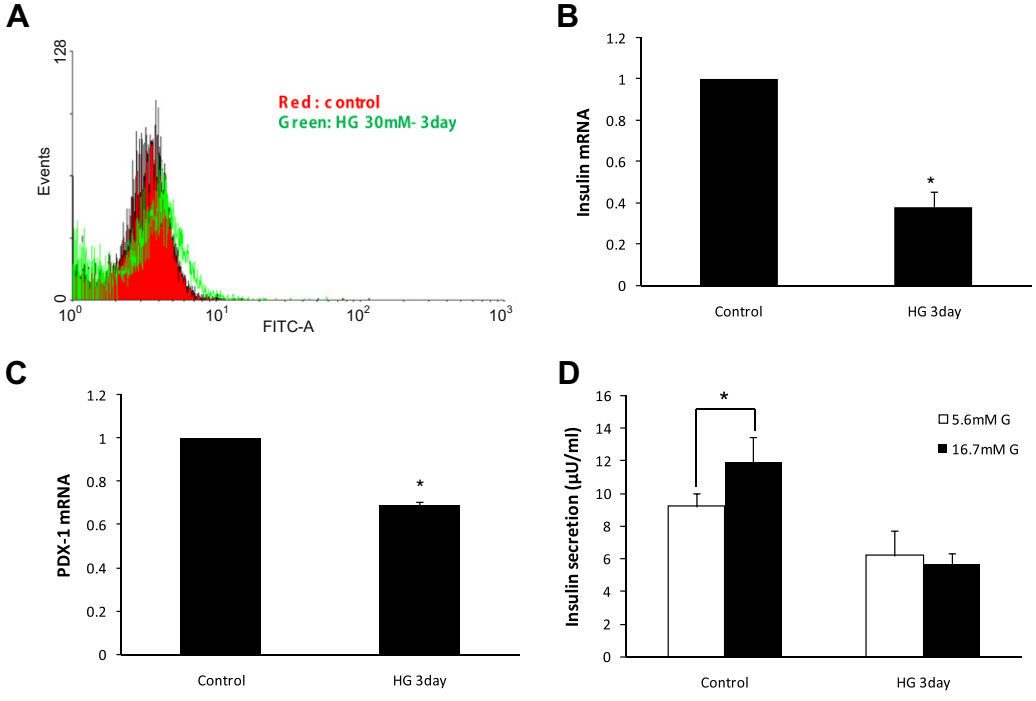

Fig. 1. Effect of 3 day-treatment with high glucose (30 mM, HG 3 day) or normal glucose (5.6 mM, Control) on intracellular peroxide level (A), mRNA expression of insulin (B) and PDX-1 (C), and glucose stimulated insulin secretion (D) in INS-1 cells. *$P < 0.05$.

CCT GGC TCC TAG CA-3′ (forward) and 5′-TGG ACA GTG AGG CCA GGA TAG-3′ (reverse).

2.6. Palmitate uptake

Palmitate uptake was determined with a modified method by Wallin et al. [8]. Briefly, cells were trypsinized and washed in ice-cold KRB in the absence of glucose. An equal amount of cells was transferred to new tubes and centrifuged. Cells were re-suspended in ice-cold KRB (11.1 mmol/L glucose) and 2.1 μCi ^{14}C-palmitate (Perkin Elemer Life Science Inc., Boston, MA) and transferred to microcentrifuge tubes (50 μL), which were prepared with a bottom layer of 6 mol/L urea solution (20 μL) over layered by a 10:3 mixture dibutyl-dinonylphthalate (200 μL). Uptake was terminated by centrifugation at 8000 rpm for 15 min. The urea layer containing the cells was transferred into scintillation vials and the radioactivity measured after adding scintillation cocktail (Aqueous Counting Scintillation, Amersham, Canada) using a liquid scintillation counter (Packard Bioscience Company, Meriden, CT).

2.7. Data analysis

All the values are expressed as means ± SE. Student's *t*-test was used for the statistical analysis, and the differences between groups were considered to be significant at p values <0.05.

3. Results

To induce glucotoxicity in the INS-1 cell line, we treated the cells with high glucose (30 mM) for 3 days in the cultured medium. The cells cultured in high glucose conditions showed decreased mRNA expressions of insulin and PDX-1, loss of GSIS, and increased intracellular peroxide level determined by FACS (Fig. 1).

To determine whether CD36 is associated with high glucose conditions in the INS-1 cell line, we measured CD36 levels following a 12 h – treatment with high glucose. The expression of CD36 was significantly elevated in the high glucose treated group as compared to controls, whereas insulin expression decreased (Fig. 2A). Silencing of CD36 suppressed the elevated CD36 mRNA expression in the high glucose condition, while insulin mRNA expression was elevated (Fig. 2B). Palmitate uptakes measured by radio-isotope tracing technique into the INS-1 cells revealed the same pattern with the changes of CD36 mRNA expression (Fig. 2C).

To identify the protective effect of CD36 inhibition on impaired insulin secretion, we suppressed CD36 expression accompanied by the treatment with high glucose for 3 days. The insulin secretion capacity was normalized by the inhibition of CD36 (Fig. 3). The intracellular peroxide level was partly recovered by CD36 inhibition.

4. Discussion

The present study demonstrated that hyperglycemic conditions increased CD36 expression and decreased insulin secretion accompanied by increased palmitate uptake and ROS level in INS-1 cells, which was reversed by suppression of CD36.

It is well known that glucotoxicity is a major cause of pancreatic beta-cell dysfunction in the diabetic state and results from increased generation of ROS associated with increased glucose oxidation [15,16]. Consistent with these previous studies, a treatment of high glucose for 3 days in INS-1 cells reduces mRNA expression and glucose-stimulated secretion of insulin which was accompanied by an elevated intracellular peroxide level compared to control in this study.

Lipotoxicity, induced by a chronically elevated FFA in beta-cells, also has been well documented in various *in vitro* experiments, however there are controversies in terms of *in vivo* experimental systems due to varying experimental conditions. A prolonged infusion of FFA was shown to improve [17–19] or to impair [20,21] beta-cell function in healthy subjects. However, it is widely accepted that sustained elevation of FFA induces beta-cell dysfunction in obese individuals [22,23] and in diabetic subjects who have a hyperglycemic tendency [24]. It is consistent with the notion that chronically elevated FFA levels do not harm the beta-cell as long as blood glucose levels are normal, but profoundly affect beta-cell function in the presence of concomitant hyperglycemia [1], suggesting a close interrelationship between glucotoxicity and lipotoxicity.

The possible mechanisms of lipotoxicity are increased levels of oxidative stress, PKC, and inflammatory signaling molecules, which are similarly involved in the process of glucotoxicity. Thus, it is speculated that glucotoxicity and lipotoxicity affect beta-cell dysfunction additively or synergistically [25].

The influx of FFA is regulated by various transporters, including CD36, scavenger receptor class B type I, and Niemann-Pick C1-Like 1 [9]. Among them, CD36 is expressed mainly in the liver and muscle tissues. Recently it was reported that CD36 is also expressed in insulin producing cells including MIN-6 cell, INS-cell, and human beta-cell [8]. The oversupply of FFA accumulates in pancreatic beta-cells via incorporation into triglycerides and contributes to

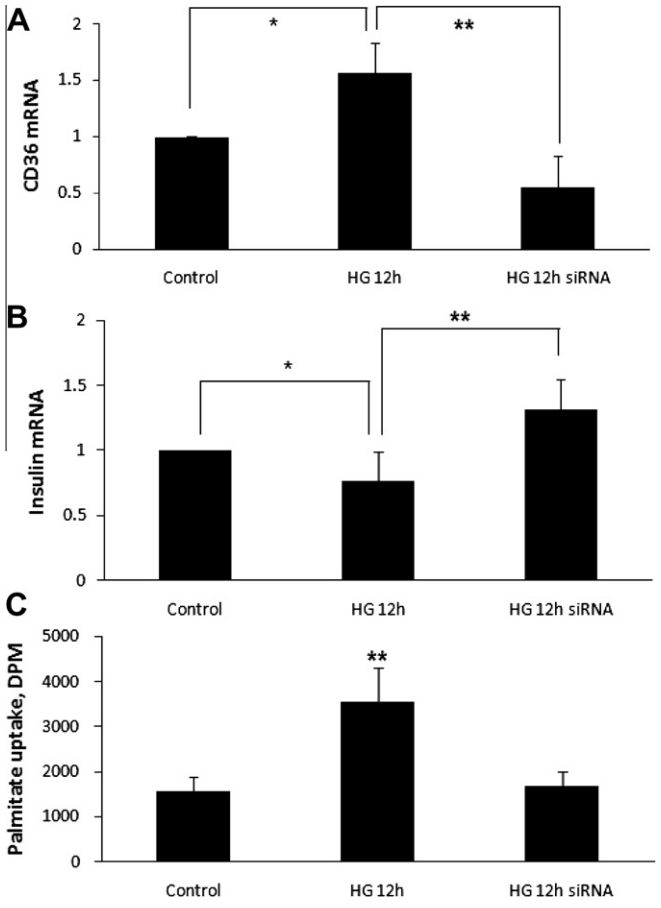

Fig. 2. The 12-h high glucose (HG 12 h) treatment increased CD36 mRNA expression in INS-1 cells, which was reversed by siRNA (A). Insulin mRNA decreased with high glucose treatment, however, it was elevated by siRNA (B). Palmitate uptake following an exposure to high glucose conditions for 12 h was significantly elevated, which was normalized by the inhibition of CD36 in INS-1 cells (C). $^{*}p < 0.05$, $^{**}p < 0.01$.

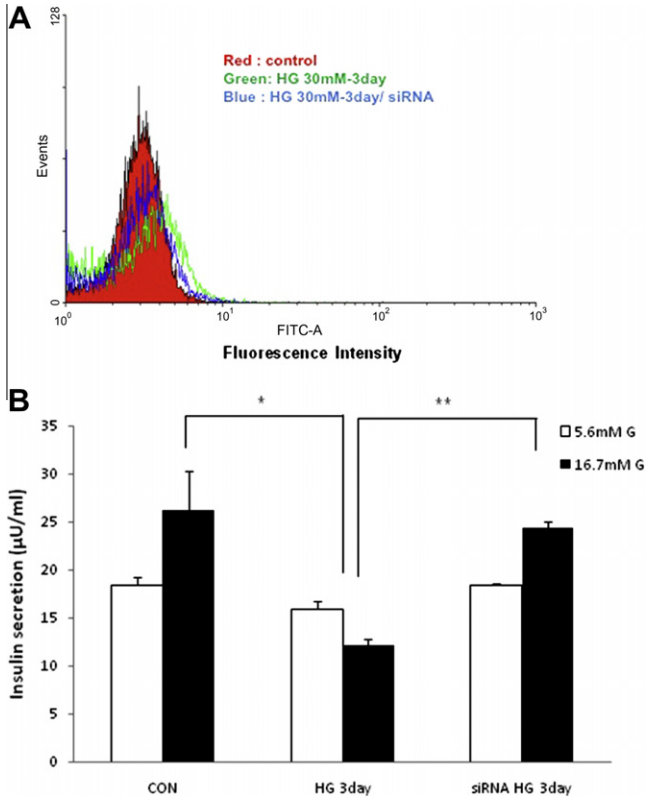

Fig. 3. Inhibition of CD36 expression by siRNA partly reversed the elevated intracellular peroxide level in 3 day high glucose conditions (HG 3 day) in INS-1 cells (A) and glucose stimulated insulin secretion was also normalized by the inhibition of CD36 (B). $^{*}p < 0.05$, $^{**}p < 0.01$.

beta-cell dysfunction [26]. Wallin et al. [8] demonstrated that the overexpression of CD36 in INS-1 cells elevated fatty acids uptake and reduced a potentiating effect of fatty acids on glucose-induced insulin secretion.

A recent report indicated that the expression of CD36 is elevated by hyperglycemia in intestinal epithelium, adipose tissue, heart, and vascular smooth muscle cells [27,28]. In the present study, we demonstrated that high glucose levels stimulated CD36 expression in INS-1 cells, which was accompanied with increased palmitate influx that was normalized by suppression of CD36. Moreover, the inhibition of CD36 ameliorated glucotoxicity in this study.

The finding that hyperglycemic conditions enhance FFA influx via CD36 stimulation which may exacerbate glucotoxicity in insulin producing cells is, to our knowledge, novel. These results were shown in the media concentration of FFA at 0.5 mM/L, which was a normal fasting FFA concentration. This finding implies that the beta-cell injury resulting from hyperglycemia may be induced even in normal lipid level if FFA influx is enhanced and just correction of hyperlipidemia is not sufficient for preserving of beta-cell function in diabetic patients. Further *in vivo* studies about CD36 related beta cell dysfunction are needed.

Though we could not estimate the isolated effect of enhancing FFA influx in INS-1 cells directly, the adverse effect of FFA was confirmed by addition of palmitate (0.5 mM/L). The addition of palmitate for 1 day in normal glucose media increased CD36 expression and ROS level and decreased insulin secretion, suggesting the induction of lipotoxicity (data not shown). Moreover, we also found that the inhibition of CD36 in high glucose conditions decreased ROS level and increased insulin secretion compared to high glucose conditions in INS-1 cells. This result agrees with previous studies that demonstrated suppression of CD36 by human growth hormone [29] improved basal glucose induced insulin secretion. Also inhibition of CD36 by a chemical inhibitor (sulfosuccinimidyloleate) resulted in preservation of insulin secretion which was suppressed by palmitate treatment [30].

We do not know the exact physiological meaning of the increase of CD36 in the high glucose state. However, we present evidence here that FFA influx affects glucotoxicity even in normal concentrations of FFA and that the inhibition of FFA influx may prevent glucotoxicity in pancreatic beta-cells.

In summary, INS-1 cells exposed to high glucose concentrations decreased insulin secretion accompanied by increases of CD36 expression, FFA influx, and intracellular peroxide level. The decreased insulin secretion by high glucose conditions was reversed by suppression of CD36. We suggest that CD36 may be a possible target for preserving beta-cell function in the diabetic state.

Acknowledgments

This research was supported by the Basic Science Research Program through the National Research Foundation of Korea (NRF) funded by the Ministry of Education, Science and Technology (2009-0069055).

References

[1] V. Poitout, R.P. Robertson, Glucolipotoxicity: fuel excess and beta-cell dysfunction, Endocrine Rev. 29 (2008) 351–366.
[2] V. Poitout, R.P. Robertson, Minireview: secondary beta-cell failure in type 2 diabetes – a convergence of glucotoxicity and lipotoxicity, Endocrinology 143 (2002) 339–342.
[3] K.C. Won, J.S. Moon, M.J. Eun, J.S. Yoon, K.A. Chun, I.H. Cho, Y.W. Kim, H.W. Lee, A protective role for heme oxygenase-1 in INS-1 cells and rat islets that are exposed to high glucose conditions, J. Korean Med. Sci. 21 (2006) 418–424.
[4] R.H. Unger, Lipotoxicity in the pathogenesis of obesity-dependent NIDDM: genetic and clinical implications, Diabetes 44 (1995) 863–870.
[5] J.D. McGarry, R.L. Dobbins, Fatty acids, lipotoxicity and insulin secretion, Diabetologia 42 (1999) 128–138.
[6] I.J. Goldberg, R.H. Eckel, N.A. Abumrad, Regulation of fatty acid uptake into tissues: lipoprotein lipase- and CD36-mediated pathways, J. Lipid Res. 50 (Suppl.) (2009) 86–90.
[7] H. Noushmehr, E. D'Amico, L. Farilla, H. Hui, K.A. Wawrowsky, W. Mlynarski, A. Doria, N.A. Abumrad, R. Perfetti, Fatty acid translocase (CD36) is localized on insulin-containing granules in human pancreatic beta-cells and mediates fatty acid effects on insulin secretion, Diabetes 54 (2005) 472–481.
[8] T. Wallin, Z. Ma, H. Ogata, I.H. Jørgensen, M. Iezzi, H. Wang, C.B. Wollheim, A. Björklund, Facilitation of fatty acid uptake by CD36 in insulin-producing cells reduces fatty-acid-induced insulin secretion and glucose regulation of fatty acid oxidation, Biochim. Biophys. Acta 1801 (2010) 191–197.
[9] Z. Ravid, M. Bendayan, E. Delvin, A.T. Sane, M. Elchebly, J. Lafond, M. Lambert, G. Mailhot, E. Levy, Modulation of intestinal cholesterol absorption by high glucose levels: impact on cholesterol transporters, regulatory enzymes, and transcription factors, Am. J. Physiol. Gastrointest. Liver Physiol. 295 (2008) 873–885.
[10] S. Jacqueminet, I. Briaud, C. Rouault, G. Reach, V. Poitout, Inhibition of insulin gene expression by long-term exposure of pancreatic beta-cells to palmitate is dependent upon the presence of a stimulatory glucose concentration, Metabolism 49 (2000) 532–536.
[11] S. Gremlich, C. Bonny, G. Waeber, B. Thorens, Fatty acids decrease IDX-1 expression in rat pancreatic islets and reduce GLUT2, glucokinase, insulin, and somatostatin levels, J. Biol. Chem. 272 (1997) 30261–30269.
[12] B. Ritz-Laser, P. Meda, I. Constant, N. Klages, A. Charollais, A. Morales, C. Magnan, A. Ktorza, J. Philippe, Glucose-induced preproinsulin gene expression is inhibited by the free-fatty acid palmitate, Endocrinology 140 (1999) 4005–4014.
[13] I. Lingvay, V. Esser, J.L. Legendre, A.L. Price, K.M. Wertz, B. Adams-Huet, S. Zhang, R.H. Unger, L.S. Szczepaniak, Noninvasive quantification of pancreatic fat in humans, J. Clin. Endocrinol. Metab. 94 (2009) 4070–4076.
[14] M.E. Tushuizen, M.C. Bunck, P.J. Pouwels, S. Bontemps, J.H. van Waesberghe, R.K. Schindhelm, A. Mari, R.J. Heine, M. Diamant, Pancreatic fat content and beta-cell function in men with and without type 2 diabetes, Diabetes Care 30 (2007) 2916–2921.
[15] R.P. Robertson, J. Harmon, P.O. Tran, V. Poitout, Beta-cell glucose toxicity, lipotoxicity, and chronic oxidative stress in type 2 diabetes, Diabetes 53 (Suppl. 1) (2004) S119–S124.
[16] J.W. Kim, K.H. Yoon, Glucolipotoxicity in pancreatic β-cells, Diabetes Metab. J. 35 (2011) 444–450.

[17] G. Boden, X. Chen, J. Rosner, M. Barton, Effects of a 48-h fat infusion on insulin secretion and glucose utilization, Diabetes 44 (1995) 1239–1242.
[18] C. Magnan, C. Cruciani, L. Clement, et al., Glucose-induced insulin hypersecretion in lipid-infused healthy subjects is associated with a decrease in plasma norepinephrine concentration and urinary excretion, J. Clin. Endocrinol. Metab. 86 (2001) 4901–4907.
[19] S. Kashyap, R. Belfort, A. Gastaldelli, et al., A sustained increase in plasma free fatty acids impairs insulin secretion in nondiabetic subjects genetically predisposed to develop type 2 diabetes, Diabetes 52 (2003) 2461–2474.
[20] G. Paolisso, P.A. Tataranni, J.E. Foley, C. Bogardus, B.V. Howard, E. Ravussin, A high concentration of fasting plasma non-esterified fatty acids is a risk factor for the development of NIDDM, Diabetologia 38 (10) (1995) 1213–1217.
[21] N. Leung, T. Sakaue, A. Carpentier, et al., Prolonged increase of plasma nonesterified fatty acids fully abolishes the stimulatory effect of 24 h of moderate hyperglycaemia on insulin sensitivity and pancreatic beta-cell function in obese men, Diabetologia 47 (2004) 204–213.
[22] A. Carpentier, S.D. Mittelman, R.N. Bergman, et al., Prolonged elevation of plasma free fatty acids impairs pancreatic beta-cell function in obese nondiabetic humans but not in individuals with type 2 diabetes, Diabetes 49 (2000) 399–408.
[23] C. Xiao, A. Giacca, G.F. Lewis, Oral taurine but not N-acetylcysteine ameliorates NEFA-induced impairment in insulin sensitivity and beta cell function in obese and overweight, nondiabetic men, Diabetologia 51 (2008) 139–146.
[24] G. Boden, X. Chen, Effects of fatty acids and ketone bodies on basal insulin secretion in type 2 diabetes, Diabetes 48 (1999) 577–583.
[25] A. Giacca, C. Xiao, A.I. Oprescu, A.C. Carpentier, G.F. Lewis, Lipid-induced pancreatic β-cell dysfunction: focus on in vivo studies, Am. J. Physiol. Endocrinol. Metab. 300 (2) (2011) E255–E262.
[26] N.J. van der Zijl, G.H. Goossens, C.C. Moors, D.H. van Raalte, M.H. Muskiet, P.J. Pouwels, E.E. Blaak, M. Diamant, Ectopic fat storage in the pancreas, liver, and abdominal fat depots: impact on β-cell function in individuals with impaired glucose metabolism, J. Clin. Endocrinol. Metab. 96 (2) (2011) 459–467. Epub 2010 Nov 17.
[27] M. Chen, Y.K. Yang, T.J. Loux, K.E. Georgeson, C.M. Harmon, The role of hyperglycemia in FAT/CD36 expression and function, Pediatr. Surg. Int. 22 (8) (2006) 647–654. Epub 2006 Jul 13.
[28] J.H. Xue, Z. Yuan, Y. Wu, Y. Liu, Y. Zhao, W.P. Zhang, Y.L. Tian, W.M. Liu, Y. Liu, C. Kishimoto, High glucose promotes intracellular lipid accumulation in vascular smooth muscle cells by impairing cholesterol influx and efflux balance, Cardiovasc. Res. 86 (1) (2010) 141–150. Epub 2009 Dec 10.
[29] L.T. Dalgaard, P. Thams, L.W. Gaarn, J. Jensen, Y.C. Lee, J.H. Nielsen, Suppression of FAT/CD36 mRNA by human growth hormone in pancreatic β-cells, Biochem. Biophys. Res. Commun. 410 (2) (2011) 345–350. Epub 2011 Jun 7.
[30] H. Noushmehr, E. D'Amico, L. Farilla, H. Hui, K.A. Wawrowsky, W. Mlynarski, A. Doria, N.A. Abumrad, R. Perfetti, Fatty acid translocase (FAT/CD36) is localized on insulin-containing granules in human pancreatic beta-cells and mediates fatty acid effects on insulin secretion, Diabetes 54 (2) (2005) 472–481.

Biochemical and Biophysical Research Communications 420 (2012) 467–472

Contents lists available at SciVerse ScienceDirect

Biochemical and Biophysical Research Communications

journal homepage: www.elsevier.com/locate/ybbrc

Identification of a novel cis-element that regulates alternative splicing of Bcl-x pre-mRNA

Jaehoon Lee [a], Jianhua Zhou [b], Xuexiu Zheng [a], Sunghee Cho [a], Heegyum Moon [a], Tiing Jen Loh [a], Kyungjin Jo [a], Haihong Shen [a,*]

[a] School of Life Science, Gwangju Institute of Science and Technology, Gwangju 500-712, Republic of Korea
[b] Nantong University, Nantong, JiangSu 226001, P.R. China

ARTICLE INFO

Article history:
Received 21 February 2012
Available online 13 March 2012

Keywords:
Pre-mRNA splicing
Bcl-x
Alternative splicing
Apoptosis
Exon inclusion
Exon skipping

ABSTRACT

Alternative splicing plays an important role in the control of apoptosis. A number of genes related to apoptosis undergo alternative splicing. Among them, the apoptotic regulator Bcl-x produces two major isoforms, Bcl-xL and Bcl-xS, through the alternative splicing of exon 2 in its pre-mRNA. These isoforms have antagonistic function in apoptotic pathway; Bcl-xL is pro-apoptotic, while Bcl-xS is anti-apoptotic. The balanced ratio of two isoforms is important for cell survival. However, regulatory mechanisms of Bcl-x splicing remain poorly understood. Using a mini-gene system, we have found that a 105 nt exonic region (E3b) located within exon 3 affects exon 2 splicing in the Bcl-x gene. Further deletion and mutagenesis studies demonstrate that this 105 nt sequence contains various functional elements which promote skipping of exon 2b. One of these elements forms a stem-loop structure that stimulates skipping of exon 2b. Furthermore our results prove that the stem-loop structure functions as an enhancer in general pre-mRNA splicing. We conclude that we have identified a cis-regulatory element in exon 3 that affects splicing of exon 2 in the Bcl-x gene. This element could be potentially targeted to alter the ratio of Bcl-xL and Bcl-xS for treatment of tumors through an apoptotic pathway.

1. Introduction

Alternative splicing plays an important role in gene regulation [1,2]. Alternative splicing process contributes to the proteomic diversity in higher eukaryotes through generating multiple mature mRNAs from a single pre-mRNA [3,4]. It is estimated that at least 95% of multi-exon pre-mRNAs undergo alternative splicing in human [5]. Regulation of alternative splicing is mediated by a variety of splicing regulators, containing RNA sequence elements (cis-regulatory elements) and protein regulators (trans-acting factors) [3,4]. These elements regulate alternative splicing by promoting or suppressing the spliceosome assembly [6]. The cis-regulatory elements are divided into enhancer and silencer elements [3,7]. A variety of cis-regulatory elements are identified in various systems [8,9].

In mammal, two families of RNA binding proteins have been well studied as trans-acting factors, the serine/arginine-rich (SR) proteins and the heterogenous nuclear ribonucleoproteins (hnRNPs) [3,10]. The members of SR family generally bind to enhancer elements and activate splicing of target exon by promoting spliceosome assembly at the adjacent splice site [11–13]. In contrast, the hnRNPs usually bind to silencer elements to inhibit inclusion of target exons [14,15]. A growing number of genetic diseases have been found to be caused by aberrant alternative splicing events [16,17].

Apoptosis, programmed cell death, is a process of cellular destruction that is required for the development and homeostasis of multicellular organisms [18]. Apoptosis is characterized by cell shrinkage, condensation of nuclei and internucleosomal degradation of DNA. Cells defective in apoptosis tend to survive with excess DNA damage and thus lead to carcinogenesis by accumulating mutations [18,19]. Apoptosis is regulated through pre-mRNA splicing [20]. Through alternative splicing, different isoforms with contrasting functions in apoptosis are produced [21,22]. The Bcl-x is a member of the Bcl-2 family which plays a key role in the control of apoptosis [23–25]. The Bcl-*x* pre-mRNA is alternatively spliced to produce two distinct mRNA variants coding different proteins, Bcl-xL and Bcl-xS [26,27]. These two isoforms have antagonistic effects on apoptosis. The longer form, Bcl-xL is anti-apoptotic, while the short form Bcl-xS is pro-apoptotic [28,29]. In numerous types of cancer cells, anti-apoptotic Bcl-xL is predominantly expressed, and its overexpression confers resistance to apoptotic stimuli such as chemotherapeutic agents [30–33]. On the other hand, pro-apoptotic Bcl-xS can induce apoptosis and enhance sensitivity to anticancer drugs [34,35]. Since the balance between Bcl-xL and Bcl-xS is important for decision of cell survival or death, modulation of

* Corresponding author. Fax: +82 62 715 2484.
E-mail address: haihongshen@gist.ac.kr (H. Shen).

0006-291X/$ - see front matter © 2012 Elsevier Inc. All rights reserved.
http://dx.doi.org/10.1016/j.bbrc.2012.03.029

Bcl-x splicing has great therapeutic potential for apoptosis-related diseases including cancer and degenerative disorders [36,37]. It is important to identify and characterize splicing regulators that specifically regulate alternative splicing of Bcl-x pre-mRNA for therapeutic applications. However, the mechanism controlling the alternative splicing of Bcl-*x* and the related regulators remain poorly understood.

In this study, we have identified a cis-regulatory element on Bcl-*x* pre-mRNA. We first realized based on our deletion analysis that a 105 nt RNA, E3b, within exon 3 promotes exon 2b skipping on Bcl-x alternative splicing. We further found that a specific RNA stem-loop structure located in E3b promotes exon 2b exclusion. This stem-loop structure functions as an enhancer in general pre-mRNA splicing.

2. Materials and methods

2.1. Plasmid construction

All primers and oligonucleotides for constructs are listed in Table 1. The Bcl-x sequence was PCR-amplified using human genomic DNA as a template to construct a wild type mini-gene. Specifically, a 1022 bp DNA containing 3′ portion of intron 2 and coding region of exon 3 of Bcl-x was produced using the primer sets (forward: In2b, reverse: Ex3b). This PCR product was cloned into pCI-neo vector. Then a 2161 bp sequence of the Bcl-x containing exon 1, intron 1, exon 2 and 5′ portion of intron 2 that was PCR-produced using primer sets (forward: Ex1a, reverse: In2a) and cloned into pCI-neo plasmid. ΔE3b mini-gene was constructed with another reverse primer (Ex3a).

To generate Bcl-x mutant constructs SL-D, -R, -1M and -3M, we performed overlapping PCR. Different primers were used for each constructs; common primers (forward: I2for, reverse: Neorev), specific primers for SL-D (forward: SLDfor, reverse: SLDrev), SL-R (forward: SLRfor, reverse: SLRrev), SL-1M (forward: SL1for, reverse: SL1rev) and SL-3M (forward: SL3for, reverse: SL3rev). The PCR products were cloned into pCI-neo vector. Different primers were used for mutants R1 (forward: R1for, reverse: R1rev) and R2 (forward: R2for, reverse: R2rev). These PCR products were cloned into ΔE3b by using restriction enzymes EcoRI and NotI. To generate Bcl-x mutant constructs E3b-1, -2, R1r, R2r and R3r, synthesized DNA oligonucleotide were cloned into ΔE3b by using restriction enzymes EcoRI and NotI.

To generate Hβ-globin mutated mini-genes, overlapping PCR was performed to generate restriction enzyme sites KpnI and SacII on exon 2 of β-globin sequence. Specific primers were used; primers for first PCR (forward: GE1for, reverse: E2Mrev), primers for second PCR (forward: E2Mfor, reverse: GE2rev). The third PCR product was cloned into pcDNA3.1(+) using restriction enzymes HindIII and EcoRI. To generate additional mutant constructs Hβ-SL, -3M, -R, synthesized DNA oligonucleotides were cloned into Hβ-globin by using restriction enzymes KpnI and SacII.

2.2. Cell culture and transfection

HeLa cells were maintained in Dulbecco's Modified Eagle's Medium (DMEM) supplemented with 10% of Fetal Bovine Serum (FBS) at 37 °C in a humidified 5% CO_2 condition. Plasmid transfections were carried out with polyethyleneimide (PEI). Four micro gram of PEI were mixed with 2 μg of plasmid in 100 μl of DMEM. The mixture was applied to cells in 900 μl of DMEM supplemented

Table 1
List of oligonucleotides.

Name	Sequence
In2b	5′-ACC CTC AGA GGC ACA GCT T-3′
Ex3b	5′-TTT CCG ACT GAA GAG TGA G-3′
Ex1a	5′-GGA AGG AGG AAG CAA GCG AGG-3′
In2a	5′-AGT AAC CCA GCC TGT CCA AGG-3′
Ex3a	5′-ATT GTT CCC ATA GAG TTC CAC-3′
I2for	5′-ACC CTC AGA GGC AC-3′
Neorev	5′-ATA AGA ATG CGG CCG CCC GGG TCG AC-3′
SLDfor	5′-GAG AGC CGA AAG GGC ACG GGC ATG ACT GTG-3′
SLDrev	5′-CAC AGT CAT GCC CGT GCC CTT TCG GCT CTC-3′
SLRfor	5′-CCG AAA GGG CGC GGA TCA CGC ATT CAC GTG TAC CGT CAC GGG CAT GA-3′
SLRrev	5′-TCA TGC CCG TGA CGG TAC ACG TGA ATG CGT GAT CCG CGC CCT TTC GG-3′
SL1for	5′-AAC CGC TGG TTT CTG ACG G-3′
SL1rev	5′-CCG TCA GAA ACC AGC GGT T-3′
SL3for	5′-GGC CAG AAA AGA TTC AAC C-3′
SL3rev	5′-GGT TGA ATC TTT TCT GGC C-3′
R1for	5′-TGC TCT GAT GCC GCA TAG T-3′
R1rev	5′-CAT GCA ATT GTC GGT CAA G-3′
R2for	5′-AAG AAT CTG CTT AGG GTT AG-3′
R2rev	5′-ATG AAC TAA TGA CCC CGT AA-3′
E3b-1.oligo	5′-GCA GCA GCC GAG AGC CGA AAG GGC CAG GAA CGC TTC AAC CGC T-3′
E3b-2.oligo	5′-ACG GGC ATG ACT GTG GCC GGC GTG GTT CTG CTG GGC TCA CTC TTC AGT CGG AAA-3′
R1r.oligo	5′-TCG AAC GAA AGC AGG AGG GGC CTC CGC ACC AAC CGC TGG TTC CTG ACG GGC ATG ACT GTG GCC GGC GTG GTT CTG CTG GGC TCA CTC TTC AGT CGG AAA-3′
R2r.oligo	5′-GCA GCA GCC GAG AGC CGA AAG GGC CAG GAA CGC TTC GGG TTT CTC GGC ACT GAT ACG ACG CGC AGC GTG GTT CTG CTG GGC TCA CTC TTC AGT CGG AAA-3′
R3r.oligo	5′-GCA GCA GCC GAG AGC CGA AAG GGC CAG GAA CGC TTC AAC CGC TGG TTC CTG ACG GGC ATG ACT GTG GCC GGT GCC GTT ACC GCC ATG AGG GGA CAT TTG-3′
GE1for	5′-ACA TTT GCT TCT GAC ACA AC-3′
E2Mrev	5′-AGA ACC GCG GGG TAC CAG GGT-3′
E2Mfor	5′-ACC CTG GTA CCC CGC GGT TCT-3′
GE2rev	5′-TCA GGA TCC ACG TGC AGC TTG-3′
Hβ-SL.oligo	5′-GCC AGG AAC GCT TCA ACC GCT GGT TCC TGA C-3′
Hβ-3M. oligo	5′-GCC AGA AAA GAT TCA ACC GCT GGT TCC TGA C-3′
Hβ-R.oligo	5′-TAC TCG AGC GTA ATC CAC CGG GGC TCG CTA C-3′

with FBS. Four hours later, media was changed. The cells were incubated for 48 h before total RNA extraction.

2.3. Total RNA extraction and RT-PCR analysis

Total RNA was extracted from transfected HeLa cells using RiboEx reagent (GeneAll) following the manufacturer's protocol. One micro gram of total RNA was reverse transcribed using oligo (dT) primer using ImProm-II™ reverse transcriptase (Promega) following the manufacturer's protocol. One micro liters of the reverse transcription reaction was amplified by PCR using a specific forward primer to the pCI-neo cDNA sequence (5′-ACG ACT CAC TAT AGG CTA G-3′), a specific reverse primer to Bcl-x exon 3 (5′-ATT GTT CCC ATA GAG TTC CAC-3′), and G-Taq polymerase (Cosmo Genetech). The PCR products were loaded onto 2% agarose gel and visualized by staining with ethidium bromide solution (0.5 μg/Ml).

3. Results

3.1. Exon 3 in Bcl-x gene contains elements that regulate alternative splicing of exon 2b

To identify cis-acting elements that are involved in the alternative splicing of Bcl-*x* pre-mRNA, we constructed a wild-type Bcl-*x* mini-gene with a deletion of ~53 kb DNA from the intron 2 (Fig. 1A). A mutant mini-gene with a deleted 105 nt (E3b) in exon 3 was also generated in order to examine if there are any regulatory elements in the exon (Fig. 1B). The wild type and E3b deletion mutant (△E3b) Bcl-*x* mini-genes were transfected into HeLa cells. After 48 h, total RNA was extracted and RT (reverse transcription) PCR experiments were conducted to analyze the splicing of Bcl-x pre-mRNA. The results in Fig. 1B showed that pre-mRNA splicing of △E3b significantly increased antiapoptotic Bcl-xL isoform. To eliminate the possibility that deletion of 105 nt changed the size of exon 3, leading to alteration of exon 2b splicing, we substituted the 105 nt of E3b with two different random sequences. Our results indicated that splicing of exon 2b in the constructs with replacements of the 105 nt is similar to that of the deletion mutant △E3b. Therefore we conclude that the 105 nt in Exon 3 (E3b) contain regulatory elements that stimulate skipping (or exclusion) of exon 2b in the alternative splicing of Bcl-x.

3.2. The 105 nt RNA (E3b) contains multiple regulatory elements for the alternative splicing of Bcl-x pre-mRNA

We next asked what regulatory elements reside within E3b. To answer this question, we first constructed two deletion mutants in which upstream 43 nt (E3b-2) or downstream 54 nt (E3b-1) is deleted (Fig. 2A). RT-PCR for alternative splicing analysis shows that deletion of both elements increased the inclusion of exon 2b of Bcl-x pre-mRNA. We conclude that both upstream 45 nt RNA and downstream 54 nt RNA affect exon 2b splicing into Bcl-x pre-mRNA. To further narrow down cis-elements, we constructed additional deletion mutation on E3b. We divided the E3b (105 nt) RNA into three 35 nt pieces evenly, then made three mutant constructs by substituting each 35 nt RNA with random sequences (E3b-R1, E3b-R2, E3b-R3) (Fig. 2A). We found that replacement of 35 nt Bcl-x RNA with a random 35 nt sequence in all three substitution mutants promotes the inclusion of Exon 2b (Fig. 2C). We deduce

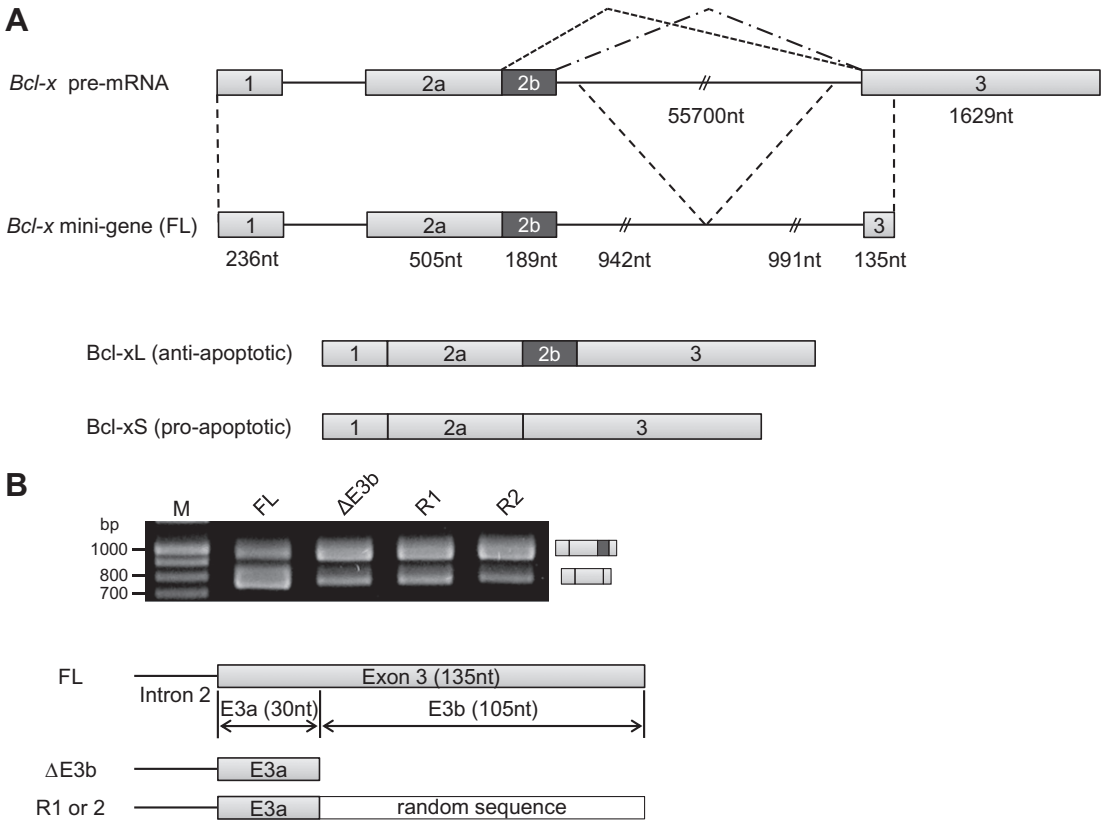

Fig. 1. Exon 3 in Bcl-x gene contains regulatory elements on its alternative splicing. (A) A mini-gene of Bcl-x is generated by deleting ~54,000 bp from Bcl-x intron 2. Alternative splicing isoforms of Bcl-x pre-mRNA are shown as the anti-apoptotic Bcl-xL (longer form) that includes exon 2b and the pro-apoptotic-xS (shorter form) that excludes Exon2b. (B) Deletion or substitution mutants were constructed and transfected into HeLa cells. RT-PCR was performed to examine Bcl-x splicing. The resulting RT-PCR products were resolved on agarose gels.

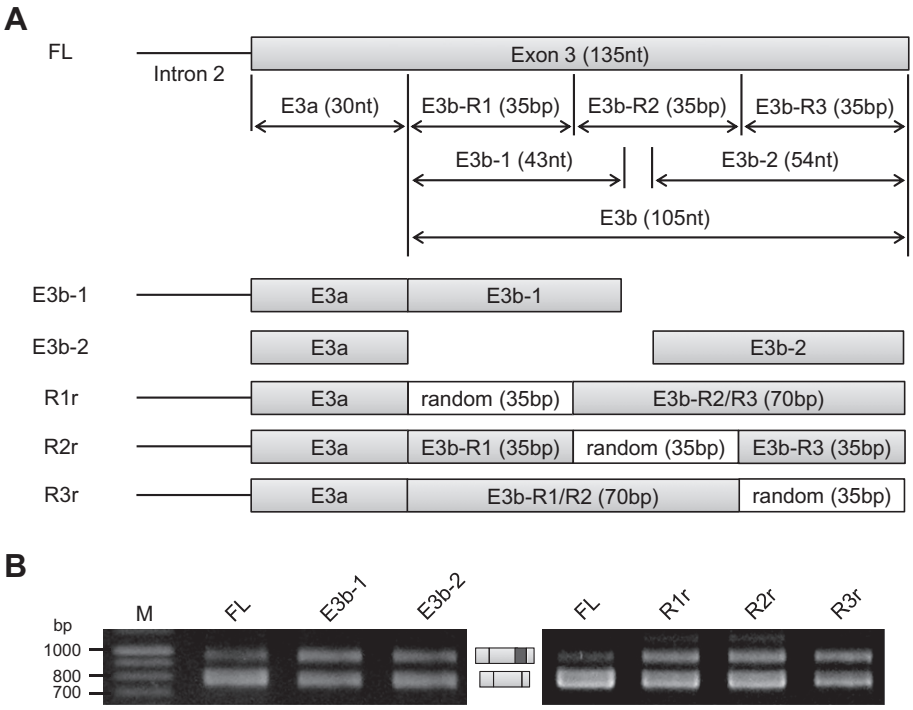

Fig. 2. The 105 nt RNA(E3b) contains regulatory elements for the alternative splicing of Bcl-x pre-mRNA. (A) Shown are various deletion or substitution mutants. In E3b-1 and E3b-2 constructs, downstream 54 nt or upstream 43 nt in 105 nt are deleted separately. In R1r, R2r and R3r constructs, 35 nt located at upstream, middle and downstream of 105 nt are substituted by random sequences. (B) RT-PCR analysis was performed after mini-genes described in (A) were transfected into HeLa cells.

that the 105 nt E3b RNA either contains multiple regulatory elements which are required for exon 2b exclusion skipping or three 35 nt sequences are interconnected that affect exon 2b splicing.

3.3. A predicted novel stem-loop structure functions as a regulator of exon 2b splicing

To pinpoint the cis-elements, we analyzed the 105 nt E3b with Mfold program [38]. We found that an *in silico* stem-loop structure could be precited in the sequence. The location, sequence and structure of the stem-loop are shown in Fig. 3A. In detail, the structure contains 27 nt and is located in the middle of 105 nt where the first 35 nt (E3b-R1) and the second 35 nt (E3b-R2) share a junction. Therefore, a substitution of either first 35 nt (E3b-R1) or the second 35 nt (E3b-R2) with a random sequence would disrupts the stem-loop element, explaining why exon 2b inclusion increases in E3b-R1 and E3b-R2. To test whether the stem-loop structure regulates alternative splicing of *Bcl-x*, we produced several mutations. First we tested if deletion (SL-D) or substitution with random sequence (SL-R) for the stem-loop structure causes the changes of alternative splicing of Bcl-x (Fig. 3A). We found that exon 2b inclusion is increased in both of the mutants (Fig. 3B). To directly answer if the stem-loop structure is important for its regulation, we disrupted the structure by introducing point mutations (SL-3M and SL-1M) (Fig. 3A). As shown in Fig. 3C, the mutants with a disrupted secondary structure increased exon 2b inclusion of Bcl-x pre-mRNA splicing. Based on the results in Fig. 3, we conclude that the stem-loop structure in the 105 nt RNA (E3b) is important for the promotion of Bcl-x exon 2b skipping.

3.4. Stem-loop sequence can function as splicing enhancer in general pre-mRNA splicing

Our results above have suggested that a stem-loop within the 105 nt RNA regulates alternative splicing of Bcl-x. We then asked whether this sequence can function as enhancer or silencer for general splicing. To answer this question, we inserted the stem-loop RNA sequence into β-globin mini-gene (Hβ) which is used for the study of general splicing mechanisms (Hβ-SL) (Fig. 4A). In the meantime, we inserted stem-loop structure disrupted mutation (Hβ-SL-3M) into the same β-globin mini-gene (Hβ). To avoid the effect of exon length on pre-mRNA splicing, we also inserted a random sequence with the same size of stem-loop into the mini-gene (Hβ-SL-R). The results in Fig. 4B showed that Hβ-SL produced more spliced products compared with Hβ-SL-3M and Hβ-SL-R, indicating that stem-loop RNA functions as an enhancer in general splicing.

4. Discussion

Similar to exons that undergo regular splicing, alternatively spliced exons also contain RNA sequences that are important for pre-mRNA splicing. These sequences include 5′ splice site, 3′ splice site, branch point and polypyrimidine tract site that are essential splicing signals required for pre-mRNA splicing. Pre-mRNA splicing of many genes requires additional RNA sequence elements, such as exon splicing enhancer (ESE). However, it seems that in addition to the essential splicing signals on pre-mRNA, enhancers or inhibitors/silencers on pre-mRNA are particularly important for regulation of alternative splicing.

Bcl-X pre-mRNA produces anti-apototic Bcl-xL and pro-apoptotic Bcl-xS through its alternative splicing of exon 2. The ratio between anti-apototic Bcl-xL and pro-apoptotic Bcl-xS plays an important role in apoptosis process. It has been hypothesized that regulation of Bcl-x pre-mRNA splicing of exon 2 presents a link between alternative splicing and apoptosis. Therefore one would expect that identification of regulatory factors for Bcl-x alternative splicing will provide a clue on how regulation of alternative splicing may influence apoptosis. To identify cis-elements that regulate alternative splicing of Bcl-x exon 2b, we generated a Bcl-x mini

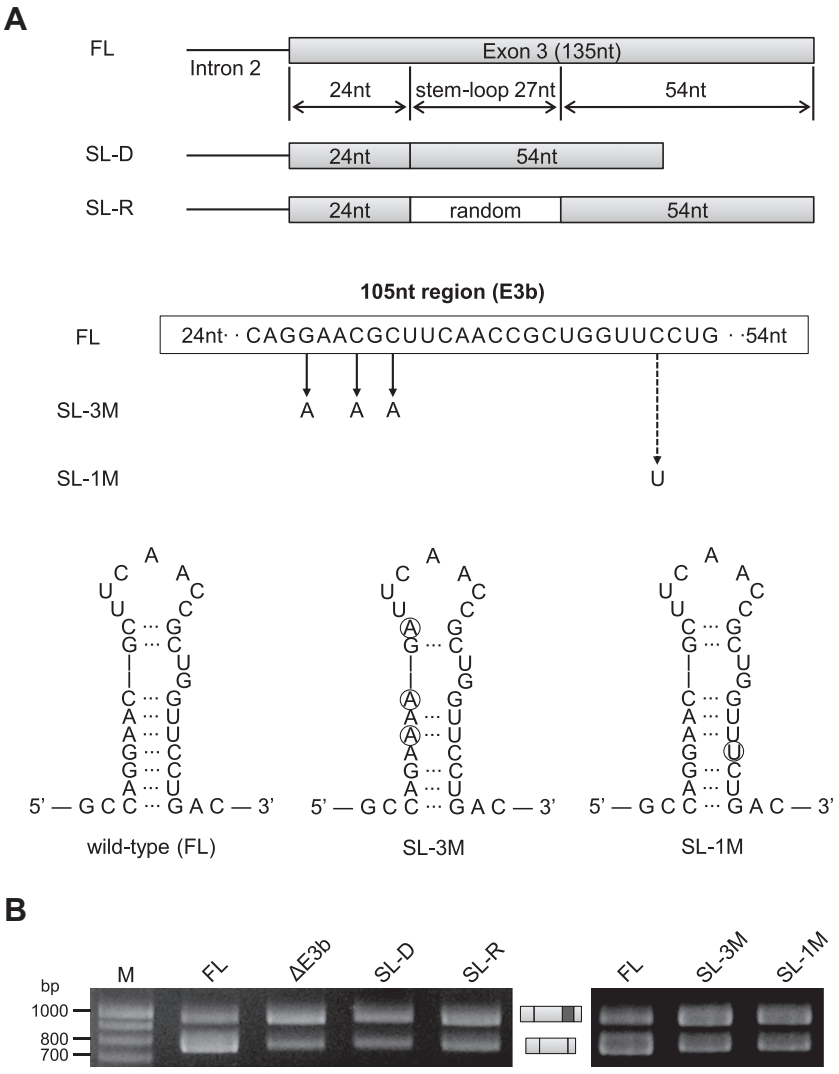

Fig. 3. A stem-loop structure in 105 nt RNA (E3b) promotes the skipping of Bcl-x exon 2b. (A) A 27 nt long stem-loop RNA structure was identified in the 105 nt E3b RNA. The sequence and structure of the stem-loop structure are shown. Mutant constructs that disrupt the secondary structure (SL-3M and SL-1M) or that replace or delete the secondary structure (SL-R, SL-D) are generated. (B) Mini-genes with the wildtype stem-loop (SL) or mutants (SL-3M, SL-1M, SL-R, SL-D) were transfected into HeLa cells. RT-PCR results show that the wild type stem-loop RNA element but not mutants promote the skipping of Bcl-x exon 2b.

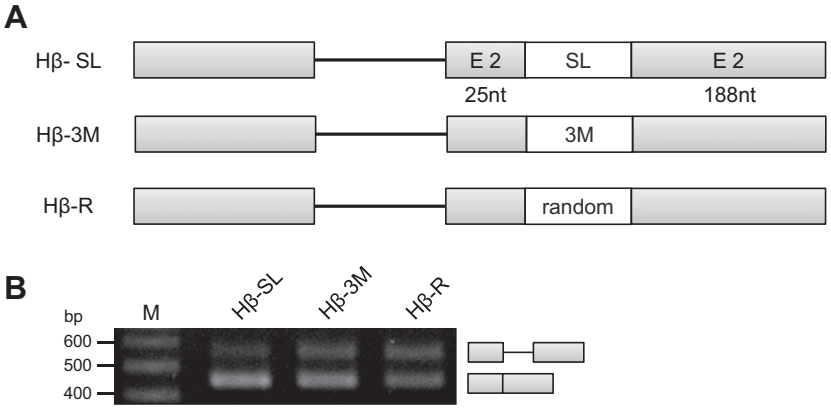

Fig. 4. The Stem-loop structure identified in 105 nt RNA (E-3b) functions as a splicing enhancer. (A) The stem-loop RNA, wild type (SL), mutant (3 M), or a control random sequence (random) was inserted into the β-globin mini-gene. (B) The constructs were transfected into HeLa cells and RT-PCR was carried out. Insertion of stem-loop RNA into β-globin gene produces more splicing products than insertion of stem-loop mutation or insertion of a random sequence.

gene system. Through deletion and random sequence substitution analysis, we show that the alternative splicing of Bcl-x is regulated by a 105 nt sequence located in exon 3b. Further investigation demonstrates that there may be multiple cis-elements in the 105 nts region of exon 3 in the Bcl-x gene that regulate inclusion and skipping of exon 2b. While we believe that it is important to

pinpoint all elements in the region, we have identified and validated at least one of these elements, a stem-loop of 27 nt in the middle of 105 nt that plays a significant role in regulation of exon 2b inclusion or exclusion (Fig 3). It appears that there is an additional element in E3b-3R 35 nt that affects exon 2b splicing (Fig 3). However, it is also possible that the E3b-3R 35 nt regulates exon 2b splicing by coordinating with the stem-loop structure.

To examine the role of the stem-loop structure, we inserted the 27 nt sequence into the β-globin mini-gene (Hβ). We found that in addition to regulating alternative splicing of Bcl-x, the stem-loop structure acts as an enhancer in general splicing (Fig. 4). The results are not surprising considering of the fact that the regulation of pre-mRNA splicing by RNA secondary structure is found in the regulation of other pre-mRNAs. For example, it was found that a RNA sequence covering exon 10 and intron 10 of Tau pre-mRNA forms a secondary structure that disrupts the base pairing between 5′ splicing site and U1 snRNA [39], regulating exon 10 inclusion or exclusion. While the mechanistic basis for the stem-loop regulation remains to be determined, we hypothesize that recruitment of specific splicing machinery to pre-mRNA and/or binding of RNA helicase that can unwind the stem-loop structure to regulate alternative splicing are two possibilities that are worth investigating.

In conclusion, we have identified a novel stem-loop RNA structure in Bcl-x pre-mRNA that functions not only as a cis-element to regulate exon 2 splicing in Bcl-x pre-mRNA but also as a enhancer in general splicing.

Acknowledgments

This work was supported by the Korea Healthcare Technology R&D Project, Ministry for Health, Welfare and Family Affairs (A100733-1102-0000100) and Mid-career Researcher Program through a National Research Foundation (NRF) grant (2011-0016757) funded by the Korea Ministry of Education, Science, and Technology (MEST).

References

[1] Q. Li, J.A. Lee, D.L. Black, Neuronal regulation of alternative pre-mRNA splicing, Nat. Rev. Neurosci. 8 (2007) 819–831.
[2] A.L. Saltzman, Q. Pan, B.J. Blencowe, Regulation of alternative splicing by the core spliceosomal machinery, Genes Dev. 25 (2011) 373–384.
[3] D.L. Black, Mechanisms of alternative pre-messenger RNA splicing, Annu. Rev. Biochem. 72 (2003) 291–336.
[4] T. Maniatis, B. Tasic, Alternative pre-mRNA splicing and proteome expansion in metazoans, Nature 418 (2002) 236–243.
[5] Q. Pan, O. Shai, L.J. Lee, B.J. Frey, B.J. Blencowe, Deep surveying of alternative splicing complexity in the human transcriptome by high-throughput sequencing, Nat. Genet. 40 (2008) 1413–1415.
[6] M.C. Wahl, C.L. Will, R. Luhrmann, The spliceosome: design principles of a dynamic RNP machine, Cell 136 (2009) 701–718.
[7] A.J. Lopez, Alternative splicing of pre-mRNA: developmental consequences and mechanisms of regulation, Annu. Rev. Genet. 32 (1998) 279–305.
[8] H. Shen, J.L. Kan, C. Ghigna, G. Biamonti, M.R. Green, A single polypyrimidine tract binding protein (PTB) binding site mediates splicing inhibition at mouse IgM exons M1 and M2, RNA 10 (2004) 787–794.
[9] C. Rothrock, B. Cannon, B. Hahm, K.W. Lynch, A conserved signal-responsive sequence mediates activation-induced alternative splicing of CD45, Mol. Cell 12 (2003) 1317–1324.
[10] A.J. Matlin, F. Clark, C.W. Smith, Understanding alternative splicing: towards a cellular code, Nat. Rev. Mol. Cell Biol. 6 (2005) 386–398.
[11] J.R. Sanford, J. Ellis, J.F. Caceres, Multiple roles of arginine/serine-rich splicing factors in RNA processing, Biochem. Soc. Trans. 33 (2005) 443–446.
[12] B.R. Graveley, T. Maniatis, Arginine/serine-rich domains of SR proteins can function as activators of pre-mRNA splicing, Mol. Cell 1 (1998) 765–771.
[13] B.R. Graveley, Sorting out the complexity of SR protein functions, RNA 6 (2000) 1197–1211.
[14] F. Del Gatto-Konczak, M. Olive, M.C. Gesnel, R. Breathnach, HnRNP A1 recruited to an exon in vivo can function as an exon splicing silencer, Mol. Cell Biol. 19 (1999) 251–260.
[15] G. Dreyfuss, V.N. Kim, N. Kataoka, Messenger-RNA-binding proteins and the messages they carry, Nat. Rev. Mol. Cell Biol. 3 (2002) 195–205.
[16] T.A. Cooper, W. Mattox, The regulation of splice-site selection, and its role in human disease, Am. J. Hum. Genet. 61 (1997) 259–266.
[17] C.L. Lorson, E. Hahnen, E.J. Androphy, B. Wirth, A single nucleotide in the SMN gene regulates splicing and is responsible for spinal muscular atrophy, Proc. Natl. Acad. Sci. USA 96 (1999) 6307–6311.
[18] S.L. McKenna, A.J. McGowan, T.G. Cotter, Molecular mechanisms of programmed cell death, Adv. Biochem. Eng. Biotechnol. 62 (1998) 1–31.
[19] M. Leist, M. Jaattela, Four deaths and a funeral: from caspases to alternative mechanisms, Nat. Rev. Mol. Cell Biol. 2 (2001) 589–598.
[20] B. Fadeel, S. Orrenius, Apoptosis: a basic biological phenomenon with wide-ranging implications in human disease, J. Intern. Med. 258 (2005) 479–517.
[21] C. Schwerk, K. Schulze-Osthoff, Regulation of apoptosis by alternative pre-mRNA splicing, Mol. Cell 19 (2005) 1–13.
[22] C.J. David, J.L. Manley, Alternative pre-mRNA splicing regulation in cancer: pathways and programs unhinged, Genes Dev. 24 (2010) 2343–2364.
[23] J.E. Chipuk, T. Moldoveanu, F. Llambi, M.J. Parsons, D.R. Green, The BCL-2 family reunion, Mol. Cell 37 (2010) 299–310.
[24] C. Akgul, D.A. Moulding, S.W. Edwards, Alternative splicing of Bcl-2-related genes: functional consequences and potential therapeutic applications, Cell Mol. Life Sci. 61 (2004) 2189–2199.
[25] Z. Huang, Bcl-2 family proteins as targets for anticancer drug design, Oncogene 19 (2000) 6627–6631.
[26] D.R. Mercatante, C.D. Bortner, J.A. Cidlowski, R. Kole, Modification of alternative splicing of Bcl-x pre-mRNA in prostate and breast cancer cells. analysis of apoptosis and cell death, J. Biol. Chem. 276 (2001) 16411–16417.
[27] L.H. Boise, M. Gonzalez-Garcia, C.E. Postema, L. Ding, T. Lindsten, L.A. Turka, X. Mao, G. Nunez, C.B. Thompson, Bcl-x, a bcl-2-related gene that functions as a dominant regulator of apoptotic cell death, Cell 74 (1993) 597–608.
[28] K. Boon-Unge, Q. Yu, T. Zou, A. Zhou, P. Govitrapong, J. Zhou, Emetine regulates the alternative splicing of Bcl-x through a protein phosphatase 1-dependent mechanism, Chem. Biol. 14 (2007) 1386–1392.
[29] G. Kroemer, The proto-oncogene Bcl-2 and its role in regulating apoptosis, Nat. Med. 3 (1997) 614–620.
[30] I. Lebedeva, R. Rando, J. Ojwang, P. Cossum, C.A. Stein, Bcl-xL in prostate cancer cells: effects of overexpression and down-regulation on chemosensitivity, Cancer Res. 60 (2000) 6052–6060.
[31] J. Watanabe, F. Kushihata, K. Honda, K. Mominoki, S. Matsuda, N. Kobayashi, Bcl-xL overexpression in human hepatocellular carcinoma, Int. J. Oncol. 21 (2002) 515–519.
[32] L. Espana, Y. Fernandez, N. Rubio, A. Torregrosa, J. Blanco, A. Sierra, Overexpression of Bcl-xL in human breast cancer cells enhances organ-selective lymph node metastasis, Breast Cancer Res. Treat. 87 (2004) 33–44.
[33] L. Shkreta, L. Michelle, J. Toutant, M.L. Tremblay, B. Chabot, The DNA damage response pathway regulates the alternative splicing of the apoptotic mediator Bcl-x, J. Biol. Chem. 286 (2011) 331–340.
[34] M.F. Clarke, I.J. Apel, M.A. Benedict, P.G. Eipers, V. Sumantran, M. Gonzalez-Garcia, M. Doedens, N. Fukunaga, B. Davidson, J.E. Dick, A.J. Minn, L.H. Boise, C.B. Thompson, M. Wicha, G. Nunez, A recombinant bcl-x s adenovirus selectively induces apoptosis in cancer cells but not in normal bone marrow cells, Proc. Natl. Acad. Sci. USA 92 (1995) 11024–11028.
[35] V.N. Sumantran, M.W. Ealovega, G. Nunez, M.F. Clarke, M.S. Wicha, Overexpression of Bcl-XS sensitizes MCF-7 cells to chemotherapy-induced apoptosis, Cancer Res. 55 (1995) 2507–2510.
[36] J.M. Adams, S. Cory, The Bcl-2 apoptotic switch in cancer development and therapy, Oncogene 26 (2007) 1324–1337.
[37] K. Kim, Silencing Bcl-X(L) in cancer therapy, Cancer Biol. Ther. 4 (2005) 398–399.
[38] M. Zuker, Mfold web server for nucleic acid folding and hybridization prediction, Nucleic Acids Res. 31 (2003) 3406–3415.
[39] A. Kar, K. Fushimi, X. Zhou, P. Ray, C. Shi, X. Chen, Z. Liu, S. Chen, J.Y. Wu, RNA helicase p68 (DDX5) regulates tau exon 10 splicing by modulating a stem-loop structure at the 5′ splice site, Mol. Cell Biol. 31 (2011) 1812–1821.

Biochemical and Biophysical Research Communications 420 (2012) 473–478

Contents lists available at SciVerse ScienceDirect

Biochemical and Biophysical Research Communications

journal homepage: www.elsevier.com/locate/ybbrc

Binding of human BiP to the ER stress transducers IRE1 and PERK requires ATP

Si Nga Sou [a], Kristina M. Ilieva [b], Karen M. Polizzi [b,*]

[a] Centre for Process Systems Engineering, Department of Chemical Engineering and Chemical Technology, Imperial College, London SW7 2AZ, United Kingdom
[b] Division of Molecular Biosciences & Centre for Synthetic Biology and Innovation, Imperial College, London SW7 2AZ, United Kingdom

ARTICLE INFO

Article history:
Received 20 February 2012
Available online 13 March 2012

Keywords:
Endoplasmic reticulum stress
Unfolded protein response
Immunoglobulin binding protein
Glucose regulated protein 78
Protein quality control
ER homeostasis

ABSTRACT

ER stress is activated in a number of important diseases such as diabetes, cancer, and neurodegeneration, but the molecular interactions governing the response are still being elucidated. In the absence of stress, protein complexes exist between the ER-resident chaperone BiP and three transmembrane signalling molecules which are responsible for signal transmission. Previous results suggested that cofactors might participate in these interactions, but the molecular details are not well understood. We coexpressed BiP and the lumenal domains of each of the three ER stress transducers and copurified the complexes in the presence of ATP and ADP in order to better understand how the complex is formed. ATP, but not ADP, was required to isolate the BiP-IRE1 and the BiP-PERK complexes, but the BiP-ATF6 complex was purified in all conditions tested. Based on the results, we hypothesize that in contrast to its mode of binding ATF6 and unfolded proteins, BiP binds to IRE1 and PERK in a different manner.

1. Introduction

The endoplasmic reticulum (ER) is the main site of quality control in protein folding. In order to maintain ER homeostasis, a highly tuned signalling mechanism known as the ER stress response monitors the level of unfolded proteins and triggers ameliorating responses if this exceeds a particular threshold. The molecular details of how this surveillance mechanism functions are still being discovered. However, the central players are the Hsp70 ER chaperone, BiP (also known as GRP78), and three transmembrane signalling proteins IRE1, PERK, and ATF6 (also called the ER stress transducers). In the resting state of the ER, IRE1, PERK, and ATF6 are each bound by BiP and no signal is transmitted. Accumulation of unfolded or misfolded protein leads to BiP dissociation and ER stress signalling, resulting in the increase of chaperone and foldase levels, attenuation of protein synthesis, and eventually, if homeostasis cannot be restored, cell death [1–3]. ER stress activation has been implicated in various protein misfolding diseases [4], diabetes [5], and cancer [6]. A greater understanding of how ER stress is triggered and how BiP rebinding occurs once homeostasis is restored is an important step towards the prevention of cell loss. We wish to begin by understanding the molecular interactions between BiP and the ER stress transducers in the resting state of the cell, in the hope that this would shed light on the biochemical components necessary to restore homeostasis.

Our initial attempts to form BiP-IRE1 complexes *in vitro* by mixing purified proteins did not result in the formation of a complex (unpublished data), which suggested perhaps the presence of one or more additional factors was required to assist in complex formation. The unidentified factor(s) could be small molecules (e.g. ATP or ADP) or accessory proteins. Both cofactors play a role in the interaction of BiP with unfolded proteins [7] and an associated nucleotide exchange factor has been shown to work with BiP to accelerate the rate of ADP/ATP exchange [8]. Seminal work by Bertolotti et al. showed that the interaction between BiP and PERK co-immunoprecipitated directly from tissue was disrupted upon addition of ATP [9]. However, a study exploring the interaction of Kar2p (the yeast BiP homolog) and IRE1 in yeast suggested that the interaction site between BiP and IRE1 was located on the ATPase domain of BiP and that it was the ATP-bound form of BiP that was able to bind IRE1 [10]. Additionally, Shen et al. easily isolated recombinant BiP-ATF6 complexes from stably transfected NIH 3T3 cells and demonstrated that the BiP-ATF6 complex was resistant to ATP-induced dissociation [11]. Therefore, the role of ATP in the BiP-ER stress transducer interaction remains unclear. We reasoned that coexpression of BiP and the ER stress transducers within a single cell would mean that small molecule factors would be present to facilitate the interaction, and purification of the complex in the presence of different additives would give us information on which small molecule factors are necessary to maintain the interaction. We chose *Escherichia coli* as a host cell in order to minimise the chance of contamination by endogenous proteins.

Abbreviations: ADP, adenosine diphosphate; ATF6, activating transcription factor 6; ATP, adenosine triphosphate; BiP, immunoglobulin binding protein; ER, endoplasmic reticulum; GST, glutathione-S-transferase; IRE1, inositol requiring enzyme 1; PERK, PKR-like ER kinase; UPR, unfolded protein response.

* Corresponding author. Fax: +44 2075943057.
E-mail addresses: si.sou07@imperial.ac.uk (S.N. Sou), k.polizzi@imperial.ac.uk (K.M. Polizzi).

0006-291X/$ - see front matter © 2012 Elsevier Inc. All rights reserved.
http://dx.doi.org/10.1016/j.bbrc.2012.03.030

We co-expressed BiP with each of the ER stress transducers and then attempted to co-purify the complexes in the presence or absence of ATP and ADP. ATP, but not ADP, was required to isolate the BiP-IRE1 and the BiP-PERK complexes, but the BiP-ATF6 complex was purified in all conditions tested. Based on the results, we hypothesize that in contrast to its mode of binding ATF6 and unfolded proteins, BiP binds to IRE1 and PERK in a different manner.

2. Materials and methods

2.1. Plasmid and strain construction

The amino acid sequences corresponding to the lumenal domains of ATF6, IRE1 and PERK were predicted using bioinformatics. First, the signal sequences of IRE1 and PERK were identified by the SignalP 3.0 Server [12] and truncated. Subsequently, the Phobius Transmembrane Topology Predictor [13] was used to identify the transmembrane domains of all three proteins which were also truncated, leaving the putative sequence of the lumenal domain. The stability and half-life of these proteins when expressed in bacteria were then predicted using the ProtParam tool [14] and further truncations were made where necessary to increase the predicted protein stability. The final constructs correspond to amino acids 399 to 670 of ATF6, 19 to 333 of IRE1, and 32 to 522 of PERK.

The inserts were PCR amplified from the MegaMan human transcriptome library (Agilent), first with blunt primers (Invitrogen) to amplify initial fragments, followed by gel purification and secondary PCR to add restriction enzyme recognition sequences. Human BiP lacking the N-terminal signal sequence (amino acid residues 20–654) was cloned into pET29a (Merck Biosciences) using the *Nde*I and *Xho*I restriction sites in frame with the C-terminal histidine tag. ATF6, IRE1, and PERK were cloned into the pGEX4T-2 vector (GE Healthcare) using the *Eco*RI and *Xho*I restriction sites in frame with the N-terminal GST tag. The T37G mutant of BiP was created using mutational primers followed by *Dpn*I digestion (Promega). All primer sequences and PCR conditions are reported in the Supplementary Information. Sequences were verified (Eurofins MWG Operon). Plasmids were transformed into *E. coli* BL21 (DE3) cells (New England Biolabs) for protein expression.

2.2. Protein expression and affinity chromatography

A single colony was grown overnight in 10 mL LB broth supplemented with 50 μg/mL ampicillin (single expression of ATF6, IRE1, or PERK), 30 μg/mL kanamycin (single expression of BiP), or both (coexpressions). Each overnight culture was added into 500 mL of LB broth with its respective antibiotics and incubated at 37 °C until cell density reached an OD_{600} of 0.5–0.7. Isopropyl β-D-1-thiogalactopyranoside (IPTG) was added to a final concentration of 0.5 mM and the cultures were incubated at 30 °C for a further 4 h to express the protein. Cells were harvested via centrifugation at 6774*g* for 15 min, the supernatant was discarded and the pellet was stored at −80 °C overnight.

The cell pellet was lysed by sonication for 3 min with 3 s pulses in 10 mL PBS-lysis (PBS-L) buffer (25 mL 10× PBS, 1% Triton X-100, 1 mM DTT, 1–2 mM PMSF, 1 mg/mL lysozyme pH 8.0). Lysate was clarified by centrifugation at 11,600*g* for 40 min and used in column affinity purification. GST-tagged proteins were purified using the Glutathione Superflow Resin (Qiagen) and His-tagged proteins by Ni–NTA Agarose (Qiagen) using a gravity flow column, both according to the manufacturer's protocol. Co-expressed cultures were purified by both methods. In preparation for the activity assay, BiP was purified with two additional wash steps: a low pH wash (20 mM Na_2HPO_4, 50 mM NaCl and 0.1% Triton X-100 at pH 5.5) and a high pH stringency wash (20 mM Na_2HPO_4, 500 mM NaCl, 0.1% Triton X-100 and 50 mM imidazole at pH 7.4) in order to dislodge bound proteins and allow for clearer analysis. These washes were not used during the His-tag purification of the co-expressed cultures as they dislodged bound ER stress transducers.

2.3. Gel electrophoresis and Western blotting

Samples were run on 12% Precast protein gel (Thermo Scientific) in 1× Tris–HEPES running buffer at 120 V for 1 h and then transferred onto a methanol-activated PVDF membrane (Invitrogen) using a semi-dry transfer system (Bio-Rad) at 0.3 A for 50 min. Bands were visualised using the Western Breeze Chromogenic Detection Kit (Invitrogen) according to the manufacturer's instructions using a 1:1000 dilution of the mouse anti-GST or anti-His primary antibody (Invitrogen) and the anti-mouse alkaline phosphatase conjugated secondary antibody supplied in the kit. Bands were visualized by incubating the membrane in 5 mL chromogenic substrate (BCIP/NBT).

2.4. BiP refolding assay

The protocol for BiP-mediated refolding of denatured β-galactosidase was adapted from Freeman and Morimoto, [15]. First, β-galactosidase (10 μg/mL, Sigma Aldrich) was denatured by incubation in 6 M guanidine hydrochloride at 30 °C for 30 min. 3.4 nM of the denatured β-galactosidase was incubated with 1.6 μM BiP in refolding buffer (25 mM HEPES, pH 7.4, 5 mM $MgCl_2$, 50 mM KCl, 2 mM ATP, 2 mM ADP, 10 mM DDT) at 37 °C. At each time point, 10 μL of this reaction was mixed with 10 μL of 0.8 M ONPG (Sigma) in a clear bottomed 96-well plate (Costar) and incubated at 37 °C for 30 min, followed by reaction termination with 50 μL of 0.5 M sodium carbonate. Absorbance of each sample was measured at 412 nm in a BMG Polstar Omega plate reader. The percentage of refolding activity was calculated by comparing sample absorbance relative to that of the non-denatured β-galactosidase. Quantitative results are presented as the mean ± SEM.

3. Results

3.1. Human BiP produced in E. coli is functional

Heterologous expression of human BiP in *E. coli* could result in a poorly folded inactive protein which would make our study of complex formation subject to artefacts. Thus, we wanted to verify that the soluble BiP protein produced in *E. coli* was indeed functional. Toward this end, we performed a refolding assay using the BiP purified with the additional low pH and high stringency washes in order to determine whether it was an active molecular chaperone. The BiP produced in *E. coli* does function in the refolding of guanidinium hydrochloride denatured β-galactosidase, restoring it to full activity in approximately 3 h (Fig. 1). The chaperone activity of BiP expressed in this study was comparable to that of the recombinant Hsp70 [16] and Hsp70 purified directly from chicken liver [17].

3.2. The BiP-ATF6 complex is stably formed

To verify that our system was capable of replicating previous results, we coexpressed BiP and ATF6 and then attempted to purify the complex in the presence or absence of ATP and ADP. Fig. 2a shows the results from the Ni–NTA purification experiment which uses the polyhistidine tag on BiP to capture the complex. The BiP-ATF6 complex was purified in all conditions, regardless of whether ATP or ADP (or neither) was present, consistent with

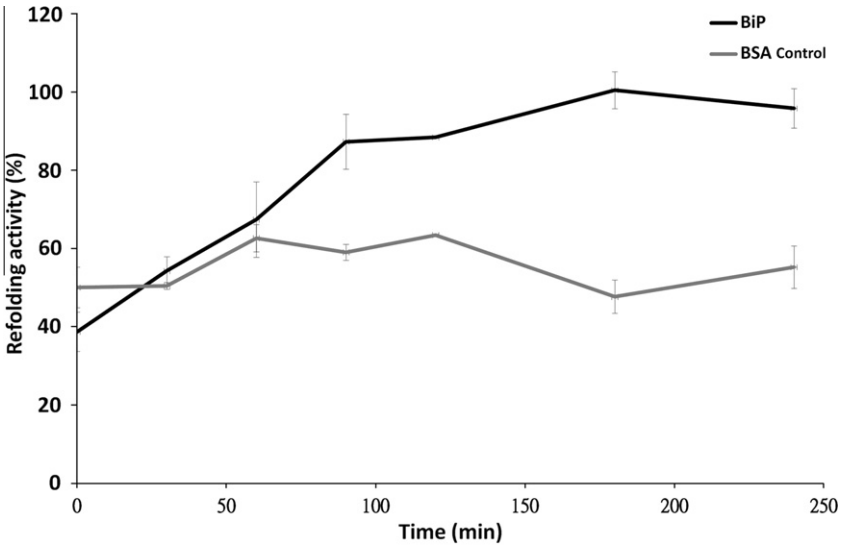

Fig. 1. Functional assay of human BiP produced in *E. coli* using unfolded β-galactosidase. Samples containing BiP (dark grey line) were monitored over time for their ability to restore β-galactosidase activity. BSA (light grey line) was used as a control for spontaneous refolding.

the report that the complex is formed stably and does not require any additional cofactor [11]. Results using the glutathione affinity chromatography to capture the complex through ATF6 were qualitatively similar, but overall protein levels were lower suggesting that excess BiP was expressed within the system (data not shown). These results confirm the utility of our coexpression system for identifying conditions for BiP interaction with other proteins.

3.3. Co-purification of the BiP-IRE1 and BiP-PERK complexes requires ATP and an ATP-induced conformational change in BiP

We then went on to investigate the interaction of BiP with IRE1 and PERK using the coexpression system. As with the ATF6 experiment, results were similar for complexes purified through either affinity tag, but the amount of protein recovered from the GST-tag experiments was much lower than with the polyhistidine tag. In particular, levels of IRE1 were very low (data not shown), so the results displayed are from the polyhistidine tag experiment. Coexpression of BiP and IRE1 (Fig. 2b) and BiP and PERK (Fig. 2c) both resulted in the formation of a complex that was only purified in the presence of ATP and absent when purified in the presence of ADP or with no cofactor. This dependence is not what would occur in the normal catalytic cycle of BiP. For unfolded proteins, BiP has a higher affinity in its ADP bound state and exchange of the ADP for ATP by a nucleotide exchange factor facilitates the release of the polypeptide, whereas ATP hydrolysis to ADP increases BiP affinity for substrate and results in another cycle of binding [7]. Thus, our data suggests that BiP binds IRE1 and PERK in a manner different than it binds unfolded proteins.

Our results are consistent with the observation made by Todd-Corlett et al. that the binding of the yeast BiP homolog Kar2p to IRE1 occurs not through the substrate binding cleft, but through a different part of the protein. Specifically, they hypothesised that ATP binding caused a conformational change in the ATPase domain that then allowed IRE1 to bind [10]. In order to explore whether this might be true in the human system, we repeated our experiments using the T37G mutant of BiP [18] which lacks the conformational change upon binding of ATP. Indeed, when coexpressing T37G BiP with IRE1 or PERK, we were no longer able to purify the complex even in the presence of ATP, suggesting that the conformational change is a necessary part of the BiP-ER stress transducer interaction (Fig. 3a and b).

4. Discussion

Taken together, our results suggest that the interaction between BiP and IRE1 and BiP and PERK requires ATP and the conformational change produced upon ATP binding to create and/or maintain complex formation. Thus, we propose a modified BiP catalytic cycle (Fig. 4) for BiP-ER stress transducer interactions. In this model, the ATP bound form of BiP is required to bind IRE1/PERK and the ADP bound form releases from the complex. The inherent ATPase activity of BiP may then result in BiP-IRE1 and BiP-PERK interactions that are dynamic, causing BiP to cycle off and back onto the ER stress transducers. During that time, if unfolded proteins are present, BiP rebinding to the ER stress transducers might be slowed by its interaction with the unfolded protein in the ADP-bound form (where affinity for unfolded proteins is high). This would allow time for other events that might contribute to ER stress activation to occur (e.g. IRE1 clustering and binding of IRE1 to unfolded protein [19]). It is possible that the BiP-unfolded protein cycle and the BiP-IRE1/PERK cycle could operate simultaneously in an unstressed cell and that an increased concentration of unfolded proteins changes the dynamics of the interactions, contributing to ER stress activation. However, further experiments would be necessary to corroborate this hypothesis.

Pincus et al. recently provided evidence for a role for BiP as a modulator of UPR, suggesting that it aids in signal deactivation by sequestering IRE1 monomers that break away from the activated signalling cluster [20]. If ATP is indeed required to reform the interaction with the stress transducers once homeostasis has been restored, there are potential implications for the ability of cells to recover from ER stress in the presence of other stressors. Energy depletion is a common event following different types of cellular stress. For example, hypoxia can lead to lower levels of ATP production [21] and may prevent cells from restoring the ER to its resting state. This could partially account for the observation that hypoxia can contribute to ER stress [22] and that prolonged IRE1 signalling occurs in cells at the centre of a tumour mass, a relatively low oxygen environment [23]. In addition, ER perturbations can result in aberrant calcium signalling, in turn leading to mitochondrial membrane potential damage and impaired ATP synthesis capabilities [24]. Calcium dyshomeostasis and ER stress induction have both been implicated in Alzheimer's disease and may have synergistic effects in disease progression [4,25]. The energy

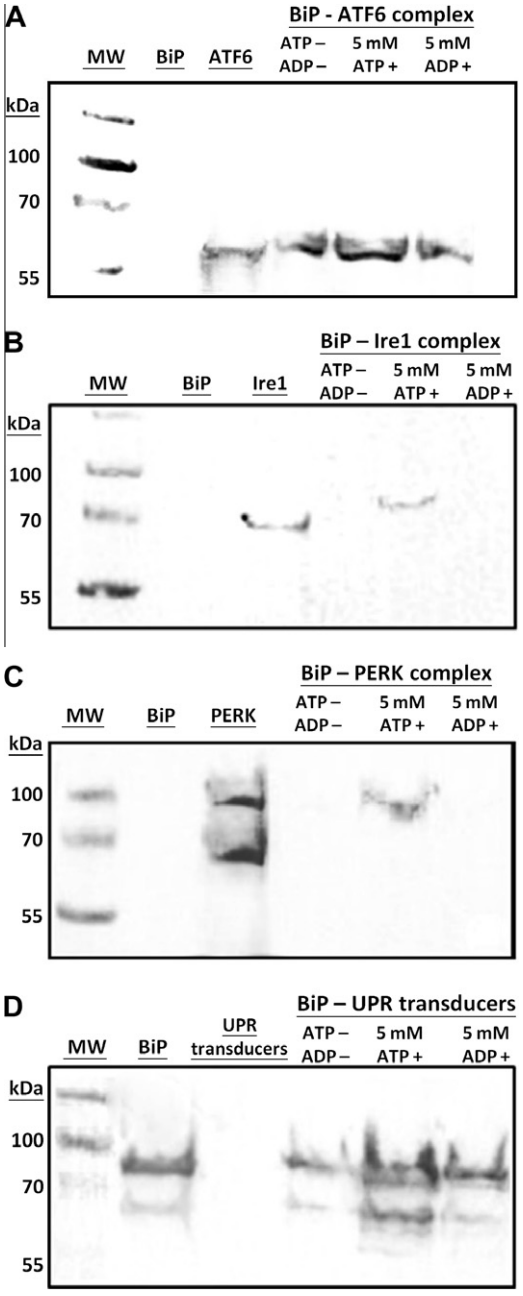

Fig. 2. Isolation of the BiP-ER stress transducer complex from the lysate of an *E. coli* population coexpressing the two proteins using Ni–NTA affinity chromatography. (A) ATF6 complex purification Western blot using the mouse anti-GST antibody as the primary antibody to detect GST-tagged proteins. Lane 1: Molecular weight marker, Lane 2: Singly expressed BiP (negative control), Lane 3: Singly expressed ATF6 (positive control), Lane 4: The complex purified without additives, Lane 5: The complex purified in the presence of 5 mM ATP, Lane 6: The complex purified in the presence of 5 mM ADP. (B) IRE1 complex purification. Western blot using the mouse anti-GST antibody as the primary antibody to detect GST-tagged proteins. Lane 1: Molecular weight marker, Lane 2: Singly expressed BiP (negative control), Lane 3: Singly expressed IRE1 (positive control), Lane 4: The complex purified without additives, Lane 5: The complex purified in the presence of 5 mM ATP, Lane 6: The complex purified in the presence of 5 mM ADP. (C) PERK complex purification. Western blot using the mouse anti-GST antibody as the primary antibody to detect GST-tagged proteins. Lane 1: Molecular weight marker, Lane 2: Singly expressed BiP (negative control), Lane 3: Singly expressed PERK (positive control), Lane 4: The complex purified without additives, Lane 5: The complex purified in the presence of 5 mM ATP, Lane 6: The complex purified in the presence of 5 mM ADP. (D) An example BiP Western blot using the mouse anti-His antibody to detect histidine tagged proteins. Lane 1: Molecular weight marker, Lane 2: Singly expressed BiP (positive control), Lane 3: Singly expressed PERK (negative control), Lane 4: The complex purified without additives, Lane 5: The complex purified in the presence of 5 mM ATP, Lane 6: The complex purified in the presence of 5 mM ADP.

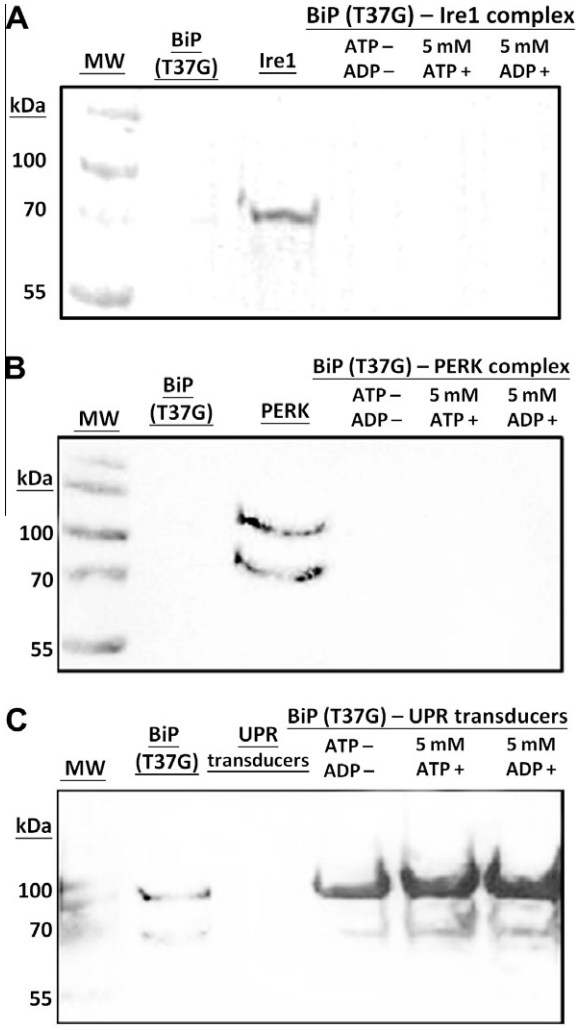

Fig. 3. Coexpression and co-purification experiment using the T37G mutant of BiP. (A) IRE1 complex purification. Western blot using the mouse anti-GST antibody as the primary antibody to detect GST-tagged proteins. Lane 1: Molecular weight marker, Lane 2: Singly expressed T37G BiP (negative control), Lane 3: Singly expressed IRE1 (positive control), Lane 4: The complex purified without additives, Lane 5: The complex purified in the presence of 5 mM ATP, Lane 6: The complex purified in the presence of 5 mM ADP. (B) PERK complex purification. Western blot using the mouse anti-GST antibody as the primary antibody to detect GST-tagged proteins. Lane 1: Molecular weight marker, Lane 2: Singly expressed T37G BiP (negative control), Lane 3: Singly expressed PERK (positive control), Lane 4: The complex purified without additives, Lane 5: The complex purified in the presence of 5 mM ATP, Lane 6: The complex purified in the presence of 5 mM ADP. (C) An example BiP Western blot using the mouse anti-His antibody to detect histidine tagged proteins. Lane 1: Molecular weight marker, Lane 2: Singly expressed T37G BiP (positive control), Lane 3: Singly expressed PERK (negative control), Lane 4: The complex purified without additives, Lane 5: The complex purified in the presence of 5 mM ATP, Lane 6: The complex purified in the presence of 5 mM ADP.

requirement of BiP-ER stress transducer complex formation may be a hurdle to restoration of homeostasis and represents a potential point of intervention for disease treatment in complex diseases with multiple etiologies.

While our results cannot directly show whether accessory proteins are necessary to form the initial BiP-IRE1 and BiP-PERK complexes, the fact that we chose *E. coli* as our expression host suggests that any such proteins required must be highly conserved. BiP is an Hsp70 with homology to DnaK of *E. coli* [26]. Accessory proteins of DnaK such as DnaJ (which stimulates its ATPase activity) or GrpE (the associated nucleotide exchange factor) might have some degree of cross interaction with the human BiP. However, the

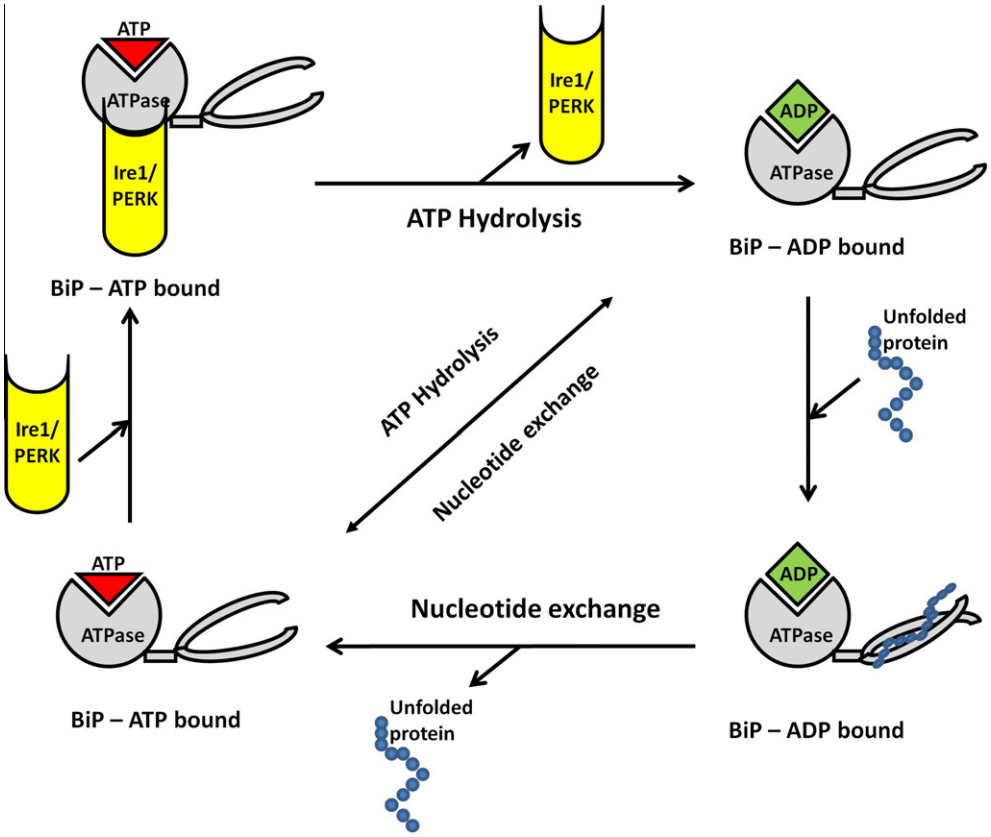

Fig. 4. Proposed binding model for BiP and IRE1/PERK.

function of a nucleotide exchange factor is to promote ADP exchange for ATP, so the presence of very high levels of ATP such as those present in our study would help to promote exchange even in the absence of a functional nucleotide exchange factor. In our case, if DnaJ promotes ATP hydrolysis by human BiP, then this could account for the fact that we purified IRE1 and PERK with a less than 1:1 stoichiometry with BiP.

Our results are based on human proteins heterologously expressed in *E. coli* which may be subject to misfolding. We have demonstrated that our purified BiP is functional, suggesting that it is not misfolded. However, for the lumenal domains of ATF6, IRE1, and PERK, there is no analogous activity assay and we cannot be sure that these proteins have adopted their native conformations in our expression system. Interestingly, the binding relationships we see do not follow what would be expected with generic unfolded proteins (where ADP would strengthen the association of misfolded protein with BiP and ATP would abolish binding) suggesting that there is a different interaction between BiP and the stress transducers in whatever conformation they adopt within our *E. coli* host. There is some evidence to suggest that at least some of the lumenal proteins might fold correctly. A crystal structure of the IRE1 lumenal domain has been obtained using *E. coli* as an expression host and the amino acid truncation used in that paper is similar to our study [27]. In addition, our results for ATF6 mirror those of Shen et al. who used mammalian cells as an expression system and also observed that the BiP-ATF6 complex was stable regardless of whether any cofactor was present [11]. However, we cannot entirely rule out protein misfolding as the root cause of our observations and so it is necessary to confirm our observations using a mammalian cell line or to compare the lumenal proteins expressed in *E. coli* to those obtained from a mammalian expression system by one or more biophysical methods determine if they have folded correctly.

Acknowledgments

This work was supported in part by an Alzheimer's Research Trust Pilot Grant (ART/PPG2009B-5). The authors thank Tanya Kapoor for creating the BiP clone. K.P. is supported by an RCUK Fellowship in Biopharmaceutical Processing. The Centre for Synthetic Biology and Innovation is generously funded by the EPSRC.

Appendix A. Supplementary data

Supplementary data associated with this article can be found, in the online version, at http://dx.doi.org/10.1016/j.bbrc.2012.03.030.

References

[1] D. Ron, P. Walter, Signal integration in the endoplasmic reticulum unfolded protein response, Nat. Rev. Mol. Cell Biol. 8 (2007) 519–529.
[2] M. Schroder, R.J. Kaufman, The mammalian unfolded protein response, Ann. Rev. Biochem. (2005) 739–789.
[3] I. Tabas, D. Ron, Integrating the mechanisms of apoptosis induced by endoplasmic reticulum stress, Nat. Cell Biol. 13 (2011) 184–190.
[4] I. Stefani, D. Wright, K. Polizzi, C. Kontoravdi, The role of ER stress-induced apoptosis in neurodegeneration, Current Alzheimer's Res. (2012).
[5] A. Volchuk, D. Ron, The endoplasmic reticulum stress response in the pancreatic beta-cell, Diabetes Obes. Metab. 12 (2010) 48–57.
[6] M. Moenner, O. Pluquet, M. Bouchecareilh, E. Chevet, Integrated endoplasmic reticulum stress responses in cancer, Cancer Res. 67 (2007) 10631–10634.
[7] M.J. Gething, Role and regulation of the ER chaperone BiP, Semin. Cell Dev. Biol. 10 (1999) 465–472.
[8] K.T. Chung, Y. Shen, L.M. Hendershot, BAP, a mammalian BiP-associated protein, is a nucleotide exchange factor that regulates the ATPase activity of BiP, J. Biol. Chem. 277 (2002) 47557–47563.
[9] A. Bertolotti, Y.H. Zhang, L.M. Hendershot, H.P. Harding, D. Ron, Dynamic interaction of BiP and ER stress transducers in the unfolded-protein response, Nat. Cell Biol. 2 (2000) 326–332.
[10] A. Todd-Corlett, E. Jones, C. Seghers, M.J. Gething, Lobe IB of the ATPase domain of Kar2p/BiP interacts with Ire1p to negatively regulate the unfolded protein response in *Saccharomyces cerevisiae*, J. Mol. Biol. 367 (2007) 770–787.

[11] J.S. Shen, E.L. Snapp, J. Lippincott-Schwartz, R. Prywes, Stable binding of ATF6 to BiP in the endoplasmic reticulum stress response, Mol. Cell. Biol. 25 (2005) 921–932.

[12] O. Emanuelsson, S. Brunak, G. von Heijne, H. Nielsen, Locating proteins in the cell using TargetP, SignalP and related tools, Nature Protoc. 2 (2007) 953–971.

[13] L. Kall, A. Krogh, E.L.L. Sonnhammer, A combined transmembrane topology and signal peptide prediction method, J. Mol. Biol. 338 (2004) 1027–1036.

[14] E. Gasteiger, A. Gattiker, C. Hoogland, I. Ivanyi, R.D. Appel, A. Bairoch, ExPASy: the proteomics server for in-depth protein knowledge and analysis, Nucleic Acids Res. 31 (2003) 3784–3788.

[15] B.C. Freeman, R.I. Morimoto, The human cytosolic molecular chaperones hsp90, Hsp70 (hsc70) and hdj-1 have distinct roles in recognition of a non-native protein and protein refolding, EMBO J. 15 (1996) 2969–2979.

[16] S. Takayama, D.N. Bimston, S. Matsuzawa, B.C. Freeman, C. AimeSempe, Z.H. Xie, R.I. Morimoto, J.C. Reed, BAG-1 modulates the chaperone activity of Hsp70/Hsc70, EMBO J. 16 (1997) 4887–4896.

[17] R.J. Schumacher, W.J. Hansen, B.C. Freeman, E. Alnemri, G. Litwack, D.O. Toft, Cooperative action of Hsp70, Hsp90, and DnaJ proteins in protein renaturation, Biochemistry 35 (1996) 14889–14898.

[18] J.Y. Wei, J.R. Gaut, L.M. Hendershot, *In vitro* dissociation of BiP-peptide complexes requires a conformational change in BiP after ATP binding but does not require ATP hydrolysis, J. Biol. Chem. 270 (1995) 26677–26682.

[19] B.M. Gardner, P. Walter, Unfolded proteins are Ire1-activating ligands that directly induce the unfolded protein response, Science 333 (2011) 1891–1894.

[20] D. Pincus, M.W. Chevalier, T. Aragon, E. van Anken, S.E. Vidal, H. El-Samad, P. Walter, BiP binding to the ER-stress sensor Ire1 tunes the homeostatic behavior of the unfolded protein response, PLoS Biol. 8 (2010).

[21] J.P. Steinbach, H. Wolburg, A. Klumpp, H. Probst, M. Weller, Hypoxia-induced cell death in human malignant glioma cells: energy deprivation promotes decoupling of mitochondrial cytochrome c release from caspase processing and necrotic cell death, Cell Death Differ. 10 (2003) 823–832.

[22] N. Badiola, C. Penas, A. Minano-Molina, B. Barneda-Zahonero, R. Fado, G. Sanchez-Opazo, J.X. Comella, J. Sabria, C. Zhu, K. Blomgren, C. Casas, J. Rodriguez-Alvarez, Induction of ER stress in response to oxygen-glucose deprivation of cortical cultures involves the activation of the PERK and IRE-1 pathways and of caspase-12, Cell Death & Disease 2.

[23] C. Koumenis, ER stress, hypoxia tolerance and tumor progression, Curr. Mol. Med. 6 (2006) 55–69.

[24] M. Giacomello, I. Drago, P. Pizzo, T. Pozzan, Mitochondrial Ca^{2+} as a key regulator of cell life and death, Cell Death Differ. 14 (2007) 1267–1274.

[25] F.M. LaFerla, Calcium dyshomeostasis and intracellular signalling in Alzheimer's disease, Nat. Rev. Neurosci. 3 (2002) 862–872.

[26] M. Wisniewska, T. Karlberg, L. Lehtio, I. Johansson, T. Kotenyova, M. Moche, H. Schuler, Crystal Structures of the ATPase Domains of Four Human Hsp70 Isoforms: HSPA1L/Hsp70-hom, HSPA2/Hsp70-2, HSPA6/Hsp70B′, and HSPA5/BiP/GRP78, PLoS One 5 (2010).

[27] J.H. Zhou, C.Y. Liu, S.H. Back, R.L. Clark, D. Peisach, Z.H. Xu, R.J. Kaufman, The crystal structure of human IRE1 luminal domain reveals a conserved dimerization interface required for activation of the unfolded protein response, Proc. Nat. Acad. Sci. USA 103 (2006) 14343–14348.

Biochemical and Biophysical Research Communications 420 (2012) 479–484

Contents lists available at SciVerse ScienceDirect

Biochemical and Biophysical Research Communications

journal homepage: www.elsevier.com/locate/ybbrc

DGKζ is involved in LPS-activated phagocytosis through IQGAP1/Rac1 pathway

Masashi Okada [a,*], Yasukazu Hozumi [a], Kiyoshi Iwazaki [a], Kentaro Misaki [b], Mitsuaki Yanagida [b], Yoshihiko Araki [b], Takashi Watanabe [c], Hitoshi Yagisawa [d], Matthew K. Topham [e], Kozo Kaibuchi [c], Kaoru Goto [a,*]

[a] Department of Anatomy and Cell Biology, Yamagata University School of Medicine, Yamagata 990-9585, Japan
[b] Institute for Environmental and Gender-specific Medicine, Juntendo University Graduate School of Medicine, Urayasu 279-0021, Japan
[c] Department of Cell Pharmacology, Nagoya University Graduate School of Medicine, Showa, Nagoya 466-8550, Japan
[d] Laboratory of Biological Signaling, Graduate School of Life Science, University of Hyogo, Kamigori 678-1297, Japan
[e] Huntsman Cancer Institute, Department of Oncological Sciences, University of Utah, Salt Lake City 84112, USA

ARTICLE INFO

Article history:
Received 7 March 2012
Available online 17 March 2012

Keywords:
Diacylglycerol kinase
IQGAP
Rac1
Macrophage
Phagocytosis

ABSTRACT

Diacylglycerol kinase (DGK) plays an important role in phosphoinositide signaling cascade by regulating the intracellular level of diacylglycerol and phosphatidic acid. The DGK family is involved in various pathophysiological responses that are mediated through unique binding partners in different tissues and cells. In this study, we identified a small GTPase effector protein, IQGAP1, as a novel DGKζ-associated complex protein. A bacterial endotoxin, lipopolysaccharide (LPS), facilitated the complex formation in macrophages. Both proteins co-localized at the edge and phagocytic cup of the cell. Furthermore, RNA interference-mediated knockdown of DGKζ or IQGAP1 impaired LPS-induced Rac1 activation. Primary macrophages derived from DGKζ$^{-/-}$ mice attenuated LPS-induced phagocytosis of bacteria. These results suggest that DGKζ is involved in IQGAP1/Rac1-mediated phagocytosis upon LPS stimulation in macrophages.

1. Introduction

Macrophages play a central role in inflammatory responses such as cytokine synthesis, free radical production, and phagocytosis by bacterial infection [1]. Phagocytosis is an important role of macrophage-mediated innate immune response to bacterial infection, which includes receptor binding, internalization, and phagosome maturation [2]. During phagocytosis in macrophages, the relative abundance of several phosphoinositides (PIs) changes drastically [2]. Phosphatidylinositol (4,5)-bisphosphate (PtdIns(4,5)P_2), constitutively presented in the plasma membrane, undergoes rapid and transient accumulation above basal levels at the site of particle engagement and propagates with the pseudopods as they extend around the particle [3]. PtdIns(4,5)P_2 promotes *de novo* actin polymerization to initiate phagocytic cup extension, whereas elimination of PtdIns(4,5)P_2 causes depolymerization of actin filaments to promote closure of the phagocytic cup [2]. The PtdIns(4,5)P_2-metabolizing proteins such as type I PtdIns-4-phosphate 5-kinase (PIP5K) and phospholipase C (PLC)γ localize to the phagocytic cup, and regulate the availability of PtdIns(4,5)P_2. Indeed, PLC inactivation attenuates phagocytosis [3]. Diacylglycerol (DG), which is generated by hydrolysis from PtdIns(4,5)P_2 by PLC, initially associates with phagocytic cup and early phagosome [3]. DG regulates the activity and/or subcellular distribution of DG effectors containing C1 domain [4]. Indeed, PKCs and RasGRPs are recruited to phagosomes [5,6]. Phosphatidic acid (PA), which can be generated by either phospholipase D (PLD)-mediated hydrolysis of phosphatidylcholine (PC) or phosphorylation of DG by DG kinase (DGK), is shown to promote macrophage activation induced by lipopolysaccharide (LPS), a component of the outer membrane from Gram-negative bacteria [7]. However, inhibition of PLD, one PA-generating pathway, does not alter target ingestion in macrophages, suggesting that the other PA-generating pathway involving DGK might contribute to phagocytosis [8].

Through the control of DG/PA balance by enzyme activity, DGKs play important roles in various signaling from receptors and modulate diverse cellular processes [9]. In mammalian cells, 10 different isoforms have been identified. They show distinct properties in terms of gene expression, enzymatic characteristics, and subcellular localization [4,10,11]. Previous report has described that LPS-induced proinflammatory cytokine production is decreased in DGKζ$^{-/-}$ bone marrow macrophages [12], demonstrating that DGKζ signaling regulates macrophage function although the role played by DGKζ in phagocytosis of macrophages remains unclear.

* Corresponding authors. Address: Department of Anatomy and Cell Biology, Yamagata University School of Medicine, 2-2-2 Iida-nishi, Yamagata 990-9585, Japan. Fax: +81 23 628 5210.
E-mail addresses: m-okada@med.id.yamagata-u.ac.jp (M. Okada), kgoto@med.id.yamagata-u.ac.jp (K. Goto).

0006-291X/$ - see front matter © 2012 Elsevier Inc. All rights reserved.
http://dx.doi.org/10.1016/j.bbrc.2012.03.057

In this study, we identified IQGAP1 as a novel DGKζ-associating partner. The interaction between IQGAP1 and DGKζ is regulated by LPS stimulation in macrophages. Furthermore, knockdown or ablation of DGKζ impairs Rac1 activation and LPS-induced phagocytosis of bacteria. Collectively, these results suggest a crucial role of DGKζ in IQGAP1-mediated Rac1 activation during the process of LPS-activated phagocytosis of bacteria.

2. Materials and methods

2.1. Reagents

The cell culture reagents were obtained from Wako. HEK293 and the murine macrophage cell line Raw264 cells were maintained in Dulbecco's modified Eagle's medium (DMEM) containing 10% heat-inactivated fetal bovine serum (FBS), 100 U/ml penicillin, 100 μg/ml streptomycin sulphate at 37 °C and 5% CO_2. LPS and latex beads were purchased from Sigma. Enzyme inhibitors were from Sigma (ET18OCH$_3$), Calbiochem (Gö6850, wortmannin), and Cayman Chemical Company (PD98059). Alexa-565-conjugated phalloidin was from Molecular Probes. Protein G-conjugated Sepharose and Glutathione Sepharose were obtained from GE Healthcare. Anti-β-actin and anti-Flag-M2 antibodies, anti-Flag-M2 agarose, and Flag peptide were purchased from Sigma. Other antibodies were from Santa Cruz (anti-IQGAP1, anti-RhoGDI, and anti-HA), and Chemicon (Anti-Rac1), and Serotec (anti-CD11b). Anti-GFP and anti-DGKζ antibodies were produced as previously described [13,14].

2.2. Plasmids construction

GFP-IQGAP1, GFP-IQGAP2, GFP-IQGAP3, and HA-Rac1 DA (constitutively GTP-bound form) were described previously [15]. Flag-tagged DGKζ, DGKζΔC, DGKζC1/3 and DGKζ1-280 were constructed as described [13,16]. GFP-IQGAP1 truncated mutants encoding amino acids 1-1248, 1070-1657, 1-863, and 764-1657 were obtained by digestion of full length IQGAP1 with *Afl*II, *Bgl*II, *Bam*HI, and *Eco*RI, respectively. For bacterial expression, the plasmid encoding GFP was amplified using PCR and subcloned into the pGEX2TK. GST-PAK1-CRIB, corresponding to the fragment encoding 67-150 of human PAK1, was amplified using PCR and subcloned into pGEX4T2. All constructs were fully verified by DNA sequencing.

2.3. Animals and peritoneal macrophage isolation

All experimental protocols using mice were performed in accordance with the guidelines and the permission of the Animal Research Center of Yamagata University. Generation of DGKζ$^{-/-}$ mice were as described [17]. All of the mice were aged between 8 and 12 weeks. Wild-type mice, C57BL6, were purchased from Japan SLC Inc. Peritoneal macrophages were elicited by intraperitoneal injection of 2 ml 4% thioglycolate (Sigma). After 4 days, the macrophages were harvested from peritoneal lavage. They were washed with 5 ml of PBS and plated in culture dishes in complete DMEM. After 1 h, non-adherent cells were washed away and the remaining cells were incubated. More than 95% of cells were CD11b-positive macrophages by fluorescent microscope analysis.

2.4. Transfection and RNAi

Cells were transfected with plasmid constructs using Lipofect-AMINE2000 (Invitrogen). All constructs for transfection were purified with EndoFree Plasmid Maxi Kit (QIAGEN). DGKζ-specific siRNA (5′-UAGUCGUGCAUACUGACCCTG-3′) was obtained from QIAGEN. IQGAP1-specific siRNA (5′-CCAACAAGAUGUUUCUGGGC-GAUAA-3′) was purchased from Invitrogen.

2.5. Immunoprecipitation, in vitro binding assay, immunoblot, and TOF-MS analyses

Co-immunoprecipitation analysis was conducted as described previously [18]. Cells were washed with ice-cold PBS and then lysed in 600 μl of lysis buffer containing 50 mM Tris/HCl (pH 7.4), 40 mM NaCl, 1 mM EDTA, 0.5% Triton X-100, 1.5 mM Na_3VO_4, 50 mM NaF, 10 mM sodium pyrophosphate, 10 mM sodium β-glycerophosphate, and protease inhibitor cocktail (Sigma). After centrifugation, the supernatant was mixed with antibody. After washing, the immunocomplexes were eluted with SDS–PAGE sample buffer. *In vitro* pull-down assay and immunoblot analysis were as described [18]. Briefly, GST-PAK1-CRIB was expressed in BL21 (DE3)pLysE strain by IPTG induction and then purified with glutathione-Sepharose. Sepharose-immobilized GST-PAK1-CRIB was mixed with cell lysate. After washing, bound proteins were eluted with SDS–PAGE sample buffer. For searching interaction molecules, immunoprecipitation and TOF-MS analysis were performed as described previously [19]. In brief, Flag-tagged DGKζ was transfected into HEK293 cells and lysed. After centrifugation for 20 min at 18,000*g* at 4 °C, the supernatant was mixed with anti-Flag-M2 agarose and washed with lysis buffer five times followed by wash buffer (20 mM Tris/HCl (pH 7.4), 150 mM NaCl) twice. The immunocomplexes were eluted with Flag peptide. After SDS–PAGE, samples are analyzed by TOF-MS with subsequent identification using the Mascot search program.

2.6. Microscopic analysis

Cells were seeded onto coverslips in 12-well dish and were fixed with 3% formaldehyde in PBS at room temperature (RT) for 10 min. The cells were then permeabilized and blocked with 0.3% Triton X-100 and 2% FBS in PBS at RT for 15 min, washed with PBS three times and subjected to immunocytochemistry as described previously [20]. Fluorescent images were taken under a Zeiss Axioplan 2 microscope equipped with a confocal laser-scanning unit (Carl Zeiss LSM510Meta).

2.7. Phagocytosis assay

Bacterial phagocytosis by macrophages was examined as described previously [21]. Briefly, the day before commencing the experiment, *Escherichia coli* strain BL21 (DE3)pLysE carrying pGEX-GFP was grown in LB and induced by IPTG. Macrophages were washed with warmed PBS and mixed with GFP-*E. coli* at a multiplicity of infection (MOI) of 40–60 in DMEM at 37 °C for 45 min. After washing and fixation, macrophages that phagocytized one or more than two GFP-*E. coli* were counted. The data were expressed mean ± SD and analyzed by Student's *t*-test. A value of $p < 0.05$ was considered to be statistically significant. For latex bead phagocytosis assay, Raw264 cells were treated with 100 ng/ml LPS and incubated at 37 °C with latex beads (1:500 final dilution) in DMEM without serum for 45 min. After fixation, cells were subjected to immunocytochemistry.

3. Results

3.1. DGKζ interacts with IQGAP

Previously, several DGKζ interacting molecules have been identified, such as α-syntrophin [22] and nucleosome assembly protein [13]. These DGKζ interacting proteins are shown to affect the subcellular localization of DGKζ and mediate its physiological functions. We sought to identify previously unknown DGKζ interacting molecules using co-immunoprecipitation and mass spectrometry.

In the immunoprecipitants of HEK293 cells transfected with Flag-DGKζ, a protein with a mass of 190 kDa was identified as human IQGAP1 (GI: 4506787), a small GTPase Rac1/Cdc42 effector [23,24]. Using immunoblot analysis, an immunoreactive band was recognized specifically by anti-IQGAP1 antibody in the Flag-DGKζ eluates but not in the control eluates (Fig. 1A). The IQGAP family comprises three subtypes [15]. To explore whether other IQGAPs can interact with DGKζ, we performed co-transfection and immunoprecipitation assay. Immunoblot analysis revealed that DGKζ was associated with GFP-IQGAP1 and IQGAP3, but not IQGAP2 (Fig. 1B). To characterize the domains responsible for association with IQGAP1, we constructed a series of DGKζ truncate mutants (Fig. 1C) and performed immunoprecipitation experiments in co-transfected HEK293 cells. Immunoblot analysis revealed that the full length, C-terminal deletion (ΔC), and amino acid 1-280 region of DGKζ associated with IQGAP1, suggesting the necessity of the N-terminal region (a.a. 1–249) of DGKζ for binding (Fig. 1D). To explore the interacting region of IQGAP1 further, we generated a series of IQGAP1 mutants (Fig. 1E). Immunoprecipitation analysis revealed that DGKζ bound efficiently to a.a. 1070–1657 and a.a. 764–1657, weakly to a.a. 1–1248, but not to the N-terminal half (a.a. 1–863) of IQGAP1. These results suggest that the RasGAP-related domain (GRD) of IQGAP1 is responsible for DGKζ binding, although RasGAP-C region could affect the binding affinity (Fig. 1F).

3.2. LPS regulates the association between DGKζ and IQGAP1 in macrophages

DGKζ-mediated responses are shown to be critical for the immune system in macrophages [12]. To examine the endogenous association between DGKζ and IQGAP1 in macrophages, we performed immunoprecipitation assay on a murine macrophage-like cell line, Raw264 cells. Endogenous IQGAP1 was detected in the anti-DGKζ immunoprecipitants (Fig. 2A, left) and vice versa (Fig. 2A, right), suggesting that DGKζ associates with IQGAP1 in Raw264 cells. Furthermore, endogenous interaction between IQGAP1 and DGKζ was also confirmed in mouse primary peritoneal macrophages (Fig. 2B). No interaction was found in the immunoprecipitants using control IgG (Fig. 2A and B).

Toll-like receptor (TLR) is well known to activate a series of intracellular signaling pathways that engender the dynamic and rapid actin reorganization through small GTPase signaling in macrophages [2]. To examine whether the interaction between DGKζ and IQGAP1 can be regulated by LPS/TLR signaling, we performed immunoprecipitation assay after LPS stimulation. In Raw264 cells without LPS treatment, DGKζ associated weakly with IQGAP1 (Fig. 2C). Intriguingly, LPS treatment enhanced DGKζ–IQGAP1 complex formation. Treatment with 100 ng/ml LPS was sufficient to induce the complex formation (Fig. 2C, lanes 3 and 4), which was enhanced in a time-dependent manner (Fig. 2D). LPS-induced complex formation between DGKζ and IQGAP1 was also observed in primary peritoneal macrophages (Fig. 2E, lanes 1 and 2). The specificity of this association between DGKζ and IQGAP1 was verified with DGKζ$^{-/-}$ primary macrophages (Fig. 2E, lanes 3 and 4). To explore how DGKζ–IQGAP1 complex formation is regulated after LPS stimulation, we performed immunoprecipitation assay using various inhibitors. Compared with the control, LPS-induced association of DGKζ and IQGAP1 was substantially blocked by inhibitors for PI3K (wortmannin), MEK (PD98059), and PKC (Gö6850), whereas PLC inhibitor, ET18OCH$_3$, had less effect on the complex formation (Fig. 2F).

We next examined the subcellular localization of DGKζ and IQGAP1. In transfected macrophages, Flag-DGKζ colocalized with endogenous IQGAP1 at the membrane edge (Fig. 2G *upper*). After

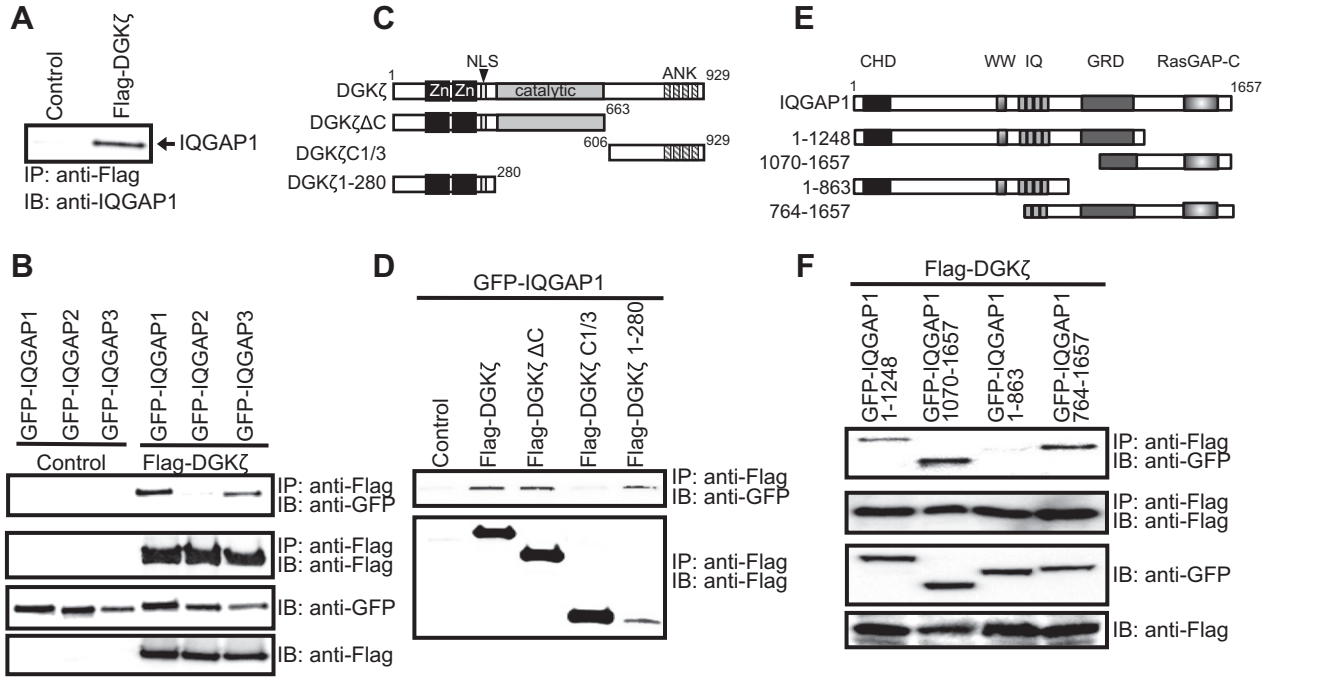

Fig. 1. DGKζ interacts with IQGAP. (A) The plasmid pcDNA3 (control) or Flag-DGKζ was transfected into HEK293 cells and immunoprecipitated. Bound proteins were eluted with 200 μg/ml Flag peptide and analyzed by immunoblotting using anti-IQGAP1. (B) GFP-IQGAP constructs and either pcDNA3 or Flag-DGKζ were co-transfected into HEK293 cells as indicated above. The lysates were immunoprecipitated and analyzed by immunoblotting. (C) Schematic diagram of the DGKζ constructs used in the experiment. NLS, nuclear localization signal; ANK, ankyrin-like repeats; Zn, zinc-finger domain. (D) GFP-IQGAP1 and several Flag-DGKζ truncates were co-transfected into HEK293 cells. Cell lysates were immunoprecipitated and analyzed by immunoblotting. (E) Schematic diagram of the IQGAP1 constructs. CHD, calponin homology domain; IQ, IQ motif/calmodulin binding domain; GRD, RasGAP-related domain; RasGAP-C, RasGAP C-terminal domain. (F) Cell lysates transfected with Flag-DGKζ and GFP-IQGAP1 truncates were mixed with the Flag antibody. The immunoprecipitants were subjected to immunoblot analysis. Three independent experiments were performed with similar results.

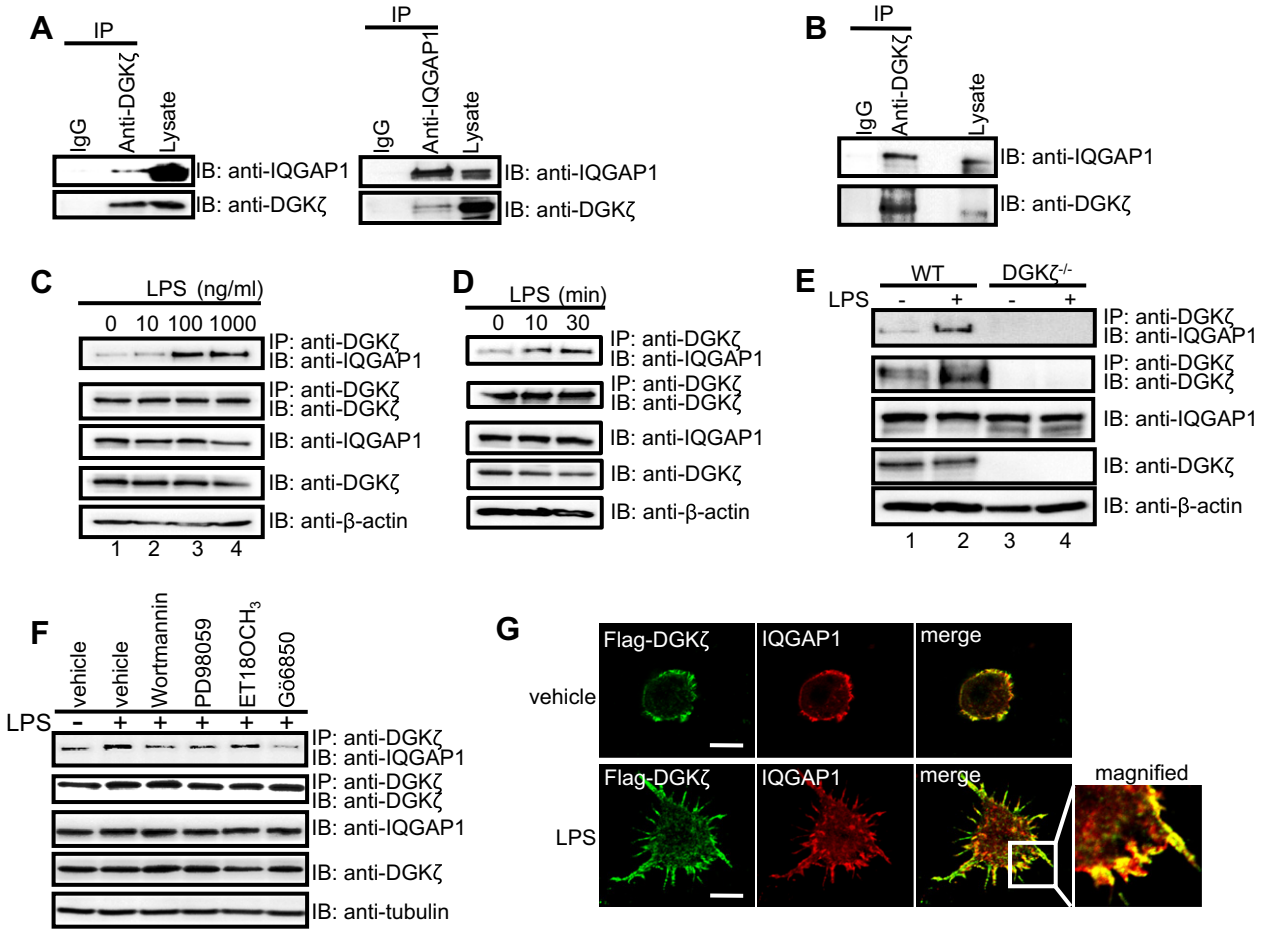

Fig. 2. DGKζ associates with IQGAP1 in an LPS-dependent manner in macrophages. (A) Raw264 cells were lysed and mixed with anti-DGKζ or anti-IQGAP1 antibodies. Normal IgG was used as a negative control. The immunocomplexes were subjected to immunoblot analysis. (B) Mouse primary peritoneal macrophages were prepared as described in Section 2. Peritoneal macrophages were lysed and immunoprecipitated by anti-DGKζ antibody and analyzed by immunoblotting. (C) Raw264 cells were treated with 10, 100, or 1000 ng/ml LPS for 10 min. The immunoprecipitation complexes using anti-DGKζ antibody were analyzed by immunoblotting. (D) Raw264 cells were left untreated or treated with 100 ng/ml LPS for 10 or 30 min and subjected to immunoprecipitation and immunoblotting. (E) The peritoneal macrophages derived from wild-type (WT) or DGKζ-deficient (DGKζ$^{-/-}$) mice were treated with 1 μg/ml LPS for 24 h, and cell lysates were immunoprecipitated and analyzed by immunoblotting. (F) Raw264 cells were left untreated or treated with 100 ng/ml LPS for 30 min in the presence of vehicle (DMSO), wortmannin (100 nM), PD98059 (50 μM), ET18OCH$_3$ (30 μM), or Gö6850 (20 nM). The lysates were immunoprecipitated and analyzed by immunoblotting. (G) Transfected Raw264 cells were treated with vehicle or 100 ng/ml LPS for 30 min and fixed. Cells were subjected to immunocytochemistry using anti-Flag and anti-IQGAP1 antibodies and analyzed by confocal microscopy. Bar, 10 μm. Three independent experiments were performed with similar results.

LPS stimulation, Flag-DGKζ was detected at the filopodia-like protrusion together with IQGAP1 (Fig. 2G, bottom), suggesting that LPS does not change significantly the subcellular localization of these proteins but induces their complex formation at the plasma membrane.

3.3. DGKζ plays a crucial role in LPS-induced phagocytosis via Rac1 activation

Reportedly, LPS-induced TLR4 signal transduction activates membrane dynamics followed by actin cytoskeleton reorganization in macrophages during bacterial phagocytosis via the Rho-GTPase family activation, such as Rac1 and Cdc42 [21]. To examine whether DGKζ affects LPS-dependent Rac1 activation in macrophages, we performed pull-down assay using GST-fused PAK1-CRIB that can bind selectively to GTP-bound active Rac1. Immunoblot analysis revealed that DGKζ RNA silencing decreased its protein levels by 80–90% and attenuated the Rac1-GTP bound form upon LPS stimulation, compared with a scrambled siRNA treatment (Fig. 3A, lane 5 versus lane 6). A similar result was obtained in IQGAP1 RNA silencing cells (Fig. 3A, lane 7 versus lane 8). Taken together, these results suggest that both DGKζ and IQGAP1 are required for LPS-dependent Rac1 activation in macrophages.

A previous report showed that IQGAP1 localizes to the phagocytic cup, and that IQGAP1 knockdown inhibits the initial step of phagocytosis in Raw264 cells [25]. Immunofluorescence analysis showed that DGKζ and IQGAP1 colocalized clearly at the phagocytic cup in LPS-stimulated Raw264 cells (Fig. 3B). Fig. 3C shows that LPS stimulation markedly enhanced the phagocytosis of *E. coli* expressing GFP, as determined quantitatively using confocal microscopy. To confirm the functional role of DGKζ in phagocytosis, we knocked down DGKζ or IQGAP1 using specific siRNAs. Knocking down of IQGAP1 clearly inhibited phagocytosis upon LPS treatment as in the previous study [25]. Similarly, when DGKζ was knocked down, LPS-dependent phagocytosis, including catching and internalization, was also decreased (Fig. 3D). Independent verification of the results described above was obtained through quantitative analysis using primary peritoneal macrophages derived from DGKζ$^{-/-}$ mice. Fig. 3E shows representative images of bacterial phagocytosis of primary macrophages. The left panel shows a macrophage that internalized only one bacterium. The right panel presents a macrophage that phagocytized more than

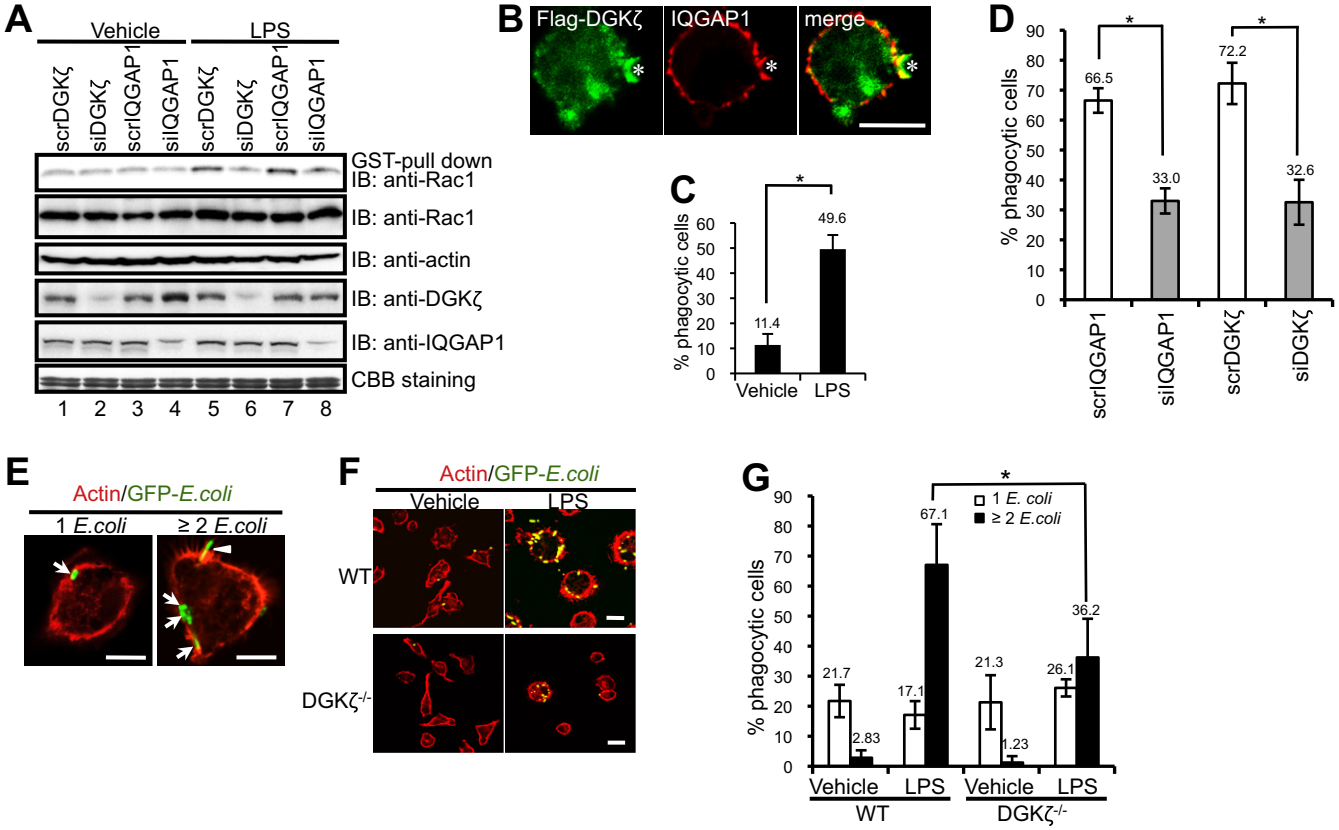

Fig. 3. DGKζ regulates LPS-induced phagocytosis via Rac1 activation. (A) The siRNA for DGKζ or IQGAP1 was transfected into Raw264 cells. After 36 h, transfected cells were treated with 1 μg/ml LPS for 24 h and analyzed by GST-PAK1-CRIB pull-down assay. (B) After treatment with LPS (100 ng/ml) for 12 h, Raw264 cells transfected with Flag-DGKζ were incubated with latex beads for 45 min. After fixation, cells were subjected to immunocytochemistry using anti-Flag and anti-IQGAP1 antibodies. A phagocytosed bead was indicated by asterisk. (C) Raw264 cells were treated with 1 μg/ml LPS for 24 h and mixed with GFP-*E. coli* at an MOI of 40–60 for 45 min at 37 °C. (D) Raw264 cells were transfected with siRNAs for DGKζ or IQGAP1 and treated with LPS. The graph shows the percentage of cells that internalized at least one GFP-*E. coli* (C and D). (E) Representative images of bacterial phagocytosis of murine peritoneal macrophages that were treated with LPS and mixed with GFP-*E. coli*. Arrows indicate internalized *E. coli*. Membrane-attached *E. coli* is indicated by arrowhead. (F) WT or DGKζ$^{-/-}$ peritoneal macrophages were treated with LPS and mixed with GFP-*E. coli*. After fixation, phalloidin-stained macrophages were analyzed by confocal microscopy. Bar, 10 μm. (G) Quantitative analysis of F. Cells that phagocytized one (open bar) or more than two (solid bar) *E. coli* were counted ($n > 100$). The data shown are means ± SD of three independent experiments. $^{*}p < 0.05$ (paired Student's *t*-test).

two bacteria. Under normal conditions without LPS treatment, phagocytosis of DGKζ$^{-/-}$ peritoneal macrophages was similar to that of wild-type (Fig. 3F and G). After LPS treatment, however, the number of macrophages that phagocytized more than two bacteria was apparently decreased in DGKζ$^{-/-}$ primary macrophages (Fig. 3F and G; 67.1 ± 13.5% in WT versus 36.2 ± 12.9% in DGKζ$^{-/-}$, $p < 0.05$). These data show that DGKζ deficiency attenuates macrophage phagocytosis upon LPS stimulation.

4. Discussion

In this study, we identified a small GTPase effector protein, IQGAP1, as a novel DGKζ-associated complex protein in macrophages. We show that either DGKζ or IQGAP1 siRNA-knockdown attenuates LPS-induced Rac1 activation. In addition, we also reveal that phagocytosis decreases significantly in Raw264 cells treated with siDGKζ and in primary macrophages derived from DGKζ$^{-/-}$ mice (Fig. 4).

In the process of phagocytosis, phagocytic cup and phagosome formation is regulated by actin reorganization. Actin polymerization at developing phagosomes is probably controlled by PtdIns(4,5)P_2, actin-related proteins and Rho family small GTPases, especially, Rac1 and Cdc42. Inhibition of these small GTPases in macrophages results in a complete blockade of phagocytosis because of defective actin assembly at nascent phagosomes [26,27]. IQGAP1 is originally identified as a target for the small GTPases,

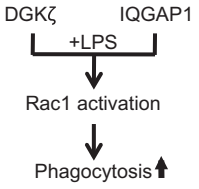

Fig. 4. Potential mechanisms of DGKζ function in LPS-induced phagocytosis. DGKζ associates with IQGAP1 in an LPS-dependent manner. Both DGKζ and IQGAP1 are required for LPS-dependent Rac1 activation. DGKζ is involved in IQGAP1/Rac1-dependent bacterial phagocytosis upon LPS stimulation in macrophages.

Cdc42 and Rac1 [24]. IQGAP binds to and stabilizes the GTP-bound form of Rac1/Cdc42 by inhibiting their intrinsic GTPase activity and by interfering with their interaction with RhoGAPs [28]. Recently, IQGAP1 has been reported to interact with Dia1, a regulator of actin polymerization [25]. Its interaction correlates with phagocytic cup formation in Raw264 cells. In this regard, we found that DGKζ interacts with GRD of IQGAP1. The GRD of IQGAP protein is shown to bind to Rac1/Cdc42 and stabilize its activity [23,28]. It is therefore plausible that DGKζ is involved in IQGAP1-mediated Rac1 activation and subsequent phagocytosis after LPS stimulation. However, it remains unclear how the interaction of DGKζ with IQGAP1 is regulated upon LPS stimulation, although our chemical inhibitor experiment suggests that LPS-induced DGKζ–IQGAP1 association is regulated by several kinase cascades, such as PI3K,

MEK, and PKC. It is possible that DGKζ and/or IQGAP1 may be modified by these kinases upon LPS stimulation.

Results of a recent study suggest that retinoic acid-inducible gene I (RIG-I) plays an important role in TLR-stimulated phagocytosis of bacteria and LPS-stimulated morphological changes, which is mediated through the binding of actin and subsequent activation of Rac1/Cdc42 signaling [21]. Whether DGKζ signaling is cross-linked with RIG-I pathway remains undetermined. However, the phenotype of RIG-I deficiency in phagocytosis after LPS resembles that of DGKζ$^{-/-}$ macrophages. Further studies are needed to elucidate this point together with the functional significance of the interaction between DGKζ and IQGAP3.

In summary (Fig. 4), we identified IQGAP1 as a novel DGKζ-associated complex protein in macrophages. DGKζ interacts with IQGAP1 in an LPS-dependent manner and is involved in IQGAP1-mediated Rac1 activation. DGKζ knockdown or gene ablation impairs LPS-activated bacterial phagocytosis. Our results suggest that DGKζ participates in IQGAP1/Rac1-mediated phagocytosis in macrophages.

Acknowledgments

This work was supported by Grants-in-Aid from The Ministry of Education, Culture, Sports, Science and Technology (MEXT) of Japan (M.O., Y.H., K.G.).

References

[1] D.M. Mosser, J.P. Edwards, Exploring the full spectrum of macrophage activation, Nat. Rev. Immunol. 8 (2008) 958–969.
[2] B.E. Steinberg, S. Grinstein, Pathogen destruction versus intracellular survival: the role of lipids as phagosomal fate determinants, J. Clin. Invest. 118 (2008) 2002–2011.
[3] R.J. Botelho, M. Teruel, R. Dierckman, R. Anderson, A. Wells, J.D. York, T. Meyer, S. Grinstein, Localized biphasic changes in phosphatidylinositol-4,5-bisphosphate at sites of phagocytosis, J. Cell Biol. 151 (2000) 1353–1368.
[4] I. Merida, A. Avila-Flores, E. Merino, Diacylglycerol kinases: at the hub of cell signalling, Biochem. J. 409 (2008) 1–18.
[5] E.C. Larsen, J.A. DiGennaro, N. Saito, S. Mehta, D.J. Loegering, J.E. Mazurkiewicz, M.R. Lennartz, Differential requirement for classic and novel PKC isoforms in respiratory burst and phagocytosis in RAW 264.7 cells, J. Immunol. 165 (2000) 2809–2817.
[6] R.J. Botelho, R.E. Harrison, J.C. Stone, J.F. Hancock, M.R. Philips, J. Jongstra-Bilen, D. Mason, J. Plumb, M.R. Gold, S. Grinstein, Localized diacylglycerol-dependent stimulation of Ras and Rap1 during phagocytosis, J. Biol. Chem. 284 (2009) 28522–28532.
[7] Y.N. Lee, H.Y. Lee, H.K. Kang, J.Y. Kwak, Y.S. Bae, Phosphatidic acid positively regulates LPS-induced differentiation of RAW264.7 murine macrophage cell line into dendritic-like cells, Biochem. Biophys. Res. Commun. 318 (2004) 839–845.
[8] K.L. Cheeseman, T. Ueyama, T.M. Michaud, K. Kashiwagi, D. Wang, L.A. Flax, Y. Shirai, D.J. Loegering, N. Saito, M.R. Lennartz, Targeting of protein kinase C-ε during Fcγ receptor-dependent phagocytosis requires the εC1B domain and phospholipase C-γ1, Mol. Biol. Cell 17 (2006) 799–813.
[9] H. Kanoh, K. Yamada, F. Sakane, Diacylglycerol kinase: a key modulator of signal transduction?, Trends Biochem Sci. 15 (1990) 47–50.
[10] M.K. Topham, R.M. Epand, Mammalian diacylglycerol kinases: molecular interactions and biological functions of selected isoforms, Biochim. Biophys. Acta 1790 (2009) 416–424.
[11] K. Goto, Y. Hozumi, T. Nakano, S.S. Saino, H. Kondo, Cell biology and pathophysiology of the diacylglycerol kinase family: morphological aspects in tissues and organs, Int. Rev. Cytol. 264 (2007) 25–63.
[12] C.H. Liu, F.S. Machado, R. Guo, K.E. Nichols, A.W. Burks, J.C. Aliberti, X.P. Zhong, Diacylglycerol kinase ζ regulates microbial recognition and host resistance to *Toxoplasma gondii*, J. Exp. Med. 204 (2007) 781–792.
[13] M. Okada, Y. Hozumi, T. Ichimura, T. Tanaka, H. Hasegawa, M. Yamamoto, N. Takahashi, K. Iseki, H. Yagisawa, T. Shinkawa, T. Isobe, K. Goto, Interaction of nucleosome assembly proteins abolishes nuclear localization of DGKζ by attenuating its association with importins, Exp. Cell Res. 317 (2011) 2853–2863.
[14] Y. Hozumi, T. Ito, T. Nakano, T. Nakagawa, M. Aoyagi, H. Kondo, K. Goto, Nuclear localization of diacylglycerol kinase ζ in neurons, Eur. J. Neurosci. 18 (2003) 1448–1457.
[15] S. Wang, T. Watanabe, J. Noritake, M. Fukata, T. Yoshimura, N. Itoh, T. Harada, M. Nakagawa, Y. Matsuura, N. Arimura, K. Kaibuchi, IQGAP3, a novel effector of Rac1 and Cdc42, regulates neurite outgrowth, J. Cell Sci. 120 (2007) 567–577.
[16] K. Goto, H. Kondo, A 104-kDa diacylglycerol kinase containing ankyrin-like repeats localizes in the cell nucleus, Proc. Natl. Acad. Sci. USA 93 (1996) 11196–11201.
[17] D.S. Regier, J. Higbee, K.M. Lund, F. Sakane, S.M. Prescott, M.K. Topham, Diacylglycerol kinase ι regulates Ras guanyl-releasing protein 3 and inhibits Rap1 signaling, Proc. Natl. Acad. Sci. USA 102 (2005) 7595–7600.
[18] M. Okada, S.W. Jang, K. Ye, Ebp1 association with nucleophosmin/B23 is essential for regulating cell proliferation and suppressing apoptosis, J. Biol. Chem. 282 (2007) 36744–36754.
[19] Y. Araki, D. Nonaka, A. Tajima, M. Maruyama, T. Nitto, H. Ishikawa, H. Yoshitake, E. Yoshida, N. Kuronaka, K. Asada, M. Yanagida, M. Nojima, K. Yoshida, K. Takamori, T. Hashiguchi, I. Maruyama, L.J. Lee, K. Tanaka, Quantitative peptidomic analysis by a newly developed one-step direct transfer technology without depletion of major blood proteins: its potential utility for monitoring of pathophysiological status in pregnancy-induced hypertension, Proteomics 11 (2011) 2727–2737.
[20] M. Okada, S.W. Jang, K. Ye, Akt phosphorylation and nuclear phosphoinositide association mediate mRNA export and cell proliferation activities by ALY, Proc. Natl. Acad. Sci. USA 105 (2008) 8649–8654.
[21] L. Kong, L. Sun, H. Zhang, Q. Liu, Y. Liu, L. Qin, G. Shi, J.H. Hu, A. Xu, Y.P. Sun, D. Li, Y.F. Shi, J.W. Zang, J. Zhu, Z. Chen, Z.G. Wang, B.X. Ge, An essential role for RIG-I in toll-like receptor-stimulated phagocytosis, Cell Host Microbe 6 (2009) 150–161.
[22] H. Abramovici, A.B. Hogan, C. Obagi, M.K. Topham, S.H. Gee, A. Hogan, L. Shepherd, J. Chabot, S. Quenneville, S.M. Prescott, M.K. Topham, S.H. Gee, Diacylglycerol kinase-ζ localization in skeletal muscle is regulated by phosphorylation and interaction with syntrophins, Mol. Biol. Cell 14 (2003) 4499–4511.
[23] S. Kuroda, M. Fukata, K. Kobayashi, M. Nakafuku, N. Nomura, A. Iwamatsu, K. Kaibuchi, Identification of IQGAP as a putative target for the small GTPases, Cdc42 and Rac1, J. Biol. Chem. 271 (1996) 23363–23367.
[24] L. Weissbach, J. Settleman, M.F. Kalady, A.J. Snijders, A.E. Murthy, Y.X. Yan, A. Bernards, Identification of a human rasGAP-related protein containing calmodulin-binding motifs, J. Biol. Chem. 269 (1994) 20517–20521.
[25] D.T. Brandt, S. Marion, G. Griffiths, T. Watanabe, K. Kaibuchi, R. Grosse, Dia1 and IQGAP1 interact in cell migration and phagocytic cup formation, J. Cell Biol. 178 (2007) 193–200.
[26] E. Caron, A. Hall, Identification of two distinct mechanisms of phagocytosis controlled by different Rho GTPases, Science 282 (1998) 1717–1721.
[27] D. Cox, P. Chang, Q. Zhang, P.G. Reddy, G.M. Bokoch, S. Greenberg, Requirements for both Rac1 and Cdc42 in membrane ruffling and phagocytosis in leukocytes, J. Exp. Med. 186 (1997) 1487–1494.
[28] M.J. Hart, M.G. Callow, B. Souza, P. Polakis, IQGAP1, a calmodulin-binding protein with a rasGAP-related domain, is a potential effector for cdc42Hs, EMBO J. 15 (1996) 2997–3005.

Biochemical and Biophysical Research Communications 420 (2012) 485

Contents lists available at SciVerse ScienceDirect

Biochemical and Biophysical Research Communications

journal homepage: www.elsevier.com/locate/ybbrc

Corrigendum

Corrigendum to "Targeting A20 enhances TRAIL-induced apoptosis in hepatocellular carcinoma cells" [Biochem. Biophys. Res. Commun. 418 (2012) 433–438]

Bingfei Dong [a,1], Guoyue Lv [a,1], Quan Wang [b], Feng Wei [a], Anita C. Bellail [c], Chunhai Hao [c], Guangyi Wang [a,*]

[a] Department of Hepatopancreatobiliary Surgery, First Hospital of Jilin University, Jilin University, 71 Xinmin Street, Changchun 130021, China
[b] Department of Gastrointestinal Surgery, First Hospital of Jilin University, Jilin University, 71 Xinmin Street, Changchun 130021, China
[c] Department of Pathology & Laboratory Medicine, Emory University School of Medicine, 1365-C Clifton Road NE, Atlanta, GA 30322, USA

The authors regret the omission of three authors from the author line in the published article. The author line and affiliations are correct as they appear above.

DOI of original article: http://dx.doi.org/10.1016/j.bbrc.2012.01.056
* Corresponding author. Fax: +86 431 8878 3331.
E-mail addresses: chao@emory.edu (C. Hao), pixie2011@hotmail.com (G. Wang).
[1] These authors contributed equally to this work.

http://dx.doi.org/10.1016/j.bbrc.2012.03.044

Biochemical and Biophysical Research Communications

Correspondence regarding production may be sent to:

Biochemical and Biophysical Research Communications, Elsevier Inc.

525 B Street, Suite 1800, San Diego, California 92101-4495, USA
Telephone +1 (619) 699-6857, Fax +1 (619) 699-6859, E-mail bbrc@elsevier.com

0006-291X(20120406)420:2;1-W

Cover photo. The cover photo graphic is taken from figure 1A of the paper 'Susceptibility of Antiviral Drugs Against 2009 Influenza A (H1N1) Virus' published in the journal (BBRC Volume 385, pages 390–394). It is reproduced by kind permission of the authors – Supot Hannongbua, et al.